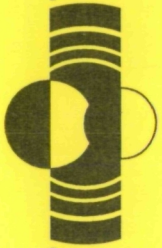


# Lunar and Planetary Science XXIV



*Abstracts of papers submitted to the  
Twenty-fourth Lunar and Planetary  
Science Conference*

**PART 1 A - F**

N94-12015  
--THRU--  
N94-12268  
Unclass

63/91 0163220

(NASA-CR-193095) TWENTY-FOURTH  
LUNAR AND PLANETARY SCIENCE  
CONFERENCE. PART 1: A-F Abstracts  
Only (Lunar and Planetary Inst.)  
597 p

467/47  
6/14  
LPI/USRA



National Aeronautics and  
Space Administration

Lyndon B. Johnson Space Center  
Houston, Texas

**LPI / USRA**

LUNAR AND PLANETARY INSTITUTE  
UNIVERSITIES SPACE RESEARCH ASSOCIATION

**LUNAR AND PLANETARY SCIENCE XXIV**

**Abstracts of Papers Submitted to the  
TWENTY-FOURTH LUNAR AND PLANETARY SCIENCE CONFERENCE**

**Sponsored by**

**National Aeronautics and Space Administration  
Lunar and Planetary Institute  
NASA Johnson Space Center**

**March 15-19, 1993**

**Part 1**

**Compiled by  
Lunar and Planetary Institute  
3600 Bay Area Boulevard  
Houston TX 77058-1113**



The Lunar and Planetary Institute is operated by the Universities Space Research Association under Contract No. NASW-4574 with the National Aeronautics and Space Administration.

Material in this volume may be copied without restraint for library, abstract service, educational, or personal research purposes; however, republication of any paper or portion thereof requires the written permission of the authors as well as appropriate acknowledgement of this publication.

---

**Page intentionally left blank**

PAGE 3, 4

**Page intentionally left blank**

# CONTENTS

Mössbauer Spectroscopy of the SNC Meteorite Zagami <i>D. P. Agerkvist and L. Vistisen</i> .....	1-1
Production of Electronic Grade Lunar Silicon by Disproportionation of Silicon Difluoride <i>W. N. Agosto</i> .....	3-2
Rates of Fluvio-Thermal Erosion on Mars <i>J. Aguirre-Puente, F. M. Costard, and R. Posado-Cano</i> .....	5-3
Giant Impact-induced Atmospheric Blow-Off <i>T. J. Ahrens</i> .....	7-4
Dispersion of the Ratios of Cosmogenic Isotopes of Noble Gases in Chondrites of Different Cosmic-Ray Exposure Ages <i>V. A. Alexeev</i> .....	9-5
Peculiarities of Distributions of the Cosmic-Ray Exposure Ages of H Chondrite Falls and Finds <i>V. A. Alexeev</i> .....	11-6
Search for Effects of a Supernova Explosion 30-40 Thousand Years Ago in Chondrites <i>V. A. Alexeev and G. K. Ustinova</i> .....	13-7
Morphology of Large Impact Craters and Basins on Venus: Implications for Ring Formation <i>J. S. Alexopoulos and W. B. McKinnon</i> .....	15-8
Effects of Microscopic Iron Metal on the Reflectance Spectra of Glass and Minerals <i>C. C. Allen, R. V. Morris, H. V. Lauer Jr., and D. S. McKay</i> .....	17-9
Encouraging Interest in Space Exploration and Planetary Science Among Navajo Primary Students <i>J. H. Allton and C. S. Allton</i> .....	19-OMED
Calorimetric Thermometry of Meteoritic Troilite: A Feasibility Study <i>J. H. Allton and J. L. Gooding</i> .....	21-10
Cold Press Sintering of Simulated Lunar Basalt <i>D. A. Altemir</i> .....	23-11
General Overview of an Integrated Lunar Oxygen Production/Brickmaking System <i>D. A. Altemir</i> .....	25-12
Thermodynamics of Lunar Ilmenite Reduction <i>B. H. Altenberg, H. A. Franklin, and C. H. Jones</i> .....	27-13
Interstellar Graphite in Murchison: Continued Search for Isotopically Distinct Components <i>S. Amari, E. Zinner, and R. S. Lewis</i> .....	29-14
Fourier Domain Target Transformation Analysis in the Thermal Infrared <i>D. L. Anderson</i> .....	31-15

PRECEDING PAGE BLANK NOT FILMED

47 INTENTIONALLY BLANK



Lineament Analysis and Tectonic Interpretation for the Tharsis Region, Mars <i>R. Anderson</i> .....	33-76
Descriptions and Preliminary Interpretations of Cores Recovered from the Manson Impact Structure (Iowa) <i>R. R. Anderson, B. J. Witzke, J. B. Hartung, E. M. Shoemaker, and D. J. Roddy</i> .....	35-77
A Space Studies Curriculum for Small Colleges and Universities <i>J. O. Annexstad and R. C. Melchior</i> .....	37-omit
Measurements of Cosmogenic Nuclides in Lunar Rock 64455 <i>J. R. Arnold, C. P. Kohl, K. Nishiizumi, M. W. Caffee, R. C. Finkel, and J. R. Southon</i> .....	39-78
Marslink <i>R. E. Arvidson, L. D. Friedman, and C. J. Stadum</i> .....	41-79
Carbon in Weathered Ordinary Chondrites from Roosevelt County <i>R. D. Ash and C. T. Pillinger</i> .....	43-20
Ejecting Basaltic Achondrites from Vesta: Hydrodynamical Impact Models <i>E. Asphaug, H. J. Melosh, and E. Ryan</i> .....	45-21
Venus Small Volcano Classification and Description <i>J. C. Aubele</i> .....	47-22
The Los Alamos Neutron Spectrometer for the Lunar Scout-I Mission <i>G. Auchampaugh, B. Barraclough, R. Byrd, D. Drake, W. Feldman, C. Moss, and R. Reedy</i> .....	49-23
Vaporization by Shock Loading of Albite, Jadeite, and Pyrex Glass: Experimental Study <i>D. D. Badjukov and T. L. Petrova</i> .....	51-24
Shock Transformations in Quartzite <i>D. D. Badjukov, E. A. Koslov, Yu. N. Zhugin, and E. V. Abakshin</i> .....	53-25
Reconstruction of the Dynamics of the 1800-1801 Hualalai Eruption: Implications for Planetary Lava Flows <i>S. Baloga and P. Spudis</i> .....	55-26
Horizontal Stresses Induced by Vertical Processes in Planetary Lithospheres <i>W. B. Banerdt</i> .....	57-27
Encouraging Female Interest in Science and Mathematics <i>N. G. Barlow</i> .....	59-omit
Increased Depth-Diameter Ratios in the Medusae Fossae Formation Deposits of Mars <i>N. G. Barlow</i> .....	61-28

Behavior of Vortices Generated by an Advancing Ejecta Curtain in Theory, in the Laboratory, and on Mars <i>O. S. Barnouin and P. H. Schultz</i> .....	63-29
Mineralogy of Chondritic Interplanetary Dust Particle Impact Residues from LDEF <i>R. A. Barrett, M. E. Zolensky, and R. Bernhard</i> .....	65-30
Estimation of Age of Dali-Ganis Rifting and Associated Volcanic Activity, Venus <i>A. T. Basilevsky</i> .....	67-31
Regional Geology of the Vega Landing Sites: Tentative Results of Photogeologic Mapping <i>A. T. Basilevsky and C. M. Weitz</i> .....	69-32
Regional Geology of the Venera Landing Sites: Tentative Results of Photogeologic Mapping <i>A. T. Basilevsky and C. M. Weitz</i> .....	71-33
Interpretation of Lunar and Planetary Electromagnetic Scattering Using the Full Wave Solutions <i>E. Bahar and M. Haugland</i> .....	73-34
Apollo 16 Core 60013/14 as a Product of Path I and Path II Regolith Evolution Processes <i>A. Basu, K. McBride, S. J. Wentworth, and D. S. McKay</i> .....	75-35
Nitrogen and Noble Gases in a Glass Sample from LEW88516 <i>R. H. Becker and R. O. Pepin</i> .....	77-36
The Stability of Hibonite and Other Aluminous Phases in Silicate Melts: Implications for the Origin of Hibonite-bearing Inclusions <i>J. R. Beckett and E. Stolper</i> .....	79-37
A Comparison of Telescopic and Phobos-2 ISM Spectra of Mars in the Short-Wave Near-Infrared (0.76-1.02 $\mu\text{m}$ ) <i>J. F. Bell III and J. F. Mustard</i> .....	81-38
An Observational Search for CO <sub>2</sub> Ice Clouds on Mars <i>J. F. Bell III, W. M. Calvin, J. B. Pollack, and D. Crisp</i> .....	83-39
Changes in Hawaiian Palagonite Fe Mineralogy Associated with Thermal Alteration: Implications for Mars <i>J. F. Bell III, R. V. Morris, and J. B. Adams</i> .....	85-40
Petrography and Preliminary Interpretations of the Crystalline Breccias from the Manson M-1 Core <i>M. S. Bell, M. K. Reagan, R. R. Anderson, and C. T. Foster Jr.</i> .....	87-41
Orbital Simulations of Satellite Escape/Capture and the Origin of Satellites such as Triton <i>L. A. M. Benner and W. B. McKinnon</i> .....	89-42
The Great 8 Ma Event and the Structure of the H-Chondrite Parent Body <i>P. H. Benoit and D. W. G. Sears</i> .....	91-43
Meteorites from Recent Amor-type Orbits <i>P. H. Benoit and D. W. G. Sears</i> .....	93-44

Natural Thermoluminescence Profiles in Lunar Cores and Implications for Meteorites <i>P. H. Benoit and D. W. G. Sears</i> .....	95-45
Metallographic Cooling Rates of L-Group Ordinary Chondrites <i>M. E. Bennett and H. Y. McSween Jr.</i> .....	97-46
Explicit 3D Continuum Fracture Modeling with Smooth Particle Hydrodynamics <i>W. Benz and E. Asphaug</i> .....	99-47
Composition and Modal Frequencies of Hypervelocity Particles <1 mm in Diameter in Low-Earth Orbit <i>R. P. Bernhard, T. H. See, and F. Hörz</i> .....	101-48
Thermal Studies of Martian Channels and Valleys Using Termoskan Data <i>B. H. Betts and B. C. Murray</i> .....	103-49
Spectral Analysis of the Gravity and Topography of Mars <i>B. G. Bills, H. V. Frey, W. S. Kiefer, R. S. Nerem, and M. T. Zuber</i> .....	105-50
Global Organization of Tectonic Deformation on Venus <i>F. Bilotti, C. Connors and J. Suppe</i> .....	107-51
Venus' Center of Mass-Center of Figure Displacement and Implications <i>D. L. Bindschadler and G. Schubert</i> .....	109-52
The Asteroid-Meteorite Connection: Forging a New Link to Vesta as the Parent Body of Basaltic Achondrite (HED) Meteorites <i>R. P. Binzel</i> .....	111-53
Alkali-Granitoids as Fragments Within the Ordinary Chondrite Adzhi-Bogdo: Evidence for Highly Fractionated, Alkali-Granitic Liquids on Asteroids <i>A. Bischoff</i> .....	113-54
Reflectance Spectra of Sulfate- and Carbonate-bearing Fe <sup>3+</sup> -doped Montmorillonites as Mars Soil Analogs <i>J. L. Bishop, C. M. Pieters, and R. G. Burns</i> .....	115-55
The Effects of Atmospheric Pressure on Infrared Reflectance Spectra of Martian Analogs <i>J. L. Bishop, C. M. Pieters, S. F. Pratt, and W. Patterson</i> .....	117-56
Stable Isotope Analyses of the Peralkaline Volcanics Gregory Rift Valley, Kenya <i>S. Black, R. Macdonald, A. E. Fallick, and M. Kelly</i> .....	119-57
<sup>230</sup> Th- <sup>238</sup> U Series Disequilibrium of the Olkaria Basalts, Gregory Rift Valley, Kenya <i>S. Black, R. Macdonald, and M. Kelly</i> .....	121-58
<sup>230</sup> Th- <sup>238</sup> U Series Disequilibrium of the Olkaria Basalts Gregory Rift Valley, Kenya: Petrogenesis <i>S. Black, R. Macdonald, and M. Kelly</i> .....	123-59
<sup>230</sup> Th- <sup>238</sup> U Series Disequilibrium of the Olkaria Rhyolites Gregory Rift Valley, Kenya: Petrogenesis <i>S. Black, R. Macdonald, and M. Kelly</i> .....	125-60



$^{230}\text{Th}$ - $^{238}\text{U}$ Series Disequilibrium of the Olkaria Rhyolites, Gregory Rift Valley, Kenya: Residence Times <i>S. Black, R. Macdonald, and M. Kelly</i> .....	127-61
Using High Spectral Resolution Spectrophotometry to Study Broad Mineral Absorption Features on Mars <i>D. L. Blaney and D. Crisp</i> .....	129-62
Using Solar Flare Track Densities to Determine the Origin of Interplanetary Dust Particles <i>G. E. Blanford</i> .....	131-63
Spectral and Multispectral Imaging Studies of Lunar Mantled Mare Deposits <i>D. T. Blewett, B. R. Hawke, P. G. Lucey, J. F. Bell III, R. Jaumann, H. Hiesinger, G. Neukum, and P. D. Spudis</i> .....	133-64
Strontium and Oxygen Isotope Study of M-1, M-3 and M-4 Drill Core Samples from the Manson Impact Structure, Iowa: Comparison with Haitian K-T Impact Glasses <i>J. D. Blum, C. P. Chamberlain, M. P. Hingston, and C. Koeberl</i> .....	135-65
Preliminary Results of Mn Partitioning Experiments on Murchison Analogues <i>J. S. Boesenberg and J. S. Delaney</i> .....	137-66
Noble Gases in LEW88516 Shergottite: Evidence for Exposure Age Pairing with ALH77005 <i>D. D. Bogard and D. H. Garrison</i> .....	139-67
$^{39}\text{Ar}$ - $^{40}\text{Ar}$ Ages of Acapulcoites and Lodranites: Evidence for Early Parent Body Heating <i>D. D. Bogard, D. H. Garrison, T. J. McCoy, and K. Keil</i> .....	141-68
Arroyo El Mimbral, Mexico, K/T Unit: Origin as Debris Flow/Turbidite, Not a Tsunami Deposit <i>B. F. Bohor and W. J. Betterton</i> .....	143-69
K/T Spherules from Haiti and Wyoming: Origin, Diagenesis, and Similarity to Some Microtektites <i>B. F. Bohor, B. P. Glass, and W. J. Betterton</i> .....	145-70
The Solubility of Gold in Silicate Melts: First Results <i>A. Borisov, H. Palme, and B. Spettel</i> .....	147-71
$^{29}\text{Si}$ NMR Spectroscopy of Naturally-Shocked Quartz from Meteor Crater, Arizona: Correlation to Keiffer's Classification Scheme <i>M. B. Boslough, R. T. Cygan, and R. J. Kirkpatrick</i> .....	149-72
Midplane Temperatures in the Solar Nebula <i>A. P. Boss</i> .....	151-73
Chondrule Formation by Clumpy Accretion onto the Solar Nebula <i>A. P. Boss and J. A. Graham</i> .....	153-74
Initiating Solar System Formation Through Stellar Shock Waves <i>A. P. Boss and E. A. Myhill</i> .....	155-75

Impact Mineralogy and Chemistry of the Cretaceous-Tertiary Boundary at DSDP Site 576 <i>J. A. Bostwick and F. T. Kyte</i> .....	157-76
Collision Lifetimes and Impact Statistics of Near-Earth Asteroids <i>W. F. Bottke Jr., M. C. Nolan, and R. Greenberg</i> .....	159-77
Age of Popigai Impact Event Using the $^{40}\text{Ar}$ - $^{39}\text{Ar}$ Method <i>R. J. Bottomley, D. York, and R. A. F. Grieve</i> .....	161-78
Minor and Trace Element Composition and Age of Yukon Probable-Microtektites <i>S. Q. Boudry-Sanders and R. L. Hervig</i> .....	163-79
A Structural Origin for the Cantaloupe Terrain of Triton <i>J. M. Boyce</i> .....	165-80
Trace-Element Abundances in Several New Ureilites <i>W. V. Boynton and D. H. Hill</i> .....	167-81
Compositional and Textural Information from the Dual Inversion of Visible, Near and Thermal Infrared Remotely Sensed Data <i>R. A. Brackett and R. E. Arvidson</i> .....	169-82
Unequilibrated, Equilibrated, and Reduced Aggregates in Anhydrous Interplanetary Dust Particles <i>J. P. Bradley</i> .....	171-83
Carbon Analyses of IDPs Sectioned in Sulfur and Supported on Beryllium Films <i>J. P. Bradley, L. Keller, K. L. Thomas, T. B. Vander Wood, and D. E. Brownlee</i> .....	173-84
Modern Shelf Ice, Equatorial Aeolis Quadrangle, Mars <i>G. R. Brakenridge</i> .....	175-85
Mineralogy Versus Bulk Composition of the Carbonaceous Chondrite Clast Kaidun II <i>F. Brandstätter, G. Kurat, A. V. Ivanov, H. Palme, and B. Spettel</i> .....	177-86
A Structural and Petrographic Investigation of the Pretoria Saltpan Impact Structure <i>D. Brandt and W. U. Reimold</i> .....	179-87
Geophysical Signature of the Pretoria Saltpan Impact Structure and a Possible Satellite Crater <i>D. Brandt, R. J. Durrheim, and W. U. Reimold</i> .....	181-88
Carbonaceous Chondrite Clasts in the Kapoeta Howardite <i>A. J. Brearley</i> .....	183-89
Chondrite Thermal Histories from Low-Ca Pyroxene Microstructures: Autometamorphism vs. Prograde Metamorphism Revisited <i>A. J. Brearley and R. H. Jones</i> .....	185-90
SXRF Determination of Trace Elements in Chondrule Rims in the Unequilibrated CO3 Chondrite, ALH A77307 <i>A. J. Brearley, S. Bajt, and S. R. Sutton</i> .....	187-91

<b>Martian Particle Size Based on Thermal Inertia Corrected for Elevation-Dependent Atmospheric Properties</b>	
<i>N. T. Bridges</i> .....	189 -92
<b>Multiple Nitrogen Components in Lunar Soil Sample 12023</b>	
<i>D. R. Brilliant, I. A. Franchi, and C. T. Pillinger</i> .....	191 -93
<b>A Reexamination of Amino Acids in Lunar Soil</b>	
<i>K. L. F. Brinton, J. L. Bada, and J. R. Arnold</i> .....	193 -94
<b>The Spectral Effects of Subsolidus Reduction of Olivine and Pyroxene</b>	
<i>D. T. Britt</i> .....	195 -95
<b>1.2- to 3.5-<math>\mu</math>m Observations of Asteroid 4179 Toutatis</b>	
<i>D. T. Britt, E. S. Howell, J. F. Bell, and L. A. Lebofsky</i> .....	197 -96
<b>Flexure and the Role of Inplane Force Around Coronae on Venus</b>	
<i>C. D. Brown and R. E. Grimm</i> .....	199 -97
<b>Viscous Relaxation of the Moho Under Large Lunar Basins</b>	
<i>C. D. Brown and R. E. Grimm</i> .....	201 -98
<b>Determining the Relative Extent of Alteration in CM Chondrites</b>	
<i>L. B. Browning, H. Y. McSween Jr., and M. Zolensky</i> .....	203 -99
<b>Identification of Cometary and Asteroidal Particles in Stratospheric IDP Collections</b>	
<i>D. E. Brownlee, D. J. Joswiak, S. G. Love, A. O. Nier, D. J. Schlutter, and J. P. Bradley</i> .....	205 -100
<b>Quantifying the Effect of Rheology on Plan-View Shapes of Lava Flows</b>	
<i>B. C. Bruno, G. J. Taylor, and R. M. C. Lopes-Gautier</i> .....	207 -101
<b>EET87513 Clast N: A CM2 Fragment in an HED Polymict Breccia</b>	
<i>P. C. Buchanan, M. E. Zolensky, A. M. Reid, and R. A. Barrett</i> .....	209 -102
<b>Can Weak Crust Explain the Correlation of Geoid and Topography on Venus?</b>	
<i>W. R. Buck</i> .....	211 -103
<b>Venus Resurfacing Rates: Constraints Provided by 3-D Monte Carlo Simulations</b>	
<i>M. A. Bullock, D. H. Grinspoon, and J. W. Head</i> .....	213 -104
<b>Scalloped Margin Domes: What are the Processes Responsible and How do they Operate?</b>	
<i>M. H. Bulmer, J. E. Guest, G. Michaels, and S. Saunders</i> .....	215 -105
<b>Yana Ring Structure, North-Eastern Siberia: A Possible Counterpart of Coronae on Venus</b>	
<i>G. A. Burba</i> .....	217 -106
<b>Russia's Contribution to Regional Geologic Mapping of Venus: 1992 Progress Report</b>	
<i>G. A. Burba, N. N. Bobina, and V. P. Shashkina</i> .....	219 -107



Landscape and Geomorphic Survey of Zhamanshin Area, Northern Kazakhstan: Preliminary Report on 1992 Field Trip Data <i>G. G. Burba Jr. and V. A. Meshcherskaya</i> .....	221-108
How Diverse is the Asteroid Belt? <i>T. H. Burbine and J. F. Bell</i> .....	223-109
Studies of the Release of Radiogenic $^{129}\text{Xe}$ from Bjurböle: Evidence Against Simple Diffusion Models <i>M. K. Burkland, T. D. Swindle, and S. L. Baldwin</i> .....	225-110
A Pattern Recognition System for Locating Small Volcanoes in Magellan SAR Images of Venus <i>M. C. Burl, U. M. Fayyad, P. Smyth, J. C. Aubele, and L. S. Crumpler</i> .....	227-111
Sources of Na for the Io Atmosphere <i>D. S. Burnett, S. B. Ellis, A. Rice, and S. Epstein</i> .....	229-112
Chemical Weathering on Mars: Rate of Oxidation of Iron Dissolved in Brines <i>R. G. Burns</i> .....	231-113
Venus Mountain-Top Mineralogy: Misconceptions About Pyrite as the High Radar-Reflecting Phase <i>R. G. Burns and D. W. Straub</i> .....	233-114
Buoyant Subduction on Venus: Implications for Subduction Around Coronae <i>J. D. Burt and J. W. Head</i> .....	235-115
The Origin of Venusian Channels: Modelling of Thermal Erosion by Lava <i>D. B. J. Bussey, S.-A. Sørensen, and J. E. Guest</i> .....	237-116
Volatiles in Fourteen Interplanetary Dust Particles: A Comparison with CI and CM Chondrites <i>R. Bustin, E. K. Gibson Jr., and S. J. Wentworth</i> .....	239-117
An Ancient Inner Lake in Ma'Adim Vallis <i>N. A. Cabrol, E. A. Grin, A. Dollfus, and G. Dawidowicz</i> .....	241-118
Spatial Variation in the Seasonal South Polar Cap of Mars as Observed by Mariner 7 <i>W. M. Calvin, T. Z. Martin, and G. B. Hansen</i> .....	243-119
The Giant Impact Produced a Precipitated Moon <i>A. G. W. Cameron</i> .....	245-120
Geology and Surface Characteristics of Bell Regio, Venus <i>B. A. Campbell and P. G. Rogers</i> .....	247-121
Lava Flows on Venus: Analysis of Motion and Cooling <i>B. A. Campbell and J. R. Zimbelman</i> .....	249-122
Stratigraphy and Sedimentology of the K/T Boundary Deposit in Haiti <i>L. Carey, H. Sigurdsson, S. D'Hondt, and J. M. Espindola</i> .....	251-123

Galileo/NIMS Near-Infrared Thermal Imagery of the Surface of Venus <i>R. W. Carlson, K. H. Baines, M. Girard, L. W. Kamp, P. Drossart, T. Encrenaz, and F. W. Taylor</i> .....	253 -124
Preliminary Report of Lunar Observations by the Near-Infrared Mapping Spectrometer (NIMS) During the Second Galileo Earth-Moon Encounter <i>R. W. Carlson, H. H. Kieffer, K. H. Baines, K. J. Becker, G. E. Danielson, K. Edwards, F. P. Fanale, J. Forsythe, L. R. Gaddis, J. C. Granahan, J. Hui, T. V. Johnson, R. Lopes-Gautier, L. W. Kamp, D. L. Matson, T. B. McCord, R. Mehlman, A. C. Ocampo, L. A. Soderblom, W. D. Smythe, J. Torson, and P. R. Weissman</i> .....	255 -125
Distribution of Vanadium and Melting of Opaque Assemblages in Efremovka CAIs <i>I. Casanova and L. Grossman</i> .....	257 -126
Metal-rich Meteorites from the Aubrite Parent Body <i>I. Casanova, T. J. McCoy, and K. Keil</i> .....	259 -127
Why Convective Heat Transport in the Solar Nebula was Inefficient <i>P. Cassen</i> .....	261 -128
Fault Geometries and Extension in the Valles Marineris, Mars <i>D. J. Chadwick and B. K. Lucchitta</i> .....	263 -129
A Two-Stage (Turbulent-Drainage) Mechanism for the Emplacement of Impact Crater Outflows on Venus <i>D. J. Chadwick and G. G. Schaber</i> .....	265 -130
Oxygen Isotopes as Tracers of Tektite Source Rocks: An Example From the Ivory Coast Tektites and Lake Bosumtwi Crater <i>C. P. Chamberlain, J. D. Blum, and C. Koeberl</i> .....	267 -131
Cratering on Gaspra <i>C. R. Chapman, G. Neukum, J. Veverka, and M. Belton</i> .....	269 -132
Basal Scarp, Paleoglacier, and Fissure Flows of Elysium Mons, Mars <i>M. G. Chapman</i> .....	271 -133
Shock Induced Reaction in Chicxulub Target Materials ( $\text{CaSO}_4$ and $\text{SiO}_2$ ) and Their Relation to Extinctions <i>G. Chen and T. J. Ahrens</i> .....	273 -134
LEW88516 and SNC Meteorites <i>J. H. Chen and G. J. Wasserburg</i> .....	275 -135
Th and U Abundances in Chondritic Meteorites <i>J. H. Chen, G. J. Wasserburg, and D. A. Papanastassiou</i> .....	277 -136
Lunar Scout Two Spacecraft Gravity Experiment <i>A. F. Cheng</i> .....	279 -137

Mission to the Moon: An ESA Study on Future Exploration <i>A. F. Chicarro</i> .....	281	138
Fractal Dimensions of Rampart Impact Craters on Mars <i>D. Ching, G. J. Taylor, P. Mouginis-Mark, and B. C. Bruno</i> .....	283	139
A Simple Model of Clastic Sediments on Mars <i>P. R. Christensen and M. C. Malin</i> .....	285	140
Thermal-Infrared Emission Spectroscopy of Natural Surfaces: Application to Coated Surfaces <i>P. R. Christensen, S. T. Harrison, P. Barbera, and S. Ruff</i> .....	287	141
Collisions of Small Spacewatch Asteroids with the Earth <i>C. F. Chyba</i> .....	289	142
Differential Scaling: Implications for Central Structures in Large Lunar Craters <i>M. J. Cintala and R. A. F. Grieve</i> .....	291	143
Impact Commminution of Glasses: Implications for Lunar Regolith Evolution <i>M. J. Cintala, S. Smith, and F. Hörz</i> .....	293	144
Microtektite-like Glass Spherules in Late Devonian (367 Ma) Shales <i>P. Claeys and J.-G. Casier</i> .....	295	145
KT Boundary Impact Glasses from the Gulf of Mexico Region <i>P. Claeys, W. Alvarez, J. Smit, A. R. Hildebrand, and A. Montanari</i> .....	297	146
First Results of the Seven-Color Asteroid Survey <i>B. E. Clark, J. F. Bell, F. P. Fanale, and P. G. Lucey</i> .....	299	147
Simulation of Possible Regolith Optical Alteration Effects on Carbonaceous Chondrite Meteorites <i>B. E. Clark, F. P. Fanale, and M. S. Robinson</i> .....	301	148
Spectral Mixing Models of S-type Asteroids <i>B. E. Clark, P. G. Lucey, J. F. Bell, and F. P. Fanale</i> .....	303	149
Remote Sensing X-Ray Fluorescence Spectrometry for Future Lunar Exploration Missions <i>P. E. Clark, L. G. Evans, and J. I. Trombka</i> .....	305	150
Carbon and Nitrogen in Type II Supernova Diamonds <i>D. D. Clayton, M. El Eid, and L. E. Brown</i> .....	307	151
Measurement of Polycyclic Aromatic Hydrocarbon (PAHs) in Interplanetary Dust Particles <i>S. J. Clemett, C. R. Macchling, R. N. Zare, P. D. Swan, and R. M. Walker</i> .....	309	152
Mars: The Initial Emplacement of Ground Ice in Response to the Thermal Evolution of its Early Crust <i>S. M. Clifford</i> .....	311	153



The Role of the Geothermal Gradient in the Emplacement and Replenishment of Ground Ice on Mars <i>S. M. Clifford</i> .....	313 -154
The Thermodynamic Case for a Water-rich Mars <i>S. M. Clifford</i> .....	315 -155
Olivine-rich Asteroids, Pallastic Olivine and Olivine-Metal Mixtures: Comparisons of Reflectance Spectra <i>E. A. Cloutis</i> .....	317 -156
Remanent Magnetism of HED Meteorites—Implications for Their Evolution and Ancient Magnetic Fields <i>D. W. Collinson and S. J. Morden</i> .....	319 -157
Graphite "Solubility" and CO Vesiculation in Basalt-like Melts at One-atm <i>R. O. Colson</i> .....	321 -158
Crystal-Chemistry and Partitioning of REE in Whitlockite <i>R. O. Colson and B. L. Jolliff</i> .....	323 -159
Power-Law Confusion: You Say Incremental, I Say Differential <i>J. E. Colwell</i> .....	325 -160
The Experimental Production of Matrix Lumps Within Chondrules: Evidence of Post-Formational Processes <i>H. C. Connolly Jr. and R. H. Hewins</i> .....	327 -161
Flash Melting of Chondrule Precursors in Excess of 1600C. Series 1: Type II (B1) Chondrule Composition Experiments <i>H. C. Connolly Jr., R. H. Hewins, and G. E. Lofgren</i> .....	329 -162
Modelling Hypervelocity Impacts into Aluminum Structures Based on LDEF Data <i>C. R. Coombs, D. R. Atkinson, A. J. Watts, J. R. Wagner, M. K. Allbrooks, and C. J. Hennessy</i> .....	331 -163
Using Lunar Sounder Imagery to Distinguish Surface from Subsurface Reflectors in Lunar Highlands Areas <i>B. L. Cooper and J. L. Carter</i> .....	333 -164
Geologic History of Central Chryse Planitia and the Viking 1 Landing Site, Mars <i>R. A. Craddock, L. S. Crumpler, and J. C. Aubele</i> .....	335 -165
Macroscopic Electric Charge Separation During Hypervelocity Impacts: Potential Implications for Planetary Paleomagnetism <i>D. A. Crawford and P. H. Schultz</i> .....	337 -166
Rhenium-Osmium Isotope Systematics of Group IIA and Group IVA Iron Meteorites <i>R. A. Creaser, D. A. Papanastassiou, and G. J. Wasserburg</i> .....	339 -167

Separation of Spallation and Terrestrial $^{14}\text{C}$ in Chondrites <i>R. G. Cresswell, R. P. Beukens, and J. C. Rucklidge</i> .....	341-168
Near-Infrared Spectra of the Martian Surface: Reading Between the Lines <i>D. Crisp and J. F. Bell III</i> .....	343-169
Geomorphology of Triton's Polar Materials <i>S. K. Croft</i> .....	345-170
Porosity and the Ecology of Icy Satellites <i>S. K. Croft</i> .....	347-171
Tectonics on Triton <i>S. K. Croft</i> .....	349-172
Post-Impact Alteration of the Manson Impact Structure <i>L. J. Crossey and P. McCarville</i> .....	351-173
Model of Optical Scatter from Microimpacts on the Hubble Telescope <i>L. B. Crowell</i> .....	353-174
Volcanism in Southern Guinevere Planitia, Venus: Regional Volcanic History and Morphology of Volcanic Domes <i>D. A. Crown, E. R. Stofan, and J. J. Plaut</i> .....	355-175
Anomalous REE Patterns in Unequilibrated Enstatite Chondrites: Evidence and Implications <i>G. Crozaz and W. Hsu</i> .....	357-176
Comparison of the Distribution of Large Magmatic Centers on Earth, Venus, and Mars <i>L. S. Crumpler</i> .....	359-177
The Magellan Volcanic and Magmatic Feature Catalog <i>L. S. Crumpler, J. C. Aubele, and J. W. Head</i> .....	361-178
Synthesis of Global Thematic Mapping, Venus: Geologic Correlations/Questions for the Magellan Gravity Mission <i>L. S. Crumpler, J. C. Aubele, and J. W. Head</i> .....	363-179
Large Volcanoes on Venus: Examples of Geologic and Structural Characteristics from Different Classes <i>L. S. Crumpler, J. W. Head, and J. C. Aubele</i> .....	365-180
Regional Mantle Upwelling on Venus: The Beta-Atla-Themis Anomaly and Correlation with Global Tectonic Patterns <i>L. S. Crumpler, J. W. Head, and J. C. Aubele</i> .....	367-181
The Granulite Suite: Impact Melts and Metamorphic Breccias of the Early Lunar Crust <i>J. A. Cushing, G. J. Taylor, M. D. Norman, and K. Keil</i> .....	369-182

Galileo EM-2 Contributions to the Lunar Control Network <i>E. Davies, T. R. Colvin, M. J. S. Belton, R. Greeley, and Galileo SSI Team</i> .....	371 183
Iron and Nickel Isotopic Mass Fractionation in Deep-Sea Spherules <i>M. Davis and D. E. Brownlee</i> .....	373 184
Trace Element Distributions in Primitive Achondrites <i>M. Davis, M. Prinz, and M. K. Weisberg</i> .....	375 185
Deviations from the Straight Line: Bumps (and Grinds) in the Collisionally Evolved Size Distribution of Asteroids <i>R. Davis, P. Farinella, P. Paolicchi, A. C. Bagatin, A. Cellino, and E. Zappala</i> .....	377 186
Small Volcanoes in Tempe Terra, Mars: Their Detailed Morphometry and Inferred Geologic Significance <i>A. Davis and K. L. Tanaka</i> .....	379 187
Shallow Crustal Discontinuities and Graben and Scarp Formation in the Tharsis Region of Mars <i>P. A. Davis, K. L. Tanaka, and M. P. Golombek</i> .....	381 188
Characteristics of Arachnoids from Magellan Data <i>C. B. Dawson and L. S. Crumpler</i> .....	383 189
A Method to Determine Asteroid Poles <i>G. De Angelis</i> .....	385-190
Cathodoluminescence Properties of Components in Enstatite Chondrites <i>J. M. DeHart and G. E. Lofgren</i> .....	387-191
Classification of Martian Deltas <i>R. A. De Hon</i> .....	389-192
Fe/Mn Constraint on Precursors of Basaltic Achondrites <i>J. S. Delaney and J. S. Boesenberg</i> .....	391 193
Compositional Heterogeneity Within a Dumbbell-shaped Apollo 15 Green Glass: Evidence for Simultaneous Eruption of Different Magmas <i>J. W. Delano</i> .....	393 194
Oxidation State of the Earth's Upper Mantle During the Last 3800 Million Years: Implications for the Origin of Life <i>J. W. Delano</i> .....	395 195
Soret Diffusion: A Possible Cause of Compositional Heterogeneity Within Tektites <i>J. W. Delano, Y.-G. Liu, and R. A. Schmitt</i> .....	397-196
Isotopic and Trace Element Characteristics of an Unusual Refractory Inclusion from Essebi <i>E. Deloule, A. K. Kennedy, I. D. Hutcheon, and A. El Goresy</i> .....	399-197

Disk-resolved Spectral Characteristics of Saturn's Medium-sized Satellites <i>T. Denk, R. Jaumann, and G. Neukum</i> .....	401 198
The Correlation of Alkalies and Aluminum During High-Temperature Volatilization of Albite and Nepheline <i>Yu. P. Dikov, M. V. Gerasimov, O. I. Yakovlev, and F. Wlotzka</i> .....	403 199
A CM Chondrite Cluster and CM Streams <i>R. T. Dodd and M. E. Lipschutz</i> .....	405 200
Relation Between Ages and Elevations of Martian Channels <i>J. M. Dohm and D. H. Scott</i> .....	407 201
Does the Thermal Wind Exist Near the Earth's Core Boundary? <i>A. Z. Dolginov</i> .....	409 202
Magnetic Fields and Nonuniform Structures of the Moon <i>A. Z. Dolginov</i> .....	411 203
Polarity Reversals and Tilt of the Earth's Magnetic Dipole <i>A. Z. Dolginov</i> .....	413 204
Are Cosmic Rays Effective for Ionization of the Solar Nebula? <i>A. Z. Dolginov and T. F. Stepinski</i> .....	415 205
On the Unique Structure of the Magnetic Fields of Uranus and Neptune <i>Sh. Sh. Dolginov</i> .....	417 206
Precession of Uranus and Neptune and Their Magnetic Field <i>Sh. Sh. Dolginov</i> .....	419 207
Dust in the Martian Atmosphere: Polarimetric Sensing <i>A. Dollfus and S. Ebisawa</i> .....	421 208
Development of a Molecular Beam Technique to Study Early Solar System Silicon Reactions <i>Q. W. Dong and M. H. Thieme</i> .....	423 209
On High-Temperature Formation of Iron-rich Olivine in the Early Solar System <i>V. A. Dorofeyeva, A. B. Makalkin, and A. B. Vityazev</i> .....	425 210
Recondensation of Chondritic Material in the Early Solar System: Results of Thermodynamic Simulation <i>V. A. Dorofeyeva, A. B. Makalkin, M. V. Mironenko, and A. V. Vityazev</i> .....	427 211
Analytic Expression for Epithermal Neutron Spectra Amplitudes as a Function of Water Content <i>D. Drake</i> .....	429 212
Noble Gas Evidence of an Aqueous Reservoir Near the Surface of Mars More Recently than 1.3 Ga <i>M. J. Drake, T. Owen, T. Swindle, and D. Musselwhite</i> .....	431 213

Exploration Planning in the Context of Human Exploration and Development of the Moon <i>M. B. Duke and D. A. Morrison</i> .....	433 214
Primordial Lightning: Evidence Preserved in Chondrites <i>D. Eisenhour and P. R. Buseck</i> .....	435 215
Micro-Zoning in Minerals of a Landes Silicate Inclusion <i>D. D. Eisenhour, P. R. Buseck, H. Palme, and J. Zipfel</i> .....	437 216
Solar Wind-Induced Secondary Ions and Their Relation to Lunar Surface Composition <i>R. C. Elphic, H. O. Funsten III, and R. L. Hervig</i> .....	439 217
A New Carbon-rich Phase ("COPS") in Antarctic Micrometeorites <i>C. Engrand, M. Maurette, G. Kurat, F. Brandstatter, and M. Perreau</i> .....	441 218
Automatic Definition of Spectral Units in the Equatorial Regions of Mars <i>S. Erard, P. Cerroni, and A. Coradini</i> .....	443 219
Composition of the Martian Aerosols Through Near-IR Spectroscopy <i>S. Erard, P. Cerroni, and A. Coradini</i> .....	445-220
Giant Radiating Dyke Swarms on Earth and Venus <i>R. E. Ernst, J. W. Head, E. Parfitt, L. Wilson, and E. Grosfils</i> .....	447-221
Re-Os Dating of IIIAB Iron Meteorites <i>T. M. Esat and V. Bennett</i> .....	449-222
Modelling of Dispersal and Deposition of Impact Glass Spherules from the Cretaceous-Tertiary Boundary Deposit <i>J. M. Espindola, S. Carey, and H. Sigurdsson</i> .....	451-223
Xe-Q in Lodranites and a Hint for Xe-L. FRO90011 Another Lodranite? <i>O. Eugster and A. Weigel</i> .....	453-224
On the Origin of $^4\text{He}$ and $^{40}\text{Ar}$ in Natural Gold <i>O. Eugster, B. Hofmann, S. Niedermann, and Ch. Thalmann</i> .....	455-225
Projectile-Target Mixing in Melted Ejecta Formed During a Hypervelocity Impact Cratering Event <i>N. J. Evans, T. J. Ahrens, M. Shahinpoor, and W. W. Anderson</i> .....	457-226
Mössbauer Spectrometer for Mineralogical Analysis of the Mars Surface: Mössbauer Source Considerations <i>E. N. Evlanov, V. A. Frolov, O. F. Prilutskii, G. V. Veselova, A. M. Rodin, and G. Klingelhöfer</i> .....	459-227
Vulcanian Explosive Eruptions: A Mechanism for Localised Pyroclast Dispersal on Venus <i>S. A. Fagents and L. Wilson</i> .....	461-228
Chondrites, S Asteroids, and "Space Weathering": Thumping Noises from the Coffin? <i>F. P. Fanale and B. E. Clark</i> .....	463-229

A Comparison of the Visible and Near Infrared Reflectance of Hydrovolcanic Palagonite Tuffs and Martian Weathered Soils	
<i>W. H. Farrand and R. B. Singer</i> .....	465
	230
The Rate of Chemical Weathering of Pyrite on the Surface of Venus	
<i>B. Fegley Jr. and K. Lodders</i> .....	467
	231
Terrestrial Case Studies of Ilmenite Exploration and Lunar Implications	
<i>S. C. Feldman and H. A. Franklin</i> .....	469
	232
Morphotectonics of Venus	
<i>V. J. Finn, V. R. Baker, and A. Z. Dolginov</i> .....	471
	232
Transmantle Flux Tectonics	
<i>V. J. Finn, A. Z. Dolginov, and V. R. Baker</i> .....	473
	234
Assimilation in Lunar Basalts and Volcanic Glasses: Implications for a Heterogeneous Mantle Source Region	
<i>A. B. Finnila, P. C. Hess, and M. J. Rutherford</i> .....	475
	235
Measuring and Distinguishing Compositional and Maturity Properties of Lunar Soils by Remote VIS-NIR Spectroscopy	
<i>E. M. Fischer and C. M. Pieters</i> .....	477
	236
Diamond Thermoluminescence Properties of Different Chondrites	
<i>A. V. Fisenko, L. L. Kashkarov, L. F. Semjonova, and C. T. Pillinger</i> .....	479
	237
The Unusual Metallic Particles in Krymka LL3.0 Chondrite	
<i>A. V. Fisenko, A. Yu. Ljul, L. F. Semjonova, and K. I. Ignatenko</i> .....	481
	238
On Possibility of Diamond Formations in Radiation Process	
<i>A. V. Fisenko, L. F. Semjonova, L. N. Bolsheva, T. V. Grachjova, A. B. Verchovsky, and Yu. A. Shukolyukov</i> .....	483
	239
The Carbon Isotopic Composition of Novo Urei Diamonds	
<i>A. V. Fisenko, L. F. Semjenova, A. B. Verchovsky, S. S. Russell, and C. T. Pillinger</i> .....	485
	240
The Fractionation of Noble Gases in Diamonds of CV3 Efremovka Chondrite	
<i>A. V. Fisenko, A. B. Verchovsky, L. F. Semjonova, and Yu. A. Shukolyukov</i> .....	487
	241
Cronstedtite and Iron Sulfide Mineralogy of CM-type Carbonaceous Chondrites from Cryogenic Mössbauer Spectra	
<i>D. S. Fisher and R. G. Burns</i> .....	489
	242
NMR Spectroscopy of Experimentally Shocked Single Crystal Quartz: A Reexamination of the NMR Shock Barometer	
<i>P. S. Fiske, A. J. Gratz, and W. J. Nellis</i> .....	491
	243
Organic Matter on the Early Surface of Mars: An Assessment of the Contribution by Interplanetary Dust	
<i>G. J. Flynn</i> .....	493
	244



Trace Element Content of Chondritic Cosmic Dust: Volatile Enrichments, Thermal Alterations, and the Possibility of Contamination <i>G. J. Flynn, S. R. Sutton, and S. Bajt</i> .....	495 245
Depletions of Sulfur and/or Zinc in IDPs: Are They Reliable Indicators of Atmospheric Entry Heating? <i>G. J. Flynn, S. R. Sutton, S. Bajt, W. Klöck, K. L. Thomas, and L. P. Keller</i> .....	497 246
New Low-Ni (Igneous?) Particles Among the C and C? Types of Cosmic Dust <i>G. J. Flynn, S. R. Sutton, S. Bajt, and W. Klock</i> .....	499 247
Mass and Spatial Distribution of Carbonaceous Component in Comet Halley <i>M. Fomenkova and S. Chang</i> .....	501 248
Primitive SNC Parent Magmas and Crystallization: Low $P_{H_2O}$ Experiments <i>D. J. Ford and M. J. Rutherford</i> .....	503 249
Phase Transitions and 2D Spherical Convection in a Large Icy Satellite <i>O. Forni, C. Federico, and A. Coradini</i> .....	505-250
Planetary Science and Astronomy in the Middle School Classroom <i>L. M. French</i> .....	507-D MIT
Do Large Impact Basins in the Southern Hemisphere of Mars Control the Distribution of Polar Structures and Deposits? <i>H. Frey and A.-M. Reidy</i> .....	509-251
Free-Air and Bouguer Gravity Anomalies and the Martian Crustal Dichotomy <i>H. Frey, B. G. Bills, W. S. Kiefer, R. S. Nerem, J. H. Roark, and M. T. Zuber</i> .....	511-252
New Mars Free-Air and Bouguer Gravity: Correlation with Topography, Geology and Large Impact Basins <i>H. Frey, B. G. Bills, W. S. Kiefer, R. S. Nerem, J. H. Roark, and M. T. Zuber</i> .....	513-253
<b>PART 2</b>	
Spectral Evidence of Size Dependent Space Weathering Processes on Asteroid Surfaces <i>M. J. Gaffey, J. F. Bell, R. H. Brown, T. H. Burbine, J. L. Piatek, K. L. Reed, and D. A. Chaky</i> .....	515
$Fe^{2+}$ -Mg Interdiffusion in Orthopyroxene: Constraints from Cation Ordering and Structural Data and Implications for Cooling Rates of Meteorites <i>J. Ganguly and V. Tazzoli</i> .....	517
Cation Ordering in Orthopyroxenes and Cooling Rates of Meteorites: Low Temperature Cooling Rates of Estherville, Bondoc and Shaw <i>J. Ganguly, H. Yang, and S. Ghose</i> .....	519
SCR $^{21}Ne$ and $^{38}Ar$ in Lunar Rock 68815: The Solar Proton Energy Spectrum over the Past 2 Myr <i>D. H. Garrison, M. N. Rao, D. D. Bogard, and R. C. Reedy</i> .....	521

Morphometric Comparison of Icelandic Lava Shield Volcanoes Versus Selected Venusian Edifices <i>J. B. Garvin and R. S. Williams Jr.</i>	523
A Mineralized Zone in Western Candor Chasma, Mars <i>P. E. Geissler, R. B. Singer, and G. Komatsu</i>	525
Trapping of Water Vapor from an Atmosphere by Condensed Silicate Matter Formed by High-Temperature Pulse Vaporization <i>M. V. Gerasimov, Yu. P. Dikov, O. I. Yakovlev, and F. Wlotzka</i>	527
Pargo Chasma and Its Relationship to Global Tectonics <i>R. C. Ghail</i>	529
First Oxygen from Lunar Basalt <i>M. A. Gibson, C. W. Knudsen, D. J. Brueneman, H. Kanamori, R. O. Ness, L. L. Sharp, D. W. Brekke, C. C. Allen, R. V. Morris, L. P. Keller, and D. S. McKay</i>	531
The Formation and Evolution of Alpha and Tellus Tesserae on Venus <i>M. S. Gilmore and J. W. Head</i>	533
Extraction and Isotopic Analysis of Medium Molecular Weight Hydrocarbons from Murchison Using Supercritical Carbon Dioxide <i>I. Gilmour and C. Pillinger</i>	535
EUVE Observations of the Moon <i>G. R. Gladstone, J. S. McDonald, and W. T. Boyd</i>	537
Cretaceous-Tertiary Boundary Spherules and Cenozoic Microtektites: Similarities and Differences <i>B. Glass, B. F. Bohor, and W. J. Betterton</i>	539
A Test of the Applicability of Independent Scattering to High Albedo Planetary Regoliths <i>J. D. Goguen</i>	541
Rheology of Water and Ammonia-Water Ices <i>D. L. Goldsby, D. L. Kohlstedt, and W. B. Durham</i>	543
Importance of Expansion and Contraction in the Formation of Tectonic Features on the Moon <i>M. P. Golombek and W. B. Banert</i>	545
Stalking the LREE-enriched Component in Ureilites <i>C. A. Goodrich and G. W. Lugmair</i>	547
Grosnaja ABCs: Magnesium Isotope Compositions <i>J. N. Goswami, G. Srinivasan, and A. A. Ulyanov</i>	549
EUROMET Ureilite Consortium: A Preliminary Report on Carbon and Nitrogen Geochemistry <i>M. M. Grady and C. T. Pillinger</i>	551
Nitrates in SNCs: Implications for the Nitrogen Cycle on Mars <i>M. M. Grady, I. P. Wright, I. A. Franchi, and C. T. Pillinger</i>	553

A Calibration of the Production Rate Ratio $P_{21}/P_{26}$ by Low Energy Secondary Neutrons: Identification of Ne Spallation Components at the $10^6$ Atoms/g Level in Terrestrial Samples <i>Th. Graf, S. Niedermann, and K. Marti</i> .....	555
New K Type Asteroids <i>J. C. Granahan, G. Smith, and J. F. Bell</i> .....	557
Martian Crater Degradation by Eolian Processes: Analogy with the Rio Cuarto Crater Field, Argentina <i>J. A. Grant and P. H. Schultz</i> .....	559
Rover Mounted Ground Penetrating Radar as a Tool for Investigating the Near-Surface of Mars and Beyond <i>J. A. Grant and P. H. Schultz</i> .....	561
Sand Transport on Mars: Preliminary Results from Models <i>R. Greeley, F. S. Anderson, D. Blumberg, E. Lo, and P. Xu</i> .....	563
Galileo Imaging Results from the Second Earth-Moon Flyby: Lunar Maria and Related Units <i>R. Greeley, M. J. S. Belton, J. W. Head, A. S. McEwen, C. M. Pieters, G. Neukum, T. L. Becker, E. M. Fischer, S. D. Kadel, M. S. Robinson, R. J. Sullivan, J. M. Sunshine, and D. A. Williams</i> .....	565
Mars Analog Site Study (MASS) <i>R. Greeley, R. Kuzmin, F. Costard, F. S. Anderson, M. A. Geringer, R. Landheim, and M. L. Wenrich</i> .....	567
Earth Imaging Results from Galileo's Second Encounter <i>R. Greenberg, M. Belton, E. DeJong, A. Ingersoll, K. Klaasen, P. Geissler, J. Moersch, W. R. Thompson, and Galileo Imaging Team</i> .....	569
Collisional and Dynamical History of Gaspra <i>R. Greenberg, M. C. Nolan, W. F. Bottke Jr., and R. A. Kolvoord</i> .....	571
Petrography, Mineralogy, and Mg Isotope Composition of Victoria: A Vigarano $\text{CaAl}_4\text{O}_7$ -bearing Type A Inclusion <i>R. C. Greenwood, A. Morse, and J. V. P. Long</i> .....	573
Explosive Mafic Volcanism on Earth and Mars <i>T. K. P. Gregg and S. N. Williams</i> .....	575
Heliocentric Zoning of the Asteroid Belt by Aluminum-26 Heating <i>R. E. Grimm and H. Y. McSween Jr.</i> .....	577
Evolutionary Implications of a Steady-State Water Abundance on Venus <i>D. H. Grinspoon</i> .....	579
Spatially Extensive Uniform Stress Fields on Venus Inferred from Radial Dike Swarm Geometries: The Aphrodite Terra Example <i>E. B. Grosfils and J. W. Head</i> .....	581

Petrologic Constraints on the Surface Processes on Asteroid 4 Vesta and on Excavation Depths of Diogenite Fragments <i>T. L. Grove</i> .....	583
The Planetary Data System Educational CD-ROM <i>E. A. Guinness, R. E. Arvidson, M. Martin, and S. Dueck</i> .....	585
Fluvial Erosion on Mars: Implications for Paleoclimatic Change <i>V. C. Gulick and V. R. Baker</i> .....	587
The Acraman Impact Structure: Estimation of the Diameter by the Ejecta Layer Thickness <i>E. P. Gurov</i> .....	589
The Karakul Depression in Pamirs—The First Impact Structure in Central Asia <i>E. P. Gurov, H. P. Gurova, R. B. Rakitskaya, and A. Yu. Yamnichenko</i> .....	591
Systematic Chemical Variations in Large IIIAB Iron Meteorites: Clues to Core Crystallization <i>H. Haack, E. R. D. Scott, G. S. Rubio, D. F. Gutierrez, C. F. Lewis, J. T. Wasson, R. R. Brooks, X. Guo, D. E. Ryan, and J. Holzbecher</i> .....	593
Assimilation of Solids During Ascent of Magmas from the Bartoy Field of the Baikal Region, Siberia <i>J. R. Haas, L. A. Haskin, J. Luhr, and S. Rasskazov</i> .....	595
Morphology and Models for the Evolution of Eastern Hecate Chasma, Venus <i>V. E. Hamilton and E. R. Stofan</i> .....	597
A Pluto Thermal Model: <i>C. J. Hansen and D. A. Paige</i> .....	599
Modeling the Reflectance of CO <sub>2</sub> Frost with New Optical Constants: Application to Martian South Polar Cap Spectra <i>G. B. Hansen and T. Z. Martin</i> .....	601
Ishtar Deformed Belts: Evidence for Deformation from Below? <i>V. L. Hansen and R. J. Phillips</i> .....	603
Why is the Moon Dark? <i>B. Hapke</i> .....	605
<sup>142</sup> Nd/ <sup>144</sup> Nd in Bulk Planetary Reservoirs, the Problem of Incomplete Mixing of Interstellar Components and Significance of Very High Precision <sup>145</sup> Nd/ <sup>144</sup> Nd Measurements <i>C. L. Harper Jr. and S. B. Jacobsen</i> .....	607
The Physical Mechanism of Comet Outbursts: An Experiment <i>W. K. Hartmann</i> .....	609
Confirmation of Saturation Equilibrium Conditions in Crater Populations <i>W. K. Hartmann and R. W. Gaskell</i> .....	611

<b>Corvid Meteoroids and a Giordano Bruno Ray are Genetically Related</b> <i>J. B. Hartung</i> .....	613
<b>Pyroxene Equilibration Temperatures in Metamorphosed Ordinary Chondrites</b> <i>R. P. Harvey, M. L. Bennett, and H. Y. McSween Jr.</i> .....	615
<b>Remote Sensing Studies of the Northeastern Portion of the Lunar Nearside</b> <i>B. R. Hawke, D. T. Blewett, P. G. Lucey, G. J. Taylor, C. A. Peterson, J. F. Bell, M. S. Robinson, J. F. Bell III, C. R. Coombs, R. Jaumann, H. Hiesinger, G. Neukum, and P. D. Spudis</i> .....	617
<b>Tessera Terrain on Venus: Implications of Tessera Flooding Models and Boundary Characteristics for Global Distribution and Mode of Formation</b> <i>J. W. Head and M. Ivanov</i> .....	619
<b>Mode of Emplacement of Lunar Mare Volcanic Deposits: Graben Formation Due to Near Surface Deformation Accompanying Dike Emplacement at Rima Parry V</b> <i>J. W. Head and L. Wilson</i> .....	621
<b>Lunar Impact Basins: New Data for the Nearside Northern High Latitudes and Eastern Limb from the Second Galileo Flyby</b> <i>J. W. Head, M. Belton, R. Greeley, C. Pieters, E. Fischer, J. Sunshine, K. Klaasen, A. McEwen, T. Becker, G. Neukum, J. Oberst, C. Pilcher, J. Plutchak, M. Robinson, T. Johnson, D. Williams, S. Kadel, R. Sullivan, I. Antonenko, N. Bridges, and the Galileo Imaging Team</i> .....	623
<b>Lunar Scout Missions: Galileo Encounter Results and Application to Scientific Problems and Exploration Requirements</b> <i>J. W. Head, M. Belton, R. Greeley, C. Pieters, A. McEwen, G. Neukum, and T. McCord</i> .....	625
<b>Lava Flow-Field Morphological Classification and Interpretation: Examples from Venus</b> <i>J. W. Head, K. Magee Roberts, L. Wilson, and H. Pinkerton</i> .....	627
<b>Modes of Formation of Lunar Light Plains and the Detection of Cryptomaria Deposits</b> <i>J. W. Head, J. Mustard, I. Antonenko, and B. R. Hawke</i> .....	629
<b>Chemical Differentiation, Thermal Evolution, and Catastrophic Overturn on Venus: Predictions and Geologic Observations</b> <i>J. W. Head, E. M. Parmentier, and P. C. Hess</i> .....	631
<b>A Mössbauer Spectrometer for the Mineralogical Analysis of the Mars Surface: First Temperature Dependent Tests of the Detector and Drive System</b> <i>P. Held, R. Teucher, G. Klingelhöfer, J. Foh, H. Jäger, and E. Kankeleit</i> .....	633
<b>Galileo Photometry of Apollo Landing Sites</b> <i>P. Helfenstein, J. Veverka, J. W. Head, C. Pieters, S. Pratt, J. Mustard, K. Klaasen, G. Neukum, H. Hoffmann, R. Jaumann, H. Rebhan, A. S. McEwen, and M. Belton</i> .....	635
<b>Emplacement of Multiple Flow Units on Very Shallow Slopes, East Kawelu Planitia Flow Field, Venus</b> <i>M. B. Helgerud and J. R. Zimbelman</i> .....	637

Near-Surface Temperature Gradients and Their Effects on Thermal-Infrared Emission Spectra of Particulate Planetary Surfaces <i>B. G. Henderson and B. M. Jakosky</i> .....	639
Bubble Coalescence in Magmas <i>R. A. Herd and H. Pinkerton</i> .....	641
Thermal Inertia and Radar Reflectivity of the Martian North Polar Erg: Low-Density Aggregates <i>K. E. Herkenhoff</i> .....	643
The Three Ages of Venus: A Hypothesis Based on the Cratering Record <i>R. R. Herrick</i> .....	645
$^{26}\text{Al}$ - $^{26}\text{Mg}$ Ages of Iron Meteorites <i>G. F. Herzog, A. E. Souzis, S. Xue, J. Klein, D. Juenemann, and R. Middleton</i> .....	647
The Ilmenite Liquidus and Depths of Segregation for High-Ti Picrite Glasses <i>P. C. Hess</i> .....	649
Overturn of Magma Ocean Ilmenite Cumulate Layer: Implications for Lunar Magmatic Evolution and Formation of a Lunar Core <i>P. C. Hess and E. M. Parmentier</i> .....	651
Geochemistry and Cosmochemistry of Fullerenes III: Reaction of $\text{C}_{60}$ and $\text{C}_{70}$ with Ozone <i>D. Heymann and L. P. F. Chibante</i> .....	653
Earth-based and Galileo SSI Multispectral Observations of Eastern Mare Serenitatis and the Apollo 17 Landing Site <i>H. Hiesinger, R. Jaumann, G. Neukum, and GLL Imaging Team</i> .....	655
Trace-Element Composition of Chicxulub Crater Melt Rock, K/T Tektites and Yucatan Basement <i>A. R. Hildebrand, D. C. Grégoire, M. Attrep Jr., P. Claeys, C. M. Thompson, and W. V. Boynton</i> .....	657
Comparison of Reflectance Spectra of C Asteroids and Unique C Chondrites Y86720, Y82162, and B7904 <i>T. Hiroi, C. M. Pieters, and M. E. Zolensky</i> .....	659
Phase Equilibria of the Magnesium Sulfate-Water System to 4 kbars <i>D. L. Hogenboom, J. S. Kargel, J. P. Ganasan, and L. Lee</i> .....	661
Experimental Constraints on $\text{CO}_2$ and $\text{H}_2\text{O}$ in the Martian Mantle and Primary Magmas <i>J. R. Holloway, K. J. Domanik, and P. A. Cocheo</i> .....	663
The Size of Complex Craters <i>K. A. Holsapple</i> .....	665

Siderophile Elements in the Upper Mantle of the Earth: New Clues from Metal-Silicate Partition Coefficients	
<i>A. Holzheid, A. Borisov, and H. Palme</i> .....	667
Gas-Grain Energy Transfer in Solar Nebula Shock Waves: Implications for the Origin of Chondrules	
<i>L. L. Hood and M. Horanyi</i> .....	669
Mass of Saturn's A Ring	
<i>L. J. Horn and C. T. Russell</i> .....	671
Impact Penetration Experiments in Teflon Targets of Variable Thickness	
<i>F. Hörz, M. J. Cintala, R. P. Bernhard, and T. H. See</i> .....	673
Simulation of Collisional Fragmentation with Explosives	
<i>K. Housen</i> .....	675
Olivines in the Kaba Carbonaceous Chondrite and Constraints on Their Formation	
<i>X. Hua and P. R. Buseck</i> .....	677
Removal of Carbonaceous Contaminants from Silica Aerogel	
<i>H.-P. Huang, I. Gilmour, C. T. Pillinger, and M. E. Zolensky</i> .....	679
The Group A3 Chondrules of Krymka: Further Evidence for Major Evaporative Loss During the Formation of Chondrules	
<i>S. Huang, P. H. Benoit, and D. W. G. Sears</i> .....	681
Petrologic Models of 15388, a Unique Apollo 15 Mare Basalt	
<i>S. S. Hughes, E. J. Dasch, and L. E. Nyquist</i> .....	683
Potassium Isotope Cosmochemistry, Volatile Depletion and the Origin of the Earth	
<i>M. Humayun and R. N. Clayton</i> .....	685
Do SiC Grains in Orgueil Differ from Those in Murchison?	
<i>G. R. Huss, I. D. Hutcheon, and G. J. Wasserburg</i> .....	687
The Depths of the Largest Impact Craters on Venus	
<i>B. A. Ivanov and P. G. Ford</i> .....	689
Tessera Terrain on Venus: Global Characterization from Magellan Data	
<i>M. Ivanov and J. W. Head</i> .....	691
Density of Impact Craters on Tessera, Venus	
<i>M. A. Ivanov and A. T. Basilevsky</i> .....	693
First Investigation of Noble Gases in the Dengli H3,8 Chondrite	
<i>M. A. Ivanova, S. S. Assonov, and Yu. A. Shukolyukov</i> .....	695
Silica-bearing Objects in the Dengli H3.8 and Gorlovka H3-4 Chondrites	
<i>M. A. Ivanova, N. N. Kononkova, and M. I. Petaev</i> .....	697

Induced Thermoluminescence Study of Experimentally Shock-Loaded Oligoclase <i>A. I. Ivliev, L. L. Kashkarov, and D. D. Badjukov</i> .....	699
Shock-Thermal History of Kapoeta Howardite Matter on Data of Thermoluminescence Analysis of Individual Mineral Grains <i>A. I. Ivliev, L. L. Kashkarov, and Yu. Yu. Korotkova</i> .....	701
A First-Order Model for Impact Crater Degradation on Venus <i>N. R. Izenberg, R. E. Arvidson, and R. J. Phillips</i> .....	703
A Discontinuous Melt Sheet in the Manson Impact Structure <i>G. A. Izett, R. L. Reynolds, J. G. Rosenbaum, and J. M. Nishi</i> .....	705
Orbital Evolution of Dust from Comet Schwassmann-Wachmann 1: A Case of One-to-One Resonance Trapping <i>A. A. Jackson and H. A. Zook</i> .....	707
Constraints on the Differentiation of the Earth from the Coupled $^{146}\text{Sm}$ - $^{142}\text{Nd}$ Systematics <i>S. B. Jacobsen and C. L. Harper Jr.</i> .....	709
Os Isotopes in SNC Meteorites and Their Implications to the Early Evolution of Mars and Earth <i>E. Jagoutz, J. M. Luck, D. Ben Othman, and H. Wänke</i> .....	711
Transition Metals in Superheat Melts <i>P. Jakes and M.-P. Wolfbauer</i> .....	713
Iron Oxide Bands in the Visible and Near-Infrared Reflectance Spectra of Primitive Asteroids <i>K. S. Jarvis, F. Vilas, and M. J. Gaffey</i> .....	715
Searching for neuKREEP: An EMP Study of Apollo 11 Group A Basalts <i>E. A. Jerde and L. A. Taylor</i> .....	717
On the Composition of neuKREEP: QMD Contamination at Apollo 11? <i>E. A. Jerde, G. A. Snyder, and L. A. Taylor</i> .....	719
Estimates of Lithospheric Thickness on Venus <i>C. L. Johnson and D. T. Sandwell</i> .....	721
Radar Properties of Several Fluidized Ejecta Blankets on Venus <i>J. R. Johnson and V. R. Baker</i> .....	723
A Monazite-bearing Clast in Apollo 17 Melt Breccia <i>B. L. Jolliff</i> .....	725
Apollo 17 Materials Viewed from 2-4 mm Soil Particles: Pre-Serenitatis Highlands Components <i>B. L. Jolliff and K. M. Bishop</i> .....	727
An Iridium-rich Iron Micrometeorite with Silicate Inclusions from the Moon <i>B. L. Jolliff, R. L. Korotev, and L. A. Haskin</i> .....	729



The Cooling Rates of Pahoehoe Flows: The Importance of Lava Porosity <i>A. C. Jones</i> .....	731
Partitioning of Nb, Mo, Ba, Ce, Pb, Th and U Between Immiscible Carbonate and Silicate Liquids: Evaluating the Effects of P <sub>2</sub> O <sub>5</sub> , F, and Carbonate Composition <i>J. H. Jones and D. Walker</i> .....	733
Complex Zoning Behavior in Pyroxene in FeO-rich Chondrules in the Semarkona Ordinary Chondrite <i>R. H. Jones</i> .....	735
Angrite LEW87051: Are the Olivines Pheno's or Xeno's? A Continuing Story <i>A. J. G. Jurewicz and G. A. McKay</i> .....	737
Partial Melting of Ordinary Chondrites: Lost City (H) and St. Severin (LL) <i>A. J. G. Jurewicz, J. H. Jones, E. T. Weber, and D. L. Mittlefehldt</i> .....	739
Experimental Partitioning of Zr, Ti, and Nb Between Silicate Liquid and a Complex Noble Metal Alloy and the Partitioning of Ti Between Perovskite and Platinum Metal <i>S. R. Jurewicz and J. H. Jones</i> .....	741
Experimental Segregation of Iron-Nickel Metal, Iron-Sulfide, and Olivine in a Thermal Gradient: Preliminary Results <i>S. R. Jurewicz and J. H. Jones</i> .....	743
The History of Mare Volcanism in the Orientale Basin: Mare Deposit Ages, Compositions and Morphologies <i>S. D. Kadel, R. Greeley, G. Neukum, and R. Wagner</i> .....	745
The Al Rais Meteorite: A CR Chondrite or Close Relative? <i>G. W. Kallemeyn</i> .....	747
Chemical and Isotopic Compositions in Acid Residues from Various Meteorites <i>N. Kano, K. Yamakoshi, H. Matsuzaki, and K. Nogami</i> .....	749
Crustal Structure and Igneous Processes in a Chondritic Io <i>J. S. Kargel</i> .....	751
Geomorphic Processes in the Argyre-Dorsa Argentea Region of Mars <i>J. S. Kargel</i> .....	753
The Rheology and Composition of Cryovolcanic Flows on Icy Satellites <i>J. S. Kargel</i> .....	755
Martian Carbon Dioxide: Clues from Isotopes in SNC Meteorites <i>H. R. Karlsson, R. N. Clayton, T. K. Mayeda, A. J. T. Jull, and E. K. Gibson Jr.</i> .....	757
Different Radiation and Metamorphic History of the Kainsaz CO 3.2 Chondrules <i>L. L. Kashkarov and G. V. Kalinina</i> .....	759

Complex Radiation-Thermal History of Kaidun Meteorite on Data of Track Study of Silicate Minerals <i>L. L. Kashkarov, N. N. Korotkova, and A. Ya. Skripnik</i> .....	761
Fractal Geometry of Some Martian Lava Flow Margins: Alba Patera <i>K. Kauhanen</i> .....	763
Tectonics of Neyterkob Corona on Venus <i>K. Kauhanen</i> .....	765
Implications of Crater Distributions on Venus <i>W. M. Kaula</i> .....	767
Megaplumes on Venus <i>W. M. Kaula</i> .....	769
Preliminary Analysis of Dione Regio, Venus: The Final Magellan Regional Imaging Gap <i>S. T. Keddle</i> .....	771
The Distribution of Large Volcanoes on Venus as a Function of Height and Altitude <i>S. T. Keddle and J. W. Head</i> .....	773
Structural Mapping of Maxwell Montes <i>M. Keep and V. L. Hansen</i> .....	775
I-Xe Structure of Ilafegh 009 and Shallowater: Evidence for Early Formation and Rapid Cooling of Impact-derived Enstatite Meteorites <i>K. Kehm, R. H. Nichols Jr., C. M. Hohenberg, T. J. McCoy, and K. Keil</i> .....	777
Explosive Volcanism and the Compositions of the Cores of Differentiated Asteroids <i>K. Keil and L. Wilson</i> .....	779
High-Resolution Seismic Reflection Survey at the Manson Crater, Iowa <i>D. A. Keiswetter, R. Black, D. W. Steeples, and R. R. Anderson</i> .....	781
Heterogeneous Plagioclase Compositions in the Maralinga CK4 Chondrite <i>L. P. Keller</i> .....	783
Carbon Abundances, Major Element Chemistry, and Mineralogy of Hydrated Interplanetary Dust Particles <i>L. P. Keller, K. L. Thomas, and D. S. McKay</i> .....	785
An Initial Perspective of S-Asteroid Subtypes Within Asteroid Families <i>M. S. Kelley and M. J. Gaffey</i> .....	787
Tidal Interaction: A Possible Explanation for Geysers and Other Fluid Phenomena in the Neptune-Triton System <i>W. D. Kelly and C. L. Wood</i> .....	789
International Testing of a Mars Rover Prototype <i>A. Kemurjian, V. Linkin, and L. Friedman</i> .....	791

An Experimental Study of Trace Element Partitioning Between Perovskite, Hibonite and Melt: Equilibrium Values <i>A. E. Kennedy, G. E. Lofgren, and G. J. Wasserburg</i> .....	793
Nitrogen Isotopic Signatures in Agglutinates from Breccia 79035 <i>J. F. Kerridge, Y. Kim, J. S. Kim, and K. Marti</i> .....	795
An Inversion of Geoid and Topography for Mantle and Crustal Structure on Mars <i>W. Kiefer, B. Bills, H. Frey, S. Nerem, J. Roark, and M. Zuber</i> .....	797
Lava Crusts and Flow Dynamics <i>C. R. J. Kilburn</i> .....	799
Isotopic Signatures and Distribution of Nitrogen and Trapped and Radiogenic Xenon in the Acapulco and FRO90011 Meteorites <i>Y. Kim and K. Marti</i> .....	801
Separation of Topographic and Intrinsic Backscatter Variations in Biscopic Radar Images: A "Magic Airbrush" <i>R. L. Kirk</i> .....	803
Global Magellan-Image Map of Venus at Full Resolution <i>R. L. Kirk, K. B. Edwards, H. F. Morgan, L. A. Soderblom, and T. L. Stoewe</i> .....	805
The Cartography of Venus with Magellan Data <i>R. L. Kirk, H. F. Morgan, and J. F. Russell</i> .....	807
Osmium Isotopes in Ivory Coast Tektites: Confirmation of a Meteoritic Component and Rhenium Depletion <i>C. Koeberl and S. B. Shirey</i> .....	809
Manson Impact Structure, Iowa: First Geochemical Results for Drill Core M-1 <i>C. Koeberl, R. R. Anderson, J. B. Hartung, and W. U. Reimold</i> .....	811
Age Determinations and Earth-based Multispectral Observations of Lunar Light Plains <i>U. Koehler, R. Jaumann, and G. Neukum</i> .....	813
Meander Properties of Venusian Channels <i>G. Komatsu and V. R. Baker</i> .....	815
Terrestrial Bitumen Analogue of Orgueil Organic Material Demonstrates High Sensitivity to Usual HF-HCl Treatment <i>A. V. Korochantsev and O. V. Nikolaeva</i> .....	817
Composition of Apollo 17 Core 76001 <i>R. L. Korotev and K. M. Bishop</i> .....	819
Composition and Maturity of the 60013/14 Core <i>R. L. Korotev, R. V. Morris, and H. V. Lauer Jr.</i> .....	821

Cat Mountain: A Meteoritic Sample of an Impact-melted Chondritic Asteroid <i>D. A. Kring</i> .....	823
Comparative Magnetic and Thermoanalytical Study of Two Enstatite Chondrites: Adhi Kot and Atlanta <i>E. Król and B. Lang</i> .....	825
Chromite-rich Mafic Silicate Chondrules in Ordinary Chondrites: Formation by Impact Melting <i>A. N. Krot and A. E. Rubin</i> .....	827
Evaporation Kinetics of Mg <sub>2</sub> SiO <sub>4</sub> Crystals and Melts from Molecular Dynamics Simulations <i>J. D. Kubicki and E. M. Stolper</i> .....	829
Spectral Study of Venus Global Topography and Geoid from Magellan and PVO Data <i>A. B. Kucinskas, N. J. Borderies, and D. L. Turcotte</i> .....	831
Vertical Structure Models of the 1990 Equatorial Disturbance on Saturn <i>D. M. Kuehn, C. D. Barnett, and R. F. Beebe</i> .....	833
Preliminary <sup>40</sup> Ar/ <sup>39</sup> Ar Age Spectrum and Laser Probe Dating of the M1 Core of the Manson Impact Structure, Iowa: A K-T Boundary Crater Candidate <i>M. J. Kunk, L. W. Snee, B. M. French, S. S. Harlan, and J. J. McGee</i> .....	835
Was Martian Mantle Wet? A Possible Consequence of Rapid Core Formation <i>K. Kuramoto and T. Matsui</i> .....	837
Water in Earth's Mantle: Hydrogen Analysis of Mantle Olivine, Pyroxenes and Garnet Using the SIMS <i>M. Kurosawa, H. Yurimoto, and S. Sueno</i> .....	839
Lunar LIGO: A New Concept in Gravitational Wave Astronomy <i>N. LaFave and T. L. Wilson</i> .....	841
Sheet Flow Fields on Venus <i>M. G. Lancaster, J. E. Guest, and K. M. Roberts</i> .....	843
Mars Exobiology Landing Sites for Future Exploration <i>R. Landheim, R. Greeley, D. Des Marais, J. D. Farmer, and H. Klein</i> .....	845
Far-Infrared Spectra of CO <sub>2</sub> Clathrate Hydrate Frosts <i>J. C. Landry and A. W. England</i> .....	847
Orientation of Planar Deformation Features (PDFs) in Quartz <i>F. Langenhorst and A. Deutsch</i> .....	849
Lunar Phase Function Effects on Spectral Ratios Used for Resource Assessment <i>S. M. Larson, J. Collins, R. B. Singer, J. R. Johnson, and D. E. Melendrez</i> .....	851
The Astrophysical Interpretation of Isotope Anomalies in Graphite and SiC Grains of Chondrites <i>A. K. Lavrukhina</i> .....	853

On Possible Mn-53 Heterogeneity in the Early Solar System <i>A. K. Lavrukhina and G. K. Ustinova</i>	855
On Origin of the Olivine Inclusions from the Kainsaz CO Carbonaceous Chondrite <i>A. K. Lavrukhina, Z. A. Lavrentjeva, A. Yu. Ljul, and K. I. Ignatenko</i>	857
Teaching Planetary Sciences to Elementary School Teachers: Programs that Work <i>L. A. Lebofsky and N. R. Lebofsky</i>	859
A Simultaneous Estimation of the Mass of Mars and Its Natural Satellites, Phobos and Deimos, from the Orbital Perturbations on the Mariner 9, Viking 1, and Viking 2 Orbiters <i>F. G. Lemoine, D. E. Smith, S. K. Fricke, and J. J. McCarthy</i>	861
Models of Thermal/Chemical Boundary Layer Convection: Potential Application to Venus <i>A. Lenardic and W. M. Kaula</i>	863
On the Relationship Between Tectonic Plates and Thermal Mantle Plume Morphology <i>A. Lenardic and W. M. Kaula</i>	865
Hellas Basin, Mars: Formation by Oblique Impact <i>G. J. Leonard and K. L. Tanaka</i>	867
Mapping the Stability Region of the 3:2 Neptune-Pluto Resonance <i>H. F. Levison and S. A. Stern</i>	869
Possible Dust Contamination of the Early Solar System <i>E. H. Levy and T. V. Ruzmaikina</i>	871
A Search for Noble-Gas Evidence for Presolar Oxide Grains <i>R. S. Lewis and B. Srinivasan</i>	873
The Seismic Response of an Aquifer to the Propagation of an Impact Generated Shock Wave: A Possible Trigger of the Martian Outflow Channels? <i>I. A. Leyva and S. M. Clifford</i>	875
INAA of CAIs from the Maralinga CK4 Chondrite: Effects of Parent Body Thermal Metamorphism <i>D. J. Lindstrom, L. P. Keller, and R. R. Martinez</i>	877
Spaceship Earth: A Partnership in Curriculum Writing <i>M. M. Lindstrom and the NASA Partners-in-Space Team</i>	879
Chondritic Ratios of Fe/Cr/Ir in Kerguelen Plateau (Hole 783C) K/T Carbonate-rich Sediments Support Asteroid-Cometary Impact at K/T Time <i>Y.-G. Liu and R. A. Schmitt</i>	881
Earth's Partial Pressure of CO <sub>2</sub> Over the Past 120 Ma; Evidence from Ce Anomalies in the Deep (>600 m) Pacific Ocean, I <i>Y.-G. Liu and R. A. Schmitt</i>	883

Geochemical Evidences for Two Chondritic-like Cometary or Asteroid Impact Before and at the K/T Boundary <i>Y.-G. Liu and R. A. Schmitt</i> .....	885
Earth's Partial Pressure of CO <sub>2</sub> Over the Past 100-500 Ma. Evidence from Ce Anomalies in Mostly Shallow Seas (<200 m) as Recorded in Carbonate Sediments, II <i>Y.-G. Liu, J. W. Reinhardt, and R. A. Schmitt</i> .....	887
Noble Gases in Twenty Yamato H-Chondrites: Comparison with Allan Hills Chondrites and Modern Falls <i>Th. Loeken, P. Scherer, and L. Schultz</i> .....	889
The First Lunar Outpost: The Design Reference Mission and a New Era in Lunar Science <i>G. E. Lofgren</i> .....	891
Experimentally Reproduced Relict Enstatite in Porphyritic Chondrules of Enstatite Chondrite Composition <i>G. E. Lofgren, J. M. DeHart, and T. L. Dickinson</i> .....	893
Liquidus Equilibria of Lunar Analogs at High Pressure <i>J. Longhi</i> .....	895
The Monzonorite-Anorthosite Connection: The Petrogenesis of Terrestrial KREEP <i>J. Longhi and J. Vander Auwera</i> .....	897
Martian Lavas: Three Complementary Remote Sensing Techniques to Derive Flow Properties <i>R. Lopes-Gautier, B. C. Bruno, G. J. Taylor, S. Rowland, and C. R. J. Kilburn</i> .....	899
Densities of 5-15 $\mu$ m Interplanetary Dust Particles <i>S. G. Love, D. J. Joswiak, and D. E. Brownlee</i> .....	901
Resolving Topographic Detail on Venus by Modeling Complex Magellan Altimetry Echoes <i>A. J. Lovell, F. P. Schloerb, and G. E. McGill</i> .....	903
Sedimentation, Volcanism, and Ancestral Lakes in the Valles Marineris: Clues from Topography <i>B. K. Lucchitta, N. K. Isbell, and A. Howington-Kraus</i> .....	905
The Clementine Instrument Complement <i>P. G. Lucey</i> .....	907
Mixing Model Analysis of Telescopic Lunar Spectra <i>P. G. Lucey, B. C. Clark, and B. R. Hawke</i> .....	909
First Results from a Laboratory Facility for Measurement of Emission Spectra Under Simulated Planetary Conditions <i>P. G. Lucey, N. Domergue-Schmidt, B. G. Henderson, and B. Jakosky</i> .....	911
Evolution of Triton's Volatile Budget <i>J. I. Lunine</i> .....	913

The Effect of an On-Orbit Near Encounter on the Number Flux Density of Micron Sized Particles <i>C. R. Maag, W. G. Tanner, T. J. Stevenson, J. Borg, J.-P. Bibring, W. M. Alexander, and A. J. Maag</i> .....	915
Suggestion for Extended Viking Magnetic Properties Experiment on Future Mars Missions <i>M. B. Madsen, J. M. Knudsen, L. Vistisen, and R. B. Hargraves</i> .....	917
Large-scale Volcanism Associated with Corónae on Venus <i>K. Magee Roberts and J. W. Head</i> .....	919
Possible Sources of [H <sub>2</sub> ] to [H <sub>2</sub> O] Enrichment at Evaporation of Parent Chondritic Material <i>A. B. Makalkin, V. A. Dorofeyeva, and A. V. Vityazev</i> .....	921
Tidal Regime of Intact Planetoid Capture Model for the Earth-Moon System: Does It Relate to the Archean Sedimentary Rock Record? <i>R. J. Malcuit and R. R. Winters</i> .....	923
On the Delivery of Planetesimals to a Protoplanet in the Solar Nebula <i>R. Malhotra</i> .....	925
Tectonic Resurfacing of Venus <i>M. C. Malin, R. E. Grimm, and R. R. Herrick</i> .....	927
Venusian 'Pancake' Domes: Insights from Terrestrial Voluminous Silicic Lavas and Thermal Modeling <i>C. R. Manley</i> .....	929
Geophysical Models of Western Aphrodite-Niobe Region: Venus <i>K. I. Marchenkov, R. S. Saunders, and W. B. Banerdt</i> .....	931
CO <sub>2</sub> -Production by Impact in Carbonates?: An ATEM and Stable Isotope (C,O) Study <i>I. Martinez, P. Agrinier, F. Guyot, Ph. Ildefonse, M. Javoy, U. Schärer, U. Hornemann, and A. Deutsch</i> .....	933
Dust Grain Resonant Capture: A Statistical Study <i>F. Marzari, V. Vanzani, and S. J. Weidenschilling</i> .....	935
Effects of Bulk Composition on Production Rates of Cosmogenic Nuclides in Meteorites <i>J. Masarik and R. C. Reedy</i> .....	937
A Decade's Overview of Io's Volcanic Activity <i>D. L. Matson, G. J. Veeder, T. V. Johnson, D. L. Blaney, and J. D. Goguen</i> .....	939
A Mission Concept of Phobos/Deimos Exploration <i>K. Matsushima, J. Saito, M. Utashima, and H. Koshiishi</i> .....	941
Size Distribution of Interplanetary Iron and Stony Particles Related with Deep-Sea Spherules <i>H. Matsuzaki and K. Yamakoshi</i> .....	943

Classificational Parameters for Acapulcoites and Lodranites: The Cases of FRO 90011, EET 84302 and ALH A81187/84190 <i>T. J. McCoy, K. Keil, R. N. Clayton, and T. K. Mayeda</i> .....	945
The Dregs of Crystallization in Zagami <i>T. J. McCoy, K. Keil, and G. J. Taylor</i> .....	947
Resolving LDEF's Flux Distribution: Orbital (Debris?) and Natural Meteoroid Populations <i>J. A. M. McDonnell</i> .....	949
Clementine: Anticipated Scientific Datasets from the Moon and Geographos <i>A. S. McEwen</i> .....	951
Global and Regional/Seasonal Color Mosaics of Mars <i>A. S. McEwen and L. A. Soderblom</i> .....	953
Lunar Multispectral Mosaics from Galileo's Second Earth-Moon Flyby <i>A. S. McEwen, T. L. Becker, M. S. Robinson, K. P. Klaasen, C. Heffernan, J. M. Sunshine, and the Galileo SSI Team</i> .....	955
Galileo SSI Lunar Observations: Copernican Craters and Soils <i>A. S. McEwen, R. Greeley, J. W. Head, C. M. Pieters, E. M. Fischer, T. V. Johnson, G. Neukum, and the Galileo SSI team</i> .....	957
Aspects of Modelling the Tectonics of Large Volcanoes on the Terrestrial Planets <i>P. J. McGovern and S. C. Solomon</i> .....	959
Grain Surface Features of Apollo 17 Orange and Black Glass <i>D. S. McKay and S. J. Wentworth</i> .....	961
JSC-1: A New Lunar Regolith Simulant <i>D. S. McKay, J. L. Carter, W. W. Boles, C. C. Allen, and J. H. Allton</i> .....	963
The Nakhla Parent Melt: REE Partition Coefficients and Clues to Major Element Composition <i>G. McKay, L. Le, and J. Wagstaff</i> .....	965
More on the Cooling History of Angrite LEW 86010 <i>G. McKay, T. Ogawa, M. Miyamoto, and H. Takeda</i> .....	967
Limited Subsolvus Diffusion in Type B1 CAI; Evidence from Ti Distribution in Spinel <i>G. P. Meeker, J. E. Quick, and J. M. Paque</i> .....	969
The Effects of Orbital and Climatic Variations on Martian Surface Heat Flow <i>M. T. Mellon and B. M. Jakosky</i> .....	971
Equatorial Ground Ice on Mars: Steady-State Stability <i>M. T. Mellon, B. M. Jakosky, and S. E. Postawko</i> .....	973



Remote Visual Detection of Impacts on the Lunar Surface <i>H. J. Melosh, N. A. Artemjeva, A. P. Golub, I. V. Nemchinov, V. V. Shuvalov, and I. A. Trubetskaya</i> .....	975
Thermogeologic Mapping of the Moon from Lunar Orbit <i>W. W. Mendell and M. A. Wieczorek</i> .....	977
Deucalionis Regio, Mars: Evidence for a Unique Mineralogic Endmember and a Crusted Surface <i>E. Merényi, K. S. Edgett, and R. B. Singer</i> .....	979
Do It Yourself Remote Sensing: Generating an Inexpensive High Tech, Real Science Lake Mapping Project for the Classroom <i>S. M. Metzger</i> .....	981
Opportunity for Early Science Return by the Artemis Program <i>C. Meyer</i> .....	983
<sup>26</sup> Al Production Profile and Model Comparisons in Canyon Diablo <i>E. Michlovich, D. Elmore, S. Vogt, M. Lipschutz, J. Masarik, and R. C. Reedy</i> .....	985
Exsolved Kirschsteinite in Angrite LEW86010 Olivine <i>T. Mikouchi, H. Takeda, H. Mori, M. Miyamoto, and G. McKay</i> .....	987
Analysis of Pyroxene Absorptions Observed in Martian Dark Regions <i>J. S. Miller and R. B. Singer</i> .....	989
Refractory Precursor Components in an Allende Ferromagnesian Chondrule <i>K. Misawa, T. Fujita, M. Kitamura, and N. Nakamura</i> .....	991
Igneous Fractionation and Subsolidus Equilibration of Diogenite Meteorites <i>D. W. Mittlefehldt</i> .....	993
Siderophile Element Fractionation in Meteor Crater Impact Glasses and Metallic Spherules <i>D. W. Mittlefehldt, T. H. See, and E. R. D. Scott</i> .....	995
Identification of New Meteorite, Mihonoseki (L), from Broken Fragments in Japan <i>Y. Miura and Y. Noma</i> .....	997
The Thickness of Eucritic Crust in the HED Parent Body <i>M. Miyamoto and H. Takeda</i> .....	999
Zaoyang Chondrite Cooling History from Pyroxene Fe <sup>2+</sup> -Mg Intracrystalline Ordering and Exolutions <i>G. M. Molin, M. Tribaudino, and E. Brizi</i> .....	1001
Relief of Some Small Landforms on Venus <i>H. J. Moore, J. J. Plaut, and T. J. Parker</i> .....	1003
Mars Brine Formation Experiment <i>J. M. Moore, M. A. Bullock, and C. R. Stoker</i> .....	1005

Catalytic Crystallization of Ices by Small Silicate Smokes at Temperatures Less Than 20K <i>M. Moore, R. Ferrante, R. Hudson, T. Tanabe, and J. Nuth</i> .....	1007
Effective Elastic Thickness of the Venusian Lithosphere with Lateral Viscosity Variations in the Mantle <i>L. Moresi</i> .....	1009
Optical Effects of Regolith Processes on S Asteroids as Simulated by Laser Impulse Alteration of Ordinary Chondrite <i>L. V. Moroz, A. V. Fisenko, L. F. Semjonova, and C. M. Pieters</i> .....	1011
Altitude Profile of Aerosols on Mars from Measurements of Its Thermal Radiation on Limb <i>V. I. Moroz, D. V. Titov, Yu. M. Gektin, M. K. Naraeva, and A. S. Selivanov</i> .....	1013
Terrestrial Impact Melts as Analogues for the Hematization of Martian Surface Materials <i>R. V. Morris, H. V. Lauer Jr., and D. C. Golden</i> .....	1015
A Hydrogen Isotope Study of CO <sub>3</sub> Type Carbonaceous Chondrites; Comparison with Type 3 Ordinary Chondrites <i>A. D. Morse, J. Newton, and C. T. Pillinger</i> .....	1017
Gamma-Ray Spectrometer for Lunar Scout II <i>C. E. Moss, W. W. Burt, B. C. Edwards, R. A. Martin, G. H. Nakano, and R. C. Reedy</i> .....	1019
The Influence of Oceans on Martian Volcanism <i>P. Mouginis-Mark</i> .....	1021
Helium-3 Inventory of Lunar Samples: A Potential Future Energy Resource for Mankind? <i>A. V. Murali and J. L. Jordan</i> .....	1023
The Spectrum of Phobos from Phobos 2 Observations at 0.3-2.6 $\mu$ m: Comparison to Previous Data and Meteorite Analogs <i>S. Murchie and S. Erard</i> .....	1025
Bright Soil Units on Mars Determined from ISM Imaging Spectrometer Data <i>S. Murchie and J. Mustard</i> .....	1027
Variations in the Fe Mineralogy of Bright Martian Soil <i>S. Murchie, J. Mustard, S. Erard, P. Geissler, and R. Singer</i> .....	1029
Solar Noble Gases Revealed by Closed System Stepped Etching of a Metal Separate from Fayetteville <i>Ch. Murer, H. Baur, P. Signer, and R. Wieler</i> .....	1031
Effects of Levitated Dust on Astronomical Observations from the Lunar Surface <i>D. L. Murphy and R. R. Vondrak</i> .....	1033
Dust-Dynamic Feedbacks in the Martian Atmosphere: Surface Dust Lifting <i>J. R. Murphy and J. B. Pollack</i> .....	1035

Nitrogen and Light Noble Gases in Parsa Enstatite Chondrite <i>S. V. S. Murty</i> .....	1037
Composition of Weakly Altered Martian Crust <i>J. F. Mustard, S. L. Murchie, and S. Erard</i> .....	1039
From Minerals to Rocks: Toward Modeling Lithologies with Remote Sensing <i>J. F. Mustard, J. M. Sunshine, C. M. Pieters, A. Hoppin, and S. F. Pratt</i> .....	1041
SO <sub>2</sub> on Venus: IUE, HST, and Ground-based Measurements, and the Active Volcanism Connection <i>C. Y. Na, E. S. Barker, S. A. Stern, and L. W. Esposito</i> .....	1043
Evaporation in Equilibrium, in Vacuum, and in Hydrogen Gas <i>H. Nagahara</i> .....	1045
REE and Other Trace Lithophiles in MAC88177, LEW88280 and LEW88763 <i>N. Nakamura and N. Morikawa</i> .....	1047
The Erevan Howardite: Petrology of Glassy Clasts and Mineral Chemistry <i>M. A. Nazarov and A. A. Ariskin</i> .....	1049
The Koshak Section: Evidence for Element Fractionation and an Oxidation Event at the K/T Boundary <i>M. A. Nazarov, D. D. Badjukov, L. D. Barsukova, G. M. Kolesov, and D. P. Naidin</i> .....	1051
Carbonaceous Xenoliths from the Erevan Howardite <i>M. A. Nazarov, F. Brändstatter, and G. Kurat</i> .....	1053
Igneous Rock from Severnyi Kolchim (H3) Chondrite: Nebular Origin <i>M. A. Nazarov, F. Brandstätter, and G. Kurat</i> .....	1055
Petrogenesis of Apollo 12 Mare Basalts, Part 1: Multiple Melts and Fractional Crystallization to Explain Olivine and Ilmenite Basalt Compositions <i>C. R. Neal and L. A. Taylor</i> .....	1057
Petrogenesis of Apollo 12 Mare Basalts, Part 2: An Open System Model to Explain the Pigeonite Basalt Compositions <i>C. R. Neal and L. A. Taylor</i> .....	1059
The Coherent Backscattering Opposition Effect <i>R. M. Nelson, B. W. Hapke, W. D. Smythe, V. Gharakanian, and P. Herrera</i> .....	1061
On Magnetodynamic Effects Initiated by a High-Speed Impact of a Large Cosmic Body Upon the Earth's Surface <i>I. V. Nemchinov, P. E. Alexandrov, V. I. Artemiev, V. I. Bergelson, and V. A. Rybakov</i> .....	1063
Determination of Cosmic Bodies Size-Velocity Distribution by Observation of Current Impacts on Mars <i>I. V. Nemchinov, A. A. Perelomova, and V. V. Shuvalov</i> .....	1065

Effects of Hydrodynamics and Thermal Radiation in the Atmosphere after Comet Impacts <i>I. V. Nemchinov, M. P. Popova, L. P. Shubadeeva, V. V. Shuvalov, and V. V. Svetsov</i>	1067
The High Resolution Stereo Camera (HRSC) for the Lunar Scout I Mission <i>G. Neukum</i>	1069
Core Formation in the Moon: The Mystery of the Excess Depletion of Mo, W and P <i>H. E. Newsom and S. Maehr</i>	1071
Dating Native Gold by Noble Gas Analyses <i>S. Niedermann, O. Eugster, B. Hofmann, Ch. Thalmann, and W. U. Reimold</i>	1073
Helium in Interplanetary Dust Particles <i>A. O. Nier and D. J. Schlutter</i>	1075
Geologic Mapping of Northern Atla Regio on Venus: Preliminary Data <i>A. M. Nikishin and G. A. Burba</i>	1077
Beta Regio Rift System on Venus: Geologic Interpretation of Magellan Images <i>A. M. Nikishin, N. N. Bobina, V. K. Borozdin, and G. A. Burba</i>	1079
Beta Regio-Phoebe Regio on Venus: Geologic Mapping with the Magellan Data <i>A. M. Nikishin, V. K. Borozdin, N. N. Bobina, and G. A. Burba</i>	1081
Largest Impact Features on Venus: Non-Preserved or Non-Recognizable? <i>O. V. Nikolaeva</i>	1083
Exposure Ages of Carbonaceous Chondrites—I <i>K. Nishiizumi, J. R. Arnold, M. W. Caffee, R. C. Finkel, J. R. Southon, H. Nagai, M. Honda, M. Imamura, K. Kobayashi, and P. Sharma</i>	1085
Identification of an Interstellar Oxide Grain from the Murchison Meteorite by Ion Imaging <i>L. R. Nittler, R. M. Walker, E. Zinner, P. Hoppe, and R. S. Lewis</i>	1087
Fragments of Ancient Lunar Crust: Ferroan Noritic Anorthosites from the Descartes Region of the Moon <i>M. D. Norman, C. Alibert, and M. T. McCulloch</i>	1089
Volatility in the Lunar Crust: Trace Element Analyses of Lunar Minerals by PIXE Proton Microprobe <i>M. D. Norman, W. L. Griffin, and C. G. Ryan</i>	1091
Impact Glasses from the Ultrafine Fraction of Lunar Soils <i>J. A. Norris, L. P. Keller, and D. S. McKay</i>	1093
$^{146}\text{Sm}$ - $^{142,143}\text{Nd}$ Formation Interval for the Lunar Mantle and Implications for Lunar Evolution <i>L. E. Nyquist, C.-Y. Shih, H. Wiessmann, and B. M. Bansal</i>	1095
Goniospectrometric Properties of a White Standard <i>A. Oehler and A. Dummel</i>	1097

Characterization of Minnesota Lunar Simulant for Plant Growth <i>J. P. Oglesby, W. L. Lindsay, and W. Z. Sadeh</i> .....	1099
Dynamics of Large Scale Impacts on Venus and Earth <i>J. D. O'Keefe and T. J. Ahrens</i> .....	1101
Tambo Quemado: Extraordinary Concentrations of REE and Refractory Trace Elements Caused by Artificial Heating <i>E. Olsen, I. Hutcheon, and C. Moore</i> .....	1103
Modelling the Gravity and Magnetic Field Anomalies of the Chicxulub Crater <i>C. Ortiz Aleman, M. Pilkington, A. R. Hildebrand, W. R. Roest, R. A. F. Grieve, and P. Keating</i> .....	1105
Self Diffusion of Alkaline-Earth in Ca-Mg-Aluminosilicate Melts, Experimental Improvements on the Determination of the Self-Diffusion Coefficients <i>O. Paillat and G. J. Wasserburg</i> .....	1107
Orthopyroxenes as Recorders of Diogenite Petrogenesis: Major and Minor Element Systematics <i>J. J. Papike, M. N. Spilde, G. W. Fowler, and C. K. Shearer</i> .....	1109
Structural Evidence for Reorientation of Miranda About a Paleo-Pole <i>R. Pappalardo and R. Greeley</i> .....	1111
Formation and Evolution of Radial Fracture Systems on Venus <i>E. A. Parfitt and J. W. Head</i> .....	1113
Thermal and Rheological Controls on Magma Migration in Dikes: Examples from the East Rift Zone of Kilauea Volcano, Hawaii <i>E. A. Parfitt, L. Wilson, and H. Pinkerton</i> .....	1115
Constraints on the Rate of Discharge and Duration of the Mangala Valles Flood <i>T. J. Parker and D. S. Gorsline</i> .....	1117
Mixing of a Chemically Buoyant Layer at the Top of a Thermally Convecting Fluid: Implications for Mantle Dynamics with Application to Venus <i>E. M. Parmentier, P. C. Hess, and C. Sotin</i> .....	1119
Abundance and Composition of Solar Kr in the H3-H6 Chondrite Acfer111 <i>A. Pedroni</i> .....	1121
First Discovery of the Organic Materials in Deep-Sea Iron Cosmic Spherule <i>H. Peng and P. Xu</i> .....	1123
C/O Atomic Ratios in Micrometer-size Crushed Grains from Antarctic Micrometeorites and Two Carbonaceous Meteorites <i>M. Perreau, C. Engrand, M. Maurette, G. Kurat, and Th. Presper</i> .....	1125
Lamellar Olivine in the Divnoe Achondrite: Evidence for High-Pressure Exsolution? <i>M. I. Petaev</i> .....	1127

<b>Opaque-rich Lithology in the Divnoe Achondrite: Petrology and Origin</b> <i>M. I. Petaev</i> .....	1129
<b>Chaunskij: The Most Highly Metamorphosed, Shock-modified and Metal-rich Mesosiderite</b> <i>M. I. Petaev, R. S. Clarke Jr., E. J. Olsen, E. Jarosewich, A. M. Davis, I. M. Steele,</i> <i>M. E. Lipschutz, M.-S. Wang, R. N. Clayton, T. K. Mayeda, and J. A. Wood</i> .....	1131
<b>Spectral Reflectance Studies of the Humorom Basin Region</b> <i>C. A. Peterson, B. R. Hawke, P. G. Lucey, G. J. Taylor, D. T. Blewett, and P. D. Spudis</i> .....	1133
<b>Venus Magmatic and Tectonic Evolution</b> <i>R. J. Phillips and V. L. Hansen</i> .....	1135
<b>Post-Igneous Redistribution of Components in Eucrites</b> <i>W. C. Phinney, D. J. Lindstrom, D. W. Mittlefehldt, and R. R. Martinez</i> .....	1137
<b>Wavelength Dependence of Limb-Darkening of Mars from Visible and Near-IR Telescopic Spectral Imaging</b> <i>E. Pierazzo and R. B. Singer</i> .....	1139
<b>Compositional Diversity of the Lunar North Pole: Preliminary Analyses of Galileo SSI Data</b> <i>C. M. Pieters, M. Belton, J. W. Head, R. Greeley, A. McEwen, E. M. Fischer,</i> <i>J. M. Sunshine, K. Klaasen, J. Plutchak, G. Neukum, T. V. Johnson, and the SSI Team</i> .....	1141
<b>Optical Effects of Space Weathering on Lunar Soils and the Role of the Finest Fraction</b> <i>C. M. Pieters, E. M. Fischer, O. D. Rode, and A. Basu</i> .....	1143
<b>MinMap: An Imaging Spectrometer for High Resolution Compositional Mapping of the Moon</b> <i>C. M. Pieters, J. W. Head, T. B. McCord, and the MinMap Team</i> .....	1145
<b>Visible-Infrared Properties of Controlled Laboratory Soils</b> <i>C. M. Pieters, J. F. Mustard, S. F. Pratt, J. M. Sunshine, and A. Hoppin</i> .....	1147
<b>A Comparison of Calculated and Measured Rheological Properties of Crystallising Lavas in the Field and in the Laboratory</b> <i>H. Pinkerton and G. Norton</i> .....	1149
<b>Magellan Vertical Polarization Radar Observations</b> <i>J. J. Plaut</i> .....	1151
<b>Eruption History of the Tharsis Shield Volcanoes, Mars</b> <i>J. B. Plescia</i> .....	1153
<b>Geology of Biblis Patera, Ulysses Patera, and Jovis Tholus, Mars</b> <i>J. B. Plescia</i> .....	1155
<b>Gravity Investigation of the Manson Impact Structure, Iowa</b> <i>J. B. Plescia</i> .....	1157

Elevated Initial $^{87}\text{Sr}/^{86}\text{Sr}$ in Ordinary Chondrite Metal <i>F. A. Podosek, J. C. Brannon, C. Perron, and P. Pellas</i> .....	1159
Crater Destruction on the Venusian Highlands by Tectonic Processes <i>H. A. Pohn and G. G. Schaber</i> .....	1161
Low-Energy Ion Implantation: Large Mass Fractionation of Argon <i>K. V. Ponganis, Th. Graf, and K. Marti</i> .....	1163
Global Blackout Following the K/T Chicxulub Impact: Results of Impact and Atmospheric Modeling <i>K. O. Pope, A. C. Ocampo, K. H. Baines, and B. A. Ivanov</i> .....	1165
Schools of the Pacific Rainfall Climate Experiment <i>S. E. Postawko, M. L. Morrissey, G. J. Taylor, and P. Mougini-Mark</i> .....	1167
U-Pb Isotopic Ages and Characteristics of Ancient (>4.0 Ga) Lunar Highland Rocks <i>W. R. Premo</i> .....	1169
U-Pb Provenance Ages of Shocked Zircons from the K-T Boundary, Raton Basin, Colorado <i>W. R. Premo and G. A. Izett</i> .....	1171
U-Pb Isotopic Systematics of Ferroan Anorthosite 60025 <i>W. R. Premo and M. Tatsumoto</i> .....	1173
Thermal Conductivity Measurements of Particulate Materials Under Martian Conditions <i>M. A. Presley and P. R. Christensen</i> .....	1175
Elemental Depletions in Antarctic Micrometeorites and Arctic Cosmic Spherules: Comparison and Relationships <i>T. Presper, G. Kurat, C. Koeberl, H. Palme, and M. Maurette</i> .....	1177
Geologic Mapping of Harmakhis and Reull Valles Region, Mars: Evidence for Multiple Resurfacing and Drainage Events <i>K. H. Price</i> .....	1179
Some Deformation Trends and Topographic Characteristics of Tesserae on Venus <i>M. Price and J. Suppe</i> .....	1181
Studying Venus Using a GIS Database <i>M. Price and J. Suppe</i> .....	1183
Oxygen Isotopic Relationships Between the LEW85332 Carbonaceous Chondrite and CR Chondrites <i>M. Prinz, M. K. Weisberg, R. N. Clayton, and T. K. Mayeda</i> .....	1185
Impact Disturbance of the Venus Atmosphere <i>A. A. Provalev and B. A. Ivanov</i> .....	1187

Chocolate Tablet Aspects of Cytherean Meshkenet Tessera <i>J. Raitala</i> .....	1189
Ridge Belt-related Scarps and Troughs: Compressional Crustal Bending on Venus <i>J. Raitala, T. Törmänen, K. Kauhanen, and T. Tokkonen</i> .....	1191
SCR Neon and Argon in Kapoeta Feldspar: Evidence for an Active Ancient Sun <i>M. N. Rao, D. H. Garrison, and D. D. Bogard</i> .....	1193
Cosmogenic-Radionuclide Profiles in Knyahinya: New Measurements and Models <i>R. C. Reedy, J. Masarik, K. Nishiizumi, J. R. Arnold, R. C. Finkel, M. W. Caffee, J. Southon, A. J. T. Jull, and D. J. Donahue</i> .....	1195
Kalkkop Crater, Eastern Cape—A New Impact Crater in South Africa <i>W. U. Reimold, F. G. Le Roux, C. Koeberl, and S. B. Shirey</i> .....	1197
Micrometeorite Dynamic Pyrometamorphism: Nonstoichiometric Clinostatite (CLEN) <i>F. J. M. Rietmeijer</i> .....	1199
Micrometeorite Dynamic Pyrometamorphism: Observation of a Thermal Gradient in Iron-Nickel Sulfide <i>F. J. M. Rietmeijer</i> .....	1201
Wavelength Dispersive Analysis with the Synchrotron X-ray Fluorescence Microprobe <i>M. L. Rivers, K. S. Thorn, S. R. Sutton, K. W. Jones, and S. Bajt</i> .....	1203
Subduction on the Margins of Coronae on Venus: Evidence from Radiothermal Emissivity Measurements <i>C. A. Robinson</i> .....	1205
Preliminary Results from Mariner 10: High Resolution Images of the Moon <i>M. S. Robinson, B. R. Hawke, K. Edwards, P. G. Lucey, and B. E. Clark</i> .....	1207
Chronology, Eruption Duration, and Atmospheric Contribution of Apollinaris Patera, Mars <i>M. S. Robinson, P. J. Mouginis-Mark, J. R. Zimbelman, and S. S. C. Wu</i> .....	1209
The Manson Impact Crater: Estimation of the Energy of Formation, Possible Size of the Impacting Asteroid or Comet, and Ejecta Volume and Mass <i>D. J. Roddy, E. M. Shoemaker, and R. R. Anderson</i> .....	1211
Comparative Hypsometric Analysis of Both Earth and Venus Topographic Distributions <i>P. Rosenblatt, P. C. Pinet, and E. Thouvenot</i> .....	1213
Derivation of the Midinfrared (5.0-25.0 $\mu\text{m}$ ) Optical Constants of Hydrous Carbonate and Sulfate <i>T. L. Roush, J. B. Orenberg, and J. B. Pollack</i> .....	1215
Euhedral Metallic-Fe-Ni Grains in Extraterrestrial Samples <i>A. E. Rubin</i> .....	1217



Named Venusian Craters <i>J. F. Russell and G. G. Schaber</i> .....	1219
A Carbon and Nitrogen Isotope Study of Carbonaceous Vein Material in Ureilite Meteorites <i>S. S. Russell, J. W. Arden, I. A. Franchi, and C. T. Pillinger</i> .....	1221
C-O Volatiles in Apollo 15 and Apollo 17 Picritic Glasses <i>M. J. Rutherford and R. A. Fogel</i> .....	1223
Formation of the Low-Mass Solar Nebula <i>T. V. Ruzmaikina, I. V. Khatuncev, and T. V. Konkina</i> .....	1225
Asteroid Collisions: Target Size Effects and Resultant Velocity Distributions <i>E. V. Ryan</i> .....	1227
Detectability of Crystalline Ferric and Ferrous Minerals on Mars <i>D. E. Sabol Jr., J. F. Bell III, and J. B. Adams</i> .....	1229
Distribution of Small Volcanic Cones on the Surface of Venus by Size and Elevation: Implications for Differential Deposition of Volcanic Features <i>Sahuaro High School Astronomical Research Class, J. F. Lockwood, Evergreen High School Research Class, M. Ellison, J. Johnson, and G. Kamatsu</i> .....	1231
Venus Pancake Dome Formation: Morphologic Effects of a Cooling-induced Variable Viscosity During Emplacement <i>S. E. H. Sakimoto and M. T. Zuber</i> .....	1233
Thermal Infrared Remote Sensing and Kirchhoff's Law: I Laboratory Measurements <i>J. W. Salisbury, A. Wald, and D. M. D'Aria</i> .....	1235
Magellan at Venus: Summary of Science Findings <i>R. S. Saunders, E. R. Stofan, J. J. Plaut, and D. A. Senske</i> .....	1237
Preliminary Estimation of Tagamite Cooling Conditions (Puchezh-Katunki Astrobleme, Russia) <i>L. Sazonova, V. Feldman, and N. Korotaena</i> .....	1239
Venus' Impact-Crater Database: Update to ~98% of the Planet's Surface <i>G. G. Schaber and D. J. Chadwick</i> .....	1241
Local Topography of Mars and Its Relationship to Surface Weathering Processes <i>M. W. Schaefer</i> .....	1243
Diapirs and Cantaloupes: Layering and Overturn of Triton's Crust <i>P. Schenk and M. P. A. Jackson</i> .....	1245
Geology of the Southern Hemisphere of Triton: No Polar Cap <i>P. Schenk and J. M. Moore</i> .....	1247
3-D Moons: The Voyager Stereo Atlas of the Outer Solar System <i>P. Schenk and J. M. Moore</i> .....	1249

Iridium in Sediments Containing Large Abundances of Australasian Microtektites from DSDP Hole 758B in the Eastern Indian Ocean and from DSDP Hole 769A in the Sulu Sea <i>G. Schmidt, L. Zhou, and J. T. Wasson</i> .....	1251
Pressure Versus Drag Effects on Crater Size <i>R. M. Schmidt</i> .....	1253
Searching for Ancient Venus <i>P. H. Schultz</i> .....	1255
Impactor Control of Central Peak and Peak-Ring Formation <i>P. H. Schultz and D. E. Gault</i> .....	1257
Further Analyses of Rio Cuarto Impact Glass <i>P. H. Schultz, T. E. Bunch, C. Koeberl, and W. Collins</i> .....	1259
C <sub>2</sub> , CN and Dust in Comet Wilson (1987VII) <i>R. Schulz, M. F. A'Hearn, P. V. Birch, C. Bowers, M. Kempin, and R. Martin</i> .....	1261
Strength and Deformation Properties of Basaltic Lava Flows on Planetary Surfaces <i>R. A. Schultz</i> .....	1263
Mars: New Evidence for Origin of Some Valles Marineris Layered Deposits <i>D. H. Scott</i> .....	1265
Post-Metamorphic Brecciation in Type 3 Ordinary Chondrites <i>E. R. D. Scott, T. J. McCoy, and K. Keil</i> .....	1267
Cathodoluminescence Observations of <i>In Situ</i> Aqueous Destruction of Chondrules in the Murchison CM Chondrite <i>D. W. G. Sears, P. H. Benoit, J. Lu, and A. S. R. Sears</i> .....	1269
Diffusive Redistribution of Water Vapor in the Solar Nebula Revisited <i>W. D. Sears</i> .....	1271
Lunar Basalt Meteorite EET 87521: Petrology of the Clast Population <i>A. S. Semenova, M. A. Nazarov, and N. N. Kononkova</i> .....	1273
Magnetic Properties and Mössbauer Analyses of Glass from the K-T Boundary, Beloc, Haiti <i>F. E. Senftle, A. N. Thorpe, L. May, A. Barkatt, M. A. Adel-Hadadi, G. S. Marbury, G. Izett, H. Sigurdsson, and F. J.-M. R. Maurasse</i> .....	1275
Rifting at Devana Chasma, Venus: Structure and Estimation of the Effective Thickness of the Elastic Lithosphere <i>D. A. Senske</i> .....	1277
Volcanic Rises on Venus: Geology, Formation, and Sequence of Evolution <i>D. A. Senske, E. R. Stofan, D. L. Bindshadler, and S. E. Smrekar</i> .....	1279
Molecular Equilibria and Condensation Sequences in Carbon Rich Gases <i>C. M. Sharp and G. J. Wasserburg</i> .....	1281

Chicxulub Impact Basin: Gravity Characteristics and Implications for Basin Morphology and Deep Structure <i>V. L. Sharpton, K. Burke, S. A. Hall, S. Lee, L. E. Marin, G. Suarez, J. M. Quezada-Muñeton, and J. Urrutia-Fucugauchi</i> .....	1283
Basaltic Magmatism on the Moon. A Perspective from Volcanic Picritic Glasses <i>C. K. Shearer and J. J. Papike</i> .....	1285
Origin of the Apollo 15 Very Low Ti Green Glass. A Perspective from the Compositional Diversity in the Very Low Ti Glasses <i>C. K. Shearer and J. J. Papike</i> .....	1287
Orthopyroxenes as Recorders of Diogenite Petrogenesis: Trace Element Systematics <i>C. K. Shearer, J. J. Papike, and G. D. Layne</i> .....	1289
Combined Backscatter Mössbauer Spectrometer/X-ray Fluorescence Analyzer (BaMS/XRF) for Extraterrestrial Surfaces <i>T. D. Shelfer, E. L. Wills, D. G. Agresti, M. M. Pimperl, M. H. Shen, R. V. Morris, and T. Nguyen</i> .....	1291
The Roughness of the Martian Surface: A Scale Dependent Model <i>M. K. Shepard, E. A. Guinness, and R. E. Arvidson</i> .....	1293
Chronology of Lunar Granite 12033,576: Resetting of Rb-Sr and K-Ca Isochrons <i>C.-Y. Shih, H. Wiesmann, D. H. Garrison, L. E. Nyquist, and D. D. Bogard</i> .....	1295
The Chondrite Mihonoseki—New Observed Fall <i>M. Shima, A. Okada, and K. Nagao</i> .....	1297
Clementine: An Inexpensive Mission to the Moon and Geographos <i>E. M. Shoemaker and S. Nozette</i> .....	1299
Research Program on the Manson Impact Crater, Iowa <i>E. M. Shoemaker, D. J. Roddy, and R. R. Anderson</i> .....	1301
Petrography of Shock Features in the 1953 Manson 2—A Drill Core <i>N. M. Short and D. P. Gold</i> .....	1303
<sup>60</sup> Fe and the Evolution of Eucrites <i>A. Shukolyukov and G. W. Lugmair</i> .....	1305
Geoid, Topography, and Convection-driven Crustal Deformation on Venus <i>M. Simons, B. H. Hager, and S. C. Solomon</i> .....	1307
Petrography and Origin of Refractory Inclusions from the Murray and Murchison C2 Chondrites <i>S. B. Simon, L. Grossman, and A. Hsu</i> .....	1309
Scattering by Venus' Surface <i>R. A. Simpson, G. L. Tyler, M. J. Maurer, E. Holmann, and P. B. Wong</i> .....	1311

Venus Gravity: New Magellan Low Altitude Data <i>W. L. Sjogren, A. S. Konopliv, N. Borderies, M. Batchelder, J. Heirath, and R. N. Wimberly</i> .....	1313
Size Distributions and Aerodynamic Equivalence of Metal Chondrules and Silicate Chondrules in Acfer 059 <i>W. R. Skinner and J. M. Leenhouts</i> .....	1315
GMM-1: A 50 <sup>th</sup> Degree and Order Gravitational Field Model for Mars <i>D. E. Smith, F. J. Lerch, R. S. Nerem, M. T. Zuber, G. B. Patel, S. K. Fricke, and F. G. Lemoine</i> .....	1317
Response of the Topography and Gravity Field on Venus to Mantle Upwelling Beneath a Chemical Boundary Layer <i>S. E. Smrekar and E. M. Parmentier</i> .....	1319
Primary Differentiation in the Early Earth: Nd and Sr Isotopic Evidence from Diamondiferous Eclogites for Both Old Depleted and Old Enriched Mantle, Yakutia, Siberia <i>G. A. Snyder, E. A. Jerde, L. A. Taylor, A. N. Halliday, V. N. Sobolev, N. V. Sobolev, R. N. Clayton, T. K. Mayeda, and P. Deines</i> .....	1321
Chronology and Genesis of High-Ti Mare Volcanism: Melting of Cogenetic Depleted and Enriched Reservoirs <i>G. A. Snyder, L. A. Taylor, and A. N. Halliday</i> .....	1323
Geochronology and Petrogenesis of the Western Highlands Alkali Suite: Radiogenic Isotopic Evidence from Apollo 14 <i>G. A. Snyder, L. A. Taylor, and A. N. Halliday</i> .....	1325
Magnesian Anorthosites from the Western Highlands of the Moon: Isotope Geochemistry and Petrogenesis <i>G. A. Snyder, L. A. Taylor, and A. N. Halliday</i> .....	1327
Differentiation of Magma Oceans and the Thickness of the Depleted Layer on Venus <i>V. S. Solomatov and D. J. Stevenson</i> .....	1329
A Tectonic Resurfacing Model for Venus <i>S. C. Solomon</i> .....	1331
The "Missing" Impact Craters on Venus <i>D. H. Speidel</i> .....	1333
Delimitation of Terrestrial Impact Craters via Pseudotachylitic Rock Distribution <i>J. G. Spray</i> .....	1335
Contributions of the Clementine Mission to Our Understanding of the Processes and History of the Moon <i>P. D. Spudis and P. G. Lucey</i> .....	1337
Impact Basins on Venus and Some Interplanetary Comparisons <i>P. D. Spudis and V. L. Sharpton</i> .....	1339

Geology and Deposits of the Serenitatis Basin <i>P. D. Spudis, B. R. Hawke, and P. G. Lucey</i> .....	1341
Earth-based Measurement of Lunar Topography Using Delayed Radar Interferometry <i>N. J. S. Stacy and D. B. Campbell</i> .....	1343
Fe/Mn in Olivine of Carbonaceous Meteorites <i>I. M. Steele</i> .....	1345
Two-Polarity Magnetization in the Manson Impact Breccia <i>M. B. Steiner and E. M. Shoemaker</i> .....	1347
Multielement Analysis of Interplanetary Dust Particles Using TOF-SIMS <i>T. Stephan, W. Klöck, E. K. Jessberger, H. Rulle, and J. Zehnpfening</i> .....	1349
Magnetically Controlled Solar Nebula <i>T. F. Stepinski and M. Reyes-Ruiz</i> .....	1351
Expectations for the Martian Core Magnetic Field <i>D. J. Stevenson</i> .....	1353
Volatile Loss from Accreting Icy Protoplanets <i>D. J. Stevenson</i> .....	1355
Fine Resolution Chronology Based on Initial $^{87}\text{Sr}/^{86}\text{Sr}$ <i>B. W. Stewart, D. A. Papanastassiou, R. C. Capo, and G. J. Wasserburg</i> .....	1357
Sm-Nd Systematics of Silicate Inclusions in Iron Meteorites: Results from Caddo (IAB) <i>B. W. Stewart, D. A. Papanastassiou, and G. J. Wasserburg</i> .....	1359
Parga and Hecate Chasmata, Venus: Structure, Volcanism and Models of Formation <i>E. R. Stofan, V. E. Hamilton, and K. Cotugno</i> .....	1361
Linear Structures on the Small Inner Satellites of Saturn <i>P. J. Stooke</i> .....	1363
The Age of the Pretoria Saltpan Impact Crater, South Africa <i>D. Storzer, C. Koeberl, and W. U. Reimold</i> .....	1365
The Role of $\text{CO}_2$ in Weathering Reactions and the Presence of $\text{S}_2$ on Venus: Implications for the Pyrite Stability Field <i>D. W. Straub</i> .....	1367
The Stability of Oxyamphiboles: Existence of Ferric-bearing Minerals Under the Reducing Conditions on the Surface of Venus <i>D. W. Straub and R. G. Burns</i> .....	1369
Parabolic Features and the Erosion Rate on Venus <i>R. G. Strom</i> .....	1371

<b>Triton's Cratering Record and Its Time of Capture</b> <i>R. G. Strom and S. K. Croft</i> .....	1373
<b>Are Plinian Type Eruptions Possible on Venus?</b> <i>S. Sugita and T. Matsui</i> .....	1375
<b>Implantation of Nitrogen: Effects of Hydrogen and Implantation Energy</b> <i>N. Sugiura, T. Futagami, and S. Nagai</i> .....	1377
<b>Determining the Composition of Olivine on Asteroidal Surfaces</b> <i>J. M. Sunshine and C. M. Pieters</i> .....	1379
<b>Discovery Venera Surface-Atmosphere Geochemistry Experiments Mission Concept</b> <i>Yu. A. Surkov, J. W. Head, R. Kremnev, K. T. Nock, and the Discovery Venera Team</i> .....	1381
<b>X-Ray Microprobe Determination of Chromium Oxidation State in Olivine from Lunar Basalt and Kimberlitic Diamonds</b> <i>S. R. Sutton, A. S. Bajt, M. L. Rivers, and J. V. Smith</i> .....	1383
<b>Microanalysis of Iron Oxidation State in Iron Oxides Using X-Ray Absorption Near Edge Structure (XANES)</b> <i>S. R. Sutton, J. Delaney, S. Bajt, M. L. Rivers, and J. V. Smith</i> .....	1385
<b>SPH Modelling of Energy Partitioning During Impacts on Venus</b> <i>T. Takata and T. J. Ahrens</i> .....	1387
<b>Hydrothermal Alteration Experiments of Olivine with Varying Fe Contents: An Attempt to Simulate Aqueous Alteration of the Carbonaceous Chondrites</b> <i>K. Takatori, K. Tomeoka, K. Tsukimura, and H. Takeda</i> .....	1389
<b>Mineralogy and Cooling History of Magnesian Lunar Granulite 67415</b> <i>H. Takeda and M. Miyamoto</i> .....	1391
<b>Ti-bearing Oxide Minerals in Lunar Meteorite Y793169 with the VLT Affinity</b> <i>H. Takeda, T. Arai, and K. Saiki</i> .....	1393
<b>A New Antarctic Meteorite With Chromite, Orthopyroxene and Metal with Reference to a Formation Model of S Asteroids</b> <i>H. Takeda, K. Saiki, M. Otsuki, and T. Hiroi</i> .....	1395
<b>Extensional History of Mars' Tharsis Region</b> <i>K. L. Tanaka and D. J. Chadwick</i> .....	1397
<b>Complex Structure of the Thaumasia Region of Mars</b> <i>K. L. Tanaka and J. M. Dohm</i> .....	1399
<b>Large, Ancient, Compressional Structures on Mars</b> <i>K. L. Tanaka and R. A. Schultz</i> .....	1401

Determination of Parameters for Hypervelocity Dust Grains Encountered in Near-Earth Space <i>W. G. Tanner, C. R. Maag, W. M. Alexander, and P. Sappenfield</i> .....	1403
Tumuli and Tubes: Teaching Scientific Techniques <i>M. J. Tatsumura, G. J. Taylor, and P. J. Mougini-Mark</i> .....	1405
Sparking Young Minds with Moon Rocks and Meteorites <i>G. J. Taylor and M. M. Lindstrom</i> .....	1407
Evaluation of Lunar Rocks and Soils for Resource Utilization: Detailed Image Analysis of Raw Materials and Beneficiated Products <i>L. A. Taylor, J. G. Chambers, A. Patchen, E. A. Jerde, D. S. McKay, J. Graf, S. Wentworth, and R. R. Oder</i> .....	1409
Production of O <sub>2</sub> on the Moon: A Lab-Top Demonstration of Ilmenite Reduction with Hydrogen <i>L. A. Taylor, E. A. Jerde, D. S. McKay, M. A. Gibson, C. W. Knudsen, and H. Kanamori</i> .....	1411
The Mg-Suite and the Highland Crust: An Unsolved Enigma <i>S. R. Taylor, M. D. Norman, and T. M. Esat</i> .....	1413
The Sand Bag Model of the Dispersion of the Cosmic Body in the Atmosphere <i>A. V. Teterev and I. V. Nemchinov</i> .....	1415
Atmospheric Breakup of a Small Comet in the Earth's Atmosphere <i>A. V. Teterev, N. I. Misychenko, L. V. Rudak, G. S. Romanov, A. S. Smetannikov, and I. V. Nemchinov</i> .....	1417
Original Size of the Vredefort Structure, South Africa <i>A. M. Theriault, A. M. Reid, and W. U. Reimold</i> .....	1419
Origin of the Vredefort Structure, South Africa: Impact Model <i>A. M. Theriault, A. M. Reid, and W. U. Reimold</i> .....	1421
Synoptic Observations of Near Surface Processes of an Insolated Ice-Dust Body Under Space Conditions: The Case of KOSI 9 and 10 <i>K. Thiel, G. Kölzer, E. Lorenz, H. Kochan, J. Gebhard, and E. Grün</i> .....	1423
Cometary Interplanetary Dust Particles? An Update on Carbon in Anhydrous IDPs <i>K. L. Thomas, L. P. Keller, G. E. Blanford, and D. S. McKay</i> .....	1425
Magellan Mission Progress Report <i>T. W. Thompson and Magellan Flight Team</i> .....	1427
Discharge Rates in Ma' Adim Vallis, Mars <i>G. D. Thornhill, D. A. Rothery, J. B. Murray, T. Day, A. C. Cook, J.-P. Muller, and J. C. Iliffe</i> .....	1429
Objective Determination of Image End-Members in Spectral Mixture Analysis <i>S. Tompkins, J. F. Mustard, C. M. Pieters, and D. W. Forsyth</i> .....	1431

Distribution and Geologic History of Materials Excavated by the Lunar Crater Bullialdus <i>S. Tompkins, C. M. Pieters, and J. F. Mustard</i> .....	1433
Core Formation by Giant Impacts: Conditions for Intact Melt Region Formation <i>W. B. Tonks and H. J. Melosh</i> .....	1435
U-Th-Pb, Sm-Nd, and Ar-Ar Isotopic Systematics of Lunar Meteorite Yamato-793169 <i>N. Torigoye, K. Misawa, G. B. Dalrymple, and M. Tatsumoto</i> .....	1437
Complex Ridged Terrain-Related Ridge Belts on Venus: Global Distribution and Classification <i>T. Törmänen</i> .....	1439
The Parent Magma of the Nakhla (SNC) Meteorite: Reconciliation of Composition Estimates from Magmatic Inclusions and Element Partitioning <i>A. H. Treiman</i> .....	1441
Intact Capture of Hypervelocity Particles on Shuttle <i>P. Tsou, D. E. Brownlee, and A. L. Albee</i> .....	1443
Photogeological Analysis of European Tectonic Features <i>B. R. Tufts</i> .....	1445
Is There Uniformitarian or Catastrophic Tectonics on Venus? <i>D. L. Turcotte</i> .....	1447
Impact-induced Devolatilization of $\text{CaSO}_4$ Anhydrite and Implications for K-T Extinctions: Preliminary Results <i>J. A. Tyburczy and T. J. Ahrens</i> .....	1449
Measurements of the Dielectric Properties of Simulated Comet Materials as Part of the KOSI 10 Experiment <i>S. Ulamec, H. Svedhem, and H. Kochan</i> .....	1451
Geology of Galileo Regio Quadrangle, Ganymede <i>J. R. Underwood Jr., R. Casacchia, A. Woronow, and M. J. Teeling</i> .....	1453
Reverse Polarity Magnetized Melt Rocks from the Chicxulub Impact Structure, Yucatán Peninsula, Mexico <i>J. Urrutia-Fucugauchi, L. E. Marin, V. L. Sharpton, and J. M. Quezada</i> .....	1455
On Modelling Nuclear Reactions in Meteorites <i>G. K. Ustinova and A. K. Lavrukhina</i> .....	1457
IMPS Albedo and Diameter for Asteroid 243 Ida <i>G. J. Veeder and E. F. Tedesco</i> .....	1459
Are the $\text{C}_8$ Light Nitrogen and Noble Gases Located in the Same Carrier? <i>A. B. Verchovsky, S. S. Russell, C. T. Pillinger, A. V. Fisenko, and Yu. A. Shukolyukov</i> .....	1461
Numerical Modeling of Impact Erosion of Atmospheres: Preliminary Results <i>A. M. Vickery</i> .....	1463



Comparison of Visible and Near-Infrared Reflectance Spectra of CM2 Carbonaceous Chondrites and Primitive Asteroids <i>F. Vilas, T. Hiroi, and M. E. Zolensky</i> .....	1465
Recondensation in the Early Solar System: Physical Conditions and Source Material <i>A. V. Vityazev, V. A. Dorofeyeva, and A. B. Makalkin</i> .....	1467
The Clementine Mission Science Return at the Moon and Geographos <i>R. W. Vorder Bruegge, M. E. Davies, D. M. Horan, P. G. Lucey, C. M. Pieters, A. S. McEwen, S. Nozette, E. M. Shoemaker, S. W. Squyres, and P. C. Thomas</i> .....	1469
Aluminum-26 Activities in Meteorites <i>J. F. Wacker</i> .....	1471
Rare Earth Elements in Individual Minerals in Shergottites <i>M. Wadhwa and G. Crozaz</i> .....	1473
Origin of High-Ti Lunar Ultramafic Glasses <i>T. P. Wagner and T. L. Grove</i> .....	1475
Rhenium-Osmium Isotope Systematics of Ordinary Chondrites and Iron Meteorites <i>R. J. Walker, J. W. Morgan, M. F. Horan, and J. N. Grossman</i> .....	1477
Diffusion-controlled Magnesium Isotopic Fractionation of a Single Crystal Forsterite Evaporated from the Solid State <i>J. Wang, A. M. Davis, A. Hashimoto, and R. N. Clayton</i> .....	1479
Limits on Differentiation of Melt "Sheets" from Basin-scale Lunar Impacts <i>P. H. Warren</i> .....	1481
Consortium Study of Lunar Meteorites Yamato-793169 and Asuka-881757: Geochemical Evidence of Mutual Similarity, and Dissimilarity vs. Other Mare Basalts <i>P. H. Warren and M. M. Lindstrom</i> .....	1483
Magnetic Record in Chondrite Meteorites <i>P. J. Wasilewski, J. L. Faris, and M. V. O'Bryan</i> .....	1485
AGB Stars as a Source of Short-lived Radioactive Nuclei in the Solar Nebula <i>G. J. Wasserburg, R. Gallino, M. Busso, and C. M. Raiteri</i> .....	1487
Multiplicity of Chondrule Heating Events and the Coarsening of Chondrule Textures <i>J. T. Wasson</i> .....	1489
Equilibrium and Fractional Crystallization of a Primitive Shergottite Composition <i>L. E. Wasylenski, J. H. Jones, L. Le, and A. J. G. Jurewicz</i> .....	1491
High D/H Ratios of Water in Magmatic Amphiboles in Chassigny: Possible Constraints on the Isotopic Composition of Magmatic Water on Mars <i>L. L. Watson, I. D. Hutcheon, S. Epstein, and E. M. Stolper</i> .....	1493

Arcuate and Circular Structures in the Tharsis Region: Evidence of Coronae on Mars <i>T. R. Watters, J. R. Zimbelman, and D. H. Scott</i>	1495
A Fresh Look at Crater Scaling Laws for Normal and Oblique Hypervelocity Impacts <i>A. J. Watts, D. R. Atkinson, S. R. Rieco, J. B. Brandvold, S. L. Lapin, and C. R. Coombs</i>	1497
Coagulation of Grains in Static and Collapsing Protostellar Clouds <i>S. J. Weidenschilling and T. V. Ruzmaikina</i>	1499
The Formation of FeO-rich Pyroxene and Enstatite in Unequilibrated Enstatite Chondrites: A Petrologic-Trace-Element (SIMS) Study <i>M. K. Weisberg, M. Prinz, R. A. Fogel, and N. Shimizu</i>	1501
Geology and Radiophysical Properties of the Venera and Vega Landing Sites <i>C. M. Weitz and A. T. Basilevsky</i>	1503
A Study of Carbonates, Sulfates, and Phosphates Using Thermal Emission Spectroscopy <i>M. L. Wenrich and P. R. Christensen</i>	1505
Weathering Features and Secondary Minerals in Antarctic Shergottites ALHA77005 and LEW88516 <i>S. J. Wentworth and J. L. Gooding</i>	1507
Petrology and Geochemistry of VLT Glasses from Double Drive Tube 79001/2 <i>S. J. Wentworth, D. J. Lindstrom, R. R. Martinez, and D. S. McKay</i>	1509
Variety in Planetary Systems <i>G. W. Wetherill</i>	1511
Elevation and Igneous Crater Modification on Venus: Implications for Magmatic Volatile Content <i>R. W. Wichman</i>	1513
Large Floor-fractured Craters and Isostatic Crater Modification: Implications for Lithospheric Thickness on Venus <i>R. W. Wichman and P. H. Schultz</i>	1515
Degradation Sequence of Young Lunar Craters from Orbital Infrared Survey <i>M. A. Wieczorek and W. W. Mendell</i>	1517
A Long-Term Change of the Ar/Kr/Xe Fractionation in the Solar Corpuscular Radiation <i>R. Wieler, H. Baur, and P. Signer</i>	1519
Multispectral Studies of Selected Crater- and Basin-filling Lunar Maria from Galileo Earth-Moon Encounter 1 <i>D. A. Williams, R. Greeley, G. Neukum, and R. Wagner</i>	1521
Equilibrium Models of Mass Distribution and Collisional Lifetimes of Asteroids <i>D. R. Williams and G. Wetherill</i>	1523

Formation of Perched Lava Ponds on Basaltic Volcanoes: Interaction Between Cooling Rate and Flow Geometry Allows Estimation of Lava Effusion Rates <i>L. Wilson and E. A. Parfitt</i> .....	1525
A Classification Scheme for the Morphology of Lava Flow Fields <i>L. Wilson, H. Pinkerton, J. W. Head, and K. Magee Roberts</i> .....	1527
CERN-derived Analysis of Lunar Radiation Backgrounds <i>T. L. Wilson and R. Svoboda</i> .....	1529
Multivariate Statistical Analysis: Principles and Applications to Coorbital Streams of Meteorite Falls <i>S. F. Wolf and M. E. Lipschutz</i> .....	1531
Characterization of the Marquez Dome Buried Impact Crater Using Gravity and Magnetic Data <i>A. M. Wong, A. M. Reid, S. A. Hall, and V. L. Sharpton</i> .....	1533
Morphologic Classes of Impact Basins on Venus <i>C. A. Wood and W. Tam</i> .....	1535
LREE Variability in CM Matrices: Another Look at Meteorite "Compaction Ages" <i>D. S. Woolum, K. Poelstra, C. Alexander, and T. Ireland</i> .....	1537
The Carbon Components in SNC Meteorites of Feldspathic Harzburgite Composition <i>I. P. Wright, C. Douglas, and C. T. Pillinger</i> .....	1539
Further Carbon Isotope Measurements of LEW 88516 <i>I. P. Wright, C. Douglas, and C. T. Pillinger</i> .....	1541
Shock Attenuation at the Slate Islands Revisited <i>S. Wu, P. B. Robertson, and R. A. F. Grieve</i> .....	1543
Convex Set and Linear Mixing Model <i>P. Xu and R. Greeley</i> .....	1545
Stable Ni Isotopes and $^{10}\text{Be}$ and $^{26}\text{Al}$ in Metallic Spheroids from Meteor Crater, Arizona <i>S. Xue, G. F. Herzog, G. S. Hall, J. Klein, R. Middleton, and D. Juenemann</i> .....	1547
Geometrical Analysis of the Microcraters Found on LDEF Samples <i>K. Yamakoshi, H. Ohashi, M. Noma, H. Sakurai, K. Nakashima, K. Nogami, and R. Omori</i> .....	1549
Antipodal Fragment Velocities for Porous and Weak Targets at Catastrophic Impacts <i>M. Yanagisawa and T. Itoi</i> .....	1551
Regolith Breccia Consisting of H and LL Chondrite Mixture <i>K. Yanai and H. Kojima</i> .....	1553

Consortium Reports on Lunar Meteorites Yamato 793169 and Asuka 881757, a New Type of Mare Basalt <i>K. Yanai, H. Takeda, M. M. Lindstrom, M. Tatsumoto, N. Torigoe, K. Misawa, P. H. Warren, G. W. Kallemeyn, C. Koeberl, H. Kojima, K. Takahashi, A. Masuda, and K. Nishiizumi</i> .....	1555
Preliminary AEM Study of the Microstructure and Composition of Metal Particles in Ordinary Chondrites <i>C. W. Yang, D. B. Williams, and J. I. Goldstein</i> .....	1557
Micrometeorite Pre-Solar Diamonds from Greenland Cryoconite? <i>P. D. Yates</i> .....	1559
The Connection Between Venus' Free Obliquity and Its CMB Oblateness <i>C. F. Yoder</i> .....	1561
Trace Element Compositions of Spinel-rich Refractory Inclusions from the Murchison Meteorite <i>S. Yoneda, P. J. Sylvester, S. B. Simon, L. Grossman, and A. Hsu</i> .....	1563
Inter- and Intra-Crystalline Oxygen Isotope Distribution of Fassaite in Allende CAI <i>H. Yurimoto, H. Nagasawa, and Y. Mori</i> .....	1565
Age and Thermochronology of K-Feldspars from the Manson Impact Structure <i>P. K. Zeitler and M. J. Kunk</i> .....	1567
Spectral Analysis of Chemisorbed CO <sub>2</sub> on Mars Analog Materials <i>A. P. Zent and T. L. Roush</i> .....	1569
Lewis Cliff 87057: A New Metal-rich E3 Chondrite with Similarities to Mt. Egerton, Shallowater and Happy Canyon <i>Y. Zhang, P. H. Benoit, and D. W. G. Sears</i> .....	1571
Chemical Zoning and Diffusion of Ca, Al, Mn, and Cr in Olivine of Springwater Pallasite <i>Y. Zhou and I. M. Steele</i> .....	1573
Comparison of Flank Modification on Ascræus and Arsia Montes Volcanoes, Mars <i>J. R. Zimbelman</i> .....	1575
Numerical Simulation of Lava Flows; Applications to the Terrestrial Planets <i>J. R. Zimbelman, B. A. Campbell, J. Kousoum, and D. J. Lampkin</i> .....	1577
Chemical Composition of New Acapulcoites and Lodranites <i>J. Zipfel and H. Palme</i> .....	1579
Diffuse Reflectance Spectra of Orthopyroxene, Olivine, and Plagioclase as a Function of Composition and Structure <i>M. E. Zolensky, L. Le, C. Galindo, R. Morris, V. Lauer, and F. Vilas</i> .....	1581
Mineralogy of Dark Clasts in Primitive vs. Differentiated Meteorites <i>M. E. Zolensky, M. K. Weisberg, R. A. Barrett, and M. Prinz</i> .....	1583

<b>K, U, and Th Behavior in Martian Environmental Conditions</b> <i>M. Yu. Zolotov, T. V. Krot, and L. V. Moroz</i> .....	1585
<b>On Dust Emissions from the Jovian System</b> <i>H. A. Zook, E. Grün, M. Baguhl, A. Balogh, S. J. Bame, H. Fechtig, R. Forsyth, M. S. Hanner, M. Horanyi, J. Kissel, B.-A. Lindblad, D. Linkert, G. Linkert, I. Mann, J. A. M. McDonnell, G. E. Morfill, J. L. Phillips, C. Polanskey, G. Schwehm, N. Siddique, P. Staubach, J. Svestka, and A. Taylor</i> .....	1587
<b>Wrinkle Ridges, Reverse Faulting, and the Depth Penetration of Lithospheric Stress in Lunae Planum, Mars</b> <i>M. T. Zuber</i> .....	1589
<b>Possible Flexural Signatures Around Olympus and Ascraeus Montes, Mars</b> <i>M. T. Zuber, B. G. Bills, H. V. Frey, W. S. Kiefer, R. S. Nerem, and J. H. Roark</i> .....	1591
<b>Author Index</b> .....	lix
<b>Sample Index</b> .....	lxxii
<b>Meteorite Index</b> .....	lxxiii
<b>Keyword Index</b> .....	lxxviii

5

163300

## Preface

This volume contains abstracts accepted by the Program Committee of the Twenty-Fourth Lunar and Planetary Science Conference.

The Program Committee was co-chaired by Douglas Blanchard (*NASA Johnson Space Center*) and David Black (*Lunar and Planetary Institute*); other members were Bruce Bohor (*U.S. Geological Survey, Denver*), Roger G. Burns (*Massachusetts Institute of Technology*), Bruce Campbell (*Smithsonian Institution*), Deborah Domingue (*Lunar and Planetary Institute*), Charles Hohenberg (*Washington University*), Lindsay P. Keller (*NASA Johnson Space Center*), Marilyn M. Lindstrom (*NASA Johnson Space Center*), Glenn MacPherson (*Smithsonian Institution*), Renu Malhotra (*Lunar and Planetary Institute*), Kurt Marti (*University of California, San Diego*), Gordon McKay (*NASA Johnson Space Center*), David Mittlefehldt (*Lockheed EMSCO*), Scott Murchie (*Lunar and Planetary Institute*), Larry Nyquist (*NASA Johnson Space Center*), William Phinney (*NASA Johnson Space Center*), Jeff Plescia (*Jet Propulsion Laboratory*), Frank A. Podosek (*Washington University*), Ben Schuraytz (*Lunar and Planetary Institute*), Virgil L. Sharpton (*Lunar and Planetary Institute*), Tomasz Stepinski (*Lunar and Planetary Institute*), Ellen R. Stofan (*Jet Propulsion Laboratory*), Paul Warren (*University of California, Los Angeles*), and Michael Zolensky (*NASA Johnson Space Center*).

Papers are arranged alphabetically by the last name of the first author. There are four indexes: authors, lunar sample numbers, meteorites, and keywords.

This abstract volume was compiled through the efforts of the Publications Services Department of the Lunar and Planetary Institute. Eleta Malewitz and Jackie Lyon provided computer service support to the preparation efforts.

Logistics and administrative support for the conference were provided by the staff of the Program Services Department, Lunar and Planetary Institute.

456160

2P

N94-12016  
56-90  
163221

P-2

**MÖSSBAUER SPECTROSCOPY OF THE SNC METEORITE ZAGAMI.**

D.P. Agerkvist and L. Vistisen, Niels Bohr Institute, Blegdamsvej 17, DK-2100 Copenhagen Ø, Denmark

We have performed Mössbauer spectroscopy on two different pieces of the meteorite Zagami belonging to the group of SNC meteorites. In one of the samples we found a substantial amount of olivine intergrown with one kind of pyroxene, and also another kind of pyroxene very similar to the pyroxene in the other sample we examined. Both samples showed less than 1 % of  $\text{Fe}^{3+}$  in the silicate phase.

The group of SNC meteorites called shergottites, to which Zagami belongs, are achondrites whose texture, mineralogy and composition resembles those of terrestrial diabases [1].

We have performed Mössbauer spectroscopy on various specimens from Zagami. The first sample we studied was obtained from British Museum (sample BM 1966, 54) and the second sample from the firm David New, Anacortes, Washington (sample DN). A small part of each sample was gently crushed to give material for the Mössbauer absorbers.

The figures 1a and 1b show Mössbauer spectra of whole rock absorbers, i.e. no separation of minerals, from the BM sample and the DN sample, respectively. Using a low-magnification optical microscope two different looking types of silicates were separated from the crushed material of the DN sample and used as Mössbauer absorbers. One of the separates was grey-green, intergrown grains, the other was clear green, larger single crystals. In Fig. 1c and 1d the Mössbauer spectra of the two different silicates from the DN sample are shown.

The two spectra in Fig. 1a and 1b are clearly different even though both are recorded on whole rock samples from Zagami. In Fig. 1a we see pyroxene only, but in Fig. 1b we see both olivine and pyroxene and a little amount of ilmenite (at about 0.7 and 1.4 mm/s). This is a surprising result that has been reported previously [2].

The spectrum of the clear green, single crystals from the DN sample in Fig. 1d consists of lines from pyroxene only. This pyroxene resembles the pyroxene from the BM sample (Fig. 1a) extremely well, the Mössbauer parameters are identically and the site distribution is almost the same. The spectrum of the grey-green, intergrowth in Fig. 1c consists of lines from both pyroxene and olivine. The amount of Fe from olivine compared to Fe from pyroxene is 60:40. The pyroxene has the same Mössbauer parameters as the clear green, single crystals, but another site distribution. Our conclusion is that in the DN sample of Zagami we find two sorts of pyroxene, one very similar to the pyroxene in the BM sample of Zagami and the other differing and being intergrown with olivine.

$\text{Fe}^{3+}$  in silicates has two lines, lying at about 0.1 and 0.7 mm/s. The line at 0.1 mm/s will be hidden in the pyroxene lines, but the line at 0.7 mm/s should be seen clearly. From this we can say that all the spectra of Zagami show less than 1 % of  $\text{Fe}^{3+}$  in the silicates. This is slightly less than has been reported for the SNC meteorite Nakhla [3]

# MÖSSBAUER SPECTROSCOPY OF ZAGAMI: D.P. Agerkvist and L. Vistisen.

and much less than normally is seen in terrestrial silicates. Anyhow, the presence of titanomagnetite in both Zagami and Nakhla (even though very different [4]) shows that the SNC meteorites are more oxidized than the basaltic achondrites.

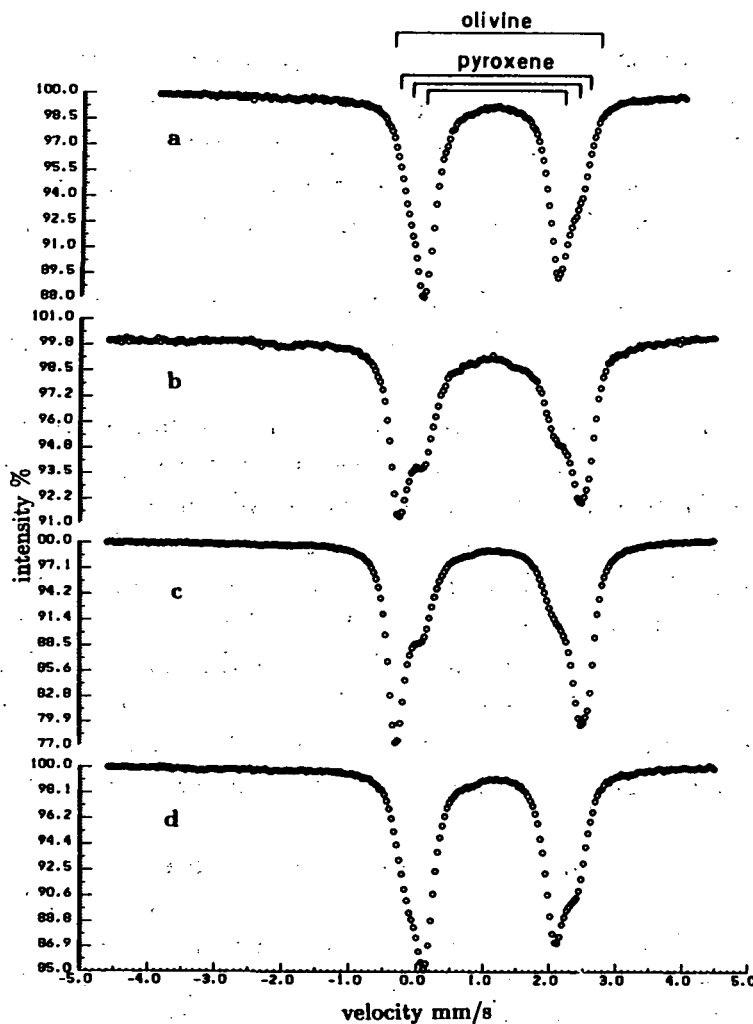


Figure 1: Room temperature Mössbauer spectra of Zagami a: BM sample, b: DN sample, c: intergrowth of pyroxene and olivine from DN sample, d: pyroxene from DN sample.

## References

- [1] McSween Jr. H.Y., (1985) *Rev. Geophys.* 23, 391.
- [2] Vistisen L., Petersen D. and Madsen M.B. (1992) *Phys. Scr.* 46, 94.
- [3] Knudsen J.M., Madsen M.B. and Vistisen L. (1991) *The Environmental Model of Mars. Proc. of the 2nd COSPAR Colloquium, Sopron, Hungary, 22-26 January 1990.* K Szegő (Ed.). (Pergamon Press, Oxford) 7.
- [4] Madsen M.B., Olsen M., Knudsen J.M., Petersen D. and Vistisen L. (1992) *Lunar Planet. Sci. Conf. XXIII*, 825.

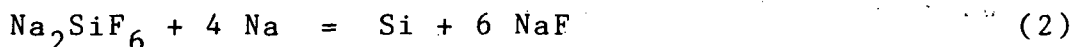


456161  
2P  
32-91  
AB-104-12017  
163222 P. 25

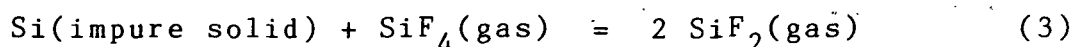
PRODUCTION OF ELECTRONIC GRADE LUNAR SILICON BY  
DISPROPORTIONATION OF SILICON DIFLUORIDE, William N. Agosto,  
Lunar Industries, P.O. Box 590004, Houston, TX 77259-0004

Waldron (1) has proposed to extract lunar silicon by sodium reduction of sodium fluorosilicate derived from reacting sodium fluoride with lunar silicon tetrafluoride. Silicon tetrafluoride is obtained by the action of hydrofluoric acid on lunar silicates. While these reactions are well understood, the resulting lunar silicon is not likely to meet electronic specifications of 5 nines purity. Dale and Margrave (2) have shown that silicon difluoride can be obtained by the action of silicon tetrafluoride on elemental silicon at elevated temperatures (1100-1200 C) and low pressures (1-2 torr). The resulting silicon difluoride will then spontaneously disproportionate into hyperpure silicon and silicon tetrafluoride in vacuum at approximately 400 C. On its own merits, silicon difluoride polymerizes into a tough waxy solid in the temperature range from liquid nitrogen to about 100 C. It is the silicon analog of teflon. Silicon difluoride ignites in moist air but is stable under lunar surface conditions and may prove to be a valuable industrial material that is largely lunar derived for lunar surface applications.

The most effective driver for lunar industrialization may be the prospects for industrial space solar power systems in orbit or on the moon that are built with lunar materials. Such systems would require large quantities of electronic grade silicon or compound semiconductors for photovoltaics and electronic controls. Since silicon is the most abundant semimetal in the silicate portion of any solar system rock (approximately 20 wt%), lunar silicon production is bound to be an important process in such a solar power project. Lunar silicon can be extracted (1) as follows:



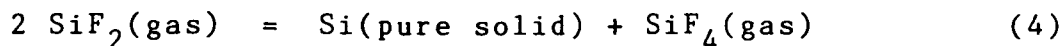
Reactions (1) and (2) are components of a hydrofluoric acid (HF) process for digestion of lunar soils that can extract all the major lunar metals except calcium, separate all the major lunar oxides, and generate lunar oxygen (1,3). Both reactions proceed at about 700 C and (2) is self sustaining once ignited (4). However the product silicon is likely to contain unacceptable levels of sodium impurity for electronic applications. That can be addressed by reacting the silicon with  $\text{SiF}_4$  at 1100 - 1200 C and pressures below a few torr to obtain  $\text{SiF}_2$  (2) as follows:



As a gas,  $\text{SiF}_2$  has a lifetime of approximately 150 sec but

W.N. Agosto

it can be condensed to a reddish brown polymer-(SiF<sub>2</sub>)<sub>x</sub>-in liquid nitrogen which converts to a tough white waxy solid at room temperature. SiF<sub>2</sub> ignites spontaneously in air but is stable in vacuum. And it can be disproportionated at 400 C in vacuum to yield hyperpure silicon and SiF<sub>4</sub> by the reverse of reaction (3):



Minor perfluorosilanes of the form --Si<sub>n</sub>F<sub>2n+2</sub>-- are also generated by the disproportionation. Gaseous products in (4) can be recycled to (3).

Reaction (3) and its reverse can of course be used to purify silicon extracted by any process such as carbon or aluminum reduction of silica. Hydrogen reduction of SiF<sub>4</sub> is another approach to silicon extraction. While it is very unfavorable thermodynamically (3), the reduction may proceed by electric discharge or the excitation of hydrogen plasma (5) and could produce silicon as pure as the product of reaction (4). Alternatively, hydrogen reduced silicon can be purified by the disproportionation of SiF<sub>2</sub>.

Silica and aluminum, as well as SiF<sub>4</sub> and hydrogen, are products of the lunar HF process. Accordingly, fluoride processing makes lunar silicon abundantly available. In addition, significant quantities of fluorine may be available on the moon. Phosphates are widely disseminated in the lunar samples, up to one modal percent in KREEP rocks and soils. Further, a large fraction of lunar phosphates are fluorine rich apatites, some exceeding 3% F (6). Such phosphates can be beneficiated by dry electrostatic processes (7) and could become substantial sources of lunar halogens.

## REFERENCES

1. Waldron R.D. (1985) Space Manufacturing 5, AIAA, Washington, DC. p. 132-149.
2. Dale L.P and Margrave J.L. (1976) J. Chem. Education, V. 53, N. 11, p. 696-699.
3. Agosto W.N. (1992) Engineering, Construction, and Operations in Space III, Space 92, Amer. Soc. of Civil Engrs., New York, p. 678-689.
4. Kapur, Nanis, and Sanjurjo (1979) Paper 60, 155th Meeting of Electrochem. Soc.
5. Kretschmer K-H et al. (February 1990) Solid State Technology, p. 53-55.
6. Heiken G. et al. (1991) Lunar Sourcebook, A Users Guide to the Moon, Cambridge U. Press, New York.
7. Fraas F. (1962) Electrostatic Separation of Granular Materials, B 603, Bureau of Mines.

456/62  
2P

53-91  
ABS-ONLY

N 94-12018  
163223

**RATES OF FLUVIO-THERMAL EROSION ON MARS. J. Aguirre-Puente<sup>(1)</sup>**

F.M. Costard<sup>(2)</sup>, and R. Posado-Cano<sup>(1)</sup>. <sup>(1)</sup> Laboratoire d'Aérothermique (UP 1301), CNRS, Meudon, France. <sup>(2)</sup> Centre de Géomorphologie (UPR A4501), CNRS, Caen, France.

On Mars, most of the outflow channels start from chaotic terrains and exhibit a rather straight valley of 1500 km long and 25 km large with few tributaries. Different interpretations of these outflow channels have been proposed. Lucchitta (1) considers them as possible glacial valleys, and Komar (2) proposed some comparisons with submarine rivers. Carr (3) suggests that these valleys were produced by catastrophic release of water from confined aquifers and Baker (4) considers them as highly turbulent catastrophic floods. In order to take into account the cold climate conditions of Mars, the presence of ground-ice and the large scale of outflows, a thermal erosion was first proposed by Costard (5). From a quantitative point of view, three thermal mathematical models were analyzed and discussed by Aguirre-Puente et al. (6).

In Arctic regions, thermal erosion is considered as the result of the ground thawing produced by the heat exchange between the water flow and ground-ice followed by a transport of sediments. On the basis of direct geomorphic evidence (Are, 7), rates of thermal erosion, in various parts of Siberian river banks, are on the order of 15 to 25 m per year.

By analogy with Arctic regions, it is reasonable to assume that the rate of thermal erosion, for Martian outflow channels, is far more efficient than the rate of fluvial erosion. The interesting case for our Martian model is a hypothetical situation where ground-ice exists with the presence of liquid water to the surface. In such a case, short duration Martian outflow channels are believed to have survived under cold climatic conditions and produced thermal erosion against frost banks.

In order to get some ideas about the order of magnitude of fluvio-thermal recession rate, a mathematical thermal model for Martian outflow channels is proposed. This model corresponds to a system undergoing a permanent thermal regime where the surface temperature is constant and equal to the phase change temperature (due to the immediate removal of melted materials). This is an ablation model. For its application, estimations of the heat transfer coefficient  $h$ , and thermal flux  $q$  are necessary. Determination of these coefficients needs the calculation of dimensionless numbers (Reynolds, Prandtl, Nusselt), and the consideration of turbulent regime of the flow.

For estimations, the following parameters are considered:

Water temperature:  $T = 5^{\circ}\text{C}$  and  $T = 1^{\circ}\text{C}$

Ground-ice temperature:  $t = 0^{\circ}\text{C}$

River cross section: 10 km

River discharge:  $Q = 3.86 \cdot 10^4 \text{ m}^3 \text{ s}^{-1}$

Velocity of the water:  $v = 0.4 \text{ m s}^{-1}$

Reynolds number:  $Re = 3 \cdot 10^5$

Nusselt number:  $Nu = 1562$

Prandtl number:  $Pr = 11.19$  (for water at  $5^{\circ}\text{C}$ )

Thermal conductivity of the frozen soil:  $k = 0.57 \text{ W m}^{-1} \text{ K}^{-1}$

Heat transfer coefficient:  $h = 780 \text{ W m}^{-2} \text{ K}^{-1}$

Thermal flux:  $q = 3900 \text{ W m}^{-2}$  for  $\Delta T = 5 \text{ K}$ ,  $780 \text{ W m}^{-2}$  for  $\Delta T = 1 \text{ K}$ .

For such a model, it is assumed that the surface keeps a constant melting temperature, and that the thermal flux is constant. For ground characteristics, two different soil porosities are

# FLUVIO-THERMAL EROSION: Aguirre-Puente, J. et al.

considered: 80% and 40% (the pores being filled with ice). With these assumptions, thermophysical properties are calculated:

Porosity $\epsilon$ :	0.4	0.8
Density $\beta$ :	$2.04 \cdot 10^3 \text{ kg m}^3$	$1.347 \cdot 10^3 \text{ kg m}^3$
Specific Heat $c_p$ :	$1.453 \cdot 10^3 \text{ J kg}^{-1} \text{ K}^{-1}$	$8 \cdot 10^3 \text{ J m}^{-1} \text{ K}^{-1}$
Thermal conductivity $k$ :	$1.572 \text{ W m}^{-1} \text{ K}^{-1}$	$0.6941 \text{ W m}^{-1} \text{ K}^{-1}$
Thermal diffusivity $\mu$ :	$0.5303 \cdot 10^{-6} \text{ m}^2 \text{ s}^{-1}$	$0.184 \cdot 10^{-6} \text{ m}^2 \text{ s}^{-1}$
Latent Heat $L$ :	$6.52 \cdot 10^4 \text{ J kg}^{-1}$	$1.98 \cdot 10^5 \text{ J kg}^{-1}$

The results obtained from the application of the ablation model give some interesting informations about the recession banks on Martian outflow channels. From the figure 1, rates of fluvio-thermal erosion are on the order of 22 m and 35 m, for one Martian month with  $\Delta = 1\text{K}$ , respectively for soil porosities' 0.8 and 0.4.

These values confirm that thermal erosion might be a strong sapping process along Martian outflow channels. As for Siberian rivers, the interaction between thermal and mechanical processes during thousand of years might contribute to the formation of large Martian outflow channels.

Our model of fluvio-thermal erosion needs some modifications to bring it closer to the reality. In order to take into account interaction between thermal processes and mechanical erosion for both one-dimensional and two-dimensional models, a research program is proposed.

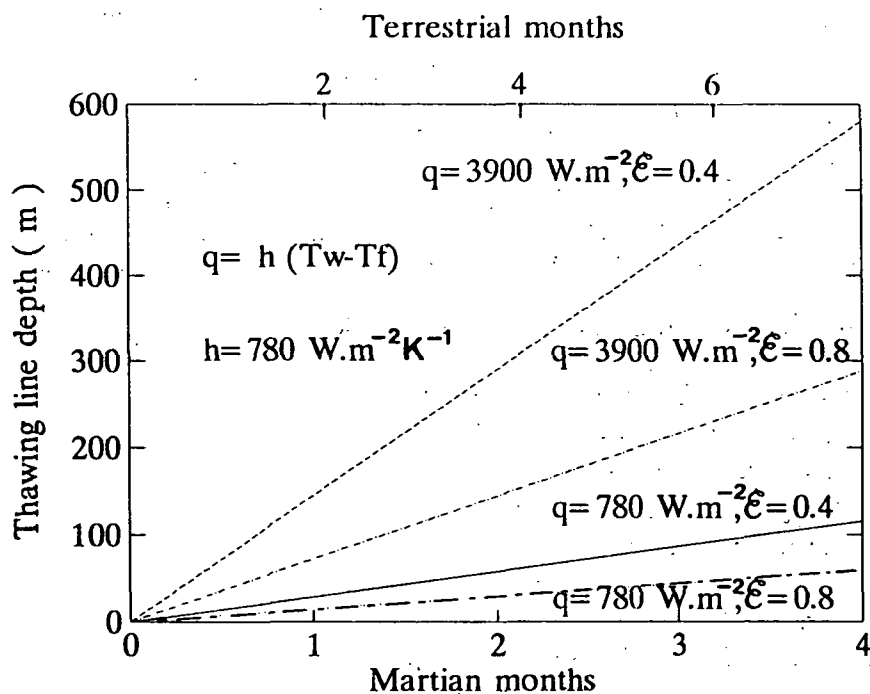


fig 5. Ablation model for short period

References: (1) Lucchitta B.K. (1982) *JGR*, 87, 9951. (2) Komar P.D. (1979) *Icarus*, 34, 156. (3) Carr M. (1979) *JGR*, 84, 2995. (4) Baker V.R. (1982) *The channels of Mars*, Univ. of Texas, Austin. (5) Costard F.M. (1989) *LPSC XX*, 189. (6) Aguirre-Puente J., Costard F.M. and Posado-Cano R. (1990). *LPSC XXI*, 7. (7) Are F.E. (1983) Proc. In *4th Int. Conf. on Permafrost*, 24.

*This work received a financial support from P.N. Planetology, I.N.S.U.*

456163

54-91

ABS ONLY

LPSC XXIV

7

N94-12019

**GIANT IMPACT-INDUCED ATMOSPHERIC BLOW-OFF; Thomas J. Ahrens, Lindhurst**  
 Laboratory of Experimental Geophysics, Seismological Laboratory 252-21, California Institute of  
 Technology, Pasadena, CA 91125.

How are the present atmospheres of the Earth, Venus, and Mars related to the earliest (primordial) atmospheres which surrounded these planets? Recent modeling of the accretion of the planets from a swarm of planetesimals orbiting the early sun demonstrates that smaller planetesimals gained specific kinetic energy at the expense of the larger planetesimals [1, 2]. As a result, runaway impact accretion and growth occurred for marginally larger objects such that in  $\sim 10^5$  years some of the  $10^{24}$  g objects grew to  $10^{26}$  g. Mutual impact of lunar and Mars size objects resulted in a series of "large body" impacts during the latter stages of accretion. Assuming the composition of the planetesimals are similar to the primitive meteorites, Lange and Ahrens [3] showed that after the Earth and Venus accreted to about 0.1 of their present mass, the volatiles ( $H_2O$ ,  $CO_2$ ,  $SO_2$ ,  $NH_3$ ,  $CH_4$  + noble gases) within the later impacting planetesimals became vaporized and produced the giant primordial atmospheres overlying a magma ocean [4] which remained during the completion of the accretion. The termination of the co-accretion of an atmosphere results from at least three different mechanisms;

(1) As the accretion rate decreased, the impact energy flux at the base of the atmosphere decreased and gradually solar heating dominated over impact heating. Surface temperatures then declined below the melting point of hydrous basalt, water condenses and forms planetary oceans.

(2) Atmospheric loss occurs via multiple impact erosion, where  $\sim 10^0$  -  $10^2$  km diameter planetesimals drove off  $\sim 10^{-3}$  to  $\sim 10^{-4}$  of the total atmosphere per event [5, 6, 7, 8, 9, 10].

Previously, Cameron [11] and Ahrens [12] considered some aspects of the effects of giant body impact on the Earth's atmosphere. To calculate the energy, and hence, approximate planetesimal size, such that upon impact the entire planetary atmosphere is blow off, I employ a different approach than previous efforts and consider a shock wave that is entirely propagated within a terrestrial planet as sketched in Fig. 1.

A key calculation is to relate the particle velocity of the solid planet-atmosphere interface,  $u_{fs}$ , antipodal to a major impact, to the atmospheric free-surface velocity,  $v_e$ , which will result from being shocked first by the moving solid planet and then isentropically released into space upon reflection of the shock wave at the effective top of the atmosphere (Fig. 2). This results in gas speeds greater than the escape velocity. The shock-induced outward atmospheric velocity,  $u_e$ , is given by:  $u_e = |u_{fs}| + u_r$ , where  $|u_{fs}|$  is the velocity of the planetary surface-atmosphere interface and  $u_r$  is the additional velocity achieved by the atmosphere upon reflection of the shock at the top of the atmosphere as sketched in Fig. 2 [13]. When  $u_e$  exceeds the planetary escape velocity, the atmosphere is considered blown-off. In a case of  $\gamma = 1.1$  to 1.3, antipodal outward rock velocities of 1.6 to 2.3 km/sec, 1 to 2.5 km/sec and 0.3 to 1.2 km/sec for the Earth, Venus, and Mars are required for this atmospheric ejection. Here  $\gamma$  is the polytropic exponent. What impact energies,  $E_{fs}$ , will produce these outward rock velocities for the terrestrial planets?

The strength of the shock-wave induced compressional wave which results upon propagation completely through planets with varying iron core sizes overlain by silicate mantles has been recently calculated for objects with core to planetary radius ratios of 0.33 and 0.47 [14]. Upon scaling Watts' calculation values of  $E_{fs} = 6$  to  $18 \times 10^{37}$  ergs are obtained for  $\gamma = 1.1$  and 1.3 in the case of the Earth, respectively. This compares to  $\sim 10^{37}$  ergs obtained earlier [12] using Hughes et al.'s [15]. calculation. For Venus,  $E_{fs} = 2$  to  $12 \times 10^{36}$  ergs and for Mars,  $E_{fs} = 3$  to  $57 \times 10^{34}$  ergs are required for complete blow-off (Fig. 3). These energies correspond to impact of projectiles in the radius range of  $10^2$  to  $10^3$  km. Impact energies corresponding to antipodal (Rayleigh) wave atmospheric excitation yield similar estimates of impact energies. It appears likely that the terrestrial planetary atmospheres were subjected to multiple partial to complete blow-offs and the present atmospheres represent the result of the last stages of accretion and possible subsequent endogenic modification.

## GIANT IMPACT-INDUCED ATMOSPHERIC BLOW-OFF; Ahrens, T. J.

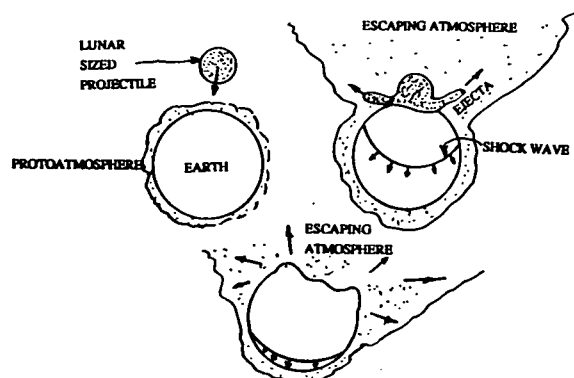


Fig. 1. Sketch of a giant planetesimal impact the Earth.

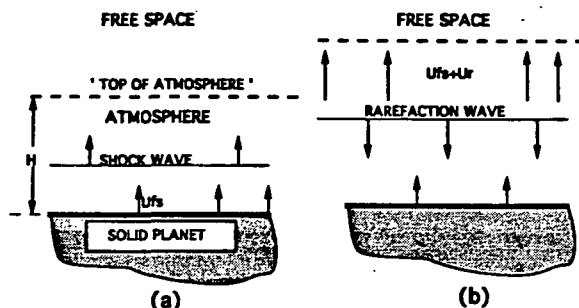


Fig. 2. Sketch of shock- and rarefaction wave-induced motion of atmosphere being driven by planetary free-surface velocity,  $u_s$ . Atmosphere geometry is approximated by a layer of scale height,  $H$ . (a) shock wave driven particle velocity,  $u_s$ . (b) increase of gas velocity to  $u_s + u_r$  upon "reflection" of shock at the "top of atmosphere."

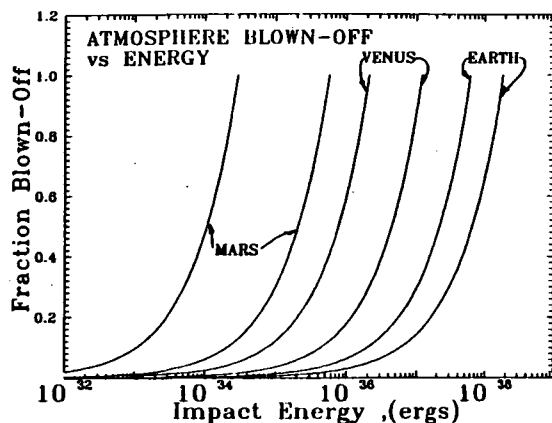


Fig. 3. Calculated fraction of atmosphere blown-off versus impactor energy for Earth, Venus, and Mars. Lower and higher energy curves for each planet corresponds to assumed polytropic exponent of ideal gas of  $\gamma = 1.1$  and  $1.3$ , respectively.

## REFERENCES:

- 1Stewart G. R. and Kaula W. M. (1980) *Icarus*, 44, 154-71.
- 2Stewart G. R. and Wetherill G. W. (1988) *Icarus*, 74, 542-53.
- 3Lange M. A. and Ahrens T. J. (1984) *Earth Planet. Sci. Lett.*, 71, 111-119.
- 4Abe Y. and Matsui T. (1985) *Proc. Lunar Planet. Sci. Conf. 15th, Part 2, J. Geophys. Res.*, 90, C545-C559.
- 5Jones E. M. and Kodis J. W. (1982) in *Geological Implications of Impacts of Large Asteroids and Comets on the Earth* (Silver L. T. and Schultz P. H., eds.), pp. 175-186. Geol. Soc. Amer. Special Paper, 6.
- 6Ahrens T. J. and O'Keefe J. D. (1987) *Proc. Hypervelocity Impact Symp., Int. J. Impact Engng.*, 5, 13-32.
- 7Ahrens T. J., et al. (1989) in *Origin and Evolution of Planetary and Satellite Atmospheres* (Atreya S. K., et al., eds.), pp. 328-385. University of Arizona Press, Tucson, AZ.
- 8Melosh H. J. and Vickery A. M. (1989) *Nature*, 338, 487-489.
- 9Vickery A. M. and Melosh H. J. (1990) in *Global Catastrophes in Earth History* (Sharpton V. L. and Ward P. O., eds.), pp. 289-300. Geol. Soc. Am. Sp. Paper, 10.
- 10Zahnle K. J. (1992) *J. Geophys. Res.*, 97, 10243-10255.
- 11Cameron A. G. W. (1983) *Icarus*, 56, 195-201.
- 12Ahrens T. J. (1990) in *Origin of the Earth* (Jones J. and Newsom H., eds.), pp. 211-227. Oxford U. Press, Houston, TX.
- 13Ahrens T. J. (1993) *Ann. Rev. Earth Planet. Sci.*, in press.
- 14Watts A. W., et al. (1991) *Icarus*, 93, 159-168.
- 15Hughes H. G., et al. (1977) *Phys. Earth and Planet. Int.*, 15, 251-263.

456190

55-90

2P

ABS ONLY

LPSC XXIV

N94-12020

DISPERSION OF THE RATIOS OF COSMOGENIC ISOTOPES OF NOBLE GASES IN CHONDRITES OF DIFFERENT COSMIC-RAY EXPOSURE AGES. V.A.Alexeev. V.I.Vernadsky Inst. of Geochem. and Analyt. Chem., Russian Academy of Sciences, Moscow, Russia

The dispersion of ratios of  $(\text{He-3}/\text{Ne-21})_c$  and  $(\text{Ne-22}/\text{Ne-21})_c$  depending on the cosmic-ray exposure ages of meteorites is analysed. The dispersion is increased at decrease of age. This effect may be stipulated by presence of more significant portion of meteorites of small preatmospheric sizes among meteorites of small radiation ages in comparison to meteorites of higher exposure age.

We have analysed the distributions of the ratios of cosmogenic isotopes of  $(\text{He-3}/\text{Ne-21})_c$  and  $(\text{Ne-22}/\text{Ne-21})_c$  in about 800 non-Antarctic (falls and finds) and Antarctic H and L chondrites depending on the cosmic ray exposure ages of meteorites. The noble gas data are from [1]. Contents of cosmogenic components were calculated by conventional procedure. The exposure ages were calculated for production rates of He-3, Ne-21, and Ar-38 according to [2] with correction of Ar-38 production rate [3].

We can see (Fig 1) the increase of dispersion at decrease of exposure age of meteorites. This regularity is the most well-defined for Antarctic H chondrites.

For quantitative estimation of this effect we divided each group of N meteorites on several subgroups with identical numbers of meteorites of  $n \geq 10$  (in Fig 1,  $n=11$ ). For every subgroup it was calculated the dispersion of  $S_i^2 = (\sum y_i^2 - (\sum y_i)^2/n)/(n-1)$ , where  $y_i$  are values of  $(\text{He-3}/\text{Ne-21})_c$  or  $(\text{Ne-22}/\text{Ne-21})_c$  ratios,  $i=1,2,\dots,n$ . Then we calculated the dispersion of all points:  $S^2 = (\sum y_i^2 - (\sum y_i)^2/N)/(N-1)$ ,  $i=1,2,\dots,N$ , determined the values of  $\alpha_i = S_i^2/S^2$  and constructed the dependence of  $\lg \alpha_i$  vs. average logarithm of age of  $(\lg T)_{av,i}$  in subgroup. The values of the coefficient "b" in equation of line of  $\lg \alpha = a + b(\lg T)_{av}$  were determined according to [4]. Such dependence is shown in Fig 2 for distribution shown in Fig 1. The values of the coefficient of "b" are given in the Table for all investigated groups of chondrites. The "-" sign of "b" coefficient means the increase of dispersion at decrease of age; the magnitude of "b" defines the significance of this effect. We can see all values of "b" is less of zero for non-Antarctic falls and Antarctic meteorites and exceed in the most cases the values of standard deviations (10) especially for H chondrites. For non-Antarctic finds this effect is manifested not for all cases; it may be stipulated by superposition of process of weathering [3].

The considered effect may be understood in the framework of model according to which meteorites may be fragments of main-belt asteroids, derived by cratering collisions [5-7]. In this case dispersion of the velocities of fragments at collisions of asteroids stipulates the different times of the evolution of this fragment orbits to the earth-crossing orbits. Smaller fragments obtain higher velocities, whereby the time of transfer of this fragments to the earth-crossing orbits is decreased and therefore their exposure ages will be mainly small. Also, we know [8] the

## DISPERSION OF THE RATIOS... Alexeev V.A.

Table. Values of "b" coefficient in equation  $y = a + bx$ 

METEORITES	H		L	
	He-3/Ne-21	Ne-22/Ne-21	He-3/Ne-21	Ne-22/Ne-21
Antarctic	-1.03+/- .34	-1.06+/- .30	-0.54+/- .66	-0.58+/- .53
Non-Ant.falls	-0.36+/- .13	-0.32+/- .08	-0.22+/- .16	-0.40+/- .09
Non-Ant.finds	-0.15+/- .25	0.12+/- .32	0.18+/- .23	-0.56+/- .30

small meteorites have high ratios of  $(\text{He-3/Ne-21})_c$  and  $(\text{Ne-22/Ne-21})_c$ . Therefore discussed effect may be stipulated by presence of bigger portion of meteorites with small preatmospheric sizes among the meteorites with small exposure ages (in comparison to meteorites with high exposure ages). More significant manifestation of this effect in Antarctic H chondrites may be stipulated by presence of bigger portion of small meteorites among cosmic bodies which were falling on the Earth  $\sim 10,000$  years ago (average terrestrial age of H chondrites [9]) in comparison to modern falls.

- REFERENCES. [1]Schultz L., Kruse H. *Meteoritics*, 1989, v.24, 155.  
 [2]Eugster O. *GCA*, 1988, v.52, 1649.  
 [3]Alexeev V.A. *This volume*.  
 [4]York D. *Canad.J. of Physics*, 1966, v.44, 1079.  
 [5]Greenberg R., Chapman C.R. *Icarus*, 1983, v.55, 455.  
 [6]Wasson J.T. *Science*, 1980, v.249, 900.  
 [7]Wetherill G.W. *Meteoritics*, 1984, v.19, 335.  
 [8]Graf Th. et al. *GCA*, 1990, v.54, 2521.  
 [9]Alexeev V.A. *LPS XXIII*, 1991, 7

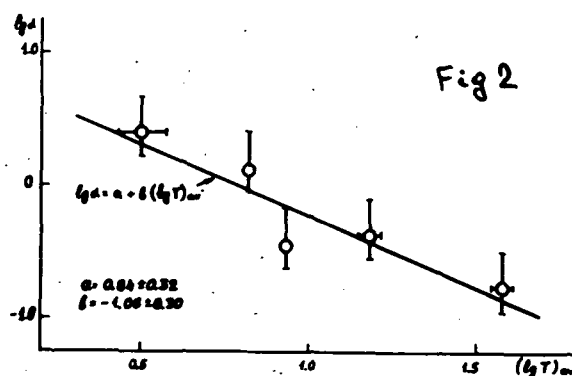
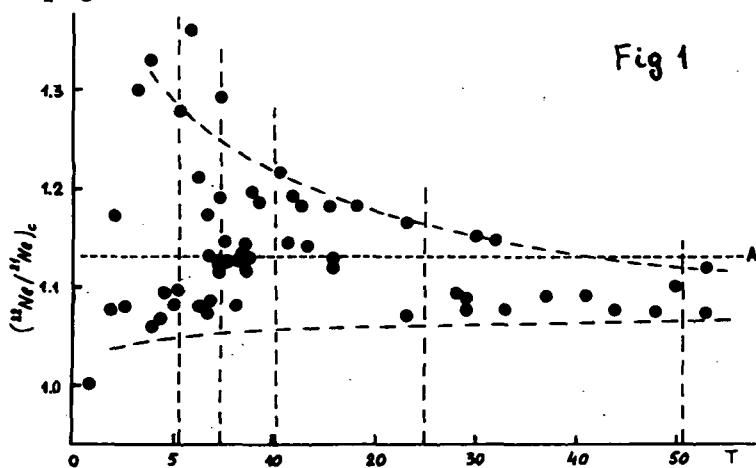


Figure captions

Fig 1 Distribution of the cosmogenic isotope ratios of  $(\text{Ne-22/Ne-21})_c$  in Antarctic H chondrites vs. exposure ages (T, My)

The vertical dashed lines divides the data on subgroups with 11 points in everyone; Av is average value of  $(\text{Ne-22/Ne-21})_c$  ratio for all points.

Fig 2 Logarithm of relative dispersion vs. exposure age of meteorites



456192

56-90

LPSC XXIV

11

ABS. ONLY  
P. 2

N94-12021

PECULIARITIES OF DISTRIBUTIONS OF THE COSMIC-RAY EXPOSURE AGES OF H CHONDRITE FALLS AND FINDS. V.A. Alexeev. V.I. Vernadsky Institute of Geochem. and Analyt. Chemistry, Russian Academy of Sciences, Moscow, Russia

Well known peak in the distribution of the cosmic-ray exposure ages of H chondrites at 6-7 My can be employed as mark in comparison of different populations of H chondrites. It is found the age corresponding to maximum of peak for non-Antarctic falls is higher by (15+/-5)% of this for non-Antarctic finds. Antarctic H chondrites occupy intermediate position. This effect is probably due to process of weathering.

It is well known the distribution of the cosmic-ray exposure ages of H chondrites have clear-cut peak at 6-7 My. This peak can be employed as mark in comparison of different populations of H chondrites, for example non-Antarctic falls and finds and Antarctic finds. This comparison may give us the information not only about meteorite parent bodies but also about changes of meteorites on the Earth. For such comparison we used the results of our calculations of the cosmic-ray exposure ages of meteorites. Ages were calculated according to contents of cosmogenic isotopes of He-3, Ne-21, and Ar-38. Production rates of isotopes were determined according to Eugster [1] with reduction of Ar-38 production rate by 15% [2]. (Such reduction allows to get the best agreement for He-3, Ne-21, and Ar-38 exposure ages [2-4].) Distributions of the average ages ( $T_{av} = (T_3 + T_{21} + T_{38})/3$ ) are shown in Fig 1. The curves of Gaussian distribution for every histogram were calculated by the method of successive approximations. Parameters of each curve allow to determined the average value of age corresponding to the maximum of peak ( $T_m$ ) and the standard deviation of this average value ( $\bar{\sigma} = \sigma/\sqrt{N}$ , where  $\sigma$  is parameter of Gaussian curve and  $N$  is the number of meteorites in the peak).

We can see (Fig 1) the age corresponding to the maximum of peak for non-Antarctic falls ( $T_m = 6.59 \pm 0.23$  My) is higher by (15+/-5)% of this for non-Antarctic finds ( $T_m = 5.64 \pm 0.22$  My). Antarctic H chondrites occupy intermediate position ( $T_m = 6.38 \pm 0.36$  My).

Similar comparison was made for the distribution of ages calculated separately for He-3, Ne-21, and Ar-38. The obtained data are shown on diagram (Fig 2). We can see the same situation.

This effect is possible stipulated by loss of cosmogenic (and not only cosmogenic of course) noble gases in process of weathering of meteorites on the Earth. According to obtained data the weathering is more significant for non-Antarctic finds in spite of relatively small their terrestrial ages (~4000 years in average [5]) in comparison to terrestrial ages of Antarctic H chondrites (~40,000 years in average [6]).

And the last. Fig 2 shows that above mentioned reduction of Ar-38 production rate is probably necessary for conformity of He-3, Ne-21, and Ar-38 ages only of non-Antarctic H chondrites. For Antarctic H chondrites such correction is unnecessary. Why? May be by reason of difference of sizes of H chondrite falls on the Earth in the past (small sizes) and now (big sizes)?

## EXPOSURE AGES... Alexeev V.A.

## REFERENCES

- [1] Eugster O. Geochim. Cosmochim. Acta, 1988, v.52, 1649
- [2] Alexeev V.A. LPS XXII, 1991, 11
- [3] Graf Th., Marti K. LPS XX, 1989, 353
- [4] Schultz L. et al. Geochim. Cosmochim. Acta, 1991, v.55, 59
- [5] Boeckl R. Nature, 1972, v.236, 25
- [6] Alexeev V.A. LPS XXII, 1991, 7

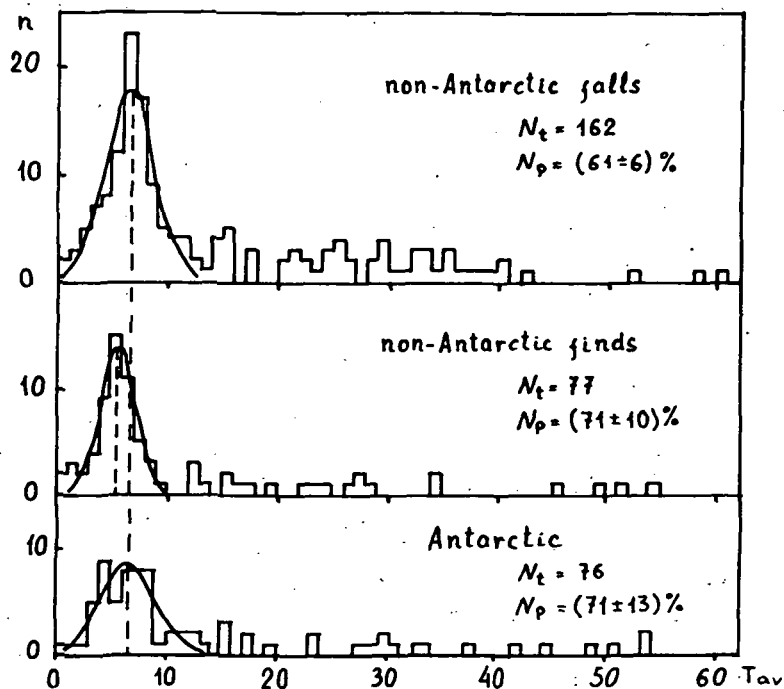


Figure captions

Fig 1

Fig 1 Distributions of the average values of cosmic-ray exposure ages ( $T_{av}$ , My) of H chondrites.

$N_t$  is total number of meteorites;  $N_p$  is portion of meteorites in peak. Dashed lines correspond to positions of maxima.

Fig 2 Positions of the peak maxima of cosmic-ray exposure ages calculated for He-3 (T3), Ne-21 (T21), and Ar-38 (T38) for non-Antarctic and Antarctic H chondrites.

Filled symbols correspond to positions of maxima in distributions of the average values of the exposure ages.

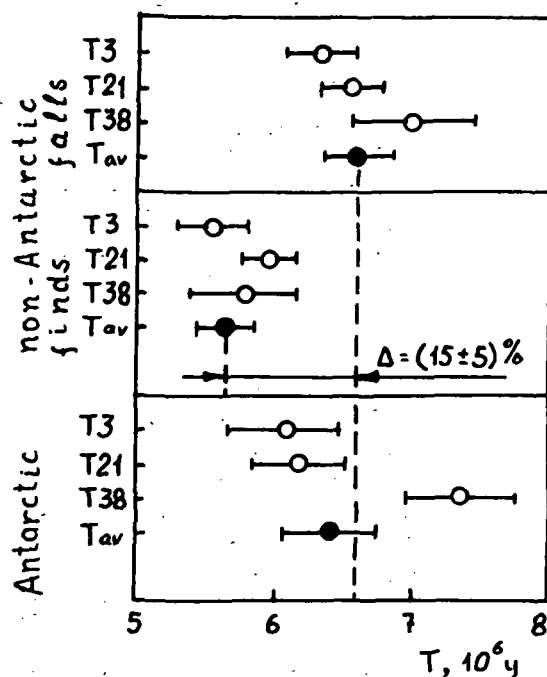


Fig 2

SEARCH FOR EFFECTS OF A SUPERNOVA EXPLOSION 30-40 THOUSAND YEARS AGO IN CHONDRITES; V.A.Alexeev and G.K.Ustinova, Institute of Geochemistry and Analytical Chemistry, Russian Academy of Sciences, Moscow 117334, Russia

The relative increases in Al-26 and Mn-53 equilibrium radioactivity of chondrites with different cosmic-ray exposure and terrestrial ages due to possible supernova explosion 30-40 thousand years ago have been calculated.

The analysis of the data on Be-10 radioactivity in the Antarctic ice core /1/ and C-14 in stalagmites /2/ has allowed /3,4/ to suppose that prominent peaks in the temporal profiles of radioactivity of these radionuclides are conditioned by a close supernova explosion 30-40 thousand years ago. The relative increase of the radiation intensity over the considered time period, reconstructed according to these data in /4/, is shown in Fig.1 (the filled and empty points have resulted from Be-10 and C-14 data, respectively; the curve is from the theory of cosmic ray generation during the supernova explosion). There are two peculiar peaks along the intensity enhancement testifying in favour of a supernova explosion as a reason for this effect: the first, with approximately double increase of intensity, is caused by immediate generation of particles during the supernova explosion, and the second, with nearly threefold intensity increase, is conditioned by the generation of accelerated particles in the vicinity of shock waves from the supernova.

To what extent could such a strong increase of the radiation intensity be manifested in radioactivity of cosmogenic nuclides in meteorites? The influence of other probable factors on the level of radioactivity of the different cosmogenic nuclides in meteorites was investigated in detail in /5/, including, in particular, the effects of cosmic ray modulation. As regards a possible display of the short-time intensity increase in the radioactivity of cosmogenic nuclides, it should be studied in connection with the observed differences of the radioactivity in the Antarctic and non-Antarctic chondrites /6/. In the non-Antarctic H- and L,LL-chondrites the average Al-26 radioactivity is the same within the limits of standard deviation; meanwhile, in the Antarctic H-chondrites it is  $15 \pm 3\%$  higher than in the Antarctic L,LL-chondrites. However, this effect is not observed for Mn-53: its average radioactivities in the Antarctic and non-Antarctic chondrites of every chemical group are mutually consistent /6/. In comparison with the non-Antarctic chondrites, the Antarctic ones are characterized also by lower average Al-26 radioactivity: by  $20 \pm 2\%$  and  $\sim 5\%$  in the case of L,LL- and H-

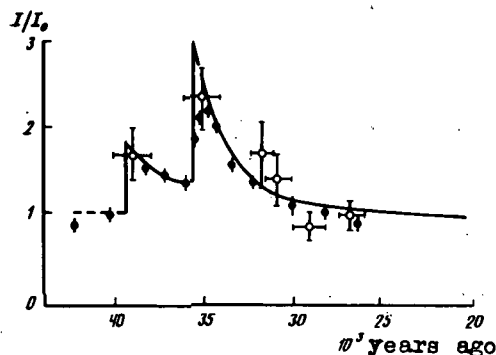


Fig.1

SUPERNOVA EFFECTS IN CHONDRITES: Alexeev V. and Ustinova G.

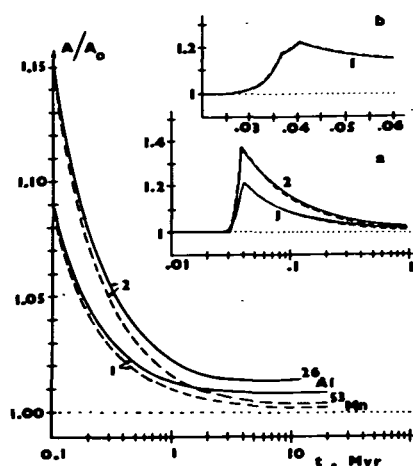


Fig.2

chondrites, successively. This effect is most surely caused by high terrestrial age of the Antarctic chondrites ( $\sim 230$  and  $\sim 40$  thousand years for L, LL- and H-chondrites, respectively) if the Al-26 radioactivity in the Antarctic H-chondrites has not been affected by any other factors.

We have calculated the relative change of Al-26 and Mn-53 equilibrium radioactivity  $A$  due to the sudden enhancement of radiation intensity, conditioned by the supernova explosion, in contemporary chondrites (Fig.2) and in the ones fallen 30 thousand years ago (see it for Al-26 in Fig.3), depending on their cosmic-ray exposure age  $t$  ( $A_0$  is the equilibrium radioactivity in absence of the explosion). The calculation was performed for two models of change of the radiation intensity: 1 - for the reconstructed behaviour of the intensity in Fig.1, and 2 - for the 2.5 times increase of it 30-40 thousand years ago.

According to Fig.2, where in inserts a and b the regions of ages, corresponding to the period of the supernova explosion, are shown on larger scales, the maximum increase of radioactivity of both the nuclides (by  $\sim 20\%$  and  $\sim 40\%$  in models 1 and 2, respectively) falls on the chondrites with cosmic-ray exposure age  $\sim 40$  thousand years, while in the case of higher ages the increase is unessential. However, the highest effect of the supernova explosion should be observed in the chondrites of  $t \sim 10$  thousand years which fell to the earth  $\sim 30$  thousand years ago. At the time of their fall the radioactivity of both the nuclides increases by  $\sim 1.6$  and  $\sim 2.5$  times in models 1 and 2, respectively. Taking into account the terrestrial age of these chondrites leads to little decrease of the radioactivity level (dashed curves in Fig.3).

Thus, the possible supernova explosion 30-40 thousand years ago did not affect essentially the Al-26 and Mn-53 radioactivity in most chondrites (Antarctic and non-Antarctic) due to their high cosmic-ray exposure age: usually  $t > 1$  Myr. An appreciate effects can only be detected in chondrites with  $t < 0.1$  Myr, e.g., in the Farmington chondrite with  $t \sim 0.05$  Myr.

### References

- [1] Raisbeck G. et al. Nature 326(1987) 273.
- [2] Vogel J.C. Radiocarbon 25(1983) 213.
- [3] Sonett C.P. et al. Nature 330 (1987) 458.
- [4] Ammosov A.E. et al. Izvestia Acad.Sci.USSR, ser.phys. 55(1991) 2037.
- [5] Lavrukhina A.K., Ustinova G.K. Meteorites as probes of cosmic ray variations. Moscow: Nauka (1990).
- [6] Alexeev V.A. LPS XXII. Houston: LPI(1991)7.

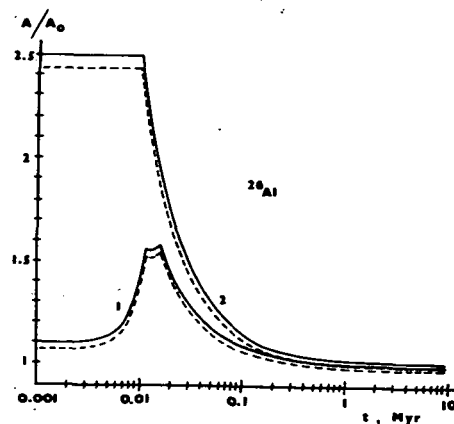


Fig.3

45696

28

58-91

N94-12023

LPSC XXIV

15

12023

163228

**MORPHOLOGY OF LARGE IMPACT CRATERS AND BASINS ON VENUS: IMPLICATIONS FOR RING FORMATION.** Jim S. Alexopoulos and William B. McKinnon, Department of Earth and Planetary Sciences and McDonnell Center for the Space Sciences, Washington University, Saint Louis, MO 63130. *R2*

A nearly complete examination of the Magellan radar data for the Venusian surface reveals 72 unequivocal peak-ring craters and 4 larger structures that we interpret to be multiringed. This report updates our earlier studies and that of the Magellan team. The general morphology of peak-ring craters, decreasing ring diameter ratio trends with increasing crater diameter, and the general size-morphology progression from complex central-peak crater to peak-ring crater on Venus and the terrestrial planets suggest similar processes of peak-ring formation. Observations are consistent with a model of dynamic collapse, downward and outward, of an unstable central peak to form a ring. We interpret the four larger ringed structures (Klenova, Lise Meitner, Mead, and Isabella) to be morphologically similar to the Orientale Basin on the Moon, and thus true multiringed basins.

**Peak-Ring Craters** Four distinct peak-ring crater types, ranging in diameter from ~30 to 110 km, have been identified on Venus. The most common forms (types A and B), which comprise ~85% of all peak-ring craters, are generally characterized by an outer, well-defined radar-bright rim, and a continuous or partial bright inner ring of concentrically arranged peaks/ridges. Less common are types C and D. Type C are characterized by a continuous ridge-like inner ring that exhibits scarp-like attributes, whereas type D are characterized by a central region with isolated but closely clustered peaks that have a concentric ring outline.

The onset diameter to peak-ring craters on Venus was initially defined at ~40 km [1-4]. However, the complete Magellan images indicate that the onset diameter may be closer to ~30 km (Fig. 1). The inner rings of these smaller peak-ring forms are comprised of small, isolated, and concentrically arranged peaks that define both a complete and partial ring, and thus are not as distinct as the coherent ring mountains of larger peak-ring craters.

Our measurements indicate that crater-rim to peak-ring diameter ratios ( $D_{out}/D_{in}$ ) are a function of crater diameter (Fig. 1). At smaller crater diameters (~30 to 35 km) ring ratios are relatively large, reaching up to ~5.2. These smaller peak-ring forms likely represent transitional forms between complex craters with central and multiple peaks and well-developed peak-ring craters. At diameters of ~40 to 70 km, ring ratios are generally larger than 2, and reach up to ~4.5. With increasing craters diameters of up to ~110 km, Venusian peak-ring craters generally show decreasing ring diameter ratios that reach, and fall below, 2.

Ring ratios also vary among the different peak-ring craters. Type A have ring ratios that range from ~1.7 to 4.9, with ~64% having ratios  $\leq 2.5$ . Although type B show a similar range of ratios (~2.1 to 5.2) as type A, ratios are relatively larger (~48% have ratios  $\leq 3.0$ ). Type C occur over a large diameter range (~52 to 102 km), but they exhibit the most distinct ring ratios, extending over a very narrow range, from ~1.8 to 2.1. Type D exhibit a relatively wide range of ring ratios from ~2.5 to 4.0, albeit over a diameter range of only a few km (near 45 km).

There are ~22 peak-ring craters with ratios of ~2 or less, 16 of which exhibit an inner ring of isolated and concentrically arranged massifs (types A and B); i.e., they have a distinct (or partial) peak ring. The 6 others are the type C peak-ring craters, which exhibit very bright radar returns from continuous ridge-like inner ring segments.

**Multiringed Basins** Three larger ringed craters, Klenova, Lise Meitner, and Mead (with diameters of ~144, 149, and 270 km, respectively) are different in morphology from the peak-ring forms. Based on ring morphology, relative ring spacing, and ejecta placement, we originally interpreted these structures to be morphologically similar to the Orientale Basin, and thus multiringed basins [1-3]. A fourth crater, Isabella (~170-km-diameter), we interpret to be a degraded multiringed basin. A cycle 2 Magellan image of Meitner confirms our initial interpretation [1-3], and also reveals the presence of radar-bright returns on the darker floor, possibly from remnants of an inner peak ring. Topographic profiles of Mead clearly show a step-down topography to the basin center across each ring, the inward facing nature of the scarp-like rings, and an outward tilt of the region between the rings. These structural attributes are analogous to those observed for Orientale, and are consistent with models [5, 6] that predict ring-faulting, megaterrace collapse, and inward rotation of lithospheric blocks.

**Large Non-Ringed Impact Craters** To understand better the morphologic nature of the transition from complex central-peak to peak-ring crater, we have systematically analyzed 96 non-ringed impact craters with diameters  $\geq 30$  km, or ~55% of all mapped craters within this size range (Fig. 2). These craters were classified as having a central peak or multiple peaks. Central-peak craters are abundant at diameters of ~30 to 40 km, become less frequent with increasing crater diameter, and then disappear at ~50-km-diameter. On the other hand, craters that

# IMPACT CRATERS AND BASINS ON VENUS: Alexopoulos J.S. and McKinnon W.B.

display multiple-peak complexes are more abundant than central-peak craters at diameters of ~40 to 50 km and, as with central-peak craters, are not present above ~50-km-diameter. Three larger craters (with diameters of ~73, 63, and 60 km), which are in the size range of being peak-ring craters, are completely flooded and show no interior structure or inner ring. The Venusian data shows that complex crater morphology is a function of crater diameter (Fig. 2). With increasing crater diameter, craters generally evolve from ones with a single, central peak to forms with multiple-peak complexes, and then to peak-ring craters. Similar studies of complex central-peak craters on the Moon and Mercury [7, 8] claim that central peak complexity is irresponsive to crater size.

**Interplanetary Comparisons** The inner rings and crater rims of Venusian peak-ring craters are morphologically similar to the inner rings and crater rims, respectively, of peak-ring craters on the Moon, Mars, and Mercury.

The morphologic transition from complex central-peak crater to peak-ring crater is generally similar on the Moon, Mars, and Mercury, although Mars is more complicated [9, 10, 11]. The morphologic sequence with increasing diameter is craters with central peaks, to transitional forms with both a central peak and inner ring, and then to peak-ring craters [9]. Craters at or near the transition on the Moon, Mercury, and Mars exhibit both a central peak and inner ring of peaks. No craters with both a central peak and distinct peak ring have been unequivocally identified on Venus.

Ring diameter ratios for the Moon and Mercury reveal similar trends to Venus, indicating that ring ratios are generally a function of crater diameter. This trend in ring ratios is not clearly evident for Mars. The smaller ringed craters on the Moon and Mercury, with relatively larger ring ratios, are usually transitional forms with both a central peak and inner ring. Craters with both a peak and inner ring on Mars also have the largest ratios, although they are generally larger than most peak-ring craters there. On Venus, smaller peak-ring forms have complete and partial peak-rings, exhibit larger ring ratios, and thus are consistent with being transitional forms, but without a central peak.

Generally, with increasing crater diameter, ring ratios decrease to ~2 and less, central peaks disappear, and interior structures are dominated by a well-developed inner ring. These observations are consistent with peak ring formation being an extension of the central-peak collapse process.

**REFERENCES** [1] Alexopoulos, J.S. *et al.*, *Lunar Planet. Sci. XXII*, 13-14, 1991; [2] Alexopoulos, J.S., and W.B. McKinnon, *Icarus*, 100, 1992 (in press); [3] Alexopoulos, J.S., and W.B. McKinnon, *LPI Contribution 789*, 2-4, 1992; [4] Schaber, G.G. *et al.*, *J. Geophys. Res.*, 97, 13257-13301, 1992; [5] Melosh, H.J., and W.B. McKinnon, *Geophys. Res. Lett.*, 5, 985-988, 1978; [6] McKinnon, W.B., and H.J. Melosh, *Icarus*, 44, 454-471, 1980; [7] Hale, W.S., and J.W. Head, *Proc. Lunar Planet. Sci. Conf. 10*, 2623-2633, 1979; [8] Hale, W.S., and J.W. Head, *Proc. Lunar Planet. Sci. Conf. 11*, 2191-2205, 1980; [9] Wood, C.A., and J.W. Head, *Proc. Lunar Sci. Conf. 7*, 3629-3651, 1976; [10] Wood, C.A., *Proc. Lunar Planet. Sci. Conf. 11*, 2221-2241, 1980; [11] Pike, R.J., in *Mercury*, 165-273, 1988.

Fig. 1

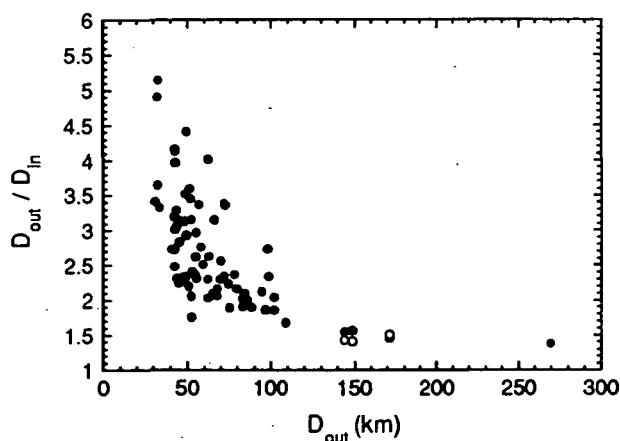
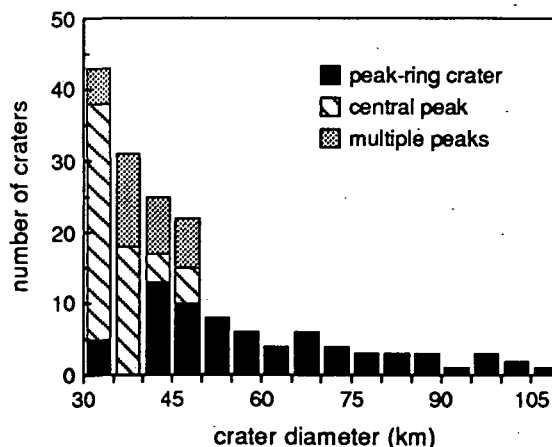


Fig. 2



456201  
2P

39-91

LPSC XXIV

5 17

ABN 94-12024  
163229

**EFFECTS OF MICROSCOPIC IRON METAL ON THE REFLECTANCE SPECTRA OF GLASS AND MINERALS**

C. C. Allen<sup>1</sup>, R. V. Morris<sup>2</sup>, H. V. Lauer, Jr.<sup>1</sup>, and D. S. McKay<sup>2</sup>

<sup>1</sup>Lockheed Engineering & Sciences Co., Houston, TX <sup>2</sup>NASA Johnson Space Center, Houston, TX

P-2

Maturity, which is a measure of the time lunar soils have been in the upper ~1mm of the surface (1), is correlated with changes in the soils' optical properties. Mature soil is darker and somewhat redder than immature soil of the same composition, and features in the reflectance spectrum become more subdued with increasing maturity (2). The maturation process also involves accumulation of agglutinitic glass and submicroscopic metallic iron particles (3). We have produced sub-micrometer iron metal blebs on the surfaces and within glass and mineral grains by the method of high-temperature reduction. This technique has permitted the determination of optical changes in samples much simpler than lunar soil, and offers a useful tool with which to investigate the maturation process.

**Experimental.** Starting materials included synthetic glass of basaltic composition, pyroxene (enstatite, augite, diopside), olivine (Fog<sub>1</sub>), and plagioclase (An<sub>80</sub>). The samples were crushed and sieved to <74  $\mu$ m. They were then reduced with flowing hydrogen in a vertical tube furnace for 3-4 hours at 1100°C. The oxygen fugacity was held three to four log units below the iron-wustite buffer. Visible and near-infrared (VIS/NIR) reflectance spectra were collected before and after reduction. Samples were also analyzed by iron Mossbauer spectroscopy (FeMS), SEM, and XRD. Complementary results are reported in this volume (4).

**Results.**

Synthetic Basalt Glass (13 wt% FeO): Heating in hydrogen resulted in complete devitrification as well as partial reduction of Fe<sup>2+</sup> to iron metal. Devitrification products, in the form of intimately mixed submicrometer crystals, included pyroxene, plagioclase, and cristobalite. The iron metal occurred as rounded blebs 0.3-1  $\mu$ m across, covering 20-30% of the surfaces of typical grains and distributed through grain interiors. The sample turned from tan to black, and all features of the reflectance spectrum were masked (Figure 1).

Enstatite (10 wt% FeO): FeMS and XRD data indicated that a small portion of the FeO in this sample was reduced. The SEM showed iron blebs approximately 0.1-0.3  $\mu$ m in size coating 10-30% of some grain surfaces. The powdered sample, originally white, was brown-gray after reaction. The strong VIS/NIR features were almost completely masked, though dips near 900 and 1900 nm remained in the spectrum of the reacted material (Figure 2).

Augite (6 wt% FeO): A limited portion of the ferrous iron in this sample was converted to metal. Rounded iron blebs, 0.2-0.7  $\mu$ m across, were sparsely scattered across some grains. In no case did these blebs cover more than 10% of a grain surface. No iron blebs were identified in grain interiors. The pale green starting powder was changed to gray during the reaction. Spectral features centered near 800 and 1000 nm were strongly but not completely masked. The continuum of the reacted material spectrum rose toward longer wavelengths.

Diopside (2 wt% FeO): Reduction of this sample yielded only traces of iron metal. The iron peaks in the FeMS and XRD spectra, if present, were below the detection limits. An SEM examination of several reacted grain surfaces disclosed a very small number of 0.5  $\mu$ m iron metal blebs, covering altogether less than 1% of the surface area. The diopside powder changed from white to pale gray. The reflectance spectrum showed only a partial masking.

Olivine (9 wt% FeO): A substantial part of the FeO in the starting olivine was reduced to iron metal. Iron blebs 0.5-1.5  $\mu$ m across coated 20-30% of the surface area on all grains examined. Blebs 0.5  $\mu$ m across were also distributed along parallel planes in the interiors of some grains. The pale green starting powder was changed to black. The reflectance spectrum of the reduced sample was essentially featureless, with reflectivity values ranging from 5-15% and a distinct rise in the continuum toward longer wavelengths. The features which characterized the starting material's spectrum were no longer visible (Figure 3).

## EFFECTS OF MICROSCOPIC IRON METAL ON REFLECTANCE SPECTRA: Allen C.C. et al.

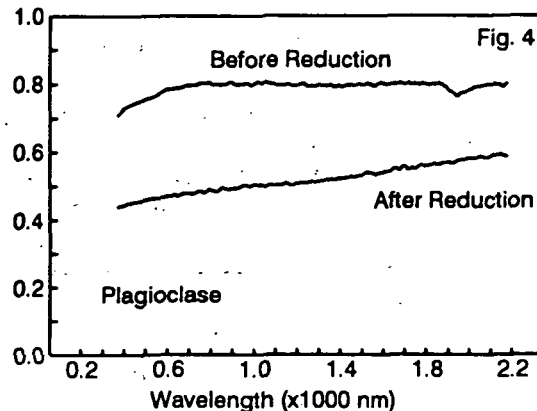
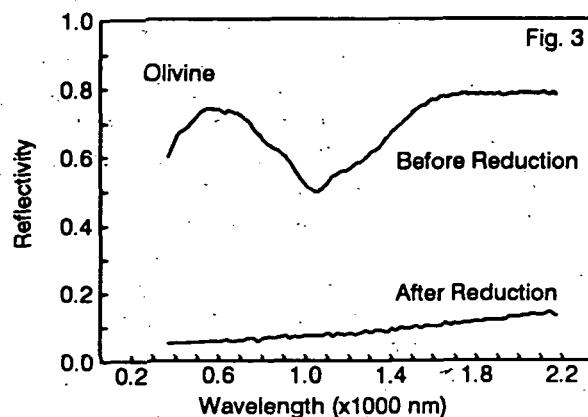
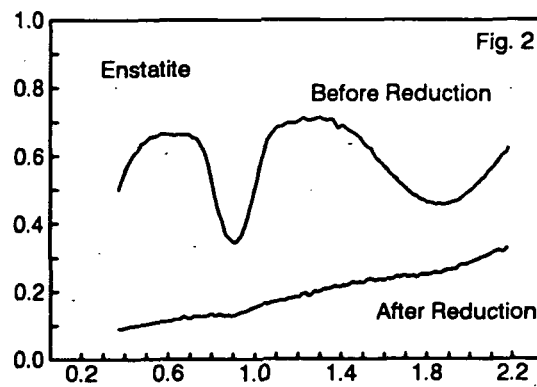
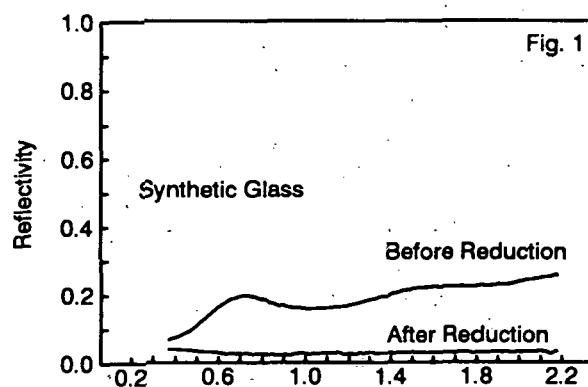
**Plagioclase (0.4 wt% FeO):** Reduction of even the very small amount of FeO in this sample produced detectable effects. Scattered iron blebs, 0.3  $\mu\text{m}$  across and smaller, decorated less than 1% of grain surfaces. The abundance of iron was below the XRD detection limit, but small peaks produced by the metal were visible in the FeMS spectrum. The powder, initially white, changed to pale gray. The reflectivity declined from 80% to less than 60% (Fig. 4).

**Discussion.** A portion of the  $\text{Fe}^{2+}$  in basaltic glass and minerals can be reduced to metal in a few hours at a temperature of 1100°C and an oxygen fugacity well below the iron-wustite buffer. Part of the iron metal forms rounded submicrometer blebs on the surfaces and in some cases within the grains. A concentration of such blebs equivalent to 20-30% of a grain's surface area can totally dominate the reflectance spectra of basaltic glass, pyroxene, and olivine. Smaller concentrations can strongly affect the spectra of pyroxene and plagioclase.

Iron metal blebs have apparently never been reported on or within silicate minerals in lunar soil. Such blebs are, however, ubiquitous in agglutinitic glass. We believe that the iron need only be in the optical path to change a mineral's reflectance spectrum. Iron blebs in glass surrounding a mineral grain would have the same effect as blebs on or within the grain itself.

The optically opaque iron metal blebs affect the glass and mineral reflectance spectra in three ways: lowering the overall reflectivity, reducing the spectral contrast of absorption features, and producing a continuum with a general rise in reflectivity toward longer wavelengths (red slope). These effects match the optical changes ascribed to the lunar maturation process (2). Our experiments indicate that high-temperature reduction provides a useful tool to study the optical properties of maturing lunar soil.

**References.** (1) Morris, R.M., 1978, *Proc. Lunar Planet. Sci. Conf. 9th*, 2287. (2) Adams, J.B. and T.B. McCord, 1973, *Proc. Lunar Sci. Conf. 4th*, 163. (3) McKay, D.S. et al, 1974, *Proc. Lunar Sci. Conf. 5th*, 887. (4) Britt, D.T., *this volume*.





## ENCOURAGING INTEREST IN SPACE EXPLORATION AND PLANETARY SCIENCE AMONG NAVAJO PRIMARY STUDENTS; J. H. Allton<sup>1</sup> and C. S. Allton, <sup>1</sup>Lockheed Engineering & Sciences Co.

Two educational projects were initiated and organized by two individuals, implemented by 15-20 Houston, Texas volunteers who contributed time and money, and helped by many more NASA and contractor professionals. Principal goals for both projects were to 1) encourage interest in space exploration and planetary science among students with little exposure to science and engineering, 2) relate space exploration and planetary science to Navajo culture and environment, 3) motivate students with little interest or incentive to study math and science and 4) complete a project within one year with a limited number of volunteers on a small budget. A space/science fair was sponsored at a small Indian boarding school in Arizona, and the winners toured the Johnson Space Center. The following year winners traveled to Houston and trained at "Mars Camp" culminating in a simulated rover traverse geology sampling mission on Mars.

Students at the 60-student boarding school in Arizona were targeted because a former Indian school teacher was available to serve as liaison between the Houston group and the school administration. Sponsorship of a space/science fair with student winners and teacher chaperones being brought to Houston to tour the Johnson Space Center was proposed to school officials. The trip to Houston was intended not only as an educational experience for the winners, but also as an incentive to all students to participate and work earnestly on their science fair projects. A broad range of topics was eligible for projects since one goal was to relate Navajo tradition with math and science. For example, one student did a statistical compilation of patterns and colors in Navajo rugs by inspecting over one hundred specimens.

The Arizona teachers had little background in space exploration and the school had few resources for projects. Houston volunteers furnished reference books, posters, maps, videos and other teaching aids. Once student projects were chosen, materials to build projects were provided. Project initiators wrote each child encouraging them with their project and answered specific questions. Working with unfamiliar teachers via letter and telephone probably lessened the effectiveness of the significant effort expended supporting these projects because of lack of feedback and actual observation about how the materials were used. The school managed the science fair and the judging. Although some criteria for judging the 23 projects were suggested by the initiators, they were not used. Student oral presentations were videotaped and provided to the Houston volunteers, so they could see the results of their efforts.

Seven students toured Johnson Space Center. In addition to the public tour, students met with an astronaut, talked with an Earth Observation specialist, and toured meteorite and closed loop plant growth laboratories. The laboratory tours were selected because they were related to specific student projects. The project initiators desired to expose students to new experiences available during the trip to Houston. Students experienced flying, collecting specimens at Galveston beach (seeing an ocean), and an educational tour of Sea World of Texas. Since the well-behaved students were used to boarding school, they adapted quite well to travel and food available. However, the tour schedule was too rushed and Houston humidity was exhausting to the Arizona natives. The students were very fascinated with trees and examined and photographed many leaves. The initiators observed a reserved response to the astronaut chat and lecture type presentations and decided that more hands-on activities would be an improvement.

The second year, the initiators decided to combine several hands-on activities into a Mars Camp. Students would attend a week-long "astronaut" training session for a geological sampling mission to Mars culminating in a simulated rover traverse mission. The major decision was whether to take Mars Camp to Arizona where it would be available to more students and in a more Mars-like terrain or to again bring students to Houston for Mars Camp. The teachers felt that the students greatly benefited from travel to Houston and recommended the trip be repeated. Thus, plans were made to take advantage of three educational resources in Houston: Challenger Center, Johnson Space Center and the Lunar and Planetary Institute.

Like the first year, a space/science fair was proposed as a way of motivating students and selecting participants in Mars Camp. However, the projects were to be selected from a list of activities

## SPACE EXPLORATION &amp; NAVAJO PRIMARY STUDENTS; J. H. Allton and C. S. Allton

related to Mars mission skills (living in space, surface exploration topics). Materials and advice were again furnished by Houston volunteers. New teachers and administrators decided to change the science fair projects from in-class science activities to Science Club activities to be worked on after school hours. Fewer students participated and the projects were of lower quality. Nearly all students who completed their project were winners.

Seven students attended Mars Camp, located at a commercial camp with a classroom near the Johnson Space Center. Mornings were spent in the classroom experimenting with space suits and robotic arms, estimating the amount of consumables needed for a trip to Mars, comparing the Martian surface features to familiar features in Arizona and New Mexico, and learning how to navigate using maps and communicate on the radio. Afternoons were spent on field trips: space mission simulation at the Challenger Center, history of space flight at Johnson Space Center, and Mars cratering and volcanic features experiments at the Lunar and Planetary Institute. Outdoor activities at the camp included practice at rover driving, rover TV operation, and soil sample collection with core tubes. Finally, the trained "astronauts" were ready for the simulated mission to Mars. The Mars rover, a modified golf cart equipped with TV and radio transmission and laser range-finder, was operated on a deserted, cold beach at Galveston. Each EVA sample collection crew included a rover driver, communicator using CB radio, and geologist who collected, bagged and labelled samples. The geologist was also supposed to use a laser range finder to plot the rover position on a map, but overnight flooding rendered the primary, mapped site inaccessible, so this mission objective had to be dropped. Students did a good job collecting and documenting samples. The wet conditions provided core samples with layering. The students did find life on "Mars" in the form a dead shark, which they proudly brought back draped across the front of the rover. Student mission controllers communicated constantly with the rover crews via radio, keeping them informed of possible hazards and recording crew observations.

Post-mission sample analyses were conducted in the classroom. Students examined samples under the microscope, performed a size analysis on sand and wrote a report about the findings of their mission to Mars. The intensive 12-hour-a-day training at Mars Camp should have been more beneficial than the previous year's tours, but feedback from students was not obtained.

Mars Camp training for a simulated rover traverse geology sampling mission to Mars neatly tied together many aspects of spaceflight and planetary exploration using hands-on activities. Driving the rover was very appealing to elementary school students. These Navajo students were verbally creative and CB communications worked well. Name tags and astronaut jumpsuits, popular at commercial space camps, were not used because previous year Navajo students were not fond of such identification.

Many volunteers were needed to implement this project. The community around Johnson Space Center is rich with people willing to contribute. This type project is suitable for activities which depend on free help because the electronics, radio and geology volunteer experts had fun. More importantly, this is an example of what a few individuals can do without the burdens of educational bureaucracy.

456208

310-90

LPSC XXIV

21

ABS-ONLY

N94-162025

# CALORIMETRIC THERMOMETRY OF METEORITIC TROILITE: A FEASIBILITY STUDY;

J. H. Allton<sup>1</sup>, and J. L. Gooding<sup>2</sup>, <sup>1</sup>Lockheed Engineering & Sciences Co. Houston, TX 77058 USA,  
<sup>2</sup>SN2/Office of the Curator, NASA Johnson Space Center, Houston, TX 77058 USA

**Summary.** Two solid-state phase transitions in troilite (FeS) can be readily measured by differential scanning calorimetry (DSC) on samples of only a few milligrams. Troilite from the Mundrabilla iron meteorite displays a DSC fingerprint which is distinct from that of terrestrial troilite from Del Norte Co., California; their response to subsequent heating also differ significantly. Further work may establish whether troilite thermometry of meteorites is possible using DSC.

**Introduction.** Troilite, the FeS mineral found mainly in meteorites, undergoes two phase transitions upon heating to temperatures well below the melting point. The  $\alpha/\beta$  transition occurs at  $411 \pm 3$  K, and the  $\beta/\gamma$  transition at  $598 \pm 3$  K [1,2]. Both transitions appear to be reversible. Earlier the unpublished DSC work by Gooding on chondrites of varying metamorphic grade hinted at differences in the  $\alpha/\beta$  transition. The purpose of this work on Mundrabilla and Del Norte troilite is to investigate the feasibility of using DSC to measure thermal histories of meteorites.

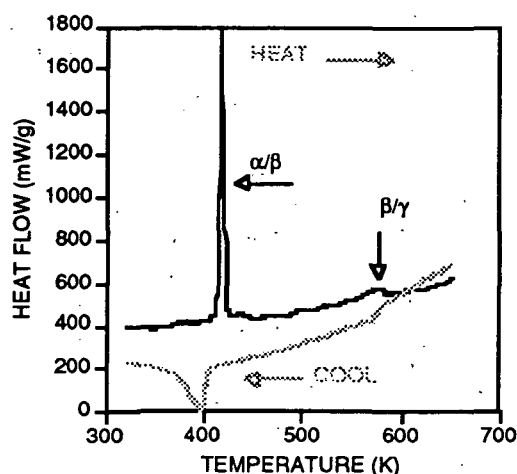
**Procedure.** Del Norte troilite (provided by C. B. Moore) samples of approximately 5 mg were placed in aluminum oxide crucibles and heated at 10 K/min in a Perkin Elmer DSC-7 under an argon purge of 20 cm<sup>3</sup>/min. Samples were heated to maximum temperatures of 473 K, 673 K or 993 K. The differential heat flow between the sample and an empty reference crucible was measured as a function of temperature both on heating and subsequent cooling. Two samples of troilite from the iron meteorite Mundrabilla (provided by E. R. D. Scott) were separately analyzed under the same conditions.

**Results.** The heating curves for Del Norte are reproducible, but do show some variation due to inhomogeneity among small samples. Phase transitions in the heating curves are correlated to transitions in the cooling curves (Fig. 1). Mundrabilla is distinct from Del Norte, implying that DSC may be of value in fingerprinting troilites (Fig. 2). For the  $\alpha/\beta$  transition in Del Norte and Mundrabilla, respectively, the temperature for onset is  $419.7 \pm 0.2$  K and  $415.4 \pm 1$  K, and the  $\Delta H$  is  $40.1 \pm 0.1$  J/g and  $29.9 \pm 4.5$  J/g. Reheating samples produced heating curves indicating that the original structure of the troilite had been altered by the initial laboratory heating. Mundrabilla troilite was significantly more altered by heating (Fig. 3). With increasing maximum temperature of heating both the onset temperature and the  $\Delta H$  of the  $\alpha/\beta$  transition systematically decreased in Del Norte, although the effects of temperature are not separated from time in these experiments (Fig. 4). Thus, transition rates also may be a factor.

**Discussion.** The straightforward conclusion of this preliminary work is that troilite phase transitions are readily measurable via DSC, and that differences exist between Del Norte and Mundrabilla troilite. Whether differences are due to thermal history or composition is not clear. For example, the negatively sloping baseline above 550 K in Mundrabilla is typical of an exothermic reaction. Mundrabilla troilite is known to contain daubreelite and graphite which may participate in redox reactions [3]. Yet, Mundrabilla is shown in Fig. 3 to be much more affected by heating, on a laboratory time scale, than is Del Norte.

The nature of the  $\alpha/\beta$  transition varies depending on troilite sample type (meteoritic, synthetic, lunar) and method of structure determination. Among areas of discussion are the existence of transition phases between  $\alpha$  and  $\beta$  forms and whether the high-temperature ( $\beta$ ) form can be quenched [4-8]. The DSC heat flow curves, by their multiplicity of peaks for a given transition, offer a way of observing the degree of phase homogeneity upon heating and the process of nucleation upon cooling.

Fig. 1. Initial heating (black) and subsequent cooling (gray) curve for Del Norte troilite.



## CALORIMETRIC THERMOMETRY OF TROILITE: Allton J. and Gooding J.

This study has not yet demonstrated that DSC can be used to elucidate thermal histories of meteorites, but the thermal alteration of troilite demonstrated in the laboratory sustains hope that DSC thermometry of meteorites may yet be established.

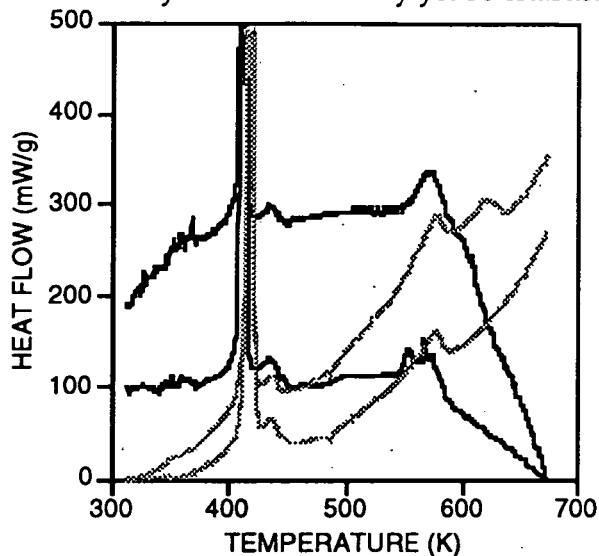


Fig. 2. Heating curves for Mundrabilla (black) and Del Norte (gray) troilites. Top of large peak at 415-420 K is truncated for display purposes only.

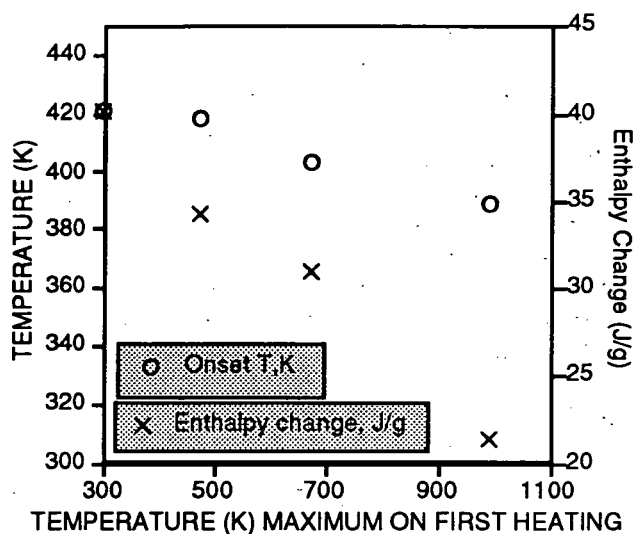


Fig. 4. Onset temperature and  $\Delta H$  values for  $\alpha/\beta$  transition from second heating curves of Del Norte troilite. The maximum temperature of first heating affects the subsequent values for onset temperature and  $\Delta H$ .

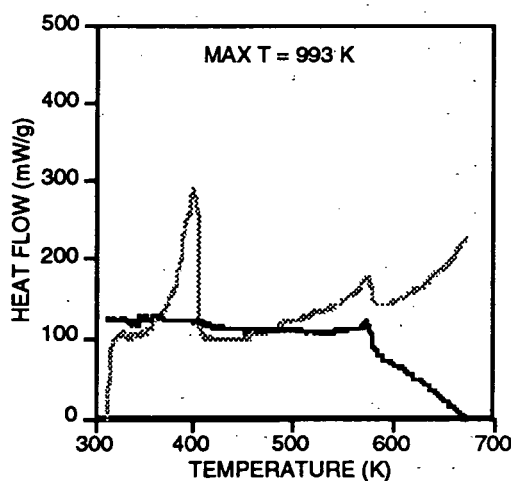
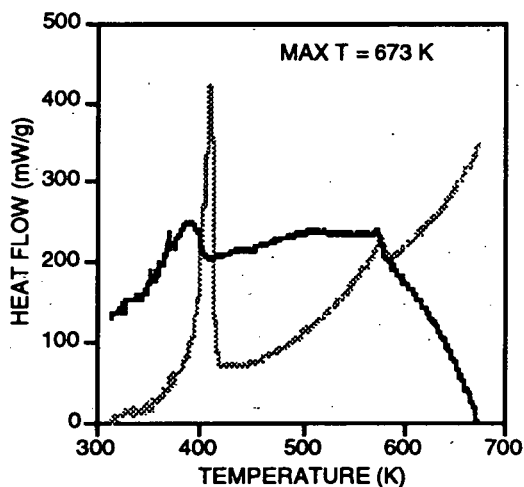


Fig. 3a and 3b. Second heating curves for Mundrabilla (black) and Del Norte (gray) troilites. Increasing maximum temperature on first heating degrades the sharpness of the transition. Mundrabilla is significantly more affected than Del Norte.

## References:

- [1] Chase M. et al. (1985) *JANAF Thermochemical Tables*, 3rd ed. p. 1194; [2] Robie R. et al. (1979) *Geol. Survey Bull.* 1452., p. 125; [3] Buchwald V. (1975) *Handbook of Iron Meteorites*, Univ. of Calif. Press; [4] Andresen F. and Torbo P. (1967) *Acta. Chem. Scand.*, 21: 2841-2848; [5] Toepel-Schadt J. and Mueller F. (1982) *Phys. Chem. Minerals*, 8:175-179; [6] Putnis, A. (1974) *Science*, 186:439-440; [7] Taylor L. and Mao K. (1970) *Science*, 170: 850-851; [8] Evans H. (1970) *Science*, 167: 621-623.

456212

2P

LPSC XXIV

23

N94-12026

511-31

ABS-ONLY

163231

P. 2

# COLD PRESS SINTERING OF SIMULATED LUNAR BASALT; D.A. Altemir, NASA/Johnson Space Center, Houston, TX, 77058.

In order to predict the conditions for which the lunar regolith may be adequately sintered, experiments were conducted in which samples of simulated lunar basalt (MLS-1) were pressed at high pressures and then heated in an electric furnace. This sintering process may be referred to as *cold press* sintering since the material is pressed at room temperature. Although test articles were produced which possessed compressive strengths comparable to that of terrestrial concrete, the cold press sintering process requires very high press pressures and sintering temperatures in order to achieve that strength. Additionally, the prospect of poor internal heat transfer adversely affecting the quality of sintered lunar material is a major concern. Therefore, the author concludes that cold press sintering will most likely be undesirable for the production of lunar construction materials.

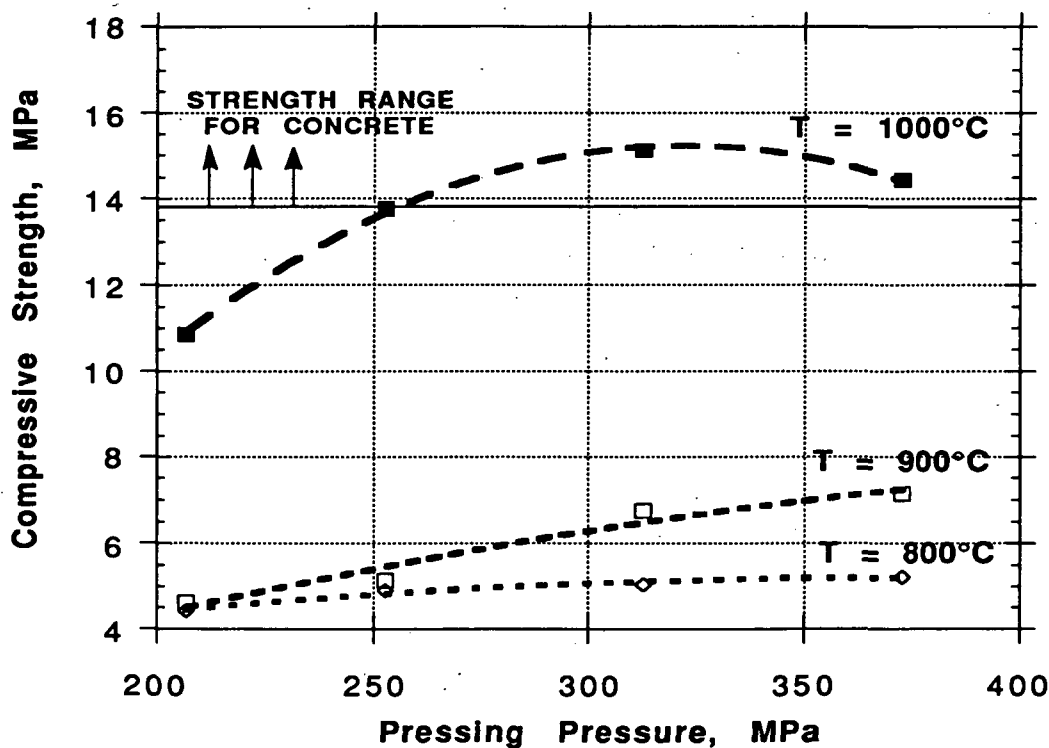


Figure 1. Compressive Strength of Simulated Lunar Basalt  
for Various Sintering Conditions.

According to the experimental results shown in Figure 1, sintered basalt with a compressive strength greater than 14 MPa may be produced by initially pressing the material at pressures above 253 MPa and subsequently heating it above 1000°C for 30 minutes. It should be noted that the samples originally possessed a maximum grain size of 500  $\mu\text{m}$  and that the sintering process took place in an argon atmosphere at ambient pressure.

In addition to the experimental compressive strength results, theoretical predictions of heat transfer were made using a SINDA'85 numerical model. Assuming typical lunar soil thermal conductivities ( $\sim 0.02 \text{ W/m}^{\circ}\text{K}$  for in situ conditions [1]), the heat transfer model suggests that severe temperature gradients are likely to occur for the radiative heating of lunar soil [2]. If similar temperature gradients occur during a real sintering process, then non-uniform properties will result in the sintered material and longer sintering times and/or smaller product dimensions will become necessary to alleviate the non-uniformity.

In summary, adequate compressive strengths were measured for sintered basalt. However, the need for extremely high pressing pressures, coupled with the issues related to poor heat transfer, will limit the viability of cold press sintering as a candidate process for the production of lunar construction materials. Therefore, alternative processes should be investigated.

The author gratefully acknowledges the contributions of Steven L. Rickman and Ron K. Lewis both of the Johnson Space Center in the area of heat transfer analysis. The many helpful discussions with Carlton C. Allen of Lockheed Engineering and Science Company during this work are also greatly appreciated.

## REFERENCES.

1. Lewis R. K. (1992). Thermal Conductivity Evaluation of Lunar Soil. *NASA Memo ES3-92-003*.
2. Horai K., Fujii N. (1972). *Lunar Geophysics, Proceedings of a Conference at Lunar Science Institute*; 18-21 October 1971. pp. 372-408.

456214 2P

LPSC XXIV

25

N94-12027

512-31

GENERAL OVERVIEW OF AN INTEGRATED LUNAR OXYGEN PRODUCTION /  
BRICKMAKING SYSTEM; D.A. Altemir, NASA/Johnson Space Center, Houston, TX 77058

ABS-ONLY

163232

P. 2

On the moon, various processing systems would compete for the same resources, most notably power, raw materials, and perhaps human attention. Therefore, it may advantageous for two or more processes to be combined such that the integrated system would require fewer resources than separate systems working independently. The synergistic marriage of two such processes — lunar oxygen production and the manufacture of bricks from sintered lunar regolith — is considered.

**DESCRIPTION OF INTEGRATED OXYGEN / BRICKMAKING PROCESS.** The integration of oxygen production with brickmaking seems to make intuitive sense and indeed is often alluded to in discussions regarding the independent processes. Figure 1 outlines one possible scenario in which oxygen production and brickmaking may be combined. In this concept, one mining operation supports both the oxygen and brickmaking operations. The oxygen production process depicted here assumes the hydrogen reduction of ilmenite and the production of bricks by hot press sintering, although other processes are certainly possible.

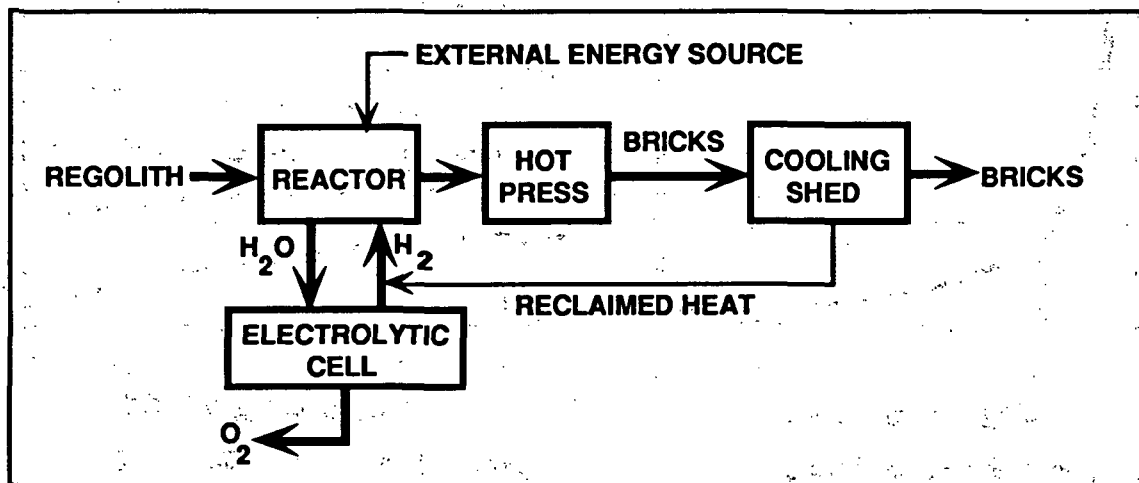


Figure 1. Lunar oxygen production/brickmaking concept.

**SYSTEM MODEL OF AN INTEGRATED PROCESS.** In general, an oxygen/brickmaking process may be modelled on the basis of mass balance:

$$\frac{M_b}{M_{O_2}} = \frac{(1 - f_{O_2})}{f_{O_2}} \quad \text{Eq. 1}$$

where

## INTEGRATED LUNAR OXYGEN PRODUCTION SYSTEM: Altemir D. A.

$$\begin{aligned}
 M_{O_2} &= \text{Mass of oxygen produced} \\
 M_b &= \text{Mass of bricks produced} \\
 f_{O_2} &= \text{Mass of oxygen produced / Reaction mass}
 \end{aligned}$$

This model assumes that the portion of reaction mass not collected as oxygen is used as feedstock for the brickmaking process. It should also be noted that  $f_{O_2}$  is a catch-all parameter that includes the influences of feedstock beneficiation, reaction efficiency, chemical equilibrium, *etc.* upon oxygen yield.  $M_b/M_{O_2}$ , plotted in Figure 2, shows how oxygen production and brickmaking are competing processes.

It can also be shown that the sensitivity of an integrated system to fluctuations in oxygen yield increases with increasing  $f_{O_2}$  values.

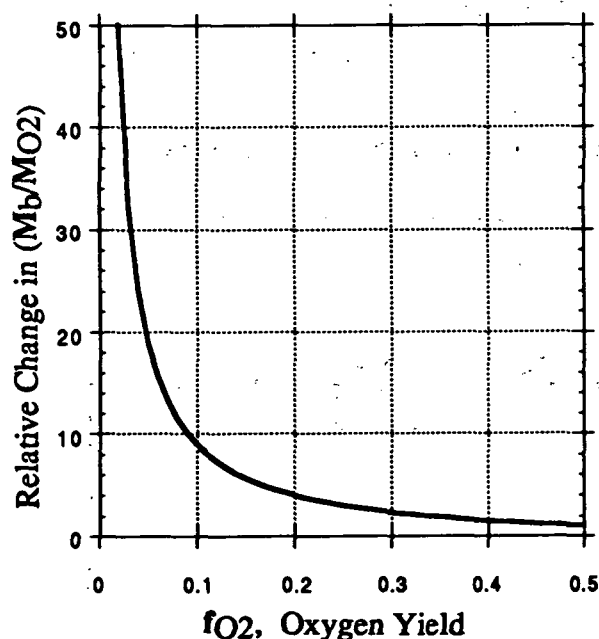


Figure 2. Brick/O<sub>2</sub> Ratio vs. oxygen yield

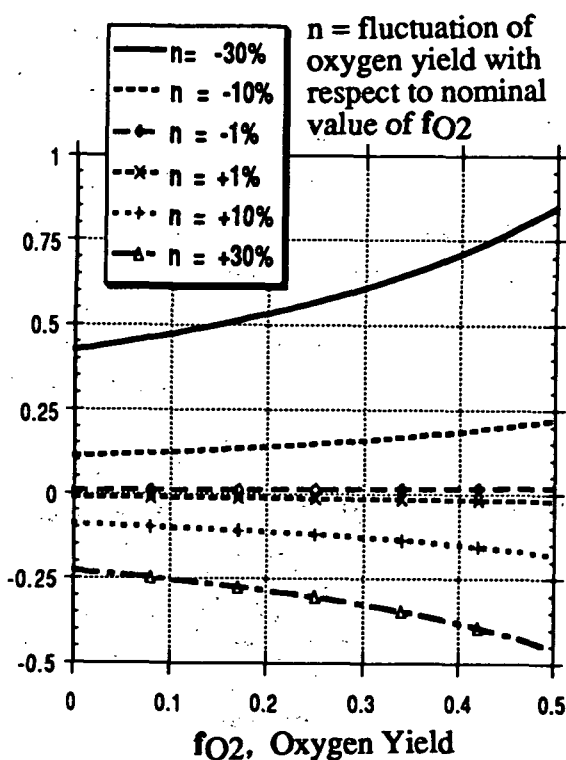


Figure 3. Sensitivity of Brick/O<sub>2</sub> Ratio to Fluctuations in  $f_{O_2}$

**CONCLUSIONS.** Conclusions to be drawn from this simple system model may vary depending upon which is valued more—oxygen or bricks. Such value judgments have been the subject of many programmatic studies some of which continue to evolve as new developments arise. Hopefully, the simple system model presented here serves to illustrate some important issues that may arise regarding certain lunar base strategies.



456216  
2P

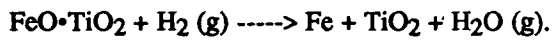
513-77  
NBS ON

N94-12028

THERMODYNAMICS OF LUNAR ILMENITE REDUCTION; B.H. Altenberg, H. A. Franklin, C. H. Jones, P-2

Bechtel, San Francisco, CA

With the prospect of returning to the moon, the development of a lunar occupation would fulfill one of the goals of the Space Exploration Initiative (SEI) of the late 1980's. Processing lunar resources into useful products, such as liquid oxygen for fuel and life support, would be one of many aspects of an active lunar base. Ilmenite ( $\text{FeTiO}_3$ ) is found on the lunar surface and can be used as a feedstock to produce oxygen. Understanding the various ilmenite-reduction reactions elucidates many processing options. Defining the thermodynamic chemical behavior at equilibrium under various conditions of temperature and pressures can be helpful in specifying optimal operating conditions. Differences between a previous theoretical analysis (Hernandez and Franklin, 1992) and experimentally determined results (Gibson et al., 1988) has sparked interest in trying to understand the effect of operating pressure on the hydrogen-reduction-of-ilmenite reaction. The overall reaction can be written



This equation demonstrates no change in the number of moles of gas present as reactant compared to the number of moles of gas present as product. Basic theory suggests that this reaction should be pressure independent. A computer simulation (Roine et al., 1989) was used to model the theoretical reduction of ilmenite with hydrogen as a function of temperatures (at  $T = 900^\circ\text{C}$ ,  $1000^\circ\text{C}$ ,  $1100^\circ\text{C}$ , and  $1200^\circ\text{C}$ ) and pressures ranging from  $10^{-3}$  bar to  $10^{+4}$  bar. This was done to gain insight as to the effect operating pressure can have on how water is won from the reduction of ilmenite with hydrogen.

For the reduction of ilmenite with hydrogen, several important conclusions are obtained. Figure 1 describes the variations in the composition equilibrium constant,  $K_x$ , as a function of pressure. At very low pressures ( $10^{-3}$  bar to 0.2 bar),  $K_x$  increases with increasing pressure. At higher pressures (20 bar to  $10^{+4}$  bar)  $K_x$  also increases with increasing pressure. In both of these regions the ratio of water vapor product to hydrogen reductant increases. Between these two pressure regimes, there exists a transition pressure range (0.2 bar to 20 bar). The trends seen in the lowest and highest pressures regions agree with those seen in the experimental work by Massieon (1992) and by Gibson et al. (1988). The points in the transition region correspond to those reported by Hernandez (1992). The computer model, HSC, uses an extensive base of empirical thermochemical data in computing the standard Gibbs function of the reaction. However, the authors of this abstract are now comparing the results to work by MacChesney and Muan (1961), Merritt and Turnbull (1974), Grey and Merritt (1981), and Borowiec and Rosenquist (1981), which deal with the stability of various solid species present in the  $\text{Fe-Ti-O}$  system. In addition, the results presented in Figure 1 are based on a model of a closed system. The simulation data presented in Figure 1 still needs to be tested in the laboratory before accepting it as a reflection of the real system. In particular, extrapolation to very high and very low pressures will need confirmation.

THERMODYNAMICS OF LUNAR ILMENITE REDUCTION; B.H. Altenberg, H. A. Franklin, C. H. Jones, Bechtel, San Francisco, CA

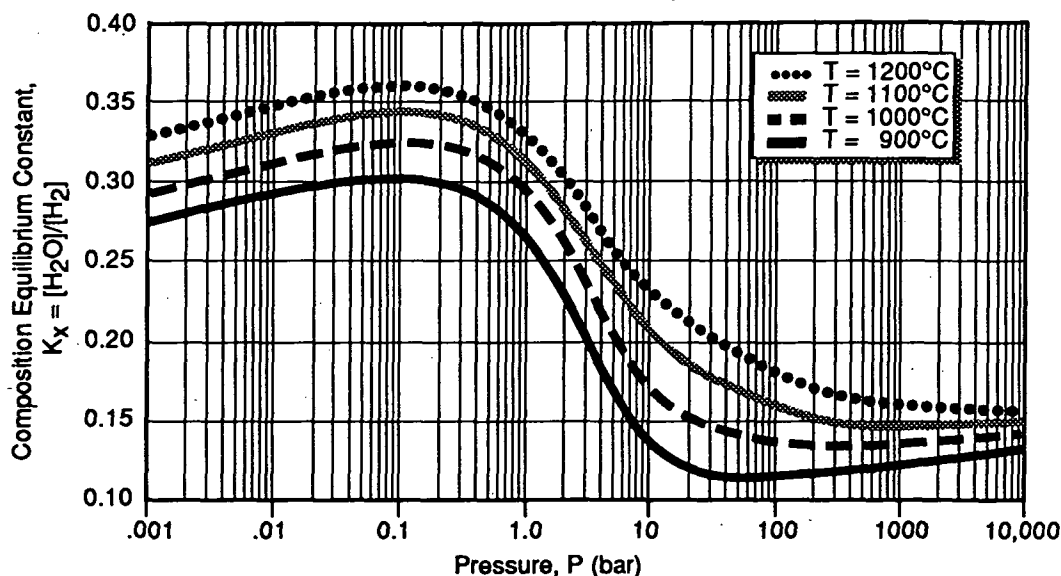


**Figure 1 Composition Equilibrium Constant as a Function of Temperature and Pressure**

The modeling performed in the generation of Figure 1 has provided insight into the effect of pressure on the reduction of ilmenite with hydrogen to form water and various solid species. It will be important to determine more precisely how the amounts of gas species and different solid species at equilibrium depend on the temperature and pressure of the system. The results to date indicate that, in the lower pressure range, the water vapor is obtained almost exclusively from the reduction of iron oxide to iron. In the highest pressure range, the water vapor obtains some of its oxygen from partially reduced oxides of titanium. The presence of these solid species was also noted in work by Allen et al. (1992).

#### References

- Allen, C. C., Gibson, M. A., Knudsen, C. W., Kanamori, H., Morris, R. V., Keller, L. P., McKay, D. S., (1992) LPI Tech. Rpt. No. 92-09, Part 1, Workshop on Geology of the Apollo 17 Landing Site, Houston, TX, p. 1-2.
- Borowiec, K., Rosenquist, T. (1981) *Scand. J. Metallurgy* 10.
- Gibson, M. A., Knudsen, C. W. (1988), AIChE Symposium on Nontraditional Applications of Chemical Reaction Engineering, 1988 Annual Meeting, Washington, D. C.
- Grey, I. E., Merritt, R. R. (1981) *J. Solid State Chem.* 37 p. 284-293.
- Hernandez, A. L., Franklin, H. A. (1992) ASCE Space '92 Conference, p. 576 - 583.
- Massieon, C. C., (1992) M. S. Thesis, University of Arizona, Dept. of Chem. Eng., Tucson, AZ.
- MacChesney, J. B., Muan, A., (1961) *Amer. Mineralogist* 46, p. 572-582.
- Merritt, R. R., Turnbull, A. G. (1974) *J. Solid State Chem.* 10, p. 252-259.
- Roine, A., Talonen, T., Syvajarvi, T., (1974-89), Outokumpu Oy, Outokumpu Research Centre, Pori, Finland.

**INTERSTELLAR GRAPHITE IN MURCHISON: CONTINUED SEARCH FOR ISOTOPICALLY DISTINCT COMPONENTS.** Sachiko Amari<sup>1,2</sup>, Ernst Zinner<sup>1</sup>, and Roy S. Lewis<sup>2</sup>, <sup>1</sup>McDonnell Center for the Space Sciences and the Physics Department, Washington University, St. Louis, MO 63130, <sup>2</sup>Enrico Fermi Institute, University of Chicago, Chicago, IL 60637.

We have measured C-, N-, and O-isotopic ratios of individual graphite grains from the Murchison density fractions KFB1 (2.1-2.15 g/cm<sup>3</sup>) and KFC1 (2.15-2.20 g/cm<sup>3</sup>). According to the C-isotopic composition, KFC1 consists of two populations: one has light C while the other has heavy C (Fig. 1). In addition to these two populations, KFB1 also contains grains whose C-isotopic ratios are approximately normal (Fig. 1). In view of these isotopic distributions it is difficult to understand why the Kr-isotopic compositions of these two separates are so different [1]. In contrast to the lighter density fractions KE1 (1.6-2.05 g/cm<sup>3</sup>) and KFA1 (2.05-2.10 g/cm<sup>3</sup>) [2], the separates KFB1 and KFC1 do not seem to contain many grains with significant <sup>18</sup>O excesses.

Graphite, the carrier of Ne-E(L), is the third type of pre-solar dust identified in primitive meteorites. Four graphite fractions (KE1, KFA1, KFB1, and KFC1) have been extracted from the Murchison meteorite by chemical etching, density and size separation [3]. Noble gas studies [1,4] have shown that there are at least two types of carriers of Ne-E(L), which have different density (1.6-2.15 g/cm<sup>3</sup> vs 2.15-2.20 g/cm<sup>3</sup>) and different Ne-E(L) release temperatures (700 vs 900-1000 °C extraction coil temperature) and two distinct components in the Kr isotopes. Ion microprobe measurements [5,6] have shown that there are differences in the distribution of C isotopic ratios among different fractions.

Two fundamental questions to be addressed are how many populations of grains can be distinguished in these graphite fractions, and whether it is possible to correlate noble gas data with isotopic data obtained with the ion microprobe. To answer these questions, we need to minimize any biases in the selection of grains from the density fractions. For the previous ion probe studies, we tended to select larger (>1.5µm) grains in order to be able to make as many measurements as possible. This time, we tried to measure all round grains that were found in a selected area on the gold foil on which grains were deposited from suspension. The size distributions in Fig. 1 reflect the difference in selection criteria. However, the distribution of KFB1 is still biased in favor of larger grains since interferences from contamination on the grain mount did not allow us to obtain reliable C-isotopic data on the smallest grains.

We measured C- and N-isotopic ratios in 72 grains from the KFB1 fraction. In the C-isotopic distribution (Fig.1), the population with heavy C is not as distinct as in the previous study. This might be due to the difference in grain size distribution. However, both studies show two populations with normal and with light C. Because of interference problems, N-isotopic ratios were measured in only two thirds of the grains. All are normal except in two grains which have heavy N (<sup>14</sup>N/<sup>15</sup>N=156±6 and 153±19).

We measured 157 grains from KFC1. This fraction has two populations with light and heavy C, the population with normal C is largely missing. Except for this population with normal C in KFB1, the isotopic distributions are similar for these two fractions (Fig. 1), in marked contrast to the <sup>86</sup>Kr/<sup>82</sup>Kr ratios, which are completely different [1]. Since the N contents of KFC1 grains are low (CN<sup>-</sup>/C<sup>-</sup> is down to 4x10<sup>-3</sup>; N is measured as CN<sup>-</sup>), the N-isotopic ratios have large errors. Most of the grains are normal. Six grains have <sup>14</sup>N/<sup>15</sup>N ratios smaller than 195, deviating from the normal ratio of 273 by more than 3σ.

The <sup>16</sup>O/<sup>18</sup>O ratios of selected grains from both fractions are plotted in Figs. 2 and 3 together with previous measurements on grains from the two lighter density fractions, KE1 and KFA1 [2]. In the latter two fractions, excesses in <sup>15</sup>N and <sup>18</sup>O are positively correlated. In this work, all grains with normal N have normal O. Among the grains with N anomalies, one from KFB1 (<sup>14</sup>N/<sup>15</sup>N=156±6) has normal O. We could not measure the other grain with heavy N because of interference problems. Of the six grains with anomalous N from KFC1, two had

interferences from adjacent grains, another three have normal O. The sixth grain (indicated by arrows in Figs. 2 and 3) is somewhat enriched in  $^{18}\text{O}$  ( $^{16}\text{O}/^{18}\text{O}=275\pm 47$ ;  $^{12}\text{C}/^{13}\text{C}=365\pm 43$ ,  $^{14}\text{N}/^{15}\text{N}=93\pm 17$ ). However, in both correlation plots (Figs. 2 and 3) this grain falls outside the trends for the KE1 and KFA1 grains with  $^{18}\text{O}$  excesses (these trends are indicated by broken lines in the figures). Grains with  $^{15}\text{N}$  and  $^{18}\text{O}$  excesses appear to be preferentially concentrated in the low density fractions. While further measurements are desirable to confirm this conclusion and to test the apparent relationship between  $^{15}\text{N}$  and  $^{18}\text{O}$  excesses and high  $^{26}\text{Al}/^{27}\text{Al}$  ratios [2], this pursuit is frustrated by the low abundance of such grains and the lack of extremely clean sample mounts necessary for such studies.

REFERENCES: [1] R. S. Lewis and S. Amari (1992) *LPS XXIII*, 775. [2] P. Hoppe *et al.* (1992) *Meteoritics* 27, 235. [3] S. Amari *et al.* (1993) *GCA*, submitted. [4] S. Amari *et al.* (1990) *LPS XXI*, 19. [5] S. Amari *et al.* (1990) *Meteoritics* 25, 348. [6] P. Hoppe *et al.* (1992) *LPS XXIII*, 553.

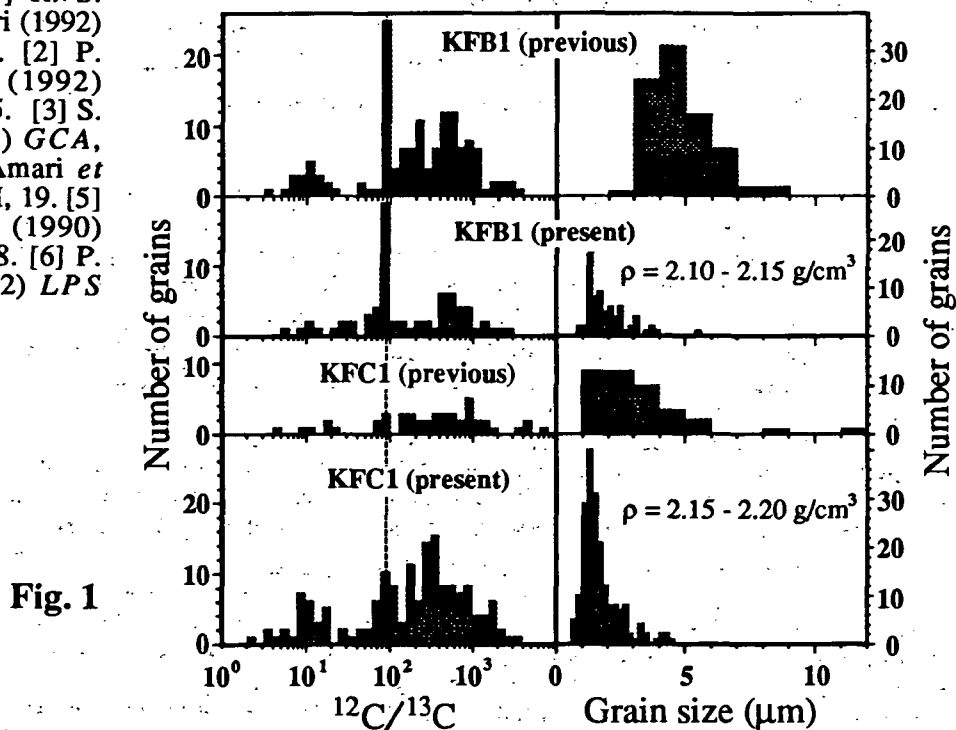


Fig. 1

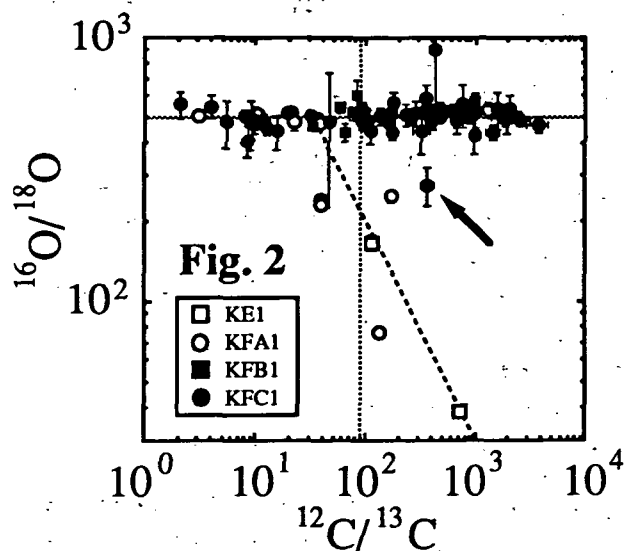


Fig. 2

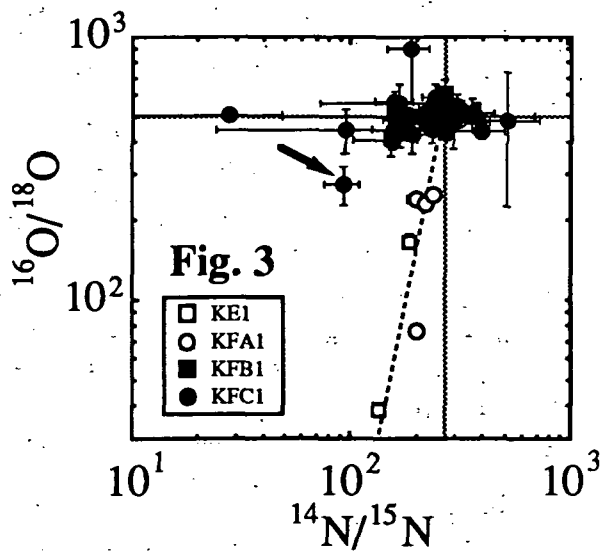


Fig. 3

456221

S 15-43

LPSC XXIV

31

ABSTRACT

N94-12030

P-2

**FOURIER DOMAIN TARGET TRANSFORMATION ANALYSIS IN THE THERMAL INFRARED;** *D. L. Anderson*, Department of Geology, Arizona State University, Tempe, AZ 85287-1404.

Remote sensing uses of principal component analysis (PCA) of multispectral images include band selection and optimal color selection for display of information content [1,2]. PCA has also been used for quantitative determination of mineral types and abundances given endmember spectra [3,4]. This abstract reports on the preliminary results of the investigation of target transformation PCA (TTPCA) in the fourier domain to both identify endmember spectra in an unknown spectrum, and to then calculate the relative concentrations of these selected endmembers.

Identification of endmember spectra in an unknown sample has previously be performed through bandmatching [5], expert systems [6], and binary classifiers [7]. Both bandmatching and expert system techniques require the analyst to select bands or combinations of bands unique to each endmember. Thermal infrared mineral spectra have broad spectral features which vary subtly with composition. This makes identification of unique features difficult. Alternatively, whole spectra can be used in the classification process, in which case there is no need for an expert to identify unique spectra. Use of binary classifiers on whole spectra to identify endmember components has met with some success [8]. These techniques can be used, along with a least squares fit approach on the endmembers identified, to derive compositional information.

An alternative to the approach outlined above uses target transformation in conjunction with PCA to both identify and quantify the composition of unknown spectra [9]. Preprocessing of the library and unknown spectra into the fourier domain, and using only a specific number of the components, allows for significant data volume reduction while maintaining a linear relationship in a Beer's Law sense [10]. The most serious problem with the PCA method is the determination of the proper number of factors in a set of unknown spectra in the presence of noise and other effects. The noise associated with laboratory spectra is the only effect incorporated in this preliminary study. Many statistical techniques attempt to determine the number of factors in an unknown spectral matrix, with limited success. The approach taken here is to iteratively calculate concentrations, reducing the number of endmember components until only non-negative concentrations remain. This technique, though computationally intense, is an unequivocal method for determining the number of components. Through this iterative process it is possible to determine both the number of components and the identity of those components from the spectral library that best match the target transformed unknown spectra. Once the proper spectral library components have been determined, PCA is used to calculate both concentrations and spectra. Least-squares errors (LLE) of calculated vs. true concentrations can be used to estimate the error associated with the technique. No such error can be determined for remotely sensed data with no ground truth. The LLE of calculated vs. library spectra can give an estimate of the error associated with the separation of imbedded verses extracted error in the unknown data matrix.

Mineral mixtures of quartz, enstatite, and calcite have been analyzed using linear least squares (LLS) analysis to determine mineral compositions for application to analysis of TIMS images of Meteor Crater [11]. Five samples varying in approximate percent composition of the three endmembers, using large crystals to minimize particle size effects, were run by Ramsey and Christensen (see also Table I). The spectra where sampled at one wavenumber (wn) resolution from 400 to 1600 wn. The first pair of each column in Table I is the percent of the component in the sample and the second column is the LLS best fit ratio.

TTPCA was run on the samples in the fourier domain for comparison to the LLS technique. A spectral library consisting of calcite, enstatite, kyanite, pyrophyllite, quartz, gypsum, and

## FOURIER DOMAIN TARGET TRANSFORMATION ANALYSIS: D.L. Anderson

tourmaline was used. Three components were found for all TTPCA runs (i.e., quartz, enstatite, and calcite were the spectra having the closest matches to the unknown samples). Table II compares the LLS concentration of sample number one with those calculated with TTPCA.

As seen in Table II, the Fourier domain TTPCA technique does as well as the LLS technique with as few as 20 Fourier coefficients. Thus, low frequency information is what distinguishes mineral spectra in the thermal infrared. Both LLS and PCA should calculate approximately the same results as both are least-squares types of analysis. TTPCA can separate out some of the imbedded error in the spectra through determination of the true number of components. Thus, it has the potential for being more accurate than LLS in the analysis of remotely sensed spectra. TTPCA can also be a fast semi-quantitative technique using a minimum number of Fourier coefficients.

**Table I**  
Comparison of Laboratory to Linear Least Squares Analysis  
of Quartz, Enstatite, Calcite Mixtures

	Sample 1		Sample 2		Sample 3		Sample 4		Sample 5	
Calcite	5	4	20	25	33	30	10	10	10	11
Enstatite	90	91	60	58	33	40	50	52	30	27
Quartz	5	5	20	18	33	30	40	38	60	62

(First of each pair is the percent volume, the second is the best fit ratio)

**Table II**  
Comparison of Laboratory to Linear Least Squares Analysis and  
Fourier Domain Target Transformation Principal Component Analysis  
of Quartz, Enstatite, Calcite Mixtures

	Sample 1	LLS	TTPCA 50pts	TTPCA 20pts	TTPCA 4pts
Calcite	5	4	4	4	5
Enstatite	90	91	91	91	88
Quartz	5	5	5	5	7

- [1] Chavez P.S. and Kwarteng A.Y. (1989) *Photog. Eng. Remote Sensing*, 55, 339.
- [2] Chavez P.S., Sides S.C. and Anderson J.A. (1991) *Photog. Eng. Remote Sensing*, 57, 55.
- [3] Smith M.O., Johnson P.E. and Adams J.B. (1985) *JGR*, 90, C797.
- [4] Johnson P.E., Smith M.O. and Adams J.B. (1985) *JGR*, 90, C805.
- [5] Crowley J.K. and R.N. Clark (1992) *JPL AVIRIS Workshop*, 29.
- [6] Kruse F.A., Lefkoff A.B. and Dietz J.B. (1992) *JPL AVIRIS Workshop*, 119.
- [7] Mazer A.S., Martin M., Lee M. and Solomon J.E. (1988) *Remote Sens. Env.*, 24, 201.
- [8] Kingston M.J., Crowley J.K. and Clark R.N. (1992) *JPL AVIRIS Workshop*, 116.
- [9] Hwang C., Severin K.G. and Hopke P.K. (1984) *Atmos. Environ.*, 18, 345.
- [10] Hoy R.M. and McClure W.F. (1989) *Appl. Spec.*, 43, 1102.
- [11] Ramsey M.S. and Christensen P.R. (1992) *JPL TIMS Workshop*, 34.

556223  
2P

516-91  
ABS ONLY

N94-12031

LINEAMENT ANALYSIS AND TECTONIC INTERPRETATION FOR THE THARSIS REGION, P-1  
MARS; Robert Anderson, University of Pittsburgh, Pittsburgh, PA 15260

The Tharsis region of Mars is critical to any study of Martian tectonics. This region (65°N and 65°S latitude; 45°W to 157.5°W longitude) is characterized by an asymmetrical dome-shaped topographic high approximately 8000 km across. Affecting over 25% of the surface area, this region has been the center of most of the major tectonic and volcanic activity that has taken place on the Martian surface. Lineament studies are the primary tool available for studying tectonic processes on terrestrial planets such as Mars. At least three major lineament systems can be delineated in the Tharsis region; north-south and east-west trending lineament systems are superimposed on an older northwest trending lineament system. Four centers of uplift have been identified based on the occurrence of radial fracture patterns. Preliminary results indicate that the formation of the Tharsis Dome may not have resulted from a single uplift event, but may instead have resulted from as many as four uplift events. The northwest trending fracture may represent a pre-existing zone of weakness which contributed to the early formation of the Tharsis Dome.

1:2,000,000 scale photomosaic maps of Mars were examined and lineaments were identified. The end points of each lineament were measured and recorded in an X-Y reference coordinate frame. Curved segments of otherwise non-rectilinear lineaments were broken into standardized length segments. The study area was divided into a predetermined matrix of cells; the length and the orientation of each lineament segment was tabulated for each cell. The lineaments were then divided into 5 degree azimuthal intervals within their respective grid cells. Each grid cell was then numerically analyzed and the frequency of each interval calculated. Density distribution plots were constructed for the region. Each contour plot was then examined for major trends or regions of high concentration of lineaments. Fourteen dominant trend directions were identified from the density plots. Assuming that uplift events result in a radial lineament pattern, four projected centers emerged. 95% of the lineaments mapped for the Tharsis region could be attributed to the four centers.

456226

S17-46

LPSC XXIV

35

ABS. ONLY

2P

N94-12032

DESCRIPTIONS AND PRELIMINARY INTERPRETATIONS OF CORES RECOVERED FROM THE MANSON IMPACT STRUCTURE (IOWA) R.R. Anderson, B.J. Witzke, and J.B. Hartung, Iowa DNR Geological Survey Bureau, Iowa City, IA 52242-1319, E.M. Shoemaker, D.J. Roddy, U.S. Geological Survey, Division of Astrogeology, Flagstaff, AZ 86001

A core drilling program initiated by the Iowa Geological Survey Bureau and U.S. Geological Survey in 1991 and 1992 collected 12 cores totaling over 1200 m from the Manson Impact Structure, a probable K-T boundary structure [1,2] located in north-central Iowa. Cores were recovered from each of the major structural terranes, with 2 cores (**M-3** and **M-4**) from the Terrace Terrane, 4 cores (**M-2**, **M-2A**, **M-6**, and **M-9**) from the Crater Moat, and 6 cores (**M-1**, **M-5**, **M-7**, **M-8**, **M-10**, and **M-11**) from the Central Peak (Figure 1). These supplemented 2 central peak cores (**1-A** and **2-A**) drilled in 1953. The cores penetrated five major impact lithologies including (1) **Sedimentary Clast Breccia (SCB)**, a polymictic breccia interpreted as a post-impact debris flow, dominated by clasts of Cretaceous marine shale, lesser numbers of Paleozoic carbonate, sandstone, and shale clasts, minor Proterozoic Red Clastics clasts, and rare clasts of igneous and metamorphic rocks and impact melt rock. These clasts are in a medium gray, calcareous, sandy, silty, shale matrix, (2) **Impact Ejecta**, an inverted sequence of Proterozoic Red Clastics and Paleozoic carbonates apparently emplaced as an overturned ejecta flap, (3) **Central Peak Crystalline Rocks (CPC)**, Proterozoic gneisses and granites up-lifted from the crystalline basement to form the Central Peak, (4) **Crystalline Clast Breccia with a Sandy Matrix (CCB-S)**, a polymictic breccia composed of clasts of Proterozoic gneisses and granites displaying abundant planar deformation features (PDFs) and other impact deformation features in a matrix of sand- to silt-sized crystalline rock fragments and mineral grains from disaggregated crystalline rocks, and (5) **Crystalline Clast Breccia with a Melt Matrix (CCB-M)**, a rock composed of clasts similar to the sandy matrix breccia in a dominantly isotropic matrix that displays regions of flow-banding, interpreted as originally melt in some areas, subsequently crystallized to varying degrees. This unit is the impact melt layer.

**Sedimentary Clast Breccia** was encountered mantling portions of all 3 major structural terranes in cores **2-A**, **M-1**, **M-2**, **M-4**, **M-6**, **M-8**, **M-9**, **M-10**, and **M-11** (Figure 1). Where it overlies the **CCB-M** on the Central Peak (especially in **M-1**) the **SCB** incorporates both angular melt rock clasts (solid when fractured and entrained in the **SCB**) and irregular "blobs" of melt rock (apparently molten or plastic when entrained). This indicates emplacement of the **SCB** debris flow very shortly after crater formation, when only a thin crust had formed on melt rock that capped the central peak. The composition of the **SCB**, dominated by the shallowest pre-impact lithologies, is similar to the anticipated composition of the latest, proximal ejecta, which is assumed to be a major source of this debris flow. Maximum **SCB** thicknesses penetrated in the Manson Impact Structure include 137 m (**M-4**) in the Terrace Terrane, 191 m (**M-2**) in the Crater Moat, and 77 m (**M-10**) on the Central Peak. The magnitude of these debris flows and their presence in all terranes of the structure, including at the center of the Central Peak (**1-A**), poses many questions about mechanisms of their transportation, mixing, and emplacement. **SCB** flows would presumably have traveled across the Terrace Terrane, down to the crater floor in the Moat area, and up and over the Central Peak. Although most previous interpretations of latest Cretaceous paleogeography concluded that epicontinental seas had completely regressed from the North American continental interior (including the Manson site), alternative stratigraphic interpretations suggest that the seaway may in fact still have been present in the area at the close of the Cretaceous. Water displaced by the impact and flooding back into the crater could have been a factor in transport of the massive **SCB** debris flow.

**Crystalline Clast Breccias** were encountered on the Central Peak. **CCB-S** was penetrated in cores **2-A**, **M-1**, and **M-11**, **CCB-M** in cores **M-1**, **M-7**, **M-8**, and **M-10**. While clast in these breccias are almost exclusively crystalline, rare shale and siltstone clasts and rare melt rock clasts are present throughout

34



# **DESCRIPTIONS AND INTERPRETATION OF MANSON CORES** Anderson, R.R. et al.

these units. Additionally, some crystalline clasts are mantled with glassy layers, reminiscent of accretionary lapilli. These clasts and the polymictic character of the breccias suggest some amount of clast movement and mixing. These breccias probably represent impact-brecciated transient crater floor, the **CCB-M** from a position nearer inside of the transient crater where temperatures were highest. The thickest sequence of **CCB-S**, 65 m, was penetrated in the **M-11** core, and the thickest **CCB-M**, 80 m, in the **M-7** core.

The **Central Peak Crystalline Rock** was encountered in the **2-A**, **M-5**, **M-7**, **M-8**, and **M-10** cores. The **CPC** is dominated by biotite oligoclase quartz gneiss, but includes other gneisses, granitic intrusives, and minor mafic lithologies. In the **M-7**, **M-8**, and **M-10** cores the **CPC** is present as large blocks separated by thin intervals of **CCB-S**, apparently intruded between the blocks. Also present in **CPC** blocks are thin pseudotachylite-like bands of melt rock which frequently cut across gneiss foliation.

The overturned flap of **Impact Ejecta** material penetrated in the **M-4** core includes Proterozoic Red Clastic strata overlying Paleozoic Cambrian, Ordovician, and Devonian strata. Although all Paleozoic units present at the time of impact are preserved (in inverted order) in the **M-4** core, they are only about 18% of their pre-impact thicknesses.

Samples from these cores are currently being investigated by over a dozen scientists. As their research advances, so will our understanding of the Manson Impact Structure and its relationship to events at the K-T boundary. Samples from these cores are available as research materials from both the U.S. Geological Survey and the Iowa DNR Geological Survey Bureau. Interested scientists are encouraged to contact the authors.

**References:** [1] Anderson, R.R. and Hartung, J.B., *Proc. Lunar Planet. Sci.* 22, 101-110, 1992.

[2] Kunk, M.J., Izett, G.A., Haugerund, R.A., and Sutter, J.F., *Science* 244, 1565-1568, 1989.

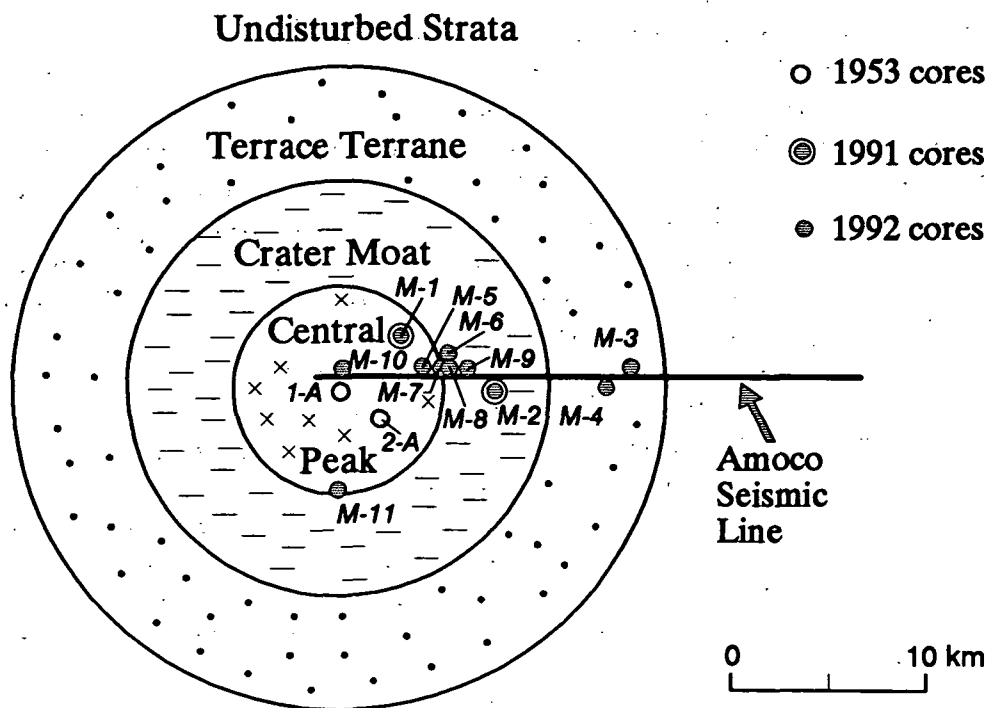


Figure 1. Location of the Manson Impact Structure cores and principal crater terranes.

A SPACE STUDIES CURRICULUM FOR SMALL COLLEGES AND UNIVERSITIES; John O. Annexstad and Robert C. Melchior, College of Social and Natural Sciences, Bemidji State University, Bemidji, MN 56601-2699.

Space Science curricula have generally been the purview of the large and/or research oriented universities with related departmental status. The advent of the NASA Space Grant Consortium Program has opened the field to a number of smaller, less research oriented schools. At Bemidji State University, we have instituted a Space Studies Minor at the undergraduate level which is designed to address the interdisciplinary nature of the space environment. This curriculum is targeted to supplement majors ranging from Geology to Elementary Education.

Bemidji State University is primarily an undergraduate institution located in Minnesota's northern lake region. The school services a large geographical but limited population area and is in the immediate vicinity of three Native American reservations. As part of the Minnesota State University System (separate from the University of Minnesota - a Land Grant University), Bemidji has strong undergraduate programs in Science, Literature, the Arts and Teacher Education.

As part of the initial proposal to form the Minnesota Space Grant Consortium, Bemidji State agreed to establish an interdisciplinary minor program in Space Studies. The minor was presented to the university curriculum committee and formally approved during the first year of the four year consortium NASA grant. Today, the program lists 30 enrolled students including a significant proportion of women and minorities, primarily Native American.

The basic core of the Bemidji Space Studies minor is comprised of three courses taught under the auspices of the Geology Department. These are Planetology I, Planetology II, and Special Problems. Planetology I, Introduction to Space Science, is a 4 quarter hour sophomore level offering that covers the topics earth, atmospheres, meteorites, moon, comets, asteroids, and living in space. The basic reference text is Morrison and Owen<sup>(1)</sup> along with heavy emphasis on material from other sources (2)(3)(4)(5). Planetology II, Introduction to the Solar System, is the second quarter offering and follows appropriate portions of the basic text<sup>(1)</sup> more closely. The 4 credit Special Problems course is built around a mini-thesis on a space theme within the student's area of major interest which is acceptable to the faculty of Space Studies.

The course of study beyond the required 12 quarter hours includes 16 quarter hours of electives. The elective portion of the minor was initially based upon courses already in place at Bemidji when the minor was submitted for approval. These include; Introduction to Environmental Science, Aerial Photography, Geographic Information Systems, Geomorphology, Introduction to Oceanography, Advanced Planetology, Public Policy Analysis, General Psychology, Astronomy, Meteorology, Bureaucracy and Society, and Introduction to Public Administration. New elective courses, either in development or currently being presented by faculty in various departments of the University include; Space Studies: Living in Isolated and Confined Environments (Psychology), Space Studies: NASA History (History), Space Law (Political Science), and Life in the Universe (Biology).

The Space Studies minor is broad enough in scope to allow students to design a personalized course of study that fits his or her major field of interest. Geology majors, for example, can focus on Planetary Geology through Advanced Planetology<sup>(6)</sup> with exposure to lunar samples and meteorite thin

## SPACE STUDIES CURRICULUM: Annexstad, John O., Melchior, Robert C.

sections, and non-science majors can emphasize management skills. Regardless of a student's major field of interest, the minor program provides an insight to the space program for all.

A very significant aspect of the minor program is the option for elementary, middle and secondary school teachers to upgrade or supplement their education with space studies courses. This has the effect of providing additional science education to K-12 students via teacher education. At Bemidji, we work closely with our future teachers and help them design curricula for use in their classrooms.

The current program will remain as a minor for the next few years but will benefit from constant course renewal and upgrading. As a smaller institution, the student population at Bemidji State is such that a major program is at present unjustified. However, as interest grows and as projected educational and employment opportunities become available, we expect to upgrade to a full fledged department. In the interim, we will continue to provide well trained undergraduates as candidates for graduate school and for entry level positions in aerospace related organizations.

## REFERENCES.

- [1] Morrison, D., and Owen, T., The Planetary System, Addison-Wesley, Reading, MA, 1987
- [2] Davis, N., The Aurora Watcher's Handbook, University of Alaska Press, Fairbanks, AK, 1992
- [3] Beatty, J.K., and Chaikin, A., The New Solar System, Sky Publishing, Cambridge, MA, 1990
- [4] Dodd, R.T., Meteorites, Cambridge University Press, New York, NY, 1981
- [5] Hartmann, W.K., Phillips, R.J., and Taylor, G.J., Origin of the Moon, Lunar and Planetary Institute, Houston, TX, 1986
- [6] Hartmann, W.K., Moons and Planets, 3rd Edition, Wadsworth, Belmont, CA, 1993

1994007561 518-91  
456345 ABS. ONLY

LPSC XXIV

39

N 9/4 = 182 033

MEASUREMENTS OF COSMOGENIC NUCLIDES IN LUNAR ROCK 64455; J. R. Arnold, C. P. Kohl, K. Nishiizumi\*, Department of Chemistry, University of California, San Diego, La Jolla, CA 92037-0317, M. W. Caffee, R. C. Finkel, J. R. Southon, CAMS, Lawrence Livermore National Lab., Livermore, CA 94551-9900

Eleven samples were ground from the glass coated surface of lunar rock 64455,82 with an average depth resolution of 50  $\mu\text{m}$  and were measured for  $^{10}\text{Be}$ ,  $^{26}\text{Al}$ , and  $^{36}\text{Cl}$  using AMS (accelerator mass spectrometry). Results show no evidence of SCR (solar cosmic ray) effects. The flat cosmogenic nuclide profiles and activity levels are consistent with a 2 My exposure history for the rock and a sample location on the bottom of the rock. These AMS measurements are some of the most precise ever obtained for these three nuclides. This precision and the demonstrated fine depth resolution will enable us to conduct a number of detailed studies of depth effects in lunar and meteoritic samples, including investigating SCR effects in the surface exposed top of the glass coating of 64455 and possibly in the underlying rock. This work is underway.

Concentrations of cosmic ray produced nuclides in lunar surface rocks provide important information on past solar activity. The most detailed study to date has been done on the highland breccia 68815, which experienced a relatively high erosion rate [1]. In this work we extend our studies of detailed depth profiles to the glass coated rock 64455.

The Apollo 16 impact melt breccia 64455 was collected from the northeast slope of Stone Mountain. It is a small object, 5.6x4.0x2.5 cm weighing 56.7 g, which was coated with a very thick (more than 2 mm) smooth glass layer. It has been concluded that the glass coating did not result from fusion of the surface of the rock itself but is actually a splash coating of impact-melted material with chemical composition similar to that of 64455 [2, 3]. This conclusion is supported by the existence of a thin (~1 mm) partially melted thermal aureole between the basalt and the glass coating.

Marti (pers. comm.) obtained a 2.01 My  $^{81}\text{Kr}$  exposure age for the glass portion of 64455,17 making it clear that 64455 was associated with the South Ray cratering event. The  $^{21}\text{Ne}$  age, 1.2 My, and the  $^{38}\text{Ar}$  age, 1.8 My, are somewhat shorter than the  $^{81}\text{Kr}$  age [4, 5]. Although its lunar surface orientation has not been definitely identified photographically, the distribution of microcraters suggests a simple lunar surface irradiation [6]. Blanford et al. measured cosmic ray tracks in 64455,14 and 64455,16 [7, 8]. The surface subsample, 14, was heavily damaged by microcraters and contained high solar flare track densities. They compared the track densities of 64455,14 with those of 68815 and concluded that the surface of rock 64455 had no erosion and that the top half of the rock had not been covered by soils [7, 8]. A slice of sample 64455,82 (10x24x19 mm) was selected for our study based on microcraters and cosmic ray tracks in the rock. In this slice all sides of the basaltic core were completely covered by glass.

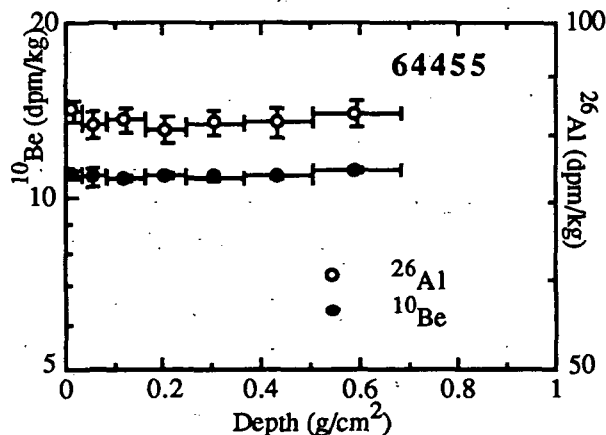
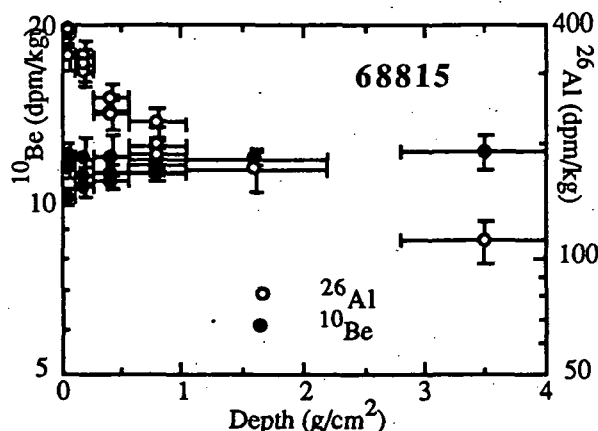
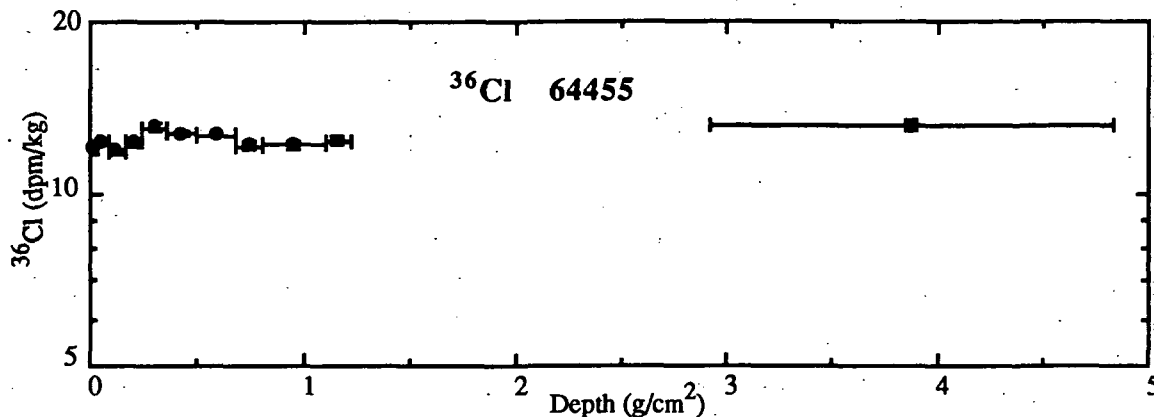
This slice of sample 64455,82 was mounted on an X-Y-Z stage [1]. About 10mm x 20 mm of surface area was ground using a dental drill with measurements at each point of a 1 mm x 1 mm grid. The grinding method was similar to that used in our previous work on 68815, but achieved a depth resolution for 64455 more than two times better [1]. In this work, we report data on 11 samples from the smooth glass surface and the rock below it. The depth intervals were 0-0.12, 0.12-0.31, 0.31-0.60, 0.60-0.90, 0.90-1.33, 1.33-1.83, 1.83-2.50, 2.50-2.93, 2.93-3.76, 3.76-4.44, and 10.7-17.7 mm. The recoveries of ground materials were usually over 90%, somewhat less for the smaller samples. The density of the glass, calculated from the grinding dimensions and the weight removed, is 2.74 g/cm<sup>3</sup>. This density is in good agreement with the density of Ca Feldspar, 2.76. Be, Al, and Cl were chemically separated from each sample.  $^{10}\text{Be}$ ,  $^{26}\text{Al}$ , and  $^{36}\text{Cl}$  were measured by AMS at LLNL [9]. The concentrations of major target elements were determined by atomic absorption spectrometry.

$^{10}\text{Be}$  and  $^{26}\text{Al}$  depth profiles in 64455,82 are shown in Fig. 1. The  $^{36}\text{Cl}$  profile is shown in Fig. 3. Fig. 2 shows  $^{10}\text{Be}$  and  $^{26}\text{Al}$  profiles in 68815 for comparison [1, 10].  $^{10}\text{Be}$  and  $^{26}\text{Al}$  concentrations were corrected to saturation using 2.0 My exposure ages for 64455 and 68815. Note the different depth scales in Fig. 1 and 2. Concentrations of the cosmogenic nuclides in 64455 are constant and do not show the SCR signature which was observed for  $^{26}\text{Al}$  in 68815 (Fig. 2). This uniformity is expected since we ground rock 64455 from its lunar subsurface side. The depths of our samples were equivalent to 6 - 7 g/cm<sup>2</sup> (2 - 2.5 cm) on the moon. The differences

\* Present address: Space Sciences Laboratory, University of California, Berkeley, CA 94720

MEASUREMENTS OF COSMOGENIC NUCLIDES IN 64455 : Arnold J. R. *et al.*

of cosmogenic nuclide concentrations in this depth range are expected to be less than a few percent [11]. Measured activities were constant within experimental errors (0.8 - 3 %). The magnitude of the  $^{10}\text{Be}$  activities and the flat  $^{26}\text{Al}$  profile are consistent with the fact that rock 64455 was exposed to cosmic rays for only 2 My and that the rock has not tumbled within the last 2 My. This experiment demonstrated the efficacy both of our high resolution grinding method and of the AMS measurements. At present, we are grinding samples from the surface which was exposed on the moon.

Fig. 1.  $^{26}\text{Al}$  and  $^{10}\text{Be}$  in 64455 (This work)Fig. 2.  $^{26}\text{Al}$  and  $^{10}\text{Be}$  in 68815 [1, 10]Fig. 3.  $^{36}\text{Cl}$  in 64455 (This work)

## References;

- [1] Kohl C.P. *et al.* (1978) *Proc. Lunar Planet. Sci. Conf. 9th*, 2299-2310.
- [2] See T.H. *et al.* (1986) *Proc. Lunar Planet. Sci. Conf. 17th*, *J. Geophys. Res.* 91, E3-E20.
- [3] Morris R.V. *et al.* (1986) *Proc. Lunar Planet. Sci. Conf. 17th*, *J. Geophys. Res.* 91, E21-E42.
- [4] Bogard D.D. and Gibson E.K. (1975) *Lunar Sci.* VI, 63-65.
- [5] Bogard D.D. *et al.* (1973) *Earth Planet. Sci. Lett.* 21, 52-69.
- [6] Schneider E. and Hörz F. (1974) *Icarus* 22, 459-473.
- [7] Blanford G.E. *et al.* (1974) *Proc. Lunar Sci. Conf. 5th*, 2501-2526.
- [8] Blanford G.E. *et al.* (1975) *Proc. Lunar Sci. Conf. 6th*, 3557-3576.
- [9] Southon J.R. *et al.* (1990) *Nucl. Inst. Meth. B52*, 301-305.
- [10] Nishizumi K. *et al.* (1988) *Proc. Lunar Planet. Sci. Conf. 18th*, 79-85.
- [11] Reedy R.C. and Arnold J.R. (1972) *J. Geophys. Res.* 77, 537-555.

456344  
28  
519-91  
ABS ONLY  
LPSC XXIV  
N94-12034  
41  
2

**MARSLINK;** R.E. Arvidson, McDonnell Center for Space Sciences, Earth and Planetary Sciences, Washington University, St. Louis, MO 63130, L.D. Friedman, and C.J. Stadum, The Planetary Society, Pasadena, CA 91106

The Marslink Project focuses on the development, dissemination, and evaluation of instructional materials about the composition, structure, and dynamics of the martian atmosphere, surface, and interior. A multi-year effort is underway so that middle and high school students can follow a full martian year of seasonal changes using data from NASA's Mars Observer spacecraft, and the Mars Observer Project has time to process and release the appropriate data sets. Monthly activity packets for students, teacher enhancement sessions, a teacher resource center, an on-call Mars data specialist, daily SPACELINK electronic bulletin board updates, and semi-annual NASA Select TV broadcasts will constitute the basis of the Marslink Project. Marslink would take advantage of: (a) the excitement of keeping abreast of activities within NASA's Mars Observer Mission from 1993 through 1996 and working with data acquired by Mars Observer and Viking spacecraft; (b) science expertise and involvement in the Mars Observer Mission at Washington University; (c) Development Team of middle and high school teachers, and research scientists who would work jointly at their home institutions and at summer writing workshops to construct activity packets; (d) dissemination capabilities associated with The Planetary Society and a number of supporting institutions; and (e) formal evaluations led by James Barufaldi, University of Texas. Monthly packets would be designed using a theme-oriented, hands-on approach for use primarily in earth science, physics, and chemistry courses. Selected material would also be of use in physical sciences and biology courses. Packets, where appropriate, would include comparisons between Mars and Earth. The Marslink Activity Book would be published by the National Science Teachers Association at the end of the project and would include background discussions, instructional materials, and project evaluations.

The nation must increase science and technology literacy among the public and the flow of students into science and engineering careers. Further, new learning methodologies are required and need to be tested. In Marslink the first major objective is to capture student interest in science on a national scale by allowing them to follow the progress of Mars Observer as it explores the red planet. Using activity packets developed as part of Marslink, they will participate in the analyses of data from the spacecraft, share in the excitement and discovery of Mars exploration, and learn basic scientific concepts in the process. Results will be related back to a better understanding of Earth by comparisons of the nature and dynamics of the atmosphere, surface, and interior of the two planets. A second major objective is to use and test the effectiveness of constructivist and theme-based learning methodologies in which students advance from concrete concepts to abstract ideas. The evaluation component of Marslink will test the impact of this learning paradigm on the ability of students to develop and understand scientific concepts from middle to high school level, in addition to probing the extent to which their interest levels have increased.

As shown in Figure 1, Marslink activities will be designed using a specific set of learning paradigms or guidelines. The paradigms are:

1. Constructivist Approach: Numerous studies (and common sense) demonstrate that students learn more efficiently when lessons or exercises build on what they already know [1].
2. Hands-on Learning: Marslink packets will feature exercises that will enable students to be active participants in the learning process as opposed to passive listeners.
3. Concrete to Abstract: Marslink will utilize the National Science Teachers Association Content Core concept [2] that students learn best when they initially encounter concepts, principles, and laws at a concrete level through direct experience. This phase will be followed by activities that present higher levels of abstraction.
4. Theme Oriented: Students learn more efficiently when ideas and concepts are placed in the context of themes [3]. Themes also overcome the encapsulation of information within the traditional scientific disciplines and associated courses. Mars Observer data will be used to address themes in weather, climate, volcanism and tectonism that cut across traditional discipline boundaries while at the same time introducing basic concepts in earth science, physics, and chemistry.
5. Phased Approach: Marslink will use California's recommendation of a three-tiered approach to

MARSLINK: Arvidson R.E. et al.

learning [4]. The first phase will begin with *Scale and Structure*, in which students explore sizes, shapes, and characteristics of the martian atmosphere, surface, and interior and comparisons with Earth. The second phase is called *Change and Evolution*, where variations in characteristics are tracked as a function of time. The third phase is *Systems and Interactions* and probes underlying physical and chemical processes and how they interact to make systems, e.g., current terrestrial martian climate systems. In fact, analysis of Mars Observer data by the mission science teams will be very much structured along this approach and Marslink activities will be able to "piggy-back" on their research efforts.

#### References Cited:

- [1] Yager R.E. (1991) *The Science Teacher*, Vol. 58, no. 6, pp. 52-57.
- [2] Aldridge B. (1992) *Scope, Sequence and coordination of Secondary School Science, Volume 1, The Content Core, a Guide for Curriculum Designers. A Project of the National Science Teachers Association*, 152 pp.
- [3] Rutherford F.J. and Ahlgren A. (1990) *Science for All Americans: A Project 2061 Report on Literacy Goals in Science Mathematics and Technology*. Oxford University Press, 240 pp.
- [4] Sachse T. (1990) *Science Framework for California Public Schools: Kindergarten through Grade Twelve*. California Dept. of Education, Sacramento, pp. 28-36.

### MARSLINK

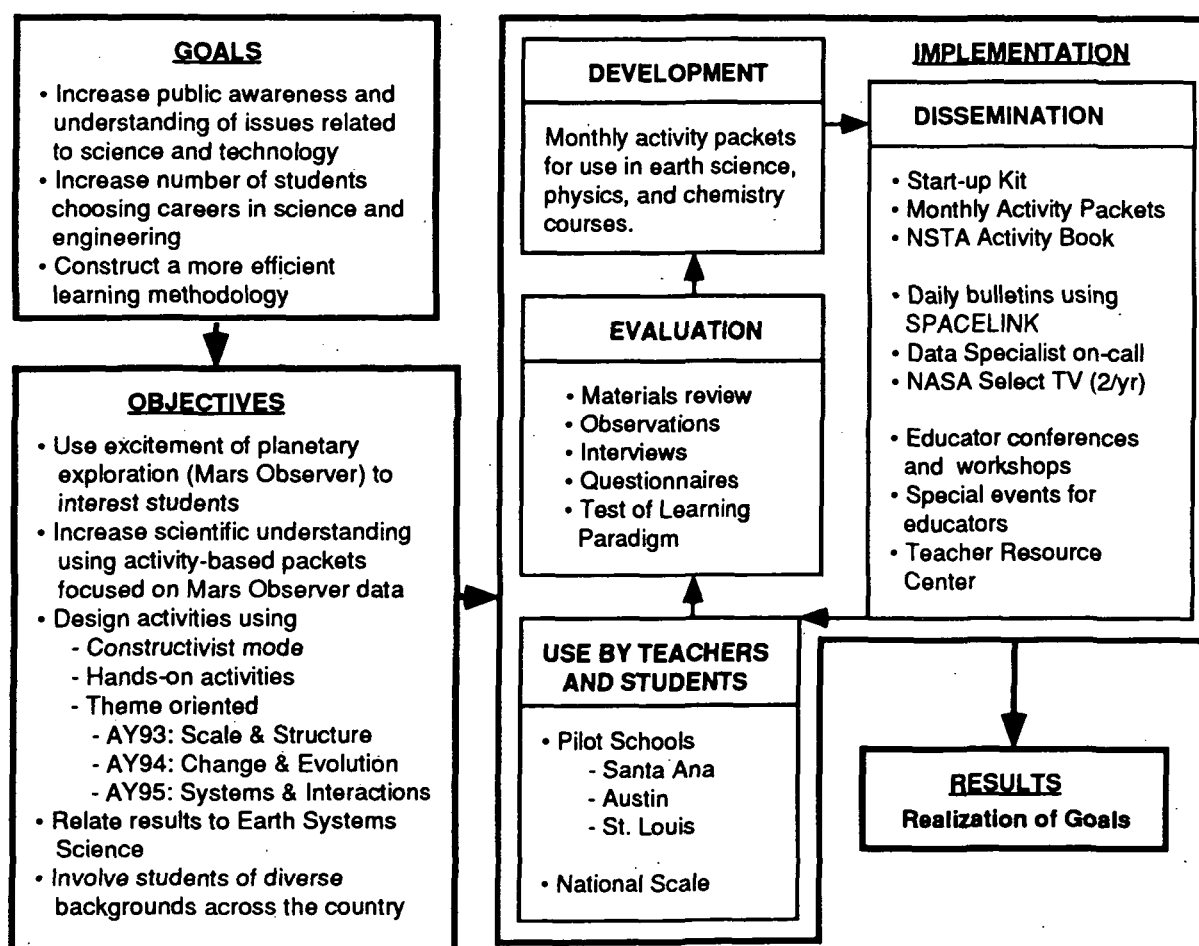


Figure 1 - Flow chart illustrating goals, objectives, and implementation of Marslink.

456348  
2P

32090  
ABS. ONLY  
16N94-12035

LPSC XXIV

43

**CARBON IN WEATHERED ORDINARY CHONDRITES FROM ROOSEVELT COUNTY;** R.D. Ash<sup>1,2</sup> and C.T. Pillinger<sup>2</sup> (1) Dept. of Geology, University of Manchester, Manchester M13 9PL. (2) Dept. Earth Sciences, Open University, Milton Keynes MK7 6AA.

A suite of Roosevelt County ordinary chondrites of known terrestrial age have been analysed for carbon content and isotopic composition. Initial results indicate that significant carbon contamination is evident only in samples with a terrestrial age greater than 40ka. These samples are of weathering grade D and E and contain three times more carbon than the less weathered samples. The soil in which they were preserved has a carbon content of *ca.* 1.5%.

Over 200 meteorites have been recovered from a series of soil depleted areas of New Mexico and west Texas. Most have been recovered from blowouts near Clovis in Roosevelt County (RC) on the high plains of New Mexico (1). The mineralogical and petrological effects of weathering upon these samples have been studied previously and show that the degree of weathering is largely dependant upon the terrestrial residence time (2).

Ordinary chondrites from Antarctica show no significantly different carbon contents from non-Antarctic samples, but may be isotopically altered due to the growth of secondary minerals (3,4). Studies of samples of the Holbrook (L6) chondrite, recovered at various times over a sixty year period, showed that the weathering of the meteorite was accompanied by an increase in carbon content (5). However the carbonaceous chondrites from the Sahara show a depletion in carbon content compared to their non-Saharan equivalents due to the loss of organic material being greater than the gain of carbon from evaporitic carbonate (6). The unequilibrated ordinary chondrite, RC 075, has a carbon content higher than any other whole rock ordinary chondrite. When the sample was analysed by stepped combustion results suggested that terrestrial organic material may account for *ca.* 50% of the carbon inventory (7).

The current study was undertaken to determine the effects of prolonged exposure to the soil and climate of Roosevelt County upon ordinary chondrites in the hope that this will enable a better understanding of the problems associated with the collection of meteoritic falls. A suite of ten grade 4 to 6 H, L and LL ordinary chondrites were analysed for carbon content and isotopic composition. These meteorites had previously had their weathering grade assessed petrographically and their terrestrial ages determined using <sup>14</sup>C contents (2).

It has been shown that the petrologic type 4, 5 and 6 ordinary chondrites have lower carbon contents than the type 3s, typically below 0.25wt% C (8,9) and that there is no discernible pattern for distinguishing between falls and finds. Most of the Roosevelt County samples show a similar range of low carbon contents, between 0.09 and 0.3wt% carbon, but the two oldest samples, with terrestrial ages in excess of 44000 and 46000 years (2), have carbon contents of 0.7 and 0.85wt%



# ROOSEVELT COUNTY WEATHERING.... Ash R.D. and Pillinger C.T.

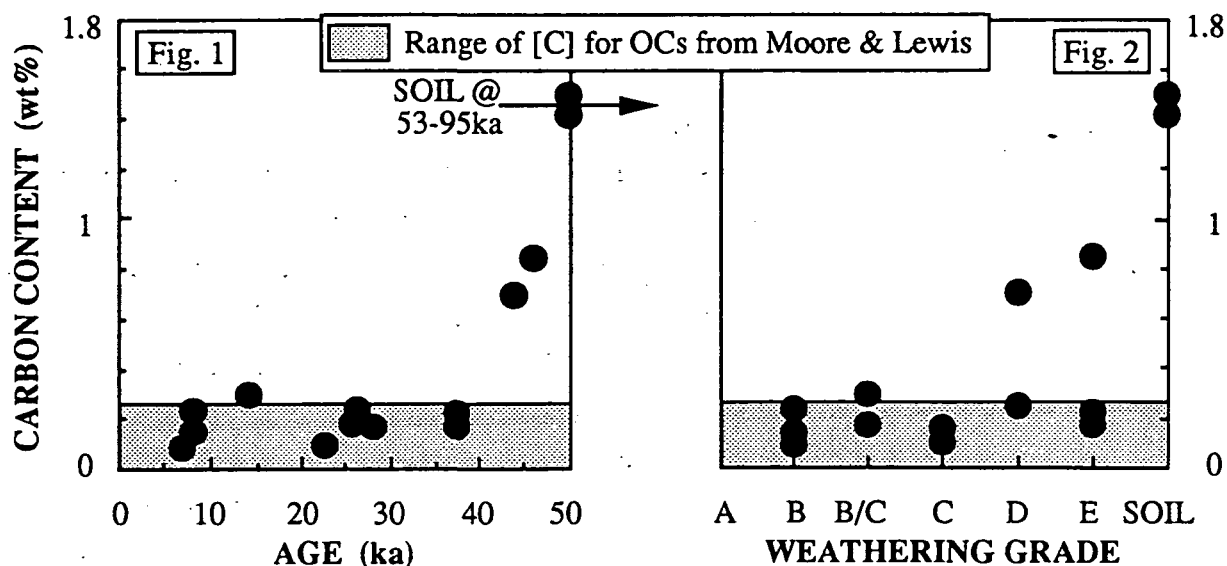
(Fig.1) Although it was shown that there is a dependence of weathering grade upon terrestrial residence time (2) one of these samples is of weathering grade D, the other E, hence the carbon contamination is not simply related to the degree of weathering (Fig.2).

The soil from Roosevelt County in which the meteorites were preserved has a higher carbon content of *ca.* 1.5 wt% carbon hence with the meteorites seem to become more soil-like in their carbon characteristics. The stratigraphic units below the RC soil have an age between 53 and 95ka (10) hence the soil must have acquired its carbon budget in less than this time.

The  $\delta^{13}\text{C}$  values have the same range as those of the type 3 ordinary chondrites, between -20 and -30‰ (9) and show no clear correlation with either carbon content, age or weathering grade. Thus far the high carbon samples show no apparent differences in  $\delta^{13}\text{C}$  from the low carbon samples, coherent with the main source of contaminant carbon being from organic material in the soil, which would be expected to have a  $\delta^{13}\text{C}$  of *ca.* -25‰.

Thus the degree of carbon contamination in Roosevelt County samples is primarily determined by their terrestrial residence time, with some weathering grade D and E samples showing no excess carbon. It is also seems likely that the contamination by organic material is a complex process dependant not only upon time, but also local conditions such as temperature soil type and soil water content.

Refs: (1) Zolensky *et al.* (1990) *Meteoritics* 25, 11. (2) Jull *et al.* (1991) *L.P.S.C. XXII*, 667. (3) Grady *et al.* (1983) *Meteoritics* 24, 1. (4) Grady *et al.* (1983) *Meteoritics* 24, 147. (5) Gibson & Bogard (1978) *Meteoritics* 13, 277. (6) Ash & Pillinger (1992) *Meteoritics* 27, 199. (7) Ash & Pillinger (1992) *Meteoritics* 27, 198. (8) Moore & Lewis (1967) *J. Geophys. Res.* 72, 6289-6292. (9) Grady *et al.* (1982) *J. Geophys. Res.* 87, A289. (10) Zolensky *et al.* (1992) *Meteoritics* 27, 460.



456349  
2P  
Ejecting Basaltic Achondrites from Vesta: Hydrodynamical Impact Models

E. Asphaug and H.J. Melosh, University of Arizona, Tucson AZ

E. Ryan, Planetary Science Institute, Tucson AZ

521-90  
ABS-ONLY  
N 94-B2036  
P. 2

Vesta is a large ( $\sim 570$  km diameter<sup>1</sup>) asteroid whose crust is mostly basaltic. Spectral heterogeneity suggests a sizable olivine feature<sup>2</sup> which may be explained as impact excavation (exposure of sub-crustal material). The spectral data probably show a localized feature  $\sim 200$  km in diameter or a diffuse feature  $\sim 400$  km in diameter<sup>3</sup>. Lightcurve irregularities suggest heterogeneity on a similar scale<sup>4</sup>. This heterogeneity may represent the crater bowl, the extent of its ejecta deposit, or indeed something unrelated to cratering. In any case drawing direct inferences about the state of Vesta's surface on the basis of these observations involves substantial speculation.

These observations lend support to the suggestion that Vesta is the Eucrite parent body<sup>5</sup>. But there is a dynamical problem: in order to deliver the Eucrites from Vesta to the 3:1 Jovian resonance (the most efficient route to Earth), ejection velocities of  $\sim 750$  km/s are required. While small fragments might be ejected at such speeds from a cratering event, large fragments seemingly cannot be (on the basis of laboratory measurements and scaling relations). This is the problem of equipartition: kinetic energy tends to be roughly evenly divided between large fragments and small fragments, such that large fragments travel proportionally slowly. This issue is the same one which stands in the way of our understanding of dynamical asteroid families: how can large fragments be ejected with great velocity?

But Vesta, as Binzel and Xu have recently confirmed<sup>6</sup>, is but the largest member of a taxonomically and dynamically distinct family of objects. The minor members of the Vesta family are basaltic achondrites between 4 and 7 km in diameter with similar  $e$  and  $\sin i$ . Since these objects extend in semi-major axis from Vesta to the 3:1 resonance, a trail is pointed from Vesta to a route to Earth. These asteroids are almost certainly derived from Vesta by an impact event, which may in turn be related to the observed olivine feature. And so we return to the question: how do we eject large fragments at high velocity without disrupting the target? Having such a good data base for Vesta (fragment sizes and velocities, and a possible crater diameter), it is an appropriate candidate for detailed study.

One possibility is that these large ejecta fragments are conglomerates formed by the gravitational aggregation of small debris; this implies that the small fragments are jetted along clustered trajectories. Such phenomena have been observed in the explosion of meter-sized rocks<sup>7</sup>, and may be related to ejecta blanket rays on the moon and other planets. A second possibility is that the impactor was much larger than previously supposed, such that point-source solutions (the basis for impact scaling) are not valid. A third possibility is the existence of inhomogeneities inside the target prior to impact (the result of a previous collisional history); pre-impact fractures can greatly enhance ejection velocities by reflecting impact energy back to the surface.

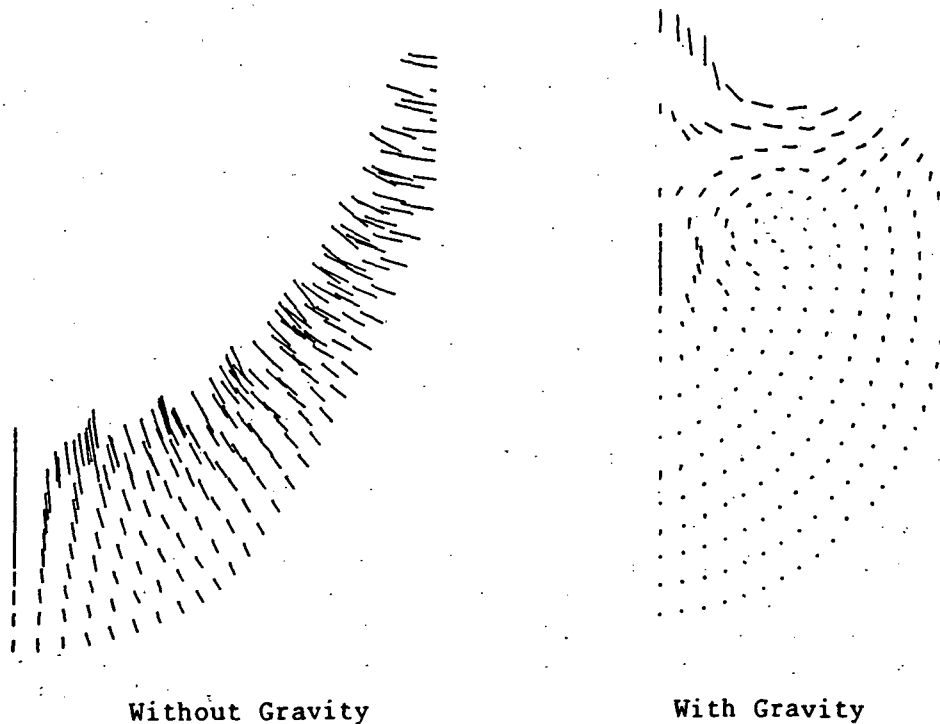
Vesta has considerable gravity and can therefore survive large impacts. Escape velocity is  $\sim 350$  m/s, such that material ejected at 10 m/s will only stay aloft for a minute or two and rise to a height of one km. If Vesta were broken into large fragments by the impact which ejected the Eucrites, its surface might still appear (at the resolution of our spectral observations) to be an intact unit in spite of extensive fracture. Fragmentation does not imply disruption; we need look no further than Phobos (whose surface gravity is only 3% that of Vesta) with all of its fracture grooves to witness this fact. As the figures below illustrate, self-gravity can preserve the stratigraphic order of rocks in an impact even when the rocks are totally disrupted.

We are still far from understanding the boundary between cratering and catastrophic disruption, particularly on targets for which strength and self-gravity both matter. But we are now able to model the underlying physical process - dynamic fragmentation - accurately with fragmentation hydrocodes such as SALE 2D<sup>8</sup> and SPH3D<sup>9</sup>. We shall present several impact scenarios for Vesta; our study is similar to a previous impact model for the formation of Stickney crater on Phobos<sup>10</sup>. We shall illustrate the effects of impactors of different sizes and velocities, and the effect of gravity and structural inhomogeneity.

# EJECTA FRAGMENTS FROM VESTA: Asphaug, Melosh and Ryan

**REFERENCES:** (1) L. Lebofsky *et al.*, *LPSC XXIII* 1991; (2) M. Gaffey, *LPSC XIV* 1983; (3) M. Gaffey, personal communication 1989; (4) A. Cellino *et al.*, *Icarus* **70** 1987; (5) M.J. Drake, in *Asteroids* 1979; (6) R.P. Binzel and Shui Xu, submitted to *Icarus* 1992; (7) G. Martelli *et al.* (preprint) 1992; (8) H.J. Melosh, E. Ryan and E. Asphaug, *JGR* **97** 1992; (9) W. Benz, *Comput. Phys. Comm.* **48** 1990; (10) E. Asphaug and H.J. Melosh, *Icarus* (in press) 1992.

**Figure 1.** The figures below show the effect of gravity alone when an impactor 40 km in radius strikes Vesta at 5 km/s. In the figure on the left, 42 minutes after impact, the target is totally dispersed and destroyed. On the right, where self-gravity is implemented, the target rebounds after 25 minutes. Note that the largest velocities (150 m/s on the right) occur in the central peak. The lines are velocity vectors; the maximum velocity is 100 m/s on the left and 150 m/s at the right for these times. The plots are in axial symmetry with the symmetry axis bounding each figure on the left; each figure was at the start of the computation a half-circle impacted from above along the axis.



# Venus Small Volcano Classification and Description

J. C. Aubele, Dept. Geological Sciences, Brown University, Providence, RI 02912

456350  
28  
N 94-122037  
163242

*Introduction.* The high resolution and global coverage of the Magellan radar image data set allows detailed study of the smallest volcanoes on the planet. A modified classification scheme for volcanoes less than 20 km in diameter is shown in Fig.1 and described. It is based on observations of all members of the 556 significant clusters or fields of small volcanoes located and described by this author during data collection for the Magellan Volcanic and Magmatic Feature Catalog [1]. This global study of approximately  $10^4$  volcanoes provides new information for refining small volcano classification based on individual characteristics. Total number of these volcanoes was estimated to be  $10^5$  to  $10^6$  planetwide based on pre-Magellan analysis of Venera 15/16 [2], and during preparation of the global catalog, small volcanoes were identified individually or in clusters in every C1-MIDR mosaic of the Magellan data set [3]. Basal diameter (based on 1000 measured edifices) generally ranges from 2 to 12 km with a mode of 3-4 km, and follows an exponential distribution similar to the size frequency distribution of seamounts as measured from GLORIA sonar images [2,3]. This is a typical distribution for most size-limited natural phenomena unlike impact craters which follow a power law distribution and continue to infinitely increase in number with decreasing size. Using an exponential distribution calculated from measured small volcanoes selected globally at random, we can calculate total number possible given a minimum size. The paucity of edifice diameters less than 2 km may be due to inability to identify very small volcanic edifices in this data set; however summit pits are recognizable at smaller diameters, and 2 km may represent a significant minimum diameter related to style of volcanic eruption. Guest, et al, [3] discussed four general types of small volcanic edifices on Venus: (1) small lava shields; (2) small volcanic cones; (3) small volcanic domes; (4) and scalloped margin domes ("ticks"). Steep-sided domes or "pancake domes" [4], larger than 20 km in diameter, were included with the small volcanic domes. For the purposes of this study, only volcanic edifices less than 20 km in diameter will be discussed. This forms a convenient cutoff since most of the steep-sided domes ("pancake domes") and scalloped margin domes ("ticks") are 20 to 100 km in diameter, are much less numerous globally than are the smaller diameter volcanic edifices (2 to 3 orders of magnitude lower in total global number [1]), and do not commonly occur in large clusters or fields of large numbers of edifices.

*Defined by Apparent Topography.* Topography is interpreted from the image and confirmed by a small number of radarclinometric profiles from Venera 15/16 and Magellan data (2,5) and stereo analysis [6] and edifices can be subdivided into four types: (1) "shield-shaped" (the most common type of small volcano on Venus [1]); (2) domical-shaped; (3) cone-shaped; and (4) flat-topped or mesa-shaped edifices. Although edifice slopes vary between these types, there is no difference in size frequency distribution of their diameters or the planimetric circularity which delineates them on the radar images. Summit pit size for all types is 0.2 to 1.8 km. Summit pit diameter (or occurrence) does not have a direct relationship to basal edifice diameter; however, pits large in relation to the diameter of the edifice occur more commonly in dome-shaped or cone-shaped edifices. Although individual flow units cannot be identified on edifice flanks at Magellan resolution, the volcanoes can be modeled by multiple centralized small-volume lava flows with a contribution by localized phreatic deposition. Steeper edifice slopes imply a greater contribution by phreatic material or a variation in geochemical evolution or eruption rate. The mesa-like or "flat-top" edifices are distinctive and similar to some seafloor volcanoes imaged by GLORIA[7]. The Venus flat-tops are characterized by a radar-dark flat summit and small central crater. One or two of this type commonly occur in fields of dominantly shield-shaped edifices. The flat-top profile is difficult to model by construction due to multiple centralized small-volume lava flows; but such a profile can be created by a perched and flooded lava pond [3]. A few of the flattops show a radar bright, striated apron of narrow width encircling the edifice base which may represent flows originating at the summit and overflowing the edge or a debris apron. Some of the topographic edifice type small volcanoes are very similar to larger and less common Venus volcanic landforms, implying a continuum of similar volcanic processes, materials or eruption rates/conditions operating at different scales. The small domical-shaped edifices frequently show the flat and patterned summit common to the larger steep-sided domes, and the flat-top type may be produced or modified in ways similar to those suggested for the larger and much less common scalloped margin domes [3].

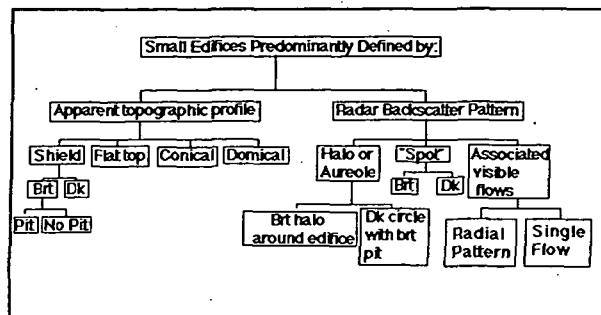
*Defined by Radar Backscatter Pattern.* Many small volcanoes are visible only as variations in radar backscatter and are interpreted to have extremely low topographic slopes. They are defined separately from the topographic edifice types because their differences in characteristics imply differences in material, volume of material, or eruption rate/conditions. Sub-divisions are: (1) Radial flow pattern; (2) halo (aureole); (3) bright or dark "spot"; and (4) defined solely on the basis of the presence of a pit or crater or by disruption of local structural trends. The radial flow pattern type is similar in diameter to the shield-shaped type but individual flows are clearly visible and well-defined. They are similar to the "anemone-type" intermediate-sized (30-40 km diameter) volcanoes first described early in the Magellan mission [8]. They occur individually within fields of dominantly shield-shaped edifices or, in a few areas, in entire fields of the radial flow pattern type. These volcanoes appear to be produced by long linear flows extruded from a circular to elongate fissure-type vent and are frequently aligned along local structural trends. Radar bright (or less commonly dark) aureoles or haloes [2,9] are sometimes associated with small but otherwise typical topographically defined edifices and may be evidence that the total volume of extrusive material associated with each vent is larger than the edifice alone. Although haloed edifices are somewhat rare, when they do occur, they commonly occur in fields rather than as a single example. This implies that the origin of the halo effect may be a regional phenomenon. The halo is either constructional and emplaced on pre-existing plains in association with the volcanic edifice or it may represent the exposed radar bright lower slopes or surrounding apron of flows of the edifice encircled by later plains material at a constant contour level. Circular radar

bright (commonly without central pits) or irregularly shaped radar dark "spots" represent very low slope shield volcanoes or extrusion of a much less viscous material than commonly occurs in the typical shield-shaped edifices. The dark irregular patches frequently occur associated with graben and may represent individual flows erupted from a point source on a fissure, similar to small localized Hawaiian rift eruptions, rather than a true constructional shield-type edifice.

**Future Work.** There are three fundamental questions regarding the small volcanic edifices on Venus: (1) what type of volcanic activity is represented by these edifices? (2) what is the volume contribution of these numerous but small volcanic source vents? and (3) what does the presence of abundant volcanoes, frequently occurring in concentrated "fields" imply for the heat flow and resurfacing history of Venus? There is now a complete data set of small volcanoes identified and located on the surface of Venus. Detailed observation has resulted in a classification of these features and preliminary interpretations of the type of volcanic activity that they represent. Detailed mapping of the geologic relationships of these small volcanoes to the plains and larger volcanic features is essential to continue to explore these questions.

**References:** [1] Head, et al, 1992, JGR 97, 13,153; Crumpler, et al, 1992, this volume; Crumpler, et al, 1992 GSA Sp Pap, in prep [2] Aubele and Slyuta, 1990, EMP 50/51, 493 [3] Guest, et al, 1992, JGR 97, 15,949 [4] Pavri, et al, 1992, JGR 97, 13,445; McKenzie, et al, 1992, 15,977 [5] C. Weitz, unpub. data, 1991 [6] Moore, et al, 1992, Int. Ven Colloq.(abst), 71 [7] USGS MISC. Invest. Series I-1792, 1986 [8] Head, et al, 1991, Science 252, 276 [9] Klose, 1990, LPSC 21 (abst) 639.

Figure 1



Defined by apparent topographic profile			
	Profile	Planview	Characteristics
Shield-shaped			Circular
Domical-shaped			Circular Some have large pits
Flat-top			Dk or Brt top, Mesa-like flanks Central pit, Some have aprons
Cone-shaped			Some show striated flanks
Defined by radar backscatter pattern			
		Planview	
Radial flow pattern			Elongated or circular pit
Halo or aureole type			Radar Brt circle surrounds small topographic edifice
Bright spot			Circular (Brt) / Irregular (Dk)
Dark Spot			No pit (Brt) / Pit (Dk)
			No topography
Defined by pit			Central pit Irregularly circular
Defined by structure>>>			

456351  
2P523-35  
ABS-ONLY

LPSC XXIV

49

N94-12038

THE LOS ALAMOS NEUTRON SPECTROMETER FOR THE LUNAR SCOUT-I MISSION; George Auchampaugh, Bruce Barraclough, Roger Byrd, Darrell Drake, William Feldman, Calvin Moss, and Robert Reedy, Space Science and Technology Division, Los Alamos National Laboratory, Los Alamos, NM 87545.

We review the current status of the Los Alamos program to develop a neutron spectrometer for the Lunar Scout-I mission, which is the first of two such missions to obtain global compositional, gravity, topography, and image maps of the lunar surface during nominal one-year missions. The neutron spectrometer will measure fast and slow (epithermal and thermal) neutrons in the ranges of 0.5 MeV to 25 MeV and 0.01 eV to more than 1 keV, respectively. The neutron spectrometer will consist of two independent instruments, a fast-neutron one and a thermal and epithermal one. The measured neutron fluxes are very sensitive to hydrogen in the top meter of the lunar surface and provide additional information about lunar composition.

The concept of using cosmic-ray-produced neutrons that escape from the Moon to study lunar surface composition dates back to Lingenfelter *et al.* [1], who in 1961 noted that hydrogen modifies the ratio of thermal and epithermal neutrons and proposed an experiment to measure lunar thermal and epithermal neutrons. Better sensitivity for detecting lunar hydrogen can be obtained by adding a sensor for detecting fast neutrons [2]. Using neutrons measured in three energy ranges (fast, epithermal, and thermal) also removes many ambiguities in the two-energy-range neutron system and provides additional information on lunar composition, such as a measure of the abundances of elements in the top meter of the lunar surface like Fe, Ti, Gd, and Sm that strongly absorb thermal neutrons [2]. No experiment to measure neutrons has flown in lunar orbit. The Mars Observer Gamma-Ray Spectrometer has the capability of detecting martian thermal and epithermal neutrons [3] and will be used to map hydrogen and carbon in the martian surface after the Mars Observer goes into orbit in August 1993.

The fast neutron sensor consists of four boron-loaded plastic scintillator rods, optically coupled to photomultiplier tubes. The boron in the scintillator provides a unique way to unambiguously identify a fast neutron. When such a neutron interacts with the plastic and is subsequently captured by  $^{10}\text{B}$ , two pulses of light are created, a prompt pulse and a delayed pulse, which are separated in time by the neutron moderation time of the scintillator. The neutron moderation time is 2.2  $\mu\text{s}$  and is governed by the amount of  $^{10}\text{B}$  loaded into the scintillator, which is approximately 1% by weight  $^{10}\text{B}$  for our scintillators. The prompt pulse provides a measure of the total energy released by the neutron as it slows down in the scintillator. A correction must be made to account for the energy that does not result in a detectable light pulse. The amplitude of the delayed pulse, which is governed by the 2.78-MeV Q-value for the  $^{10}\text{B}(n,\alpha)$  reaction, provides a unique way to identify a neutron. Gamma rays in coincidence with a prompt pulse would have random amplitudes. An event is tagged by three pieces of data: the prompt pulse amplitude, the delayed pulse amplitude, and the time interval between them. The data are stored in several formats: (a) single events, where the pulse heights in each rod are recorded; (b) 1-rod events; (c) 2-rod events; and (d) 3&4-rod events. Calculations show that the directional information provided by the four rods can be used to correct the data for cosmic-ray-generated spacecraft neutron background, thereby eliminating the need for a boom. The instrument has energy resolution of about 30% for 5-MeV neutrons, gamma-ray rejection comparable to that obtainable using pulse shape discrimination with liquid scintillators, and previous flight heritage. See reference 4 for more details on the operation of the instrument.

Thermal and epithermal neutrons will be measured with  $^3\text{He}$  gas proportional counters. The epithermal counter will be wrapped with cadmium and the "thermal" neutron counter with tin. The thickness of tin is chosen so that the epithermal response of the "thermal" counter matches that of the epithermal counter. In this way, a thermal neutron flux is obtained by a difference between the "thermal" and epithermal count rates. The

LUNAR SCOUT NEUTRON SPECTROMETER: Auchampaugh G. *et al.*

counters can be effectively shielded from the thermal/epithermal spacecraft neutron background with little weight penalty, thereby also eliminating the need for a boom. Similar counters have been flown in Earth orbits.

We will report on neutron science issues relating to the Lunar Scout-I mission and on the current configurations, potential weight, power and telemetry rates of these instruments.

References: [1] Lingenfelter R.E., Canfield E.H., and Hess W.N. (1961) *J. Geophys. Res.*, **66**, 2665. [2] Feldman W.C., Reedy R.C., and McKay D.S. (1991) *Geophys. Res. Lett.*, **18**, 2157. [3] Boynton W.V. *et al.* (1992) *J. Geophys. Res.*, **97**, 7681. [4] Feldman W.C., Auchampaugh G.F., and Byrd R.C. (1991) *Nucl. Instrum. & Methods*, **A306**, 350. \* Work done under the auspices of the US DOE.

#56352

524-27

LPSC XXIV

51

ABS ONLY

163244  
N94-12039

VAPORIZATION BY SHOCK LOADING OF ALBITE, JADEITE, AND PYREX GLASS: EXPERIMENTAL STUDY. D.D.Badjukov(1) and T.L.Petrova(2);(1) - Vernadsky Institute of Geochemistry and Analytical Chemistry, Kosygin St. 19, Moscow 117975, Russia; (2) - Institute of Lithosphere, Staromonetny per., Moscow.

Produced by shock experiments impact melts of albite, jadeite and pyrex glass demonstrate a loss of both Na and Al relative to Si, which can be due to selective vaporization. It is suggested that the high volatility of Al is related to volatility of a Na-Al compound of proposed  $\text{NaAlO}_2$  composition. The similar loss of Al and Na seems to be possible during tektite-forming processes.

A degree of selective vaporization and modification of a melt chemical composition during impact processes is still poorly understood. The selective vaporization of some elements has been shown by shock experiments [1,2]. The vaporization and condensation processes can take place in the lunar regolith [3]. On this base there are hypotheses explaining differentiation of planetary bodies through the impact vaporization [4]. On the other hand studies of tektites, impact glasses and lunar soils show that bulk compositions of impact melts are not modified significantly. In order to estimate degree of the vaporization during shock fusion, chemical compositions of experimentally produced impact melts were studied. We chosen Al-containing compositions, because a high volatilization of Al during unequilibrated evaporation had been demonstrated [5,6].

Powder samples of pure albite and jadeite were shocked in steel cylindrical containers surrounded by high explosive. Due to a geometry of a shock wave propagation and a porosity of the samples, high pressure and temperature were generated in an area located along the sample cylinder axis. Unfortunately, we cannot determine achieved shock parameters exactly, but an estimation gives the peak pressure of about 70 GPa and the shock temperature of about 5000 C. For the study chips of vesiculated glasses were picked up from central part of the samples. In addition, we studied melt containing particles produced by impact experiments on a light gas gun. The experiments were carried out with pyrex glass projectiles, which were launched with velocity of 6 km/s onto a silicate target. The peak pressure depending on impedances of the targets varied from 51 to 65 GPa. Remelted projectile glasses adhering to the shock fused agglutinates were studied. The produced glasses were analyzed by electron probe with using the broad beam method.

The albite and jadeite glasses contain steel droplets, which could come into the melt from walls and bottoms of the containers. In addition, black areas of the albite glass contain dissolved iron as a minor component and the jadeite glass is slightly enriched in Fe. Initial pyrex glass analyses totaled of about 84.5 wt%, that should be due to presence of boron. The shock fused pyrex glass has totals of about 86%, that suggest a B loss during the impact fusion. The compositions of the glasses (Fig.1) show loss of Na and Al too. Assuming that Si was not lost during the shock fusion, the loss of an evaporated matter can be estimated to be about 4 wt.% for the albite and jadeite glasses and to be 3.6 wt.% for the fused pyrex glass. Selective loss of Al is more pronounced, when we consider the ratios of  $\text{Na}_2\text{O}$  and  $\text{Al}_2\text{O}_3$  to  $\text{SiO}_2$  (Fig.2). The Al loss for the pyrex glass appears to be smaller, although it lies out of the range of the analytical uncertainties. The calculated atomic Na/Al ratio in the vapor is equal to 1.3 for the albite and jadeite glasses and to 26 for the fused pyrex glass. This difference could be due to the higher Na/Al ratio in the melt of pyrex glass relative to albite and jadeite, that could lead to the enrichment of the vapor phase in Na.

The unusual behavior of Al as a volatile element conflict with the relative sequence of the element volatilities [7], i.e. Al is lost more readily than Si. The behavior of Al can be explained by the formation of Na-Al clusters in the impact melt. If it is so, then vaporization of Na-Al compound would increase the volatility of Al with provided that the compound has a high volatility. On the base of Na/Al ratio in vapor phase for albite and jadeite glasses the composition of the compound may be  $\text{NaAl}_2\text{O}_4$ . Thus, a presence of Na could increase the volatility of Al, and vice versa, a presence of Al could decrease the volatility of Na. This suggestion is supported by the pattern of the Na and K depletion in fused projectiles, produced by laboratory cratering experiments [1]. When an Al-free soda-lime glass melts shows a loss of Na and K, basalt glass melts with 16 wt.%  $\text{Al}_2\text{O}_3$  do not lose significant amount of Na by a smaller loss of K. However, in contrast to our results the experiments did not show any loss of Al, that may be due to very short time of melt existence. High rate of Al volatilization was observed by a experimental vaporization of feldspars [6].

Tektites is a most suitable object among other impact glasses for a search of traces of selective vaporization. For this reason we constructed a  $\text{Na}_2\text{O}/\text{SiO}_2$ - $\text{Al}_2\text{O}_3/\text{SiO}_2$  diagram of average compositions of some tektites groups, irgisites, and their proposed parent materials (Fig.3). In general Figure 3 is similar to Figure 2.



## VAPORIZATION BY SHOCK LOADING

Badjukov, D.D. and Petrova, T.L.

There are two causes for this similarity. The first may be the appearance of the effect of high rate of the Al volatilization. The second may be due to a variety of a quartz content in target rocks. If the latter is true, then any elements (e.g. Mg) should display a depletion similar to Al. However, the  $MgO/SiO_2$  ratio is higher in the tektites except for moldavites, than that in the target rocks. It may indicate a selective loss of Al and Na, because it is difficult to propose the local enrichment of the targets in quartz and Mg-bearing minerals at the same time. On the other hand the suggestion about the Na and Al depletion of the tektite groups depends on choice of parent material.

REFERENCES. [1] Hoerz, F., H. Feghtig, J. Janicke, and E. Schneider//1983, Proc. Lunar Planet. Sci. Conf. 11th, pp.B353-B363; [2] Yakovlev, O.I. and A.Yu. Lyul'// 1992, Geochemistry, N2, pp.323-327 (Russ.); [3] Keller, P.K., and D.S. McKay//1992, Proc. Lunar Planet. Sci. Conf. 22th, pp.137-141; [4] Yakovlev, O.I.// 1989, Cosmochemistry and Comparative Planetology, Moscow, pp. 127-142 (Russ.); [5] Nagahara, H., I. Kushiro// 1989, LPSC XX, abstr., pp.754-755; [6] Yakovlev, O.I., Yu.P. Dikov, and M.V. Gerasimov//1992, LPSC XXIII, abstr., pp. 1557-1558; [7] Walter, L.S. and J.E. Giutornich//1967, Solar Eng. 11, N3, pp. 163-169; [8] von Engelhardt, W., E. Luft, J. Arndt, H. Schock, W. Weiskirchner //1987, GCA, V.51, pp.1425-1444; [9] Koeberl, C.// 1992, GCA, V.56, pp.1033-1064; [10] Jones, W.B.//1985, GCA, V.49, pp.2569-2576; [11] Izokch, E.P.//1986, in: 'Extraterrestrial matter and Earth', pp.159-203

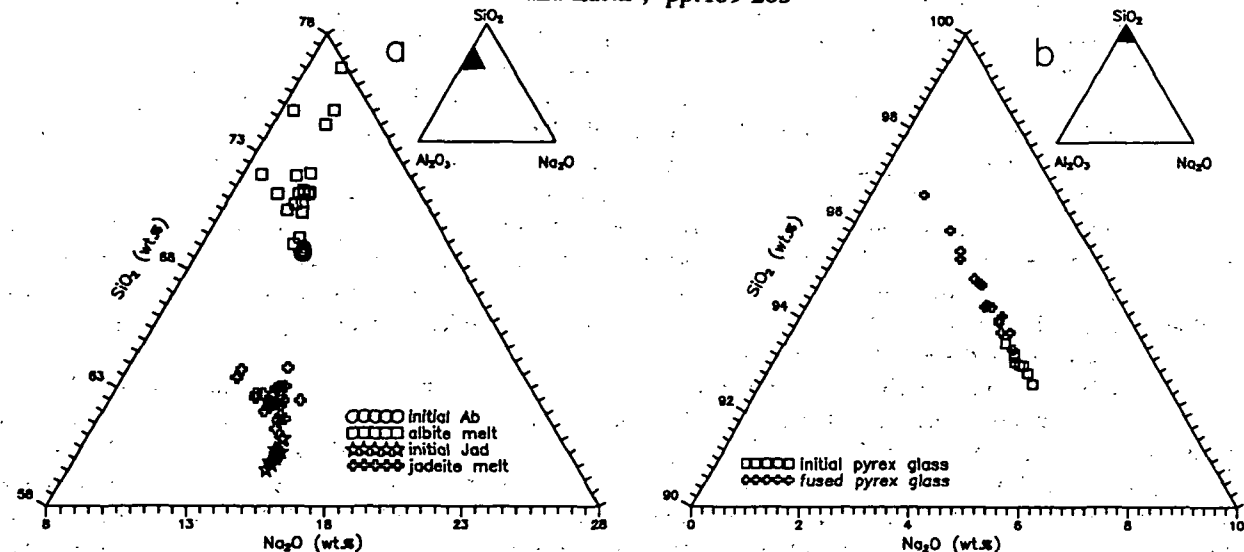


Fig. 1. Bulk chemistry of melts for albite, jadeite (a), and pyrex glass experiments onto a  $Al_2O_3$ - $SiO_2$ - $Na_2O$  diagram.

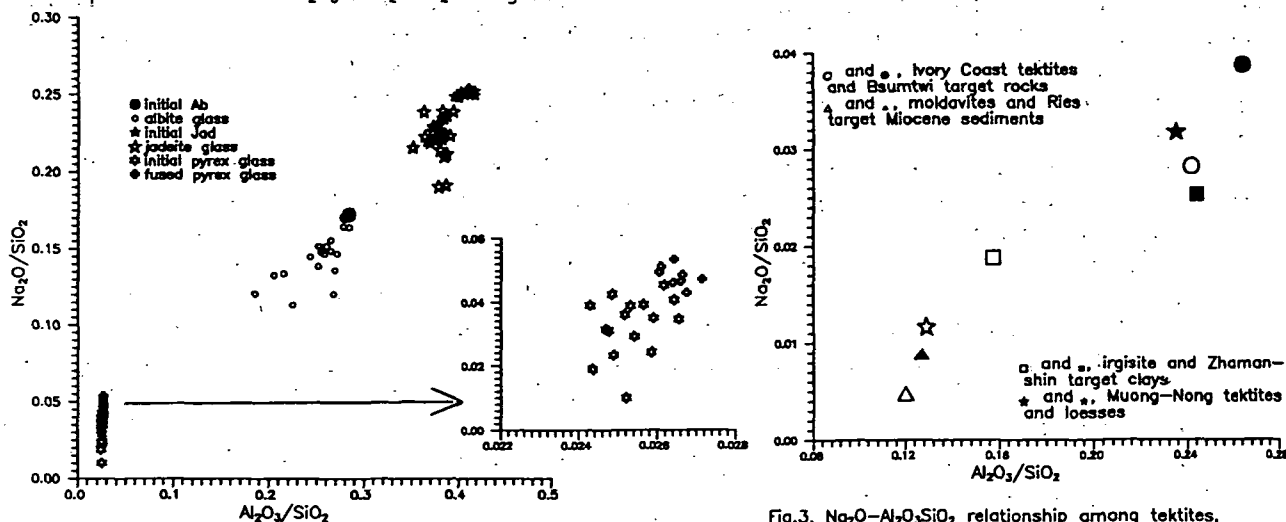


Fig. 2.  $Na_2O$ - $Al_2O_3$ - $SiO_2$  relationships among melts produced by shock experiments. The composition of the melts shows depletion both  $Na_2O$  and  $Al_2O_3$  relative to initial matter.

Fig. 3.  $Na_2O$ - $Al_2O_3$ - $SiO_2$  relationship among tektites, irgites (open symbols) and their proposed source rocks (solid symbols). Data from (8 - 11).

456353

2P

S25-27

ADS ONLY

N94-163245-12040

**SHOCK TRANSFORMATIONS IN QUARTZITE.** D.D.Badjukov(1), E.A.Koslov(2), Yu.N.Zhugin(2), and E.V.Abakshin(2), (1) -Vernadsky Institute of Geochemistry and Analytical Chemistry, Kosygin St. 19, Moscow 117975, Russia; (2) - Institute of Technical Physics, Chelyabinsk-70, Russia

In the paper we report results of studies of experimental shock metamorphism in a quartzite sample. Shock pressure increases in the experiment from a rim to a center of the bowl-shaped sample due to a design of a recovery assembly. The section along an equatorial plane shows a progressive development of shock metamorphism. On the base of observations it is proposed, that diaplectic glass can be a product of quenching of a melt.

Experimental shock metamorphism of minerals and rocks has been intensively studied by many workers [1,2, and others]. However, used facilities and shock recovery assemblies provide a realization of the experiments only at discrete shock pressure in an each shot. Thus, there is possibility to miss some details of shock effects distribution over a pressure range. The task of this work is to study developing of shock effects through a section of a recovered sample of quartzite with non-uniform distribution of shock pressure. A method of the shock loading of the spherical samples by converging of a shock wave has been reported previously [3]. In the experiment the shock wave passed through a bowl-shaped sample from the outer rim towards the center of a quartzite sphere. Shock pressure rises from a distance about one third of the radius to the sample center due to the shock wave convergence. A pattern of the shock loading in the sample includes a pass of the first shock wave, an isentropic pressure rise, a pass of the second reflected shock wave, and a release. The calculated distribution of the shock pressure of the first shock wave and the final peak pressure along a radius of the sphere is shown on Fig.1. The matter picked up from an equatorial section of the sample was studied by optical and X-ray techniques.

Visually a white outer ring, a glassy foggy ring, and a glassy transparent central part can be separated in the equatorial section of the sample. Observations on a thin section demonstrate progressive development of shock metamorphism towards the center of the sphere sample. According to an appearance of shock effects it is possible to separate a few zones. i) The zone of intensive irregular fracturing (Fig. 2a). There are narrow veins filled with a frictionally-produced glass. ii) The zone of developing of sets of deformation planar features. Amount of quartz grains containing the sets of planar features increases towards the center of the sample (Fig. 2b and Fig. 2c respectively). iii) The zone of decreasing of refractive indices and partial isotropization. Areas of developing of a glass are not observed. Practically all quartz grains contain the sets of planar features. iv) The zone of developing of diaplectic glass. At the beginning of the zone there are regions of the diaplectic quartz with planar features and very low birefringence. Identification of the diaplectic glass is based on its refractive index, that is about of 1.48 and partial reverting to a crystalline state by annealing. Aggregates of a non-identified phase are observed too (Fig. 2d). According to microprobe analyses this phase consists of practically pure silica with enrichment in Al and Mg relative to the matrix glass. A X-ray powder diffractogram of the phase differs from that of known silica phases. After annealing the aggregates of the phase were recrystallized, that shows their metastability and, perhaps, a high-pressure origin. v) The zone of a melt glass without any crystalline inclusions.

Boundaries between the zones are very gradual, except for a boundary between the zone of partial isotropization (iii) and the zone of diaplectic glass (iv). In Fig. 2e this boundary is marked by arrows. The relative thicknesses of the zones together with the estimations of shock pressure according to broadening of X-ray diffraction peaks [4] and optical observations are shown in Fig. 1.

The pattern of the developing of the shock metamorphic effects along the radius of the sample is in a good agreement with results reported earlier [1,2,4]. However, the sharp boundary between the diaplectic quartz and the diaplectic glass, and a gradual boundary between the diaplectic glass and the fused glass have never been observed in recovered quartz samples. This relationship among the diaplectic glass, melt glass, and quartz may be due to a fusion of the silica on the shock wave front or immediately behind that, as it was proposed for mechanism of diaplectic glass formation [6,7]. This silica melt could be quenched in the pressure release wave, which is recovered after a pressure release as a diaplectic glass. Temperatures in the release wave increase with decreasing of a distance to the center due to a rise of the shock pressure along the sample radius. Hence, the silica melt in certain point of the sample will not be quenched in a solid state after a final release. This liquid will not have a sharp phase boundary with the melt quenched by higher pressure, because there is not a formation of a new phase and a refractive index of the glass should depend only on pressure and temperature of its quenching. The sharp boundary could be formed in a case, if the diaplectic glass forms by reversing of a high-pressure phase in the solid state by a release. Then the boundary will be absent only by equality of refractive indices of the diaplectic and fused glasses. This condition have a low probability, because in this case the diaplectic and fused glasses would be different phases with a different history of formation. On the other hand the diaplectic glass should have sharp boundary with crystalline quartz at a point, where the Hugoniot state of quartz intercepts the curve of silica melting. Above this point the melt should be coexisting with the crystalline quartz. The suggestion about melting of quartz in shock wave supported also by presence of the aggregates of the unknown phase, amount of which decreases towards the sample center. It would be very interesting to check the presence of liquid state of silica in pressure range of 35 - 40 GPa by direct measurements of some physical properties of silica.

**REFERENCES.** [1] Horz F., 1968, // in: French, B.M., and Short, N.M., eds., Shock metamorphism of natural materials: Baltimore, Mono Book Corp., p.243-254; [2] Stoffler D., 1974 // Fortsh. Miner. V.51, p.256-289; [3] Litvinov B.A., E.A.Kozlov, Yu.N.Zhugin et al., 1991 // DAN, V.319, N6, p.1428-1429 (in Russian); [4] Badjukov D.D., 1986 // Meteoritika, N.45, p.122-130, (in Russian); [5] Grady D.E., 1977 // in: Manghani M.H., and Akimoto S.I., eds., High-pressure research. Academic Press, N.Y., p.389-438; [6] Arndt J., W.Hummel, and I.Gonzalez-Cabeza, 1982 // Phys. Chem. Minerals., V.8, p.230-239

## SHOCK TRANSFORMATIONS IN QUARTZITE

Badjukov, D.D. et al.

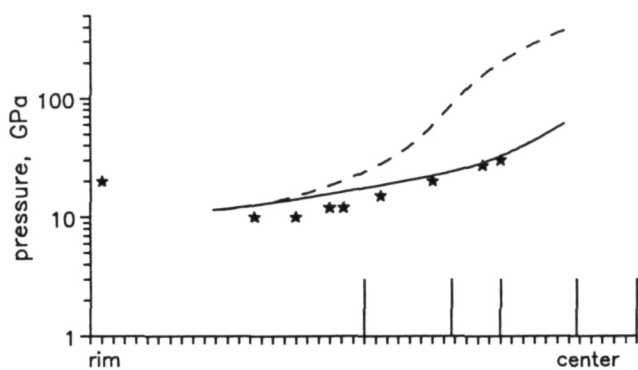


Fig. 1. Pressure distribution along a radius of the quartzite sphere. The initial and final pressures are shown as the solid and dashed lines respectively. Pressure estimations in the recovery sample are shown as asterisks.

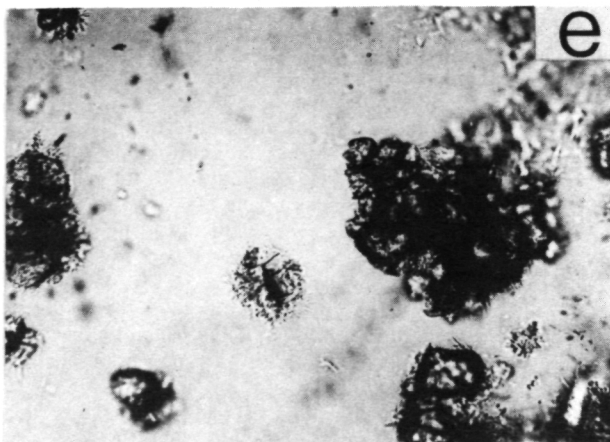
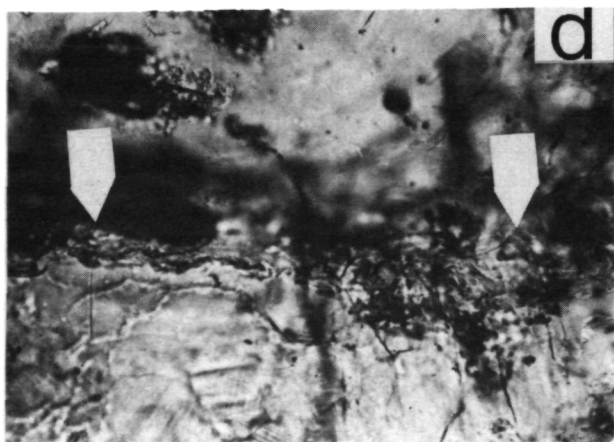
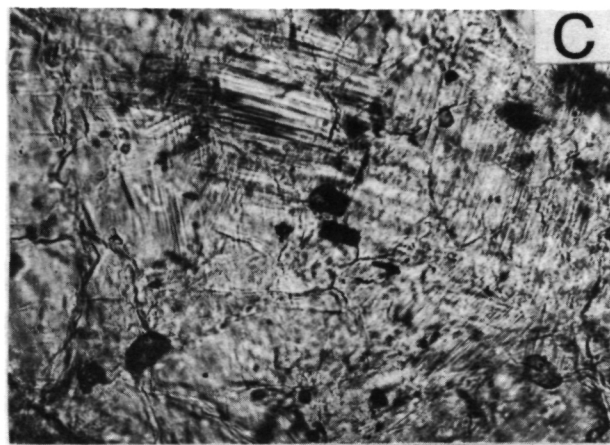
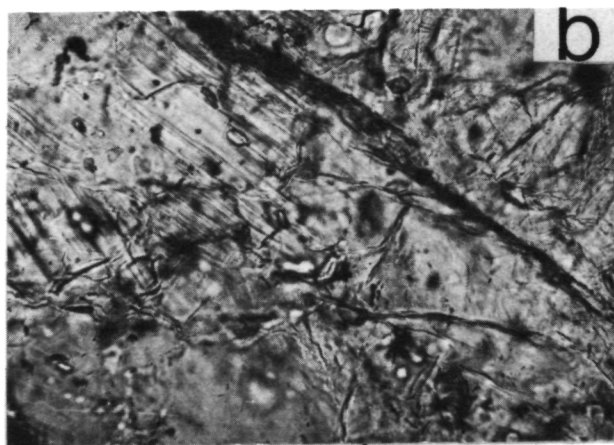


Fig. 2. Transmitted light photomicrographs of the shocked quartzite. Shock pressure increases from (a) to (e). (a) The zone of irregular fracturing. (b) The zone of planar features. (c) An area of the zone of the planar features near the boundary with the zone of decreasing refractive indices. (d) The boundary between diaplectic quartz and diaplectic glass. (e) Aggregates of a new-formed phase in diaplectic glass. Long edge is about 0.4 mm, par.pols.

46-6354  
28

526-46

LPSC XXIV

55

ABS. 5/14/7

N94-12041

**RECONSTRUCTION OF THE DYNAMICS OF THE 1800-1801 HUALALAI ERUPTION:**  
**IMPLICATIONS FOR PLANETARY LAVA FLOWS** Stephen Baloga<sup>1</sup> and Paul Spudis<sup>2</sup> 1. Code SLC, P-2  
 NASA Headquarters, Washington DC 20546 2. Lunar and Planetary Institute, Houston TX 77058

The 1800-1801 eruption of alkalic basalt from the Hualalai volcano, Hawaii provides a unique opportunity for investigating the dynamics of lava flow emplacement with eruption rates and compositions comparable to those that have been suggested for planetary eruptions. Field observations [1] suggest new considerations must be used to reconstruct the emplacement of these lava flows. These observations are: 1) The flow traversed the 15 km from the vent to the sea so rapidly that no significant crust formed and an observation of the eruption reported that the flow reach the sea from the vent in approximately 1 hour; 2) The drainage of beds of xenolith nodules indicates a highly fluid, low viscosity lava; 3) Overspills and other morphologic evidence for a very low viscosity host fluid; 4) No significant longitudinal increase in flow thickness that might be associated with an increase in the rheological properties of the lava; and 5) the relatively large size of channels associated with the flow, up to 80 meters across and several km long [1].

Models for many geologic mass movements and fast moving fluids with various loadings and suspensions, approximate the flow velocity by

$$u = \sqrt{\frac{hg \sin \theta}{C_f}} \quad (1)$$

where  $g$  is gravity,  $\theta$  is the slope, and  $C_f$  is a *dimensionless* friction factor that has to be determined empirically. The velocity  $u$ , the friction factor, and the original depth of the flow are all unknown so additional considerations must be used to develop inferences about the dynamics of the eruption. There are four zones identified where the slope and width are roughly constant in each reach. These values are shown in Table 1. Requiring the model to be applicable in each zone allows the unknown quantities to be estimated for the early flooding stage of eruption before a channel network developed.

For the early stage of emplacement, we assume that the volumetric flowrate  $Q (= u h w)$  is a quantity that is approximately conserved along the flow path. In the steady state, this flowrate has a single value,  $Q_0$ , that is the same in each zone, i.e.,

$$Q_0 = u_i h_i w_i \quad (2)$$

where the subscript  $i$  refers to a particular zone. By using eq. (1) in eq. (2), we get a constraint on the ratio of the thickness of the flow in each section given by :

$$\frac{h_i}{h_r} = \left( \frac{w_r}{w_i} \right)^{2/3} \left( \frac{\sin \theta_r}{\sin \theta_i} \right)^{1/3} \quad (3)$$

where the thickness of the flow in a particular zone is given relative to a reference value that must be determined by field observation. The reference values are taken as those in zone 1 although any zone could be chosen. Table 1 shows the thickness of the flow in each of the zones based on the measured values of the flow widths and slopes and a field estimate of 5 m for the depth in zone 1. Although it is difficult to establish flow thicknesses from post-emplacement conditions, we consider the values in the Table to be consistent with field observations.

## HUALALAI 1801 LAVA FLOW AND PLANETARY IMPLICATIONS: Steve Baloga and Paul Spudis

TABLE 1

Zone	L (km)	W(m)	Slope	u(m/s)	h (m)
1	3.5	1400	12.5°	10 <sup>1</sup>	5
2	4	1150	9.5°	9.8	6
3	5	1200	3.8°	7.1	7.9
4	2.5	2500	1.2°	3.8	7.2

The continuity of the volumetric flowrate along the path of the flow and eq. (4) can be used to express the velocity in each of the zones as

$$u_i = u_1 \left( \frac{w_1 \sin \theta_1}{w_i \sin \theta_i} \right)^{1/3} \quad (4)$$

The velocity in each of the zones can be reconstructed by knowing one velocity in a particular zone. Guest *et al.* [1] have estimated a minimum local flow velocity in zone 1 to be 10 m/s. Using this result as the reference value, Table 1 gives the zonal flow velocities. This set of velocities indicates that the transit time from the crater to the ocean was about 35 minutes.

This type of model produces a longitudinal thickness profile that is relatively flat in spite of the dramatic changes in slope and flow width. In contrast, the 1A flow of the Mauna Loa eruption increased in thickness along the flow path from a few meters or less to more than 25 m near the front. This flow required between 4-5 days to attain its full extent and was accompanied by a significant increase in the rheological parameters of the magma during transit.

Two significant characteristics of the emplacement can be computed from the values reconstructed above, namely, the volumetric flowrate and the friction coefficient. From the definition of flowrate, we find that the flow rate must have been  $7 \times 10^4 \text{ m}^3/\text{s}$  and the uncertainties in the estimates suggest that the flowrate could be even higher. This is almost two orders of magnitude higher than the 1950 Mauna Loa eruption, which attained a peak of  $3000 \text{ m}^3/\text{s}$  [2].

As a check of the consistency of the model, we have examined the flow conditions in the deepest channels. The largest channel is approximately rectangular in shape with a width of 80m and a depth of 18m. The parameters derived above give a depth of 37m for this channel geometry. This channel must have been completely filled at some point during the eruption and the reconstructed eruption conditions easily fulfill this requirement.

**Conclusions** The overall dimensions of the flow are consistently reproduced by a dynamic model taken from turbulent, mass movements, and sedimentation theory produces results consistent with measured dimensions and field observations. The eruption rate must have been approximately  $10^5 \text{ m}^3/\text{sec}$ , roughly two orders of magnitude higher than the 1950 Mauna Loa flow, and comparable to eruption rates cited for large lava flows on Mars and the Moon. The 1800-1801 eruption of the Hualalai volcano is a better analog for planetary eruptions with the high effusion rates than other terrestrial eruptions.

**REFERENCES** [1] Guest J.E. *et al.* (1993) *Geology*, submitted [2] Malin M. (1980) *Geology* 8, 306

456355  
2P

527-46

ABS ONLY

LPSC XXIV

57

N94-314270 42

# HORIZONTAL STRESSES INDUCED BY VERTICAL PROCESSES IN PLANETARY LITHOSPHERES; W. B. Banerdt, Jet Propulsion Laboratory, California Institute of Technology, Pasadena, CA 91109

Understanding the state of stress in the elastic lithosphere is of fundamental importance for planetary geophysics, as it is the link between the observed geologic structures on the surface and the processes which form and modify these structures. As such it can provide valuable constraints for the difficult problem of determining interior structure and processes. On the Earth, most large-scale, organized deformation can be related to lateral tectonics associated with plate dynamics; however, the tectonics on many extra-terrestrial bodies (such as the Moon, Mars, and most of the outer-planet satellites) appears to be primarily vertical in nature, and the horizontal stresses induced by vertical motions and loads are expected to dominate the deformation of their lithospheres [e.g., 1-3]. The largest stress contributions from vertical loading come from the flexure of the lithosphere, which induces both bending moments and membrane stresses. We are concerned here only with non-flexural changes in the state of stress induced by processes such as sedimentary and volcanic deposition, erosional denudation, and changes in the thermal gradient that induce uplift or subsidence. This analysis is important both for evaluating stresses for specific regions in which the vertical stress history can be estimated, as well as for applying the proper loading conditions to global stress models. It is also of interest for providing a reference state of stress for interpreting stress measurements in the crust of the Earth [e.g., 4].

A great deal of confusion exists in the literature about the effects of vertical changes in the lithosphere on its horizontal state of stress ( $\sigma_h$ ). Much of this confusion can be traced to an uncertainty in the type of lateral boundary condition applied to the lithospheric column. Generally, a lateral constraint condition has been assumed [e.g., 5-7] in which the horizontal displacement is assumed to vanish due to the "resistance" of the surrounding rock. McGarr [8] pointed out fundamental logical inconsistencies in the lateral constraint assumption, and argued on both theoretical and observational grounds that this situation is "thoroughly improbable". In its place, he advocated a fixed-stress boundary condition, in which the state of stress in the region outside the area involved in the vertical changes is unaffected. This is physically equivalent to placing a fixed-displacement boundary at an infinite distance. Actual boundary conditions for a real lithosphere almost certainly lie between the lateral constraint and fixed stress cases. Thus these two end members can be used to place bounds on the magnitude of deviatoric stresses induced in the lithosphere by vertical processes. However, previous derivations of  $\sigma_h$  for these situations [7,8] contain errors resulting from incorrect physical assumptions.

**Lateral Constraint.** In this case changes in the vertical stress results in an additional horizontal stress due to a combination of elastic lateral stress accommodation ("Poisson stress"), isostatic subsidence or uplift on a sphere, and thermal re-equilibration. An implicit assumption in previous derivations is that the three contributions to the stress are independent and can be computed separately and simply superposed to arrive at an expression for the stress [7]. Such is not the case. For example, the horizontal expansion induced by vertical compression acts to help support the lithosphere in a spherical geometry, reducing the vertical displacement and hence the compression due to isostatic subsidence on a sphere. As the three mechanisms are not independent, they must be solved simultaneously as an elastic problem in a spherical geometry. Whereas for the Earth the difference between the two approaches is negligible, the error in using superposition can be quite large for smaller planets, with a strong dependence on assumed lithosphere thickness (see Fig.1).

**Fixed Stress.** In order to calculate stresses in the loaded region, McGarr [8] required that horizontal forces balance and solved for the resulting stresses [e.g., 9]. He further assumed that changes in the overburden thickness are equivalent to changes in the elastic lithosphere thickness, changes in the temperature of the lithosphere affect the lithosphere thickness through thermal expansion alone, and thermal erosion and underplating of the lithosphere can be modelled as thickness changes alone, independent of other thermal effects.

The three latter assumptions are inconsistent with current understanding of the relationship between temperature and the structure of the lithosphere. For a given geologic material, the effective thickness of the elastic lithosphere is determined by the depth to a critical isotherm, which is in turn a function only of the heat flux or thermal gradient. The addition or removal of overburden will not result in any change to the total lithosphere thickness once thermal re-equilibration has occurred. In addition, the lithosphere is, in general, composed of two major layers: a crustal layer and an elastic mantle layer, both of which overlie ductile mantle. Changes (e.g., erosion, deposition) near the surface involve material with the density of crustal rocks

## HORIZONTAL STRESSES: Banerdt W. B.

whereas the compensating changes at the base of the lithosphere (due to vertical migration of the critical isotherm) involve the mantle, which has a higher density. Thus the integrated vertical stress will decrease and the buoyancy of the column will increase. These corrections produce significant changes in the horizontal stress results. For a nominal set of parameters typical sedimentary basins on the Earth, the corrected expression results in a ratio of horizontal to vertical stress of about  $-0.2$ , versus  $+0.3$  for the original derivation [8]. Note that if the base of the elastic lithosphere is within the crust, there is no net change in the mechanical state after addition or removal of material at the surface, and the induced horizontal stress is zero.

**Geometric Constraint.** The above discussion regarding the fixed stress boundary condition applies only to two-dimensional structures, such as a long ridge or syncline. However, many planetary loading problems involve quasi-circular features like impact basins or volcanic constructs. In this situation the proper boundary condition is less ambiguous, as lateral constraint is furnished by the resistance (due to the circumferential, or "hoop" stress) of the surrounding material to radial expansion or contraction. The ratio of horizontal to vertical stress in this case is given by  $\nu/2$ , in the absence of thermal or spherical effects. For comparison, this ratio would be  $\nu/(1-\nu)$  for lateral constraint, 0 for a fixed stress, and 1 for hydrostatic conditions (Fig. 2). In addition, a radially decreasing horizontal stress is induced in the region surrounding the load, in contrast to the other cases discussed previously.

It should be noted that these stresses are not included in thin shell or thin plate elastic models, such as those typically used to infer lithosphere thickness from mascon or volcanic loads [e.g., 2, 10-11], due to the approximations inherent in the formulation. Thus they should be added to those solutions in order to more accurately estimate the state of stress. Whereas the radial positions of stress peaks will not be influenced, the relative magnitudes of the principal stresses, which determines the style of faulting, will change, possibly affecting the interpretation of the models.

**References:** [1] Melosh, *Proc. LPSC 9th* 3513, 1978; [2] Solomon & Head, *JGR* 84:1667, 1979; [3] Banerdt et al, in *Mars* 249, 1992; [4] McGarr & Gay, *Ann. Rev. Earth Planet. Sci.* 6:405, 1978; [5] Price, *Fault & Joint Development in Brittle & Semi-Brittle Rock*; [6] Voigt & St. Pierre, *Adv. Rock Mech., Proc. 3rd Cong. Int. Soc. Rock Mech.*, IIA:580, 1974; [7] Haxby & Turcotte, *Geol.* 4:181, 1976; [8] McGarr, *JGR* 93:13609, 1988; [9] Artyushkov, *JGR* 78:7675, 1973; [10] Banerdt, *JGR* 91:403, 1986; [11] Comer et al, *Rev. Geophys.* 23:61, 1985.

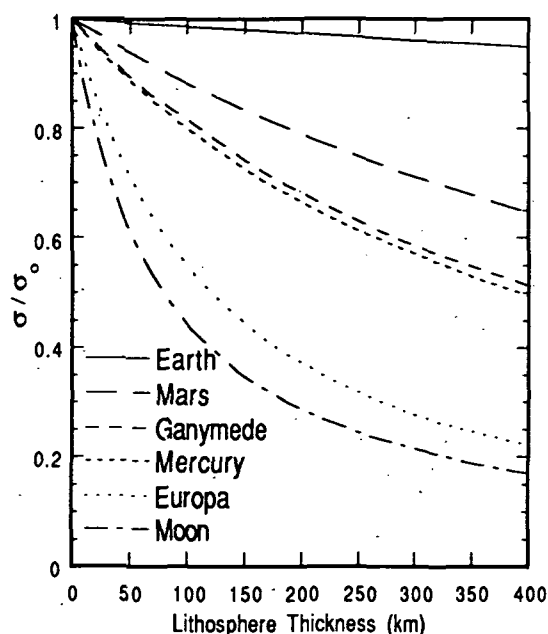


Fig. 1. Ratio of horizontal stress calculated from a fully spherical elastic solution to that calculated by superposition of individual contributions, as a function of lithosphere thickness, for various planets and satellites. Nominal values for elastic constants, thermal expansion coefficients, and thermal gradients have been assumed. Values deviating significantly from 1 indicate that the derivation of [7] gives a poor approximation to the stress.

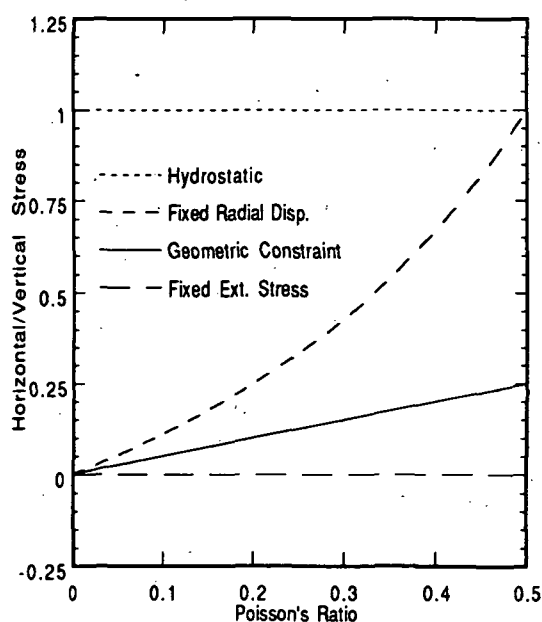


Fig. 2. Ratio of the elastically induced horizontal stress to the vertical load stress for various boundary conditions.

ENCOURAGING FEMALE INTEREST IN SCIENCE. AND MATHEMATICS. N. G. Barlow, Lunar and Planetary Institute, 3600 Bay Area Blvd., Houston, TX 77058.

The United States has begun a new initiative to improve the science literacy of our students. Classroom curricula are being rewritten with an increased emphasis on the understanding of concepts rather than memorization of facts and figures. Studies have shown that students learn more when they are actively involved in a project. Science fairs and science camps have been the traditional means by which students have participated in science activities beyond the classroom environment. However, studies reveal that young women and students of various ethnic backgrounds have not participated as fully in these activities as white males, either because they have not been informed about the event or more commonly because they have not been encouraged to participate by parents, teachers, counselors, and other adults. Today a number of programs are being offered specifically for these groups which have traditionally been underrepresented in scientific and engineering fields. Examples of such programs for young women are Expanding Your Horizons workshops, programs with Girl Scouts, Girls Clubs of America Operation SMART program, and mentoring programs initiated by various professional women's organizations.

Generating enthusiasm for science and mathematics in our young people must begin long before secondary school and college if we are to succeed. Children up through about the 4th grade level tend to be very excited by science, particularly dinosaurs and space exploration. However, a recent study of 3000 students in grades 4 through 10 across the United States indicates that both boys and girls tend to lose interest in science and mathematics during this time period (1). In elementary school, 75% of the girls and 82% of the boys said they "liked" science, but by high school only 63% of girls and 75% of boys agreed with that statement. Similar declines are seen in mathematics: 81% of girls and 84% of boys like math in elementary school, declining to 61% of girls and 72% of boys in high school. The study also found that a strong sense of self-esteem is correlated with favorable impressions of mathematics and science for both girls and boys.

Faced with these statistics, many scientists are involved in efforts to improve science education in America. Before these efforts will be successful, however, three common myths must be laid to rest.

(1) *Astronomy cannot be taught to elementary school students because it is too technical.* Space and space exploration are fields which excite young children. We can capitalize on the visual aspect of planetary science and astronomy to further the inherent interest these children have in their surroundings. In addition, basic concepts such as the organization of the solar system, the relative sizes of the planets, the cause of seasons, and basic geologic processes operating on the planets and moons can be taught to the students through numerous creative hands-on activities.

(2) *Students are being encouraged in math and science in order to produce more future scientists and engineers.* The vast majority of students will not become engineers or professional scientists. However, they will be the voters (and some will be the politicians) of the future and thus have input into the funding of science programs. Our main goal should be to produce a scientifically literate population who will see the opportunities and benefits of a strong science program.

(3) *Special programs are not necessary for those groups who have been traditionally underrepresented in the technical fields.* Women constitute approximately 10% of the astronomy and planetary science communities; the numbers of ethnic minorities such as African-Americans and Hispanics in these fields is even lower (2). Many people argue that gender-only or race-only scientific programs and activities should not be encouraged since we live in an integrated society and we all need to learn to work together. This would be fine if the educational opportunities were equal among women, ethnic minorities, and white males. Unfortunately, numerous studies indicate that women and minority students do not receive the same quality or quantity of education that white males do (3). Special science programs geared toward specific groups show these students that science is fun and relevant to their daily lives while often providing them with role models. Students also tend to participate more fully in the activities when they are in a group of their peers—for example, in mixed gender situations, many girls are afraid that they will be unattractive to the boys if they act too interested or do better in science and math



## ENCOURAGING FEMALES IN SCIENCE/MATH: Barlow, N.G.

than their male colleagues. We often think this situation no longer exists in the 1990's, particularly when we use our own children as our guidelines. Unfortunately, this situation is still much too true for the vast majority of students who do not come from enlightened families such as our own. Special programs for the groups traditionally underrepresented in the sciences help to overcome many of the notions which keep these students from fully participating in, understanding, and enjoying science.

Several scientific programs aimed specifically at young women have been initiated in recent years. Often they have originated through partnerships of women's organizations and schools or Girl Scouts/Girls Club. The four programs described below are just a sampling of the ways in which young women are being acquainted with the joys of science.

(1) *Expanding Your Horizons*. Expanding Your Horizons (EYH) workshops were first organized by female scientists in the 1970's following a study by a University of California Berkeley sociologist which found that only 8% of college freshmen women had the necessary math background to pursue technical careers (compared to 50% of freshmen men). EYH workshops are one-day events where young women (generally intermediate school aged students) have the opportunity to participate in hands-on workshops dealing with various areas of science. The workshops are conducted by female scientists and engineers, who not only lead the activities but also talk with the young women about academic preparation, salaries, future opportunities, and any other topics the girls have questions about.

(2) *Girl Scouts*. Girl Scouting is more than just selling cookies these days. Increasingly, Girl Scout councils are taking advantage of opportunities to expose the scouts to math and science programs. The Lunar and Planetary Institute has had considerable success working with the San Jacinto Girl Scout Council in offering "Youth in Space", a program for 7th and 8th graders which provides the scouts with a weekend of planetary science activities. The scouts learn about our solar system through many hands-on activities, then focus on the Martian environment in order to produce their final project: a Mars base. Other organizations, such as the Association of Women Geoscientists, also work with Girl Scout Councils to provide opportunities for young women to experience science beyond the classroom (4).

(3) *Girls Clubs*. Girls Clubs of America have instituted a program called Operation SMART, which encourages every girl in Science, Math, and Relevant Technology. The program has three components, one for elementary students (ages 6 to 11), one for early adolescents (ages 11-14) and one for high school students (ages 14-18). The elementary and early adolescent components utilize a variety of materials and activities to emphasize scientific inquiry, exploration, empowerment, and equity. The high school component also incorporates a more rigorous science content and career preparation materials. The Girls Clubs also have forged partnerships with science centers to provide the girls with opportunities to interact with the scientific expertise provided through numerous community organizations.

(4) *Mentoring Programs*. Numerous organizations have initiated science/math mentoring programs. Several branches of the American Association of University Women have begun such mentoring programs with local junior high and high schools. The Association for Women in Science has initiated nationwide mentoring programs for female undergraduates. These programs provide young women with opportunities to experience science beyond the classroom environment and link them with women scientists and engineers who can answer their questions and help guide them during periods of decision making.

REFERENCES: (1) *Shortchanging Girls, Shortchanging America*, American Association of University Women, 1991. (2) *AAS Membership Survey: Final Report and Recommendations*, 1991. (3) *The AAUW Report: How Schools Shortchange Girls*, American Association of University Women, 1992. (4) *AWG-Girl Scouts USA 1992 Wider Opportunity*, Gaea, XV, 1992.

456356  
2P

528-91  
ABR 02047  
N94-123048

LPSC XXIV

61

INCREASED DEPTH-DIAMETER RATIOS IN THE MEDUSAE FOSSAE FORMATION DEPOSITS OF MARS. N. G. Barlow, Lunar and Planetary Institute, 3600 Bay Area Blvd., Houston, TX 77058.

P-2

Depth to diameter ratios for fresh impact craters on Mars are commonly cited as approximately 0.2 for simple craters and 0.1 for complex craters. Recent computation of depth-diameter ratios in the Amazonis-Memnonia region of Mars indicates that craters within the Medusae Fossae Formation deposits found in this region display greater depth-diameter ratios than expected for both simple and complex craters.

Photoclinometric and shadow length techniques have been used to obtain depths of craters within the Amazonis-Memnonia region. 37 craters in the 2 to 29 km diameter range and displaying fresh impact morphologies were identified in the area of study (9°S to 15°S latitude, 170°W to 180°W longitude). This region includes the Amazonian aged upper and middle members of the Medusae Fossae Formation (Amu and Amm) and Noachian aged cratered (Npl<sub>1</sub>) and hilly (Nplh) units (1). The Medusae Fossae Formation is characterized by extensive, flat to gently undulating deposits of controversial origin (2, 3, 4). These deposits appear to vary from friable to indurated.

Early analysis of crater degradation in the Medusae Fossae region suggested that simple craters excavated to greater depths than expected based on the general depth-diameter relationships derived for Mars (5). However, too few craters were available in the initial analysis to estimate the actual depth-diameter ratios within this region. Although the analysis is continuing, we are now beginning to see a convergence towards specific values for the depth-diameter ratio depending on geologic unit.

The simple to complex transition diameter appears to occur around 5 km in this region, similar to values obtained by Pike for other regions of Mars (6). Fresh impact craters superposed on the Noachian aged units display similar depth-diameter ratios as those found for the planet on average: simple craters have a depth-diameter ratio of approximately 0.23 ( $\pm 4$ ) whereas the ratio for complex craters is closer to 0.15 ( $\pm 3$ ). However, both simple and complex craters within the Medusae Fossae Formation deposits are deeper than craters of similar size outside the deposits (Table 1). Within the Medusae Fossae Formation, simple craters display a depth-diameter ratio of approximately 0.29 ( $\pm 5$ ) and complex craters have a ratio of 0.21 ( $\pm 4$ ). Thus simple craters within the Medusae Fossae Formation deposits are approximately 79% deeper than similarly sized craters outside the deposits. Complex craters are 71% deeper in the deposits than in surrounding areas.

The increase in depth-diameter ratio for the impact craters within the Medusae Fossae Formation deposits is almost certainly the result of textural differences between these deposits and other geologic units on Mars. Geomorphic analysis of features within these deposits suggests that the material is fine-grained and easily erodible. Laboratory experiments suggest that impact into fine-grained material can dramatically alter the morphometric properties of the resulting impact craters (7). Continuing analysis of depth-diameter ratios across Mars will provide further insight into the areal variation of near-surface properties.

REFERENCES: (1) Scott, D.H. and Tanaka, K.L. (1986) *USGS Map I-1802-A*. (2) Scott, D.H. and Tanaka, K.L. (1982) *JGR*, **87**, 1179-1190. (3) Schultz, P.H. and Lutz, A.B. (1988) *Icarus*, **73**, 91-141. (4) Forsythe, R.D. and Zimbelman, J.R. (1990) *LPSC XXI*, 383-384. (5) Barlow, N.G. (1992) *LPSC XXIII*, 63-64. (6) Pike, R.J. (1988) *Mercury*, 165-273. (7) Schultz, P.H. (1992) *JGR*, **97**, 11623-11662.

## DEPTH-DIAMETER IN MEDUSAE FOSSAE: Barlow, N.G.

TABLE 1

## DEPTHS AND DIAMETERS OF CRATERS IN ANALYSIS

DIAMETER (D) (KM)	DEPTH (d) (KM)	RATIO (d/D)
28.0*	1.35	0.05
6.0*	1.13	0.19
28.5	2.48	0.09
3.1	0.77	0.25
2.7	0.66	0.24
2.7	0.66	0.24
2.0	0.44	0.22
4.3*	1.16	0.27
8.2*	2.13	0.26
2.7*	0.95	0.35
10.0*	3.08	0.31
2.5*	0.98	0.39
2.5*	0.79	0.32
3.8*	0.98	0.26
3.8*	1.08	0.28
9.9*	2.25	0.23
10.8	1.35	0.13
6.8*	1.35	0.20
19.1	1.17	0.06
5.2	0.78	0.15
3.5	0.73	0.21
4.6	0.73	0.16
3.5	0.73	0.21
2.6	0.43	0.17
8.4	1.28	0.15
6.8	1.10	0.16
3.4	0.73	0.21
7.0	1.29	0.18
7.4	1.29	0.17
3.9	0.72	0.19
9.6	1.61	0.17
2.5	0.57	0.23
2.5	0.57	0.23
4.6	0.89	0.19
4.0	0.72	0.18
5.0	1.08	0.22
6.9	1.15	0.17

\*Fresh impact craters within Medusae Fossae Formation Deposits.

456357  
2P529-34  
ABS. ONLY  
163-11

LPSC XXIV

63

N94-12044

# BEHAVIOR OF VORTICES GENERATED BY AN ADVANCING EJECTA CURTAIN IN THEORY, IN THE LABORATORY, AND ON MARS. O.S. Barnouin and P.H. Schultz, Dept. of Geological Sciences, Brown University, Providence, R.I. 02912.

**Introduction:** Several papers [1, 2, 3, 4] assess the interaction between an atmosphere and advancing ejecta to assess possible atmospheric processes affecting ejecta emplacement. Ejecta travel through an atmosphere in two modes [1]: larger ejecta blocks follow ballistic trajectories unhindered by the atmosphere; finer ejecta are entrained in a turbulent basal cloud, which develops as the advancing ejecta curtain generates strong atmospheric winds. Laboratory experiments [1, 2, 3] reveal that this cloud of fine ejecta produce ramparts, flow lobes, or radial scouring that superposes larger ballistic ejecta emplaced earlier. Martian [1, 2, 3], Venusian [4, 5] and terrestrial ejecta facies [1, 6] can be interpreted in terms of processes observed in the laboratory with appropriate first-order corrections for scaling. A continuum model [7] of the atmospheric flow around an advancing inclined plate simulated and reproduced some of the complex flow patterns observed in front and at the top of the curtain [3]. Here we consider improvements to the model to compare quantitatively the approximate position of ejecta deposition (i.e. run-out distance) with laboratory experiments and martian ejecta facies.

**Theory:** At the time of crater formation, the bulk of the ejecta comprises a relatively thin ejecta wall forming an inclined curtain [8]. Since shock processes and comminution during excavation [9] ensures that a large fraction of this ejecta is small with respect to the curtain width, the base of the curtain forms an impermeable wall with respect to the atmosphere. As a consequence, the atmosphere sees the ejecta curtain as a continuous plate-like structure in the laboratory and on Mars [3]. A Kutta-Joukowski estimate [6] allows calculating the circulation generated by this analogy with the advancing curtain. The circulation must generate two vortices to conserve angular momentum in the atmosphere in the vicinity of the curtain as it decelerates to its minimum velocity at the end of crater excavation. A stronger flow separation vortex occurs below, behind the continuous portion of the curtain. If the curtain moves from left to right, then this lower vortex rotates in a counterclockwise direction with a circulation greater than the circulation generated by the ejecta curtain at a given time, reflecting remnant angular momentum from an earlier time. A second vortex shed at the top of the continuous curtain rotates in the opposite direction, with a circulation equal to the difference between that generated by the advancing curtain and the lower vortex. The strength of this upper vortex increases until the ejecta curtain reaches its minimum speed. As the curtain starts accelerating again [3], angular momentum is no longer supplied to the upper vortex; hence, it dissipates by diffusion. The lower vortex, however, regains the strength previously lost until the curtain becomes discontinuous, i.e. permeable to the flow. At this point, vorticity generated at the base of the curtain within the boundary layer [6] interacts with the vortex generated behind the curtain, thereby perhaps strengthening still further. This vortex entrains the finer grain fraction of the thinning ejecta curtain and proceeds outwards, driven by the horizontal momentum imparted to it by the curtain but losing strength by diffusion.

For an incompressible flow, each vortex generated by the curtain is described by the vorticity equation

$$\frac{D\omega}{Dt} = \omega \nabla \cdot \mathbf{v} + \nu \nabla^2 \omega$$

rate of change  
of vorticity = rate of deformation  
of the vortex lines + net rate of  
viscous diffusion

where  $\omega$  is the vorticity vector of the flow,  $\mathbf{v}$  is the velocity vector of the flow, and  $\nu$  is the kinematic viscosity. This equation does not entirely describe the behavior of the vorticity in a stratified incompressible flow. An additional term is required because the center of mass of a fluid particle in a density gradient does not coincide with its geometric center. Since pressure acts through this point, the fluid parcel should rotate, producing additional vorticity affecting large scale vortices. For simplicity, such effects are not considered. Although an axisymmetric geometry is assumed, the vortices shed by the ejecta curtain are viewed as two dimensional. These simplifying assumptions yield the vorticity diffusion equation:

$$\frac{D\omega}{Dt} = \nu \nabla^2 \omega$$

Considering the flow in the vortex to be irrotational, then a solution of this diffusion equation is the Oseen vortex:

$$v_{\theta} = \frac{\Gamma}{2\pi r} (1 - \exp(-r^2/4\nu t))$$

where  $v_{\theta}$  is the angular flow velocity,  $r$  is the radius from the vortex center,  $\Gamma$  is the circulation of the vortex and  $t$  is time. Such a model has been used effectively to determine the decay of laminar vortices and, with some modification, large scale turbulent vortices shed behind airfoils [10, 11].

Aerodynamic forces decelerate individual ejecta to a velocity where they are entrained in the Oseen vortex. The maximum particle size that the vortex entrains is determined simply by equating the weight of a spherical body to the drag force generated by  $v_{\theta}$ , the flow velocity in the vortex.

**Laboratory:** Laboratory experiments performed at the NASA Ames Vertical Gun Range verify both qualitatively

## EJECTA CURTAIN GENERATED VORTICES: Barnouin, O.S. and Schultz, P.H.

[2,3] and quantitatively [6] the theoretical justification for the flow generated by the advancing ejecta curtain. At the time of crater formation, two vortices are observed, and as expected, a weaker, short-lived vortex forms at the top of the curtain. The stronger vortex forms behind the base of the curtain and gains strength once the ejecta curtain accelerates outwards beyond the crater rim [1, 2, 3].

At low pressures (0.06 bar atmosphere), most ejecta are ballistically emplaced for a crater formed in pumice by a projectile travelling at 2 km/s, but the atmosphere entrains a small fraction of the ejecta. Because the pumice target has a bimodal grain size distribution, with peaks at 80  $\mu$  and 25  $\mu$  [3], a subtle rampart is produced. Application of the Oseen vortex suggests the vortex winds should carry the 80  $\mu$  particles for 0.25 times the total time of crater formation (38 ms), provided that these particles are sufficiently decelerated for entrainment by the maximum circulation generated by the curtain. The 25  $\mu$  particles, if entrained, will be carried for only a slightly longer time (98 ms). The theoretical results are therefore consistent to first order with observations.

The Oseen vortex also can be used to determine the time at which both the 80 and 25  $\mu$  pumice particles are deposited over a range of atmospheric pressures and densities. Multiplying the theoretical time of deposition by the outward velocity (from the film record) provides a first-order estimate of the ejecta run-out distance. This approach provides a consistent match between theory and experiments, thereby establishing confidence for extrapolation to broader scales.

**Planetary scales:** Several conditions must be met for the above model to apply at martian scales. First, the model requires that the flow around the continuous portion of the ejecta curtain remains incompressible. Thus, the velocity of this curtain must be subsonic at the time of crater formation. This condition is true for Mars for craters up to 100 km in diameter [2, 3]. Second, the atmosphere needs to recover from the initial impact blast by the time of crater completion. On Mars, the pressure satisfies this requirement as it returns to ambient conditions well before crater formation [3, 4]. Third, turbulent flow enhances viscous diffusion in the vortices generated at large scales and requires that the viscosity term  $\nu$  in the Oseen vortex be replaced by an effective viscosity  $\nu_{eff} = \nu + a\Gamma$ . The constant  $a$  is determined empirically by observing the time for vortices shed by airfoils to diffuse together.

The flow-like nature of the inner ejecta facies for martian craters could be the result of water released during impact that decreases basal shear of the larger initially ballistically emplaced ejecta near the rim [3,12]. The Oseen vortex, therefore, is most relevant for the role of curtain generated winds controlling run-out distances of the outer ejecta deposits. The theory suggests that maximum winds (just below the speed of sound) carry particles up to 4 cm in diameter. However, because these maximum vortex winds rapidly decay by diffusion, this maximum particle size is entrained by the vortex flow for only a brief instant. From rim-to-rampart distances [3], preliminary analyses indicate that if ramparts consist of 3 cm diameter particles carried by the vortex, then the basal vortex must have traveled outwards with a velocity approximately equal to the minimum curtain velocity at the time of crater formation. If the ramparts are made of smaller grain sizes, this velocity can be less. Theory, hence, suggests that curtain generated winds deposit finer ejecta after the larger ballistically emplaced ejecta, consistent with the observed depositional sequence on Mars [1, 2, 3, 12].

If we assume that the derived minimum velocity equals the expected outward vortex velocity in the present day martian atmosphere, then the Oseen vortex suggests that craters of similar sizes but with different run-out distances result from either, or the combination of two situations. If the run-out distance is greater than commonly expected from [3] then: 1.) the particles in the rampart or flow-lobe are smaller than 3 cm in diameter, the reference particle diameter; and/or 2.) the atmospheric density at impact is larger than today, possibly from impact released volatiles, a thicker atmosphere in the martian past, or both. For two side-by-side 5 km diameter craters in the Hesperian ridged plains (28.6 S, 241.9 W), similar target properties should result in common ejecta sizes assumed to equal the 3 cm reference diameter in the ejecta facies observed. However, one of the craters has thin distal lobes that extend to about 2.5 crater radii while the other has a contiguous rampart at the typical rim-to-rampart distance of 1.7-1.8 crater radii [3]. Application of the model suggests that the density of the atmosphere must have been close to 0.080 kg/m<sup>3</sup> when the first crater, but close to present day conditions at 0.018 kg/m<sup>3</sup> [13] for the second. This factor of 4 change in density and, hence, pressure could have resulted from precession-driven climate changes [3].

**Conclusion:** Although the Oseen vortex does not describe the final stages of ejecta emplacement in an atmosphere [3], it does provide a clue to the run-out distance before deposition of ejecta of different grain sizes in the laboratory. At large scales, the Oseen vortex model may provide information on either the grain size (i.e. local geology) or the atmospheric environment of the ejecta through time. However, the model has limitations: it does not include the effects of a stratified atmosphere; viscous diffusion in the core of the large vortices where the flow is supersonic; and, another process similar to a hydraulic jump but which occurs in vorticity, i.e. vortex breakdown.

**References:** [1] Schultz and Gault, 1979, *JGR* 84,7669-7687. [2] Schultz and Gault, 1982, *GSA* special paper 190, 153-174. [3] Schultz, 1992a, *JGR* 97, 11623-11662. [4] Schultz, 1992b, *JGR* 97, 16183-16248. [5] Phillips et al., 1991, *Science* 252, 288-296. [6] Schultz and Grant, 1989, *LPSC XX*, 972-973. [6] Barnouin and Schultz, *LPSC XXIII*, 65-66. [8] Gault et al., 1968, *Shock Metamorphism of Natural Materials*, Mono, 219-229. [9] Schultz and Mendell, *PLPSC IX*, 2857-2883. [10] Squire, 1965, *Aero. Quarterly* XVI, 302-306. [11] Panton, 1984, *Incompressible Flow*, Wiley & Sons., 288. [12] Carr et al., 1977, *JGR* 82, 4055-4065. [13] Seiff and Kirk, 1977, *JGR* 82,4364-4378.

456358  
2f

530-25  
ABS ONLY

4-6-12045

**MINERALOGY OF CHONDRITIC INTERPLANETARY DUST PARTICLE IMPACT RESIDUES FROM LDEF**

R.A. Barrett<sup>1</sup>, M.E. Zolensky<sup>2</sup>, and R. Bernhard<sup>1</sup>; <sup>1</sup>Lockheed ESCO, 2400 NASA Rd. 1, Houston, TX 77058, <sup>2</sup>SN2, NASA Johnson Space Center, Houston, TX 77058.

**SUMMARY:** A detailed structural and compositional analysis of several impactor residues was performed utilizing transmission electron microscopy, energy dispersive spectroscopy, and electron diffraction. Residues from the interior of several craters in gold surfaces were removed with a tungsten needle, mounted in EMBED-812 epoxy, and ultramicrotomed. The presence in these residues of equilibrated ferromagnesian minerals, recrystallization textures, glass, and melted metal and sulfide bodies decorating grain boundaries is indicative of varying degrees of shock metamorphism in all impact residues we have characterized.

**INTRODUCTION:** Impactor residues in materials exposed on the Long Duration Exposure Facility (LDEF) satellite are being characterized to establish the nature and abundance of meteoritic and orbital debris materials in the low-Earth orbit (LEO) environment [1], and also the effect hypervelocity impacts will have on spacecraft. In this study, simple techniques were developed for the study of selected chondritic (containing Si, Mg, Fe, +/- Al, Ca, S, Mn, and Ni in appropriate amounts) impactor residues in shallow craters in gold plates, from the LDEF experiment of Fred Horz [2-4]. A detailed structural and compositional analysis of several of these impactor residues was performed utilizing transmission electron microscopy, energy dispersive spectroscopy, and electron diffraction. The immediate goal of this continuing work has been to determine the effects of the impact process on impactor mineralogy and mineral composition of chondritic interplanetary dust particles (IDPs), and to compare these impactor residues to chondritic IDPs collected from the stratosphere.

**SAMPLE PREPARATION AND ANALYTICAL PROCEDURES:** Residues from the interior of several craters in gold [2] were removed with a tungsten needle, mounted in EMBED-812 epoxy, and ultramicrotomed into 90nm-thick sections. Observation of the sections on carbon-coated copper grids was done by transmission electron microscopic techniques using JEOL 100CX and 2000FX analytical electron microscopes. Chemical analyses of crystalline areas were performed with a PGT System 4 and energy dispersive X-ray spectrometer and reduced with the PGT dedicated software. The structural state of all analyzed materials were assessed by electron diffraction, which proved to be a critical step, considering the non-crystalline nature of many materials observed.

**RESULTS:** We examined the mineralogy of residues from three impact features: nos.102, 121, and 295. Impact residue 102 has very finely-divided crystalline pyroxene and olivine, showing abundant evidence of intense shock, these being planar deformation features, mosaicism, and, in some instances, evidence of recrystallization (120° grain intersections). Compositional analyses of these ferromagnesian phases are now being performed. The matrix consists of frothy ferromagnesian glass. Spherical bodies of Fe-Ni metal and pyrrhotite abound locally, particularly at grain boundaries. (See Figure 1.) Impact residue 121 contains fragmental grains of olivine (Fo<sub>57-67</sub>), orthopyroxene (En<sub>63-64</sub>), Fe-Ni metal, and abundant glass. The olivine and pyroxene grains show abundant evidence of shock (see above for criteria). Impact residue 295 contains shocked, fragmental olivine (Fo<sub>56-71</sub>) and orthopyroxene (En<sub>71</sub>), pyrrhotite, and glass.

The compositions of olivines and orthopyroxenes in all residues characterized in this study are equilibrated compared to anhydrous chondritic IDPs, and also Fe-rich compared to hydrous chondritic IDPs. They are also Fe-rich as compared to ferromagnesian from partially melted chondritic IDPs [5], which are typically on the order of Fo<sub>90</sub> and En<sub>90</sub>. The presence of equilibrated and shocked ferromagnesian minerals, recrystallization textures, glass, and melted metal and sulfide bodies decorating grain boundaries, is indicative of varying degrees of shock metamorphism in all impact residues we have characterized. Our failure to locate any magnesian olivines or pyroxenes is illustrative of the pervasive shock metamorphism of these particular residues. Nevertheless, we are continuing to search for more pristine IDP impactor residues.

**MINERALOGY OF LDEF IMPACT RESIDUES: Barrett R.A. et al.**

Acknowledgments: We thank Fred Horz for providing some of the best impact examples from his LDEF experiment and his discussions.

REFERENCES: [1] See et al. (1990) Planetary Science Branch Special Pub. 84, JSC 24608, 586 p.; [2] Horz and Bernhard (1992) NASA Tech. Memorandum 104750, 210 p.; [3] Bernhard and Horz (1992) LPSC XXIII, p. 93-94.; [4] Bernhard et al. (1993) Proceedings of the Second LDEF Post-Retrieval Symposium (in press); [5] Zolensky and Barrett (1993) Microanalytical J. (in press).

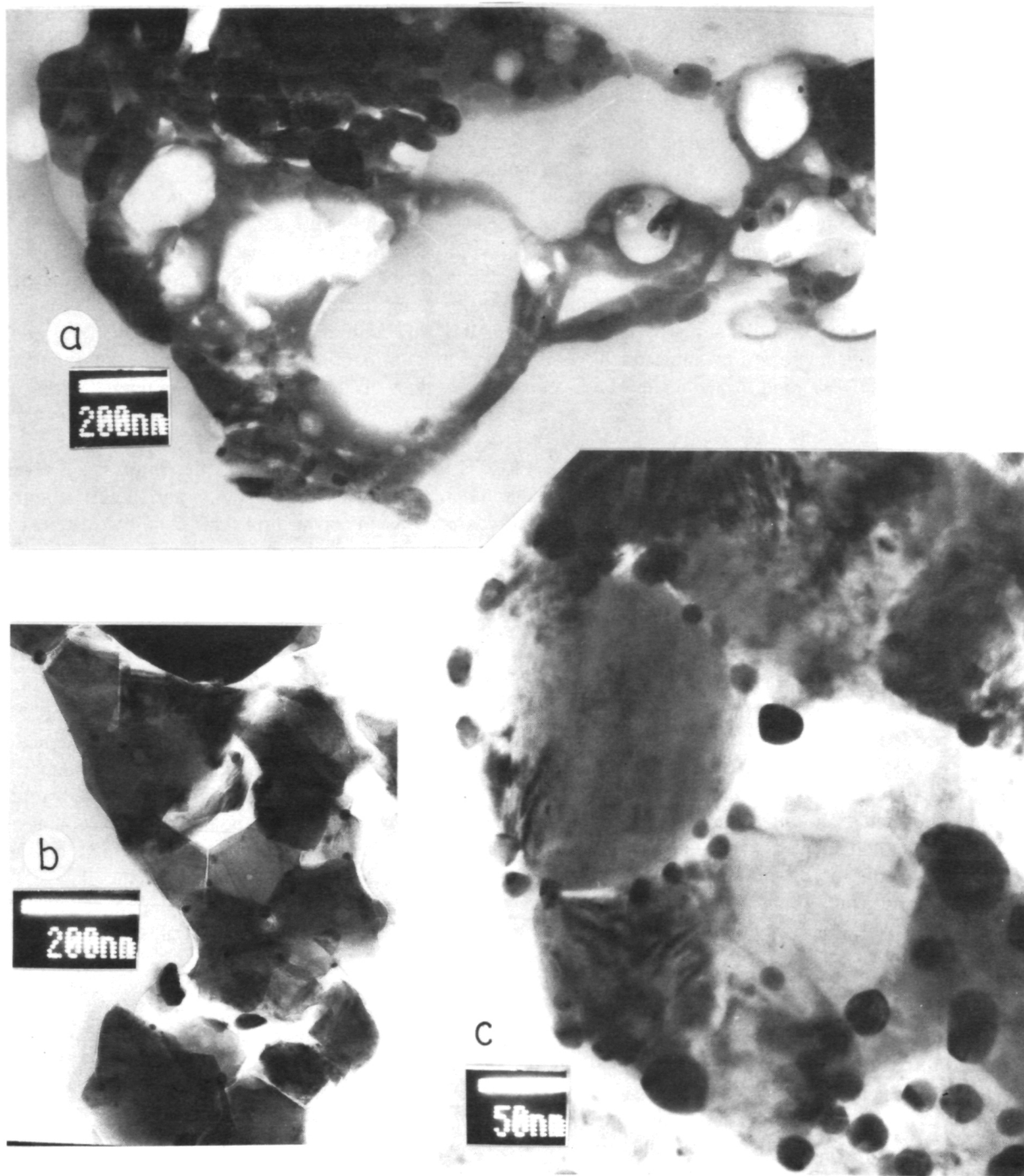


Figure 1 Impact shock effects in chondritic IDP residue 102: (a) frothy ferromagnesian glass, (b) 180° olivine grain intersections, and (c) metal and sulfide blebs decorating olivine grain boundaries.

456359 2P 531-91 ABS. ONLY N94-12046

ESTIMATION OF AGE OF DALI-GANIS RIFTING AND ASSOCIATED VOLCANIC ACTIVITY, VENUS; A.T. Basilevsky, Department of Geological Sciences, Brown University, Providence, Rhode Island 02912; permanent affiliation, Vernadsky Institute, Moscow, 117975, Russia.

This paper deals with the estimation of age for the Dali and Ganis Chasma rift zones and their associated volcanism based on photogeologic analysis of stratigraphic relations of rift-associated features with impact craters which have associated features indicative of their age. The features are radar-dark and parabolic, and they are believed to be mantles of debris derived from fallout of the craters' ejecta [1]. They are thought to be among the youngest features on the venusian surface, so their "parent" craters must also be very young, evidently among the youngest 10% of Venus' crater population [1].

Dali Chasma and Ganis Chasma are a part of a system of rift zones contained within eastern Aphrodite and Atla Regio which is a significant component of Venus tectonics [2,3]. The rifts of this system are fracture belts which dissect typical venusian plains with rare islands of tessera terrain (Fig. 1). The rift zone system consists of several segments following each other (Diane, Dali, Ganis) and forming the major rift zone line, about 10,000 km long, which has junctions with several other rift zones, including Parga Chasma Rift. The junctions are usually locations of rift-associated volcanism in the form of volcanic edifices (Maat and Ozza Montes) or plain-forming flows flooding some areas within the rift zones and the adjacent plains [2,4].

Within the Dali-Ganis rift zones there are several impact craters, and three of them, Sitwell (16.64 N, 190.38 E), Luxemburg (2.37 N, 198.24 E), and Von Schuurman (5.03 S, 199.99 E), have prominent dark parabolic features included in the list of [1].

Crater Sitwell is located at the northern part of the Ganis Rift Zone within the rift-forming fracture belt that dissects the plain and tessera island there. Sitwell is 34.5 km in diameter and it has a prominent central peak, a flat bottom, and a prominent rim merging into a 10 to 15 km wide ejecta blanket (Fig. 2). The crater is clearly superimposed on the fractures of Ganis Rift and the fractures do not cross any elements of the crater. The radar-dark parabolic feature associated with Sitwell is superimposed partly on the plains and partly on the tessera island. All the surface within the parabolic fracture is darkened, including most fractures which, east and west of the parabolic feature, look brighter than within the feature, evidently due to the debris mantle covering the surface. But several fractures within the parabolic feature north of the crater look brighter. They seem to have steeper slopes with more effective resurfacing due to the down slope mass wasting, or they might have formed or had movement after the formation of Sitwell, formation, thus indicating a possible continuation of rifting activity.

Crater Luxemburg is in the area of junction between Dali, Ganis, Parga and two unnamed rifts between Maat Mons and Ozza Mons. Luxemburg is 40 km in diameter and it has a central peak and a flat bottom with some knobs and a prominent rim merging into a 7-15 km wide ejecta blanket (Fig. 3). The crater is superimposed on lavas from Ozza Mons and possibly on some rift-forming fractures. However, several fractures from the rift disrupt the crater ejecta, rim and floor. West of the crater, these fractures are buried by lava flows emanating from the volcano, Maat. The dark parabolic feature associated with Luxemburg is superimposed on the moderately-bright Ozza lava flows and on the adjacent Rusalka Planitia volcanic plain, making them appear darker. But the bright lava flow north of Maat is unaffected by the dark parabolic feature that crosses it.

Crater Von Schuurman is located on the Rusalka Planitia plain, adjacent to the Dali Rift Zone and partly affected by rift fracturing. Von Shuurman is 29 km in



## AGE OF DALI-GANIS RIFTING: Basilevsky A.T.

diameter and it has a prominent central peak and a flat bottom: part is radar-bright, part is intermediate in brightness, and there is a prominent rim merging into a 5 - 20 km wide ejecta blanket, (Fig. 4). The crater is superimposed on NE-SW trending fractures which are the marginal part of the Dali rift zone. The fractures are buried by the crater ejecta. The dark parabolic feature is superimposed on both the Rusalka Planitia plain and on the rift-associated lavas dissected by rift fractures.

**Conclusion:** The described stratigraphic relations between these three craters and rift-associated features mean that at least the last stages of tectonic and volcanic activity associated with the Dali-Ganis rift zones are contemporaneous to the time of formation of young impact craters, with associated radar-dark parabolic features. If these craters represent the youngest 10% of the venusian crater population [1], and the average age of the venusian surface is about 500 million years [5], it means that the Dali-Ganis rifting and rift-associated volcanism were active as recently as during the last 50 million years.

**References:** [1] Campbell D.B. *et al.*, *JGR*, 97, E10, 16,249-16,278, 1992. [2] Head J.W. *et al.*, *JGR*, 97, E8, 13,153-13,198, 1992. [3] Solomon S.C. *et al.*, *JGR*, 97, E8, 13,199-13,256, 1992. [4] Senske D.A. *et al.*, *JGR*, 97, E8, 13,395- 13,420, 1992. [5] Schaber G.G. *et al.*, *JGR*, 97, E8, 13,257-13,302, 1992. [6] Phillips R.J. *et al.*, *JGR*, 97, E10, 15,923-15,948, 1992.

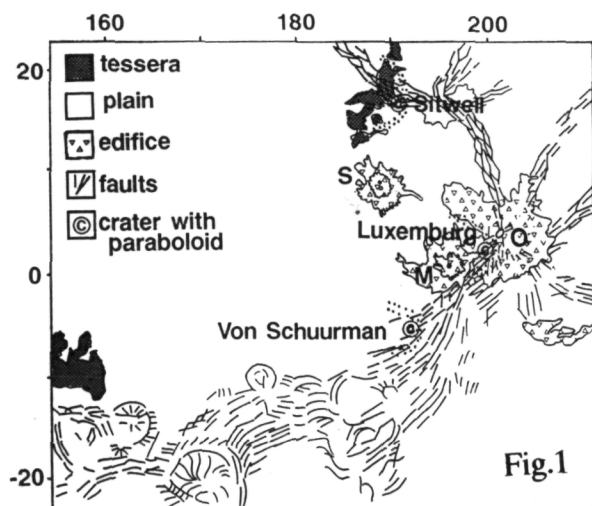


Fig.1

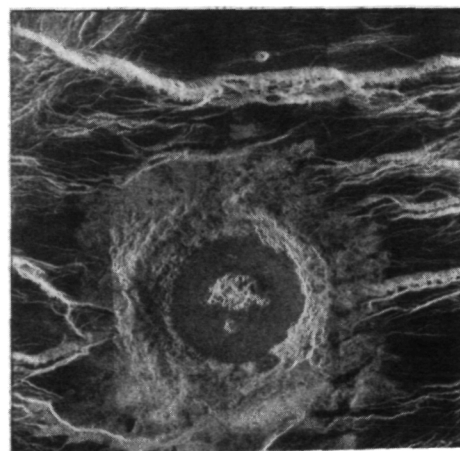


Fig.2

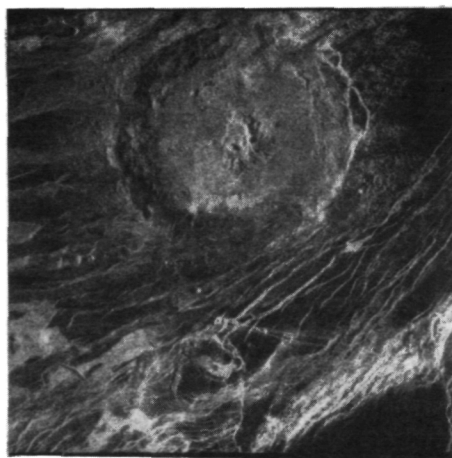


Fig.3



Fig.4

456360  
28  
532-91  
173 only  
163252  
N94-12047

REGIONAL GEOLOGY OF THE VEGA LANDING SITES: TENTATIVE RESULTS OF PHOTOGEOLOGIC MAPPING; A.T. Basilevsky<sup>1</sup> and C.M. Weitz<sup>2</sup>; 1) Department of Geological Sciences, Brown University, Providence, RI 02912; permanent affiliation is with the Vernadsky Institute, Moscow, 117975, Russia; 2) Jet Propulsion Laboratory, Pasadena, CA 91109.

Introduction: The regional geology of the two *Vega* landing sites, where geochemical measurements on the venusian surface were made, was studied using *Magellan* C1-MIDRP imagery and MIT-processed altimetry for the large region which we will call the *Vega* region (22.90° N to 22.90° S and 154.12° W to 211.12° E). The results of the analysis were compiled in the form of a synoptic geologic map of about 1:10 m scale.

Description: The majority of this region is dominated by plains with an altitude level close to the mean planetary radius. [1] The plains have several islands of tessera terrain. The plains and tessera terrains are dissected by a system of rift zones with volcanic centers at some of the rift junctions, including the well-known edifices of Ozza Mons and Maat Mons. One more well-known volcanic edifice, Sapas Mons, is located to the west of the rift zones.

Plains are typical venusian plains, but compared to the plains of the *Venera* region, they are less spotty with vast radar-dark and radar-bright units [2,3]. At least three age units maybe distinguished within the plains. Older plains often have a fractured surface and low ridges about 10 km long. They occur mostly at the central-northern part of the region around the tessera block of Nokomis Montes. These plains are embayed by intermediate-age plains, which represent the majority of the plains found in the *Vega* region. They generally have a network of wrinkle ridges and other features typical of the venusian plains. The material in these intermediate age plains was sampled by the *Vega 1* and *Vega* landers and determined to be a tholeiitic composition. The younger plains are associated with the rift zones. They are formed by lava flows either originating from the volcanic edifices of Maat and Ozza Montes, or from the rift zones with no morphologically prominent edifices. Their boundaries with the plains of intermediate age are unclear in many places. Typical characteristics of the younger plains are the absence of the wrinkle ridges network. This makes sense because the association of younger plains with the rift implies an extensional environment while the wrinkle ridges formation implies a compressional one.

Islands of tessera are present in several parts of the *Vega* region, perhaps representing a tessera basement underlying the plain-forming material. However, the tessera islands are much less abundant here compared to the *Venera* region [3]. This implies a larger thickness of the plain-forming lavas. Volcanic centers have been identified in several places on the plains with center to center spacing about 500 to 600 km, similar to the *Venera* region [3]. But in the center of the western part of the *Vega* region, the radar-dark lava flows form a large 1000 x 2000 km field, the southern end of which contacts the Dali Rift Zone. Inside this lava field there are several corona-like features (with the spacing also close to 500 km) which are probably the sources for the lava flows coalescing in the single lava field. Steep-sided volcanic domes are not typical for this region. We have mapped only one of them on the plain about 1,500 km southeast of Maat Mons.

Rift zones occupy a significant part (about 20%) of the region. The largest rift zone in the region is Diana Chasma. It travels along the southern margin of the region for more than 4000 km, and it consists of a peculiar combination of coronae and corona-like features, forming broad E-W trending chain, and linear fracture belts, which are typically expressed as topographic troughs. In the eastern part of the *Vega* region, the Diana Rift Zone becomes a

## VEGA LANDING SITE GEOLOGY, A.T. Basilevsky and C.M. Weitz

system of fracture belts trending SW-NE. At the broad area around 0° N latitude and 200° E longitude, there is a junction between Devana Chasma, Ganis Chasma, Parga Chasma, and two other unnamed rifts. At this junction are the two large volcanic edifices, Ozza and Maat Mons. Lavas from Ozza Mons flood some parts of the rifts fracture belts and are dissected by some rift-associated fractures. This implies contemporaneous tectonic deformations and volcanism. Lavas from Maat Mons are superimposed both on lavas from Ozza Mons and on rift-associated fractures. They are evidently the youngest volcanics of the area under study. Further north, a fracture belt in Ganis Chasma travels northward and then to the northwest. At the area around 17° N latitude and 196° E longitude, where a junction occurs between the Ganis Rift and two unnamed rift zones, there is a volcanic center with lava flows flooding the surrounding plains.

Within the rift zones of the *Vega* region, there are three impact craters with associated dark parabolic features. One of them, Von Schuurman, is superimposed on the Dali Chasma Rift. Another, Sitwell, is superimposed on the Ganis Rift and may have been followed by some rift-associated fracturing. The third one, Luxemburg, is superimposed on lavas of the Ozza edifice and dissected by Dali Chasma fractures, which, in turn, are covered by lavas from Maat Mons. This implies that at least the last stages of tectonic and volcanic activity associated with rift zones of the *Vega* region are contemporaneous to the formation of the craters which are young enough to preserve their associated radar-dark parabolic features. Those craters evidently belong to the youngest 10% of the venusian crater population [4], and this means that the rifting and rift-associated volcanism of this area were active here as recently as during the last 50 m.y. [5]

At 9° N latitude and 189° E longitude, the volcanic edifice of Sapas Mons looks as fresh and prominent as Ozza Mons and Maat Mons, but it has no visible association with the described rift zones. It rises about 2 km above the intermediate-age plains of Rusalka Planitia and its lavas cover the volcanics of the plains. Its flanks and the plains around it are disrupted by a radial fracture system. Sapas Mons seems to be an example of the volcanic activity as young as the activity of the rift zones of the *Vega* region. However, it probably originated from an ascending mantle plume that is not associated with the rift zones.

**Conclusions:** Geologic analysis of the Magellan images and altimetry for the broad region around the Vega 1 and 2 landing sites has shown that the dominant terrain of this area is volcanic plains. Three age units were identified within the plains and the Vega 1 and 2 landers both sampled the intermediate age plain. The plains formation was predated by the formation of tessera terrain which now forms several islands and probably occurs as a basement beneath the plain-forming material for the entire region. The formation of the intermediate age plain was followed by rifting and young volcanism, a significant part of which was associated with the rift zones. Stratigraphic relations of rift-associated features with very young impact craters show that the rift activity occurred in this area as recently as during the last 50 m.y..

**References:** 1) Ford, P.G. and G. H. Petengill, *JGR*, 97, E8, 13,103-13,114, 1992. 2) Weitz, C.M. and A.T. Basilevsky, LPSC XXIV Abstracts, this volume, 1993. 3) Basilevsky, A.T. and C.M. Weitz, LPSC XXIV Abstracts, this volume, 1993. 4) Campbell et al., *JGR*, 97, E10, 16,249-16,278, 1992. 5) Basilevsky, A.T., LPSC XXIV Abstracts, this volume, 1993.

456361  
2P

533-91

LPSC XXIV

71

ABS ONLY

N94-112048

REGIONAL GEOLOGY OF THE VENERA LANDING SITES: TENTATIVE RESULTS OF PHOTOGEOLOGIC MAPPING; A.T. Basilevsky<sup>1</sup>, and C.M. Weitz<sup>2</sup>; 1) Department of Geological Science, Brown University, Providence, RI 02912. Permanent affiliation is with the Vernadsky Institute, Moscow, 117975, Russia; 2) Jet Propulsion Laboratory, Pasadena, CA 91109.

**Introduction:** The regional geology of the five *Venera* landing sites, where geochemical measurements and TV observations on the venusian surface were made, was studied based on the photogeologic analysis of the Magellan C1-MIDRP imagery for the large area that we will call the *Venera* region (38° N to 22.6° S and 268° to 344° E). The results of the analysis were compiled in the form of a synoptical geologic map at about 1:10 M scale. MIT-processed Magellan altimetry was also used for the analysis. [1]

**Description:** The majority of this region is dominated by plains with an altitude close to the mean planetary radius of 6051.84 km [1]. The northwestern part of the region is dominated by the Beta Regio domical uplift and the southwestern part by Phoebe Regio. Beta and Phoebe Regios and some plains are dissected by long fracture belts associated with rift zones.

**Plains** of this region, where material was sampled by the *Venera* 8, 9, 10, 13 and 14 landers, represent typical plains of Venus [2], with features of several types: lava flows and volcanic domes, ridges and fractures, coronae and corona-like features, islands of tessera, impact craters, and radar-dark debris mantles and wind streaks. The following is a short description of some of these features of the plains.

**Islands of Tessera** on most of the *Venera* region plains are usually several tens of km across and many are located approximately a few hundred km from each other to form clusters of tesserae with the distance between the clusters about 1000 to 1500 km. The tessera islands are embayed by the plains and are evidently the outcrops of a tessera basement underlying the plains. In the tessera clusters, the thickness of the plain-forming material is on the order of the topographic range within tessera terrain at distances of a few hundred km, which is some hundred meters. Between the tessera clusters, the plain thickness must be larger.

Fields of lava flows, clusters of gentle-sloped volcanic domes, and coronae and corona-like features represent the visible centers of volcanic activity. The total number of these centers on the *Venera* region plains is about 30. They form clusters of 2 to 5 centers with the average center to center distance in the clusters about 500-600 km, and cluster to cluster distance about 1000 to 2000 km. If these clusters of volcanic activity are related to the ascending plumes of the mantle material, which are essentially thermal diapirs, then the center to center distance may be used for estimating the depth of the feeding layer for the diapirs. According to the model by [3], the feeding layer depth is about 40% of the average distance between the diapirs. This gives a depth for the feeding layer in the *Venera* region as deep as 200 to 250 km.

**Steep-sided domes**, whose presence at the *Venera* 8 and 13 areas correlates with nontholeiitic composition of the surface material [4], are present in many localities on the plains. The total number of steep-sided domes in the region is 48. A significant part of them form clusters with 2-6 domes in each and a typical 30-40 km dome to dome distance. Part of the domes are a few hundred km from each other, and a few are isolated from other ones by distances from 1000 to 2000 km. In most cases the steep-sided domes are associated with the previously discussed centers of volcanic activity. If the observed volcanic centers are placed over magma chambers, the differentiation of magma in the chambers and/or assimilation by magma of the material of the lower crust of Venus might be a mechanism to generate the viscous lavas which formed the steep-sided domes.

**Beta Regio** is a domical topographic rise about 2000 km across whose summit stands 4-4.5 km above the adjacent plains. Its geologic description was recently updated by Senske *et al.* [5], who confirmed early interpretations that Beta Regio represents uplifted terrain over an ascending mantle plume, *e.g.* [6]. The uplifted area is mostly made of a mosaic of tessera

## VENERA SITES GEOLOGY, A.T. Basilevsky and C.M. Weitz

and embaying plain, which was sampled by the *Venera 9* spacecraft. Geologic mapping of the *Venera 9* site has shown that the plain was formed before the Beta uplift [2]. The southern summit of Beta is a volcano, Theia Mons, sitting at the junction of three branches of the Devana Chasma Rift. Theia Mons' summit and flanks are covered by lavas which are among the youngest volcanic units of the area.

South of Beta Regio, the Devana Chasma Rift Zone travels about 3000 km through the plains, generally southward, and then splits into several less prominent fracture belts as it enters the eastern boundary of the Phoebe Regio topographic uprise and the adjacent plain. North of Phoebe Regio, the rift zone has two associated volcanic centers with lava flows covering the adjacent plains. The distance between these two volcanic centers is about 1000 km. At the triple junction of the rift zones at the southeast end of Phoebe Regio, there is one more rift-associated volcanic center with lavas embaying the surrounding tessera terrains and volcanic plain. All these rift zones appear very young, which is supported by the fact that the crater Bonheur on the plain between Beta and Phoebe Regiones is dissected by the fractures from the rift zone. Bonheur is a crater with low emissivity material on its floor, which is believed to be evidence that the crater is very young [7].

The Phoebe Regio Uplift is a 1000 x 2000 km island of tessera terrain which is embayed by the adjacent plains. This tessera looks similar to the tessera of Beta Regio and both large and small islands of this terrain extend from the eastern flank of Beta to the large block 800 km island east of Phoebe. This large tessera block east of Phoebe has its eastern part dissected by several other rift zones, and at their junction there is another volcanic center with lavas embaying the tessera and the adjacent plains. Bindschandler *et al.* [8], based on consideration of *Magellan* imagery and *Pioneer Venus* gravity data, interpreted Phoebe Regio as a surface expression of mantle coldspots or a region of downwelling. Our mapping shows that in the recent geologic period, Phoebe Regio definitely was not a downwelling area because the rift zones dissecting it are evidence of extension. The downwelling hypothesis may be applied to the formation of the tessera, composing Phoebe, but because Phoebe tessera is just one of several large islands of tessera in this region, the coldspot theory should be tested on a much broader area.

Conclusion: Geologic analysis of the *Magellan* imagery and altimetry for the broad region, where the *Venera 8,9,10,13*, and *14* landers made geochemical measurements of the surface material, has shown that the dominant terrain of this area is volcanic plains. The plain-forming material sampled by the *Venera* landers represents mostly tholeiitic basalts with some amount of nontholeiitic volcanics. The plains flooded the preexisting tessera terrain, which may underlie all of the region under study. It is not clear now whether the plains were formed by overlapping lava flows from numerous volcanic centers, or whether the majority of the plain-forming materials were formed by some events of larger scale and the observed centers represent only the last stages of the plain-forming volcanism in this area. The plain-formation was followed by the domical uplift of Beta Regio over the ascending mantle plume and by rifting and associated volcanism, which represent the youngest traces of endogenic geologic activity in this region.

References: 1) Ford P.G. and Pettengill G.H., *JGR*, 97, E8, 13,103-13,114, 1992. 2) Weitz C.M. and Basilevsky A.T., LPSC-XXIV abstracts, 1993. 3) Turcotte D.L. and Schubert G., *Geodynamics*, New York, Wiley, 1982. 4) Basilevsky A.T. *et al.*, *JGR*, 97, E10, 16,315-16,336, 1992. 5) Senske D.A. *et al.*, *JGR*, 97, E8, 13,395-13,420, 1992. 6) Stefan E.R. *et al.*, *Geol. Soc. Am. Bull.*, 101, 143-156, 1989. 7) Weitz C.M. *et al.*, *Int. Coll. on Venus*, 129-131, 1992. 8) Bindschandler D.L. *et al.*, *JGR*, 97, E8, 13,495-13,532, 1992.

456362  
2P

534-91  
ABS. QUL  
N9/4-12049  
1632342

LPSC XXIV

73

INTERPRETATION OF LUNAR AND PLANETARY ELECTROMAGNETIC SCATTERING USING THE FULL WAVE SOLUTIONS; E. Bahar and M. Haugland, Department of Electrical Engineering, University of Nebraska, Lincoln, NE 68588-0511

Bistatic radar experiments carried out during the Apollo 14, 15 and 16 missions provide a very useful dataset with which to compare theoretical models and experimental data. Vesecky, et al.[1] report that their model for near grazing angles compares favorably with experimental data. However, for angles of incidence around  $80^\circ$ , all the analytical models considered by Vesecky, et al.[1] predict values for the quasi-specular cross sections that are about half the corresponding values taken from the Apollo 16 data. (See Fig. 1) In this work, questions raised by this discrepancy between the reported analytical and experimental results are addressed. The unified full wave solutions are shown to be in good agreement with the bistatic radar taken during Apollo 14 and 16 missions. (See Fig. 1) Using the full wave approach, the quasi-specular contributions to the scattered field from the large scale surface roughness as well as the diffuse Bragg-like scattering from the small scale surface roughness are accounted for in a unified self-consistent manner. Since the full wave computer codes for the scattering cross sections contain ground truth data only, it is shown how it can be reliably used to predict the rough surface parameters of planets based on the measured data.

[1] Vesky, J.F., Sperley, E.J., and, Zebker, H., "Electromagnetic Wave Scattering at Near-Grazing Incidence from a Gently Undulating, Rough Surface," Proceedings of IGARSS'88 Symposium, Edinburgh, Scotland, Ref ESA SP-284 (IEEE 88CH2497-6), Vol. 3, pp 1579-1583, September 13-16, 1988.

Comparison of unified full wave theory with other models

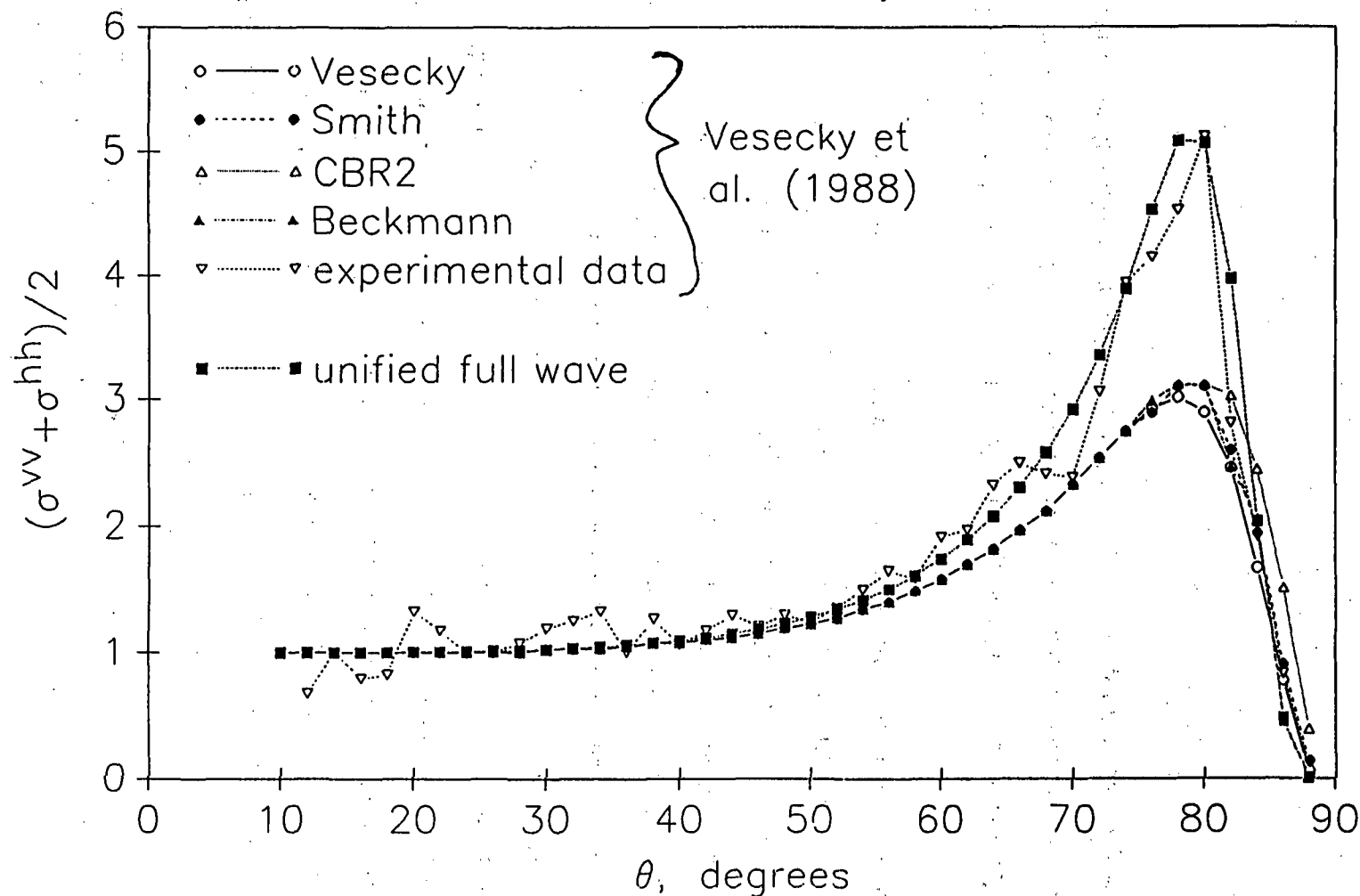


Fig 1 Comparison of the unified full wave solution with other models.

456363  
2p  
S35-91  
N94-12050  
2

**APOLLO 16 CORE 60013/14 AS A PRODUCT OF PATH I AND PATH II  
REGOLITH EVOLUTION PROCESSES; A. Basu, Department of Geological  
Sciences, Indiana University, Bloomington, IN. 47405, and LPI,  
Houston, TX. 77058; K. McBride and S.J. Wentworth, LESC,  
Houston, TX. 77058; D.S. McKay, NASA-JSC, Code SN 14, Houston,  
TX. 77058, U.S.A.**

We have made a petrographic study of 12 samples along the 62 cm profile of Apollo 16 core 60013/14, taken at Station 10' near the lunar module. The basic core description and maturity variations have been discussed earlier [1-4]. This core is important because it enables a stratigraphic comparison with nearby cores 60001-7 and 60009/10. These cores form a triangle with sides 35-40m. FMR data show a maturity-match between 60009/10 and 60013/14 [3,5]. Unfortunately, segments of the core 60001-7 are too disturbed for any cm scale comparison [6].

We present new data on the grain size distribution (Table-1) and the modal petrography (Table-2) for six samples from six levels of 60013 using the same approach and rationale used for 60014 [4]. We have combined the new data with our previous data on 60014 [4] to plot the variations of grain size distributions and grain type abundances, in the 500-1000 $\mu$ m and 90-150 $\mu$ m size fractions, with depth (Figs. 1-3). Agglutinate abundances match the  $I_S/FeO$  profile (Fig. 4), and both show a significant break at a depth of about 45 cm, with lower maturity material below that point [3,8]. Grain size distributions show that for all analyzed samples, the mean grain size is below 90 $\mu$ m. The two lowest samples are somewhat more coarse-grained than the rest of the core. The break at about 45 cm is the most prominent feature of the core and was described during the initial dissection as a pronounced change in color from dark to light [2]. As emphasized by [8], it now seems clear that this break is primarily one of maturity rather than of bulk chemical composition.

In our data, the abundances of single feldspar grains (Felds) and feldspathic fragmental breccias (FFBx) are positively correlated with each other down to a depth of about 27 cm. Below that depth, the correlation between these two components is not particularly good. This correlation does not mainly result from closure driven by variations in the major components (crystalline breccias at the larger grain size and crystalline breccias plus agglutinates at the finer grain size); the variations in the much less abundant feldspathic components does not mirror, in most cases, the variations in these major components as would be expected from simple closure relationships (Fig. 2,3). In the lower part of the core below about 41 cm, the feldspar fragments correlate (in a positive sense) better with the crystalline breccia lithic fragments and do not correlate positively with the feldspathic fragmental breccias. In normal reworking or Path I soil evolution [7], feldspars correlate negatively with feldspar-rich lithic fragments; the lithic fragments are systematically comminuted and destroyed and single mineral grain abundance increases. Conversely, in Path II evolution (mixing), daughter feldspars and parent lithic fragments may be mixed into soils as endmember pairs, and the ratio between the two will then reflect the ratio in the original endmember, rather than any reworking in the mixed soil. This suggests that single feldspars in these two stratigraphic intervals were derived principally from these two types of breccias respectively; this derivation occurred in processes that operated prior to the emplacement of the stratigraphic segments at this location. The major source of feldspars in the lower core may be from crystalline breccias and this lower core may include an endmember which contained these two components as a set. The segment between 27 cm and 41 cm is intermediate. It may reflect some degree of *in situ* reworking, or may simply reflect a more complex mixing. We infer that Path II processes operated to produce much of the mineralogic variability, which then may have been subdued or modified by subsequent Path I processes. It is likely that both processes were dominant during different and possibly even in overlapping episodes. One implication of this interpretation is that two major populations of feldspars may be present, and the relative abundance of each may change significantly with depth.

Finally, fragments of mare basalts are extremely rare in the >90 $\mu$ m fraction; green and orange glasses are also rare. Therefore, the chemical mare basalt component [8] must be in the finer fractions, and the mare basalt glasses [9] could be a part of an ancient regolith.

Table 1. Grain size distribution (60013 wt%)

Depth(cm)	33.5	41.0	43.0	48.5	54.5	61.5
Split	226	227	228	229	230	231
>1mm	6.7	7.9	9.3	3.5	14.7	11.3
0.5-1mm	8.1	7.5	6.6	5.4	5.4	7.1
250-500 $\mu$ m	10.4	9.5	8.6	8.1	8.1	11.3
150-250 $\mu$ m	9.3	9.4	8.3	7.4	6.8	8.3
90-150 $\mu$ m	10.8	9.8	9.9	9.2	8.1	9.4
<90 $\mu$ m	54.2	56.0	57.1	66.3	56.8	52.7

REFERENCES : [1] Schwarz, C. (1991) LPSC XXII, pp. 1201-1202; [2] Schwarz, C. (1992) LPSC XXIII, pp. 1249-1250; [3] Morris, R.V. and Lauer, H.V. (1992) LPSC XXIII, p. 935; [4] Basu, A. et al. (1992) LPSC XXIII, pp. 71-72; [5] McKay D.S. et al. (1976) PLSC 7th, pp. 295-313; [6] Korotev, R. (1991) PLPSC 21st, pp. 229-289; [7] McKay, D.S. et al. (1974) PLSC 5th, pp. 887-906. [8] Korotev et al. (1993) This Vol.; [9] Delano, J. (1992) LPSC XXIII, pp. 305-306.

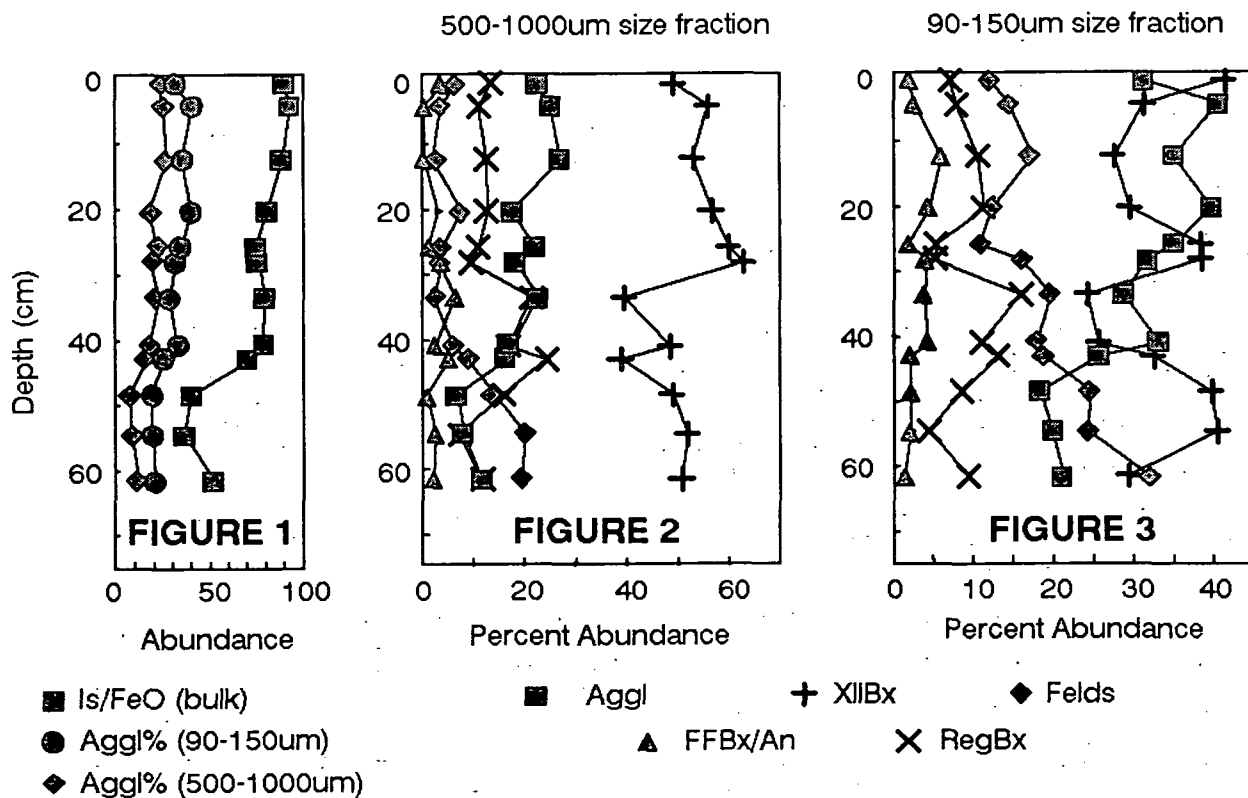


## REGOLITH EVOLUTION AT 60013/14: Basu, A. et al.

Table 2. Petrographic Modal Analysis of Core 60013

Split Depth(cm)	(500-1000 $\mu$ m)						(90-150 $\mu$ m)					
	233	248	263	278	293	308	239	254	269	284	299	314
	33.5	41.0	43.0	48.5	54.5	61.5	33.5	41.0	43.0	48.5	54.5	61.5
Aggl	22.8	17.6	16.6	7.0	8.3	11.7	28.7	33.2	25.7	18.3	19.8	21.2
RegBx	21.4	16.9	24.3	16.0	7.4	11.7	16.0	11.0	13.3	8.5	4.4	9.4
FFBx	6.7	2.8	5.5	1.0	2.7	2.3	3.9	4.5	2.2	2.2	2.2	1.3
XlIBx	39.5	48.5	38.8	49.0	51.8	50.7	24.2	25.7	32.5	39.8	40.5	29.4
Felds	2.6	6.3	9.0	14.0	20.3	19.5	19.6	17.9	18.8	24.6	24.2	32.0
Pyrox	0.0	0.0	0.6	1.0	0.0	0.0	2.9	2.2	2.6	1.8	2.2	2.6
OrGl	0.0	0.0	0.0	0.0	0.0	0.0	0.0	0.3	0.0	0.0	0.9	0.0
GrGl	0.0	0.0	0.6	4.0	0.0	0.7	0.6	0.3	0.0	0.3	0.9	0.0
YlGl	0.6	0.7	0.0	0.0	0.0	0.0	0.9	0.9	0.3	0.6	0.9	0.3
ClGl	0.6	0.7	0.0	1.0	0.0	0.7	2.2	2.6	3.5	2.2	1.5	1.6
KBasalt	2.6	2.1	0.6	0.0	0.0	0.0	0.0	0.0	0.3	0.0	0.0	0.0
MBasalt	0.0	0.0	0.0	0.0	0.9	0.7	0.0	0.0	0.0	0.0	0.0	0.0
Other	2.6	4.2	3.4	7.0	8.3	1.5	0.6	0.9	0.3	1.2	1.9	2.0
Total	99.4	99.8	99.4	100	99.7	99.5	99.6	99.5	99.5	99.5	99.4	99.8
Ngrain	149	142	144	100	108	128	306	307	307	316	313	306

## MATURITY AND PETROLOGIC PROFILES OF 60013/14



456365

536-25

LPSC XXIV

77

ABS ON N94-12051

NITROGEN AND NOBLE GASES IN A GLASS SAMPLE FROM LEW88516; R. H. Becker and R. O. Pepin, School of Physics and Astronomy, University of Minnesota, Minneapolis, MN 55455.

The Antarctic meteorite LEW88516 has been classified (1) as a member of the SNC group of meteorites, specifically a shergottite. It is reported to be remarkably similar in mineralogy, petrogenesis and chemistry to the previously known ALH77005 shergottite (1-5), with both being compositionally distinct from other shergottites (2). LEW88516 shows pervasive shock features (2,3) and has been found to contain glass veins attributable to a shock origin (2). In an effort to determine whether the glass in LEW88516 contains any of the isotopically-heavy trapped nitrogen component observed in EETA 79001 glass (6,7), as well as the related high- $^{40}\text{Ar}/^{36}\text{Ar}$  and high- $^{129}\text{Xe}/^{132}\text{Xe}$  components (8,9), we undertook an analysis of an 11.9 mg glass sample (LEW88516,4) provided to us by H. Y. McSween, Jr. as part of a consortium study of this meteorite.

Nitrogen and noble gases were extracted from LEW88516,4 in a series of combustion steps at increasing temperatures followed by a final pyrolysis, using essentially the same procedures as those reported in (6) for EETA79001. Initial steps at 550°C were intended to remove any surface-sited nitrogen-containing contaminants, while the 700°C step was expected to show the onset of release of a trapped argon component, based on our previous data for EETA 79001 (6). It was hoped that the bulk of any trapped gas release would be concentrated in one of two steps at 1100°C and ~1400°C, maximizing our analytical sensitivity. Results of the analysis are shown in Tables 1 and 2. Except for He and Ne, data obtained for the 550°C steps will be omitted from further consideration on the assumption that they represent terrestrial contamination.

Table 1. Light noble gas and nitrogen yields and isotopic ratios from 11.9 mg of LEW 88516,4.

Step	$^4\text{He}$ $\delta^{15}\text{N}(\text{‰})$	$^3\text{He}$	$^{22}\text{Ne}$	$^{20}\text{Ne}/^{22}\text{Ne}$	$^{21}\text{Ne}/^{22}\text{Ne}$	$^{36}\text{Ar}$	$^{40}\text{Ar}$	$^{38}\text{Ar}$	ppm N	
550°C	8.	1.62	0.0654	6.8	0.168	0.0842	27.5	0.0144	0.295	5.0
	13.	0.03	0.0055	1.7	0.013	0.0076	2.0	0.0023	0.019	1.3
550°C	< 6.	0.205	0.1642	9.59	0.0421	0.0581	8.4	0.0117	0.001	----
	----	0.005	0.0068	0.72	0.0017	0.0076	1.4	0.0026	0.003	----
700°C	36.	1.80	0.2294	7.97	0.2103	0.0220	11.2	0.0031	0.105	4.7
	13.	0.04	0.0073	0.55	0.0050	0.0092	1.5	0.0025	0.009	3.1
1100°C	20.	2.83	0.671	2.59	0.6427	0.122	530	0.079	0.257	5.8
	15.	0.06	0.018	0.15	0.0079	0.052	30	0.013	0.017	2.0
1400°C	17.9	0.597	0.507	1.23	0.742	0.259	235	0.1007	0.011	42
	9.8	0.012	0.014	0.22	0.012	0.026	13	0.0087	0.003	34

Noble gas amounts given in units of  $10^{-8}$  ccSTP/g. Errors given below the values. There are additional systematic errors of  $\pm 10\%$  on He yields,  $\pm 15\%$  on Ne yields, and  $\pm 10\%$  on Ar yields.

On the face of it, there is nothing that stands out in our data. He and Ne, especially  $^3\text{He}_{\text{sp}}$  ( $\sim 7 \times 10^{-8}$  ccSTP/g) and  $^{21}\text{Ne}_{\text{sp}}$  ( $\sim 8 \times 10^{-9}$  ccSTP/g), are comparable to the amounts reported for ALH77005 (9). The  $^{40}\text{Ar}$  seen could be generated, given the K content of LEW88516 (5), in about

N AND NOBLE GASES IN LEW88516: <sup>1</sup>Becker R. H. and Pepin R. O.

$3.5 \times 10^9$  years. The  $\delta^{15}\text{N}$  values appear very ordinary, but there is a small enhancement in  $^{129}\text{Xe}$  in the last step. On the whole, the trapped component being sought is not obviously present.

Table 2. Kr and Xe data from 11.9 mg of LEW 88516,4.

Step.	$^{84}\text{Kr}$	$^{132}\text{Xe}$	$^{129}\text{Xe}/^{132}\text{Xe}$
550°C	$1.534 \pm 0.070$	$0.580 \pm 0.055$	$0.976 \pm 0.037$
550°C	$0.551 \pm 0.051$	$0.343 \pm 0.042$	$1.016 \pm 0.033$
700°C	$0.151 \pm 0.092$	$0.555 \pm 0.052$	$0.972 \pm 0.034$
1100°C	$1.765 \pm 0.058$	$0.311 \pm 0.077$	$0.976 \pm 0.070$
1400°C	$1.16 \pm 0.13$	$0.220 \pm 0.062$	$1.136 \pm 0.085$

Gas amounts in units of  $10^{-10}$  ccSTP/g. There are additional systematic errors of  $\pm 15\%$  on the Kr yields and Xe yields.

If, however, one compares our  $^{40}\text{Ar}$  yield to that of ALH77005 (9), whereby one sees a five-fold enhancement in our LEW88516 sample, and considers that the shergottites in general have apparently lost their radiogenic  $^{40}\text{Ar}$  in a relatively recent shock event (10), another interpretation becomes possible. One can assume that  $^{40}\text{Ar}$  is predominantly trapped, with only a small radiogenic contribution. On that basis, a comparison with  $^{40}\text{Ar}$  data for EETA 79001 (6,7) indicates that there is about 20% of the EETA 79001 trapped component in LEW88516 glass. As the trapped component in EETA 79001 contributed about 84 ppb N (7), this would imply  $\sim 17$  ppb of the heavy component in LEW88516. For a  $+600\%$  to  $+650\%$  N component, we would expect to see a  $25\%$  to  $30\%$  effect in  $\delta^{15}\text{N}$ . If one recalls that the shergottites contain "indigenous" nitrogen released at temperatures above  $700^\circ\text{C}$ - $800^\circ\text{C}$  which lies in the range of  $-15\%$  to  $-25\%$  (11,12), the observed  $\delta^{15}\text{N}$  values are in fact consistent with the presence of this amount of trapped component. The excess of  $^{129}\text{Xe}$  seen at  $1400^\circ\text{C}$ , taking into account the uncertainties of the measurement, is also consistent with the presence of about 20% of the trapped component seen in EETA 79001. We would thus conclude that in fact there is a shock-implanted trapped component in the LEW88516 glass similar to that seen in EETA 79001, but lower in amount by about a factor of five.

REFERENCES: (1) Mason B. (1991) Antarctic Meteorite Newsletter, 14:2, 19. (2) Lindstrom M.M., Mittlefehldt D.W., Treiman A.H., Wentworth S.J., Gooding J.L., Morris R.V., Keller L.P. and McKay G.A. (1992) Lunar Planet. Sci., XXIII, 783-784. (3) Harvey R.P. and McSween H.Y., Jr. (1992) Meteoritics, 27, 231-232. (4) Wadhwa M and Crozaz G. (1992) Meteoritics, 27, 302-303. (5) Dreibus G., Jochum K.H., Palme H., Spettel B., Wlotzka F., and Wänke H. (1992) Meteoritics, 27, 216-217. (6) Becker R.H. and Pepin R.O. (1984) Earth Planet. Sci. Lett., 69, 225-242. (7) Wiens R.C., Becker R.H. and Pepin R.O. (1986) Earth Planet. Sci. Lett., 77, 149-158. (8) Bogard D.D., Nyquist L.E. and Johnson P. (1984) Geochim. Cosmochim. Acta, 48, 1723-1739. (9) Swindle T.D., Caffee M.W. and Hohenberg C.M. (1986) Geochim. Cosmochim. Acta, 50, 1001-1015. (10) Bogard D.D., Husain L. and Nyquist L.E. (1979) Geochim. Cosmochim. Acta, 43, 1047-1055. (11) Fallick A.E., Hinton R.W., Mathey D.P., Norris S.J., Pillinger C.T., Swart P.K. and Wright I.P. (1983) Lunar Planet. Sci., XIV, 183-184. (12) Wright I.P., Pillinger C.T. and Grady M.M. (1992) Meteoritics, 27, 309.

456366

537-25

LPSC XXIV

79

AES ONLY

N 9/43-152 052

# THE STABILITY OF HIBONITE AND OTHER ALUMINOUS PHASES IN SILICATE MELTS: IMPLICATIONS FOR THE ORIGIN OF HIBONITE-BEARING INCLUSIONS.

J.R. Beckett and E. Stolper. Division of Geological and Planetary Sciences 170-25, California Institute of Technology, Pasadena, CA 91125

**Abstract.** Phase fields in which hibonite (Hib) and silicate melt coexist with spinel (Sp),  $\text{CaAl}_4\text{O}_7$  (CA2), gehlenitic melilite (Mel), anorthite (An) or corundum (Cor) in the system  $\text{CaO-MgO-Al}_2\text{O}_3\text{-SiO}_2\text{-TiO}_2$  (CMAS) were determined and activity models developed for melilite (Mel) and Hib solid solutions. Experimentally determined partition coefficients for Ti between Hib and coexisting melt,  $D_{\text{Ti}}$ , vary from 0.8 to 2.1 and generally decrease with increasing  $\text{TiO}_2$  content in the liquid (L). Based on Ti partitioning between Hib and melt, bulk inclusion compositions and Hib-saturated liquidus phase diagrams, the Hib in Fluffy Type A inclusions (FTA's) from Allende and at least some of the Hib from Hib-rich inclusions is relict; much of the Hib from Hib-glass spherules probably crystallized from a melt under nonequilibrium conditions. Bulk compositions for all of these Ca-Al-rich inclusions (CAIs) are consistent with an origin as Mel + Hib + Sp + perovskite (Pv) proto-inclusions in which Mel was partially altered. In some cases, the proto-inclusion was partially or completely melted with vaporization occurring over a period of time sufficient to remove any Na introduced by the alteration process but frequently insufficient to dissolve all of the original hibonite. If equilibration temperatures based on Hib-bearing CAIs reflect condensation in a cooling gas of solar composition, then Hib + Cor condensed at  $\sim 1260^\circ\text{C}$  (referenced to  $10^{-3}$  atm) and Hib + Sp  $\pm$  Mel at  $\sim 1215 \pm 10^\circ\text{C}$ . Simple thermochemical models for the substitution of trace elements into the Ca-site of meteoritic Hib suggest that virtually all Eu is divalent in early condensate Hibs but that  $\text{Eu}^{2+}/\text{Eu}^{3+}$  decreases by a factor of 20 or more during the course of condensation, primarily because the ratio is proportional to the partial pressure of Al, which decreases dramatically as aluminous phases condense. The relative sizes of Eu and Yb anomalies in meteoritic Hibs and CAIs may be influenced by this effect.

**Introduction.** Hib-bearing CAIs occur in carbonaceous, ordinary and enstatite chondrites but there is little consensus on how these inclusions formed. Based on textural, compositional and isotopic arguments, some appear to have crystallized from melts while others are interpreted to be vapor-to-solid condensates and/or vaporization residues (1-2). We conducted isothermal crystallization experiments in CMAS at 1 bar, 1350-1550°C. Our results are used to evaluate whether or not Hib could have crystallized from specific CAI bulk compositions and as a basis for constraining vapor-Hib equilibria in the primitive solar nebula.

**Starting Compositions and Results.** Fifteen bulk compositions with 0-5 wt%  $\text{TiO}_2$  were selected to map out portions of the Hib saturation surface in CMAS by crystallization experiments. Hib is a binary [ $\text{CaAl}_2\text{O}_9$  (HIB) -  $\text{CaMgSiAl}_3\text{O}_{19}$  (MSH)] or ternary [HIB - MSH -  $\text{CaMgTiAl}_3\text{O}_{19}$  (MTH)] solution,  $\text{Ti}^{4+}$  being slightly incompatible ( $D_{\text{Ti}} \sim 0.8$ ) to strongly compatible ( $D_{\text{Ti}} \sim 2.1$ ) with lower  $D_{\text{Ti}}$  at higher bulk Ti. Projected compositions of Hib-saturated melts (Fig. 1) are similar to those of (3) and are generally lowered by  $\sim 1$  wt% HIB for every 1 wt% increase in  $\text{TiO}_2$ . Hib is destabilized slightly under reducing conditions. There are also regions near the An and Sp vertices (shaded in Fig. 1) for which there are no Hib-saturated melts because Hib melts incongruently to Cor + L and if sufficient HIB is added to any Hib-saturated melt, Hib + L becomes unstable for the same reason. Hib is in a reaction relationship with L along Cor-Sp-Hib-L and CA2-Sp-Hib-L except possibly close to the Mel-CA2-Sp-Hib-L invariant point, CA2 along CA2-Mel-Hib-L and Cor along An-Cor-Hib-L.

**Did Meteoritic Hibonite Crystallize from Melts?** A few Hib-bearing inclusions contain glass and were therefore at least partially molten at some point. Most of these have bulk compositions consistent with near-liquidus Hib and apparent  $D_{\text{Ti}}$  values consistent with experimentally determined values. This suggests that there are at least Hib overgrowths on relict cores and possibly that all of the Hib crystallized from a melt. Glass compositions (1,4-5) are, however, well below the Hib-saturation surface suggesting that rapid cooling rates prevented nucleation of otherwise stable phases and that the liquid line of descent therefore passed through their saturation surfaces. Bulk compositions of some of the glass-bearing inclusions are far below the Hib saturation surface. Provided that sections used to obtain bulk compositions were representative, Hib is quite unlikely to appear early in the crystallization sequence, which suggests that at least some of the Hib is relict unless nucleation is much easier for Hib than for the other phases. Hib in FTA's is texturally early but bulk compositions are well below the saturation surface and Ti contents of Hib are often much higher than consistent with an early crystallizing phase. This suggests that Hib is relict with respect to melting events in these inclusions.

**Condensation Sequences.** We derived a binary solution model with one ordering parameter for Mel, a ternary model for Hib with perfect ordering of Mg-Si couples in adjacent tetrahedra, and used available thermodynamic data for end-member Sp, Mel, Hib, oxides and vapor species (6-8) to constrain the stability of meteoritic Hib-bearing phase assemblages. Based on the reactions [1]  $\text{HIB} + \text{Mg}_{(\text{g})} + \text{SiO}_{(\text{g})} + \text{O}_{2(\text{g})} = \text{MSH} + \text{Cor}$  and [2]  $\text{HIB} + \text{SiO}_{(\text{g})} + 2\text{Mg}_{(\text{g})} + 1.5\text{O}_{2(\text{g})} = \text{MSH} + \text{Sp}$  and assuming solar abundances of vapor species, we obtain temperatures for meteoritic Hib referenced to  $10^{-3}$  atm of Hib + Cor  $\sim 1260^\circ\text{C} \rightarrow \text{Hib} + \text{Sp} \pm \text{Mel} \sim 1215 \pm 10^\circ\text{C}$ .

## THE STABILITY OF HIBONITE IN SILICATE MELTS: Beckett J.R. and Stolper E.

These refer to the points at which vapor-solid equilibrium ceased and may or may not correspond to initial condensation of phases. However, the relative temperatures are consistent with observed textures and therefore a condensation sequence. The equilibration temperatures of Hib-bearing inclusions with Sp but no Mel are indistinguishable from those with Sp+Mel+Hib although both they and the Cor + Hib temperatures are  $>70^\circ$  below calculated equilibrium condensation temperatures of Mel for a cooling gas of solar composition (9). This may reflect the relative ease of nucleation in the vapor for Sp and Mel or fractionation of an aluminous phase.

**Eu Anomalies.** Available data are insufficient for accurate calculations of absolute concentrations of trace elements (TE) in condensate Hib, primarily because neither individual standard state free energies of formation for end-member components nor differences in free energies between them are known. Data of (10), however, constrain the relative free energies of formation from the oxides of  $\text{Eu}^{2+}\text{Al}_{12}\text{O}_{19}$  (EuH2) and  $\text{Eu}^{3+}\text{MgAl}_{11}\text{O}_{19}$  (EuH3)  $[\bar{G}_{\text{EuH2}}^{\text{ox}} - \bar{G}_{\text{EuH3}}^{\text{ox}}]$  to  $-58 \pm 8$  kJ/mole at  $1470^\circ\text{C}$ . The exchange reaction [3]  $\text{EuH3} + \text{Al}_{(\text{g})} = \text{EuH2} + \text{Mg}_{(\text{g})}$  can therefore be used to calculate  $\text{Eu}^{2+}/\text{Eu}^{3+}$  in condensate Hib. This leads for trace Eu to [4]  $X_{\text{EuH2}}/X_{\text{EuH3}} = [2X_{\text{MTH}}/(X_{\text{Hib}} + X_{\text{MTH}}/2)][P_{\text{Al}}/P_{\text{Mg}}]\exp[-\Delta\bar{G}_{\text{r}(3)}/RT]$ , where  $P_i$  are partial pressures in the vapor,  $X_i$  mole fractions in Hib and  $\Delta\bar{G}_{\text{r}(3)}$  the standard state free energy of reaction [3]. Note that  $\Delta\bar{G}_{\text{r}(3)}$  of an exchange reaction such as [3] that takes into account the phase that the TE is substituting into must be evaluated to describe correctly partitioning of a TE between Hib and vapor. This leads invariably to an explicit dependence of TE concentrations on  $P_i$  of one or more major element species in the vapor. Previous calculations (11-12) neglected this aspect of TE condensation but it can have a significant influence. Fig. 2 shows calculated  $\text{Eu}^{2+}/\text{Eu}^{3+}$  in equilibrium condensate Hib based on (9). We increased the crystal chemistry term (i.e. the first expression in brackets in [4]) linearly from 0.11 at  $1455^\circ\text{C}$  to 1.94 at  $1217^\circ\text{C}$  to account for observed variations in meteoritic Hib. Initially,  $\text{Eu}^{2+}/\text{Eu}^{3+}$  rises, an artifact of how the Hib composition was assumed to change that may not occur in natural systems, but the steadily declining  $P_{\text{Al}}$  due to condensation of aluminous phases soon causes a decline in  $\text{Eu}^{2+}/\text{Eu}^{3+}$  that continues until Hib no longer coexists with vapor. Details of Fig. 2 are strongly dependent on various assumptions, but two features are likely to survive improvements in the thermodynamic database and condensation scenarios. {1} Most Eu in condensate Hib is divalent. Previous calculations used  $\text{Eu}^{3+}$  only and therefore underestimated total Eu concentrations, possibly by as much as 2-3 orders of magnitude. {2}  $\text{Eu}^{2+}/\text{Eu}^{3+}$  decreases significantly during equilibrium condensation, by a factor  $> 20$  in Fig. 2. Thus, the size of the Eu anomaly relative to that of the trivalent cation Yb can be expected to change in a way that reflects the degree of condensation (at least prior to the appearance of Pv) and this may be an important factor in determining the relative sizes of Eu and Yb anomalies in meteoritic inclusions.

**References.** (1) Ireland T. et al. (1991) *G.C.A.* 55, 367. (2) Grossman J. et al. (1988) *EPSL* 91, 33. (3) Beckett J. and Stolper E. (1987) *LPSC XVIII*, 56. (4) Kurat G. (1975) *Tschermak's Min. Pet.* 22, 38. (5) MacPherson G.J. (1991) personal communication. (6) Berman R. (1988) *J. Petrol.* 29, 445. (7) Hallstedt B. (1990) *J. Am. Ceramic Soc.* 73, 15. (8) Chase M. et al. (1985) *J. Phys. Chem. Ref. Data* 14, Suppl. 1. (9) Ward T. (1991) personal communication. (10) Drake M. and Boynton W. (1988) *Met.* 23, 75. (11) Boynton W. (1975) *G.C.A.* 39, 569. (12) Davis A. and Grossman L. (1979) *G.C.A.* 43, 1611.

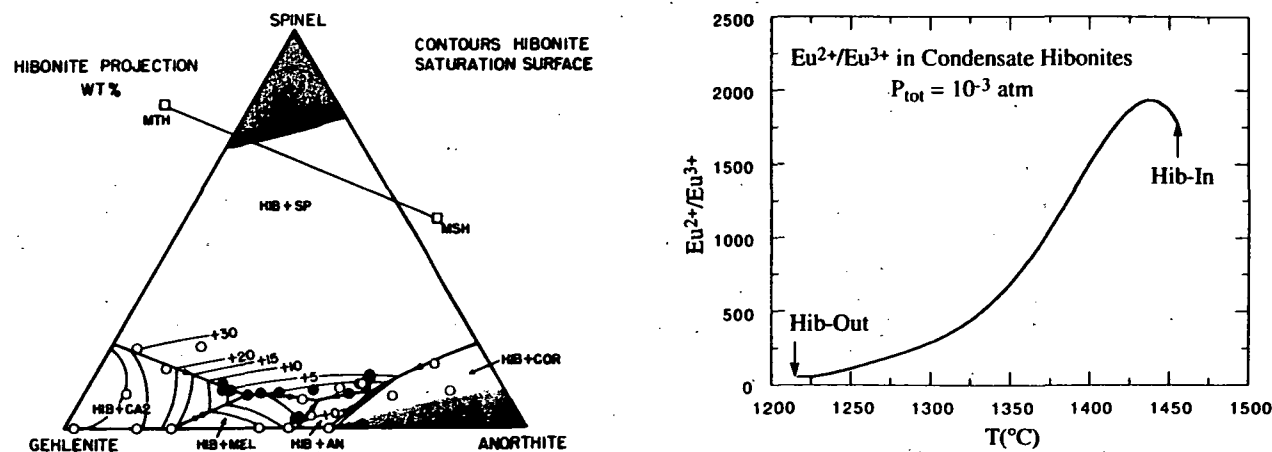


Fig. 1. Hib-saturated liquidus phase diagram ( $<2.5$  wt%  $\text{TiO}_2$ ) projected from HIB and  $\text{TiO}_2$  onto the composition plane formed by gehlenite, anorthite and spinel contoured in wt% HIB. Multiply-saturated liquids from literature cited in 1 (open symbols) and this study (closed symbols).

Fig. 2. Calculated  $\text{Eu}^{2+}/\text{Eu}^{3+}$  in condensate Hib assuming equilibrium condensation at a total pressure of  $10^{-3}$  atm in a cooling gas of bulk solar composition.

456367

338-89  
ABS. ONLY

LPSC XXIV

81

N 94612053

**A COMPARISON OF TELESCOPIC AND PHOBOS-2 ISM SPECTRA OF MARS IN THE SHORT-WAVE NEAR-INFRARED (0.76-1.02  $\mu\text{m}$ )** James F. Bell III (NRC/NASA Ames, Space Sciences 245-3, Moffett Field, CA 94035) and John F. Mustard (Brown University, Dept. of Geological Sciences, Providence RI 02912).

**The Problem:** Recent analyses of near-IR (0.76-3.16  $\mu\text{m}$ ) Mars surface reflectance spectra obtained by the Phobos-2 ISM instrument during early 1989 have revealed the presence of substantial variability in surface spectral properties [1-3]. Strong absorption features seen in the 0.85-1.05  $\mu\text{m}$  region are up to 10-15% deep relative to the local continuum [2,3] and have been interpreted as evidence of  $\text{Fe}^{2+}$  and  $\text{Fe}^{3+}$ -bearing minerals (pyroxenes and iron oxides, respectively). Though these observed band depths are comparable to those seen in laboratory reflectance spectra [e.g., 4-6], they are up to three times larger than most previously reported band depths for Mars spectra at these wavelengths. Thus, we have posed the following questions: (1) Do the ISM data accurately represent the spectral behavior of the Martian surface in the near-IR? If so, are the differences between the ISM spectra and decades of previous groundbased observations a result of (a) differences in spatial resolution, or (b) changes in the spectral character of the martian surface and/or atmosphere with time? If not, are the differences due to calibration errors in the groundbased data, the ISM spectra, or both?; and (2) If these large band depths are indeed real, what are the implications for Mars surface mineralogy and past/present weathering environments?

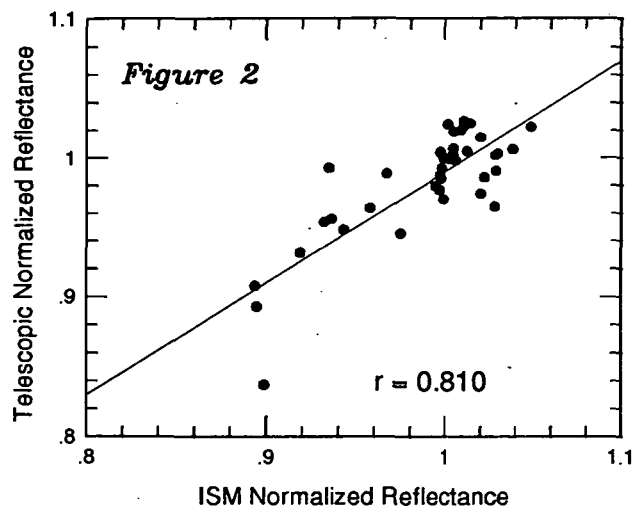
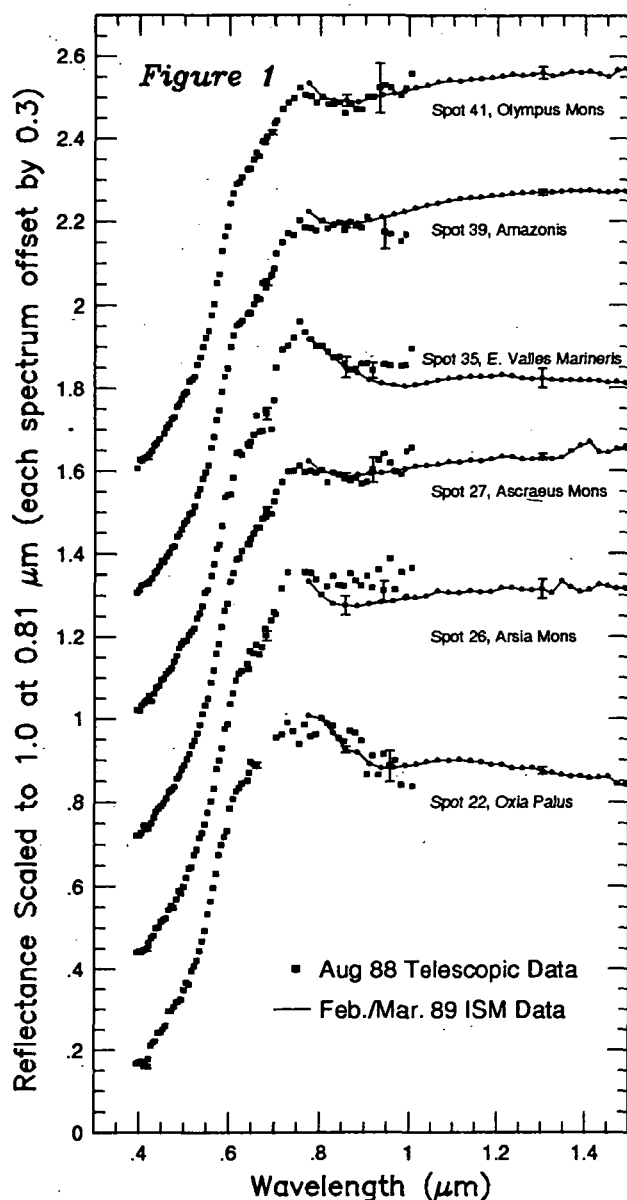
**The Data:** Groundbased telescopic observations of Mars in the visible to near-IR (0.4-1.0  $\mu\text{m}$ ) were obtained from Mauna Kea Observatory during the 1988 opposition by Bell *et al.* [7]. Earlier measurements in the near-IR have been summarized by Singer *et al.* [8], McCord *et al.* [9], and Bell and McCord [10]. The spatial resolution of these data ranges from 150-2000 km, and calibration is relative to standard stars and/or returned lunar samples. Near-IR (0.76-3.14  $\mu\text{m}$ ) imaging spectrometer data of Mars were acquired from orbit by the ISM instrument onboard the Phobos-2 spacecraft in February and March 1989, approximately 6 months after the 1988 telescopic observations. Data were acquired with a spatial resolution of 22 km/pixel over 11 regions, focusing on Tharsis, Valles Marineris, Arabia, and Syrtis Major-Isidis. Data were calibrated in two steps: 1) using pre- and in-flight calibrations to account for known instrumental and atmospheric effects, and 2) relative to a spectral model for Mars [1,2].

**Comparison Procedure:** Six regions of variable albedo and geologic setting were identified where ISM and 1988 opposition telescopic coverage either overlapped physically or sampled the same surface geologic unit [11]. The areal sizes and positions of the regions measured telescopically were compiled by Bell *et al.* [7]. ISM pixels falling within these spots were averaged to produce a spatially convolved spectrum that simulates what would have been seen telescopically (neglecting the effects of the Earth's atmosphere). To facilitate comparisons of absorption band positions and relative strengths, the convolved ISM data and the 1988 telescopic spectra were scaled to unity at 0.81  $\mu\text{m}$  and are presented in Fig. 1. The data have also been convolved to equivalent band pass normalized reflectances in the region of spectral overlap (0.76-1.02  $\mu\text{m}$ ). A scatter diagram of telescopic vs ISM reflectances is shown in Fig. 2.

**Results:** Of the six regions compared (Fig. 1), four exhibit remarkably good agreement between the telescopic and ISM data (Spots 22, 27, 35, 41). Another shows differences within acceptable bounds of the noise (Spot 26). The final spot exhibits differences associated with the 0.85-0.95  $\mu\text{m}$  band (Spot 39). However, it should be noted that telescopic data from 0.93-0.98  $\mu\text{m}$  are occasionally contaminated by a telluric water vapor feature. Overall, the impression is that, when properly convolved to simulate telescopic spatial resolution, the ISM data are consistent with groundbased telescopic measurements of the same regions taken only a few Mars months earlier. The depth of the absorption features seen in the 0.8-1.0  $\mu\text{m}$  region are qualitatively consistent between the two data sets. However, quantitative comparisons can be complicated when using multiplicatively scaled data. Nevertheless, a correlation coefficient of 0.81, as a simple statistical measure of similarity, was computed for the data shown in Figure 2.

**Discussion and Implications:** Our simple study indicates that, at coarse spatial resolution, both ISM and groundbased telescopic spectra of Mars are in general agreement, despite being calibrated independently. This provides assurance that the observations of the Martian surface spectral properties at finer spatial scales with the ISM data are accurate. It also confirms that there is significant and meaningful spectral heterogeneity on Mars at fine spatial scales, even in regions that appear to be mantled by the global dust on larger spatial scales [3,10]. Differences between the convolved ISM data and the telescopic measurements for local areas may be related to changing surface and/or atmospheric conditions between the

## TELESCOPIC-ISM COMPARISON: J.F. Bell III and J.F. Mustard



time the two data sets were acquired. Specifically, the ISM convolved spectrum for Spot 39 shows a  $\approx 5\%$  absorption feature centered near  $0.85\text{--}0.90 \mu\text{m}$  while the telescopic spectrum does not. This could be due to transient surface or atmospheric phenomena such as the presence of poorly-crystalline airborne or surface-mantling dust in this region during August 1988 that had cleared by the time the region was measured by ISM in 1989. We believe that the deep (10-15%) absorption features reported in the ISM spectra for regions like Syrtis Major [2] and subtle but spatially coherent differences in weak spectral features observed in high albedo regions [3] are a manifestation of the order of magnitude increase in spatial resolution of the ISM data over the telescopic measurements. This finding has important implications. First, it demonstrates that high spatial resolution spectral observations can detect mineralogic variability over all ranges of Mars albedo and surface geology. Further increases in spatial resolution can be expected to provide greater information on the compositional diversity of the Martian surface. Second, Mustard *et al.* [2,12] have interpreted the band near  $0.95 \mu\text{m}$  and related band near  $2.1 \mu\text{m}$  to indicate the presence of calcic pyroxene. Based on morphologic associations, this implies that relatively unaltered pyroxene-bearing volcanic materials occur on the Martian surface and must occupy a large percentage of each pixel's  $400 \text{ km}^2$  field of view where detected. Given the paradigm that the surface of Mars is highly altered, the presence of relatively pristine volcanic material is surprising and also exciting. If relatively fresh volcanic materials (secondary crust) are exposed on the surface, perhaps unaltered primary crust is also exposed in the ancient cratered terrains and could be sensed by remote means. If not, then the fresh volcanics seen on current Mars may be in a metastable weathering environment, effectively "frozen in time" by the currently low temperature, humidity, and oxygen partial pressure. The problem of how and when oxidative weathering occurred may therefore be tractable by carefully targeted data collection with high spatial and spectral resolution.

**References:** [1] Erard S. *et al.* (1991) *PLPSC* 21, 437-455. [2] Mustard J.F. *et al.* (1993) *JGR*, in press. [3] Murchie S.L. *et al.* (1992) *LPSC XXIII*, 941-942. [4] Adams J.B. (1974) *JGR*, 79, 4829-4836. [5] Cloutis E.A. and M.J. Gaffey (1991) *JGR*, 96, 22,809-22,826. [6] Morris R.V. *et al.* (1985) *JGR*, 90, 3126-3144. [7] Bell J.F. III *et al.* (1990) *JGR*, 95, 14,447-14,463. [8] Singer *et al.* (1979) *JGR*, 84, 8415-8426. [9] McCord T.B. *et al.* (1982) *JGR*, 87, 3021-3032. [10] Bell J.F. III and T.B. McCord (1989) *Icarus*, 77, 21-34. [11] Murchie S.L. and N.R. Izenberg (1991) *LPSC XXII*, 941-942. [12] Mustard J.F. *et al.* (1991) *LPSC XXII*, 951-952.

539-91

45-6369

ABS ONLY

LPSC XXIV

83

N 94-12 054

AN OBSERVATIONAL SEARCH FOR CO<sub>2</sub> ICE CLOUDS ON MARS; James F. Bell III (NRC/NASA Ames, MS 245-3, Moffett Field CA 94035), Wendy M. Calvin (USGS Branch of Astrogeology, Flagstaff AZ 86001), James B. Pollack (NASA Ames, MS 245-3, Moffett Field CA 94035), and David Crisp (JPL/Caltech MS 169-237, Pasadena CA 91109).

**Introduction:** CO<sub>2</sub> ice clouds were first directly identified on Mars by the Mariner 6 and 7 infrared spectrometer limb scans [1]. These observations provided support for early theoretical modeling efforts of CO<sub>2</sub> condensation [2]. Mariner 9 IRIS temperature profiles of north polar hood clouds were interpreted as indicating that these clouds were composed of H<sub>2</sub>O ice at lower latitudes and CO<sub>2</sub> ice at higher latitudes [3]. The role of CO<sub>2</sub> condensation on Mars has recently received increased attention because (a) Kasting's [4] model results indicated that CO<sub>2</sub> cloud condensation limits the magnitude of the proposed early Mars CO<sub>2</sub>/H<sub>2</sub>O greenhouse, and (b) Pollack *et al.*'s [5] GCM results indicated that the formation of CO<sub>2</sub> ice clouds is favorable at all polar latitudes during the fall and winter seasons. These latter authors have shown that CO<sub>2</sub> clouds play an important role in the polar energy balance, as the amount of CO<sub>2</sub> contained in the polar caps is constrained by a balance between latent heat release, heat advected from lower latitudes, and thermal emission to space. The polar hood clouds reduce the amount of CO<sub>2</sub> condensation on the polar caps because they reduce the net emission to space [5].

There have been many extensive laboratory spectroscopic studies of H<sub>2</sub>O and CO<sub>2</sub> ices and frosts [*e.g.*, 6-9, 13]. In this study, we use results from these and other sources to search for the occurrence of diagnostic CO<sub>2</sub> (and H<sub>2</sub>O) ice and/or frost absorption features in groundbased near-infrared imaging spectroscopic data of Mars. Our primary goals are (a) to try to confirm the previous direct observations of CO<sub>2</sub> clouds on Mars; (b) to determine the spatial extent, temporal variability, and composition (H<sub>2</sub>O/CO<sub>2</sub> ratio) of any clouds detected; and (c) through radiative transfer modeling, to try to determine the mean particle size and optical depth of polar hood clouds and thus to assess their role in the polar heat budget.

**Data Set:** The telescopic data examined here were obtained in November 1990 at the NASA IRTF on Mauna Kea using the ProtoCAM near-IR imaging spectrometer [10]. The data set is composed of whole-disk images of Mars at 83 wavelengths between 1.3 and 4.0  $\mu$ m ( $R = 100$ ). Data reduction and calibration details are discussed elsewhere [11]. Results are presented here using relative band depth (RBD) maps of the planet. RBD maps are ratios between co-registered images obtained in an absorption band to images that represent the local continuum, where a spectrum of the whole disk has first been divided from all the data in order to remove telluric contamination. Thus, RBD maps show the spatial variations in an absorption band relative to the global "average" depth of that feature [11]. Laboratory frost spectra of CO<sub>2</sub> [7] and H<sub>2</sub>O [12] were convolved to the spectral resolution of the telescopic data for comparison and simulation of the RBD maps.

**Results and Discussion:** Four wavelength regions were examined in detail: 2.04, 2.44, 3.33, and 3.02  $\mu$ m. These wavelengths exhibit absorptions due to both H<sub>2</sub>O and/or CO<sub>2</sub> frost in pure lab spectra [*e.g.*, 6-9]. In Figure 1 we present local-continuum-removed CO<sub>2</sub> and H<sub>2</sub>O frost data convolved to the spectral resolution of the telescopic data. The local continua were chosen at the same wavelengths as the continua used for the RBD maps, and thus this figure simulates an endmember case (pure frosts) of what could be seen in the image data. The RBD maps corresponding to each of these wavelength regions are shown in Figure 2.

All four RBD maps reveal substantial spatial structure in the north polar region. Specifically, maps at 2.04, 2.44, and 3.33  $\mu$ m all show a region of enhanced absorption in the north polar region (north of 50°). This polar enhancement is consistent with that observed in a 3.0/2.5  $\mu$ m ratio map (Figure 3) that has been interpreted as evidence of water ice in the polar hood [11]. Figures 1a,b show that the polar features in Figure 2 at 2.04 and 2.44  $\mu$ m may in fact be due to water ice; however, the feature at 3.33  $\mu$ m cannot be caused by water (Figure 1c) and is more likely due to either CO<sub>2</sub> frost or an unidentified surface or atmospheric absorber. Comparison with Figures 2a, 2b, and 3 shows that the 3.33  $\mu$ m absorber extends farther south than the features ascribed to water frost. It is interesting to note that the 3.33  $\mu$ m band has also been reported in Mariner 7 spectra of the Mars south polar cap [13]. The 3.02  $\mu$ m RBD image shows a remarkable



**Figure 1:** Pure H<sub>2</sub>O and CO<sub>2</sub> frosts convolved to our telescopic resolution with a local continuum removed (solid dots). These data provide an endmember simulation of the Band Depth Maps seen in Figure 2.

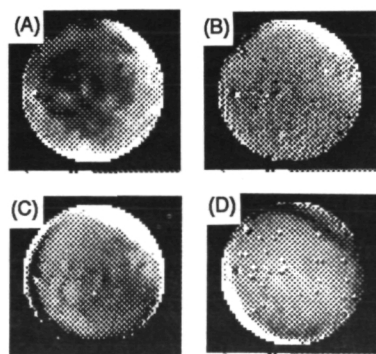
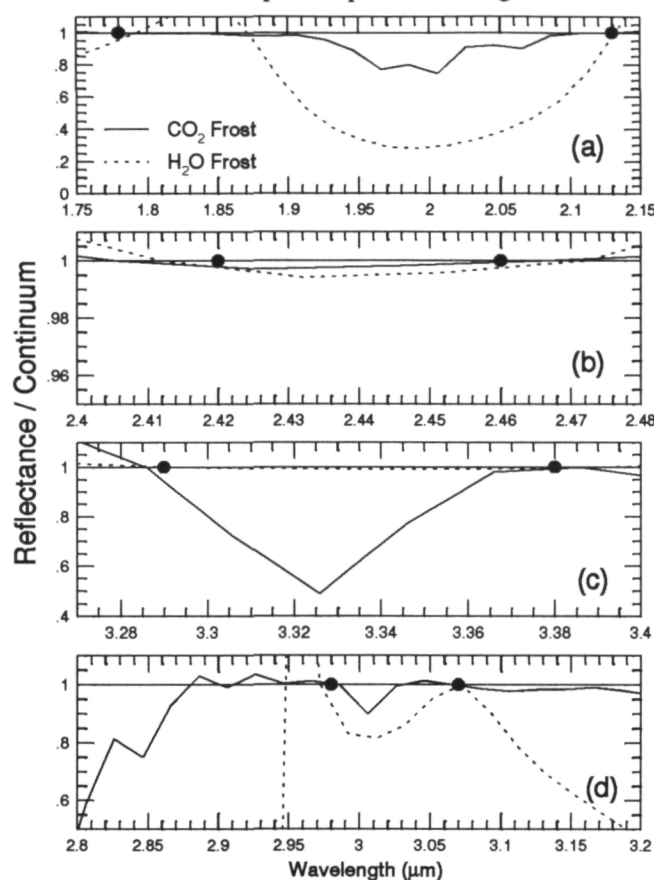


**Figure 2:** RBD Maps using the continuum values of Fig. 1.: (A) 2.04  $\mu\text{m}$ ; (B) 2.44  $\mu\text{m}$ ; (C) 3.33  $\mu\text{m}$ ; and (D) 3.02  $\mu\text{m}$ . Bright is  $>$  disk average band depth; dark is  $<$  than average [11]. North is at 2:00.

dark band (weaker than average band depth) that circles the north polar region between latitudes  $\approx 50^\circ$  to  $65^\circ$ . The polar surface north of  $\approx 65^\circ$  does not show enhanced absorption. Figure 1d reveals that water ice should be more absorbing than CO<sub>2</sub> ice for this choice of continuum points, however the sense of the absorption should yield a bright feature (greater than average band depth) rather than a dark band in the RBD map. It is possible that the dark band may be related to the small "emission" peak seen near 3.05  $\mu\text{m}$  in the continuum-removed spectrum of CO<sub>2</sub> frost in Figure 1d. The alternative, that the dark band is due to water ice in the polar hood, is inconsistent with the fact that no absorption is evident north of  $65^\circ$ . The spatially-confined nature of this feature also raises the possibility of a surface, rather than an atmospheric, origin, possibly related to polar cap edge phenomena involving mixtures of H<sub>2</sub>O/CO<sub>2</sub> ice and dust.

In summary, these data reveal compelling evidence for solid CO<sub>2</sub> absorption features at 3.33 and 3.02  $\mu\text{m}$ . The feature at 3.33  $\mu\text{m}$  is most diagnostic of CO<sub>2</sub>, and the spatial distribution of this feature is consistent with the occurrence of CO<sub>2</sub> clouds in the north polar hood. The spatial distribution of the 3.02  $\mu\text{m}$  feature is more enigmatic because it occurs as an "emission" feature in continuum-removed data and in a spatially-confined north polar annulus. There is as yet no definitive evidence demonstrating a surface or atmospheric origin for either of these two bands; however, this will be the subject of intense future study.

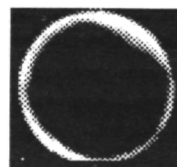


**Figure 3:** Ratio image of 2.5 to 3.0  $\mu\text{m}$  that shows uniform limb darkening and additional polar absorption attributed to H<sub>2</sub>O ice clouds [11] (bright = greater 3  $\mu\text{m}$  band depth).

**References:** [1] Herr and Pimentel (1970) *Science*, 167, 47. [2] see review in James *et al.* (1992) in *Mars*, pp. 946-948, Univ. Arizona Press. [3] Briggs and Leovy (1974) *BAMS*, 55, 278. [4] Kasting (1991) *Icarus*, 94, 1. [5] Pollack *et al.* (1990) *JGR*, 95, 1447. [6] Kieffer (1970) *JGR*, 75, 501. [7] Fink and Sill (1982) in *Comets*, pp. 164-202, Univ. Arizona Press. [8] Warren (1984) *Appl. Optics*, 23, 1206. [9] Warren (1986) *Appl. Optics*, 25, 2650. [10] Bell and Crisp (1991) *LPSC XXII*, 73. [11] Bell and Crisp (1993) *Icarus*, in press. [12] The H<sub>2</sub>O frost spectrum used was calculated by one of us (WMC) using Hapke modeling and the optical constants of Warren (1984). [13] Calvin (1990) *JGR*, 95, 14743.

456370

340-46

NBS. 6114

LPSC XXIV

N94-12055

163260

P-2

**CHANGES IN HAWAIIAN PALAGONITE FE MINERALOGY ASSOCIATED WITH THERMAL ALTERATION: IMPLICATIONS FOR MARS;** James F. Bell III (NRC/NASA Ames, Space Sciences 245-3, Moffett Field CA 94035), Richard V. Morris (Planetary Science, SN4, NASA JSC, Houston TX 77058), and John B. Adams (Dept. of Geological Sciences, Univ. Washington, Seattle WA 98195).

*Summary:* We have studied six Hawaiian palagonitic tephra samples (PH-1 through PH-6) from a site where a Mauna Loa lava flow has partially embayed a Mauna Kea cinder cone. Tephra samples that were not affected by the lava flow (PH-5, PH-6) consist of partially palagonitized coarse-grained glassy Hawaiitic particles whose iron mineralogy is dominated by nanophase ferric oxide (np-Ox) and olivine. Samples closest to the lava flow (PH-1 through PH-4) have been strongly altered and their iron mineralogy is dominated by np-Ox, magnetite, and hematite. This suite of samples has many spectral similarities to Martian bright regions, and thus this localized thermal alteration event may be an analog to similar processes on Mars that lead to the production of small amounts of crystalline ferric oxides within a poorly-crystalline or amorphous palagonitic matrix.

*Introduction and Background:* We have analyzed a series of thermally altered palagonitic tephra samples from Puu Huluhulu cinder cone on Mauna Kea, Hawaii, as part of an ongoing analysis of terrestrial materials that exhibit spectral similarities to Mars. Previously, we reported our findings on the relative abundances of poorly- and well-crystalline ferric oxides in these samples [1]. In this abstract we present a more detailed analysis of the iron mineralogy in our samples and particularly of the variations in iron mineralogy as a function of the degree of thermal alteration. Our interpretations rely primarily on Mössbauer and reflectance spectroscopic techniques. Additional details concerning the sample site, other physical properties of the samples, and laboratory techniques can be found in Bell *et al.* [2].

*Results:* The iron-bearing phases that were needed to model the Mössbauer spectra of our samples are presented in Table 1, along with their corresponding Mössbauer parameters. The identification of pyroxene is tentative (IS is usually  $> 1.1$  mm/s) and is based on analysis of XRD data. The magnetite is strongly cation deficient and/or has Ti substituted at the octahedral sites. We cannot rule out the presence of Ti substitution in the hematite as well. The nanophase iron oxide (np-Ox) doublet results from octahedrally coordinated ferric iron and has been confirmed to arise from np-Ox particles based on selective DCB extraction results [3]. We cannot identify the mineralogy of these nanoscale (20-50 nm) particles further without high resolution TEM or single area electron diffraction analysis.

TABLE 1. Average Mössbauer Parameters at 293 K for Iron-Bearing Phases in Palagonitic Soils PH-1 Through PH-6

Phase	IS, mm/s	QS, mm/s	B <sub>hf</sub> , T
<i>Ferrous Doublets</i>			
Olivine	1.13±0.02	2.87±0.03	
Pyroxene	0.98±0.02	2.36±0.03	
Glass	0.99±0.02	2.05±0.02	
<i>Ferric Doublet</i>			
Nanophase iron oxide	0.35±0.02	0.69±0.04	
<i>Magnetic Sextets</i>			
Hematite	0.38±0.02	-0.18±0.02	51.5±0.2
Magnetite (octahedral)	0.66±0.02	-0.08±0.02	46.7±0.2
Magnetite (tetrahedral)	0.29±0.02	-0.03±0.02	49.5±0.2

*Variations with Degree of Thermal Alteration:* The relative percentage area of each of the iron-bearing phases in the Mössbauer spectra of our samples is presented in Table 2. Nanophase ferric oxide has the largest fractional area in all samples, with the highest values occurring in the <20  $\mu\text{m}$  size fraction. This is consistent with the observation by Morris *et al.* [4] that np-Ox is associated with the most palagonitized material. Ferrous iron is present in olivine in all samples. Ferrous iron in glass is also present in the least altered samples (PH-4 through PH-6) but it is absent in the most altered samples (PH-1 through PH-3). The opposite is true for ferrous iron in pyroxene. This implies that the glass weathers faster than olivine and that pyroxene formation is related to the thermal alteration event. A similar coupling is observed between magnetite and the thermal alteration event. Hematite is found only in the zone closest to the heat source, where temperatures would have been the highest.

*Implications for Mars:* We have previously demonstrated that this suite of samples has many spectral similarities to Mars [1]. Our results here demonstrate that even a small influx of heat and energy (e.g., lava flows, dikes, craters) interacting with unaltered or palagonitized volcanic tephra results in the alteration of more poorly ordered phases to more crystalline ones. This process provides a way to generate the crystalline hematite recently discovered spectroscopically on Mars [5,6] and also (possibly) a way to generate pyroxene [7,8], although this is much more speculative. The mineral assemblage observed in our samples can be produced by processes other than small-scale thermal alteration; however, there is abundant photogeologic evidence that thermal alteration has operated on the Martian surface, and this hypothesis can be tested in the future by more detailed remote sensing, mapping, and eventual sampling.

TABLE 2. Relative percent spectral areas of phases from Mössbauer data for < 1 mm, 500-1000  $\mu\text{m}$ , and < 20  $\mu\text{m}$  size fractions of palagonitic soils PH-1 (closest to heat source) through PH-6 (farthest from heat source). All values in percent; errors are  $\pm 2\%$  absolute.

Sample	Size Fraction	Olivine	Pyroxene	Glass	np-Oxide	Hematite	Magnetite
PH-1	<1 mm	6	7	0	57	12	19
	500-1000 $\mu\text{m}$	8	3	0	57	8	24
	<20 $\mu\text{m}$	1	2	0	79	7	11
PH-2	<1 mm	10	8	0	72	0	10
	500-1000 $\mu\text{m}$	10	6	0	76	0	8
	<20 $\mu\text{m}$	6	5	0	82	0	8
PH-3	<1 mm	9	12	0	73	0	7
	500-1000 $\mu\text{m}$	11	15	0	69	0	5
	<20 $\mu\text{m}$	5	6	0	83	0	8
PH-4	<1 mm	9	0	2	90	0	0
	500-1000 $\mu\text{m}$	10	0	4	86	0	0
	<20 $\mu\text{m}$	6	0	0	94	0	0
PH-5	<1 mm	8	0	11	81	0	0
	500-1000 $\mu\text{m}$	8	0	21	70	0	0
	<20 $\mu\text{m}$	3	0	0	97	0	0
PH-6	<1 mm	8	0	23	70	0	0
	500-1000 $\mu\text{m}$	10	0	27	64	0	0
	<20 $\mu\text{m}$	5	0	1	94	0	0

*References:* [1] Bell J.F. III, Morris R.V., and Adams J.B. (1992) *LPSC XXIII*, 81. [2] Bell J.F. III, Morris R.V., and Adams J.B. (1993) *JGR*, in press. [3] Morris R.V. *et al.* (1993), *Geochem. Cosmochem. Acta*, in press. [4] Morris R.V. *et al.* (1990) *JGR*, 95, 14427. [5] Morris R.V. *et al.* (1989) *JGR*, 94, 2760. [6] Bell J.F. III *et al.* (1990) *JGR*, 95, 14447. [7] Singer R.B. *et al.* (1979) *JGR*, 84, 8415. [8] Mustard J.F. *et al.* (1993) *JGR*, in press.

456371

541-46

LPSC XXIV  
1135 N 94-12056<sup>87</sup>  
163261

**PETROGRAPHY AND PRELIMINARY INTERPRETATIONS OF THE  
CRYSTALLINE BRECCIAS FROM THE MANSON M-1 CORE. M.S. Bell, M.K.**

**Reagan, R.R. Anderson, and C.T. Foster Jr., Department of Geology, University of Iowa, Iowa  
City, IA 52242**

The M-1 core was drilled on the eastern edge of the central uplift within the Manson Impact Structure in Iowa. The lower 107.9 m (~~106.4 to 214.3 m~~ below ground surface) of the core consists of crystalline breccias. Twelve intervals of thin sections from this core have been studied for preliminary discussion. The breccias are divided into three units by matrix size and abundance. Unit 1 is characterized by a high volume fraction of matrix (ave. 0.54), and a decreasing proportion of matrix with depth. This matrix (106.4 to 147 m) is nearly isotropic and consists of grains  $< 0.005$  to  $< 0.02$  mm in length. The matrix between 112 and 146 meters depth consists of a crystalline intergrowth of felsic and opaque minerals with or without chlorite. This was the hottest section of the core after impact, and may have undergone high temperature metamorphic recrystallization. Unit 2 is transitional between units 1 and 3 (147 - 161 m), and is delineated by a rapid increase in grain size to .01-.04 mm and a decrease in matrix abundance to 10 %. Unit 3 (161 to 214.3) has a coarse, often porous matrix, whose abundance changes from about 10 % at the top to about 2 % at the base. Grain sizes range from 0.01-0.1 mm over this interval and coarsen with depth. Changes in the character of the matrix as well as the changes in clast lithology and abundance outlined below suggest that unit 3 is in-situ brecciated basement with injected melt and shale fragments; unit 1 is a crater veneer deposit consisting of transported basement materials and unit 2 is a mixed zone between units 1 and 3. **END**

The top of unit 1 consists of intermixed sedimentary (3%) and crystalline basement (5%) clasts. The sedimentary clasts are predominantly Proterozoic siltstones. The abundance of the sedimentary clasts decrease to less than 1% within about 1 m, although they are scattered throughout the rest of the core. The basement clasts are mostly granophyric granite and biotite gneiss. Mineral grains in these clasts sometimes exhibit shock effects, and some clasts appear to have been melted by the impact. Polycrystalline quartz clasts less than 0.8 mm in length are abundant (~20%). Most have irregular shapes, but some have a lens-shaped cross-section and smooth boundaries. Mineral clasts include quartz, K-feldspar, biotite, and zircon. Grain shapes range from angular to subrounded. Some grains have no internal deformation, whereas others have a variety of deformation features related to shock metamorphism. Quartz grains have single shock lamellae (type A of [1]), multiple and decorated shock lamellae (types B-D of [1]), or multiple lamellae and a pale brown color from the presence of numerous minuscule inclusions not associated with specific shock lamellae. Some quartz grains are choked with inclusions and lack obvious shock-lamellae, whereas others have been converted to diaplectic and thetomorphic glass. Shock deformation features are scarce in mineral grains at 111.8 m and most of the core appears recrystallized. Deeper within the hot section of unit 1, shock-features regain prominence. Shocked quartz grains in this section often have annealed borders and fractures. All quartz grains have halos of small epidote and phlogopite crystals. Some granophyre clasts are relatively intact whereas others consist of quartz and feldspar melts that are recrystallized to polycrystalline quartz and Na-rich K-feldspar.

The thermal effects seen in the hot section of unit 1 disappear in unit 2. Mineral clast sizes increase with depth in unit 2, as does mineral angularity and degree of shock metamorphism in

**PETROGRAPHY OF THE MANSON M-1 CORE -M.S. Bell et al.**

basement clasts. Clasts associated with unit 3 make their first appearance. Polycrystalline quartz grains decrease in abundance downward through unit 2 and are absent in unit 3.

Granophyric granite and biotite gneiss remain abundant in unit 3. Amphibolite also becomes abundant, especially towards the bottom of the core gabbroic rocks and diabases are relatively common, and volcanic rock fragments are rare. Melt fragments that are often altered, recrystallized, and sometimes vesicular are scattered down through the core. Mineral clasts are larger, more abundant, and more angular in unit 3 than in overlying units, and their size and abundance increases downward through the upper part of unit 3. Mineral clasts include blue-green to brown hornblende, K-feldspar, plagioclase, quartz, biotite, magnetite, clinopyroxene, and allanite (?). With the exception of shale clasts, all clasts within unit 3 exhibit shock metamorphic features.

These preliminary data suggest that there are major lithologic differences between units 1 and 3. Unit 3 has abundant amphibolite clasts, coarse mineral and matrix grains, and ubiquitous shock deformational features. There is no evidence of high temperatures within this unit except for the rare melt fragments. Unit 1 is dominated by granophyric granite, biotite gneiss, and associated minerals. Shock metamorphic features are common, but not ubiquitous. The matrix in the upper portion of the unit is exceedingly fine grained and nearly isotropic. The lower portion of the unit was hot enough to generate a finely crystalline groundmass and reaction rims on quartz. The transitional nature of unit 2 suggests that it is a mixture of units 1 and 3, with unit 1 traits increasing upward, and unit 3 downwards. Our preliminary interpretation is that unit 1 represents in-situ basement that was brecciated, mixed, and shock metamorphosed by impact. The rare shale and glass fragments present in unit 3 were likely injected into the jumble during impact. Unit 1 consists of diverse basement lithologies that were transported to the site during or shortly after impact. It may be a fallback breccia, but the high temperatures toward the base, and the mixed zone underneath suggest it was emplaced by flow. Our preferred interpretation is that it is a crater lining deposit generated during impact. Polycrystalline and monocrystalline quartz grains within unit 1 are identical in morphology and degree of shock to those seen in the upper layer of the K-T boundary horizons in the western U.S. [2], suggesting that unit 1 may be the local equivalent of this layer. Additional petrographic analyses and electron microprobe studies are planned to test these hypotheses.

[1] Robertson, P.B., Dence, M.R., and Vos, M.A. (1966) in French, B.M. and Short, N.M., Shock metamorphism of natural materials, Mono Book Corp., p. 433-452

[2] Izett, G.A. (1990) Geol. Soc. Am. Spec. Pap. 249, 100 p.

456372

5/20/90  
12/8/87

LPSC XXIV

89

N 94-132057

# **ORBITAL SIMULATIONS OF SATELLITE ESCAPE/CAPTURE AND THE ORIGIN OF SATELLITES SUCH AS TRITON;** Lance A.M. Benner and William B. McKinnon, Department of Earth and Planetary Sciences and McDonnell Center for the Space Sciences, Washington University, Saint Louis, MO 63130-4899.

We investigate satellite escape/capture in the context of the restricted, circular three body problem as applied to the Sun, Neptune, and Triton. We have computed a large number of coplanar prograde and retrograde orbital simulations over a range of initial distances and velocities. The satellite starts at superior conjunction within  $\sim 2$  Hill radii of Neptune and has a velocity orthogonal to the Sun-planet line. Orbits with these initial conditions can be reflected with respect to time [1], so an escape is simply the reverse of a capture. We numerically integrate the equations of motion to compute the satellite's position until it escapes, collides with Neptune, or after  $\sim 100$  planetary years, fails to escape, when computations cease. The initial distance  $x$  and velocity  $v$  in the restricted problem uniquely define the Jacobi constant  $C$ , a conserved energy-like quantity. Plots of the simulation outcomes in the prograde and retrograde  $C, x$  phase spaces (Figs. 1 and 2) reveal distinct zones in which temporary satellites approach the planet closely enough that permanent capture can be effected by gas drag with a protoplanetary nebula [2,3] or by collision with a pre-existing satellite [4]. Single and double close-flybys constitute the most common possible capture orbits. Long term ( $\geq 10$  planetary years), multiple flyby orbits occur near the stability limits between bound and unbound orbits, and are more common among retrograde captures.

Figures 1 and 2 summarize several tens of thousands of prograde and retrograde simulations, respectively, where each point indicates the result of one simulation. Individual  $C, x$  curves represent orbits computed from a constant initial eccentricity relative to the planet. Curves on the left in the plots depict simulations begun at pericenter; simulations on the right began at apocenter. The simulation outcomes are divided into six categories: 1. capture: minimum distance  $R_{\min} \leq 30 R_N$  ( $R_N$  = radius of Neptune), where a protoplanetary nebula or pre-existing satellite system could exist; 2. collision with the planet; 3. no capture: initial distance = minimum distance; 4. no capture:  $R_{\min} \geq 30 R_N$ ; 5. no escape:  $R_{\min} > 30 R_N$ ; 6. no escape:  $R_{\min} \leq 30 R_N$ .

The capture zones are adjacent to and generally mask narrow collision regions. Potential capture orbits are  $\sim 3$  times more numerous among retrograde than among prograde simulations, in part because of the greater stability of retrograde orbits at large planetary distances. Prograde orbits about Neptune become unbound if  $C \leq 3.00585$ , when the zero velocity curves open at the inner Lagrangian point  $L_2$ . No similar condition exists for retrograde objects. Instead, an irregular band of bound orbits (indicated by many very close crosses) extends from the upper left to the lower right in Fig. 2, but appears blank near the legend. The complicated structure in the figures is a consequence of the nonlinear nature of the three body equations of motion [5], which indicate that satellite capture is a fundamentally nonlinear process.

Although the present orbit of Triton is retrograde, prograde simulations may also be relevant to Triton because some capture orbits alternate between prograde and retrograde inclinations. Similar  $C, x$  phase space behavior should exist for planets with smaller and larger masses and scale according to their Hill spheres. Consequently, these integrations are applicable to other possibly captured objects such as the prograde and retrograde outer moons of Jupiter, Phoebe, and perhaps Nereid.

Additional work is in progress to fill the gaps in the  $C, x$  phase space where computations are not yet complete.

REFERENCES: [1] Roy, A.E., and M.W. Ovendon (1955), *Mon. Not. R. Astron. Soc.* **115**, 296-309; [2] Pollack, J.B., J.A. Burns, and M.E. Tauber (1979) *Icarus* **37**, 587-611; [3] McKinnon, W.B., and A.C. Leith (1993) *Icarus*, in revision; [4] Goldreich, P., N. Murray, P.Y. Longaretti, and D. Banfield (1989) *Science* **245**, 500-504; [5] Murison, M.A. (1989) *Astron. J.* **98**, 2346-2359.

## SATELLITE ESCAPE/CAPTURE ZONES: Benner L.A.M. and McKinnon W.B.

FIG. 1: PROGRADE COPLANAR CAPTURE/ESCAPE FOR NEPTUNE

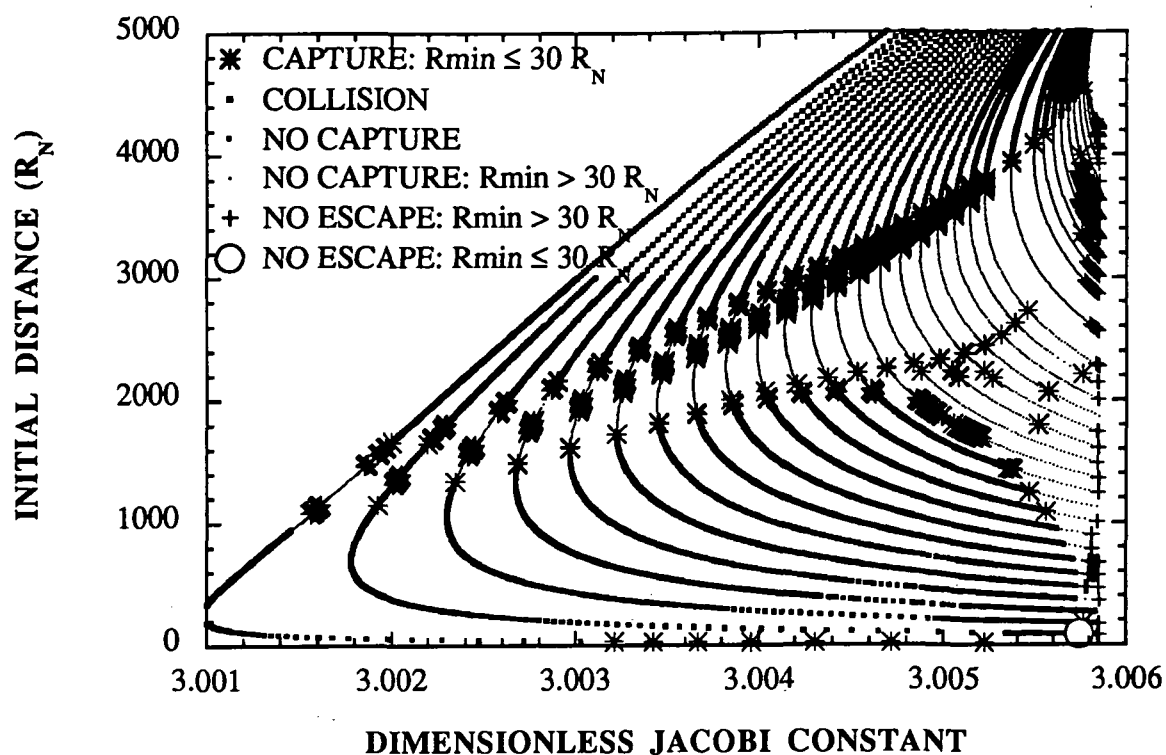
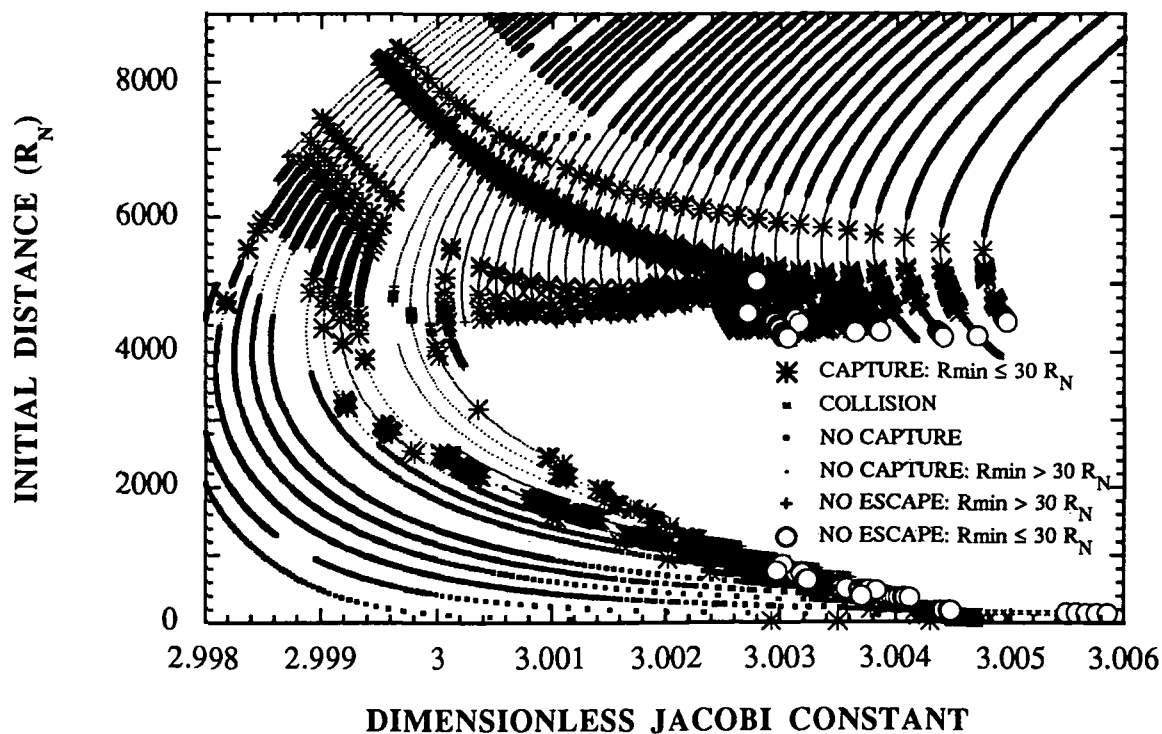


FIG.2: RETROGRADE COPLANAR CAPTURE/ESCAPE FOR NEPTUNE



456373

543-90  
ABS ONLY

LPSC XXIV

91

N 94-1612058

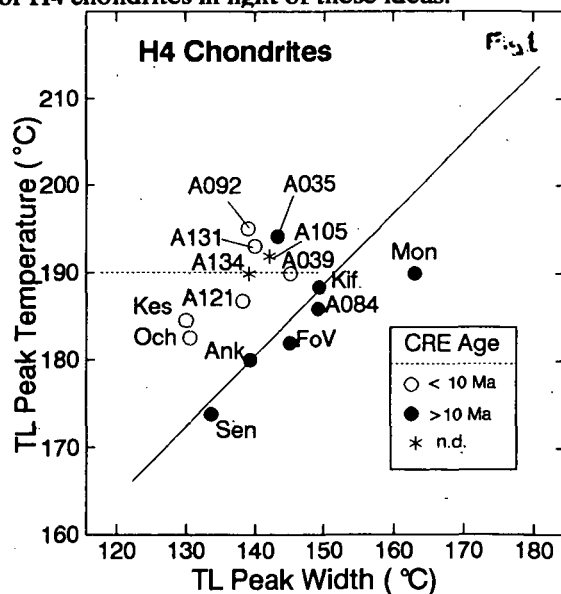
# THE GREAT 8 MA EVENT AND THE STRUCTURE OF THE H-CHONDRITE PARENT BODY. P.H. Benoit and D.W.G. Sears, Cosmochemistry Group, Dept. Chemistry and Biochemistry, University of Arkansas, Fayetteville, AR 72701 USA.

We have recently identified two groups of H5 chondrites with distinct thermal histories, one of which (the "unusual" group) has cosmic ray exposure ages of  $\sim 8$  Ma and is only found in the Antarctic meteorite collection and the other which is found in both Antarctic and non-Antarctic collections. We suggested that these groups are indicative of changes in the meteorite flux over the last million years. We have extended our work to H4 chondrites and find that the groups are also apparent. The most likely origin of the unusual group of H-chondrites is thermal processing during the 8 Ma event which was the source of large numbers of meteoroid fragments.

**INTRODUCTION.** The H-chondrites have been the subject of several recent controversies, including the question of whether Antarctic and non-Antarctic meteorites are or are not the same [1] and whether there is or is not evidence for stratigraphic layering in the original parent body [2,3,4]. We have identified two distinct groups of H5 chondrites in the Antarctic collection [5,6]. One group has induced thermoluminescence (TL) peak temperatures  $< 190^\circ\text{C}$  and metallographic cooling rates between 5 to 50 K/Myr, similar to modern H5 falls. It also has a variety of cosmic ray exposure ages, many being  $> 10^7$  years. The other group has TL peak temperatures  $> 190^\circ\text{C}$ , metallographic cooling rates of 100 K/Myr and cosmic ray exposure ages of  $\sim 8$  Ma. The members of this group were generally smaller than those of the  $> 190^\circ\text{C}$  group (including the modern falls) during cosmic ray exposure. Detailed study of the cosmogenic nuclide concentrations of these groups indicates that they are not solely the result of pairing of a few unusual meteorites [7]. It is likely that the  $> 190^\circ\text{C}$  group was an important part of the H-chondrite flux about 1 million years ago, but has since decreased in importance relative to the  $< 190^\circ\text{C}$  group [5]. In [6] we discussed several possible origins for the  $> 190^\circ\text{C}$  group, including multiple H-chondrite parent bodies, unusual parent body structure, and creation during the 8 Ma event. In this paper, we present new data for H4 chondrites in light of these ideas.

**RESULTS.** We collected induced TL, metallographic cooling rate, and petrographic data for 13 H4 chondrites, 9 of which were from Antarctica and for which cosmogenic noble gas data were available [8]. Unlike our H5 samples, most of the H4 samples had not been previously examined in detail and thus it was necessary to eliminate some heavily shocked meteorites. Our data are shown in Figs 1 and 2. On a plot of TL peak temperature vs. peak width (Fig. 1) four meteorites, including three non-Antarctic falls, plot close to the trend defined by the larger non-Antarctic H-chondrite database. All four have cosmic ray exposure (CRE) ages in excess of 10 Ma. The remainder cover a broad range of TL peak temperatures from 185 to  $196^\circ\text{C}$ , and all, with the exception of A035, have CRE ages  $< 10$  Ma. There is no clear clustering of two groups, with a separation at a peak temperature of  $190^\circ\text{C}$ , but there are three groups, one following the trend for non-Antarctic H-chondrites, a second with peak temperatures between 185 and  $195^\circ\text{C}$  and a third with peak temperatures  $> 195^\circ\text{C}$ . We obtained metallographic cooling rates for all our samples except for A262 and Kesen (Fig. 2). The data show that, with the exception of FoV, (1) the H4s, like the H5s, show two major groups of metallographic cooling rates, one between 5 - 50 K/Myr and the other with rates of  $\sim 150$  K/Myr and (2) the samples with the highest TL peak temperatures also have the highest cooling rates. The TL groups of H4 chondrites are less resolved than H5 chondrites on the Berne plot, probably because there is less diversity among the present samples since their meteoroid bodies were fairly large. In addition, the group with the highest TL peak temperatures and the highest metallographic cooling rates also have significant amounts of implanted gases, as their  $^{22}\text{Ne}/^{21}\text{Ne}$  is much greater than most ordinary chondrites.

**CONCLUSIONS.** We have previously discussed several possible origins for the unusual, fast-cooled,  $> 190^\circ\text{C}$  group of H-chondrites [6]. Among the possibilities are (1) stratification in the parent body (2) multiple





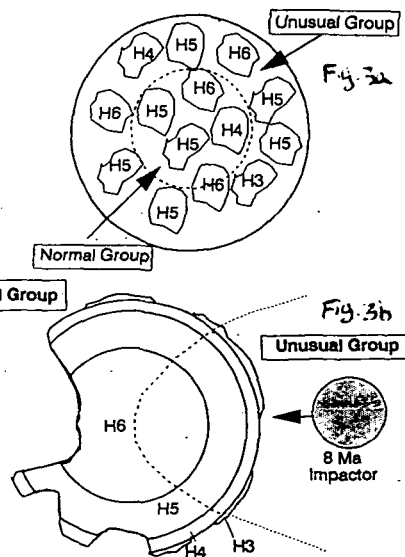
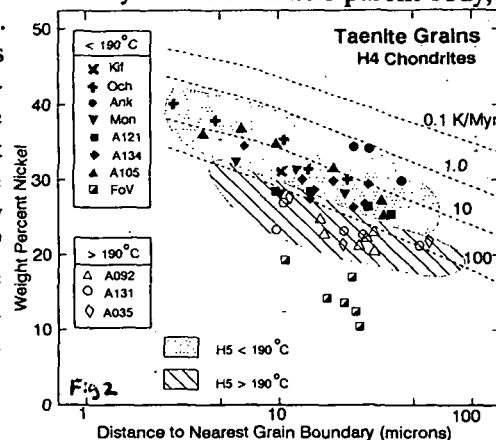
## THE 8 MA EVENT AND THE H CHONDRITE PARENT BODY: Benoit P.H. and Sears D.W.G.

parent bodies (3) a "rubble pile" parent and (4) alteration of a stratified body during the 8 Ma event. We discuss each of these possibilities in light of the current data.

The existence of a single metamorphically stratified H-chondrite body has been the subject of much discussion [2,3,4]. Metallographic cooling rate data have argued against such a simple structure [4], but recent metallographic work and Ar-Ar dating of meteorites selected for their very low degree of shock seems to support stratification [2,3]. The present TL and metallographic data indicate that the  $>190^\circ\text{C}$  group is very unlikely to represent the near-surface of a simple stratified body. Since both TL groups are found in both the H4 and H5 chondrites, one would have to suggest a layering of H5-H4-H5-H4, which is not in accord with a simple concentric metamorphic sequence. The second possibility, that of origin of the groups in different H-chondrite parent bodies, also seems unlikely. In this case, it would be necessary for the two bodies to impact each other in the 8 Ma event, with large numbers of fragments of both bodies surviving the event, or both bodies would have to be impacted at about the same time by other objects. The rubble pile model is vastly more flexible than the others; It would be possible to generate the two groups in all petrologic types by depth placement within the reassembled parent body, with the  $>190^\circ\text{C}$  group forming the outer layer of the body (Fig. 3a). During the 8 Ma event, this outer layer would be more subject to comminution than the more protected  $<190^\circ\text{C}$  group and hence might be fragmented into smaller pieces. If this is the case, however, why do *all* the H-chondrites with CRE ages  $>8$  Ma belong to the  $<190^\circ\text{C}$  group? It would seem more likely that previous less-catastrophic events would preferentially sample this outermost layer of  $>190^\circ\text{C}$  material but this is not observed. The final possibility, that of formation of the  $>190^\circ\text{C}$  group *during* the 8 Ma event has the advantage of simplicity. It is apparent from CRE ages that, if there is only one H-chondrite parent body, fragments have spalled off it many times over the last 40 Ma [9]. The event which produced all the fragments with  $\sim 8$  Ma CRE ages was clearly a very large one, considering about a third of all H-chondrites were involved in it. If the event was a large-scale collision/impact (Fig. 3b), the  $>190^\circ\text{C}$  group might be the product of a rapid pulse of heat in the area around the impact region. The rest of the body might be fragmented, but would be less affected by the heat pulse, and thus could serve as a source for the "normal"  $<190^\circ\text{C}$  group, including most modern falls. The rocks in the  $>190^\circ\text{C}$  source region would be prone to heavy comminution and thus might be expected to produced smaller meteoroid bodies. In this model one would expect the H6 chondrites to have metallographic cooling rate and TL trends similar to those of the H5 chondrites; preliminary TL results suggest that this is the case [6]. The present data and our earlier results [5,6] indicate that, while the great 8 Ma event has severely affected the H-chondrites, it should be possible, by careful sample selection, to examine the original stratigraphy of the H-chondrite parent body. Metallographic and nuclear track cooling rates seem to bear this out [2,3] and suggest a stratified body similar to the L and LL bodies. **Acknowledgements:** We wish to thank the Meteorite Working Group of NASA and the National Museum of Natural History (US) for samples and J. Wagstaff and V. Yang for access to the Johnson Space Center microprobe. Supported by NASA grant NAG 9-81.

**References:** [1] Dennison J.E. and Lipschutz M.E. (1987) *GCA*, 51, 741. [2] Lipschutz M.E., Gaffey M.J., and Pellas P. (1989) in *Asteroids II*, Univ. Arizona Press, 740. [3] Pellas P. and Fiéni C. (1988) *LPS XIX*, 915. [4] Taylor G.J., Maggiore P., Scott E.R.D., Rubin A.E., and Keil K. (1987) *Icarus*, 69, 1. [5] Benoit P.H. and Sears D.W.G. (1992) *Science*, 255, 1685 [6] Benoit P.H. and Sears D.W.G. (1993) *Icarus*, in press. [7] Schultz L. Weber F. and Begemann, *GCA*, 55, 59. [8] Schultz L. and Kruse H. (1989) *Meteoritics*, 24, 155. [9] Graf T. and Marti K. (1989) *Meteoritics*, 14, 271.

**Meteorite name abbreviations used:** A035 = ALHA79035; A039 = ALHA79039; A084 = ALHA78084; A092 = ALHA81092; A105 = ALHA81105; A121 = ALHA80121; A131 = ALHA80131; A134 = ALHA78134; A262 = ; Ank = Ankober; FoV = Forest Vale; Kif = Kiffa; Kes = Kesen; Mon = Monroe; Och = Ochansk; Sen = Sena.



456374

344-90

ABS. ONLY

LPSC XXIV

93

94-12059

R-2

**METEORITES FROM RECENT AMOR-TYPE ORBITS.** P.H. Benoit and D.W.G. Sears, Cosmochemistry Group, Dept. Chemistry and Biochemistry, University of Arkansas, Fayetteville, AR 72701, USA.

*Observations of observed falls (including three photographed falls) have shown that most meteorites derive from meteoroids in orbits similar to those of Earth-crossing (Apollo) asteroids with perihelia close to 1 AU. We report here the discovery of a recent meteorite shower in Antarctica, the members of which have very high natural thermoluminescence levels. It is apparent from these data that (1) the shower has been on Earth only a short time (terrestrial age  $\sim 1000$  years) and (2) the meteorite probably came to Earth through rapid ( $<10^5$  years) evolution from an orbit with perihelion  $>1.1$  AU, similar to Amor asteroids. Only a very small number of meteorites, including a few modern falls, appear to have had similar orbital histories.*

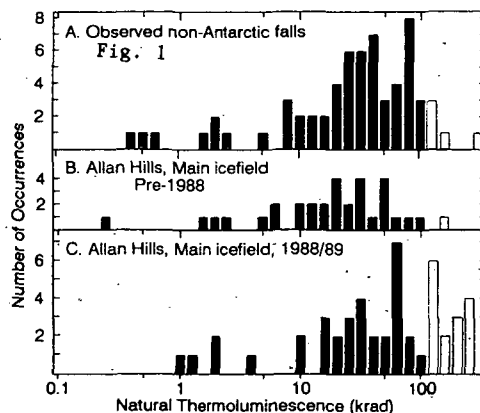
On January 14-15, 1989, a party from the European Meteorite Recovery expedition (EUROMET) discovered 59 meteorites in an area of the Allan Hills blue ice field ( $159^{\circ}20'W$ ,  $76^{\circ}45'S$ ) which only days earlier had been searched with negative results [1,2]. The discovery of such a large number of samples was largely fortuitous; many are very small ( $<20$  g) and would have been blown away by the strong winds of the region [2,3]. An additional, related sample was found by an American ANSMET expedition three years earlier. Natural thermoluminescence (TL) measurements were made on a number of these meteorites as part of their initial characterization. Of the 50 EUROMET samples we measured, 15 had very high levels of natural TL ( $>100$  krad) (Table 1). Such high natural TL levels are not only unusual by Antarctic meteorite standards but are higher than all but a very few non-Antarctic falls, the large majority of which have natural TL levels between 20-80 krad (Fig. 1). Although our conservative criteria for pairing [4], identify seven groups of samples (Table 1), the circumstances of recovery and their common classification suggest that most of them are from a single meteorite, the exception being ALH88020. The total mass of this fall, designated ALH85110, is nearly 0.5 kilogram and might be considerably more, since we have not examined all samples found in the vicinity.

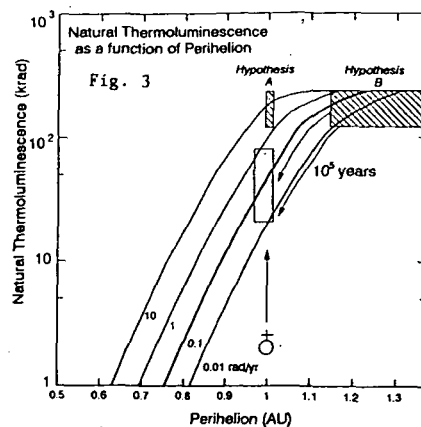
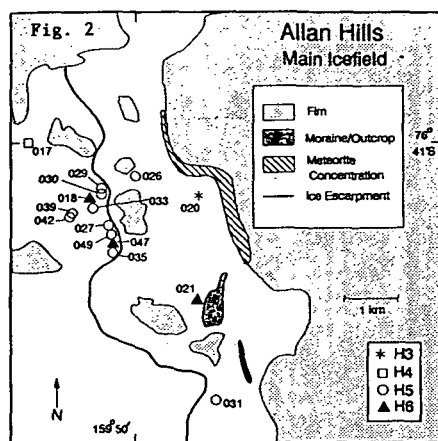
All but four of the samples were found along a line near the ice escarpment along the west edge of the Allan Hills blue ice field (Fig. 2), most of the samples covering a region about 1.5 km wide and 2 km long. The SE-NW trend of these samples may reflect concentration by wind in crevasses during previous periods of surface exposure [2], or the strewn field of a single meteorite fall. If the latter is the case, larger additional masses may in future be found at one end of this trend line [5].

The very high natural TL levels of these meteorites indicates that they have not been on Earth very long. Confirming this, A.J.T. Jull (per comm.) measured  $^{14}C$  activities in two members of the ALH85110 group corresponding to terrestrial ages of  $350 \pm 1300$  and  $2,300 \pm 1300$  years. These terrestrial ages are extremely short by Antarctic meteorite standards; at the Allan Hills Main ice field most meteorites have terrestrial ages well in excess of 40,000 years and are often on the order of  $10^5$  years [6].

Even with such short terrestrial ages, the natural TL levels of these meteorites are unusually high, higher than virtually all recent falls. There are two ways in which very high levels of natural TL can be obtained in meteoroid bodies, shown schematically in Fig. 3. A meteoroid body must either (a) be exposed to radiation levels at least 10 times that of typical bodies or (b) be irradiated at lower temperatures than are typical by being in orbits with unusually large perihelia and impacting the Earth before adjusting its TL level to that appropriate at 1 AU.

The dose rate experienced by a sample depends on the external cosmic ray flux and the depth of the point ("shielding") in relation to the size of the body. We have calculated the effects of shielding [7] and find that high TL levels should be restricted to very small meteorites and therefore this does not explain data for modern falls with very high natural TL levels (Table 1). Shielding effects could, however, at least partly explain the range of natural TL seen among the present samples. An order of magnitude greater external cosmic ray flux is also unlikely. While such high dose rates could be obtained through solar cosmic rays, these are too low in energy to contribute to the flux more than a few centimeters below the surface of a meteoroid





body. Another possibility is that these bodies have been in unusual orbits which were at least partly beyond the heliosphere, i.e., in orbits with very large aphelion or perhaps with high inclinations [8]. However, data from the Pioneer and Voyager spacecraft indicate that the cosmic ray flux outside the heliosphere is only a factor of 2-3 higher than a 1 AU [9], far less than the factor of 10 needed to explain the very high natural TL levels.

The remaining possibility, that meteorites with very high natural TL levels were irradiated while in large perihelion orbits and reached Earth without adjusting their TL, clearly depends on the kinetics of the TL decay process. Calculations (summarized in Fig. 3) show that equilibrium natural TL levels for meteoroid bodies will be very high ( $>150$  krad) at perihelion  $>1.1$  AU and will reach a saturation level in perihelion  $>1.2$  AU. Approximately  $10^5$  years are required for TL levels to decay from an equilibrium level of 250 krad at  $\geq 1.1$  AU to 80 krad at 1 AU [10]. While this is a short period of time relative to the orbital evolution of most meteoroid bodies, orbital calculations suggest that rapid changes in perihelion are possible on less than this time scale in some cases [11]. Less than 5% of ordinary chondrites have very high natural TL levels (Fig. 1), suggesting that few meteoroid bodies undergo such rapid perihelion changes. It is probably not a coincidence that one of the best-characterized of these meteorites, Jilin, has a two-stage irradiation history in which the most recent stage is only about 0.4 Ma long [12]. If this interpretation is correct, these rare meteorites are the only documented samples from meteoroid bodies in orbits similar to Earth-approaching (Amor) asteroids, although it has been suggested that three Amor asteroids are potential sources for basaltic meteorites [13].

In summary, we have identified a major Antarctic meteorite shower which is an H-chondrite breccia and which was found along a geographic trend line which may reflect a preserved strewn field or wind concentration of small meteorites in ice crevasses. The meteorite has been on Earth only  $\sim 1000$  years and had experienced a very unusual orbital history, probably involving a change of perihelion from  $\geq 1.1$  AU to 1 AU within the last few hundred thousand years. Only a very small number of other meteorites have had similar histories.

**Acknowledgements:** We wish to thank EUROMET, L. Schultz, and the U.S. Antarctic Meteorite Working group for samples and documentation and J. Roth and H. Sears (Univ. Arkansas) for technical assistance. This research sponsored by NASA grant NAG 9-81.

**References:** [1] EUROMET (1991) *LPS XXII*, 359. [2] Delisle G. and Sievers J. (1991) *JGR* 96, 15577. [3] Cassidy W., Harvey R., Schutt J., Delisle G., and Yanai K. (1992) *Meteoritics* 27, in press. [4] Benoit P.H., Sears H., and Sears D.W.G. (1992) *JGR* 97, 4629. [5] Pedersen H., Canut de Bon C. and Lindgren H. (1992) *Meteoritics* 27, 126. [6] Nishiizumi K., Elmore D., and Kubik P.W. (1989) *EPSL* 93, 299. [7] Benoit P.H. and Sears D.W.G. (1993) this meeting. [8] Traub-Metlay S. and Benoit P.H. (1992) *LPS XXIII*, 1443. [9] McDonald F.B., Moraal H., Reinecke J.P.L., Lal N., and McGuire R.E. (1992) *JGR* 97, 1557. [10] Benoit P.H., Jull A.J.T., McKeever S.W.S., and Sears D.W.G. (1993) *Meteoritics*, in press. [11] Hahn G. and Lagerkvist C. (1988) *Cel Mech.* 43, 285. [12] Heusser G., Ouyang Z., Kirsten T., Herpers U., and Englert P. (1985) *EPSL* 72, 263. [13] Cruikshank D.P., Tholen D.J., Hartmann W.K., Bell J.F., and Brown R.H. (1991) *Icarus* 89, 1.

TABLE 1.

Sample	Class	Weight (g)	Natural TL (krad at 250°C)	Pairing*
<b>ALLH</b>				
85110	H5	22.2	148 $\pm$ 2	A
88017	H4	70.4	130 $\pm$ 1	
88018	H8	67.1	108 $\pm$ 1	B
88020	H3	53.7	210 $\pm$ 2	
88021	H6	51.0	170 $\pm$ 1	
88028	H5	37.1	127 $\pm$ 1	C
88027	H5	31.6	177 $\pm$ 1	A
88029	H5	29.1	226 $\pm$ 2	D
88030	H5	28.5	120 $\pm$ 3	C
88031	H4-5	27.8	160 $\pm$ 1	A
88033	H5	27.3	118 $\pm$ 1	C
88036	H5	26.6	123 $\pm$ 4	C
88039	H5	24.9	145 $\pm$ 1	A
88042	H5	22.8	238 $\pm$ 1	D
88047	H8	20.6	109 $\pm$ 1	B
88048	H5	20.1	225 $\pm$ 4	D
<b>Observed Falls</b>				
Bo Xian	L4	13000	207 $\pm$ 1	
Jilin	H5	4000000	290 $\pm$ 15	
Sandov	L4	328000	130 $\pm$ 7	
Tennasilm	L4	28500	120 $\pm$ 6	
Oldong	L5	1300	125 $\pm$ 1	

\* Letter indicates assignment to groups of meteorite fragments thought to have been pieces of the same body immediately prior to fall. Grouping is on the basis of compositional and TL properties.

45-6375

545-91

ABS. ONLY

LPSC XXIV

95

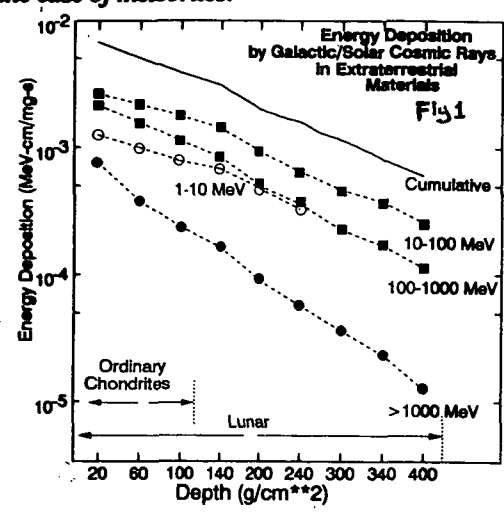
N94-12060

# **NATURAL THERMOLUMINESCENCE PROFILES IN LUNAR CORES AND IMPLICATIONS FOR METEORITES.** P.H. Benoit and D.W.G. Sears, Cosmochemistry Group, Dept. Chemistry and Biochemistry, University of Arkansas, Fayetteville, AR 72701.

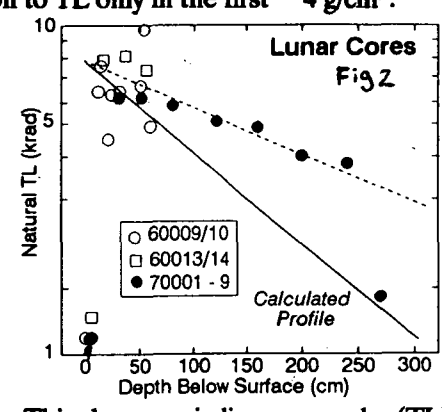
P-2

Meteorites and lunar samples have been irradiated by high energy cosmic rays, typically for millions of years. In addition to producing isotopic changes, the irradiation creates ionization which may be recorded in the form of stored thermoluminescence (TL) in certain minerals, the most important of which is feldspar. One aspect of interpreting the TL of these samples is the effect of "shielding" or depth control, which is particularly important for meteorites, since they have lost an unknown amount of mass during atmospheric entry. Here we report theoretical calculations which we compare with samples from lunar cores for which we have excellent stratigraphic control. We then discuss the implications for these results for the TL of meteorites, which have a different irradiation geometry. We find that, in general, calculated profiles are similar to those observed in lunar samples and meteorites. Additional effects, such as orbital (thermal) history and terrestrial age must also be considered in the case of meteorites.

**Calculations:** We use the calculated cosmic ray flux of Michel *et al.* [1] which is based on the flux on the Moon. This flux estimate is probably approximately correct for most meteorites but might be too low by a factor of 2-3 for meteorites in high inclination or large aphelion orbits [2]. The flux from Michel *et al.* [1] includes both primary and secondary protons. Thermoluminescence levels in materials are governed by the amount of energy deposited per unit volume rather than any specific nuclear reaction. Thus, we assume that only charged particles (i.e., largely protons) contribute to the TL build-up, as these are much more efficient at depositing energy in matter than are primary and secondary neutrons. We convert the cosmic ray energy spectrum to energy deposited using "stopping power" curves for a material near in atomic number to the samples [3]. These curves emphasize the importance of the lower energy cosmic rays (10 - 100 MeV) in TL build-up, especially the secondary particles. The shape of the TL profile can be estimated by finding the cumulative energy deposited as a function of depth. This calculated profile is fairly shallow on a log(energy) vs. depth plot, with a drop of about a factor of 5 over 400 g/cm<sup>2</sup> (Fig. 1). Additional calculations show that lower energy solar cosmic rays (<100 MeV primary particles)[4] will make a significant contribution to TL only in the first ~ 4 g/cm<sup>2</sup>.



**Lunar Cores.** We have measured the natural TL of three lunar cores: 60009/10 (8 samples); 60013/14 (4 samples); and 70001-70009 (8 samples). These data are shown in Fig. 2. In all three cores the uppermost sample has a very low level of natural TL. This is because of the high temperatures experienced by the top 5-10 cm of lunar regolith due to diurnal heating [5]. The TL profiles reach a plateau of ~7 krad in all three cores in the interval of 10-100 cm, including the entire length of 60009/10 and 60013/14. It is, however, possible that the samples in the 10-40 cm range have also been affected by diurnal heating but to a much lesser degree than those in the uppermost 10 cm. These data are in accord with earlier TL studies of lunar cores [6]. In the 70001-70009 core there is a gradual drop in TL from 100-250 cm. This decrease is linear on a log(TL) vs. depth plot (Fig. 2) and thus is qualitatively similar to the calculated profile for simple 2 $\pi$  geometry (Fig. 1). However, the TL profile in 70001-70009 is shallower than that predicted by the calculations, showing a range of only a factor of ~2 verses the expected factor of ~4. The deepest sample, at ~270 cm, has very low TL relative to the other samples. This cannot be interpreted in terms of core history, since it appears that the stratigraphy has not been radically changed for at least 10<sup>7</sup> years [5,7], far greater than the ~10<sup>5</sup> years needed for TL to achieve equilibrium at 1 AU [8]. It is more likely that this sharp drop reflects changes in the energy spectrum, such that particles of sufficient energy are not present in great enough quantity to produce "normal" TL levels at these depths.

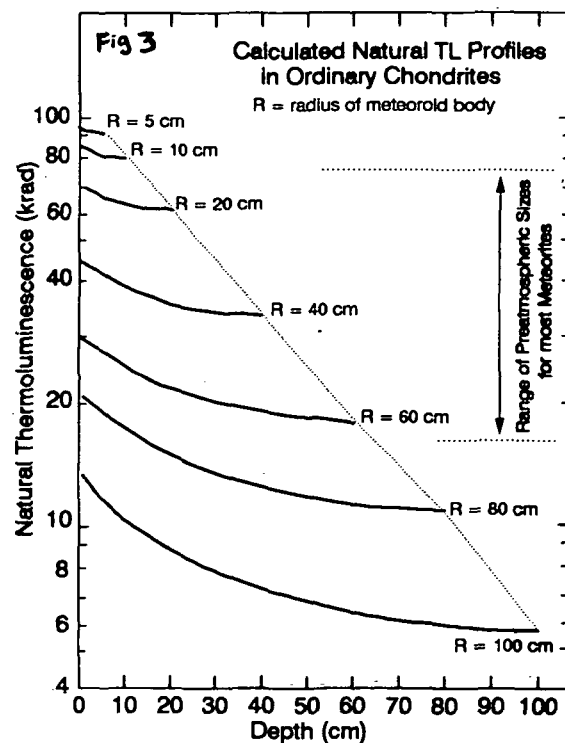


**Implications for meteorites:** In light of these data and calculations, it should be possible to calculate TL profiles for meteoroid bodies as well, making appropriate corrections for  $4\pi$  irradiation. Our calculations are similar in nature to those of Honda [9] for cosmogenic nuclides. The results for meteoroid bodies of various radii ( $R$ ) are shown in Fig. 3. In order to obtain absolute TL calibration, it is necessary to use TL values for meteoritic samples from known pre-atmospheric locations. In the present case, we use values for samples near the center of Knyahinya (as determined by cosmogenic nuclide profiles [10]; preatmospheric radii  $\sim 65$  cm). We are presently seeking other additional calibration samples. Lunar core data could also be used for this purpose, but "anomalous fading" [11] must also be accounted for in these samples in order to compare their natural TL levels directly to meteorites. It is apparent from these calculations that the TL profile for an individual meteorite is fairly flat, with the smallest meteoroids showing the smallest range. The range is greatest in the largest meteoroid bodies, but exceeds 10 krad only in those with preatmospheric radii of  $>120$  cm. Considering bodies between  $\sim 60$  cm and  $\sim 4$  cm in radius, encompassing all meteoroid bodies currently studied in detail [10], the range in TL is only about a little more than a factor of three (i.e., 20 - 65 krad). This compares favorably with the range in natural TL observed in modern ordinary chondritic falls, most of which have TL between 20 - 70 krad [12] (however, see [8] for some exceptions) and with the TL profiles of individual meteoroids such as St. Severin.

**Conclusions:** (1) The expected shape for TL profiles under  $2\pi$  geometry irradiation can be calculated from estimated proton fluxes. The calculated profile has a fairly shallow slope as a function of depth, ranging over less than a factor of 10 over a thickness of  $400 \text{ g/cm}^2$ . TL profiles of three lunar cores, especially 70001-70009 seems to fit the shape of this calculated profile. (2) After corrections for  $4\pi$  geometry irradiations, TL profiles in ordinary chondrites also have fairly shallow slopes as a function of depth, ranging over less than a factor of 2 for the largest meteoroid bodies. The expected range of TL in a full range of meteoroid sizes is only a factor of 3, which is similar to the range observed in samples from various modern falls. (3) While natural TL values of meteorites partly reflect their size during irradiation ("shielding"), they also reflect the recent thermal history of meteoroid bodies, including orbital effects [8,12] and terrestrial age [13].

**Acknowledgments:** LAPST supplied the lunar samples and G. Kurat (Naturhistorisches Museum Wien) supplied Knyahinya samples used in this study. Funded by NASA grant NAG 9-81 and NSF DPP 9115521.

[1] Michel R., Dragovitsch P., Cloth P., Dagge G., and Fülges D. (1991) *Meteoritics*, 26, 221. [2] McDonald F.B., Moraal H., Reinecke J.P.L., Lal N., and McGuire R.E. (1992) *JGR* 97, 1557. [3] Friedlander G., Kennedy J.W., Macias E.S., and Miller J.M. (1981) *Nuclear and Radiochemistry*, 3rd edition. [4] Michel R., Brinkmann G., and Stück R. (1982) *EPSL* 59, 33. [5] Vaniman D., Reedy R., Heiken G., Olhoeft G., and Mendell W. (1991) in *Lunar Sourcebook*, 27. [6] Walker R.M., Zimmerman D.W., and Zimmerman J. (1971) *Proc. LPSC* 4, 308. [7] Pepin R.O., Dragon J.C., Johnson N.L., Bates A., Coscio M.R., and Murthy V.R. (1975) *Proc. Lunar Sci. Conf.* 6th, 2027. [8] Benoit P.H. and Sears D.W.G. (1993) this meeting. [9] Honda M. (1962) *JGR*, 67, 4847. [10] Graf Th., Signer P., Wieler R., Herpers U., Sarafin R., Vogt S., Fieni Ch., Pellas P., Bonani G., Suter M., and Wolff W. (1990) *GCA*, 54, 2511. [11] Sears D.W.G., Benoit P.H., Sears H., Batchelor J.D., and Symes S., *GCA*, 55, 3167. [12] Benoit P.H., Sears D.W.G., and McKeever S.W.S. (1991) *Icarus* 94, 311. [13] Benoit P.H., Jull A.J.T., McKeever S.W.S., and Sears D.W.G. (1993) *Meteoritics*, in press.



456378

S 46-90

LPSC XXIV

97

NBS ONLY

N 94-132061

P-2

## METALLOGRAPHIC COOLING RATES OF L-GROUP ORDINARY CHONDRITES.

Marvin E. Bennett and Harry Y. McSween Jr., Department of Geological Sciences, University of Tennessee, Knoxville, TN 37996-1410.

Shock metamorphism appears to be a ubiquitous feature in L-group ordinary chondrites. Brecciation and heterogeneous melting obscure much of the early history of this meteorite group and have caused confusion as to whether L chondrites have undergone thermal metamorphism within onion-shell [1] or rubble-pile [2] parent bodies. Employing the most recent shock criteria [3], we have examined 55 Antarctic and 24 non-Antarctic L chondrites in order to identify those which have been least affected by post-accretional shock. Six low-shock samples (those with shock grade less than S4) of petrographic types L3-L5 were selected from both populations and metallographic cooling rates were obtained following the technique of Willis and Goldstein [4]. All non-Antarctic L6 chondrites inspected were too heavily shocked to be included in this group. However, 4 shocked L6 chondrites were analyzed in order to determine what effects shock may impose on metallographic cooling rates.

Metallographic cooling rates were derived by analyzing the cores of taenite grains and then measuring the distance to the nearest grain edge. Taenites were identified using backscatter imaging on a Cameca SX-50 electron microprobe. Using backscatter we were able to locate homogeneous, rust-free, nearly spherical grains. M-shaped profiles taken from grain traverses were also used to help locate the central portions of selected grains. All points which contained phosphorus above detection limits were discarded. Plots of cooling-rate data are summarized in Fig. 1. Data from the high-shock samples are presented in Fig. 1a. The lack of coherency of cooling rates for individual samples is indicative of heterogeneous cooling following shock. This diagram confirms the statement expressed by numerous workers that extreme care must be taken when selecting samples of L chondrites for cooling-rate studies.

Data for the 6 non-Antarctic low-shock samples are presented in Fig 1a. Incoherence of individual samples in this plot is due in part to the analytical technique (the difficulty in finding the exact center of asymmetrical grains) and the slight level of shock (most L chondrites observed were shocked to S3) in these 'least-shocked' samples. The samples do, however, display a general trend in cooling rates. The lowest metamorphic grade yielded the slowest cooling rates and an increase in grade follows an increase in cooling rate. This is the opposite relationship to that predicted by the onion-shell model. Fission track studies of several L chondrites have suggested an origin in an onion-shell parent body [1], but the database used in that study was very limited when compared to both fission track and metallographic cooling rate data for H and LL chondrites [1,2,5]. This study should greatly increase the current database for L chondrite metallographic cooling rates.

Cooling rates for 4 analyzed Antarctic L chondrites are presented in Fig 1c. These samples have experienced cooling in a much narrower range than the 4 non-Antarctic L chondrites (0.2 to 100 as opposed to 0.1 to 600 K/Myr in the non-Antarctic L chondrites). They do not show the apparent correlation between metamorphic grade and cooling rate seen in non-Antarctic L chondrites, casting doubt on the validity of any such correlation in this group.

Taylor et al. [2] used results similar to those obtained in this study to suggest that H and LL ordinary chondrite parent bodies were broken up and gravitationally reassembled as rubble-piles. If this disruption took place before the asteroid reached the blocking temperature of Fe-Ni metal, then cooling rate patterns similar to those shown by our non-Antarctic samples could prevail: Antarctic L chondrites yield no correlation between cooling rate and metamorphic grade. If both Antarctic and non-Antarctic L chondrites were derived from the same parent body, then the trend suggested by the non-Antarctic samples is an artifact of the small sample size. If they were derived from different parent bodies, there is still no evidence in either population to support onion-shell bodies. All metallographic cooling rates may have been controlled by a rubble-pile structure, as has been quantitatively shown to be possible if reassembly times for the disrupted parent body were relatively short [6].

## METALLOGRAPHIC COOLING RATES: Bennett, M.E. and McSween, H.Y.

**References:** [1] P. Pellas and D. Storzer (1981) *Proc. R. Soc. London*, Ser. A **374**, 253-270, [2] G.J. Taylor, P. Maggiore, E.R.D. Scott, A.E. Rubin and K. Keil (1987) *Icarus* **69**, 1-13. [3] D. Stöffler, K. Keil and E.R.D. Scott (1991) *Geochim. Cosmochim. Acta* **55**, 3845-3867. [4] J. Willis and J.I. Goldstein (1983) *Proc. LPSC* **14**, B287-B292. [5] P. Pellas and C. Fiéni (1988) *Proc. LPSC* **19**, 915-916. [6] R.E. Grimm (1985) *J. Geophys. Res.* **90**, 2022-2028.

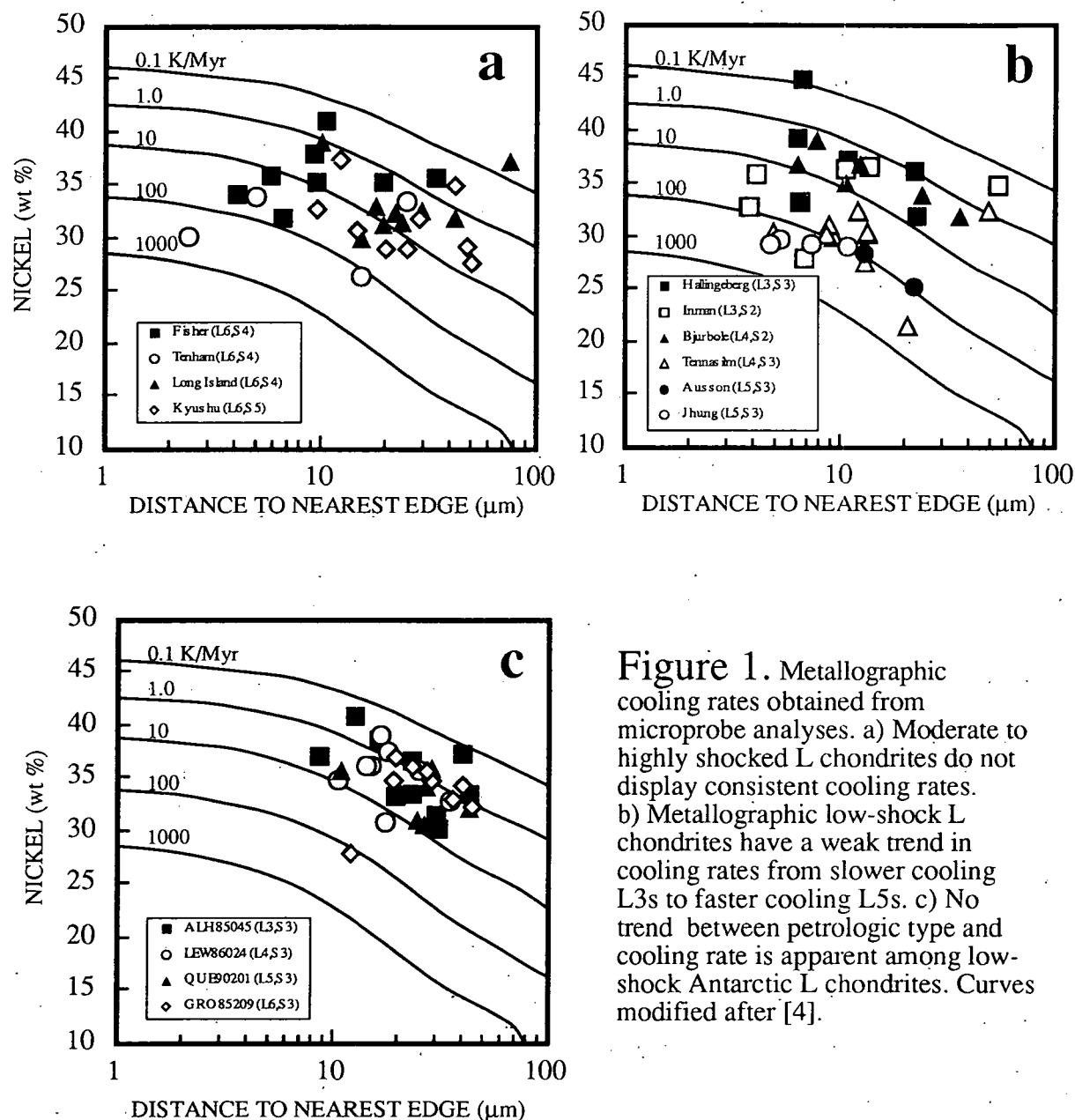


**Figure 1.** Metallographic cooling rates obtained from microprobe analyses. a) Moderate to highly shocked L chondrites do not display consistent cooling rates. b) Metallographic low-shock L chondrites have a weak trend in cooling rates from slower cooling L3s to faster cooling L5s. c) No trend between petrologic type and cooling rate is apparent among low-shock Antarctic L chondrites. Curves modified after [4].

456380

547-90  
ABS ONLY

LPSC XXIV

99

N 94-132062

**Explicit 3D Continuum Fracture Modeling with Smooth Particle Hydrodynamics**

W. Benz (Steward Observatory) and E. Asphaug (Lunar Planetary Laboratory) University of Arizona, Tucson AZ 85721

Impact phenomena shaped our solar system. From the accretion of the planetesimals 4.6 billion years ago to the comparatively recent spallations of meteorites from their parent bodies, which take them to Earth, this ceaseless process has left no bit of solid matter untouched.

As usual for most solar system processes, the scales are far different than we can address directly in the laboratory. Impact velocities are often much higher than we can achieve, sizes are often vastly larger, and most impacts take place in an environment where the only gravitational force is the mutual pull of the impactors. Laboratory studies are limited to disruptive impacts with typical velocities  $\approx 3$  km/s, and typical target diameters  $\approx 6$  cm, in an imposed terrestrial gravitational environment. We must extrapolate from these data by upwards of five orders of magnitude before we reach the size range of asteroids, comets and planetesimals.

It is unlikely that analytical scaling relations for disruption can be extrapolated meaningfully by so many orders of magnitude, since fracture processes are nonlinear and complex. To experiment far beyond laboratory scales, numerical models are the only real alternative. Of course, numerical models are not without problems and limitations either. The first obvious difficulty is to accurately integrate the hydrodynamics and the fracture physics in three spatial dimensions, which by itself is not a totally trivial task! In addition, the predictive power of these models relies upon the limited data available concerning rate-dependent strengths for relevant materials, and upon good equations of state. In any case, it is essential that this tool be properly tested. For this, reproducing laboratory experiments is certainly a necessary condition.

The Smooth Particle Hydrodynamics (SPH)<sup>1</sup> technique has been applied in the past to the simulations of giant impacts<sup>2</sup>. In these simulations, the colliding objects were so massive (at least a sizeable fraction of the Earth's mass) that material strength was negligible compared to gravity. This assumption can no longer be made when the bodies are much smaller. To this end, we have developed a 3D SPH code that includes a strength model<sup>3,4</sup> to which we have added a von Mises yielding relation for stresses beyond the Hugoniot Elastic Limit. At the lower stresses associated with brittle failure, we use a rate-dependent strength based on the nucleation of incipient flaws whose number density is given by a Weibull distribution. Following Grady and Kipp<sup>5</sup> and Melosh *et al.*<sup>6</sup>, we introduce a state variable  $D$  ("damage"),  $0 \leq D \leq 1$ , which expresses the local reduction in strength due to crack growth under tensile loading.

Unfortunately for the hydrodynamics, Grady and Kipp's model predicts which fragments are the most probable ones and not the ones that are really formed. This means, for example, that if a given laboratory experiment is modeled, the fragment distribution obtained from the Grady-Kipp theory would be equivalent to a ensemble average over many realizations of the experiment. On the other hand, the hydrodynamics itself is explicit and evolves not an ensemble average but very specific fragments. Hence, there is a clear incompatibility with the deterministic nature of the hydrodynamics equations and the statistical approach of the Grady-Kipp dynamical fracture model. We remedy these shortcomings by making the incipient flaw distribution explicit, i.e. particles carry activation strains which are distributed at random with a probability of occurrence given by the Weibull distribution. If the local principal axis strain exceeds this limit, damage starts to grow. By growing explicit cracks together with statistical cracks (damage) at the sub-particle scale, we ensure that material strength and fragmentation is independent of model resolution.

We tested our scheme by simulating laboratory impact experiments on basalt spheres<sup>7</sup>. In these experiments, a 0.2g nylon bullet impacts a 3cm radius basalt sphere off-axis at about 3 km/s and results in core-type fragmentation and extensive spallation. (Our simulation is shown in Fig. 1 at  $t=4$ ms.) Since these experiments have been recorded on two high-speed cameras, information about the dynamics of the debris can be obtained from the analysis of the recording. For example, Nakamura *et al.* were able to reconstruct quantities like spatial velocity and angular momentum of the flying



# SPH Fracture Model: W. Benz and E. Asphaug

debris which we use in addition to the fragment mass spectrum to check the numerical results. These comparisons show that the numerical results are a close match to the experiments. In particular, our largest fragment is found to be a core with a mass of 34% of the initial target mass, a result within 6% of the experimental value. In addition, the core's spatial velocity as well as the other fragment velocities are found to be well within the observational error bars. Fig. 2 shows the experimental fragment mass distribution of the largest fragments together with the experimental result, using two different random seeds for the Weibull flaws. These are the explicit fragments shown in Fig. 1.

Our model reproduces laboratory experiments in some detail; we shall therefore present its application to the simulation of colliding asteroids.

**References:** (1) Benz, *Comput. Phys. Comm.* **48** 1990; (2) Benz, Slattery and Cameron, *Icarus* **66** 1986; (3) Libersky and Petshek (preprint) 1992; (4) Wingate and Fisher (preprint) 1991; (5) Grady and Kipp, *Int. J. Rock Mech. Min. Sci. and Geomech. Abstr.* **17** 1980; (6) Melosh, Ryan and Asphaug, *JGR* **97** 1992; (7) Nakamura and Fujiwara, *Icarus* **92** 1991.

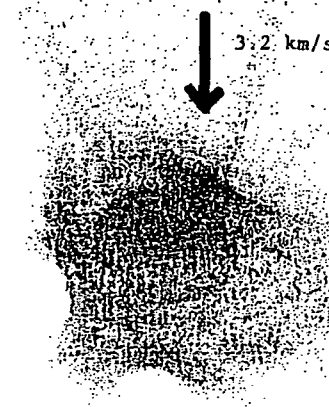
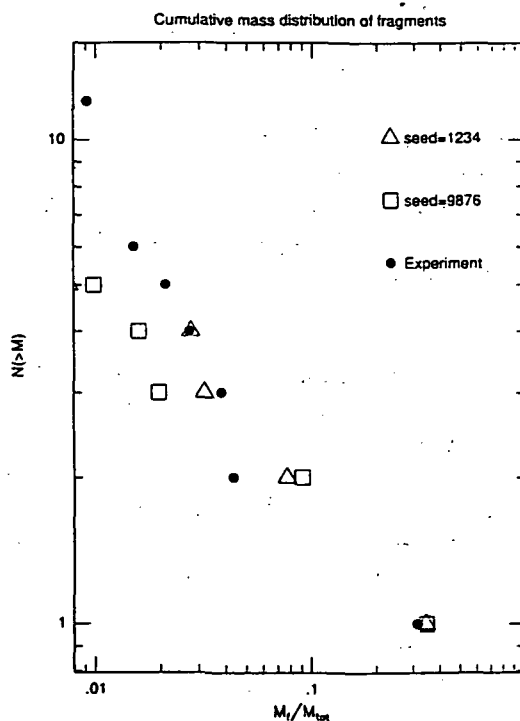


**Fig. 1:** A core-type fragmentation event modeled with our 3D SPH fragmentation code. Note the sizable core and the large surface spalls. The time is 4000  $\mu$ s after impact, extrapolated from a hydrocode completion time of 60  $\mu$ s. The original basalt target was 6cm in diameter, impacted at 3.2 km/s.

**Fig. 2:** Cumulative mass distributions for the several largest fragments. Two simulations with different random seeds (at  $t=60\mu$ s) are compared with experiment. The largest fragments ( $M_i/M_{tot} \sim 0.3$ ) are cores. In both simulations, the largest spall failed to break into two pieces; otherwise the distributions are in good agreement.

456381

548-90  
ABS-024

LPSC XXIV

101

N 94-312063

# COMPOSITION AND MODAL FREQUENCIES OF HYPERVELOCITY PARTICLES <1 mm IN DIAMETER IN LOW-EARTH ORBIT; R.P. Bernhard<sup>1</sup>, T.H. See<sup>1</sup> and F. Hörz<sup>2</sup>, <sup>1</sup>Lockheed ESC, C23, Houston, TX, 77058, <sup>2</sup>NASA Johnson Space Center, SN4, Houston, TX 77058.

**Introduction:** We have continued to systematically analyze the projectile residues associated with hypervelocity impact features on the surfaces of the "Chemistry of Micrometeoroid Experiment" (CME) that was in low-Earth orbit (LEO) for 5.7 years aboard the Long Duration Exposure Facility (LDEF). Details of the CME instrument are presented in [1]. Last year we reported [2] on the systematic analysis, via SEM-EDX methods, of all craters >20  $\mu\text{m}$  in diameter (*i.e.*, 199) on the collectors from LDEF's trailing edge (location A03; 0.85 m<sup>2</sup> of high-purity gold), and ~200 craters >75  $\mu\text{m}$  in diameter from the aluminum 1100 (>99% aluminum) substrates from the forward-facing surfaces. This latter group represents <20% of all craters on the A11 collectors, because the particle flux is substantially higher for the forward-facing orientations relative to the trailing-edge surfaces [3 & 4]. To date, we have analyzed some 600 craters on the A11 aluminum collectors, yet this report summarizes only 400 features, because not all of the results have been completely reduced and entered into our database.

**Compositional Classes of Particles:** As previously described by [2 & 3], the distinction between natural and man-made impactors can generally be made with ease, and, in many cases, impactors can be assigned to compositional subclasses. Among the natural particles, those of chondritic compositions dominate, followed by monomineralic residues of either olivine or pyroxene, and Fe-Ni sulfides. Man-made particles of pure aluminum abound on the gold surfaces and a "miscellaneous" category was established which is dominated by paint flakes, but also includes metal alloys such as stainless steel, and Cu and Ag containing electronic components. The relative frequencies of these particle types as a function of crater size are illustrated in Figure 1.

**Craters With No Detectable Residue:** Note in Figure 1 that ~50% of all craters do not contain detectable residues, most likely due to loss by complete vaporization. Using mean impact velocities of 12 and 19 km/s for natural particles encountering the A03 and A11 surfaces [4], and equation-of-state (EOS) for aluminum 1100 and gold [5], one calculates rather similar peak pressures (430 GPa for the aluminum and 460 GPa for the gold) for both CME surfaces using model projectiles composed of anorthosite [EOS by 6]. These pressures will lead to almost complete vaporization of anorthosite [6]. Nevertheless, it is important to emphasize that aluminum projectiles cannot be detected on the A11 aluminum substrates (*i.e.*, a significant fraction of the "unknown" craters could be the result of aluminum projectiles).

**Modal Projectile Frequency and Flux:** Using the above mean impact speeds of [4] for all craters resulting from natural impactors, and those of [7] for man-made particles ( $V_{\text{mean}}$ ; A03 = 1.75 km/s;  $V_{\text{mean}}$ ; A11 = 7.85 km/s) we converted the measured crater diameters into projectile masses using the equations of [1] for the

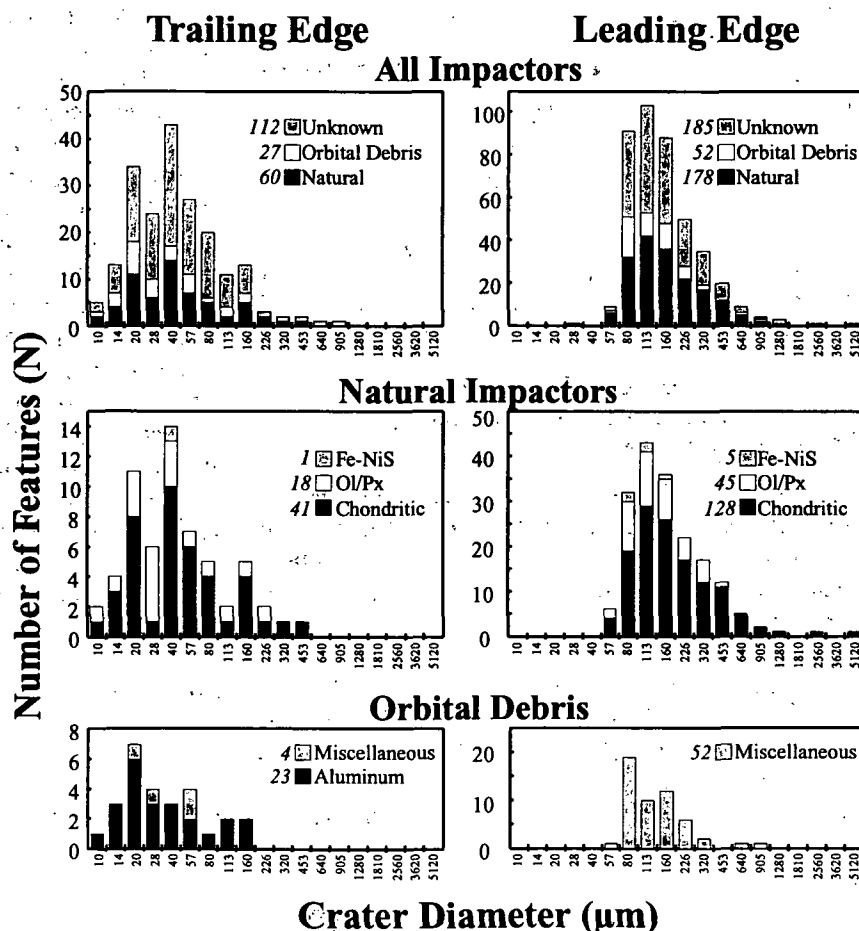


FIGURE 1. Relative frequencies of the different compositional crater classes, as defined by this study, of ~600 impactors that encountered the trailing- and leading-edge CME surfaces.

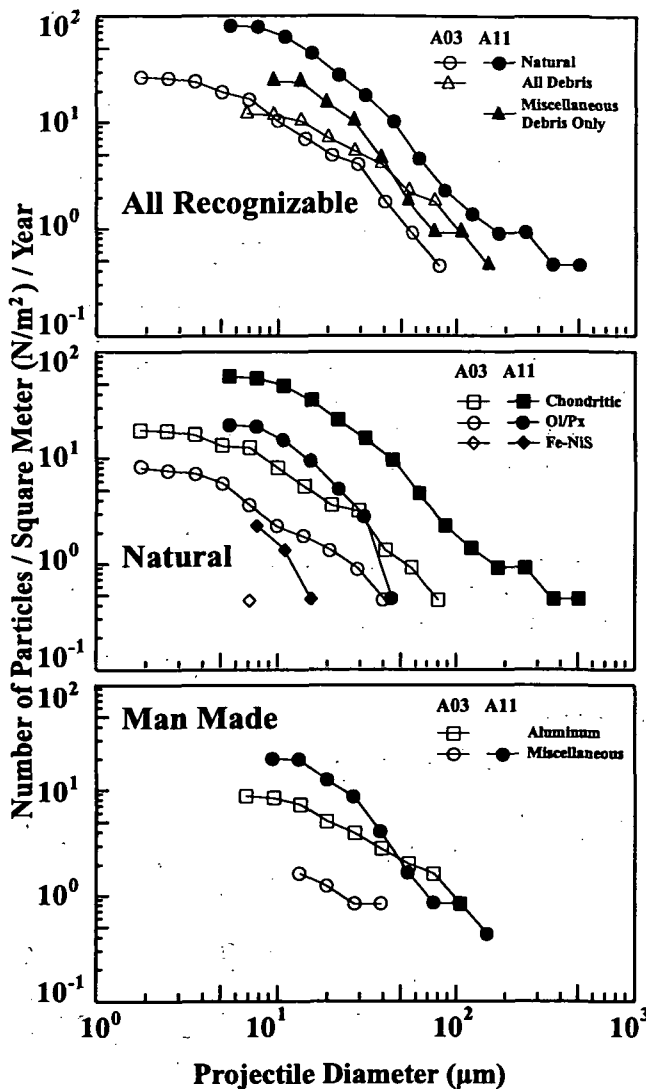


Figure 2. The absolute particle fluxes of specific projectile types, both natural and man-made.

with "massive" projectiles (i.e., resulting in an effective shift to the right in Figure 1), whereas a "large" crater assigned to "fast" projectiles would yield a relatively modest projectile mass, resulting in an effective shift to the left in Figure 1. Note that the frequency of orbital debris particles seems substantially smaller than that of natural impactors in the trailing-edge data of Figure 1, while Figure 2 portrays debris particles to be more populous than natural impactors.

gold surfaces, and those of [8] for aluminum collectors, assuming a projectile density of  $2.7 \text{ g/cm}^3$ . This conversion resulted in the cumulative mass-frequencies and fluxes for specific particle classes that are depicted in Figure 2. The relative (modal) frequency of the three major natural particle classes seems invariant with viewing direction. Furthermore, natural particles seem to dominate the forward-facing direction (A11), yet the frequency of man-made particles equals, if not exceeds the natural impactors for the trailing edge (A03). These data were modeled in detail by [7] who concluded that a substantial population of presently unaccounted for debris sources must exist in highly elliptic, low-inclination orbits. Such orbits are typically occupied by transfer vehicles of geosynchronous payloads. If the modal frequency of man-made particles observed for the A03 surfaces were applied to establish the (possibly) missing aluminum impactors on the A11 surfaces, one would obtain more craters than have been observed. We have difficulties understanding these findings as they seem to be inconsistent with considerations regarding particle dynamics, which require that the substantial population of aluminum impactors on the rear surfaces should somehow be manifested on the forward-facing surfaces as well [7].

**Concluding Remark:** Relative frequencies of projectile types as inferred from the observed frequency of laboratory analysis versus crater size (Figure 1) may differ significantly from the relative and absolute frequencies based on projectile mass (Figure 2). The wide range of impact velocities (1.7 to 19 km/s) required to determine projectile masses call for substantially different conversion factors of crater diameter to projectile mass. This may cause "small" and "low" velocity craters in Figure 1 to be associated

**References:** [1] Hörz, F. et al. (1991) in *LDEF-69 Months in Space, First Post Retrieval Symposium, NASA CP-3134*, p.487-501. [2] Hörz, F. and Bernhard, R.P. (1992) *NASA TM 104750*, 220 pp. [3] Zolensky, M.E. et al. (1992) in *LDEF-69 Months in Space, Second Post Retrieval Symposium, NASA-CP*, in press. [4] Zook, H.A. (1991) in *LDEF-69 Months in Space, First Post Retrieval Symposium, NASA CP-3134*, p. 569-579. [5] Marsh, S.P., ed. (1980) *LASL Shock Hugoniot Data*, Univ. California Press, 658 pp. [6] Ahrens, T.J. and O'Keefe, J.D. (1976) in *Impact and Explosion Cratering*, Roddy et al. eds., Pergamon Press, p. 639-656. [7] Kessler, D.J. (1992) in *LDEF-69 Months in Space, Second Post Retrieval Symposium, NASA-CP*, in press. [8] Cour Palais, B.G. (1987), *Int. J. Impact Engineering*, 5, p. 221-237.

456382

549-91

ABS ONLY  
P. 2

LPSC XXIV

N 9 4-312064 103

## THERMAL STUDIES OF MARTIAN CHANNELS AND VALLEYS USING TERMOSKAN DATA; B. H. Betts and B. C. Murray, California Institute of Technology

The Termoskan instrument on board the Phobos '88 spacecraft acquired the highest spatial resolution thermal data ever obtained for Mars [1,2]. Included in the thermal images are 2 km per pixel observations of 4 major channel and valley systems: Shalbatana Vallis (extending within the Termoskan data from approximately 2°S, 46°W to 5°N, 44°W); Simud Vallis, Hydraotes Chaos, and the associated outflow channel connecting it with the eastern end of Vallis Marineris (all connected from 7°S, 36°W to 5°N, 37°W); Al-Qahira Vallis (20°S, 199°W to 14°S, 195°W); and Ma'adim Vallis (20°S, 183°W to 16°S, 184°W). Simultaneous broad band visible channel data were obtained for all but Ma'adim Vallis. We find that all 4 valley systems have higher inertias than their surroundings, consistent with previous thermal studies of martian channels [3,4,5]. We conclude that the higher inertia is likely due to some intrinsic difference associated with the channel floors, rather than due only to dark aeolian deposits as suggested by some previous studies. Our conclusion is based largely upon the localized nature of the dark deposits in contrast with the thermal homogeneity of the channel floors. Thus, these channels and valleys show an uncommon (for Mars) connection between morphology and inertia.

All four channel systems were observed near midday. They all are cooler than their surroundings by 3 to 10 K. The thermal boundaries very closely follow the channel boundaries (to within Termoskan's 2 km per pixel resolution), in contrast with visible boundaries in and around the channels which do not (see Figure 1). In the visible, all of the valleys and channels appear either darker or similar in brightness to their surroundings. Thus, all have higher thermal inertia than their surroundings. Due to uncertainties in using Termoskan's visible channel to directly determine albedos [1], we are using Viking albedo data [6] in conjunction with visible channel data. Combining this information with Termoskan temperatures and a thermal model of the Martian surface, we estimated thermal inertias of the channels and their surroundings. For example, we have derived for the outflow channel south of Hydraotes Chaos an approximate thermal inertia of  $12.5 (10^{-3} \text{ cal cm}^{-2} \text{ s}^{-1/2} \text{ K}^{-1})$  compared to 9.0 for the surrounding terrain. For idealized, homogeneous surfaces, this would correspond to grains sizes of approximately 1.8 mm within the channel and 0.6 mm outside [7].

Although dark high inertia deposits occur in parts of some of the valleys, the data imply that they do not dominate the inertia of the valley floors as proposed for Al-Qahira and Ma'adim Vallis by Zimbelman [4] based upon areally limited Viking IRTM data. Several observations lead us to this conclusion: the channel floors are cooler (higher inertia) than the surroundings even where they are not significantly darker than the surroundings and certainly where they are much brighter than presumed aeolian intracrater deposits in nearby craters; thermal boundaries closely follow the channel boundaries, whereas visible boundaries do not; and the visible dark "deposits" are much patchier than the fairly uniform thermal regions within the channels.

The data are consistent with Christensen and Kieffer's [3] idea that one process, possibly associated with channel formation, increased the inertia throughout the channels and a second probably aeolian process concentrated a coarse, low albedo component in certain areas. The channel floors as a whole may have higher inertia due to increased particle size or increased occurrence of boulders related to the initial channel formation, e.g., from flow debris. Alternatively, increased bonding may have occurred on channel floors as a result of increased availability of water in the channels due to their original formation, sapping, or some other process.

The channels and valleys studied here are examples of features whose inertia correlates with morphology, something that is rare on Mars [8]. Other than within the localized dark aeolian deposits, the inertia of the channel floors may actually reflect a process associated with channel formation. This possibility makes continued and future studies of these features highly desirable.

REFERENCES: [1] Murray, B.C., M.K. Naraeva, A.S. Selivanov, B.H. Betts, T. Svitek, V.D. Kharlamov, M.L. Santee, Y.M. Gektin, D.A. Fomin, D.A. Paige, A.S. Panfilov, D. Crisp, J.W. Head, S.L. Murchie, and T.Z. Martin (1991), *Planetary and Space Science*, Vol. 39, No. 1/2, pp. 237-265.; [2] Selivanov,

## THERMAL STUDIES OF CHANNELS AND VALLEYS: Betts B. H. and Murray B. C.

A.S., M.K. Naraeva, A.S. Panfilov, Yu. M. Gektin, V.D. Kharlamov, A.V. Romanov, D.A. Fomin, and Ya. Ya. Miroshnichenko, [1989], *Nature*, 341, 593-595; [3] Christensen, P.R. and H.H. Kieffer (1979) *JGR*, 84, 8233-8238; [4] Zimbelman, J.R. (1986) in *Symposium on MECA*, LPI, 112-114; [5] Zimbelman, J.R., and L.A. Leshin (1987) *JGR*, 92, E588-E596; [6] Pleskot, L.K. and E.D. Miner (1981) *Icarus*, 45, 179-201; [7] Kieffer, H. H., S.C. Chase, E.D. Miner, G. Munch, G. Neugebauer (1973) *JGR*, 78, 4291-4312; [8] Christensen, P.R. and H.J. Moore (1992) in *Mars* (Kieffer, Jakosky, Snyder, and Matthews, eds.), 686-729.



Figure 1: Termoskan thermal (top) and visible (bottom) images centered approximately upon 1°S, 40°W. North is top. In the thermal image, darker is cooler. The edge of Valles Marineris is at the bottom. Note the cool and reasonably uniform channel and valley floors of Shalbatana Vallis (A), and the outflow channel (B) leading to Hydraotes Chaos (C). The thermal boundaries closely match the boundaries of the channel floors and depart significantly from albedo boundaries seen the visible image. Note also the dark, presumably aeolian deposits localized within the southern portions of Shalbatana Vallis and spreading onto the surrounding plains.

456384

550-91  
ABS ONLY

LPSC XXIV

105

N 94-12065

P 2

## SPECTRAL ANALYSIS OF THE GRAVITY AND TOPOGRAPHY OF MARS

Bruce G. Bills<sup>1</sup>, Herbert V. Frey<sup>1</sup>, Walter S. Kiefer<sup>1,2</sup>, R. Steven Nerem<sup>1</sup>, Maria T. Zuber<sup>3,1</sup>

1: Laboratory for Terrestrial Physics, NASA/GSFC, Greenbelt, MD 20771; 2: Lunar and Planetary Institute, Houston, TX 77058;

3: Dept. Earth and Planetary Sciences, Johns Hopkins Univ., Baltimore, MD 21218

New spherical harmonic models of the gravity and topography of Mars place important constraints on the structure and dynamics of the interior. The gravity and topography models are significantly phase coherent for harmonic degrees  $n \leq 30$  (wavelengths  $\geq 700$  km). Loss of coherence below that wavelength is presumably due to inadequacies of the models, rather than a change in behavior of the planet. The gravity/topography admittance reveals two very different spectral domains: for  $n > 4$ , a simple Airy compensation model, with mean depth of  $\sim 100$  km, faithfully represents the observed pattern; for degrees 2 and 3, the effective compensation depths are 1400 and 550 km, respectively, strongly arguing for dynamic compensation at those wavelengths.

The gravity model has been derived from a reanalysis of the tracking data for Mariner 9 and the Viking Orbiters [1]. The topography model was derived by harmonic analysis of the USGS digital elevation model of Mars [2]. Before comparing gravity and topography for internal structure inferences, we must ensure that both are consistently referenced to a hydrostatic datum. For the gravity, this involves removal of hydrostatic components of the even degree zonal coefficients [3]. For the topography, it involves adding the degree 4 equipotential reference surface [4], to get spherically referenced values, and then subtracting the full degree 50 equipotential.

Figure 1 illustrates the variance spectra of orthometric heights and gravity anomalies. Also shown for comparison are curves proportional to  $\{n(n+1)\}^{-1}$  with constants of proportionality  $(A,B) = (8,1) 10^{-7}$ . The topographic and gravitational variance spectra of the Earth, Moon, Mars and Venus are all well approximated by power laws of this sort [5,6]. Note that this spectral form for gravity represents a steeper decay than is implied by the usual "Kaula's rule" [7,8], but the constraint of finite variance requires asymptotic behavior similar to this.

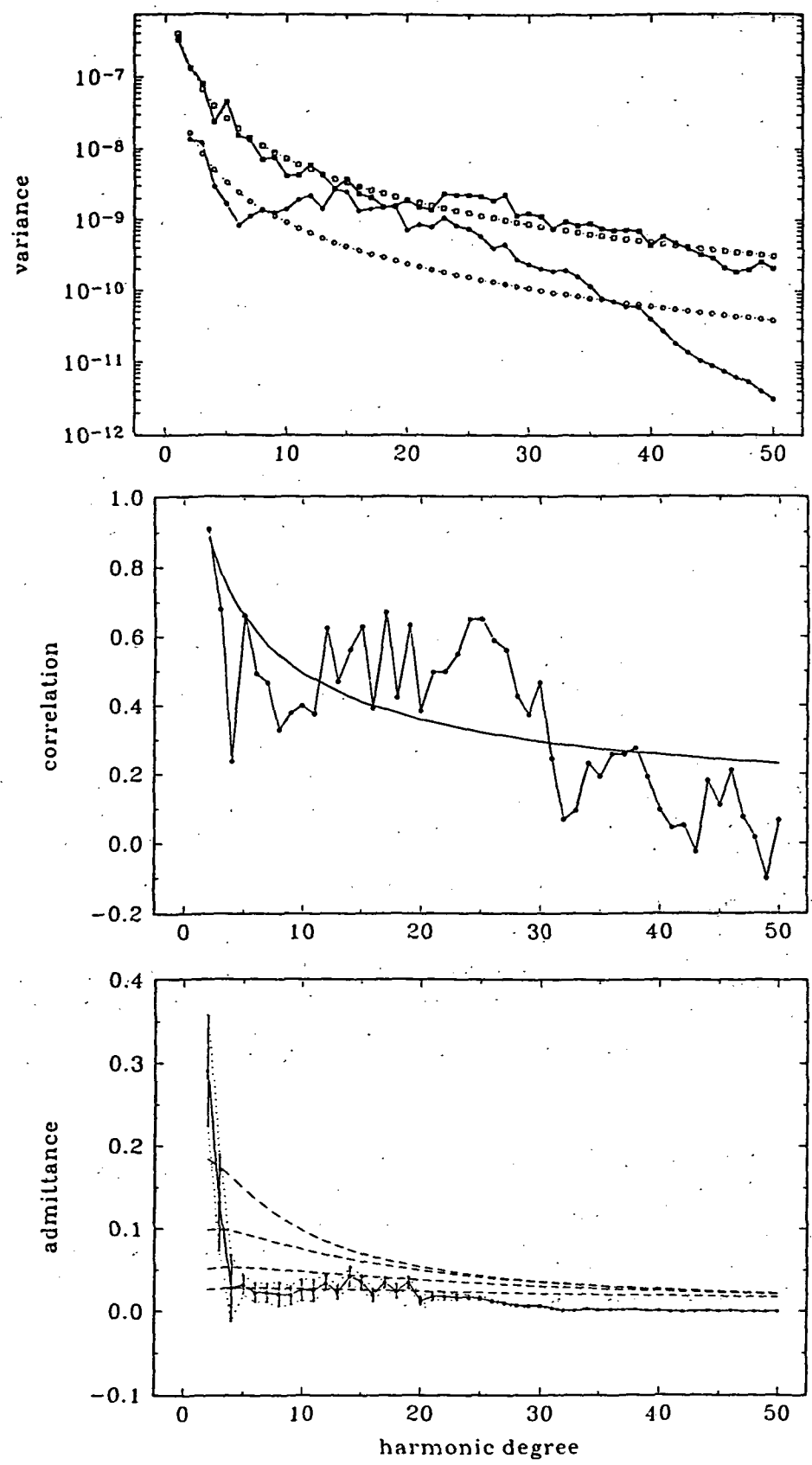
The variance spectra only address the relative amplitudes of the gravity and topography signals. Another important means of comparing them is to examine their phase coherence. The degree correlation coefficient provides a means of examining this coherence. It is a normalized cross-variance. Figure 2 illustrates the correlation spectrum for gravity and topography of Mars, and the 99% significance level. The dip in coherence at degrees 4, 8 and 9 may be real feature of the planet, or may simply reflect errors in the gravity or topography models. In general, the topography is more prone to long wavelength errors, and the gravity is more prone to short wavelength errors. The *a priori* expectation for the high degree behavior is that the correlation should remain consistently high. The decline in coherence beyond degree 30 is likely due to errors in the gravity model, though it should be noted that the correlation is still significant out to degree 40. The peak at degrees 36-38 is due to a resonance in the Viking orbits that amplified signals at those degrees [9].

Figure 3 compares the empirical gravity/topography spectral admittance with the theoretical values expected for Airy compensation [10], with depths of (100, 200, 400, 800) km. Pratt compensation curves for depth  $2d$  are virtually identical to Airy curves for depth  $d$  [11,12]. At harmonic degrees greater than 3, an Airy model with 100 km depth fits the observations quite well. However, degrees 2 and three require much greater depths. The implication is that the longest wavelengths are dynamically supported [13].

## References

- (1) D.E. Smith et al., this volume. (2) USGS Map I-2030, 1989. (3) Sleep and Phillips, JGR 90, 4469-4489, 1985. (4) Jordan and Lorell, Icarus 25, 146-165, 1975. (5) Bills, Kiefer and Jones, JGR 92, 10335-10351, 1987. (6) Turcotte, JGR 92, E597-E601, 1987. (7) Balmino, Moynot, and Vales, JGR 87, 9735-9746, 1982. (8) Smith et al., JGR 95, 14,155-14,167, 1990. (9) F.G.R. Lemoine, dissertation, U. Colorado, 1992. (10) Haxby and Turcotte, JGR 83, 5473-5478, 1978. (11) Dahlen, JGR 87, 5987-6002, 1984. (12) Hager, EPSL 63, 97-109, 1983. (13) W.S. Kiefer et al., this volume.

B.G. Bills et al. Mars Gravity and Topography



456386

351-91  
ABS ONLY

LPSC XXIV

107

N94-12066

**GLOBAL ORGANIZATION OF TECTONIC DEFORMATION ON VENUS:** Frank Bilotti,  
Chris Connors, and John Suppe; Department of Geological and Geophysical Sciences,  
Princeton University, Princeton, NJ 08544

P. 2

The geographic organization of surface deformation on Venus as on Earth is a key to understanding the global tectonic system. To date we have mapped the distribution of three unambiguous tectonic land forms on Venus: 1) Linear foldbelts analogous to those at plate margins of the Earth, 2) Linear rift zones, analogous to continental rifts on the Earth, and 3) Distributed plains deformation in the form of wrinkle ridges and extensional faults and fractures. The linear foldbelts are the dominant structural style in the northern hemisphere; Ninety percent of the planet's foldbelts lie above the equator [1]. In contrast, compressive deformation in the southern hemisphere is dominated by two large, sweeping patterns of wrinkle ridges. The two hemispheres are divided by an equatorial region that is largely covered by rift zones and several large tessera blocks. A tectonic model of generally poleward convergence of the northern hemisphere explains the distribution of foldbelts and rift zones (figure 1). In our model (figure 2), a northern hemispherical plate (or system of plates) moves poleward and deforms along discrete, predominately longitudinal bands.

We recognize four types of foldbelts based on their relationships to other large-scale tectonic features on Venus. There are foldbelts that lie within the low plains, foldbelts associated with coronae, novae and chasmata, foldbelts that lie at the margins of poly-deformed tessera plateaus, and the folded mountain belts around Lakshmi Planum [2]. Figure 1 shows the area distribution of these foldbelts as a function of latitude. We see a geometric increase in the area of foldbelts when normalized to percent area at a given latitude. This increase is consistent with our model of poleward convergence. Also, the orientations of most foldbelts are either approximately north-south or parallel to lines of latitude in the northern hemisphere. This observation is also consistent with the model in that the longitudinal bands are the result of the decreasing area of the sphere as the plate moves poleward and the latitudinal belts are the direct result of poleward compression. Both result from only a few hundred kilometers of northward motion.

Rifts on Venus are unlike those of the Earth's ocean basins in that the amount of extension is much less. An analysis based on inference from structural evidence as well as a rifted crater in Devana Chasma [3] reveals that the range of extension for a typical Venusian rift is in the range of a few tens to a few hundreds of kilometers. Using a simplified area balance for the poleward convergence model, we find that the amount of north-south extension required to produce all the northern hemisphere foldbelts is in the range of 100-300 km. Figure 1 also shows the area distribution of rifts on Venus. While the area of rifts is not a direct measure of extension, we can conclude that the distribution of rifts is consistent with the poleward convergence model.

The trends of wrinkle ridges have been mapped over the planet (figure 3) and several large, sweeping patterns evidently reflect long-wavelength topography. Using wrinkle ridges as paleo-stress indicators, we have developed local and regional stress trajectory maps. These stress maps seem to indicate that the large-scale crustal stresses involved in formation of wrinkle ridges are derived from the regions of high topography near the equator [4]. The wrinkle ridge stressmaps are also very consistent with stress maps of Banerdt [5] who models stress distribution resulting from the support of long-wavelength loads. This suggests that the correlation of topography and gravity on Venus is vitally linked to the planets stresses and tectonics. We have yet to determined if the stresses associated with wrinkle ridge formation are contemporaneous with or related to the northward motion evidenced by the planet's foldbelts.

References: [1] Bilotti, F., Connors, C. and Suppe, J. (1992) Int'l Colloquium on Venus, 10 (abs). [2] Connors, C. and Suppe, J., (1992) Wkshp. on Mtn. Belts on Venus and Earth (abs). [3] Solomon, S.C., et al, (1992) JGR, 97, E8, 13,199. [4] Bilotti, F. and Suppe, J., (1992) GSA abstracts, v. 24, no. 7, A195 (abs). [5] Banerdt, W.B., (1986) JGR, 91, B1, 403.



GLOBAL ORGANIZATION OF TECTONIC DEFORMATION ON VENUS: F. Bilotti, C. Connors, and J. Suppe

figure 1

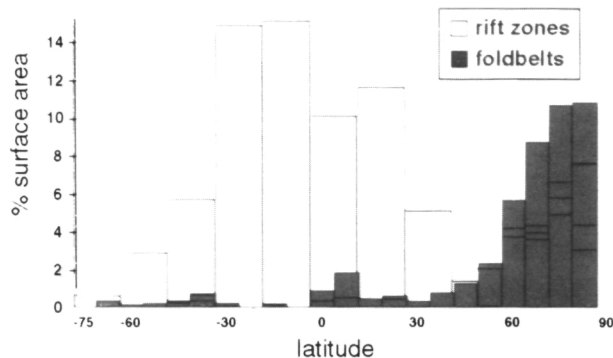


figure 2

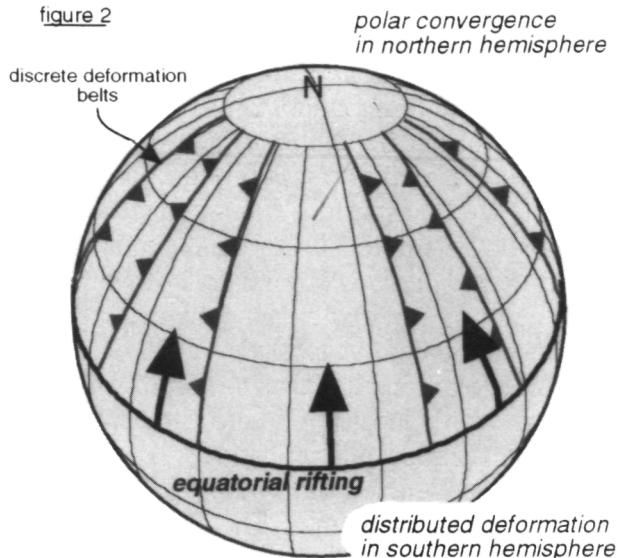


figure 1: Histograms of area of rift zones and foldbelts as a function of latitude. We find that the highest concentration of rifts occurs a few degrees below the equator whereas the area of foldbelts increases toward the north pole as prescribed by the model (fig. 2).

figure 2: Global model of deformation on Venus. Poleward convergence results in decrease in surface area of the crust which causes a poleward increase in compressive deformation. The observed poleward geometric increase in percent area of foldbelts (fig. 1) and the predominately longitudinal/latitudinal orientations of northern hemisphere foldbelts agree with the model prediction for a few hundred kilometers of northward motion.

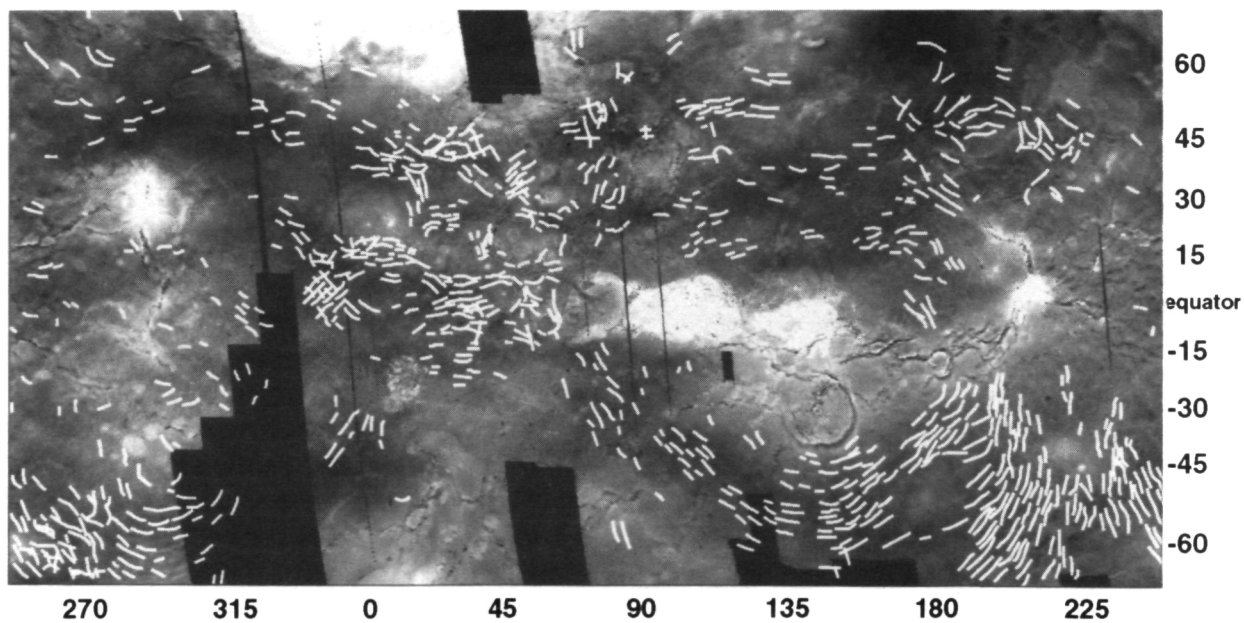


figure 3: Global distribution of wrinkle ridge trends (white lines) superimposed on Venus topography (low areas are black, high areas white). Wrinkle ridges do not occur above  $\approx 6052$  km. Note the high correlation of wrinkle ridges to long-wavelength topography in the southern hemisphere as well as the very coherent, large-scale patterns.

456387

552-91

ABS-ONLY

LPSC XXIV

109

N94-132067

p 2

**VENUS' CENTER OF MASS - CENTER OF FIGURE DISPLACEMENT AND IMPLICATIONS.** D.L. Bindschadler and G. Schubert, Dept. Earth and Space Sciences, UCLA, Los Angeles, CA 90024-1567.

Earth, Moon, Mars, and Venus all have centers of mass (C.M.) that are displaced from their centers of figure (C.F.) by amounts which range from ~340 meters (Venus, [1]) to ~2.5 km (Mars, [2]). These offsets have all been calculated from the first degree terms in spherical harmonic expansions of topography. We describe an alternate method for calculating C.M. - C.F. offsets directly from a global topographic data set and apply it to Venus. Using Magellan altimetry, we find that Venus' C.F. is displaced approximately 280 meters from its C.M. in the direction of Western Aphrodite Terra (4.4° S, 135.8° E). We investigate several simple models for this offset and find that it is most consistent with thickened crust in Ovda and Thetis Regionis (which constitute most of W. Aphrodite). The location of the C.F. offset also places constraints on the degree of crustal thickening in Western Ishtar Terra and/or this highland's mode of origin. We favor a model in which offset due to thick crust in Western Ishtar Terra is balanced by an opposing offset due to cold, downwelling mantle material beneath the highland.

We derive a method for obtaining a C.F. offset directly from a planetary topographic data set. Consider a sphere of radius  $a$  which has a spherical cap of angular radius  $\alpha$  and excess elevation  $h$  centered on the planet's north pole (Fig. 1). The C.F. offset relative to a coordinate system centered on the sphere is just the first moment of the surface area with respect to  $\underline{r}$ , divided by the surface area, where  $\underline{r}$  is the vector between a point on the surface and the center of coordinates and integration is performed over latitude and longitude.

$$\delta \underline{r}_{CF} = \frac{\int \int \underline{r} dA}{\int \int dA} \quad (1)$$

By symmetry, the C.F. offset is in the z-direction and to  $O(h/a)$  is given by

$$\delta z_{CF} = \frac{3}{8} h (1 - \cos \alpha) \quad (2)$$

To calculate the C.F. offset directly from topography, we treat each  $1^\circ \times 1^\circ$  region on the surface as a spherical cap whose angular radius varies with latitude and whose thickness is given by the average of Magellan altimetry measurements within the region (Pioneer Venus altimetry was used to fill gaps in Magellan coverage). Since the topography data are centered on the planetary C.M., offsets for each region can be summed to yield a C.F. - C.M. offset. We find a C.F. offset of 280 meters in the direction 4.4° S, 135.8° E. As a test, we used *Bills and Kobrick's* [1] harmonic expansion of Pioneer Venus (PV) topography to generate a  $1^\circ \times 1^\circ$  data set and found a C.F. offset of 339 meters toward 6.7°N, 148.8°E, essentially identical to their result of 339 meters toward 6.6°N, 148.8°E. The differences between the Magellan and PV results are most likely the result of both the higher spatial resolution and greater areal coverage of the Magellan data.

Numerous explanations have been given for C.M. - C.F. offsets of Mars and Moon, but the most likely suggestions which may also apply to Venus are (1) large-scale heterogeneities in crustal thickness and (2) similarly large asymmetries in mantle density associated with convection. For the first case, consider a cap of excess crustal thickness  $h + h_c$  (Fig. 1). Using the above formula for the C.F. offset and a similar one for the C.M. offset (integrating for mass instead of area over the volume rather than the area of the body), one finds that to  $O(h/a)$ , the C.F. offset with respect to the C.M. is

$$\frac{\Delta z_{CF}}{a} = \frac{3\Delta\rho_c}{8\rho} (1 - \cos 2\alpha) \left( \frac{h}{a} + \frac{h_c}{a} \right) \quad (3)$$

where  $\rho$  is mantle density and  $\rho_c = \rho - \Delta\rho_c$  is the crustal density

As an example of the second cause of C.F. offset, we ignore any possible crustal thickness variations. Instead, we consider a cap of height  $h$ , density  $\rho$ , and angular radius  $\alpha$  which is supported from below by a conical region (e.g., between dashed lines in Fig. 1) of hot mantle with density  $\rho_T = \rho - \Delta\rho_T$ . The C.F. offset in this case is (to  $O(h/a)$ )

$$\frac{\Delta z_{CF}}{a} = \frac{3\Delta\rho_T}{32\rho} (1 - \cos 2\alpha) \quad (4)$$

# VENUS' C.M. - C.F. OFFSET: Bindschadler, D.L., and G. Schubert

Using these formulas, we compared a number of models for the C.F. offset with the observed offset. Given the likelihood that complexly deformed plateau-shaped highlands such as Ovda Regio and W. Ishtar Terra are regions of excess crustal thickness [3,4], we calculated offsets due to spherical caps of thick crust (2) centered at the locations of seven plateau-shaped highlands (Table 1). We also considered eight volcanic rises, treating them as spherical caps supported by low-density (presumably relatively hot) underlying mantle (Table 1). For a given highland, the magnitude of the modeled offset is a function of the crustal or thermal density difference and the size of the highland ( $\alpha$ ), while the direction of the offset is controlled by the location of the highland. It is clear that regions of thick crust are more efficient at creating offset because crust-mantle density differences are large compared to likely thermal density variations (which are averaged over the entire portion of the mantle beneath a thermally-uplifted region).

Numerous combinations of highlands were tried to provide a best fit to the observed C.F. offset. Although an exhaustive examination of all possible combinations of highlands remains to be completed, the best fit was found for a model which included only Ovda and Thetis Regiones as regions of thick crust. For ~40-50 km of excess crust at these locations, the model yielded C.F. offsets of ~240-280 m toward 6°S, 101°E. Models with only volcanic rises yielded offsets clustered near 290°E, 15°-30°N. Models which include W. Ishtar Terra tend to shift the C.F. offset north of its observed location. Using a model which only included Ovda, Thetis, and W. Ishtar, we found that to remain with ~15° of latitude of the observed C.F., W. Ishtar Terra must have an excess crustal thickness not more than half that of Ovda and Thetis Regiones ( $\leq 25$  km based on the best-fit model above). The poor fit for models including Ishtar Terra is surprising given the clear geologic evidence of crustal thickening there [5,6]. One possible explanation, which is consistent with previous models for W. Ishtar [7,3], is that a region of high-density (cold) downwelling mantle exists beneath W. Ishtar Terra. Such a coldspot would provide an offset equal to that shown in (4), but in the opposite direction. For an excess crustal thickness of 20 km in W. Ishtar, the mantle beneath the region would have to be ~70°C cooler on average to yield no net offset.

**References:** [1] Bills and Kibrick, *J. Geophys. Res.*, **90**, 827-836, 1985. [2] Bills and Ferrari, *J. Geophys. Res.*, **83**, 3497-3508, 1978. [3] Bindschadler et al., *J. Geophys. Res.*, **97**, 13,495-13,532, 1992. [4] Herrick and Phillips, *J. Geophys. Res.*, **97**, 16,017-16,034, 1992. [5] Kaula et al., *J. Geophys. Res.*, **97**, 16,085-16,120, 1992. [6] Crumpler et al., *Geology*, **14**, 1031-1034, 1986. [7] Bindschadler and Parmentier, *J. Geophys. Res.*, **95**, 21,329-21,344, 1990.

TABLE 1. Venus Highland Locations

REGION	CLAT	CLON	$\alpha$
VOLCANIC RISES			
Beta	28.00	284.00	13.38
W. Eistla	22.00	356.00	8.02
Atla	1.00	189.00	8.02
Bell	33.00	44.00	6.55
Dione	-33.00	326.00	7.56
Ulfrun	18.00	222.00	8.45
Themis	-40.00	292.00	10.36
Imdr	-44.00	212.00	5.34
PLATEAU-SHAPED HIGHLANDS			
Ovda	-5.00	90.00	14.17
Thetis	-8.50	129.00	9.26
Tellus	40.00	85.00	8.79
Alpha	-25.00	4.00	6.41
Phoebe	-11.00	282.00	6.55
Ishtar	67.00	345.00	11.72
Laima	55.00	55.00	5.07

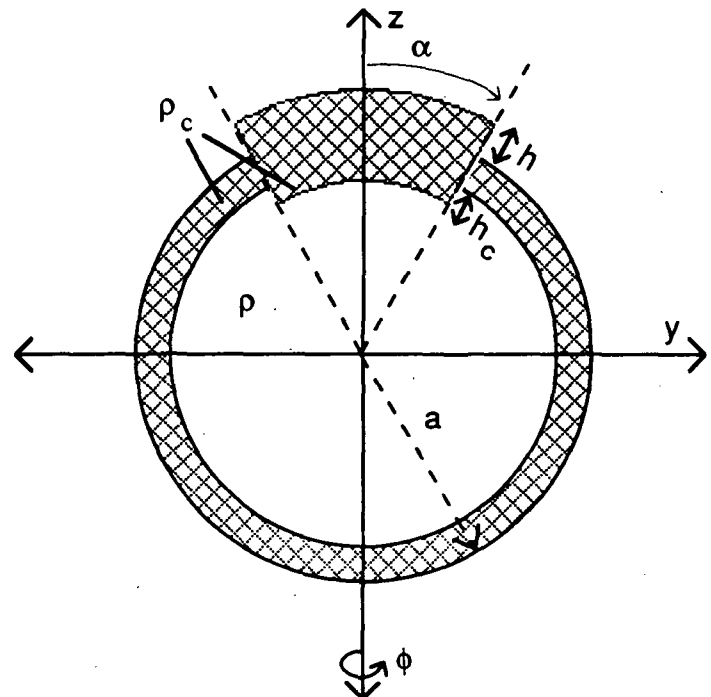


Figure 1 (at right). Sketch of model used to calculate C.F. - C.M. offset for region of thick crust. X-axis points out of paper. Region of interest has excess crustal thickness  $h+h_c$ .

456388

553-90

LPSC XXIV

111

ABS-ONLY

N94-12068

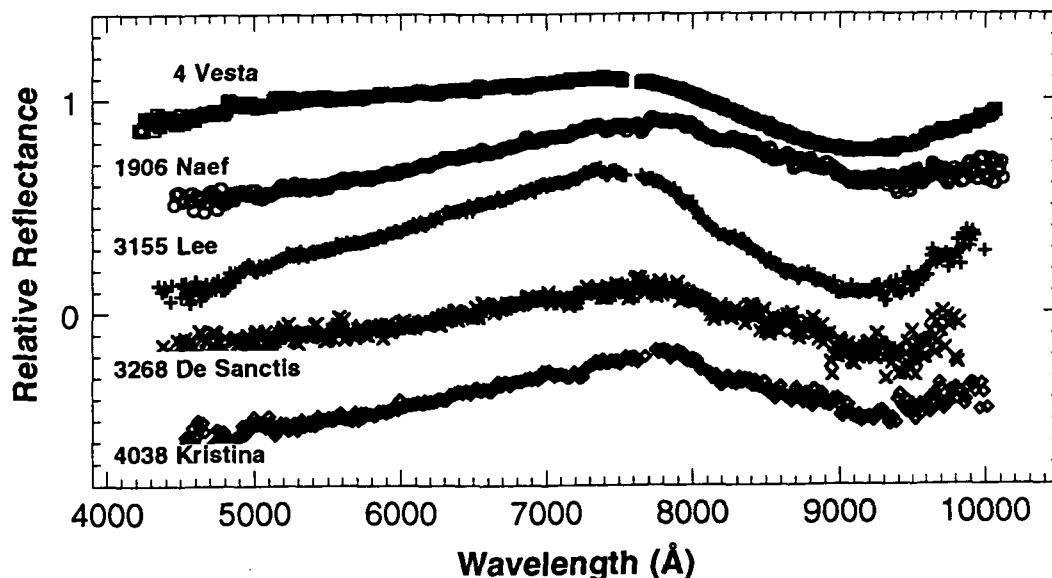
P-1

**THE ASTEROID-METEORITE CONNECTION: FORGING A NEW LINK TO VESTA AS THE PARENT BODY OF BASALTIC ACHONDRITE (HED) METEORITES;** R. P. Binzel, Department of Earth, Atmospheric, and Planetary Sciences, Massachusetts Institute of Technology, Cambridge, MA 02139

Asteroid 4 Vesta has been at the center of the debate over the identity of the howardite-eucrite-diogenite (HED) parent body since the early 1970s (1,2). Despite its unique (among the 500 largest asteroids) compositional match to HED meteorites, substantial dynamical difficulties in delivering fragments from Vesta to the Earth (3) have precluded any conclusive HED parent body link. These dynamical difficulties arise because Vesta's orbital location is far from known resonances. Consequently, it has been argued as dynamically improbable that meteoroid-sized (~1 km) fragments could be excavated from Vesta with sufficient velocities to reach the resonances. Through new astronomical observations (4), numerous small (4-7 km) asteroids between Vesta and the 3:1 resonance have been discovered to have eucrite and diogenite compositions. Based on similar orbital elements to Vesta, all of these new asteroids are likely large impact fragments excavated from Vesta. Their current orbits imply ejection velocities in excess of 700 m/sec. Smaller (~1 km) fragments can therefore be expected to have been ejected with velocities  $\geq 1$  km/sec, sufficient to reach the 3:1 and  $\nu_6$  resonances. Thus it now appears to be dynamically viable for Vesta to be linked as the HED parent body.

The figure below presents a sample of the new observations which were obtained with the 2.4-m Hiltner telescope of the Michigan Dartmouth M.I.T. Observatory. All spectra show the distinct characteristic of basaltic achondrites, a deep pyroxene absorption band beyond 9000 Å. Several of these, including 3155 Lee (below), show much deeper bands with centers at shorter wavelengths, characteristic of diogenite meteorites (5). To date, more than 15 of these small basaltic achondrite asteroids have been found within the range of 2.31-2.45 AU, where Vesta is located at 2.36 AU and the 3:1 resonance is at 2.50 AU. Also, all have orbital eccentricity and  $\sin i$  (inclination) values within  $\pm 0.02$  of Vesta. More than 100 other small asteroids outside this range have been observed, but none show basaltic achondrite spectra. This exclusivity further strengthens the tie of the new basaltic achondrite discoveries to Vesta.

- (1) T. B. McCord, J. B. Adams, and T. V. Johnson, *Science* **168**, 1445 (1970).
- (2) M. J. Drake, in *Asteroids*, T. Gehrels, Ed. (Univ. of Arizona Press, Tucson, 1979), p. 765.
- (3) G. W. Wetherill, *Phil. Trans. Roy. Soc. London A* **323**, 323 (1987).
- (4) R. P. Binzel and S. Xu, *Science* (submitted).
- (5) M. J. Gaffey, *J. Geophys. Res.* **81**, 905 (1976).



456389

554-90

LPSC XXIV

113

ABS. ONLY

N94-12069

P-2

**ALKALI-GRANITOIDS AS FRAGMENTS WITHIN THE ORDINARY CHONDRITE ADZHI-BOGDO: EVIDENCE FOR HIGHLY FRACTIONATED, ALKALI-GRANITIC LIQUIDS ON ASTEROIDS.** A. Bischoff, Institut für Planetologie, Wilhelm-Klemm-Str. 10, 4400 Münster, Germany.

Adzhi-Bogdo is an ordinary chondrite regolith breccia (LL3-6; (1)) that fell October 30, 1949 in Gobi Altay, Mongolia (2). The rock consists of submm- to cm-sized fragments embedded in a fine-grained clastic matrix. The breccia contains various types of clasts, some of which must be of foreign heritage. Based on chemical compositions of olivine some components have to be classified as L-type. Components of the breccia include chondrules, impact melts (some are K-rich, similar to those found in other LL-chondrites (3,4)), highly recrystallized rock fragments ("granulites"), pyroxene-rich fragments with achondritic textures, and alkali-granitoid fragments that mainly consist of K-feldspar and quartz or tridymite. Probably, this is the first report on granitoids from asteroids. It can be ruled out that these fragments represent huge rock assemblages of the parent body like granites do on Earth. Therefore, to avoid misunderstandings, these rocks will be designated as granitoids.

In one thin section four granitoids were observed (compare Fig. 1). The main phases within these clasts are K-feldspar ( $Or \approx 95$ ) and  $SiO_2$ -phases (tridymite, quartz). Minor phases include albite, Cl-apatite, whitlockite, ilmenite, zircon, Ca-poor pyroxene ( $Fs_{66-83}$ ), and an unidentified Na,Ti-bearing silicate. In Table 1 the modal compositions of the fragments are given. Based on chemical composition and on optical properties quartz appears to be the  $SiO_2$ -phase in two fragments, whereas tridymite seems to occur in the other two. The calculated formula of the unknown Na,Ti-rich silicate is very close to  $(Na,Ca)_{2.7}(Fe,Mg)_6Ti_{1.3}Si_7O_{24}$ . Quartz and K-feldspar can reach sizes of up to  $700 \mu m$  (Fig. 1). Thus, the fragments can be described as coarse-grained (by chondritic standards). This is especially the case considering that quartz and K-feldspar are very rare minerals in ordinary chondrites. Representative analyses of minerals from some granitoid clasts are given in Table 2. Based on the mineral compositions and the modal abundances (Table 1) the bulk compositions were calculated. Except for the ilmenite-rich fragment (B) the other three have similar bulk compositions.  $SiO_2$ - (72-79 wt%),  $Al_2O_3$ - (11-14 wt%), and  $K_2O$ -contents (9-12 wt%; up to 165-times CI) are very high, whereas concentrations of FeO, MgO, and CaO are below 1 wt% in all three fragments (Table 3). The K/Na-ratio of the granitoids varies between 5.5 and 32.

Besides these granitoid rocks, pyroxene-rich fragments occur that show exsolution textures that are similar to those found in eucrites. Augite grains exsolve Ca-poor pyroxene and Ca-poor pyroxenes exsolve Ca-pyroxene lamellae. The Ca-poor pyroxenes and the Ca-rich pyroxenes have Fs-contents of about 34-50 and 25-30 mol%, respectively. Other minor phases within some of these clasts include K-feldspar, Cl-apatite, Na-rich plagioclase, an  $SiO_2$ -rich phase, chromite, troilite, and metals. Based on the occurrence of these phases, it appears that these fragments are somehow related to the granitoids; however, the Fs-contents of pyroxene are much higher in the latter. A very similar orthoclase-pyroxene fragment was found in the Vishnupur chondrite and discussed as "part of a larger foreign unit" (4).

Discussion. Based on the mineralogy the four clasts (Table 1) have to be classified as alkali-granitoids. So far, it is not clear, whether they were formed on the LL-chondrite parent body or whether they represent fragments of an achondritic projectile. They may have formed in small intrusions representing the last differentiate of a melt during large-scale melting of a parent body (achondritic parent body; compare Warren et al. (5) describing the lunar granites which also should be better classified as granitoids) or during local (partial) melting related to thermal or impact metamorphism on an ordinary chondrite parent body.

References: (1) Wlotzka F., Meteoritical Bulletin (1993), submitted; (2) Graham A.L. et al. (1985), Catalogue of Meteorites, Univ. Arizona Press, Tucson, 460 pp.; (3) Fodor R.V. and Keil K. (1978) Spec. Publ. No. 19, UNM; (4) Wlotzka F. et al. (1983), GCA 47, 743-757; (5) Warren P. et al. (1983), EPSL 64, 175-185.

PRECEDING PAGE BLANK NOT FILMED

112

## GRANITOIDS ON ASTEROIDS: A. Bischoff

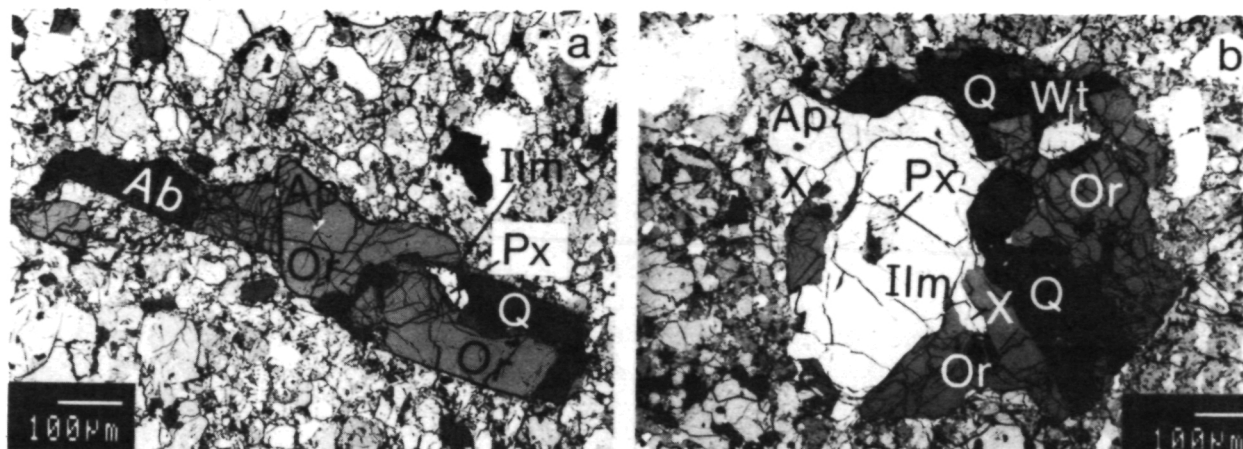


Fig. 1: Alkali-granitoids as fragments within the Adzhi-Bogdo ordinary chondrite regolith breccia; Q-Quartz; Ap-Apatite; Px-Pyroxene; Or-K-feldspar; Ilm-Ilmenite; Ab-Albite; X-unidentified Na,Ti-rich silicate; Wt-Whitlockite.

Table 1: Modal analyses of granitoids occurring as clasts in the Adzhi-Bogdo ordinary chondrite (LL) as obtained by point-counting; the unknown phase is a Na,Ti-bearing silicate (Tab. 2); all data in vol%. Fragments A and B are shown in Fig.1.

Fragment	A	B	C	D
SiO <sub>2</sub> -phase	22.9	26.0	43.7	30.0
K-feldspar	58.9	35.0	55.9	68.8
Albite	15.8	-	-	-
Pyroxene	1.3	1.6	-	-
Ilmenite	0.8	21.7	<0.1	0.1
Apatite	0.3	4.9	-	0.8
Whitlockite	-	1.6	-	-
Zircon	<0.1	<0.1	0.3	0.2
Unknown phase	-	9.2	-	-
Total	100.1	100.1	100.0	99.9

Table 3: Calculated bulk composition of granitoids in Adzhi-Bogdo based on modal composition and mineral analyses (compare Tables 1 and 2); data in wt%.

Fragm.	A	B	C	D
SiO <sub>2</sub>	72.2	53.2	78.6	72.8
TiO <sub>2</sub>	0.4	12.8	0.1	0.2
Al <sub>2</sub> O <sub>3</sub>	14.0	6.5	11.2	13.1
FeO	1.0	13.5	0.2	0.3
MnO	<0.1	0.2	<0.1	<0.1
MgO	0.1	1.0	<0.1	<0.1
CaO	0.3	3.4	<0.1	0.4
Na <sub>2</sub> O	2.0	0.9	0.6	0.4
K <sub>2</sub> O	9.8	5.8	9.2	11.3
P <sub>2</sub> O <sub>5</sub>	0.1	2.7	<0.1	0.3
Total	100.0	100.0	100.3	99.0

Table 2: Representative analyses of phases in granitoids; 1: Cl-apatite; 2: Whitlockite; 3: Quartz; 4: K-feldspar (Or<sub>96.4</sub>Ab<sub>3.5</sub>); 5: Pyroxene (Fs<sub>66.3</sub>En<sub>32.8</sub>); 6: Ilmenite; 7: Ti,Na-rich silicate; 8: Tridymite; all data in wt%; n.a.= not analyzed.

	1	2	3	4	5	6	7	8
SiO <sub>2</sub>	-	-	99.4	64.9	48.4	-	42.1	97.0
TiO <sub>2</sub>	<0.07	-	<0.04	<0.04	0.47	54.3	10.1	0.20
Al <sub>2</sub> O <sub>3</sub>	-	<0.10	-	18.4	-	-	0.26	1.53
FeO	<0.18	3.3	<0.04	0.20	38.2	43.7	35.5	<0.07
MnO	<0.05	<0.10	-	<0.01	0.76	0.95	0.24	-
MgO	-	2.0	<0.03	<0.04	10.6	2.0	3.7	<0.02
CaO	52.7	45.2	<0.01	<0.02	0.42	-	0.27	-
Na <sub>2</sub> O	0.31	3.1	-	0.39	<0.04	-	8.2	0.79
K <sub>2</sub> O	<0.10	<0.08	-	16.5	-	-	-	0.18
P <sub>2</sub> O <sub>5</sub>	41.1	45.1	n.a.	n.a.	n.a.	n.a.	n.a.	n.a.
Cl	4.9	<0.10	n.a.	n.a.	n.a.	n.a.	n.a.	n.a.
Total	99.41	99.08	99.52	100.50	98.89	100.95	100.37	99.79

**REFLECTANCE SPECTRA OF SULFATE- AND CARBONATE-BEARING  $\text{Fe}^{3+}$ -DOPED MONTMORILLONITES AS MARS SOIL ANALOGS.**

P 2

Janice L. Bishop & Carlé M. Pieters, Brown University, Providence, RI 02912;  
Roger G. Burns, Massachusetts Institute of Technology, Cambridge, MA 02139.

**Introduction.** Ferric smectites and ferrihydrite may be common alteration products of igneous lithologies on Mars,<sup>1,2</sup> and experiments involving montmorillonite enriched with  $\text{Fe}^{3+}$  support the likelihood of ferric smectites on Mars.<sup>3,4,5</sup> Mössbauer spectroscopy has been used to identify ferrihydrite [ $\text{Fe}_4(\text{O},\text{OH},\text{H}_2\text{O})_{12}$ ] as the primary ferric material in  $\text{Fe}^{3+}$ -doped montmorillonite.<sup>5</sup> Ferrihydrite is especially interesting due to its role as a precursor in the formation of hematite and goethite.<sup>6,7</sup> Reflectance spectroscopy in the visible and infrared regions are coupled with Mössbauer spectroscopy in this study to characterize the ferric material in montmorillonites containing  $\text{Fe}^{3+}$ , as well as carbonates or sulfates, in the interlayer region.

**Methods.** SWy-1 montmorillonite from the Clay Mineral Society, Source Clays Repository was converted to the  $\text{Fe}^{3+}$ -form using a  $\text{FeCl}_3$  solution.<sup>5</sup> An additional aliquot was exchanged to  $\text{Fe}^{3+}$  in a similar manner, then the solution was stirred with dry ice for 10 days in a covered vessel, resulting in a carbonate-bearing montmorillonite. A sulfate-bearing sample was prepared by adding a  $\text{Fe}_2(\text{SO}_4)_3$  solution in place of the  $\text{FeCl}_3$  solution. Samples prepared in this study were completed at pH 4-5, as opposed to former procedures involving an ion exchange resin which raised the pH to ~7.<sup>5</sup> All samples were freeze dried to form a powder and dry sieved to < 45  $\mu\text{m}$ . Visible reflectance spectra were measured with Halon as the standard on the bidirectional RELAB spectrometer at Brown University. Infrared reflectance spectra were measured under  $\text{H}_2\text{O}$ - and  $\text{CO}_2$ - purged conditions relative to a diffuse gold surface using a Nicolet 740 FTIR also at Brown University. Mössbauer spectra were measured at room temperature and at 4.2 K using cryogenic facilities at MIT.

**Results and Discussion.** Figure 1 shows reflectance spectra from 0.3 - 1.2  $\mu\text{m}$  of natural SWy montmorillonite, and our new samples containing ferrihydrite,  $\text{Fe}^{3+}$ -carbonate and  $\text{Fe}^{3+}$ -sulfate in the clay interlayer regions. Although the natural (Na/Ca) SWy has ~4 wt %  $\text{Fe}_2\text{O}_3$  in structural sites, the additional interlayer  $\text{Fe}^{3+}$  in the ferric-exchanged SWy provides significantly greater spectral evidence for ferric iron. Reflectance spectra of the Fe-enriched clay silicates in Figure 1 include a weak shoulder at ~0.45  $\mu\text{m}$ , a steep rise from 0.5  $\mu\text{m}$  to 0.75  $\mu\text{m}$  with an inflection near 0.6  $\mu\text{m}$ , a reflectance maxima at ~0.75  $\mu\text{m}$  and a broad absorption at ~0.9  $\mu\text{m}$ . Visible reflectance spectra of ferrihydrite-montmorillonite assemblages<sup>5,8</sup> compare well with telescopic data<sup>9,10</sup> and ISM data<sup>11</sup> of Mars. The  $\text{Fe}^{3+}$  electronic transitions responsible for these features have been characterized in detail.<sup>12,13</sup>

$\text{H}_2\text{O}$ - and  $\text{CO}_2$ - purged reflectance spectra from 1.8 - 4.4  $\mu\text{m}$  of natural SWy montmorillonite, and the samples containing ferrihydrite,  $\text{Fe}^{3+}$ -carbonate and  $\text{Fe}^{3+}$ -sulfate are shown in Figure 2. The spectrum of the ferric sulfate-bearing sample exhibits a stronger and broader 3  $\mu\text{m}$  absorption and also a strong shoulder at 1.95  $\mu\text{m}$ . These absorption features are probably due to interactions between the interlayer  $\text{H}_2\text{O}$  and the  $\text{SO}_4^{2-}$  ions due to the polarity of the sulfate bonds. The spectrum of the ferric carbonate-bearing sample exhibits minor differences from the spectrum of the ferrihydrite-montmorillonite in the 3  $\mu\text{m}$  region. The magnitude of the molecular water absorption from 2.9 - 3.1  $\mu\text{m}$  (3500 - 3200  $\text{cm}^{-1}$ ) is stronger and the reflectance is brighter at wavelengths greater than 3.25  $\mu\text{m}$  in the spectrum of the ferric carbonate sample.

Figure 3 shows reflectance spectra from 5 - 20  $\mu\text{m}$  of these samples. The ferric sulfate montmorillonite spectrum in Figure 3 exhibits a feature due to the  $\text{SO}_4^{2-}$  stretching vibration at 1150 - 1200  $\text{cm}^{-1}$  (~8.5  $\mu\text{m}$ ) and may contain a  $\text{SO}_4^{2-}$  bending vibration at 650 - 700  $\text{cm}^{-1}$  (~15  $\mu\text{m}$ ).<sup>14</sup>

Room temperature Mössbauer spectra for natural SWy montmorillonite and ferrihydrite montmorillonite assemblages show single quadrupole doublets.<sup>5,8</sup> The natural SWy gave only a single doublet at 4.2 K; however, the ferrihydrite montmorillonite, ferric sulfate montmorillonite and ferric carbonate montmorillonite all exhibited an additional sextet indicating magnetic ordering and are under further study. Mössbauer spectra of the ferric sulfate montmorillonite sample, however, do not indicate features characteristic of jarosite.



*Sulfates & Carbonates in Fe<sup>3+</sup>-montmorillonites; J. L. Bishop, C. M. Pieters & R. G. Burns*

Figure 1: Reflectance Spectra (0.3 – 1.2  $\mu\text{m}$ )

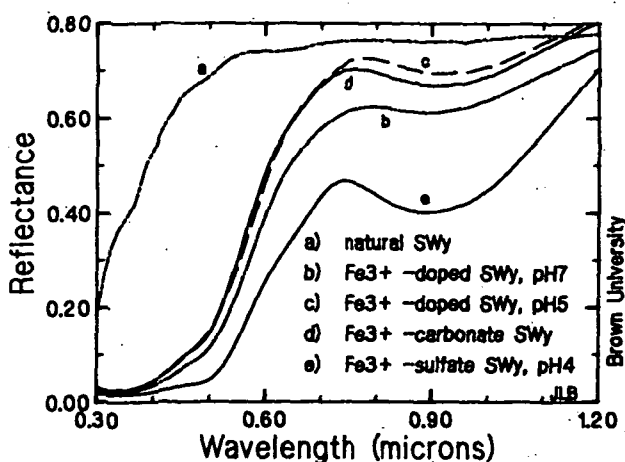


Figure 2: Reflectance Spectra (1.8 – 4.4  $\mu\text{m}$ )

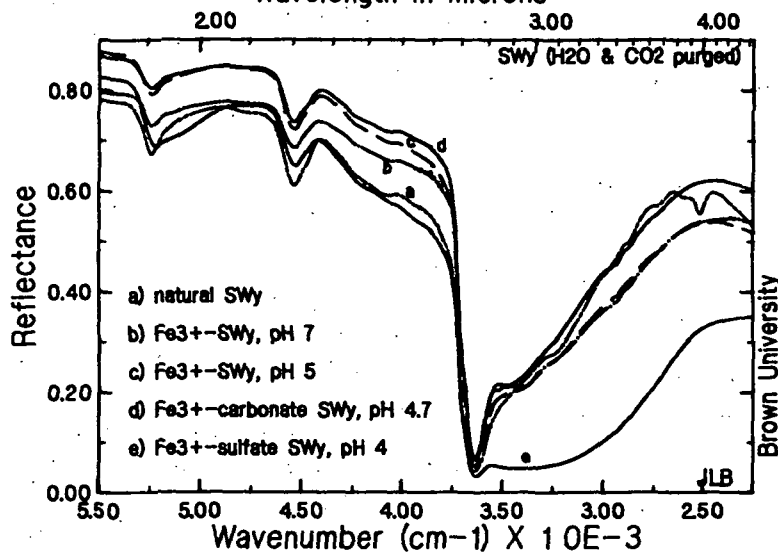
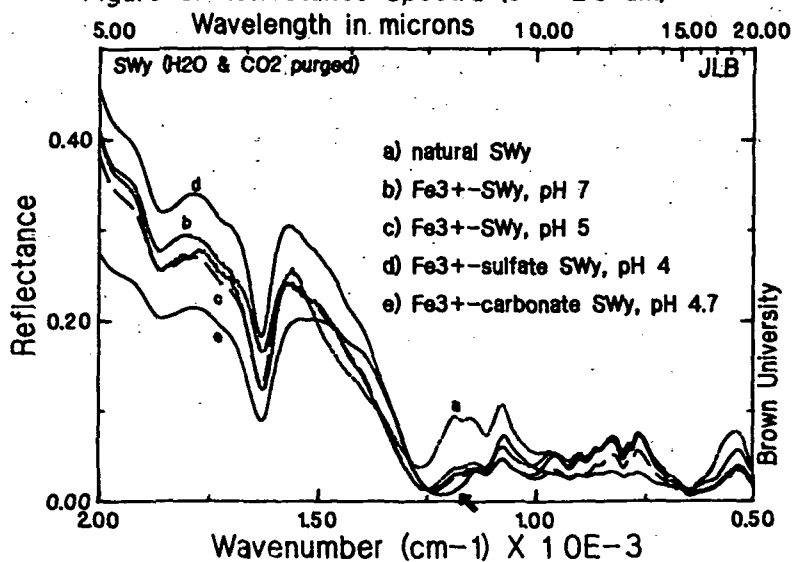


Figure 3: Reflectance Spectra (5 – 20  $\mu\text{m}$ )



**Conclusions.** The surface soils on Mars contain a silicate component, ferric iron and also smaller quantities of other elements.<sup>15</sup> We have initiated this study to explore the possibility of ferric salt formation in smectites. Our preliminary results indicate that the presence of small amounts of carbonates and sulfates formed in clay silicates do not dramatically effect the spectral features. Perhaps this will lead to new duricrust models. Continued studies are in progress to include a broader Martian geochemistry in soil analogs.

**Acknowledgements.** Support through the NASA Graduate Student Researchers Program at NASA-ARC, Moffett Field, is greatly appreciated by J. Bishop. Additional NASA support for this research under grants NAGW-28 at Brown Univ. and NAGW-2220 at MIT is also much appreciated. RELAB is a multi-user facility supported by NASA under grant NAGW-748. The Nicolet is supported under a grant from the Keck Foundation.

**References.** <sup>1</sup>Gooding, Wentworth & Zolensky (1991) *Meteoritics* 26: 135. <sup>2</sup>Treiman, Barrett & Gooding (1993) *Meteoritics*, submitted. <sup>3</sup>Banin & Rishpon (1979) *J. Molec. Evolut.* 14: 133. <sup>4</sup>Banin et al. (1988) *Origins of Life* 18: 239. <sup>5</sup>Bishop, Pieters & Burns (1993) *Geochimica et Cosmochimica Acta*, submitted. <sup>6</sup>Cornell, Giovanoli & Schindler (1987) *Clays Clay Min.* 35: 21. <sup>7</sup>Eggleton & Fitzpatrick (1988) *Clays Clay Min.* 36: 111. <sup>8</sup>Bishop, Pieters & Burns (1992) *Lunar & Planet. Sci.* XXIII: 111. <sup>9</sup>Bell, McCord & Owensby (1990) *J.G.R.* 95: 14,447. <sup>10</sup>McCord et al. (1977) *Icarus* 31: 25. <sup>11</sup>Mustard et al. (1993) *J.G.R.*, in press. <sup>12</sup>Morris et al. (1985) *J.G.R.* 90: 3126. <sup>13</sup>Sherman, Burns & Burns (1982) *J.G.R.* 87, 10169. <sup>14</sup>Nakamoto (1986) *Infrared and Raman Spectra of Inorganic & Coordination Compounds*. <sup>15</sup>Clark et al. (1977) *J.G.R.* 82: 4577.



456391

556-9N94-12071  
ABS ONLY

LPSC XXIV - 117

**THE EFFECTS OF ATMOSPHERIC PRESSURE ON INFRARED REFLECTANCE SPECTRA OF MARTIAN ANALOGS.**

163276 P. 2

Janice L. Bishop, Carlé M. Pieters, Stephen F. Pratt & William Patterson, Brown University, Providence, Rhode Island 02912.

**Introduction.** The use of terrestrial samples as analogs of Mars soils are complicated by the Martian atmosphere. Spectral features due to the Martian atmosphere can be removed from telescopic spectra of Mars<sup>1</sup> and ISM spectra of Mars,<sup>2,3</sup> but this does not account for any spectral differences resulting from atmospheric pressure or any interactions between the atmosphere and the surface. We are examining the effects of atmospheric pressure on reflectance spectra of powdered samples in the laboratory. Contrary to a previous experiment with granite,<sup>4</sup> no significant changes in albedo or the Christiansen feature were observed from 1 bar pressure down to a pressure of 8  $\mu\text{m}$  Hg. However, reducing the atmospheric pressure does have a pronounced affect on the hydration features, even for samples retained in a dry environment for years.

**Methods.** Infrared reflectance spectra were measured in these experiments using a Nicolet 740 FTIR, a biconical off-axis detection attachment produced by Specac and a new environmental chamber designed by Connecticut Instruments. This system allows spectral measurements to be made of particulate samples under a controlled atmospheric environment down to  $10^{-3}$  torr. The pressure of the sample chamber is reduced gradually over a number of hours so as not to disturb the sample. The Nicolet-environmental chamber configuration also allows spectral measurements to be made at temperatures up to 300 °C and down to -200 °C. In this preliminary study SWy-1 montmorillonite from the Clay Mineral Society-Source Clays Repository was used.

**Results and Discussion.** Normalized reflectance spectra from 5500  $\text{cm}^{-1}$  - 3000  $\text{cm}^{-1}$  (~1.8  $\mu\text{m}$  - 3.3  $\mu\text{m}$ ) of natural SWy montmorillonite at various pressures are shown in Figure 1. The shape of the reflectance features at 3  $\mu\text{m}$  and 1.9  $\mu\text{m}$  were substantially altered by changes in atmospheric pressure, while the reflectance features at 2.75  $\mu\text{m}$  and 2.2  $\mu\text{m}$  remained largely unchanged. As the atmosphere was removed from the sample chamber, water is desorbed from the clay interlayer regions and grain surfaces. At atmospheric pressures below 10 mm Hg the intensities of the 3  $\mu\text{m}$  and 1.9  $\mu\text{m}$  water features become much weaker, while the 2.75  $\mu\text{m}$  and 2.2  $\mu\text{m}$  structural OH features remain strong.

Reflectance spectra from 1800  $\text{cm}^{-1}$  - 1575  $\text{cm}^{-1}$  (5.55  $\mu\text{m}$  - 6.35  $\mu\text{m}$ ) of natural SWy montmorillonite at various pressures are shown in Figure 2. The absorption feature shown in these spectra is due to the bending vibrations of molecular H<sub>2</sub>O in the interlayer clay regions.<sup>5</sup> This feature is observed at about 1635  $\text{cm}^{-1}$  (~6.12  $\mu\text{m}$ ) under the normal H<sub>2</sub>O- and CO<sub>2</sub>-purged conditions at 1 bar in the Nicolet. After reducing the atmospheric pressure in the sample chamber below 10 mm Hg this absorption feature shifts gradually to longer wavelengths. The vibrational energies of the interlayer water molecules are dependent on the type of interlayer cation, the nature of bonding to the clay surface and the degree of H-bonding between other H<sub>2</sub>O molecules. The absorption feature at 1625  $\text{cm}^{-1}$  (~6.15  $\mu\text{m}$ ) in spectra measured under low pressures probably is related to water molecules directly bound to the interlayer cations. At higher pressures there is more water adsorbed in the clay interlayer regions and additional absorptions occur (at shorter wavelengths) due to water bound either to other water molecules or the clay surfaces.

The Christiansen feature in reflectance spectra of montmorillonites occurs near 8  $\mu\text{m}$ .<sup>6</sup> A shift in the Christiansen feature to shorter wavelengths was observed in the reflectance spectra of granite as a result of decreasing atmospheric pressure below ~1mm Hg.<sup>4</sup> However, in reflectance spectra of SWy montmorillonite measured here the Christiansen feature at 7.9  $\mu\text{m}$  (1265  $\text{cm}^{-1}$ ) is invariant from 1 bar to 8  $\mu\text{m}$  Hg (although not shown). Further work is needed to characterize the effect of low pressure on spectral features.

*Effects of Atmospheric Pressure on IR Reflectance Spectra; J. L. Bishop et al.*

**Conclusions.** The atmospheric environment of clay samples has a pronounced effect on their reflectance spectra. Although the sample examined here had been stored in a desiccator over Drierite for over two years, the spectra still showed a decrease in intensity of the water features indicating further water desorption from the sample at Mars-like pressures. Investigations of the spectral features due to hydration in clays<sup>7</sup> suggest the necessity of studying the atmospheric effects on Mars soils in order to more fully understand the hydration features in spectra of Mars. Reflectance spectra of Mars soil analogs such as ferric-rich smectites, ferric oxides/oxyhydroxides and palagonite are expected to exhibit spectral changes as well when measured under Mars-like pressures. Many spectral investigations of Mars analogs show greater spectral contrast than do observational spectra of Mars. Perhaps spectra of these analogs would more closely resemble Mars spectra when measured under Mars-like atmospheric pressures.

Figure 1: Near Infrared Reflectance as a Function of Pressure  
(Normalized to 1.0 @ 2.05  $\mu$ m)

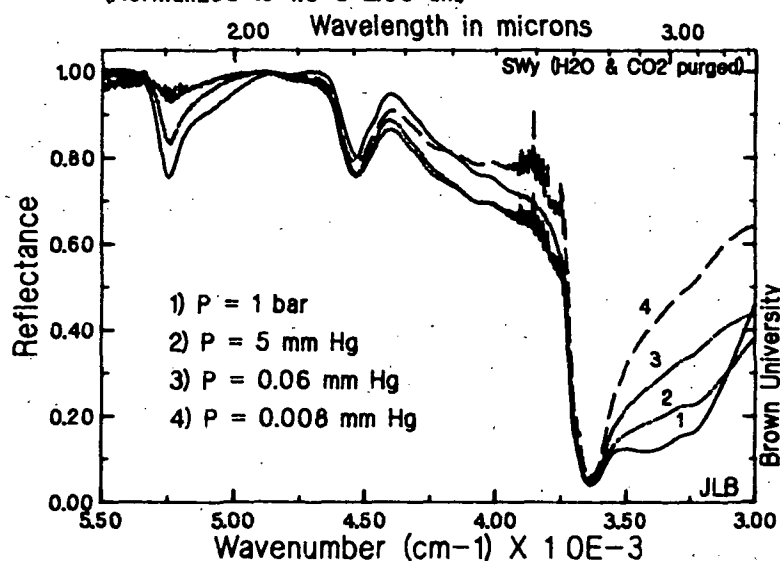
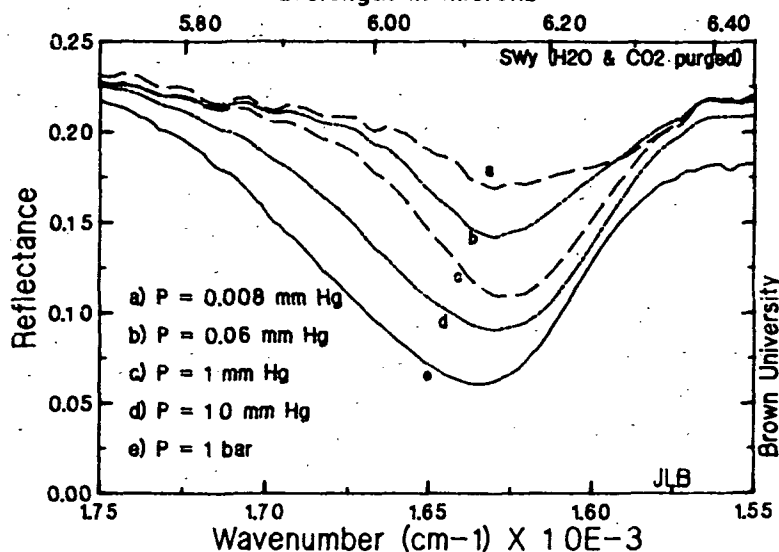


Figure 2: Reflectance Spectra as a Function of Pressure  
Wavelength in microns



**Acknowledgements.**

Support for this research through the NASA Graduate Student Researchers Program (JLB) and under grant NAGW-28 is greatly appreciated. RELAB is a multi-user facility supported by NASA under grant NAGW-748. The Nicolet is supported under a grant from the Keck Foundation.

**References.**

- <sup>1</sup>Clark, Swayze, Singer & Pollack (1990) *J.G.R.* 95: 14463.
- <sup>2</sup>Mustard et al. (1993) *J.G.R.*, in press.
- <sup>3</sup>S. Erard et al. (1991) *Proc. Lunar & Planet. Sci* 21: 437.
- <sup>4</sup>Logan, Hunt, Salisbury & Balsamo (1973) *J.G.R.* 78: 4983.
- <sup>5</sup>Farmer, ed. (1974) *The Infrared Spectra of Minerals*.
- <sup>6</sup>Salisbury, Walter, Vergo & D'Aria (1992) *Infrared (2.1 - 25  $\mu$ m) Spectra of Minerals*.
- <sup>7</sup>Bishop & Pieters (1992) *Lunar & Planet Sci*, XXIII: 109.

45693

557-46  
ABS-LOWPSC XXIV  
N 94-12072 119

STABLE ISOTOPE ANALYSES OF THE PERALKALINE VOLCANICS GREGORY RIFT VALLEY, KENYA. P. 2

S.Black\*<sup>1</sup>, R Macdonald\*<sup>1</sup>, A.E.Fallick,\*<sup>2</sup> and M. Kelly\*<sup>1</sup>.

\*<sup>1</sup> Environmental Science Division, Lancaster University, Lancaster, LA1 4YQ, UK.

\*<sup>2</sup> SURRC, East Kilbride, Glasgow, G75 0QU, UK

$\delta^{18}\text{O}$  analyses of the Naivasha rhyolites, basalts, Menengai trachytes and the Yatta phonolite are presented together with D/H analyses of the Naivasha rhyolites.  $\delta^{18}\text{O}$  results vary from 5.7‰ to 8.90‰ which is within the reported range of  $\delta^{18}\text{O}$  analyses for continental volcanics. Closure temperatures calculated from the basalts and rhyolites show equilibration to be at magmatic temperatures. D/H values range from -40‰ to -148‰ indicating that the rhyolites have undergone large scale degassing.

The results of the  $\delta^{18}\text{O}$  analyses of the Naivasha rhyolites can be seen in figure 1, these analyses were carried out on glass samples. The analytical precision has been estimated at better than  $\pm 0.1\text{‰}$  for the rhyolite samples due to the good quality of the volcanic glass with the yield of oxygen between 11.5-15.5  $\mu\text{mol/mg}^{-1}$ .

The results range from 6.6-8.6‰ with a mean  $\delta^{18}\text{O}$  value of  $7.11 \pm 0.53$  (n=41) with a general trend amongst the rhyolites to have increasingly heavy oxygen with the youngest magmas. The Group 1 centre displays  $\delta^{18}\text{O}$  values of 6.6-7.5 to the Ololbutot centre with  $\delta^{18}\text{O}$  values of 6.7-8.1 although considerable variation exists within each group ( $\pm 0.47$ ). Figure 2 shows the a quartz feldspar mineral separate diagram after (1). The Naivasha rhyolite data plots in the magmatic temperature window generating temperatures of  $780^\circ\text{C} \pm 120^\circ\text{C}$  which is within the field of the theoretical temperatures of comendite magmas (2) ( $800^\circ\text{C}$ ). No disequilibria has taken place in the rhyolites indicating that there has been no post eruptive alteration of the oxygen from any of the mineral phases or whole rocks.

The oxygen isotope analyses of the Naivasha basalts can be seen in figure 1. The majority of the basalts have  $\delta^{18}\text{O}$  values around 6.0‰ (n=10) with the hawaiiite, SB28 and the LBS basalts displaced to higher  $\delta^{18}\text{O}$  values of 6.5-7.1‰. These values are not typical for MORB ( $5.7 \pm 0.2\text{‰}$ ) (3) but are well within the reported range of continental basalts (5-7.5‰) (3). Variation in ultramafic nodules from Africa have given  $\delta^{18}\text{O}$  values of 3-7‰ (4) indicating that the mantle may not be totally homogenous or that high temperature fractionation of  $\delta^{18}\text{O}$  may occur at depth in the mantle. The small variation observed in the Naivasha basalts and the low equilibration temperatures (5) would tend to suggest that the source was isotopically heterogeneous and had not undergone fractionation.

The oxygen isotopes analyses of the Menengai trachytes can be seen in figure 1. The mean  $\delta^{18}\text{O}$  composition of the trachytes is  $7.04 \pm 0.93\text{‰}$  (n=27) No mineral separates were analysed. All the analysed groups i.e. Leat I, Leat II and the post-caldera volcanics (6) have at least a bimodal distribution on a histogram of the  $\delta^{18}\text{O}$  compositions (figure 1). The distributions of Leat I and Leat II are very similar to the Naivasha comendites with material being recorded from 5.8-8.8‰.

Samples are shown on figure 1 from Oldoinyo Lengai natrocarbonatite volcano (7) and from the Yatta phonolite (5) for comparison with the other eruptive centres.

# STABLE ISOTOPE ANALYSES OF THE PERALKALINE VOLCANICS; S. Black *et al.*

The  $\delta^{18}\text{O}$  when plotted against the D/H analyses of the rhyolites (figure 3) gives some information concerning the water content and its origin and the behaviour from formation. The degassing of the Naivasha rhyolites has been dealt with elsewhere (8), but the data in figure 3 shows that the hydrothermal system has not interacted with the magma. The hydrothermal system is largely controlled by the meteoric water from rainfall and Lake Naivasha with little magmatic water present in the geothermal system. This is the first comprehensive study of  $\delta^{18}\text{O}$  analyses on peralkaline volcanic rocks in the Kenya Rift Valley and will provide a useful database for future study, and will provide a useful guide for other planetary rift volcanic interpretations.

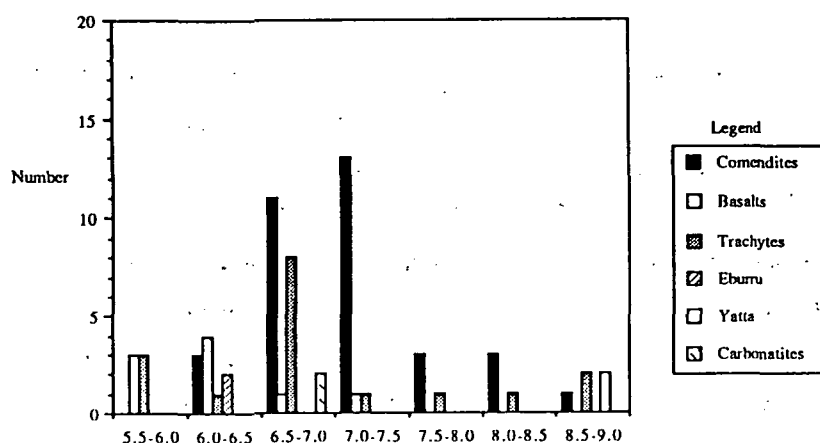


Figure 1. Histogram of the oxygen isotope analyses of the Kenya Rift peralkaline volcanic rocks.

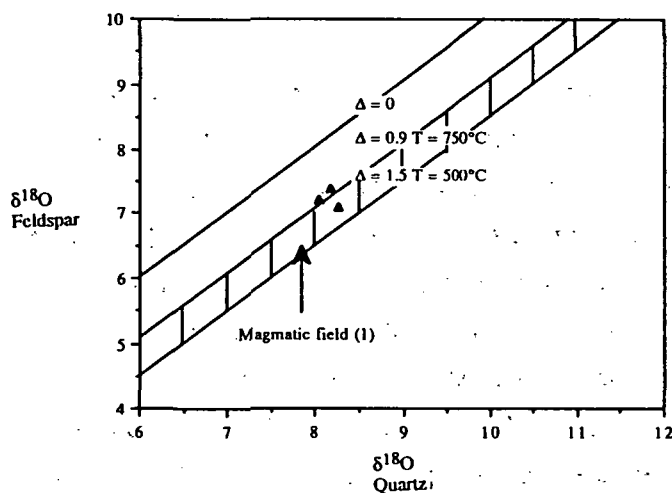


Figure 2. The oxygen results of the mineral separates from the Naivasha rhyolites. After (1).

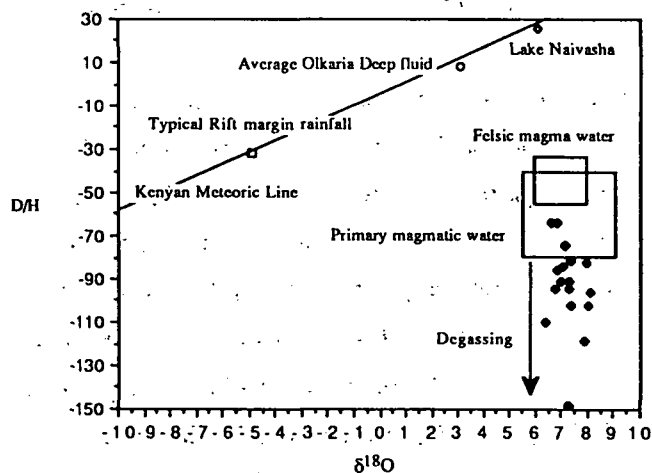


Figure 3. A diagram showing the oxygen and hydrogen isotope analyses

REFERENCES. (1) Gegory and Criss (1986), *Min. Soc. Am.* V16, 91. (2) Bailey and Macdonald (1970), *Contr. Min. Pet.* 28, 340, (3) Taylor and Sheppard (1986), *Min. Soc. Am.* V16, 227. (4) Kyser (1986) *Min. Soc. Am.* V16, 141 (5) Black PhD Univ. Lancaster (6) Black *et al.* (in prep) (7) Dawson *et al.* (in press) (8) Wilding and Macdonald *Contr. Min. Pet.* (in press)

456396

358-46  
ABS ONLY

LPSC XXIV

121

N 94-132083

p. 2

**<sup>230</sup>Th-<sup>238</sup>U SERIES DISEQUILIBRIUM OF THE OLKARIA BASALTS GREGORY RIFT VALLEY, KENYA.**

S.Black, R Macdonald and M Kelly. Environmental Science Division, Lancaster University, Lancaster, LA1 4YQ, UK.

U-Th disequilibrium analyses of the Naivasha basalts show a very small (<sup>238</sup>U/<sup>230</sup>Th) ratios which are lower than any previously analysed basalts. The broadly positive internal isochron trend from one sample indicates that the basalts may have source heterogeneities, this is supported by earlier work (2).

The Naivasha complex comprises a bimodal suite of basalts and rhyolites. The basalts are divided into two stratigraphic groups each of a transitional nature. The early basalt series (EBS) which were erupted prior to the Group 1 comendites (>20,000 years B.P.) and, the late basalt series (LBS) which erupted temporally between the Broad Acres and the Ololbutot centres (9180-3280 years B.P.) (1).

The basalts represent a very small percentage of the overall eruptive volume of material at Naivasha (< 2%). The analysed samples come from four stratigraphic units in close proximity around Ndabibi, Hell's Gate and Akira areas (appendix 5A). The earliest units occur as vesicular flows (Plb<sup>1</sup>, (2) from the Ndabibi plain. These basalts are olivine-plagioclase phyric with the associated hawaiites being sparsely plagioclase phyric. An absolute age of 0.5Ma was estimated for these basalts (3). The next youngest basalts flows (Plb<sup>2</sup>, (2)) occur as younger tuff cones in the Ndabibi area and are mainly olivine-plagioclase-clinopyroxene phyric with one purely plagioclase phyric sample. The final phase of activity at Ndabibi resulted in much younger tuff cones consisting of airfall ashes and lapilli tuffs. Many of these contain resorbed plagioclase phenocrysts with sample number 120c also being clinopyroxene phyric (2).

The isotopic evidence for the basalt formation is presented in (2) but briefly the following conclusions and data are as follows:

- i) The two basalt groups (EBS and LBS) and hawaiites have indistinguishable Sr-Nd isotope ratios of 0.70446-0.70550 and 0.51276-0.51251 respectively.
- ii) The lead isotope data in contrast distinguishes the three groups with the hawaiites and LBS having the most and least radiogenic <sup>206</sup>Pb/<sup>204</sup>Pb ratios respectively. The <sup>207</sup>Pb/<sup>204</sup>Pb ratios are more radiogenic than the majority of OIB sources.
- iii) <sup>87</sup>Sr/<sup>86</sup>Sr ratios are the more radiogenic than any of the other analysed Kenyan basalt.

U-Th disequilibrium occurs at a 2σ confidence level in 75% of the Naivasha basalts analysed, ranging from 4 to 65% excess <sup>230</sup>Th relative to <sup>238</sup>U. In light of the results presented elsewhere (4), these results are taken to indicate primary radionuclide ratios. All the basalt samples show a depleted (<sup>230</sup>Th/<sup>238</sup>U) < 1,

corresponding to K values of 0.5 to 0.7 (5), indicating that recent fractionation of uranium from thorium has occurred. Figure 1 shows a (<sup>238</sup>U/<sup>232</sup>Th)-(<sup>230</sup>Th/<sup>232</sup>Th) diagram for the Naivasha basalts with other basalt complexes shown for reference. The Naivasha basalts plot to the left of the equiline above the Naivasha comendites, and display some of the lowest (<sup>238</sup>U/<sup>230</sup>Th) ratios measured in any basalt to date.

The internal isochron for SB28 is shown in figure 2. The steep positive slope indicates that this sample indicates the presence of source heterogeneities. The thorium isotope systematics are strongly influenced by binary mixing

**$^{230}\text{Th}$ - $^{238}\text{U}$  SERIES DISEQUILIBRIUM BASALTS; S Black *et al.***

probably with the observed Kenyan basement samples. The olivine trend is given as no  $^{238}\text{U}$  analysis was successfully conducted. SB 28 is almost hawaiitic in composition and is clearly an admixture between crust and primary magma and thus gives no adequate age.

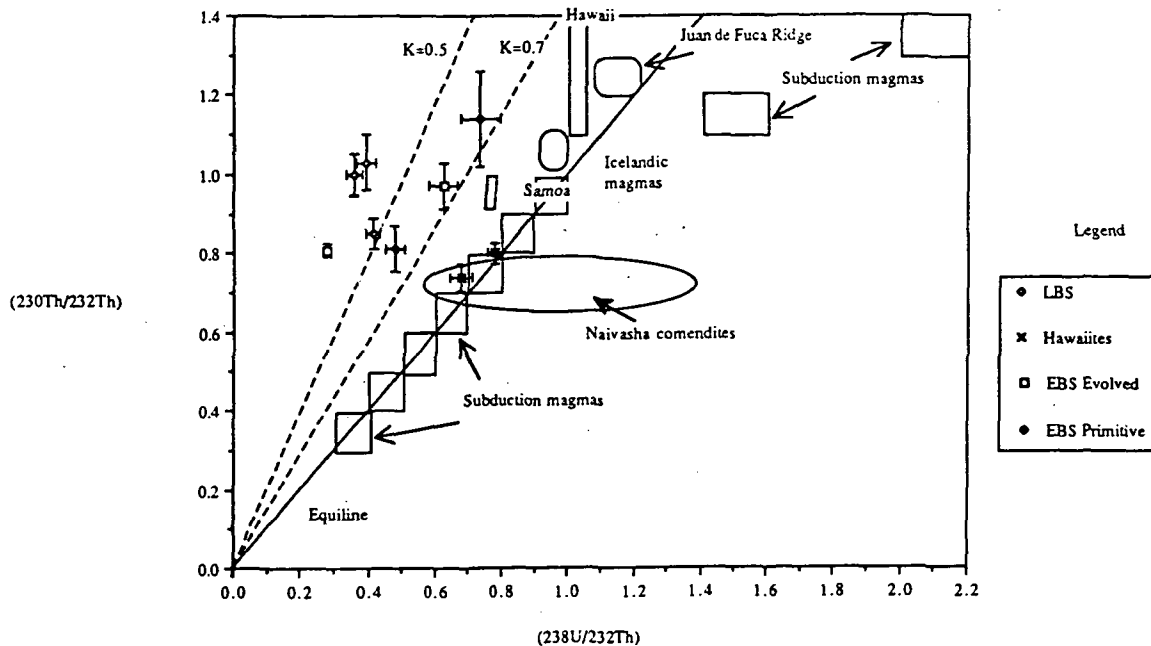


Figure 1. ( $^{238}\text{U}/^{232}\text{Th}$ )-( $^{230}\text{Th}/^{232}\text{Th}$ ) diagram for the Naivasha basalts with other data shown for reference.

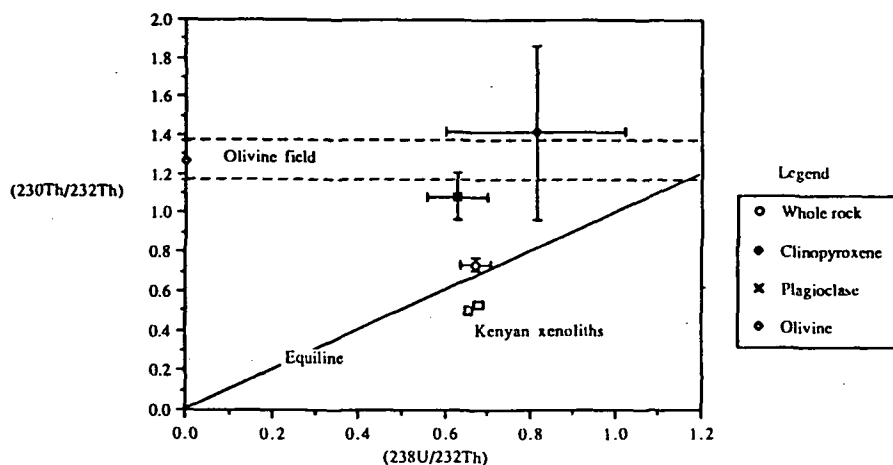


Figure 2. ( $^{238}\text{U}/^{232}\text{Th}$ )-( $^{230}\text{Th}/^{232}\text{Th}$ ) internal isochron diagram for SB28. The olivine field is shown as no U analysis was conducted on it.

REFERENCES (1) Clarke *et al.* (1990) BGS Rep. (2) Davies and Macdonald (1987) *J. Pet.* 28, 979-1008. (3) Bliss (1979) PhD Univ. Lancaster. (4) Black PhD Univ. Lancaster. (5) Condomines *et al.* (1988), *EPSL*, 90, 243-263.

456401

559-46  
ABS. ONLPSC XXIV  
94-12074  
163279-1

123

<sup>230</sup>Th-<sup>238</sup>U SERIES DISEQUILIBRIUM OF THE OLKARIA BASALTS GREGORY RIFT VALLEY, KENYA: PETROGENESIS.  
S.Black, R Macdonald and M Kelly. Environmental Science Division, Lancaster University, Lancaster, LA1 4YQ, UK.

Strong mixing trends on a (<sup>230</sup>Th/<sup>232</sup>Th) versus Th diagram show that the basalts are mixed magmas which have undergone interaction with the crust. Instantaneous Th/U ratios are less than time integrated ones but these exceed the Th/U ratios in the MORB and OIB sources. This indicates that the mantle may have undergone some metasomatic fluxing, crustal contamination of the basalts will also enhance these ratios.

Early activity on the Akira plain is represented by early basalts and hawaiites. The early basalt samples are known to predate the earliest comendites (1). The most recent phase of activity is represented by another cinder cone 40-50 m high being feldspar and clinopyroxene phyrlic. Inclusions which occur in the comendites vary in size and distribution. The largest and most porphyritic are the trachytes (up to 40 cm) with alkali feldspar phases up to 6 mm and small pyroxenes in the groundmass. The second set of inclusions are smaller (up to 10 cm) and are largely aphyric. The distribution of the inclusions are not uniform, the Broad Acres (C5) lavas contain 2-5% (1). The size of the inclusions decrease from south to north, as does the abundance of the trachytic inclusions. (1) concluded that the trachytic inclusions were derived from AFC of high TiO<sub>2</sub> hawaiitic material and isotopically variable crust with the hawaiite probably being derived from a fractionated alkali basalt.

(2) showed the basalts from both groups (EBS and LBS) to be relatively radiogenic in terms of <sup>207</sup>Pb/<sup>204</sup>Pb and <sup>87</sup>Sr/<sup>86</sup>Sr isotope ratios. Both suites exhibit trace element variations which appeared to be related to the relative amounts of Proterozoic amphibolite facies crust assimilated during magma transport. The basalts show high Sr and low Zr contents with high LREE ratios and considerable ranges in La and Yb, with all the basalts showing positive Eu anomalies (1.03-1.33). Cumulate plagioclase fractionation and alumina-rich clinopyroxene fractionation in the source region could have led to the unusual signatures in the Naivasha basalts. The mantle source region was concluded to have a "Dupal"-type isotopic and trace element signature (2)

Figure 1 shows the major element variations in the Naivasha basalts, hawaiites and magmatic inclusions. The crustal influences in the basalts can be seen in the steady rise of K<sub>2</sub>O (0.5-4.5%) with decreasing MgO (9.9-1.0%)

It is possible to use a (<sup>230</sup>Th/<sup>232</sup>Th) versus Th (figure 2) plot to further illustrate the role of mixing in the Naivasha basalts. Mixing trends will produce curved arrays whereas fractional crystallisation will produce straight horizontal vectors on figure 2. Several different mixing trends can be noted for all the basalts and magmatic inclusions.

i) The trachytic inclusions BB85-26 and 469a could be formed by AFC processes involving fractionated basaltic material (ND30) and comenditic material (002). End members of Th = 2.5ppm (<sup>230</sup>Th/<sup>232</sup>Th) = 0.82, and Th = 40ppm (<sup>230</sup>Th/<sup>232</sup>Th) = 0.775 mean that admixtures of only > 10% of rhyolitic material need be incorporated to produce the trachytic inclusions. This could explain the inclusions high <sup>87</sup>Sr/<sup>86</sup>Sr of 0.70767.

K<sub>Th</sub> and <sup>208</sup>Pb\*/<sup>206</sup>Pb\* and Th/U measured and <sup>208</sup>Pb\*/<sup>206</sup>Pb\*. Figures 3 shows the results of the above data for the Naivasha basalts with a correlation band for MORB and OIB data and other basaltic data shown for comparison taken from (3) and (4).

# $^{230}\text{Th}$ - $^{238}\text{U}$ SERIES DISEQUILIBRIUM BASALT PETROGENESIS; S Black *et al.*

The data, on figure 3 with the exception of 124, plot on a near horizontal line across the diagram indicating that the fractionation of U and Th is very recent and not the result of previous Th/U fractionations. The OIB, MORB and subduction data plot in trends with vertical components indicating older Th/U fractionations. The Naivasha basalts plot on a line corresponding to a  $^{208}\text{Pb}^*/^{206}\text{Pb}^*$  ratio of 0.972. The crustal component marked on figure 3 which was determined from the average crustal component determined from (5) which gave a  $^{208}\text{Pb}^*/^{206}\text{Pb}^*$  ratio of 0.972. The  $K_{\text{Th}}$  value of the crustal component is taken to be similar to the Kenyan xenoliths analysed during this study. Crustal contamination of a basalt with a  $K_{\text{Th}}$  of 2-3 with a crustal source of  $K_{\text{Th}}$  of 5-6 will produce elongate horizontal trends as observed in figure 3 if the  $^{208}\text{Pb}^*/^{206}\text{Pb}^*$  ratios of the basalt and contaminant are the same. This has enhanced the already existing elongate trends formed by the recent formation of the basalts.

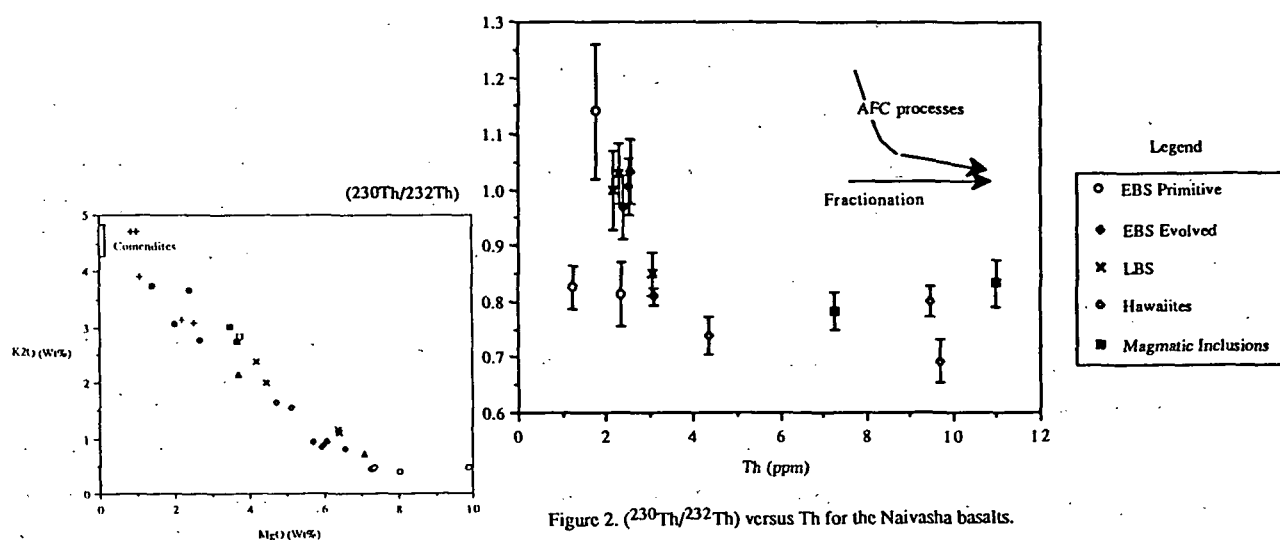


Figure 2.  $(^{230}\text{Th}/^{232}\text{Th})$  versus Th for the Naivasha basalts.

Figure 1.  $\text{MgO}$  versus  $\text{K}_2\text{O}$  for the Naivasha basalts, hawaiiites and magmatic inclusions.

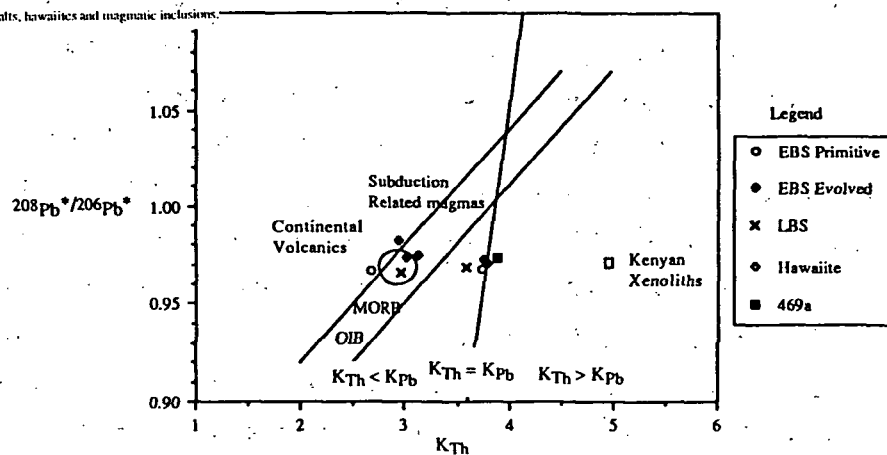


Figure 3. Th-Pb correlation showing the Naivasha basalts in relation to the MORB and other mantle sources.

- REFERENCES (1) Bone (1987) PhD Univ. Lancaster. (2) Davies and Macdonald (1987), *J. Pet.*, 1009-1031. (3) McDermott and Hawkesworth (1991), *EPSL*, 104, 1-15. (4) Gill and Williams (1990), *Geochim. Cosmochim. Acta*, 54, 1227-1442. (5) Macdonald *et al.* (1987), *J. Pet.*, 28, 979-1008.



456402

560-46

LPSC XXIV

125

RRS ONLY

N94-12075

<sup>230</sup>Th-<sup>238</sup>U SERIES DISEQUILIBRIUM OF THE OLKARIA RHYOLITES GREGORY  
RIFT VALLEY, KENYA: PETROGENESIS.

S.Black, R Macdonald and M Kelly.

Environmental Science Division, Lancaster University, Lancaster, LA1 4YQ, UK.

Positive correlations of (<sup>238</sup>U/<sup>230</sup>Th) versus Th show the rhyolites to be products of partial melting. Positive correlations of U and Cl and U and F show that the U enrichment in the rhyolites is associated with the halogen contents which may be related to the minor phenocryst phase fractionation. Instantaneous Th/U ratios exceed time-integrated Th/U ratios providing further evidence of the hydrous nature of the Olkaria rhyolite source.

Excess (<sup>238</sup>U/<sup>230</sup>Th) in the subduction related rocks has been associated to the preferential incorporation of uranium in slab derived fluids, but no evaluation of the size of this flux has been made. The majority of the Naivasha samples show a (<sup>238</sup>U/<sup>230</sup>Th) > 1 (figure 1) and plot close to the subduction related samples indicating the Naivasha rhyolites may also have been influenced by fluids during their formation as speculated by (1). In general samples with high (<sup>238</sup>U/<sup>230</sup>Th) ratios reflecting recent enrichment of uranium relative to thorium have high thorium contents, thereby the high (<sup>238</sup>U/<sup>230</sup>Th) ratios are restricted to the most incompatible element enriched magmas (figure 1) and, hence, are a good indication that the rhyolites were formed by partial melting.

If a fluid phase had some influence on the formation of the rhyolites then the uranium and thorium may have some correlation with F and Cl contents which can be mirrored by the peralkalinity. Figure 2 shows the plots of uranium against F and Cl contents. The positive correlation indicates that the uranium enrichments are associated with the halogen contents. There seems to be a greater correlation for U against Cl than F indicating that the U may be transported preferentially as Cl complexes.

If U was added preferentially to the source of the comendites recently (< 300,000 years B.P.) this may result in (<sup>238</sup>U/<sup>230</sup>Th) ratios > 1. Uranium and thorium are known to be mobile in the presence of fluids and since uranium is enriched it would suggest that uranium is more mobile, particularly in the presence of CO<sub>2</sub>-rich fluids (2, 3, 4, 5, 6, 7, 8). U could reach the magmas in two main ways;

- i) The U-rich fluid could flux the crust and increase the percentage of melting, and thus produce (<sup>238</sup>U/<sup>230</sup>Th) ratios > 1 in the magma.
- ii) The U-rich fluid could react to form secondary minerals in the source region resulting in subsolidus metasomatism thereby increasing the (<sup>238</sup>U/<sup>230</sup>Th) ratios. The time between metasomatism and partial melting will be reflected in the (<sup>230</sup>Th/<sup>232</sup>Th), i.e. the longer the time the higher the resulting (<sup>230</sup>Th/<sup>232</sup>Th) will be from ingrowth of (<sup>230</sup>Th) from (<sup>238</sup>U).

Figure 3 shows a <sup>208</sup>Pb\*/<sup>206</sup>Pb\* versus K<sub>Th</sub> plot showing a time integrated plot of the Th/U ratios. The <sup>208</sup>Pb\*/<sup>206</sup>Pb\* ratios are used to infer old Th/U ratios, and are the ratios of <sup>208</sup>Pb to <sup>206</sup>Pb since 4.55Gy. These are calculated by subtracting the primordial lead (derived from the Canyon Diablo meteorite), from the determined ratios. The K<sub>Th</sub> factor (7) is equal to 3.034/(<sup>230</sup>Th/<sup>232</sup>Th) and represents recent Th/U modifications, whereas the Pb isotopes will only respond slowly to modifications in Th/U ratios and will represent older fractionation events.

# $^{230}\text{Th}$ - $^{238}\text{U}$ SERIES DISEQUILIBRIUM PETROGENESIS; S Black *et al.*

Thus horizontal vectors on figure 3 are an indication of recent fractionation, and vertical components are older enrichments. (9) demonstrated that some of the subduction related volcanism was formed from older enrichments, some of their data is displayed on figure 3 for comparison. The broad horizontal lying trend defined by the Naivasha rhyolite data suggests that the Th/U fractionation has been recent. The solid black line in figure 4 is the locus of points whose time integrated and instantaneous Th/U ratios are equal, and is the geochron for 4.55Gy. Points to the right of this line have instantaneous Th/U ratios higher than their time integrated ratios indicating that hydrous metasomatism has taken place beneath this part of the sub-continental lithosphere.

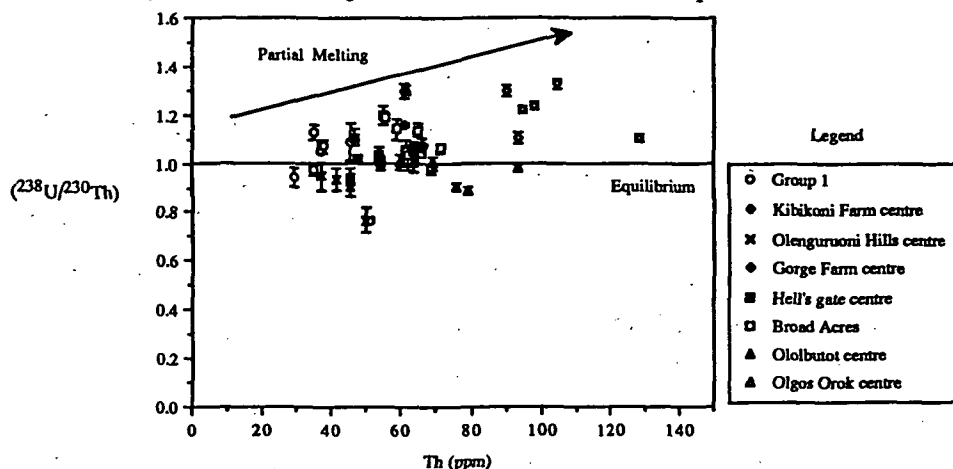


Figure 1.  $(^{238}\text{U}/^{230}\text{Th})$  versus Th for the Naivasha comendites.

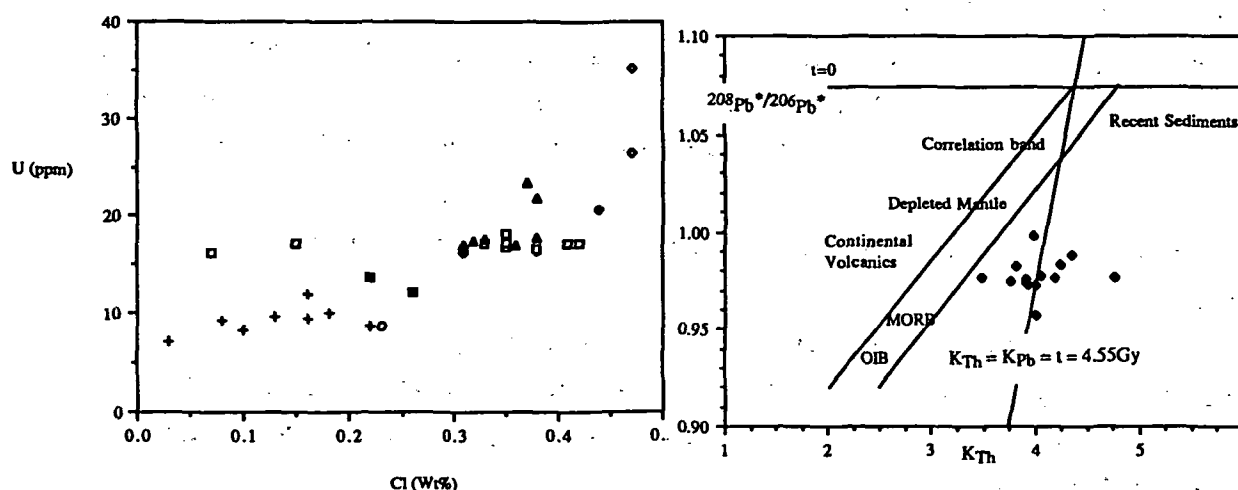


Figure 2. U versus Cl for the Naivasha comendites.

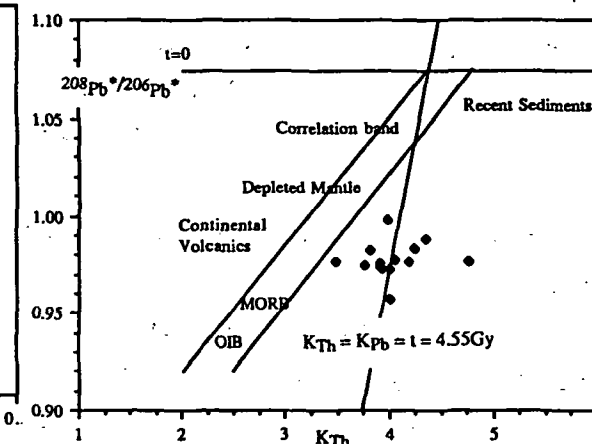


Figure 3. Th-Pb correlation showing the Naivasha rhyolites. Most of the data plots either close to or to the right of the geochron.

REFERENCES (1) Macdonald *et al.* (1987) *J. Pet.*, 28, 979-1008. (2) Williams *et al.* (1986) *Geochim. Cosmochim. Acta*, 50, 1249-1259. (3) Vanlerherberge *et al.* (1989) *Terra Cognita*, 7, 367. (4) Condomines *et al.* (1988) *EPSL*, 90, 243-263. (5) Pyle (1990) PhD. Univ Cambridge (6) Pyle *et al.* (1991) *EPSL*, 105, 378-396 (7) Gill and Williams (1990) *Geochim. Cosmochim. Acta*, 54, 1427-1442. (8) Williams *et al.* (1992), In Ivanovich and Harmon (1992). (9) McDermott and Hawkesworth (1990) *EPSL*, 105, 1-15.

456403  
561-46  
ABS ONLY  
N 94-1632812076  
R-2

**<sup>230</sup>Th-<sup>238</sup>U SERIES DISEQUILIBRIUM OF THE OLKARIA RHYOLITES GREGORY RIFT VALLEY, KENYA: RESIDENCE TIMES.**  
S.Black, R Macdonald and M Kelly. Environmental Science Division, Lancaster University,  
Lancaster, LA1 4YQ, UK.

67% of the rhyolites analysed show U-Th disequilibrium, ranging from 27% excess thorium to 36% excess uranium. Internal and whole rock isochrons give crystallisation/formation ages between 65 ka and 9 ka, in every case these are substantially older than the eruptive dates. The residence times of the rhyolites (U-Th age minus the eruption date) have decreased almost linearly with time, from 45 ka to 7 ka, suggesting a possible increase of activity within the system related to increased basaltic input. The long residence times are mirrored by large <sup>222</sup>Rn fluxes from the centres which cannot be explained by larger U contents.

The area west and south of Lake Naivasha, Kenya is occupied by a multicentred volcanic field, some 240 km<sup>2</sup> in extent. There are at least eighty small volcanic centres in the GOVC. Most occur either as steep sided domes or form lavas and/or pyroclastic deposits, usually of rather restricted lateral extent. Domes range from features less than 500 m in basal diameter and less than 50 m high to prominent features 340 m in height and 2 km in basal diameter. Distinct topographic features are formed by groups of coalescing domes and lava flows, such as the Olenguruoni Hills, Kibikoni, Gorge Farm and Broad Acres. These are informally referred to here as centres, e.g. the Gorge Farm centre (1, 2, 3)

The earliest activity is represented by Group 1, and was concentrated to the west of Lake Naivasha. However, domes around Orgaria have the same composition and are taken to be time-equivalent. The next phase was the eruptions at Kibikoni and Olenguruoni, which were broadly synchronous. Possibly overlapping those eruptions, but mainly later than them, was the activity at the Gorge Farm centre, which, in turn, was post-dated by emplacement of the Broad Acres and Hell's Gate Groups. The most recent activity has been that of the Ololbutot area (4)

The rhyolites are extremely high in F ( $\leq 1.3\%$ ) and Cl ( $\leq 0.5\%$ ). Recent work (5) has shown that the pre-eruptive H<sub>2</sub>O contents of the rhyolites are also high up to 3%; there has apparently been both open and closed system degassing of the comendites prior to eruption (5).

U-series disequilibrium analyses have been conducted on samples from all the rhyolite centres with ages being available for all but one centre using both internal and whole rock isochrons. The eruptive age of any Olkaria comendite is known to better than a few thousand years and, in some cases, to better than a few hundred years (4). This allows us to assess the significance of U-Th series disequilibria dates for those rocks. If internal isochrons give ages that can reasonably be considered to be eruptive ages, then we have a useful technique for refining the temporal evolution of the complex. If the isochrons give ages different to the eruptive ages, then some other interpretation such as crystallisation dates or formation dates of the magma is implied (6).

U-Th disequilibrium occurs at a 2 $\sigma$  confidence level in 67% of the Naivasha rhyolites, ranging from 27% excess thorium to 36% excess uranium. In light of the analytical accuracy of the results presented elsewhere (7) the disequilibria are considered to be primary.

The relationship between the U-Th age of the Naivasha rhyolites and their inferred residence time is given in figure 1. The residence time of the magma is taken to represent the age of magma formation, i.e. the U-Th age minus the

# $^{230}\text{Th}$ - $^{238}\text{U}$ SERIES DISEQUILIBRIUM; S.Black, *et al.*

eruption date. Where the exact eruption age is not available the average age for the date from the units below and above the particular centre are taken. There is a positive correlation in figure 1 with residence times of the magmas have dropped linearly from 45,000 years for the Group 1 centre to just over 7,000 years for the Ololbutot Group. The Gorge Farm centre shows a similar linear trend from several internal isochrons giving varying ages from the same centre. This indicates that the rhyolites are erupting magmas which have undergone linearly varying residence times possibly from within each centre. These relatively long residence times indicated for some centres, which are unusual for small rhyolitic bodies which have undergone a short eruptive history of only 20,000 years, and is the first quantitative recording in a continental setting using U-Th disequilibria.

The long residence time for some of the magmas at Naivasha is also suggested by data from (4). Figure 2 shows the  $^{222}\text{Rn}$  and  $\text{CO}_2$  data from the Olkaria complex and Longonot from soil gas measurements. The Naivasha complex has higher radon and  $\text{CO}_2$  fluxes than Longonot, Suswa or the Eburru complex. Although the Olkaria complex has higher uranium and thorium contents this does not sufficiently explain the two orders of magnitude difference in radon recorded by (4). No evidence exists for uranium mineralisation or increased  $^{226}\text{Ra}$  activity in the ground water to sufficiently explain the  $^{222}\text{Rn}$  excess (4). The eruption age of the Longonot effusives is very similar to the Olkaria complex (figure 3) and one possible reason for this increased flux is a longer residence time for the magma. The Suswa and Eburru volcanics exhibit  $^{238}\text{U}$  disequilibria (8) and therefore the large  $^{222}\text{Rn}$  excesses are not simply a disequilibrium phenomenon.

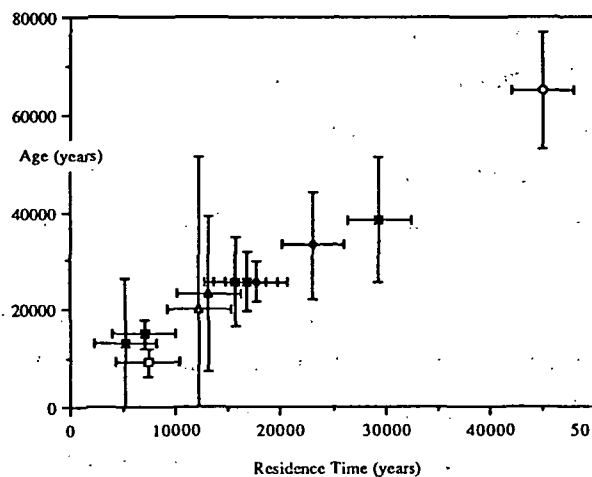


Figure 1. Plot showing residence time versus U-Th age. Note the linear decrease

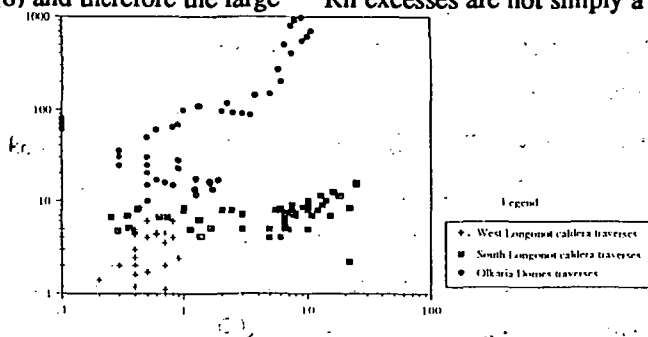


Figure 2. Plot showing Rn versus  $\text{CO}_2$  for the soil gas traverses near Naivasha. The higher Rn comes only from the rhyolite areas.

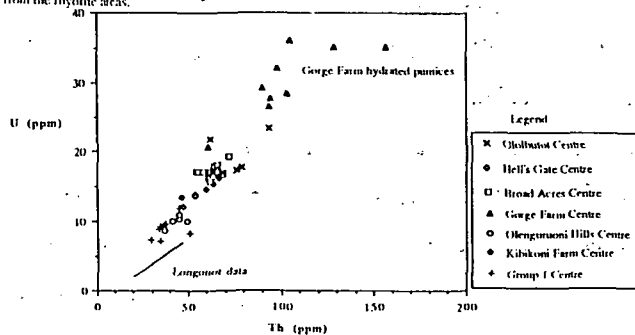


Figure 3. U versus Th plot. U and Th contents of the rhyolites are higher than the surrounding volcanics but this cannot explain the high Rn contents.

REFERENCES (1) Macdonald *et al.* (1987) *J. Pet.*, 28, 979-1008 (2) Davies and Macdonald (1987) *J. Pet.*, 28, 1009-1031 (3) Bone (1987) PhD, Univ. Lancaster. (4) Clarke *et al.* (1990) BGS Rep.. (5) Wilding *et al.* (1992) *Cont. Min. Pet.* (in press) (6) Condomines *et al.* (1988) *EPSL*, 90, 243-263 (7) Black PhD, Univ. Lancaster. (8) Black *et al.* (in prep).

456404

562-91  
ABS. ONLY

LPSC XXIV

129

N94-12077  
163282

USING HIGH SPECTRAL RESOLUTION SPECTROPHOTOMETRY TO STUDY BROAD MINERAL ABSORPTION FEATURES ON MARS; D. L. Blaney and D. Crisp, Jet Propulsion Laboratory, California Institute of Technology, MS183-501, 4800 Oak Grove Drive, Pasadena, Ca 91109.

Traditionally telescopic measurements of mineralogic absorption features have been made using relatively low to moderate ( $R=30-300$ ) spectral resolution. Mineralogic absorption features tend to be broad so high resolution spectroscopy ( $R>10,000$ ) does not provide significant additional compositional information. Low to moderate resolution spectroscopy allows an observer to obtain data over a wide wavelength range (hundreds to thousands of wavenumbers) compared to the several wavenumber intervals that are collected using high resolution spectrometers. However, spectrophotometry at high resolution has major advantages over lower resolution spectroscopy in situations that are applicable to studies of the Martian surface, i.e. at wavelengths where relatively weak surface absorption features and atmospheric gas absorption features both occur.

The nature of weak absorption features can be easily identified at wavelengths at or near regions where atmospheric absorptions also occur using high resolution spectrophotometry. At high resolution, individual atmospheric lines can be resolved removing any ambiguity about whether a feature is caused by an atmospheric gas or by a mineralogic feature. This is applicable in the 4 - 5  $\mu\text{m}$  region where there is absorption, emission, and scattering by atmospheric  $\text{CO}_2$  (4.3 and 4.8  $\mu\text{m}$ ), CO (4.6  $\mu\text{m}$ ), and water vapor ( $> 4.8 \mu\text{m}$ ).

A weak absorption feature (5-10% band depth) has been observed near 4.5  $\mu\text{m}$  and has not been reproduced in models by atmospheric gases [1,2,3]. Sulfate minerals have strong absorptions around 4.5  $\mu\text{m}$  caused by the  $2\nu_3$  overtone of the sulfate fundamental [4]. The observed feature however, does not match the measured spectra of known terrestrial sulfate minerals [1,2,3] so the identification of this feature remains tentative. Analysis of this absorption feature's band depth and shape is problematic because it lies on the wing of the 4.3  $\mu\text{m}$   $\text{CO}_2$  band. The continuum is defined not only by the albedo outside the absorption band but also by the atmosphere.

In addition to the problems encountered in the study of a mineralogic absorption feature in the wings of an atmospheric band, analysis is further complicated because the measured light includes similar contributions from reflected solar radiation and emitted thermal radiation. Thermal masking of mineralogic absorption features may occur. Even strong surface albedo features near 4.5  $\mu\text{m}$  will not produce deep spectral features because reductions in the reflected solar flux are almost completely compensated by increases in the emitted thermal flux (Kirchoff's Law) at high temperatures ( $T \sim 270 \text{ K}$ ). At slightly lower temperatures ( $T \sim 250 \text{ K}$ ), thermal emission tends to subdue surface absorption features making them more difficult to detect [2,3]. Therefore, a technique

## HIGH RES. SPECTROPHOTOMETRY OF MARS: D.L. Blaney and D. Crisp

which separates atmospheric gas absorptions from albedo changes caused by mineralogy would be useful in better understanding the optical properties of both the surface and the atmosphere.

High spectral resolution spectroscopy answers this need. Rather than covering a broad wavelength range, several limited wavelength regions are selected to address specific questions about a known absorption feature. These wavelength regions must be selected carefully using not only lower resolution spectra of the absorption feature but also detailed knowledge of the line structure of the atmospheric gases. At high resolution, individual atmospheric gas lines are resolved, eliminating doubt about whether it is a gas or mineralogic absorption. The continuum produced by surface absorption between the lines is well defined and the atmospheric gas portion of the spectra is distinct. The small windows of transparency between the lines provide direct information about the mineralogy of the absorbers. Atmospheric modeling is also easier as individual line strengths of different gases can be measured in the spectra.

**References:** [1]. Blaney, D.B. and T.B. McCord, submitted to *J. Geophys Res.* 1992. [2]. D. Crisp and D.L. Blaney, *MSATT Meeting*, Boulder, Co, Sept. 1991. [3]. Blaney, D.L., and D. Crisp, *Bulletin of the American Astronomical Society*, Vol.23, No.3, p 1183, (1991). [4]. V. Farmer (ed.) *Mineralogical Soc. of London Monograph 4*, London England, 427, 1974.

456405

563-90

LPSC XXIV

131

ABS ONLY

N94-12078

USING SOLAR FLARE TRACK DENSITIES TO DETERMINE THE ORIGIN OF INTERPLANETARY DUST PARTICLES, George E. Blanford, University of Houston-Clear Lake, Houston, TX 77058.

Sandford [1] theoretically explored the use of solar flare track densities in interplanetary dust particles (IDPs) to distinguish whether they were of cometary or asteroidal origin. He determined that there were differences in the characteristic distributions of track densities that would occur from these two possible sources. Flynn [2,3] examined the heating of IDPs on atmospheric entry and concluded that IDPs must be predominantly from asteroidal sources because these asteroidal particles would have sufficiently low velocities to survive atmospheric heating with little or no modification whereas cometary particles would ordinarily have velocities that are much higher. This paper looks at what we can learn by combining the approaches of Sandford [1] and Flynn [2,3].

Determining the buildup of tracks in an IDP follows the procedure of Sandford [1]. He used the formulas derived by Wyatt and Whipple [4] to follow the change in eccentricity and semimajor axis of a particle under the influence of radiation pressure and Poynting-Robinson drag [5]. We have modified these formulas to include solar wind drag as 30% of Poynting-Robinson drag. The modified formula for the time to go from eccentricity  $e_j$  to eccentricity  $e_{j+1}$  ( $e_j > e_{j+1}$ ) is given by

$$\tau_j = 9.58 \times 10^6 \frac{s \rho C^2}{\nu} \int_{e_{j+1}}^{e_j} \frac{e^{0.762} de}{(1 - e^2)^{3/2}}$$

where  $s$  is the radius,  $\rho$  is the density, and  $\nu$  is the absorption coefficient of the particle in cgs units. Burns et al. [6] have shown that a Mie coefficient should be used in general rather than an absorption coefficient. However, IDPs that are large enough to handle and analyze fall in a size range in which geometrical optics should apply and an absorption coefficient should be adequate. Results reported here are for  $s = 10^{-3}$  cm,  $\rho = 1$  g/cm<sup>3</sup>, and  $\nu = 1$ . The constant  $C$  is given by

$$C = a_0 e_0^{-0.881} (1 - e_0^2)$$

where  $a_0$  and  $e_0$  are the initial semimajor axis and eccentricity of the particle. The track density is then given by

$$\rho_{track} = \sum_{i,j} A \left[ \frac{\Delta p_i}{r_i^\beta} \right] \tau_j$$

where  $A$  is the track production rate at 1 AU which is assumed to follow an inverse square law from the Sun such that  $\beta = 2$ . Results reported here use a preliminary value of  $A = 6 \times 10^5$  cm<sup>-2</sup> yr<sup>-1</sup> [7]. The fraction of an orbital period  $\Delta p_i$  between  $r_i$  and  $r_{i+1}$  ( $r_i > r_{i+1}$ ) is given by

$$\Delta p_i = \frac{1}{\pi} \left\{ \sin^{-1} \left[ \frac{r - a}{ae} \right] - \frac{1}{a} \left[ a^2 e^2 - (r - a)^2 \right]^{1/2} \right\}_{r_{i+1}}^{r_i}$$

## Using Track Densities for IDP Origins: G.E. Blanford

These formulas were coded such that  $\Delta p_i$  was calculated in steps of  $r_i/100$  and time intervals were calculated for steps of  $a/100$  or  $\Delta e = 0.0001$  whichever was greater. The integration was finished when the line of nodes reached values of 1.017 AU and 0.983 AU. The geocentric velocities of the particle were also calculated at the nodal crossings.

Accumulated track densities and geocentric nodal crossing velocities were calculated for a representative set of the following groups of planetary bodies: Aten, Apollo, Amor, Hungaria, Phocaea, Cybele, and Hilda asteroids, archetypes of the Hirayama families among the first 240 catalogued asteroids, comets with  $q > 1.5$  AU  $Q < 6$  AU, and many of the comets associated with meteor streams or showers. Orbital elements were taken from [8,9,10]. Results are plotted in Fig. 1. Calculated track densities have values consistent with most experimental measurements of  $10^9$ - $10^{10}$   $\text{cm}^{-2}$  [11].

It is known that high velocity particles will volatilize in the atmosphere (eg. [2,3]). For this reason we would not expect IDPs to come significantly from Apollo, Aten, from most of the Amor asteroids, and comets responsible for meteor showers [12]. Excluding these sources we find that track densities are rather closely packed together for sources that have low velocities at nodal crossing. There are comets with low eccentricities and perihelia  $> 1.5$  AU which should contribute low velocity particles to the stratospheric dust collection. The statistical uncertainty of measuring track densities of  $\sim 10^{10}$   $\text{cm}^{-2}$  in grains of  $\sim 2.5 \times 10^{-9}$   $\text{cm}^{-2}$  will be  $\pm 2 \times 10^9$   $\text{cm}^{-2}$ . This degree of resolution would make it possible to distinguish particles derived from Amor asteroids from low eccentricity comets and Trojan asteroids. It is doubtful that we could distinguish other sources using track density measurements.

References: [1] Sandford S.A. (1986) *Icarus* 68, 377-394. [2] Flynn G.J. (1989) *Icarus* 77, 287-310. [3] Flynn G.J. (1990) *Proc. Lunar Planet. Conf.* 20th, 363-371. [4] Wyatt S.P. and Whipple F.L. (1950) *Astrophys. J.* 111, 134-141. [5] Jackson A.A. and Zook B.A. (1992) *Icarus* 97, 70-84. [6] Burns J.A. et al. (1979) *Icarus* 40, 1-48. [7] Blanford et al. (1975) *Proc. Lunar Sci. Conf.* 6th, 3557-3576. [8] Williams J.G. (1989) In *Asteroids II* (Binzel, Gehrels, Matthews eds.), 1034-1072. (UA Press). [9] *Ephemerides of the Minor Planets for 1992*. [10] Marsden B.G. (1986) *Catalogue of Cometary Orbits*, 5th ed. (IAU). [11] Thiel K. et al. (1991) *Nucl. Tracks Radiat. Meas.* 19, 109-716. [12] Sandford S.A. and Bradley J.P. (1989) *Icarus* 82, 146-166.

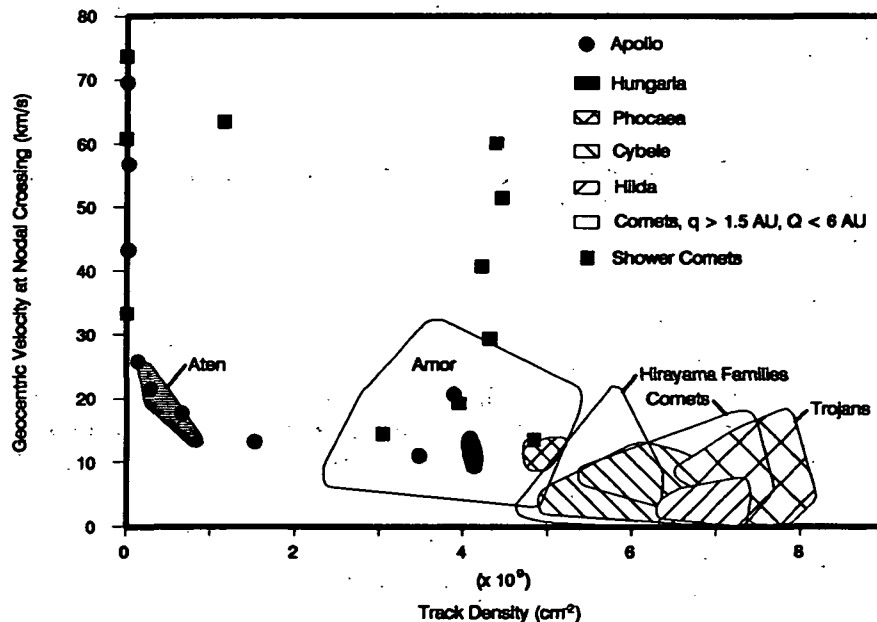


Fig. 1. Geocentric velocities at nodal crossing versus track densities in 20  $\mu\text{m}$  dust grains originating from different families of planetary bodies which have decayed by Poynting-Robinson drag. Low velocity grains have similar orbital elements which leads to similar track densities.



456406

564-81  
ABS only

LPSC XXIV

133

N 94-132079

**SPECTRAL AND MULTISPECTRAL IMAGING STUDIES OF LUNAR MANTLED MARE DEPOSITS;** D.T. Blewett, B.R. Hawke, P.G. Lucey, Planetary Geosciences/SOEST, Univ. of Hawaii, 2525 Correa Rd., Honolulu, HI 96822; J.F. Bell III, NASA-ARC, Moffet Field, CA 94035; R. Jaumann, H. Hiesinger, G. Neukum, DLR, Oberpfaffenhofen, FRG; P.D. Spudis, Lunar & Planetary Inst., Houston, TX 77058

Near-IR reflectance spectra (0.6-2.5  $\mu\text{m}$ ) and CCD images in the extended visible range (0.4-1.0  $\mu\text{m}$ ) obtained with Earth-based telescopes have been used to investigate the composition and origin of formations in the Schiller-Schickard region of the Moon. Of particular interest are the Schickard light plains, which represent an area of mantled mare basalt, or cryptomare. Here local pre-existing mare basalts were eroded and incorporated into a highlands-rich deposit by ejecta from the Orientale Basin. Spectral observations of mature and immature highland and mare surfaces, as well as dark-halo crater materials provide information on the mafic mineralogy of features in the area. Analyses of the "1  $\mu\text{m}$ " absorption band and spectral mixing models indicate that selected spots in the light plains contain on the order of 50% mare basalt. CCD image cubes can be used to map the amount of basalt in the light plains and evaluate changes with radial distance from Orientale.

**INTRODUCTION:** Lunar light plains deposits, which cover some 4-7% of the nearside [1], have been one of the most troubling features in the study of lunar geology. This flat, smooth landform often appears to have ponded in depressions and is characterized by albedo and crater densities intermediate between those of the highlands and the maria. The light plains were interpreted by early geologic mappers to be volcanic in origin, perhaps ash sheets or low viscosity silicic lavas [e.g., 2]. The Apollo 16 mission sampled the Cayley Formation, an archetypal light plains unit, and discovered non-volcanic breccias - forcing a re-interpretation of the light plains. In the time since Apollo, three major types of light plains have been recognized. First, there may be examples of true volcanic light plains. A strong case has been made [3,4,5] for an extrusive KREEP volcanic origin of the Apennine Bench Formation [6], a classic occurrence of light plains in the Imbrium Basin and near the Apollo 15 site. Second, some light plains may represent assemblages containing much impact melt. For example, the light plains unit in the interior of Orientale Basin has been interpreted to contain a relatively large proportion of impact melt [7]. The third type of light plains is believed to have been emplaced in a fluidized state as the result of the debris surge produced by the impact of basin secondary-forming projectiles. This mode of formation was responsible for the Cayley Formation in the central highlands [8] as well as the light plains in the Schiller-Schickard (SS) region [9,10].

The SS light plains represent an important subtype of the debris surge-derived light plains. Near-IR reflectance spectroscopy has demonstrated [9,10] that the dark-haloed impact craters in the SS region excavated mare basalt from beneath the higher-albedo highlands-rich plains unit deposited by the Orientale debris surge. Such mantled mare (cryptomare) are found elsewhere on the Moon and have important implications for the extent and timing of lunar basaltic volcanism [e.g., 11,12,13]. In addition, the presence of a spectrally distinct substrate (mare basalt) allows an evaluation of the local mixing process [14], i.e., the degree to which the basin ejecta erodes local material and incorporates it into the resulting deposit. Recent analyses of Earth-based telescopic spectra [15] and Galileo imagery [16,17] have provided more information on the composition and distribution of surface units in the SS region. The purpose of this report is to describe the results of our ongoing analysis of spectral data for this interesting area.

**DATA and ANALYSIS:** We have been working with two data sets for the SS region: near-IR reflectance spectra and multispectral images. The spectra (0.6-2.5  $\mu\text{m}$ ) [18] have been analyzed [15] to extract information on the "1  $\mu\text{m}$ " mafic absorption features as well as other spectral parameters. Of principal interest for determining mineralogy are the wavelength location of the reflectance minimum and the band depth. Also, mixing relationships were studied using a linear model [19]. Portions of the spectra longward of 2  $\mu\text{m}$  (thermal contamination) and in the vicinity of water bands were not included in the analysis. Additional insight into mixing systematics and endmember identification can be had through the application of principal components analysis [20].

SPECTRAL STUDY OF MANTLED MARE DEPOSITS: Blewett D.T. *et al.*

Multispectral images (12 colors between 0.4 and 1.0  $\mu\text{m}$ ) of the Moon were collected with a CCD camera using the 61 cm telescope on Mauna Kea. Information concerning data reduction and calibration can be found elsewhere [21]. The twelve images of a scene of the region surrounding Schiller and the eastern portion of Schickard crater were assembled into an image cube. The SIPS image processing software [22] was used for analysis. Potential endmembers within the image were evaluated using a spectral angle mapping technique, and least-squares linear unmixing analysis performed.

**RESULTS and DISCUSSION:** Schickard crater contains two major mare basalt patches and a light plains deposit. The composition of the local highlands material is revealed by a spectrum for a crater on the rim of Schickard. The band minimum (0.92  $\mu\text{m}$ ) and relatively shallow depth are characteristic of a noritic anorthosite. Spectra for the Schickard mare deposits as well as for dark-haloed impact craters in the region have deeper bands with minima longward of 0.97  $\mu\text{m}$ , as expected for the high-Ca pyroxene in basalt. Spectra for the Schickard light plains exhibit intermediate band minima and depths, indicating the presence of a significant component of mare basalt. Two-endmember (mare and highlands) mixing calculations for a light plains spectrum show that the proportion of basalt included is approximately 50%.

The Schiller plains, immediately to the southwest of Schiller crater, have a generally mare-like appearance on Lunar Orbiter photos, but have been mapped as "dark plains" attributed to ash fall deposition [23]. Spectra for the Schiller plains show a strong mare basalt signature; therefore we interpret the Schiller plains to be a post-Oriente mare surface contaminated with highlands debris from nearby craters. Our mixing results indicate that ~70% mare basalt is required to model a spectrum of the Schiller plains. This finding is supported by analysis of the image cube. Four endmembers (fresh mare, mature mare, fresh highlands, mature highlands) within the scene were selected. Endmember abundance images produced by the mixing model give high mare contents for the Schiller plains, with only minor contribution from highlands spectral types. This small component of highlands material is probably derived mostly from the 64 km diam. Copernican crater Zucchi, located ~250 km to the SW. Zucchi rays and secondaries are abundant on the Schiller plains.

Light plains are found on the floor of Schiller crater. A spectrum of the floor material has a band minimum of 0.93  $\mu\text{m}$ , indicative of a highlands mineral assemblage. The abundance images confirm that the floor of Schiller has a greater highlands affinity than the basalt-dominated Schiller plains. Wargent crater also has an occurrence of light plains on its floor. A dark-halo impact crater has penetrated the plains unit and exposed mare basalt [15].

This research represents one phase of our study of lunar light plains, of which the cryptomaria are a special case. Investigation of cryptomaria can provide key information on the subject of ancient mare volcanism. Additionally, the cryptomaria hold clues to a greater understanding of ballistic erosion and sedimentation processes. We have investigated a variety of mantled basalt units in the SS region. In the floor of Schickard highlands-rich basin ejecta has covered and incorporated pre-existing mare basalt. The light plains in Wargent have also mantled mare material. The Schiller plains however, are an expanse of post-Oriente mare that has undergone slight modification by impact debris from surrounding highlands craters. The light plains on the floor of Schiller crater appear to have only a minor component of mare basalt.

**References:** [1] Oberbeck V.R. *et al.* (1974) *Proc. LSC 5th*, 111. [2] Milton D.J. & Hodges C.A. (1972) U.S.G.S. Misc. Inv. Map I-748. [3] Hawke B.R. and Head J.W. (1978) *Proc. LPSC 9th*, 3285. [4] Spudis P.D. (1978) *Proc. LPSC 9th*, 3379. [5] Spudis P.D. *et al.* (1988) *Proc. LPSC 18th*, 155. [6] Hackman R.J. (1966) U.S.G.S. Misc. Inv. Map I-463. [7] Head J.W. (1974) *Moon* 11, 327. [8] Eggleton R.E. & G.G. Schaber (1972) *Ap. 16 Prelim Sci. Rept.*, 29-7. [9] Hawke B.R. & Bell Jeffrey F. (1981) *Proc. LPSC 12th*, 665. [10] Bell Jeffrey F. and B.R. Hawke (1984) *J. Geophys. Res.* 89, no. B8, 6899. [11] Schultz P.H. & Spudis P.D. (1979) *Proc. LPSC 10th*, 2899. [12] Schultz P.H. & Spudis P.D. (1983) *Nature* 302, No. 5905, 233. [13] Hawke B.R. *et al.* (1985) *Earth, Moon, Planets* 32, 257. [14] Oberbeck V.R. *et al.* (1975) *Moon* 12, 19. [15] Blewett D.T. *et al.* (1992) *LPS XXIII*, 123. [16] Belton, M.J.S. *et al.* (1992) *Science* 255, 570. [17] Mustard J.S. *et al.* (1992) *LPS XXIII*, 957. [18] McCord T.B. *et al.* (1981) *J. Geophys. Res.* 86, no. B11, 10883. [19] Singer R.B. & McCord T.B. (1979) *Proc. LPSC 10th*, 1835. [20] Smith M.O. *et al.* (1985) *Proc. LPSC 15th*, C797. [21] Neukum *et al.*

456407

565-46  
ABS. ONLY

LPSC XXIV 135

N 946 1-28080

**STRONTIUM AND OXYGEN ISOTOPE STUDY OF M-1, M-3 AND M-4  
DRILL CORE SAMPLES FROM THE MANSON IMPACT STRUCTURE, IOWA:  
COMPARISON WITH HAITIAN K-T IMPACT GLASSES.** Joel D. Blum, C. Page  
Chamberlain and Michael P. Hingston, Dept. of Earth Sciences, Dartmouth College, Hanover, NH  
03755; Christian Koeberl, Institute of Geochemistry, Univ. of Vienna, A-1010 Vienna, Austria.

Strontium and oxygen isotope analyses were performed on 8 samples from the M-1, M-3, and M-4 cores recently drilled at the Manson impact structure. The samples were three clastic sedimentary rocks (of probable Cretaceous age) which occurred as clasts within the sedimentary clast breccia, two samples of crystalline rock breccia matrix, and three samples of dolomite and limestone. The  $^{87}\text{Sr}/^{86}\text{Sr}$  (corrected to 65 Ma) ratios were much higher than those in impact glasses from the Haitian Cretaceous-Tertiary (K-T) boundary. Isotope mixing calculations demonstrate that neither the silicate or carbonate rocks analysed from the Manson crater, or mixtures of these rocks, are appropriate source materials for the Haitian impact glasses. However, the  $^{87}\text{Sr}/^{86}\text{Sr}_{(65\text{Ma})}$  ratio and  $\delta^{18}\text{O}$  value of the Ca-rich Haitian glasses are well reproduced by mixtures of Si-rich Haitian glass with platform carbonate of K-T age.

The Manson, Iowa impact structure has a diameter of 35 km, making it the largest well-preserved impact crater in the United States. Both the Manson [1] and Chicxulub, Mexico [2,3] structures have radiometric ages indistinguishable from the K-T boundary and the age of Haitian impact glasses [3,4]. Although the Manson structure is smaller than the Chicxulub structure (~180 km diameter), it may be considered at least one element in the events that led to the mass extinctions at the K-T boundary. Impact glasses from the K-T section in Haiti [4,5] have been crucial in establishing a connection with documented impact processes [5-7] and provide an opportunity to test the connection between specific impact structures and the impact glasses.

In this study 8 drill core samples from the M-1, M-3, and M-4 holes, recently drilled at the Manson impact structure, were analysed (Fig. 1). Drillhole M-1 is located at the flank of the central peak of the structure, while M-3 and M-4 are located in the terrace terrane of the structure. Details of drillhole locations, core stratigraphy and some major element analyses of these samples can be found in ref [8]. The crater is completely covered by Quaternary glacial deposits that are underlain by Cretaceous clastic sediments and flat-lying carbonate sediments of Phanerozoic age, as well as Proterozoic red clastic, metamorphic, volcanic and plutonic sequences (e.g. [9]). Core samples are referred to below by the drill hole name (i.e., M-1, M-3, M-4) followed by the depth in feet.

Three samples of Cretaceous shale (M1-186.0), silty sandstone (M1-194.1), and siltstone (M2-320.8) have  $^{87}\text{Sr}/^{86}\text{Sr}_{(65\text{Ma})}$  ratios of 0.71324–0.73161 and  $\delta^{18}\text{O}$  values of 12.4–14.3‰; two samples of glassy matrix in crystalline rock breccia (M1-359.6 and M1-475.3) have  $^{87}\text{Sr}/^{86}\text{Sr}_{(65\text{Ma})}$  ratios of 0.72244–0.72498 and  $\delta^{18}\text{O}$  values of 8.7–8.9‰; and three samples of dolomite (M4-1116.0 and M4-1200.0) and limestone (M3-274.1) have  $^{87}\text{Sr}/^{86}\text{Sr}_{(65\text{Ma})}$  ratios of 0.70803–0.71000 and  $\delta^{18}\text{O}$  values of 23.4–26.6‰. Strontium analyses by Premo [10] of the Pierre Shale in Colorado (thought to be equivalent to the shale found at Manson) yielded  $^{87}\text{Sr}/^{86}\text{Sr}_{(65\text{Ma})}$  ratios of 0.71004–0.72520. Analyses of Si-rich impact glass from the K-T boundary in Haiti yield  $^{87}\text{Sr}/^{86}\text{Sr}_{(65\text{Ma})}$  ratios of 0.70820–0.70878 [5,11] and  $\delta^{18}\text{O}$  values of 6.2–9.0‰ [5,12] whereas analyses of Ca-rich impact glass from the K-T boundary in Haiti yield a  $^{87}\text{Sr}/^{86}\text{Sr}_{(65\text{Ma})}$  ratio of 0.70796 [5] and  $\delta^{18}\text{O}$  values of 13.1–14.5‰ [5,12]. A single analysis of Si-rich melt rock from the Chicxulub structure yielded  $^{87}\text{Sr}/^{86}\text{Sr}_{(65\text{Ma})}$  ratios of 0.70837 [13] and a similar Si-rich melt rock from Chicxulub analyzed by us yielded a  $\delta^{18}\text{O}$  value of 8.2‰.

In a previous study [12] we suggested that the variation in  $\delta^{18}\text{O}$  and major element composition of the Ca-rich (yellow) Haitian glasses could be readily explained by a mixture of 58% of the most Si-rich (black) glass with 42% platform carbonate to produce the most Ca-rich impact glasses. Although we were able to show that the impact glasses were mixtures of siliceous rocks with carbonates we were unable to differentiate between the Manson and Chicxulub structures as both have appropriate combinations of the two target lithologies [12,17]. With the additional data presented here we suggest that the Manson structure is not likely to be the source of either the Si-rich or Ca-rich Haitian K-T glasses.

## ISOTOPIC STUDY OF MANSON CORES: Blum J.D. et al.

On Fig. 1 we have plotted  $^{87}\text{Sr}/^{86}\text{Sr}(65\text{Ma}) - \delta^{18}\text{O}$  mixing hyperbolas for several relevant endmember compositions. Curve A was calculated using average values for Si-rich clastic rocks and carbonates from Manson as endmembers. Curve B was calculated using average values of glassy matrix and carbonate from Manson as endmembers. Curve C was calculated by starting with average values for the Si-rich Haitian impact glasses as one endmember, considering the Ca-rich glass as a 58% mixture of the first endmember and 42% mixture of an unknown Ca-rich endmember (following ref [12]), and then calculating the values for the hypothetical Ca-rich endmember. The figure inset shows curve C at an expanded scale along with the estimated value for marine carbonates at 65 Ma [14, 15] which is close to our calculated carbonate endmember.

Several conclusions can be drawn from the data and mixing calculations. First, neither the Si-rich or Ca-rich rocks analyzed from the Manson drillholes are plausible source rocks for the Haitian K-T glasses. Second, the glassy matrix from the crystalline rock breccia in hole M-1 is isotopically distinct from the analyzed clastic rocks supporting the hypothesis that the glassy matrix formed from the Proterozoic crystalline basement. And third, although more data are needed to be conclusive, the isotopic composition of Haitian K-T glasses are consistent with a mixture of melt rock from the Chicxulub crater with marine carbonate of K-T age—strengthening the link [2,3,13,16,17] between the Chicxulub impact structure and the Haitian K-T impact glasses.

**ACKNOWLEDGEMENTS:** We are grateful to the U. S. Geological Survey and the Iowa Geological Survey Bureau for core samples, and to R. Anderson and J. Hartung for logistical support and discussions. This work is supported by the NSF (to JDB and CPC), the Sloan Foundation (to JDB) and the Austrian FWF Proj. No. P8794-GEO (to CK).

**REFERENCES:** [1] Kunk MJ, et al. (1989) *Science* 244, 1565-1568. [2] Sharpton VL, et al. (1992) *Nature* 359, 819-821. [3] Swisher CC, et al. (1992) *Science* 257, 954-958. [4] Izett GA, et al. (1991) *Science* 252, 1539-1542. [5] Sigurdsson H, et al. (1991) *Nature* 353, 839-842. [6] Koeberl C and Sigurdsson H (1992) *GCA* 56, 2113-2129. [7] Koeberl C (1992) *GCA* 56, 4329-4332. [8] Koeberl C, et al. (1993) LPSC XXIV (this issue). [9] Hartung JB, et al (1990) *GSA Spec. Pap.* 247, 207-221. [10] Premo WR (1992) LPSC XXII, 1099-1100. [11] Premo WR and Izett GA (1992) *Meteoritics* 27, 413-423. [12] Blum JD and Chamberlain CP (1992) *Science* 257, 1104-1107. [13] Hildebrand A, et al. (1991) *Geology* 19, 867-871. [14] Burke WH, et al. (1982) *Geology* 10, 516-519. [15] O'Neil JR and Clayton RN (1964) in *Isotopic and Cosmic Chemistry* (North-Holland, Amsterdam), 157-168. [16] Kring DA and Boynton WV (1992) *Nature* 358, 141-144. [17] Koeberl C (1993) *Geology* 21 (in press).

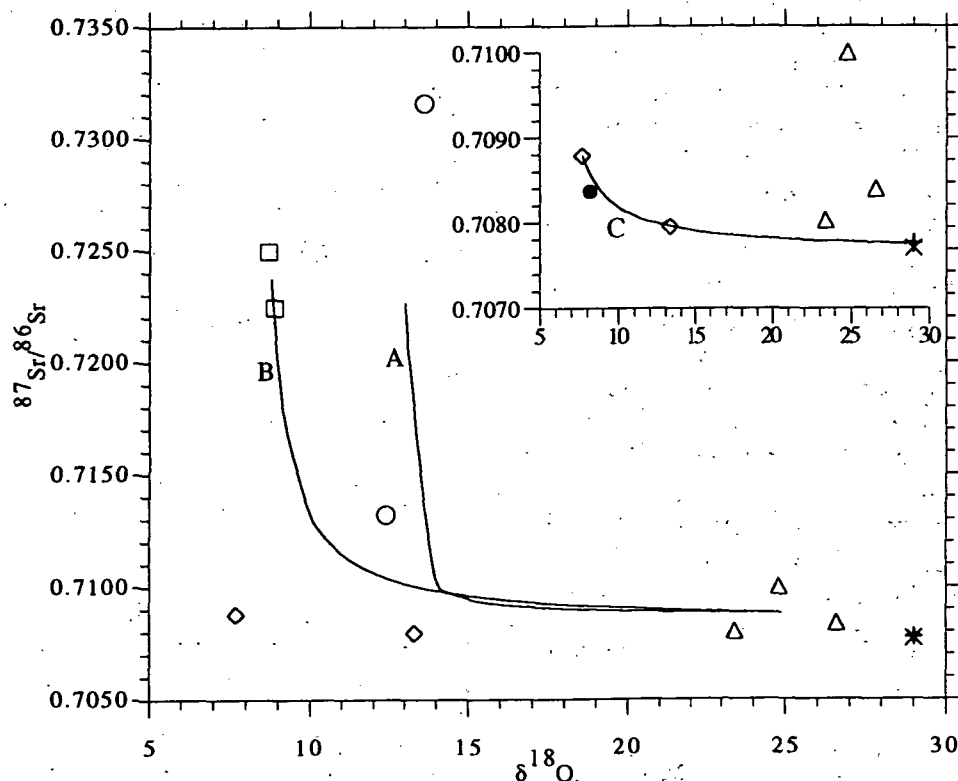


Fig. 1: Plot of  $^{87}\text{Sr}/^{86}\text{Sr}(65\text{Ma})$  versus  $\delta^{18}\text{O}$  for clastic sedimentary rocks (circles), glassy matrix (squares) and carbonates (triangles) from Manson core samples. Also included are Haitian impact glasses (diamonds), a calculated hypothetical platform carbonate endmember (plus sign), an estimated K-T age carbonate (X) and a value for meltrock from Chicxulub (solid circle). Curves A, B and C are mixing hyperbolas between average compositions of several rock types. Inset shows impact glasses and carbonates at expanded scale. See text for references, sample descriptions and discussion of figure.

456408

566-46  
ABSON 47

LPSC XXIV

137

N 94-12081

**PRELIMINARY RESULTS OF MN PARTITIONING EXPERIMENTS ON MURCHISON ANALOGUES;** Joseph S. BOESENBERG and Jeremy S. DELANEY; Dept Geological Sciences, Rutgers University, New Brunswick, NJ 08903

**INTRODUCTION:** Eucrites, howardites, and diogenites have Fe/Mn ratios between 30 and 45, while carbonaceous chondrites have much higher values between 90 and 150. [1] first showed that basaltic achondrites could evolve from a precursor chondritic material through simple partial melting. These experiments indicated that chondritic material heated to temperatures near 1180 °C with a fugacity of one log unit below the iron-wüstite buffer curve, produced a eucritic mineralogy that contained olivine, pigeonite, plagioclase, spinel, glass, and metal. The partial melting experiments of [2] on anhydrous Murchison and Allende also showed that HED compositions were produceable at temperatures between 1130 °C and 1325 °C with fugacities below and above the iron-wüstite buffer curve. However, the MnO abundances of [2] were too low to produce suitable Fe/Mn ratios for HEDs. We present below our results of partial melting experiments on Murchison analogues that involved temperatures between 1180 °C and 1580 °C and fugacities below the iron-wüstite buffer curve. Our experiments resulted in MnO abundances nearly twice that of [2] and indicate that the production of basaltic achondrite-like Fe/Mn ratios from precursor chondritic material are possible.

**METHODS:** To determine whether the initial FeO and MnO abundances within carbonaceous chondrites needed modification by some MnO enrichment process prior to melting to produce eucritic ratios, four analogues with varying Fe/Mn ratios were prepared from oxides. Compositions with initial Fe/Mn ratios of 140 (actual Murchison ratio), 100, 60, and 20 were used. The ratios, based on analyses by [3], were calculated with respect to the total iron within Murchison, not just the bulk FeO it contained, and were then normalized for the seven oxides of SiO<sub>2</sub>, Al<sub>2</sub>O<sub>3</sub>, Cr<sub>2</sub>O<sub>3</sub>, FeO, MnO, MgO, and CaO that were contained within our compositions. The oxide mixes were then ground into fine powders, made into 100 mg pellets, suspended on platinum wire, and placed into a Deltech vertical muffle tube furnace. The  $f(\text{O}_2)$  was calibrated for 0.5 log units below the iron-wüstite buffer curve at 1600 °C using a CO/CO<sub>2</sub> gas mixture and was left at this constant gas ratio for all runs. The charges thus underwent slightly different fugacities at different temperatures, but were always between 0.5 and 1.0 log unit below the iron-wüstite buffer curve. Charges 005-012 were melted in the furnace at 1580 °C for 0.5 hours and then cooled at 1800 °C/hour to their respective isothermal temperature (Table 1). All charges were quenched from their isothermal temperatures. Charges 003-016 were air quenched, while 017 and 019 were water quenched. Due to time constraints some experiments did not reach equilibrium. The final compositions were analyzed by electron microprobe using an accelerating voltage of 15kv and a beam current of 10nA.

**RESULTS:** Iron loss to the platinum wire was the major problem in the experiments. Preliminary estimates indicate approximately 5-15% FeO loss at 1180 °C with amounts approaching 90% FeO loss at temperatures of 1580 °C and fairly long duration. Subsequent low temperature experiments will be run using iron wire, to minimize this problem. Our Fe/Mn 140 experiments yielded eucritic MnO abundances of 0.4 to 0.7 wt% in the glasses, 0.4 to 0.5 wt% in the olivines, and 0.4 to 0.7 wt% in the pyroxenes. Higher MnO abundances were found in the Fe/Mn 100, 60, and 20 experiments. The final Fe/Mn ratios from the Fe/Mn 140 experiments were generally between 10 and 60 within the glasses (Fig. 1) and 20 to 80 in the olivines (Fig. 2).

The exact reason why our experiments yielded different MnO abundances than [2] is not yet clear. A variable may be that our experiments involved oxide compositions, while [2] started with natural Murchison.

**CONCLUSIONS:** Eucritic MnO abundances and Fe/Mn ratios are produceable from chondritic source material at temperatures from 1180 °C to 1580 °C under reducing conditions. Although our experiments did not reproduce [1] or [2] exactly, they did demonstrate further

## MN EXPERIMENTS ON MURCHISON ANALOGUES: Boesenberg &amp; Delaney

the possibility of HED origins from precursor carbonaceous chondritic material through simple partial melting.

Future experiments investigating Fe/Mn ratios and HED origins will contain (1) longer run times to insure equilibrium; (2) an expanded oxide composition to include NiO, TiO<sub>2</sub>, and Na<sub>2</sub>O; (3) Fe-wire to hold the low temperature experiments; (4) a greater range of oxygen fugacities; and (5) water quenching of all charges.

REFERENCES: [1] Stolper (1977) GCA 41, 587-611; [2] Jurewicz et al. (1992) GCA in press; [3] Jarosewich (1990) Meteoritics 25, 323-337.

Table 1

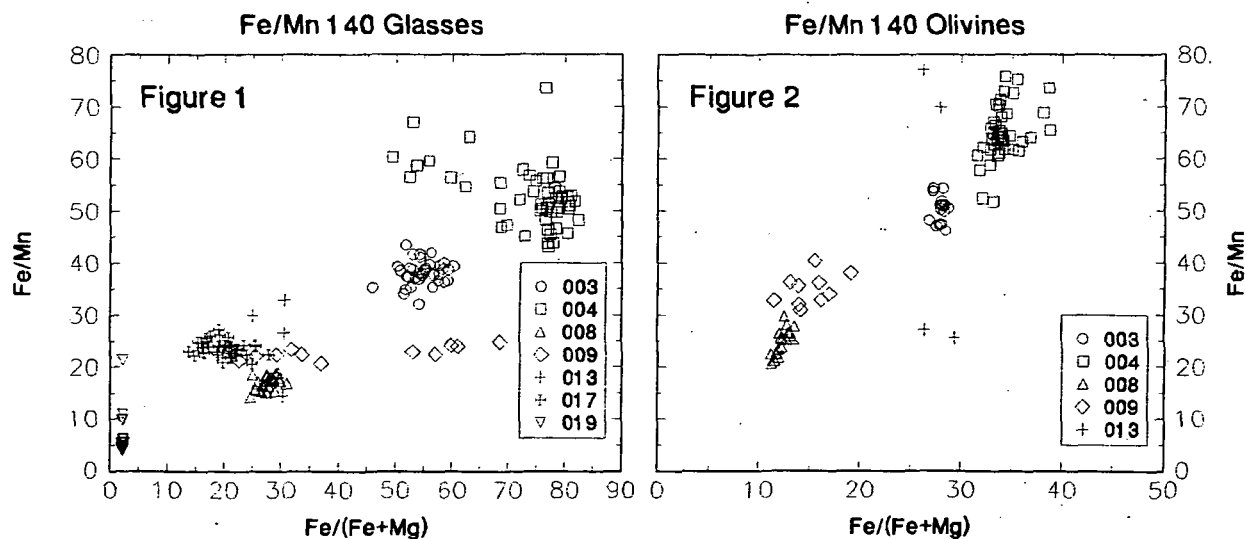
Charge	Fe/Mn	Temp °C (Time in hrs)	Phases Present
003	140	1253 (47)	gl+oli+pyx+sp+mtl
004	140	1300 (21)	gl+oli+sp+mtl
005*	20	1580 (0.5) » 1325(16.5)	gl+oli+pyx+mtl
006*	60	1580 (0.5) » 1325(16.5)	gl+oli+pyx+mtl
007*	100	1580 (0.5) » 1325(16.5)	gl+oli+pyx+mtl
008*	140	1580 (0.5) » 1325(16.5)	gl+oli+pyx+mtl
009*	140	1580 (0.5) » 1180(40.5)	gl+oli+pyx+mtl+(sil)
010*	100	1580 (0.5) » 1180(40.5)	gl+oli+pyx+mtl
011*	60	1580 (0.5) » 1180(40.5)	gl+oli+pyx+mtl
012*	20	1580 (0.5) » 1180(40.5)	gl+oli+pyx+mtl
013	140	1180 (39)	gl+oli+pyx+sp+mtl+p lag+(sil)
014	100	1180 (39)	gl+oli+pyx+sp+mtl+p lag+(sil)
015	60	1180 (39)	gl+oli+pyx+sp+mtl+p lag+(sil)
016	20	1180 (39)	gl+oli+pyx+sp+mtl+p lag+(sil)
017	140	1580 (1)	gl
019	140	1580 (10)	gl

Fe/Mn =starting composition's ratio based on total Fe.

(sil) =relic silica grains found.

\* =melted at 1580 °C for 30 minutes and cooled to respective isothermal temperature at 1800 °C/hr.

The following charges were run simultaneously: (005 & 006); (007 & 008); (009-012); (013-016).



456409

367-25  
ABS ONLY

LPSC XXIV

139

N94-12082

NOBLE GASES IN LEW88516 SHERGOTTITE: EVIDENCE FOR EXPOSURE AGE PAIRING WITH ALH77005. D.D. Bogard and D.H. Garrison<sup>1</sup>, NASA, Johnson Space Center, Houston, TX 77005 (1-also Lockheed-ESC)

LEW88516 contains excess amounts of radiogenic  $^{40}\text{Ar}$  and  $^{129}\text{Xe}$  that are slightly greater than those observed in ALH77005, but in the same relative proportion as much larger excesses observed in EET79001. Cosmogenic  $^3\text{He}$  and  $^{21}\text{Ne}$  abundances in LEW88516 are very similar to those for ALH77005 and are consistent with a common initiation of cosmic ray exposure -2.8 Myr ago for four of the five shergottites. Exposure of these four shergottites could have been under different shielding in a common meteoroid, or in several objects.

**Introduction:** LEW88516, a 13 gram meteorite found in Antarctica, has recently been identified as a shergottite [1,2] and is the ninth member of the SNC group of meteorites which many believe to have been derived from Mars. Shock effects in LEW88516 are "ubiquitous and extreme", maskelynite is present, and the sample is "cut by veins of glass and vitrophyre" [2,3,4,5]. The petrology and chemical composition of LEW88516 are generally similar to ALH77005 and different from other SNC meteorites, which suggests possible pairing of these two meteorites [2]. However, modest differences between the two meteorites exist, including the fact that they were recovered about 500 miles apart.

**Noble Gas Abundances:** The isotopic abundances of noble gases were measured in two temperature extractions (450°C and 1600°C) of an 85 mg whole rock sample of LEW88516. The 450°C extraction released some adsorbed atmospheric gases, much of the radiogenic  $^4\text{He}$  and cosmogenic  $^3\text{He}$ , and possibly a small amount of trapped gas. The 1600°C extraction released >97% of the total cosmogenic Ne and Ar. The isotopic composition of heavier Xe isotopes in the 1600°C extraction generally was within uncertainties of that for atmosphere and previous measurements of trapped Xe in EET79001 [6]. One exception is  $^{129}\text{Xe}$ , for which the measured  $^{129}\text{Xe}/^{132}\text{Xe}$  ratio of  $1.149 \pm 0.011$  is significantly higher than this ratio for atmospheric, AVCC, or solar components. Relative to atmospheric Xe composition, we calculate an excess  $^{129}\text{Xe}$  abundance of  $7 \times 10^{-12} \text{ cm}^3\text{STP/g}$  for LEW88516.

The total  $^{40}\text{Ar}$  in LEW88516 was  $5.93 \times 10^{-6} \text{ cm}^3\text{STP/g}$ , of which 96.7% was released at 1600°C. The measured K concentrations of LEW88516 and ALH77005 are 199 ppm [5] and 230 ppm (JSC unpublished data), respectively. This K content for LEW88516 would have produced only  $-15 \times 10^{-8} \text{ cm}^3\text{STP/g}$  of radiogenic  $^{40}\text{Ar}$  during the -180 Myr Rb-Sr age determined for the other four shergottites [7], leaving an excess  $^{40}\text{Ar}$  of  $5.78 \times 10^{-6} \text{ cm}^3\text{STP/g}$ . By analogy to the other shergottites [6], we attribute the excess  $^{40}\text{Ar}$  and  $^{129}\text{Xe}$  in LEW88516 to a shock-implanted, trapped component. The quantities of excess  $^{40}\text{Ar}$  and  $^{129}\text{Xe}$  in LEW88516 ( $5.7 \times 10^{-6}$  and  $7 \times 10^{-12} \text{ cm}^3\text{STP/g}$ , respectively) are similar to excesses measured in ALH77005 ( $1.2 \times 10^{-6}$  and  $5 \times 10^{-12} \text{ cm}^3\text{STP/g}$ , respectively) but are considerably less than excesses measured in shock-melt phases of EET79001 [6]. However, the excess  $^{40}\text{Ar}/^{129}\text{Xe}$  ratio of  $8 \times 10^5$  in LEW88516 is similar to the ratio of  $12 \times 10^5$  found for several phases of EET79001. Thus, our sample of LEW88516 contained slightly greater amounts of a trapped, Martian-like component than did ALH77005.

**Cosmogenic Abundances & Exposure Ages:** The measured  $^{21}\text{Ne}$  and  $^{38}\text{Ar}$  were >99% and -76% cosmogenic, respectively. We calculated abundances of the cosmogenic component using the lever rule and assumed end-member compositions of: trapped  $^{21}\text{Ne}/^{22}\text{Ne} = 0.029$  and  $^{36}\text{Ar}/^{38}\text{Ar} = 5.32$ ; and cosmogenic  $^{21}\text{Ne}/^{22}\text{Ne} = 0.91$  and  $^{36}\text{Ar}/^{38}\text{Ar} = 0.7$ . The concentration of cosmogenic  $^{38}\text{Ar}$  in LEW88516 ( $2.5 \times 10^{-9} \text{ cm}^3\text{STP/g}$ ) is somewhat higher than that measured in ALH77005 ( $1.8 \times 10^{-9} \text{ cm}^3\text{STP/g}$ ), even if we account for a higher measured Ca content for LEW88516 [5]. Cosmogenic  $^{21}\text{Ne}$  and  $^3\text{He}$  in LEW88516 are similar to those measured for ALH77005, but are different from those measured in other SNC meteorites, especially EET79001, Chassigny, and the nakhlites. Figure 1 is a plot of cosmogenic  $^3\text{He}$  and  $^{21}\text{Ne}$  concentrations against the cosmogenic  $^3\text{He}/^{21}\text{Ne}$  ratio for all SNC meteorites. Except for the addition of LEW88516 data, it is reproduced from Figs. 10 and 11 of Bogard et al. [6]. Measured  $^{21}\text{Ne}$  data have been corrected for differences in target element abundances by normalizing to the composition of ordinary chondrites [see 6]. These  $^{21}\text{Ne}$  corrections were small (-3%) for LEW88516 and ALH77005, but amounted to a factor of -2 for Shergotty and Zagami. No corrections were applied to  $^3\text{He}$ . The concentrations of cosmogenic He and Ne in SNC meteorites define three distinct groups: EET79001; Chassigny and the three nakhlites; and the remaining four shergottites. Using  $^{21}\text{Ne}$  production rates given by [8], these three groups have distinctly different exposure ages of -0.6 Myr, -12 Myr, and -2.8 Myr, respectively. Nishiizumi et al. [9] reported that the  $^{10}\text{Be}$  exposure age for ALH77005 is  $2.5 \pm 0.3$  Myr. Measured  $^{10}\text{Be}$  activities and the prediction of a nearly constant  $^{10}\text{Be}/^{21}\text{Ne}$  ratio as a function of

## NOBLE GASES IN LEW88516: Bogard &amp; Garrison

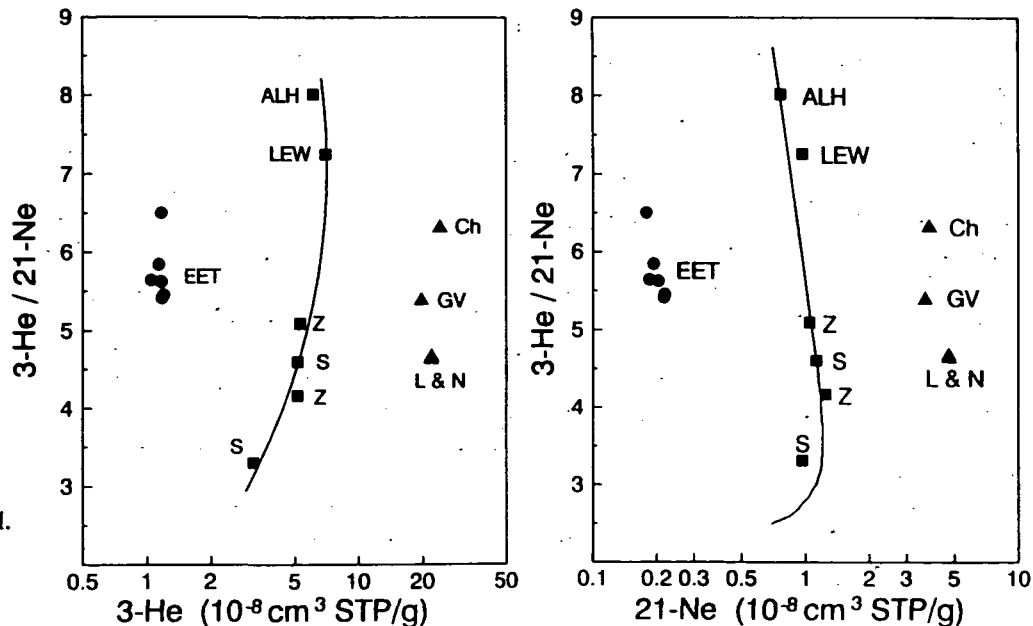
shielding for ordinary chondrite composition [10] can also be used to calculate exposure ages. From the  $^{10}\text{Be}$  activity of 16.6 dpm/kg measured in LEW88516 [11] and the relationship given by [10], we calculate a  $^{10}\text{Be}/^{21}\text{Ne}$  exposure age for LEW88516 of 3.0 Myr. The exposure age groupings of Fig. 1 are not significantly affected by the terrestrial ages determined from cosmogenic radionuclides, which are ALH77005 = 0.19 Myr [12], EET79001 = 0.012 Myr [13], and LEW88516 = <0.05 Myr [11].

**Shielding Groups:** The curves through the middle data sets of Fig. 1 define the expected variations in the cosmogenic composition due to cosmic ray shielding in a single body for a common exposure age and have been taken from the model of [14]. Analogous curves representing a greater exposure age could be passed through the Chassigny--nakhilite data. Thus, the variations observed in cosmogenic He and Ne among ALH77005, LEW88516, Shergotty, and Zagami could be explained as due to irradiation in a common object under conditions of different shielding for a period of 2.5-3.0 Myr. Similarly, variations among Chassigny and the three nakhilites be explained as due to irradiation in a common object for ~12 Myr under conditions of different shielding [6]. Lesser shielding is represented by larger  $^3\text{He}/^{21}\text{Ne}$  ratios.

LEW88516 cosmogenic He and Ne data lie close to and probably within uncertainties of the ALH77005 data (Fig. 1). Similar  $^3\text{He}/^{21}\text{Ne}$  and  $^{10}\text{Be}$  indicate that LEW88516 and ALH77005 were irradiated under similar shielding. Because the chemical compositions of these two shergottites are not greatly different from that of ordinary chondrites, their cosmogenic  $^3\text{He}/^{21}\text{Ne}$  ratios can probably be compared to shielding systematics in chondrites in order to estimate the amount of cosmic ray shielding. Thus, the relatively high  $^3\text{He}/^{21}\text{Ne}$  ratios suggest irradiation within a few cm of the surface. The recovered ALH77005 specimen was 5-10 cm in diameter, and LEW88516 was only 1-2 cm. Furthermore, measurements of cosmic ray particle tracks indicate that <1 cm of ablation loss occurred for ALH77005 during atmospheric entry [15]. Thus, both LEW88516 and ALH77005 were exposed with minimal shielding to cosmic rays for an apparent common period of 2.5-3.0 Myr. Shergotty and Zagami could have been irradiated at somewhat greater depths in the same object. However, substantial compositional differences between LEW88516 and ALH77005 on the one hand and Shergotty and Zagami on the other might suggest that these four shergottites were exposed to cosmic ray irradiation within at least two objects. LEW88516 and ALH77005 could have been irradiated in a single object. However, different  $^{36}\text{Cl}$  activities [11] and the significant distance between their recovery sites indicate that LEW88516 and ALH77005 fell to earth at different times, and thus existed as separate objects in space prior to their fall. In conclusion, it is likely that four of the five shergottites were ejected from their parent meteoroid by a common event ~2.8 Myr ago, but it is not clear whether most of their cosmic ray exposure occurred in a single object or in multiple objects.

**References:** [1] Mason, *Ant. Met. Newsletter* 14:2, 1991; [2] Lindstrom et al., *LPSC XXIII*, 1992; [3] Delaney, *Meteoritics* 27, p.213, 1992; [4] Harvey & McSween, *ibid*, p.231; [5] Dreibus et al., *ibid*, p.213; [6] Bogard et al., *G.C.A.* 48, p.1723, 1984; [7] Shih et al., *G.C.A.* 46, p.2323, 1982; Nyquist et al., *LPSC XVII*, p.624, 1986;

[8] Eugster, *G.C.A.* 52, p.1649, 1988; [9] Nishiizumi et al., *G.C.A.* 50, p.1017, 1986; [10] Graf et al., *G.C.A.* 54, p.2521, 1990; [11] Nishiizumi et al., *Meteoritics* 27, p.270, 1992; [12] Schultz & Freundel, *Meteoritics* 19, p.310, 1984; [13] Jull & Donahue, *G.C.A.* 52, p.1309, 1988; [14] Nyquist, *LPSC XV*, p.613, 1984; [15] Bhandari et al., *G.C.A.* 50, p.1023, 1986.





56B-46  
456414 ABS ONLY  
N94-12883

<sup>39</sup>Ar-<sup>40</sup>Ar AGES OF ACAPULCOITES AND LODRANITES: EVIDENCE FOR  
EARLY PARENT BODY HEATING; D.D. Bogard, D.H. Garrison (NASA Johnson Space  
Center, Houston, TX 77058), T.J. McCoy, and K. Keil (Planetary Geosciences, Dept. of Geology and  
Geophysics, SOEST, University of Hawaii at Manoa, Honolulu, HI 96822).

**Abstract.** New age dating of acapulcoites (Acapulco, Monument Draw) and lodranites (Gibson) allow us to reconstruct the history of their parent body in a chronological framework. These meteorites originated on a common parent body -4.55 Ga ago. Non-collisional heating caused partial melting, with lodranites having been heated slightly higher than acapulcoites. This parent body cooled to the Ar closure temperature at -4.51 Ga for acapulcoites and -4.48 Ga for lodranites. The difference in ages is consistent with the higher temperature and longer cooling time for lodranites. Cooling probably occurred at a few to tens of °C/Ma, with slower cooling rates at lower temperatures.

**Previous Work.** Acapulcoites and lodranites are samples of a single parent body [1] which experienced low degrees of partial melting [2,3]. These rocks have roughly chondritic compositions but achondritic textures. Acapulcoites were heated to just above the Fe,Ni-FeS eutectic (-980°C) [2], whereas lodranites were heated slightly more (-1000-1050°C) and experienced silicate partial melting [3]. These temperatures are broadly consistent with oxygen isotopic [1] and two-pyroxene [2] geothermometry. A diverse range of cooling rates has been reported, depending on the method used. For Acapulco alone, cooling rates of -100°C/Ma from 900-1000°C, 20,000-70,000°C/Ma from 500-750°C [4], and -1.7°C/Ma at -300-100°C [5] have been estimated. These cooling rates imply very different times, from <1 Ma to >400 Ma, to cool to low temperatures, and possibly a complex thermal history.

Isotope chronology can provide a powerful tool to help unravel the formation and thermal history of these meteorites. Unfortunately, previous efforts have yielded uncertain results. A  $4.60 \pm 0.03$  Ga Sm-Nd isochron age for Acapulco is significantly older than the widely accepted 4.55-4.56 Ga age of the solar system, suggesting that Acapulco may be the oldest precisely dated object [6]. U-Pb studies of Acapulco only suggested an early re-equilibration [7]. <sup>39</sup>Ar-<sup>40</sup>Ar profiles for the acapulcoites Y-74063 and ALH 78230 [8] suggest "plateau" ages of  $4.556 \pm 0.053$  and  $4.531 \pm 0.021$ , respectively, but individual temperature extractions have much wider age ranges and the ages are derived from a limited number of temperature extractions. No age dating of lodranites has been reported.

**Results.** Figures 1 a-c give our <sup>39</sup>Ar-<sup>40</sup>Ar ages and K/Ca ratios as a function of cumulative release of <sup>39</sup>Ar for stepwise temperature extractions of Acapulco, Monument Draw, and Gibson. Six extractions of Acapulco, releasing 22-97% of the <sup>39</sup>Ar, define a "plateau" age of  $4.50 \pm 0.01$  Ga (error is one  $\sigma$  of deviations from the mean). Thirteen extractions of Monument Draw, releasing 0.2-99% of the <sup>39</sup>Ar, define an age of  $4.52 \pm 0.02$  Ga; nine extractions releasing 85% of the <sup>39</sup>Ar define an age of  $4.514 \pm 0.011$  Ga. Seven extractions of Gibson, releasing 8-99% of the <sup>39</sup>Ar, define a "plateau" age of  $4.48 \pm 0.02$  Ga. In addition, all extractions of Monument Draw define a highly linear ( $r^2 = 0.99995$ ) isochron of <sup>40</sup>Ar/<sup>36</sup>Ar vs. <sup>39</sup>Ar/<sup>36</sup>Ar, which passes through <sup>40</sup>Ar/<sup>36</sup>Ar = 0, and whose slope corresponds to an age of  $4.523 \pm 0.005$  Ga, identical to the "plateau" age. (Errors quoted for these ages include all analytical uncertainties but do not include an additional -1% uncertainty in the age of the hornblende monitor.) Ages of Monument Draw and Gibson (irradiated together) differ at the limits of their analytical uncertainties, suggesting that Gibson is 20-40 Ma younger.

The K/Ca ratios and rate of Ar release indicate the presence in each meteorite of two K-bearing phases, high K/Ca plagioclase and low K/Ca pyroxene. Using temperature release data for Ar from each phase we calculated the diffusivity parameter  $D/a^2$ . Assuming a cooling rate of 10°C/Ma and using diffusivity data from an Arrhenius plot for Monument Draw, we calculate closure temperatures [9] of -275°C for plagioclase and -470°C for pyroxene. Given the much higher heating temperatures, complete Ar degassing from these meteorites would be expected, even at moderately fast cooling rates. Because the two phases have different closure temperatures but no observable age difference (i.e., <30 Ma, Fig. 1), the parent body must have cooled from -470°C to 275°C at >7°C/Ma. To cool from the peak temperature of -980°C of Monument Draw to the 275°C closure temperature in ~30 Ma (i.e., 4.55 Ga minus 4.52 Ga), suggests an average cooling rate of the parent body of -25°C/Ma. Clearly, neither very fast [4] nor very slow [5] cooling rates predominated during cooling of these meteorites. Cooling probably occurred at tens of °C/Ma above 500°C, decreasing gradually to a few °C/Ma below 300°C. Gibson apparently was completely degassed of planetary <sup>36</sup>Ar, whereas Acapulco

<sup>39</sup>Ar-<sup>40</sup>Ar AGES OF ACAPULCOITES AND LODRANITES: Bogard et al.

and Monument Draw released <sup>36</sup>Ar at the highest extraction temperatures in concentrations comparable to type 5-6 ordinary chondrites.

**Discussion.** The <sup>39</sup>Ar-<sup>40</sup>Ar data presented here are entirely consistent with the petrologic [2,3] and oxygen isotopic [1] information about acapulcoites and lodranites. We can now reconstruct the history of the acapulcoite-lodranite parent body in a chronological framework.

**Accretion.** The parent body was of chondritic composition and accreted 4.55-4.56 Ga ago. Unless substantiated by additional data, the  $4.60 \pm 0.03$  Sm-Nd age for Acapulco is assumed not to represent parent body accretion. The assertion of a common parent body for these meteorites is entirely consistent with similarities in oxygen isotopic compositions [1], mineralogy and mineral composition [2,3], and cosmic-ray exposure ages indicative of excavation in a single impact event (R. Wieler, pers. comm., 1992).

**Heating by Non-collisional Sources.** After accretion, the parent body was heated to the point of partial melting (Fe,Ni-FeS cotectic for acapulcoites; cotectic and silicates for lodranites). The heat source for this melting was non-collisional (e.g., <sup>26</sup>Al, electromagnetic induction). No evidence for shock exists in the silicates, which is consistent with well-defined <sup>39</sup>Ar-<sup>40</sup>Ar release patterns. High two-pyroxene geothermometer temperatures (-950-1100°C) suggest that partial melting did not result from local excursions in shock pressures. The evidence for "early re-equilibration" seen in the U-Pb system [8] probably reflects this early heating. The higher temperature estimated for Gibson possibly caused total loss of <sup>36</sup>Ar and lower K concentrations (Fig. 1).

**Cooling.** The parent body cooled below the Ar closure temperature -4.51 Ga ago for acapulcoites and -4.48 Ga ago for the Gibson lodranite. Cooling decreased gradually from tens of °C/Ma at higher temperatures to a few °C/Ma at low temperatures. Neither very fast or very slow cooling predominated. Lodranites were heated -100°C higher than acapulcoites, requiring longer cooling times and, thus, explaining the younger age. There is no evidence that these meteorites experienced any significant thermal event after closure of the Ar chronometer. These <sup>39</sup>Ar-<sup>40</sup>Ar ages of 4.48-4.52 Ga are identical to the upper range of <sup>39</sup>Ar-<sup>40</sup>Ar ages shown by unshocked ordinary chondrites [10]. The acapulcoites and lodranites apparently formed in a manner and time scale analogous to metamorphism on parent bodies of ordinary chondrites.

**References.** [1] Clayton et al. (1992) *LPSC XXIII*, 231-232. [2] McCoy et al. (1992) *LPSC XXIII*, 871-872. [3] McCoy et al. (1992) *Meteoritics* 27, 258-259. [4] Zipfel et al. (1992) *LPSC XXIII*, 1585-1586. [5] Pellas and Fieni (1992) *LPSC XXIII*, 1051-1052. [6] Prinzhofer et al. (1992) *GCA* 56, 797-815. [7] Göpel et al. (1992) *Meteoritics* 27, 226. [8] Kaneoka et al. (1992) *Proc. NIPR Symp. Antarct. Met.* 5, 224-232. [9] Dodson (1973) *Contrib. Min. Pet.* 40, 259-274. [10] Turner et al. (1978) *Proc. 9th LPSC*, 989-1025.

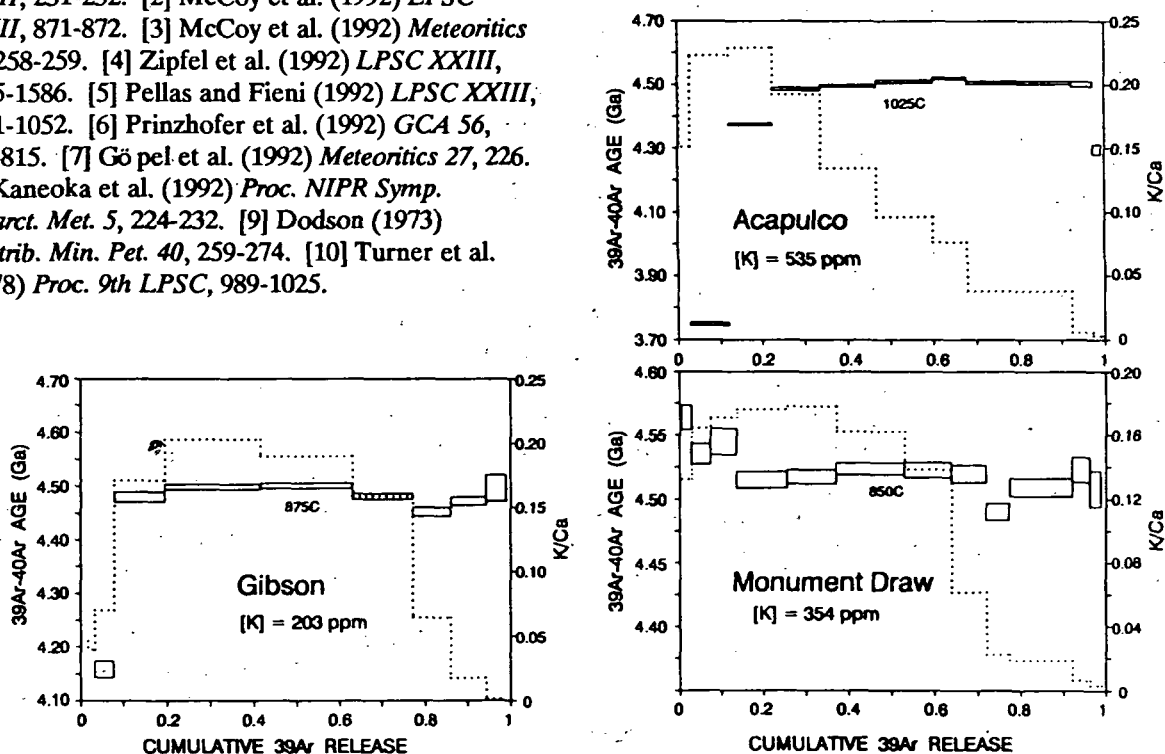


Figure 1. Plot of <sup>39</sup>Ar-<sup>40</sup>Ar ages ("boxes" contain all analytical uncertainties) and K/Ca ratios (dotted lines) vs. cumulative release of <sup>39</sup>Ar for acapulcoites and lodranites. Determined K concentrations are also shown.

456416

568-46  
ABS ONLY

LPSC XXIV

143

N 94-182084

ARROYO EL MIMBRAL, MEXICO, K/T UNIT: ORIGIN AS DEBRIS  
FLOW/TURBIDITE, NOT A TSUNAMI DEPOSIT; Bruce F. Bohor and William J. P. Z.  
Betterton, U.S. Geological Survey, MS 972, Box 25046, Denver, CO 80225

Coarse, spherule-bearing, clastic units have been discovered at 10 marine sites that span the K/T boundary in northeastern Mexico [1]. We examined one of the best exposed sites in Arroyo el Mimbrel, northwest of Tampico [2]. The Mimbrel outcrop displays a layered clastic unit up to 3 m thick enclosed by marly limestones of the Mendez (Latest Maastrichtian) and Velasco (Earliest Danian) Formations. At its thickest point, this channelized clastic unit is comprised of 3 subunits: 1) a basal, poorly-sorted, ungraded calcareous spherule bed ~1 m thick containing relict impact glass and shocked mineral grains, 2) a massive set of laminated calcite-cemented sandstones up to 2 m thick with plant debris at its base, 3) capped by a thin (up to 20 cm) set of rippled sandstone layers separated by silty mudstone drapes containing a small (921 pg/g) iridium anomaly [2]. This tripartite clastic unit is conformably overlain by marls of the Velasco Formation. We also visited the La Lajilla site east of Ciudad Victoria [1]; its stratigraphy is similar to Mimbrel's, but its clastic beds are thinner and less extensive laterally.

The Mimbrel clastic unit has been interpreted previously as being deposited by a megawave or tsunami produced by an asteroid impact on nearby Yucatan (Chicxulub crater) [1,2]. However, a presumed 400-m paleodepth of water at the Mimbrel site [2], channeling of the spherule subunit into the underlying Mendez Formation marls, and the overtopping of the basal, spherule-bearing subunit (1) by the laminated sandstone subunit (2), all suggest a combined debris flow/turbidite origin for this clastic unit similar to that proposed for Upper Pleistocene sand/silt beds occurring elsewhere in the Gulf of Mexico [3]. In this latter model, the sediment source region for the clastic unit is the lower continental shelf and slope escarpment. For the K/T unit at Mimbrel, we propose that thick ejecta blanket deposits composed mostly of spherules were rapidly loaded onto the lower shelf and slope from an impact-generated ejecta curtain. After deposition a debris flow was initiated, either by a megawave (tsunami) or earthquake shocks caused by impact, or by the inherent instability of this thick ejecta deposit on the slope escarpment. This mass of spherules and associated local shelf sands plunged down the slope and out onto the basin floor in a channelized debris flow. In this scenario, larger and heavier spherules formed the base of the flow that cut and filled the channel, while smaller and lighter siliclastic grains from co-transported sands formed the upper turbiditic part of the flow. These turbidite sands formed lobate, laminated, graded beds that overrode the confines of the channel itself as the flow subsided. The uppermost rippled and clay-draped subunit (3) formed from the settling of fine clastic components on top of the flow-laminated sands, contemporaneous with the arrival of the last of the fine-grained vapor cloud components (Ir-rich fireball layer). Thus, this clastic unit appears to have been deposited from a debris flow/turbidite, and not directly from a giant impact-generated wave.

Smit et al. [2] state that oversteepening and overturning of the channel rims at the base of this clastic unit are due to "escape" of unconsolidated Mendez marls and that the base of the spherule bed roughly follows the bedding of the underlying deformed marl, both features indicating a lack of an angular unconformity at the top of the Mendez. However, we interpret the oversteepened channel rims and the bedding in the underlying deformed marls paralleling the base of the spherule bed as soft sediment deformation features due to loading; the deformed bedding in the top of the Mendez beneath the channel probably does not represent primary bedding. Moreover, we and others [2] further noted that the spherule bed contains interclasts

## ARROYO EL MIMBRAL: Bohor, B.F. and Betterton, W.J.

of limestone and Mendez marl at its base; we consider these rip-up clasts further evidence of channel cutting. For these reasons, we suggest that the clastic unit at the Mendez-Velasco boundary rests on a disconformity formed by scouring at the base of a channelized debris flow, and not the angular unconformity of Hay [4].

Spherule shapes and sizes at Mimbral are similar to those at Haiti. However, being a redeposited bed, these Mexican spherules are set in a matrix of secondary calcite, rather than the original matrix of fine-grained impact glass altered to palagonite as found at Haiti. At Mimbral, the glass matrix was winnowed out during aqueous transport. Most Mimbral spherules consist of hollow clay (chlorite-smectite) shells, but some contain relict cores of impact glass. Some of the smaller shells consist of a dark green inner rim of chlorite, surrounded by an outer, lighter-colored rim of chlorite-smectite altered from a palagonite precursor. Many relict glass cores and fragments are encased in sparry calcite, indicating that their palagonite (or hydrated glass) rims were abraded away during transport in the debris flow. The impact glasses at Mimbral are mostly dark brown (black), but some are dark green mixed with amber, light green and, rarely, yellow. Preliminary analyses of the black and yellow glasses (Table 1) show a close correspondence with the compositions of Haitian impact glasses of similar colors [5]. However, the light green and dark green glasses from Mimbral have no analogs among the Haitian glasses. Smit et al. [2] designate these light green glasses as K-rich, but our analyses specifically show low K, Ca and Mg for this class compared to dark brown glasses, along with a strikingly-low value for total oxides (Table 1); the latter probably indicates high water content. The dark green glasses are commonly altered to chlorite on weathered surfaces. We also separated a few relict glass fragments from the spherule bed at La Lajilla, although none have been reported from here before [6]. These glass fragments were dark brown and light green, with semi-quantitative analyses similar to Mimbral glasses of these colors. **Acknowledgements.** We thank Billy Glass for providing the Mimbral glass analyses, and Gene Foord for the X-ray diffraction studies. Work partially supported by NASA Grant T-5715 to BFB.

**REFERENCES:** [1] Alvarez, W. et al. (1992) *GSA Absts. Prog.* **24**, A331. [2] Smit, J. et al. (1992) *Geology* **20**, 99-103. [3] Nelson, C.H. et al. (1992) *Geology* **20**, 693-696. [4] Hay, W.W. (1960) in *Proc. Inter. Geol. Cong. 21st*, Copenhagen, Pt. 5, 70-77. [5] Sigurdsson, H. et al. (1991) *Nature* **349**, 482-487. [6] Margolis, S.V. et al. (1992) *GSA Absts. with Prog.* **24**, A331. [7] Maurrasse, F. and Sen, G. (1991) *Science* **252**, 1690-1693.

TABLE 1. COMPARISON OF MIMBRAL AND HAITI RELICT GLASS ANALYSES

	Mimbral, Mexico Relict Glasses					Beloc, Haiti Glasses	
	Dk. Brn.	Yellow	Dk. Grn.	Lt. Grn.	K-rich[2]	Dk. Brn.[5]	Yellow[7]
SiO <sub>2</sub>	60.43	50.38	60.68	60.82	66.20	63.09	49.06
Al <sub>2</sub> O <sub>3</sub>	15.75	13.78	15.41	14.88	18.73	15.21	13.19
FeO	6.42	5.15	3.63	4.35	5.67	5.44	5.14
MgO	3.79	4.64	1.16	2.46	2.64	2.74	4.09
CaO	7.21	23.66	3.76	5.21	0.84	7.26	24.54
K <sub>2</sub> O	1.27	0.61	1.11	0.91	3.68	1.59	0.63
Na <sub>2</sub> O	2.65	2.15	1.46	0.99	0.84	3.63	2.10
TiO <sub>2</sub>	0.78	0.64	0.83	0.70	0.02	0.67	0.64
MnO	---	---	---	---	0.00	0.14	0.16
Total	98.34	101.2	88.10	90.38	98.83	99.76	99.56

456418

570-46  
ABS-ONLY

LPSC XXIV

145

N 94-12085  
R-2

**K/T SPHERULES FROM HAITI AND WYOMING: ORIGIN, DIAGENESIS, AND SIMILARITY TO SOME MICROTEKTITES;** Bohor, B.F.<sup>1</sup>, Glass, B.P.<sup>2</sup>, and Betterton, W.J.<sup>1</sup>

<sup>1</sup>U.S. Geological Survey, MS 972, Box 25046, Denver, CO 80225; <sup>2</sup>Dept. of Geology, University of Delaware, Newark, DE 19716

Spherules with relict glass cores in the K/T boundary bed of Haiti allow for a comparison of these bodies with hollow goyazite shells in the K/T boundary claystone of Wyoming and with younger microtektites of the Ivory Coast strewn field. Samples of the Haitian beds from undisturbed sections at Beloc, as determined by Jehanno et al. [1], contain both hollow shells and relict glass cores rimmed by palagonite [2] that has been partially converted to smectite. These palagonite rims developed from hydration zones formed when hot, splash-form droplets of andesitic impact glass [3] were deposited into water. Mutual collisions between these droplets in the ejecta curtain [4] may have formed point-source stresses on their surfaces. Initiation of hydration would be facilitated at these surface stress points and propagated radially into the glass. The inner surface of these merged hemispherical fronts appears mammillary (Fig. 1), which is reflected as scalloping in Haitian relict glass cores.

In the Western Interior, hollow spherules in the melt ejecta layer of the K/T boundary unit were designated as Type 1 spherules by Bohor and Betterton [5]. The shells of these spherules are replaced by goyazite at Dogie Creek and Teapot Dome in southern Wyoming, allowing for detailed comparisons with Haiti spherules. All of the features characteristic of palagonite rims in Haiti, such as mammillary inner surfaces, cracks and interior vesicles rimmed with palagonite, and banded and fibroradial texture, strongly resemble features of the goyazite shells in Wyoming. We propose that palagonite rims in Haiti and goyazite shells in Wyoming are identical manifestations of glass hydration and palagonite formation processes operating at both aqueous depositional sites and resulting in Type 1 spherules. The thick Haitian spherule beds (Units 1, 2) contain rare shocked quartz grains but no magnetoferrite, underscoring their identity as a melt ejecta layer (ejecta blanket) equivalent in origin to that of the Western Interior but more proximal to the impact crater.

All of the K/T Type 1 spherules display typical splash-form, melt-droplet shapes characteristic of microtektites. Microtektites in the Ivory Coast strewn field have compositions similar to those of the Haitian relict glasses. Scalloped surfaces displayed by these Ivory Coast microtektites (Fig. 2a) are mimicked by scalloped Haitian relict glass cores (Fig. 2b) and by scalloping on secondary mineral casts pseudomorphing dissolved glass cores in Wyoming (Fig. 2c). Ivory Coast microtektites [6] also display U-shaped grooves (Fig. 3a), duplicated in Haitian relict glass cores (Fig. 2b). In Wyoming hollow shells, these grooves are formed by surface fractures rimmed with goyazite after palagonite (Fig. 3b). These morphological similarities between Type 1 spherules in the K/T melt ejecta layers from Haiti and Wyoming and Ivory Coast microtektites are further evidence in support of the hypothesis that Type 1 spherules are, in fact, altered microtektites [7]. **Acknowledgements:** Haiti samples provided by Dave Larue. BFB partially supported by NASA Grant T-5715. **REFERENCES:** [1] Jehanno, C. et al. (1992) *EPSL* **109**, 229-241; [2] Lyons, J.B. and Officer, C.B. (1992) *EPSL* **109**, 205-224; [3] Sigurdsson, H. et al. (1991) *NATURE* **349**, 482-487; [4] Bohor, B.F. and Betterton, W.J. (1992) *LPSC* **23**, 135-136; [5] Bohor, B.F. and Betterton, W.J. (1990) *LPSC* **21**, 107-108; [6] Glass, B.P. (1974) *GSA Bull.* **85**, 1305-1314; [7] Bohor, B.F. and Betterton, W.J. (1991) *Meteoritics* **26**, 320.

## ORIGIN OF K/T SPHERULES: Bohor, B.F. et al.

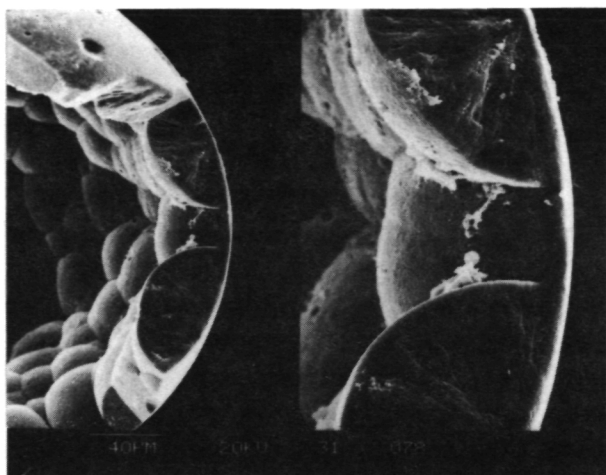


Fig. 1. Teapot Dome--goyazite replacing palagonite mammillary shells.

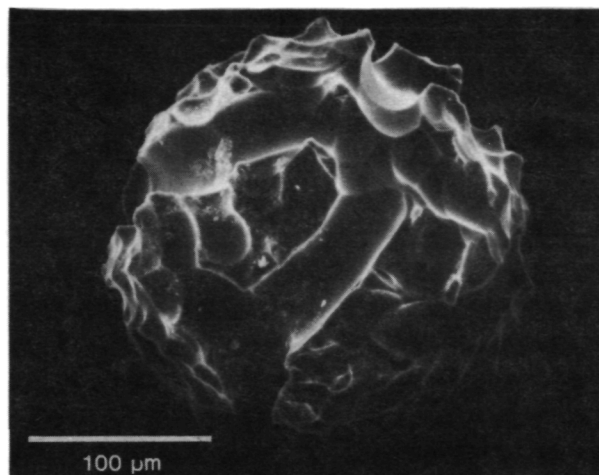


Fig. 2a. Ivory Coast microtektite--scalloped with U-groove.

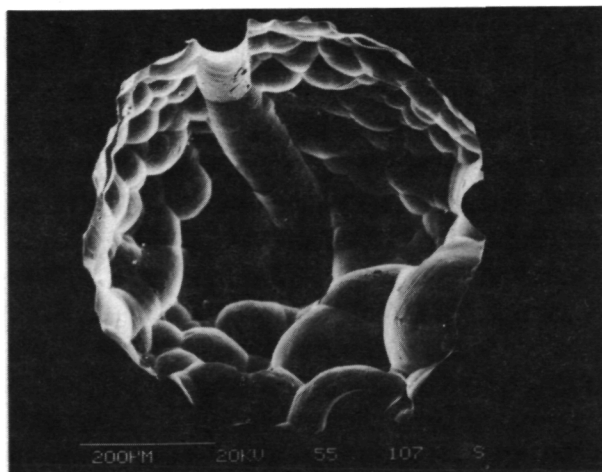


Fig. 2b. Haitian relict glass core--scalloped with U-groove.

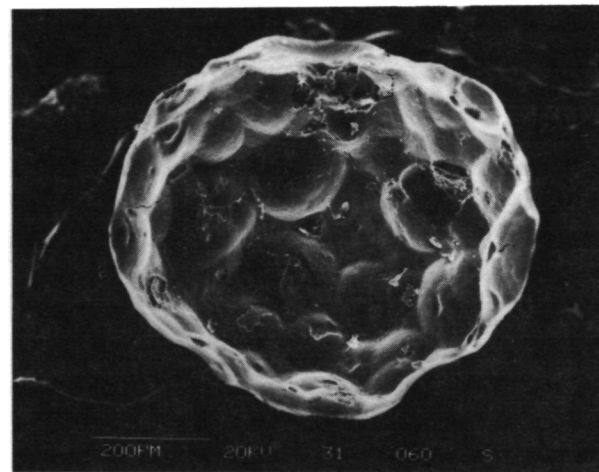


Fig. 2c. Teapot Dome--scalloped secondary mineral cast (core).

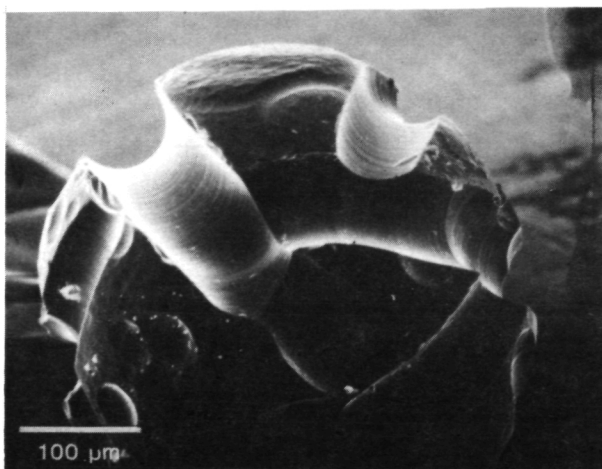


Fig. 3a. Ivory Coast microtektite. U-grooves on scalloped surface.

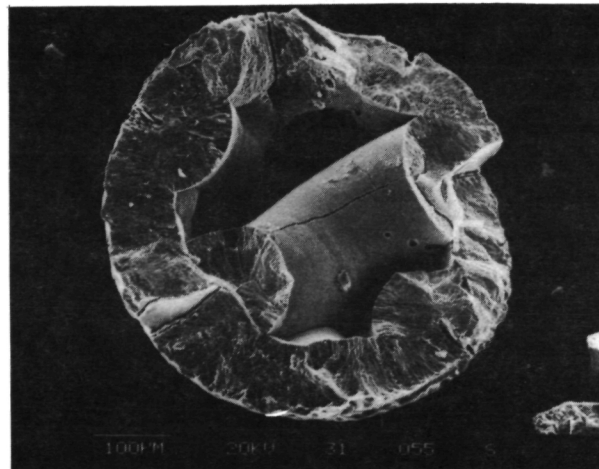


Fig. 3b. Teapot Dome. Surface cracks rimmed with goyazite after palagonite.

571-26  
NBS ONLY  
456420  
163291  
N 94-12086

**THE SOLUBILITY OF GOLD IN SILICATE MELTS: FIRST RESULTS.** A. Borisov, H. Palme, B. Spettel. MPI für Chemie, Saarstrasse 23, 6500 Mainz, Germany

The effects of oxygen fugacity and temperature on the solubility of Au in silicate melts were determined. Pd-Au alloys were equilibrated with silicate of anorthite-diopside eutectic composition at different T-fO<sub>2</sub> conditions. The behaviour of Au was found to be similar to that of Pd reported recently [1]. Au solubilities for alloys with 30 to 40 at. % Au decrease at 1400°C from 12 ppm in air to 160 ppb at a log fO<sub>2</sub> = -8.7. The slope of the log(Me-solubility) vs. log(fO<sub>2</sub>) curve is close to 1/4 for Au and the simultaneously determined Pd suggesting a formal valence of Au and Pd of 1+. Near the IW buffer Pd and Au solubilities become even less dependent on fO<sub>2</sub> perhaps reflecting the presence of some metallic Au and Pd.

**Experimental.** As in earlier work [1,2] liquid silicate droplets (2-3 mm diameter) were equilibrated with 0.5-1.0 mm wide metal band loops (Au<sub>45</sub> Pd<sub>55</sub>, at%) inside a furnace with controlled oxygen fugacity for about 50 hours. After removal of metal loops glasses were analysed for Au and Pd by INAA. By successive removal of surface layers and reanalyses of Au and Pd, profiles through the glass were obtained. From these data homogeneous Pd and Au distribution within the glass is inferred indicating that equilibrium was achieved in the experiments. Quantitative energy dispersive analyses (SEM) of the Au-Pd loops showed significant selective Au evaporation (typically 5-24% of the initial Au-content) from the alloy during the experiments. Particularly severe Au-losses (61-67%) were recorded when H<sub>2</sub>/CO<sub>2</sub> gas mixtures were used for fO<sub>2</sub> control.

**Results.** Results of the experiments are graphically displayed in Figs. 1 and 2. Combined analytical uncertainties are typically in the order of 10%. The slopes of log(Me solubility) vs. log(fO<sub>2</sub>) at 1400°C are close to 1/4 for both, Pd and Au (Fig.1), indicating the effective valence of 1+, instead of 2+ and 1+ (or perhaps 3+) for Pd and Au, respectively. This is similar to the behaviour of Ir [2] and Pd [1] recently reported. At more reducing conditions (around IW) there is a significant decrease of the slope for both metals, associated with increasing scatter of the results. A change of slope in reducing conditions was earlier found in experiments with pure Pd [1]. The existence of Pd<sup>0</sup> was suggested as one of the possible reasons of this behaviour. The reason for the large spread in the low fO<sub>2</sub> region in the present experiments using alloys is, however, unknown. Additional experiments will be performed to clarify this question.

At constant fO<sub>2</sub> (air) Au and Pd solubilities increase with increasing temperature (Fig.2) opposite to the behavior of metals of the Fe group but in agreement with earlier data on Pd [1]. Extrapolation of our data to 1450°C leads to solubilities of about 197 ppm Pd and 14 ppm Au comparable to results by Capobianco [3] (Pd=290±60, Au=14±2 ppm) for silicate melts equilibrated with solid Pd<sub>66</sub>Au<sub>34</sub> alloy in air. Both melt compositions are similar with respect to SiO<sub>2</sub> and MgO content, but different in CaO and Al<sub>2</sub>O<sub>3</sub> which may be responsible for the small difference in Pd solubility.

By comparing Pd solubility in equilibrium with pure Pd [1] and with Au-Pd alloys (this work), activity coefficients of Pd in Au-Pd alloys ( $\gamma_{\text{Pd}}$ ) were extracted. Their values (0.9-1.2) are compatible, within error limits, with activity coefficients calculated from thermodynamic data [4] and with values extracted from experimental data [3].

**D<sup>Pd</sup>/D<sup>Au</sup> (iron metal/silicate melt).** Over a wide range of oxygen fugacities the ratio of Pd to Au concentrations (weight ratio = 12±1) was found to be constant in our experiments (Fig. 1). By considering the Pd-Au-alloy composition, appropriate activity coefficients [4] and normalizing to unit activities for Au and Pd, a ratio of 3.6 is obtained reflecting the difference between Au and Pd solubility in silicate melts.

Metal silicate partition coefficients, D(met/sil), were calculated from solubilities according to  $D(\text{Fe/melt}) = 1/(c_i \cdot \gamma_i \cdot B_i)$ , where  $c_i$  is the solubility in equilibrium with pure Au or Pd,  $\gamma_i$  is the activity coefficient of metal  $i$  in Fe-metal and  $B_i$  is a coefficient for converting mole fractions of metal  $i$  in Fe-metal into weight fractions. From this and from estimates of the activity coefficient ratio of Pd and Au in Fe-metal ([4, 5]:  $\gamma_{\text{Pd}}/\gamma_{\text{Au}}$  in solid Fe = 0.12) a partition coefficient ratio of  $D^{\text{Pd}}/D^{\text{Au}} = 1.2$  is obtained. Extrapolation to lower oxygen fugacities are made on the assumption that the dependence of Au and Pd metal/silicate partition coefficients on oxygen fugacity is the same for both metals.

**Conclusions:** At 1350°C and oxygen fugacities appropriate for core formation in the Earth (log fO<sub>2</sub> = IW-2)  $D^{\text{Pd}}$  was estimated to be about  $1.6 \cdot 10^7$  [1]. From this and the results of this study a partition coefficient  $D^{\text{Au}} = 2 \cdot 10^7$  is

## GOLD SOLUBILITY IN SILICATE MELTS Borisov A. et al.

calculated for the same conditions. The similarity of Pd and Au metal/silicate partition coefficients, as well as the similar temperature dependence indicate similar behaviour of both elements during metal-silicate fractionation. Since Ir, another highly siderophile element, has a significantly higher metal-silicate partition coefficient we have concluded earlier [1] that the contents of highly siderophile elements in the upper mantle were not established by metal-silicate separation as suggested, for example, by [6] but are rather the result of accretion of a late chondrite-like veneer to the Earth. Additional arguments against a global core mantle equilibrium are given in a companion abstract [7].

References: [1] Borisov A. et al. (1993) *GCA*, submitted; [2] Borisov A. et al. (1992) *LPSC XXIII*, 139; [3] Capobianco C.J. (1990) *LPSC XXI*, 164; [4] Kubaschewski O. and Cousell J.F. (1971) *Monatshefte für Chemie* 102, 1724; [5] Hultgren R. et al. (1973) Selected values of thermodynamic properties of binary alloys, *American Society for metals, Metals Park, Ohio*; [6] Murthy V.R. (1991) *Science*, 253, 303; [7] Holzheid A. et al. (1993) *this volume*.

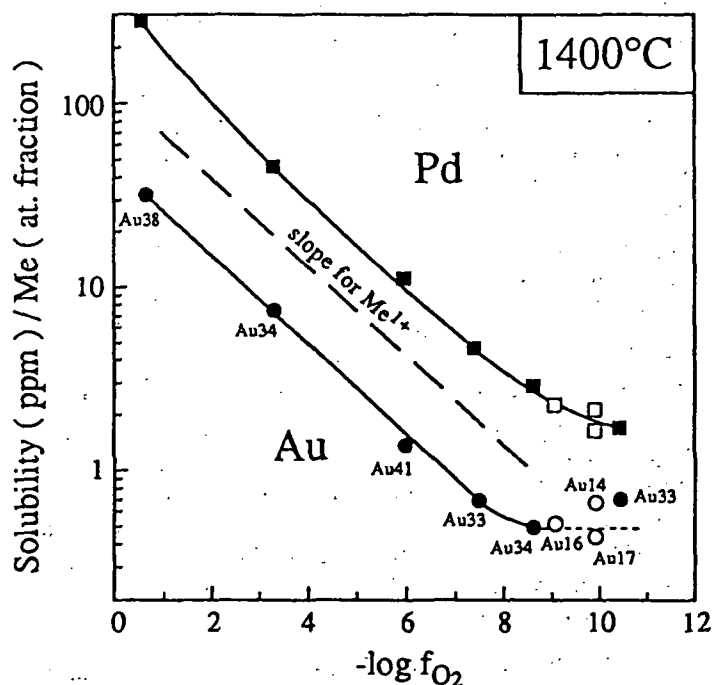


Fig.1. Effect of  $fO_2$  on Au and Pd solubilities. Open symbols -  $H_2/CO_2/N_2$  gas mixtures, solid - air,  $CO_2/N_2$  or  $CO/CO_2/N_2$  gas mixtures. Alloy compositions (at.%) are indicated. Dashed line - solubility for metal dissolved as  $Me^{1+}$ .

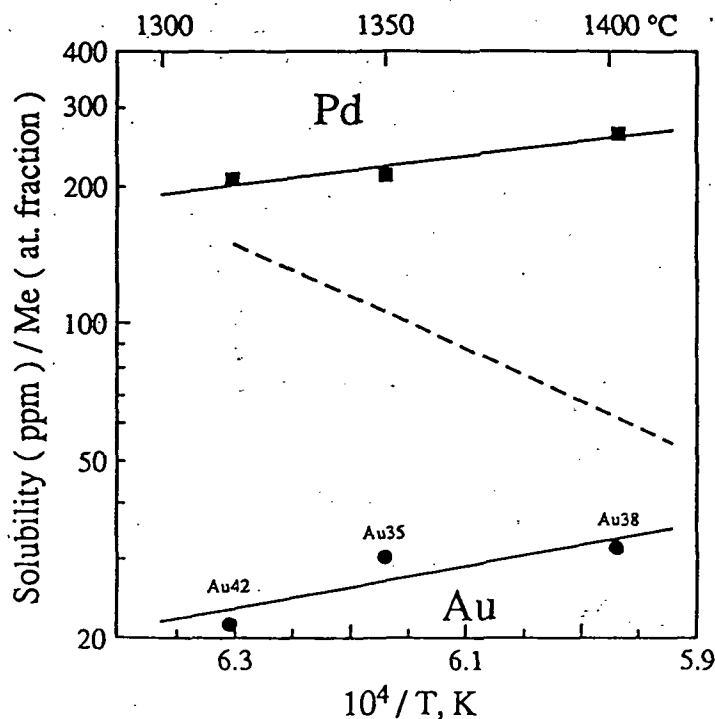


Fig.2. Effect of temperature on Au and Pd solubilities in silicate melts at constant  $fO_2$  (air). Dashed-line indicates typical slope for elements of the Fe-group.



450422

372-25

ABS ONLY

LPSC XXIV

149

N9 4-12087

<sup>29</sup>Si NMR SPECTROSCOPY OF NATURALLY-SHOCKED QUARTZ FROM METEOR CRATER, ARIZONA: CORRELATION TO KIEFFER'S CLASSIFICATION SCHEME\* M. B. Boslough<sup>1</sup>, R. T. Cygan<sup>1</sup>, and R. J. Kirkpatrick<sup>2</sup>, <sup>1</sup>Sandia National Labs, Albuquerque, NM 87185 and <sup>2</sup>U. of Illinois, Urbana, IL 61801.

We have applied solid state <sup>29</sup>Si nuclear magnetic resonance (NMR) spectroscopy to five naturally-shocked Coconino Sandstone samples from Meteor Crater, Arizona, with the goal of examining possible correlations between NMR spectral characteristics and shock level. This work follows our observation of a strong correlation between the width of a <sup>29</sup>Si resonance and peak shock pressure for experimentally shocked quartz powders [1,2]. The peak width increase is due to the shock-induced formation of amorphous silica, which increases as a function of shock pressure over the range that we studied (7.5 to 22 GPa). The Coconino Sandstone spectra are in excellent agreement with the classification scheme of Kieffer [3] in terms of presence and approximate abundances of quartz, coesite, stishovite, and glass. We also observe a new resonance in two moderately shocked samples that we have tentatively identified with silicon in tetrahedra with one hydroxyl group in a densified form of amorphous silica.

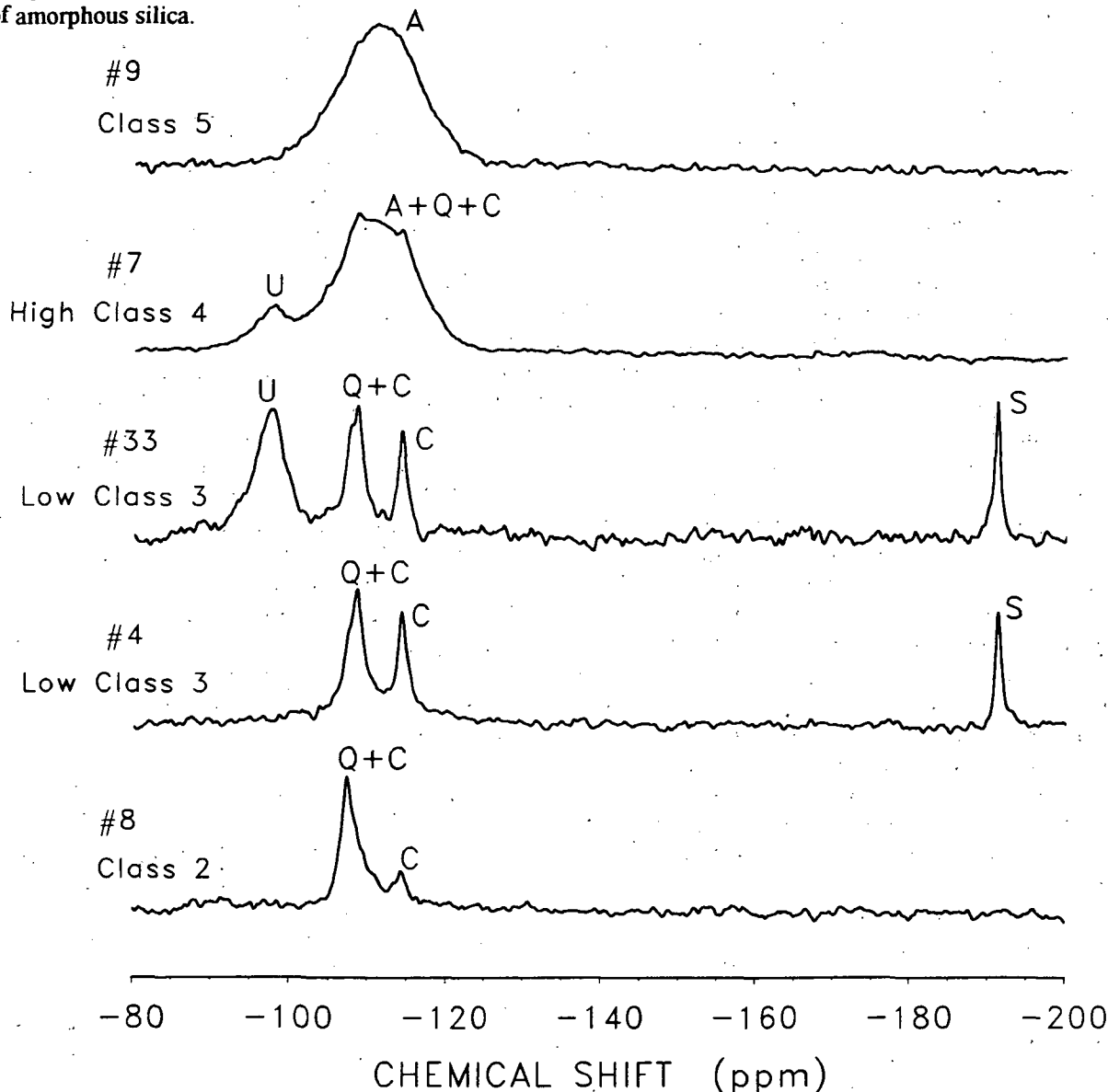


Figure 1. <sup>29</sup>Si NMR spectra of five shocked Coconino Sandstone samples. Resonance identifications are (Q) quartz, (C) coesite, (S) stishovite, (A) Q<sup>4</sup> sites in amorphous silica, and (U) unknown site tentatively identified as Q<sup>3</sup> (one OH) Si sites in a densified form of hydroxylated amorphous silica.

\*This work performed at Sandia National Laboratories supported by the U.S. Department of Energy under contract DE-AC04-76DP00789.

<sup>29</sup>Si NMR SPECTROSCOPY OF NATURALLY-SHOCKED QUARTZ: Boslough, M. B. *et al.*

We have previously suggested that NMR spectra be used as a "shock barometer", or at least as an identification technique for shocked quartz. However, our measurements to date have been limited to laboratory-shocked samples. Because the duration of shock loading can be many orders of magnitude longer for large impacts, major differences are to be expected. To address these possible differences, we have now turned our attention to naturally-shocked samples. Application of solid state NMR spectroscopy to such samples has been limited. Smith and Blackwell [4] measured spectra of coesite and stishovite taken from shocked Coconino Sandstone as part of a comparative study of silica polymorphs. Yang *et al.* [5] showed that this technique is very sensitive to high-pressure silica phases from whole rock samples of shocked Coconino Sandstone, and is capable of yielding accurate coesite/stishovite ratios. McHone *et al.* [6] applied the technique to samples collected from the K/T boundary and reported the detection of trace amounts of stishovite, although this interpretation has been disputed [7].

In the present work, we obtained spectra for five samples of Coconino Sandstone representing shock classes 2-5 (Fig. 1). The following is a preliminary summary of our observations. Class 2 (sample #8): mostly quartz, small amounts of coesite and possibly amorphous silica, no stishovite. Class 3 (sample #4): mostly quartz, more coesite than sample #8, some amorphous silica, and stishovite. Class 3 (sample #33): same as sample #4, but with an additional peak, possibly due to Q<sup>3</sup> (one OH) Si sites in a dense form of hydroxylated amorphous silica. Class 4 (sample #7): mostly amorphous silica, with some quartz and coesite, no stishovite, contains a less intense peak possibly associated with the same Q<sup>3</sup> site as in sample #33. Class 5 (sample #9): almost entirely amorphous silica, no stishovite. Of particular note are the surprisingly strong stishovite resonances in the Class 3 samples; the stishovite peak observed by Yang *et al.* [5] is significantly weaker. We also observed a more intense X-ray line ( $2\theta = 30.2^\circ$ ) for stishovite, implying there is more of this phase in our samples. The only samples for which we observe stishovite are those previously identified as Class 3.

The presence of an unidentified peak with a chemical shift of about -98 ppm in two of our samples (#33 and #7) is especially noteworthy. There is no X-ray diffraction evidence for significant amounts of any crystalline material other than the three silica polymorphs. There are several lines of evidence that this resonance corresponds to Si in tetrahedra with one hydroxyl group in a dense form of hydroxylated amorphous silica:

- 1) The large intensity implies that, unless it is a major phase, it has a very short relaxation time ( $T_1$ ), consistent with previous observations for shock-produced amorphous silica.
- 2) The shift to higher frequency (smaller negative ppm value) is consistent with a denser phase than a similar phase formed at one atmosphere for a given Si coordination. A dense amorphous phase has been identified in NMR spectra obtained by Nellis *et al.* [8] from crystalline quartz shocked to 33 GPa, with a resonance centered at about -106 ppm, an upfield shift of about 6 ppm from -112 ppm for normal-density silica glass [9]. The resonance for Q<sup>3</sup> (one OH) Si sites in a normal-density gel is at about -102 ppm [10]. Our observed peak position of about -98 would be consistent with densification by roughly the same amount as the amorphous silica associated with shocked quartz.
- 3) The peak is broad, indicating a wide range of Si-O-Si bond angles typical of amorphous material, and is inconsistent with Si in clay or feldspar.
- 4) The target Coconino Sandstone was wet, and there is TEM evidence for vesicular "froth" (consisting of amorphous material produced by steam separation) in Class 3 samples [11].
- 5) We have observed in a previous NMR study of clinoptilolite that shock loading can generate hydroxyl groups [12].

Further work is required to confirm the identification of the unknown phase, and to answer other questions. NMR proton cross-polarization techniques can be used to enhance Si resonances near protons, as would be the case for this phase. NMR relaxation studies can provide characteristic fractal dimensions as has been done for amorphous material in experimentally-shocked quartz [13]. We are also in the process of obtaining NMR spectra for other naturally shocked samples, in particular for quartz from the K/T boundary, that may have seen a radically different loading and unloading history than the Meteor Crater samples.

**References:** [1] Cygan *et al.* (1990) In *Proc. Lunar Planet Sci. Conf.* 20th, 451-457. [2] Cygan *et al.* (1992) In *Proc. Lunar Planet Sci. Conf.* 22nd, 127-136. [3] Kieffer (1971) *J. Geophys. Res.* 76, 5449-5473. [4] Smith and Blackwell (1984) *Nature* 303, 223-225. [5] Yang *et al.* (1986) *Meteoritics* 21, 117-124. [6] McHone *et al.* (1989) *Science* 243, 1182-1184. [7] Izett (1990) *GSA Special Paper* 249. [8] Nellis *et al.* (1992) *EOS* 73, No. 43, 594. [9] Oestrike *et al.* (1987) *Geochim. Cosmochim. Acta* 51, 2199-2209. [10] Phleiderer *et al.* (1990) *J. Phys. Chem.* 94, 4189-4194. [11] Kieffer *et al.* (1976) *Contrib. Mineral Petrol.* 59, 41-93. [12] Cygan *et al.* (1992) *EOS* 73, No. 14, 360. [13] Boslough *et al.* (1992) *EOS* 73, No. 43, 594.

**Acknowledgments:** S. Kieffer kindly provided us with well-documented samples from her previous work. G. Turner obtained the NMR spectra. This work was funded by NASA's PMG program.

## MIDPLANE TEMPERATURES IN THE SOLAR NEBULA. A. P. Boss,

DTM, Carnegie Institution of Washington, 5241 Broad Branch Road N.W., Washington DC 20015.

Cosmochemical analyses of meteorites imply that maximum temperatures in the inner solar nebula were on the order of 1300 K, yet standard viscous accretion disk models predict much lower midplane temperatures ( $\sim 300$  K at 2 AU to 3 AU) in a minimum mass nebula. A second-order accurate radiative hydrodynamics code has been used to construct models of the late-phase solar nebula appropriate for low-mass star formation ( $\dot{M} \sim 10^{-6}$  to  $10^{-5} M_{\odot} \text{ yr}^{-1}$ ). For a minimum mass ( $0.02 M_{\odot}$ ) nebula and a solar-mass protostar, the new models show that compressional heating due to mass accretion onto the nebula and subsequent vertical contraction of the nebula are sufficient to lead to midplane temperatures  $T_m > 1400$  K at 1 AU and  $T_m > 1000$  K at 2.5 AU.

**INTRODUCTION.** Low volatile metal abundances [1] and variations in Mg and Si abundances [2] have been interpreted to require temperatures in the range 1200 K to 1400 K in the inner solar nebula at the time of dust grain coagulation. On the other hand, rapid formation of the giant planets [3,4] seems to require coeval temperatures low enough ( $\sim 150$  K) at 5 AU and beyond to allow icy dust grains to coagulate. Classical viscous accretion disks have long been favored as solar nebula models [5], yet heating due to viscous dissipation seems only capable of producing midplane temperatures  $T_m \sim 150$  K to 300 K at 2 AU [6,7] unless the nebula is much more massive than a minimum mass nebula [8,9]. Numerical hydrodynamical models of solar nebula formation have been limited to high mass accretion rates and/or to relatively massive disks [10,11,12]. Here we present numerical calculations that overcome both of these previous drawbacks.

**NUMERICAL METHODS.** A new set of axisymmetric (2D) radiative hydrodynamical models of solar nebula formation has been calculated with a spatially second-order accurate code [13]. The equations of hydrodynamics, self-gravitation, and radiative transfer in the Eddington approximation are solved on a spherical coordinate grid extending from 1 AU to 10 AU. Compared to viscous accretion disk models, the hydrodynamical models include (i) compressional energy generated by molecular cloud core infall and vertical contraction of the nebula, (ii) the detailed vertical structure of the nebula, and (iii) Rosseland mean dust grain opacities and radiative transfer.

**INITIAL MODELS.** Acceptably low mass accretion rates are ensured for both the central protosun and the solar nebula by starting the models from an approximate equilibrium solution for the vertical structure of a self-gravitating, non-thin, adiabatic disk in near-Keplerian orbit around a solar-mass protosun. The midplane density is taken to be a power-law in radius ( $\rho_m \propto r^{-3/2}$ ), and the vertically infalling molecular cloud core is given the same form. This results in  $\dot{M}_s \rightarrow 0$  and  $\dot{M}_d \sim 10^{-6}$  to  $10^{-5} M_{\odot} \text{ yr}^{-1}$ .

**RESULTS.** In order to best determine the steady state midplane temperature profile, a variety of models were run with varied initial spherically symmetric temperature profiles. If the final temperature was higher than the initial temperature, then the initial temperature was assumed to be a lower bound on the steady state value, and vice versa. Thirteen such models were used to define a *composite* temperature profile that was then used as the initial temperature distribution for the final *composite* model shown in Figure 1. The disk undergoes a small amount of contraction during the evolution, while the infalling molecular cloud halo is preferentially accreted along the rotation axis. The temperature distribution rapidly changes from being spherically symmetric to a distribution with the highest temperatures in the optically thick disk. The midplane temperature does not change significantly from the initial profile, indicative of a steady state solution. The model temperatures are slightly lower than the midplane temperatures previously calculated on the basis of effective (photospheric) temperatures inferred at 1 AU from observations of T Tauri disk-star systems [14]. Midplane pressures in the inner nebula are  $\sim 10^{-6}$  to  $10^{-5}$  atm.

## SOLAR NEBULA MODELS: Boss, A.P.

**CONCLUSIONS.** The new models imply that a minimum mass nebula orbiting a solar-mass protostar and undergoing mass accretion at the appropriate rate should be compressively heated to  $T_m > 1400$  K at 1 AU and to  $T_m > 1000$  K at 2.5 AU, but with  $T_m \sim 100$  K at 5 AU and beyond. These temperatures seem to be in good agreement with the cosmochemical constraints for the inner solar system and with the need to coagulate icy grains in the outer nebula at the same time.

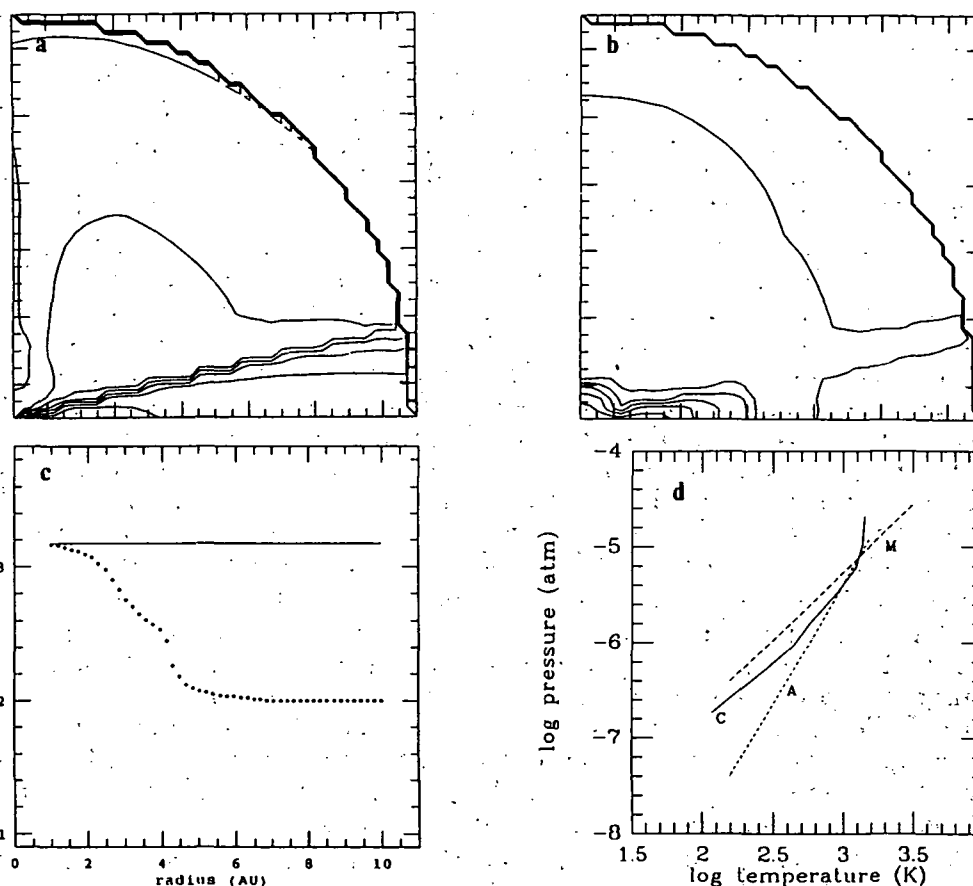


Figure 1. Results for the composite solar nebula model: (a) log density contours (factors of 10 change); (b) log temperature contours (factors of 1.6 change); (c) log midplane temperature (horizontal line = 1500 K); and (d) midplane pressure-temperature relation for the composite model (C), the adiabat used to define the initial model (A), and a standard viscous accretion disk adiabat (M) [7]. In (a) and (b), the rotation axis is the left border and the midplane is the bottom border; the box is 10 AU across.

**REFERENCES.** [1] Palme, H. and Boynton, W. V. (1992). In *Protostars & Planets III*, eds. Levy, Lunine, & Matthews (Tucson: Arizona), in press. [2] Larimer, J. W. and Wasson, J. T. (1988). In *Meteorites and the Early Solar System*, eds. Kerridge & Matthews (Tucson: Arizona), 394. [3] Lissauer, J. J. (1987). *Icarus* **69**, 249. [4] Stevenson, D. J. and Lunine, J. I. (1988). *Icarus*, **75**, 146. [5] Cameron, A. G. W. (1978). *Moon Planets* **18**, 5. [6] Cabot, W., Canuto, V. M., Hubickyj, O. and Pollack, J. B. (1987). *Icarus* **69**, 423. [7] Wood, J. A. and Morfill, G. E. (1988). In *Meteorites and the Early Solar System*, eds. Kerridge & Matthews (Tucson: Arizona), 329. [8] Morfill, G. E. (1988). *Icarus* **75**, 371. [9] Ruden, S. P. and Pollack, J. B. (1991). *Ap. J.* **375**, 740. [10] Tscharnuter, W. M. (1987). *Astron. Ap.* **188**, 55. [11] Boss, A. P. (1989). *Ap. J.* **345**, 554. [12] Bodenheimer, P., Yorke, H. W., Rózycka, M. and Tohline, J. E. (1990). *Ap. J.* **355**, 651. [13] Boss, A. P. and Myhill, E. A. (1992). *Ap. J. Suppl.* **83**, 311. [14] Cassen, P. (1992). *Lunar Planet. Sci. XXIII*, 207.

456444

544-92  
ABS = ONLY

LPSC XXIV

153

N 94-12089  
103297  
A-2

**CHONDRULE FORMATION BY CLUMPY ACCRETION ONTO THE SOLAR NEBULA.** A. P. Boss & J. A. Graham, DTM, Carnegie Institution of Washington, 5241 Broad Branch Road N.W., Washington DC 20015.

Chondrule textures and compositions appear to require rapid heating of precursor grain aggregates to temperatures in the range 1500 K to 2100 K, cooling times on the order of hours, and episodic and variable intensity events in order to produce chondrule rims and chemically distinct groups. Nebula shock waves have been proposed by Hood and Horanyi as a physical mechanism that may be capable of meeting the meteoritical constraints. Motivated by astronomical observations of the close environments of young stars, we suggest that the source of the nebula shock waves may be clumpy accretion onto the solar nebula - that is, episodic impacts onto the nebula by discrete cloud clumps with masses of at least  $10^{22}$  g. If the cloud clumps are massive enough ( $\sim 10^{26}$  g), the resulting shock wave may be able to propagate to the midplane and process precursor aggregates residing in a dust sub-disk.

**INTRODUCTION.** Laboratory analyses of meteoritical chondrules provide constraints on physical conditions in the solar nebula at the time of their formation. The spheroidal shape of most chondrules implies a molten phase [1], while their granular and porphyritic textures require cooling rates of  $\sim 1000$  K per hour [2]. Maximum temperatures were probably in the range 1500 K to 2100 K, depending on whether or not unmelted dust grains impacted the molten grains [3] and on the initial heating rate [4]. The initial heating must have taken place in less than an hour because chondrule compositions are not in equilibrium with nebular gas at these temperatures [1]. These physical conditions seem to require a localized heating event, and given the widespread occurrence of chondrules in primitive meteorites [5], and high temperature rims on many chondrules [6], chondrule formation must have been episodic. Compositional differences [7] imply that the formation mechanism was able to produce a range of end-products, perhaps indicative of variable intensity processing. A number of imaginative ideas have been advanced for chondrule formation [1,5,8]. Shock waves within the nebula [9] appear to be capable in principle of matching these constraints, provided an episodic source of shock waves is identified. Here we point out that astronomical observations of young stars suggest that clumps of gas and dust may impact the nebula at high enough velocities to cause shock wave processing in at least the outer layers of the solar nebula [10].

**OBSERVATIONS OF YOUNG STARS.** Three types of observations suggest the presence of clumps of optically thick matter in the close environments of young stars. (A) Irregular variations occur in the brightness of young stars over short (days) time periods [11] without accompanying spectral changes [12,13]. (B) Changes in the illumination of extended reflection nebulae are apparently caused by shadowing of the central star [14,15]. (C) Night-to-night changes in spectral features are attributed to accretion of low density circumstellar matter [16]. All of these observations are consistent with the presence of opaque clouds of gas and dust with speeds up to 250 km/sec. Estimates of the masses of the obscuring clouds are  $> 10^{22}$  g [15,17]. While the origin of such clumps is unclear and their lifetimes are likely to be short (years), they may result from the interaction of outflowing stellar winds with infalling or disk gas.

**CLUMP-NEBULA IMPACTS.** If clumps of gas and dust are moving at high velocity and high inclinations in the vicinity of young stars, they will eventually impact the disk, leading to localized heating and possibly driving shock waves into the nebula (Figure 1). Using conservation of the vertical component of the momentum and assuming that the shock front propagates like a cylindrical snowplow through the underlying nebula, the surface density of processed disk matter  $\sigma_d$  is related to the clump surface density  $\sigma_c$  by  $\sigma_d = \sigma_c(v_c/v_z - 1)$ , where  $v_z$  is the vertical shock velocity and  $v_c \sim 50$  km/sec is the clump impact velocity. Detailed calculations of dust grain shock heating [9] show that shock speeds of at least  $v_z \sim 5$  km/sec are required to thermally process chondrule precursor aggregates.

## CHONDRULE FORMATION: Boss, A. P., &amp; Graham, J. A.

Assuming that clump-disk impacts occur repetitively and that each impact processes a fresh batch of aggregates, the total fraction of the nebula dust aggregates which can be thermally processed  $F_p$  is

$$F_p \approx 0.8 \left[ \frac{t_i}{10^6 \text{ yr}} \right] \left[ \frac{f_i}{52 \text{ yr}^{-1}} \right] \left[ \frac{M_c}{10^{22} \text{ g}} \right] \left[ \frac{10^3 \text{ g cm}^{-2}}{\sigma_n} \right],$$

where  $t_i$  is the duration of the impact phase,  $f_i$  is the impact frequency,  $M_c$  is the clump mass, and  $\sigma_n$  is the nebula surface density. Clump masses of order  $10^{26}$  g may be necessary however in order for the shock waves to propagate all the way to the midplane of a minimum mass nebula.

**CONCLUSIONS.** Given the existence of clumpy disk accretion, the resulting nebular shock waves appear to be capable of thermally processing a significant fraction of nebula dust aggregates. However, processing will only occur close to the nebula surface unless the impacting clumps are considerably more massive ( $\sim 10^{26}$  g) than the present observational lower bound of ( $\sim 10^{22}$  g). Further observational evidence for clumpy disk accretion is necessary to learn if this scenario is reasonable.

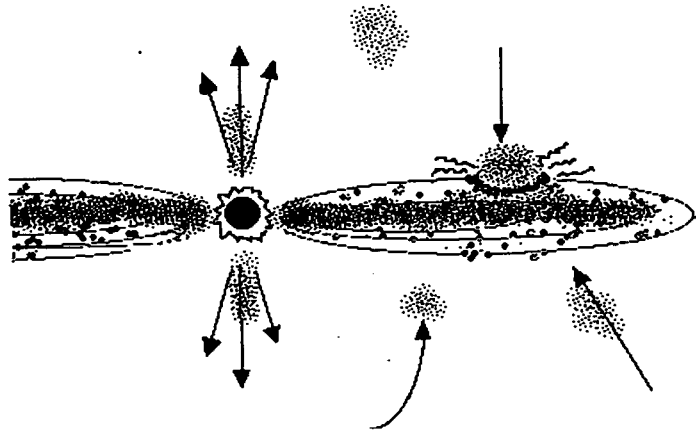


Figure 1. Schematic diagram (not to scale) of the clumpy disk accretion scenario for chondrule formation. Opaque clumps of gas and dust moving at high velocity close to young stars (possibly with bipolar outflows) may strike the disk, dissipating kinetic energy and driving shock waves which thermally process precursor dust aggregates in the disk.

**REFERENCES.** [1] Wood, J. A. (1988). *Ann. Rev. Earth Planet. Sci.* **16**, 53-72. [2] Hewins, R. H. (1988). In *Meteorites and the Early Solar System*, eds. Kerridge & Matthews (Tucson: U. Arizona), pp. 660-679. [3] Connolly, H. C., B. D. Jones, & R. H. Hewins (1991). *Meteoritics* **26**, 329. [4] Hewins, R. H. (1992). *Meteoritics* **27**, 232. [5] Grossman, J. N., A. E. Rubin, H. Nagahara, & E. A. King (1988). In *Meteorites and the Early Solar System*, eds. Kerridge & Matthews (Tucson: U. Arizona), pp. 619-659. [6] Kring, D. A. (1991). *Earth Planet. Sci. Lett.* **105**, 65-80. [7] Sears, D. W. G., L. Jie, P. H. Benoit, J. M. DeHart, & G. E. Lofgren (1992). *Nature* **357**, 207-210. [8] Levy, E. H. (1988). In *Meteorites and the Early Solar System*, eds. Kerridge & Matthews (Tucson: U. Arizona), pp. 697-711. [9] Hood, L. L., & M. Horanyi (1991). *Icarus* **93**, 259-269. [10] Boss, A. P., & J. A. Graham (1993). *Icarus*, submitted. [11] Bellingham, J. G., & G. S. Rossano (1980). *Astron. J.* **85**, 555-559. [12] Gahm, G. F., C. Fischerström, R. Liseau, & K. P. Lindroos (1989). *Astron. Astrophys.* **211**, 115-130. [13] Graham, J. A. (1989). *Publ. Astron. Soc. Pac.* **101**, 880. [14] Graham, J. A., & A. C. Phillips (1987). *Publ. Astron. Soc. Pac.* **99**, 91-98. [15] Lightfoot, J. F. (1989). *Mon. Not. R. Astron. Soc.* **239**, 665-675. [16] Graham, J. A. (1992). *Publ. Astron. Soc. Pac.* **104**, 479-488. [17] Hughes, J. D., P. Hartigan, J. A. Graham, J. P. Emerson, & F. Marang (1991). *Astron. J.* **101**, 1013-1020.

# INITIATING SOLAR SYSTEM FORMATION THROUGH STELLAR SHOCK WAVES. A. P. Boss & E. A. Myhill, DTM, Carnegie Institution of Washington, 5241 Broad Branch Road N.W., Washington DC 20015.

Isotopic anomalies in presolar grains and other meteoritical components require nucleosynthesis in stellar interiors, condensation into dust grains in stellar envelopes, transport of the grains through the interstellar medium by stellar outflows, and finally injection of the grains into the presolar nebula. The proximity of the presolar cloud to these energetic stellar events suggests that a shock wave from a stellar outflow might have initiated the collapse of an otherwise stable presolar cloud. We have begun to study the interactions of stellar shock waves with thermally supported, dense molecular cloud cores, using a three spatial dimension (3D) radiative hydrodynamics code. Supernova shock waves have been shown by others to destroy quiescent clouds, so we are trying to determine if the much smaller shock speeds found in, e.g., asymptotic giant branch (AGB) star winds, are strong enough to initiate collapse in an otherwise stable, rotating, solar-mass cloud core, without leading to destruction of the cloud.

**INTRODUCTION.** The presence of noble gas isotopic anomalies in presolar SiC grains seems to require nucleosynthesis in a red giant star [1,2,3] and subsequent ejection of the products in the strong stellar wind that accompanies the asymptotic giant branch (AGB) phase of stellar evolution. A few SiC grains have C, N, and Si isotopic abundances quite different from the majority, possibly requiring their production in a supernova explosion [4]. Cr isotope anomalies in carbonaceous chondrites seem to require mixing products from several nucleosynthetic sources [5]. Given the need for rapid injection of certain newly-synthesized isotopes (e.g.,  $^{26}\text{Al}$ ) into the presolar cloud [2], the evident proximity of the presolar cloud to these energetic stellar sources suggests that collapse may have been initiated by the very stellar shock wave that injected the isotopically anomalous grains [2,6]. Previous hydrodynamical studies of the interaction of stellar shock waves with molecular clouds have been limited to supernova shock fronts ( $\sim 1000$  km/sec) that completely destroy even massive molecular clouds [7-10]. Here we begin an investigation of the interaction of much slower shock waves ( $\sim 25$  km/sec) characteristic of, e.g., AGB star winds [11], protostellar outflows, or distant supernovae, with the hope of finding shock waves that can initiate collapse without destroying the cloud.

**NUMERICAL METHODS.** The calculations are being performed with a temporally and spatially second-order accurate radiative hydrodynamics code written in spherical coordinates [12]. The equations of hydrodynamics, self-gravitation, and radiative transfer in the Eddington approximation are solved by finite-differences on an Eulerian grid. Extensive testing on a variety of test cases has verified the accuracy of the code [12]. The numerical grid used for the present calculations spans 51 points in radius, 23 points in latitude ( $\pi/2 \geq \theta \geq 0$  assuming equatorial symmetry), and 64 points in azimuth ( $2\pi \geq \phi \geq 0$ ).

**INITIAL MODELS.** The quiescent presolar cloud consists of a spherically symmetric,  $1M_{\odot}$ , cold (10 K), centrally condensed ( $\rho_c = 20\rho_R$ ), molecular cloud core. The cloud is assumed to be in solid body rotation such that  $E_{\text{rot}}/|E_{\text{grav}}| = 0.04$ ; the density is perturbed by a low level of random noise. Instead of introducing a gas pressure perturbation [13] to represent the shock wave, the ram pressure of the shock wave is modeled by introducing an initial radial *velocity* perturbation over one hemisphere of the cloud's spherical boundary (at  $R = 10^4$  AU) with  $v_R = v_s \sin\theta \cos\phi$ ,  $v_s = 10$  to 25 km/sec.

**RESULTS.** Figure 1 shows the results for a model with  $v_s = 25$  km/sec. The initial cloud (a) is strongly compressed by the shock front but is not destroyed during the interval calculated so far (d). The central density ( $\rho_c$ ) increases by a factor of 34 during this early phase; a sustained increase in  $\rho_c$  will indicate the successful initiation of collapse. The velocity shear between the rapidly infalling shocked gas and the initial cloud core may lead to Kelvin-Helmholtz (KH) instability [14] and hence mixing. We find that the Richardson number is of the order necessary for instability.

## INITIATING FORMATION: Boss, A.P. &amp; Myhill, E. A.

**CONCLUSIONS.** Impacting a quiescent, rotating molecular cloud core with a shock front in the range of 10 to 25 km/sec may lead to the initiation of cloud collapse without totally destroying the collapsing cloud – continued calculations are necessary to determine the final result. If we determine that sustained collapse is possible, we will focus on following the trajectories of presolar dust grains injected into the cloud by the shock front, with the goal being to gain a preliminary understanding of the processes of mixing and transport during solar system formation.

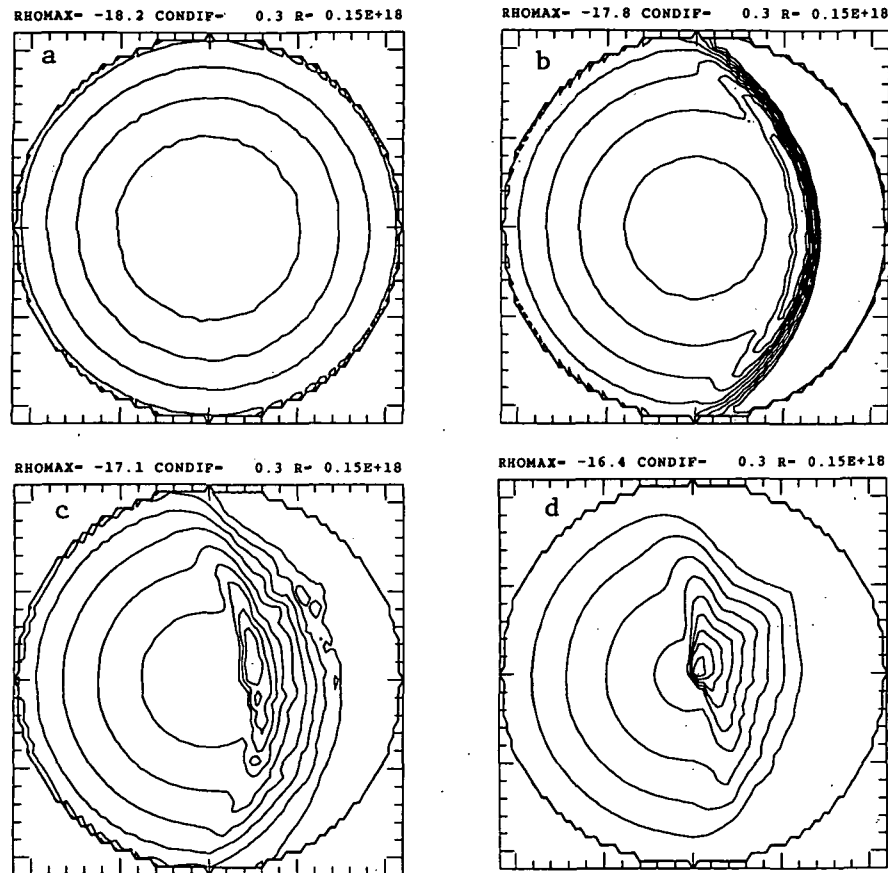


Figure 1. Equatorial density contour plots for the model with  $v_s = 25$  km/sec at four times: (a) 0.0, (b) 0.16, (c) 0.51, and (d) 0.62 free fall times. The initially stable cloud (a) rotates counterclockwise. The shock wave converges (b,c) on the center of the cloud (d), driving it toward gravitational collapse.

REFERENCES: [1] Lewis, R. S., Amari, S., & Anders, E. (1990). *Nature* **348**, 293-298. [2] Cameron, A. G. W. (1993). In *Protostars & Planets III*, eds. E. H. Levy, J. I. Lunine, & M. S. Matthews (Tucson: U. Arizona), in press. [3] Brown, L. E., & Clayton, D. D. (1992). *Science* **258**, 970-972. [4] Amari, S., Hoppe, P., Zinner, E., & Lewis, R. S. (1992). *Astrophys. J.* **394**, L43-L46. [5] Rotaru, M., Birck, J. L., & Allègre, C. J. (1992). *Nature* **358**, 465-470. [6] Cameron, A. G. W., & Truran, J. W. (1977). *Icarus* **30**, 447-461. [7] Krebs, J., & Hillebrandt, W. (1983). *Astron. Astrophys.* **128**, 411-419. [8] Tenorio-Tagle, G., & Rozyczka, M. (1986). *Astron. Astrophys.* **155**, 120-128. [9] Bedogni, R., & Woodward, P. R. (1990). *Astron. Astrophys.* **231**, 481-498. [10] Stone, J. M., & Norman, M. L. (1992). *Astrophys. J.* **390**, L17-L19. [11] Pottasch, S. R. (1984). *Planetary Nebulae* (Dordrecht: D. Reidel), p. 277. [12] Boss, A. P., & Myhill, E. A. (1992). *Astrophys. J. Suppl.* **83**, 311-327. [13] Kimura, T., & Tosa, M. (1991). *Mon. Not. R. Astron. Soc.* **251**, 664-669. [14] Chandrasekhar, S. (1961). *Hydrodynamic and Hydromagnetic Stability* (New York: Dover), p. 491.



456453

376-46

ABS ONLY

LPSC XXIV

157

N94-12091

**IMPACT MINERALOGY AND CHEMISTRY OF THE CRETACEOUS-TERTIARY**

**BOUNDARY AT DSDP SITE 576** Jennifer A. Bostwick and Frank T. Kyte. Institute of Geophysics and Planetary Physics, University of California, Los Angeles, CA 90024

We have identified the K/T boundary in pelagic clay sediments from cores at DSDP Site 576 in the western North Pacific (32°21.4'N, 164°16.5'E). Detailed geochemical and trace mineralogical analyses of this boundary section are in progress and initial results indicate similarities and differences relative to the only other clay core investigated in detail; DSDP Site 596, a locality in the western South Pacific (1,2). Peak Ir concentrations of 13 ng/g in DSDP Hole 576B are virtually identical with those observed in the South Pacific, but in the North Pacific this peak is much narrower and the integrated Ir fluence of ~85 ng cm<sup>-2</sup> is ~4 times lower (320 in Hole 596). Of the 34 elements measured, only Ir and Cr were found to have anomalous concentrations in K/T boundary samples.

Trace mineral residues were obtained by washing away clays and sequential chemical leaches (including HF) to remove typical hydrogenous and biogenous sediment components (e.g., zeolites and radiolarian opal). We attempted to quantitatively recover the entire trace mineral assemblage for grains >30µm in diameter. Our mineral residues were dominated by two phases: quartz and magnesioferrite spinel. Other non-opaque mineral grains we have positively identified were trace K-feldspar, plagioclase, corundum, and muscovite. Of these only K-feldspar exhibited planar deformation features (PDF). We have not found abundant plagioclase, as in the South Pacific suggesting that this phase was either not preserved in the North Pacific, or that in the south, it has a non-impact (i.e. volcanic) source.

PDF in quartz were commonly obscured by secondary overgrowths on the surfaces of quartz grains, presumably from diagenetic reprecipitation of silica dissolved from opaline radiolarian tests that are common in these sediments. However, careful examination revealed that most grains had multiple sets of PDF. Of the 133 quartz grains >30µm analyzed, 62% showed evidence of shock. The largest shocked grain recovered to date had a maximum diameter of 160µm, consistent with other sites in the Pacific. Our preliminary estimate of the total number of shocked quartz grains >30µm in diameter is ~400 grains cm<sup>-2</sup>. As with the Ir, this is considerably lower than the shocked quartz abundance in Hole 596 (~1800 cm<sup>2</sup>). Analyses of the size distribution of the shocked quartz indicates that the number of grains increases with decreasing size. No peak abundance is observed for any size above 30µm, a marked difference from size distributions reported for sites from the western interior of North America (3).

Magnesioferrite spinel is the most abundant component in the nonopaque fraction of the trace minerals. Qualitative analyses indicate that it is relatively Al-rich, as at other Pacific sites (4,5). Spinel occurs in a variety of morphologies including

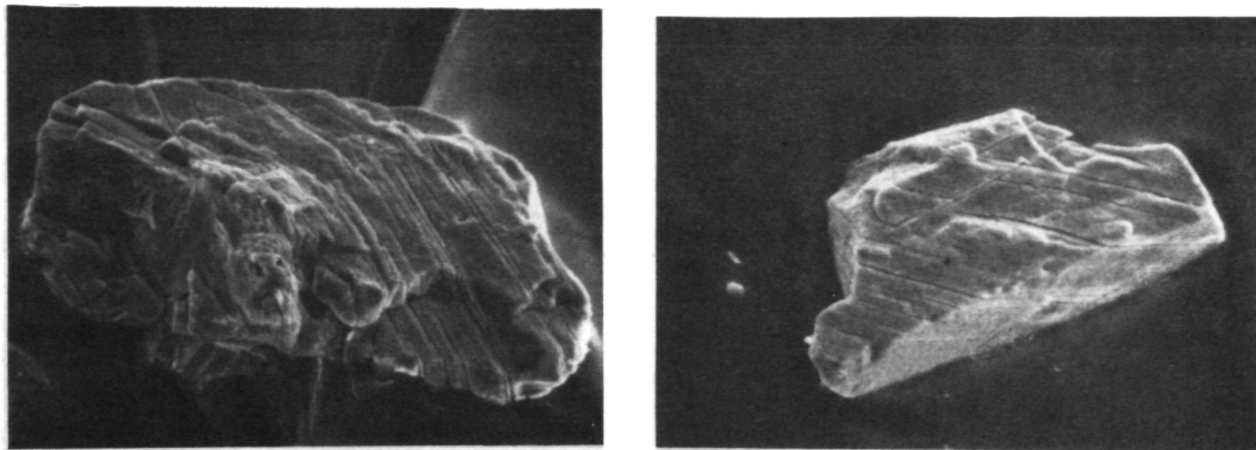


Figure 1. Shocked quartz grains with multiple sets of PDF (left 68  $\mu\text{m}$ , right 54  $\mu\text{m}$ ) that are commonly discontinuous due to secondary quartz overgrowths.

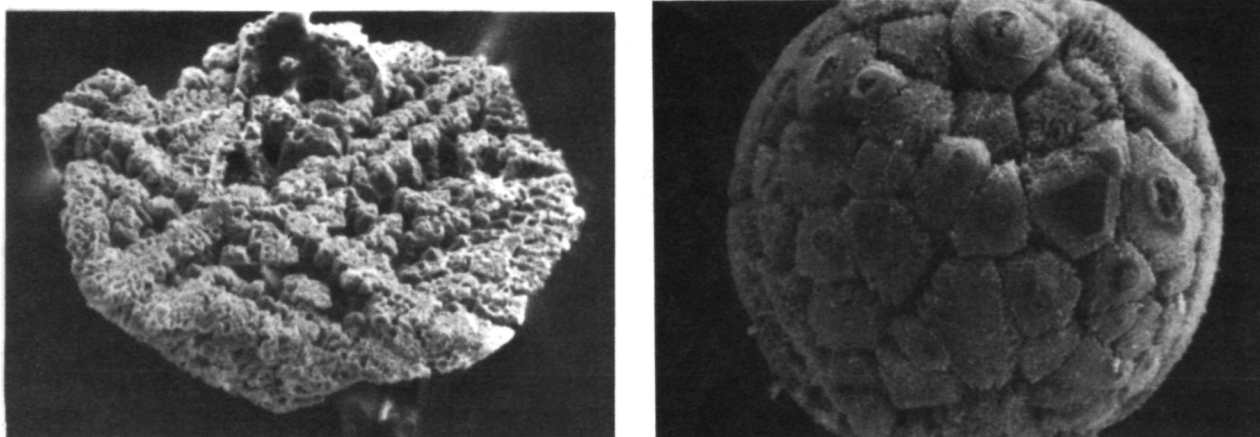


Figure 2. Left; Magnesioferrite intergrowth (65  $\mu\text{m}$ ) with preferential orientation of mineral grains. Right; spherule (58  $\mu\text{m}$ ) with intricate sponge-like Fe-rich (mineralogy unknown) on surface. Dark, smooth surfaces are magnesioferrite.

single grains, spherules and aggregates, the largest being ~140  $\mu\text{m}$  in size. Some spinel may be derived from silicate spherules which were observed in bulk sediments, but destroyed by our extraction procedure.

REFERENCES. 1) Zhou Z., Kyte F.T., and Bohor B.F., (1991) *Geology* **19**, 694. 2) Bohor B.F. and Betterton W.J. (1991) *LPSOXXII*, 119. 3) Izett G.A. (1990) *GSA Spec. Pap.* **249**. 4) Kyte F.T. and Smit J. (1986) *Geology* **14**, 485. 5) Kyte F.T., Zhou L. and Bohor B.F. (1991) *Meteoritics* **26**, 361.

456454

572-90

ABS-ONLY

LPSC XXIV

159

N9 4-4B 20792

COLLISION LIFETIMES AND IMPACT STATISTICS OF NEAR-EARTH ASTEROIDS;  
W. F. Bottke Jr., M. C. Nolan, and R. Greenberg, Lunar and Planetary Lab., University of Arizona

We have examined the lifetimes of Near-Earth asteroids (NEAs) by directly computing the collision probabilities with other asteroids and with the terrestrial planets. We compare these to the dynamical lifetimes, and to collisional lifetimes assumed by other workers. We discuss the implications of the differences.

The lifetimes of NEAs are important because, along with the statistics of craters on the Earth and Moon, they help us to compute the number of NEAs and the rate at which new NEAs are brought to the vicinity of the Earth. Assuming that the NEA population is in steady-state, the lifetimes determine the flux of new bodies needed to replenish the population. Earlier estimates of the lifetimes ignored (or incompletely accounted for) the differences in the velocities of asteroids as they move in their orbits, so our results differ from (for example) Greenberg and Chapman (1983, *Icarus* 55, 455) and Wetherill (1988, *Icarus* 76, 1) by factors of 2 to 10.

We have computed the collision rates and relative velocities of NEAs with a) each other, b) the main-belt asteroids, and c) the terrestrial planets, using the corrected method described by Bottke *et. al.* (1992, *GRL*, in press). The many recent discoveries of NEAs provide a more complete sample than was previously available, which presumably gives a better representation of the orbital distribution of NEAs.

We find that NEAs typically have shorter collisional lifetimes than do main-belt asteroids of the same size, due to their high eccentricities, which typically give them aphelia in the main belt. Consequently, they spend a great deal of time in the main belt, and are moving much slower than the bodies around them, making them "sitting ducks" for impacts with other asteroids. They cross the paths of many objects, and their typical collision velocities are much higher (10-15 km/s) than the collision velocities (~ 5 km/s) among objects within the main belt. These factors combine to give them substantially shorter lifetimes than had been previously estimated.

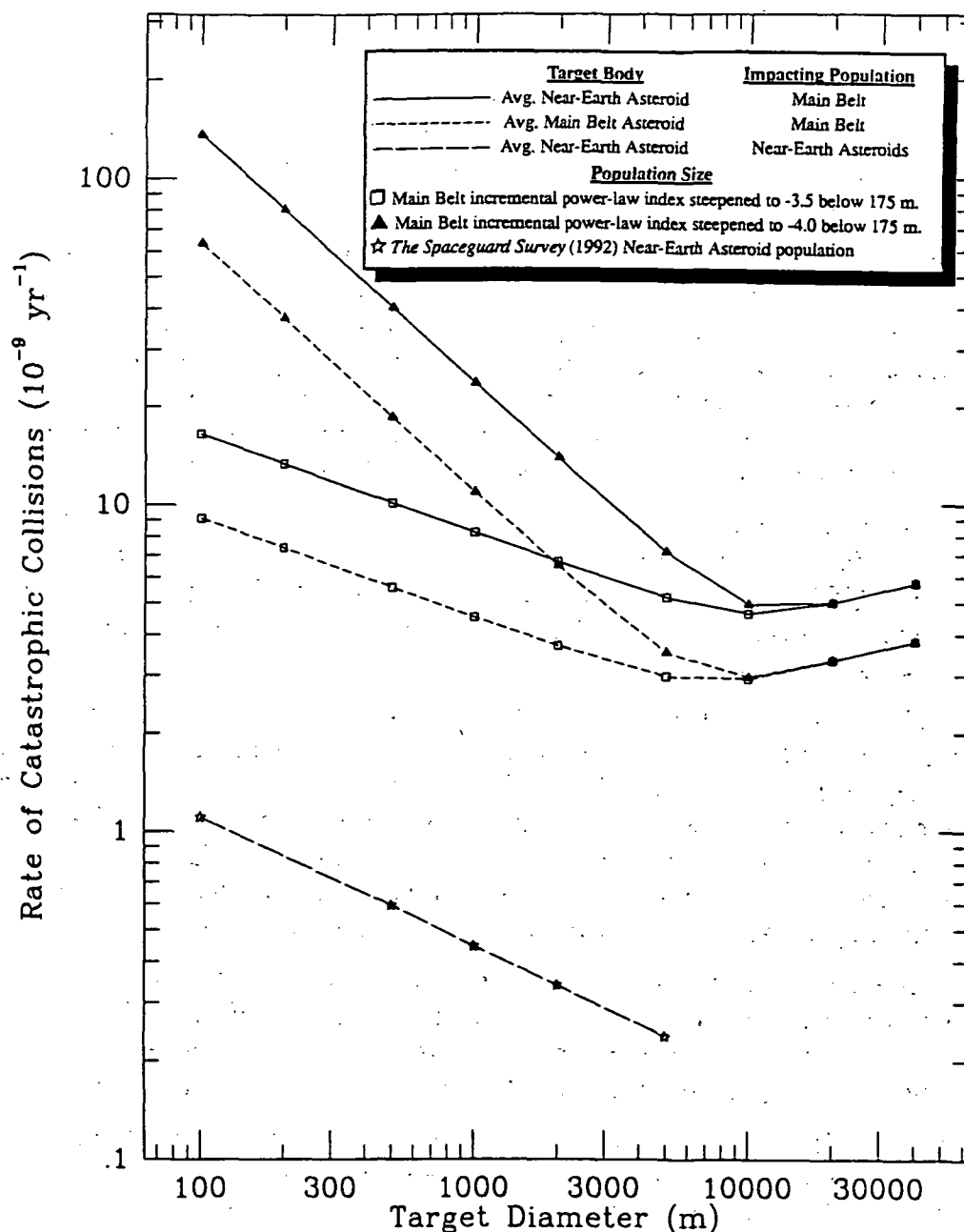
These short lifetimes imply one or more of the following: a) there are sources of NEAs other than those we understand, b) the known source mechanisms are more effective than has been suggested, possibly because there are more small objects in or near resonances than we can observe, or c) that earlier suggestions that many NEAs are extinct comets may be correct.

All these possibilities have implications for the impact rate of bodies onto the Earth. If the source mechanisms are more effective than believed, then the orbital distribution of NEAs will be dynamically "young", implying that Earth impacts are most likely at the asteroid's perihelion, observable as PM falls.

We have also computed the probability distributions for impact velocities between the Earth and observed NEAs, using the technique of Bottke and Greenberg (1993, *BAAS* 24, 960). Unlike previous methods, each possible orbital geometry for collision between pairs of bodies is included in the distribution according to its probability, rather than simply an average velocity for each NEA as in previously published velocity histograms. NEAs have a wide range of eccentricities, so that impacts can occur over a wide range of velocities. This method is important because it gives a complete representation of the probability of extreme (high and low) impact velocities, which can affect impact energy at the Earth.

C-4

## COLLISION LIFETIMES: W. F. Bottke Jr., M. C. Nolan, and R. Greenberg



For a target asteroid, which is an average member of a given orbital class, we show (as a function of its size) the frequency of catastrophic disruption events due to impacts from another class. Note that:

1. Near-Earth asteroids passing through the Main Belt are disrupted twice as often as Main Belt asteroids of the same size, due to their higher impact velocities. This result is independent of the size distribution of Main Belt asteroids.
2. Disruptions between average Near-Earth asteroids and the Near-Earth asteroid population occur at least 1-2 orders of magnitude less frequently than collisions with the Main Belt population. Therefore, they are not significant and can be neglected (except for the Atens, where few Main Belt crossings occur).

456455

578-46

LPSC XXIV

161

P.B.S. ONLY

N 94-1209.3

## AGE OF POPIGAI IMPACT EVENT USING THE $^{40}\text{Ar}$ - $^{39}\text{Ar}$ METHOD

R. J. Bottomley, Canadian Union College, College Heights, Alberta, Canada, T0C 0Z0, D. York, University of Toronto, Toronto, Ontario, Canada, M5S 1A7, and R. A. F. Grieve, Geophysics Division, Geological Survey of Canada, Ottawa, Ontario, Canada, K1A 0Y3.

The Popigai impact structure of central Siberia is the largest known impact crater in the Commonwealth of Independent States with an original diameter of some 100 km. The age of the crater is constrained by the existing stratigraphy to a period between 5-65 Ma (1). Attempts to date the impact event using conventional K-Ar on whole rock samples and fission track dating on glasses yield a spread of ages between 30 and 45 Ma (1-4). Argon step-heating analyses of several whole-rock samples performed with the Argon Laserprobe at the University of Toronto indicated an age of impact of about 36 Ma (5). However, a more recently reported  $^{40}\text{Ar}$ - $^{49}\text{Ar}$  result on glass separated from a suevite sample gave a 65 Ma age (6) and raised the possibility that Popigai was involved with the K/T boundary event. We have pursued further analyses at the University of Toronto on a broader spectrum of Popigai samples. These results confirm an age of about 36 Ma for the formation of this crater, and indicate that Popigai was not associated with the K/T boundary event.

We now have a total of 10 step-heating runs on a five different samples. These runs displayed several types of spectral shapes including plateaux. These assorted spectral shapes are common in melt rock morphologies and are indicative of the complex interaction of the different argon reservoir sites in these rocks (7).

Of the five different Popigai samples, two display horizontal plateaux on an age spectrum plot, two others display a step-wise rising pattern to a final age consistent with the plateaux age found in the previous samples, while the fifth sample gives a plot which oscillates around the approximate plateaux age with higher ages in the lower temperature fractions and lower ages in the higher temperature steps. All of these patterns are consistent with a resetting of the argon clock between 35-36 Ma ago. A simple average of the appropriate plateau fractions gives an estimate of the age of the Popigai impact event of  $35.7 \pm 0.8$  Ma. Thus analysis of whole rocks (as opposed to glass from suevites) indicates that Popigai was not associated with the K/T boundary event.

REFERENCES: (1) Masaitis, V.L., Mikhailov, M.V., and Selivanovskaya, T.V. (1975) Popigai Meteor Crater Nauka Press, Moscow 124pp; (2) Firsov, L.V. (1970) Dok. Nauk SSSR 194 664-666; (3) Komarov, A.N. and Rayhlin, A.I. (1976) Dok Nauk SSSR 228 673-676; (4) Storzer, D. and Wagner, G.A. (1979) Meteoritics 14 541-542; (5) Bottomley, R.J., and York, D. (1989) LPSC XX 101-102; (6) Deino, A.L., Garvin, J.B., and Montanari, A. (1991) LPSC XXII 297-298; (7) Bottomley, R.J., York, D., and Grieve, R.A.F., (1990) Proc. Lunar Planet. Sci. Conf. 20th, 421-431.

456456

379-90  
NBS ONLY

LPSC XXIV

163

N94-12094

V-2

MINOR AND TRACE ELEMENT COMPOSITION AND AGE OF YUKON PROBABLE-MICROTEKTITES; S. Q. Boundy-Sanders, Department of Geology, UC Berkeley, Berkeley, CA 94720 and R. L. Hervig, CSSS, Arizona State University, Tempe, AZ 85287.

Major, minor, and trace element composition of the candidate microtektites from Yukon Territory suggest a possible impact site of hydrothermally altered limestone and sand or chert, or possibly a carbonatite. Their REE/chondrite curve is similar in character to, but higher than, shale composites of North America, Australia, and Europe. Relative to these same composites, the Yukon droplets are enriched in Y, F, S, Sr, P, Mn, Mg, and Ca. They are depleted in Rb, Li, Th, Nb, Ti, K, Na, Fe, Si, and Al. Biostratigraphic constraints on the droplets indicate they are Middle to Late Devonian, more likely Middle Devonian, in age.

Table 1 shows major elements analyzed by electron probe, and minor and trace elements analyzed mostly by ion probe, with some repeated by electron probe. The high calcium and magnesium contents suggest a carbonate-rich source [1]. Alumina is low compared to shale composites and other microtektites and indicates a paucity of micas or clays. The extremely low Fe, K, and Na preclude any significant igneous component, except possibly carbonatite. The major element composition most strongly suggests a sedimentary carbonate-and-silica source, either dolomitic limestone and quartz sand, or dolomitic limestone and chert, in either case with minor amounts of clays or micas, but virtually no alkali feldspar or mafic grains. A sedimentary input is also suggested by the rare earth element pattern of the droplets, which is compared in Figure 1 to published shale composites [2-7] and the Beloc K-T glasses [8]. The Yukon REE pattern is similar in character to shale composite patterns, but richer in REE by 20 to 100%. Water content was measured by ion probe at  $<0.2$  wt % -- below the range for igneous rocks.

Of particular interest is the extremely high fluorine content of the droplets. The analyses will require careful calibration, but both electron and ion probe analyses indicate abundances of 1 wt %. Such high values are found in only a few environments, which we can evaluate based on major and trace element chemistry. Fluorine can be abundant in micas and clays, but the low alumina content of the Yukon droplets indicates that these phases were a minor component of the source and could only have provided a small portion of the observed REE. Fluorapatite could provide both F and REE, but the F/P weight ratio is inappropriate (0.2 for typical fluorapatite and ~4 for the Yukon droplets) and indicates that this too is at best only a partial contributor of F and REE. The most feasible source of fluorine appears to be fluorite- which would typically be found in hydrothermally altered limestone or in carbonatite and would likely be associated with high-REE minerals. Fluorine and REE values as high as these are found only in bodies of restricted size, and the data necessitate that the meteorite impact melted principally F-rich material. This indicates a small crater ( $<1/2$  km diameter) and therefore a small meteorite.

Sulfur values in the droplets are high and comparable to values in the Beloc glasses. However, since we don't know the source of the Yukon droplets, we can't identify a source phase as readily as Sigurdsson and co-workers were able to do for the Beloc glasses [8]. Evaporites, sedimentary-exhalative massive sulfides, Mississippi Valley-type deposits, and pyrite precipitated during prolonged worldwide oceanic anoxia are common in Early and Middle Paleozoic sedimentary rocks. All represent feasible sources for the sulfur. At this point, the sulfur represents a promising test of any proposed site but we don't yet regard it as a particularly useful beacon for locating potential sites.

The Yukon droplets are crystal-free glass and have a highly homogeneous composition. These attributes rule out origins as volcanic ejecta, fly ash, slag, and fulgurites [9-12]. All data so far are consistent with an impact origin of the Yukon droplets, and all other interpretations are ruled out by multiple lines of evidence.

A new biostratigraphic age constraint is provided by conodonts from Oklahoma, occurring with the same radiolarian species found at the Yukon droplet site. The conodonts suggest the droplets are more likely Middle than Late Devonian in age [13].

We gratefully acknowledge electron probe analyses by Charles E. Meyer of the U.S. Geological Survey, Menlo Park, and helpful discussions with Don Burt and John Holloway at ASU.

PRECEDING PAGE BLANK NOT FILMED

-162  
EXHIBITION ROOM

## COMPOSITION OF YUKON MICROTEKTITES: Boundy-Sanders S. Q. and Hervig R. L.

Oxide or element@	Yukon range	Shale composites	Beloc+	Element	Yukon range	Shale composites	Beloc+	Oxide or Element@	Yukon range	Shale composites	Beloc+
SiO <sub>2</sub>	44-47	62-63	48-52	La	51-55	32-41	18	U	1.1-4.8	3.1-3.2	1.2
Al <sub>2</sub> O <sub>3</sub>	7.5-8.6	18-19	12-14	Ce	94-99	73-81	36	Th	2.7-3.8	11-15	4.2-5.3
FeO	0.34-0.59	6.5-7.4	4.7-5.3	Pr	11-12	7.9-10	--	Zr	200-230	200-210	147
MgO	5.9-7.2	2.2-2.9	3.9-4.1	Nd	41-51	32-40	19	Nb	4.0-6.2	19-20	--
CaO	35-36	1.3-4.2	21-25	Sm	11-14	5.6-7.3	4.2	Cs	17-18	5-15	1.3
K <sub>2</sub> O	0.59-0.78	3.4-3.8	0.49-0.92	Eu	1.9-2.5	1.1-1.5	1.1	Be	0.8-0.9	--	1.1
Na <sub>2</sub> O	0.43-0.57	1.1-1.5	2.0-3.1	Gd	--	4.7-6.0	4.3	B	110-140	100	28
TiO <sub>2</sub>	0.40-0.55	0.8-1.0	0.53-0.81	Tb	1.3-2.1	0.77-1.0	0.7	Li	26-35	60-75	12.5
MnO	0.22-0.40	0.11-0.13	0.10-0.16	Dy	9.5-12	4.4-5.8	4.8	H <sub>2</sub> O	<0.2	--	--
SO <sub>3</sub>	0.57-0.91	--	0.77-0.92	Ho	2.2-2.9	1.0-1.2	--				
F	9000-11000	--	190	Er	5.5-8.9	2.9-3.6	--				
P	2400-3200	700-960	--	Tm	0.8-1.0	0.40-0.56	0.5				
Ba*	450-1100	580-650	760	Yb	--	2.8-3.3	2.8				
Sr	440-540	200-450	1200	Lu	0.7-1.1	0.43-0.58	0.37				
Rb	22-38	140-160	21	Y	77-83	27-30	--				

**Table 1.** Oxide and elemental composition of the Yukon droplets, with shale composites [2-4] and Beloc K-T glasses [5] for comparison. Symbols: @: Oxides except H<sub>2</sub>O and F by electron probe in weight %. Elements other than F are in ppm, H<sub>2</sub>O in wt. %, and were analyzed by ion probe. \*: range of compositions in Yukon droplets includes analyses by both electron and ion probe. +: values for Beloc glasses include several analytical methods; single values in Beloc column are averages. Major element data modified from [1].

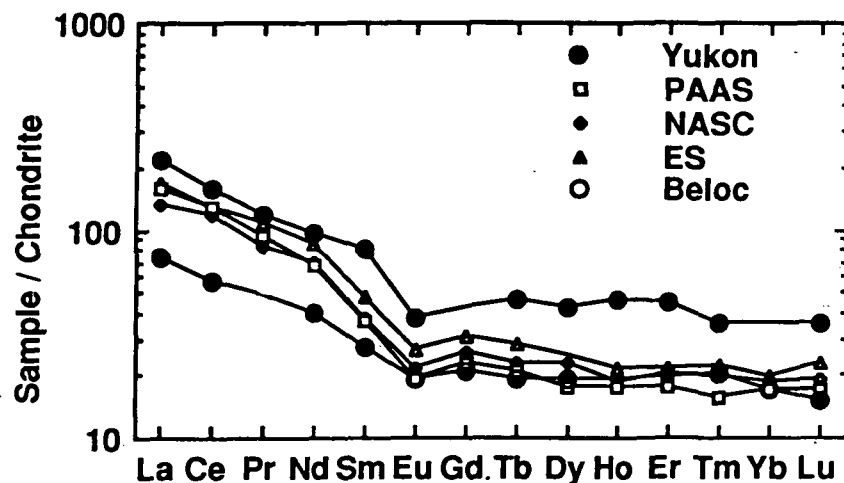


**Figure 1.** Rare earth pattern of Yukon droplets compared to shale composites and Beloc glasses [8]. PAAS = Post-Archean average Australian shale [5]; NASC = North American shale composite [6]; ES = European shale [7].

**REFERENCES** [1] Boundy-Sanders S. Q., Meyer C. E. and Jones D. L. (1992) *Eos*, 73(43), 328. [2] Taylor S. R. and McLennan S. M. (1985) *The continental crust: Its origin and evolution*, Blackwell. [3] Clarke F. (1924) *The data of geochemistry*, USGS Bull., 770. [4] Krauskopf K. B. (1967) *Introduction to Geochemistry*, McGraw-Hill. [5] Nance W. B. and Taylor S. R. (1976) *GCA*, 40, 1539. [6] Haskin L. A. et al. (1968) *J. Radioanal. Chem.*, 1, 337. [7] Haskin M. A. and Haskin L. A. (1966) *Science*, 154, 507. [8] Sigurdsson H., D'Hondt S. and Carey S. (1992) *EPSL*, 109, 543. [9] Keller G. et al. (1987) *Meteoritics*, 22, 25. [10] Byerly G. R., Hazel J. E. and McCabe C. (1990) *Meteoritics*, 25, 89. [11] Storzer D. (1992) *LPSC XXIII*, 1373. [12] Essene E. J. and Fisher D. C. (1986) *Science*, 234, 189. [13] P. Noble, pers. commun., 1992.

454460

ABSC 0147

163300

P. 2

A Structural Origin for the Cantaloupe Terrain of Triton: Joseph M. Boyce, Solar System Exploration, NASA, Washington D.C. 20546.

Cantaloupe terrain is unique to Triton. It is Triton's oldest terrain and includes about 250,000 km sq. region displaying sparsely cratered, closely spaced, nearly circular dimples about 30-40 km across. This terrain is found on no other planet because, only on Triton the final major global thermal pulse 1) caused completed (or nearly) interior melting resulting in a cooling history where large thermal stresses shattered and contorted a thin, weak lithosphere, and 2) occurred after heavy bombardment so that the surface features were preserved. The cantaloupe terrain is composed of intersecting sets of structures (folds and/or faults) that have developed as a result of global compression generated by volumetric changes associated with cooling of Triton's interior. Further, it is proposed that these structures developed after the period of heavy bombardment, and resulted from the last major global thermal epoch in Triton's unique history (either caused by tidal or radiometric heating). Initially, as the body cooled and the structures formed, their surface topography was most likely modified by thermal relaxation of the warm surface ices.

Difficulty in explaining this peculiar terrain is reflected in the number and variety of proposed origins including; a combination of viscous relaxation, collapse and sublimation (1, 2), interference pattern of intersecting structure sets (3,4), explosive volcanism (4,5,6), and diapirism (7). The lack of superposition and the uniformity in size and shape of the dimples suggest that impact cratering, collapse, sublimation or volcanism are not likely origins. Diapirism is also improbable because of 1) the necessity for major density instabilities in a highly differentiated body (ammonia-water liquid and coexisting ice phases have similar densities and are stable), 2) the lack of radial structures around the dimples, 3) the dimensions and uniformity in the spacing and size of the dimples is inconsistent with the general physical constraints of diapir formation, and 4) models for diapir development specific to Triton (8) are inconsistent with dimple size vs spacing (predicting ascent of only 1.0-1.5 times the views's radius before stopping). In addition, periglacial processes that form such features as pingos, patterned ground, alases, and 'oriented' lakes require freeze/thaw processes and mechanical properties of ices that are inconsistent with the large size of the features (dimples). Periglacial models raise mechanical problems with the materials involved.

Models for the early history of Triton all predict an initial period of global melting and differentiation associated with accretion. The density of Triton suggests that it formed in the solar nebula (9) though other later processes have altered its original composition (10,11,12). The peculiar orbit of Triton suggests capture (13,14,15), depending on the capture mechanism, may have resulted in substantial tidal heating during circularization of its orbit. The epoch of tidal heating may have lasted more than 500 m.y., and caused complete melting and



Cantaloupe Terrain: Boyce, J.M.

extensive chemical evolution of Triton (15,16). Stevenson and Gandhi (1990) predict that, even without tidal effects, internal heating and melting would be prolonged by decay of radiogenic elements in the high rock fraction of the satellite. In either case, significant global melting of Triton is predicted to continue for several hundred million years to a billion years after accretion. Triton may still be molten layer beneath about 200 km (10,12). Lunine and Nolan (1992) suggests that the early molten state may have been prolonged further due to the insulative effects of a transient atmosphere created by out-gassing of volatiles driven out by the thermal event.

Therefore, Triton has most likely undergone significant global heating, interior melting and differentiation, stabilization of the surface and subsequent cooling well after accretion. The sparsely cratered nature of all terrains (including the cantaloupe terrain) observed on Triton (Strom et al, 1990) is consistent with formation after heavy bombardment.. If this is correct, then on Triton, unlike other bodies, processes associated with the initial cooling of a molten or nearly molten body may have been recorded a the surface undestroyed by the "gardening" of heavy bombardment. (18,19,20,21) have pointed out the importance of the initial state and evolutionary path of a planet on the models of the thermal stress state. They indicate that thermal stresses are generally greater in the crust of bodies that were initially totally molten (like Triton) compared to those in bodies where only the outer portion was melted (Those that may have been accreted cold objects).

In other bodies like Mercury (22), thermal stresses generated from global cooling and contraction have resulted in widely spaced thrust faults, whereas on Triton, thermal stresses produced more closely-spaced folds and faults sets. This difference in structural style is probably due to differences in lithospheric properties (thickness, strength, etc.), the magnitude of stress (directly dependent on the thermal history), and when the structures formed, relative to the period of heavy bombardment.

References: 1) Smith, B. et. al, 1989, Science, 246, 1422-1449; 2) Boyce, J., Rogers, 1992, LPSC, 100; 3) Boyce, J., 1990, LPSC, 121; 4) Croft, S., 1990, LPSC, 245; 5) Strom, R., 1990, Science, 250, 437-440; 6) Schenk, P., 1992, LPSC, 1215-1216; 7) Schenk, P. & Jackson, M., 1992, Geology, in press; 8) Kirk, R., & Brown, R., 1991, LPSC, 721-722; 9) Lewis, J. 1971, Icarus, 15, 175; 10) Stevenson, D., et. al, 1986, in Satellites, 39-88; 11) Shock, E., & McKinnon, W., 1991, LPSC, 1251-1252; 12) Stevenson, D. & Gandhi, 1990, LPSC, 1202-1203; 13) McKinnon, W., 1984, Nature, 311, 355-358; 14) Goldreich, P. et. al., 1989, Science, 245, 500-504; 15) McKinnon, W., & Benner, L., 1990, LPSC, 777-778; 16) Ross, M., & Schubert, G., 1990, GRL, 17, 1749-1752; 17) Lunine, J., & Nolan, M., 1992, Icarus, 100, 221-234; 18) Solomon, S., 1986, in Origin of the Moon, 435-452; 19) Solomon, S., & Chaikin, J., 1976, Proc. LPSC, 3229-3243; 20) Binder, A., & Lange, 1980, JGR, 85, 3194-3243; 21) Binder, A., 1986, in Origin of the Moon, 411-433; 22) Strom, R., 1975, JGR, 80, 2478-2507.

456461

S81-25  
ABS ONLY

LPSC XXIV

167

N 943-102096

TRACE-ELEMENT ABUNDANCES IN SEVERAL NEW UREILITES William V. Boynton  
and Dolores H. Hill, Lunar and Planetary Laboratory, University of Arizona, Tucson AZ 85721

**Summary:** Four new ureilites are analyzed for trace-element abundances. Frontier Mountain (FRO) 90054 is an augite-rich ureilite and has high REE abundances with a pattern expected of augite. FRO 90036 and Acfer 277 have REE patterns similar to the V-shape pattern of other ureilites. Nuevo Mercurio (b) has very high REE abundances, but they look like they are due to terrestrial alteration. The siderophile-element pattern of these ureilites are similar to those of known ureilites.

**Introduction:** Ureilites are a group of enigmatic meteorites whose origin is unknown [1]. There appears to be a consensus that they have undergone igneous processing, but beyond that there is little agreement on the petrology of ureilites. Suggestions have been made that they formed by Ostwald ripening [2], as a residue from partial melting [3], as a cumulate [4], or by a three-stage [5] or a four-stage [6] igneous fractionation process. Their petrogenesis has been reviewed recently by Spitz [7].

**Samples:** In this work we have analyzed three new ureilites (FRM 90036 and FRO 90054, from Antarctica, and Acfer 277, from the Sahara) as part of a consortium effort lead by Robert Hutchison of the British Museum (Natural History), and a fourth meteorite Nuevo Mercurio (b) found in Zacatecas Mexico and supplied by Ron Farrell of Bethany Sciences. The consortium samples are described as heavily shocked (FRO 90036), lightly shocked and augite rich (FRO 90054), and moderately shocked (Acfer 277) [8]. Nuevo Mercurio (b) has been described by Treiman and Berkley [9]. It is a Group 1 ureilite (Kenna-like) and is altered from terrestrial exposure, containing calcite and silica in cracks and up to 1% nickel oxide in grain boundary alterations.

**Experimental:** So far the samples have been analyzed only via INAA using the U of A low-flux Triga reactor. Ureilites are known to have low REE abundances that require radiochemical separations to properly determine the shape of the REE pattern. We expect to have RNAA results for the REE at the conference.

**Results:** The siderophile-element abundances are plotted in Fig. 1a; literature data are shown in Fig 1b for comparison. The refractory, incompatible siderophiles (Re, Os, W, Ir) are correlated with each other and are more abundant than the volatile, compatible elements. At this time, only Ir could be determined among the former group in Nuevo Mercurio (b) as its abundance is low and the others are below detection limits. This incomplete siderophile-element pattern is consistent with this ureilite having abundances like that of Alan Hills (ALH) A81101, the only other ureilite with refractory siderophiles as low as the volatile siderophiles. Because of the formation of NiO in this meteorite due to alteration, the significance of this result cannot yet be determined. The W data in the two Frontier Mountain samples seem high. Contamination may well be responsible for this result, but at this time we do not fully understand the collection and curation processes and thus cannot say whether this hypothesis is likely.

The REE are plotted in Fig 2a, and literature data are shown in Fig 2b. The pattern of Nuevo Mercurio (b) is unlike that of any other ureilite and may well be a weathering artifact. Sample FRO 90054 has the highest REE of any known ureilite. The pattern is similar to that expected of an augite, and the data suggests that augite probably dominates the REE abundances. Unless augite is particularly coarse grained and heterogeneous, this result is not likely to be simply a sampling artifact, as we analyzed three splits totaling 460 mg, and each split showed a similar result. Without the RNAA data, it is difficult to say much about the REE in the other new ureilites except to say that they appear to have a normal V-shape pattern.

**Discussion:** At this early stage in our study, these new data provide little additional insight into the petrology of ureilites. Clearly no new arguments can be made to chose between the various hypotheses that have been offered. Nevertheless, the presence of FRO 900054, which

## TRACE-ELEMENTS IN UREILITES: Boynton W.V. and Hill D.H.

may be an end member in the igneous fractionation process, may be able to contribute to our understanding once the consortium can combine the constraints provided by the different investigations.

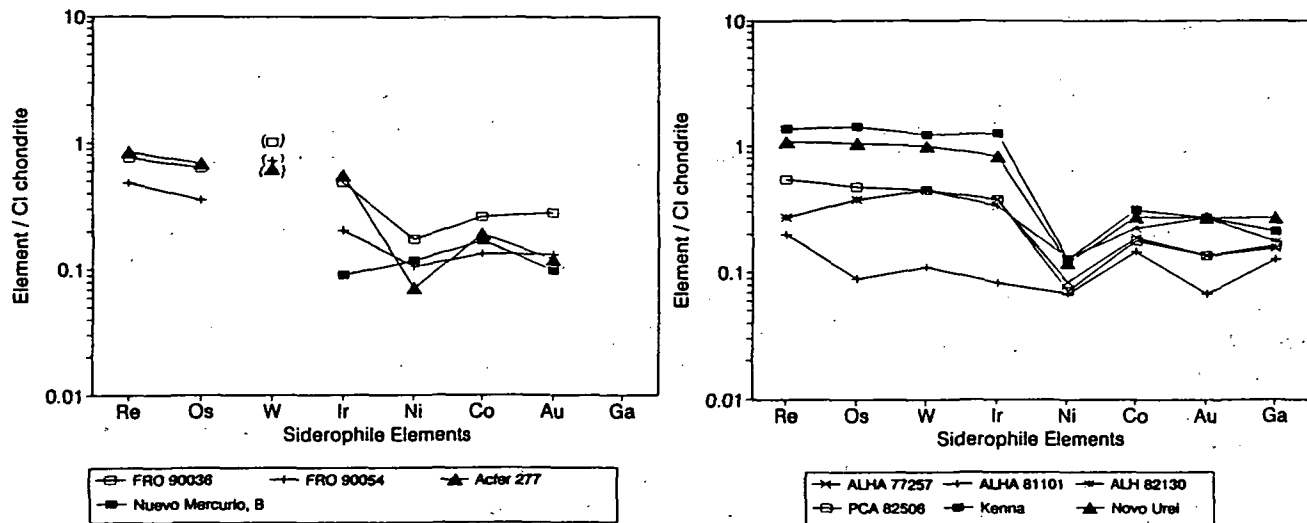


Figure 1. Siderophile-element data in ureilites; this work (a) and literature data from [1] (b). The new ureilites show the same type of pattern with the incompatible siderophiles (Re, Os, W, Ir) enriched by constant amounts relative to the compatible siderophile elements (Ni, Co, Au, Ga).

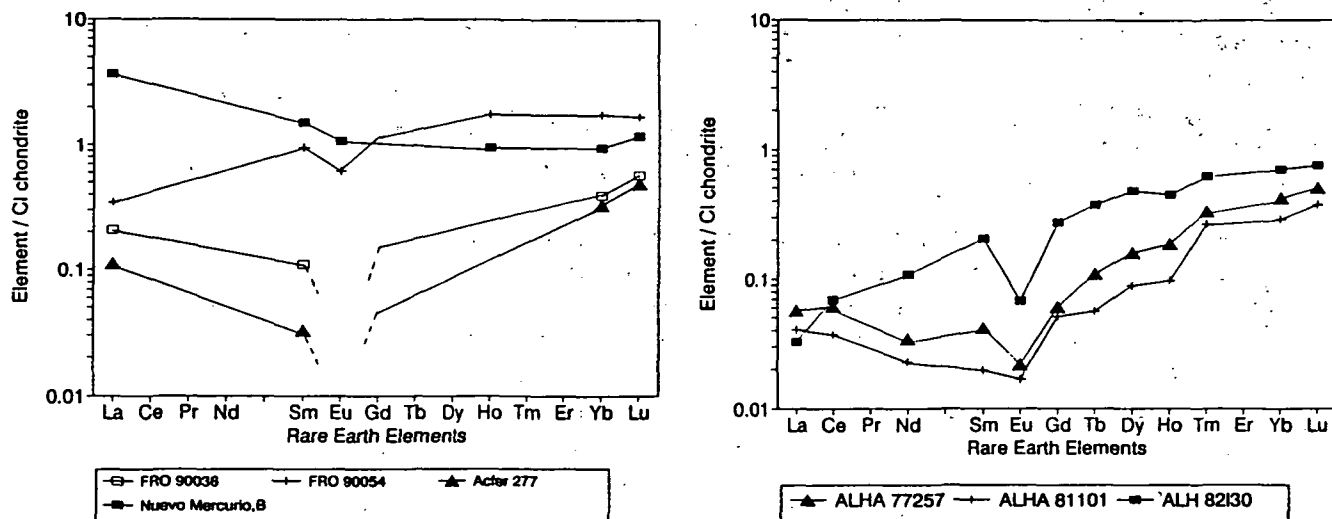


Figure 2. Rare-earth-element data in ureilites; this work (a) and literature data from [1] (b). Frontier Mountain 90054 has higher REE abundances than any known ureilite. The pattern is not the typical V-shape pattern or linear pattern found in other ureilites. It is similar to that expected of augite. The pattern of Nuevo Mercurio (b) may be due to terrestrial alteration

- References:** [1] Spitz A.H. and Boynton W.V. (1991) *Geochim. Cosmochim. Acta* **55**, 3417-3430. [2] Takeda H. (1987) *Earth Planet. Sci. Lett.* **81**, 358-370. [3] Boynton W.V., Starzyk P.M. and Schmitt R.A. (1976) *Geochim. Cosmochim. Acta* **40**, 1439-1447. [4] Berkley, J.L., Taylor G.J., Keil K., Harlow G.E. and Prinz M. (1980) *Geochim. Cosmochim. Acta* **44**, 1579-1597. [5] Goodrich C.A. and Jones J.H. (1987) *Lunar Planet. Sci.* **XVIII**, 347-348. [6] Goodrich C.A., Jones J.H. and Spitz A.H. (1987b) *Meteoritics* **22**, 392-394. [7] Spitz A.H. (1991) Ph.D. Thesis, The University of Arizona, Tucson, 232 pp. [8] Robert Hutchison (1992) personal communication. [9] Treiman A.H. and Berkley J.L. (1992) *Lunar Planet. Sci.* **XXIII**, 1449-1450.

456462

582-43  
ABS ONLY

LPSC XXIV

169

N94-12097

COMPOSITIONAL AND TEXTURAL INFORMATION FROM THE DUAL INVERSION OF VISIBLE, NEAR AND THERMAL INFRARED REMOTELY SENSED DATA; Robert A. Brackett and Raymond E. Arvidson, Department of Earth and Planetary Sciences, McDonnell Center for the Space Sciences, Washington University, St. Louis, MO 63130; 314-935-4888; Internet: brackett@wunder.wustl.edu.

A technique is presented that allows extraction of compositional and textural information from visible, near and thermal infrared remotely sensed data. Using a library of both emissivity and reflectance spectra, endmember abundances and endmember thermal inertias are extracted from AVIRIS (Airborne Visible and Infrared Imaging Spectrometer) and TIMS (Thermal Infrared Mapping Spectrometer) data over Lunar Crater Volcanic Field, Nevada, using a dual inversion. The inversion technique is motivated by upcoming Mars Observer data and the need for separation of composition and texture parameters from subpixel mixtures of bedrock and dust.

*Dataset:* The analysis used data from two instruments flown during the Geologic Remote Sensing Field Experiment (GRSFE) in 1989 at which time remote sensing data from visible to radar wavelengths were acquired over Lunar Crater Volcanic Field, Nevada, simultaneously with ground observations [1]. AVIRIS is a visible and near-infrared spectrometer that acquires 224 channels of data from 0.4  $\mu\text{m}$  to 2.5  $\mu\text{m}$ . TIMS is a thermal infrared spectrometer which acquires 6 bands of data from 8.0  $\mu\text{m}$  to 12.0  $\mu\text{m}$ . These two instruments imaged Lunar Crater Volcanic Field, a Miocene-age caldera complex located in northern Nye County, Nevada, dominated by rhyolite ash-flows, basalt cones and flows, and typical arid to semi-arid landforms (e.g., development of desert pavements, desert varnish, alluvial fans, caliche, and playa and aeolian deposits) [2].

*Inversion:* Initially, field and/or laboratory spectra (both reflectance and emission) are acquired for a set of endmembers that are chosen to represent the lithologic units present in the field area (e.g., rhyolite, basalt, playa, sand, caliche). The AVIRIS and TIMS images are corrected for atmospheric effects using the LOWTRAN-7 software and reduced to units of reflectance and emittance, respectively [3]. The AVIRIS dataset is then used in a linear mixing model to determine for each pixel the areal abundance of each endmember [4]. These endmember abundances are then used as a constraint on the inversion of several TIMS scenes obtained at multiple times during the diurnal cycle. The emittance,  $F(\lambda)$ , received by a given TIMS band is assumed to be the sum of the radiance of the  $N$  endmembers of the pixel:

$$F(\lambda) = \sum_{i=1}^N f_i \varepsilon_i(\lambda) \sigma T_{k,i}^4$$

where  $f_i$  is the fractional area of endmember  $i$ ,  $\varepsilon_i(\lambda)$  is the emissivity spectra of endmember  $i$ ,  $\sigma$  is the Stefan-Boltzmann constant, and  $T_{k,i}$  is the kinetic temperature of endmember  $i$ . Note that  $f_i$  is known from the linear inversion of AVIRIS data and  $\varepsilon_i(\lambda)$  is obtained from

## DUAL INVERSION OF VISIBLE AND IR REMOTE DATA, Brackett R.A. and Arvidson R.E.

field and/or laboratory spectra.  $T_{k,i}$  is the sole unknown parameter in this equation. This equation is cast into the form of a set of linear equations and inverted for the kinetic temperature of each endmember. One inversion is performed for each time of day at which a TIMS scene was acquired. The result is a map of kinetic temperature versus time of day for each endmember. This inversion does not require the assumption of constant emissivity in TIMS band 6 (*cf.* [5]) or isothermal endmembers [6]. A nonlinear inversion is then performed to extract apparent thermal inertia [7] of the endmembers from these thermal histories of each endmember at each pixel. Note that apparent thermal inertia is  $\approx \sqrt{k\rho c}$ , where  $k$  is thermal conductivity,  $\rho$  is density, and  $c$  is specific heat [8, 9]. The inversion results in maps of the apparent thermal inertia of each of the endmembers.

*Assumptions:* Several assumptions are implicit in this inversion: first, that macroscopic mixing dominates microscopic mixing [4]; second, that the endmember spectra in reflectance correspond to the endmember spectra in emission; third, that the surface is vertically homogenous at the scale of the diurnal skin depth; finally, that environmental parameters (*e.g.*, latent heat, sensible heat flux) are small. This final assumption is testable using a simple one-dimensional thermal conduction model [10], constrained by field meteorological observations acquired during GRSFE.

*Discussion:* The model employed offers the opportunity to extract compositional and textural information for a variety of endmembers within a given pixel. Geologic inferences concerning grain size, abundance, and source of endmembers can be made directly from the inverted data. These parameters are of direct relevance to Mars exploration, both for Mars Observer and for follow-on missions.

## REFERENCES:

- [1] Arvidson R. *et al.* (1991) CD-ROM Volume USA\_NASA\_PDS\_GR\_0001.
- [2] Kleinhampl F. and J. Ziony (1985) Geology of Northern Nye County, Nevada.
- [3] Kneizys F. *et al.* (1988) User's Guide to LOWTRAN-7 Rep. AFGL-TR-88-0177.
- [4] Singer R. and T. McCord (1979) Proc. Lunar Sci. Conf. **10** p. 1835-1848.
- [5] Kahle A. and R. Alley (1992) Rem. Sens. Environ. **42** p. 107-111.
- [6] Gillespie A. (1992) Rem. Sens. Environ. **42** p. 137-145.
- [7] Price J. (1977) J. Geophys. Res. **82** p. 2582-2590.
- [8] Kahle A. and R. Alley (1985) Photogrammetric Eng. and Rem. Sens. **51** p. 73-75.
- [9] Jakosky B. (1979) J. Geophys. Res. **84** p. 8252-8262.
- [10] Kahle A. (1977) J. Geophys. Res. **82** p. 1673-1680.

456463

383-90

LPSC XXIV

171

ABS ONLY 94-132098

P. 2

**UNEQUILIBRATED, EQUILIBRATED, AND REDUCED AGGREGATES IN ANHYDROUS INTERPLANETARY DUST PARTICLES, J. P. Bradley, MVA Inc., 5500/200 Oakbrook Pkwy., Norcross, GA 30093**

Track-rich anhydrous IDPs are probably the most primitive IDPs because a) they have escaped significant post-accretional alteration, b) they exhibit evidence of (nebular) gas phase reactions [1-3], c) their mineralogy is similar to comet Halley's dust [4], d) some of them exhibit comet-like IR spectral characteristics [5]. However, basic questions about the mineralogy and petrography of anhydrous IDPs remain unanswered, because they contain aggregated components that can be heterogeneous on a scale of nanometers (Fig. 1). In some IDPs, aggregates account for >75% of the volume of the particle. The aggregates have been systematically examined using an analytical electron microscope (AEM), which provides probe-forming optics and (x-ray and electron) spectrometers necessary to analyze individual nanometer-sized grains. The AEM results reveal at least three mineralogically distinct classes of aggregates in anhydrous IDPs, with mineralogies reflecting significantly different formation/aggregation environments.

The IDPs studied are U219C2, U219C11, U220A19, U222B28, U230A3, W7027A11, and W7027H14. They were embedded, thin-sectioned, and examined using brightfield and darkfield imaging. Mineral compositions were measured using energy-dispersive x-ray spectroscopy (EDS) and electron energy-loss spectroscopy (EELS). Local solid state environments of specific elements within aggregates were investigated using energy-loss near edge structure analysis (ELNES) (Fig. 2) [5]. Crystallographic parameters of mineral grains were determined using lattice fringe imaging, selected area electron diffraction, and microdiffraction.

Three classes of aggregates were studied: unequilibrated, equilibrated, and reduced aggregates. **Unequilibrated aggregates (UA's)** contain crystalline grains, typically between 1 and 40 nm diameter, embedded in non-crystalline material (Fig. 1). Bulk compositions of UA's are approximately chondritic although sulfur is often significantly depleted [6]. The compositions of individual grains and (non-crystalline) matrix were investigated using EDS and ELNES. EDS analyses suggest that most grains contain either major Fe and minor Ni, or major Fe and S. Microdiffraction patterns confirmed that the grains are kamacite (FeNi) and FeS respectively. Figure 2 (column A) shows the O-K, Mg-K, Si-K, and Fe-L core scattering edges from an unequilibrated aggregate. Mg-K and Si-K edges from both crystalline and non-crystalline silicates are shown in columns B and C. Comparison of near edge structures for Mg and Si (columns A through C) suggest that most of the Mg and Si in the aggregate are within a non-crystalline environment (i.e. glass) rather than crystals. The near edge structure of the O-K edge (column A) is compatible with silicate glass or crystals, although there is evidence (arrowed) of oxides (e.g. magnetite) (see [7]). EDS analyses suggest that the non-crystalline matrix typically contains major Mg and Si, and sometimes Al, Ca, and Fe, although the matrix composition can vary significantly on a nanometer scale. **Equilibrated aggregates (EA's)** exhibit distinct igneous textures and grain sizes between 0.1 and 0.5  $\mu\text{m}$ . Olivine and pyroxene (with equilibrated Mg/Fe ratios), Fe-sulfides, and feldspathic glass are the most common minerals. Petrographic evidence suggests that EA's may have formed from UA's by melting and recrystallization, possibly in the solar nebula. **Reduced aggregates (RA's)** contain FeNi metal, FeNi carbides, and Fe-rich sulfides embedded in carbonaceous material. The FeNi carbides and carbonaceous material may have formed by catalytic reactions between FeNi metal and carbon-containing gas (e.g. CO) [2]. RA's may contain organic carbon.

In summary, anhydrous IDPs contain at least three types of aggregates. On a scale of <0.1  $\mu\text{m}$ , glass is the predominant silicate in anhydrous IDPs, and the abundance of glass suggests a possible link between aggregates in anhydrous IDPs and IR silicate emission from comets and interstellar grains [4]. Kamacite, which is rare as large grains, is the most abundant nanometer-sized grain in UA's. Metallic Fe provides further evidence for the survival of high temperature condensates in anhydrous IDPs [1, 3, 8, 9].

## References

- [1] Bradley, J. P., Brownlee, D. E., Veblen, D. R. (1983) *Nature*, 301, 473. [2] Christoffersen R. and Buseck, P. R. (1983) *Science*, 222, 1327. [3] Klöck, W., Thomas, K. L., McKay, D. S., & Palme, H. (1989) *Nature*, 339, 126. [4] Bradley, J. P., Humecki, H. J., Germani, M. S. (1992) *Ap. J.*, 394, 643. [5] Taftø, J. and Zhu, J. (1982) *Ultramicroscopy*, 9, 349. [6] Bradley, J. P. (1988) *Geochim. Cosmochim. Acta*, 52, 889. [7] Bradley, J. P. (1991), *Meteoritics*, 26(4), 322a. [8] Christoffersen, R. and Buseck, P.R. (1986) *Science*, 234, 590. [9] Zolensky, M. E. (1987) *Science*, 237, 1466.

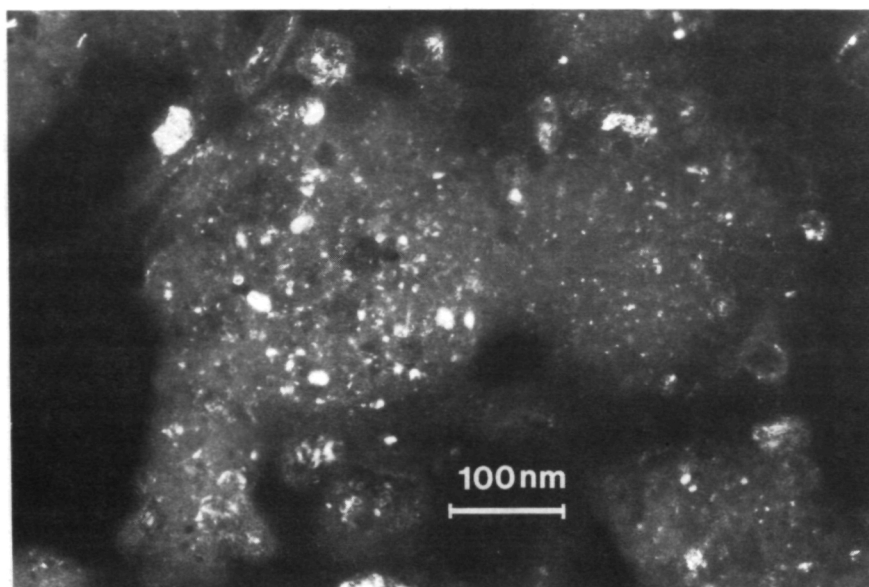


Figure 1. Darkfield micrograph of unequilibrated aggregates in IDP U22019.

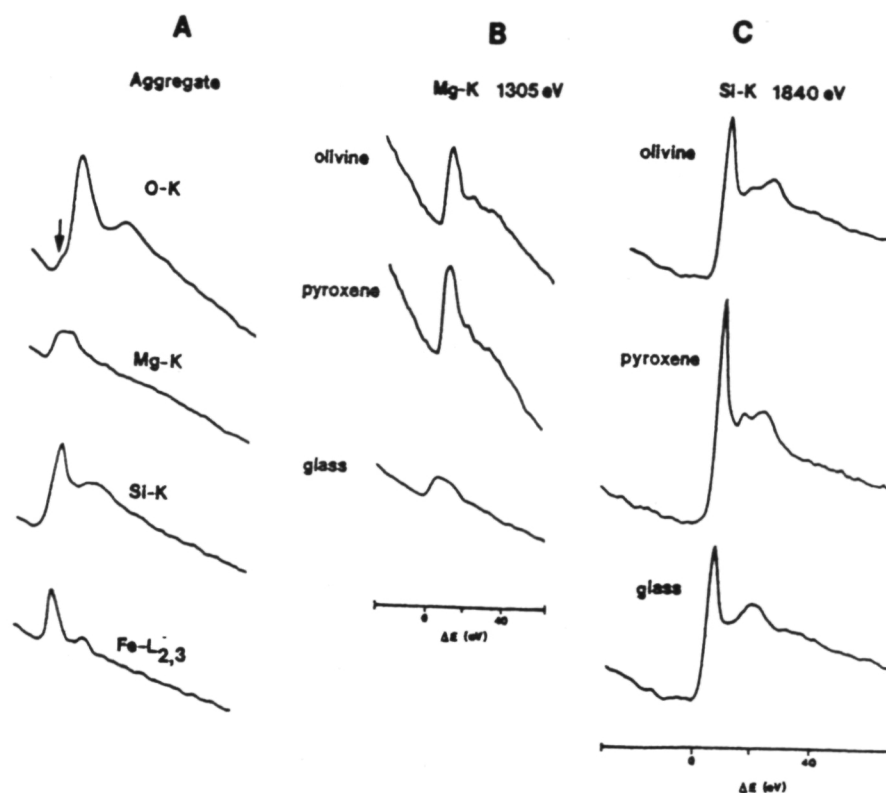


Figure 2. Column A - O, Mg, Si, and Fe energy-loss core scattering edges from an unequilibrated aggregate. Column B -- Mg-K edges in crystalline silicates and glass. Column C -- Si-K edges from crystalline silicates and glass.

456464

584-25

ABS ONLY

LPSC XXIV

173

N94-123099

P-2

**CARBON ANALYSES OF IDPS SECTIONED IN SULFUR AND SUPPORTED ON BERYLLIUM FILMS**, J. P. Bradley<sup>1</sup>, L. Keller<sup>2</sup>, K. L. Thomas<sup>3</sup>, T. B. Vander Wood<sup>1</sup>, and D.E. Brownlee<sup>4</sup>. <sup>1</sup>MVA Inc., 5500/200 Oakbrook Pkwy., Norcross, GA 30093; <sup>2</sup>NASA JSC, SN4, Houston, TX 77058; <sup>3</sup>Lockheed, Code 23, Houston, TX 77058; <sup>4</sup>University of Washington, Seattle, WA 98195.

Carbon is the only major element in interplanetary dust whose abundance, distribution and chemical state are not well understood. Information about carbon could clarify the relationship between the various classes of IDPs, conventional meteorites, and sources (e.g. comets vs. asteroids). To date, the most reliable estimates of C abundance in IDPs have been obtained by analyzing particles on thick-flat Be substrates using thin-window energy-dispersive spectroscopy in the SEM [1, 2]. These estimates of C abundance are valid only if C is homogeneously distributed, because detected C x-rays originate from the outer 0.1  $\mu\text{m}$  of the particle [1]. An alternative and potentially more accurate method of measuring C abundances is to analyze multiple thin sections (each  $<0.1 \mu\text{m}$  thick) of IDPs. These efforts however, have been stymied because of a lack of a suitable non-carbonaceous embedding medium and the availability of C-free conductive substrates. We have embedded and thin-sectioned IDPs in glassy sulfur, and transferred the thin sections to Be support films  $\sim 25 \text{ nm}$  thick. The sections were then analyzed in a 200 KeV analytical TEM. S sublimates rapidly under vacuum in the TEM, leaving non-embedded sections supported on Be. Apart from quantitative C (and O) analyses, S sectioning dramatically expands the range of analytical measurements that can be performed on a single IDP.

An IDP mounted on a stereomicroscope hot stage is enveloped within a droplet of molten sulfur (100 - 400  $\mu\text{m}$  diameter). The droplet is agitated with a tungsten or glass needle until the IDP is well embedded in the sulfur. After the sulfur droplet has cooled and solidified, it is mounted on the end of a regular epoxy stub for ultramicrotomy. The sulfur is trimmed with a glass knife and sectioned as if it were epoxy [3]. The sections (50-100 nm thick) are floated on water and transferred to continuous Be films (20-25 nm thick) supported on TEM grids (Fig. 1).

Thin-sections were analyzed in a TEM (JEOL 2010) equipped with an ultrathin window EDS system. The Cliff-Lorimer thin-film correction procedure was employed to measure C and other elements [4]. We used silicon carbide (SiC) supported on Be to derive an experimental K-factor (relative to Si) for C, and NIST thin-film glass SRM2063, synthetic  $\text{Ni}_2\text{SiO}_4$ , and mineral standards to derive K-factors for the other elements. While acquiring x-ray spectra from the standards, we monitored the electron energy loss spectroscopy (EELS) zero loss and plasmon regions to confirm that light element x-ray absorption was minimized.

Table 1 (column 1) lists an EDS thin-film analysis of spurrite ( $2\text{Ca}_2\text{SiO}_4 \cdot \text{CaCO}_3$ ); column 2 lists the theoretical element abundances for spurrite. Comparison of columns 1 and 2 illustrates the potential of thin-film analysis for light element measurements. The relative error of the C analysis is  $<25\%$  (c.f. columns 1 and 2), although both the precision and accuracy of thin-film analysis need to be established by analyses of multiple C-bearing standards. Relative error of  $\sim 25 \text{ wt } \%$  is typical for heavier elements at similar concentrations [5]. Table 1, columns 3-5 list analyses of thin sections of IDP L2006H5 which had been embedded in S, thin-sectioned using ultramicrotomy, and mounted on thin (25 nm thick) Be films on Cu TEM grids. L2006H5 is a hydrated IDP whose carbon abundance was measured at 8.0 wt % in the SEM prior to sulfur embedding and thin-sectioning (column 6). The relative analytical error of SEM carbon analysis (column 6) is reported to be on the order of 20% [1].

We have developed a particle thin-sectioning method which does not require organic embedding media and carbon support substrates. Thin sections can now be mapped for light elements (C, N, and O) using EDS or EELS mapping procedures. Electron energy loss near edge structure analysis (ELNES) can be used to investigate the state of the carbon, and organic carbon can be measured using infrared (IR) microspectroscopy. Unsectioned material can be recovered from the sulfur mount, simply by heating and sublimation of the sulfur, and be made available for other purposes such as noble gas measurements and trace element analysis.



## IDPs SECTIONED IN SULFUR, J.P. Bradley

## References

[1] Thomas K. L., et al., (1993) *Geochim Cosmochim. Acta*, in press. [2] Keller, L., et al., (1993) *LPSC*, this volume. [3] Bradley, J. P. (1988) *Geochim Cosmochim. Acta*, 52, 889. [4] Cliff, G., and Lorimer, G.W., (1975) *J. Microsc.*, 103, 203. [5] Germani M. S., Bradley, J. P., and Brownlee, D. E. (1991) *Earth Planet. Sci. Lett.*, 101, 162.

Table 1 - Quantitative thin-film analyses

	<u>1</u>	<u>2</u>	<u>3</u>	<u>4</u>	<u>5</u>	<u>6</u>
C	3.03	2.7	11.73	7.89	6.15	8.0
O	37.4	39.58	43.87	38.58	39.4	36.3
Mg	-	-	5.2	4.83	5.32	8.6
Al	-	-	1.23	1.47	1.26	1.2
Si	13.94	12.64	14.42	16.82	17.2	17.6
S	-	-	5.96	8.9	8.32	7.4
Ca	45.62	45.1	-	-	-	0.2
Cr	-	-	0.35	0.4	0.32	0.2
Fe	-	-	16.46	20.19	21.32	18.5
Ni	-	-	0.76	0.85	0.87	1.1

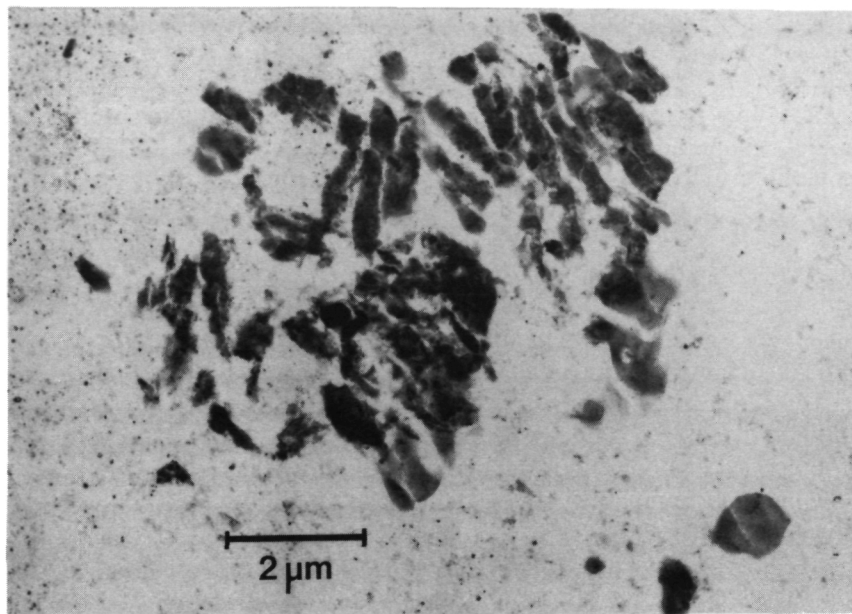


Figure 1. Brightfield micrograph of a thin section of IDP L2005H5 supported on a polycrystalline beryllium film.

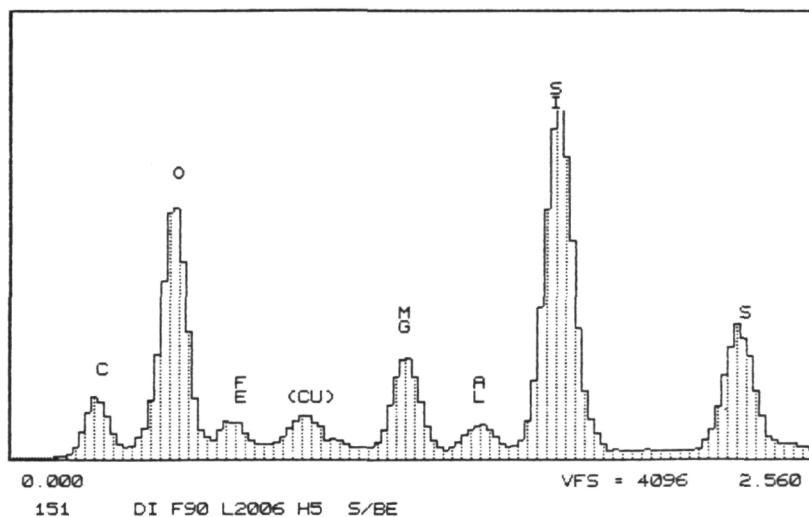


Figure 2. Energy dispersive x-ray spectrum of a thin section of IDP L2005H5. (Cu) is a system peak.

585-91

ABS ONLY

LPSC XXIV

175

456466

N 94-12100

## MODERN SHELF ICE, EQUATORIAL AEOLIS QUADRANGLE, MARS

G. R. Brakenridge, Surficial Processes Lab, Dept. of Geography, Dartmouth  
College, Hanover NH 03755 USA

As part of a detailed study of the geological and geomorphological evolution of Aeolis Quadrangle, I have encountered evidence suggesting that near-surface ice exists at low latitudes and was formed by partial or complete freezing of an inland sea. The area of interest is centered at approximately  $-2^{\circ}$ ,  $196^{\circ}$ . It lies within the "Younger channel and floodplain material, undivided" unit mapped at this location by the Greeley and Guest (1987) 1:15,000,000 geological map. The area also lies within one of the several broad regions of low thermal inertia discussed by Paige (1992, *Nature*, v. 356, p. 43-45) as potential locations of stable ground ice at low latitudes. As seen in a suite of Viking Orbiter frames obtained at a range of  $\sim 600$  km (frames 725A35-A19), the plains surface at this location is very lightly cratered or uncratered, and it is thus of late Amazonian age. It exhibits an unusual pattern of intersecting, very low-relief linear or sinuous ridges that may define ridge-interior, polygon-shaped, mainly angular but sometimes rounded ice cakes and ice floes (see figure). The ice, if it exists, is now frozen together into extensive composite floes that exhibit features analogous to terrestrial shelf ice, such as shear zones and pressure ridges. Scattered  $\sim 10$  km diameter craters form isolated, still-subaerial uplands that are more heavily cratered: these uplands are apparently older than the surrounding "ice floes" and are embayed by the ice-covered sea or the grounded ice (see figure). Extant topographic data indicate that the Amazonian plains at this location occupy a trough whose surface lies at least 1000 m below the Mars datum. A reasonable hypothesis is that quite recent surface water releases, perhaps associated with final evolution of large "outflow chasms" to the south, but possibly from other source areas, filled this trough, that ice floes formed almost immediately, and that either grounded ice or an ice-covered sea still persists. In either case, the thin (a few meters at most) high albedo, low thermal inertia cover of aeolian materials was instrumental in allowing ice preservation, and at least the lower portions of this dust cover may be cemented by water ice. Detailed mapping using Viking stereopairs and quantitative comparisons to terrestrial shelf ice geometries are underway.

## MODERN SHELF ICE, MARS: G. R. Brakenridge

FIGURE. Viking Orbiter frames 725A35,A33, A31 illustrating possible eolian dust-covered shelf ice. Dimensions of scene below are approximately 9.7 x 23 km.



456467

586-90  
ABS. ONLY

LPSC XXIV

177

N94<sup>3</sup>12101

**MINERALOGY VERSUS BULK COMPOSITION OF THE CARBONACEOUS CHONDRITE CLAST KAIDUN II.** F. Brandstätter and G. Kurat, Naturhistorisches Museum, Postfach 417, A-1014 Vienna, Austria, A.V. Ivanov, Vernadsky Institute of Geochemistry and Analytical Chemistry, Moscow 117975, Russia, H. Palme and B. Spettel, Max-Planck-Institute für Chemie, D-65 Mainz, Germany.

Kaidun is an unusual chondritic meteorite. Its main mass is of CR-type (Kaidun I) and contains CI-like (Kaidun II), EL, and EH clasts [1,2]. As already noticed in [2] the classification of Kaidun II based on mineralogy and bulk chemical criteria does not allow an unambiguous assignment to CI. Here we report on the bulk chemical composition and the mineralogy of the Kaidun II clasts. The results of our investigation show that Kaidun II has some characteristics of both CI and CM chondrites. A possible relationship to the texture and composition of micrometeorites is indicated.

**Mineralogy** Kaidun II consists mainly of matrix dominated by phyllosilicates (serpentine and saponite, [3]) and variable amounts of opaque phases (mostly magnetite and pyrrhotite) with morphologies typical of CIs. Less abundant, but not rare are isolated grains ( $< 10\mu\text{m} - 30\mu\text{m}$ ) of anhydrous silicates and carbonates [4]. Among the silicates forsteritic olivine (Fo96 - Fo99) is most abundant followed by enstatite. In addition, a few grains of Fe-rich olivine (down to Fo42) and Ca-rich pyroxene have been encountered. Calcite is the dominant carbonate, less common is dolomite.

**Mineral composition** The Mg-rich olivines have generally high minor element contents. CaO, MnO and Cr<sub>2</sub>O<sub>3</sub> vary from  $<0.02-0.62$ ,  $<0.02-2.5$  and  $0.13-1.30$  wt.-%, respectively. The contents of Al<sub>2</sub>O<sub>3</sub> and TiO<sub>2</sub> are on average  $<0.05$  wt.-%. Enstatites (0.80-3.50 wt.-% FeO) are also rich in minor elements. The ranges for CaO, MnO, Cr<sub>2</sub>O<sub>3</sub>, Al<sub>2</sub>O<sub>3</sub> and TiO<sub>2</sub> are 0.37-2.15, 0.05-0.51, 0.02-0.97, 0.10-1.86 and 0.05-0.18 wt.-%, respectively. Calcites are relatively rich in FeO (1.1-1.3 wt.-%) and poor in MnO ( $<0.02-0.05$ , whereas the dolomites are rich in FeO (4.1-4.7 wt.-%) and in MnO (2.1-4.5 wt.-%).

**Matrix composition** The bulk composition of the matrix in Kaidun II has been determined by electron microprobe defocussed beam technique. Normalized elemental abundances (average of 54 analyses) and averaged analyses of CI and CM matrices as given by [5] are listed below.

Na/Si	Mg/Si	Al/Si	S/Si	K/Si	Ca/Si	Ti/Si	Cr/Si	Mn/Si	Fe/Si	Ni/Si	
0.025	0.620	0.068	0.444	0.006	0.046	0.004	0.019	0.011	1.907	0.096	KaidunII
0.013	0.796	0.090	0.147	0.015	0.015	0.002	0.022	0.009	1.072	0.099	CI,[5]
0.031	0.828	0.116	0.221	0.006	0.041	0.004	0.018	0.012	1.859	0.120	CM,[5]

**Bulk composition** Three samples of Kaidun MKD2, MKD7 (compact type) and MKD8 (fluffy type) which were assumed to be of CI-type composition have been analyzed by neutron activation analysis. MKD2 corresponds to the sample previously described as Kaidun II [1, 2]. CI-normalized abundances of lithophile and siderophile elements are shown in Figures 1 and 2, respectively.

**Discussion** Except for the generally high MnO contents forsteritic olivines in Kaidun II are similar in their minor element contents to forsterites in CI chondrites (e.g., [6]). Low-Fe, Mn-enriched olivines (and pyroxenes) are not known to occur in CI and CM chondrites. However, they have been described from chondritic porous IDPs and UOCs [7] and micrometeorites [8]. The abundance and chemical composition of carbonates in Kaidun II shows some distinct differences to carbonates previously described from CIs and CMs [9,10,11]. In Kaidun II, like in CMs, calcite is the most abundant carbonate. In contrast, dolomite [9] or subequal amounts of dolomite and ferroan magnesite [10] are most abundant carbonates in CIs. The Kaidun calcites are clearly richer in Fe and poorer in Mn when compared to calcites from CIs as well as to those from CMs [9]. The bulk matrix composition of Kaidun II (Table) shows some significant similarities with CM matrices. Si-normalized abundances of Fe, Mn, Cr, Ti, Ca, and K closely match the corresponding CM abundances. For Al and Mg the relation Kaidun II  $<$  CI  $<$  CM holds, whereas S abundances are definitely higher when compared to CI and CM matrices. The Ni/Si ratio is similar to the CI matrix average. The Na/Si ratio is intermediate between that of CI and CM matrices. A comparison of bulk elemental abundances of the MKD2 (Kaidun II), MKD7 and MKD8 (Fig.1,2) reveals some significant differences among these samples. **MKD2:** Refractory lithophile elements are slightly enriched ( $1.07-1.3\times\text{CI}$ ), a feature typical for CM

## KAIDUN II, MINERALOGY VERSUS COMPOSITION: F. Brandstätter et al.

chondrites. Moderately volatile lithophiles show an inconsistent abundance pattern. Cr, Mn, and K are close to CI, while Zn is depleted ( $.75 \times \text{CI}$ ). Sodium and the highly volatile Br are enriched by 1.4 and  $1.6 \times \text{CI}$ , respectively. Siderophile elements show an almost unfractionated overall pattern. The moderately volatiles Fe, Ni and Co are slightly enriched. MKD8 exhibits an abundance pattern which is essentially identical with MKD2 being slightly higher in the refractory REE La, Sm and Eu. MKD7 is clearly distinct from MKD2 and MKD8 having lower abundances of volatile lithophiles and siderophiles. The abundances of the element pairs Fe,Mn and Se,Zn which are used to discriminate between carbonaceous chondrite classes also reveal some inconsistencies. According to Se,Zn MKD2 and MKD8 fall between CI and CM, MKD7 is close to C3. In a Fe vs. Mn plot MKD7 again plots near C3 whereas MKD2 lies between CM and C3, MKD8 is closer to CM. Samples MKD2 and MKD8 are similar to the Yamato-82042 carbonaceous chondrite which was described as the first CM1 meteorite [12].

**Summary** The Kaidun II clast shows some conflicting mineralogical and chemical characteristics that do not allow an unambiguous assignment to the well established carbonaceous chondrite classes. The overall texture of the matrix-rich clast and morphology of opaques are typical for CIs. Bulk matrix and bulk sample compositions reveal similarities with CMs. In addition, the presence of low-Fe Mn-enriched olivines and the relatively high abundance of enstatite resembles some micrometeorites.

**References** [1] A.V.Ivanov et al. (1986) *Meteoritika*, 45, 3-19. [2] A.V. Ivanov (1989) *Geochemistry International*, 26, 84-91. [3] M.E. Zolensky et al. (1991) *LPSC XXII*, 1565. [4] F. Brandstätter et al. (1992) *Meteoritics*, 27, 206. [5] H.Y. McSween and S.M. Richardson (1977) *Geochim. Cosmochim. Acta*, 41, 1145-1161. [6] I.M. Steele (1990) *Meteoritics*, 25, 301-307. [7] W. Klöck et al. (1989) *Nature*, 339, 126-128. [8] T. Presper et al. (1992) *Meteoritics*, 27, 278. [9] J.A. Johnson and M.Prinz (1991) *LPSC XXII*, 643. [10] J.F. Kerridge et al. (1980) *Meteoritics*, 15, 313. [11] K. Fredriksson and J.F. Kerridge (1988) *Meteoritics*, 23, 35-44. [12] M.M. Grady et al. (1987) *Mem. Natl. Inst. Polar Res., Spec. issue*, 46, 162-178.

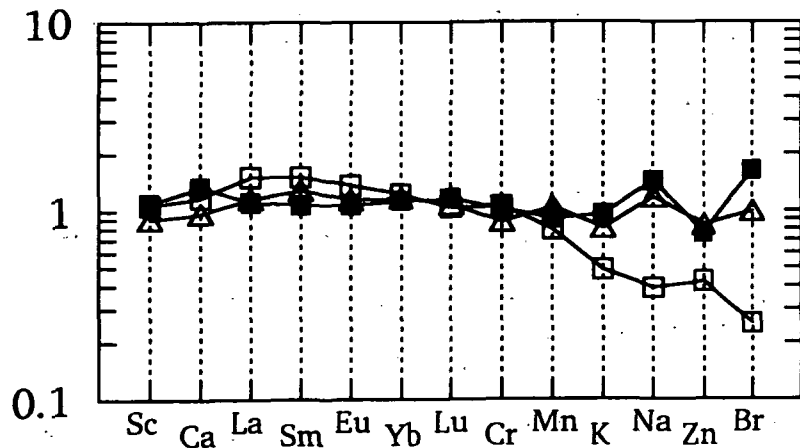


Fig. 1 CI-normalized abundances of lithophile elements in Kaidun samples

■ MKD2  
□ MKD7  
△ MKD8

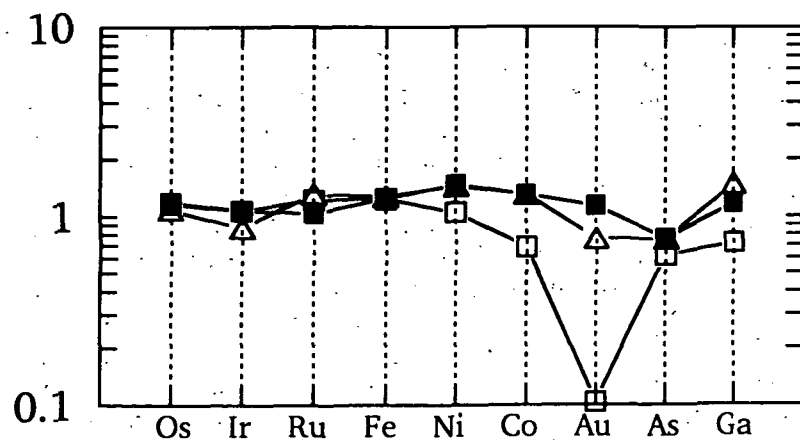


Fig. 2 CI-normalized abundances of siderophile elements in Kaidun samples

■ MKD2  
□ MKD7  
△ MKD8

587-46  
456470  
NOS ONLY  
N 94-123P02  
R 2

**A STRUCTURAL AND PETROGRAPHIC INVESTIGATION OF THE PRETORIA SALTPAN IMPACT STRUCTURE; D. Brandt<sup>1</sup> and W. U. Reimold<sup>2</sup>, <sup>1</sup>Dept. of Geology, <sup>2</sup>Economic Geology Research Unit, at the Dept. of Geology, University of the Witwatersrand, P.O. WITS 2050, R.S.A.**

## INTRODUCTION

The Pretoria Saltpan crater is located in the southern portion of the Bushveld Igneous Complex, some 40 km NNW of Pretoria, South Africa, at 25°24'30"S/28°04'59"E. The near-circular structure of 1.13 km diameter exhibits a well-preserved, uptilted granite rim. Granitic breccia overlies Karroo sediment in places, indicating a post-Karoo age for the cratering event. The coincidence of the spatial occurrence of the crater with respect to various alkaline and ultramafic intrusives has been the main argument put forward against an impact origin for the structure [1,2]. Detailed mapping of the crater rim exposures and the crater environs was carried out and revealed many occurrences of intrusives in the whole region. Structural analysis along the rim revealed the presence of typical impact crater-related structures. Comparative petrographic and chemical studies of crater-related and non-related intrusives showed close similarities between these sample suites.

**GEOLOGICAL AND STRUCTURAL RESULTS:** Small basic and alkaline intrusive bodies are present in the otherwise granitic rim, and were previously thought to have a radial or peripheral disposition with respect to the crater center. However, detailed mapping (Fig.1.) has revealed that most of the intrusives have no such preferred orientation. In most cases the dykes or sills have been faulted both radially and concentrically by a post-intrusive event. Deformation in the crystalline rim, generally composed of strongly altered, coarse-grained Nebo granite, is not as clear as that encountered in impact craters with well-defined target stratigraphy. However, sets of tight, closely spaced, originally horizontal sheeting joints together with the granite foliation could be used to determine changes in attitude of the rim rocks. Closer to the crater floor, the rim granite dips gently inwards and there is evidence for shallow dipping, closely spaced shear surfaces. Towards the rim crest the granite dips outwards to varying degrees, indicative of upwarping. Ejecta debris (granitic fragmental breccia) is found in an inverted stratigraphic sequence at various localities along the rim. The rim is broken by concentric thrust faults and radial fractures (see inset, Fig.1), that are responsible for the numerous depressions seen on the rim crest. These near-vertical faults display a scissor-type displacement in the southern section of the rim. The mid-section of the rim appears to consist of an anticline, which is locally displaced along some inward-dipping faults, similar to those described e.g. from the Odessa crater [3], as well as some outward dipping faults. A few concentric normal faults, well known from other terrestrial impact structures, are present too. Aerial photographic analysis revealed radial and concentric fractures in the immediate crater surroundings. Overall, the Pretoria Saltpan Crater is structurally similar to the Odessa Crater, with some similarity and strikingly similar dimensions to Meteor Crater. The jointing patterns of the crater rim and environs are markedly different to those observed in the surrounding region, and exhibit a well defined radial and concentric pattern, which can be related to strain deformation.

**PETROLOGY:** Chemical compositions of the country rocks, as well as of various basic and alkaline intrusives from within the crater and from the crater environs were determined for the first time. Fig.2, CIPW normative compositions, represents the total variability of the samples collected from the crater and its environs. Increasing alteration of trachyte from within the crater and from the region leads to increasing enrichment in SiO<sub>2</sub>. The lamprophyres are typically silica undersaturated, but show varying Feldspar/Mafic ratios. Lamprophyre pyroxene compositions (Fig.3) from the crater are almost identical to those from the environs. The ranges of selected trace element abundances for lamprophyre samples from within the crater are shown in Fig.4. Superimposed are the abundances for several samples collected outside of the crater. The variations seen may be attributed to alteration processes or minor variations within the parent magma body. These results are all strongly suggestive of a common source for the intrusives from within and outside of the crater.

## CONCLUSION

The Pretoria Saltpan structure occurs in an area of alkaline activity, the age of which has been tentatively determined at about 1.36 Ga [4]. The cratering event is significantly younger at about 220 000a ago [5]. Clearly the petrographic and structural observations above are all in keeping with an impact origin for the Pretoria Saltpan Impact Structure.

**ACKNOWLEDGEMENTS:** The authors of this paper would like to thank the Barringer Crater Co. for their financial support in these studies.

**REFERENCES:** [1] Wagner, P. A., 1922, Geol. Surv. South Africa Mem. 20, 136p. [2] Feuchtwanger, 1973, Hons. Proj., Dept. of Geology, Univ. of Wits., unpublished. [3] Shoemaker, E. M. & Eggleton, R. E., 1961, Proc. Geophysical Lab./Lawrence Radiation Crat. Symp., p A1-A27. [4] Partridge, T. C. et al., 1990, Meteoritics 25, p. 396. [5] Storzer, D. et al., 1993, this volume.

## STRUCTURE AND PETROGRAPHIC INVESTIGATION OF THE PRETORIA SALTPAN CRATER: Brandt D. and Reimold W.U.

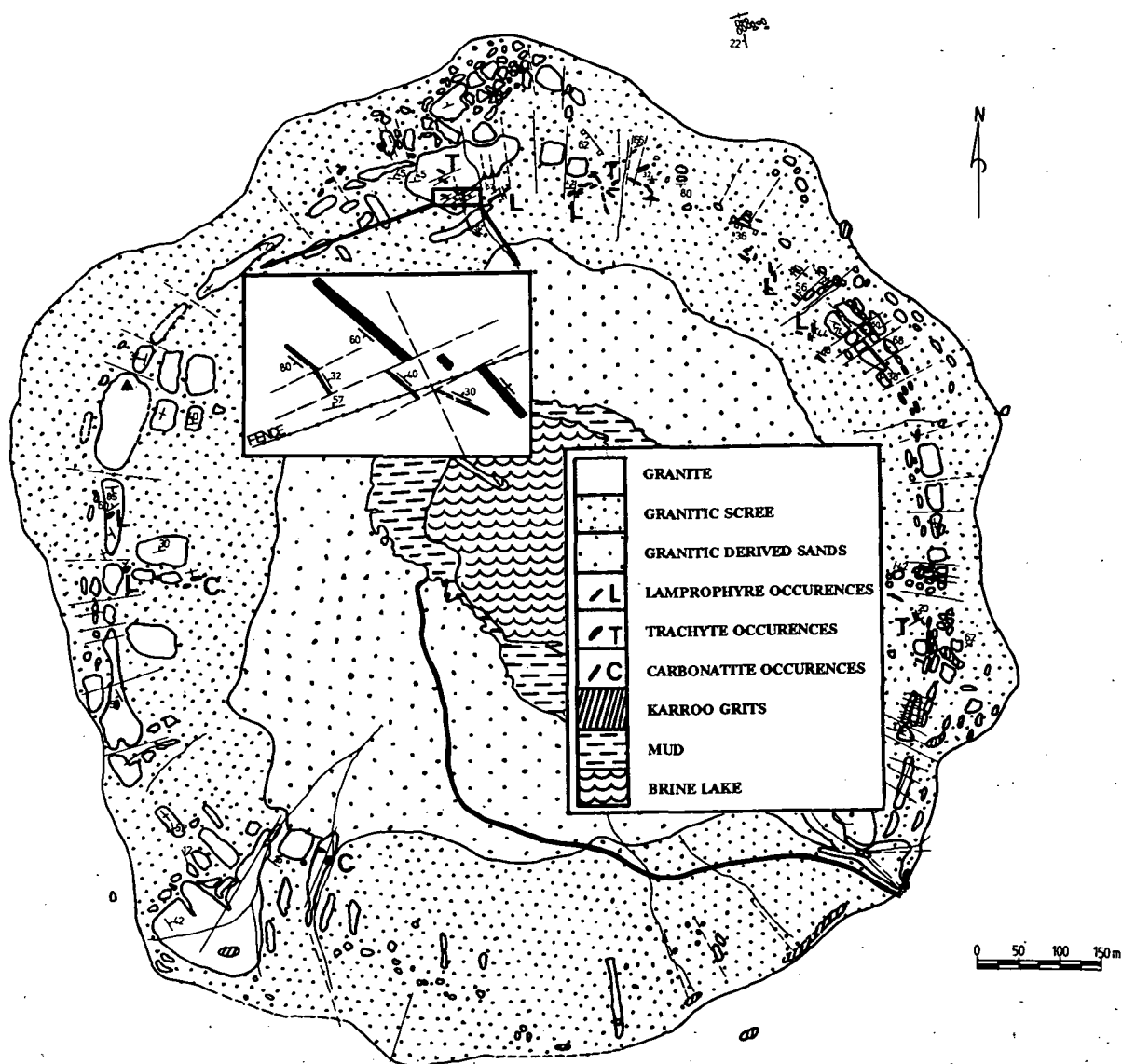


FIG.1. Geological Map of the Pretoria Saltpan Impact Crater.

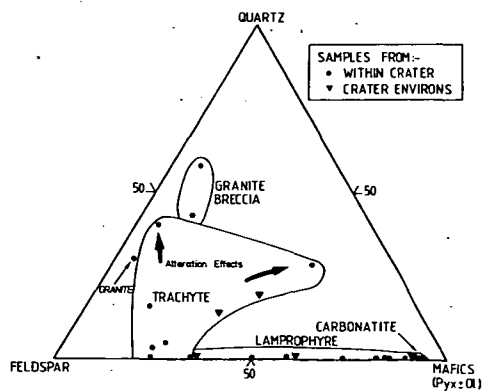


FIG.2. CIPW normative mineralogy.

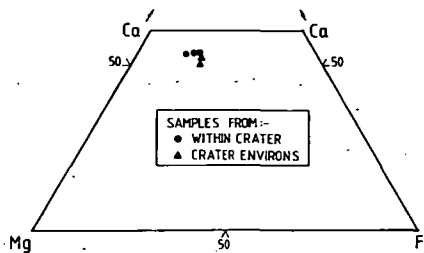


FIG.3. Pyroxene Compositions in Lamprophyres.

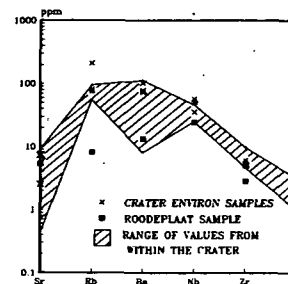


FIG.4 Lamprophyre Trace Elements (Rock/MORB), using values of Pearce (1983).

456472

588-46  
ABS ONLY

LPSC XXIV

181

N 94 - 12 103

P-2

**GEOPHYSICAL SIGNATURE OF THE PRETORIA SALTPAN IMPACT STRUCTURE AND A POSSIBLE SATELLITE CRATER; D. Brandt<sup>1</sup>, R. J. Durrheim<sup>2</sup> & W. U. Reimold<sup>3</sup>, <sup>1</sup>Dept. of Geology, <sup>2</sup>Dept. of Geophysics, <sup>3</sup>Econ. Geol. Res. Unit, Dept. of Geology, University of the Witwatersrand, P.O. WITS, 2040, Johannesburg, R.S.A.**

**INTRODUCTION**

The Pretoria Saltpan Crater is located in the southern portion of the Bushveld Igneous Complex, some 40 km NNW of Pretoria, South Africa, at 25°24'30"S/28°04'59"E. An origin by impact for this crater structure was recently confirmed [1]. The results of the only gravity reconnaissance carried out over the crater to date [2] failed to support an impact origin. With the aid of recent results obtained from a central drill-core, it was necessary to carry out more geophysical work which would include a gravity profile of higher resolution. A second, smaller, circular depression (about 400 m in diameter) to the SW of the crater is suggestive of a twin crater. This site had never been investigated, and thus various geophysical surveys were conducted.

**RESULTS:**

**I MAIN CRATER:** Thirty-three gravity stations were located along a single north-south traverse (Fig.2), extending ca. 300 meters beyond the crater rim. Both the gravity (Fig.1c) and topographic profiles (Fig.1a) are relative to an arbitrary base station near the crater floor. Due to the severe topography the gravity data reductions included terrain corrections. A centred anomaly (Fig.1c) of -3.2 mgals was obtained. A density of 2,67 g/cm<sup>3</sup> was used for the relatively undisturbed surrounding granite. The low density muds, which fill the crater floor, are believed to be the primary contributor to the observed anomaly. Known parameters, i.e., densities and layer thicknesses, were used in constructing the gravity model seen in Fig.1d. The subsurface configuration was approximated using a number of slabs, the strike lengths of which decrease from the centre of the model outwards, in order to simulate the roundness of the actual body in plan view. The various densities used for each slab are tabulated in Fig.1d. The size of the negative anomaly plus the known densities may be used to infer the 3-dimensional geometry of the crater fill. Unlike the earlier interpretation [1], the data presented here appears to be compatible with the anatomy of a simple bowl-shaped impact crater. The magnetic anomaly (Fig.1b) which was obtained along the same traverse as the gravity profile exhibits the known regional trend together with signatures of the lamprophyric dykes found on the northern, inner slopes of the crater rim [3], but rules out the possibility that a magnetic volcanic pipe could exist below the crater sediments.

**II POSSIBLE SATELLITE CRATER:** The small circular depression (Fig.3), situated some 3.5 km to the southeast of the Pretoria Saltpan Crater is approximately 3 m deep. A very small gravity anomaly (Fig.4b) was found, contrary to what would be expected of an impact crater. However, it most probably represents the regional gravity trend. As in the case of the gravity, the magnetic anomaly (Fig.4a) only represents the regional magnetic trend. It does, however, exclude the possibility of the existence of a magnetic volcanic or kimberlite pipe of some sort. A ground probing radar survey was conducted across the feature, but was unsuccessful in that the wet upper conductive mud unit prevented penetration of the signals. Refraction seismic profiles and resistivity profiles indicated lithological breaks at 0.76 m and 26 m. Trenching revealed a calcrete-type layer at 0.76 m, and it is possible that at a depth of 26 m the granite floor to the depression is reached.

**CONCLUSION**

The negative gravity anomaly of the main crater that the gravity model produced, as well as the magnetic signature is within reasonable limits of an impact crater of these dimensions. The small circular feature which has the physical shape of a possible satellite impact structure does not show any typical geophysical signatures. As it is the only such feature in the entire area it should not be overlooked as a possible satellite crater. A drilling program may reveal interesting results and an explanation to the still inconclusive geophysical results.

**ACKNOWLEDGEMENTS:** The authors would like to thank the Barringer Crater Co. for their financial contribution to this project.

**REFERENCES:** [1] Reimold, W. U. et al., 1992, *Geology* 20, p. 1079-1082. [2] Fudali, R. F., 1973, *J. of Geol.* 81, 495-507. [3] Brandt, D. and Reimold, W.U., this volume.





2456474

589-46  
ABS ONLY

LPSC XXIV

183

N94-12104

**CARBONACEOUS CHONDRITE CLASTS IN THE KAPOETA HOWARDITE.** Adrian J. Brearley, Institute of Meteoritics, Department of Earth and Planetary Sciences, University of New Mexico, Albuquerque, New Mexico 87131. P-2

A petrographic and mineralogical study of a number of carbonaceous chondrite clasts in the Kapoeta howardite has been carried out. Most of the clasts have mineralogical and chemical properties which link them to the CM carbonaceous chondrites. Some clasts contain chondrules which often have well-developed fine-grained rims, but many have been extensively brecciated. PCP-rich objects are common and pentlandite and pyrrhotite also occur. Calcite has also been found. The remainder of the clasts are extremely fine-grained and appear to be closely related to CI carbonaceous chondrites. In these clasts magnetite framboids are common and fine-grained sulfides and magnetite occur disseminated throughout the matrix.

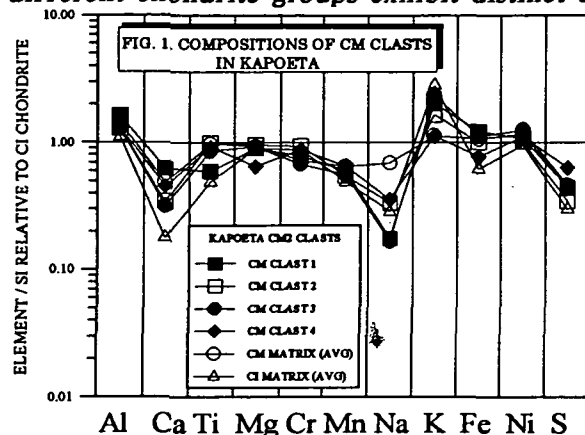
**Introduction.** Some achondritic breccias, particularly the howardites, and polymict ureilites [1,2,3] contain relatively abundant carbonaceous chondrite clasts. These materials appear to have been added to the achondrite parent bodies from impacts into the regolith at a late stage in the evolution of the parent body. The presence of carbonaceous chondritic clasts in achondrites represents an important additional resource of primitive meteoritic material which has not been fully exploited. The possibility that new chondrite types may be present within these breccias also exists, but detailed studies are lacking. Recent studies of brecciated achondrites, such as the Bholgati and Jodzie howardites [1,2] and the Nilpena polymict ureilite [3] have shown that several types of carbonaceous chondrite clasts, with affinities to the CM, CI and CR groups can occur in these meteorites. In addition, clasts in the Kapoeta howardite were described by [4] which appeared to be C2 carbonaceous chondrites. However, to date no comprehensive petrological or mineralogical studies of clasts in Kapoeta have been carried out. As part of a continuing study of carbonaceous chondrites and chondritic clasts in brecciated meteorites I have commenced a detailed study of clasts in the Kapoeta howardite. It is appropriate to reexamine clasts in this meteorite in view of the recent, significant advances in our understanding of the carbonaceous chondrites.

Seven thin sections of Kapoeta have been studied in detail using optical microscopy, SEM and electron microprobe. Transmission electron microscopy of selected carbonaceous clasts is planned. This study and the work of Pun [5] show that a significant number of such clasts (3 modal%) is present in Kapoeta. The clasts are typically angular although some tend to be subrounded and range in size from up to 3 mm down to tens of microns. The smaller clasts occur frequently and detailed SEM studies often reveal 10-20 clasts in a single thin section with sizes less than 200  $\mu\text{m}$ . Preliminary results from this study suggest that two main carbonaceous chondrite types, CM and CI, are represented among the clast population in Kapoeta.

**CM carbonaceous chondrite clasts.** The majority of clasts in Kapoeta appear to have affinities to the CM group based on their mineralogical and chemical characteristics. The clasts are characterized by the presence of chondrules or chondrule fragments set in a dark fine-grained matrix. Some clasts contain chondrules that are mantled by fine-grained rims which sometimes show textural and compositional zoning typical of CM2 meteorites [6]. There is considerable variation in the textural characteristics of the clasts in terms of their degree of brecciation. Some clasts show textures which have been described by [6] as being indicative of primitive accretionary rocks. These clasts contain chondrules with well developed rims set in a matrix of subrounded PCP-rich objects. These objects probably consist of tochilinite or tochilinite intergrown with serpentine. In these clasts there is no evidence of brecciation. A whole range of textures from this primitive accretionary texture to highly brecciated clasts exists. In the latter case, there are no intact chondrules and the clasts are dominated by angular fragments of olivine and pyroxene intimately mixed with the fine-grained matrix. It is notable that the most highly brecciated clasts appear to have the lowest abundance of PCP in the matrix.

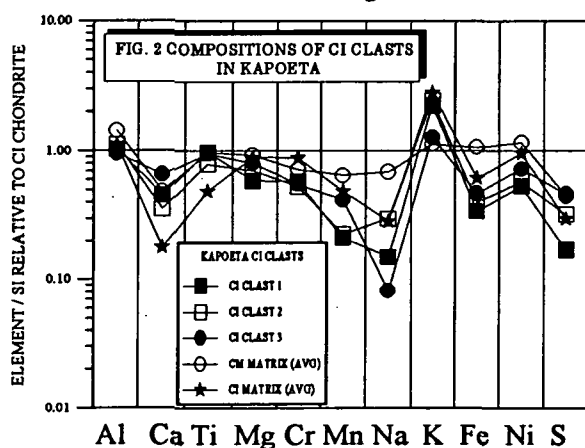
# CARBONACEOUS CHONDRITE CLASTS IN KAPOETA: Brearley A.J.

The matrix compositions in 10-15 different CM-like clasts have been determined by electron microprobe analysis using a 10  $\mu\text{m}$  beam. Elemental ratio diagrams for matrix are a useful way of discriminating between carbonaceous chondrite types, because matrices in the different chondrite groups exhibit distinct enrichment and depletion patterns relative to bulk CI



values. Normalised element ratio patterns for a number of clasts in Kapoeta are shown in Fig. 1. The data show some variability, but all are consistent with carbonaceous chondrite matrix. The observed compositional variations may be a reflection of the varying degrees of aqueous alteration and brecciation in different clasts. Despite these variations, the shapes of the patterns are generally comparable from one clast to another. In all cases the matrices are depleted in Ca, Ti, Cr, Mn Na and S and enriched in K and Ni. The patterns are most consistent with CM matrix, but some elements, Ni and K in particular, are more like CI matrix. However, overall the available petrological and mineralogical data show that these clasts have close affinities to CM chondrites.

**CI-like clasts.** A number of dark clasts have been observed which exhibit close affinities to CI chondrites. These clasts are very fine-grained, tend to be fractured and have fine-grained opaques (magnetite and sulfides) disseminated throughout the matrix. No chondrules have been found but rare silicate fragments occur. In several clasts framboids of magnetite are extremely



abundant, but no magnetite with a plaquette morphology has been observed. Bulk matrix data for 3 CI clasts are shown in Fig. 2 and provide good evidence for a CI link. The elemental ratios for these clasts show larger fractionations for Mn, Na, K, and Ni than are observed in CM matrix, but are similar to CI matrix. The exact depletions are not identical to average CI matrix values and there are differences from clast to clast suggesting that there may be some mineralogical differences on a fine-scale.

**Conclusions.** Of the clasts studied so far in Kapoeta, the bulk appear to have close affinities to CM chondrites whilst the remainder are dominantly CI-like. Further detailed mineralogical studies are in progress to confirm this. No clasts with affinities to CR, CO or CV meteorites have yet been found. The wide variety of textures observed in the CM-like clasts suggest that either samples from several distinct impacts are present or that the clasts are fragments of a CM2 regolith breccia. It is clear that alteration and regolith processing on the CM2 parent body had occurred extensively prior to impact onto the howardite regolith [2]. The presence of relatively unprocessed accretionary CM rock fragments illustrates that these materials can survive an extended and complex history of regolith and impact processing. Such clasts provide an additional and important resource of primitive material for unraveling the evolution of the CM (and CI) chondrites.

**Acknowledgments.** I am grateful to Dr Elbert King for kindly providing the sample of Kapoeta used in this study. Funding was provided by NASA grant NAG -9-497 to J.J. Papike (P.I.).

**References** [1] Bunch, T.E. et al. (1979) GCA 43, 1727-1742. [2] Reid, A.M. et al. (1990) GCA 54, 2161-2166. [3] Brearley, A.J. and Prinz, M. (1992) GCA 56, 1373. [4] Wilkening, L.L (1973) GCA 37, 1985. [5] Pun, A.P. (1991) MSc. Thesis. University of New Mexico. [6] Metzler, K. et al. (1992) GCA 56, 2873.

**CHONDRITE THERMAL HISTORIES FROM LOW-CA PYROXENE MICROSTRUCTURES: AUTOMETAMORPHISM VS PROGRADE METAMORPHISM REVISITED.** Adrian J. Brearley and Rhian H. Jones, Institute of Meteoritics, Department of Earth and Planetary Sciences, University of New Mexico, Albuquerque, New Mexico 87131.

In order to constrain the thermal histories of chondritic meteorites we have carried out a detailed study of the microstructures of low-Ca pyroxenes produced experimentally and in types 4 and 5 ordinary chondrites. We have performed cooling experiments on synthetic  $\text{MgSiO}_3$  at cooling rates between 2 and  $10000^\circ\text{C/hr}$  from the protopyroxene stability field into that of orthopyroxene (OPX) and annealed the products of these experiments for a variety of annealing times. There are clear microstructural differences between samples which have been cooled and those which have been subsequently annealed. A comparison of the microstructures observed in our experimental samples with those in H4-5 ordinary chondrites shows that they cannot have experienced a single stage cooling history, as proposed for the autometamorphism model.

**Introduction.** The petrologic type 3 to 6 ordinary chondrites represent a metamorphic sequence which is characterized by increasing degrees of thermal annealing, homogenization of silicate compositions and recrystallization of fine-grained matrix and chondrule mesostasis. The exact thermal history which produced the metamorphism is still a subject of some controversy. Many workers have argued that annealing occurred as a result of prograde metamorphism within a parent body [1]. In this model the parent bodies accreted cold and the metamorphism resulted from secondary heating of the asteroid. The alternative model is that the petrologic sequence is produced by primary cooling from high temperature (autometamorphism) [2,3]. In this model material accreted hot ( $\sim 700\text{--}800^\circ\text{C}$ ) and early accreted material cooled more slowly (types 5-6) than material accreted late (types 3-4). The principal evidence to support this model comes from low-Ca pyroxenes microstructures and experimental annealing of striated low-Ca pyroxene from an H4 chondrite [4,5]. We have reexamined the evidence for autometamorphism based on a systematic experimental and TEM study of phase transitions in synthetic low-Ca pyroxene and studies of low-Ca pyroxene in a type H chondrite. Our results demonstrate that the evidence used to support the autometamorphism model is by no means as convincing as has been claimed.

There are three principal polymorphs of enstatite-rich low-Ca pyroxene; protopyroxene, orthopyroxene (OPX) and clinopyroxene (CPX). Protopyroxene is only stable at high temperatures and during cooling inverts to OPX. Increasingly slower degrees of cooling result in higher proportions of OPX [6]. If protopyroxene is cooled rapidly it inverts to metastable CPX at low temperatures ( $<500^\circ\text{C}$ ). This CPX will invert to OPX if it is reheated within the OPX stability field. Low-Ca pyroxenes in ordinary chondrites consist of intergrowths of CPX and OPX polymorphs and the proportion of OPX increases with petrologic type.

Two sets of experiments were carried out: a) cooling experiments in which protoenstatite is cooled at different cooling rates from high temperature through the proto-ortho inversion temperature and then quenched and b) annealing experiments in which the products of the cooling experiments are annealed for different periods of time. The first set of experiments have implications for the initial cooling histories of chondrules and autometamorphism. The annealing experiments address the question of prograde vs autometamorphism.

**Cooling experiments.** Experiments were carried out at cooling rates of 10000, 1000, 100, 10 and  $2^\circ\text{C/hr}$  and the run products were examined by TEM techniques. From high resolution electron micrographs we have been able to measure directly the proportions of OPX and CPX (quenched proto) in each sample. The degree of transformation as a function of cooling rate is shown in Fig. 1. Based on an extrapolation of these data complete transformation of protopyroxene to OPX requires a cooling rate of  $0.03^\circ\text{C/hr}$ . For a cooling interval of 1000 to  $500^\circ\text{C}$  this would take 1.9 years. At fast cooling rates (100,  $1000^\circ\text{C/hr}$ ) development of OPX is extremely heterogeneous and individual regions (500 nm wide) can vary from 14 to 80 vol% OPX. At slow cooling rates ( $2, 10^\circ\text{C/hr}$ ) OPX is homogeneously developed throughout the crystal. We have measured the field widths (measured in the a direction) of OPX and CPX lamellae in each of these samples. The proto to OPX transformation appears to proceed by the nucleation of thin

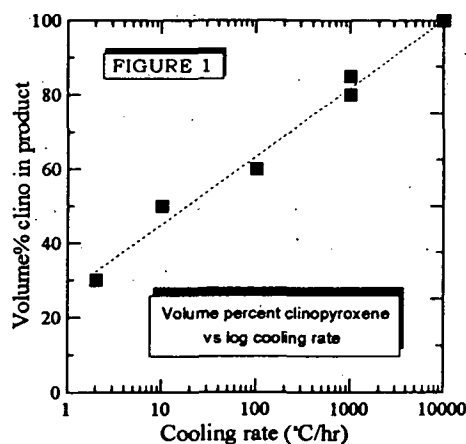
## CHONDRITE THERMAL HISTORIES: Brearley, A.J. and Jones, R.H.

(1-2 unit cells) lamellae of OPX, rather than coarsening of early formed lamellae. Development of OPX lamellae greater than 10 unit cells thick only occurs at the slowest cooling rates.

**Annealing experiments** Annealing experiments have been carried out on  $\text{MgSiO}_3$  and iron-bearing compositions. For enstatite, we have annealed the products of 1000 and 10000°C/hr cooling experiments for periods of up to 24 days at 800, 900 and 980°C. For the compositions  $\text{En}_{85}\text{Fs}_{15}$  and  $\text{En}_{84}\text{Fs}_{15}\text{Wo}_1$ , 10000°C/hr material has been annealed for 1 week at 1045°C. For enstatite, no transformation has occurred in any of the annealing experiments. For Fe-bearing compositions, there is some minor evidence of transformation, suggesting that the transformation may be slightly faster than for  $\text{MgSiO}_3$ , although this may be also due to the higher annealing temperatures. In these samples we observe a coarsening of the OPX lamellae.

**Discussion.** [4] showed that after annealing striated low-Ca pyroxene from the Quenggouk (H4) chondrite for 1 week at 800°C, the sample inverted to 100% OPX. These data were used to argue that Quenggouk could not have been annealed at high T, because this would have destroyed the striated microstructure. Thus the striated microstructure was inferred to be the result of primary cooling from high temperatures. Our experiments show that this argument is highly flawed. The rate of transformation is a strong function of the amount of OPX in the starting material. For samples with low proportions of OPX the reaction rate is extremely slow. The data of [4] show only that if the Quenggouk pyroxene, in its present state, were heated at 800°C for a week, it would transform to OPX. However, this ignores the possibility that the pyroxene may initially have had a much higher CPX content. The microstructure in Quenggouk could have formed by annealing of such material for extended periods of time at high T.

We have examined low-Ca pyroxenes in the unshocked H4 chondrite Conquista by TEM and compared the microstructures with our experimental samples. Conquista contains 32 vol% OPX, which based on Fig. 1 indicates a cooling rate of 300°C/hr, assuming single stage cooling



from high temperature. For this cooling rate the maximum field width of OPX which could develop (based on our experimental data) is between 5 and 10. However, in Conquista rare lamellae up to 56 unit cells thick and several lying between 13 and 23 occur. Our experimental data show that during single stage cooling thick OPX lamellae do not form, even at cooling rates of 2°C per hour. Thus the microstructures in Conquista are not consistent with single stage cooling from high temperature (autometamorphism). The low degree of transformation and the thick OPX lamellae are not compatible with such a thermal history. However, the data are consistent with a two stage thermal history which would be expected for prograde metamorphism. With the exception of the very wide OPX lamellae, the distribution of ortho and clino

lamellae widths in Conquista bears a very close resemblance to that for samples cooled at ~1000°C. Thus the microstructures in Conquista can be interpreted as annealing of low-Ca pyroxene produced by rapid cooling during chondrule formation. Some of the preexisting OPX lamellae coarsen as a result of annealing during reheating in a parent body environment. This is likely to be a sluggish process which occurred over several million years.

**Conclusions.** Our experimental data and high resolution TEM observations of low-Ca pyroxene from the H4 chondrite, Conquista show that the microstructures present are not consistent with a single stage cooling model from high temperatures. However, they are entirely consistent with a two stage model involving reheating of rapidly cooled chondrule pyroxene within a parent body environment. We conclude that the autometamorphism model, which has been largely based on pyroxene microstructures, is no longer a viable model to explain the thermal histories of the ordinary chondrites. Funded by NASA grant NAG 947 to J.J. Papike (P.I.).

**References:** [1] Dodd, R.T. (1981) *Meteorites: A Petrological-Chemical Synthesis*, Cambridge University Press. [2] Hutchison, R. et al. (1980) *Nature* 287, 787. [3] Watanabe, S. et al. (1985) *EPSL* 72, 87. [4] Ashworth, J.R. et al. (1984) *Nature* 308, 259. [5] Ashworth, J.R. (1980) *EPSL* 46, 167. [6] Smyth, J.R. (1974). *Am. Min.* 59, 345.

456477

Sg 1-96

LPSC XXIV

187

N 94-102106

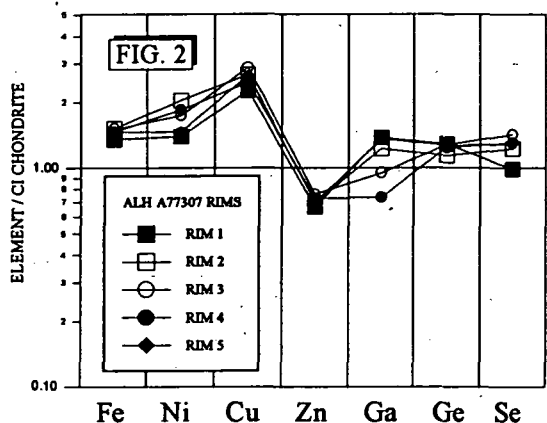
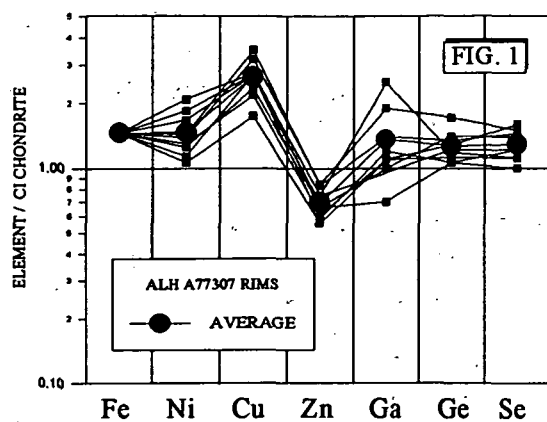
**SXRF DETERMINATION OF TRACE ELEMENTS IN CHONDRULE RIMS IN THE UNEQUILIBRATED CO<sub>3</sub> CHONDRITE, ALH A77307.** Adrian J. Brearley<sup>1</sup>, Saša Bajt<sup>2,3</sup>, and Steve R. Sutton<sup>2,3</sup> <sup>1</sup>Institute of Meteoritics, Department of Earth and Planetary Sciences, University of New Mexico, Albuquerque, New Mexico 87131. <sup>2</sup>Dept. of Applied Sciences, Brookhaven National Laboratory, Upton, NY 11973. <sup>3</sup>Dept. of Geophysical Sciences, University of Chicago, Chicago, IL 60637.

We have determined the concentrations of Ni, Cu, Zn, Ga, Ge and Se in five chondrule rims in the CO<sub>3</sub> chondrite ALH A77307 (3.0) using the synchrotron X-ray fluorescence (SXRF) microprobe at Brookhaven National Laboratory. The data show that the trace element chemistry of rims on different chondrules is remarkably similar, consistent with data obtained for the major elements by electron microprobe. These results support the idea that rims are not genetically related to individual chondrules, but all sampled the same reservoir of homogeneously mixed dust. Of the trace elements analysed Zn and Ga show depletions relative to CI chondrite values, but in comparison with bulk CO chondrites all the elements are enriched by ~1.5 to 3.5 x CO. The high concentrations of the highly volatile elements Se and Ga and moderately volatile Zn (1.5 to 2 x CO) in rims show that matrix is the major reservoir of volatile elements in ALH A77307.

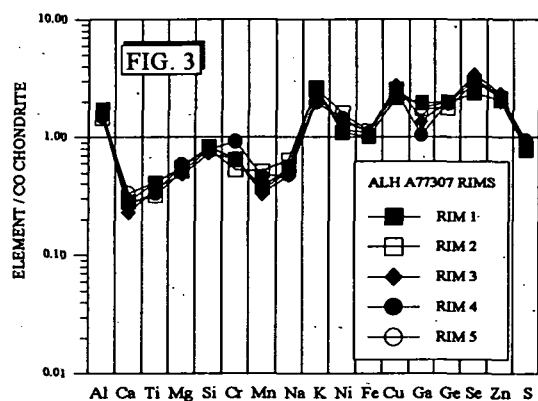
**Introduction.** Allan Hills A77307 is the most unequilibrated of the CO<sub>3</sub> carbonaceous chondrites [1]. Such unequilibrated chondrites represent some of the least processed samples of meteoritic material available for study. They may preserve, to varying degrees, evidence of processes which took place during the earliest stages of the formation of our solar system. One of the major components of the CO<sub>3</sub> chondrites is a dark, fine-grained matrix which occurs interstitially to chondrules. The origin of this material and matrix materials in other chondrites has long been a question of considerable controversy e.g. [2,3,4]. In order to address the origin of matrix it is important to characterize these materials as fully as possible. Although mineralogical and major element compositions have become more widely available as a result of detailed transmission electron microscope (TEM) and electron microprobe studies, trace element compositions of matrix are extremely rare. Because the trace element geochemistry of matrix can provide important geochemical constraints on the origin of matrix, we have commenced a study of the trace element compositions of fine-grained matrix in the CO<sub>3</sub> chondrites, using the SXRF microprobe at Brookhaven National Laboratory.

**Analytical techniques.** Polished thin sections of ALH A77307 were prepared on Suprasil glass slides. Several chondrules with well-developed fine-grained rims were selected for study and their major element compositions were determined by electron microprobe for 6-10 spots on each rim using a 10 µm beam. Trace element concentrations were determined by SXRF microprobe at the same locations on the sample used to acquire the electron microprobe analyses. Between 6 to 10 analyses were carried out on each chondrule rim using a beam size of 8 x 10 µm. Because of the intense Fe peak a 170 µm thick Al filter was used on the fluorescent beam. Concentrations of Ni, Cu, Zn, Ga, Ge and Se were determined.

**Trace element chemistry.** The results of several analyses in different positions on one rim are reported in Fig.1 normalised to CI abundances. The plot shows that there is some variation from point to point for all the elements analysed, especially Ga. This spread in Ga values is due to the relatively large uncertainty resulting from its low concentration levels. However, overall the data for Ni, Cu, Zn, Ge and Se are relatively closely clustered. Some of the variation in the data can be attributed to localized variations in the matrix composition on the scale of 10 µm which have also been observed in electron microprobe analyses [3]. It is notable that the relative enrichments and depletions for each analytical spot are essentially identical. The average trace element compositions from the five different rims, normalised to CI chondrite values, are also shown in Fig. 2. This plot clearly shows that the trace element compositions of individual rims are essentially identical, with Ni, Cu, Ge and Se all showing enrichments relative to CI

TRACE ELEMENTS IN CHONDRULES RIMS IN ALH A77307: Brearley, A.J. *et al.*

in ALH A77307 are not related to chondrules. One of the major observations from this study is that the highly volatile elements Se and Zn are significantly enriched (2 to 3.5 x CO) in rims as is the moderately volatile element Ga relative to bulk CO chondrite values. Se and Ga also show modest enrichments relative to CI chondrite values illustrating that matrix is indeed the major reservoir for these elements in ALH A77307. The only other analysis of CO3 matrix [5] was carried out by neutron activation analysis from a matrix fragment in Ornans. These data show



evidence for lower enrichments for the volatile elements Se, Zn and Ga (~1.5 x CO) than our SXRF analyses, but differ in other important respects in having higher refractory abundances in comparison with the microprobe data as noted by [5]. Fig. 3 illustrates that ALH A77307 matrix has suffered extremely complex fractionations, consistent with the presence of a number of different matrix components with different origins [3]. Overall, matrix appears to be depleted in refractory elements, but is enriched in the moderately volatile siderophile and chalcophile elements, consistent with the view that matrix did not suffer extensive high temperature processing prior to accretion. The high volatile contents also argue strongly against a chondrule origin for rim materials. **Acknowledgements.** Funding was provided by NASA grants NAG 9-437 to J.J. Papike (P.I) and NAG9-106 to Stev Sutton (P.I.).

**References.** [1] Scott, E.R.D. and Jones, R.H. (1990) GCA 54, 2485. [2] Kornacki, A.S. and Wood, J.A. (1984) GCA 48, 1663. [3] Brearley, A.J. (1993, in press) GCA 57. [4] Alexander, C.M. *et al.* (1989) EPSL 95, 187-207. [5] Rubin, A.E. and Wasson, J.T. (1988) GCA 52, 425.

abundances. Zn is consistently depleted, but Ga shows variable behavior, presumably due to the errors noted above. Overall it appears to be enriched relative to CI abundances. In Figure 3 the trace element data, combined with major element data for the same rims, are plotted, normalised to CO chondrites. There is a remarkable compositional homogeneity of individual rims in ALH A77307. Relative to bulk CO all the trace elements are enriched, particularly Se which shows enrichments of up to 3.5 x CO values.

**Discussion.** The trace element data clearly demonstrate the remarkable compositional homogeneity of rims on different chondrules, which has previously been reported for major elements in ALH A77307 [3]. These results support the idea that this fine-grained material represents a single reservoir of dust which was sampled by chondrules. Mineralogically, rim material has been shown to consist of an ultrafine-grained, highly unequilibrated assemblage of amorphous material, silicates, oxides and sulfides, which was clearly mixed extremely thoroughly on a fine scale. The absence of any variation in the mean trace element abundances from rim to rim is strong evidence to support the arguments presented elsewhere [3] that rim materials

are not related to chondrules. One of the major observations from this study is that the highly volatile elements Se and Zn are significantly enriched (2 to 3.5 x CO) in rims as is the moderately volatile element Ga relative to bulk CO chondrite values. Se and Ga also show modest enrichments relative to CI chondrite values illustrating that matrix is indeed the major reservoir for these elements in ALH A77307. The only other analysis of CO3 matrix [5] was carried out by neutron activation analysis from a matrix fragment in Ornans. These data show evidence for lower enrichments for the volatile elements Se, Zn and Ga (~1.5 x CO) than our SXRF analyses, but differ in other important respects in having higher refractory abundances in comparison with the microprobe data as noted by [5]. Fig. 3 illustrates that ALH A77307 matrix has suffered extremely complex fractionations, consistent with the presence of a number of different matrix components with different origins [3]. Overall, matrix appears to be depleted in refractory elements, but is enriched in the moderately volatile siderophile and chalcophile elements, consistent with the view that matrix did not suffer extensive high temperature processing prior to accretion. The high volatile contents also argue strongly against a chondrule origin for rim materials.

456481

592-910

ABS ONLY

LPSC XXIV

189

N 94-12107

**MARTIAN PARTICLE SIZE BASED ON THERMAL INERTIA CORRECTED  
FOR ELEVATION-DEPENDENT ATMOSPHERIC PROPERTIES** N.T. Bridges,  
U.S. Geological Survey, Menlo Park, CA 94025

Thermal inertia is commonly used to derive physical properties of the Martian surface. If the surface is composed of loosely consolidated grains, then the thermal conductivity derived from the inertia can theoretically be used to compute the particle size [1]. However, one persistent difficulty associated with the interpretation of thermal inertia and the derivation of particle size from it has been the degree to which atmospheric properties affect both the radiation balance at the surface and the gas conductivity. These factors vary with atmospheric pressure so that derived thermal inertias and particle sizes are a function of elevation [2]. Here, by utilizing currently available thermal models and laboratory information, a fine component thermal inertia map [3] has been convolved with digital topography to produce particle size maps of the Martian surface corrected for these elevation-dependent effects. Such an approach is especially applicable for the highest elevations on Mars, where atmospheric back radiation and gas conductivity are low.

The original Viking thermal model (VTM) [4] assumed a constant back radiation equal to 2% of the noontime insolation. In contrast, the Haberle and Jakosky thermal model (HJTM) [5] takes into account the radiative properties of a time varying and dusty CO<sub>2</sub> atmosphere. The larger back radiation in the HJTM results in lower thermal inertias and derived particle sizes than the VTM. However, neither model explicitly considers the decline in atmospheric back radiation with elevation. As back radiation decreases, the derived thermal inertia increases. Atmospheric dust increases back radiation in addition to that due to CO<sub>2</sub> alone and thus lowers the derived thermal inertia, with the magnitude of the this change increasing with pressure in proportion to the dust opacity. Finally, the particle size inferred from the thermal inertia depends mostly on the gas conductivity within the pore space gas [6]. The gas conductivity within the pores is a function of the spacing between adjacent particles and the atmospheric pressure, so that the particle size derived from the thermal inertia is proportional to surface pressure.

To produce the particle size maps, the fine component thermal inertia and digital topography were compared to two lookup tables on a pixel by pixel basis. To compute the change in thermal inertia with elevation a lookup table from [7] that lists the change in thermal inertia with different amounts of back radiation was used. Two different computer runs, one using the VTM and another using an approximated version of the HJTM were conducted. For the VTM, back radiation was set to 2% at an elevation of 0 km and modeled to decay exponentially with a scale height of 10 km. For the HJTM, CO<sub>2</sub> back radiation independent of dust was modelled to decay with elevation as outlined in [2] from a value of 4% at -2 km, which is the elevation of Viking Lander 1 where the original HJTM was applied. The dust component of the HJTM back radiation was set proportional to an opacity of 0.4 at -2 km, with the opacity decaying exponentially in proportion to the scale height. After the thermal inertias were corrected for elevation, they were converted to particle size by comparing them to another lookup table that listed particle size as a function of pressure (and hence elevation) and thermal inertia. This table was based on laboratory measurements reported in the literature [6,8-12].

The resulting particle size maps show that relative variations in thermal inertia across the Martian surface translate well to similar relative variations in particle size using both the VTM and HJTM for elevations near 0 km. However, at high elevations, the elevation-corrected particle size can be up to 1-2 orders of magnitude larger than the uncorrected value. For example, the Tharsis shield volcanoes generally show an elevation-corrected particle size larger than dust, in contrast to previous interpretations of a thick dust mantle overlying these constructs (Figure 1). However, based on terrestrial experience, widespread sheets of sand-sized particles are implausible over these shield volcanoes. The high inferred particle size is more likely due to lava flows only partially and/or thinly mantled by dust. Dust within depressions separated by bedrock outcrops generally smaller than the 15 cm-size rocks modelled by [3] and/or bedrock covered by a veneer of dust thinner than the dust diurnal skin depth will have an average inferred particle size larger than dust. This model is consistent with the variable albedo of the Tharsis volcanoes, where changes in



## MARTIAN PARTICLE SIZE: Bridges, N.T.

brightness may be caused by erosion and deposition of dust on exposed rock outcrops [13-14]. It also agrees with the strong diffuse radar backscatter of Tharsis that indicate a rough surface at the radar penetration depth [15]. The increase in apparent particle size with elevation may mean that the Tharsis volcanoes contain the least dust near their summits and the most toward their lower regions.

### References

- (1) Jakosky, B.M. (1986) *Icarus*, **66**, 117-124. (2) Jakosky, B.M. (1979) *Jour. Geophys. Res.*, **84**, 8252-8262. (3) Christensen, P.R. (1986) *Icarus*, **68**, 217-238. (4) Kieffer, H.H. et al. (1977) *Jour. Geophys. Res.*, **82**, 4249-4291. (5) Haberle, R.M. and Jakosky, B.M. (1991) *Icarus*, **90**, 187-204. (6) Weschler, A.E. et al. (1972) *Prog. Astronaut. Aeronaut.*, **28**, 215-241. (7) Zimbelman, J.R. (1984) PhD Dissertation, Ariz. St. Univ., 302 pp. (8) Deissler, R.G and Boegli, J.S. (1958) *Trans. Am. Soc. Mech. Eng.*, **80**, 1417-1425. (9) Fountain, J.A. and West, E.A. (1970) *Jour. Geophys. Res.*, **75**, 4063-4069. (10) Masamune, S. and Smith, J.M. (1963) *Ind. Eng. Chem. Fundam.*, **2**, 136-143. (11) Weschler, A.E. and Glaser, P.E. (1965) *Icarus*, **4**, 335-352. (12) Woodside, W. and Messmer, J.H. (1961) *Jour. Appl. Phys.*, **32**, 1688-1699. (13) Lee, S.W. et al. (1982) *Jour. Geophys. Res.*, **87**, 10,025-10,041. (14) Christensen, P.R. (1986) *Jour. Geophys. Res.*, **91**, 3533-3545. (15) Simpson, R.A. et al. (1978) *Icarus*, **33**, 102-115.

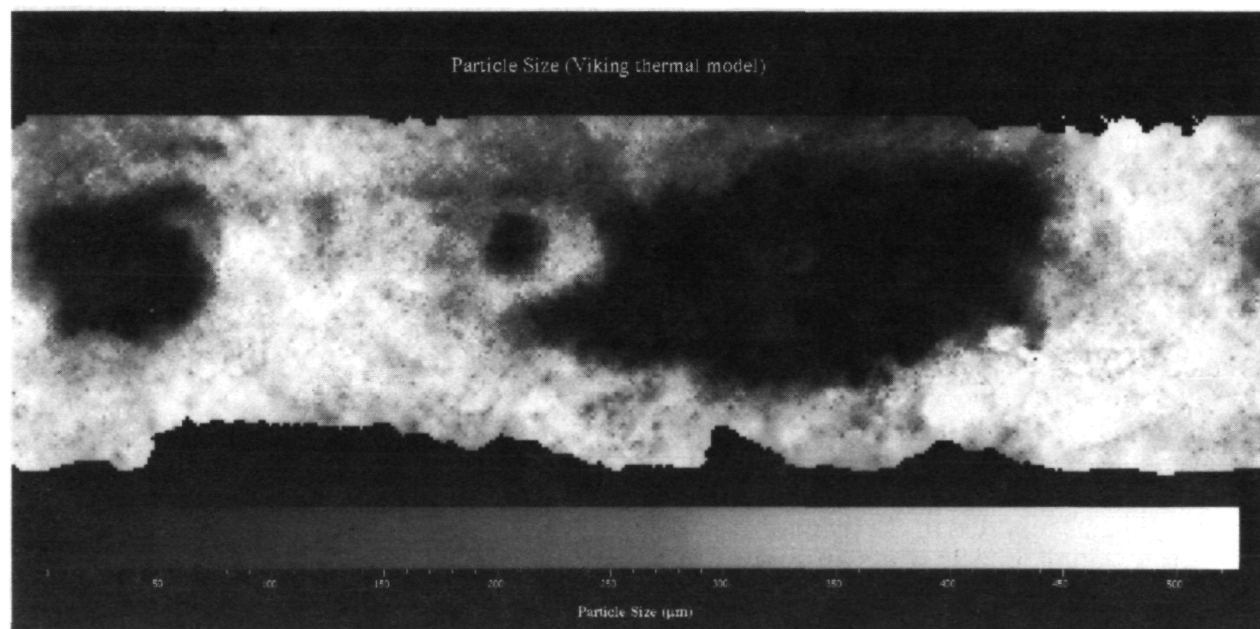


Figure 1. Particle size on Mars using the Viking thermal model corrected for elevation-dependent atmospheric properties. Map extends from 0° W on the right to 360°W on the left. Bright splotch at middle right, within dark region, is Olympus Mons.

456483

39B-91  
ABS ONLYLPSC XXIV  
N94-12108  
163373

191

**MULTIPLE NITROGEN COMPONENTS IN LUNAR SOIL SAMPLE 12023.** D.R. Brilliant, I.A. Franchi and C.T. Pillinger, Planetary Sciences Unit, The Open University, Milton Keynes MK7 6AA.

Nitrogen is one of the enigmatic elements in lunar soils and breccias. The large range in  $\delta^{15}\text{N}$  values found within lunar soils was initially attributed to a secular increase in the  $^{15}\text{N}/^{14}\text{N}$  ratio of 50% within the solar corona, and hence in the implanted nitrogen within the lunar regolith (1). However, more recent explanations have proposed a two (or many) component mixing model of solar wind nitrogen with some hypothetical non-solar components (2,3). Such components could include indigenous lunar nitrogen (4), nitrogen contained in interstellar grains in primitive meteorites (5,6) and magnetospheric nitrogen from the terrestrial atmosphere (7).

To understand the makeup of multi-component mixtures it is advantageous to have carbon and noble gas data measured simultaneously, particularly in the case of lunar soils, where the solar wind is a likely fundamental contributor of nitrogen. To this end, a new nitrogen instrument has been adapted to give some of the desired data in parallel. Here we report conjoint measurements of N abundance and  $\delta^{15}\text{N}$ , together with  $\text{N}/^{36}\text{Ar}$  and  $^{36}\text{Ar}/^{38}\text{Ar}$  ratios obtained during a stepped combustion of lunar soil 12023. The results are preliminary to a much more comprehensive investigation of well characterised fractions of the sample which we still have available from a previous study (8). Stepped combustion of a sample of 12023,7 yielded 94 ppm nitrogen with a  $\delta^{15}\text{N} = +22.2\text{‰}$ , as well as the characteristic heavy-light-heavy pattern observed for lunar samples (4). The low temperature maximum was  $+75.1\text{‰}$  at  $550^\circ\text{C}$ , the minimum at  $800^\circ\text{C}$  with  $\delta^{15}\text{N} = -16.7\text{‰}$  and the high temperature  $\delta^{15}\text{N}$  peak is  $+90.6\text{‰}$  at  $1250^\circ\text{C}$ . The major releases of nitrogen occurred between  $650^\circ\text{C} - 800^\circ\text{C}$  in the form of a double peak; a third, substantial release occurred at  $1150^\circ\text{C}$  yielding 14.2 ppm of nitrogen coinciding with a small but recognisable drop in  $\delta^{15}\text{N}$  against a regularly increasing trend.

The  $^{36}\text{Ar}$  and  $^{38}\text{Ar}$  release profiles at face value resemble those of nitrogen but whilst  $\text{N}/^{36}\text{Ar}$  varies by nearly a factor of three (Fig. 1) with quite clearly defined mixing trends between different components, the  $^{36}\text{Ar}/^{38}\text{Ar}$  remains virtually constant between about 5.9 and 6.3 (*N.B.* no effort has been made to calibrate the mass spectrometer absolutely for argon or correct for mass fractionation effects; these are considered to be constant and raw data without blank subtraction are used throughout). If the consistency of the  $^{36}\text{Ar}/^{38}\text{Ar}$  is accepted as a measure of the solar wind contribution then the variation of  $\text{N}/^{36}\text{Ar}$  is interpreted as recognising input of nitrogen from different non solar wind sources. The alternative, that  $\text{N}/^{36}\text{Ar}$  is being fractionated by a factor of  $\approx 3$  by some diffusive process between different minerals or phases seems highly unlikely but clearly will be explored by the analysis of physical separates. On the basis of the total dataset, there is evidence of a component of nitrogen liberated at low temperature  $<600^\circ\text{C}$  enriched in  $^{15}\text{N}$ . A major contributor to the nitrogen from the contemporary solar wind (possibly 50% of the total) comes off between  $700^\circ$  and  $1000^\circ\text{C}$  when the  $\text{N}/^{36}\text{Ar}$  is about 10. The true  $\delta^{15}\text{N}$  of this component is difficult to discern but may be  $\approx +10\text{‰}$ . The problem of establishing its  $\delta^{15}\text{N}$  value is related to the fact that a smaller, isotopically lighter ( $<-16\text{‰}$ ) fraction is liberated in the temperature range  $760$  to  $900^\circ\text{C}$  during which the  $\text{N}/^{36}\text{Ar}$  ratio changes to at least 13. Whether this

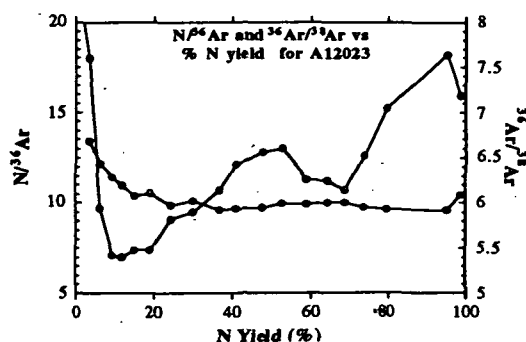
# MULTIPLE LUNAR NITROGEN COMPONENTS: Brilliant *et al.*

is the so called ancient lunar nitrogen is open to question; if it ultimately has a  $\delta^{15}\text{N} < -200\text{‰}$  it is of low relative abundance in 12023. From the data here however we can say that the light nitrogen is not found in the interior of complex particles. The "ancient surfaces" component can be directly equated with the major release at 1100 to 1150°C coinciding with the anticipated melting temperature of the soil. This relatively large amount of gas must have an isotopic composition close to the 10‰ suggested for the major component discussed earlier to account for the dip of only 5‰ in the overall upward  $\delta^{15}\text{N}$  trend. There is no possibility that this pulse of nitrogen can be a spallogenic component because (i) the amounts observed are totally unreasonable (ii) if spallogenic gas was released in amounts of this magnitude the  $\delta^{15}\text{N}$  would go off-scale (spallogenic nitrogen has a  $^{14}\text{N}/^{15}\text{N}$  ratio *ca.* 1) and (iii) the  $^{36}\text{Ar}/^{38}\text{Ar}$  ratio shows no increase of cosmogenic  $^{38}\text{Ar}$ . However since the  $\delta^{15}\text{N}$  is increasing regularly all across the high temperature extraction region, a small amount of spallogenic nitrogen is being released at least up to 1250°C. The  $\text{N}/^{36}\text{Ar}$  ratio of what we believe to be ancient particles is slightly higher than that proposed for contemporary surfaces but this might be a genuine fractionation effect.

At a conservative estimate we can see four different nitrogen components in 12023. The major solar wind contributed gas is sited in two locations which can readily be discerned. Further analyses of physically separated particles, and higher resolution heating programmes, with conjoint data gathering to include carbon measurements, and use of pyrolysis to supplement combustion extraction techniques, can be expected to shed more light on problems concerning the nitrogen budget of the lunar soil which are long overdue for solution.

## References:

- (1) Kerridge J.F. (1989), *Science* **245**, 480 - 86. (2) Geiss J. and Bochsler P. (1982) *Geochim. Cosmochim. Acta* **46**, 529 - 48. (3) Kerridge J.F., Bochsler P., Eugster O. and Geiss J. (1992). *Proc. Lunar. Planet. Sci. Vol. 22*, 239 - 48. (4) Becker R.H. and Clayton R.N. (1975), *Proc. Lunar Sci. Conf. 6th*, 2131 - 49. (5) Norris S.J., Wright I.P. and Pillinger C.T. (1983), *Meteoritics* **18**, 366 - 67. (6) Brilliant D.R., Franchi I.A. and Pillinger C.T. (1992) *Meteoritics* **27**, 206-207. (7) Geiss J. and Bochsler P. (1991), *The Sun in Time* (eds. C.P. sonnett, M.S. Giampapa, M.S. Matthews), Univ. of Arizona, Tuscon, 98 - 117. (8) Gardiner L.R., Woodcock M.R. and Pillinger C.T. (1977) *Proc. Lunar. Sci. Conf. 8th*, 2817-2839.



456484

594-91  
ABS ONLY

N 94-12334109

A REEXAMINATION OF AMINO ACIDS IN LUNAR SOIL; K. L. F. Brinton and J. L. Bada, The Scripps Institution of Oceanography, University of California, San Diego, La Jolla, CA 92093-0212

J. R. Arnold, Department of Chemistry, University of California, San Diego, La Jolla, CA 92093-0317

Amino acids in lunar soils provide an important indicator of the level of prebiotic organic compounds on the moon. The results provide insight into the chemistry of amino acid precursors, and furthermore, given the flux of carbonaceous material to the moon, we can evaluate the survival of organics upon impact. The amino acid contents of both hydrolyzed and unhydrolyzed hot-water extracts of Apollo 17 lunar soil were determined using o-phthalaldehyde/N-acetyl cysteine (OPA/NAC) derivatization followed by HPLC analysis [1]. Previous studies of lunar amino acids were inconclusive, as the technique used (derivatization with ninhydrin followed by HPLC analysis) was unable to discriminate between cosmogenic amino acids and terrestrial contaminants [2]. Cosmogenic amino acids are racemic, and many of the amino acids found in carbonaceous meteorites such as Murchison, i.e.  $\alpha$ -amino-i-butyric acid (aib), are extremely rare on Earth. The ninhydrin method does not distinguish amino acid enantiomers, nor does it detect  $\alpha$ -alkyl amino acids such as aib, whereas the OPA/NAC technique does both.

The sample 78421,16 was collected during the Apollo 17 mission. Two 1 g portions were hot-water extracted for 24 h. The extract of one sample was directly analyzed, while the other was acid-hydrolyzed for 23 h in 6 N HCl prior to analysis. Control blanks were processed and analyzed concurrently with both samples. The samples were derivatized with OPA/NAC for 15 minutes in order to maximize the detectability of aib, and then analyzed by HPLC [2]. See Table 1 for the results.

Table 1: Amino acid analysis results, blank corrected and reported in ng/g, with an estimated error of  $\pm 20\%$ . All determinations are based on retention time only. Sample 78421 was analyzed in this study, while the 72501 results are reported by Fox et al. [1].

	<u>78421</u>		<u>72501</u>	
	unhydrolyzed	hydrolyzed	unhydrolyzed	hydrolyzed
D,L-Aspartate	0.0	0.0	0.1	0.7
D,L-Serine	0.5	0.9	0.1	0.3
D,L-Glutamate	0.0	0.2	0.0	0.7
Glycine	3.5	10.6	1.7	7.1
D-Alanine	0.0	0.2		
L-Alanine	1.1	1.2	0.3*	1.1*
Aib	0.3	0.2	0.0	0.0

\*Fox et al. did not distinguish between alanine enantiomers [1].

The excess of L-alanine over D-alanine and the high abundance of serine indicate the presence of terrestrial contamination. However, in this study we

## A REEXAMINATION OF AMINO ACIDS IN LUNAR SOIL: Brinton K. L. F. et al.

did not attempt to resolve the serine enantiomers as we were specifically looking for aib, which has never before been detected in lunar soils. The peaks corresponding to aib and D-alanine in the hydrolyzed fraction are indicative of indigenous lunar amino acid precursors.

Previous investigations have shown that aqueous solutions of HCN, upon hydrolysis, yield glycine and small amounts of other amino acids [1, 3]. In our work, the large increase in glycine upon hydrolysis supports the surmise that the precursor responsible for the amino acids is HCN indigenous to lunar soil.

Using the value of 12.1  $\mu\text{g/g}$  (hydrolyzed) for aib in the Murchison meteorite [4], and 1-2% for carbonaceous chondritic debris in lunar soil, we have estimated the aib content of lunar soil to be 0.1-0.2  $\mu\text{g/g}$ , assuming 100% survivability. (We obtain a similar value, to within an order of magnitude, by examining the long term accumulation of IDP's.) Since our results show the actual aib content of lunar soil to be  $<0.3 \text{ ng/g}$ , we calculate the impact survivability of aib on the lunar surface to be approximately  $10^{-3}$ . This is likely to be an overestimate, since aib may also be a product of the acid hydrolysis of HCN [3].

Studies of amino acids on the moon are important in evaluating whether organic compounds required for the origin of life on Earth may have been supplied from extraterrestrial sources. Our results suggest that, although amino acids may be present on the moon, they are more likely derived from precursor molecules, rather than being components of extraterrestrial debris [5].

## REFERENCES

- [1] Zhao M. and Bada J. L. (1989) *Nature*, 339, 463.
- [2] Fox S. W., Harada K., and Hare P. E. (1976) *GCA*, 40, 1069.
- [3] Yuasa S., Flory D., Basile B., and Oró J. (1984) *J. Mol. Evol.*, 20, 52.
- [4] Cronin J. R. and Pizzarello S. (1983) *Adv. Space Res.*, 3, 5.
- [5] Chyba C. and Sagan C. (1992) *Nature*, 355, 125.

456 485

395-25  
ABR ONLY

LPSC XXIV 195

N 9 4-1321510

**THE SPECTRAL EFFECTS OF SUBSOLIDUS REDUCTION OF OLIVINE AND PYROXENE.** D.T. Britt. Lunar and Planetary Laboratory, University of Arizona, Tucson, AZ 85721. P2

**Introduction:** The surfaces of atmosphereless bodies are subjected to a variety of chemical, thermal, accretionary, and shock processes related to their regolith environment. These processes are responsible for a number of alterations that occur in regoliths. Alterations include particle size commutation, implantation of solar wind gases, formation of agglutinates, spectral darkening, and, in the lunar case, the development of the very strong red continuum slope in the visible and near infrared spectra. A great deal of work has pointed to the role of agglutinates as the principal agent for darkening and reddening the lunar soil [1]. The measures of regolith maturity are strongly linked to the accumulation of agglutinates [2]. Recent work has suggested that the finest fractions of agglutinitic glass are major source of the spectral red slope [3]. In particular, the red slope is most strongly associated with the agglutinitic glasses that are rich in blebs of sub-micron sized metal particles. It is thought that these metal particles, because of their size and scattering efficiently relative to the wavelength of light, are responsible for the red continuum slope. This fine fraction of metal particles is produced primarily by reduction of  $\text{Fe}^{2+}$  from silicates [4]. One mechanism for the reduction process is the reaction of solar implanted wind protons with the regolith soil during impact events. In this case the presence of hydrogen creates a reducing environment and the thermal pulse from the impact greatly speeds the reaction kinetics. To explore other reducing and thermal environments a series of experiments were done using samples in evacuated capsules buffered by Tantalum and heated to subsolidus temperatures.

**Experimental:** To achieve oxygen fugacities below the iron-wustite buffer grains of mineral samples were placed in an evacuated capsule and buffered with Tantalum [5]. The mineral samples were olivine from South Point, Hawaii ( $\text{Fo}_{89}$ ), and pyroxene from Webster, North Carolina ( $\text{En}_{88}$ ). Both samples were made up of grains between 0.5-2 millimeters in diameter. Samples were separately heated to 1250 °C, held at that temperature for 22 hours, and then slowly cooled. The olivine sample was crushed and reheated to 1250 °C for 10 hours to simulate regolith processing.

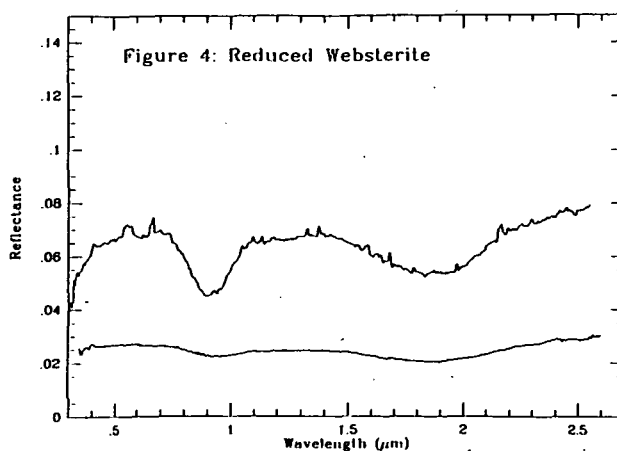
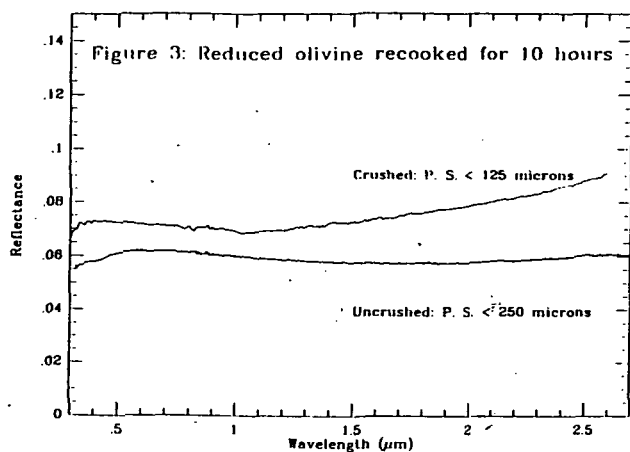
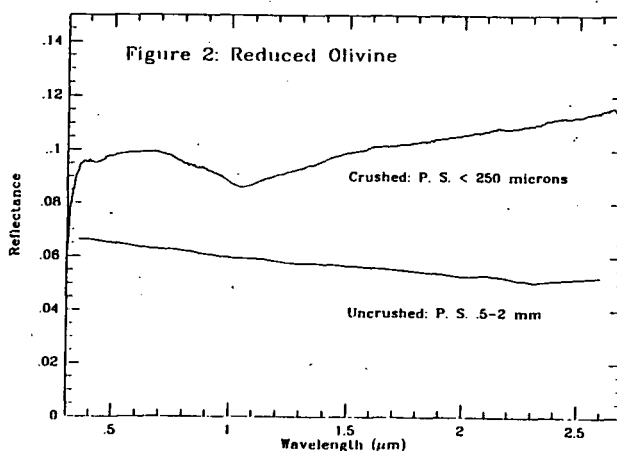
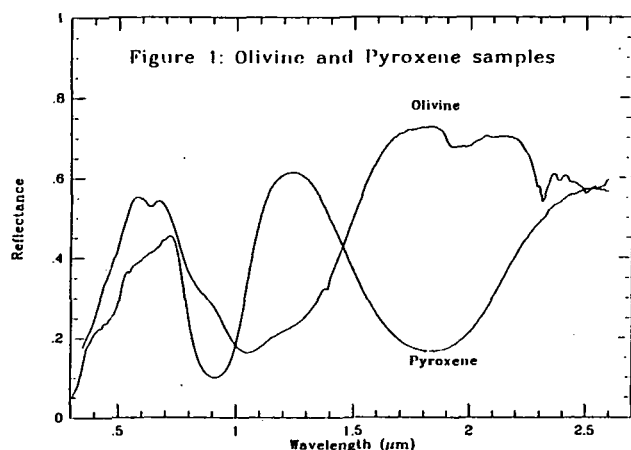
**Discussion:** Shown in Figure 1 are the bidirectional reflectance spectra of the olivine and pyroxene samples before reduction. Both samples show the characteristic high reflectance and strong absorption bands of olivine and pyroxene. For the olivine the reflectance at 0.55  $\mu\text{m}$  is 54% and there are several strong  $\text{Fe}^{2+}$  absorption bands that combine to form one large band centered at 1.03  $\mu\text{m}$ . The sample of low-calcium pyroxene is characterized by  $\text{Fe}^{2+}$  bands centered at 0.91 and 1.83  $\mu\text{m}$  and a reflectance of 37% at 0.55  $\mu\text{m}$ . Shown in Figure 2 are spectra of the olivine sample after reduction; note that the scale is much expanded from Figure 1. The lower spectrum is the sample before crushing and the upper spectrum is the same sample after it was crushed to a particle size of less than 250  $\mu\text{m}$ . Both spectra show dramatic changes to the optical properties of olivine as a result of reduction. In the case of the spectrum of the uncrushed material, the reflectance of the olivine has been reduced from 54% to 6.5% at 0.55  $\mu\text{m}$  and the strong absorption band at 1.03  $\mu\text{m}$  has been completely eliminated. The negative continuum slope of this spectrum is probably related to the large particle size of the olivine grains. Examination of thin sections made from grain mounts of this sample show that the reduction process has caused the formation of thin layers of elemental iron blebs concentrated on the surface, grain boundaries, and cleavage planes of the olivine grains. This layer is an optically thick coating that effectively masks the distinctive spectral signature of the bulk olivine. Crushing physically exposes the unaltered interior of the olivine grains and brings out a much reduced olivine band. This band is highly suppressed by the presence of opaque blebs formed during the reduction process and its depth has dropped from 73% in the original material to 14% in the reduced material. Reflectance is also highly suppressed at 10%. Another spectral change is the blue/UV charge transfer absorption edge has moved from 0.57  $\mu\text{m}$  to an abrupt absorption edge at 0.35  $\mu\text{m}$ . The sample also shows a slight red continuum slope in the IR. Shown in Figure 3 are spectra of the crushed sample after it was reheated in reducing conditions at 1250 °C for 10

## REDUCTION OF OLIVINE AND PYROXENE: D.T. Britt

hours. The additional reduction has produced opaque coatings that have lowered the samples reflectance back to 6% and again masked the olivine absorption. Crushing raises the reflectance only slightly to 7.3%, exposes a very highly suppressed 6% olivine band, and shows an increased red continuum slope. Shown in Figure 4 are the effects of reduction on the pyroxene sample. In the uncrushed sample reflectance and absorption features are very strongly suppressed. Reflectance drops from 37% to 2.7%, band depth in the 1.0  $\mu\text{m}$  band drops from 81% to 15%, and band depth in the 2.0  $\mu\text{m}$  band drops from 71% to 19%. With crushing exposing fresh material reflectance increases to 6.7% and band depth to 34% and 25% respectively.

**Conclusions:** Subsolidus reduction of common rock-forming minerals can take place rapidly in conditions of low  $f\text{O}_2$  and brief pulses of high temperature. This process forms a physically thin but optically thick opaque layer on the optically active surfaces of the material. Although the bulk chemistry of the material is not significantly changed, the optical properties are dramatically effected. This process can significantly reduce reflectance and attenuate absorption features of spectrally diagnostic minerals. Similar results are reported in this volume by Allen et al. [6].

**References:** [1] Adams J.B. and McCord T.B. (1971) PLC 2, 2183-2195. [2] McKay D.S. et al. (1971) PLC 2, 755-773. [3] Pieters C.M. et al., (1991) LPS XXIII, 1071-1072. [4] Morris R.V. (1980) PLC 11, 1697-1712. [5] Fogel B.F. (1991) Personal Communication. [6] Allen C.C., et al. (1993) LPS XXIV, in press.



456487

596-90  
ABS. ONLY

LPSC XXIV

197

N 9/43-1/2 1 1 1  
P 7

**1.2-to 3.5- $\mu$ m OBSERVATIONS OF ASTEROID 4179 TOUTATIS.** D.T. Britt<sup>1</sup>, E.S. Howell<sup>1</sup>, J.F. Bell<sup>2</sup>, and L.A. Lebofsky<sup>1</sup>. (1) Lunar and Planetary Laboratory, University of Arizona, Tucson, AZ 85721. (2) Planetary Geosciences Division, SOEST, University of Hawaii, Honolulu, HI 96822.

**Introduction:** The close Earth approach of the Apollo asteroid 4179 Toutatis during the winter of 1992-1993 has provided a unique opportunity for detailed ground-based observations of a near earth asteroid (NEA). Because of their relatively small size NEAs are usually far too faint to be observable by most ground-based instruments. This opposition by Toutatis was, however, exceptionally favorable. Toutatis approached within 0.03 AU of Earth and was as bright as 11th visual magnitude. This made the object observable in a wide variety of wavelengths including radar, thermal IR, near IR, and visual.

**Observations:** We obtained 1.2-to 3.5- $\mu$ m photometry of Toutatis on the night of January 3-4, 1993. Howell observed Toutatis with a 1.2-to 2.5- $\mu$ m CVF spectrophotometer, using the Multiple Mirror Telescope on Mount Hopkins in Arizona. Within two hours of that observation, Britt and Bell obtained J, H, K, 2.95  $\mu$ m, 3.12  $\mu$ m, and 3.35  $\mu$ m broad-band filter photometry using NASA's Infrared Telescopic Facility at the Mauna Kea Observatory in Hawaii. Since Toutatis has a very slow rotation period of approximately ten days, these observations are essentially of the same area on the object [1]. During the observations Toutatis was at or very near zenith, visual magnitude was approximately 12.8, phase angle was 15.2°, and the distance from Earth was approximately 0.182 AU. Toutatis was only 1.158 AU from the sun, so the 3.0  $\mu$ m data has a substantial thermal contribution.

**Results:** Only preliminary data reductions have been done. The 1.2-to 2.5- $\mu$ m CVF data show an absorption band centered near 2.0  $\mu$ m suggesting that pyroxene is a major contributor to the spectrum of Toutatis. In addition, the spectral slope between the broad-band J and K filters (1.25 and 2.2  $\mu$ m respectively) is about 6-10%, which is a modest red slope for an S class asteroid. The shape of the CVF spectrum obtained at the MMT was closely matched by the J, H, K broad-band filter data from the IRTF. The thermal correction for the 3.0  $\mu$ m data is particularly challenging because Toutatis is very close to the Sun, rotates very slowly, and radar images show it to have a very complex shape [2]. Preliminary reductions of these data indicate that Toutatis is, as expected for an S class asteroid, anhydrous, but standard thermal models do not apply directly to this object and further work remains to be done.

**References:** [1] Spencer, J.R. (1993) Personal Communication. [2] Ostro, S.J. (1993) Personal Communication.



456488

SAT-91

ABS-ON-27

LPSC XXIV

199

N 94-1621172

P 2

**FLEXURE AND THE ROLE OF INPLANE FORCE AROUND CORONAE ON VENUS.**

C. David Brown and Robert E. Grimm, Department of Geology, Arizona State University, Tempe, AZ 85287-1404.

**Introduction.** Large coronae on Venus, such as Artemis and Latona, are rimmed by conspicuous trenches and associated outer rises. Sandwell and Schubert [1] have observed that these systems resemble terrestrial subduction zones in planform and have succeeded in fitting an elastic plate bending equation to the inferred flexural topography. However, the first zero-crossing bending moments required are  $-2.5 \times 10^{17}$  N for Artemis and  $-5.0 \times 10^{16}$  N for Latona. Since these moments are similar in magnitude to those of subducting slabs on Earth, a rollback subduction mechanism has been proposed to explain the flexure around the largest coronae, although a differential thermal subsidence model is sufficient to account for the topography around some coronae [1]. The purpose of this study is to investigate the effect of inplane force as a possible alternative to large applied moments in producing flexure at Artemis and Latona.

The close correlation of gravity to topography on Venus implies the absence of a low viscosity zone and the strong coupling of the lithosphere to mantle convection [2]. If coronae are the surface manifestations of mantle plumes, they may be the sites of active convective stress coupling. As the upwelling reaches the lithosphere, it spreads radially outward, inducing shear tractions on the base of the plate. In addition, the hot, expanding corona may load the surrounding plate horizontally. Both the basal shear stresses and radial loading can be treated as an equivalent compressive inplane force in the mechanical lithosphere, which contributes to the bending of the outlying plate.

Using a model that relates inplane force to the measured gravity anomalies [2], we calculate a rough value of the inplane force at Artemis. Recent Pioneer Venus spherical harmonic gravity models [3] indicate a geoid anomaly of about 75 m over Artemis, which corresponds to an estimated inplane force on the order of  $-1 \times 10^{13}$  N/m. The gravity model is unable to resolve Latona, but we assume an inplane force of similar dimensions. We can constrain the maximum possible inplane force based on the expected rheology by using the approximate 5 K/km thermal gradient inferred from the best fit 30 km elastic plate at Artemis and Latona [1]. For a dry olivine flow law in the upper mantle [4], the compressional load limit of the 60 km thick mechanical lithosphere is  $-4 \times 10^{13}$  N/m. This value is equivalent to a load of  $-8 \times 10^{13}$  N/m on a 30 km thick elastic plate.

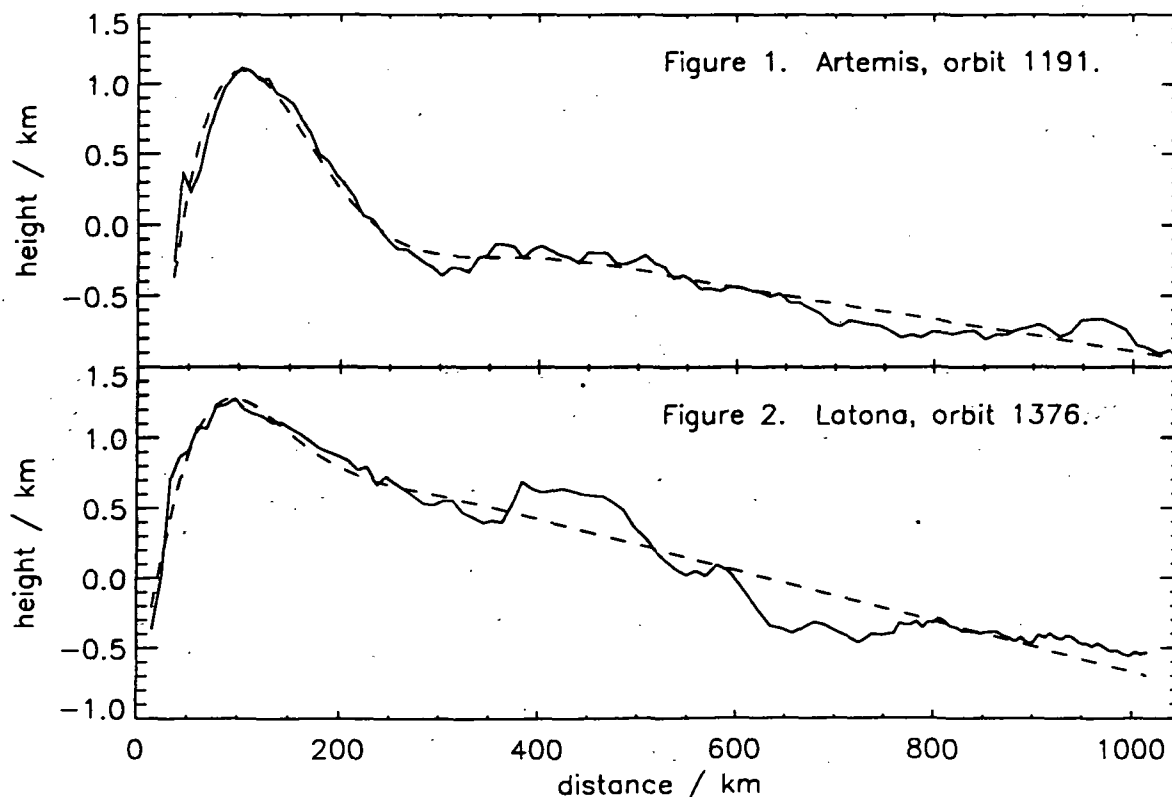
**Results.** To represent the effects of basal shear on flexure, an elastic plate bending equation that incorporates inplane force is used [5]. In this model, the applied moment ( $M$ ) at the trench axis, inplane force ( $N$ ), and trench depth ( $y_0$ ) all affect the amplitude of the flexure. The plate bending equation is fit to the Artemis topography from Magellan orbit 1191, and the Latona topography from orbit 1376. For the case of zero inplane force, this model yields a good fit to Artemis with  $M = -2.7 \times 10^{17}$  N,  $y_0 = 2$  km, and an elastic plate thickness of  $T_e = 30$  km. These results are comparable to a first zero crossing moment of  $M_0 = -2.0 \times 10^{17}$  N [1]. However, a better fit is offered by a case of zero applied moment,  $N = -8.1 \times 10^{13}$  N/m,  $y_0 = 2$  km, and  $T_e = 30$  km. Although this fit is excellent, the inplane force exceeds the estimate from gravity and may be at the yield strength of the lithosphere. If we assume an inplane force of  $-4.0 \times 10^{13}$  N/m, then a moment  $M = -1.2 \times 10^{17}$  N and a deeper trench ( $y_0 = 3$  km) are required to achieve a good fit to Artemis (Fig. 1). Latona is best fit by  $M = -4.7 \times 10^{16}$  N,  $y_0 = 2$  km, and  $T_e = 20$  km for zero inplane force. Again, the topography is just as well fit by a zero bending moment, with  $N = -1.9 \times 10^{13}$  N/m,  $y_0 = 2$  km, and  $T_e = 20$  km (Fig. 2).

# FLEXURE AND INPLANE FORCE ON VENUS Brown, C. D. and R. E. Grimm

**Discussion.** By estimating reasonable values of inplane force, we are able to model flexure at Artemis and Latona by minimizing the applied moment. The Latona topography can be matched by a model with no applied moment. However, a sizable bending moment is still required to fit the topography at Artemis. If the corona ridge is isostatically compensated, a subducted slab may need to be invoked to give such a large bending moment. Two-thirds of the uncompensated ridge topography at Artemis is necessary to provide a first zero crossing moment of  $-2.5 \times 10^{17}$  N with no inplane force [6]. Thus, if we assume that the ridge is only partially compensated, we may be able to explain the flexure by means of a  $-4.0 \times 10^{13}$  N/m inplane force and a  $-1.2 \times 10^{17}$  N bending moment. Since the coronae ridges sometimes exhibit flexure on both sides and are relatively narrow, partial compensation may be a valid supposition. If so, basal shear stresses caused by mantle convection may be the source of much of the flexure seen around coronae.

The large curvatures and extreme flexure at Artemis and Latona indicate that plastic failure is taking place and elastic plate bending models are not entirely adequate in this case [7]. Some terrestrial subduction zones can not be fit by an elastic plate bending equation and require an elastic-plastic model [8]. Also to be considered on Venus is the effect of lateral heterogeneity in the lithosphere outlying the corona, specifically a changing thermal gradient and plate thickness. Studies using an inelastic flexure model are in progress, and should give us greater insight into the flexural structures at Artemis and Latona.

**References.** [1] Sandwell, D. T. and G. Schubert (1992), *JGR*, 97, 16,069. [2] Phillips, R. J. (1990), *JGR*, 95, 1301. [3] Nerem, R. S. (1991), *Eos Trans. AGU*, 72, 174. [4] Chopra, P. N. and M. S. Paterson (1984), *JGR*, 89, 7861. [5] Parsons, B. and P. Molnar (1976), *Geophys. J. R. Astr. Soc.*, 45, 707. [6] Sandwell, D. T., and G. Schubert (1992), *Science*, 257, 766. [7] Phillips, R. J. and S. Mueller (1992), *Eos Trans. AGU*, 73, Fall Meeting Suppl., 327. [8] McAdoo, D. C., J. G. Caldwell, and D. L. Turcotte (1978), *Geophys. J. R. Astr. Soc.*, 54, 11.



456492

598-91  
ABS. ONLY

LPSC XXIV

201

N 94-10121313

Pr 2-3

**VISCOUS RELAXATION OF THE MOHO UNDER LARGE LUNAR BASINS.**

C. David Brown and Robert E. Grimm, Department of Geology, Arizona State University, Tempe, AZ 85287-1404.

**Introduction.** Viscously relaxed topography on the Moon is evidence of a period in lunar history of higher internal temperatures and greater surface activity. Previous work has demonstrated the viscous relaxation of the Tranquillitatis basin surface [1]. Profiles of the lunar Moho under nine basins were constructed from an inversion of lunar gravity data [2]. These profiles show a pattern of increasingly subdued relief with age, for which two explanations have been proposed [2]. First, ancient basins may have initially had extreme Moho relief like that of younger basins like Orientale, but, due to higher internal temperatures in early lunar history, this relief viscously relaxed to that observed today. Second, ductile flow in the crust immediately after basin formation resulted in an initially shallow basin and subdued mantle uplift. The intent of the work described in this paper is to test the first hypothesis.

**Model and Data.** The viscous relaxation model used here represents the near-surface rheology of the Moon as an isoviscous layer of viscosity  $\eta_1$  over an isoviscous halfspace of viscosity  $\eta_2$  [3]. The layer represents the crust, and the halfspace the mantle; thus, an important limitation of this model is that the viscosity discontinuity is imposed at the same depth as the compositional (density) boundary. The surface and Moho topography are obtained from published plots [2] and are scaled horizontally to the size of Orientale using the main ring diameter of each basin [4]. It is assumed that the main ring is the same tectonic feature for each basin, so it is representative of the basin size. Since most of the basins are within 15% of the size of Orientale, it was decided that vertical scaling of the topography was unnecessary.

**Results.** Tests of relaxation are carried out by using different relaxation times ( $t$ ) with both Orientale and Serenitatis starting profiles. The viscosity of the layer and halfspace are also varied, but this causes no change in the shape of the final profiles. An inviscid halfspace was modeled by setting  $\eta_2 = 10^{-10} \eta_1$ , but for all relative viscosities up to  $\eta_2 = 10^{-1} \eta_1$  the times required to achieve the same amount of relaxation are identical. Increasing or decreasing the absolute viscosity of the layer increases or decreases the relaxation time proportionally; therefore the value of  $t/\eta_1$  is independent of both the relative viscosities of the layer and halfspace and the absolute viscosities of each, as long as  $\eta_2 < \eta_1$ . In the results described below, the viscosities of the two regions are fixed to  $\eta_1 = 10^{24}$  Pa-s and  $\eta_2 = 10^{21}$  Pa-s.

The Serenitatis basin profile can not be fit by a relaxed Orientale profile. The peak of the Serenitatis mantle uplift is about 70% of the maximum Orientale uplift, but the narrow Orientale profile does not relax to the broad Serenitatis contour while retaining 70% of its original relief. Nectaris is reasonably well fit by the relaxed Orientale profile with  $t/\eta_1 = 6.3 \times 10^{-8}$  Pa<sup>-1</sup> (Fig. 1). Similarly, Tranquillitatis is roughly fit by a relaxed Orientale profile, though not quite as well. The best fit value of  $t/\eta_1$  is  $1.3 \times 10^{-7}$  Pa<sup>-1</sup>, which is comparable to the result for the surface topography [1]. In general, the relaxed Serenitatis starting profile offers a better fit to many of the basins than the relaxed Orientale profile. The closest fit found in this study is the relaxed Serenitatis profile to the Nubium uplift (Fig. 2). The excellent match strongly suggests that Serenitatis and Nubium had similar initial uplift shapes.  $t/\eta_1$  for this fit is  $9.5 \times 10^{-8}$  Pa<sup>-1</sup>. Note that values of  $t/\eta_1$  for the relaxed Serenitatis profile can not be compared to the Orientale results since the "initial" Serenitatis profile is presumably in a more advanced state of relaxation. The relaxed Serenitatis fit to Tranquillitatis

# LUNAR MOHO RELAXATION Brown, C. D. and R. E. Grimm

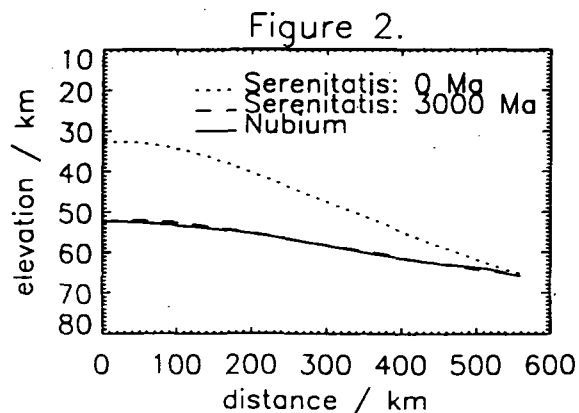
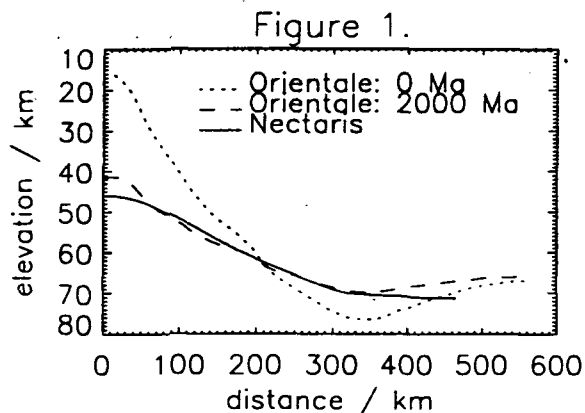
is better than the fit of the Orientale starting profile. Here  $t/\eta_1 = 6.3 \times 10^{-8} \text{ Pa}^{-1}$ . However, the Nectaris profile can not be fit by a relaxed Serenitatis profile; as with the poor fit of the Orientale starting profile to Serenitatis, this result seems to indicate that Serenitatis is an inappropriate starting profile for Nectaris.

**Discussion.** In general, Orientale is an inadequate starting profile for examination of viscous relaxation. Its creation later than the other basins at the nearside-farside boundary where the crust is thicker indicates that the conditions of its formation were unique. However, the better fit of the relaxed Orientale profile to Nectaris than the relaxed Serenitatis profile does demonstrate that there was some variation in the initial mantle uplift shapes among the old basins and therefore significant heterogeneity in conditions which controlled the Moho uplift. The results of this work show that Nubium and Tranquilitatis probably had initial uplifts like that of Serenitatis, and Nectaris had a starting profile more like that of Orientale.

Orientale is commonly assigned an age of 3.8 Ga, and we assume the time of significant possible viscous relaxation on the nearside ended at this time. Since Nectaris formed at 3.92 Ga [4],  $t = 0.12 \text{ Ga}$ . Using the best fit value of  $t/\eta_1$  for Orientale relaxed to Nectaris, we constrain the lunar mantle viscosity at this time to be less than  $10^{22} \text{ Pa-s}$ , which agrees with the value  $\eta_2 = 10^{21} \text{ Pa-s}$  favored by lunar thermal evolution models [5]. If a later "freeze-in" of the Nectaris profile is assumed (3.7 Ga), the maximum mantle viscosity must be about an order of magnitude greater, thus the result of the Nectaris fit supports the assumption that at least some nearside basins had stopped relaxing by the end of the Lower Imbrian.

The near-perfect fit of the viscously relaxed Serenitatis profile to Nubium offers strong evidence for viscous relaxation over several tens or hundreds of millions of years. If the lithosphere was very thin and the viscosities were much less, the uplifts could presumably relax soon after formation. But this explanation seems to rely heavily on the contribution of heat from the impact, since thermal models of the Moon's evolution typically limit the temperature in the upper 100 km to be less than  $800^\circ\text{C}$  in the first 0.5 Ga [5]. It would be unlikely for viscosities to be substantially lower than  $10^{21} \text{ Pa-s}$  at such temperatures. However, if the impact heat is the primary contributor to immediate relaxation, it is difficult to explain why the Orientale uplift remains so high, 60 Ma after Serenitatis formed and relaxed.

**References.** [1] Solomon, S. C., R. P. Comer, and J. W. Head (1982), *JGR*, 87, 3975. [2] Bratt, S. R., S. C. Solomon, J. W. Head, and C. H. Thurber (1985), *JGR*, 90, 3049. [3] Drew, W. A. (1982), B. S. Thesis, MIT, unpublished. [4] Wilhelms, D. E. (1987), *The Geologic History of the Moon*, U. S. G. S. Prof. Paper 1348. [5] Cassen, P., R. T. Reynolds, F. Graziani, A. Summers, J. McNellis, and L. Blalock (1979), *Phys. Earth Planet. Inter.*, 19, 183.



456851

2f

5.99 - 90

ABS 04/7

LPSC XXIV

203

N 94-139114

p-2-

# DETERMINING THE RELATIVE EXTENT OF ALTERATION IN CM CHONDRITES

Lauren B. Browning<sup>1</sup>, Harry Y. McSween, Jr.<sup>1</sup>, and Michael Zolensky<sup>2, 1</sup> Department of Geological Sciences, University of Tennessee, Knoxville, TN 37996-1410, <sup>2</sup> Solar System Exploration Division, NASA Johnson Space Center, Houston, TX 77058.

The aqueous alteration of CM chondrites provides a record of the processes attending the earliest stages of parent body evolution [1]. However, resolving the alteration pathways of chondritic evolution requires a means for distinguishing the relative extent of alteration that individual samples have experienced. We propose three new indices for gauging the relative degree of alteration in CM chondrites based on modal and compositional analyses of 7 CM falls. The proposed alteration parameters are consistent with the basic tenets of several previous models [2,3,4] and correlate with additional indices to produce an integrated method for determining the relative extent of alteration. The model predicts the following order of progressive alteration: Murchison (MC)  $\leq$  Bells (BL)  $<$  Murray (MY)  $<$  Cochabamba (CC)  $<$  Mighei (MI)  $<$  Nogoya (NG)  $\leq$  Cold Bokkeveld (CB).

The broad range of CM phyllosilicate compositions observed within individual meteorites is fundamental to the characterization of the aqueous alteration process. Chemical analyses of CM phyllosilicates suggest that these phases became systematically enriched in Mg and depleted in Fe with increasing alteration [2]. This is consistent with the results of mass balance calculations, which support the progression from Fe<sup>3+</sup>-rich cronstedtite to Mg-rich serpentine as alteration proceeded [3]. We submit that the relative extent to which this mineralogical progression is completed can be monitored by a stoichiometric approximation based on the amount of Si-substitution in matrix phyllosilicates. The proposed Fe<sup>3+</sup>/(2-Si) alteration indicator relies on a phyllosilicate stoichiometry, [(Fe, Mg)<sub>3-x</sub>(Al, Fe<sup>3+</sup>)<sub>x</sub>(Si<sub>2-x</sub>(Al, Fe<sup>3+</sup>)<sub>x</sub>)O<sub>5</sub>(OH)<sub>4</sub>], which accommodates a continuous transition from cronstedtite to serpentine compositions. Decreasing Fe<sup>3+</sup>/(2-Si) ratios signify increasing alteration. To test this parameter, mean Fe<sup>3+</sup>/(2-Si) ratios were calculated from an average of 14 microprobe analyses of matrix phyllosilicate crystals in each meteorite except Cochabamba, from which only defocused beam matrix analyses are currently available. We also intend to determine the oxidation states of Fe in each sample by mössbauer spectroscopy.

It is generally accepted that the phyllosilicates of CM chondrites were produced at the expense of anhydrous silicates by aqueous reactions [1,2]. Because the volume of phyllosilicates should, therefore, increase during progressive alteration [4], we propose two new alteration parameters which monitor the volumetric production of CM phyllosilicates. These indices are based on the modal analyses of 1 to 3 thin sections from each of the analyzed falls. The first, the percent of remnant anhydrous matrix silicates, represents the volume of primary olivines and pyroxenes in the matrix that were not altered by aqueous alteration. Figure 1 shows that decreasing volume percentages of remnant silicates in the CM matrix correlate with decreasing Fe<sup>3+</sup>/(2-Si) ratios. This supports previous proposals that the systematic alteration of anhydrous silicates is accompanied by the production of phyllosilicates which are progressively more depleted in Fe [2,3]. The anomalous volume of remnant silicates in CB is probably the result of the breakup of chondrules during advanced stages of alteration. The second modal-based alteration index is the percent of phyllosilicates within chondrules and aggregates. This parameter indicates that chondrules and aggregates are also systematically consumed by progressive alteration (Fig. 1b).

The production of CM phyllosilicates by low-temperature aqueous reactions suggests additional correlations that can be tested. For example, since phyllosilicates are the dominant hydrous phase in CM chondrites, a positive correlation should exist between phyllosilicate volume and bulk H abundance, which reflects H<sub>2</sub>O or OH<sup>-</sup> content [7]. Figure 2 shows a strong negative correlation between Fe<sup>3+</sup>/(2-Si) and H values, which is consistent with this hypothesis. In addition, the alteration order predicted by the proposed parameters correlates with the oxygen isotopic signature. Both  $\delta^{18}\text{O}$  (Fig. 3) and  $\delta^{17}\text{O}$  show progressive enrichment with increasing phyllosilicate abundance, as also noted by [8].

## CM CHONDRITES: Browning, L. B., McSween, H. Y., and Zolensky, M.

The comparison of several parameters yields an order of alteration consistent with whole-rock signatures, although analytical errors prevent the development of an absolute scale of alteration. Use of several parameters also provides a basis for identifying points exhibiting anomalous behavior. Applications of the  $\text{Fe}^{3+}/(2-\text{Si})$  ratio should prove beneficial in characterizations of small CM samples where modal and bulk analyses are not feasible.

**References:** [1] M. Zolensky and H. Y. McSween (1988) *In: Meteorites and the Early Solar System* (eds. J. F. Kerridge and M. S. Matthews), 114-143, [2] K. Tomoka and P. R. Buseck (1985) *Geochim. Cosmochim. Acta* 49, 2149-2163, [3] H. Y. McSween (1987) *Geochim. Cosmochim. Acta* 51, 2469-2477, [4] H. Y. McSween (1979) *Geochim. Cosmochim. Acta* 43, 1761-1770, [5] L. Van Der Plas and A. C. Tobi (1965) *Am. J. of Science* 263, 87-90, [6] W. R. Van Schmus and J. M. Hayes (1974) *Geochim. Cosmochim. Acta* 38, 47-64, [7] J. F. Kerridge (1985) *Geochim. Cosmochim. Acta* 49, 1707-1714, [8] R. N. Clayton and T. K. Mayeda (1989) *LPSC* 20, 169-170.

\***Acknowledgements:** We are grateful for the oxygen isotope data provided by R. N. Clayton.

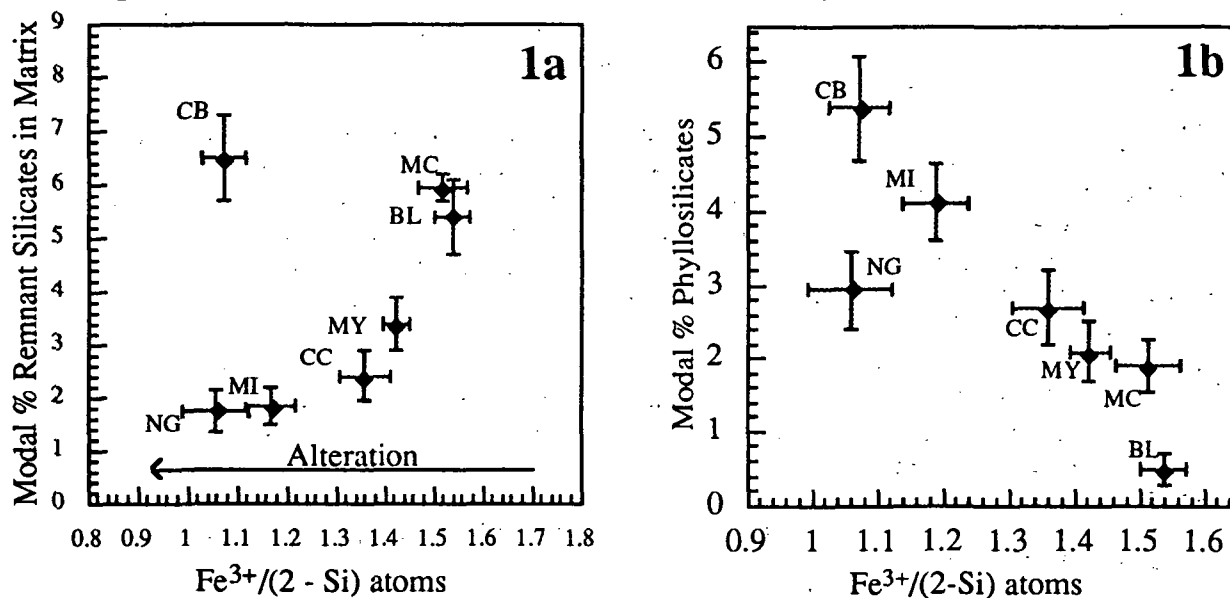


**Figure 1.** Comparison of proposed alteration parameters showing analytical and  $1\sigma$  modal counting errors.

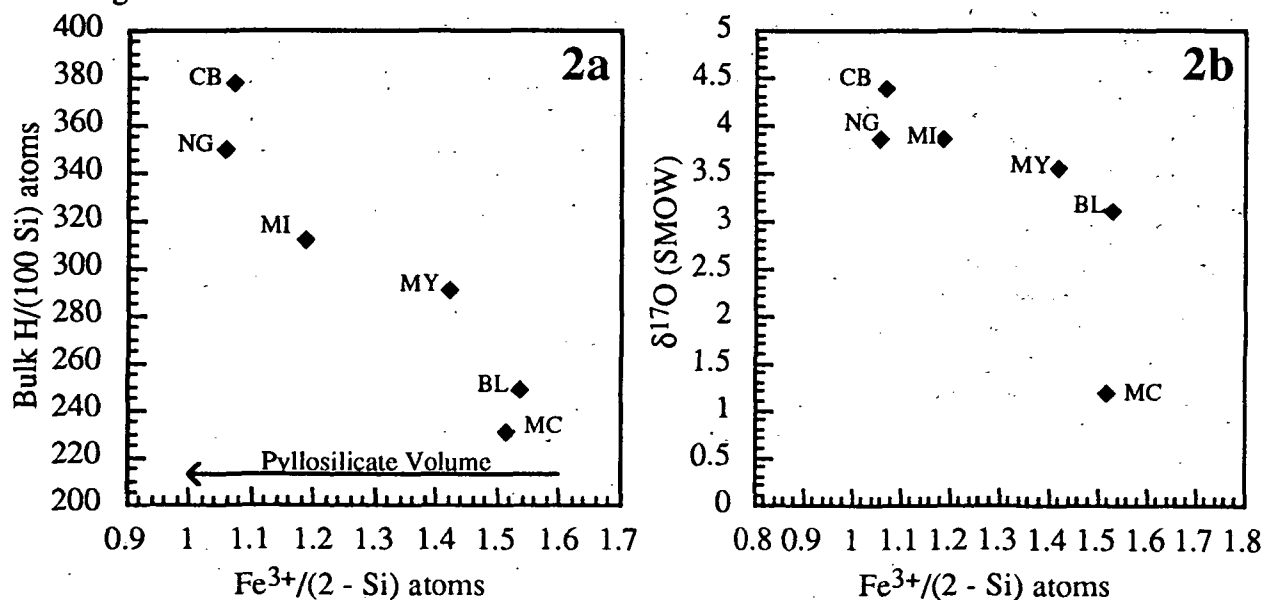


**Figure 2.** Comparison of bulk hydrogen abundance (a) and  $\delta^{17}\text{O}^*$  values (b) with the  $\text{Fe}^{3+}/(2-\text{Si})$  parameter. Hydrogen data taken from [6,7].

457852

5100-90

ABS. ONLY

LPSC XXIV

205

N 94-132115

Pr 2

**IDENTIFICATION OF COMETARY AND ASTEROIDAL PARTICLES IN STRATOSPHERIC IDP COLLECTIONS.** D.E. Brownlee, D. J. Joswiak, S. G. Love, Dept of Astronomy, Univ. Of Washington, Seattle, WA 98195, A.O. Nier, D.J. Schlutter, Dept. of Physics, Univ. of Minnesota, Minneapolis, MN 55455, and J. P. Bradley, MVA Inc., 5500 Oakbrook Parkway, Atlanta, GA, 30093.

N 94CROSS

We have determined He release temperature curves for a specially processed set of 5 $\mu$ m to 15 $\mu$ m stratospheric IDPs whose masses, densities and compositions have been accurately measured. The He release temperature in combination with atmospheric entry calculations yields a most probable entry velocity for each particle and association with either an asteroidal (low velocity) or cometary (high velocity) origin. We find that over half of the 5-15 $\mu$ m IDPs have entry velocities consistent with asteroidal origin and that at least 20% have cometary origins. A few of the asteroidal particles are porous aggregates and it appears that there may be close material similarities among some primitive asteroids and comets. In the processing of individual 5 $\mu$ m IDPs and determination of entry velocities we preserve a few dozen microtome slices that can be used for a variety of detailed TEM, IR and ion probe studies. These procedures provide laboratory samples that can be generically associated with asteroids and comets and are in a sense a limited sample return mission from these primitive bodies.

Earth encounter velocity is a distinguishing property of cometary and asteroidal dust [1,2]. The 1AU nodal crossing velocities estimated by Zook & Jackson [3] give typical asteroidal and cometary entry velocities into the atmosphere of 12 km s<sup>-1</sup> and 19 km s<sup>-1</sup>, respectively. For identical 10 $\mu$ m particles entering at 45° this velocity contrast results in a >300 °C difference in peak atmospheric heating. Using measured peak temperature we can calculate the entry velocity required to produce this temperature and clearly distinguish typical cometary dust particles on elliptical orbits from low inclination, low eccentricity dust that has spiraled in from the asteroid belt by Poynting Robertson drag.

In this project we determine the maximum heating temperature by measuring the temperature dependence of He release from particles subjected to pulsed step-wise heating [4]. The particles are heated to successively higher temperatures by 5s thermal pulses that mimic heating curves for atmospheric entry. Tests of lunar grains and IDPs have shown that the temperature release curves are reliable indicators of prior heating and degassing of the samples [4,5]. Estimated errors due to material differences and other factors are believed to be less than 100 °C. The smallest IDPs that can effectively be analyzed by this step-wise heating technique are 5 $\mu$ m and so we have chosen this diameter as our preferred IDP size. The remarkable ability to do the He analysis on 10<sup>-10</sup>g IDPs is the result of technique refinements [5] and increasing He concentrations of smaller IDPs that approach 1 cc (STP) g<sup>-1</sup> at 5 $\mu$ m diameter. The great advantage of using the smallest IDPs is that they are the least modified during atmospheric entry. For 5  $\mu$ m IDPs, typical 12 km s<sup>-1</sup> particles are heated to 400-500 °C and 19 km s<sup>-1</sup> particles are heated to 800-900 °C. Larger cometary particles are heated to higher temperatures and may be significantly altered.

The particles used for this study were specially picked from U2 collection surfaces to provide a random sampling of the smallest IDPs. They include a large

number of 5 $\mu$ m particles, a size that is not commonly removed from surfaces and curated. We picked particles and mounted them on special TEM mounts that carry 100 particles each in a square array. All particles were processed and analyzed by identical techniques. We did quantitative elemental analysis in the SEM at 20KV using the EDX techniques described by Schramm et al. [6]. To determine entry velocities from measured peak heating temperatures it is necessary to know the mass and density of each particle. We made this determination in the TEM with 120KV electrons using the technique described by Love et al. [7]. Individual particle masses are determined by absolute measurement of the Fe mass and dividing this by the fractional abundance of Fe. We believe that the mass, density and peak temperature measurements are sufficiently accurate to distinguish typical asteroidal and cometary particles.

The computation of velocity from peak heating temperatures is done with the atmospheric entry model of Love and Brownlee [8]. Velocities are computed for 45°, the most probable entry angle. Entry at shallower angles results in lower temperatures, but only a small fraction of particles enter at low enough angles to yield serious underestimates of velocity. A situation producing erroneously high implied velocity could occur when a 5 $\mu$ m particle is generated by fragmentation of a larger particle deep in the atmosphere. Due to the higher air density, such a particle is much more strongly heated than one that enters as an initially small particle. However, the extremely high He concentrations in the IDPs analyzed, indicate that their surfaces were exposed to space and that they are not fragments of larger particles. They have much higher He concentrations than found in gas-rich meteorites.

To date we have analyzed enough particles to show that the majority of small IDPs have low entry velocities consistent with asteroidal origin. We have also clearly identified cometary particles that are present at an abundance of >20%. An initial finding is that porous IDPs are found with both asteroidal and cometary orbits. Although much more work remains to be done, this finding suggests significant similarities between comets and at least one class of asteroid material. To significantly expand our ability to study particles that are destructively analyzed for He we have recently developed a procedure where a few dozen microtome slices are removed from each 5 $\mu$ m particle before it is run for He. This preserves a set of material with known generic origin that can be extensively studied. It is hoped that this work will provide vital information for comparison of the mineralogical, elemental and isotopic properties of asteroids and comets at the micron and sub-micron size scales. Using the sulfur embedding techniques discussed by Bradley et al. [9] we believe it will be possible to directly study cometary organics preserved in 5 $\mu$ m IDPs.

References: [1] G. Flynn, ICARUS 77, 287, 1989; [2] S. Sandford and J. P. Bradley, ICARUS 82, 146, 1989; [3] H. Zook and A. Jackson, ICARUS 97, 70, 1992; [4] A.O. Neir and D. Schlutter, Meteoritics 25, 263 [5] A.O. Neir and D. Schuttter LPSC 24, (this volume); [6] L. S. Schramm and D. E Brownlee, Meteoritics 24, 99, 1989; [7] S. G. Love, D. Joswiak and D. E Brownlee, LPSC 24 (this volume); [8] S. G. Love and D. E Brownlee, ICARUS 89, 26, 1991; [9] J. P. Bradley, L. Keller, K.L. Thomas, T.B. Vander Wood and D. E. Brownlee, LPSC 24, (this volume).



456853

3101-46

LPSC XXIV

207

MS CN 9/4-132116

QUANTIFYING THE EFFECT OF RHEOLOGY ON PLAN-VIEW SHAPES OF LAVA FLOWS; B.C. Bruno, G.J. Taylor (Planetary Geosciences, Dept. of Geology & Geophysics, University of Hawaii, Honolulu, HI 96822) and R.M.C. Lopes-Gautier (Jet Propulsion Laboratory, California Institute of Technology, Mail Stop 183-601, Pasadena, CA 91109).

**Introduction.** This study aims at quantifying the effect of rheology on the plan-view shapes of lava flows. Plan-view shapes of lava flows are important because they reflect the processes governing flow emplacement and may provide insight into lava flow rheology and dynamics. In our earlier investigation (1), we report that plan-view shapes of tholeiite basalts are fractal, having a characteristic shape regardless of scale. We also found we could use the fractal dimension (a parameter which quantifies flow margin convolution) to distinguish between the two major types of basalts: a'a and pahoehoe. Encouraged by these earlier results, we are currently developing a similar method for use on silicic flows and present our preliminary work.

**Data.** This analysis of silicic lavas is based on measurements of 10 flows. All of these measurements are from images; no field data have been taken to date. We selected only those lava flow margins that appear unaffected by topography. We divide these flows into two categories based on silica content, separating the basaltic andesites (SiO<sub>2</sub>: 52-58%) from the more silicic flows (SiO<sub>2</sub>: 61-74%).

**Methodology.** This analysis of silicic flows utilizes the same methodology as our earlier basaltic analysis. We calculate the fractal dimensions (D) of lava flow margins using the "structured-walk" method (2). In this method, the apparent length (L) of a lava flow margin is measured by walking rods of different lengths (r) along the margin. Since smaller rod lengths traverse more smaller-scale embayments and protrusions in the flow margin, L increases as r decreases. A linear trend on a log L vs. log r plot ("Richardson plot") indicates the data are fractal. D can then be calculated as  $D=1-m$ , where m is the slope of the linear least squares fit line to the data.

### Results and Discussion.

1) *Basaltic lava flows are fractals.* Our previous analysis of basaltic lava flows indicates that both a'a and pahoehoe flow margins are fractals, within the range of scale studied (r: 0.125m to 2.4km). Richardson plots are linear (Fig. 1a), demonstrating self-similarity.

2) *More silicic lava flows are generally not fractals.* Silicic lava flows tend to exhibit scale-dependent behavior within the range of scale studied (r: 10m to 4.5km). Typical Richardson plots for basaltic andesite (Fig. 1b) and dacite (Fig. 1c) are non-linear (not fractal), most notably for the dacite. Unlike the basaltic case, D tends to increase as r increases (Fig 2). This breakdown of fractal behavior at increased silica content is presumably related to the higher viscosities and yield strengths, which suppress smaller-scale features. Plan-view shapes of basaltic andesites typically have finger-like lobes, hundreds of meters in diameter. Superimposed upon these fingers are smaller-scale features, resembling crenulations. As silica content increases further, the lobes tend to widen (>1 km for typical dacites), protrude less from the main mass of the lava flow, and the smaller crenulations disappear.

3) *New Remote Sensing Tool.* We are in the process of developing a remote sensing tool that uses fractal parameters to quantitatively distinguish lava flows of different rheologies. There may be a critical value of r, related to silica content, which serves as a boundary for self-similar behavior (i.e., a value of r above which the flow appears fractal). This critical value may be related to lobe dimensions and/or the degree of suppression of smaller-scale features. We are currently investigating this hypothesis by simulating suppression of smaller-scale features on a synthetic fractal. Starting with an ideal fractal (Fig. 3a), we filter out the smaller-scale features, causing it to no longer be fractal (Fig 3b). Applying the same methodology described above, we generate Richardson plots (Fig. 4). The result is distinctly non-linear (not fractal; Fig. 4b), with a breakdown of fractal behavior at some critical value of r. This critical value is related to the size of the small-scale features suppressed. We liken the ideal case to basaltic flows, and the modified case to silicic flows. Silicic flows may also have critical values, and may be remotely distinguished by these values. We will compare our results to those of other remote sensing techniques aimed at quantifying lava flow morphology (3).

**References.** (1) Bruno, B.C. *et al.* (1992), *Geophys. Res. Lett.* 19, 305-308. (2) Richardson, L.F. (1961) *Genl. Syst. Yearbook* 6, 139-187. (3) Lopes-Gautier, R.M.C. *et al.* (1992), this volume (and references therein).

## QUANTIFYING PLAN-VIEW SHAPES OF LAVA FLOWS: Bruno, B.C. et al.

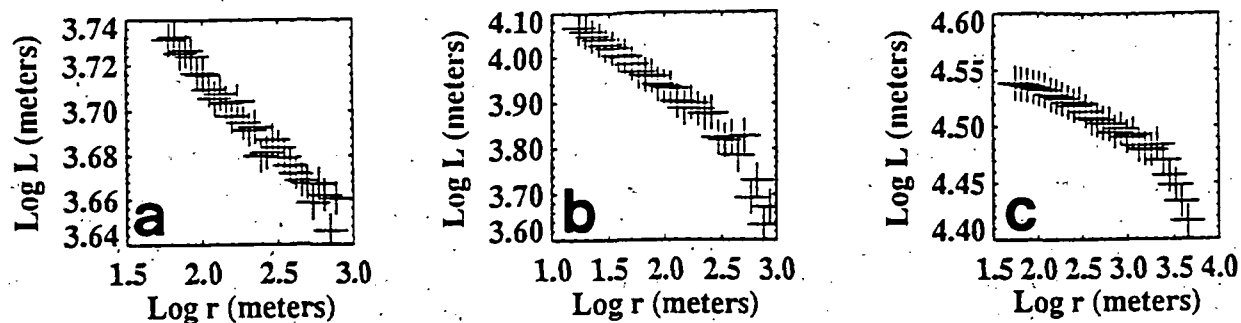


Figure 1. Typical Richardson plots for representative lava flows: (a) a'a basalt, (b) basaltic andesite, (c) dacite.

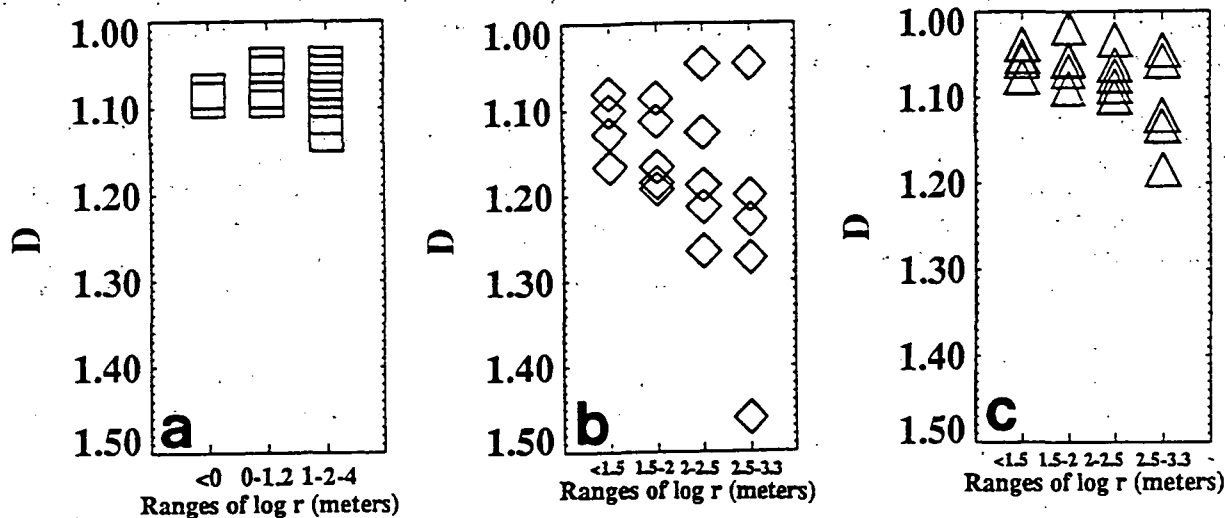


Figure 2. D vs. log r for all measured lava flows: (a) a'a basalts, (b) basaltic andesites, (c) dacites.

Figure 3. (a) Ideal Koch Triad (fractal); (b) Modified Koch Triad (not fractal), generated by filtering out smaller-scale features from (a). We compare (a) with basalt, as both are self-similar. We compare (b) with more silicic flows (e.g., dacite), where high viscosities and yield strengths suppress smaller-scale features.

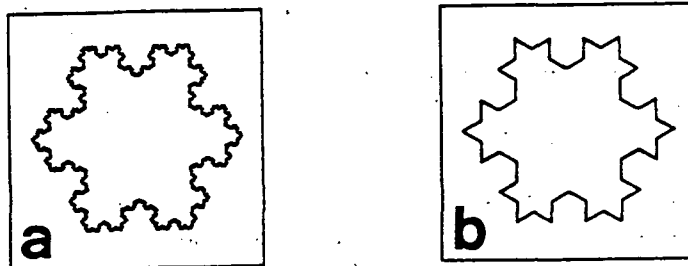
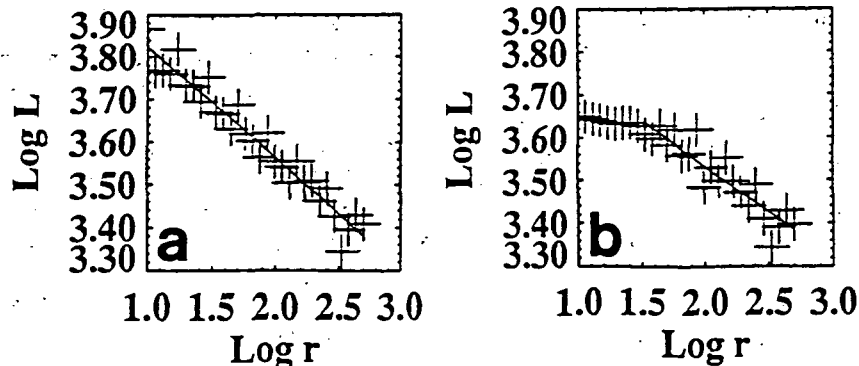


Figure 4. Richardson plots. Axes are in data numbers. (a) Ideal Koch Triad: linear plot, compare with basaltic plot (Fig. 1a); (b) Modified Koch Triad: non-linear plot, compare with dacitic plot (Fig. 1c).



5102-91  
456854, ABS ONLY

N 94-12117  
p 2

**EET87513 CLAST N: A CM2 FRAGMENT IN AN HED POLYMICT BRECCIA;** P.C. Buchanan<sup>1</sup>,

M.E. Zolensky<sup>2</sup>, A.M. Reid<sup>1</sup>, and R. A. Barrett<sup>3</sup>; <sup>1</sup>Department of Geosciences, University of Houston, Houston, TX 77204-5503; <sup>2</sup>SN2, NASA Johnson Space Center, Houston, TX 77058; <sup>3</sup>Lockheed ESCO, 2400 NASA Rd. 1, Houston, TX 77058.

**I. INTRODUCTION.** Xenoliths of material resembling carbonaceous chondrites have been found in several HED polymict breccias (e.g. Kapoeta, Bholghati). Most workers [1-5] have concluded that these clasts are related to CM2 meteorites on the basis of texture, bulk composition, and mineralogy. The present study reports data on clast N, a carbonaceous chondrite fragment from the howardite EET87513 large enough (~4x5mm on the surface of the slab from which it was separated) to extract bulk samples for INAA and oxygen isotope analysis and to provide a thin section for electron microprobe, SEM, and TEM analysis. Preliminary data for this clast have been reported in Buchanan et al. [6] and Zolensky et al. [7]. INAA was performed at Oregon State University by Y.-G. Liu and R. A. Schmitt and bulk oxygen isotopic composition was determined at the University of Chicago by T. K. Mayeda and R. N. Clayton. These data confirm that EET87513 clast N is a fragment of CM2 material.

**II. DESCRIPTION/DISCUSSION.** EET87513 clast N is composed of fine-grained, opaque matrix and coarser-grained, ferromagnesian silicates (Fig. 1), with some of the latter present as chondrules and aggregates (up to 250µm in diameter). Size range of chondrules and aggregates is consistent with that reported for CM2 meteorites [8]. These coarse-grained silicates are predominantly olivine (Fo60-89) with lesser amounts of orthopyroxene (Wo1-5En90-98). Matrix makes up ~75 vol. % of the clast and is composed primarily of concentrations of sulfides (pyrrhotite and pentlandite) and fine-grained silicates which form flowing, undulating textures wrapping around larger silicate grains, chondrules, and aggregates. Fuchs et al. [9] and Bunch et al. [4] describe similar textures in Murchison and in CM-like clasts from the howardite Jodzie. McSween [10] reports that CM2 meteorites contain 57-85 vol. % matrix.

Preliminary results of STEM analysis of matrix minerals from EET87513 clast N are published in Zolensky et al. [7]; the dominant matrix mineral in this clast is flaky and platy serpentine intergrown with minor amounts of flaky saponite. Fig. 2 shows the 7Å basal lattice fringes of this serpentine which are corrugated with abundant edge dislocations. Zolensky et al. [7] interpret this morphology as indicating that matrix material of this clast has been heated to less than ~400°C. Matrix saponite, though not found in most CM2 meteorites, has been found in Murray [13] and in the heated CM meteorite Belgica-7904 [11, 12, 13] and apparently indicates high water:rock ratios and/or temperatures during aqueous alteration [13]. Other matrix minerals present include chromite, tochilinite, tochilinite-serpentine [13], pyrrhotite, pentlandite, enstatite, olivine, diopside, and carbonaceous spheres [7].

In Fig. 3, bulk lithophile and siderophile element composition of EET87513 clast N [Y.-G. Liu and R. A. Schmitt, personal communication] are normalized to CI composition [14] and compared with bulk compositional ranges of CM, CO, and CV chondrites reported in Kallemeyn and Wasson [15]. Except for anomalous enrichments in the elements Sm and Au and depletion in Lu, these data suggest that EET87513 clast N is either a CM or CO chondrite. In Fig. 4, bulk oxygen isotope composition of this clast [T. K. Mayeda and R. N. Clayton, personal communication] is compared with ranges of oxygen isotope compositions for CR, C3, and CM chondrites taken from Clayton [16]; the composition falls to the <sup>16</sup>O-rich end of the CM trend.

**III. CONCLUSIONS.** On the basis of texture, matrix mineralogy, bulk composition, and oxygen isotopic composition, EET87513 clast N is a fragment of CM2 material. Matrix saponite indicates that this clast probably underwent aqueous alteration with higher water:rock ratio and/or temperature than typical CM2 materials [13]. Morphology of matrix serpentine indicates that this clast has been heated to less than ~400°C following aqueous alteration [7].

**REFERENCES.** [1] Wilkening L.L. (1973) *Geochim. Cosmochim. Acta* 37, 1985-1989; [2] Smith M.R. (1982) Ph.D. dissertation, University of Oregon, 193 pp.; [3] Bunch T.E. (1975) *Proc. Lunar Sci. Conf.* 6th, 469-492; [4] Bunch T.E. et al. (1979) *Geochim. Cosmochim. Acta* 43, 1727-1742; [5] Kozul J. and Hewins R.H. (1988) *Lunar Planet. Sci.* 19, 647-648; [6] Buchanan P.C. et al. (1990) *Lunar Planet. Sci.* 21, 141-142; [7] Zolensky M.E. et al. (1992) *Lunar Planet. Sci.* 23, 1587-1588; [8] King T.V.V. and King E.A. (1978) *Meteoritics* 13, 47-72; [9] Fuchs L.H. et al. (1973) *Smithsonian Contributions to the Earth Sciences* 10, Smithsonian University Press, Washington, 39 pp.; [10] McSween H.Y. Jr. (1979) *Geochim. Cosmochim. Acta* 43, 1761-1770; [11] Tomeoka K. (1990) *Proc. NIPR Symposium on Antarctic Meteorites* 3rd, 40-54; [12] Zolensky M.E. et al. (1991) *Papers presented to the 16th Symposium on Antarctic Meteorites*, National Institute of Polar Research, Tokyo, 195-196; [13] Zolensky M.E. et al. (1992) submitted to *Geochim. Cosmochim. Acta*; [14] Anders E. and Grevesse N. (1989) *Geochim. Cosmochim. Acta* 53, 197-214; [15] Kallemeyn G.W. and Wasson J.T. (1981) *Geochim. Cosmochim. Acta* 45, 1217-1230; [16] Clayton R.N. (1992) submitted to *Annual Review of Earth and Planetary Sciences*.

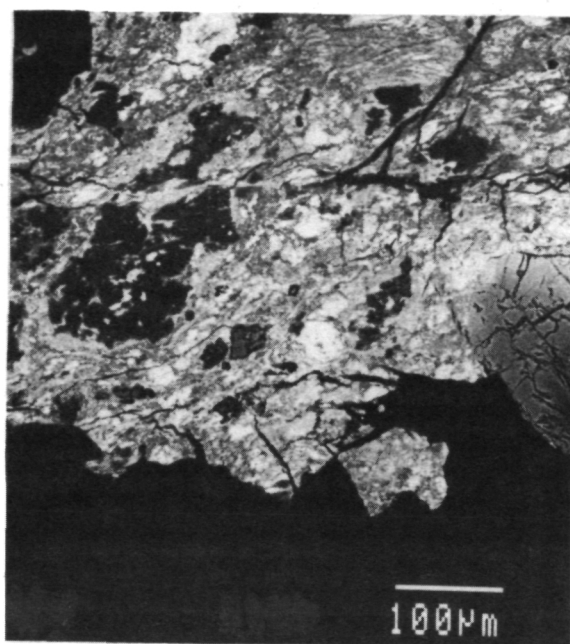


Fig. 1 BSEI of a portion of EET87513 clast N.

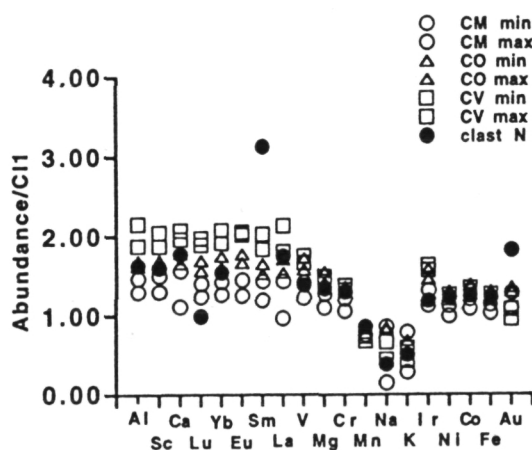


Fig. 3 Bulk abundances of lithophile and siderophile elements for EET87513 clast N [Liu and Schmitt, personal communication] normalized to CI compositions [14] and compared with ranges of abundances for CM, CO, and CV meteorites reported in Kallemeyn and Wasson [15]. Squares represent maximum and minimum values for CV chondrites. Triangles represent maximum and minimum values for CO chondrites. Circles represent maximum and minimum values for CM chondrites.

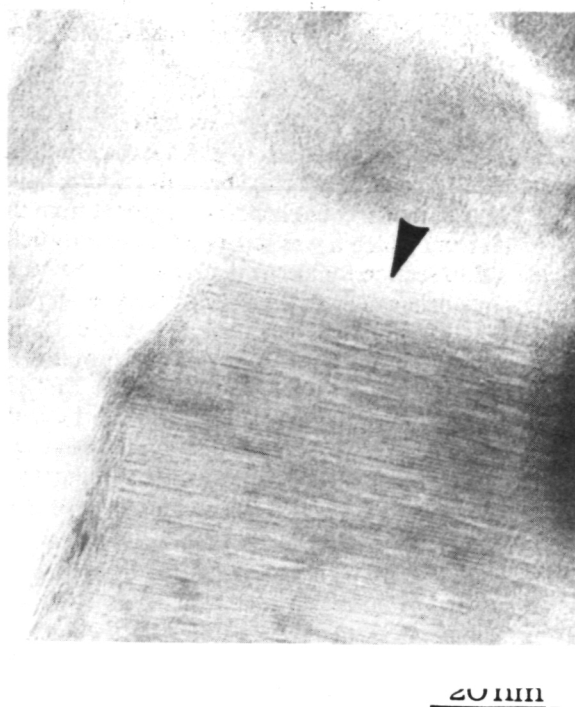


Fig. 2 TEM image of a flake of matrix serpentine from EET87513 clast N. 7 Å basal lattice fringes are obvious and are corrugated (arrow).

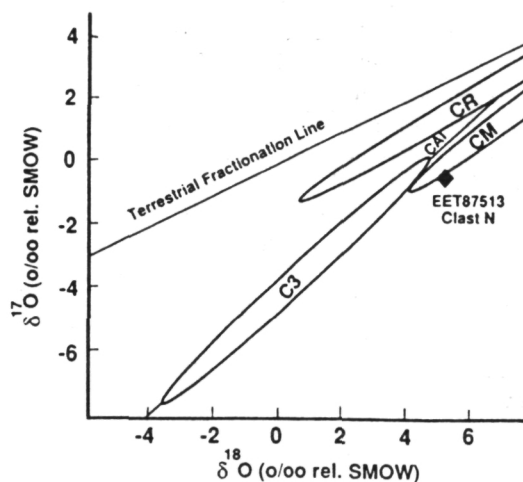


Fig. 4 Bulk oxygen isotopic composition of EET87513 clast N [Mayeda and Clayton, personal communication] compared with ranges of compositions for C3, CR, and CM chondrites taken from Clayton [16]. Terrestrial fractionation line and refractory inclusion line are also shown [16].

456855 S103-91  
ABSONLY  
P-2

N 94-3132-118

## CAN WEAK CRUST EXPLAIN THE CORRELATION OF GEOID AND TOPOGRAPHY ON VENUS?

W. Roger Buck, Lamont-Doherty Geological Observatory and the Department of Geological Sciences, Columbia University, Palisades NY 10964. Present Address: Science Institute, University of Iceland, Reykjavik, Iceland.

The effect on geoid and topography of low viscosity crust overlying a steady-state convecting mantle is estimated under the assumption that the shear between crust and mantle does not alter the mantle flow. The weak crustal layer can change the sign of the geoid to topography ratio (admittance). The positive long wavelength admittance for Venus is consistent with a weak crust overlying a mantle with a viscosity that increases strongly with depth.

The accepted interpretation of the strong positive correlation of geoid and topography on Venus, is that the convecting mantle of Venus has a constant viscosity with depth [1-4]. According to these workers, topography results from vertical normal stresses caused by mantle convection and highlands occur where mantle upwells. For topography to be supported by normal stress, the time scale for crustal flow must be long compared to the time scale for changes in the pattern of mantle flow. Because the high surface temperature of Venus may cause the crust to have a low viscosity, this assumption may be false. Topography should then be dominated by shear coupling between the crust and mantle.

In the absence of a crustal layer convection in a constant viscosity layer gives rise to a geoid anomaly that correlates positively with surface topography. When the viscosity in the layer increases with depth by several orders of magnitude the surface topography and geoid anomaly become anti correlated [5].

Consider that mantle convection in the absence of crust produces a 100 meter variation in geoid height  $\Delta N$ . In the case of a constant mantle viscosity the geoid high is above the mantle upwelling and in the case of strongly depth dependent mantle viscosity the geoid high is above the downwelling. Next, consider a low density, low viscosity crustal layer overlying a steady-state mantle convection cell. Convective normal stresses deflect the crust-mantle boundary, but do not affect the surface in steady-state, as noted in [6]. If the top of the mantle cell moves with a horizontal velocity of  $u_p$  and is of lateral dimension  $L$ , then shear stresses cause a difference in elevation between the surface above the mantle downwelling and over the upwelling of:

$$\Delta w = \frac{\partial w}{\partial x} L = \frac{3u_p \mu L}{g \rho_c h^2}$$

where  $g$  is the acceleration of gravity,  $w$  is topography.  $h$ ,  $\rho_c$  and  $\mu$  are the thickness, density and viscosity of the crust, respectively. In the limit that the crust is invicid the surface topography conforms to the geoid. Topographic differences should be the sum of the topography related to geoid variations and due to shear coupling as given above.

Assume that the stresses within the crust are small enough to have a negligible effect on the pattern and rate of mantle convection. Then the geoid anomaly  $\Delta N$  will be the combination of that due to convection in the absence of a crustal layer and that due to the topography and crustal thickness variations caused by the shear coupling between the mantle and crust.

Figure 1 shows the steady state topography for a range of conditions of shear coupling between crust and mantle for the two cases of mantle viscosity. Note the parameter on the horizontal axis is proportional to the elevation difference resulting from shear coupling. Figure 2 shows the same variation of the geoid height difference across the convecting cell. The admittance defined as the ration of geoid to topography is shown in Figure 3.

# Correlation of Geoid and Topography on Venus W. R. Buck

For Venus the observed admittance at long wavelength is of order 0.02-0.04 [2]. For the weak crust model, the sign of the admittance is positive and of magnitude 0.1 only for the model with a mantle viscosity that increases with depth. For convection cells on the order of 1000-5000 km and a crust of order 10 km thick the crustal viscosity would be in the range of  $10^{17}$  to  $10^{18}$  Pa s to give the observed admittance and elevation differences.

This model of a weak crust for Venus suggests that the mantle of Venus may have a similar viscosity structure as the Earth. Also all highlands must be underlain by mantle downwellings. Previously, [7] I showed that this kind of model might lead to low surface slopes in the lowlands and higher slopes in highlands due to thermal differences in the crust mantle system. Temporal variations in the rate of mantle convection can lead to either dominantly compressive or extensional features in highlands.

**REFERENCES** [1] Phillips R. J. and Malin M. C. (1984) *Ann. Rev. EPS*, 12, 411. [2] Kiefer W. S., Richards M. A., Hager B. H. and Bills B. G. (1986) *GRL*, 13, 14. [3] Kaula W. M. (1990) *Science*, 247, 1191. [4] Kiefer W. S. and Hager B. H. (1991) *JGR*, 96, 20,947. [5] Robinson E. M. and Parsons B. (1988) *JGR*, 93, 3144. [6] Bindshadler D. L. and Parmentier E. M. (1989) *JGR*, 95, 21,329.; [7] Buck W. R. (1992) *GRL*, 19, 2111.

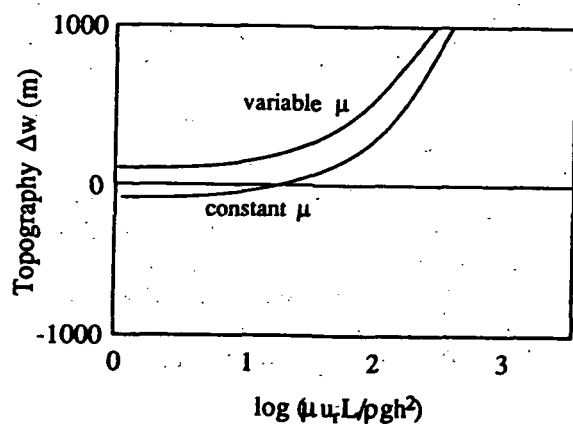


Figure 1

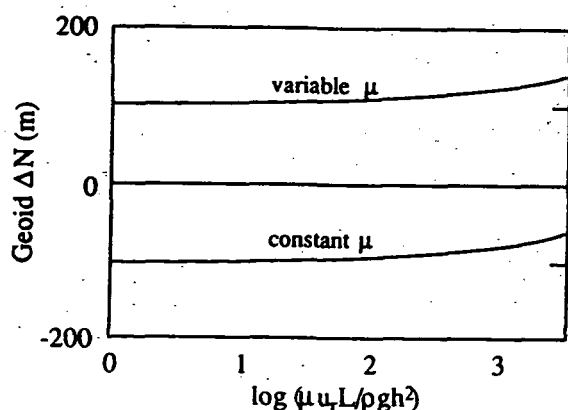


Figure 2

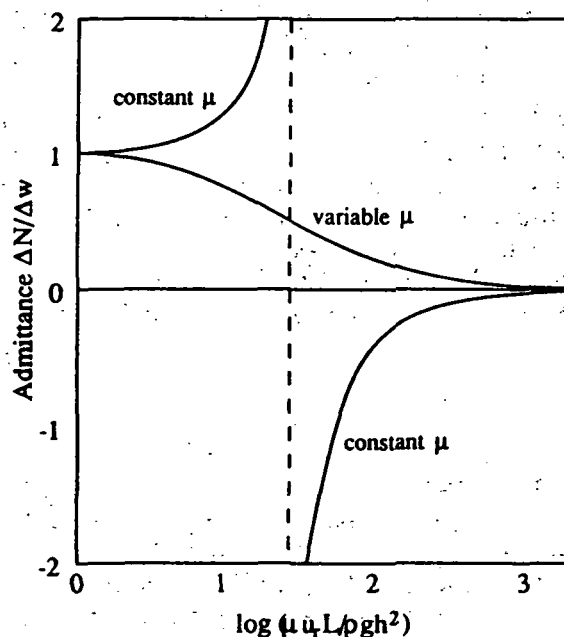


Figure 3

47

456856 5104-81  
PBS only  
P. 2  
LPSC XXIV  
N 94-312419 213

## VENUS RESURFACING RATES: CONSTRAINTS PROVIDED BY 3-D MONTE CARLO SIMULATIONS

M. A. Bullock, D. H. Grinspoon, University of Colorado, Laboratory for Atmospheric and Space Physics and the Department of Astrophysical, Planetary and Atmospheric Sciences, Boulder, CO 80309, J. W. Head, Department of Geological Sciences, Brown University, Providence, RI 02912

We have implemented a 3-D Monte Carlo model that simulates the evolving surface of Venus under the influence of a flux of impacting objects and a variety of styles of volcanic resurfacing. For given rates of impact events and resurfacing, the model predicts the size-frequency and areal distributions of surviving impact craters as a function of time. The number of craters partially modified by volcanic events is also calculated as the surface evolves. We find that a constant, global resurfacing rate of approximately  $0.4 \text{ km}^3/\text{yr}$  is required to explain the observed distributions of both the entire crater population, and the population of craters partially modified by volcanic processes.

An examination of the Venus impact cratering record revealed by Magellan thus far suggests interesting implications for its resurfacing history. In particular one feature of the observed crater population demands an explanation: The total density of craters suggests a surface which is approximately 500 million years old, yet the craters themselves are nearly all apparently in a state of perfect preservation [1]. The surface is young compared with the age of the planet, therefore some process is removing craters. Yet there are very few partially degraded, or partially buried craters observed. Schaber *et al.* [2] report only 4-6 % partially embayed craters. Any process that was removing craters gradually such as chemical or physical weathering, aeolian erosion or burial, viscous relaxation or volcanic flooding would be expected to leave a suite of craters in various states of degradation. Two hypotheses have recently been presented to explain the observed crater population.

The first hypothesis, the single production age or "spasmodic volcanism" model, is that resurfacing rates on Venus were quite high up to some point in the past and then rapidly declined, allowing subsequent crater preservation in pristine form [2,3,4]. The age of this change in surface activity may be roughly constrained by crater densities. The second hypothesis is that there has been a relatively constant rate of "regional resurfacing" [1,4]. Although statistical analyses of the spatial distribution of observed craters reveals that they are consistent with complete spatial randomness, ruling out extensive resurfacing events over large areas in the last  $5 - 10 \times 10^8$  years, this hypothesis suggests that the characteristic scale of the resurfacing events which dominate the steady-state evolution of the surface is smaller than the scale of randomness of the craters.

The resurfacing of Venus is modeled as the time evolution of the competing processes of impact cratering and volcanism [5]. The computer simulation of the planetary surface is represented on a 3-D grid, with a surface resolution of 5 km and a vertical resolution of 100 m. The total grid represents an area of  $4 \times 10^8 \text{ km}^2$ , the approximate surface area of Venus. Monte Carlo methods are used to randomly place impact craters, at rates and diameters derived from the observed mass distribution of Earth and Venus crossing asteroids and comets [6]. Rim heights are calculated from the diameter/height relationships for lunar impact craters [7]. A wide range of volcanic features are represented on the planet. The observed size-frequency distribution for volcanic features on Venus [4] is used to randomly select volcanic forms and to place them on the planet. Again, the observed distribution is fit to a power law for the Monte Carlo simulation. The areal extent of shield fields, large volcanoes, and lava floods is determined in the simulations by sampling the appropriate distributions for the feature type from Magellan data [4]. Lava flow features are modeled using an energy minimization technique to simulate the effects of local topography on the shape and extent of flows. By performing simulations with a wide range of resurfacing rates, we have seen that no fewer than 30% of the surviving craters are partially embayed by lavas, for resurfacing rates greater than  $2 \text{ km}^3/\text{yr}$ . At these resurfacing rates, the

model also shows that a steady state between crater impacts and volcanic resurfacing is established in less than 600 m.y. We therefore conclude that an equilibrium regional resurfacing is inconsistent with the observed number of partially embayed craters.

A unique solution to the problem of a constant resurfacing rate is provided by the constraints of the total number of impact craters, their spatial randomness, and by the number of partially embayed craters. The evolution of the crater population for a constant global resurfacing rate of  $0.37 \text{ km}^3/\text{yr}$  is shown in the two figures below. Figure 1 is a plot of the total number of surviving impact craters as a function of time. The low diameter cut off is 16 km, selected to adjust for the fall-off of low diameter impact craters due to atmospheric effects. A total of approximately 900 craters survive after 500 m.y., as shown by the solid line. The evolution of a pure production surface is shown by the dotted straight line. Figure 2 shows that the total number of partially embayed craters is about 5% of the total population.

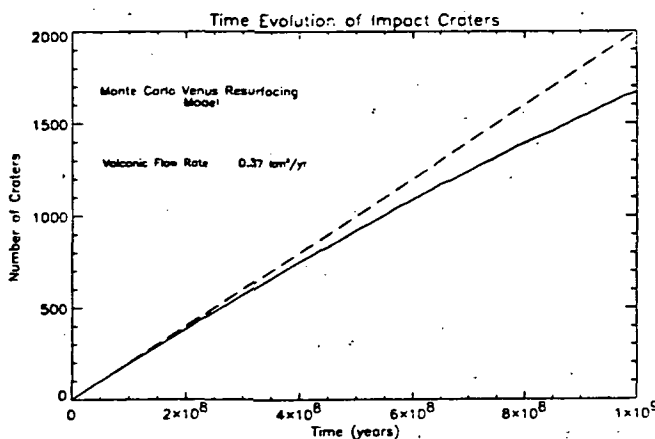


**Figure 1.** Time Evolution of Impact Craters

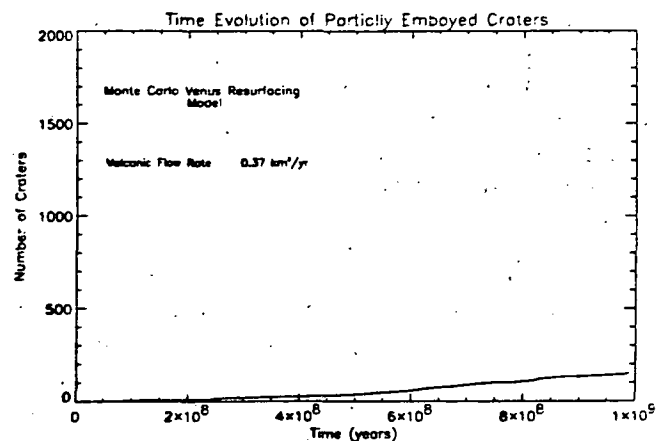


**Figure 2.** Time Evolution of Partially Embayed Impact Craters

Our results thus far suggest that the most likely scenario for the history of Venus' surface is that the observed crater population is the record of a relatively pristine surface that has undergone volcanic resurfacing on a regional scale at an average rate of about  $0.4 \text{ km}^3/\text{yr}$ . If the present crater population is one that has accumulated after some global catastrophic event, the age of the surface, as constrained by the spatial randomness and number of partially embayed craters is slightly greater than the crater production age, and is estimated to be about 500 m.y.

**References:** [1] Phillips, R.J. et al. (1991) *Science*, 252, 288. [2] Schaber, G.G. et al. (1992) *JGR*, 97, 13,257. [3] Head, J.W. et al. (1992) *JGR*, 97, 13,153. [4] Phillips, R.J. et al. (1992) *JGR*, 97, 15,923. [5] Bullock, M.A. et al. (1992) *Lunar and Planetary Science XXXIII*, 175. [6] Shoemaker, E.M. et al. (1989) *Reports of the planetary geology and geophysics program: 1988*. [7] Melosh, H.J. (1989) *Impact Cratering*, Oxford University Press, New York.



48

456857

5105-91

ABJ. OXLEY

LPSC XXIV

94-12120<sup>215</sup>  
763326

**SCALLOPED MARGIN DOMES: WHAT ARE THE PROCESSES RESPONSIBLE AND HOW DO THEY OPERATE ?** M H Bulmer, J E Guest (Univ. London Observatory. NW72QS, UK), G. Michaels, S Saunders (JPL 230-225 Pasadena CA 91109)

p. 2

Studies of scalloped margin domes (SMD) indicate the scallops are the result of slope failure. SMD's have similar but smaller average diameters (26.5 km) to unmodified domes (29.8 km), and the majority plot at altitudes ranging from 0.5-4.7 km, (figure 1) relative to the mean planetary diameter. A range of morphological types exist from those least modified to those that show heavy modification. Of the 200 SMD's examined, 33 have clearly discernible debris aprons. Examination and comparison of debris aprons with mass movement features on the Moon, Mars and in sub-aerial and submarine environments on Earth<sup>1</sup> using H/L against area (km<sup>2</sup>), suggests there are three main types of failure; debris avalanche, slumps and debris flow.

The five examples (figure 2) representing the morphological range within the SMD's, show the different modified forms and the different types of slope failures that have occurred. A large percentage of SMD's have narrow "flutes" on their perimeters possibly resulting from failures similar to those that give "block and ash" type flows on Earth. Radar bright material at the base of edifice appears analogous to crumble breccia around terrestrial domes. There is evidence that breaching on the flank causes material inside to flow out. This suggests that the failure in some cases occurred contemporaneous with the main eruptive phase. Evidence for sector collapse can be seen where a large part of the edifice has been removed and radar bright hummocky terrain lies at its base and on the surrounding plains. Such large failures occur on all the examples in the morphological range characterised by collapsed topography with a wide opening to one side of the edifice that forms a well defined amphitheatre. The existence of more than one amphitheatre gives the edifice the appearance of being scalloped. The hummocky nature of the collapsed material is a typical feature of dry volcanic debris avalanche deposits, each hummock consisting of one or more megablocks. The maximum run-out distance ranges from 12-55 km, the maximum width from 5-52 km and the maximum area from 52-2140 km<sup>2</sup>. More coherent failures situated close to the base of the edifice have characteristics of slump-type landslides. A well defined backscar is often visible and the deposits remain as a semi-coherent mass with a number of large blocks. One of the steep sided conical examples has a slump complex which contains blocks that may have undergone rotation. The maximum run-out distances of these deposits ranges from 8-34 km, the maximum width from 3-36 km and the maximum area from 77-375 km<sup>2</sup>.

Other processes of modification include magma withdrawal which results in a downsag seen most frequently on the lower domical structures. This may have occurred at the end of the main eruptive phase as a result of withdrawal or loss of volume through vesicle collapse. The existence of steep sided calderas suggest withdrawal also occurred catastrophically. The evidence of explosive activity remains uncertain but the existence of pits on the edge of a number of domes may be related to such activity. Heavily modified domes with only a fraction of the edifice remaining suggests topographic relaxation over time takes place.

The global distribution of domes<sup>1,2</sup> shows that many of the least modified domes are situated close to the margins of basins. From examination of seven unmodified domes it is suggested they show the shape expected for an axisymmetric gravity current spreading unimpeded over a horizontal surface<sup>3</sup>. Other forms of domes found away from these areas may have had a different rheology resulting in them undergoing modification. It is therefore necessary to examine the eruptive conditions under which domes form. There are a number of key factors that control dome formation: the effusion rate, rheological properties of the magma, thickness of the carapace, oversteepening of the margins, cooling rates, atmospheric effects and explosive activity.

These factors are being studied using theoretical models and laboratory experiments.

References: (1) Bulmer et al. in press. (2) Pavri et al. (1992) J. Geophys. Res., 97, 13,445-13,476. (3) McKenzie et al. (1992) J. Geophys. Res., 97, 15,967-15,976.

# SCALLOPED MARGIN DOMES: PROCESSES AND OPERATION

Bulmer, M.H. et al.

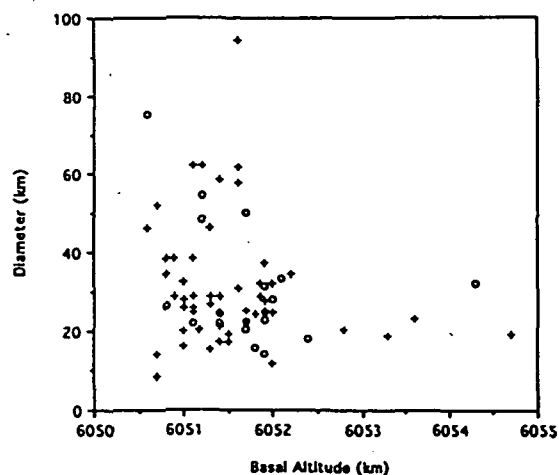
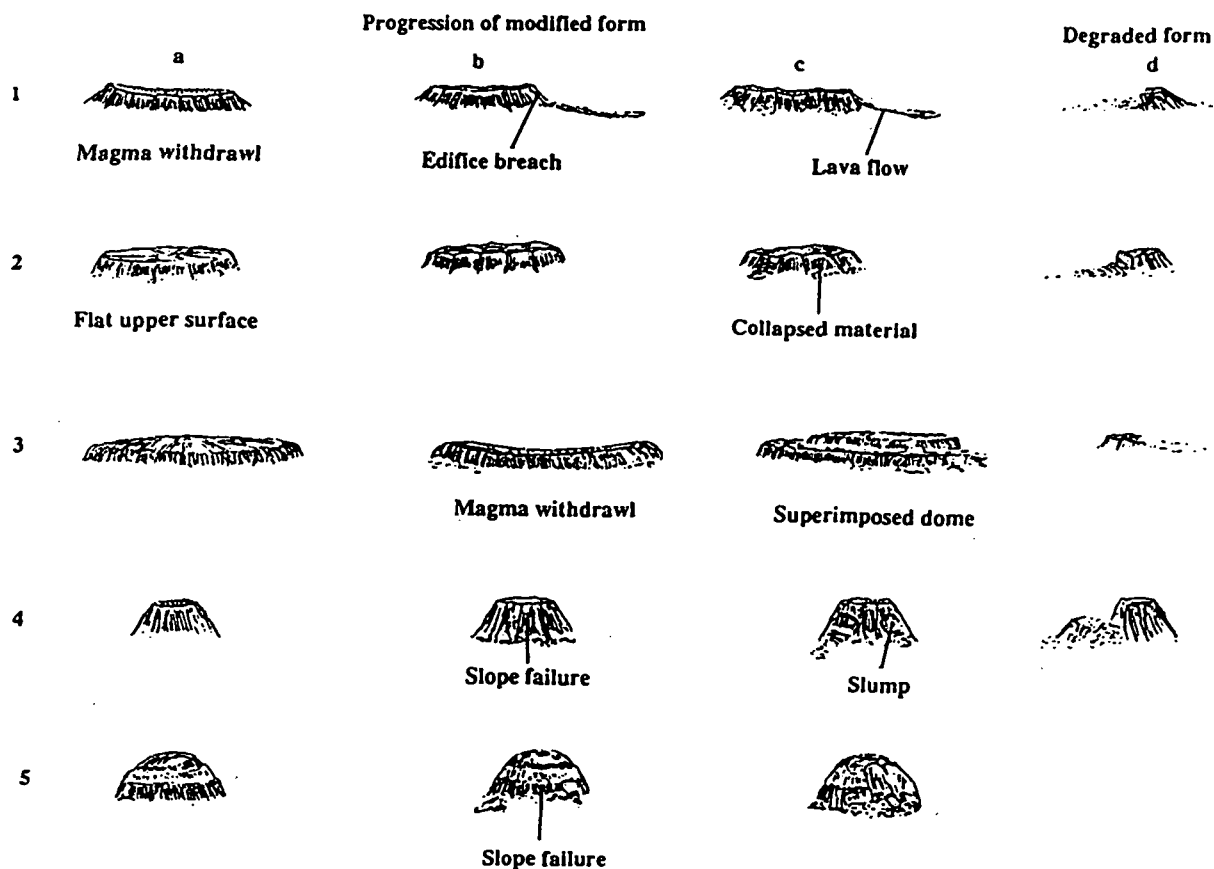


Figure 1 Plot of basal altitude with dome diameter for scalloped margin domes and unmodified domes.

Figure 2 Schematic representation of the formation of different types of scalloped margin domes.



S106-46

ABS ONLY

456858

N 94-12121

# YANA RING STRUCTURE, NORTH-EASTERN SIBERIA: A POSSIBLE COUNTERPART OF CORONAE ON VENUS

G.A.Burba, Vernadsky Institute, Moscow, 117975, Russia

An arch of Verkhoyansky Range in NE Siberia, Russia, is considered here as W and S parts of the rim of the large ring structure, referred hereafter as Yana Ring Structure (YRS) after the name of Yana River. It have general appearance similar to coronae on Venus and could be considered as the terrestrial counterpart of coronae.

The structure is located between 63 and 70°N, 125 and 140°E (fig. 1). The outer diameter of YRS (between the rim feet) is 680-700 km. The rim crest diameter is 500-520 km. The inner diameter (between the inner feet of the rim) is 320-350 km. The rim of YRS consist of the following topographic features: W segment is Orulgan Range (N part of Verkhoyansky Range), SW and S segments consist of S part of Verkhoyansky Range, SE segment is Elginskoye Ploskogorye (Tableland), E segment is Chersky Range (its part W of Indigirka River), NE segment is Selennyakhsky Range, and NW segment is Kular Range. Inside this ring of mountains Yanskoye Ploskogorye (Tableland) is located.

The circular outlines of YRS are marked with the large river valleys located outside: Lena River (lower of Aldan River mouth) is located W from YRS, Aldan River (lower of Amga River mouth) is from S, Indigirka River (between 64 and 67° N.lat.) is from E, and Selennyakh River (the part running N to S) is from NE.

The ring patterns inside the mountainous rim of YRS are marked with the tributaries of Yana River. The largest ring here, 300 km in diameter, consists of Bytangay (with Bellyakh) River at W, Nelgese and Derbeke Rivers at S/SE, and Tuostakh River at E.

The typical altitudes of YRS mountain rim are 1000-2000 m. The maximal ones are: 2400 m in W part of the rim, 2300 m in S, 1600 m in SE, 2200-2500 m in E, 1300-1500 m in N. The central part of YRS have typical altitudes of 400-600 m. There are lowlands with altitudes 50-200 m to the S, W, N, and NW outside YRS. Oymyakonskoye Nagorye (Highland) is located SE of YRS at 500-1500 m altitudes.

It should be recognized from this description YRS have a general appearance of circular highland with its central plateau located 1000-2000 m lower than surrounding mountain rim, but 300-400 m higher than plains of lowlands located outside the rim. Such topographic patterns are typical for coronae on Venus (1). The diameter of YRS is equal to the largest coronae on Venus. There are only 3 or 4 structures of such or larger size on the whole Venus. This calls to compare morphology and geologic evolution of YRS with morphology and models of coronae evolution, especially the largest ones, to search the similarities and/or differences in geologic histories of the structures on the Earth and Venus.

Reference: 1. G.A.Burba, V.P.Shashkina (1992). Topographic comparison of coronae on Venus and Transylvanian ring structure on the Earth. In: Lunar and Planetary Science XXIII, pp. 183-184.

## YANA RING STRUCTURE IN SIBERIA. Burba, G.A.

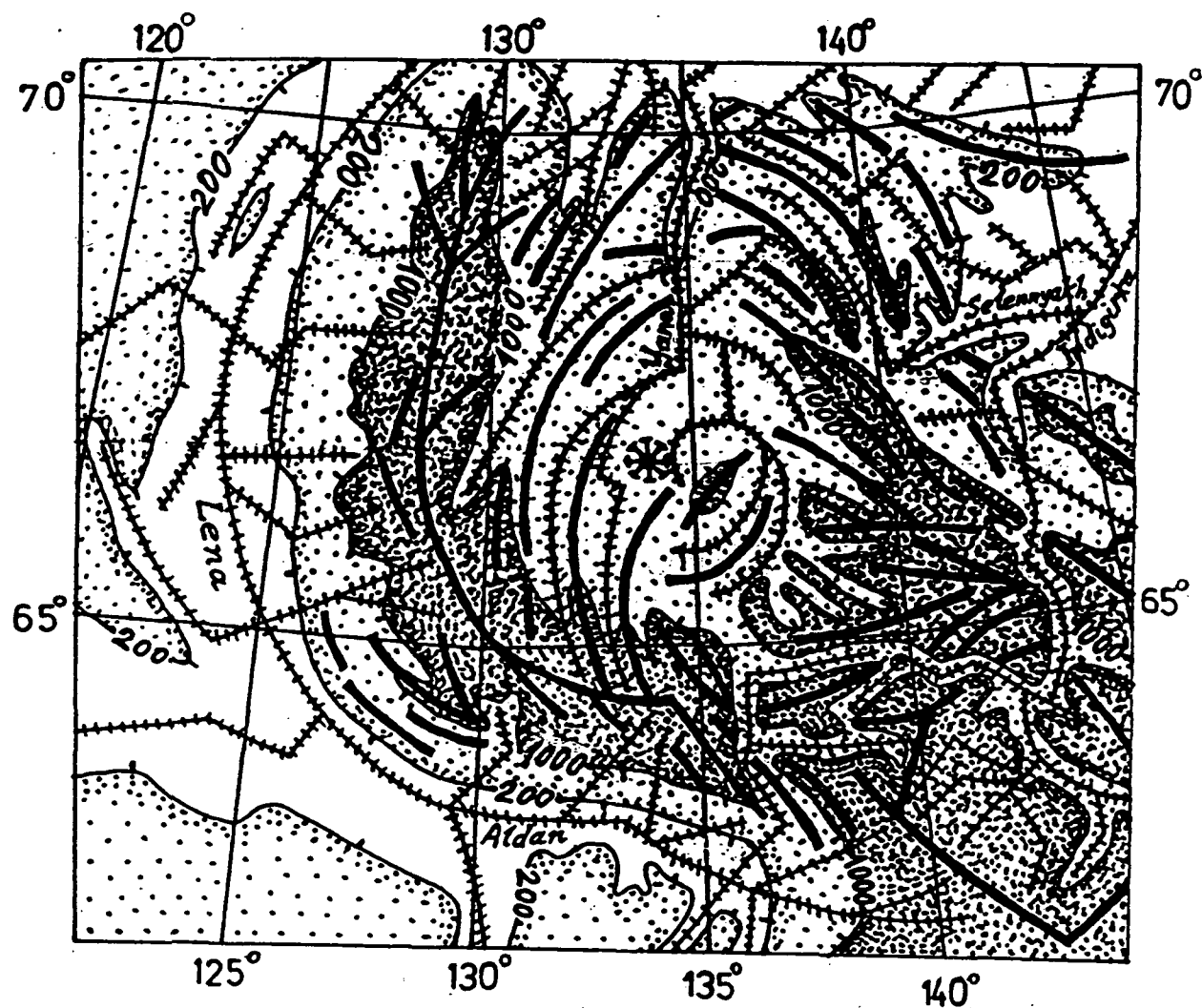


Fig.1. Sketch map of  
Yana Ring Structure (YRS)

- axis of mountain ranges;
- ++++ lineated segments of river valleys;
- ~ 200 and 1000 m topographic contours;
- \* centre of the structure

N 94-12122  
p. 2

50 456859

RUSSIA'S CONTRIBUTION TO REGIONAL GEOLOGIC MAPPING OF VENUS:  
1992 PROGRESS REPORT; G.A.Burba, N.N.Bobina, V.P.Shashkina,  
Vernadsky Institute, Moscow, 117975, Russia

26 sheets of geologic map in Magellan C1-formate were produced by 6 geologists and 3 cartographers in Russia during 1992. 45 more sheets are in progress. The work is coordinated by Vernadsky Institute.

The Magellan SAR images in form of C1-formate photomaps were used as a base for geologic-geomorphic regional mapping of Venus at ~1:8,000,000 scale. This work took place in Russia at Vernadsky Institute and at the Department of Geology, Lomonosov Moscow University. The work is going on since January 1992 after the initiative of Magellan Project Scientist Dr.R.S.Saunders. The aim is to produce a preliminary geologic survey of Venus with the new high resolution images obtained by Magellan. The coordination of Russia's efforts is under responsibility of this abstract authors. It took place at the cartografic division, Laboratory of comparative planetology and meteoritics, Vernadsky Institute, Russia's Academy of Sciences.

By this time six geologists are involved in the project. Four of them are from Vernadsky Institute (VI), and two - from Moscow University (MU). By December 1992 there are 26 sheets compiled and 19 sheets more are in progress. So far 45 C1-formate geologic map sheets are planning to be produced in Russia (there are 181 C1-formate sheets to cover the whole surface of Venus). The number of sheets to be produced could be increased.

The listing of C1 sheets by the authors is given here. Both compiled sheets and those in progress (in parenthesis) are shown. The numbers before the authors' name are the same as inside the circles on fig.1 (see next page) to label the blocks of sheets.

1. V.P.Kryuchkov (VI) - 75N164, 75N254, 60N180, 60N208, 60N236.
2. A.A.Pronin (VI) - 75N299, 75N338, 60N319, 60N348.
3. I.V.Shalimov (MU) - 75N254, 60N263, 45N244, 45N265, 30N243, (30N261, 15N232, 15N249, 15N266).
4. E.N.Slyuta (VI) - 15N180, 00N180, 15S180.
5. A.M.Nikishin (MU) - 30N279, 15N197, 15N283, 00N283, (30N171, 30N189, 30N297, 15N215, 15N300, 00N197, 00N215, 00N300, 00N317, 00N352, 15S197, 15S215, 15S283, 15S300, 15S317).
6. M.A.Ivanov (VI) - 15S009, 15S335, 15S352, 30S009, 30S351.

The maps exist now in individual author's legends. They should come through the cartographic editing to be incorporated together into the continuous map. Their legends should become one common legend. All authors have used morphology as the main principle of

## REGIONAL GEOLOGIC MAPPING OF VENUS, Burba, G.A. et al.

their legends: terrain types and structures of geologic significance are shown on the maps. In some cases different authors follow different ways to show the structures of the same type. Most of the authors have outlined coronae only within the ring of topographically high ridges. But one of the authors (MAI) consider coronae and lava flows going outwards from coronae as the same unit. Two of the authors have shown age consequence of terrain types in the legends. Such way is considering to make the maps more meaningful. It resembles more or less the usual terrestrial geologic maps, based on stratigraphic principle. Accompanying abstracts in this volume present short descriptions of legends and/or geologic setting for some sheets (1-3).

References: 1. A.M.Nikishin, N.N.Bobina, V.K.Borozdin, G.A.Burba (1993). Beta Regio rift system ... (This vol.).  
2. A.M.Nikishin, V.K.Borozdin, N.N.Bobina, G.A.Burba (1993). Beta Regio - Phoebe Regio ... (This vol.). 3. A.M.Nikishin, G.A.Burba (1993). Geologic mapping of Northern Atla Regio ... (This vol.).

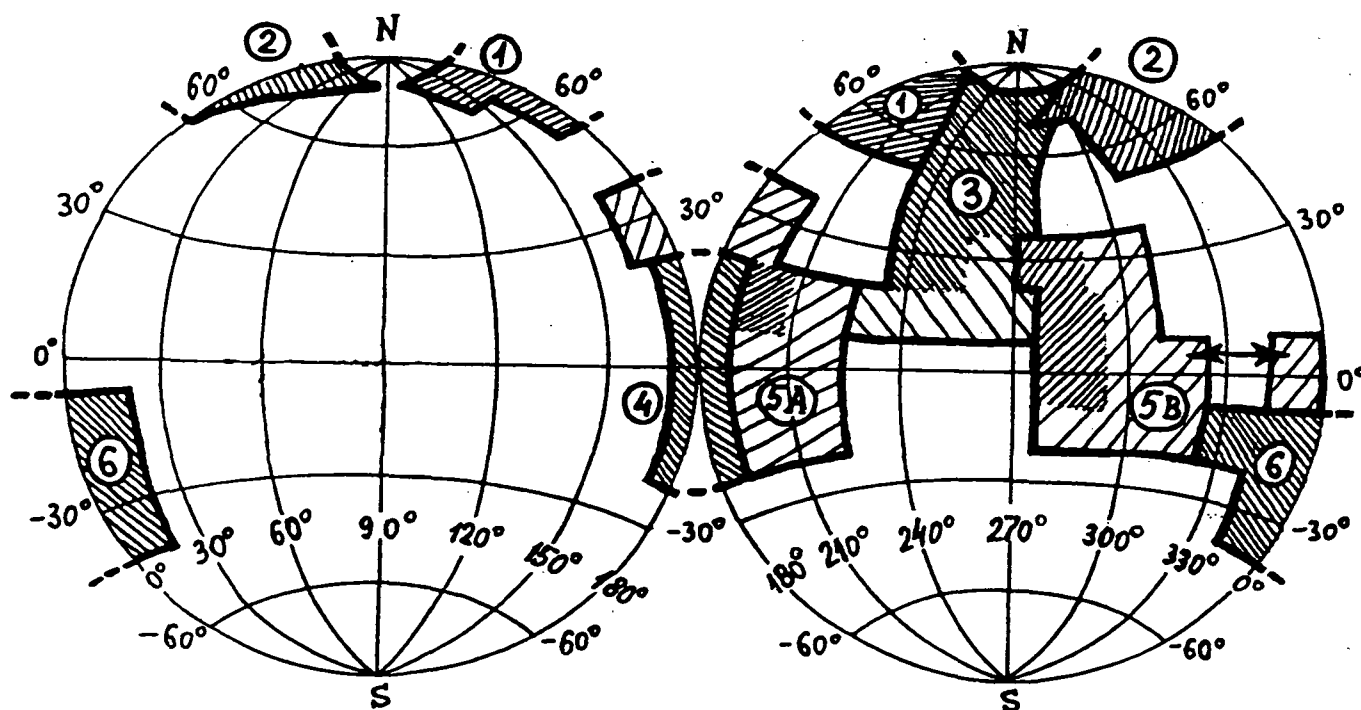


Fig.1. Locator map of C1 sheets under consideration

Close lineation - compiled geologic maps  
Sparse lineation - geologic maps in progress

Numbers of the blocks of map sheets (encircled) are the same as in the list of authors on the preceding page

5108-46

AB3. N94-12123

LPSC XXIV

231

456860

163328 P-2

LANDSCAPE AND GEOMORPHIC SURVEY OF ZHAMANSHIN AREA, NORTHERN KAZAKHSTAN: PRELIMINARY REPORT ON 1992 FIELD TRIP DATA  
G.G.Burba, Jr. and V.A.Meshcherskaya, Geographical Department, Moscow University, Moscow, 119899, Russia

**ABSTRACT.** June 1992 geographical expedition to Zhamanshin crater area made a landscape and geomorphic survey of this impact structure. 42 observational points in the area of 300 sq. km give new data on the geographical processes in the impact crater. The data obtained could be applied to search for unknown impact structures anywhere through the traces of such features in landscapes.

**INTRODUCTION.** Studies of the terrestrial impact structures were connected mainly with geologic (in broad sense) methods. We have undertook an attempt to study the natural complexes of the impact structure with the usual geographic methods - landscape and geomorphic survey. Such approach could help to recognise unknown now impact structures through their traces survived in landscape - geographical complex most sensible to the changes of environment.

**CHOISE OF THE OBJECT AND GENERAL DATA.** High degree of knowledge and prominence in modern topography define Zhamanshin crater as suitable example to begin geographic investigations of the natural complexes of terrestrial impact craters.

Zhamanshin stow is located in semidesert plain of the Northern Kazakhstan ( $48^{\circ}20'N$ ,  $60^{\circ}58'E$ ) with topographic levels of 150-300 m. It looks as planimetrically isometric depression of 100-150 m deep and have 13-km diameter between the rim crests. It is relict of impact crater aged around 0.75 m.y. [1].

In June 1992 the authors, undergraduate students, have undertook geographical investigations of Zhamanshin area. During the expedition data were obtained on geomorphic exogenic processes (VAM) and on landscapes (GGB).

**THE GOALS OF THE EXPEDITION.** The following tasks were planned before the field trip.

- (1) To define modern natural complexes of Zhamanshin area through the geologic-geomorphic and soil-vegetation differences, the main directions of material movement with exogenic processes, gravitational, aeolian, and insolation conditions and patterns of hydrologic net.
- (2) To estimate if crater's landscapes or their structure/patterns are unique if compare with landscapes of the surrounding region.
- (3) To estimate the role of catastrophie impact origin for the following evolution of the cratrer's natural complexes.
- (4) Is there any correlation between modern landscape patterns and the original geologic structure of the crater?

**THE FIELD OBSERVATIONS.** During the field trips landscape and geomorphic cross-sections were constructed. They cross the crater N to S and E to W and are 13-16 km long. Trips along crater rim and the areas outside the crater took place. After that areas within the crater were investigated in accordance with pre-field mapping with the satellite image. During the field trips an area of about 300 sq. km was surveyed.

# LANDSCAPE/GEOMORPHIC SURVEY OF ZHAMANSHIN CRATER Burba, G.G., Jr. and Meshcherskaya, V.A.

Observations took place at 42 points located at the bottom and rim of the crater and outside of crater. Each point was described in details with geologic-geomorphic data, surface soil, deep section of soil, hydrologic patterns, botanical square. Rocks and vegetation were sampled for collection. Detailed studies of the field data are in progress. The preliminary landscape map of Zhamanshin crater area is given at fig.1. The map shows different landscape areals which will be described elsewhere.

REFERENCE: 1. P.V.Florensky, A.I.Dabizha. Zhamanshin meteoritic crater. Moscow: Nauka, 1982 [in Russian].

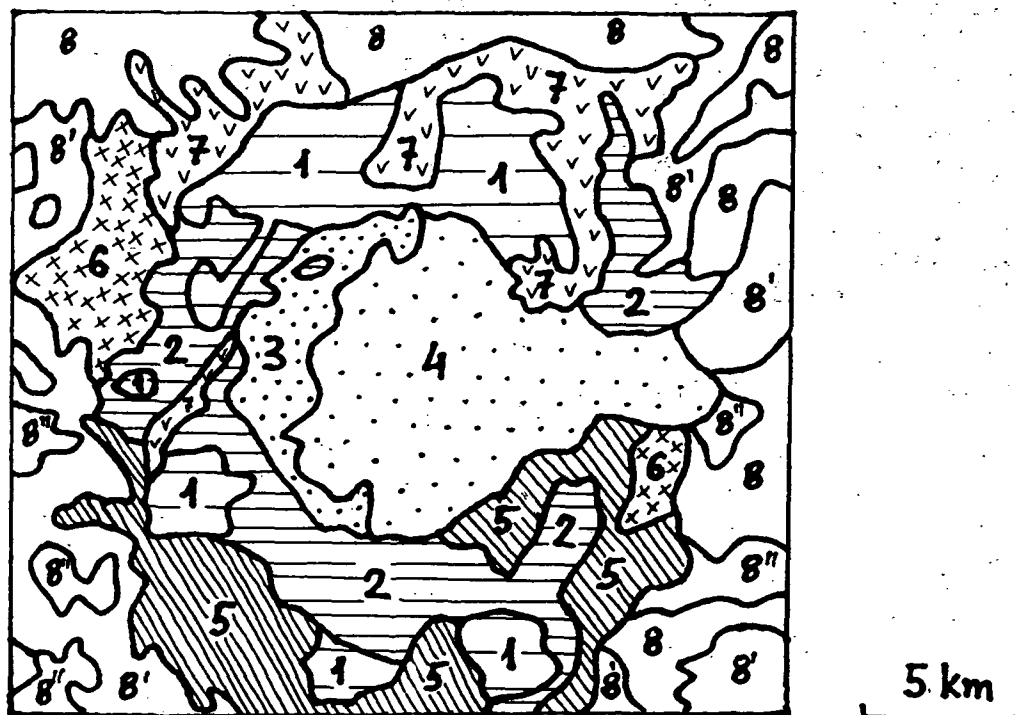


Fig.1. Preliminary landscape map of Zhamanshin crater area

Different landscape types are labeled 1 through 8. Types 1 and 2 are connected with highlands; types 3, 4, and 8 - with lowlands; types 5, 6, and 7 - with slopes from high to low areas. Types were established after analyses of geomorphic position, soils, vegetation, hydrologic patterns and are to be described elsewhere.



52

456861

5109-90  
ABS ONLY

LPSC XXIV

223

N 94-312124  
P-2

HOW DIVERSE IS THE ASTEROID BELT? Thomas H. Burbine (Smithsonian Astrophysical Observatory, Cambridge, MA 02138) and Jeffrey F. Bell (Planetary Geosciences Div., Dept. of Geology & Geophysics, SOEST, Univ. of Hawaii, Honolulu, HI 96822)

For approximately twenty years, many different asteroid taxonomies, which used many different observational data sets, have been developed to try to group asteroids into classes that contain members with similar spectral characteristics. However to understand the structure of the asteroid belt, the resulting classes are only useful if they are grouping together asteroids with somewhat similar mineralogies and thermal histories. Until recently, these taxonomies have focused on spectral reflectance data from 0.3 to 1.1  $\mu\text{m}$  and visual albedo. But in the last five years, observational data sets (e.g. 0.8 to 2.5  $\mu\text{m}$  spectra, CCD spectra, 3  $\mu\text{m}$  spectra, radar albedos) for a small number of asteroids have been compiled that can give a better mineralogical interpretation, but whose use in asteroid taxonomy has been relatively limited. Analyses of these "supplementary" data sets show that most asteroid classes contain members with different compositions and/or thermal histories. To understand the diversity of the asteroid belt, the number of objects with these observations must be expanded and used in the next generation of taxonomies.

The most widely used taxonomy [1] groups asteroids according to similarities in seven colors taken from 0.3 to 1.1  $\mu\text{m}$  in the eight-color asteroid survey (ECAS) [2] and rough similarities in visual albedo (pre-IRAS) when available. No mineralogical interpretations are used in forming the classes, however the same spectral information that is used in classifying can be used to give a rough interpretation of surface composition. The "supplementary" data sets allow for a more complete mineralogical interpretation as shown in Table I. Due to the small number of asteroids that have these observations (Table I), these data sets have had limited uses in taxonomy except in the work of a few researchers (e.g. [3], [4], [5]). However these data sets can be used to "test" a class by seeing how consistent the mineralogical interpretations are for the members of the class. If members of the same class have different mineralogical interpretations from the analyses of these data sets, the most obvious conclusions are that the class contains asteroids with different surface compositions or one of the observations is in error.

Analyses of these data sets shows that most classes contain members with different mineralogies. Many of the classes (C, D, F, M, and T) contain both hydrated and non-hydrated members [6], which implies at least two types of surface material in these classes. The two known hydrated M-asteroids (55 Pandora and 92 Undina) are most likely composed of some type of carbonaceous material, while the non-hydrated ones may or may not have surfaces of metallic iron. The one known non-hydrated M (16 Psyche) has a very high radar albedo [7] that implies a metallic surface. The T-asteroids appear to contain at least two mineralogically distinct types [8] [9] from the analysis of 0.8 to 2.5  $\mu\text{m}$  [10] and 3  $\mu\text{m}$  [6] spectra. One type (96 Aegle, 114 Cassandra, and 233 Asterope) is non-hydrated and moderately red-sloped, while the other type (308 Polyxo) is hydrated and much redder sloped. The spectrum of the first type of T-asteroid has been noticed to have similarities with both the spectra of troilite [9] and an EH4 chondrite (Abee) [11]. One asteroid class (G) was thought to contain both hydrated and non-hydrated members, however the one non-hydrated G-type (148 Gallia) (GU) appears to be a misclassified S on the basis of CCD spectra [12].

The S-class also appears to be very mineralogically diverse. The S-class has members that appear to be differentiated and exhibit silicate compositions on the surface ranging from pure olivine through olivine-pyroxene mixtures to pure pyroxene or pyroxene-feldspar mixtures [13]. There also appears to be "primitive" asteroids in the S-asteroid population. One example is the K-class, which was separated by Bell (3) from the S-class and linked with a CO/CV chondritic composition on the basis of albedo ( $-0.09$ ) and flat 0.8 to 2.5  $\mu\text{m}$  spectra. Another example are 387 Aquitania and 980 Anacostia [14]. Both asteroids have a 2  $\mu\text{m}$  feature and no corresponding 1  $\mu\text{m}$  feature, which is anomalous for an assemblage of olivine and/or pyroxene. This 2  $\mu\text{m}$  feature has been attributed to spinel and these two asteroids have been proposed to have a CO/CV composition enriched in spinel-bearing inclusions.

To try to display the diversity of the asteroid classes, a revised Bell superclass table [15] (Table II) has been formulated. Asteroid classes that have members with dissimilar surface compositions have been subdivided and then placed into the superclass (primitive, metamorphic, or igneous) that best explains the degree of metamorphic heating that each subclass is believed to have undergone. The symbols for the subclasses of the S-class are S (olivine-pyroxene mixture), So (olivine-rich) [4], Sp (pyroxene-rich) [4], and Ss (spinel-rich). The classes (C, D, F, M, and T) with hydrated and non-hydrated members have each been given either the symbol h after the class name (e.g. Ch) to represent a hydrated subclass or the symbol n to represent a non-hydrated one. It is not clear where the subclass Tn should be placed since a troilite composition would imply an igneous thermal history while an EH4 composition would imply a metamorphic thermal history. Single letter asteroid classes (K and Z [16]) that were not included in Tholen's original taxonomy [1] are placed in parentheses. A representative asteroid of each class (or subclass) is also given, however it is unknown if the properties of that asteroid is characteristic of other members of the class.

Most asteroid classes contain members with different surface compositions and/or thermal histories based on the analyses of these supplementary data sets. These observations appear critical for understanding the structure of the asteroid belt and need to be done for a large number of asteroids so a taxonomy that truly reflects the diversity of the asteroid belt can be created.

## HOW DIVERSE IS THE ASTEROID BELT? Burbine T. H. and Bell J. F.

Table I

Observational Data Sets	Absorption Features (Present or Absent) and Other Significant Information
ECAS spectra (0.3-1.1 $\mu\text{m}$ ) (~589 asteroids)	Ultraviolet feature due to $\text{Fe}^{+2}$ , Part of 1 $\mu\text{m}$ feature due to olivine and/or pyroxene
Visual albedo (Mainly IRAS) (~1800 asteroids)	Elimination of some possible surface compositions
0.8-2.5 $\mu\text{m}$ spectra (52 channels) (~120 asteroids)	Other part of 1 $\mu\text{m}$ feature, 1.1 $\mu\text{m}$ feature due to feldspar, 2 $\mu\text{m}$ feature due to pyroxene and/or spinel, Continuum slope
3 $\mu\text{m}$ spectra (~50 asteroids)	3 $\mu\text{m}$ feature due to hydrated silicates
CCD spectra (0.4-1.0 $\mu\text{m}$ ) (~200 asteroids)	Very weak features believed to be due to iron oxides in phyllosilicates, Better determination of part of 1 $\mu\text{m}$ feature
Radar albedos (~32 asteroids)	Estimation of metal abundance as a function of porosity

Table II

Bell Superclass	Class	Inferred Minerals	Analogous Meteorites	Asteroid Example
Primitive	Dn	organics	(none)	721 Tabora
	P	organics	(none)	65 Cybele
	Cn+Fn	anhydrous silicates, C	(none)	31 Euphrosyne
	(K)	ol, pyx, carbon	CO and CV chondrites	221 Eos
	Ss	spinel	CO and CV chondrites	387 Aquitania
Metamorphic	(Z)	organics	(none)	5145 Pholus
	Th	clays, organics	(none)	308 Polyxo
	B+Ch+Fn+G	clays, opaques	altered carb. chondrites	10 Hygiea
	Dh	clays, organics	(none)	773 Irmintraud
	Q	pyx, ol, grey NiFe	H, L, LL chondrites	1862 Apollo
Igneous	Mh	clays	altered carb. chondrites	55 Pandora
	V	pyx, plag, ol	basaltic achondrite	4 Vesta
	R	ol, pyx	ol-rich achondrites?	349 Dembowska
	S	ol, pyx, red NiFe	lodranites, irons	6 Hebe
	So	ol, red NiFe	pallasites	354 Eleonora
	Sp	pyx, plag, red NiFe	basaltic achondrites?	1036 Ganymed
	A	ol	brachinites	446 Aeternitas
	Mn	NiFe	irons	16 Psyche
	E	Fe-free pyx	aubrites	64 Angelina
	(Mars)		(SNC meteorites)	
	(Moon)		(lunar meteorites)	

(The superclass of the Tn subclass is still being debated.)

**References:** [1] Tholen, D. J. (1984) Ph.D. Thesis, Univ. of Ariz., Tucson. [2] Zellner, B. *et al.* (1985) *Icarus* **61**, 355-416. [3] Bell, J. F. *et al.* (1988) *Meteoritics* **23**, 256-257. [4] Howell, E. S. *et al.* (1993) Submitted to *JGR Planets*. [5] Merényi, E. *et al.* (1992) *Bull. Amer. Astron. Soc.* **24**, 939. [6] Jones, T. D. *et al.* (1990) *Icarus* **88**, 172-192. [7] Ostro, S. J. *et al.* (1985) *Science* **229**, 442-446. [8] Burbine, T. H. and Bell, J. F. (1991) *Lunar Planet. Sci.* **22**, 155-156. [9] Britt, D. T. *et al.* (1992) *Meteoritics* **27**, 207. [10] Bell, J. F. *et al.* (1988) *Lunar Planet. Sci.* **19**, 57-58. [11] Burbine, T. H. Jr. (1991) M.S. Thesis, Univ. of Pittsburgh. [12] Sawyer, S. R. (1991) Ph.D. Thesis, Univ. of Texas, Austin. [13] Gaffey, M. J. *et al.* (1993) Submitted to *Icarus*. [14] Burbine, T. H. *et al.* (1992) *Meteoritics* **27**, 424-434. [15] Bell, J. F. (1986) *Lunar Planet. Sci.* **17**, 985-986. [16] Mueller, B. E. A. *et al.* (1992) **97**, 150-154.

456862

5110-90  
ABS ONLY

-LPSC XXIV

225

N 94-12125

P. 2

STUDIES OF THE RELEASE OF RADIOGENIC  $^{129}\text{Xe}$  FROM BJURBÖLE: EVIDENCE AGAINST SIMPLE DIFFUSION MODELS; M. K. Burkland<sup>1</sup>, T. D. Swindle<sup>1</sup>, and S. L. Baldwin<sup>2</sup>,  
<sup>1</sup>Lunar and Planetary Laboratory and <sup>2</sup>Department of Geosciences, University of Arizona, Tucson, AZ 85721 USA.

The I-Xe system, based on the decay of 15.7 Ma  $^{129}\text{I}$ , is a potentially precise chronometer of early solar system events. However, it is not known how the system responded to thermal events during the post-formation histories of ordinary chondrites, severely limiting the usefulness of this system [1]. Isothermal experiments on Bjurböle for different heating durations suggest that at least three domains are responsible for the thermal release of radiogenic  $^{129}\text{Xe}$  ( $^{129}\text{Xe}^*$ ) and that the system may be less susceptible to thermal resetting than some calculations indicated.

Two scenarios for the release of  $^{129}\text{Xe}^*$  have been proposed. In one, the mobility of  $^{129}\text{Xe}^*$  is governed by diffusion in mineral grains. This leads to predicted closure temperatures comparable to, or less than, metamorphic temperatures [2]. In the second, mineral grains that solidified at specific temperatures trapped  $^{129}\text{I}$  within them, and the resulting  $^{129}\text{Xe}^*$  is only released when those minerals melt, such that isotopic closure occurs at the temperature of solidification.

#### Procedure:

We measured the retention of  $^{129}\text{Xe}^*$  in Bjurböle (L4) for different run durations and temperatures. Crushed ( $<250\text{ }\mu\text{m}$ ) samples were heated to 1000°C, 1100°C, or 1200°C, for times ranging from 1 hour to 14 days. Splits of the samples were fused and analyzed in a VG5400 noble gas mass spectrometer [4]. Samples of the crushed, but unheated, Bjurböle were also analyzed. The fraction lost was calculated as  $(^{129}\text{Xe}^*_{\text{unheated}} - ^{129}\text{Xe}^*_{\text{treated}}) / (^{129}\text{Xe}^*_{\text{unheated}})$ .

Amounts of  $^{129}\text{Xe}^*$  were corrected for trapped  $^{129}\text{Xe}$  (and blanks) by assuming a  $^{129}\text{Xe}/^{132}\text{Xe}$  ratio of  $1.01 \pm 0.03$  in the trapped component, which encompasses air (0.98) and Bjurböle trapped Xe (1.04). Duplicate analyses were performed on all time-temperature steps except the 1100°C-1 hour step.

#### Results:

Approximately 12% of the total  $^{129}\text{Xe}^*$  is released at  $\leq 1000^\circ\text{C}$  in the first hour of heating (Fig. 1a). Heating for 2.5 orders of magnitude longer releases little, if any, more  $^{129}\text{Xe}^*$ . The fraction released during the longer heatings is less than the amount predicted by [2] for diffusion from a single domain.

Figure 1c shows the loss profile at 1200°C from 1 to 24 hours along with the predicted diffusion curve [2]. Again the diffusion curve based on parameters derived from standard stepwise heating does not match the data. Approximately 80% of the  $^{129}\text{Xe}^*$  outgassed, regardless of heating time. The remaining 20% must be released either by melting or by diffusion with much different parameters than those predicted.

Figure 1b shows a profile of increasing loss with time at 1100°C that suggests a diffusion process. However, the fact that the  $^{129}\text{Xe}^*$  which appears to be diffusing at 1100°C seems to have been almost fully retained at 1000°C and almost fully released at 1200°C suggests diffusion parameters that would lead to a relatively high closure temperature for this domain as well.

The results suggest that  $^{129}\text{Xe}^*$  in Bjurböle is released from at least three different domains. One domain outgasses completely at 1000°C, although little can be said about the release mechanism. The second, containing the majority of

C-5

N

RELEASE OF  $^{129}\text{Xe}^*$  FROM BJURBÖLE: Burkland M. K. et al.

the  $^{129}\text{Xe}^*$ , appears to diffuse out at about  $1100^\circ\text{C}$  in these experiments. The third domain retains  $^{129}\text{Xe}^*$  after 24 hours at  $1200^\circ\text{C}$ , indicative of a very retentive mineral site.

An Arrhenius plot of the data (Fig. 2) is consistent with the results of standard stepwise heating [2]. But a systematic variation of two log units at  $1000^\circ\text{C}$  and  $1200^\circ\text{C}$  with extended heating indicate that simple diffusion from a single type of site is not an adequate description of the system. Rather, a mixture of sites with different release properties is required.

## References:

- [1] Swindle T. D., and Podosek F. A. (1988) In Meteorites and the Early Solar System, 1127.
- [2] Caffee M. W., Hohenberg C. M., Swindle T. D., and Hudson B. (1982) Proc. Lunar Planet. Sci. Conf. 13th, in J. Geophys. Res. 87, A303.
- [3] Wood J. A. (1967) J. Geophys. Res. 72, 6397.
- [4] Burkland M. K., and Swindle T. D. (1992) Lunar Planet. Sci. XXIII, 185.
- [5] Jordan J., Kirsten T., Richter H. (1980) Z. Naturforsch. 35a, 145.

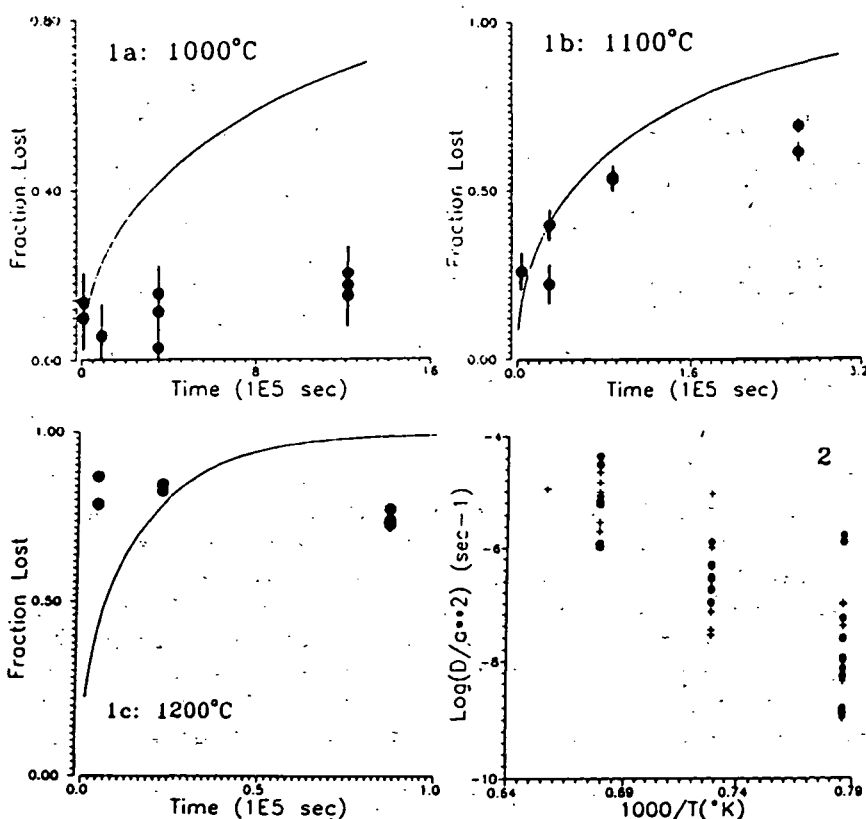


Fig. 1: Fraction of  $^{129}\text{Xe}^*$  released vs. time during extended heating of Bjurböle at  $1000^\circ\text{C}$  (1a),  $1100^\circ\text{C}$  (1b), and  $1200^\circ\text{C}$  (1c). Data from this work are compared with predictions of diffusion calculations (curve), using diffusion parameters from [2] based on data of [5].

2 Fig. 2: Arrhenius plot of data from this work (●) and calculations from [2] (+), based on data of [5]. In this work, longer heating times consistently give lower values of  $D/a^2$ .

456963

5111-91

LPSC XXIV

227

ABS. ONLY

94-12126

P-2

**A PATTERN RECOGNITION SYSTEM FOR LOCATING SMALL VOLCANOES IN MAGELLAN SAR IMAGES OF VENUS;** M.C. Burl, U.M. Fayyad, and P. Smyth, Jet Propulsion Lab M/S 525-3660, California Institute of Technology, Pasadena, CA 91109.  
J.C. Aubele and L.S. Crumpler, Dept. of Geological Sciences, Brown University, Providence, RI 02912.

**INTRODUCTION.** The Magellan data set constitutes an example of the large volumes of data that today's instruments can collect, providing more detail of Venus than was previously available from Pioneer Venus, Venera 15/16, or ground-based radar observations put together [1]. However, data analysis technology has not kept pace with data collection and storage technology. Due to the sheer size of the data, complete and comprehensive scientific analysis of such large volumes of image data is no longer feasible without the use of computational aids. In this paper we report on our progress towards developing a pattern recognition system for aiding in the detection and cataloging of small-scale natural features in large collections of images. Combining classical image processing, machine learning, and a graphical user interface, we are initially targeting the detection of the "small-shield" volcanoes (less than 15km in diameter) that constitute the most abundant visible geologic feature [2] in the more than 30,000 synthetic aperture radar (SAR) images of the surface of Venus. Our eventual goal is to provide a general, trainable tool for locating small-scale features where scientists specify what to look for simply by providing examples and attributes of interest to measure. This contrasts with the traditional approach of developing problem-specific programs for detecting specific patterns. This paper reports on our approach and initial results in the specific context of locating small volcanoes.

It is estimated, based on extrapolating from previous studies and knowledge of the underlying geologic processes, that there should be on the order of  $10^5$  to  $10^6$  of these volcanoes visible in the Magellan data [3,4]. Identifying and studying these volcanoes is fundamental to a proper understanding of the geologic evolution of Venus. However, locating and parameterizing them in a *manual* manner is forbiddingly time-consuming. Hence, we have undertaken the development of techniques to partially automate this task. The primary constraints for this particular problem are that the method must be reasonably robust and fast. Unlike most geological features, the small volcanoes of Venus can be ascribed to a basic process that produces features with a short list of readily defined characteristics differing significantly from other surface features on Venus [2]. For pattern recognition purposes the relevant criteria include (1) a circular planimetric outline, (2) known diameter frequency distribution from preliminary studies, (3) a limited number of basic morphological shapes, and (4) the common occurrence of a single, circular summit pit at the center of the edifice.

**THE APPROACH.** There has been little prior work on detecting *naturally* occurring objects in remotely-sensed SAR images. Most pattern recognition algorithms are geared towards detecting straight edges or large changes in texture/reflectivity. While this works well for detecting man-made objects, edge detection and Hough transform approaches deal poorly with the variability and speckle noise present in SAR imagery [5,6]. This, along with the desirability of developing a general tool rather than manually programming each detection problem, led us to develop an approach based on the block diagram shown in Figure 1.

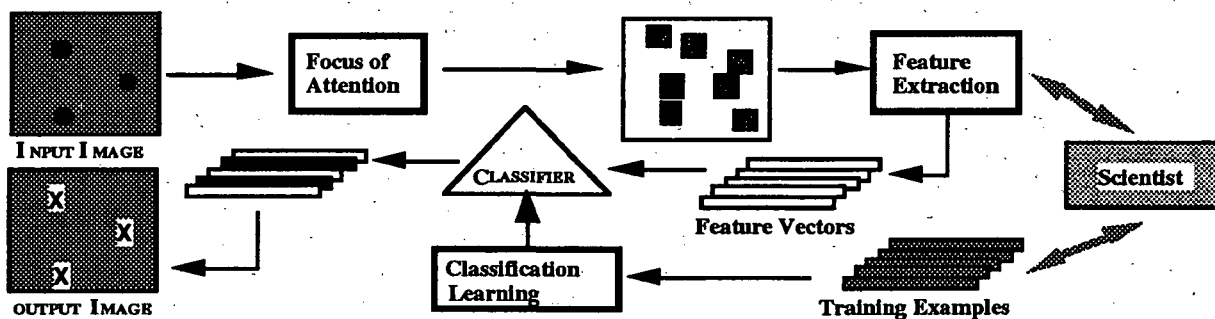


Figure 1. Overview of the Detection System

The system consists of three main components:

1. **Focus of attention (FOA):** this component is designed primarily for computational efficiency. Its function is to quickly scan an input image and roughly determine regions of interest (regions potentially containing objects similar to those specified by the scientist). It is thus an inaccurate detector and is expected to generate a large number of false detections (*false alarms*) as long as it detects the majority of true regions of interest. It thus serves as a filter that reduces the number of pixels to consider by one or two orders of magnitude.
2. **Feature extraction (FE):** On each of the regions of interest selected by the FOA component, we can now afford to perform more sophisticated computation. The FE component measures a set of general features of a region of interest (e.g. average intensity, area, relative areas of segments grown within the region, and so

## PATTERN RECOGNITION SYSTEM: Burl M. C. et al.

forth), as well as a host of problem-specific attributes defined by the scientist (if any). A scientist may have certain measures that are known to provide useful information in determining whether a detected object does indeed belong to the target class (e.g. eccentricity, expected brightness ratios, extent, and so forth). Using the standard and user-provided feature definitions, the FE component transforms each region of interest detected by the FOA component into a feature vector consisting of attribute measurements computed on the pixels in that region.

3. **Classification learning:** The task of this component is to discriminate between false alarms and true detections. At this stage, the regions of interest have all been translated into feature vectors and the learning component has to decide which feature vectors belong to which class based on the training data set provided by the user (see below). This component can employ any one of a variety of learning algorithms. Based on the training data, it produces a classifier that performs the discrimination task to disregard false alarms when the system is used to analyse a new set of images.

The system functions in two modes: the *training* and the *detection* modes. In the training mode, a scientist brings up some images and labels regions in the image containing objects of interest. The labeling is performed via an interface we developed for Sun workstations that allows the user to simply point the mouse and select a region, specifying a symbolic name for the object contained in it (class), the extent of the region (size), and the probability associated with that class. The probability is given by selecting one of three confidence ranges. These ranges reflect the certainty of the scientist regarding the membership of an object in the class of interest. In addition, the scientist is able to provide definitions for features or attributes to be measured for each region of interest as described above. The training data collected in this manner is then used to automatically produce a classifier that distinguishes between true detections and false alarms generated by the FOA component for the images from which the training data was drawn. We use three different types of learning algorithms that generate three different types of classifiers: decision trees [7], neural networks, and nearest-neighbour classifiers. The first two construct a model (classifier) based on the training data. The third simply classifies a feature vector based on the class of the nearest vector in the training data based on a distance measure defined on the feature vectors. The FOA algorithm used is a simple statistical method known as constant false alarm rate (CFAR) detector. It performs well for detecting a bright center in a relatively darker surround. This detects the summit pits of volcanoes, which form a fairly bright compact center. False alarms are caused by craters, grabens, and other bright features in the data. In order to detect volcanoes of variable sizes (1-15km in diameter), the CFAR detector is applied at multiple resolutions of the same image [8].

In the detection mode, the system processes large amounts of image data by applying the FOA, the FE, and then the classifier to produce the final list of detected volcanoes. Note that this list can be automatically produced as a catalog of all volcanoes detected, arranged by position and listing whatever properties are desirable for inclusion in the catalog.

**CURRENT STATUS AND RESULTS.** We have constructed several training sets using F1-MIDR images (at the 75m/pixel resolution) labeled by two of the authors (JCA and LSC) to get an initial estimate of the performance of the system. The FOA component, typically detects more than 80% of all the volcanoes, while generating 5-6 times as many false alarms. Using the nearest neighbour classifier, we can classify the regions of interest into volcanoes and false alarms with an estimated accuracy of 81%. Similar accuracy results are reported in [9]. It is important to clarify that these are initial results pending proper and general solutions to the FOA, FE, and classification problems. These early results are, however, encouraging. With further effort we hope to be able to significantly improve the accuracy rates for the volcano detection problem. Demonstrating the general applicability of this approach to the detection of other Venusian features as well as images from other missions will be the next step. So far our emphasis has been placed mainly on developing the computer tools to allow scientists to browse through images and produce training data sets (as well as partial catalogs) within a single integrated workstation environment.

**ACKNOWLEDGMENTS.** Research described in this paper was carried out in part by the Jet Propulsion Laboratory, California Institute of Technology, under a contract with the National Aeronautics and Space Administration.

## REFERENCES

- [1] *Science*, special issue on Magellan data, April 12, 1991..
- [2] J. E. Guest et al., *Journal Geophys. Res.*, 97, E10, 15949, 1992.
- [3] J. C. Aubele and E. N. Slyuta, *Earth, Moon and Planets*, 50/51, 493--532, 1990.
- [4] J. W. Head et al., *Journal Geophysical Res.*, 97, E8, 13,153-13,197, 1992.
- [5] A.M. Cross, *Int. J. Remote Sensing*, 9,no.9, 1519-1528, 1988.
- [6] S. Quegan et al., *Phil. Trans. R. Soc. London*, A 324, 409-421, 1988.
- [7] U.M. Fayyad, et.al. *Proc. of 6th Space Op. & Research Conference (SOAR-92)*, Houston, TX, 1992.
- [8] P. Smyth et al, "Multi-Resolution Pattern Recognition of Small Volcanoes in Magellan Data", *Proc. of the Int. Venus Colloq.*, California Institute of Technology, August 1992.
- [9] C.R. Wiles and M.R.B. Foreshaw, LPSC XXIII (abst), 1527-1528, 1992.

456864

5112-91  
ABS-ONLY

LPSC XXIV

229

P N94-12127

SOURCES OF Na FOR THE IO ATMOSPHERE. D.S. Burnett, Susan B. Ellis, A. Rice, S. Epstein. Geological and Planetary Sciences Cal Tech Pasadena, Ca, 91125.

The physics and geology of Io have been extensively studied, but there has been little discussion of the chemistry. Relatively little is known about Io chemistry, but there are constraints. Further, it will be a long time before improvements will result from direct observation, given the severe difficulties with the Galileo mission. We are interested in exploring, via laboratory simulation experiments, plausible thermochemical and photochemical processes which determine the nature and amounts of surface constituents of Io.

The well-known density of Io shows that the planet overall is rocky. Because the orbit of Io is well within the magnetosphere of Jupiter and because Io only has a thin, transient SO<sub>2</sub> atmosphere, the surface is continually sputtered with magnetospheric ions. Complex processes ionize and accelerate the Io surface atoms to keV and MeV energies. Remarkably, only S, O, and Na ions were found by Voyager. Sputtering also produces an atomic cloud of Na and S (O not observable) with a trace of K. Both gaseous and solid SO<sub>2</sub> are known from spectroscopic studies. A trace of H<sub>2</sub>S and possibly CO<sub>2</sub> are present. Geologic features are interpreted in terms of elemental S, but there is no direct evidence for this constituent. We thus have a rocky planet which does not have rocks on the surface.

Our general goal is to understand the cycling of Na, S, and O through the crust and atmosphere on present-day Io and to understand how Io evolved to this state. A specific objective has been to determine the phases on the surface which are the source of the Na in the atmosphere of Io. There are 3 viable hypotheses for the nature and origin of the Io surface Na compounds: (I) Na<sub>2</sub>SO<sub>4</sub> from SO<sub>2</sub>-rock interactions [1]; (II) Na-sulfides from elemental S, rock interactions [2,3]; (III) directly-erupted volcanic Na [2,4], as atoms or, more reasonably, as NaO molecules. The viability of mechanism II was demonstrated by experiments which showed that liquid elemental S reacting with silicate glass at 1100-1200K produces Na-sulfides, most likely Na<sub>2</sub>S<sub>2</sub> [3]. The Na-sulfides could be entrained in S magmas (or dissolved at higher temperatures) and transported to the surface during S volcanism. The issue arises, however, whether elemental S is required to explain the Na-rich surface. Although widely accepted [see e.g. 5], elemental S is not a confirmed surface constituent [e.g. 6,7]. Consequently, it is important to test the alternative represented by mechanism I which does not require elemental S.

We have performed mechanism I simulations to test whether direct interaction of SO<sub>2</sub> with silicate materials (SO<sub>2</sub> alteration) can produce Na-S compounds. Experiments carried out under oxidizing conditions with a SO<sub>2</sub>-O<sub>2</sub> gas phase showed extensive interaction for a wide variety of silicate compositions at 1123K (mid-level crustal temperature for Io) [1]. Characterization by scanning electron microscopy (SEM) revealed extensive sulfate surface deposits for all experiments, but the nature of the sulfate changed systematically with the silicate Ca/Na ratio. Mixtures of CaSO<sub>4</sub> and Na-rich sulfate were formed from basaltic compositions having higher Ca/Na, but only alkali-rich sulfates formed from more granitic (low Ca/Na) compositions. For crystalline albite and an albite-orthoclase eutectic glass composition, K and Al-rich sulfates were formed. Many analyses show significant S excesses which are best interpreted as due to the presence of bisulfate (HSO<sub>4</sub>) components, and NaHSO<sub>4</sub> deserves consideration as an Io surface mineral.

Here we report studies of "direct" interaction mechanisms with pure SO<sub>2</sub> which do not involve external redox agents: (A). SO<sub>2</sub> disproportionation which can be represented

## SOURCES OF Na FOR THE IO ATMOSPHERE: Burnett et al.

schematically:  $\text{SO}_2 + \text{Na}_2\text{O} = \text{S} + \text{Na}_2\text{SO}_4$  or (B). sulfite formation:  $\text{SO}_2 + \text{Na}_2\text{O} = \text{Na}_2\text{SO}_3$ . For 4/7 compositions, no reaction products were seen with the SEM for the same temperatures and times as the oxidizing conditions experiments [1]. However, deposits on cm-sized silicate slices were always observed by photoelectron spectroscopy, which is much more sensitive than the SEM, and can distinguish oxidized and reduced S compounds. In all experiments where samples were not exposed to air for longer than about 10 minutes both oxidized and reduced S peaks were observed (Figure and Table). The reduced S peak disappears when samples are exposed to air for periods greater than a week, so both reduced and oxidized S compounds appear to form in all experiments, indicating mechanism A. A second set of experiments with powdered samples to provide greater surface area for reaction is undergoing infra-red characterization, but at high temperature, these sample capsules were filled with a yellow gas suggesting that elemental S is the reduced disproportionation product, as opposed to the alternative of Na-sulfide formation.

Assuming that burial of  $\text{SO}_2$  to temperatures approaching those of our experiments is plausible and that somewhat less oxidizing conditions do not qualitatively change the results,  $\text{SO}_2$ -rock alteration is a viable mechanism to account for the Io surface enrichment in Na. Overall, the model I simulations indicate that elemental S is not required to form Na compounds in crustal igneous interactions. The possibility of elemental S on Io can be regarded as a totally separate issue from the problem of the surface Na enrichment. Thus, the presence of Na compounds provides no constraint on elemental S, but, in turn, igneous formation of Na-S compounds is not tied to models of Io which contain elemental S. Measurements of minor constituents (e.g. K,Ca) in the Io atomic cloud and torus are the key to resolving these alternatives.

On a short time scale ( $< 10^3$  yr), except for minor effects of sputter erosion, relatively little chemistry occurs for Io surface materials. The dominant process is crustal recycling. Thermochemical reaction rates are probably negligible at Io surface temperatures, but due to heating during recycling (and to a lesser extent due to shallow intrusion of magmas), it is plausible that thermochemical equilibrium would be achieved. In this case it is likely that, regardless which of the above mechanisms extracts Na from silicate source regions, Na ends up as  $\text{Na}_2\text{SO}_4$  (or possibly  $\text{NaHSO}_4$ ). Sulfates are not observed in the Io reflectance spectrum [8], but the observational upper limit is sufficiently high that sufficient  $\text{Na}_2\text{SO}_4$  could be present to supply the Na atmosphere.

References: [1] M.L. Johnson and D.S. Burnett (1993) J.G.R. Planets, in press. [2] G.R. van Hecke and D.B. Nash (1984) unpublished manuscript. [3] M.L. Johnson and D.S. Burnett (1990) Geophys. Res. Lett. 17, 981-984. [4] F. Fanale, et al. (1982) In Satellites of Jupiter, D. Morrison, ed., 756-781, U.Ariz. Press Tuscon. [5] J.I. Moses and D.B. Nash (1991) Icarus 89, 277-304. [6] B. Hapke (1989) Icarus 75, 56-76. [7] A.S. McEwen and J.I. Lunine (1989) J. 450-478. [8] R.R. Howell et al. (1989) Icarus 78, 27-37.

Sample	XPS Spectra	SEM
Albite	Nothing	Nothing
AbOr Eutectic Glass (a)	2 Peaks	Nothing
Obsidian (a)	2 Peaks	Nothing
Sodalime Glass (b)	(Oxidized Only)	Na-S
Ab <sub>8</sub> AnDi Glass (b)	(Oxidized Only)	Na-S + Ca-S
Chondrule Glass	2 Peaks	Na-S + Ca-S
Alkali Basalt (a)	2 Peaks	Nothing

(a) Less than 10 min. air exposure.

(b) Air exposed for > 1 week; reduced peak probably lost.

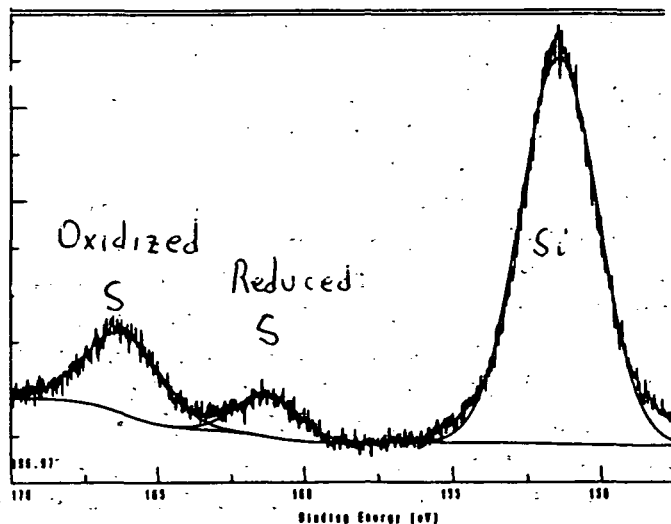


FIGURE Photoelectron spectrum of Mono obsidian +  $\text{SO}_2$  reaction products.



45865- 3113-91  
ABS. ONLY N 94-12128 231  
163333-  
P-2

## CHEMICAL WEATHERING ON MARS: RATE OF OXIDATION OF IRON DISSOLVED IN BRINES

Roger G. Burns, Department of Earth, Atmospheric and Planetary Sciences, Massachusetts Institute of Technology, Cambridge, MA 02139.

**Overview.** Salts believed to occur in Martian regolith imply that brines occur on Mars, which may have facilitated the oxidation of dissolved  $\text{Fe}^{2+}$  ions after they were released during chemical weathering of basaltic ferromagnesian silicate and iron sulfide minerals. Calculations show that the rate of oxidation of  $\text{Fe}^{2+}$  ions at  $-35^\circ\text{C}$  in a 6M chloride-sulfate brine that might exist on Mars is about  $10^6$  times slower than the oxidation rate of iron in ice-cold terrestrial seawater.

**Introduction.** The existence of ferric-bearing materials on Mars bears testimony to the fact that, at some time during the evolution of the martian regolith, oxidative weathering has occurred of the ferromagnesian silicate and iron sulfide minerals which were originally present in the basalts that flowed onto the surface of the planet. Less certain are the chemical environments, reaction rates and timing of the oxidation events. Intuitively, chemical weathering is expected to have progressed most rapidly when warmer, wetter conditions prevailed on Mars, since the processes of dissolution and oxidation of  $\text{Fe}^{2+}$ -bearing olivines, pyroxenes and sulfides are facilitated in aqueous environments [1]. Such reactions would be inhibited in the present-day frozen surface of Mars. However, periodic melt-waters suspected to occur in equatorial regions of Mars and the possible existence of brine eutectics in the regolith could provide chemical environments in which aqueous oxidation of dissolved  $\text{Fe}^{2+}$  is still occurring near the Martian surface. Factors affecting the rate of oxidation of iron at low temperatures in brine solutions are addressed here.

**Rate Equations.** The most commonly verified rate law for the oxidation of dissolved ferrous iron at near-neutral pH ( $\geq 4.5$ ) is given by

$$-d[\text{Fe}^{2+}]/dt = k_1 [\text{Fe}^{2+}] P_{\text{O}_2} \{\text{OH}^-\}^2 \quad (1)$$

where  $[\text{Fe}^{2+}]$  is the molar concentration of dissolved iron,  $P_{\text{O}_2}$  is the partial pressure of oxygen saturating the aqueous solution,  $\{\text{OH}^-\}$  is the activity of hydroxyl ions, and  $k_1$  is the rate constant [2-5]. On Earth, in water saturated with atmospheric oxygen, the rate constant near  $25^\circ\text{C}$  has a value  $k_1 = (8.0 \pm 2.5) \times 10^{13} \text{ M}^{-2} \text{ atm}^{-1} \text{ min}^{-1}$ , or  $\log_{10} k_1 = 13.9$  [2,3]. Note that the activity of  $\text{OH}^-$  ions in eq. (1) is linked to the pH (where  $\text{pH} = -\log_{10}\{\text{H}^+\}$ ) by the ionic product of water,  $K_w = \{\text{H}^+\}\{\text{OH}^-\}$ , which is the equilibrium constant for the dissociation of water ( $\text{H}_2\text{O} = \text{H}^+ + \text{OH}^-$ ). At  $25^\circ\text{C}$ ,  $K_w = 1 \times 10^{-14} \text{ M}^2$  or  $\text{p}K_w = 14$ , so that acidic solutions prevail when  $\text{pH} < 7$ . At  $0^\circ\text{C}$ ,  $\text{p}K_w = 14.93$ , so that solutions are acidic when  $\text{pH} < 7.46$ .

Equation (1) indicates that the rate of oxidation of dissolved  $\text{Fe}^{2+}$  ions is strongly dependent on pH, decreasing one hundred-fold for each unit decrease of pH. Thus, reaction rates are lowered in acidic solutions, such as those resulting from oxidative weathering of iron sulfides [6,7] and the precipitation of acid rainwater that contains dissolved volcanic gases. Temperature also has a strong effect on the rate of oxidation of  $\text{Fe}^{2+}$  expressed by eq. (1), which is reported to decrease by a factor of 10 for a temperature decrease of  $15^\circ\text{C}$  [2]. Such a rate decrease may be accounted for by the temperature variation of  $K_w$  and the resultant decrease of  $\{\text{OH}^-\}$  at constant pH [3]. Since solubilities of dissolved gases increase at low temperatures, the higher solubility of oxygen in cold water partially offsets the effect of lower temperature on rates of oxidation of  $\text{Fe}^{2+}$  ions. For example, the concentration of dissolved oxygen in pure water at  $25^\circ\text{C}$  ( $[\text{O}_2] = 2.58 \times 10^{-4} \text{ M}$ ) increases to  $[\text{O}_2] = 4.57 \times 10^{-4} \text{ M}$  at  $0^\circ\text{C}$  [8]. To account for the solubility of oxygen, the rate equation for the oxidation of dissolved  $\text{Fe}^{2+}$  is expressed as

$$-d[\text{Fe}^{2+}]/dt = k_0 [\text{Fe}^{2+}] [\text{O}_2] \{\text{OH}^-\}^2, \quad (2)$$

where  $[\text{O}_2]$  is the molar concentration of dissolved oxygen [9]. The rate constant in air-saturated pure water at  $25^\circ\text{C}$  is  $k_0 = 2.37 \times 10^{16} \text{ M}^{-3} \text{ min}^{-1}$ , or  $\log k_0 = 16.375$ . The temperature variation of  $k_0$  may be estimated from  $\log k_0 = 21.56 - 1545/T$  (where  $T$  is in degrees Kelvin) [9], yielding  $\log k_0 = 15.90$  in air-saturated pure water at  $0^\circ\text{C}$ . At  $-25^\circ\text{C}$ ,  $\log k_0 = 15.33$ .

# RATE OF OXIDATION OF IRON IN BRINES ON MARS: Burns, R. G.

**Salinity Dependence.** To determine the effect of salinity on the oxidation of  $\text{Fe}^{2+}$  in aqueous solutions, it is necessary to make corrections for variations of the pH and the concentration of dissolved oxygen with rising ionic strength. For example, in reference seawater with salinity,  $S = 35 \text{ ‰}$  (i.e. 3.5 wt. % dissolved salts), corresponding to the ionic strength  $I \approx 0.7 \text{ M}$ , the concentration of dissolved oxygen at  $0^\circ\text{C}$  decreases to  $[\text{O}_2] = 3.58 \times 10^{-4} \text{ M}$  [8] due to a salting-out effect. At  $25^\circ\text{C}$ ,  $\text{pK}_w = 13.62$ , so that seawater is acidic at  $\text{pH} < 6.81$ . At  $0^\circ\text{C}$ , seawater is acidic at  $\text{pH} < 6.82$ . The effect of salinity on the rate of oxidation of  $\text{Fe}^{2+}$  dissolved in air-saturated seawater is expressed by [9]

$$\log k_I = 21.56 - 1545/T - 3.29 \sqrt{I} + 1.52 I. \quad (3)$$

Thus, in reference seawater at  $25^\circ\text{C}$ ,  $\log k_I$  is lowered to 14.69. At  $0^\circ\text{C}$ ,  $\log k_I = 14.21$ . Extrapolation to  $-25^\circ\text{C}$ , yields  $\log k_I \approx 13.64$ . The decreased rate constant in seawater results from the slower rate of oxidation of  $\text{FeCl}^+$  ion-pairs relative to  $\text{Fe}^{2+}$  ions in pure water.

**Oxidation of  $\text{Fe}^{2+}$  in Brines.** Studies of the effects of ionic strength and ion interactions on the oxidation of  $\text{Fe}^{2+}$  in brine solutions with ionic strengths as high as  $I = 6\text{M}$  [10] have yielded the following expression for the rate constant

$$\log k_B = 21.56 - 1545/T + 0.470 \sqrt{I} - 646 \sqrt{I}/T + 0.723 I \quad (4)$$

Rates of oxidation of  $\text{Fe}^{2+}$  ions initially decrease with increasing ionic strength [10]. However, above  $I \approx 2\text{M}$ , reaction rates increase; in  $6 \text{ M NaCl}$  solutions, for example, rate constants are comparable to values in pure water. In  $6\text{M NaCl}$  brines at  $25^\circ\text{C}$  and  $0^\circ\text{C}$ , the values of  $\log k_I$  are 16.55 and 15.59, respectively, leading to an estimated value of  $\log k_B \approx 14.63$  at  $-25^\circ\text{C}$ . The rate constants are also anion dependent; they decrease in the order  $\text{HCO}_3^- > \text{Br}^- > \text{Cl}^- > \text{NO}_3^- > \text{SO}_4^{2-}$ . Rates of oxidation of  $\text{Fe}^{2+}$  are considerably lower in sulfate solutions than in chloride solutions, reflecting the greater stability of the  $\text{FeSO}_4^0$  ion-pair relative to the  $\text{FeCl}^+$  ion-pair [10]. Thus, rate constants for the oxidation of  $\text{Fe}^{2+}$  ions in mixed-anion  $\text{Cl}^-$ - $\text{SO}_4^{2-}$  brines with  $I = 6\text{M}$  are roughly half the rate constants in pure ice-water at  $0^\circ\text{C}$ , corresponding to  $\log k_B \approx 15.6$ . At  $-25^\circ\text{C}$ , the estimated  $\log k_B \approx 15.0$  for the oxidation of  $\text{Fe}^{2+}$  ions in a chloride-sulfate brine with  $I = 6\text{M}$ . In this brine, the estimated concentration of dissolved oxygen is  $[\text{O}_2] \approx 3.5 \times 10^{-4} \text{ M}$ .

**Oxidation of  $\text{Fe}^{2+}$  in Brines on Mars.** The high concentrations of  $\text{S}$ ,  $\text{Cl}$  and, perhaps,  $\text{Br}$  analysed in the martian soil by the Viking Lander XRF experiment [11] suggest that salts containing  $\text{SO}_4^{2-}$ ,  $\text{Cl}^-$  and, perhaps,  $\text{Br}^-$ ,  $\text{NO}_3^-$  and  $\text{CO}_3^{2-}$  anions may exist near the surface of Mars [12]. Aqueous solutions permeating these salts may have ionic strengths exceeding  $5\text{M}$ , based on ion concentrations estimated from the XRF analyses [12,13]. A variety of brine eutectics proposed for Mars [14,15], including the mixture of ice +  $\text{MgCl}_2 \cdot 12\text{H}_2\text{O}$  +  $\text{MgSO}_4 \cdot 7\text{H}_2\text{O}$ , could maintain a fluid phase at temperatures as low as  $-35^\circ\text{C}$  [14], thereby creating an environment for the oxidation of dissolved  $\text{Fe}^{2+}$  ions.

The concentration of oxygen in a brine equilibrated with the Martian atmosphere ( $\text{P}_{\text{O}_2} \approx 10^{-5} \text{ bar}$ ) would be about  $2 \times 10^{-4}$  smaller than that at the same temperature in an aerated brine on Earth. The rate of oxidation of dissolved  $\text{Fe}^{2+}$  in an aerated brine on Mars is about  $0.3 \text{ ppm Fe}^{2+}$  per year, based on trends summarized above. Assumptions made in this calculation are: (1) the existence on Mars of a  $6\text{M}$  brine containing  $\text{Cl}^- + \text{SO}_4^{2-}$  anions; (2) a rate constant of  $\log k_B = 15.0$  at  $-25^\circ\text{C}$ ; (3)  $\text{pH} = 6$  and  $\text{pK}_w = 13.5$  in this brine; (4) dissolved  $[\text{O}_2] = 7 \times 10^{-8} \text{ M}$ ; and (5) the concentration of dissolved iron is maintained at  $[\text{Fe}^{2+}] = 10^{-4} \text{ M}$  by the solubility of siderite. Therefore, oxidation of  $\text{Fe}^{2+}$  dissolved in a brine on Mars is about  $10^6$  times slower than the rate of oxidation of  $\text{Fe}^{2+}$  ions dissolved in  $\text{pH } 8$ , ice-cold terrestrial seawater.

**References.** [1] R.G.Burns, *Lunar Planet. Sci.*, XXIII, 187 (1992); *MSATT/LPI Tech. Rept.*, 92-04, 8 (1992); [2] W.Stumm & G.F.Lee, *Ind. Eng. Chem.*, 53, 143 (1961); [3] W.Sung & J.J.Morgan, *Environ. Sci. Tech.*, 14, 561 (1980); [4] W.Davison & G.Seed, *Geochim. Cosmochim. Acta*, 47, 67 (1983); [5] E.J.Roekens & R.E.Van Grieken, *Marine Chem.*, 13, 195 (1983); 15, 281 (1984); [6] R.G.Burns, *Proc. 18th LPSC*, 713 (1988); [7] R.G.Burns & D.S.Fisher, *JGR*, 95, 14415 (1990); [8] B.B.Benson & D.Krause Jr, *Limnol. Oceanogr.*, 29, 620 (1984); [9] F.J.Millero, S.Sotolongo & M.Izaguirre, *Geochim. Cosmochim. Acta*, 51, 793 (1987); [10] F.J.Millero & M.Izaguirre, *J. Soln. Chem.*, 18, 585 (1989); [11] B.C.Clark et al., *JGR*, 87, 10059 (1982); [12] B.C.Clark & D.C.Van Hart, *Icarus*, 45, 370 (1981); [13] R.G.Burns, *Proc. 17th LPSC, JGR*, 92, E570 (1987); [14] G.W.Brass, *Icarus*, 42, 20 (1980); [15] A.P.Zent & F.P.Fanale, *JGR*, 84, D439 (1986); [16] Research supported by NASA grant NAGW-2049.

456867

5114-91  
ABS. ONLYLPSC XXIV  
N 9 4 7 1 2 3 1 2 9<sup>233</sup>**VENUS MOUNTAIN-TOP MINERALOGY: MISCONCEPTIONS ABOUT PYRITE AS THE HIGH RADAR-REFLECTING PHASE**Roger G. Burns and D'Arcy W. Straub, Department of Earth, Atmospheric and Planetary Sciences, Massachusetts Institute of Technology, Cambridge, MA 02139. P. 2

**Overview.** Altitude-dependent, high radar-reflectivity surfaces on Venus are observed on most mountainous volcanic terranes above a planetary radius of about 6054 km. However, high radar-reflectivity areas also occur at lower altitudes in some impact craters and plain terranes. Pyrite ( $\text{FeS}_2$ ) is commonly believed to be responsible for the high radar reflectivities at high elevations on Venus, on account of large dielectric constants measured for sulfide-bearing rocks that were erroneously attributed to pyrite instead of pyrrhotite. Pentlandite-pyrrhotite assemblages may be responsible for high reflectivities associated with impact craters on the Venusian surface, by analogy with Fe-Ni sulfide deposits occurring in terrestrial astroblemes. Mixed-valence  $\text{Fe}^{2+}$ - $\text{Fe}^{3+}$  silicates, including oxyhornblende, oxybiotite and ilvaite, may contribute to high radar-reflecting surfaces on mountain-tops of Venus.

High radar-reflectivity regions on the surface of Venus [1], corresponding to areas with low radiothermal emissivities, are an enigma. They appear to predominate at high altitudes above a critical planetary radius of about 6054 km on highlands (e.g., Ovda Regio, Thetis Regio, Maxwell Montes), large shield volcanoes (e.g., Ozza Mons, Theia Mons, Gula Mons) and other smaller and rifted volcanoes (e.g., Rhea Mons) [2]. However, areas of high radar reflectivity are occasionally observed in low-lying terranes, including some impact craters (e.g., Boleya, Stanton, Stuart, Mead) [2]. These high radar-reflectivity regions are indicative of surface rocks with relatively large bulk dielectric constants resulting from mineral constituents that may possess high electrical conductivities [1]. Fresh, dry, unweathered, compact igneous and plutonic rocks have relatively small intrinsic dielectric constants [3]. Therefore, to account for the electrical properties of the surface of Venus, a variety of Fe, Mn and Ti oxide minerals with large dielectric constants have been proposed, including ilmenite ( $\text{FeTiO}_3$ ), perovskite ( $\text{CaTiO}_3$ ), hematite ( $\text{Fe}_2\text{O}_3$ ), and pyrolusite ( $\text{MnO}_2$ ) [4]. However, major proportions (>10 volume %) of these minerals must be present in the surface rocks to account for their high radar reflectivities, posing geochemical problems of segregating such comparatively minor minerals. The bulk dielectric constant of a rock matrix may be raised when it is "loaded" with fragments of electrically conducting inclusions [1]. The most popular candidate as a "loaded dielectric" is pyrite,  $\text{FeS}_2$ , which is postulated to be disseminated in amounts approaching 15 volume % throughout surface rocks at high elevations on Venus, apparently accounting for many of the high radar-reflectivity areas [1,2].

The choice of pyrite as the high radar-reflectivity phase at high altitudes on Venus was influenced by dielectric constant measurements made on, supposedly, pyrite-bearing rocks [5]. Evidence for this association may be flawed, however. One rock-type used in those room temperature dielectric constant measurements [5] consisted of two specimens of metamorphosed volcanic rocks from New Hampshire. The mineralogy of the metavolcanic rocks comprised major proportions of plagioclase feldspar, Fe-bearing biotite, chlorite and accessory magnetite, together with minor iron sulfide assemblages consisting of pyrite (4 to 5 volume %  $\text{FeS}_2$ ), pyrrhotite (2 to 4 %  $\text{Fe}_{1-x}\text{S}$ ) and chalcopyrite (up to 2 %  $\text{CuFeS}_2$ ). The metavolcanic rocks yielded bulk dielectric constants ( $\epsilon$ ) of about 20, which are significantly larger than typical values ( $\epsilon = 5$  to 10) for mafic igneous rocks [3] and pure monomineralic pyrite ( $\epsilon = 10.4$  to 12.1; [6]). A second rock-type used in the early dielectric constant measurements [5] comprised three samples of high-grade sulfide ore from Sudbury, Ontario, Canada. The ore specimens were reported [5] to contain 40 to 45% pyrite, 40 to 45% chalcopyrite, and <5% pyrrhotite. The mineral identifications were based on optical reflectivities observed in surfaces of polished rock-sections viewed under the microscope. In principle, pyrite with a high reflectivity ( $R = 55\%$ ) is readily distinguishable from pyrrhotite ( $R = 40\%$ ) and chalcopyrite ( $R = 45\%$ ). However, the high electrical conductivities ( $\sigma$ ) of the three Sudbury ore samples ( $\sigma = 3 \times 10^3$  to  $7.5 \times 10^5 \text{ ohm}^{-1} \text{ m}^{-1}$ ) prevented dielectric constant

## MINERALS ON THE SURFACE OF VENUS: Burns, R. G. and Straub, D. W.

measurements being made, which appeared to correlate with high proportions of pyrite in the specimens [5]. These high dielectric constants for sulfide-bearing metamorphic rocks and ores, which were attributed to electrical properties of pyrite, and not pyrrhotite, appear to have influenced subsequent interpretations of Venusian radiothermal emissivity measurements derived from the Pioneer Venus radar mapper experiments [1] and the current Magellan radiometer experiment [2], as well as chemical equilibrium reactions believed to occur on Venus that have focused mainly on thermodynamic properties of pyrite [7]. These chemical reactions involving pyrite are evaluated elsewhere [8].

However, the mineralogy reported [5] for the Sudbury sulfide ore is probably incorrect. The sulfide deposits at Sudbury are an economic source of nickel, which occurs in pentlandite,  $(\text{Fe,Ni})_9\text{S}_8$ , intimately associated with major pyrrhotite and accessory pyrite and chalcopyrite [9]. Pentlandite has a higher reflectivity ( $R = 50\%$ ) than pyrrhotite ( $R = 40\%$ ) and was apparently misidentified as pyrite [5]. Pentlandite and pyrrhotite both have metallic properties, but pentlandite is non-magnetic. Therefore, the immeasurably high dielectric constant (due to high electrical conductivity) of the Sudbury ore [5], which appeared to correlate with pyrite (plus chalcopyrite) abundance, probably originated, instead, from the pyrrhotite-pentlandite assemblage.

An important inference about Venus surface mineralogy that may be drawn from the electrical properties of the Sudbury ore samples is they provide a clue to the origin of the high radar reflectivities associated with some impact craters on the planet. The Sudbury deposits resulted from an astrobleme that impacted the Earth about 1.85 b.y. ago [10]. Basaltic magma (now norite) flowed into the impact crater associated with the astrobleme to form the Sudbury lopolith, in which massive Fe-Ni sulphide ores were deposited around the perimeter of the crater [9,10]. We suggest that pyrrhotite-pentlandite assemblages occur in many impact craters on Venus, too, accounting for the high radar reflectivities of impact-related parabolic features observed there at low altitudes on the Venusian surface [11].

Controversy also exists over the thermodynamic stability of pyrite on Venus [12,13], which is discussed elsewhere [8]. Such ambiguities over the stability of pyrite, and whether or not pyrite influences the radiothermal emissivity of the Venusian surface above the 6054 km planetary radius, led us to explore alternative explanations for the high radar-reflectivity areas of Venus [14]. Stability fields of mixed-valence  $\text{Fe}^{2+}\text{-Fe}^{3+}$  silicates (e.g., oxyhornblende, oxybiotite, ilvaite), render these mineral assemblages as viable candidates, rather than pyrite, for the high radar-reflectivity assemblages observed at high elevations on the surface of Venus. The stability of oxyamphiboles on Venus is discussed in an accompanying abstract [15].

**References.** [1] G.H. Pettengill, P.G. Ford & S. Nozette, *Science* 217, 640 (1982); P.G. Ford & G.H. Pettengill, *Science* 220, 1379 (1983); G.H. Pettengill, P.G. Ford & B.D. Chapman, *JGR* 93, 14881 (1988); [2] R.J. Wilt, *Ph.D. Thesis, MIT* (1992); G.H. Pettengill, P.G. Ford & R.J. Wilt, *JGR* 97, 13091 (1992); [3] M.J. Campbell & J. Ulrichs, *JGR* 74, 5687 (1969); G.V. Keller, in *Practical Handbook of Physical Properties of Rocks and Minerals* (R.S. Carmichael, ed., CRC Press, Boca Raton, Florida), p. 359 (1989); [4] J.B. Garvin et al., *Lunar Planet. Sci.* XVI, 262, 264 & 266 (1985); [5] S.D. Nozette, *Ph.D. Thesis, MIT* (1982); [6] D.E. Husk & M.S. Seehra, *Solid State Comm.* 27, 1147 (1978); [7] S.Nolette & J.S. Lewis, *Science* 216, 181 (1978); [8] D.W. Straub, *Lunar Planet. Sci.* XXIV, this vol. (1993); [9] A.J. Naldrett, in *The Geology and Ore Deposits of the Sudbury Structure* (E.G. Pye, A.J. Naldrett & P.E. Giblin, eds), *Ontario Geol. Surv. Spec. Vol. 1*, 309 (1984); A.J. Naldrett, *Magmatic Sulfide Deposits*, Oxford Univ. Press (1989); [10] R.S. Dietz, *J. Geol.* 72, 412 (1964); G.G. Morrison, in *ref.* [9], p. 513 (1984); [11] J.J. Plant & R.E. Arvidson, *JGR* 97, 16279 (1992); [12] J. A. Wood et al., *Lunar Planet. Sci.* XXII, 1519 (1991); XXIII, 1551 (1992); D.B. Klose, J.A. Wood & A. Hashimoto, *JGR* 97, 16353 (1992); [13] B. Fegley Jr & A.H. Treiman, in *Venus and Mars: Atmospheres, Ionospheres and Solar Wind Interactions* (J. G. Luhmann, M. Tatralayay & R. O. Pepin, eds), *AGU Geophys. Monograph* 66, 7 (1992); B. Fegley Jr, A. H. Treiman & V. I. Sharpton, *Proc. Lunar Planet. Sci.* 22, 3 (1992); [14] R.G.Burns & D.W. Straub, *Intern. Colloq. Venus, LPI Contrib. No. 789*, p.15 (1992); *EOS, Trans. Amer. Geophys. Un.*, 73, 332 (1992); *Lunar Planet. Sci.*, XXIII, 1375 (1992); [15] D.W. Straub & R.G. Burns, *Lunar Planet. Sci.* XXIV, this vol. (1993); [16] Research supported by NASA grants NAGW-2049 and 2220.

456868

5115-91

ABS ONLY

LPSC XXIV

235

N 94 - 12130

168335

p. 1

# Buoyant Subduction on Venus: Implications for Subduction Around Coronae

J.D. Burt and J.W. Head, Dept. of Geological Sci., Brown University, Providence, R.I., 02912

Potentially low lithospheric densities, caused by high Venus surface and perhaps mantle temperatures [1], could inhibit the development of negative buoyancy-driven subduction and a global system of plate tectonics/crustal recycling on that planet [2]. No evidence for a global plate tectonic system has been found so far, however, specific features strongly resembling terrestrial subduction zones in planform and topographic cross-section have been described, including trenches around large coronae and chasmata in eastern Aphrodite Terra [3,4,5]. The cause for the absence, or an altered expression, of plate tectonics on Venus remains to be found. Slab buoyancy may play a role in this difference, with higher lithospheric temperatures and a tendency toward positive buoyancy acting to oppose the descent of slabs and favoring underthrusting instead. This study seeks to explore the effect of slab buoyancy on subduction and to define the conditions which would lead to underthrusting versus those allowing the formation of trenches and self-perpetuating subduction. Applying a finite element code to assess the effects of buoyant forces on slabs subducting into a viscous mantle, we find that mantle flow induced by horizontal motion of the convergent lithosphere greatly influences subduction angle, while buoyancy forces produce a lesser effect. Induced mantle flow tends to decrease subduction angle to near an underthrusting position when the subducting lithosphere converges on a stationary overriding lithosphere. When the overriding lithosphere is in motion, as in the case of an expanding corona, subduction angles are expected to increase.

An initial stage of this work [6] involved estimating the changes in slab buoyancy due to slab heating and pressurization over the course of subduction. Modelling a slab, descending at a fixed angle and heated by conduction, radioactivity, and the heat released in phase changes, slab material density changes due to changing temperature, phase, and pressure were derived. In brief, slabs were found to remain positively buoyant until they had penetrated to a depth of 250 to 300 km. Thus, during the early stages of subduction, slabs must overcome positive buoyancy forces to achieve net negative buoyancy and promote self-sustained subduction. The rate at which buoyancy forces can force a slab to rise through a viscous mantle may be important in determining the slab fate.

To understand better the effects of buoyancy on slab descent a finite element code was applied to a simplified model of a slab subducting into a viscous mantle. The model consists of a lithospheric slab descending at an initial 45 degree angle into the mantle. The density structure includes a basaltic crust and peridotite mantle, with the basalt-eclogite phase change applied at a depth of 100 km. The complexities of density variation due to pressure and temperature were ignored. The depleted mantle layer, the mantle residue remaining after crustal material was removed by partial melting, was also not included. Its low density relative to the undepleted mantle would add somewhat to the positive buoyancy of the slab. Buoyancy forces appropriate to the crustal thickness were applied, using basaltic densities above the basalt-eclogite phase change, and eclogite densities below. The mantle and slab materials differ in viscosity by a factor of 100. The convergence velocity was imposed where the slab enters the mantle and horizontally along the surface of the model as a surface boundary velocity. Meanwhile, horizontal velocities were set to zero beneath the stationary overriding lithosphere. Side boundary conditions were imposed to allow passage of material into and out of the model region, while a zero shear stress condition was used at the bottom boundary. Changes in the subduction angle were then estimated as the slab lengthened according to the convergence rate.

Figure 1 illustrates the mantle flow pattern resulting from this model. Generally, the flow shown proceeds from right to left in concert with the convergent lithospheric motion at the surface. Horizontal lithospheric motion appears to cause this mantle flow. The slab partially deflects the mantle flow, but, impinging on the slab base, the flow causes the subduction angle to decrease. While positive slab buoyancy also has the effect of decreasing the subduction angle, the mantle flow induced by the horizontal motion of the lithosphere at the surface dominates.

Figure 2, plotting slab length against subduction angle, shows the effect over time of the mantle flow on the subduction angle. Starting with a 50 km slab initially dipping 45 degrees, the graph shows the angle decreases rapidly, reaching a minimal value near 15 degrees within 15 to 20 million years. This result appears consistent for a range of subduction rates and crustal thicknesses. The significance of the minimum angle is uncertain, but it may represent the diminishing influence of mantle flow as the slab profile shrinks. Slab buoyancy alone has a lesser effect, yielding a similar decrease in the subduction angle, but over a longer time span. Thus, it appears that mantle flow induced by the horizontal motion of the converging lithosphere at the surface dominates in governing the changing angle of subduction.

Two consequences derive from this result. First, a slab must subduct much further, to lengths near 1000 km, over a much longer time, before negative buoyancy is attained. Second, mantle flow induced by

the convergent motion of the slab will reduce the subduction angle and force the slab into a nearly underthrusting position. In order for subduction to become self-sustained through the negative buoyancy of the slab, other means may be necessary to mitigate or eliminate the effects of the induced mantle flow. These means might include the attachment of a slab to a deepening crustal root which, upon becoming negatively buoyant itself, delaminates and sinks taking the slab with it. Another alternative is presented by the case of subduction on the periphery of a corona.

In the model of Sandwell and Schubert [3], a radially expanding corona may override the lithosphere on its border and cause that lithosphere to subduct. In this scenario the overriding lithosphere of the corona is moving horizontally while the subducting material sinks vertically. This contrasts with the situation given in the model where the overriding lithosphere remains stationary and the subducting material first converges horizontally before descending. This would lead to a reversal of the induced flow in the mantle and cause it to impinge on the upper side of the slab. Due to the apparent dominance of the effects of mantle flow over buoyancy forces, increasing subduction angles may be favored despite positive buoyancy in the subducting slab. This enhances the tendency of the slab to reach negative buoyancy. Thus, in the case of subduction resulting from corona growth, self-perpetuating subduction may be possible leading to further corona expansion.

In the case of overturn initiated by a growing negatively buoyant lithosphere [7] or depleted mantle layer [8], the negative buoyancy of the slab guarantees continued subduction. If, in these cases, appreciable horizontal movement and convergence of lithosphere were to develop, then induced mantle flow may affect the subduction angle, but it could not prevent or slow further recycling.

**References:** [1] Phillips R.J. and Malin M.C. (1982) in *Venus*, Hunten D.M. et al. eds., U. AZ Press, Tucson, p.159-214. [2] Anderson D.L. (1981) *Geophys. Res. Lett.*, 8, 309-311. [3] Sandwell D.T. and Schubert G. (1992) *J. Geophys. Res.*, 97, 16069-16084. [4] Schubert G., Sandwell D.T., and Johnson C.L. (1992) *Eos*, 329. [5] McKenzie D., Ford P.G., Johnson C., Parsons B., Sandwell D., Saunders S., and Solomon S.C. (1992) *J. Geophys. Res.*, 97, 13533-13544. [6] Burt J.D. and Head J.W. (1992) *Geophys. Res. Lett.*, 19, 1707-1710. [7] Turcotte D.L. (1992) *International Colloquium on Venus*, 127. [8] Parmentier E.M. and Hess P.C. (1992) *Geophys. Res. Lett.*, 19, 2015-2018.

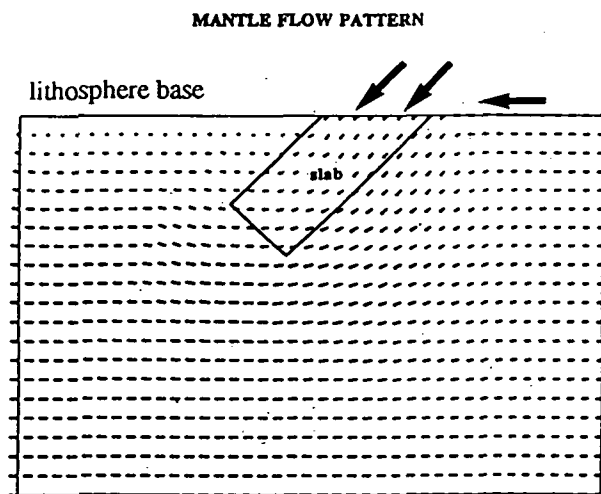


**Figure 1:** Mantle flow pattern. Flow trends right to left. Base of lithosphere is at top.

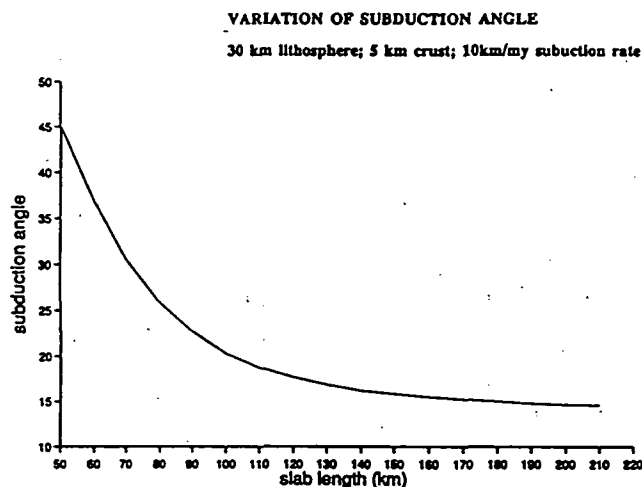


**Figure 2:** Variation of subduction angle for 30 km lithosphere, 5 km crust, 10 km/my subduction rate.

**THE ORIGIN OF VENUSIAN CHANNELS: MODELLING OF THERMAL EROSION  
 BY LAVA;** D.B.J. Bussey, S-A. Sørensen, J.E. Guest, University of London Observatory, University  
 College London, London, NW7 2QS, U.K.

Magellan imagery has revealed that channels, apparently volcanic in origin, are abundant on the surface of Venus [1]. There has been much debate about the origin of these channels. Are they the result of erosional (either thermal or mechanical) or constructional processes?

A common characteristic of the simple sinuous channels (described by Baker as 'canali' [1]) is that they show evidence of erosion near their source and then become purely constructional, forming levees and in some cases roofing over completely [2].

One method of showing that thermal erosion is capable of producing the type of channels seen is to use computer modelling incorporating the physical conditions on Venus and the physical characteristics of the different types of lava that may have been erupted.

It is possible to calculate, relatively easily, two channel parameters. The first is the erosion rate, which combined with eruption duration, gives depth. The second is for how long after leaving the source the erupted lava will continue to be capable of thermal erosion before constructional processes dominate. Making assumptions about the rheology of the lava (e.g. assume it behaves as a Bingham plastic) along with the slope angle yields a flow velocity and therefore a distance over which thermal erosion will take place.

Due to the resolution (both vertical and horizontal) of the Magellan altimetric data, the distance from the source that the channel is erosional can be much more accurately measured than the depth of the channel. This will remain the case until stereo imagery becomes available for large areas of the planet.

Until a solid crust is formed on top of the lava, heat is lost by radiation and convection to the atmosphere. At the same time heat is transferred to the underlying rock by conduction. This heats up the rock until its solidus temperature is reached. At this point latent heat must be supplied before the rock actually enters the liquid phase, whereupon the melted rock is amalgamated into the lava and removed. Loss of heat at the top of the lava by radiation and the bottom of the lava by conduction leads to heat flow within the lava by both convection and conduction. Of the two however, convection has a much shorter time scale and is therefore much more effective.

Once a crust has formed heat loss by convection stops and heat loss by radiation is much reduced due to the crust being at a lower temperature than the liquid lava. Lava then loses heat by conduction into the crust which gradually thickens. As the lava loses internal energy, by melting the ground rock, it is itself cooled. Eventually the lava will be cooled to such an extent that it will no longer have enough internal energy to continue to melt the rock. At this point the channel becomes purely constructional in nature.

As mentioned previously there are two different quantities to be modelled. The erosion rate and the distance from the vent that the lava retains its erosional capability. In the first approximation this can be accomplished using a simple one dimensional model of temperature distribution as a function of time at various distances from the vent. The model is solved by using the principle of finite differences. Preliminary findings for erosion rate near the source for a komatiite lava flowing over a basalt ground rock are shown in figures 1 & 2. Figure 1 represents Venusian flow whilst figure 2 is for Earth. The graphs show vertical distance eroded against time. The present model predicts an erosion rate of approximately 25 cm a day on Venus and 16 cm a day on Earth. The value for Earth is significantly lower than that predicted by Huppert [3].

**ORIGIN OF VENUSIAN CHANNELS: D.B.J. Bussey et al.**

Even with this lower rate the preliminary quantitative results presented here indicate that even for short eruption durations thermal erosion can be an important process, given the right conditions, in the production of channels.

**REFERENCES:**

- [1] Baker V.R. et al. (1992) *JOURNAL GEOPHYSICAL RESEARCH* 97 pp 13421 - 13444.
- [2] Bussey D.B.J. et al. (1992) *INTERNATIONAL COLLOQUIUM ON VENUS LPI Contribution No. 789* pp 18 - 19.
- [3] Huppert H.E. et al. (1984) *NATURE* Vol 309 pp 19 - 23.

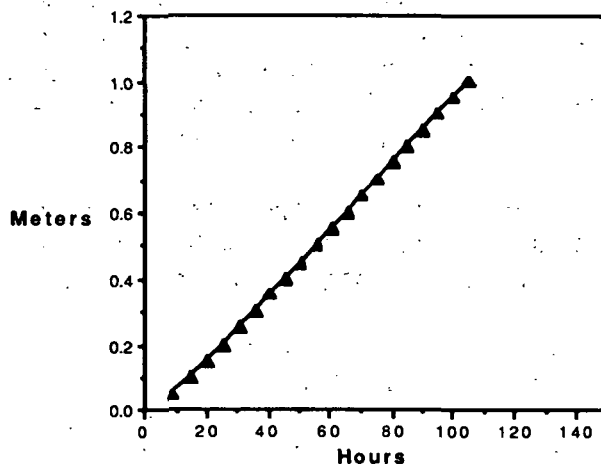


**Fig. 1.** A plot of vertical distance eroded versus time on Venus.

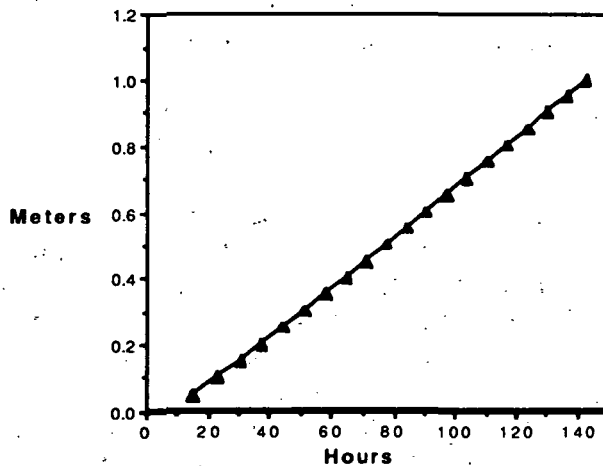


**Fig. 2.** A plot of vertical distance eroded versus time on Earth.



456871

5117-90  
ABS ONLY

LPSC XXIV

239

N 9 4 4 3 2 B 3 2

**VOLATILES IN FOURTEEN INTERPLANETARY DUST PARTICLES: A**  
**COMPARISON WITH CI AND CM CHONDRITES.** R. Bustin, Chemistry Dept.,  
Arkansas College, Batesville, AR 72501, E.K. Gibson, Jr., SN4 Planetary Sciences,  
NASA-JSC, Houston, TX 77058 and S.J. Wentworth LESC, NASA-JSC, Houston, TX 77058.

In an attempt to classify the nature of volatiles within interplanetary dust particles (IDPs) we have studied 14 IDPs using a laser microprobe/mass spectrometer (LM/MS) technique. Volatile abundances and distributions found for the IDPs are compared with those measured for carbonaceous chondrites in order to determine if the IDPs are related to the parent bodies of these primitive meteorites (See Gibson, 1992 for review of volatiles associated with IDPs).

IDPs and carbonaceous chondrites have been analyzed using the techniques of Hartmetz et al. (2-4). Individual IDPs and pieces of CI, CM and CV carbonaceous chondrites similar in size have been mounted on gold foils, cleaned by rinsing with hexane and freon to remove silicone oil from the IDPs. Particles have been further cleaned by treatment with an atomic oxygen plasma. Each particle analyzed has been subjected to EDX-SEM analysis to determine the composition of the particles prior to analysis; 13 of the 14 IDP particles were of chondritic composition, based on the similarity of their elemental compositions and those of chondritic meteorites, particularly the carbonaceous chondrites (Table 1). Individual samples are vaporized under vacuum using a Q-switched Nd/YAG laser (1.06 microns) and the released volatiles directly analyzed with a quadrupole mass spectrometer. Spectral information obtained has been processed using the procedures of Hartmetz et al. (2-4). The IDPs used in this study were from the Large Area Collectors L2005 and L2006 flown aboard a NASA ER-2 aircraft during a series of flights that were made within west-central North America during the fall of 1989.

The volatile abundances observed within the 14 IDPs varied dramatically from almost no volatiles (L2005B21) to what is considered volatile-rich (L2006A12) because of the presence of several hydrocarbon "families" in addition to species such as C, O, CO, CO<sub>2</sub>, and COS. Table 2 lists the indigenous volatile species found for the 14 IDPs studied. As noted earlier by Hartmetz et al. (2-4) IDPs are porous and may retain silicone oil and/or freon residues from the collection devices or hexane used to remove the silicone oil from the surface; species is considered to be indigenous only if it does not occur in the mass spectrum of silicone oil, freon, or hexane. Nine of the 14 particles analyzed in our study are believed to be hydrated IDPs and five are anhydrous particles. Table 3 lists the major classes of volatiles which we have observed for all of the IDPs analyzed to date in our laboratory.

One of the more unusual particles analyzed is L2006B16 which was observed to contain unusually large amounts of carbon in its EDX spectrum. Thomas et al. (5) noted a fragment of this sample contained between 40 and 50 wt. % carbon. Our analysis of the particle showed it contained a form of carbon which released essentially only CO during vaporization. We do not know if the carbon was graphite or another unusual variety of carbon. Trace amounts of sulfur-related volatiles were also observed. Particle L2006B16 is an unusual IDP as our analysis and those of Thomas et al. (5) have shown.

To give some idea about how representative a 10-20 micron sized particle really is as compared to its parent body, small particles of Murchison (CM) and Orgueil (CI) were analyzed. There was considerable diversity in the volatiles released from individual 10 to 20 micron particles analyzed from the carbonaceous chondrites. The diversity is consistent with the heterogeneity observed by SEM/EDS. Some particles appeared to be only mineral grains (i.e. released only CO and CO<sub>2</sub> from carbonates, or SO<sub>2</sub> from sulfates, or CS<sub>2</sub> and/or COS from sulfides, or OH or H<sub>2</sub>O from hydrated minerals); some particles did not release volatiles typical of meteoritic volatiles, and others were fairly representative of the meteorite matrix as observed by Hartmetz et al. (4). All meteorite particles were not the same size. In most cases, the larger particles (20 micron-sized particles) gave spectra most similar to the parent meteorite. For both Orgueil and Murchison, a composite of all particles yielded a spectrum similar to that of the parent meteorite. Sulfur-bearing species, aliphatic hydrocarbon groups, polycyclic aromatic hydrocarbons, carbonates, and water were present in each of these. Based on the total ion

chromatograms, the IDPs had the least amount of total volatiles; small Murchison particles had only slightly more volatiles (1.15 times); and small Orgueil particles had about 2.3 times as much volatile materials as the IDPs. Direct analysis of the groundmass in an individual piece of Murchison with the LM/MS technique produced only 1.4 times as much volatiles as the IDPs, but the analysis of 40 to 50 micron-sized particles or Orgueil evolved 20 times as much volatile material as the IDPs. These results are in keeping with previous studies which noted volatile differences (4).

In order to envision what a parent body containing all 14 or our IDPs might resemble, a composite spectrum was prepared. Backgrounds were subtracted and the resulting spectrum can be considered to give a representative spectrum of a possible IDP "parent body". The IDP composite spectrum is very much like the spectra obtained from the CM carbonaceous chondrite. The most obvious difference is the decreased intensity of the sulfur-related peaks. Although clearly present, the SO and SO<sub>2</sub> peaks are much smaller for the IDP composite spectrum as compared to either the CM and CI spectrum. The composite IDP spectrum resembles the Murchison spectrum and may be another indicator that the IDPs parent body are related to the CM carbonaceous chondrite-type parent bodies.

**References:** (1) Gibson, E.K., Jr. (1992) *J. Geophys. Res.-Planets* E3, 3865-3875; (2) Hartmetz et al. (1990) *Proc. 20th LPSC* 343-355; (3) Hartmetz et al. (1991a) *Proc. 21st LPSC* 557-567.; (4) Hartmetz et al. (1991b) *Proc. 21st LPSC* 527-539. (5) Thomas et al. (1993) this volume.

TABLE 1 EDX/SEM ELEMENTAL ANALYSIS OF IDPs

Particle	Major and (Minor) Components <sup>1</sup>
L2005B21	Si, Fe, Mg, O, (Al)
L2005C21	Si, S, Mg, O, Fe, Ca, Na, Al
L2005C24	Si, Mg, Fe, O, Ca, (Al)
L2005C26	Si, Mg, Fe, O, (Ca), (Al), (Ni)
L2005C28	S, Si, Fe, Mg, O, (Al), (Ni)
L2005C30	Si, Mg, Fe, O, (Ca), (Ti), (Al), (Na)
L2005D27	Si, Mg, O, S, Fe, (Na), (Al), (Ca)
L2005D34	Si, Mg, O, Na, Fe
L2005E38	Si, Mg, Fe, O, (Na)
L2005E39	Si, Mg, C, Fe, O, (Na)
L2006A6,7	C, Si, Na, (O)
L2006A12	Si, Mg, O, Fe, (Ca), (C), (Na), (Al)
L2006A26	Si, Ca, Mg, O, Fe, C
L2006B16	Si, Mg, O, Fe, C

<sup>1</sup>Elemental abundances listed in order of abundance with minor amounts placed in parentheses. Sulfur abundances are difficult to know accurately because of the overlap of the sulfur peak with the strong background gold peak from the sample mount.

TABLE 2. INDIGENOUS VOLATILE SPECIES PRESENT IN IDPs

Particle	Volatile Components Measured within IDP
L2005B21	OH
L2005C21	C, C <sub>2</sub> H <sub>5</sub> , O <sub>2</sub> or S, SO <sub>2</sub> , C <sub>5</sub> H <sub>6</sub> , C <sub>6</sub> H <sub>6</sub> , C <sub>6</sub> H <sub>7</sub> , C <sub>6</sub> H <sub>5</sub> CH <sub>3</sub>
L2005C24	OH, C <sub>2</sub> H <sub>5</sub> , C <sub>2</sub> H <sub>6</sub> , C <sub>4</sub> or SO, C <sub>4</sub> H, C <sub>5</sub> H <sub>8</sub> , C <sub>5</sub> H <sub>9</sub> , C <sub>6</sub> H <sub>6</sub> , C <sub>6</sub> H <sub>5</sub> CH <sub>3</sub>
L2005C26	C, CH, and higher molecular weight hydrocarbons
L2005C28	CH, OH, C <sub>5</sub> H <sub>7</sub> , CS <sub>2</sub> , C <sub>6</sub> H <sub>6</sub> , C <sub>6</sub> H <sub>7</sub> , C <sub>7</sub> H <sub>11</sub>
L2005C30	OH, C <sub>2</sub> H <sub>5</sub> , C <sub>2</sub> H <sub>6</sub> , CO <sub>2</sub> , C <sub>5</sub> H <sub>8</sub> , C <sub>5</sub> H <sub>9</sub>
L2005D27	C, C <sub>2</sub> H <sub>5</sub> , CO <sub>2</sub> , SOH <sub>7</sub> , SO <sub>2</sub> , CS <sub>2</sub> , C <sub>6</sub> H <sub>6</sub> , C <sub>6</sub> H <sub>7</sub> , C <sub>6</sub> H <sub>5</sub> CH <sub>3</sub> , C <sub>7</sub> H <sub>9</sub> , C <sub>7</sub> H <sub>11</sub> , C <sub>7</sub> H <sub>16</sub>
L2005D34	CH, OH, C <sub>6</sub> H <sub>6</sub>
L2005E38	OH, O <sub>2</sub> or S, SO
L2005E39	C, C <sub>2</sub> H <sub>5</sub> , C <sub>5</sub> H <sub>5</sub> , C <sub>5</sub> H <sub>6</sub> , C <sub>5</sub> H <sub>7</sub>
L2006A6,7	C, OH, C <sub>2</sub> H <sub>5</sub> , CO <sub>2</sub> , C <sub>5</sub> H <sub>5</sub> , C <sub>5</sub> H <sub>6</sub> , C <sub>6</sub> H <sub>6</sub>
L2006A12	C, C <sub>2</sub> H <sub>5</sub> , CO <sub>2</sub> , C <sub>5</sub> H <sub>5</sub> , C <sub>5</sub> H <sub>7</sub> , C <sub>6</sub> H <sub>6</sub>
L2006A26	NONE
L2006B16	CO, SO

TABLE 3. OVERVIEW OF VOLATILE SPECIES IDENTIFIED IN 28 IDPs

Little or No Indigenous Volatiles	Large Amount of Indigenous Volatiles	Carbonaceous Material	Carbonates	Water or Hydroxyl	Sulfur Species
L2001D3	L2002C4	L2002C4	L2003D2	L2005B21	L2002C4
L2004D3	L2003D2	L2003D2	L2006A6,7	L2005C24	L2003D2
L2005B21	L2003E3	L2004C3	L2006A12	L2005C28	L2004C3
L2005C21	L2004C3	L2003E3	U2034D7	L2005C30	L2004D3
L2005C24	L2006A12	L2005C21		L2005D34	L2005C21
L2005C26	U2017A4	L2005C24		L2005E38	L2005C24
L2005C28	U2017A5	L2005C26		L2006A6,7	L2005C26
L2005C30	U2022G13	L2005D34		L2006B16	L2005E38
L2005D27	U2034D7	L2005E39		U2022F5	L2006A12
L2005D34		L2006A6,7		U2022F20	L2006B16
L2005E38		U2034D7		U2034D7	U2017A4
L2006A26					U2017A5
L2006B16					U2022G13
U2015B20					U2034D7
U2015F20					
U2022F5					
U2034D1					

Samples listed are a composite of all the IDPs analyzed via LM/MS technique and have been previously reported in (2-4) and this study.

456873

S118'-91  
ADS. ONLY

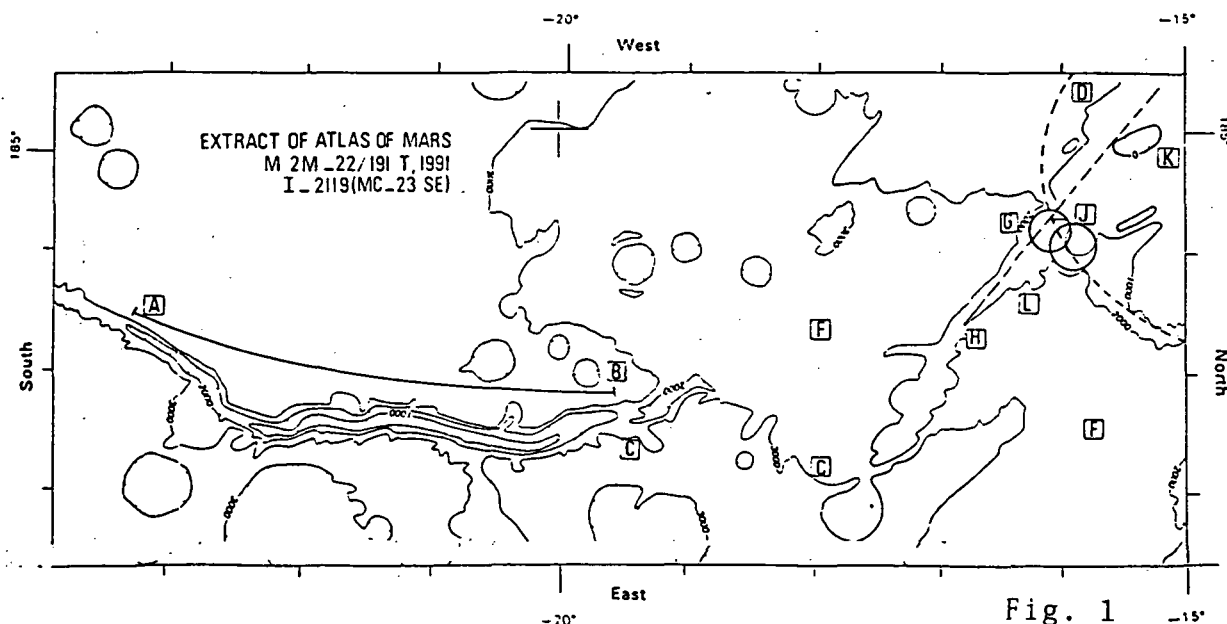
LPSC XXIV

241

N94-12133

AN ANCIENT INNER LAKE IN MA'ADIM VALLIS. N.A CABROL, E.A GRIN, A, DOLLFUS (Observatoire de Paris-Meudon) ; G. DAWIDOWICZ (Université Paris I-Sorbonne)

The survey of Ma'adim Vallis and crater Gusev area by the new topographic Aeolis southeast map allows to document the hydrodynamics processes which occurred in the valley. The inner Ma'adim Vallis hypsometric and volume deposits analyses point out that Gusev impact was subsequent to the first incision of Ma'adim Vallis in the craterized upland. The study of the deposit distributions as revealed by the topography leads to reconstruct the chronology of three major events in the Aeolis Region : Ma'adim incision, Gusev impact and Apollinaris Patera/flow interactions.



The recent topographic map [USGS, I-2119, 1991] [Fig.1] of the Ma'adim Vallis region shows the craterized upland level horizontality between  $-30^{\circ}$  Lat. and  $-18^{\circ}$  Lat. against the previous Mariner 9 topography [USGS, I-1001, 1976], which led to consider an average slope of .3 per cent with downstream segments up to 1 per cent. According to the new data, the whole Ma'adim top level is delimited by an elevation of 3000 m all along its course, by parallel steep valley sides. Conversely to usual hydrodynamics of low gradient stream flows, Ma'adim channel appears rectilinear and meanderless, without substantial drainage system. The new topographic data reveal the presence of an apparent 240 km long mid-valley overdeepening down to 2000 m with respect to the plateau level [Fig.1 A to B]. This overdeepening is linked to the outlet - located in the crater Gusev bottom (level 0) - by a subsequent 200 km long reverse slope [Fig.1C and Fig 4C].

A longitudinal profile of the downstream segment deduced from the topographic map shows a strong discrepancy with an equilibrium profile of a mature stream flow [Fig.4 E]. The main difference is given by the reverse slope. Considering the downstream global feature organization, the following model is able to illustrate the reverse slope set up by fluvial dynamics. It is envisioned a series of chronological events and sedimentary depositions. The model includes

## ANCIENT LAKE IN MA'ADIM VALLIS. N.A CABROL et al.

the presence of voluminous sedimentary deposits in the downstream segment of Ma'adim Vallis, which reach the level 2000 m [Fig.4C]. Such a deposit, could be produced by a stream slow down. This amount of deposits, could be due to a long period of flow stagnation. The process which leads to a flow stagnation in the valley was produced by the catastrophic event which produced a natural dam [Fig.3 and 4.D]. Upstream to this dam, the stream flow generated an inner valley lake [Fig.3E]. The legacy of an ancient Ma'adim Vallis inner lake is revealed by features such as : reverse slope downstream ; lateral terraces reaching the topographic level 2500 m, which corresponds to the downstream deposit level ; smooth sediments on the last section of the plateau, on the both sides of Ma'adim Vallis.

Our scenario correlates the whole feature interaction chronology. It is supposed that the earlier Ma'adim stream run down to the northern plain - beyond the actual position of Apollinaris, as attested by the presence of a paleo- channel section - until the crater formation induced by the Gusev impact on the valley. The southern rampart of Gusev generated a natural dam which interrupted the stream course, creating the inner valley lake. The surface of the lake reached a topographic level above 2000 m and overtoped the banks with aqueous sediments widely spreaded over large areas. As a legacy of this episod, several old impact craters are submerged by large amount of thick sedimentary deposits. After this lacustrine phasis, a double-impact destroyed the rampart dam generating an outlet in the inner valley lake [Fig.5G]. The water run through this opening and filled the crater Gusev, overtoping the lower northern rampart. During this episod, a 1000 m deep and 130 km long channel is eroded in the lacustrine sediment; in the last section of Ma'adim Vallis [figs.1H,5 H].

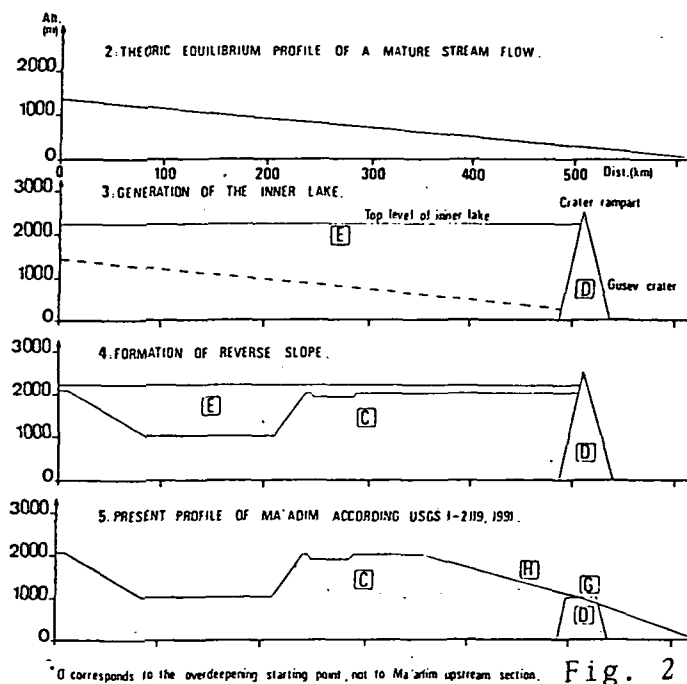


Fig. 2

This channel is well delimited on the topographic cartography by the isohypse 2000 m. The excavated volume was transported inside the crater Gusev. The more voluminous material extracted from the broken rampart are visible at the valley outlet [Fig.1J] whereas the fine material is widely distributed on the bottom of the crater Gusev. A radar scan of Roth et al (1989) shows a tilted slope from the axis of the outlet towards the eastern Gusev rampart which is explained by an asymmetric filling due to the position of the valley outlet relatively to the crater [Fig.1K]. The bottom of the double impact-crater corresponds to the last level of deposits. It is also noticed the 2 km width channel incised in this sediments by the residual water of Ma'adim. The crater Gusev lake was evacuated by a northern channel which is now partially obliterated by the Apollinaris Patera lava flows.

456874 S19-91  
ABS. ONLY P. N94-6P2-134

**SPATIAL VARIATION IN THE SEASONAL SOUTH POLAR CAP OF MARS AS OBSERVED BY MARINER 7;** Wendy M. Calvin U. S. Geological Survey, Flagstaff, AZ 86001, Terry Z. Martin Jet Propulsion Lab, Pasadena, CA 91109 and Gary B. Hansen Univ. of Washington/JPL

Spatial variations in infrared spectra of the seasonal south polar cap of Mars were noted by the original Mariner 7 IRS instrument team [1,2] as well as in subsequent examinations of the Mariner 7 data set [3,4]. Up to now, however, there has been little effort to synthesize this information to understand variations in the south seasonal cap as a function of position or latitude. We attempt to quantify the spectra by providing estimates of CO<sub>2</sub> grain sizes as well as upper limits on the amount of water frost contained in the polar collar.

In Fig. 1 we present the variation in brightness at two wavelengths as well as the band depth of a weak CO<sub>2</sub>-ice feature at 2.28  $\mu$ m as a function of spectrum number or subsequent location on the cap. Corresponding latitudes range monotonically from -62 to -77.5. The data set is fully described in [5]. Both intensity curves indicate a transition region from partial to full frost coverage. The brightness at 2.2  $\mu$ m indicates that by spectrum number 130 the spectrometer footprint was completely within the cap. However, the brightness at 3.1  $\mu$ m jumps significantly between spectra numbers 130 and 131, which led the instrument team to suggest the presence of water ice in a collar around the cap [2]. In addition, Fig. 1 shows the variation in band depth of a CO<sub>2</sub> feature at 2.28  $\mu$ m. This band is evident in laboratory measurements of CO<sub>2</sub> ices but is weak in CO<sub>2</sub> frost spectra [4,6,7,8] which implies that long path lengths are required before this absorption feature becomes apparent and that it can be a sensitive indicator of path length and/or grain size.

Although previous researchers noted variation in the bands at 2.28 and 2.34 as well as 3.1 and 3.3  $\mu$ m, it is evident in Fig. 1 that the variation in band depth is slight until spectrum number 145, which displays a dramatic increase. In conjunction with this increase, the intensity level at 3.1  $\mu$ m also drops. The intensity at 2.2  $\mu$ m remains almost constant until after spectrum number 145, which suggests that the cap was most likely a CO<sub>2</sub> frost on a CO<sub>2</sub>-ice surface. A thin layer of fine frost will keep the reflectance level high and dominate areas of strong absorption. In areas of weak absorption, light penetrates farther into a more transparent ice layer, and the spectrum is dominated by characteristics of transmission through the ice.

The spectra beyond number 145 are characterized by overall weaker intensities at all wavelengths and the virtual absence of characteristic CO<sub>2</sub>-ice features at 2.28, 2.34, 3.0 and 3.3  $\mu$ m. These conditions could be caused by continued increasing path lengths in CO<sub>2</sub> ice or coverage by ice clouds. With further modeling we hope to discriminate between these contributing factors.

In Fig. 2 we compare the full spectra, corrected only for the solar incidence angle, of three of the most significant areas. Spectrum number 130 is in the polar collar and number 134 is typical of spectra 131-142. The suppression of spectrum 130 beyond 3  $\mu$ m we attribute to the strong absorption by water ice in this region. In the corrected spectra [5] there is evidence that water ice may exist throughout the cap, which would imply an increased concentration in the collar region. Spectrum number 145 shows the peak in the depths of absorption features at 2.28 and 2.34 and the near absence of CO<sub>2</sub> features at 3.0 and 3.3  $\mu$ m, which appear to be correlated with extremely long path lengths in CO<sub>2</sub> ice. However, the presence of water ice can also contribute to the suppression beyond 2.9  $\mu$ m.

Model calculations of the reflectance of CO<sub>2</sub> as a function of grain size, using CO<sub>2</sub> absorption coefficients derived by [4,8], are useful for quantifying path lengths in the seasonal south cap. Estimates in [4] indicated equivalent grain sizes of millimeters to centimeters. More recent calculations suggest even larger grain sizes, on the order of several centimeters. In addition, calculated mixtures of water and CO<sub>2</sub> ice provide limits on the amount of water ice in the polar collar. Preliminary calculations indicate an upper limit of 1 wt%. Models are being refined to further constrain this value.

**REFERENCES** [1] Herr, K. C. and G. C. Pimentel (1969), *Science*, 166, 496. [2] Pimentel, G. C., P. B. Forney, and K. C. Herr (1974), *JGR*, 79, 1623. [3] Martin, T. Z. (1988), *BAAS*, 20, 851. [4] Calvin, W. M. (1990), *JGR*, 95, 14743. [5] Martin, T. Z. (1993), *JGR*, in press. [6] Larson, H. P. and U. Fink (1972), *Astrophys. J.*, 171, L91. [7] Kieffer, H. (1970), *JGR*, 75, 501. [8] Hansen, G. B., unpublished data.

## SPATIAL VARIATION: Calvin W. M. et al.

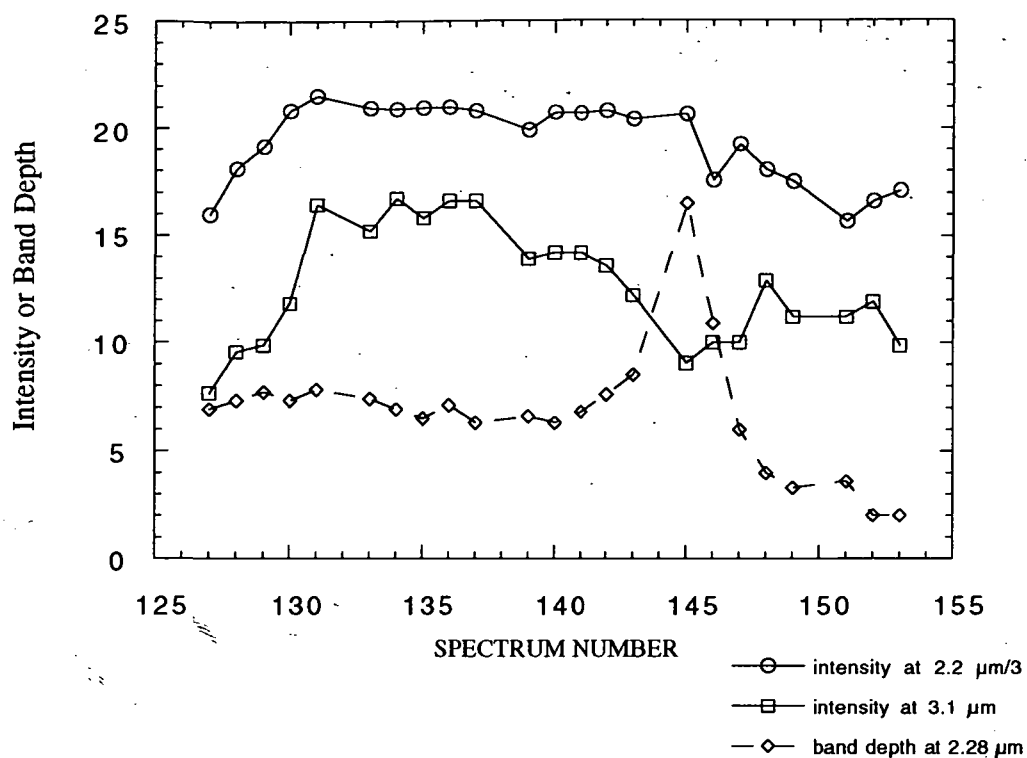


Figure 1: Intensity variations as a function of position in the polar cap.

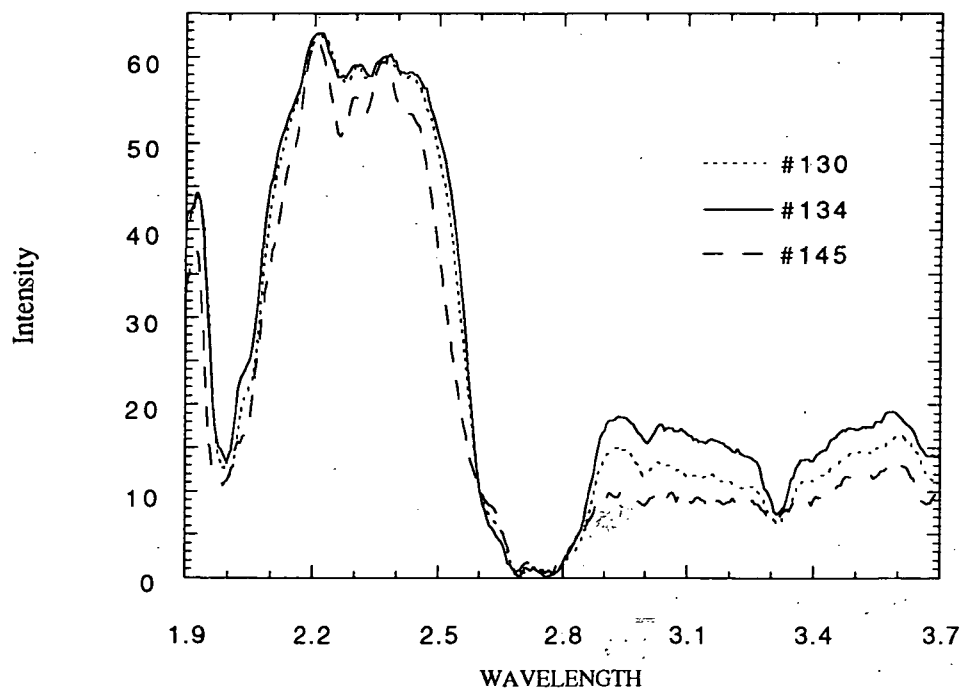


Figure 2: Raw spectra of three different positions in the cap.

456876

5120 - 90  
ABS. ONLY

LPSC XXIV

245

N 94-12135  
p. 2

**THE GIANT IMPACT PRODUCED A PRECIPITATED MOON.** A. G. W. Cameron,  
Harvard-Smithsonian Center for Astrophysics.

The author's current simulations of Giant Impacts on the protoearth show the development of large hot rock vapor atmospheres. The Balbus-Hawley mechanism will pump mass and angular momentum outwards in the equatorial plane; upon cooling and expansion the rock vapor will condense refractory material beyond the Roche distance, where it is available for lunar formation.

During the last seven years the author, together with several colleagues, has carried out a series of numerical investigations of the Giant Impact theory for the origin of the Moon (1-4). These involved three-dimensional simulations of the impact and its aftermath using Smooth Particle Hydrodynamics (SPH), in which the matter in the system is divided into discrete particles whose motions and internal energies are determined as a result of the imposed initial conditions. Densities and pressures are determined from the combined overlaps of the particles, which have a bell-shaped density distribution characterized by a smoothing length. In the original series of runs all particle masses and smoothing lengths had the same values; the matter in the colliding bodies consisted of initial iron cores and rock (dunite) mantles. Each of 41 runs used 3,008 particles, took several weeks of continuous computation, and gave fairly good representations of the ultimate state of the post-collision body or bodies but at best crude and qualitative information about individual particles in orbit.

During the last two years the author has been using an improved SPH program in which the masses and smoothing lengths of the particles are variable, and the intent of the current series of computations is to investigate the behavior of the matter exterior to the main parts of the body or bodies subsequent to the collisions. These runs are taking times comparable to a year of continuous computation in each case; they use 10,000 particles with 5,000 particles in the target and 5,000 in the impactor, and the particles thus have variable masses and smoothing lengths (the latter are dynamically adjusted so that a particle typically overlaps a few tens of its neighbors). Since the matter in the impactor provides the majority of the mass left in orbit after the collision, and since the masses of the particles that originated in the impactor are smaller than those in the target, the mass resolution in the exterior parts of the problem is greatly improved and the exterior particles properly simulate atmospheres in hydrostatic equilibrium.

So far three runs have completed calculations; these have target to impactor mass ratios of 5:5 (reported at the 1992 LPSC (5)), 6:4, and 7:3. Six additional runs are currently under way; these all have mass ratios of 8:2 and a variety of collisional angular momenta ranging from 1.2 to 2.2 times the present angular momentum of the Earth-Moon system. Most of these runs have progressed enough to support the conclusions about the calculations discussed below.

I have taken the initial temperatures of all colliding bodies to be 2,000 K, which is high enough realistically to represent a history of collisional accumulation and low enough to suppress thermal evaporation of matter from the surface. In the Giant Impact and in the subsequent fallout of most of the material from the impactor into the protoearth, a significant part of the surface regions of the protoearth, typically about a hemisphere, is heated to about 14,000 K or more. If the colliding masses are nearly equal the heating is more evenly spread throughout the merged body, whereas if the impactor is a lot smaller than the target, the heating is more concentrated toward the surface which thus tends to be hotter than in the former cases. Wherever this hot rock appears in a surface region, rock vapor evaporates and forms a hydrostatic atmosphere around the body. This rock vapor is simply the vapor phase of the dunite equation of state developed by Jay Melosh (3); future studies will need to treat the chemistry more realistically.

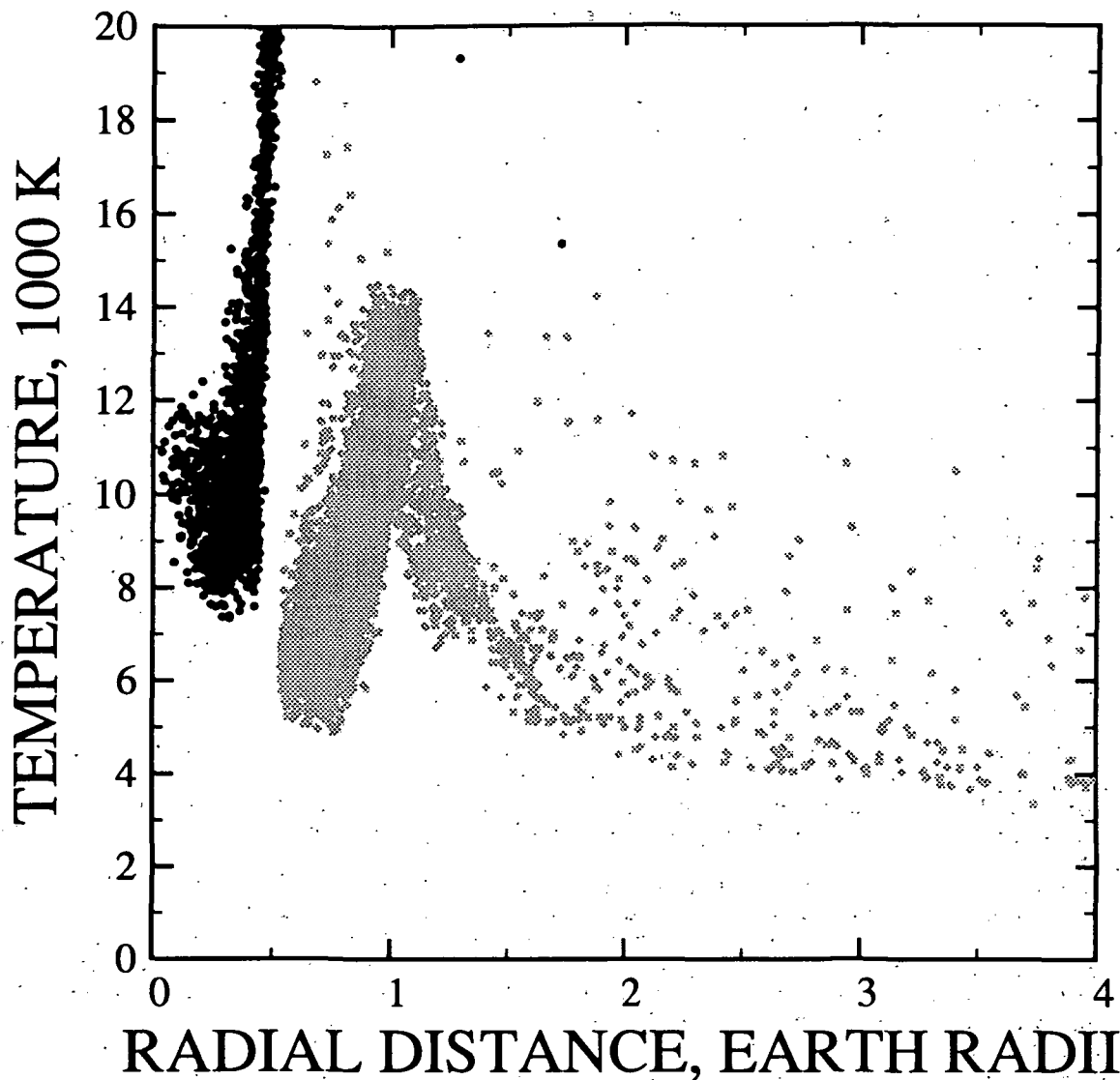
I show in the figure the radial distribution of the temperatures of the particles in the mass ratio 7:3 case; the iron particles are shown in black and the rock particles in gray. Out to 4 earth radii the rock vapor is at 4,000 K or higher, which means that it has a substantial electrical conductivity. The angular velocity of these rock vapor particles decreases outwards from near to the condensed surface, and the corresponding specific angular momentum initially increases but then also steadily falls off with increasing radius.

In all cases, the fallout from the impactor after the collision initially puts most of the iron core of the impactor and a significant part of its mantle into a single hemisphere of the target, initially producing a rotating elongated mass distribution. This is very effective in transferring angular momentum to the remaining external orbiting particles. Thus, as the infallen material settles toward a rotationally symmetric distribution, the external material is generally torqued to larger radial distances away from the central body, leaving the material within the first few earth radii consisting almost entirely of the evaporated rock vapor.

The rest of the story is an inference since the relevant physical processes are not included in the code. Within the last two years there has been a remarkable series of papers by S. A. Balbus and J. F. Hawley (6) which demonstrate that there is a powerful instability in a differentially rotating conducting fluid with a seed vertical component of the magnetic field; this leads to a rapid outward flow of angular momentum as long as differential rotation persists. The operation of this instability in the high temperature rock vapor atmosphere (which will inevitably be threaded by a magnetic field) will therefore transport angular momentum outwards from the condensed part of the mantle to produce rigid rotation within the atmosphere out to the Kepler point (at which the material goes into orbit about the central body). For a Giant Impact that produces a protoearth with about a 4 hour rotational period, the Kepler point lies close to the tidal Roche lobe at a little less than 3 earth radii. Beyond the Kepler point the Balbus-Hawley

## THE GIANT IMPACT PRODUCED A PRECIPITATED MOON

Cameron, A. G. W.



mechanism cannot shut down, and so it will continue to pump mass and angular momentum outwards in the equatorial plane, maintaining a small departure from rigid rotation below the Kepler point.

As the vapor flows away from the protoearth it progressively expands and cools and the most refractory components will condense from it, forming small planetesimals. The Balbus-Hawley mechanism will gradually become ineffective as the electrical conductivity decreases, but the remaining noncondensed vapor can probably undergo thermal escape from the protoearth, carrying away some of the angular momentum. The condensed materials, being beyond the Roche distance, are then free to accumulate into the Moon. The Moon thus formed would have a very refractory composition, but it will most probably accumulate some of the material from the impactor, that was left over from the Giant Impact and torqued to several earth radii, but which was never heated too strongly and thus contains less refractory material. The precipitation nature of this lunar formation scenario is reminiscent of some ideas of Ringwood (7).

According to these ideas, the angular momentum of the Earth-Moon system unexpectedly appears to be a remarkably significant quantity, being related to the approximate equality of the Kepler point and the Roche distance. This work was supported in part by NAGW-1598.

**References:** (1) Benz, W., Slattery, W. L., and Cameron, A. G. W. (1986) *Icarus*, **66**, 515-535; (2) Benz, W., Slattery, W. L., and Cameron, A. G. W. (1987) *Icarus*, **71**, 30-45; (3) Benz, W., Cameron, A. G. W., and Melosh, H. J. (1989) *Icarus*, **81**, 113-131; (4) Cameron, A. G. W., and Benz, W. (1991) *Icarus*, **92**, 204-216; (5) Cameron, A. G. W. (1992) 23rd LPSC, 199-200; (6) S. A. Balbus and J. F. Hawley in this or the reverse order, *Astrophys. J.*, **376**, 214-222 (1991); **376**, 223-233 (1991); **392**, 662-666 (1992); **400**, 595-609 (1992); **400**, 610-621 (1992); (7) Ringwood, A. E. (1979) *Origin of the Earth and Moon*, Springer-Verlag, New York.



456078

5121-91

ARJ

CON

94

LPC

XSTV

163341

121367

2

**GEOLOGY AND SURFACE CHARACTERISTICS OF BELL REGIO, VENUS;** Bruce A. Campbell, *Center for Earth and Planetary Studies, National Air and Space Museum, Washington, D.C., 20560*, Patricia G. Rogers, *Planetary Geology and Geophysics Program, Solar System Exploration Division, NASA, Washington, DC 20546*.

**Introduction.** Bell Regio is a broad topographic rise located at approximately 30°N, 45°E which extends ~1500 km in the N-S direction and is characterized by extensive volcanism. In this work, the geology and surface characteristics of Bell Regio are examined in order to understand the geologic evolution of the region and the surface characteristics of the major volcanic units. Relationships between Magellan SAR backscatter values and altimeter-derived rms slope data are analyzed, and terrestrial SAR data are used to suggest possible surface morphologies.

**Geologic Setting.** Southern Bell Regio contains at least three large volcanic centers: Tepev Mons, which rises approximately 5 km above the plains to the east, and two unnamed source regions. The first of these sources lies immediately SE of Tepev Mons, and has a 15-km diameter central caldera. The second source area is a much larger region of radial lava flows and chains of pit craters centered between Tepev Mons and the crater Potanina. Large northeast-trending fragmented tessera blocks lie to the west and south of these three volcanic centers, and there are several small coronae to the northwest. Northern Bell Regio is dominated by the corona Nefertiti [1,2,3].

Lava flows associated with the three large volcanic centers in southern Bell Regio embay the surrounding dark ridged plains and tessera blocks. The tesserae in turn are embayed and fragmented by the ridged plains, and are thus assumed to be the oldest units in the region. The ridged plains are next in the stratigraphic sequence, and are composed of two major units distinguished by E-W and SE-NW wrinkle-ridge patterns. The boundary between these two plains units is largely obscured by younger volcanic flows.

Four major volcanic flow units are observed in Bell Regio. The oldest is an extensive, relatively radar-dark group of flows radiating from the volcanic center between Tepev Mons and Potanina crater. The next youngest unit is comprised by the radar-bright flows to the south and southwest, which truncate the earlier dark flows and may have erupted from fractures concentric to the eastern volcanic center. The Tepev Mons summit lava apron appears to have formed next, creating an oval collection of interfingering mottled and dark flows. Finally, activity centered on the small caldera to the SE of Tepev Mons erupted a series of radar-bright flows which encircle the Tepev summit apron and embay portions of the northern tessera fragments.

The large volcanic center to the east of Tepev Mons may be responsible for the bulk of the vast flow fields in southern Bell Regio. There are major differences in the style of volcanism between these two centers; Tepev Mons has a pair of well-defined calderas with a relatively limited apron of narrow flows, while the eastern center has a poorly defined central region, long chains of radial pit craters, and much more extensive lava flows. This variation in edifice structure and flow volume may be related to the difference in vertical relief between these two regions. The great height of Tepev Mons may have led to trapping of magma within the edifice and subsequent formation of the summit calderas with relatively minimal surface effusion. In contrast, the lower-elevation eastern region may have provided an easier environment for horizontal magma motion, dike formation, and areally distributed volcanism [3].

**Analysis of Radar Data.** SAR backscatter cross-sections and altimeter-derived rms slopes were tabulated for a number of representative geologic units from footprint location information in the ARCDR records and C1-MIDR image data. Only footprints which fell completely within the boundaries of a unit were selected in order to minimize mixing of terrain types. Figure 1 presents the results of this analysis for seven surface units. The

flows examined have rms slopes ranging from  $10^\circ$  to  $90^\circ$ . Absolute HH cross-section values (no scatter-law correction made) range from approximately 0.025 (-16 dB) to 0.17 (-8 dB).

In general, there appears to be only a weak positive correlation between the rms slope and the backscatter cross-sections for these flows. This suggests that the scales of roughness responsible for quasi-specular scattering close to the nadir are not necessarily produced by the same mechanisms which cause the smaller-scale roughness. This is a reasonable result, since in terrestrial flows the large-scale folds and pressure ridges are relatively independent of the rubble or fragmental glass which forms the small-scale texture.

Comparing these results to data for Hawaiian flows presented in [4], we find that the two brightest flow units shown in Figure 1 are consistent with surfaces of "transitional" to "a'a" texture on Earth. Application of these terrestrial criteria to the entire SAR image shows that only a small group of flows (the north arcuate bright flow and the distal portions of the bright southern flow in particular) are sufficiently radar-bright to match Hawaiian a'a terrains. The vast flow fields south and east of Tepev Mons are characterized by radar brightnesses in the range of terrestrial pahoehoe flows. If terrestrial experience holds [5], this implies relatively low magma effusion rates for these deposits, and their probable emplacement in the form of slowly developed tube-fed flow fields.

The radar-bright lava flows in southern Bell Regio tend to have well-defined margins and often appear to be superimposed on other flow units. There may be several reasons for this result: 1) an observational bias due to the tendency of bright flows to stand out from the background, 2) rougher (a'a-type) flows tend to be thicker than pahoehoe flows, and are thus less likely to be cut by later thin units, or 3) the rough lava flows were late events in the volcanic development of each eruptive center.

**References.** [1] Janle, P., et. al., (1987) *Earth, Moon, and Planets*, 39, 251-273; [2] Solomon, S., et. al. (1992) *JGR*, 97, 13199-13255; [3] Head, J., et. al. (1992) *JGR*, 97, 13153-13197; [4] Campbell, B. A. and D. B. Campbell (1992) *JGR*, 97, 16293-16314; [5] Rowland, S., and G. Walker, (1990), *Bull. Volc.*, 52, 615-628.

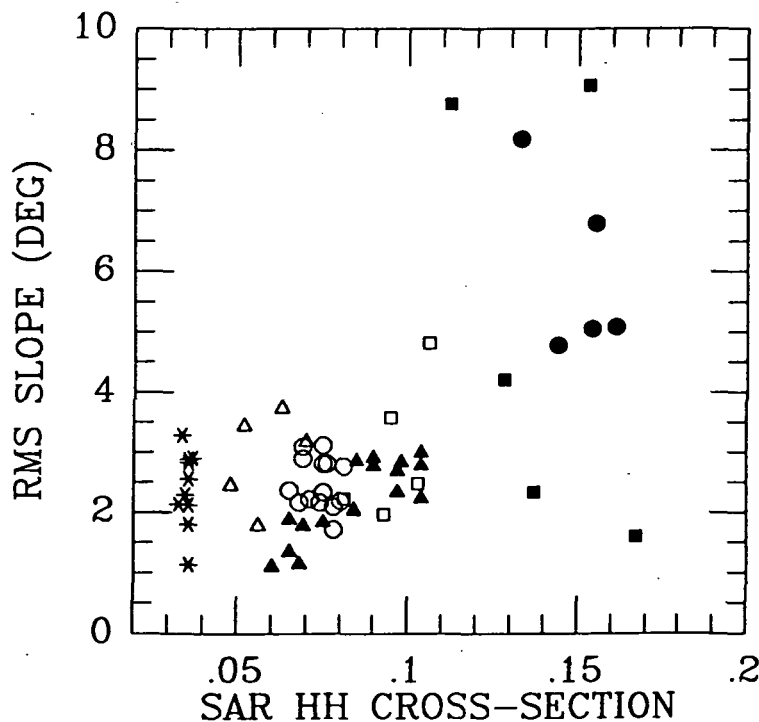


**Figure 1.** Plot of altimeter-derived rms slope values vs. mean HH backscatter cross-section for seven lava flows in southern Bell Regio. Each flow is represented by a different symbol, and each data point represents the rms slope value for one altimeter footprint along the chosen flow, and the average of all C1-MIDR values within that footprint. Terrestrial SAR data suggest that pahoehoe flows at these incidence angles are typically no brighter than about 0.12; only the two brightest lava flows fall above this value. The two radar parameters exhibit only a weak positive correlation.

456881

5122-81  
AES ONLY

LPSC XXIV

249

N 94-137

LAVA FLOWS ON VENUS: ANALYSIS OF MOTION AND COOLING. Bruce A. Campbell and James R. Zimbelman, *Center for Earth & Planetary Studies, National Air & Space Museum, Washington, DC, 20560.*

**Introduction.** Effusive volcanism is a major mechanism for resurfacing on Venus. The large edifice complexes are marked by lava flow fields which extend hundreds of kilometers from their apparent source vents. Earlier work on the emplacement of lava predicted few major differences in flow length between Venus and the Earth (for similar magmas) based primarily on assessment of the relative rates of heat loss to their respective atmospheres [1]. This analysis, combined with the obvious presence of very long lava flows on Venus, has led to suggestions that basalt magmas on Venus may be of generally lower viscosity or that magma effusion rates exceed terrestrial norms. If correct, these hypotheses might imply systematically different chemical and dynamic characteristics for volcanic processes on Venus, and a somewhat catastrophic history for many of the large edifices and flow fields. In this abstract, we re-examine the mechanics of magma motion and cooling, and discuss some of the issues involved in analyzing flows on Venus.

**Flow Motion.** Magma motion can be described by two expressions for the flow of a Bingham plastic material. The first could be termed "gravity-driven flow", and the flow per unit area through an interface is [2]:

$$q = (1/v)[h^3 \rho g \sin \theta / 3 - y h^2 / 2 + y^3 / (6 \rho^2 g^2 \sin^2 \theta)]$$

where  $v$  is viscosity,  $\rho$  is density,  $g$  is acceleration due to gravity,  $y$  is yield strength,  $h$  is the height of the flow, and  $\theta$  is the slope of the underlying ground. The second mechanism can be called "pressure-driven flow", where the  $\sin \theta$  term in the above equation is replaced by  $\tan \phi$ ,  $\phi$  being the slope of the upper magma surface. This latter case becomes most important when the topographic gradient is very small, since it expresses the tendency of a flow to spread out over a flat surface due to its internal pressure gradient. Flow will not commence until the depth reaches a critical height, which is different for the two cases:

$$\text{Gravity: } h_c = y / \rho g \sin \theta \quad \text{Pressure: } h_c = y / \rho g \tan \phi$$

If the yield strength is zero, which is expected for melts very close to the liquidus, then the above expressions reduce to those for Newtonian flow, and the critical height disappears. It is evident that the gravity-driven flow mechanism will act slowly on shallow slopes unless the yield strength is relatively low. The pressure-driven case may flow much more readily over flat terrain by exploiting the slope along the front of the liquid body (which may reach 30 degrees or more).

**Flow Cooling.** The loss of heat from a lava flow predominantly takes place through the upper surface, where energy is lost by radiation and convection to the atmosphere. Soon after eruption, basalts form a cooler crust at this top margin. Heat is then lost by conduction through the crust, whose lower surface temperature slows heat transfer to the atmosphere, and by more efficient energy transfer from hot core material exposed along cracks [3]. Terrestrial experience suggests that heat lost by a lava flow is typically accommodated by increases in the thickness of the crust rather than by major changes in core temperature.

The growth of a crust on a lava flow has been modeled previously with the assumption of a fixed upper surface temperature [4]. We carried out a similar analysis but permitted the crust surface temperature to vary with time so as to remain in thermal equilibrium with the heat flux from below and the radiative/convective losses to the atmosphere. By balancing the heat flux at top and bottom, we can at any moment calculate the temperature of the crust surface, and thus iteratively model the growth of the crust as a function of time. Our results support those of [1] in that flow crusts form much more rapidly on Venus, but after about 1 day crustal thickness will be greater on terrestrial flows (the crossover thickness is ~50 cm).

The above discussion of flow cooling is appropriate only for flows which move over the ground surface transporting an integral crust. If the lava becomes sufficiently crusted over

to form tubes, then heat loss from the magma may become negligible over distances of 10's to 100's of km. Only at the flow front or in breakouts along the tube will magma rapidly lose heat to the atmosphere. Tube formation is generally limited to low to moderate effusion rate flows, since at higher discharge rates tubes will either overflow or never form due to rapid recycling of the surface crust.

**Practical Applications.** Using the models for flow motion and cooling discussed above to analyze real flows is difficult. Laboratory data for basalt viscosity and yield strength are very limited, and in all cases use remelted material. Field measurements have been used to estimate magma rheology, but these approaches must assume a particular flow law in order to extract the parameters. Lab analysis shows that melts close to the liquidus can have nearly zero yield strengths. Even when held at a fixed temperature, a basalt melt will increase in viscosity and yield strength until equilibrium is reached [5,6].

Why a lava flow stops moving is also very much in debate: it can occur when the crust thickens to a point at which the central hot core no longer exceeds the critical depth for flow, when the flow core cools sufficiently to raise the yield strength and viscosity, or when the magma supply ceases and the flow halts at its critical depth.

**Lava Flows on Venus.** The basic issue we address is the presence of long (100's of km) lava flows, many of which are characterized by surface roughness comparable to that of terrestrial pahoehoe surfaces [7], emplaced on slopes of less than 1 degree. The great length of these flows is often cited as evidence for rather high effusion rates or low magma viscosity, but the lack of significant surface roughness argues for low magma effusion rates based on terrestrial experience [8].

Several general statements can be made for lavas on Venus: 1) magma viscosity will be increased over equivalent terrestrial basalts due to the lack of water, 2) eruption temperatures will be slightly higher, causing reduced viscosity, 3) volatile exsolution is suppressed by the atmosphere, delaying the onset of crystallization and lowering the viscosity further, and 4) the more rapid formation of a crust on Venus shields the core from the atmosphere, and is likely to lessen the total heat loss by a significant amount [1,5,6]. The degree to which these mechanisms operate is uncertain, but they may permit a lower average viscosity and a more favorable cooling regime for basaltic magmas on Venus.

We propose that most lava flows on the major Venus highland edifices are similar to terrestrial basalts, with common effusion rates of 1-10 m<sup>3</sup>/s, and that such low-volume eruptions form the vast aprons and mottled fields characteristic of these constructs. The radar-bright flows are most likely isolated cases of higher-volume eruptions (on the order of 100-1000 m<sup>3</sup>/s) which produce a surface textures. The great lengths of the smooth flows are not necessarily indicative of larger eruption rates or lower viscosity; tube-fed flows on Earth might travel equal distances were they not stopped by the ocean or regional topography. Eruptions in the lowlands of Venus may be of much higher volume flow rates since magma is not expected to stall within the crust prior to eruption [9].

**Numerical Models.** We are investigating the differences in lava flow emplacement on Venus and the Earth using numerical simulations based on the magma motion and cooling models discussed above. This work treats each small region of the flow as a discrete element, and solves for local flow rates and heat loss to the atmosphere or ground [10]. Early results are encouraging [11], and we are expanding the range of behaviors to better simulate the emplacement process.

**References.** [1] Head, J., and L. Wilson, (1986), *JGR*, 91, 9407-9446; [2] Dragoni, M., et al., (1986), *J. Volc. & Geotherm. Res.*, 30, 305-325; [3] Crisp, J., and S. Baloga, (1990), *JGR*, 95, 1255-1270; [4] Turcotte, D., and G. Schubert, (1982), *Geodynamics*; [5] McBirney, A., and T. Murase, (1984), *Ann. Rev. Earth Planet Sci.*, 12, 337-357; [6] Asimow, D., and J. Wood., (1992), *JGR*, 97, 13643-13666; [7] Campbell, B. A. and D. B. Campbell (1992) *JGR*, 97, 16293-16314; [8] Rowland, S., and G. Walker, (1990), *Bull. Volc.*, 52, 615-628; [9] Head, J. et al., (1992), *JGR*, 97, 13153-13198; [10] Ishihara, K. et al., (1990), *IAGVCEI Proc.*, 2, 174-207; [11] Zimbelman, J., et al., (1993), this volume.

456882

S123-46

AB5, ON27

LPSC XXIV

N94-3132138

251

STRATIGRAPHY AND SEDIMENTOLOGY OF THE K/T BOUNDARY DEPOSIT IN HAITI; S. Carey, H. Sigurdsson, S. D'Hondt, Graduate School of Oceanography, University of Rhode Island, Narragansett, R.I. 02882 and J.M. Espindola Instituto de Geofisica, UNAM Ciudad Universitaria, Mexico City, Mexico.

The K/T boundary sequence is exposed in uplifted carbonate sediments of the southwest peninsula of Haiti. It is found at 15 localities within the Beloc formation, a sequence of limestone and marls interpreted as a monoclinial nappe structure thrust to the north. This tectonic deformation has affected the K/T boundary deposit to varying degrees. In some cases the less competent K/T deposit has acted as a slip plane leading to extensive shearing of the boundary layer, as well as duplication of the section. The presence of glassy tektites, shocked quartz and an Ir anomaly directly link the deposit to a bolide impact. Stratigraphic and sedimentological features of the tripartite sequence indicate that it was formed by deposition from ballistic fallout of coarse tektites, emplacement of particle gravity flows and fine grained fallout of widely dispersed impact ejecta.

In sections with limited tectonic disruption, the K/T deposit consists of at least three distinct units that are separated by relatively sharp contacts (fig. 1). At the base is a 20 to 30 cm thick, light olive brown smectite unit (1) with little or no carbonate. It contains smectite spherules which are the alteration products of impact glass or tektites. The second unit from the base consists of 20 to 40 cm light olive grey spherules, which range up to 15 mm in diameter. Unit 2 is distinctive in being poorly sorted and ungraded. It contains carbonate and clay rip-up clasts up to 4 cm in length. The unit is sometimes cross-bedded and at some locations the contact with the underlying unit is clearly erosive. Overall the unit fines upward and the upper parts consist of alternating cm to mm scale lenses of smectite and carbonate sediment. Spherules are very abundant in the lower part of the unit but very poorly sorted. The top-most unit in the K/T sequence is a reddish yellow brown smectite, 0.5 to 1 cm thick (unit 3, fig. 1). This unit contains shocked quartz grains and is associated with an iridium anomaly of 28 ng/g [1]. A high content of octahedral and dendritic crystals of Ni-rich spinel, of probable extraterrestrial origin, is also characteristic of this unit.

The size and shape of tektites and carbonate fragments in units 1 and 2 (fig.1) have been determined by image analysis of cut vertical sections from plaster casts of the deposit. In the basal section the mean of the maximum diameter varies strongly with stratigraphic height, varying from about 3 mm at the base to 1 mm at the top (fig. 2). Most of the tektites are not perfectly spherical but are instead slightly ovoid in shape (aspect ratio ~0.75). Tektites from unit 2 have similar morphologies to those of unit 1 but include some that are significantly larger in size. In addition, tektites and carbonate clasts of unit 2 show evidence of preferential alignment of their long axis.

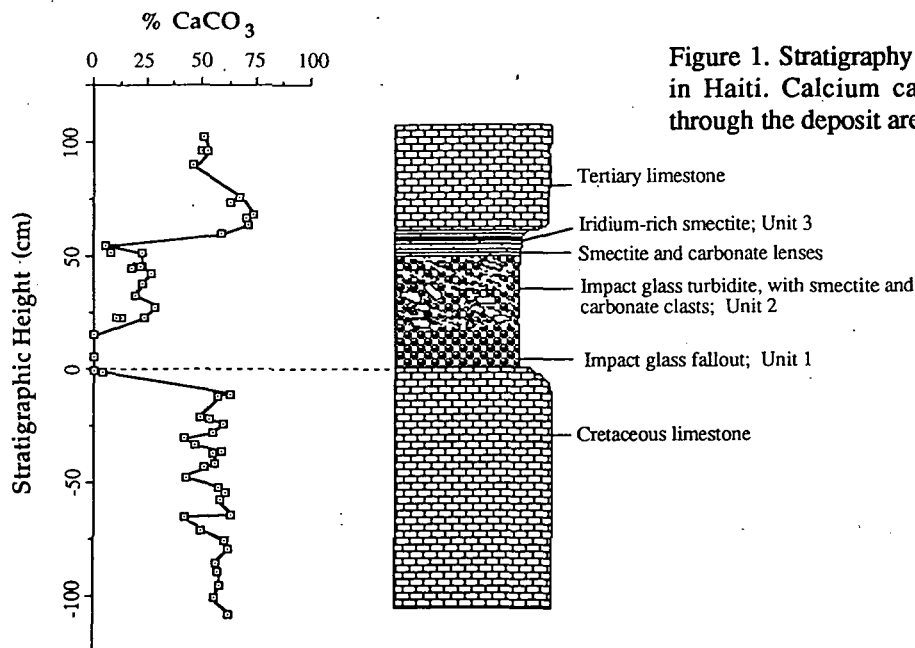


Figure 1. Stratigraphy of the K/T boundary sequence in Haiti. Calcium carbonate contents of samples through the deposit are shown on the left.

## STRATIGRAPHY OF K/T BOUNDARY DEPOSIT IN HAITI Carey, S. et al.

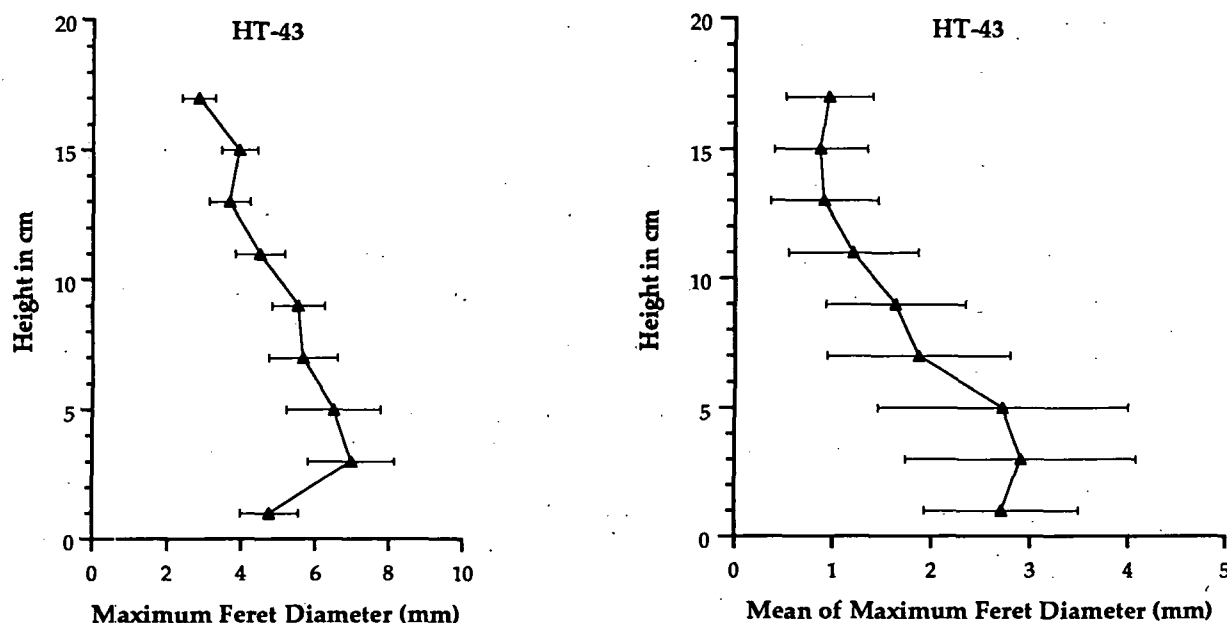


Figure 2. Variation in the maximum (left) and the mean of the maximum diameter (right) as a function of stratigraphic height in unit 1 of the K/T boundary deposit in Haiti. Data collected by image analysis.

The K/T section at Beloc is interpreted as a depositional sequence resulting from the impact of a bolide with the earth. Stratigraphic relations indicate that the sequence consists of several different sedimentary processes. The basal unit is attributed to ballistic fallout of tectite spherules based on the normal grading, good sorting, and low carbonate contents. Lack of orientation of elongate particles provides support for deposition by passive settling through the water column following ejection and transport of particles through the atmosphere. In contrast, the presence of rip-up clasts, cross-bedding and an erosive contact with the underlying unit indicates that unit 2 was deposited from some type of particle gravity flow. The presence of Cretaceous microfossils in this unit is consistent with incorporation of sediment into the flow during transport. The preferential alignment of tectites can also be attributed to the production of particle fabric during deposition of turbidity currents and grain flows.

There are two potential mechanisms for the origin of the flow that deposited unit 2. The first is that the flow was derived directly from a bolide impact and consisted of a mixture of hot particles and gas that moved across the water surface at high velocity. As the flow moved away from source it eventually mixed with water and made the transition to the submarine environment. A second possibility is that unit 2 represents gravity flow or current redeposition of impact glass spherules caused by far field effects of the impact. An impact of the size proposed for the K/T boundary is likely to have generated large magnitude earthquakes and tsunamis. Both of these phenomenon can trigger remobilization of sediment in the marine environment. The sequence at Beloc suggests that there was sufficient time to allow deposition of tectites by fallout before the unit 2 flow arrived. It is interesting to note that the more proximal K/T sections at Mimbral, Mexico does not appear to contain an undisturbed tectite fall unit. This sequence is attributed largely to a megawave or tsunami deposit associated with the impact [2].

[1] Jehanno, C., D. Boclet, L. Froget, B. Lambert, E. Robin, R. Rocchia and L. Turpin (1992) *Earth Planet. Sci. Lett.*, 109, 229-241.

[2] Smit, J., A. Montanari, N.H.M. Swinburne, W. Alvarez, A.R. Hildebrand, S. V. Margolis, P. Claeys, W. Lowrie and F. Asaro (1992) *Geology*, 20, 99-103.

456884

S124-91

ABS ONLY

LPSC XXIV

253

N 9/4-3-124 39

**GALILEO/NIMS NEAR-INFRARED THERMAL IMAGERY OF THE SURFACE OF VENUS;** R. W. Carlson, K. H. Baines, M. Girard, L. W. Kamp (JPL), P. Drossart, T. Encrenaz (Paris-Meudon Observatory), F. W. Taylor (Oxford University)

Numerous highland and lowland features on the surface of Venus are observed in multispectral imagery acquired at  $\sim 50$  km spatial resolution by the Near-Infrared Mapping Spectrometer (NIMS) on board the Galileo spacecraft in February, 1990. Specifically, such features are observed at  $1.18 \mu\text{m}$ , a wavelength particularly sensitive to thermal emission from the hot, lower atmosphere ( $< 10$  km) and surface, and show up particularly well when this image is "de-clouded" using a simultaneously-acquired  $2.3\text{-}\mu\text{m}$  image of the upper, cloudy atmosphere. Due to the steep atmospheric temperature gradient (approximately 8 degrees per kilometer), hot lowland areas appear relatively bright, while cooler, highland areas appear dark (due to the steep atmospheric temperature gradient - approximately 8 degrees per kilometer - surface temperatures span approximately 100 K over the 13 kilometer range of surface altitudes observed in this image).

Prominent highland features include Maxwell Montes ( $\sim 12$  km altitude), Alpha Regio (2.5 km), Eistla Regio ( $\sim 2.0$  km), Bell Regio (2-3 km), and the western edge of Aphrodite Terra (2-2.5 km). Low-lying regions include Sedna Planitia ( $-1.0$  km), Tinatin Planitia ( $-0.5$  km), and the Bereghinya Planitia (0 km). From correlations with radar altimetry maps, such imagery may place useful constraints on surface emissivity and temperature variations, as well as on the nature of continuum opacity of  $\text{CO}_2$  in the 1-micron region.

456886

525-89  
ABS ONLY

LPSC XXIV

255

N 94-12140

**PRELIMINARY REPORT OF LUNAR OBSERVATIONS BY THE NEAR-INFRARED MAPPING SPECTROMETER (NIMS) DURING THE SECOND GALILEO EARTH-MOON ENCOUNTER;** R.W. Carlson<sup>1</sup>, H.H. Kieffer<sup>2</sup>, K.H. Baines<sup>1</sup>, K.J. Becker<sup>2</sup>, G.E. Danielson<sup>3</sup>, K. Edwards<sup>2</sup>, F.P. Fanale<sup>5</sup>, J. Forsythe<sup>4</sup>, L.R. Gaddis<sup>2</sup>, J.C. Granahan<sup>5</sup>, J. Hui<sup>1</sup>, T.V. Johnson<sup>1</sup>, R. Lopes-Gautier<sup>1</sup>, L.W. Kamp<sup>1</sup>, D.L. Matson<sup>1</sup>, T.B. McCord<sup>4,5</sup>, R. Mehlman<sup>6</sup>, A.C. Ocampo<sup>1</sup>, L.A. Soderblom<sup>2</sup>, W.D. Smythe<sup>1</sup>, J. Torson<sup>2</sup>, P.R. Weissman<sup>1</sup>, <sup>1</sup>Jet Propulsion Laboratory, Pasadena, Calif.; <sup>2</sup>U.S. Geological Survey, Flagstaff, Ariz.; <sup>3</sup>California Institute of Technology, Pasadena, Calif.; <sup>4</sup>SETS Technology, Inc., Mililani, Hawaii; <sup>5</sup>Univ. of Hawaii, Honolulu, Hawaii, <sup>6</sup>Univ. of California, Los Angeles, Calif.

The Galileo encounter with the Earth-Moon system on December 8, 1992, provided a unique opportunity to observe the Moon. Galileo's closest approach to the Moon was at an altitude of about 110,000 km above an area at about latitude 60N, longitude 60E. During the 12 hours surrounding the time of lunar closest approach, 12 observational sequences were executed by the near-infrared mapping spectrometer (NIMS), many in coordination with other Galileo instruments. These NIMS observations provided nearly complete coverage of the illuminated crescent from phase angles of 123° to 14°. This phase-angle coverage with nearly constant illumination is not possible from Earth; it is expected to provide substantial new information on the nature of the lunar photometric function over wavelength [1]. As of January 1993, most of the analysis has focused on the highest resolution data (55 km/pixel).

NIMS covers the spectral region of 0.7-5.2  $\mu\text{m}$  with 12-nm bandwidth with 2 silicon detectors and 25-nm bandwidth longward of 1  $\mu\text{m}$  with 15 InSb detectors (see [2] for a detailed description of the instrument and its many operating modes). NIMS builds up spectral images by measuring 17 wavelengths at a time, spaced uniformly over the full spectral range, along a strip of 20 pixels imaged by the scanning secondary mirror in 1/3 s. The spectrometer grating can be stepped to the adjacent "comb" of wavelengths while the scan mirror is changing direction. In this "full-map" mode, a line of 20 complete spectra is acquired in 4-1/3 s. Slow motion of the scan platform approximately perpendicular to the NIMS mirror scan builds up swaths of coverage 20 pixels wide; up to 4 swaths were required to cover the lunar disk. Of the lunar observations, 4 were in full-map mode; 4 were in "short-map" mode (obtained by double-stepping the grating between mirror scans requiring 2-1/3 s to acquire a spectrum); and 4 had a fixed grating position (1/3 s for a spectral comb).

Spectral registration is at present based on reconstructing the geometry of the NIMS observations by using the engineering data of platform attitude and the spacecraft trajectory. Because of the strong brightness gradients that occurred over the lunar target, NIMS spectra were very sensitive to small motions of the scan platform while a complete spectrum was acquired; such motions included both the planned slew and erratic motions. For this reason, it is often necessary to remove from the spectrum a pattern correlated among the 17 detectors for each grating position in that spectrum. Thus far, this "de-patterning" has been done separately for each pixel. Major improvements by the spacecraft team to reduce random jitter have made the data collected from the second Earth-Moon encounter much cleaner and easier to reduce than data from the first encounter [3].

The NIMS spectral range includes the overlap region between solar reflection and thermal emission; this region must be carefully treated to extract reflection or emission spectra, and the de-patterning must be carried out simultaneously but separately for the two sources.

Because NIMS was designed to operate at Jupiter, many of the bands beyond 1.1  $\mu\text{m}$  were saturated on the Moon except near the terminator. Due to this saturation, our global lunar studies with the NIMS are limited to the 0.7- to 1.1- $\mu\text{m}$  region. Fortunately, this is an important region containing a broad absorption feature near 1  $\mu\text{m}$  attributed to pyroxenes and olivine. In addition, high-quality unsaturated spectra covering the entire NIMS spectral range (0.7-5.2  $\mu\text{m}$ ) are available

254  
PRECEDING PAGE BLANK NOT FILMED



## SECOND GALILEO EARTH-MOON ENCOUNTER: Carlson, R.W. et al.

for a 20-degree-wide strip along the terminator in the highest spatial resolution mosaic collected. This strip extends from western Mare Frigoris, through the north polar region, down to Mare Marginis on the lunar farside. These data allow analysis of NIMS spectra containing both the 1- $\mu$ m features as well as important features in the 2- to 2.5- $\mu$ m region attributed largely to pyroxenes and glasses.

The NIMS radiometric response is quite sensitive to the thermal environment in which the instrument is operated. Consequently, onboard calibration targets are used to validate and refine the instrument response. Unfortunately, observations of the reflected solar radiation from the photometric calibration target (PCT) that were acquired during the encounter were also largely saturated (again because the instrument was designed to operate at Jupiter). Hence the initial analysis of the NIMS lunar spectra involved dark-current correction, then ratioing of the spectra to that of a standard area (usually a relatively bland highland region), resulting in normalized spectra from which instrument and solar spectral functions were removed. The de-patterning autocorrelation techniques mentioned above were then applied to suppress artifacts introduced by scan-platform jitter.

The 1- $\mu$ m band was analyzed for the entire high-resolution north polar mosaic. This data set covers mostly the nearside north polar region and Frigoris, Imbrium, Serenitatis, Tranquilitatis, Fecunditatis, and Crisium Maria. The parameter that can most rigorously be derived is the 1- $\mu$ m band depth, which shows large variations in mafic mineral content both in highlands and maria. Parts of Mare Frigoris and Mare Imbrium show the strongest absorption; parts of the Crisium basin ejecta and highlands west of Mare Tranquilitatis show the weakest. Preliminary studies of the 1- $\mu$ m band shape and of slopes of the continuum near that band show that the NIMS observations can be analyzed with more refined techniques to yield information related to the total pyroxene/olivine abundance, the Ca content of the pyroxenes, and the Fe/Mg abundance. Like the 1- $\mu$ m bands, absorption features in the 2- to 2.5- $\mu$ m region reveal variations over the maria covered by the terminator strip mentioned above. As an example, comparison of spectra in western Mare Frigoris and flooded crater floors north of Mare Marginis show similar depths and shapes for the 1- $\mu$ m bands but quite different strengths for the 2- to 2.5- $\mu$ m bands, which are much stronger in Mare Frigoris. These observations suggest variations in the relative abundance of olivine and pyroxene as well as in pyroxene composition, which largely control shapes and depths of the two bands.

NIMS observations of the north polar region also provide unique spectral and geometric coverage that allows a search for absorption features associated with water in some form that might exist in the polar regions; our analysis in this area is underway.

In anticipation of the relatively high temperatures in Jupiter's atmosphere in the 5- $\mu$ m region, NIMS has an extremely wide sensitivity range beyond 4.3  $\mu$ m. For the lunar observations, this range will allow useful measurements from 200 to 350 K. As a consequence, NIMS observations near the poles and on the lunar farside, outside the range of Earth-based observations or the Apollo orbits, can provide new information on the physical properties of the lunar surface.

References: [1] Lane, A.P., and Irvine, W.M. (1973) *Astron. Jour.*, 78, 267; [2] Carlson, R.W. et al. (1992) *Space Sci. Rev.*, 60, 457-502; [3] McCord, T.B. et al. (1993) work in progress.

**DISTRIBUTION OF VANADIUM AND MELTING OF OPAQUE ASSEMBLAGES IN EFREMOVKA CAIs**. I. Casanova<sup>1,2</sup> and L. Grossman<sup>2,3</sup>. <sup>1</sup>Dept. of Geology, Field Museum of Natural History, Roosevelt Rd. at Lake Shore Dr., Chicago, IL 60605-2496; <sup>2</sup>Dept. of the Geophysical Sciences, The University of Chicago, 5734 S. Ellis Ave., Chicago, IL 60637; <sup>3</sup>Enrico Fermi Institute, The University of Chicago, 5640 S. Ellis Ave., Chicago, IL 60637.

**Abstract.** A petrographic and chemical study of compact Type A CAIs from the Efremovka CV3 chondrite strongly suggests that the opaque assemblages (OAs) that they contain were molten at temperatures below the CAI silicate solidus, and that the V-rich magnetite presently observed in association with OAs formed by *in situ* oxidation of their FeNi.

**Introduction.** The study of the distribution of vanadium in Ca-, Al-rich inclusions can provide important information about the oxidation of their opaque assemblages and the origin of the magnetite that they commonly contain. The two different views about this problem are those of [1], who propose that formation of magnetite took place prior to incorporation into the CAI, and [2], who suggest that the magnetite originated by *in situ* oxidation of the FeNi of the OAs. Most available information about magnetite in OAs stems from study of Allende CAIs, where the often extensive sulphidization obscures the textural relationships between FeNi and magnetite in the assemblage. Ca-, Al-rich inclusions from the reduced subgroup of CV3 chondrites contain OAs that, in general, are devoid of the sulphides that characterize their Allende (oxidized CV3) relatives. In this work, we report petrographic observations and electron microprobe analyses of three compact Type A CAIs (EF1, 2 and 3) from the Efremovka CV3 chondrite. In light of trace element analyses [3] of CAIs in reduced CV3s (Vigarano, Leoville and Efremovka), including the three inclusions studied here, experimental data on metal/silicate vanadium partitioning behaviour [4], phase equilibria in the Fe-Ni-P system [5], and magnetite stability conditions [6], our results provide a plausible model for the formation of V-rich magnetite in opaque assemblages.

**Results.** EF1, 2 and 3 consist of melilite (>60 % by volume), spinel (8-23 %), perovskite (2-8 %), and minor to accessory amounts of fassaite and OAs. Fassaite occurs almost exclusively as amoeboid intergrowths with the perovskite and/or forming rims (of up to a few tens of microns in width) around the OAs. OAs with fassaite rims are found included in or attached to euhedral spinel grains, and enclosed in melilite crystals as well. The concentration of vanadium is constant in and among spinel grains of the same inclusion ( $\text{SPEF}_1 = 0.86 \pm 0.05$  wt.%  $\text{V}_2\text{O}_3$ ,  $N=10$ ;  $\text{SPEF}_2 = 0.47 \pm 0.08$ ,  $N=10$ ;  $\text{SPEF}_3 = 0.77 \pm 0.06$ ;  $N=12$ ). In contrast, fassaite grains are generally zoned: those not spatially associated with OAs display well-defined zoning profiles, with rim compositions of 0.77-1.22 wt.%  $\text{V}_2\text{O}_3$  and cores containing up to 2.10 wt%; fassaite grains rimming OAs are also zoned and somewhat richer in  $\text{V}_2\text{O}_3$  (1.61-2.34 wt.%) but, unlike the isolated fassaite grains, they often display complicated zoning profiles. Single perovskite grains in the studied inclusions always have homogeneous  $\text{V}_2\text{O}_3$  contents but display a wide compositional range within an individual CAI ( $\text{PVEF}_1$ : 0.32-1.32 wt.%  $\text{V}_2\text{O}_3$ ;  $\text{PVEF}_2$ : 0.67-2.21;  $\text{PVEF}_3$ : 1.16-2.33). Melilite V contents are below the detection limit in all grains analyzed (< 50 ppm). In the OAs, vanadium exists exclusively as an oxide, in V-rich magnetite. High-resolution X-ray scans of the V, Cr and Fe  $K\alpha$  lines revealed that vanadium concentrates in discrete micron- to submicron-sized areas dispersed throughout the metallic FeNi of the OA. Analyses of the largest of these (5  $\mu\text{m}$  across) show that they are V-, Cr-rich magnetite; thus, the vanadium is not in solid solution in the metal. Magnetite grains in EF3-OA1 (a large, 100  $\mu\text{m}$ -diameter opaque assemblage in EF3) are anhedral; the coarser-grained ones occur preferentially at and near the edges of the assemblage and are somewhat poorer in vanadium (19-22 at.% V) than the ones in the interior (21-25 at.% V). EF3-OA1 contains two distinct textural components: the larger one is heart-shaped (named The Heart), 80  $\mu\text{m}$  across, has a bulk Ni content of 9.2 wt.% (determined by broad-beam microprobe analyses) and consists of skeletal crystals of kamacite oriented parallel to the (111) plane of their taenite host, determined according to the method described by [7]. The Heart is partially rimmed by a band of variable width (<1-5  $\mu\text{m}$ ) of calcium phosphate, which locally forms euhedral crystals. The smaller mass is attached to The Heart and elongated in shape (and accordingly named The Leech). It lacks taenite and is not rimmed by phosphate (except at the contact with The Heart); it also contains a small (7x2  $\mu\text{m}$ ) bleb of pure powellite (W-free,  $\text{CaMoO}_4$ ), and another even smaller inclusion (2x1  $\mu\text{m}$ ) of an unidentified W-Mo-S-Ca mineral (plausibly a fine intergrowth of powellite and molybdenite). Despite the fact that chemical compositions of kamacite (4.2-6.7 at.% Ni) and magnetite (19-25 at.% V) in The Heart and The Leech are indistinguishable, their distinct mineralogies and textural relationship strongly suggest that they were once individual opaque assemblages that partially coalesced in the molten state.

**Formation of V-rich magnetite in OAs:** Vanadium-rich magnetite in CAIs is always spatially associated with opaque assemblages. On the other hand, there is no relationship between the bulk vanadium content of CAIs in reduced CV3 chondrites and the amount of opaque assemblages that they contain. Although the OAs may have been previously enriched in vanadium relative to the CAI through reduction of this element from the CAI liquid (since  $D_V^{\text{liq.metal/liq.sil.}} \sim 5000$  at 1533°K and  $\log f_{\text{O}_2} = -19$ , according to extrapolation from experimental data by [4] for partitioning of V between S-bearing liquid metal and a silicate liquid of basaltic composition), it is likely that

some vanadium was already present in the reduced state dissolved in the metal of the OA. However, the lack of correlation between the V and, for instance, the Ir concentrations in CAIs [3], indicates that the bulk vanadium enrichment of the CAI relative to CI (factors of 16, 3 and 24, for EF1, 2 and 3, respectively) is not due to the presence of different amounts of OAs. Experimental data by [6] show that magnetite and an  $\text{Fe}_x\text{Ni}_y$  alloy can coexist at equilibrium only at  $T < 950^\circ\text{K}$  if the composition of the alloy is such that  $y < 15$  (as observed in our Efremovka OAs). At those temperatures, the oxygen fugacity required for magnetite-metal equilibrium ( $\log f_{\text{O}_2} = -22$ ) is about six orders of magnitude higher than that of a gas of solar composition. Therefore, even if magnetite were present in the OAs prior to their incorporation into CAIs, the magnetite would have been unstable and, consequently, reduced to metal under the  $f_{\text{O}_2}$ - $T$  conditions typical of CAI silicate liquids ( $T \geq 1500^\circ\text{K}$ ,  $\log f_{\text{O}_2} \sim -19$ ; [8]). Incorporation of the OAs into the CAIs at subsolidus (and more oxidizing) conditions is unlikely since OAs, especially the smaller ones, are commonly mantled by fassaite and enclosed in euhedral spinel grains (an early-crystallizing phase). Then, despite the probable effect of the high V contents of magnetite on the magnetite-FeNi equilibrium conditions, it is safe to say, in light of these data and in agreement with [2], that the magnetite nucleated at temperatures well below the solidus of the CAI, and therefore must have formed *in situ*.

**Vanadium in CAI silicates:** Spinel compositions suggest that vanadium is compatible in this mineral. Then, the homogeneity of the vanadium contents among different spinel grains within the same CAI suggests that crystallization of this mineral in EF1, 2 and 3 occurred in a narrow temperature interval. Subsequent cooling would induce the oxidation of vanadium [2] that may then be included as  $\text{V}^{3+}$  in perovskite and fassaite crystallizing from the late CAI residual liquid. The fassaite grains that crystallized around OAs may have incorporated more vanadium (from the locally V-enriched OAs) than the isolated ones. This can explain the higher V concentrations in fassaite rims (relative to isolated fassaite grains) and the relative depletion of V in the magnetites from the exterior (relative to the ones in the interior) of the OAs, due to nucleation and growth of magnetite at lower temperatures in areas that had been depleted in V by the earlier crystallization of fassaite.

**OA-CAI equilibrium:** If the currently observed V contents reflect equilibrium partitioning for this element between the opaque assemblages and the CAI silicates, it is possible to estimate the OA/CAI vanadium distribution coefficient when final (after cooling and oxidation) OA-CAI equilibrium was achieved. Thus, the apparent metal/silicate distribution coefficient can be calculated according to the expression:  $D_v^{\text{OA/CAI}} = [\text{V}]_{\text{OA}}/[\text{V}]_{\text{sil}}$ , where  $[\text{V}]_{\text{OA}} = x_{\text{mt}}[\text{V}]_{\text{mt}}$  and  $[\text{V}]_{\text{sil}} = x_{\text{sp}}[\text{V}]_{\text{sp}} + x_{\text{fas}}[\text{V}]_{\text{fas}} + x_{\text{pv}}[\text{V}]_{\text{pv}}$ ,  $x_i$  and  $[\text{V}]_i$  being the mass fractions and vanadium concentrations, respectively, of the indicated minerals. Modal and microprobe analyses yield values of  $D_v^{\text{OA/CAI}} = 9$  for EF1, 5 for EF2, and 8 for EF3, which are in very good agreement with V-distribution values in three Allende CAIs ( $D_v^{\text{OA/CAI}} = 6-60$ ) estimated by [2].

**Melting of OAs:** The metal that now constitutes the major part of the OAs must have been at least partially molten at the time of complete solidification of CAI silicates. According to experimental results on the phase relationships in the Fe-Ni-P system [5], an alloy containing  $>8.9$  wt.% Ni and 1.2 wt.% P will melt at  $1333^\circ\text{K}$ , well below the considered CAI solidus temperature ( $\sim 1500^\circ\text{K}$ ). The bulk P content of EF3-OA1 must have been at least 1.2 wt.% (estimated by assuming that all P currently in phosphate was dissolved in the metal at those  $f_{\text{O}_2}$ - $T$  conditions). Therefore, and at least in Efremovka, the presence of sulphur is not necessary to induce melting of the OA since the P contents of the FeNi alloys were high enough to maintain the metal partially molten until after their host CAI silicates were completely crystallized.

In summary, based on considerations of magnetite-FeNi equilibrium conditions, the observed spatial association between V-rich magnetite and metal in the OAs, and the close textural relationship between the OAs and euhedral spinel grains, we conclude that V-rich magnetite formed *in situ* in CAIs by oxidation of the metal of OAs at low temperatures (below  $950^\circ\text{K}$ ). Considering also that the OAs probably remained molten after the complete solidification of the CAI silicates, a plausible sequence of events in the history of the OAs in CAIs from EF1, 2 and 3 is as follows: (1) melting of the CAI-OA and reduction of some V from the CAI liquid at  $T \geq 1500^\circ\text{K}$  and  $\log f_{\text{O}_2} \sim -19$ ; (2) nucleation and growth of euhedral spinel crystals and melilite above  $1500^\circ\text{K}$ ; (3) cooling of the CAI and oxidation of V; (4) crystallization of fassaite and perovskite from the residual, Ti-rich, CAI liquid; (5) solidification of the FeNi alloys in the OAs (approximately at  $1333^\circ\text{K}$ ); and (6) nucleation and growth of magnetite ( $T \leq 950^\circ\text{K}$ ) within and around opaque assemblages. The investigation of OAs in CAIs from the reduced CV3 chondrites opens an interesting field of further research aimed at understanding the origin of opaque assemblages and the relationships with their CAI hosts.

**REFERENCES:** [1] ARMSTRONG J.T. et al. (1985) *GCA* 49: 1001-1022; [2] BLUM J.D. et al. (1989) *GCA* 53: 543-556; [3] SYLVESTER P.J. et al. (1993) *GCA* (submitted); [4] DRAKE M.J. et al. (1989) *GCA* 53: 2101-2111; [5] DOAN A.S., Jr. and GOLDSTEIN J.I. (1970) *Met. Trans.* 1: 1759-1767; [6] MCMAHON B.M. and HAGGERTY S.E. (1980) *Proc. Lunar. Planet. Sci. Conf.* 11th: 1003-1025; [7] BUCHWALD, V.F. (1969) *GCA* 33: 152-153; [8] BECKETT J.R. and GROSSMAN L. (1986) *Lunar Planet. Sci.* XVII: 36-37.

458891

5127-90

ABS-0111

LPSC XXIV

259

N 9 4-12142  
A 337

P-2

**METAL-RICH METEORITES FROM THE AUBRITE PARENT BODY.** I. Casanova<sup>1</sup>, T.J. McCoy<sup>2</sup> and K. Keil<sup>2</sup>; <sup>1</sup>Dept. of Geology, Field Museum of Natural History, Chicago, IL 60605 and Dept. of Geophysical Sciences, Univ. of Chicago, Chicago, IL 60637 USA; <sup>2</sup>Planetary Geosciences, Dept. of Geology and Geophysics, School of Ocean and Earth Science and Technology, Univ. of Hawaii at Manoa, Honolulu, HI 96822 USA.

**ABSTRACT.** We studied three metal-rich meteorites—Mt. Egerton, Horse Creek and LEW 88055—and suggest that they formed in the aubrite parent body. LEW 85369 and 88631 may also have a common origin, but these rocks have not yet been studied in detail. This body was probably heated to about 1600 C by a very strong heat source. While molten, metal agglomerated into sizeable nodules which never segregated efficiently to form a core, but were trapped in the silicate mantle. Different clasts and lithologies in aubrites solidified and cooled under local equilibrium conditions of oxygen fugacity, and with different thermal histories. Impacts mixed clasts from throughout the parent body, creating the typical aubrite breccias.

**INTRODUCTION.** The meteorites of the enstatite clan comprise a suite of chondrites (both unequilibrated and equilibrated); metal-rich impact melts from the EL chondrite parent body (Ilafegh 009, Happy Canyon) [1]; achondrites (aubrites); and stony-irons (Mt. Egerton, LEW 88055). All are characterized by highly reduced mineral assemblages. Some iron meteorites (Horse Creek, LEW 85369, LEW 88631) show strong geochemical and/or mineralogical affinities to this group. This broad petrologic spectrum makes the enstatite meteorites a unique group for the study of the early evolution of their source asteroids. Previous workers [2] have proposed the existence of four different parent bodies for the meteorites of the enstatite clan, represented by the EH and EL chondrites, the aubrites and Shallowater. The highly reduced nature of the silicates in the Tucson iron is suggestive of a close relationship to the meteorites of the enstatite clan, but their oxygen isotopic composition (R.N. Clayton, pers. comm., 1992) is clearly distinct from any other enstatite chondrite or aubrite.

**RESULTS.** We have identified five metal-rich meteorites which probably formed in the aubrite parent body. Here we discuss their mineralogy and petrology, with emphasis on their similarities to known enstatite achondrites, particularly the well-studied Norton County aubrite. **Mt. Egerton:** This metal-rich aubrite is estimated to contain about 21 wt % metallic Fe, Ni as angular crystals between large enstatite laths. Enstatite is the dominant mineral, followed by metal, with minor diopside; Ti and Cr-bearing troilite, brezinaite and schreibersite also occur. Mineral and oxygen isotopic compositions are well within the range of those of aubrites [3]. We have now identified SiO<sub>2</sub> intimately associated with, and sometimes rimming, Si-bearing metal. SiO<sub>2</sub> has previously been found in Norton County, where it sometimes rims perryite-bearing metal [4]. Texturally, enstatite in Mt. Egerton is similar to that in the pyroxenitic clasts in Norton County, which have distinctive intergrowths of pyroxenes indicative of co-crystallization [4], rather than gravitational accumulation. Mt. Egerton differs from Norton County in being much richer in metal and showing no indication of brecciation. The unfractionated, chondritic trace element composition of metal in Mt. Egerton is similar to that of metal in aubrites [5]. We classify Mt. Egerton as an unbrecciated metal-rich aubrite with igneous textures. **LEW 88055:** This small (1.7 g) meteorite consists of a highly reduced silicate assemblage of enstatite, diopside, albite and K-feldspar in a host of Si-free kamacite, with ferroan alabandite, Ti-bearing troilite, daubréelite and schreibersite. These minerals are similar in composition to those in aubrites [6], except for K-feldspar, which is unknown in the enstatite achondrites. Albitic feldspar is present in significant amounts (albite/K-feldspar ~5), and albite, K-feldspar and diopside all occur associated with or rimming metal. The meteorite was intensely shocked, as evidenced by twinning in some enstatite grains and Neumann bands in the kamacite host [6]. We suggest that this rock is probably a fragment from a metal-enriched portion of an aubrite, as is indicated by its mineralogy, composition and shock features. A previous model for its origin involving impact of two objects formed under different oxygen fugacities in different regions of the nebula [6] does not seem warranted. The fact that its metal is Si-free may be the result of poor sampling of this minute meteorite: aubrites are known to contain metal of widely

variable Si contents, including grains that contain no appreciable amounts ( $<200$  ppm) of reduced silicon in solid solution [5]. **Horse Creek:** This is a 570 g, Si-bearing iron meteorite, also with an unfractionated, chondritic trace element composition similar to that of aubrites [5, 7], that contains perryite and schreibersite exsolution lamellae. No silicates are included in, or attached to, the metal. Although considerably larger than the common metal nodules in aubrites, its geochemical and mineralogical similarities suggest that it formed in the same parent body. **LEW 85369 and 88631:** These two small (6.3 and 3.2 g, respectively) meteorites are both Si-bearing irons and have affinities with the metallic portions of the meteorites described above. Unfortunately, neither meteorite has been completely described. LEW 88631 apparently contains perryite, which has not been noted in LEW 85369. They may be paired, and we suggest that more detailed study may confirm their parentage from the aubrite parent body.

**DISCUSSION.** The mineralogy and mineral compositions of these meteorites are consistent with their derivation from the aubrite parent body. **Heating of the Aubrite Parent Body:** The igneous textures of the lithologies of the aubrites and their largely monomineralic ( $>85\%$  enstatite) nature imply that they crystallized from a magma of nearly pure enstatite. This melt must have been heated to at least  $1560^{\circ}\text{C}$  (melting point of enstatite at 1 bar), implying the existence of a very strong heat source early in the history of the solar system. **Metal Agglomeration:** It has been suggested that Mt. Egerton and Horse Creek are samples from the core-mantle boundary and core, respectively, of the aubrite parent body [3]. We argue that their chondritic siderophile element abundance ratios indicate that they were not parts of a fractionally crystallizing core but, rather, represent local concentrations of metal trapped in the mantle of the aubrite parent body. Since the aubrite magma was of nearly pure enstatite composition, crystallization was limited to a very narrow temperature interval. Thus, solidification may have been rapid, allowing for the trapping of sizeable metal nodules in the silicate mantle. Furthermore, at these high magmatic temperatures, convection may have been vigorous and contributed to keep small metal particles in the aubrite mantle. **Metal/Silicate Intergrowth During Solidification:** In Mt. Egerton and LEW 88055, textures are indicative of co-crystallization of pyroxene and the interstitial nature of the metal indicates that it was trapped between the growing pyroxenes. In both rocks, late crystallizing silicates (e.g., diopside, K-feldspar, albite,  $\text{SiO}_2$ ) are intimately associated with or rim the metal. **Subsolidus Cooling:** Previous studies of aubrites [4] suggest cooling rates of  $5\text{--}50^{\circ}\text{C/Ma}$  for individual Fe,Ni metal particles. An independent, although not quantitative, means of assessing the cooling rate is through examination of perryite,  $(\text{Ni,Fe})_8(\text{Si,P})_3$ , in the metallic fraction of aubrites and the metal-rich members of the clan. Perryite occurs in Mt. Egerton, Horse Creek, LEW 88631 and the cm-sized metallic nodules of Norton County mainly as long, thin lamellae ( $30\text{ }\mu\text{m}$  by a few mm), oriented parallel to the (111) plane of the Fe,Ni host crystal. This texture is indicative of an origin by subsolidus exsolution. No relationship exists between the bulk Si contents of metal particles and the presence of perryite: for instance, a cm-sized Fe,Ni nodule in Norton County with 1.1 wt % bulk Si contains no perryite, while another nodule with only 0.5 wt % displays well-developed perryite lamellae. This observation strongly suggests that perryite exsolution is controlled by the thermal history, and not the bulk Si content. Thus, our examination of perryite confirms that metal particles from the aubrite parent body experienced different thermal histories. It would appear that crystallization and/or cooling of metal particles also occurred at different local oxygen fugacities, as suggested by the presence of both Si-bearing and Si-free metal. **Impact Mixing:** The coexistence of slowly and rapidly cooled silicate lithologies in Norton County has been proposed as evidence for breakup and reassembly of the aubrite parent body [4]. The presence of perryite-bearing and perryite-free metal particles which appear to have had different thermal histories, is further evidence of extensive impact mixing of aubrite ingredients. During parent body evolution, LEW 88055 was heavily shocked, while Mt. Egerton completely escaped brecciation.

**REFERENCES:** [1] McCoy *et al.* (1992) LPSC XXIII: 869-870. [2] Keil, K. (1989) *Meteoritics* 24: 195-208. [3] Watters and Prinz, M. (1980) LPSC XI: 1225-1226. [4] Okada *et al.* (1988) *Meteoritics* 23: 59-74. [5] Casanova *et al.* (1993) GCA, in press. [6] Prinz *et al.* (1991) *Meteoritics* 26: 386. [7] Wolf *et al.* (1983) GCA 47: 2257-2270.

456893

5428-92

LPSC XXIV

261

ABS. ONLY

N 9 4 1 2 1 8 4 3

P-2

# WHY CONVECTIVE HEAT TRANSPORT IN THE SOLAR NEBULA WAS INEFFICIENT; P. Cassen, NASA-Ames Research Center, Moffett Field, CA 94035.

The radial distributions of the effective temperatures of circumstellar disks associated with pre-main sequence (T Tauri) stars are relatively well-constrained by ground-based and spacecraft infrared photometry and radio continuum observations [see the compilation in (1)]. If the mechanisms by which energy is transported vertically in the disks are understood, these data can be used to constrain models of the thermal structure and evolution of solar the nebula (2). Several studies of the evolution of the solar nebula have included the calculation of the vertical transport of heat by convection (3, 4, 5, 6). Such calculations rely on a mixing length theory of transport and some assumption regarding the vertical distribution of internal dissipation. In all cases, the results of these calculations indicate that transport by radiation dominates that by convection, even when the nebula is convectively unstable. We present here a simple argument that demonstrates the generality (and limits) of this result, regardless of the details of mixing length theory or the precise distribution of internal heating. It is based on the idea that the radiative gradient in an optically thick nebula generally does not greatly exceed the adiabatic gradient.

A well-known result from radiative transfer theory for a plane-parallel, optically thick medium, in which the flux is constant, is that the temperature at depth is related to the effective temperature  $T_e$  by

$$T = T_e \left( \frac{3}{4} \tau_0 \right)^{1/4},$$

where  $\tau_0$  is the optical depth of the layer, defined by

$$\tau_0 = \int_0^\infty \rho \kappa dz = \bar{\kappa} \Sigma / 2,$$

$\bar{\kappa}$  is the mass averaged Rosseland mean opacity, and  $\Sigma/2$  is the surface density of the layer (half nebula thickness). In general, one may write

$$T_m = T_e (\eta \tau_0)^{1/4}$$

where  $T_m$  is the midplane temperature and  $\eta$  is a number less than (but of order) unity for smoothly distributed energy sources. (For instance,  $\eta = 3/8$  if the energy sources are uniform with respect to the volume density of the layer.)

The corresponding relationship for an adiabatic temperature profile can be found from the expression for the vertical distribution of temperature:

$$T = T_m (1 - z^2/h^2),$$

where

$$h = \frac{\Omega}{c_s} \sqrt{\frac{\gamma - 1}{2}},$$

$\Omega$  is the local orbital frequency,  $\gamma$  is the ratio of specific heats, and  $c_s$  is the midplane sound speed. The scale height  $h$  is related to the nebula surface density  $\Sigma$  and midplane volume density  $\rho_0$  by

$$\Sigma = 2\rho_0 h \int_0^1 (1-u^2)^{\frac{1}{\gamma-1}} du = \zeta \rho_0 h,$$

## CONVECTION IN THE NEBULA; P. Cassen

where the value of the integral  $\zeta = 0.982$ . The effective temperature is given by  $T_e = T(\tau = 2/3)$ . For an optically thick nebula, one expects that the  $\tau = 2/3$  level is close to  $h$ , in which case

$$\frac{2}{3} = \int_{1-\varepsilon}^1 h \kappa \rho_0 (1-u^2)^{1/(\gamma-1)} du \approx \int_0^{\varepsilon} h \kappa \rho_0 (2x)^{1/(\gamma-1)} dx = \frac{\gamma-1}{\gamma} h \kappa \rho_0 (2\varepsilon)^{\gamma/(\gamma-1)}.$$

Here,  $\varepsilon = 1 - (z_e/h) \ll 1$ ,  $z_e = z(\tau = 2/3)$ , and  $\kappa$  is the Rosseland mean opacity near  $\tau = 2/3$ . This expression yields the result

$$T_m = T_e [3(\gamma-1) \kappa \Sigma / 4 \gamma \zeta]^{(\gamma-1)/\gamma} = T_e [3(\gamma-1) \kappa \tau_0 / 2 \gamma \zeta \bar{\kappa}]^{(\gamma-1)/\gamma}.$$

Therefore, the ratio

$$\frac{T_m(\text{radiative})}{T_m(\text{adiabatic})} = \frac{\eta^{1/4}}{[3(\gamma-1) \kappa / 2 \gamma \zeta \bar{\kappa}]^{(\gamma-1)/\gamma}} \tau_0^{1/4 - (\gamma-1)/\gamma} = (\bar{\kappa} / \kappa)^{2/7} \eta^{1/4} \tau_0^{-.03} \quad \text{for } \gamma = 7/5.$$

In the temperature range 160 - 1500 K, the Rosseland mean opacity *decreases* due to the evaporation of opacity-producing solids, but *increases* with temperature in those ranges within which no important solid species evaporates (7). The result is that  $\bar{\kappa} / \kappa$  will commonly be less than one, and in no case (for  $50 \text{ K} < T < 1500 \text{ K}$ ) be greater than about three. Thus the midplane temperature that is obtained for conditions of radiative equilibrium cannot be substantially modified by convection, which could only reduce it to the adiabatic value, at best.

The significance of this result is that the problem of understanding the thermal structure of observed circumstellar disks is reduced to a one-parameter ( $\tau_0$ ) issue. In general, one may then define the problem of inferring nebula thermal evolution from observations of T Tauri stars in terms of the determination of only *two* parameters, the mass accretion rate from the disk to the star  $\dot{M}$  and the optical depth  $\tau_0$ . To see this, note that for disks in which the effective temperature is well-represented by a power law in radius (the usual case), conservation of energy, quite generally, requires

$$\frac{GM_* \dot{M}}{2R_*} = \int_{R_*}^{\infty} 4\pi r \sigma T_1^4 (r/r_1)^{-4q} dr.$$

The quantities  $M_*$ ,  $R_*$ ,  $T_1(r_1)$ , and  $q$  can all, in principle, be determined from observations, and therefore so can  $\dot{M}$  [see, for instance, (8)]. One can, for example, derive the result (for  $q = 3/4$ ) that the requirement that silicates be melted at the midplane at 1 AU is:

$$\dot{M} \tau_0 \geq 4 \times 10^{-3},$$

where  $\dot{M}$  is measured in solar masses/year. At present, determination of the optical depth  $\tau_0$  requires coagulation theory.

References: (1) Beckwith, S. *et al.* (1990) *A. J.* **99**, 924. (2) Cassen, P. *LPSC XXIII* 207-208. (3) Lin, D. N. C. and Papaloizou, J. (1980) *M.N.R.A.S.* **191**, 37. (4) Lin, D. N. C. and Papaloizou, J. (1985) in *Protostars and Planets II* (Black and Matthews, eds.) U. of Arizona Press. (5) Ruden, S. P. and Lin, D. N. C. (1986) *Ap. J.* **308**, 883. (6) Watanabe, S. *et al.* (1990) *Ap. J.* **358**, 282. (7) Pollack *et al.* *Ap. J.* (submitted). (8) Bertout, C. *et al.* (1988) *Ap. J.* **330**, 350.

456896  
5129-91  
ABS. ONLY  
N 94-12,149  
f-2  
FAULT GEOMETRIES AND EXTENSION IN THE VALLES MARINERIS, MARS;

D.J. Chadwick and B.K. Lucchitta, U.S. Geological Survey, Flagstaff, AZ 86001.

The central troughs of the Valles Marineris system on Mars are generally regarded to be of tectonic origin because they are linear and bounded by faults [1,2]. Their radial orientation to the Tharsis rise suggests that at least their incipient formation was influenced by the formation of the rise [3], but the exact role of Tharsis is not yet well understood. Collapse and erosion may have significantly modified the original tectonic troughs [4].

To better understand the magnitude and mechanism of crustal extension across the Valles Marineris, we have studied the attitudes of trough-wall faults that parallel the long axes of the troughs. Our results will help to determine if the extension is related to the Tharsis rise, to a local arch along which the troughs lie, or to other mechanisms.

Fault-plane attitudes were obtained by performing a photogrammetric study of fault traces in the walls of Candor and Melas Chasmata. If the exposed wall faults in this study are not major trough-bounding faults, we assume that these major faults are buried at the base of the walls and have similar geometries to the exposed faults. We have obtained three-dimensional coordinates of several points along each fault trace and constructed three-point solutions to their geometries (Table 1). As expected, the results show that the faults dip toward the interior of the troughs, suggesting that they are indeed normal faults associated with trough formation.

We have measured eight fault geometries thus far, and all but one have an average dip of over  $70^\circ$  (Table 1). The average value of all the dips is about  $75^\circ$ , which is significantly higher than the  $65^\circ$  predicted for deep faults by Byerlee's law [5]. A pre-existing, vertical joint fabric may have caused the graben-bounding faults to form at steeper angles near the surface [6]. Such a joint fabric has influenced graben-bounding faults in Canyonlands National Park, Utah [7]. We are still investigating other possible causes for the unusual dips on the Martian faults.

If the graben-bounding faults are planar and typically dip at about  $75^\circ$ , extension across six faults in the widest part of the Valles Marineris is about 16 km. This value was calculated by using a structural displacement of 10 km for Ophir, Candor, and Coprates Chasmata that was based on observations and inferences concerning downdropped plateau rock [8]. If  $60^\circ$  dips are assumed, as suggested by Schultz [8], the amount of extension across the troughs would be about 35 km. Thus, the strain across the Valles Marineris may be considerably less than previously estimated.

The Sirenum province on the southwest side of the Tharsis rise occupies a wedge of about  $45^\circ$  azimuth around Tharsis [9, Figure 1]. This region has about 30 grabens that are oriented radially to the center of Tharsis and are considered to be a consequence of Tharsis-centered tectonism. The extension across these grabens is estimated to be about 1 km [9]. If Sirenum is an indicator of the amount of extension produced solely by the Tharsis rise, and if a simple model is assumed in which similar amounts of strain occur all around Tharsis, then the 90-degree wedge of azimuth on the east side of Tharsis that is occupied by the Valles Marineris province would be expected to have about 2 km of strain. (The strain in this wedge is concentrated almost entirely within the Valles Marineris and their immediate vicinity.) Therefore, an additional 14 km or more of extension across the Valles Marineris would have to be the result of other processes.



## VALLES MARINERIS FAULTS: Chadwick, D.J., and Lucchitta, B.K.

A 4-km-high arch associated with the central Valles Marineris troughs has been invoked as the source of much of the extension in the troughs [6,10]. However, we calculated the increase in circumference (and extension) due to the arch when superposed on an initially spherical Mars to be only about 1 km.

Overall, it appears that regional and local uplift may account for less than a quarter of the extension across the Valles Marineris if the bounding faults typically dip 75°. However, regionally inhomogeneous stresses associated with the Tharsis rise may concentrate additional extension in certain areas, such as the Valles Marineris. This situation requires further investigation. If Tharsis-centered stresses are not sufficient to account for all of the observed extension, as our preliminary results suggest, then an active mechanism--such as rifting due to mantle upwelling--may be invoked for much of the observed strain.

TABLE 1: GEOMETRIES OF VALLES MARINERIS FAULTS IN STUDY

FAULT LOCATION	STRIKE (DEG.)	DIP (DEG.)	DIP DIRECTION	FAULT LAT. LON. (DEGREES)
N.E. CANDOR	104.6	72.0	SSW	-6.8, 66.3
N.E. CANDOR	107.8	85.8	SSW	-6.9, 66.4
NORTH CANDOR	94.8	72.6	S	-5.6, 71.9
NORTH MELAS	105.1	73.3	SSW	-7.8, 71.4
SOUTH CANDOR	122.5	70.6	NE	-8.2, 72.8
NORTH MELAS	48.8	84.6	SSW	-8.9, 73.7
NORTH MELAS	52.4	74.9	SE	-9.0, 73.8
NORTH MELAS	103.7	52.5	SSW	-9.1, 74.0

- [1] Blasius, K.R. et al. (1977) *J. Geophys. Res.*, 82, 4067-4091; [2] Lucchitta, B.K. et al., (1992) *Mars*, University of Arizona Press, 453-492; [3] McCauley, J.F. et al. (1972) *Icarus*, 17, 289-327; [4] McCauley, J.F., (1978) *U.S. Geological Survey Misc. Inv. Series Map I-897*; [5] Byerlee, J. (1978) *Pure and App. Geophys.*, 116, 615-626; [6] Tanaka, K.L. and Golombek, M.P. (1989) *Proc. LPSC*, 383-396; [7] McGill, G.E. and Stromquist, A.W. (1979) *J. Geophys. Res.*, 84, 4547-4563; [8] Schultz, R.A. (1991) *J. Geophys. Res.*, 96, 22,777-22,792; [9] Tanaka, K.L. and Chadwick, D.J., this volume; [10] Witbeck, N.E. et al. (1991) *U.S. Geological Survey Misc. Inv. Series Map I-2010*.

456899

S130-91

LPSC XXIV

265

P25-ONLY

N 94-12145

P2

A TWO-STAGE (TURBULENT-DRAINAGE) MECHANISM FOR THE EMPLACEMENT OF IMPACT CRATER OUTFLOWS ON VENUS; D.J. Chadwick and G.G. Schaber, U.S. Geological Survey, Flagstaff, AZ 86001

Several emplacement mechanisms have been proposed for the unique flow features associated with 402 of the 912 [1] impact craters found on Venus to date [2-5]. Studies based on rheological models [2] and laboratory results [5] have suggested two separate depositional flow mechanisms: a turbulent emplacement and a lavalike emplacement. Schultz [5] proposed a progressive transition from the turbulent to the lavalike mechanism during deceleration of some turbulent flows. He suggested that these composite flows were emplaced prior to the deposition of the normal ejecta.

After an examination of the geomorphologic, stratigraphic, and topographic relations of the flows associated with the 402 craters, we suggest that most of the outflows result from a two-stage emplacement process. In the first stage, a turbulent, proximal part is usually emplaced downrange of the impact site *after* the other ejecta materials. In the second stage, a distal part, composed of low-viscosity melt, slowly drains via dendritic channels from the proximal deposit and flows like lava (Figure 1). A few flows have been identified that appear to have been emplaced prior to the ejecta; these flows likely result from a different mechanism.

**Proximal Part of Flows.** The proximal parts of outflows are characterized by high radar reflectivity, dendritic channel systems, and the ability to flow up slopes. About 87% of the outflows originate on the downrange side of the associated impact crater [4], and all appear to be stratigraphically higher than the other ejecta materials (Figure 2). The outflow deposits are thought to be relatively thin, because they commonly do not completely bury subjacent blocky ejecta.

**Distal Part of Flows.** The distal parts of the crater outflows commonly have a lower backscatter than the proximal parts, and some appear quite smooth (Figure 1). The distal flows are fed by material that has drained from the channels in the proximal flows. Channels not present in all flows; their formation may depend on the ratio of melt to solid clasts in the proximal deposit. The distal flows moved down slopes, filled small grabens, and were ponded by ridges, behavior that mimics flows from obvious volcanic sources.

The position of the proximal flows atop the continuous ejecta, their common occurrence downrange of the impact site, and their richness in melt make them analogous to terrestrial suevite deposits, which are turbulently emplaced [6]. The proximal flow may have originally comprised the transient crater lining, composed of vapor, melt, and shocked clasts [7]. These materials can be considered a late stage of ejecta, imparted with downrange momentum by the impactor and ejected as a turbulent cloud during crater rebound. An origin of the flows from within the craters would explain why many flows appear to originate at crater rims (Figure 2).

On Venus, suevites may contain 40% more melt than on Earth for a given crater diameter, and melt may remain molten an order of magnitude longer [8,9]. Thus, upon deposition of the proximal "suevite" part of the crater outflows, the melt fraction appears to have coalesced and drained out, creating the channels and long, thin, distal flows.

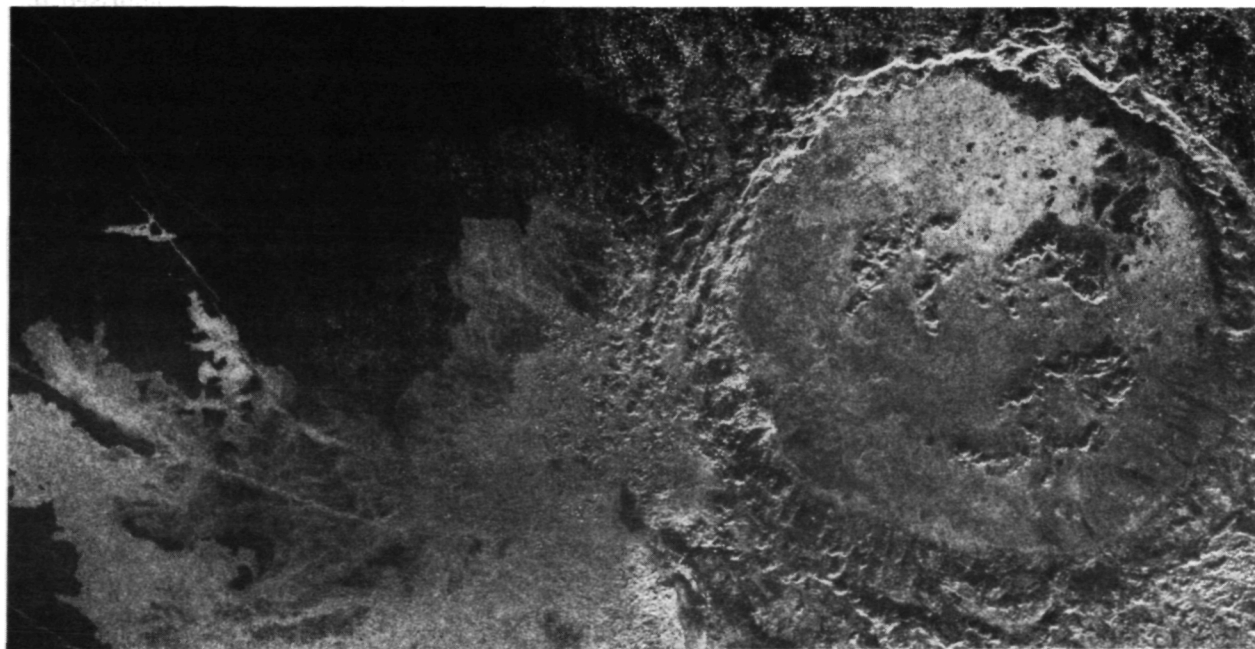
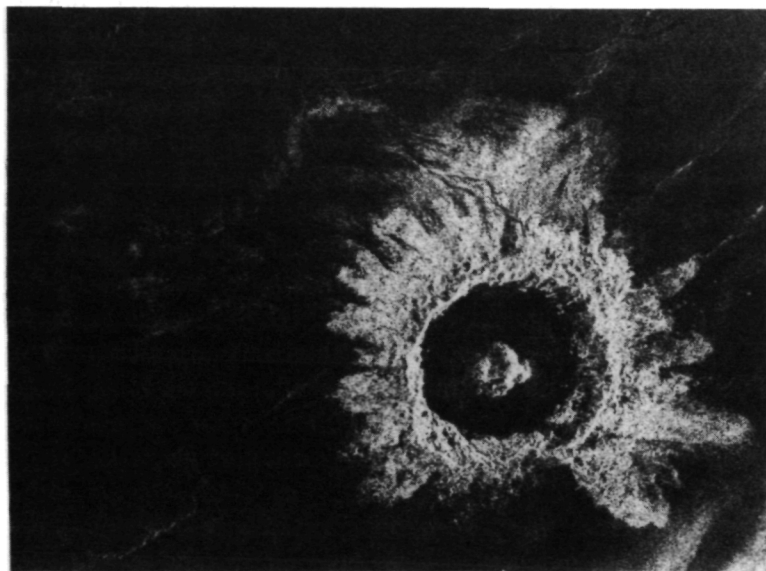
The proximal part of the outflows is best expressed at craters produced by lower angle impacts, which are identified by a missing segment of ejecta in the uprange direction (Figure 1). Craters produced by higher angle impacts may have the proximal part subdued or in some cases absent. We suggest that in these cases proximal flow deposition has occurred but is less concentrated than in lower angle impacts because the transient crater lining is not imparted with as much downrange momentum, and is thus more evenly distributed over subjacent ejecta. This probably explains why higher angle impacts are less likely to produce flows (36%) than lower angle impacts (51%). It may also explain why the flows tend to be smaller when produced by higher angle impacts, and why these flows are more numerous and less likely to be confined to a single azimuthal direction, as they are in lower angle impacts.

## TWO-STAGE MECHANISM: Chadwick D. J. and Schaber G. G.

References: [1] Schaber and Chadwick, this volume; [2] Asimow, P.D. and Wood, J.W. (1992) *J. Geophys. Res.*, 97, 13,643-13,666; [3] Chadwick, D.J. et al. (1992) Papers Presented to the International Colloquium on Venus, *LPI Contribution Number 789*, 20-21; [4] Schaber, G.G. et al. (1992) *J. Geophys. Res.*, 97, 13,257-13,303; [5] Schultz, P.H. (1992) *J. Geophys. Res.*, 97, 16,183-16,248; [6] Horz, F. (1982) *Spec. Pap. Geol. Soc. Am.*, 190, 39-54; [7] Roddy, D.J. et al. (1987) *Int. J. Impact Engng.*, 5, 525-541; [8] Ivanov, B.A. (1992) *J. Geophys. Res.*, 97, 16,167-16,181; [9] Grieve, R.A.F. and Cintala, M.J. (1992) *LPSC XXIII*, 451-452.

**Figure 1.** (Top) Kahlo crater, 36 km in diameter, located at lat. -59.85, long. 178.8. North is at the top. Note the missing segment of ejecta on the south side, indicating the uprange direction. The bright feature on the north side of the crater is the proximal deposit. Note the NW-trending channels that have fed the dark distal flow to the northwest of the crater. The distal flow has flowed downhill to the WSW.

**Figure 2.** (Bottom) Stuart crater, 69 km in diameter, located at lat. -30.75, long. 20.2. The distal flow fills a small graben and buries normal ejecta. Closer to the crater, ejecta blocks were too large to be completely inundated by the proximal flow. Note the flow on the crater rim and floor.



ORIGINAL PAGE  
BLACK AND WHITE PHOTOGRAPH

45690 3

5131-90

LPSC XXIV

267

ABS ONLY

N 94-162146

P. 3

**OXYGEN ISOTOPES AS TRACERS OF TEKTITE SOURCE ROCKS: AN EXAMPLE FROM THE IVORY COAST TEKTITES AND LAKE BOSUMTWI CRATER**

C. Page Chamberlain and Joel D. Blum, Dartmouth Laboratories for Isotope Tracers in the Environment (DLITE), Department of Earth Sciences, Dartmouth College, Hanover, New Hampshire 03755; Christian Koeberl, Institute of Geochemistry, University of Vienna, A-1010 Vienna, Austria.

Oxygen isotope studies of tektites and impact glasses provide an important tool to help in identifying the target lithologies for terrestrial impacts, including the K-T boundary impact [1]. However, such studies may be complicated by modification of the original oxygen isotope values of some source rocks during the tektite formation process either by vapor fractionation [2] or incorporation of meteoric water [3]. To further investigate the relationship between the oxygen isotopic composition of tektites and their source rocks we have studied Ivory Coast tektites and samples of impact glasses and bedrock lithologies from the Bosumtwi Crater in Ghana—which is widely believed to be the source crater for the Ivory Coast tektites [4-7]. Our preliminary results suggest that the phyllites and metagraywackes from the Bosumtwi Crater were the predominant source materials for the impact glasses and tektites and that no significant oxygen isotope modification ( $\leq 1\%$   $\delta^{18}\text{O}$ ) took place during impact melting. This contrasts with previous studies of moldavites and Australasian tektites and their sedimentary source materials which suggests a 4 to 5% lowering of  $\delta^{18}\text{O}$  due to meteoric water incorporation during impact melting [1,3,12].

In this study we have measured oxygen isotope values for each major bedrock lithology from the Lake Bosumtwi crater, impact glasses found at the crater, and Ivory Coast tektites. These data complement the original work by Taylor and Epstein [7], on the oxygen isotopes of the Ivory Coast tektites, which showed that the  $\delta^{18}\text{O}$  values were the highest of any known tektites. Taylor and Epstein [7] suggested that the Ivory Coast tektites represent impact glasses from high  $\delta^{18}\text{O}$  metasediments, soils, or deeply weathered granitic rocks which are exposed at the Bosumtwi Crater. At the time of Taylor and Epstein's study [7], however, there were no oxygen isotope data from the Bosumtwi crater target rocks for comparison.

The Bosumtwi Crater is an approximately 11 km diameter impact crater, which lies 300 km east of the Ivory Coast tektite strewn field. The bedrock is comprised of predominantly 2000 Ma [8,9] phyllites and interbedded greywackes metamorphosed to greenschist facies, that collectively belong to the Lower Birimian System. Southeast of the lake are basaltic lavas with minor interbedded greywackes of the Upper Birimian. Intruded within the metamorphic rocks are microgranite and dolerite dikes and a relatively large (~2 km in diameter) intrusive body called the Pepiakese Granodiorite. Within the crater are impact glasses and fall-back breccias (suevites) that formed during impact. The impact glasses within the crater yield K-Ar ages ranging from of 1.2 to 1.4 Ma [10] which are in close agreement with K-Ar ages of 1.1 to 1.3 Ma the Ivory Coast tektites [6,10,11].

In our study we have determined the  $\delta^{18}\text{O}$  values of the metasediments from the Lower Birimian System, the Pepiakese intrusive rocks, and the microgranites from the Bosumtwi crater. The major and trace element concentrations of these same target rocks were presented in a previous study [4]. We also determined  $\delta^{18}\text{O}$  values of 5 Ivory Coast tektites and 4 Bosumtwi impact glasses. The  $\delta^{18}\text{O}$  values of the target rocks range from a low of 8.6 to 8.9‰ for the Pepiakese intrusive to a high of 11.3 to 13.6‰ for the metasediments and microgranites (Fig. 1). The  $\delta^{18}\text{O}$  values measured here for the Bosumtwi impact glasses range from 12.6 to 14.3‰ (Fig. 1) and for the Ivory Coast tektites range from 11.7 to 12.9‰ (Fig. 1). Somewhat higher  $\delta^{18}\text{O}$  values of 12.8 to 14.6‰ were previously reported for the Ivory Coast tektites [7].

It has been argued [4], based on major and trace element data, that the Ivory Coast tektites were derived from melting a mixture of ~75% Lower Birimian System metasediments and ~25% Pepiakese intrusive rocks. The Pepiakese intrusive was thought to be a major source material for the tektites because the intrusive has high concentrations of Ni, Cr, Ca and Mg which, when mixed with the average metasediments, yields compositions similar to the tektites [4].

## OXYGEN ISOTOPES IN TEKTITES: Chamberlain C.P., Blum J.D., and Koeberl C.

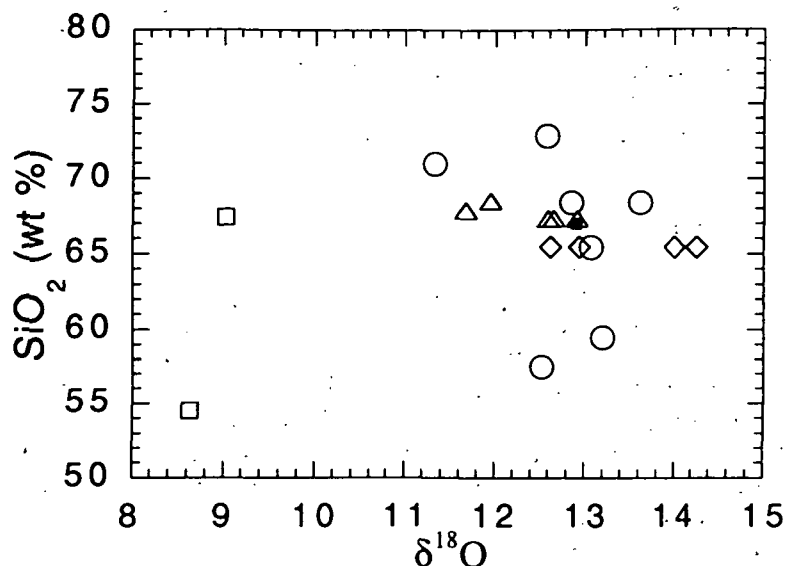


Fig. 1: Oxygen isotope values of Ivory Coast tektites (triangles), Bosumtwi impact glass (diamonds) and Bosumtwi bedrock lithologies including Lower Birimian metasediments (circles), Pepiakese intrusives (open squares) and microgranite (filled square).

The oxygen isotope data presented here support the hypothesis that the tektites and suevites were largely derived from the melting of metasediments (Fig. 1), but the  $\delta^{18}\text{O}$  values of the Pepiakese intrusive rocks are much lower than the tektites (by  $\sim 4\text{‰}$ ) and the tektites show no evidence for a major ( $>10\%$ ) contribution from this low  $\delta^{18}\text{O}$  component (Fig. 1). However, the oxygen isotope data alone cannot rule out the Pepiakese intrusive as a possible target rock for the tektites because if the impactor melted a deeply weathered portion of the Pepiakese intrusive then the  $\delta^{18}\text{O}$  values of the intrusive might be shifted towards values similar to the metasediments. Osmium isotope measurements of Ivory Coast tektites suggest a significant meteoritic component [13] which may help to explain the high refractory element content of the tektites without a large contribution from the Pepiakese intrusive.

Our data suggest that there was no significant ( $>1\text{‰}$ ) modification of oxygen isotope values during impact melting at the Bosumtwi Crater. Other studies, however, have shown that the  $\delta^{18}\text{O}$  values of tektites and source rocks can be significantly different. For example, the  $\delta^{18}\text{O}$  of moldavites are  $4.5\text{‰}$  lower than the surficial sands from which they are derived [3], and the  $\delta^{18}\text{O}$  values of Australasian tektites are  $\sim 4\text{‰}$  lower than would be expected based on proposed target lithologies [1,7,12]. To explain the lowering of  $\delta^{18}\text{O}$  values for moldavites Engelhardt et al. [4] argued that the source rocks contained a significant component ( $\sim 25\%$ ) of isotopically light oxygen from meteoric water that was mixed into the target material during tektite formation. Why are the  $\delta^{18}\text{O}$  systematics of Ivory Coast tektites different from the moldavites and Australasian tektites? One possibility is that the  $\delta^{18}\text{O}$  values of the Ivory Coast rocks have not been lowered because the metasedimentary target rocks have a relatively low porosity compared to the unmetamorphosed sedimentary rocks involved in the other two impact events. Thus, the porosity of target rocks may be an important factor controlling the oxygen isotope systematics of tektites.

**ACKNOWLEDGEMENTS:** We are grateful to WB Jones for target rocks and the Smithsonian Institutions (Washington) for Bosumtwi impact glasses. This work is supported by the NSF and the Sloan Foundation.

**REFERENCES:** [1] Blum JD and Chamberlain CP (1992) *Science*, 257, 1104-1107. [2] Walter LS and Clayton RN (1967) *Science*, 156, 1357-1358. [3] Engelhardt W et al. (1987) *GCA*, 51, 1425-1443. [4] Jones WB (1985) *GCA*, 49, 2569-2576. [5] Shaw HF and Wasserburg GJ (1982) *Earth Planet. Sci. Lett.*, 60, 155-177. [6] Koeberl C et al. (1989) *Meteoritics* 24, 187. [7] Taylor HP and Epstein S (1966) *Science*, 153, 173-175. [8] Schnetzler CC et al. (1966) *Science*, 151, 817-819. [9] Kolbe P et al. (1967) *GCA*, 31, 869-875. [10] Gentner et al. (1964) *Earth Planet. Sci. Lett.*, 2, 83-86. [11] Zahringer J. (1963) *Radioactive Dating*, IAEA, Vienna, 289-305. [12] Blum JD et al. (1992) *GCA*, 56, 483-492. [13] Koeberl C and Shirey SB (1993) LPSC XXIV (this issue).

456906

ABS ONLY

N 94-312147

CRATERING ON GASpra; Clark R. Chapman (Planetary Science Inst./SAIC, Tucson, AZ), Gerhard Neukum (DLR, Berlin/Oberpfaffenhofen, Germany), Joseph Veverka (Cornell Univ., Ithaca, NY), and Michael Belton (NOAO, Tucson, AZ)

The October 1991 *Galileo* flyby of Gaspra shows that its crater population is dominated by fresh craters several hundred meters in diameter and smaller. They appear to represent a production population because the spatial density is relatively low (few overlaps) and because fresh craters are very abundant; equilibrium could be attained at diameters near to or below the resolution limit of the best image. These craters are the first direct record of the population of main-belt asteroids some tens of meters in diameter.

We have counted, measured, and classified craters primarily from the highest resolution, "high phase" image, on which over 600 craters are visible in 90 sq. km (Fig. 1); earlier counts [1] were made on the lower resolution four-color images, which show an order of magnitude fewer craters because of the resolution limit. The population index (exponent of the differential power law approximately describing the crater sizes) has a very high negative value ( $-4.3 \pm 0.3$ , meaning that the log-log slope is "steep"), appreciably steeper than the value of -3.5 thought to reflect collisional equilibrium according to theory.

The Gaspra crater population is very different from that observed on Phobos (Fig. 2); Phobos's craters may reflect either (a) equilibrium from much greater production of the same population or (b) a different population due to circum-Martian debris. However, Gaspra's population is similar to crater populations observed on the Moon and Mars at these sizes. It is also similar to the near-Earth asteroid population recently identified by Spacewatch [2]. This lends strength to the idea that a common production function has been cratering all objects throughout at least the inner solar system, and that it is *not* a simple power law [3].

Gaspra's fresh craters are superposed on a landscape that appears "smoothed" at a vertical scale of hundreds of meters. A significant population of "soft", subdued crater-like features is visible with diameters commonly around 500 meters and larger. Some of these are associated with the linear grooves on Gaspra and may reflect sinkholes or other kinds of endogenic collapse features. Others may be pre-existing impact craters deeply blanketed or otherwise much degraded.

At its grossest scales, Gaspra is a highly irregular object. One or more "facets" were recognized in the four-color sequence, and one of these (over 8 km across) is well seen on the limb in the high-phase image. Another 5 km scale feature is visible emerging from the southern terminator in the image. We initially speculated from these images (both from approximately the same perspective) that Gaspra's shape might reflect its origin by large cratering, spallation, and chipping away from an initially larger precursor body. However, the largest of these facets would exceed the largest crater relative to body radius ever observed on a planet or satellite or expected from collisional fragmentation models. Not only would Gaspra have been disrupted and dispersed by such cratering events, but later facet-forming events would be expected to have destroyed earlier facets.

Playback in November 1992 of a full sequence of lower-resolution images of Gaspra covering a full rotation period has clarified the question of large or very large craters on Gaspra. Much of Gaspra's surface has now been seen. Two intermediate size craters about 3 km in diameter have been identified, but there is no crater approaching even half the radius of Gaspra. Furthermore, the new perspectives of Gaspra reveal a peanut-like shape, suggestive (although less obvious) of the contact binary shapes of the two other imaged asteroids, Castalia [4] and Toutatis [5]. It is intriguing that the most prominent grooves observed on the high-phase image are near the "neck" between the two "lumps".

We expect that Gaspra, as we now know it, was created from a larger parent body by a sequence of collisions beginning 4.5 b.y. ago. Perhaps Gaspra's gross configuration of two connected lumps reflects a part of a rubble pile or compound precursor body that was disrupted. Subsequent large, sub-catastrophic

CRATERING ON GASPPRA: C.R. Chapman *et al.*

collisions would have seismically shaken proto-Gaspra and, provided that ejecta velocities are low, created a "rubble pile" or at least deep, coarsely worked surface layers analogous to the lunar megaregolith. Perhaps Gaspra's subdued craters enable us to peer back through this last collision.

Since the creation of Gaspra's present surface, there has been cratering by the steep production function. The density of such craters is very low at visible size ranges, implying that Gaspra is relatively youthful. Scaled to a calculated 0.5 Gyr age for bodies of its size, based on asteroid collision models and assuming that Gaspra does not have metallic strength, we estimate its cratering lifetime could be as young as 0.2 Gyr, with large (factor 3) modelling uncertainties.

The cumulative volume of all visible craters could create a regolith only <10 meters deep, even if most ejecta were retained by Gaspra's weak gravity. Given Gaspra's very low escape velocity, most such ejecta are probably lost, so Gaspra's modern soil-like regolith, which is produced by the steep production function just as it is for the upper several meters on the Moon, is probably very thin: centimeters to a few meters at most. Gaspra could even be essentially bare. In any case, this is an inadequate environment for any mature weathering and reworking of Gaspra's visible surface during the last 0.2 Gyr. Indeed, depending on how far the steep production function extends to craters as small as ten meters, Gaspra could be subject to substantial erosion or "sand-blasting" by the saturation of small impacts. Any pre-existing megaregolith could have been eroded away to depths of tens of meters or more during the past 0.2 Gyr.

References: [1] Belton, M.J.S. (1992), *Science*, **57**, 1647-1652; [2] D. Rabinowitz (1993) *Astrophys. J.*, in press; [3] G. Neukum *et al.* (1975) *The Moon*, **12**, 201-229; [4] R. S. Hudson (1992) *EOS*, **73**, Oct. 27, 335; [5] S. Ostro (1993), presentation at "Hazards Due to Comets and Asteroids" meeting, Tucson, AZ, Jan. 1993 (see *NY Times*, 4 Jan. 1993, pg. 1).

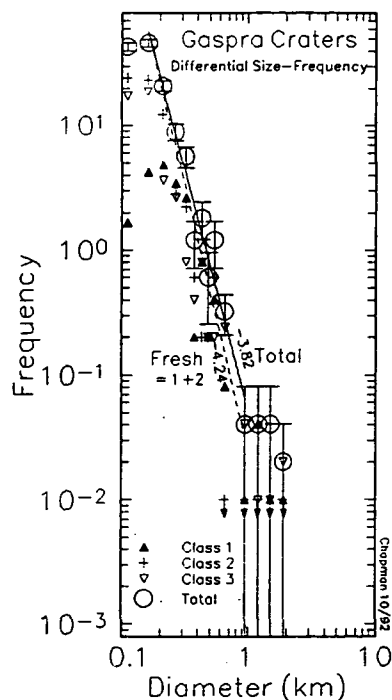


Fig. 1. Differential size-frequency plot for three morphologic classes of craters on Gaspra (1=very fresh, 2=nearly fresh, 3=soft). Least squares fits for classes 1+2 and for the total are shown, excluding incomplete data.

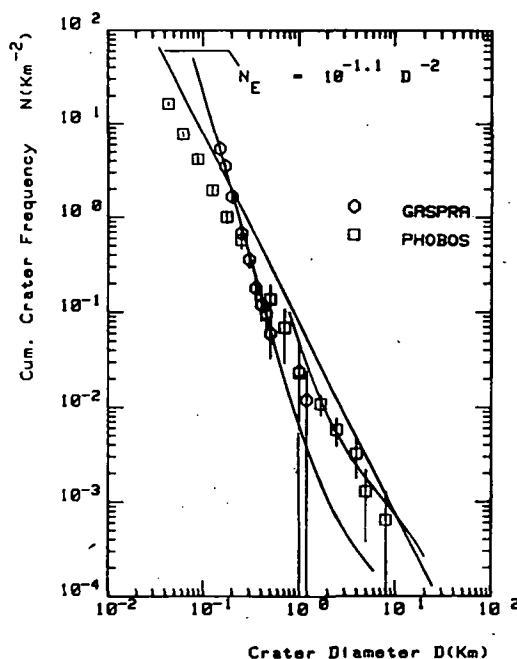


Fig. 2. Independent cumulative counts of primarily fresh Gaspra craters compared with (a) Phobos counts due to Thomas and Veverka and (b) a model equilibrium line.

456909

5133-91  
ABS ONLY

LPSC XXIV

271

N 94312148  
A 2

**BASAL SCARP, PALEOGLACIER, AND FISSURE FLOWS OF  
ELYSIUM MONS, MARS; Mary G. Chapman, U.S. Geological Survey,  
Flagstaff, Ariz. 86001**

Geological mapping at 1:500,000 scale of the Granicus Valles area west of Elysium Mons (MTM quadrangles 30227, 30222, and 25227) indicates that (1) the oldest deposits in the area are Upper Hesperian lavas of the Elysium shield; (2) a basal scarp formed by Early Amazonian faulting around the northwest flank of Elysium Mons triggered growth of Elysium Fossae; (3) a glacier or an ice sheet west and north of the scarp was of long duration; (4) water and lava flows from Elysium Fossae became dominant during and after glacial recession; and (5) the last volcanic-fissure-related flows resulted in linear chains of small domes on the Elysium shield.

A northeast-trending scarp forms a boundary between the shield of Elysium Mons and the varied materials that fill lower lying Utopia Planitia [1]. Upper Hesperian lavas of the shield [2] are cut by the scarp (between lat 28.1° N., long 223.1° and lat 28.8° N., long 222.4°), but younger shield lavas [2] partly bury it. The scarp is interpreted to be the expression of a hinge fault (west side down) that may have been associated with extensional regional stress along a pre-existing zone of weakness [1]; because the scarp lies along the trend of a major wrinkle ridge in Lower Hesperian ridged plains at about lat 16°-19° N., long 230°, about 600 km southwest of the map area [3]. The scarp was instrumental in the growth of Elysium Fossae northwest of the volcano [1]. Six major theater-headed fossae, including Granicus Valles, lie along the scarp. The fault likely breached a perched water source beneath the Elysium shield; spring sapping along fissures above the scarp could then have caused the theater-headed fossae to form. Hot-spring activity is very possible, as this sapping is closely associated with regional volcanism. Other older parallel scarps above and east of the basal scarp appear to be the foci of other Elysium Fossae, but no evidence of water erosion or deposition is associated with these fossae.

The basal scarp appears to have been the west boundary of a glacier or ice sheet that covered the area during a prolonged period in the Early Amazonian. Although some workers have interpreted all rough-textured deposits northwest of Elysium as lahars [4] or erosional plains [5], many high-standing, rough, and flat-topped mounds trend along fissures of the Elysium Fossae west and north of the scarp; the mounds resemble Icelandic table mountains and moberg ridges. Previous workers have suggested that these types of subglacial volcanoes occur in other areas of Elysium [6,7,8] and have found evidence of volcano-ground ice interactions in the general area [5,9]. The mounds are associated with low-standing, much smoother appearing deposits containing nested concentric (collapse) pits [9,10] and irregular channels. These deposits are locally bounded by lobate scarps and have been termed lahars [4], but they are more likely jökulhlaups formed by eruption of hot lava beneath the ice sheet. The Granicus Valles are suggested to have been initiated by subglacial fluvial activity [8]; this interpretation is supported by the occurrence of an inner channel ridge that bears a striking resemblance to some channel eskers noted elsewhere on Mars and Earth [11]. The ice sheet may have been a frozen remnant of a paleolake in Utopia Planitia [12, 13] that lapped against the basal scarp of Elysium Mons. The northern part of the mons, north of the scarp, may have been covered by a glacier, because it contains ice-related features [5,9], table mountains, and moberg ridges.



## SCARP, PALEOGLACIER OF ELYSIUM MONS: Chapman, M.G.

All of the rough-textured deposits discussed above are cut by channels and embayed by both shield and fossae lavas [1], indicating that water and lava flows from Elysium Fossae became dominant after glacial recession.

Some of the youngest volcanic activity in the area is expressed by small domes and associated flows. The domes occur in linear chains paralleling the trend of Elysium Fossae and are interpreted to be volcanoes that formed along fissures on the flank of Elysium Mons. They are products of the last fissure-related eruptions on the Elysium shield and attest to the depletion of the area in ground and surface ice.

Hot springs along the basal scarp and subglacial volcanoes west of the scarp are likely locations for nonphotosynthetic microbial ecosystems in subsurface habitats on Mars [14]. For this reason the northwestern part of Elysium Mons is a potential area for future Mars missions to determine the prior existence of exobiologic life.

References

- [1] Chapman, M.G. (1992) LPSC XXIII, 221-222.
- [2] Tanaka, K.L., Chapman, M.G., and Scott, D.H. (1992) USGS Map I-2147.
- [3] Scott, D.H., and Tanaka, K.L. (1986) USGS Map I-1802-A.
- [4] Christiansen, E.H. (1989) *Geology*, 17, 203-206.
- [5] Mouginis-Mark, P.J., Wilson, L., Head, J.W., Brown, S.H., Hall, J.L., and Sullivan, K.D. (1984) *Earth, Moon and Planets*, 30, 149-173.
- [6] Hodges, C.A., and Moore, H.J., (1978) LPSC IX, 523-525.
- [7] Allen, C.C. (1979) *JGR*, 84, 8048-8059.
- [8] Anderson, D.M. (1992) MSATT LPI Tech. Rep. 92-08, 1.
- [9] Mouginis-Mark, P.J. (1985) *Icarus*, 64, 265-284.
- [10] Fagan, J.J., Weiss, D., Steiner, J., and Franke, O.L. (1981) NASA TM 84211, 308-311.
- [11] Kargel, J.S., and Strom, R.G. (1992) *Geology*, 20, 3-7.
- [12] Baker, V.R., Strom, R.G., Gulick, V.C., Kargel, J.S., Komatsu, G., and Kale, V.S. (1991) *Nature*, 352, 589-594.
- [13] Scott, D.H., Chapman, M.G., Rice, J.W. Jr., and Dohm, J.M. (1992) LPSC Proc., 22, 53-62.
- [14] Boston, P.J., Ivanov, M.V., and McKay, C.P. (1992) *Icarus*, 95, 300-308.

456913

5134-46  
ABS ONLY

LPSC XXIV

N 94-12149<sup>273</sup>

P. 2

C

# SHOCK INDUCED REACTION IN CHICXULUB TARGET MATERIALS (CaSO<sub>4</sub> AND SiO<sub>2</sub>) AND THEIR RELATION TO EXTINCTIONS

Guangqing Chen and Thomas J. Ahrens, Lindhurst Laboratory of Experimental Geophysics, Seismological Laboratory, California Institute of Technology, Pasadena, CA 91125

The global platinum element rich layer, presence of shocked quartz grains (in some cases with stishovite) and observation of tektite rich layer precisely at the K-T boundary are the three major arguments for the extinction bolide impact hypothesis of Alvarez *et al.*[1]. Tektites (spherules) from Beloc in Haiti and Mimbrel in Mexico received particular interest because of their geological proximity to the Chicxulub impact structure, which is a leading candidate for at least one of the K-T impact craters. Although in most localities the original glass has weathered to clay minerals, some shock-induced glass is found in outcrops and drill cores which is used for <sup>38</sup>Ar/<sup>39</sup>Ar dating[2]. The glassy tektites have been found to be chemically similar and coeval at 65.0 Ma with Chicxulub melt rock.

Two kinds of K-T spherules were discovered: (1) a silicic black glass, and (2) a yellow glass, enriched in Ca, Mg and S. The high sulfur content of the glass and the abundance of anhydrite (CaSO<sub>4</sub>) in the carbonate-evaporite sequence observed in Drill Holes Y-1 and Y-2 at Chicxulub prompted studies of calcium sulfate devolatilization. Two types of reactions are considered:



Reaction (1) is found both theoretically and experimentally to require a higher temperature (Fig. 1)[3, 4]. Reaction (2) involves silicate, which, for simplicity, we employ SiO<sub>2</sub> in the following:

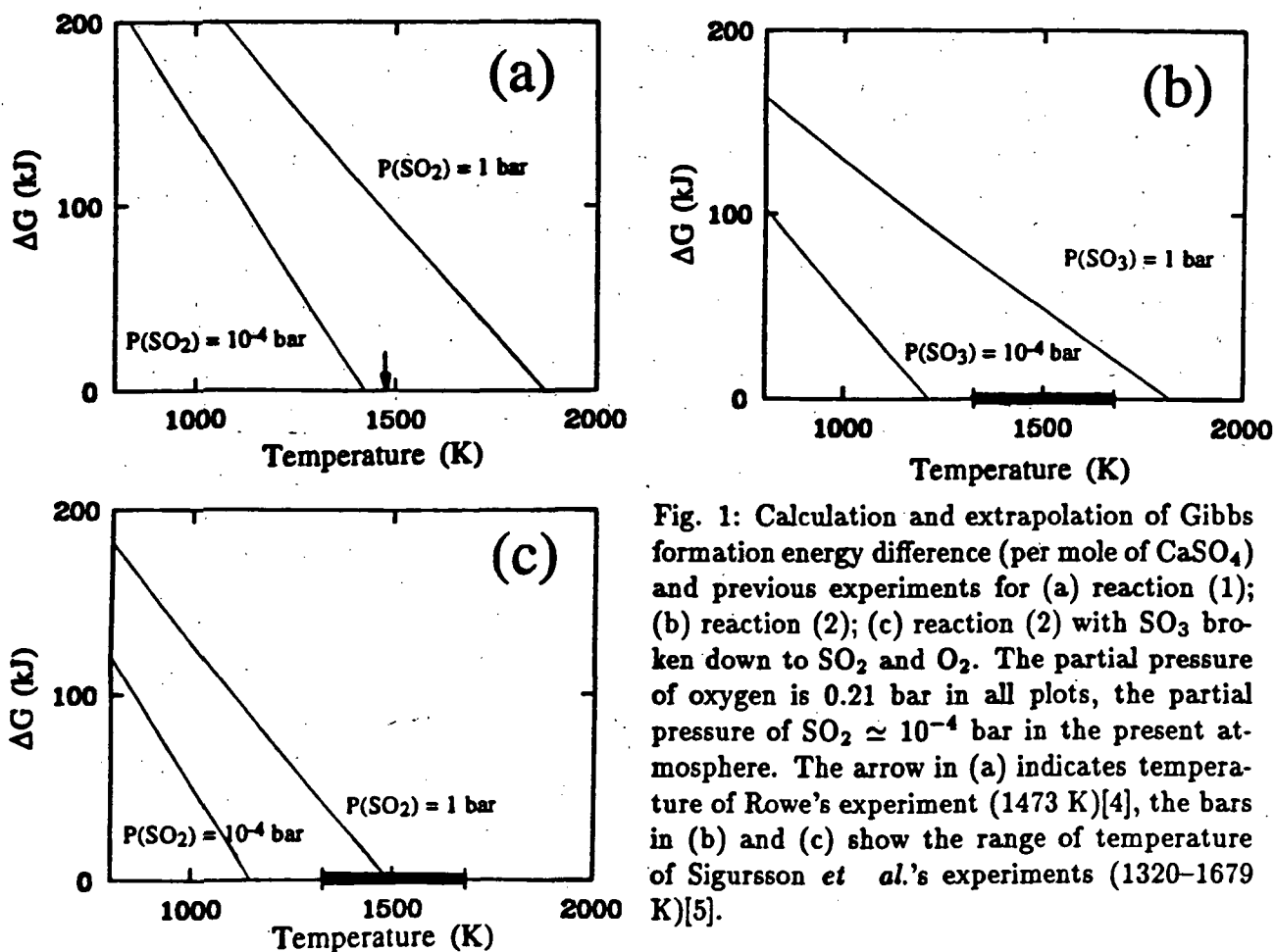
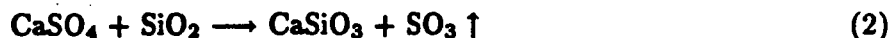


Fig. 1: Calculation and extrapolation of Gibbs formation energy difference (per mole of CaSO<sub>4</sub>) and previous experiments for (a) reaction (1); (b) reaction (2); (c) reaction (2) with SO<sub>3</sub> broken down to SO<sub>2</sub> and O<sub>2</sub>. The partial pressure of oxygen is 0.21 bar in all plots, the partial pressure of SO<sub>2</sub>  $\approx 10^{-4}$  bar in the present atmosphere. The arrow in (a) indicates temperature of Rowe's experiment (1473 K)[4], the bars in (b) and (c) show the range of temperature of Sigursson *et al.*'s experiments (1320–1679 K)[5].

## SHOCK INDUCED REACTION: Chen G. and Ahrens T. J.

Synthetic glasses compositionally similar to Haitian glasses were produced from an anhydrite plus andesite mix by heating in a normal atmosphere to temperatures of 1,320–1,679 K[5]. In order to simulate the K-T impact more closely, we studied the second reaction under shock conditions.

A 20 mm gun was used to launch projectiles up to 2 km/s. The starting mix of anhydrite and quartz powders (grain size  $\sim 4\text{--}30\ \mu\text{m}$ ) with molar ratio 0.9 : 1 was encased in stainless steel containers. Shock pressures are calculated using one dimensional impedance match method with an averaged Hugoniot from high pressure phase quartz and anhydrite (Table 1).

Table 1: Parameters of the anhydrite-quartz recovery experiments

Shot number	Sample porosity	Flyer plate	Impact velocity (km/s)	Pressure (GPa)
1098	18%	W	2.06	43.7
1099	24%	Ta	1.58	27.4

The recovered samples were analyzed with SEM. A (quenched) melted phase is found extensively in products of shot #1098. Calcium silicate is present and sulfur content decreases by a factor of about 4 relative to calcium (i. e. melt composition:  $(\text{CaSO}_4)_{0.25}(\text{CaSiO}_3)_{0.75}$ ). For shot #1099, very little (no more than a few percent) starting material reacted. Thus these two experiments confined the range of threshold pressure for the reaction. Comparing to calcium carbonate devolatilization, which starts at  $\sim 10\ \text{GPa}$ [6], anhydrite devolatilization is considerably more difficult.

Degassed sulfur oxides could induce severe negative environmental changes. After oxidation and hydrolysis of  $\text{SO}_2$  and  $\text{SO}_3$ , sulfuric acid aerosol can form. The aerosol particles backscatter the solar radiation and this results in a rapid lowering of the earth surface temperature. Determining the amount of sulfur oxides driven into the atmosphere upon the formation of a structure like the Chicxulub crater is essential to the evaluation of the intensity of the effect. There is a factor-of-30-discrepancy between the estimates by Sigursson *et al.*[5] and Brett[7] in the mass of sulfur oxides which could have been induced in the Chicxulub impact event. Sigursson *et al.*'s estimate of  $6.4 \times 10^{15}\ \text{g}$  of sulfur mass is based on the total amount of the yellow glass inferred to be produced ( $5 \times 10^{16}\ \text{kg}$ ), (extrapolated from its abundance in the Beloc section). Degassed sulfur mass is then inferred from sulfur that remains in the glass, using degassing fractions found in historic volcanic eruptions. Brett's calculation ( $4 \times 10^{17}\ \text{g}\ \text{SO}_2$ , or  $2 \times 10^{17}\ \text{g}$  in sulfur mass from Chicxulub) assumes complete degassing within radius of 13.8 km of a 500 m-thick anhydrite bed at 1 km below surface. We think Sigursson's estimate does not include  $\text{SO}_2$  derived from reaction (1), which does not produce yellow glass, and may be an underestimate. Brett's value is likely an overestimate because evaporite degassing might be incomplete due to the relatively high pressure required. Our experiments suggest carbonate devolatilization was more extensive than that of sulfates, as suggested by Blum and Chamberlain[8], therefore in the long term  $\text{CO}_2$  induced global warming might have predominated over the cooling effect of  $\text{H}_2\text{SO}_4$  aerosol; but on a short time scale,  $\text{H}_2\text{SO}_4$  cooling and acid rain could be important extinction mechanisms.

[1] L. W. Alvarez, W. Alvarez, F. Asaro, H. V. Michel, *Science*, 208, 1095 (1980). [2] C. C. Swisher III, J. M. Grajales-Nishimura, A. Montanari, S. V. Margolis, P. Claeys, W. Alvarez, P. Renne, E. Cedillo-Pardo, F. J. M. R. Maurrasse, G. H. Curtis, J. Smit, M. O. McWilliams, *Science*, 257, 954 (1992). [3] R. A. Robie, B. S. Hemingway, J. R. Fisher, *Thermodynamic Properties of Minerals and Related Substances at 298.15 K and 1 Bar ( $10^5$  Pascals) Pressure and at Higher Temperatures*. *USGS Bull.*, 1452. [4] J. J. Rowe, G. W. Morey, C. C. Silber, *J. Inorg. and Nucl. Chem.*, 29, 925 (1967). [5] H. Sigurdsson, Ph. Bonté, L. Turpin, M. Chaussidon, N. Metrich, M. Steinberg, Ph. Prade, S. D'Hondt, *Nature*, 353, 839 (1991). [6] J. D. O'Keefe, T. J. Ahrens, *Nature*, 338, 247 (1989). [7] R. Brett, *Geochim. et Cosmo. Acta*, 56, 3603 (1992). [8] J. D. Blum, C. P. Chamberlain, *Science*, 257, 1104 (1992).

456914

N94-3P2150

**LEW88516 AND SNC METEORITES;** J. H. Chen and G. J. Wasserburg, The Lunatic Asylum, Div. of Geological and Planetary Sciences, California Institute of Technology, Pasadena, CA 91125

We report on the isotopic composition of Pb and the concentration of Pb, U and Th in a sample of LEW88516 (LEW). LEW was a 13-g stone recovered from Antarctica and was classified as a new member of the Shergottite group [1,2,3]. This work was undertaken with the hope that LEW might yield new information to elucidate further the origin and evolution of Shergottites and other SNC meteorites. We have previously studied U-Th-Pb in other Shergottites, namely Shergotty, Zagami, EETA79001 and ALHA77005 [4,5] as well as Nakhla. The results indicate that the initial leads of these Shergottites were well defined, were distinct from each other, and have high  $^{204}\text{Pb}/^{206}\text{Pb}$  (from 0.0652 to 0.0739). These leads evolved in different reservoirs over most of solar system history in a low  $^{238}\text{U}/^{204}\text{Pb}(\mu) \approx 5$  environment. The U-Th-Pb isotopic systems are quite regular which unambiguously indicate an event of U-Th-Pb fractionation at  $\sim 200$  m.y. in accord with Shih *et al.* [6]. The details of the data arrays are complex. The young age is in general agreement with some of the ages obtained by other methods, but precise concordance between the different methods is not established.

Through the courtesy of the consortium led by H. Y. McSween, a 0.3-g interior sample of LEW was allocated to us for this work. This sample was processed in the Meteorite Processing Laboratory at the Johnson Space Center, Houston, Texas. The LEW sample was analyzed the same way as those described previously in our laboratory [4]. LEW was first etched in a mixture of 2 ml 1 M HBr and 2 ml 2 M HCl at  $75^\circ\text{C}$  for 1 hour. We expected that this treatment would remove both surficial U-Th-Pb and dissolve accessory minerals including troilite, whitlockite and chlorapatite. Some of the other minerals as well as mesostasis and glass might also be attacked. After the leach solution was removed, the sample was etched again in 2 ml 1 M  $\text{HNO}_3$  at  $\sim 75^\circ\text{C}$  for 1 hour. This step would further attack the mesostasis and glass, but not seriously attack the major minerals. The residue was separated from the leach solution and was dissolved in HF,  $\text{HNO}_3$ ,  $\text{HClO}_4$ , HCl and HBr. A mixture of  $^{233}\text{U}$ - $^{236}\text{U}$ - $^{205}\text{Pb}$  and  $^{229}\text{Th}$  tracers was added to the leaches and residue before further treatments.

The U-Th-Pb results on LEW and other Shergottites are shown in Table 1. The "total" was calculated from the data of leaches and residue. The first leach removed more than 50% of U, Th and Pb, but did not seem to preferentially dissolve any phases rich in U, Th but poor in Pb. The second leach also did not significantly fractionate U-Th-Pb. The lead isotopic composition and the  $^{232}\text{Th}/^{238}\text{U}(\kappa)$  ratios in both leaches are very similar. The residue has less radiogenic lead and low  $\kappa$  and  $\mu$  values indicating some U-Th-Pb fractionation. The total LEW yields a  $\mu$  value of 4.9 which is from factors of 2 to 3.5 lower than those of other Shergottites (see Table 1). The lead isotopic composition of leaches and residue in LEW are similar to those of other Shergottites in particular, ALHA77005. In a  $^{207}\text{Pb}/^{206}\text{Pb}$  versus  $^{204}\text{Pb}/^{206}\text{Pb}$  diagram, the LEW data plot near the 4.56 AE isochron (Fig. 1). The lead data indicate evolution of the LEW parent body in a reservoir with low  $\mu < 5$  (Fig. 1). The U-Pb isotopic relationships (Fig. 2) for LEW generally follow those of other Shergottites. These U-Pb data suggest a simple two-stage evolution of a  $\sim 4.5$ - $4.65$  AE old parent body which had experienced a young ( $\sim 170$  m. y.) event with lead loss.

In summary, the new results on LEW are remarkably similar to those of ALHA 77005 and supports the other observations based on the mineralogy, petrology and bulk composition. The clear distinction between the Shergottites and Nakhla ( $S \neq N \approx C$ ) is confirmed [5]. We consider that the Shergottites and possibly all the SNCs were derived from an impact on the regolith of a differentiated terrestrial type planetary body (Mars?) with a high content of volatiles as compared to the earth.

Refs. [1]Mason (1991) *Antarctic Meteorite Newsletter* 14:2,19. [2]Lindstrom *et al.* (1992) *LPSC* 23,783. [3]Harvey and McSween (1992) *Meteoritics* 27,232. [4]Chen and Wasserburg (1986) *GCA* 50,955. [5]Chen and Wasserburg (1987) *LPSC* 17, 113. [6]Shih *et al.* (1982) *GCA* 46,2323.

## LEW88516 AND CHONDRITES: Chen J. H. and Wasserburg G. J.

Table 1. Shergottite U-Th-Pb data

Samples	$^{238}\text{U}^a$	$^{232}\text{Th}^a$	$^{204}\text{Pb}^a$	$\frac{^{208}\text{Pb}}{^{206}\text{Pb}}$	$\frac{^{207}\text{Pb}}{^{206}\text{Pb}}$	$\frac{^{204}\text{Pb}}{^{206}\text{Pb}}$	$\frac{^{232}\text{Th}}{^{238}\text{U}}$	$\frac{^{238}\text{U}}{^{204}\text{Pb}}$
LEW88516								
Leach-1	0.0195	0.0795	0.0030	2.4411 (50)	0.9372 (21)	0.0718 (3)	4.08	6.55
Leach-2	0.0056	0.0223	0.0010	2.4574 (51)	0.9435 (12)	0.0714 (3)	3.97	5.84
Residue	0.0055	0.0154	0.0023	2.5396 (54)	0.9730 (12)	0.0768 (3)	2.77	2.41
TOTAL	0.0306	0.1172	0.0063	2.4785 (52)	0.9509 (19)	0.0735 (2)	3.82	4.91
EETA79001	0.0784	0.345	0.0071	2.2881 (39)	0.8966 (14)	0.0642 (1)	4.40	11.00
ALHA77005	0.0628	0.2526	0.0042	2.4309 (27)	0.9308 (5)	0.0715 (1)	4.02	15.10
Shergotty-3A	0.504	1.892	0.0291	2.3793 (11)	0.9210 (4)	0.0681 (1)	3.75	17.30
Shergotty-3C	0.4169	1.717	0.0258	2.3741 (20)	0.9200 (7)	0.0678 (1)	4.12	16.13
Zagami	0.3847	1.582	0.0371	2.4497 (18)	0.9519 (6)	0.0717 (1)	4.11	10.38

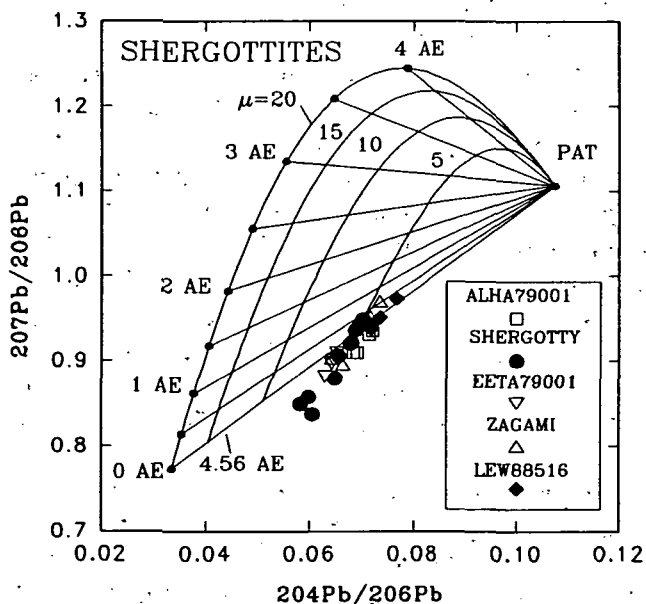
<sup>a</sup>Abundances (nmol/g)

Figure 1.

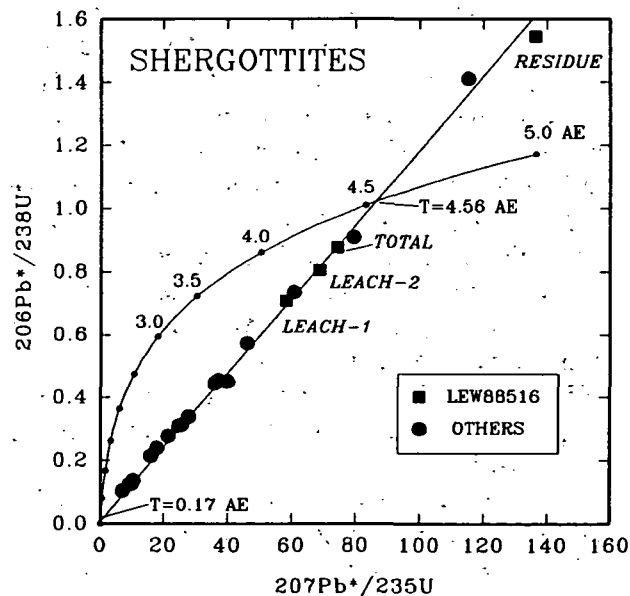


Figure 2.

456917

S136-90

LPSC XXIV

277

NBS N941251

**Th AND U ABUNDANCES IN CHONDRITIC METEORITES;** J. H. Chen, G. J. Wasserburg and D. A. Papanastassiou, The Lunatic Asylum, Division of Geological and Planetary Sciences, California Institute of Technology, Pasadena, CA 91125

P2

We present new precise analyses of  $^{232}\text{Th}/^{238}\text{U}$  in CI and CM meteorites. The relative abundance of these nuclides is important in estimates of the age of r-process elements [1,2,3]. The cosmochronology based upon the  $^{232}\text{Th}/^{238}\text{U}$  ratio ( $\kappa$ ) as was first proposed by Fowler and Hoyle [1] depends on the precise determinations of these two different elements in meteorites and on the production ratios. Both parameters are subject to substantial errors. Recent recalculations of this chronology have used selected values from compilations but do not adequately address the errors in terms of a reliable data base [3]. Morgan and Lovering [4,5] provided extensive neutron activation analyses for ordinary chondrites which yield an average  $\kappa$  of  $3.6 \pm 0.4$ . Their work on carbonaceous chondrites showed a wide range in  $\kappa$  from 2 to 6. More recent investigations by isotopic dilution have established: a) highly variable  $\kappa$  from 2.7 to 11 in Allende Ca-Al-rich inclusions and a value of 3.6 in the Orgueil CI1 chondrite [6,7]; b) a range from 2.71 to 6.63 for 7 L-type chondrites [8] and a range from 2.7 to 4.4 for 6 L, H, and LL chondrites [9]. The compilations of Anders and Ebihara [10] and Anders and Grevesse [11] are often cited for  $(^{232}\text{Th}/^{238}\text{U})_{\odot}$  and are based on a single Th analysis of Orgueil. While we consider their data selection to be reasonable, we do not consider this as an adequate basis for cosmochronological calculations.

We have acquired a set of high precision  $^{238}\text{U}$  ( $C_U$ ) and  $^{232}\text{Th}$  ( $C_{Th}$ ) concentration data by selecting different sample sizes and different specimens. As it is well recognized that carbonaceous chondrites have undergone aqueous alteration attributed to processes in the asteroidal source, we have measured  $C_U$  and  $C_{Th}$  in various acid leaches and residues to determine variations in  $\kappa$  that could reflect U mobilization or to the heterogeneous distribution of trace minerals. We also looked for isotopic heterogeneity in U. The  $^{238}\text{U}/^{235}\text{U}$  ratios were measured in most samples and they all agree within  $\sim 1\%$  with normal terrestrial U. Meteorites were dissolved in acids; residues were further attacked in teflon bombs. Four samples of Murchison, CM2, ranging from 0.1 to 2.9 g were analyzed (Table 1) and show ranges of  $\kappa$  from 3.37 to 4.16. To ascertain whether U and Th reside in labile sites, a 3.13-g sample of Murchison was leached in water and then in dilute HCl for 24 hours at  $80^\circ\text{C}$ . Although carbonates, sulfates and other phyllosilicates are ubiquitously present in Murchison, these leaches do not remove a significant amount of U and Th (#5, Table 1). The values of  $C_U$ ,  $C_{Th}$ , and  $\kappa$  in the residue are very close to other Murchison samples. To further investigate the effect of strong acid leaches, another 3.29-g sample of Murchison was etched for 8 days at  $80^\circ\text{C}$  with 6M HCl and then 7M  $\text{HNO}_3$  (#6, Table 1). The results show that in the HCl leach 63% U and  $\sim 40\%$  Th were removed. In the  $\text{HNO}_3$  leach,  $\sim 22\%$  and  $\sim 47\%$  Th were removed. The remaining residue has  $\sim 16\%$  U and  $\sim 13\%$  Th and a  $\kappa$  value of 3.8. The total  $C_U$  and  $C_{Th}$  in #6 agree with the previous analyses of Murchison, but leaches and residue clearly show major Th/U fractionation during leaching. The HCl leach removes more U than Th while the  $\text{HNO}_3$  leach removes Th preferentially. We earlier reported the U-Th results on a small powdered sample (#1, Table 1) of Orgueil [12] which shows a low  $\kappa=2.59$ . In this work, we analyzed two larger samples (#2 and #3, Table 1). The new results show  $\kappa$  of 3.68 and 3.77 respectively. In comparison, the Orgueil sample #1 has the same  $C_{Th}$  but has much higher  $C_U$ . Orgueil contains up to 5 volume % carbonates and abundant sulfates which present strong evidence for the action of an aqueous fluid on the CI parent body. To investigate whether U and Th in Orgueil are more labile than in Murchison, we treated another sample (#4, Table 2) with the following acids for 1 to 3 hours at  $80^\circ\text{C}$ : dilute acetic acid, 0.1 M HCl, 6M HCl, 7M  $\text{HNO}_3$ , and dissolved the residue separately. The U,Th results shown in Table 1 indicate that 1) large degree of Th/U fractionation in each leach, 2) the acetic acid removed a large amount of U (20%), but little Th (1%), 3) 6M HCl removes over 81% Th and 55% U, 4) residue has less than 3% U and Th, and 5) total sample has the same  $C_U$ ,  $C_{Th}$  and  $\kappa$  as the others. Another Orgueil sample (#5) which was consisted of  $\sim 30\%$  fusion crust was also treated with acetic acid and the residue dissolved without any further acid leach. The low Th content in the dilute HCl leach is most probably due to the insolubility of Th in this acid. The results also show 1) the acetic acid removed a large fraction (15%) of U, but little Th (0.5%), 2) the residue has a  $\kappa=3.57$  and 3) the total has a lower  $\kappa=3.07$ . We separated a 0.054-g sample of fusion crust ( $>80\%$ ). The result shows indeed that fusion crust contains 80% higher U and 20% higher Th than the average of other Orgueil. It is evident that a large fraction of U (15 to 20%) in Orgueil resides in labile sites which may have been produced by aqueous alterations. This is distinct from what we observed for Murchison. From Rb-Sr systematics, Macdougall *et al.* [13] concluded that carbonates in Orgueil had crystallized within 100 m.y. of the formation of the parent body. They also concluded that at least some of the Ca-sulfate present had formed at some later time. We also analyzed total rock samples of the CM2 group:

Th AND U ABUNDANCES IN CHONDRITIC METEORITES: Chen J.H. *et al.*

Adelaide, Belgica, Mighei, Murray; CO3 group: Allende, Ornans, Kainsaz; L group: Barwell, Glatton, Leedey and LL group: St. Severin. The results of all analyses, including prior high precision data [8,9,12] are shown in Fig. 1. There is a wide range for  $\kappa$  from 2.7 to 6.6; (Fig. 2) in agreement with previous workers. For all chondrites we obtain  $3.9 \pm 0.8$ . For CI and CM2 carbonaceous chondrites, using our new data and that of Tatsumoto *et al.* [6] we obtain a well-defined mean of  $3.7 \pm 0.1$  (Orgueil #1 is excluded). Insofar as CI and CM meteorites represent the Holy Grail, this is our best estimate for this parameter. Based on these results we consider that  $^{232}\text{Th}/^{238}\text{U}$  in chondrites shows a highly peaked distribution at  $\sim 3.7$ . Division Contribution 5233(797).

References: [1]Fowler and Hoyle (1960)*Ann. Phys.* 10, 280. [2]Schramm and Wasserburg G. J. (1970) *Ap.J.* 162, 57. [3]Cowan *et al.* (1991) *Ann. Rev. Astronomy Astrophys.* 29. [4]Morgan and Lovering (1967). [5]Morgan and Lovering (1968) *Talanta* 15, 1079. [6]Tatsumoto *et al.* (1976) *GCA* 40, 617. [7]Chen and Tilton (1976) *GCA* 40, 635. [8]Unruh (1982) *EPSL* 58, 75. [9]Hagee *et al.* (1990) *GCA* 54, 2847. [10]Anders and Ebihara (1982) *GCA* 46, 2363. [11]Anders and Grevesse (1989) *GCA* 53, 197. [12]Chen *et al.* (1992) *LPSC XXIII*, 223. [13]Macdougall *et al.* (1984) *Nature* 307, 249.

Table 1. Murchison and Orgueil U-Th data

Murchison	<sup>238</sup> U (pM/g)	<sup>238</sup> U (%)	<sup>232</sup> Th (pM/g)	<sup>232</sup> Th (%)	<sup>232</sup> Th/ <sup>238</sup> U	Orgueil	<sup>238</sup> U (pM/g)	<sup>238</sup> U (%)	<sup>232</sup> Th (pM/g)	<sup>232</sup> Th (%)	<sup>232</sup> Th/ <sup>238</sup> U
#1 WR	53.0	--	220.1	--	416 (2)	#1 WR	50.6	--	131.2	--	2.59 (1)
#2 WR	45.3	--	160.0	--	3.53 (1)	#2 WR	33.4	--	125.9	--	3.77 (5)
#3 WR	43.7	--	177.0	--	4.05 (3)	#3 WR	35.5	--	130.5	--	3.68 (1)
#4 WR	50.6	--	170.4	--	3.37 (5)	#4					
#5						HAc	6.6	21	1.0	1	0.150 (1)
Water	0.02	0.05	0.014	0.008	0.60 (5)	0.1M HCl	4.5	14	6.3	5	1.410 (2)
0.1M HCl	0.02	0.04	0.002	0.001	0.13 (5)	6M HCl	17.5	55	101.0	81	5.76 (3)
Residue	43.4	99.9	170.1	100	3.92 (4)	7M HNO <sub>3</sub>	2.4	55	12.7	10	5.33 (2)
Total	43.4	100	170.1	100	3.92 (4)	Residue	0.9	3	3.3	3	3.87 (2)
#6						Total	31.8	100	124.3	100	3.91 (2)
6M HCl	28.5	62.9	67.6	39.6	2.37 (1)	#5Fusion Crust Rich Frag.					
HNO <sub>3</sub>	9.7	21.5	80.1	47.0	8.23 (8)	HAc	5.9	14	0.5	0.4	0.080 (1)
Residue	7.1	15.6	22.9	13.4	3.23 (02)	Residue	34.9	86	124.7	99.6	3.57 (3)
Total	45.3	100	170.7	100	3.77 (02)	Total	40.8	100	125.1	100	3.07 (3)
Avg. of #1 to #6	46.9		178.1		3.80 (28)	#6 Fusion Crust	60.7	--	153.6	--	2.53 (1)
						Avg. of 2-4	33.6	--	126.9	--	3.79 (9)

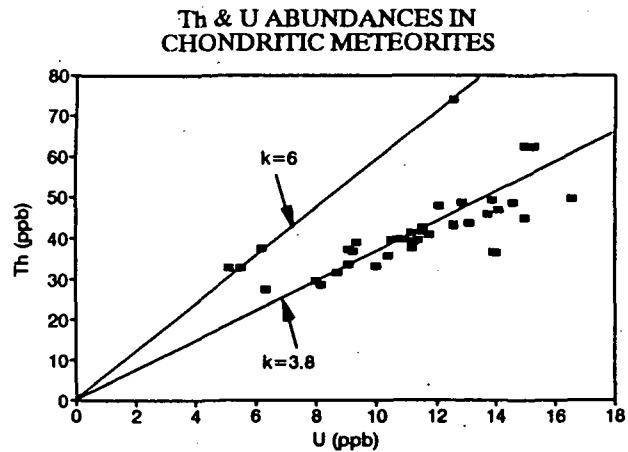


Figure 1

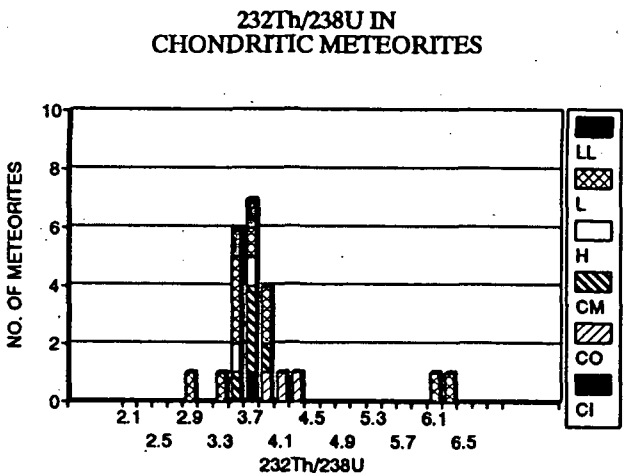


Figure 2

456918  
5137-91  
ABS ONLY  
N 94-1-25152  
P.S.F.

LUNAR SCOUT TWO SPACECRAFT GRAVITY EXPERIMENT; Andrew F.Cheng,  
Johns Hopkins Applied Physics Laboratory, Laurel, MD, 20707.

Measurement of the gravity field of the Moon has a high science priority because of its implications for the internal structure and thermal history of the Moon, and it has a high priority for future exploration activities because of the influence of lunar gravity on spacecraft navigation and orbit maintenance. The current state of knowledge in the lunar gravity field (and the uncertainty in the knowledge) is based primarily on data accumulated from the Lunar Orbiter and Apollo programs. Data are sparse and emphasize the equatorial band ( $\pm 30^\circ$ ) on the near side of the Moon. There are no tracking data on the far side and only the Lunar Orbiter V provides a small amount of high inclination data. A host of gravity models developed from different combinations of tracking data have large discrepancies in their predictions of spacecraft motion and orbit lifetimes. There are also large disagreements in the Mercator projections of the gravity acceleration from each model, especially on the far side, where the contours tend to have no obvious relationship with the local topography. The science and engineering requirements for global gravity field mapping will be satisfied with continuous radiometric tracking of Lunar Scout I in a low polar orbit using the Deep Space Network and Lunar Scout II in a high elliptical orbit.

In order to meet the science gravity field requirements, it [1] has been estimated that the radiometric velocity measurements should be less than 0.5 mm/s and possibly as low as 0.1 mm/s to average 10 seconds of gravity acceleration. This can be met using coherent two-way doppler with a DSN measurement accuracy of 0.3-1.0 mm/s with S-band. This accuracy will satisfy exploration requirements for spacecraft navigation, expressed as spacecraft position error propagation with time.

The gravity field of the Moon will be mapped during the Scout Program using a two spacecraft concept. In the two spacecraft concept, one spacecraft is placed in a high altitude eccentric orbit while the second spacecraft is in a low altitude polar orbit. The gravity experiment requires a radio frequency that will permit two-way Doppler tracking between the spacecrafts and the DSN. Both spacecraft carry NASA standard transponder systems for data transmission to Earth as well as for tracking and orbit determination. Data sufficient to produce a gravity field map could be acquired within one month with this system.

The nominal Scout Program mission plan calls for Lunar Scout I to remain in the 100km polar mapping orbit at the end of its mapping phase while Lunar Scout II will be inserted into an elliptical orbit for far-side tracking of Scout I. (DSN tracking of Lunar Scout I during its low altitude orbit will provide an initial gravity map of the Moon. Substantial improvements in the lunar gravity model can be obtained by this method.) Full scale global mapping with the high precision achievable with the two spacecraft concept will be completed during the flight of Lunar Scout II.

A possible alternative is the utilization of a spacecraft subsatellite released by a parent orbiting spacecraft and subsequently tracked. The changes in the relative distances between the two spacecraft as the Moon is orbited provide a precise measurement of the lunar gravity field.

[1] Lunar Observer: A Comprehensive Orbital Survey of the Moon, Mission and System Definition Summary, JPL D-8607, April 15, 1991.



**MISSION TO THE MOON: AN ESA STUDY ON FUTURE EXPLORATION** *Pi2*

A.F. Chicarro, Space Science Department, ESA/ESTEC, 2200 AG Noordwijk, The Netherlands.

**Background:** The increasing worldwide interest in the continuation of lunar exploration has determined ESA to carry out an investigation of the motivations to return to the Moon to establish a permanent or a semi-permanent manned lunar base. This study also considers the possible role Europe could play in the future exploration and possible utilisation of the Moon (1).

**Study goals:** The study concentrated in this first phase mainly on scientific questions, leaving technological issues such as transportation, the role of humans, infrastructure and policy matters to a later phase. It only partially considered questions relating to the exploitation of lunar resources and the impact of human activities on science. For the purpose of this study, the scientific issues were divided into three main areas:

- Science of the Moon, which includes all investigations concerning the Moon as a planetary body (geophysics, geochemistry, geology, origin of the Earth-Moon system, interaction of the Moon with its environment).
- Science from the Moon, using the Moon as a platform, hence including observatories in the broadest sense (interferometry, very-low-frequency astronomy, astrometry, planetary astronomy, solar physics and solar wind plasma, high energy physics).
- Science on the Moon, which includes not only questions related to human activities in space but also the development of artificial ecosystems beyond the Earth (exobiology, radiation biology and protection, artificial ecosystems and biological support systems, human physiology and medicine).

**Science of the Moon:** Lunar sciences will concentrate on the scientific objectives, technical elements and mission scenarios of a 4-step renewed exploration programme:

- A lunar polar orbiter, to provide complete geophysical, geochemical and geological mapping, and full high resolution coverage of the lunar surface.
- Surface stations and rovers, to determine the internal structure of the Moon, the chemical and mineralogical composition of selected sites, and to perform traverses across geological boundaries.
- Sample return missions, to further investigate the most relevant sites on the Moon about which our knowledge is very limited, such as the highlands and the far side.
- A lunar outpost/base, to provide support to field geologists in sampling and in-situ observations of the lunar surface, as well as to allow the refurbishment of surface stations and rovers.

**Science from the Moon:** A number of disciplines will take advantage of the stable lunar ground, the slow rotation of the Moon, its atmosphere-free sky and, on the far side, its radio-quiet environment. Two techniques which will make unique use of the lunar platform are UV to sub-millimetre interferometric imaging and very-low-frequency astronomy. A logical sequence should be:

## LUNAR EXPLORATION IN ESA Chicarro A.F.

- To undertake an in-depth design study of an intermediate baseline ( $\sim 100$  m) space-based optical interferometer providing milliarcsec resolution.
- To initiate two conceptual studies for very long baseline ( $> 100$  m) lunar interferometers to cover the UV to IR and the sub-millimetre domains.

Planetary and solar science will also be considered, while the specific requirements of astrometry will be of a comparatively low priority. Very-low-frequency astronomy will be addressed by a short-term small study. The lunar surface offers a unique opportunity to investigate the history of radiations such as solar wind, solar flare particles, galactic cosmic rays, or solid particle fluxes.

**Science on the Moon:** One of the goals of life sciences is evidently to provide information prerequisite for establishing a manned lunar base. This includes studies of the human physiology under reduced gravity, radiation protection and life support systems, and monitoring of the solar activity (predicting and alerting). The studies which should be performed on the Moon rather than on the Space Station should be identified during the next phase of the study. A second goal of life sciences consists in establishing – for the first time – an artificial ecosystem on a celestial body beyond the Earth. Life sciences studies, including these two major interrelated goals, could benefit from the same technical elements described in the 4-step approach for lunar exploration.

**Utilisation of the Moon:** The infrastructure required by the permanent presence of Man on the Moon will make use of available resources to support the exploration activities. Regarding Helium-3 as fuel for fusion energy, the non trivial question of mining large amounts of lunar soil in order to extract the available Helium-3 can await a later stage of lunar exploration. A question which needs to be kept in mind and to be further studied is whether human activity, and in particular mining, will not disturb the lunar environment in such a way that the unique scientific activities on the Moon are badly hampered.

**Future studies:** Already this first phase of the study has confirmed that there is not only significant interest in Europe for all lunar science disciplines but that there is also significant expertise in many fields. In-depth scientific studies are only recommended in those fields where a potentially significant European role has been identified. Several fields are not recommended a second study phase: second generation very-low-frequency astronomy (involving large structures), high energy physics (cosmic rays), the exploration of the Moon for Helium-3 as fuel for fusion. Future activities will focus on three main areas of Science of/from/on the Moon, outlined above.

**Concluding remarks:** Depending on the financial resources devoted to the exploration of the Moon in Europe, and on the time frame in which these could become available, a European contribution to lunar exploration could materialize as moderate elements (e.g., a lunar polar orbiter, surface stations, a precursor interferometer) early in the sequence of missions, or be part of a larger undertaking later (e.g., sample return missions, full-fledged interferometers, a lunar base). Lunar investigations are preferably to be performed within the framework of a broad international collaboration. Europe can play an important role in most fields of scientific investigation of Science of/from/on the Moon. Furthermore, ESA should evaluate its role in transportation systems and other technological developments, human exploration, as well as in programmatic and policy matters, in a broader study involving other ESA Directorates.

**Reference:** (1) ESA's Lunar Study Steering Group, *Mission to the Moon: Europe's Priorities for the Scientific Exploration and Utilisation of the Moon*, European Space Agency, ESA SP-1150, 190 pp., 1992.

456925

5139-91

NBS ONLY

LPSC XXIV

283

N 9 4 2 1 2 5 4

FRACTAL DIMENSIONS OF RAMPART IMPACT CRATERS ON MARS; Delwyn Ching, G. Jeffrey Taylor, Peter Mouginis-Mark, and Barbara C. Bruno (Planetary Geosciences, Dept. of Geology and Geophysics, University of Hawaii, Honolulu, HI 96822).

P. I

**Introduction.** Ejecta blanket morphologies of Martian rampart craters may yield important clues to the atmospheric densities during impact, and the nature of target materials (e.g., hard rock, fine-grained sediments, presence of volatiles). In general, the morphologies of such craters suggest emplacement by a fluidized, ground hugging flow instead of ballistic emplacement by dry ejecta (1,2). We have quantitatively characterized the shape of the margins of the ejecta blankets of 15 rampart craters using fractal geometry. Our preliminary results suggest that the craters are fractals and are self-similar over scales of  $\approx 0.1$  km to 30 km. Fractal dimensions (a measure of the extent to which a line fills a plane) ranges from 1.06 to 1.31. No correlations of fractal dimension with target type, elevation, or crater size were observed, though the data base is small. The range in fractal dimension and lack of correlation may be due to a complex interplay of target properties (grain size, volatile content), atmospheric pressure, and crater size. The mere fact that the ejecta margins are fractals, however, indicates that viscosity and yield strength of the ejecta were at least as low as those of basalts, because silicic lava flows are not generally fractals (2).

**Methodology.** Craters were selected from different areas on Mars to obtain a variety of target materials, crater sizes, locations, and elevations. Ejecta margins were digitized from enlarged images, and fractal dimensions were calculated by the ruler or structured walk method. Fractal dimension, a measure of power-law scaling, can be calculated from (e.g., 4):  $L(\delta) = \delta^{1-D}$ , where  $L(\delta)$  is the length of the perimeter of the ejecta margin, using a ruler of length  $\delta$ .  $D$  is the fractal dimension. When  $\log L(\delta)$  is plotted versus  $\log \delta$ , the slope is  $1-D$ . Such plots are called Richardson plots.

**Results and Discussion.** A typical Richardson plot is shown in Fig. 1; the good fit to a line ( $R^2 = 0.96$ ) indicates self-similar, hence fractal, scaling. Fractal dimensions ( $D$ ) measured on 15 ejecta margins range between 1.06 and 1.31. There is no obvious relationship between  $D$  and target type (Fig. 2), elevation (Fig. 3), or crater diameter (Fig. 4). Nevertheless, we can draw some preliminary conclusions about emplacement mechanisms. (1) The fact that ejecta margins of rampart craters appear to be fractals probably indicates that the material behaved as a low viscosity fluid with small yield strength. This interpretation stems from the observations that basalt lava flows are fractals (5), whereas more silicic flows (hence more viscous flows with significant yield strengths) are not fractals (3). Thus, rampart and lobed ejecta were not emplaced like terrestrial debris flows with high yield strengths, a conclusion reached previously (1, 6,7). (2) The fractal margins of rampart craters give some hints about the internal processes operating during ejecta deposition because, in general, fractal shapes are produced by nonlinear processes. Thus, the fractal nature of the margins of rampart crater ejecta blankets is consistent with the idea that turbulence (a highly nonlinear process) in entrained atmosphere plays a key role in ejecta emplacement on Mars (2). (3) The lack of a simple correlation between fractal dimension and target material, elevation, and crater size (Figs. 2-4) indicates that the final crater shape results from a complex interplay of

target properties (including volatile content), crater size, and atmospheric pressure. A larger data base will allow a more thorough exploration of the effects of the variables, so some trends may become more apparent as we acquire more data.

**References.** (1) Carr, M. H., et al. (1977) *J. Geophys. Res.* 82, 4055-4065. (2) Schultz, P. H. (1992) *J. Geophys. Res.* 97, 11,623-11,662. (3) Bruno, B.C., et al., this volume. (4) Turcotte, D. L. (1992) *Fractals and Chaos in Geology and Geophysics*. (5) Bruno, B. C. et al. (1992) *Geophys. Res. Lett.* 19, 305-308. (6) Mouginis-Mark, P. J. (1980) *Icarus* 45, 60-76. (7) Mouginis-Mark, P. J. (1987) *Icarus* 71, 268-286.

**Acknowledgment.** This work was supported by a Hawaii Space Grant College undergraduate fellowship to Delwyn Ching.

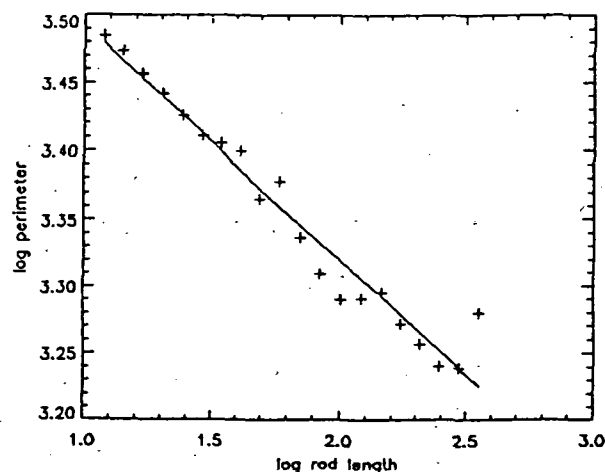


Fig. 1. Richardson plot for Martian crater Arandus. Good fit indicates self-similar, or fractal, scaling.

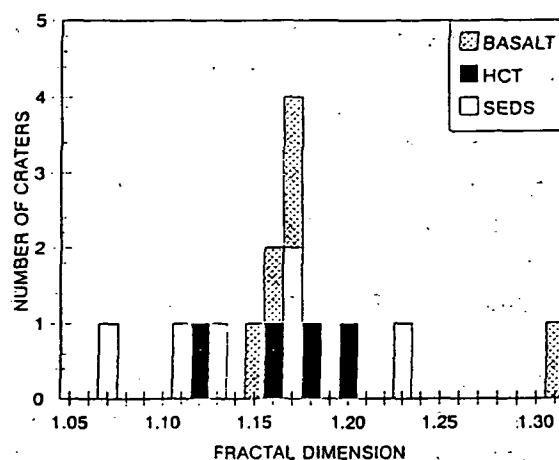


Fig. 2. Histogram of fractal dimensions of Martian rampart craters. Note the lack of correlation with type of target material.

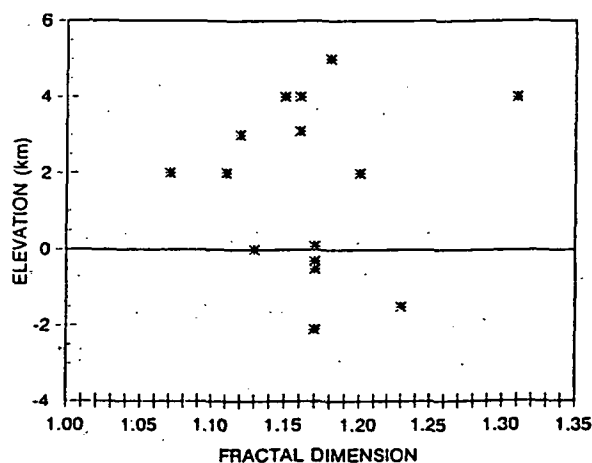


Fig. 3. Plot of elevation vs. fractal dimension of the margins of Martian rampart craters.

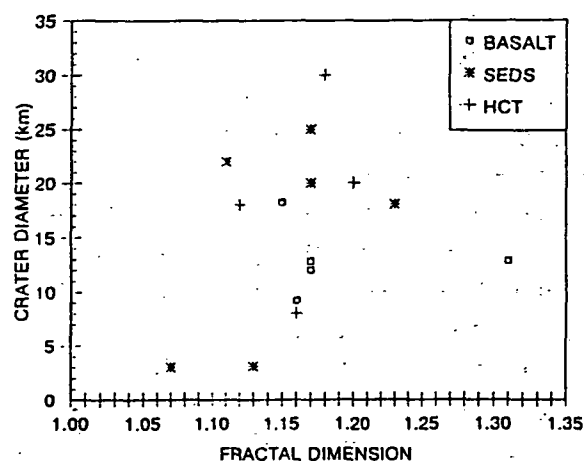


Fig. 4. Plot of crater diameter vs. fractal dimension.

456928

5140-91

ABS. ON 28

LPSC XXIV

285

94-12155

A SIMPLE MODEL OF CLASTIC SEDIMENTS ON MARS: Philip R. Christensen, Department of Geology, Arizona State University, Tempe, AZ 85287-1404 and Michael C. Malin, Malin Space Science Systems, Inc., 3535 General Atomics Court, Suite 250, San Diego, CA 92121

P-2

In preparation for the start of Mars Observer operations at Mars later this year, Viking Infrared Thermal Mapper (IRTM) observations have been synthesized into a simple but geologically coherent conceptual model for use in establishing targets for coordinated Thermal Emission Spectrometer (TES) and Mars Observer Camera (MOC) observations. The model is based on three assumptions that are, at best, only partly true: that albedo is a measure of the presence or absence of dust; that thermal inertia is a measure of the weighted average particle size; and that rock abundance is a measure of the statistical thickness of fine sediment (i.e., that the observed areal abundance of rock reflects the whole or partial burial of rocks). Using this model, it is possible to show that, on the scale of 30 km, mantles of wind-transportable sediment (dust and sand) are at most about 1 m thick, and that on a global average such mantles are about 35 cm thick.  $3.8 \times 10^{19}$  cm<sup>3</sup> of such sediment covers Mars equatorward of  $\pm 60^\circ$  latitude. Using the model, interpretation of digital maps of IRTM data focus attention not only on areas where dust is the primary sediment (e.g., Arabia Terra), but also on areas where sand is the primary sediment (e.g., eastern Valles Marineris) and where rocks and other coarse materials are abundant (e.g., eastern Kasei Vallis).

Three IRTM data sets are used in the analysis: Viking 1 and 2 pre-dawn observations mosaiced into a global map of single-point thermal inertias at  $0.5^\circ$ /bin resolution, Pleskot and Miner's<sup>1</sup> global albedo map using the best available, clear-period IRTM observations ( $1^\circ$ /bin), and Christensen's<sup>2</sup>  $1^\circ$ /bin rock abundance map. Uncertainty analyses indicate these data sets to be accurate to 5%, 2%, and 20%, respectively.

The assumption that rock abundance on Mars reflects the thickness of mantling fine material is the same as assuming that, in the absence of such mantling, the size frequency and areal density distribution of rocks would be the same everywhere. This is clearly a simplistic view, but one which may not be unreasonable at the scales and for the purposes of the analyses reported here. The areal density curve for the Viking Lander 1 (VL-1) site is very similar to that derived for the Viking Lander 2 (VL-2) site, offset by linear scaling factor. Although it is clear that the mechanisms that create and transport rocks on Mars need not necessarily create the same size frequency and hence areal density relationships, it is not likely that the populations are radically dissimilar. Using IRTM observations to establish the maximum areal density of rocks  $\geq 15$  cm in diameter ( $\approx 30\%$ ), a simple model using hemispherical "rocks" relates thickness of mantling sediment to the amount of a rock still exposed above the mantle. The use of cubical "rocks" changes the results only slightly. If the assumption that there is a single rock abundance function from which all surfaces evolve is incorrect (i.e., that some areas are intrinsically devoid of rocks), then the estimates made by invoking the assumption probably represent upper limits to the average mantle thickness. In areas of intrinsically fewer rocks, a thinner mantle is needed to reduce the visible rock abundance to the observed values. Greater abundances of fewer, larger rocks relative to smaller rocks may permit slightly thicker mantles, but both the 30% maximum rock abundance determined from IRTM investigations and studies of size/frequency relationships of boulders on Earth, Mars, and the Moon argue that this effect is likely to be of limited areal extent.

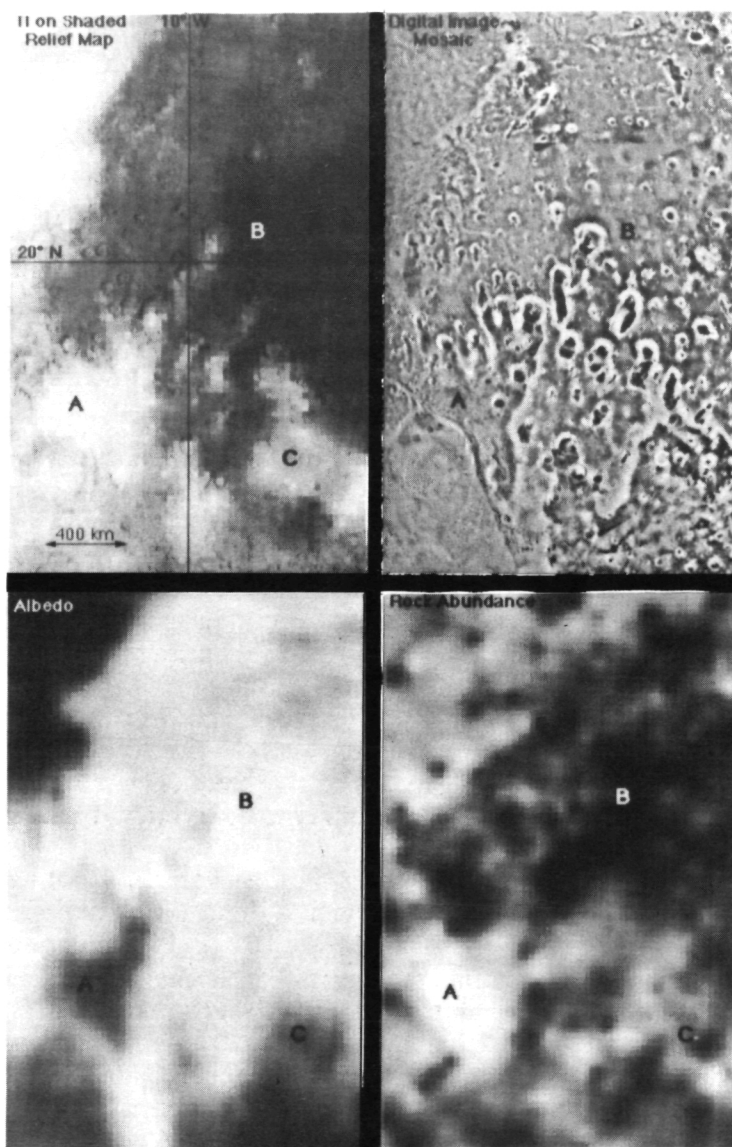
Figure 1 shows sections of the four data sets used in the analysis: clockwise from top left are thermal inertia superimposed on a shaded relief map, a digital image mosaic of Viking Orbiter images, rock abundance, and albedo. The pictured area (Oxia Palus) is one believed to contain wind-transportable sediments (dust, sand, and possibly gravel)<sup>4,5</sup>. In Figure 1, three "end-member" surface types are noted, although there are many surfaces that fall between these. High thermal inertia, low albedo, and high rock abundance (A) denote surfaces with rocks and a thin mantle of sand. Low thermal inertia, high albedo, and low rock abundance denote surfaces where rocks are mostly buried by dust. Surfaces with intermediate thermal inertia, low to intermediate

## SEDIMENTS ON MARS: Christensen, P. R. and M. C. Malin

albedo, and intermediate to low rock abundance are interpreted to have rocks buried to varying degrees by sand; dust brightens the surface but is not a major component of the deposits.

The model, consistent with previous analyses (e.g., Christensen's<sup>2,3</sup> arguments that martian sediment mantles are between 0.1 and 5.0 m thick, with the preferred value between 1 and 2 m) can be used to make quantitative predictions concerning the thickness of wind transportable sediment that may be tested by Mars Observer. Refined thermal inertia and rock abundance estimates are targeted to be addressed early in the TES data analysis effort. One end of the rock population should be visible in MOC images, as should the additional effects of topographic concentration at higher spatial resolution. The Mars '94 and '96 descent and balloon imaging experiments should provide additional tests at smaller spatial scales.

References: <sup>1</sup>Pleskot, L. K. and E. D. Miner (1981) *Icarus* **45**, 179-201. <sup>2</sup>Christensen, P. R. (1986) *Icarus* **68**, 217-238. <sup>3</sup>Christensen, P. R. (1986) *J. Geophys. Res.* **91**, 3533-3545. <sup>4</sup>Presley, M. A. and R. E. Arvidson (1988) *Icarus* **75**, 499-517. <sup>5</sup>Arvidson, R. E., E. A. Guinness, M. A. Dale-Bannister, J. Adams, M. Smith, P. R. Christensen, and R. B. Singer (1989) *J. Geophys. Res.* **94**, 1537-1587.



456930

5141-25

ABSTRACT

LPSC XXIV

287

N 94-123156

**THERMAL-INFRARED EMISSION SPECTROSCOPY OF NATURAL SURFACES: APPLICATION TO COATED SURFACES;** Philip R. Christensen, Arizona State University, Tempe, AZ, Stephanie T. Harrison, Goddard Space Flight Center, Greenbelt, MD, Paul Barbera, Steve Ruff, Arizona State University, Tempe, AZ. P 2

Thermal-infrared vibrational spectroscopy has great potential for remotely determining the composition of planetary surface materials, taking advantage of fundamental molecular vibrational modes that produce spectral features in the range from  $\sim 3$  to  $>50 \mu\text{m}$ . Much of the current interest in the thermal infrared wavelength region stems from the deployment of multi-spectral scanners, such as the Thermal Infrared Multispectral Scanner (TIMS) (1) and the Mars Observer Thermal Emission Spectrometer (TES) (2). In order to support these missions, it is necessary to develop an appropriate library of laboratory measurements. 5

The purpose of this work was to develop a technique which, with a very limited set of assumptions, can be used to determine the emissivity of natural surfaces directly using emitted energy. To date, virtually all laboratory spectra have been obtained using reflection or transmission methods (3-6) with only a limited number of measurements taken in emission (7-9). In contrast, remotely-sensed thermal-infrared data from planetary surfaces are obtained by measuring the emitted energy. For ideal conditions in which the surface is isothermal and all of the reflected and emitted energy can be measured, reflection and emission are intimately related through Kirchhoff's law. These conditions are not always met, however, in nature nor in a laboratory. For example, bidirectional or biconical reflection measurements are not appropriate for a quantitative assessment of emissivity (5). Radiative transfer modeling to account for potential non-ideal conditions is complex, as scattering by particles close to the wavelength in size may be significant (8; 10-12). As a result, all of the effects of environment are difficult to fully model. For these reasons we have chosen to obtain data in emission in order to more closely replicate remotely-acquired data and to investigate the range of conditions over which reflectance and emittance can be directly related.

One of the major complications to the collection of emission data is the difficulty in separating energy of interest emitted by the sample from that emitted by the instrument and surroundings and reflected off the sample. There are three basic approaches to this problem: 1) calculate the background energy reflected from the sample, assuming the reflectivity of the sample is given by Kirchhoff's law; 2) obtain measurements at several sample temperatures with a fixed background temperature to determine the reflected energy directly; and 3) cool the sample chamber walls to limit background emission. We have developed a laboratory technique for determining calibrated emissivities of natural surfaces using the first two of these techniques. Equations have been developed to account for the energy reflected from the environment and to determine directly the sample temperature using hot and cold blackbody targets. In method one, only a hot sample measurement is made and the reflected background energy is removed by modeling; in method two the sample is cooled and the reflected energy is measured directly. The second major difficulty inherent in emission measurements is the determination of the sample temperature. This problem has been addressed by fitting a blackbody curve over a region where the sample emissivity is assumed to be unity, and then scaling the sample emission back to the temperature of the blackbody (13). A result of this scaling is that the derived emissivities have been normalized to unity at some point and cannot be considered absolute values. However, for most rocks and minerals, there is some wavelength region between 6 and  $50 \mu\text{m}$  in which the initial assumption is very nearly met. Estimates of the error in this technique suggest that relative emissivity can be obtained to approximately 1%, and absolute emissivities to 2-15%, depending on the validity of the assumption that the emissivity of the sample is unity at some wavelength.

The emissivity determined here agrees well with hemispherically integrated reflectance data assuming Kirchhoff's law. There are significant differences, however, between emission and

bidirectional or biconical reflectance measurements. These differences arise because these reflectance measurements are not appropriate for conversion to emissivity using Kirchoff's law. Once emissivity has been determined, these data can be used in quantitative studies to model the physics of the interactions between complex surfaces and the outgoing energy. The initial study presented here has investigated the effect of surface coatings, one of many non-ideal effects on the thermal emission from planetary surfaces. These results are directly applicable to emission spectra obtained for varnished terrestrial rocks, and may be relevant to the study of dust-coated surfaces on Mars.

Granite and granodiorite suites were collected with varying degrees of varnish. The distribution of varnish was determined using SEM photographs and spectra were obtained of each varnished sample. To model the effect of varnish, two linear models are developed: the first assumes linear mixing of independent emission from the substrate and varnish (checkerboard model); the second models transmission through an absorbing/emitting medium. For a checkerboard model the resulting emissivity should vary linearly with abundance, whereas for coatings the emissivity should vary linearly with the factor  $e^{-kx}$ , and exponentially with coating thickness. It was found that there is a linear relationship between the spectral contribution of the varnish and the median varnish thickness, both in wavelength regions where varnish is relatively transparent and where it is strongly absorbing. These results are consistent with the checkerboard model and indicate that patches of varnish dominate the surface, consistent with the competing processes of varnish growth and spallation on rock surfaces. The SEM observations confirm the wide variation in varnish thickness at small scales. In detail, the spectral properties reflect the combined effect of both the checkerboard and layer models. Although the number of thick varnish patches *decreases* roughly exponentially with increasing thickness, their effect on the spectrum *increases* exponentially with thickness. Thus, the result appears roughly linear with the degree of varnish.

In addition to providing a measure of varnish thickness, the spectral data can be used to estimate the composition of the substrate through varnish layers up to 40-50  $\mu\text{m}$  in median thickness using spectral regions in which the varnish is relatively transparent. Conversely, if the spectrum of substrate material is known, then the composition of the coating can be determined by a linear separation of the substrate and composite spectrum. This approach proved successful and a close match was found between the derived varnish spectrum and that of mixed layer clays, in agreement with earlier work by Potter and Rossman (14). Thus, for rock coatings typical of those found in desert environments on Earth, thermal infrared spectral observations provide an excellent means for penetrating relatively thick (median thickness up to ~40-50  $\mu\text{m}$ ) layers of this material to probe the composition of the underlying rock. For remote sensing applications on Mars this wavelength region should provide a powerful tool for compositional mapping of coated and dust-covered rocks.

## References

- 1) Palluconi, F. D. and G. R. Meeks, Thermal infrared multispectral scanner (TIMS): An investigator's guide to TIMS data, Jet Propulsion Laboratory, Pub. Number 85-32, 14 p., 1985.
- 2) Christensen, P. R., D.L. Anderson, S. C. Chase, R. N. Clark, H. H. Kieffer, M. C. Malin, J. C. Pearl, J. Carpenter, N. Bandeira, F. G. Brown and S. Silverman, *J. Geophys. Res.*, **97**, 7719-7734, 1992.
- 3) Salisbury, J. W. and L. S. Walter, *J. Geophys. Res.*, **94**, 9192-9202, 1989.
- 4) Walter, L. S. and J. W. Salisbury, *J. Geophys. Res.*, **94**, 9203-9213, 1989.
- 5) Salisbury, J. W., L. S. Walter, N. Vergo and D. M. D'Aria, *Infrared (2.1-25  $\mu\text{m}$ ) Spectra of Minerals*, The Johns Hopkins University Press, Baltimore and London, 1991.
- 6) Moersch, J. E. and P. R. Christensen, *Bull. Amer. Astron. Soc.*, **23**, 1183, 1991.
- 7) Brown, R. J. and B. G. Young, *Appl. Opt.*, **14**, 9227-9234, 1975.
- 8) Conel, J. E., *J. Geophys. Res.*, **74**, 1614-1634, 1969.
- 9) Salisbury, J. W., in *Abstracts of the 10th Annual International Geoscience and Remote Sensing Symposium*, **3**, 1775-1778, 1990.
- 10) Hapke, B., *J. Geophys. Res.*, **86**, B4, 3039-3054, 1981.
- 11) Clark, R. N., G.A. Swayze, R. B. Singer and J. B. Pollack, *J. Geophys. Res.*, **95**, 14,463-14,480, 1990.
- 12) Salisbury, J. W. and A. Wald, *Icarus*, **96**, 121-128, 1992.
- 13) Kahle, A. B., D. O. Madura and J. M. Soha, *Appl. Opt.*, **19**, 2279-2290, 1980.
- 14) Potter, R. M. and G. R. Rossman, *Science*, **196**, 1446-1448, 1977.



45694/

S142-90  
R135 ONLY

LPSC XXIV

289

N94-162157

COLLISIONS OF SMALL SPACEWATCH ASTEROIDS WITH THE EARTH; C.F. Chyba,  
National Research Council Associate, Laboratory for Extraterrestrial Physics, Code  
693, NASA Goddard Space Flight Center, Greenbelt, MD 20771 U.S.A. P-2

Rabinowitz *et al.* [1] have reported the discovery, with the Spacewatch Telescope, of 8 Earth--approaching objects smaller than 100 m in diameter. I have calculated the probability and velocity of collision with Earth for each of these objects, using Öpik's equations, including terms for Earth's eccentricity [2]. Using a code we have successfully employed to model the Tunguska and Revelstoke atmospheric explosions [3], I have simulated the entry of these objects into Earth's atmosphere, assuming iron, stony, carbonaceous, and cometary compositions. The smallest of these objects (with tens to hundreds of kilotons of kinetic energy) pose a substantial threat at the surface only if they are iron objects. (An object is taken to "pose a substantial threat" if it either craters the ground, or explodes in the atmosphere with sufficient energy at low enough altitude to create an overpressure at the surface capable of felling trees or destroying buildings.) Larger objects, with energies greater than about a megaton, devastate the surface regardless of whether they are of iron, stony or carbonaceous composition. Iron objects crater the ground, whereas stony and carbonaceous objects explode in the atmosphere low enough to fell trees and damage buildings over thousands of square kilometers. Spacewatch objects, if presumed to be of carbonaceous composition, are as dangerous as their stony counterparts, as the former objects' lower yield strengths (and hence, higher explosion altitudes) are roughly compensated for by their larger masses (as derived from their lower albedos for a given observed magnitude). Although comets are intrinsically less dangerous than asteroids, the 90 m diameter Spacewatch objects devastate hundreds of square kilometers at the surface even if cometary.

The orbital elements and approximate diameters for the 8 Spacewatch objects smaller than 100 m in diameter are shown in the following table. Also listed are these objects' collision probabilities and velocities with Earth.

object	q (AU)	Q (AU)	i (deg)	diameter* (m)	impact velocity (km s <sup>-1</sup> )	impact probability (Gyr <sup>-1</sup> )
1990 UN	0.81	2.6	3.7	90	17.3	7
1991 BA	0.71	3.8	2.0	7	21.3	7
1991 TT	1.00	1.4	14.8	28	14.0	110
1991 TU	0.94	1.9	7.7	9	13.8	10
1991 VA	0.93	1.9	6.5	17	13.8	11
1991 XA	0.98	3.6	5.3	90	14.4	9
1992 DU	0.96	1.4	25.1	50	17.9	7
1992 JD	1.00	1.1	13.6	50	13.3	160

\*These diameters, from [1], assume an albedo of 0.0945, the geometric mean between a spherical S-type asteroid and a C-type asteroid with albedos of 0.186 and 0.048, respectively.

Typical Earth--crossing asteroid terrestrial collision probabilities are in the range 1--10 Gyr<sup>-1</sup>. The objects 1991 TT and 1992 JD have exceptionally high impact probabilities with Earth; other objects are at the high end of the "typical" range.

## COLLISIONS OF ASTEROIDS: Chyba C. F.

This, as well as many of these objects' low impact velocities (the median terrestrial collision velocity for Earth-crossing asteroids is 15 km/sec [4]), are of course the result of their Earth-like heliocentric orbits.

Using our Tunguska/Revelstoke code [2], I have calculated the fates of the 8 Spacewatch objects in the terrestrial atmosphere, assuming iron, stony, carbonaceous, and cometary compositions, for the most probable incidence angle of 45°. Iron and stony objects were assigned radii appropriate to an S-type asteroid albedo, with densities of 7.9 and 3.5 g/cm<sup>3</sup>, respectively. Carbonaceous and cometary objects were assigned radii appropriate to a C-type asteroid albedo, with densities of 2.2 and 1.0 g/cm<sup>3</sup>. The results of these simulations are summarized in the following table. If these objects are instead presumed to be of iron composition, each reaches the terrestrial surface, with the exception of 1991 BA, which catastrophically explodes at an altitude of about 2.5 kilometers with an energy of nearly 30 kilotons.

Object	S-type asteroids			C-type asteroids			Comets*	
	radius† (m)	energy (kton)	altitude (km)	radius† (m)	energy (kton)	altitude (km)	energy (kton)	altitude (km)
1990 UN	30	20,000	10	60	82,000	8	37,000	15
1991 BA	3	10	22	6	60	32	25	43
1991 TT	10	200	15	20	600	20	700	27
1991 TU	3	10	16	6	50	27	25	38
1991 VA	7	70	15	14	350	23	150	32
1991 XA	30	10,000	9	60	60,000	8	25,000	15
1992 DU	20	3,000	14	35	15,000	11	7,000	22
1992 JD	20	2,000	12	35	8,000	14	4,000	21

\*Comet radii are taken to equal those of C-type asteroids (albedos assumed equal).

†These are radii for spherical objects; the Tunguska/Revelstoke code employed here [3] treats objects as initially "cubical" cylinders; I take these objects to have masses (hence, explosion energies) identical to those listed here (and therefore slightly different cylindrical radii).

Rabinowitz [1] emphasizes that the discovery rate of small Spacewatch objects is 10 to 100 times higher than that obtained via extrapolation of the mass-number distribution of larger objects. Nevertheless, his calculated impact fluxes with the Earth yield frequencies of Tunguska-like atmospheric explosions that, given the uncertainties, are consistent with previous [5] estimates that such events occur once every several hundred years.

References: [1] Rabinowitz, D.L. (1993) *ApJ*, to be published; T. Gehrels, *Spacewatch discoveries to date*, personal communication, November 1992. [2] Öpik, E.J. (1976) *Interplanetary Encounters*, Elsevier, New York. [3] Chyba, C.F., Thomas, P.J., and Zahnle, K.J. (1993) *Nature*, to be published January 1993. [4] Chyba, C.F. (1991) *Icarus* 92, 217. [5] Morrison, D. et al. (1992), *The Spaceguard Survey*, NASA.

**DIFFERENTIAL SCALING: IMPLICATIONS FOR CENTRAL STRUCTURES IN LARGE LUNAR CRATERS.** M.J. Cintala<sup>\*</sup> and R.A.F. Grieve<sup>\*</sup>. <sup>\*</sup>Code SN4, NASA Johnson Space Center, Houston, TX 77058; <sup>\*</sup>Geophysics Div., Geological Survey of Canada, Ottawa, Ontario K1A 0Y3

The change in morphology of central structures with crater size on the terrestrial planets has been studied by many investigators.<sup>1-4</sup> While the progression of morphological change essentially follows the same basic pattern, the appearance of central peaks, and the transitions from single to multiple peaks and peaks to peak rings occur at crater diameters that appear to be dependent on parameters associated with the target planet.<sup>5-7</sup> Statistical data, morphological information, and model results exist for central structures in large craters, but the amount of "ground truth" is comparatively meager. What, for instance, is the amount of stratigraphic uplift in craters? Answers to questions such as this will provide useful constraints on models of origin for central structures, and would help in interpretation of remote-sensing data. This contribution uses terrestrial information and model calculations to estimate the amount of stratigraphic uplift for central-peak craters on the Moon — the only planet other than Earth for which sufficient topographic data are available.

**Sources of Information:** Morphometric data for the terrestrial craters used below were obtained from a literature search. Morphometric information for the lunar craters was taken from 8 and supplemented with our own measurements from the Lunar Topographic Orthophotomap and Lunar Topophotomap series. Depths of impact melting on the Moon were calculated with a model of impact heating described elsewhere.<sup>9</sup> Chondritic projectiles impacting anorthosite normal to the planetary surface at a nominal velocity of  $15 \text{ km s}^{-1}$  were used in all cases. Transient-cavity dimensions were calculated with relationships given by Schmidt and Housen,<sup>10</sup> and extrapolation to final crater diameters was made using the "modification-scaling" relationship of Croft.<sup>11</sup>

**Approach and Results:** The amount of stratigraphic uplift for terrestrial craters has been addressed previously<sup>13,14</sup> and, on the straightforward basis of geometry, was equated to the depth of excavation during the formation of the crater.<sup>14</sup> At impact velocities characteristic of planetary encounters, however, considerable volumes of target material are melted by the shock.<sup>15,16</sup> This forms the basis of the hypothesis for the remainder of this contribution; that is, the minimum depth of origin of central-peak material for any crater formed by impact normal to the surface is equal to the maximum depth of impact melting (Fig. 1). In principle, the actual depth of origin can be somewhat deeper, if the ejection process removes additional material in the center of the crater, below the zone of melting.<sup>14</sup> Figure 2 presents this minimum depth of origin of the central peak for impacts at 7.5, 15, and  $30 \text{ km s}^{-1}$ . Note the very weak dependence on impact velocity, and the break in slope corresponding to the assigned diameter of transition from simple to complex morphology (18.7 km).<sup>17</sup> Additional data not shown here indicate that the dependence on projectile type is as weak as that on impact velocity. Assuming that the calculated depth of melting is reasonable, and having available topographic data to provide the depth from the preexisting target surface to the top of the central peak, the stratigraphic uplift for a set of lunar craters can then be estimated (see Fig. 1). (Because highland topography complicates estimation of the preexisting target surface, only topographic data for craters located in mare terrain are used here.) The results of this derivation are plotted in Figure 3, which also

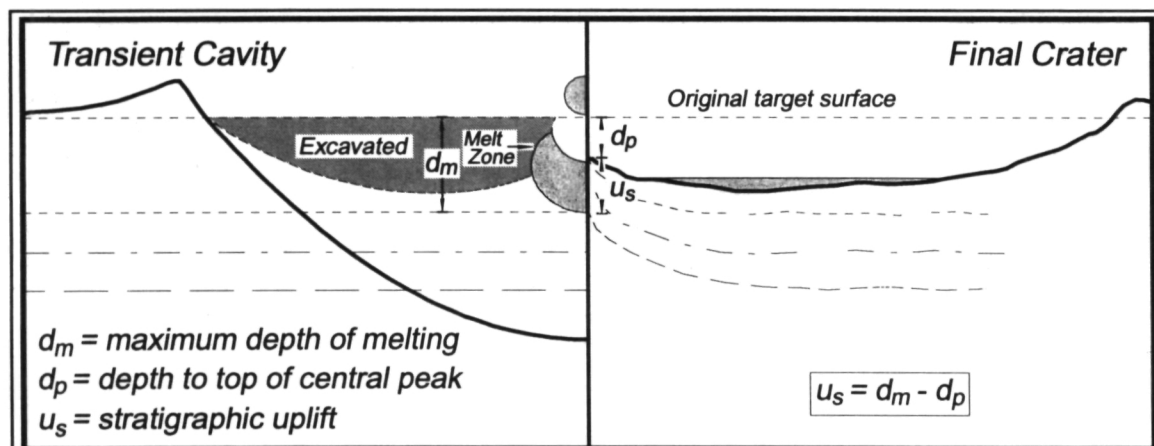


**Figure 1.** Schematic illustration of the relationship between the stratigraphic uplift, maximum depth of melting, and depth to the top of the central peak. The region labeled "Excavated" was estimated from a Z-model calculation ( $z=2.71$ );<sup>12</sup> material below that region is displaced, but not ejected, during formation of the transient cavity. The three dashed and dotted lines below the original target surface represent idealized strata before and after uplift.

## CENTRAL STRUCTURES IN LARGE CRATERS: M.J. Cintala and R.A.F. Grieve

includes the available data for terrestrial craters. Most of the terrestrial data points represent craters in sedimentary or mixed sedimentary and crystalline targets; this must be noted, since there is evidence that the cratering process in such targets will differ somewhat from that in crystalline rock,<sup>18</sup> as is essentially the case for the lunar craters. Even given this, the lunar and terrestrial estimates are in very good agreement, particularly since much of the scatter in the terrestrial data is undoubtedly due to erosion.

**Discussion:** Assuming that excavation in large craters is similar to that described by the Z-model,<sup>12</sup> the most deeply excavated material is derived from a relative position somewhere between the central peak and the cavity wall (Fig. 1). Nevertheless, it is apparent from Fig. 2 that even the minimum depth of origin of central peaks can be substantial. The top of the central peak for a crater the size of Copernicus,

for example, would come from a minimum depth of 10 km, irrespective of impact velocity or impactor type. This value supports the interpretations of Pieters,<sup>19</sup> but also suggests caution, due to the pervasive presence of impact melt. Finally, the values of stratigraphic uplift presented here for the Moon were derived from the same principles used in other applications of differential scaling.<sup>20-22</sup> The degree of agreement between the lunar and terrestrial estimates of stratigraphic uplift lend additional support to the potential validity of this approach.

**References:** 1 R.B. Baldwin (1963) *The Measure of the Moon*. (Chicago) University of Chicago Press, 448 pp. 2 C.A. Wood (1968) *Comm. Lunar Planetary Lab.* 7, 157. 3 W.K. Hartmann and C.A. Wood (1971) *The Moon* 3, 2. 4 R.J. Pike (1980) *PLPSC 11th*, 2159. 5 C.A. Wood and J.W. Head (1976) *PLPSC 7th*, 3629. 6 W.S. Hale and J.W. Head (1979) *PLPSC 10th*, 2623. 7 M.J. Cintala *et al.* (1977) *PLPSC 8th*, 3409. 8 W.S. Hale and R.A.F. Grieve (1982) *PLPSC 13th*, in *JGR* 87, A65. 9 M.J. Cintala (1992) *JGR* 97, 947. 10 R.M. Schmidt and K.R. Housen (1987) *Internat. J. Impact Engin.* 5, 543. 11 S.K. Croft (1985) *PLPSC 15th*, in *JGR* 90, 828. 12 D.E. Maxwell (1977) *Impact and Explosion Cratering* (D.J. Roddy, R.O. Pepin, and R.B. Merrill, eds.), Pergamon (New York), 1003. 13 R.A.F. Grieve (1980) *Precambrian Res.* 10, 217. 14 R.A.F. Grieve *et al.* (1981) *Multi-Ring Basins* (P.H. Schultz and R.B. Merrill, eds.), *PLPSC 12A*, 37. 15 D.E. Gault and E.D. Heitowit (1963) *Proc. 6th Hypervel. Impact Symp.*, 419. 16 J.D. O'Keefe and T.J. Ahrens (1977) *PLPSC 8th*, 3357. 17 R.J. Pike (1988) *Mercury* (F. Vilas, C.R. Chapman, and M.S. Matthews, eds.), University of Arizona Press (Tucson), 165. 18 S.W. Kieffer and C.H. Simonds (1980) *Rev. Geophys. Space Phys.* 18, 143. 19 C.M. Pieters (1982) *Science* 215, 59. 20 M.J. Cintala and R.A.F. Grieve (1991) *Lunar Planet. Sci. XXII*, 213. 21 M.J. Cintala and R.A.F. Grieve (1991) *Lunar Planet. Sci. XXII*, 215. 22 R.A.F. Grieve and M.J. Cintala (1993) *Meteoritics*, in press.

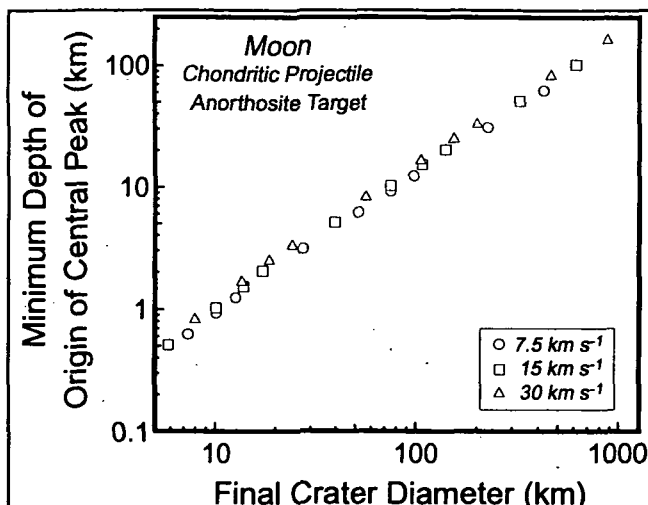


**Figure 2.** Minimum depth of origin of central peaks as a function of final crater diameter for a range of impact velocities. Note the weak dependence on velocity.

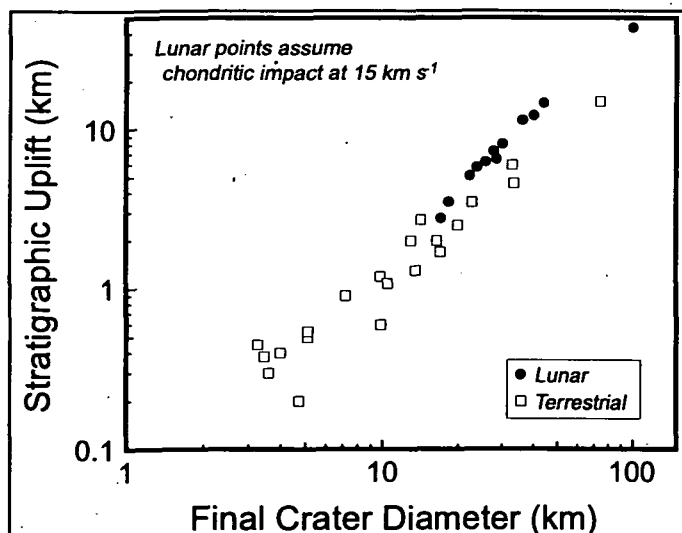


**Figure 3.** Derived stratigraphic uplift for a subset of lunar mare craters as a function of final crater diameter. Included for comparison are points for those terrestrial craters for which data are available.

456944

S144-91

ABS. 5.15.1

LPSC XXIV

293

N94-12159

**IMPACT COMMINATION OF GLASSES: IMPLICATIONS FOR LUNAR REGOLITH EVOLUTION.** Mark J. Cintala, <sup>☆</sup> Sheila Smith, <sup>†</sup> and Friedrich Hörz. <sup>☆</sup> <sup>☆</sup> Code SN4, NASA Johnson Space Center, Houston, TX 77058. <sup>†</sup> 1992 LPI Summer Intern; Dept. of Physics, Baylor University, Waco, TX 76798.

Glasses are important parts of every lunar regolith sample, whether in the form of indigenous melts such as mesostasis or pyroclastics, or as quenched impact melts. The modal proportions of agglutinitic impact melts alone can exceed 50% for some mature regoliths,<sup>1</sup> and glasses are commonly the most dominant single component of lunar soils. They therefore participate in and possibly affect all evolutionary processes to which regoliths are subjected, such as comminution and attendant chemical fractionation as a function of grain size, the retention of solar-wind products, the production of superparamagnetic iron, and others. Because they are such an integral part of lunar regoliths, a more complete understanding of regolith evolution must include the role played by these vitreous components. This contribution examines the comminution behavior of a variety of glasses and a fine-grained basalt under conditions of repetitive impact, and compares this behavior to those of crystalline components, such as lithic fragments<sup>2</sup> and major rock-forming minerals.<sup>3</sup>

**Experimental Conditions:** Three distinct types of glass were used in these experiments: obsidian (a compact, dense specimen whose source is unknown); 2.29 g cm<sup>-3</sup>), tephra (a frothy, pyroclastic glass from Kilauea Iki; 1.32 g cm<sup>-3</sup>), and dragonite (an annealed, lead-rich, synthetic glass in the form of 3-mm spheres [Jaygo, Inc.]; 3.05 g cm<sup>-3</sup>). In addition, a basalt hornfels (3.12 g cm<sup>-3</sup>)<sup>4</sup> was used as a fine-grained endmember with little or no glass. All targets were exposed to normal atmospheric conditions, and thus were subjected to the strength-modifying effects of water; direct extrapolation to dry environments (such as the lunar surface) must be made with caution,<sup>5</sup> although relative comparisons should be acceptable. As in previous experiments,<sup>3</sup> the starting mass of each fragmental target was 500 g, with an initial fragment size of 2–4 mm. Stainless-steel projectiles with a diameter of 3.18 mm and a mass of 0.13 g impacted each target 25 times at a nominal velocity of 1.4 km s<sup>-1</sup>; actual velocities averaged 1.42 km s<sup>-1</sup>. Each impact was normal to the upper surface of the target charge, and the chamber pressure was 30-mm Hg equivalent for each shot. Stainless-steel buckets were used as target containers, with a lid and baffle system employed to minimize loss of ejecta. The charges were sieved after the first and fifth

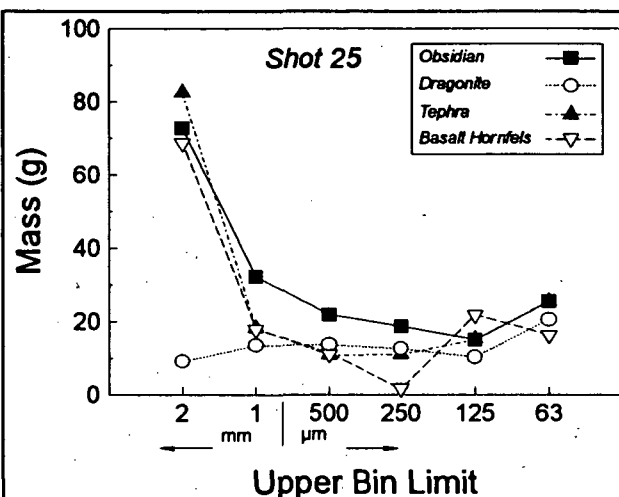


**Figure 1.** Size distributions for the four glass targets after the final shot in each series. Note the enhancement in the 63–125  $\mu\text{m}$  bin for the cryptobasalt.

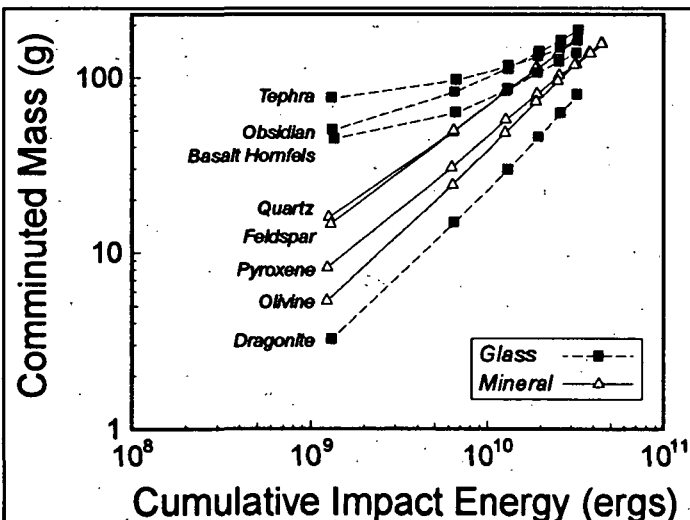


**Figure 2.** Comminuted masses for the four glassy targets used in this study. Also included for comparison are the results for four monomineralic targets.<sup>3</sup>

shots, and after every five shots thereafter. After sieving, each fraction was weighed and all fractions were recombined and mixed for the next shot. After each 25-shot series was completed, a 0.5-g aliquot taken from the <63- $\mu\text{m}$  fraction was wet sieved and the size fractions weighed; these data were used in surface-area calculations.

**Data:** This study considers only the comminuted fraction of the initial 500-g target — that is, that portion of the impacted target with grain sizes smaller than 2 mm. **Size Distributions** — The size distributions for the four targets after the final shot in each series are plotted in Figure 1. The tephra and obsidian follow trends common to such experiments, while the dragonite presents a very flat distribution. The distribution for the basalt hornfels is similar in shape to those of the obsidian and tephra, except for the marked lack of material in the 125–250  $\mu\text{m}$  bin and the enhancement of mass in the 63–125  $\mu\text{m}$  range. This relative depletion and enhancement is

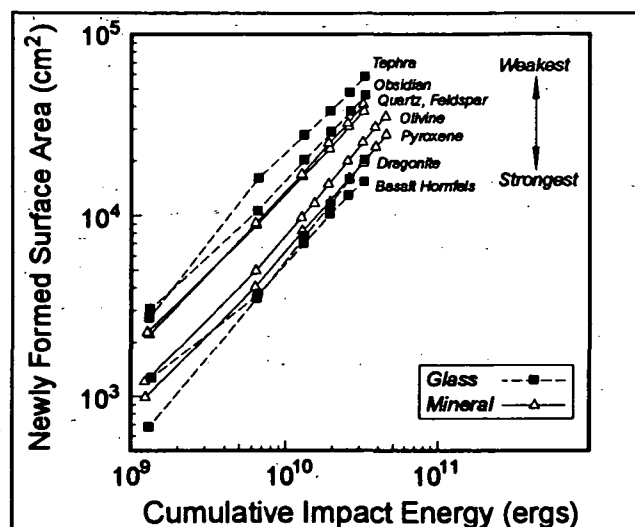


**Figure 3.** Newly formed surface area for the four glassy targets. Also included for comparison are the results for four monomineralic targets from a previous study.<sup>3</sup>

overall than the dragonite. Since the dragonite is intended for use as a grinding medium, its resistance to fracturing is not surprising. Because they have the highest new surface areas, the tephra and obsidian are judged to be the least resistant to comminution.<sup>6</sup> The dragonite generally breaks into finer fragments (Fig. 1), and thus possesses more surface area than the basalt hornfels. The relationship between these two materials is somewhat analogous to the differences observed between pyroxene and olivine in an earlier study,<sup>3</sup> in that the dragonite (olivine, in the earlier study) is more resistant to comminution in quantity, but breaks into finer pieces than the hornfels (pyroxene). The difference between the olivine and pyroxene was attributed to the fact that the pyroxene had to be fragmented with a hammer to generate the 2-4-mm fragments, and thus was "preconditioned" (undoubtedly including the introduction of microcracks and other flaws), while the olivine was already available as a gravel in that size range. This situation is repeated with the "pristine" dragonite and the similarly preconditioned basalt hornfels; it is probable that the polycrystalline nature of the hornfels and the spherical dragonite "grains" also contributes to the variations between the two targets. **All Targets** — A given mass of the three natural targets in the glass series is at least as easy if not easier to comminute than either of the two most susceptible minerals studied, feldspar and quartz. The weakest materials in terms of creating new surfaces are the tephra and obsidian, in that order, followed closely by the feldspar and quartz. Because the definition of "comminuted mass" is somewhat arbitrary, the surface area is a better measure of the ease with which a material is comminuted.<sup>6</sup> When considered in this light, the basalt hornfels is the strongest of all the natural materials measured. This is a somewhat surprising result, since the "matrix" of this particular basalt is plagioclase; while it is not quite as weak as the obsidian or tephra, it is barely stronger (Fig. 3). This is perhaps analogous to the case of a water-saturated frozen soil, which is significantly stronger than pure ice.<sup>8</sup> A simple interpretation of this phenomenon is that the silicate grains effectively impede propagation of fractures and microcracks by limiting the continuity of the ice matrix. It can then be argued that the effectively greater strength of the basalt is due to an analogous role played by the non-feldspar crystals in the rock. On this basis, we would expect that glassy basalts would behave in a similar fashion. Should this be confirmed by experiments in progress, an implication might be that the sources of the glass component in the finest fractions of regoliths are dependent on the state of the glass itself (e.g., agglutinates, glass droplets, interstitial glass in basalts or impact melts, etc.). Finally, the low resistance of the natural glasses to comminution is in keeping with experimental<sup>2</sup> and observational<sup>9</sup> evidence of enrichment of the finest grain-sizes of lunar regoliths with the most easily fragmented materials — in this case, glasses and feldspar.

**References:** 1 Morris, R.V. (1976) *PLSC 7th*, 1801. 2 F. Hörz et al. (1984) *PLPSC 15th*, in *JGR*, 89, C183. 3 M.J. Cintala and F. Hörz (1992) *Meteoritics*, 27, 395. 4 P.W. Weiblen et al. (1990) *Engineering, Construction, and Operations in Space II* (S.W. Johnson and J.P. Wetzel, eds.) Am. Soc. Civil Engin. (New York), 98. 5 Blacic, J.D. (1985) *Lunar Bases and Space Activities of the 21st Century* (W.W. Mendell, ed.) Lunar and Planetary Institute (Houston), 487. 6 M.J. Cintala and F. Hörz. (1988) *PLPSC 18th*, 409. 7 M.J. Cintala and F. Hörz (1984) *LPSC 15*, The Lunar and Planetary Institute (Houston), 158. 8 S.K. Croft et al. (1979) *JGR* 84, 8023. 9 J.M. Devine et al. (1982) *PLPSC 13th*, in *JGR* 87, A260.

characteristic of polycrystalline targets, in which fragmentation occurs preferentially along grain boundaries.<sup>6</sup> On the basis of this distribution, the average crystal dimension in the basalt hornfels can be predicted to lie between 63 and 125  $\mu\text{m}$ , an assessment in very good agreement with petrographic information.<sup>4</sup>

**Comminuted Masses** — The comminuted masses are plotted against cumulative impact energy in Fig. 2. The dragonite is substantially different from the three natural targets, although it appears to approach them as the impacts accumulate. The distributions for the obsidian and tephra are very similar, even with their relatively large density difference. **Surface Areas** — The areas of the newly formed surfaces<sup>7</sup> for the four targets are illustrated in Fig. 3, again as a function of cumulative impact energy. The obsidian and tephra continue to exhibit similar trends, but the dragonite in this plot is very similar to the basalt hornfels.

**Discussion: Glassy Targets** — In terms of mass produced, the three natural targets are the easiest to fragment, and they also possess shallower slopes

456 946

5145-91

N 94 - 12160  
ABS. 002/16 33651

LSC XXXV 1995

**MICROTEKTITE-LIKE GLASS SPHERULES IN LATE DEVONIAN (367 MA) SHALES.**

P. Claeys<sup>1</sup> and J-G Casier<sup>2</sup>. <sup>1</sup>Dept. Geology, Univ. Calif. Davis Ca. 95616; <sup>2</sup>Royal Inst. Nat. Sci. Brussels-Belgium.

p 2

Glass spherules are found closely associated with the Frasnian-Famennian (FF) boundary in two sections, Senzeille and Hony, located in the Dinant basin in the South of Belgium. These spherules are interpreted based on their chemistry and low water content as impact produced microtektite-like glass. Craters of Late Devonian ages include the Siljan Ring (Sweden), Charlevoix (Quebec) and Taihu Lake (China). The occurrence of microtektite-like glass closely associated with the FF mass extinction is intriguing. The relationships between the impact and the extinction event deserve further study.

In the Hony section, the spherule layer occurs at the very the base of Lower *triangularis*, the first conodont zone of the Famennian approximately 5 to 10 cm above the FF boundary. At Senzeille where the biostratigraphy is unclear, the spherule layer is present approximately 4.5 m above the base of the Senzeille shales [1]. In both location after crushing and acid dissolution of the shale, the spherule layer has produced between 0.03 and 0.1 mg of glass / g of sediment. Similar glass spherules have been reported from the Famennian Qidong section in China [2]. These Chinese glass spheres are found in the Lower *crepida* conodont zone and are according to conodont time scale +/- 1.5 m. y. younger than the Belgian ones.

The glassy spherules from Hony and Senzeille range in diameter from less than 50 microns to over 1 mm (250 microns in average). They are clear transparent (50%), yellowish (25%), reddish (5%) or have a dark metallic shine (20%). They are well rounded, less commonly they display elongated, dumbbell or tear drop shapes. Many are compound spherule or have small attached microspherules. The spherules are isotropic in polarized light and display conchoidal fractures. Their refractive indices varies from 1.48 to 1.56. Polished section examined under the SEM are smooth and glassy. A few spherules exhibit one or two large vesicles. No crystallites are present in the glass.

The spherules are often coated by a fine rim of calcite and clay minerals. This coating and their original low water content may explain their preservation for 367 m. y. In addition preservation may have been enhanced by rapid burial, abundance of fine grained silica, high organic content and the low porosity/permeability of the sediment in both location.

The glass spherules are interpreted as impact produced microtektites-like glass based on the following evidences: 1) Their morphology, shape and surface appearance, 2) The glass "exotic" chemistry and range of composition (Table), 3) The glass high K<sub>2</sub>O/Na<sub>2</sub>O ratio and high [Al<sub>2</sub>O<sub>3</sub>/(Na<sub>2</sub>O+K<sub>2</sub>O)], 4) The lack of high temperature microliths in the glass matrix and 5) The low water content of the glass (0.009 Wt. % determined by FTIR spectroscopy).

The glass chemistry appears quite similar at both location (Table). The range of composition is broader than commonly reported for microtektites [3]. This range might be explained by an inhomogenous target rock. The Al-rich and Fe-rich glass composition suggest the presence of pelitic sediments mixed with carbonates to produce the high Ca glass. The high silica (> 88 %) glass from Hony occurs as darker zone under SEM-BSE in the glass matrix. Similar high-Si zones have been described in microtektite glass from the Famennian Qidong section in China and interpreted as partially melted quartz grains [2]. Quartz inclusions have also been reported in Muong-Nong type tektites and impact glasses [4; 5].

Several impact craters of Late Devonian ages may be considered as possible sources for the Belgian glass spheres. The two best candidates so far, are the Siljan Ring in Sweden, the largest impact structure in Europe (52 Km in diameter) and the Charlevoix structure in Quebec (46 Km in diameter). The Siljan Ring has been dated by <sup>40</sup>Ar-<sup>39</sup>Ar method at 368 +/- 1 m.y. and Charlevoix crater at 350 +/- 20 m. y. (K-Ar method) [6]. The age of the FF boundary is estimated to be 367 Ma. [7]. The Siljan Ring target rock composition appears rather consistent with the Senzeille and Hony glass chemistry. The Siljan Ring is composed of Precambrian granites and Upper Silurian sandstones, shales and limestones [6]. Charlevoix crater rocks are a mixture of Precambrian

## 367Ma microtektites Claeys &amp; Casier.

granite, gneiss, migmatites, charnockite, gabbro and anorthosite [6]. The Taihu lake (>70 Km in diameter) in China has only recently been identified as an impact crater. It is according to Wang [3] the possible source for the Chinese microtektites.

The discovery of preserved microtektites-like particles in two Late Devonian sections demonstrates that an impact occurred at or near the FF boundary. This boundary is also marked by one of the largest mass extinction in the fossil record [8]. At this point we believe there is not yet enough evidence to definitively correlate the FF mass extinction with the impact taking place in what appears to be the very base of the Famennian. The discovery of the microtektite layer at Hony just a few cm above the extinction event is intriguing and the possible link between extinction and impact certainly deserves further study. Now that the FF boundary has been strictly defined [9], we believe that this question can be resolved in the near future. It will require the same type of global research program that so successfully demonstrated the connection between impact and extinction at the Cretaceous-Tertiary boundary.

	HONY GLASS				SENZEILLE GLASS [1]			
SiO <sub>2</sub>	60.00	49.38	62.32	88.60	63.46	50.41	40.0	44.78
Al <sub>2</sub> O <sub>3</sub>	24.58	32.89	21.16	4.02	22.78	30.90	18.97	20.21
FeO	3.96	8.33	1.49	0.95	1.58	7.25	31.75	5.40
MgO	1.05	1.49	0.93	0.45	2.12	2.37	2.12	2.10
CaO	0.46	1.96	9.77	0.05	3.26	4.11	1.46	23.11
K <sub>2</sub> O	7.28	3.00	2.64	2.97	4.71	2.96	2.11	2.16
Na <sub>2</sub> O	0.70	0.97	0.57	0.12	1.01	0.80	0.79	0.55
TiO <sub>2</sub>	1.38	1.27	0.70	2.28	0.60	1.04	0.65	0.60
MnO	<DL	0.09	0.10	<DL	0.16	0.10	1.11	0.15
Cr <sub>2</sub> O <sub>3</sub>	<DL	<DL	<DL	<DL	<DL	<DL	0.09	0.09
NiO	<DL	<DL	<DL	<DL	<DL	<DL	0.10	0.05
S	<DL	<DL	0.17	<DL	<DL	<DL	0.30	<DL
TOTAL	99.41	99.38	99.85	99.44	99.68	99.94	99.45	99.20

Table of microprobe analyses of the Hony and Senzeille glasses. All Fe as FeO. An average of at least 10 analyses are presented for each distinctive group.

- [1] Claeys Ph. *et al.*, 1992. Science, 257, 1102-1104.
- [2] Wang K., Science 256, 1546-1549.
- [3] Glass B. P. *et al.* 1985. Proc. 16 th LPSC part I D175-D196.
- [4] Koeberl C. Sec. Inter. Conf. on Natural Glassses, Prague 1987, 371-377.
- [5] Koeberl C., 1986. Ann. Rev. Earth Planetary Sci. 14 320-350.
- [6] Grieve R. A. F. *et al.*, 1988. LPI Technical Report No 88-03, 89 p.
- [7] Harlan W. B. *et al.*, 1989. Cambridge Univ. Press.
- [8] Raup D. M. and Sepkoski J. J. Jr., 1982. Science, 215, 1501-1503.
- [9] House M. R. and Feist R., 1992. IUGS, International Commission on Stratigraphy, 10p.



456 947

5146-46  
ABS. ONLY

LPSC XXIV

297

V9 4-12161

## KT BOUNDARY IMPACT GLASSES FROM THE GULF OF MEXICO REGION

P. Claeys<sup>1</sup>, W. Alvarez<sup>2</sup>, J. Smit<sup>3</sup>, A. R. Hildebrand<sup>4</sup>, A. Montanari<sup>5</sup>, <sup>1</sup>Dept. Geology, Univ. Calif., Davis 95616; <sup>2</sup>Dept. Geology & Geophysics, Univ. Calif., Berkeley 94720; <sup>3</sup>Dept. Sediment. Geol., Free Univ. Amsterdam; <sup>4</sup>Geological Survey Canada, 1 Observatory Crescent, Ottawa Canada K1A 0Y3; <sup>5</sup>Osservatorio Geologico di Coldigioco, 62020 Frontale di Apiro (MC) Italy.

Cretaceous-Tertiary boundary (KTB) tektite glasses occur at several sites around the Gulf of Mexico. Contrary to rumor among KTB workers, glass fragments have been found by several researchers in the base of the spherule bed at Arroyo el Mimbral in NE Mexico. The presence of green, red, and transparent glass fragments at Mimbral only, demonstrates that the Mimbral glass is not a laboratory contamination by Beloc glass. The chemistry and ages of the glass are consistent with an origin from the Chixculub impact crater in Yucatan. No evidence supports a volcanic origin for the KTB glasses.

Tektite glass from the KT boundary was first discovered at Beloc, Haiti [1; 2] and subsequently at DSDP sites 536 and 540, and at Arroyo el Mimbral in NE Mexico [3; 4]. At Beloc and Mimbral, glass particles occur as remnant cores within altered chlorite-smectite spherules. Informal discussions among KT workers have made it clear that finding glass in these sections is not always easy. Preserved glass occurs concentrated in local portions of the spherule bed because of irregular lithification and weathering intensity. Glass abundance is very low (<2% of the spherule fraction), and many spherule-bearing samples do not yield glass. Collections of samples from this outcrop taken on four different field expeditions over a two-year period have yielded glass fragments in three different laboratories:

- Glass was first found in the February 1991 collection taken at the time of the discovery of the KT Mimbral clastic bed by Smit, Montanari, Swinburne and Alvarez [3]. The discovery of glass was made independently by Hildebrand (Geological Survey of Canada) and by S. V. Margolis and Claeys (University of California at Davis), and reported by telephone to Smit and Alvarez at Berkeley on the same day (May 16, 1991).

- Hildebrand revisited the Mimbral outcrop in December 1991, and glass was again found independently in the samples from that trip by Hildebrand and by Margolis and Claeys.

- Montanari revisited the Mimbral outcrop in April 1992, and glass was once again found by Margolis and Claeys.

- Smit and T. Roep revisited the Mimbral outcrop in November 1992, together with R. Rocchia. Smit has found glass in samples taken then, from a different part of the outcrop than was previously sampled.

The glass is commonly preserved within clear sparry calcite crystals in the center of the spherules. Glass cores were also found preserved in the center of chlorite-smectite clay spherules. In the U.C. Davis procedure, samples of the spherule bed are disaggregated by ultrasound and digested over night in buffered acetic acid. The insoluble residue is then sieved to eliminate the finer fraction (<62 $\mu$ m). The glass fragments are hand-picked under the binocular microscope. The Mimbral outcrop has so far yielded less glass, and of generally smaller size fragments, than Beloc. Concentration of glass varies by more than a factor of 1000 from point to point in the Mimbral outcrop. The highest abundances found to date occur in the basal 2 cm of the spherule layer. Similar variability in glass concentration has been found in the Beloc outcrops.

The glass from Mimbral ranges in size from 0.1 mm to 3 mm and shows a great variety of color: dark brown to black (35%), amber-yellow (25%), green (20%), transparent (10%), red (10%). Individual glass grains from Mimbral contain widely varying compositions ranging from green to yellow glass within a single grain. The amber and black-to-green glasses have also been described at the Beloc KTB site in Haiti, [1; 2] but to our knowledge the red, green and transparent glasses have no equivalent at Beloc. At DSDP site 540 and 536 small (<50  $\mu$ m) green, brown amber and clear-colored glass fragments have also been found [4].

The glass from Mimbral and Beloc displays surface features such as etching, dissolution pits, furrows and sculpting similar to tektites [3, 5, 6]. The glasses are isotropic under polarized light and have a comparable range in refraction indexes (1.51 to 1.55 at Mimbral, 1.52-1.54 at Beloc [2]).

Polished section of Beloc and Mimbral samples appear smooth and free of microliths [1; 2; 3; 6]. Under SEM-BSE a few fragments of the Mimbral glass exhibit inhomogeneities and vague flow structure with variable proportions of Fe and Si. Similar flow structure and schlieren with high and low Si have also been described from the highSi-K Beloc glass samples [6].

The black and yellow glasses from Beloc and Mimbral appear very similar (Table). The fairly abundant Mimbral K-rich glass does not seem to have a Beloc equivalent. Koeberl and Sigurdsson [6] have reported only one fragment of a high Si-K glass rather distinct from the Mimbral composition (Table). The DSDP glass appears to have a feldspathic composition (Table) [4].

The water content, determined by FTIR spectroscopy, on the Beloc and Mimbral black glass is 0.03 and 0.05 wt% H<sub>2</sub>O respectively. This is definitively in the range expected for tektites and impact glasses and an order of magnitude lower than volcanic glasses [7]. These value confirm the data obtained for the Beloc glass by Koeberl and Sigurdsson [6].

The surface morphology, the absence of crystallites in the matrix, the chemistry and low water content of the glass all demonstrate the impact origin of the KTB glass. The volcanic origin of the Beloc glass proposed by Jehanno et al. [8] is unwarranted. The glass chemistry and ages confirm Chixculub as the KTB impact crater [9; 10; 11; 12]. The discovery of KTB glass at several sites around the Gulf of Mexico defines a KTB strewnfield and justifies the use of the term tektite for the KTB glass.

Table : Microprobe analyses of the KTB glasses from the Gulf of Mexico. All Fe as FeO.

	Black Mimbral [3]	Black Beloc [av. 2; 3]	Yellow Mimbral [3]	Yellow Beloc [6]	K-rich Mimbral [3]	Hi Si-K Beloc [6]	DSDP Leg 77 [av. 4]
SiO <sub>2</sub>	62.99	63.14	52.2	48.73	66.20	86.00	65.47
Al <sub>2</sub> O <sub>3</sub>	15.73	14.96	12.4	13.25	18.73	6.93	20.68
FeO	5.32	5.37	4.73	4.98	5.67	2.45	0.40
MgO	3.01	2.77	3.9	4.02	2.64	1.15	0.12
CaO	6.88	7.18	22.96	24.71	0.84	0.38	2.65
K <sub>2</sub> O	1.5	1.55	0.58	0.65	3.68	2.21	6.99
Na <sub>2</sub> O	3.34	3.46	2.02	2.54	0.84	0.38	2.63
TiO <sub>2</sub>	0.7	0.73	0.56	0.64	0.02	0.47	0.05
MnO	0.13	0.17	0.14	0.15	0.0	0.05	0.03
S	nd	0.0	nd	0.22	nd	0.0	nd
TOTAL	99.65	99.33	99.49	99.89	98.62	100.02	99.02

[1] Sigurdsson H. *et al.* 1991. *Nature* 349 482-486. [2] Izett G. 1991. *Jour. Geophys. Res.* 96, E4, 20879-905. [3] Smit J. *et al.* 1992. *Geology* 20, 99-103. [4] Alvarez W. *et al.* 1992. *Geology* 20, 697-700. [5] Glass B. P., 1990. *Tectonophysics* 171, 393-404. [6] Koeberl C. and Sigurdsson H., 1992. *Geochem. Cosmochem. Acta* 56, 2113-2129. [7] Koeberl C. and Beran A. *Proc. 18 th Lunar Planet. Sci. Conf.* 403-408. [8] Jehanno C. *et al.* 1992. *Earth Plan. Sci. Letters* 109, 229-241. [9] Hildebrand *et al.*, 1991 *Geology* 19, 867-871. [10] Swisher C C. *et al.* 1992, *Science* 257, 954-958. [11] Blum J.D. and Chamberlain C. P. 1992. *Science*, 257, 1104-1107. [12] Sharpton V. L. *et al.*, 1992, *Nature* 359, 819-821.

5147-90  
 456949  
 ABS ONLY  
 P. 2  
 N 9 46 1 2616 2

**FIRST RESULTS OF THE SEVEN-COLOR ASTEROID SURVEY;** Beth E. Clark, Jeffrey F. Bell, Fraser P. Fanale and Paul G. Lucey, Planetary Geosciences, University of Hawaii at Manoa, 2525 Correa Road, Honolulu, Hawaii, 96822

**Introduction:** The new Seven-Color infrared filter system (SCAS), designed specifically to capture the essential mineralogical information present in asteroid spectra, is composed of seven broad-band filters which allow for IR observations of objects as faint as 17th magnitude (Figure 1). The first test of the SCAS system occurred in July, 1992. In four nights at the IRTF on Mauna Kea, Hawaii, over 67 objects were observed. Five of the observations were to test the new system for accuracy relative to previous observations with the high-resolution 52-Color Infrared Survey [1], and with the Eight-Color Asteroid Survey (ECAS) [2]. In three cases, the match to previous data is good. In two cases the match to previous observations is not so good. In addition, sixty S-Type asteroids have been newly measured with the SCAS system. Forty of those asteroids have also been observed with the ECAS system. Among the new observations is infrared data of 371 Bohemia, a mainbelt asteroid which was classified "QSV" according to its UBV colors in the taxonomic system of D.J. Tholen [3]. There are no corresponding ECAS data for 371. Q-type asteroids are of special interest as they are proposed to be the elusive parent bodies of the ordinary chondrite meteorites [4]. Most Q-types are Earth-crossing asteroids [5], and have not yet been observed in the infrared (except, perhaps, 371). Positive identification of a large mainbelt Q-type would be of major importance in the scheme of the geological structure of the asteroid belt. Without visible wavelength data, however, the classification of 371 Bohemia remains ambiguous. Figure 2 shows an attempt to conjoin Bohemia SCAS data with ECAS data of both a typical Q-Type asteroid and an average S-Type asteroid. This figure thus illustrates the importance of visible wavelength data to the SCAS system. In other words, without ECAS data of 371 Bohemia we cannot use its spectral characteristics to identify it as a possible parent body of ordinary chondrite meteorites.

**Analysis:** As illustrated for the 52-Color data [6], the three parameters of albedo, continuum slope and 1-micron band depth were extracted from the new SCAS spectra combined with the ECAS data. In general, the clustering of S-type asteroids into a separate population from ordinary chondrite meteorites is preserved, despite the lower resolution and the sampling of fainter asteroids for our new SCAS data. Since only part of the new SCAS data set have corresponding ECAS data, a more general analysis technique of only the seven-color data is also presented here. Three specific color ratios of the SCAS bandpasses are plotted against each other. The 0.91/1.05 micron ratio is an indicator of the shape of the 1-micron mafic absorption band. The 1.30/1.55 micron ratio is an indicator of the slope coming out of the 1-micron absorption, and the 2.16/2.30 micron ratio is indicative of the 2-micron pyroxene absorption band. We have used the Hapke reflectance model [7] to calculate model spectra for the end-members Cpx, Opx, Ol, and FeNi metal. These model spectra were then convolved to the SCAS bandpasses and the above color ratios were calculated for systematic increases (at the equal expense of the other components) of each component, from 0% to 100%. The vectors which arise with mineral systematics are shown in Figure 3. For example, as the mafic minerals causing the absorption band near 1-micron switch from more Opx-rich to more Olivine and Cpx-rich, the ratio of the 0.91 to 1.05 micron filters crosses from less than unity to greater than unity. As work progresses, these clear trends will be useful in the characterization of S-asteroid sub-classes.

**Conclusion:** Attempts are underway to analyze spectral data for mineralogic heterogeneity within the S-type asteroid class [8,9,10]. Combining this SCAS data set with previous 52-color observations, a total of 100 S-type objects have now been observed. This large data set presents an opportunity to search for definitive trends in the spectra which indicate mineralogical sub-classes within the S-class. It is important, however, to augment all infrared observations of asteroids with the visible wavelength data in order to unambiguously identify potential meteorite parent bodies.

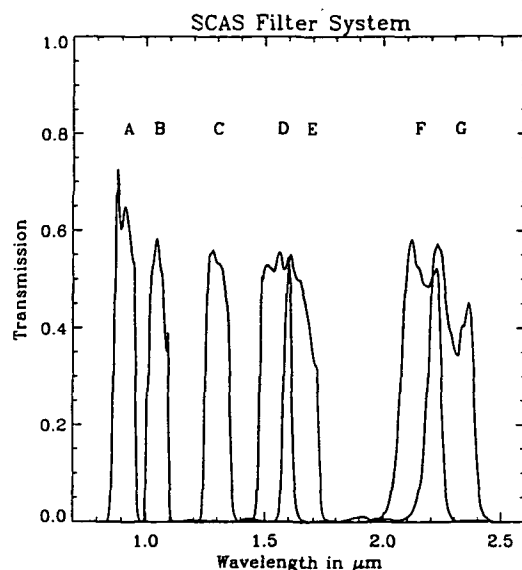
**Acknowledgements:** We thank J. Granahan, D. Tholen, M. Robinson (Univ. Hawaii), C. Kaminski and B. Golisch (NASA IRTF) for indispensable help.

**References:** [1] Bell et al. *LPSC*, XIX, 57-58, 1988 [2] Zellner et al. *Icarus*, 61, 355-416, 1985 [3] Tholen, *Asteroids II*, 1139-1150, 1989 [4] Bell et al., *Asteroids II*, 921-948, 1989 [5] Tholen, D.J. *Ph.D. Dissertation*, Univ. of Ariz., 1984 [6] Fanale et al. *JGR*, preprint, 1992 [7] Hapke et al. *JGR*, 86, 3039-3054, 1984 [8] Chapman, preprint, 1991 [9] Howell et al. *Bull. Amer. Astron. Soc.*, 23, 1140, 1992 [10] Gaffey et al., preprint, 1992.

## SEVEN COLOR ASTEROID SURVEY: Clark et al.

**FIGURE 1**

The new seven-color infrared filter system, designed to capture the essential mineralogical information present in asteroids spectra.

**FIGURE 2**

Attempts to conjoin asteroid 371 Bohemia with ECAS data of both a typical Q and a typical S-type spectrum. This figure illustrates the fact that ECAS wavelength data is necessary to the SCAS system.

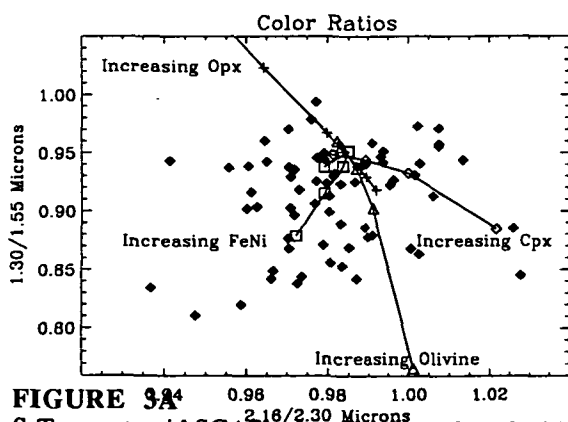
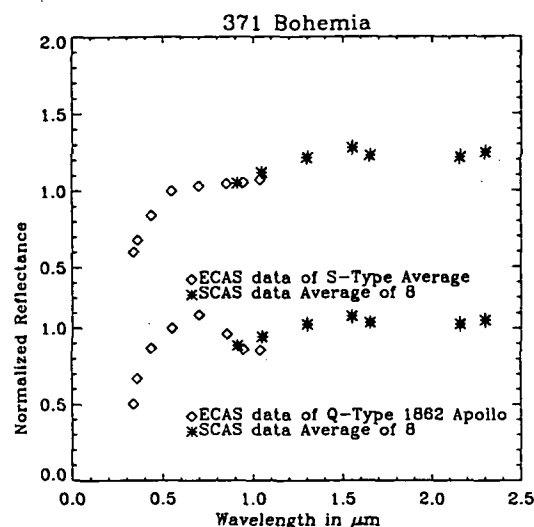


**FIGURE 3A**  
S-Type asteroid SCAS color ratios are plotted with filled diamonds and compared with color ratio trends found by calculating Hapke model systematic mineral component variations, from equal mixtures to pure end-members as indicated.

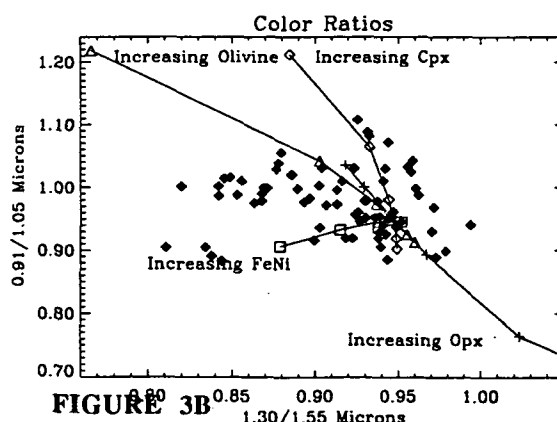


**FIGURE 3B**  
Same as in Figure 3A. Note that the 0.91/1.05 color ratio is a sensitive indicator of mafic mineral composition, and can distinguish between olv/cpx-rich and opx-rich asteroid surface assemblages.

456950

5148-90

ABS ON 94-12163

LPSC XXIV

301

**SIMULATION OF POSSIBLE REGOLITH OPTICAL ALTERATION EFFECTS ON CARBONACEOUS CHONDRITE METEORITES;** Beth E. Clark, Fraser P. Fanale and Mark S. Robinson, Planetary Geosciences, University of Hawaii at Manoa, 2525 Correa Road, Honolulu, Hawaii, 96822

**Introduction:** As the spectral reflectance search continues for links between meteorites and their parent-body asteroids the effects of optical surface alteration processes need to be considered. We present the results of an experimental simulation of the melting and recrystallization that occurs to a carbonaceous chondrite meteorite regolith powder upon heating. As done for the ordinary chondrite meteorites [1] we show the effects of possible parent-body regolith alteration processes on reflectance spectra of carbonaceous chondrites (CC's). For this study six CC's of different mineralogical classes were obtained from the Antarctic Meteorite Collection: two CM meteorites, two CO meteorites, one CK, and one CV. Each sample was ground with a ceramic mortar and pestle to powders with maximum grain sizes of 180 and 90 microns. The reflectance spectra of these powders were measured at RELAB (Brown University) from 0.3 to 2.5 microns. Following comminution, the 90 micron grain size was melted in a nitrogen controlled-atmosphere fusion furnace at an approximate temperature of 1700° Celsius. The fused sample was immediately held above a flow of nitrogen at 0° Celsius for quenching. Following melting and recrystallization, the samples were reground to powders and the reflectance spectra were remeasured. Figure 1 shows the effects on spectral reflectance for a sample of the CM carbonaceous chondrite called Murchison.

**Results:** The above procedure was followed in order to simulate the possible alteration of meteorite parent-body optical surfaces by heating due to impact or fusion crust development. As can be seen in Figure 1, the spectral effects of simulated regolith alteration by melting and comminution are significant. Following alteration the fused sample shows an increase in reflectance of about 40% as well as an apparent band center wavelength shift of about 0.2 microns, from 0.8 to 1.0 microns. This would indicate a correspondingly significant change to the mineralogy of the altered sample. Shown in Figure 2 are photomicrographs of polished grain mounts of Murchison, before (a) and after alteration (b). The altered sample shows typical quench textures and a clear increase in crystal size. In addition, it appears that metallic components in the altered sample have either agglomerated to form larger grains or have been enhanced in total number, possibly by carbon reduction of iron from the mafic silicates. Using an electron microprobe, we are in the process of determining the compositions of both the altered and unaltered sample. With known compositions we will be able to determine the cause of the wavelength shift of the 1-micron band as well as the cause of the apparent metal-enhancement.

**Discussion:** Until recently, regolith breccias have not been commonly identified among the carbonaceous chondrite meteorites [2, 3]. It is therefore not clear as to what effects weathering in the space environment may have upon carbonaceous chondrite parent body asteroids. The reflectance spectra of faint asteroids such as the P, D, T, C, G, B and F-Types are dark and relatively featureless making it difficult to establish definitive links with known meteorite types. The task is further complicated by surface processes which may be altering reflectance spectra. Some dark asteroids have been shown to spectrally resemble shock-blackened ordinary chondrites [4]. Others have been shown to resemble CM and CV carbonaceous chondrites [5, 6]. The details of the spectra vary significantly [7, 8, 9, 10]. Thus several questions remain unresolved, e.g: How well-sampled is the dark asteroid population? And how representative are the carbonaceous chondrite meteorites of the main belt asteroids? As work progresses we will show the extent to which the possible regolith processes of melting and quenching of CO, CM, CV, and CK carbonaceous chondrites can affect their optical properties and influence the search for their parent body asteroids.

**Acknowledgements:** We thank Tim McCoy, Ed Scott and Joann Sinton (University of Hawaii) for help with thin sections, Steve Pratt (Brown University) for RELAB measurements, Klaus Keil (University of Hawaii) for the generous donation of Allende meteorite chips, and the Antarctic Meteorite Working Group, also for generous meteorite donations.

**References:** [1] Clark et al. *Icarus*, 97, 288-297, 1992 [2] Scott et al. *Geochim et Cosmochim Acta*, 56, 1992 [3] Metzler et al. *Geochim et Cosmochim Acta*, 56, 2873-2897, 1992 [4] Britt and Pieters, *LPSC XX*, 111-112, 1989 [5] Burbine, T.H. Master's Thesis, Univ. of Pittsburgh, 1988 [6] Lebofsky et al., *Icarus* 48: 453-459, 1981 [7] Bell et al., *LPSC XIX*, 57-58, 1988 [8] Britt and Lebofsky, *LPSC XXIII*, 161, 1992 [9] Gaffey, M.J. *J. Geophys. Res.* 81, 905-920, 1976 [10] Howell et al. *Bull. Amer. Astron. Soc.*, 23, 1140, 1991.

## SIMULATION OF REGOLITH ALTERATION: Clark et al.

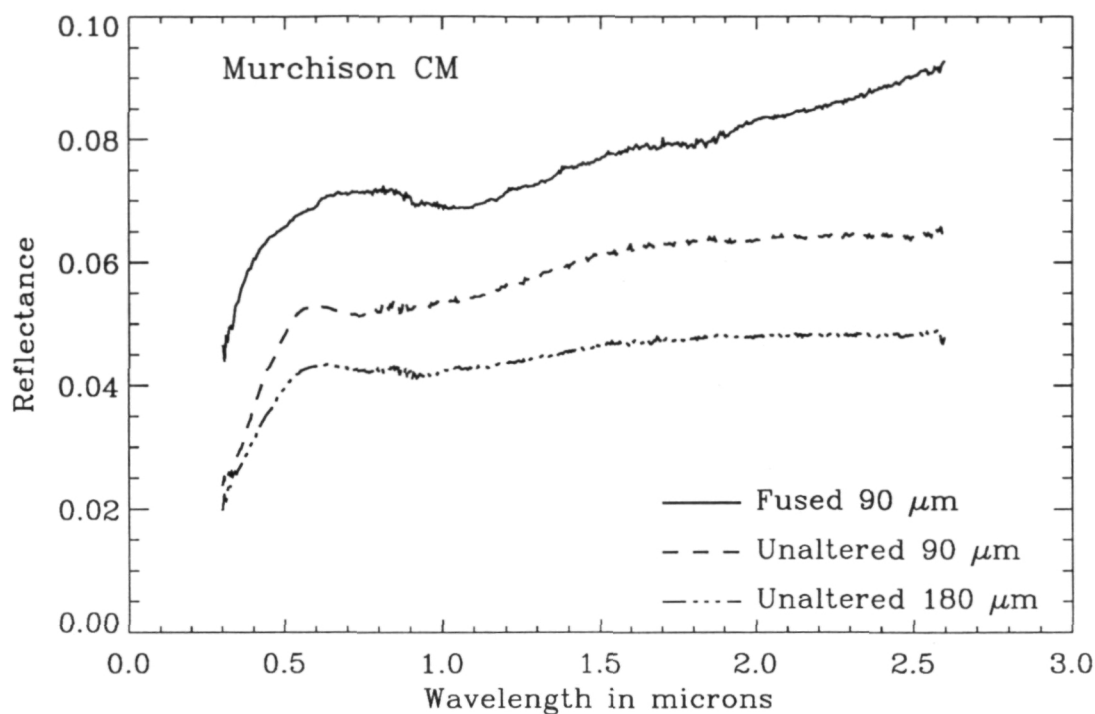


**Figure 1** Simulated regolith alteration by melting, quenching and comminution shows significant optical alteration. In this plot the unaltered meteorite powders are compared with the fused portion of the CM carbonaceous chondrite Murchison. Note the apparent wavelength shift of the mafic mineral absorption feature, as well as the dramatic overall increase in reflectance after alteration.

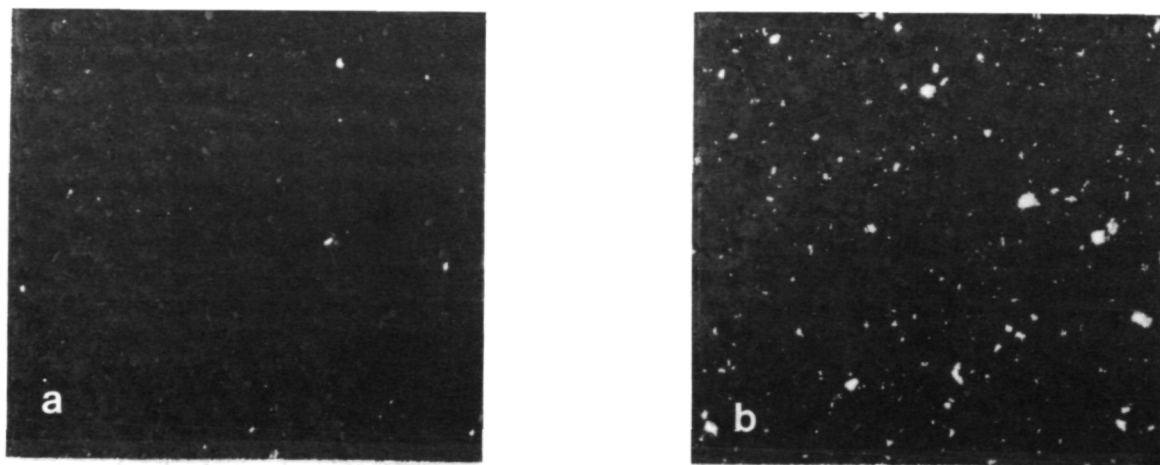


**Figure 2** Reflected light photomicrographs of polished grain mount thin sections of the CM carbonaceous chondrite Murchison before (a) and after alteration (b). Note the apparent enhancement of the metallic component seen after alteration by melting and quenching in a nitrogen atmosphere.

456955

5149-90

ABS ONLY

LPSC XXIV

303

N 9 4 - 13364

SPECTRAL MIXING MODELS OF S-TYPE ASTEROIDS; Beth E. Clark, Paul G. Lucey, Jeffrey F. Bell, and Fraser P. Fanale, Planetary Geosciences, University of Hawaii at Manoa, Honolulu, Hawaii, 96822

p 2

**Introduction:** This paper presents the results of an attempt to determine S-Type asteroid mineralogies with the use of Hapke theory spectral mixing modelling [1]. Previous attempts to understand the spectral variations present in this single class of asteroids have concentrated on spectral parameters such as absorption band center wavelengths, band area ratios, and geometric albedos [2, 3]. The procedure taken here is to utilize the Hapke spectral reflectance model to calculate single scatter albedo as a function of wavelength for a suite of candidate end-member materials. These materials are then mixed linearly in single scatter albedo space and the mixture is converted, assuming intimate particle mixing, back to reflectance for the spectrum matching routine. A total of 39 S-Type asteroids selected from the Bell et al. survey [4], have been matched with mixture model spectra.

**Procedure:** It is customary when analyzing asteroid spectral data to first normalize the spectra to 1.0 at 0.56 microns, thus eliminating albedo information until other means of analysis are completed. Part of the rationale behind this has been the fact that asteroid albedos are not known to a high degree of confidence, and cannot therefore be used as anything but rough guides as to asteroidal composition. For this paper, we first quantify the uncertainty in model composition which may be due to poorly constrained albedo. Next, we take the available published IRAS albedos to be the actual reflectance at 0.56 microns for each asteroid. The end-members we used are low-iron orthopyroxene and clinopyroxene, nickel-iron metal from the DRP IIAB meteorite, forsteritic olivine, and anorthositic plagioclase. All spectra of end-members were measured at the RELAB facility at Brown University [5, 6, 7]. In addition to the meteoritic metal component, a dark, spectrally flat absorber was added to the suite of end-members after initial attempts to use only metal resulted in systematic over-reddening of mixture model spectra. Scattering properties of the mafic minerals were approximated by taking an average of the legendre polynomial coefficients of mafic minerals analyzed by [8]. Each end-member has three different grain size ranges: < 45 microns, 45 - 75 microns, and 75 - 125 microns. To minimize procedural differences, spectra were first interactively fit with mixtures at the 45 - 75 micron average grain size range. In only two of thirty-nine S-Type spectra was a match with this grain size range impossible to achieve, whereas both other ranges resulted in strange average model compositions. Thus we make the preliminary assumption that S-Type asteroids have surface optical properties dominated by a 45 - 75 micron grain size fraction. Although this is probably an oversimplification of the actual surface grain size distribution we take it as a starting point until more information becomes available.

**Results:** Shown in Figure 1 are the compositions resulting from the model fits in terms of clinopyroxene vs. orthopyroxene, both values being normalized to total percentage mafic silicates. The lack of structure or clumping in this figure suggests that if important subgroups exist within the S-type population, their cpx to opx ratios form a smooth continuum and thus some other criteria is necessary for subgroup identification. In general, the spectral subgroups within the S-type asteroid population which have been identified by Gaffey et al. [3], have been verified by this analysis. These subgroupings were identified based on their positions on a plot of band I area/band II area vs. band I center position, a technique which appears to concentrate on the relative strength of the mafic absorption bands. We note, however, that a spectrum which appears to reflect an olivine/metal - rich assemblage may also be modelled with a mixture of plagioclase and clinopyroxene with equally minimized residuals. This possibility is indeed mildly suggested by the correlation seen in Figure 2. Thus, unless independent evidence is brought to bear, the non-uniqueness of these model fits is a considerable constraint on their usefulness. It is possible that ambiguities may be resolved by higher-precision fitting with different end-member minerals. This possibility will be explored in future.

**Discussion:** The largest single source of potential error in mixing model analyses is in the choice of end-member minerals. This is because the single-scatter albedo has been shown to be the most important Hapke parameter in characterizing mineral spectral properties, leaving refinements such as the phase function coefficients, the reflection geometry, and other parameters of secondary importance [8, 9]. Single particle phase function coefficients are however, important for the metallic component. We found that incorrect values of phase coefficients resulted in differences of overall reflectance of model spectra of up to 40%, which is quite significant when the albedo is an important parameter. Because the phase coefficients have not been measured specifically for the nickel-iron metal used here we chose to take the

## S-TYPE ASTEROID SPECTRAL MIXING MODEL: Clark et al.

average of the scattering properties of those types of metal that were measured by [8]. We note, however, that this is a potentially important source of error, and it seems that much work remains to be done before we fully understand the role of metallic components in mineral mixtures. Finally, we note several systematic errors in the results that were, given the end-members and grain sizes discussed above, impossible to eliminate. The first was a very consistent mismatch in the spectral shapes of the actual and model spectra in the wavelength regions of 0.3 to 0.5 microns and from 2.2 to 2.5 microns. The residual errors in these regions could very often be minimized by a balanced exchange of the spectrally flat neutral component with the metallic nickel-iron component. Thus if these errors were not due to choice of silicate mineral end-members, their source may lie in the inappropriate representation of the metallic component of S-type asteroid mineral mixtures.

**Acknowledgements:** We thank T. Hiroi (Johnson Space Center) for his generous help with metallic spectra, M. Gaffey (Rensselaer Polytech) for helpful discussions, J. Sunshine (Brown Univ.) for useful discussions and pyroxene spectra, J. Mustard (Brown Univ.) for good advice, and S. Pratt (also at Brown Univ.) for help with the RELAB spectral library.

**References:** [1] Hapke, *JGR*, **86**, 3039-3054, 1981 [2] Gaffey *LPSC*, **XXI**, 399-340, 1990 [3] Gaffey et al, *preprint*, 1992 [4] Bell et al., *LPSC*, **XIX**, 57-58, 1988 [5] Sunshine et al. *JGR*, **95**, 6955-6966, 1990 [6] Cloutis and Gaffey, *JGR*, **96**, 22,809-22,826, 1991 [7] Hiroi, *personal communication*, 1992 [8] Mustard and Pieters, *JGR*, **94**, 13,619-13,634, 1989 [9] Mustard and Pieters, *JGR*, **92**, E617-E626, 1987.

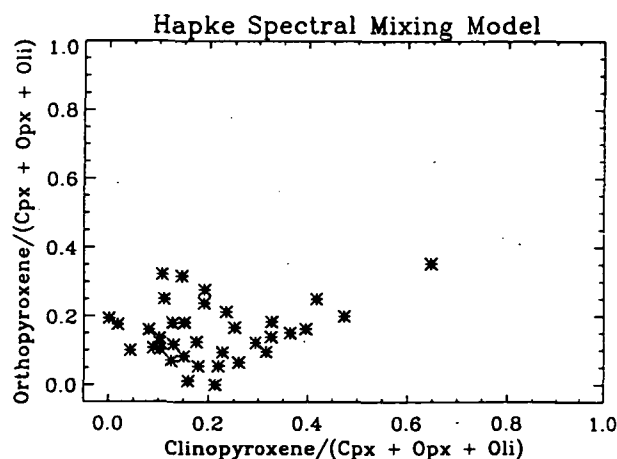


**Figure 1** Compositions resulting from Hapke model fits to 39 S-Type asteroids from the Bell et al. survey [4]. Note the lack of structure and clumping.

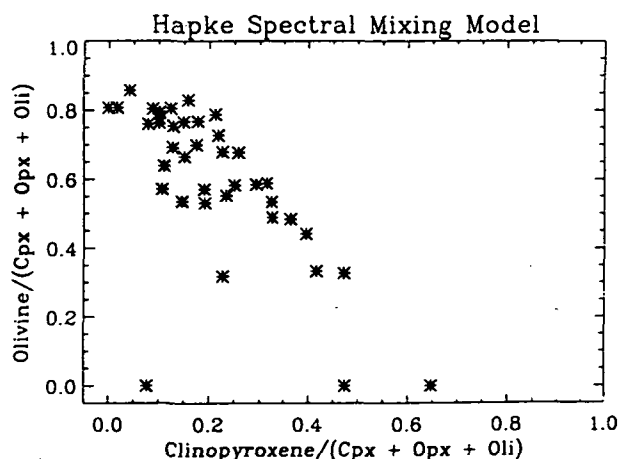


**Figure 2** Compositions of the same S-Type asteroid model fits as above, showing a rough correlation between total clinopyroxene and total olivine among the mafic mineral components. This correlation may be due in part to the non-uniqueness of spectral model fits, i.e. a spectrum which can be fit with olivine and metal can be fit equally well with clinopyroxene and plagioclase.



456959

S/50-91  
ABS ONLY

LPSC XXIV

305

N 9 4 1 2 1 6 5

P. 2

**Remote Sensing X-Ray Fluorescence Spectrometry for Future Lunar Exploration Missions** Pamela E. Clark, Albright College, Reading, PA., Larry G. Evans, Computer Sciences Corporation, Calverton, MD., Jacob I. Trombka, NASA, Goddard Space Flight Center, Greenbelt, MD.

Measurement of discrete line X-ray emission from space can be used to obtain both qualitative and quantitative elemental surface composition information. Remote orbital X-ray elemental analysis is the measurement of characteristic X-rays following the interaction of solar X-rays with the surface of a given solid body. Thus, X-ray emission from a surface is strongly dependent on the incident solar spectrum as well as on the chemical composition of the surface (1,2,3). In this paper, the relationship between the solar flux and the major lunar element fluorescence and scattered X-ray flux is characterized. A model had been developed to calculate lunar surface X-ray fluorescence emission spectra under a variety of solar conditions, and in particular conditions that might be expected for a Lunar Scout mission proposed for 1995 or 1996. This time period should be during solar minimum.

As mentioned above the X-ray emission is strongly dependent on the incident solar spectra. The solar flux is highly variable not only in intensity but in spectral shape (4,5,6). Generally speaking the differential energy spectrum of solar X-ray emission falls sharply with increasing energy. Thus, lower Z elements (e.g. Mg, Al, and Si) are more easily excited than the higher Z elements (e.g. Fe and Ti). When there is solar activity the intensity of the incident solar flux increases and the spectrum hardens. The higher Z elements can then be excited and fluorescent emission can be easily detected at orbital altitudes.

The X-Ray Fluorescent (XRF) spectrometer that flew on the Apollo 15 and 16 mission two decades ago measured lines from Mg, Al, and Si. Most of the information obtained was during a so-called quiescent sun period. The mission lasted only seven days so that there were not enough time for active sun periods to occur in order to obtain information on the higher Z elements. Even during this short period of time, elemental composition maps for about 10% of the lunar surface were obtained for Mg, Al, and Si (2,3,7,8).

If one flies a similar, but improved XRF instrument on a Lunar Scout in the 1995-1996 time frame, our calculation indicated that elemental composition for most of the lunar surface can be obtained for Mg, Al, and Si with better spatial resolution. Because of the longer time in orbit and the solar activity produced even at solar minimum, maps of elemental composition for Ca, Fe, and Ti as lower spatial resolution can also be obtained. Examples of these results for two different lunar compositions and five different solar conditions are shown in Table 1.

The theoretical models developed for this program were used to predict the Apollo 15 and 16 results and compared very well with the experimental results. Detailed results for a variety of sun conditions and typical lunar composition have been obtained. These results have been used to design the remote XRF spectrometer system proposed for the Lunar Scout orbital mission.

## REMOTE SENSING X-RAY: Clark, P. et al.

Table 1 XRF Integration Times for Compositional Determination  
Apollo 16 Composition

<u>Solar Conditions</u>	<u>Mg</u>	<u>Al</u>	<u>Si</u>	<u>Ca</u>	<u>Ti</u>	<u>Fe</u>
Low-Level Quiet	310s	75s	100s	1h	1500h	130h
Normal Quiet Sun	170s	37s	32s	0.3h	270h	16h
Subflare	37s	7s	6s	82s	22h	2h
Low-Level Flare	8s	1s	<1s	2s	500s	19s
High-Level Flare	2s	<1s	<1s	<1s	48s	2s

## Apollo 12 Composition

<u>Solar Conditions</u>	<u>Mg</u>	<u>Al</u>	<u>Si</u>	<u>Ca</u>	<u>Ti</u>	<u>Fe</u>
Low-Level Quiet	170s	200s	97s	2h	99h	42h
Normal Quiet Sun	97s	98s	30s	0.5h	19h	5h
Subflare	22s	16s	6s	130s	1.5h	0.5h
Low-Level Flare	5s	3s	<1s	2s	43s	7s
High-Level Flare	1s	<1s	<1s	<1s	4s	<1s

References: 1) Adler, I. and J. Trombka. 1970 GEOCHEMICAL EXPLORATION OF THE MOON AND PLANETS. 2) Clark, P. 1979 Chapter 6: In CORRECTION, CORRELATION AND THEORETICAL CONSIDERATION OF LUNAR X-RAY FLUORESCENCE INTENSITY RATIOS. U Maryland Dissertation. 3) Adler, I. and J. Trombka. 1977 Orbital chemistry-lunar surface analysis from the X-ray and gamma ray remote sensing experiments. PHYS. CHEM EARTH. 10: 17. 4) Kreplin, R., K. Dere, D. Horan, J. Meekins. 1977 The solar spectrum below 10A. SOLAR OUTPUT AND ITS VARIATION. 5) Donnelly, R. 1976 Empirical models of solar flare x-ray and EUV emission for use in studying their E and F region effects. JGR 81: 4745. 6) Solar Geophysical Data Comprehensive Reports, Part II. Data for May, September, and December 1986. 7) Bielefeld, M., C. Andre, E. Eliason, P. Clark, I. Adler, and J. Trombka. 1977 Imaging of the lunar surface from orbital X-ray data. PROC LUN SCI CONF 8TH 1: 901. 8) Clark, P. and R. Hawke. 1981 Compositional variation in the Hadley Apennine Region. PROC LUN SCI CONF 12B. 727.

456961

S161-90

ABS. 011

N94-PS-X2V160

163377

## CARBON AND NITROGEN IN TYPE II SUPERNOVA DIAMONDS:

Donald D. Clayton, Mounib El Eid, and Lawrence E. Brown, Department of Physics and Astronomy, Clemson University, Clemson SC 29634-1911

p. 2

Abundant diamonds found in meteorites seem either to have condensed within supernova interiors during their expansions and coolings or to have been present around those explosions. Either alternative allows implantation of Xe-HL prior to interstellar mixing [1,2,3]. A puzzling feature is the near normalcy of the carbon isotopes, considering that the only C-rich matter, the He-burning shell, is pure  $^{12}\text{C}$  in that region. That last fact has caused many to associate supernova carbon with  $^{12}\text{C}$  carbon, so that its SUNOCONS have been anticipated as very  $^{12}\text{C}$ -rich. We show that this expectation is misleading because the  $^{13}\text{C}$ -rich regions of Type II's have been largely overlooked in this thinking. We here follow the idea [1,2] that the diamonds nucleated in the  $^{12}\text{C}$ -rich He shell, the only C-rich site for nucleation, but then attached  $^{13}\text{C}$ -rich carbon during turbulent encounters with overlying  $^{13}\text{C}$ -rich matter. That is, the initial diamonds continued to grow during the same collisional encounters that cause the Xe-HL implantation. Instead of interacting with the small carbon mass having  $13/12=0.2$  in the upper He zone [2], however, we have calculated the remnants of the initial H-burning core, which left behind  $^{13}\text{C}$ -rich matter as it receded during core hydrogen burning. Howard *et al.* [3] described why the velocity mixing would be essential to understanding the implantation of both the Xe-H and Xe-L components. Velocity mixing is now known to occur from the X-ray and gamma-ray light curves of supernova 1987A.

Using the stellar evolution code developed at Göttingen [4] we calculated at Clemson the evolution of a grid of massive stars up to the beginning of core He burning. We paid attention to all H-burning reactions throughout the star, to the treatment of both convection and semiconvection, and to the recession of the outer boundary of the convective H-burning core as the star expands toward a larger redder state. This program was to generate a careful map of the CNO isotope distribution as He burning begins. Figure 1 shows our result for the  $30M_{\odot}$  star, which does not become a Wolf-Rayet star according to our prescription for mass-loss rate but evolves at almost constant mass. The H-burning shell ignites near  $8M_{\odot}$  when the final core has been exhausted of H. Very significant is the  $^{13}\text{C}$ -rich matter evident in Fig. 1 between 17 and  $22M_{\odot}$ . The  $^{13}\text{C}$  concentration was fixed by semiconvective mixing episodes from the top of the receding H-burning core. The heretofore unemphasized feature of this is that as that convective core receded, it left behind matter that had undergone only very slight H burning, so that  $^{13}\text{C}$  had been enriched from  $^{12}\text{C}(\alpha,\gamma)^{13}\text{N}$  but the  $^{12}\text{C}$  abundance itself had not been burned down to the low value to which it ultimately falls in equilibrium in the CNO cycles. That is, the mass between 17 and  $22M_{\odot}$  resembles matter that has only just begun to burn hydrogen. This composition remains almost unaltered outside the He core while it continues its entire presupernova evolution. Figure 1 also shows that within  $18M_{\odot}$  the  $^{12}\text{C}$  and  $^{13}\text{C}$  are both depleted by their more complete conversion to  $^{14}\text{N}$ . This causes the 17- $22M_{\odot}$  region of this  $30M_{\odot}$  star to have disproportionate influence on the 12/13 ratio outside the He core. The comparison with the initial solar abundances at the surface (now near  $27M_{\odot}$  of this initially  $30M_{\odot}$  star) shows that the matter outside the He core at  $9M_{\odot}$  is actually  $^{13}\text{C}$ -rich. It is the attachment of this carbon to the nucleated diamonds that prevents the SUNOCONS from remaining highly  $^{12}\text{C}$ -rich. This solution was previously suggested [2] in a more qualitative discussion. If the  $0.0016M_{\odot}$  of  $^{13}\text{C}$  ejected finally is mixed with the roughly  $0.14M_{\odot}$  of  $^{12}\text{C}$  created later in the He-burning shell, there would result a 12/13 ratio near 90 outside the carbon core. So only slight  $^{12}\text{C}$  richness is to be expected.

Additional  $^{12}\text{C}$  is synthesized later in the He-exhausted core, raising the  $^{12}\text{C}$  yield and making the bulk supernova yield roughly  $12/13=2-3$  times solar. But if we can speculate that only the carbon outside the final carbon core attaches effectively to the diamonds, perhaps

CARBON AND NITROGEN: Clayton D. D. et al.

owing to the catalytic necessity of hydrogen for diamond growth in a plasma [5], we can glimpse a reason for the near normalcy of carbon in the diamonds.

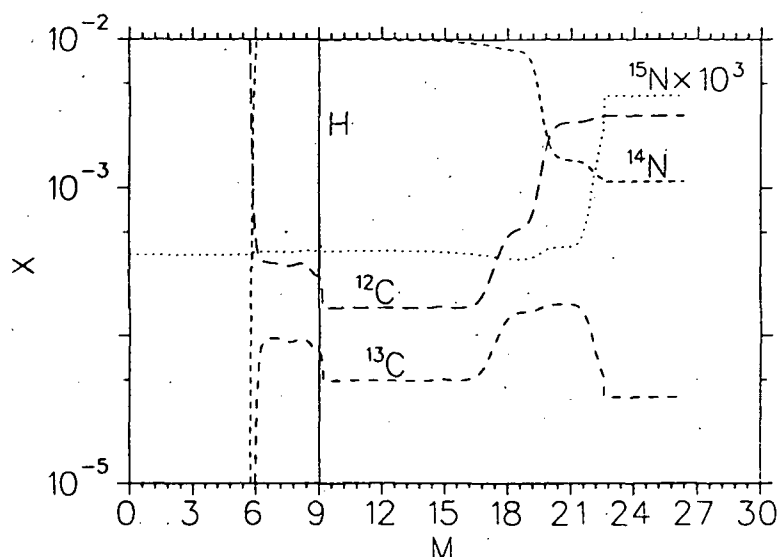
Next consider the nitrogen isotopes in Figure 1. Within  $19M_{\odot}$  the  $^{14}\text{N}$  is augmented to values near  $X(14)=0.02$ , with the result that  $M(14)=0.21M_{\odot}$  is contained at that time--approximately a factor 10 larger than the initial N content of the outer  $10M_{\odot}$  of that star. About half of this  $^{14}\text{N}$  is later destroyed by He burning creating the  $^{18}\text{O}$  yield of Type II's.

The  $^{15}\text{N}$  on the other hand later ejected. This bulk nitrogen yield is  $14/15=0.10/3.4 \times 10^{-5} = 3000$ , roughly tenfold greater than solar.

This easily accounts for the  $^{14}\text{N}$ -richness of the diamonds, but excessively so since they have  $^{15}\text{N}=-340$  [6]. An unidentified factor has favored inserting N from the outer part of stars in preference to the pure  $^{14}\text{N}$  in the He shell. The answer will depend in part on whether N must, like Xe, be implanted or whether it can be condensed during the diamond growth.

The new feature is the hydrodynamic instabilities that occur early

after the core bounce and thermonuclear explosion. These cause both inward and outward plumes of matter [7]. Some explosive oxygen, containing also Xe-L, bursts through the He shell where the diamonds will later nucleate, for example. The disruption of layered radial flow introduces the possibility of mild shocks later as one fluid element overtakes another. It is then that the Xe-L and the Xe-H can be implanted. This implantation is at much lower speeds than one normally thinks of in relation to lunar studies. Indeed, a solar-wind-speed Xe atom would either crash through a  $25\text{\AA}$  diamond or disrupt it or both--but not be captured by it. The desired speeds will allow penetration of the surface barrier of the diamond without later leaving another surface. This problem seems to merit study. In much the same spirit the  $^{13}\text{C}$ -rich carbon in the hydrogen plasma may facilitate further diamond growth for several years. Without the disruption of the radial flow the collisions would soon cease owing to the  $t^{-3}$  decline of particle density. A proper description of the growth of the diamonds will exceed our grasp for some time but will, in the end if this description is correct, offer unparalleled insights into the fluid mechanics and chemical reactions within the expanding supernova interior.



**References:** [1] Clayton, D.D. 1981 *Proc. Lunar Planet Sci* **12B**, 1781; [2] Clayton, D.D. 1989 *Astrophys. J.* **340**, 613; [3] Howard, W.M. et al. 1992 *Meteoritics* **27**, 404; [4] El Eid, M. & Langer, N. 1986 *Astron. Astrophys.* **167**, 274; [5] e.g. *SCIENCE* **258**, 736; [6] Lewis, R.S. et al. 1983 *Nature* **305**, 767; [7] Arnett, W.D. et al. 1989 *Ap.J(Lett.)* **341**, L63; 1991 *Astrophys. J.* **367**, 619.

456962

5152-90  
ABS ONLYLPSC XXIV  
N 94-12167  
763372.1

p. 2

**MEASUREMENT OF POLYCYCLIC AROMATIC HYDROCARBON (PAHs) IN INTERPLANETARY DUST PARTICLES;** S. J. Clemett, C. R. Macchling, and R. N. Zare, Department of Chemistry, Stanford University, Stanford, CA 94305-5080.

P. D. Swan and R. M. Walker, McDonnell Center for the Space Sciences, Physics Department, Washington University, One Brookings Drive, St. Louis, MO 63130-4899.

We report here the first definitive measurements of specific organic molecules (PAHs) in interplanetary dust particles (IDPs). An improved version of the microbeam-two-step laser mass spectrometer ( $\mu\text{L}^2\text{MS}$ ) described previously [1,2] was used for the analysis. Two IDPs gave similar mass spectra showing an abundance of PAHs. Control samples, including particles of probable terrestrial origin from the same stratospheric collector, gave either null results or quite different spectra. We conclude that the PAHs are probably indigenous to the IDPs and are not terrestrial contaminants.

The instrument used to study the particles is a two-step laser mass spectrometer. Constituent neutral molecules of the sample are first desorbed with a pulsed infrared laser beam focussed to 40  $\mu\text{m}$ . In the second step, PAHs in the desorbed plume are preferentially ionized by a pulsed UV laser beam. Resulting ions produced by resonant absorption are extracted into a reflectron time-of-flight mass spectrometer. This instrument has high spatial resolution, high ion transmission, unlimited mass range and multichannel detection of all ion masses from a single laser shot.

IDPs studied at WU are analyzed by several techniques [3]. Following EDS measurements, IDPs are crushed between quartz plates and adhering material is transferred to a KBr crystal for micro-FTIR absorption measurements [4] and/or micro-Raman [5] studies. Material on the other quartz plate is transferred to Au foils and isotopic measurements are made using a modified Cameca IMS-3F ion probe [6]. The KBr mounts proved satisfactory for analysis by  $\mu\text{L}^2\text{MS}$ . The molecular data were obtained on particles originally studied by F. Stadermann [7].

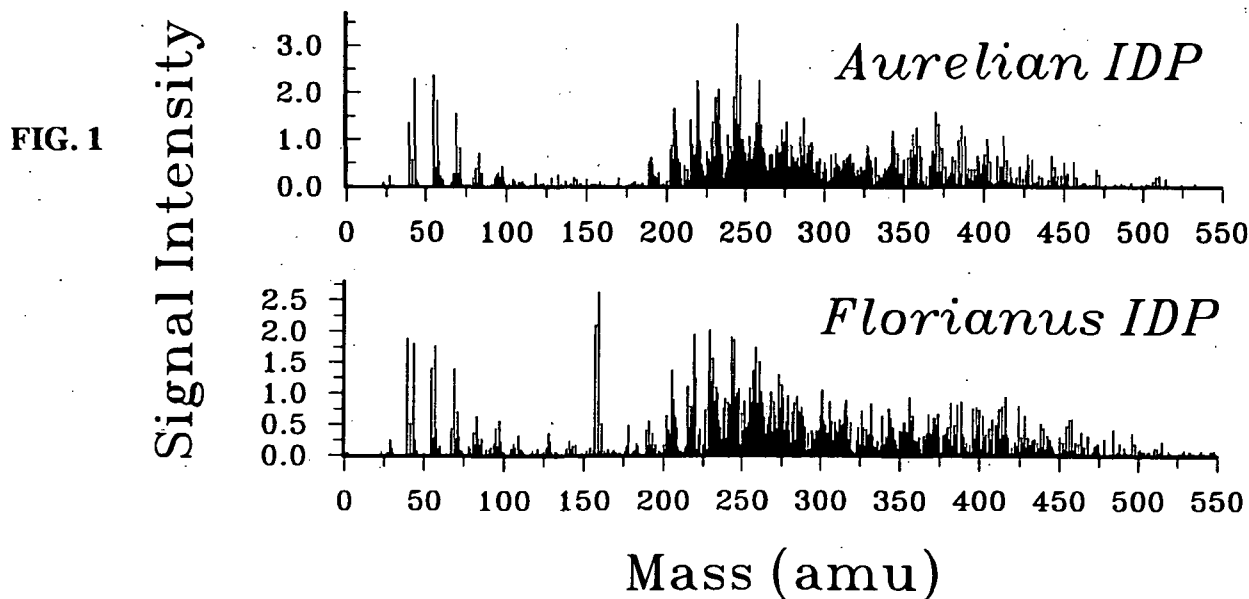
Positive results were obtained on two IDPs, Aurelian and Florianus. Both particles are certainly extraterrestrial; each has a chondritic elemental spectrum and both have large deuterium enrichments (up to  $\delta\text{D} = 771 \pm 85\text{‰}$  for Aurelian and  $\delta\text{D} = 1120 \pm 100\text{‰}$  for Florianus). In addition, Florianus has a large  $^{15}\text{N}$  enrichment ( $\delta^{15}\text{N} = 411 \pm 20$ ) [8]. Florianus has a typical pyroxene type IR spectrum while Aurelian has an IR spectrum characteristic of layer-lattice silicate IDPs [4]. Prior to shipping to Stanford the relevant dust fragments were relocated on the KBr mounts and remeasured by FTIR spectroscopy. A mark was then scribed on the KBr to locate the particles. Laser shots made at various locations on the KBr mount away from the marked IDPs gave negative results.

The  $\mu\text{L}^2\text{MS}$  results for Aurelian and Florianus are shown in Fig. 1. With the exception of the peaks in the Florianus spectrum at 155-165 amu, which we attribute to isotopomers of dipotassium bromide cation, the spectra are qualitatively similar although different in detail. Both show three major mass envelopes, one near 60 amu, one at moderate mass peaking at 250 amu, and one at high mass peaking at 370 amu. The moderate mass envelope has the largest intensity, followed in decreasing order by the high and low mass envelopes. The low mass envelope is dominated by inorganic species such as Na, K, and Fe. In contrast, the moderate and high mass envelopes contain clear signatures of PAHs and their alkylated derivatives, indicated by clusters of peaks separated by 14 amu as a consequence of the successive addition of methylene ( $-\text{CH}_2$ ) groups to the PAH skeletons. This identification is based on extensive experience with standard samples and the fact that the UV laser is tuned to selectively photoionize such molecules. The virtual absence of low mass PAHs (between 78-192 amu) such as alkyl-benzenes, alkyl-naphthalenes, and alkyl-phenanthrenes on these IDP spectra should be noted. This is consistent with the evaporation of these more volatile, lower mass organic components from an IDP during prolonged exposure in space, as well as loss by heating during atmospheric entry.

The zeptomole ( $10^{-21}$  mole) sensitivity of  $\mu\text{L}^2\text{MS}$  coupled with the wide scale distribution of PAHs in the terrestrial environment makes it difficult to prove that the observed molecules are not terrestrial contaminants. To examine this question samples of the silicone oil from collector U-47 were put on a fine-grained silica substrate (Cabosil) and looked at with  $\mu\text{L}^2\text{MS}$ . The xylene used to clean the IDPs and the Fomblin oil used in the SEM diffusion pumps were similarly studied. None of these samples gave spectra similar to those seen in Aurelian or Florianus. As a final test, we studied two particles that we had previously identified as "probable terrestrial contaminants" from collector U-47. One particle was dominated by Si, O, and Al, and the second by Ca, O, and Si. Both particles were measured in the ion probe and neither had measurable isotopic anomalies in H, N, C, or Mg. The total integrated yield of masses measured by  $\mu\text{L}^2\text{MS}$  was  $\leq 5\%$  that measured in Aurelian; the mass spectrum showed no evidence of PAHs within the detection limits. The fact that control particles which had been exposed to the same environment as Aurelian and Florianus did not show abundant PAHs lends strong support to the indigenous origin of the PAHs in the IDPs.

The results reported here are perhaps not surprising in view of prior indirect evidence for the presence of complex organic molecules in IDPs [5,6,8,9]. PAHs have also been previously measured using  $\mu\text{L}^2\text{MS}$  in various meteorites and their acid residues [1,10,11,12]. It is interesting to note however that the mass patterns seen by us in Aurelian and Florianus are different than those previously found in other extraterrestrial materials. Much work remains to be done to elucidate the nature of the organic molecules and their relationship to other properties of IDPs. The effects of heating during entry also need to be studied. To the extent that certain IDPs may represent the most primitive materials available, continued studies of the type described here can be expected to better elucidate the nature of the original organic materials in the solar system. These issues are now amenable to study thanks to the unprecedented sensitivity and specificity of  $\mu\text{L}^2\text{MS}$ .

**References:** [1] Kovalenko L. J. *et al.* (1992) *Analytical Chemistry*, **64**, 682-690. [2] de Vries M. S. *et al.* (1992) *Rev. Sci. Instrum.* **63** (6), 3321. [3] Fahey *et al.* (1985) In *Properties and Interactions of Interplanetary Dust*, Reidel, 149-155. [4] Sandford S. and Walker R. (1985) *Ap. J.* **291**, 838-851. [5] Allamandola L. *et al.* (1987) *Science* **237**, 56-59. [6] McKeegan K. D. *et al.* (1985) *Geochim. Cosmochim. Acta* **49**, 1971-1987. [7] Stadermann, F. J. *et al.* (1990) *LPSCXXI*, 1190-1191; Stadermann F. J. (1991) Ph.D. thesis, University of Heidelberg, Germany. [8] di Brozolo R. and Fleming R. H. (1992) *LPSC XXIII*, 1123. [9] Gibson E. K. and Hartmetz C. P. (1991) *LPSC XXII*, 439. [10] Hanh J. H. *et al.* (1988) *Science* **239**, 1523. [11] Zenobi R. *et al.* (1989) *Science* **246**, 1026. [12] Zenobi R. *et al.* (1992) *Geochim. Cosmochim. Acta* **56**, 2899.



456965

S153-91  
ABS ONLY

LPSC XXIV

311

N 9 4-132168

P-2

**MARS: THE INITIAL EMPLACEMENT OF GROUND ICE IN RESPONSE TO THE THERMAL EVOLUTION OF ITS EARLY CRUST**, Stephen M. Clifford, Lunar and Planetary Institute, Houston, Texas.

**Introduction** -- Given the geomorphic evidence for the widespread occurrence of water and ice in the early martian crust, and the difficulty involved in accounting for this distribution given the present climate, it has been suggested that the planet's early climate was originally more Earth-like, permitting the global emplacement of crustal  $H_2O$  by direct precipitation as snow or rain [1,2]. The resemblance of the martian valley networks to terrestrial runoff channels, and their almost exclusive occurrence in the planet's ancient ( $\sim 4$  billion year old) heavily cratered terrain, is often cited as evidence of just such a period. An alternative school of thought suggests that the early climate did not differ substantially from that of today. Advocates of this view find no compelling reason to invoke a warmer, wetter period to explain the origin of the valley networks. Rather, they cite evidence that the primary mechanism of valley formation was groundwater sapping, a process that does not require that surface water exist in equilibrium with the atmosphere [3-5]. However, while sapping may successfully explain the origin of the small valleys, it fails to address how the crust was initially charged with ice as the climate evolved towards its present state. Therefore, given the uncertainty regarding the environmental conditions that prevailed on early Mars, the initial emplacement of ground ice is considered here from two perspectives: (1) that the early climate started warm and wet, but gradually cooled with time, and (2) that it never differed substantially from that of today.

**Early Climate: Warm and Wet** -- The density and distribution of the valley networks throughout the heavily cratered terrain suggests that, regardless of whether early Mars started warm or cold, groundwater was abundant in the planet's early crust. However, given an initially warm start, an inevitable consequence of both the decline in Mars' internal heat flow and the transition to colder temperatures would have been the development of a freezing front within the regolith that propagated downward with time -- creating a thermodynamic sink for any  $H_2O$  within the crust. Initially, water may have entered this developing region of frozen ground from both the atmosphere and underlying groundwater. However, as ice condensed within the near-surface pores, it effectively sealed off the deeper regolith from any further atmospheric supply. From that point on, the only source of water for the thickening cryosphere would have been the geothermally-driven flux of vapor arising from the presence of groundwater at depth. Indeed, calculations by Clifford [6] indicate that a geothermal gradient as small as  $15 \text{ K km}^{-1}$  could supply the equivalent of 1 km of water from higher temperature (higher vapor pressure) depths to the colder (lower vapor pressure) base of the cryosphere every  $10^6 - 10^7$  years. Given the higher geothermal heat flow expected to have characterized the planet 4 b.y. ago, this supply of vapor may have been as much as 3 - 5 times greater in the past.

Pollack *et al.* [2] estimate that if the primary mechanism driving climate change was the removal of a massive (1 - 5 bar)  $CO_2$  atmosphere by carbonate formation, then the transition from a warm to cold early climate must have taken between  $1.5 \times 10^7$  to  $6 \times 10^7$  years. For transition times this slow, the downward propagation of the freezing front at the base of the cryosphere is sufficiently small (when compared with the geothermally-induced vapor flux arising from the groundwater table) that the cryosphere should have remained saturated with ice throughout its development.

From a mass balance perspective, the thermal evolution of the early crust effectively divided the subsurface inventory of water into two evolving reservoirs: (1) a slowly thickening zone of near-surface ground ice and (2) a deeper region of subpermafrost groundwater. One possible consequence of this evolution is that, if the planet's initial inventory of outgassed water was small, the cryosphere may have eventually grown to the point where all of the available  $H_2O$  was taken up as ground ice [7]. Alternatively, if the inventory of  $H_2O$  exceeds the current pore volume of the cryosphere, then Mars has always had extensive bodies of subpermafrost groundwater. As argued by Clifford [8], this latter possibility is strongly supported by the apparent occurrence of outflow channels as recently as the Mid- to Late Amazonian [e.g., 9,10].

**Early Climate: Like the Present** -- Of course, if early Mars was cold from the start, the initial emplacement of ground ice would have differed significantly from that described by the warm scenario. This possibility was first considered by *Soderblom and Wenner* [7] who suggest that the initial emplacement of crustal  $H_2O$  was the result of the direct injection and migration of juvenile water derived from the planet's interior. There are at least two ways in which this emplacement may have occurred. First, by the process of thermal vapor diffusion [6], water exsolved from cooling magmas will migrate from the warmer to colder regions of the crust. Upon reaching the cryosphere, this  $H_2O$  will then be distributed throughout the frozen crust by a variety of thermal processes [11]. As a result, any part of the cryosphere that overlies or surrounds an area of magmatic activity, will quickly become saturated with ice. The introduction of any additional water will then result in its accumulation as a liquid beneath the frozen crust, where, under the influence of the growing local hydraulic head, it will spread laterally in an effort to reach hydrostatic equilibrium. As this flow expands beneath areas where the cryosphere is not yet fully charged with ice, thermal vapor diffusion [6] and the other thermal processes discussed by *Clifford* [11] will redistribute  $H_2O$  into the frozen crust until its pore volume is either saturated or the local source of groundwater is finally depleted.

However, the fate of water released to the cold martian atmosphere is significantly different. The direct injection of a large quantity of vapor into the atmosphere (e.g., by volcanism) will lead to its condensation as ice on, or within, the surrounding near-surface regolith. As the available pore space in the upper few meters of the regolith is saturated with ice, it will effectively seal off any deeper region of the crust as an area of potential storage. From that point on, any excess vapor that is introduced into the atmosphere will be restricted to condensation and insolation-driven redistribution on the surface until it is eventually cold-trapped at the poles. Should such polar deposition continue, it will ultimately lead to basal melting [12], recycling water back into the crust beneath the caps. As the meltwater accumulates beneath the polar cryosphere, it will create a gradient in hydraulic head that will drive the flow of groundwater away from the poles. As the flow expands radially outwards, it will pass beneath regions where -- as a result of vapor condensation from the atmosphere -- only the top few meters of the cryosphere have been saturated with ice. As before, the presence of a geothermal gradient will then lead to the vertical redistribution of  $H_2O$  from the underlying groundwater until the pore volume of the cryosphere is saturated throughout. In this way, the early martian crust may have been globally charged with water and ice without the need to invoke an early period of atmospheric precipitation.

This analysis suggests that, whether the early martian climate started warm or cold, thermal processes within the crust played a critical role in the initial emplacement of ground ice. An important consequence of this fact is that, below the depths of equatorial desiccation predicted by *Clifford and Hillel* [13] and *Fanale et al.* [14], the cryosphere has likely been at or near saturation throughout its development -- or at least until such time as the total pore volume of the cryosphere grew to exceed the total volume of planet's outgassed inventory of water. The existence of outflow channels with apparent ages of less than 1 billion years [9,10] raises considerable doubt as to whether this last stage in the evolution of the martian cryosphere has yet been reached.

**References:** [1] Masursky et al. (1977). *J. Geophys. Res.*, **82**, 4016-4038. [2] Pollack et al. (1987). *Icarus*, **71**, 203-224. [3] Wallace, D., and C. Sagan (1979). *Icarus*, **39**, 385-400. [4] Carr, M.H. (1983). *Icarus*, **56**, 476-495. [5] Brakenridge et al. (1985). *Geology*, **13**, 859-862. [6] Clifford, S.M. (1991). *Geophys. Res. Lett.*, **18**, 2055-2058. [7] Soderblom, L.A., and D.B. Wenner (1978). *Icarus*, **34**, 622-637. [8] Clifford, S.M. (1993), *these abstracts*. [9] Tanaka, K.L., and D.H. Scott (1986). *LPSC XVII*, 865-866. [10] Mouginis-Mark, P.J. (1990). *Icarus*, **84**, 362-373. [11] Clifford, S.M. (1993), *these abstracts*. [12] Clifford, S.M. (1987). *J. Geophys. Res.*, **92**, 9135-9152. [13] Clifford, S.M. and D. Hillel (1983). *J. Geophys. Res.*, **88**, 2456-2474. [14] Fanale et al. (1986). *Icarus*, **67**, 1-18.



456967

5154-91  
ABS. ON 27

EPSC XXIV

313

N 9 4 1 6 9

# THE ROLE OF THE GEOTHERMAL GRADIENT IN THE EMPLACEMENT AND REPLENISHMENT OF GROUND ICE ON MARS, Stephen M. Clifford, Lunar and Planetary Institute, Houston, Texas.

P. 2

Knowledge of the mechanisms by which ground ice is emplaced, removed, and potentially replenished, are critical to understanding the climatic and hydrologic behavior of water on Mars, as well as the morphologic evolution of its surface [1,2]. Because of the strong temperature dependence of the saturated vapor pressure of H<sub>2</sub>O, the atmospheric emplacement or replenishment of ground ice is prohibited below the depth at which crustal temperatures begin to monotonically increase due to geothermal heating. In contrast, the emplacement and replenishment of ground ice from reservoirs of H<sub>2</sub>O residing deep within the crust can occur by at least three different thermally-driven processes, involving all three phases of water. In this regard, Clifford [2] has discussed how the presence of a geothermal gradient as small as 15 K km<sup>-1</sup> can give rise to a corresponding vapor pressure gradient sufficient to drive the vertical transport of 1 km of water from a reservoir of groundwater at depth to the base of the cryosphere every 10<sup>6</sup> - 10<sup>7</sup> years. This abstract expands on this earlier treatment by considering the influence of thermal gradients on the transport of H<sub>2</sub>O at temperatures below the freezing point.

In the gas phase, the transport of H<sub>2</sub>O through unsaturated frozen ground occurs by the process of thermal vapor diffusion where, as noted above, the presence of a temperature gradient creates a corresponding vapor pressure gradient that drives the diffusion of vapor from the warmer depths to the colder near-surface crust [2]. However, sub-freezing temperatures affect this process in two important ways. First, because the vapor flux at any depth is proportional to the local saturated vapor pressure, the magnitude of vapor transport necessarily declines as the diffusing vapor rises higher in the frozen crust. Second, this decline in temperature and saturated vapor pressure causes a portion of the ascending vapor flux to condense and freeze, preferentially blocking the smallest pores present in the pore system. This condensation can both substantially retard diffusion and choke off much of the pore network long before the larger pores are filled with ice. With time, however, these blockages succumb to the same thermal process that led to their formation. Thus, vapor will sublime from the ice plugs formed in the warmer, deeper regions of the cryosphere and redistributes itself -- through a repeated process of condensation, sublimation, and diffusion -- to the colder near-surface crust. In this way, the process of thermal vapor diffusion will continue until the cryosphere is ultimately saturated with ice.

The possibility of liquid phase transport arises from the fact that both adsorbed water and water in small capillaries can survive in frozen soil down to very low temperatures. Under conditions where the unfrozen water content is high enough to provide thin film continuity, the presence of a temperature gradient creates a corresponding gradient in soil water potential  $\Delta\psi$  -- a quantity that reflects the difference in effective pressure between the phases of ice and unfrozen water present in the soil. Under atmospheric conditions (*i.e.*, in the absence of a confining pressure), the magnitude of this pressure difference can be calculated from a form of the Clausius-Clapeyron equation [3,4], given by

$$\frac{dP_w}{dT} = \frac{L_f}{TV_w} \quad (1)$$

where  $P_w$  is the pressure (or hydraulic head) of soil water,  $L_f$  is the latent heat of fusion ( $= 3.35 \times 10^5$  J kg<sup>-1</sup>), and  $V_w$  is the specific volume of water ( $= 1/\rho$ ) at the crustal temperature  $T$ . Equation (1) indicates that the pressure difference between ice and water in the soil increases by  $\sim 1.2 \times 10^6$  Pa K<sup>-1</sup> for crustal temperatures below 273 K. After Smith and Burn [5] and Williams and Smith [4], the liquid flow (per unit area) that occurs in response to this temperature-induced pressure difference is given by

$$q_l = - \frac{k_f g}{\nu} \frac{d\psi}{dT} \frac{dT}{dz} \quad (2)$$

where  $k_f$  is the permeability of the frozen soil,  $g$  is the acceleration of gravity,  $\nu$  is the kinematic viscosity, and  $d\psi/dT$  ( $\equiv dP_w/dT$ ) is the temperature-dependent gradient in soil water potential. Assuming a geothermal gradient of 15 K km<sup>-1</sup>, a value of  $d\psi/dT = 1.2 \times 10^6$  Pa K<sup>-1</sup> (from eq. (1)), and a frozen permeability of  $\sim 2 \times 10^{-7}$  darcies (a value appropriate for a silty clay soil at a temperature just below freezing [4,6]), the resulting vertical flux of liquid water through the base of the cryosphere is found to be  $\sim 4.3 \times 10^{-5}$  m yr<sup>-1</sup>, or roughly 0.4 km every 10<sup>7</sup> years. It should be cautioned, however, that this flux is highly sensitive to both the local lithology and effective confining pressure of the crust; therefore, because these conditions are so poorly constrained at the base of the cryosphere, this estimate has an inherent uncertainty of as much as two orders of magnitude. Note also, that because the permeability of frozen soil declines with decreasing temperature, the magnitude of liquid transport will necessarily decline as the water reaches the colder and shallower regions of the crust.

Finally, in addition to the movement of  $H_2O$  vapor and liquid through the cryosphere, transport in the solid phase can occur by the process of thermal regelation; where, as before, the direction of transfer is from warm to cold [7,8]. As discussed by Williams and Smith [4], the process of regelation involves the movement of both ice and unfrozen water through a saturated (or nearly saturated) frozen soil. Fundamental to this process is the thermodynamic relationship between freezing point depression and the effective pressure difference between the ice and water phases present in the pores. As the geothermal gradient drives the flow of water through the unfrozen films that permeate the cryosphere, the entry of liquid water at the warm end of the pores causes a local increase in water pressure that decreases the effective pressure difference between the ice and water phases. In response to this reduction, the local freezing point will increase by an amount sufficient to cause a small quantity of water to freeze at the warm end of the pore. This freezing causes an increase in ice pressure at the pore's cold end where it increases the local difference in effective pressure between the ice and water phases -- thus, lowering the local freezing point. Water released by the subsequent melting of ice from the cold end of the pore then becomes part of the thin-film flow that enters the colder ice-filled pores located higher in the crust, whereupon the whole process is again repeated.

Note that because each of these thermal processes operate by driving the movement of water from warmer to colder regions of the crust, the transport of  $H_2O$  through the martian cryosphere is necessarily a one-way street. That is, if one attempts to introduce water into the cryosphere via the atmosphere, the maximum depth of penetration is necessarily limited to the maximum depth at which climatic temperature variations are sufficient to overwhelm the influence of the local geothermal gradient. For the surface temperature variations expected at mid- and equatorial latitudes from the periodic changes in martian obliquity and orbital elements, this depth is not likely to exceed several meters [9,10].

In contrast, when water is supplied to the cryosphere from below, the processes of thermal vapor diffusion, thermal liquid transport, and regelation, will permit its eventual redistribution throughout the frozen crust. This fact has a number of important consequences. For example, should an ice-rich region be buried by lavas, sediments, or some other type of deposit, the resulting increase in insulation provided by the depositional layer will cause local crustal temperatures to rise, permitting the buried ground ice to be thermally redistributed into the overlying mantle.

The ability of  $H_2O$  to thermally migrate through the cryosphere also has implications for the sublimation of equatorial ground ice. As the sublimation front propagates deeper into the crust, it may ultimately reach a depth where the diffusive loss of ground ice is exactly balanced by the upward thermal migration of  $H_2O$  through the cryosphere -- a condition that could significantly limit equatorial desiccation to depths shallower than those predicted by current models [10,11]. Unfortunately, the processes governing the transport of  $H_2O$ , both to and from the sublimation front, are sufficiently complex that calculating a specific depth at which this equilibrium condition is reached is virtually impossible without a more detailed knowledge of a number of crustal parameters (e.g., lithology, porosity, pore size, specific surface area, heat flow, salt content, etc.).

In summary, three processes -- thermal vapor diffusion, thermal liquid transport, and regelation -- are capable of transporting  $H_2O$  throughout the cryosphere, the direction of transport being from warmer to colder regions of the crust. Note that these processes will occur wherever there exists a crustal temperature gradient, a subsurface reservoir of  $H_2O$ , and the continuity of pore space between the source region and the near-surface crust. In this way, ground ice that was removed by impacts or sublimation to the atmosphere could have been replenished on a global scale, without the need to invoke exotic scenarios of climate change. A more detailed discussion of the potential role of these processes in the hydrologic evolution of Mars is currently in press [1].

**References:** [1] Clifford, S.M. (1993). *J. Geophys. Res.*, in press. [2] Clifford, S.M. (1991). *Geophys. Res. Lett.*, 18, 2055-2058. [3] Edlefsen, N.E. and A.B.C. Anderson (1943). Thermodynamics of soil moisture, in: *Hilgardia*. [4] Williams, P.J. and M.W. Smith (1989). *The Frozen Earth*, Cambridge Univ. Press. [5] Smith, M.W. and C.R. Burn (1987). *Cold Regions Sci. and Technology*, 13, 143-152. [6] Smith, M.W. (1985). *Can. J. Earth Sci.*, 22, 283-290. [7] Miller et al. (1975). *Soil Sci. Soc. Am. Proc.*, 39, 1029-1036. [8] Miller, R.D. (1980). Freezing phenomena in soils, in: *Applications of Soil Physics* (D. Hillel, ed.), Academic Press. [9] Toon et al. (1980). *Icarus*, 44, 552-607. [10] Fanale et al. (1986). *Icarus*, 67, 1-18. [11] Clifford, S.M. and D. Hillel (1983). *J. Geophys. Res.*, 88, 2456-2474.

456968

555-91

AB5 0227

LPSC XXIV

315

N 94-152170

THE THERMODYNAMIC CASE FOR A WATER-RICH MARS, Stephen M. Clifford, Lunar and Planetary Institute, Houston, Texas.

P. 2

**Introduction** -- Carr [1,2] has reviewed the geologic evidence for a water-rich Mars and has concluded that it is consistent with an outgassed inventory of  $H_2O$  equivalent to global ocean 0.5 - 1 km deep. The most persuasive support for this conclusion comes from the martian outflow channels, whose distribution, size, and range of ages, suggests that a significant body of groundwater was present on Mars throughout much of its geologic history [1-4]. In this abstract, the thermodynamic implications of the outflow channels are considered. The results of this analysis suggest that if the outflow channels were carved by the discharge of groundwater in diffusive and thermodynamic equilibrium with the overlying frozen crust, it implies a minimum planetary inventory of water in excess of 300 m. However, if the global inventory of groundwater on Mars at the time of outflow channel formation was as high as the 500 m estimate of Carr [2], then the *total* inventory of water on Mars could well exceed 750 m.

**Channel Discharge and the Global Inventory of Groundwater** -- Based on a conservative estimate of how much material was eroded to form the outflow channels ( $\sim 5 \times 10^6 \text{ km}^3$ ) and the maximum sediment load that the flood waters could have carried ( $\sim 40\%$  by volume [5]), Carr [2] has calculated that a minimum cumulative channel discharge of  $7.5 \times 10^6 \text{ km}^3$  of  $H_2O$  (equivalent to global ocean  $\sim 50$  m deep) was required to form the circum-Chryse channels. For at least two reasons, this calculation has likely underestimated the volume of groundwater initially present in the Chryse drainage basin. First, if the channels are not the product of a single catastrophic event, but represent the cumulative effect of multiple episodes of outbreak and erosion, then the channel flood waters may have been far less turbulent and carried far less sediment per unit volume than the assumed maximum value of  $40\%$  [7]. If so, the total volume of water required to produce the channels could have easily been several times greater than the value of 50 m estimated by Carr [2]. Second, any portion of the local aquifer whose absolute elevation lay below that of the visible channel source region would have remained undrained [6]. Since the zone of saturation could extend several kilometers or more beneath the lowest elevation in the basin, this could represent a substantial quantity of untapped groundwater. Finally, without a more detailed knowledge of the large-scale permeability of the martian crust, it is unclear whether the reservoir of groundwater that was tapped in the formation of the channels represented only a small portion of the basin's reserves, all of the basin, or includes water derived from a more extensive regional or global aquifer system (e.g., Clifford [8]). The answer to this question is crucial to the validity of Carr's [2] estimate that the global inventory of groundwater on Mars is equivalent to a global ocean 500 m deep. This estimate is based on the assumption that the Chryse channels drained all of the groundwater present in the Chryse basin and that the water content of the crust in this region is representative of the entire planet (a surface area roughly ten times greater).

**The Martian Cryosphere as a Thermodynamic Sink for  $H_2O$**  -- As discussed elsewhere [8,9], a prior condition for the existence of any large volume of groundwater on Mars is that the pore volume of the cold-trap represented by the cryosphere must first be saturated with ice. In support of this conclusion, consider the hydrologic response of Mars to the thermal evolution of its early crust. The density and distribution of the valley networks throughout the heavily cratered terrain has suggested to some that early Mars was once warm and wet [10,11]. However, given both the decline in planet's internal heat flow and the transition to colder temperatures, a freezing front eventually developed within the regolith that propagated downward with time -- creating a thermodynamic sink for any  $H_2O$  within the crust. Calculations by Clifford [12] indicate that, given an available reservoir of groundwater at depth, a geothermal gradient as small as  $15 \text{ K km}^{-1}$  is sufficient to drive a thermally-induced vapor flux equivalent to 1 km of water to the base of the cryosphere every  $10^6 - 10^7$  years (a flux that was likely 3 - 5 times greater 4 b.y. ago, given the higher heat flow expected to have characterized the planet at that time). This vapor flux is high enough that the cryosphere should have remained saturated with ice throughout its development -- or at least until such time as the total pore volume of the cryosphere grew to exceed the total volume of planet's outgassed inventory of water. However, the existence of outflow channels with apparent ages of less than 1 billion years [3,4] raises considerable doubt as to whether this last stage in the evolution of the martian cryosphere has yet been reached -- suggesting that an inventory of water in excess of that stored in the cryosphere has persisted on Mars until very recent times, and may continue to persist to the present day.

Given geologically conservative estimates of martian crustal porosity ( $< 20\%$ ), thermal conductivity ( $\sim 2.0 \text{ W m}^{-1} \text{ K}^{-1}$ ), and heat flow ( $\sim 30 \text{ mW m}^{-2}$ ) [9], the present cryosphere is estimated to have a minimum pore volume in the range of 400 - 500 m. At the time the outflow channels formed ( $\sim 2$  b.y.a.), the planet's geothermal heat

flow was likely a factor of two higher. This would have reduced the pore volume of the cryosphere to ~ 250 - 300 m. Given Carr's [2] minimum estimate of the amount of groundwater required to erode the channels (50 m), this implies a minimum global inventory of water of ~ 300 m. If Carr's [2] 500 m estimate of the global inventory of groundwater at this time is correct, then a total planetary inventory of H<sub>2</sub>O in excess of 750 m is implied.

While the theoretical argument for a water-rich Mars based on the thermodynamic implications of the outflow channels is persuasive, it falls short of an actual proof. Unfortunately, at present, the channels are the best evidence for a water-rich Mars that we have. However, as the exploration of Mars continues, there will be opportunities for more direct investigations of the subsurface that should resolve this issue conclusively. While prospects for a Mars Deep Drilling Project are likely to remain dim for the foreseeable future, at least two other geophysical methods, active seismic exploration and electromagnetic sounding, could be used to map and inventory the distribution of ground ice and groundwater beneath the planet's surface. The detection of groundwater at locations far removed from any obvious source of transient production -- such as active geothermal regions or volcanoes -- would establish beyond any reasonable doubt that Mars is water-rich. In the absence of such evidence, the thermodynamic arguments presented here suggest that the minimum inventory of water on Mars, consistent with the inferred timing and discharge of the outflow channels, is ~ 300 m.

**References:** [1] Carr, M.H. (1986). *Icarus*, **68**, 187-216. [2] Carr, M.H. (1987). *Nature*, **326**, 30-35. [3] Tanaka, K.L., and D.H. Scott (1986). *LPSC XVII*, 865-866. [4] Mouginis-Mark, P.J. (1990). *Icarus*, **84**, 362-373. [5] Komar, P.D. (1980) *Icarus*, **42**, 317-329. [6] Carr, M.H. (1979). *J. Geophys. Res.*, **84**, 2995-3007. [7] Baker et al. (1992). in: *Mars*, Univ. of Arizona Press. [8] Clifford, S.M. (1993). *J. Geophys. Res.*, in press. [9] Clifford, S.M. (1993), *these abstracts*. [10] Masursky et al. (1977). *J. Geophys. Res.*, **82**, 4016-4038. [11] Pollack et al. (1987). *Icarus*, **71**, 203-224. [12] Clifford, S.M. (1991). *Geophys. Res. Lett.*, **18**, 2055-2058.

456969

S156-90  
ASS. ONLYN94-12171<sup>317</sup>  
LPSC XXIV  
163370

OLIVINE-RICH ASTEROIDS, PALLASITIC OLIVINE AND OLIVINE-METAL MIXTURES: COMPARISONS OF REFLECTANCE SPECTRA; E.A. Cloutis, 4 Huntstrom Road N.E., Calgary, Alberta, Canada T2K 5W3

P 2

The recent acquisition of high resolution 0.3-2.6 $\mu$ m reflectance spectra of a number of olivine-rich asteroids [1,2] permits analysis of their surface compositions to be made on the basis of new and existing laboratory spectral data for pallasitic olivines [3] and olivine-metal mixtures [4,5]. Analysis of the spectral data for the latter has revealed a number of spectral parameters which can be used to constrain olivine and metal abundances, grain sizes and olivine compositions.

**Pallasite Olivine Spectra.** The 0.3-2.6 $\mu$ m reflectance spectra of <45 $\mu$ m size olivine separated from the Imilac pallasite (OLV201) (5 nm resolution,  $i=0^\circ$ ,  $e=15^\circ$ ) is shown along with those of some terrestrial olivines (Figure 1). Compositions of the samples are provided in Table 1. The OLV201 spectrum does not exhibit any marked dissimilarities from the terrestrial olivine spectra [3]. Consequently compositional differences between terrestrial and pallasitic olivines cannot be invoked to explain spectral differences between laboratory olivine-metal mixtures and olivine-rich asteroids [4].

**Olivine-Metal Mixture Spectra.** Increasing the amount of metal in an olivine-metal mixture results in a number of diagnostic spectral changes, mostly due to the red sloped spectrum of powdered meteoritic metal [6]. These include an increase in the 1.8-2.5 $\mu$ m slope (nearly flat for pure olivine), a decrease in the wavelength position of the intersection of a horizontal line tangent to the reflectance spectrum at the 0.5-0.7 $\mu$ m reflectance peak with the long wavelength wing of the absorption band near 1.05 $\mu$ m (horizontal tangent intercept- HTI) and an increase in the ratio of the reflectance at 1.8 $\mu$ m to that at the 0.5-0.7 $\mu$ m reflectance peak. Of these parameters, the HTI is the most diagnostic indicator of metal content because it is relatively insensitive to changes in olivine composition and particle size and small amounts of pyroxene [5]. The 2.5/1.8 $\mu$ m reflectance ratio is sensitive to small amounts of pyroxene and the 1.8/0.5-0.7 $\mu$ m reflectance ratio is sensitive to changes in both metal abundance and olivine chemistry [5]. Deconvolution of olivine-rich spectra is therefore best accomplished by measuring the HTI to constrain metal abundances (Figure 2) and the 1.8 $\mu$ m/band minimum reflectance ratio to constrain particle sizes (Figure 3).

**Olivine-Rich Asteroid Spectra.** The wavelength position of the HTI and 1.8 $\mu$ m/band minimum reflectance ratio for the olivine-rich asteroids 113 Amalthea, 246 Asporina, 354 Eleonora and 446 Aeternitas are shown in Figures 2 and 3, respectively, along with the values for terrestrial olivines [5], the Imilac olivine and Brenham pallasite olivine (<30 $\mu$ m grain size) [4]. No polarimetry data are available for these asteroids to constrain grain sizes; consequently the asteroid data have been plotted for a mean grain size of 150 $\mu$ m (see below). The HTI is relatively insensitive to grain size- a factor of 4 change in olivine and/or metal grain size would affect the metal abundance determination by at most 15% [5]. The asteroid HTI values clearly fall outside the range for terrestrial and pallasitic olivines and indicate surficial metal abundances of between ~30 and 40 wt% with 113 Amalthea and 446 Aeternitas being the most metal poor and metal rich, respectively.

The 1.8 $\mu$ m/band minimum reflectance ratios of the various samples are shown in Figure 3 as a function of grain size. The values for the olivine-rich asteroids (plotted at 150 $\mu$ m grain size) are consistent with either pure fine grained olivines or olivine-metal mixtures. The dashed lines indicate the extrapolated data for varying amounts of metal as a function of grain size. Since the HTI was used to constrain metal abundances, the data in Figure 3 indicate that the surfaces of these asteroids contain a spectrally significant amount of <150 $\mu$ m sized material. This size represents an upper limit since small amounts of pyroxene which may be present, as evidenced by shallow absorption bands in the 1.8-2.5 $\mu$ m regions of the asteroid spectra, will tend to increase this reflectance ratio [7].

**ACKNOWLEDGMENTS.** This study was supported by a grant-in-aid from the Geological Society of America and Sigma Xi- The Scientific Research Society. Thanks to S.F. Pratt and C.M. Pieters for the spectral measurements of some samples with the Reflectance Experiment Laboratory (RELAB) at Brown University. RELAB is a multiuser facility supported by NASA under NAGW-748.

**REFERENCES.** [1] Bell J.F., Owensby P.D., Hawke B.R. and Gaffey M.J. (1988) *LPSC XIX*, 57. [2] Hiroi T., Bell J.F., Takeda H. and Pieters C.M. (1992) *17th Symp. Antarctic Meteorites*, 53. [3] King T.V.V. and Ridley W.I. (1987) *JGR* 92, 11457. [4] Bell J.F., Gaffey M.J. and Hawke B.R. (1984) *Meteoritics* 19, 187. [5] Cloutis E.A. (1989) *LPSC XX*, 173. [6] Cloutis E.A., Gaffey M.J., Smith D.G.W. and Lambert R. St J. (1990) *JGR* 95, 8323. [7] Cloutis E.A., Gaffey M.J. Jackowski T.L. and Reed K.L. (1986) *JGR* 91, 11641.

## OLIVINE-RICH ASTEROIDS E.A. Cloutis

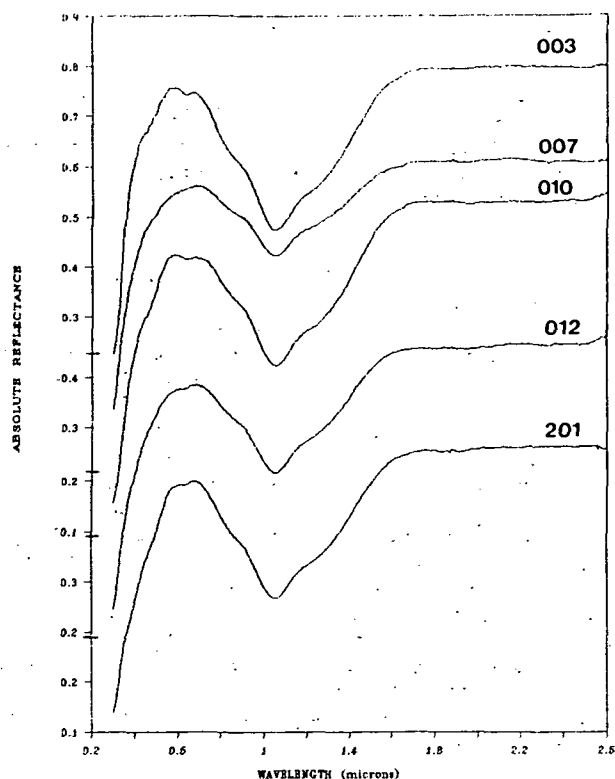


Figure 1. Reflectance spectra of <45 $\mu$ m size terrestrial olivines (003, 007, 010, 012) and Imilac pallasite olivine separate (201).

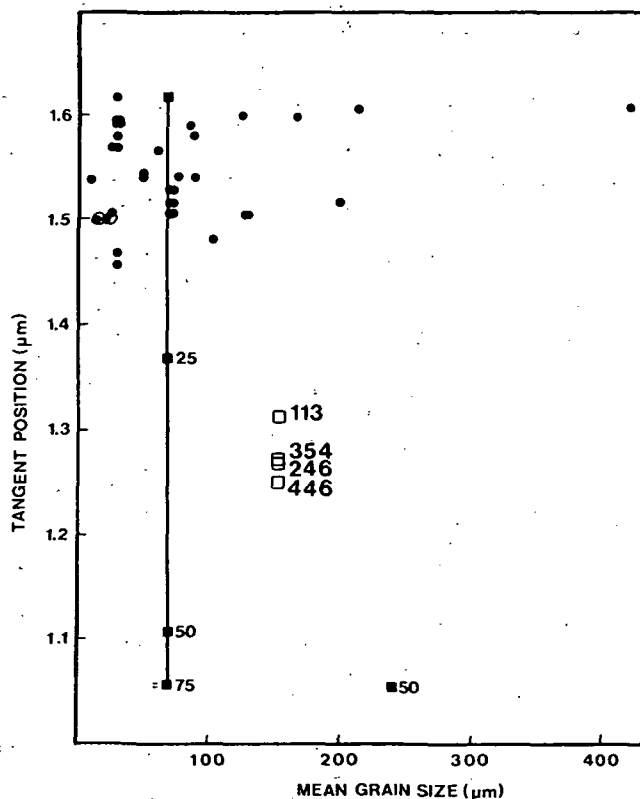


Figure 2. HTI (see text) versus particle size. Terrestrial olivines (filled circles), pallasitic olivines (open circles), olivine rich asteroids (open squares), olivine-metal mixtures (filled squares). Numbers indicate metal abundances in olivine-metal mixtures. Asteroids identified by their numeric prefixes.

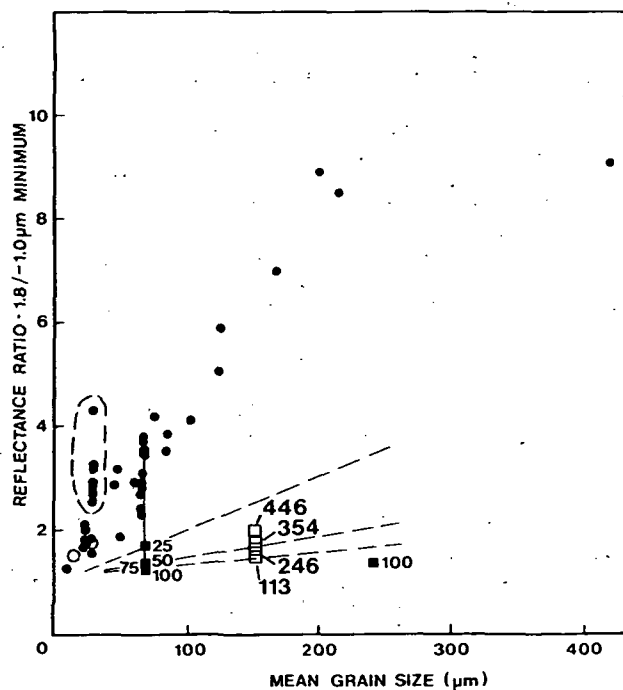


Figure 3. Reflectance ratio 1.8 $\mu$ m/band minimum versus grain size. Symbols are the same as in Figure 2.

Table 1. Compositions of Spectrally Characterized Olivines.

	003	007	010	012	201
SiO <sub>2</sub>	40.64	41.72	40.42	40.95	40.36
FeO	9.25	3.12	11.11	8.05	12.00
Fe <sub>2</sub> O <sub>3</sub>	0.59	N.D.	N.D.	N.D.	N.D.
MgO	49.13	54.65	48.25	50.83	47.76
MnO	0.09	0.19	0.15	0.10	0.26
NiO	0.33	0.01	0.43	0.40	0.01
CaO	0.07	0.63	0.19	tr.	tr.
TiO <sub>2</sub>	0.00	0.00	tr.	0.00	tr.
Cr <sub>2</sub> O <sub>3</sub>	0.01	tr.	0.13	0.00	0.02
CoO	0.04	0.01	0.04	0.06	0.03
Fo	90.4	96.9	88.5	91.8	87.6
Fa	9.6	3.1	11.5	8.2	12.4

tr.= trace (<0.01); N.D.= not determined

456970

S157-90

LPSC XXIV

319

ABS ONLY

N94-12172

REMANENT MAGNETISM OF HED METEORITES - IMPLICATIONS FOR THEIR EVOLUTION AND ANCIENT MAGNETIC FIELDS: D.W.Collinson and S.J.Morden, Department of Physics, The University, Newcastle upon Tyne, England.

The magnetic properties of extraterrestrial materials, in particular natural remanent magnetization (NRM), is a potentially useful study for detecting ancient Solar System magnetic fields and for elucidating meteorite evolutionary processes. Results reported here are for howardites Kapoeta, Petersburg, Le Teilleul and EET 87503, eucrites Sioux County and Millbillillie, and diogenites Shalka and Johnstown. Significant features of their magnetism are within-sample inhomogeneity of NRM directions in several of the meteorites and within-sample uniformity of axes of anisotropy of magnetic susceptibility. Both these phenomena bear on the meteorites' evolution and the timing of the magnetization process.

The carrier of the magnetic properties in these achondrites is mainly low-nickel kamacite. Intensity of magnetization, as received, is mainly in the range  $(1 - 70) \times 10^{-6} \text{ Am}^2 \text{ kg}^{-1}$ , with Petersburg, which contains considerably more kamacite than the others, around  $10^{-3} \text{ Am}^2 \text{ kg}^{-1}$ .

The character of the NRM is investigated by alternating field demagnetization, to test for primary and secondary components, and by breaking samples into mutually oriented fragments (typically 1 g mass) and comparing directions of NRM in these fragments. A range of behaviour is observed when these techniques are applied. Petersburg, Kapoeta, Sioux County and Johnstown show scattered within-sample NRM, together with highly irregular behaviour on demagnetization. Erratic changes occur in both direction and intensity of NRM, with no clear evidence of secondary magnetization components: however, during the demagnetization process a component of stable NRM does persist in all these meteorites.

Shalka and EET 87503 show approximately homogeneous, initial within-sample NRM, which persists during demagnetization in Shalka. In EET 87503, homogeneity is lost on demagnetization, and relatively well-defined but scattered primary NRM directions are revealed in different fragments.

More conventional demagnetization behaviour is shown by Le Teilleul and Millbillillie. Although there is within-sample scatter of NRM directions in Le Teilleul, the intensity decays smoothly on demagnetization, and the NRM is stable in different fragments. Millbillillie differs from the other achondrites studied in that there is uniformity of primary NRM direction throughout the sample with smooth intensity decay curves.

Thus, a range of NRM properties and demagnetization behaviour is observed in these achondrites. The significance of the scattered within-sample NRM is that the constituent fragments must have acquired their magnetization before their final accumulation into the meteorite material, and that there were no subsequent magnetizing events. Such an event, e.g. heating above  $\sim 70^\circ \text{C}$  and cooling, would remagnetize the meteorite uniformly if a magnetic field was present, or demagnetize it in the absence of a field. The event resulting in the formation of the meteorite as now seen clearly did not remagnetize the fragments.

With two exceptions, a magnetic property common to these meteorites is within-sample uniformity of anisotropy of magnetic susceptibility. This reflects a common fabric in the samples caused by the shape of magnetic particles, and foliation (disc-like shape) is commonly observed. This fabric appears to have been imparted to the meteorites through shock at the time of final accumulation, or during a subsequent shock event. The

## MAGNETISM OF HEDs: Collinson D.W. &amp; Morden S.J.

exceptions are Millbillillie and Johnstown, in which the anisotropy axes are randomly directed among different fragments.

The evidence from these magnetic properties of HEDs is generally of a magnetizing event on the parent body prior to break-up and re-accumulation of meteorite material. The latter event did not substantially alter the NRM of the accumulating fragments, nor was there subsequent remagnetization. The most likely origin of the NRM is a thermoremanence, acquired when the material was heated on the parent body to  $> \sim 800^{\circ}\text{C}$  and cooled in the presence of a magnetic field. It is this magnetization which is now seen in the separated meteorite fragments. Millbillillie and Le Teilleul appear to have had a somewhat different history. Their uniform NRM indicates that it was acquired either during or after final accumulation, possibly during the shock event which broke them off the parent bodies.

Whether the magnetic field which imparted NRM to the HEDs was of internal or external origin cannot be definitely determined, but a parent body field of internal origin is not ruled out. The ability of asteroidal sized bodies to support core dynamo-generated magnetic fields is uncertain, but accumulating evidence from lunar magnetism (1) and other meteorite studies (2) now points to the existence of such fields. Because of NRM inhomogeneity, only in Millbillillie and Le Teilleul can any estimate of magnetizing field strength (palaeointensity) be made. Two independent methods applied to Millbillillie are in good agreement, giving a mean value in the range 20 - 30  $\mu\text{T}$  (3), similar to other achondrite estimates (2). In view of the widespread occurrence of NRM inhomogeneity in meteorites (4)(5), a check on this phenomenon should be an essential preliminary to palaeointensity determinations.

Current research in progress includes investigation of irregular demagnetization behaviour, which prevents important evidence of different NRM components from being obtained. If present, these components would point towards other magnetizing events and thus other meteorite evolutionary events. A parallel study of remanent magnetism is being carried out on a range of lunar breccias, to investigate whether their similarity to HEDs extends to their magnetic properties. Preliminary results suggest that the breccias so far investigated were magnetized at the time of their formation.

- REFERENCES: (1) Fuller, M. and Cisowski, S.M. (1987) in "Geomagnetism", 2, Ed. Jacobs, Academic Press. (2) Cisowski, S.M. (1987) in "Geomagnetism", 2, Ed. Jacobs, Academic Press. (3) Morden, S.J. (1992) Meteoritics (in press). (4) Morden, S.J. and Collinson, D.W. (1992) E.P.S.L. 109, 105. (5) Collinson, D.W. (1991) Meteoritics, 26, 1.



456971

3158-91

ABS ONLY 94-12978

LPSC XXIV

321

## GRAPHITE "SOLUBILITY" AND CO VESICULATION IN BASALT-LIKE MELTS AT ONE-ATM

R. O. Colson, Dept. of Earth and Planetary Sciences & McDonnell Center for the Space Sciences,  
Washington University, St. Louis, MO 63130.

P. 2

The identity and source of the vapor phase that caused lunar lava-fountaining and vesiculation in lunar basalts continues to be of interest because of its implications for the composition and state of the lunar interior [e.g. 1] and because of its implications for lunar resources [e.g. 2]. In light of the apparent near-absence of  $H_2O$  on the Moon, it has been suggested that the vapor phase may be  $CO_2$ -CO [3, 1, 2]. This premise is supported by the presence of carbon on the surface of volcanic glass beads [4]. However, although the rapid exsolution of  $CO_2$  from a melt during decompression [5] may be consistent with fire-fountaining, it fails to provide a satisfying explanation for vesiculation in mare basalt where exsolution of the gas phase would more reasonably be related to cooling/crystallization at low pressure rather than decompression from high pressure. Also, geochemical trends in lunar volcanic glasses suggest that their source has an oxygen fugacity more reducing than the iron-wustite buffer [6, 7], an oxygen fugacity that is inconsistent with presence of dissolved  $CO_2$ -CO at depth [1]. I report here results of experiments in which a vesicular "basalt" is produced from a melt equilibrated with graphite and pure CO gas at one atmosphere pressure. The vesiculation is apparently related to exsolution of CO or a CO species during cooling of the melt or growth of quench crystals. Additionally, particulate carbon dispersed through the quenched sample suggests that elemental carbon is either in solution in the melt prior to quenching or tends to go into suspension perhaps as colloid-like particles. These two observations may provide insight into the nature of fire-fountaining and vesiculation on the Moon.

200-300mg of Fe-free basalt-like powdered silicate ( $SiO_2$ - $MgO$ - $Al_2O_3$ - $CaO$ ) was added with iron or nickel metal to a graphite capsule. The capsule lid fit snugly but was not sealed. The experiment was run in pure CO at 1485°C for 25 minutes then quenched in air. Based on the highly accurate "glow test" which uses how long it takes the sample to stop glowing to estimate cooling rate, the sample cooled at about 20-30° per sec. The quenched sample was glassy, with a cloudy dark-grey color (suggesting presence of small particles suspended in the glass). The density (darkness) of the grey color varied in a regular pattern, apparently reflecting convective mixing either during the experiment or during its quench. The glass was free of vesicles. The same sample was returned to the furnace for 33 minutes at 1454°C and again quenched, sectioned and examined. This sample was highly vesicular, appearing frothy before sectioning. Ignoring vesicles, the sample was 85-90% glass by volume with 5-10% skeletal to euhedral olivine and pyroxene crystals bordered by feathery quench crystals extending 3-6 micrometers from the crystal edges. These results have been duplicated multiple times with subsequent experiments terminated at either the first (glass) stage or crystal/vesicle stage and samples have been sectioned and examined under BEI and with a microprobe.

The most likely identity of the particulate material suspended in the glass is carbon. This carbon may have been in solution in the melt during the experiment but exsolved during the quench or it may have been in suspension in the melt, perhaps as colloid-like particles. The gas forming the vesicles would seem to have to be CO or some CO species such as a carbonyl, since the experiments were done in pure CO. These observations suggest substantial solubility of both CO and C in the melt. To test this, I have done a series of experiments varying activities of CO and C independently. To avoid the possibility that spectroscopic techniques, such as Raman spectroscopy, which have failed find CO in silicate melts in other studies [8], may be failing to detect CO actually present, I have done preliminary analyses using an SEM energy dispersive x-ray method with a 5kV electron beam, and an ultra-thin 1000Å Parylene window. An example carbon peak profile is given in Fig. 1. Because of large uncertainties, the results given in Table 1 and Fig. 2 are somewhat ambiguous, particularly in light of the unexpectedly large apparent concentrations. However, results are consistent with substantial solubility of both C and CO in these melts. I am currently trying to use the SIMS instrument here at Washington University to place better constraints on the concentration, presence or absence of carbon in these experiments.

At low pressure, solubility of  $CO_2$  is quite low [5], and, much more so than water, is rapidly or explosively exsolved as pressure decreases. Thus, an explanation of vesicles in basalt by this means would seem to require that vesicles were formed by exsolution during decompression at pressures much

# GRAPHITE "SOLUBILITY" AND CO VESICULATION IN BASALT-LIKE MELTS: Colson, R. O.

higher than those at the lunar surface and were somehow retained in the melts after eruption (unlike vesiculation on Earth where water continues to boil out of the melts after eruption). It is much easier to suppose that vesicles formed as the mare basalts cooled and crystallized at surface conditions, as has been demonstrated to be possible by these experiments.

In light of these experiments, CO and CO<sub>2</sub> as the gas species responsible for lunar fire-fountaining can also be reconciled with a very low interior oxygen fugacity. At oxygen fugacities at or below the iron-wustite buffer, and at depth in the Moon, carbon exists primarily as elemental carbon. This carbon will exist as graphite and, if a melt is present, either in solution or suspension in the melt. If the melt moves upward, perhaps due to density differences with surrounding rock, the resulting decrease in pressure will result in reduction of FeO in the melt by the elemental carbon as shown in Fig. 3. This will produce metallic Fe and CO during ascent of the magma. [1] pointed out how carbon floated in the melt would react with FeO and CO<sub>2</sub> to increase gas volume, but his calculations presumed a high oxygen fugacity at depth and thus a gas phase at depth dominated by CO<sub>2</sub>. These experiments indicate that such high oxygen fugacities are not necessary.

[1] Sato M. (1979) PLPSC 10th, 311-325. [2] Colson R. O. (1992) PLPSC 22, 427-436. [3] Housley R. M. (1978) PLPSC 9th, 1473-1484. [4] McKay D. S. and Wentworth S. J. (1992) LPI Tech Rep 92-09, 31-36. [5] Pan V. et al. (1991) GCA 55, 1587-1595. [6] Steele A. M. et al. (1992) GCA 56, 4075-4090. [7] Delano J. W. (1990) LPSC XXI, 278-279. [8] Pawley A. R. et al. (1992) EPSL 110, 213-225.

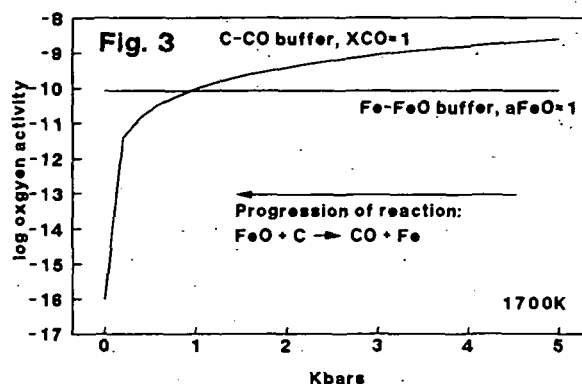
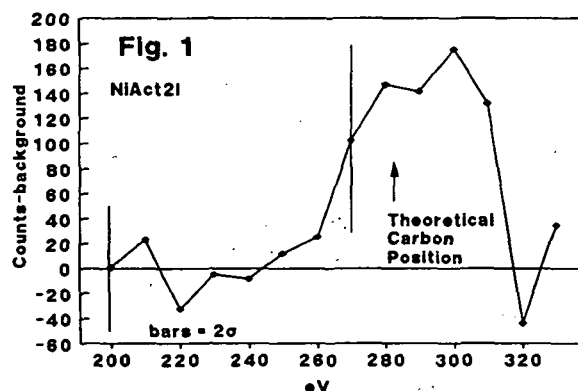
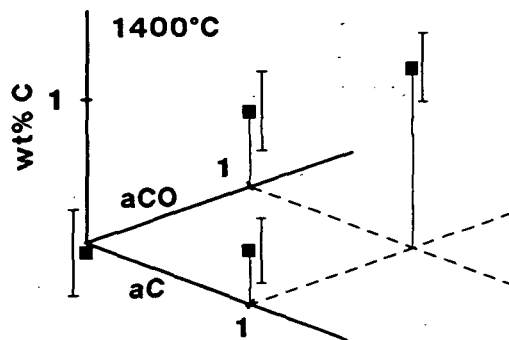
Funding was provided by NASA through UA/NASA Space Engineering Center for Utilization of Local Planetary Resources.

Table 1.

Label	total C (wt%)	aCO	aC
FeActA, NiAct2I	1.08 ± 0.24	1	1
NiActG2	0.605 ± 0.27	1	0
NiAct2M, FeAct2C	0.35 ± 0.22	0	1
NiActE1	-0.07 ± 0.3	0	0

1σ uncertainty

Fig. 2



## CRYSTAL-CHEMISTRY AND PARTITIONING OF REE IN WHITLOCKITE

R. O. Colson and B. L. Jolliff, Dept. of Earth and Planetary Sciences & McDonnell Center for the Space Sciences, Washington University, St. Louis, MO 63130.

Partitioning of REE in whitlockite is complicated by the fact that two or more charge-balancing substitutions are involved [1, 2] and by the fact that concentrations of REE in natural whitlockites are sufficiently high such that simple partition coefficients are not expected to be constant even if mixing in the system is completely ideal [1, 2]. The present study combines preexisting REE partitioning data in whitlockites [1] with new experiments in the same compositional system and at the same temperature (~1030°C) to place additional constraints on the complex variations of REE partition coefficients and to test theoretical models for how REE partitioning should vary with REE concentration and other compositional variables. With this data set, and by combining crystallographic and thermochemical constraints with a SAS simultaneous-equation best-fitting routine, it is possible to infer answers to such questions as 'what is the speciation on the individual sites Ca(B), Mg, and Ca(IIA) (where the ideal structural formula is  $\text{Ca(B)}_{18}\text{Mg}_2\text{Ca(IIA)}_2\text{P}_{14}\text{O}_{56}$ )', 'how are REE charge-balanced in the crystal', and 'is mixing of REE in whitlockite ideal or nonideal'. This understanding is necessary in order to extrapolate derived partition coefficients to other compositional systems and provides a broadened understanding of the crystal chemistry of whitlockite. Conclusions include:

- 1) Our experiments yield partition coefficients for La in addition to the values for Nd, Sm, and Yb reported in previous experiments. This gives us improved knowledge of the REE partitioning pattern.
- 2) Substantial Fe, in addition to Ca and vacancies, substitutes on the Ca(IIA) sites in whitlockite. Fe on the Ca(IIA) sites in whitlockite has not been previously suggested to our knowledge.
- 3) The ratio Fe/Ca on the Ca(IIA) sites increases strongly as the number of vacancies on the site increases due to increasing REE in the mineral. This indicates that Fe, Ca, and vacancies do not mix ideally on the Ca(IIA) site. The nonideal interaction among Ca, Fe, and vacancies on the site is expected to effect not only concentrations of Fe on Ca(IIA), but to provide a (possibly large) nonideal contribution to variations in REE partition coefficients with composition.
- 4) Although modeling of REE partitioning as the sum of a "saturating" substitution (REE on Ca(B) charge-balanced by substitution of a vacancy for Ca or Fe on Ca(IIA)), and an "unsaturating" substitution (REE on Ca(B) charge-balanced by substitution of Si for P) accounts for most of the variation in REE partitioning [1, 2], small but significant differences between the ideal-solution model and observed partition coefficients in these experiments suggest that the system is not entirely ideal.
- 5) Simple regular-solution modeling of the nonideal interaction of Fe and vacancy on the Ca(IIA) sites explains not only the variation in Ca/Fe on Ca(IIA), but the nonideal variations in REE partition coefficients with REE concentrations as well. This provides both improved modelling of the variation in partitioning with REE concentration and the means for extrapolating from these experimental compositions to the typically more Fe-poor compositions of natural systems.
- 6) Tests using the SAS statistical system suggest that other charge-balancing substitutions, such as substitution of a vacancy for Mg (or Fe) on a Mg site, are not significant in these experiments.

The presence of Fe on Ca(IIA) sites is illustrated by Fig. 1. The curve on the figure illustrates the variation modeled by the SAS fitting routine. The SAS routine uses the constraint that activities of the major components and temperature are roughly constant in these experiments, and thus, for ideal mixing, ratios of the major elements on each of the sites Ca(B), Mg sites, and Ca(IIA) will be constant and can be estimated by a statistical fitting routine. The average ratio of  $\text{Ca}/(\text{Fe}+\text{Mn}+\text{Mg})$  on the Ca(IIA) sites predicted by the SAS routine is  $0.72 \pm 0.2$ . The explanation for the change in slope in Fig. 1 is as follows: at low REE concentrations, most REE are charge-balanced by substitution of a vacancy on the Ca(IIA) site [1, 2], thus the decrease in  $\text{Mg}+\text{Fe}+\text{Mn}$  with increasing REE is related to replacement of  $\text{Mg}+\text{Fe}+\text{Mn}$  both on Ca(B) sites (where REE substitute) and Ca(IIA) sites (where charge-balancing vacancies substitute). However, at higher REE concentrations, the Ca(IIA) sites become saturated with vacancies and additional REE are charge-balanced by Si substituting for P, thus the slope at high-REE concentrations is related only to replacement of REE in Ca(B) sites. Thus, the steeper slope at low REE concentrations reflects the presence of  $\text{Mg}+\text{Fe}+\text{Mn}$  in the Ca(IIA) sites (consideration of Mg and Fe separately suggests that Fe, not Mg, is on the Ca(IIA) sites).

Fig. 2 is similar to Fig.1 but only considers those REE that are charge-balanced by vacancy on

## CRYSTAL-CHEMISTRY AND PARTITIONING OF REE IN WHITLOCKITE: Colson and Jolliff

Ca(IIA). Because the ratio of Ca/(Mg+Fe+Mn) on Ca(B) sites is high ( $75.9 \pm 1.4$ , by the SAS routine), the slope on this figure is related primarily to the ratio of Ca/(Mg+Fe+Mn) on Ca(IIA), thus the slope would be roughly constant if Ca/(Mg+Fe+Mn) on Ca(IIA) were constant. The observed slope for the 4 most REE-poor points is  $-0.156 \pm 0.05$ . For the 10 most REE-rich points the slope is  $-0.44 \pm 0.12$ . These slopes correspond roughly to Ca/Fe ratios on Ca(IIA) of 2.5 and 0.17 respectively. If we consider a simplified regular solution model for mixing of 3 components on Ca(IIA) in which all interaction parameters other than  $W_{\text{Fe,vacancy}}$  are zero, then  $W_{\text{Fe,vacancy}}$  can be estimated from the change in Ca/Fe as  $-3.25 (\ln \gamma_{\text{Fe}} = W_{\text{Fe,vacancy}} X_{\text{vacancy}})$ , where  $X_{\text{vacancy}}$  = vacancy on the Ca(IIA) sites in excess of one).

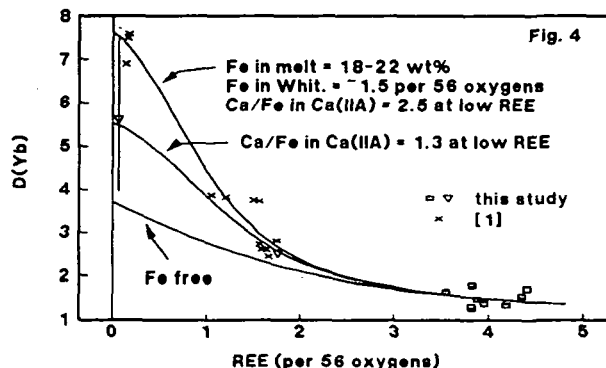
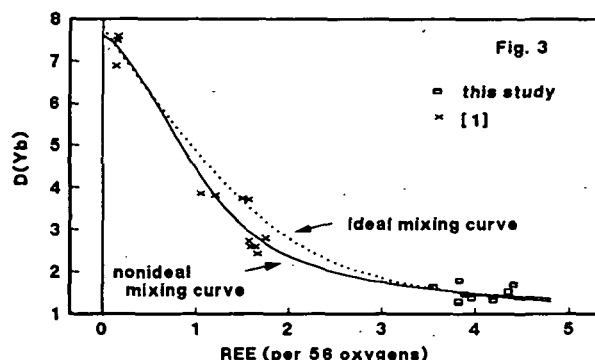
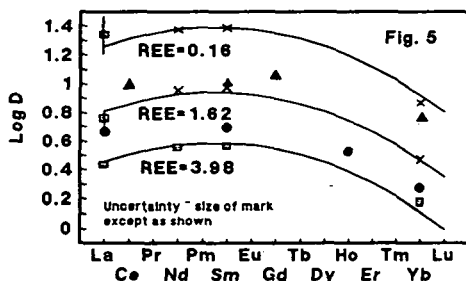
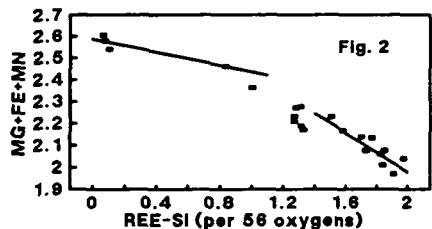
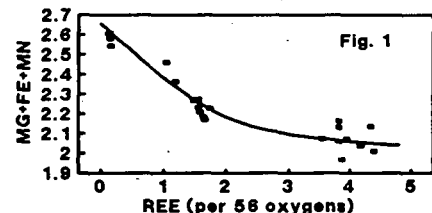
This nonideality is expected to effect the way partitioning varies with both REE concentrations and Fe concentrations in the system. Variations in  $D_{\text{Yb}}$  with REE concentrations are shown in Fig. 3. The ideal curve is as modeled in [2] and as suggested by [1]. The nonideal curve incorporates  $W_{\text{Fe,vacancy}}$  as calculated above from data independent of Fig. 3. The improved modeling of the variation of  $D$  with REE concentrations supports the premise that nonideal interaction between Fe and vacancies on Ca(IIA) sites effects not only the Ca/Fe ratio in Ca(IIA) but the value of REE partition coefficients as well.

Figure 4 illustrates the theoretically-calculated dependence of Yb partitioning on Ca/Fe ratio in Ca(IIA) (related to Fe activity in the system). Note that a substantial effect of Fe concentration is expected at low REE concentrations where higher Fe concentrations result in higher  $D$  values. This is important in interpreting the experiments reported here because Fe concentrations in the experimental whitlockite (1.2-1.6 per 56 oxygens) are higher than in typical lunar whitlockites (0.02-1.2). However, at REE concentrations more typical of lunar whitlockites (e.g. 1.4-2.0 REE per 56 oxygens) the effect of Fe concentration is greatly diminished. In an attempt to confirm this dependence of  $D$  on Fe concentration, we did some experiments in which melt Fe was about 50% lower (inverted triangles). However, low concentrations of Yb in the melt for the lowest REE experiment (60-100ppm) resulted in large uncertainties in the microprobe analyses such that this test is inconclusive.

Figure 5 illustrates REE  $D$  patterns at 3 different REE concentrations from data from McKay and this study. Data from [3] (circles) and [4] (triangles) are shown for comparison (other symbols are as in Fig. 3). The fit curves presume ideal mixing of the REE on Ca(B) sites and fit REE to a parabola  $a/a$  [5].

[1] McKay et al. (1987) LPSC XVIII, 625-626. [2] Jolliff et al. (1993) GCA, accepted. [3] Murrell et al. (1984) LPSC XV, 579-580. [4] Dickenson and Hess (1983), LPSC XIV, 158-159. [5] Philpotts (1978) GCA 42, 909-920.

Acknowledgements: Funding for this work was provided by NASA grant NAG 95-6.



464017

5160-65  
ABS. ONLY

LPSC XXIV

325

N 9 4 1 2 1 5

POWER-LAW CONFUSION: YOU SAY INCREMENTAL, I SAY DIFFERENTIAL; Joshua E. Colwell, Laboratory for Atmospheric and Space Physics, University of Colorado, Box 392, Boulder, CO 80309

P-2

Power-law distributions are commonly used to describe the frequency of occurrences of crater diameters, stellar masses, ring particle sizes, planetesimal sizes, and meteoroid masses to name a few. The distributions are simple, and this simplicity has led to a number of misstatements in the literature about the kind of power-law that is being used: differential, cumulative, or incremental. Although differential and cumulative power-laws are mathematically trivial, it is a hybrid *incremental* distribution that is often used, and the relationship between the incremental distribution and the differential or cumulative distributions is not trivial. In many cases the slope of an incremental power-law will be nearly identical to the slope of the cumulative power-law of the same distribution, *not* the differential slope. I argue for a consistent usage of these terms and against the oft-made implicit claim that incremental and differential distributions are indistinguishable [1-3].

The number of occurrences in a power-law is a function of the independent variable  $x$  and two other parameters,  $C_d$  and  $q$ :  $dN = N(x)dx = C_d x^{-q} dx$ .  $N(x)dx$  is the number of occurrences for values of  $x$  in the range  $[x, x + dx]$  where  $dx$  is a differential. This is the *differential* distribution. Integrating the differential distribution immediately provides the standard relationship between the differential and cumulative distributions:  $N(> x) = C_c x^{-b}$ , where  $b = q - 1$  and  $C_c = C_d/b$ . This describes the *cumulative* distribution. Both of these distributions treat  $x$  as a continuous variable. In practice the independent variable takes on only discrete values,  $x_i$ .

The set of  $x_i$  forms a number of *bins*; the  $i$ th bin is bounded by  $x_i$  and  $x_{i+1}$ . The number of events that is computed or counted in this discrete case is the number that occur for all  $x$  within a bin. That is,  $N_i$  is the number of events that occur for  $x$  in the range  $[x_i, x_{i+1}]$ . This is an *incremental* distribution, and it is this distribution that is computed in discrete computer algorithms, measured, or observed (as in crater counting, for example).

In order to span a large range in  $x$  with a reasonable number of bins,  $i_{max}$ , logarithmic bins are used. Then,  $x_{i+1} = (1 + \beta)x_i$ , where  $\beta$  is a bin spacing parameter. Suppose that the discrete counting produces a distribution that is fit by a power-law:  $N(x = x_i) = Kx_i^{-\gamma}$ , where  $N(x = x_i)$  is a measured fit to the histogram (data),  $N_i$ . When incremental distributions are published, the value of  $\beta$  is needed in order to interpret the meaning of  $\gamma$  (see below). In order to have a mathematically tractable distribution one must relate  $\gamma$  to either  $b$  or  $q$ .

It is simplest to derive the cumulative distribution from the incremental distribution by summing over  $N_i$ . Let  $N_c(x > x_i)$  be the discrete cumulative distribution computed from the incremental distribution.  $N_c(x > x_i)$  is the number of events that occur at  $x > x_i$  in the measured or computed incremental distribution, and

$$N_c(x > x_i) = K \sum_{j=i}^{i_{max}} x_j^{-\gamma} = Kx_i^{-\gamma} \sum_{j=0}^{i_{max}-i} (1 + \beta)^{-j\gamma} \propto x^{-\alpha} \quad (1)$$

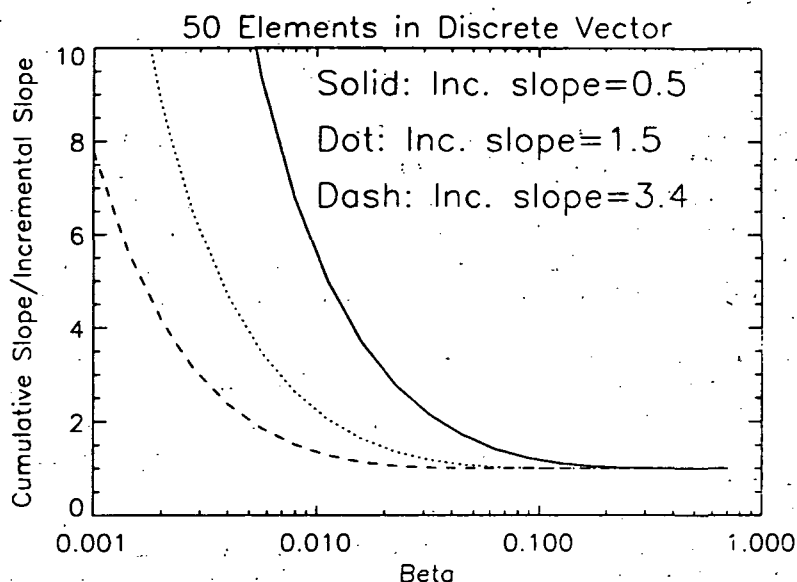
The power-law index of  $N_c(> i)$ , denoted  $\alpha$ , is the *measured* value of the slope of the cumulative power-law distribution,  $b$ . It, like  $\gamma$ , is a measured value. It is not equal to  $\gamma$  since the summation on the right side of Eq. (1) is dependent on  $i$ . Thus  $\gamma \neq b$ , and  $\gamma \neq q$ . That is, a power-law fit to an incremental distribution will not, in general, have the same slope as either the differential or the cumulative distribution.

In the figure the ratio of  $\alpha$  to  $\gamma$  is plotted for  $\gamma = 0.5, 1.5$ , and  $3.4$  with  $i_{max} = 50$ . These results demonstrate that for  $\beta \gtrsim 0.1$ ,  $\gamma \gtrsim 1$ , and at least 50 logarithmic bins,  $\alpha \approx \gamma$ , and the power-law index measured from an incremental distribution with logarithmic bins ( $\gamma$ ) will be very nearly equal to the power-law index for a continuous cumulative distribution ( $b$ ). This has been noted by Hartmann [4, p. 58] in his discussion of crater counts with  $\beta = .414$  and  $\gamma = 1.83$ . This result might be expected for a steep distribution (large  $\gamma$ ), but the figures show that it is true even for relatively shallow distributions ( $\gamma = 0.5$ ) as long as  $\beta \gtrsim 0.2$  for a distribution spanning 50 bins or more.

Crater size frequency distributions are often plotted on an R plot [e.g. 5]. The R plot is obtained by dividing the observed distribution by  $dN = D^{-3}dD$ , a differential distribution. As described above, the observed distribution will not likely have the same slope as the differential distribution of the same population. Depending on the details of the binning and the range in crater diameter the incremental

distribution may have a different slope than the cumulative distribution as well. The measured incremental distribution must be summed to form a cumulative distribution and then differentiated before dividing by the  $-3$  differential power-law to obtain the proper  $R(D)$  for the  $R$  plot.

Simulations of the accretion of planetesimals and the disruption of asteroids and planetary satellites use logarithmic bins usually with  $\beta = \sqrt{2} - 1$  or  $\beta = 1$  [e.g. 6-9]. For these simulations, the histogram of number of bodies in each size bin will most likely have a nearly identical slope to the cumulative size distribution. The differential size distribution is steeper than these incremental distributions by 1 in the power-law index.



The ratios of the measured power-law indices for the cumulative distributions to the incremental distributions ( $\alpha/\gamma$ ) for different  $\gamma$ .

#### REFERENCES

- [1] Fujiwara, A. et al. 1989. Experiments and Scaling Laws for Catastrophic Collisions, in *Asteroids II* (R. Benzel, T. Gehrels, M. S. Matthews, Eds.), Univ. of Arizona Press, Tucson.
- [2] Petit, J.-M., and P. Farinella 1993. Modelling the Outcomes of High-Velocity Impacts between Small Solar System Bodies. *Cel. Mech.* (in press).
- [3] Weidenschilling, S. J., C. R. Chapman, D. R. Davis, and R. Greenberg 1984. Ring Particles: Collisional Interactions and Physical Nature, in *Planetary Rings* (R. Greenberg and A. Brahic, eds.), University of Arizona Press, Tucson, pp. 367-416.
- [4] Hartmann, W. K. 1984. Does Crater "Saturation Equilibrium" Occur in the Solar System? *Icarus* 60, 56-74.
- [5] Strom, R. G. 1987. The Solar System Cratering Record: Voyager 2 Results at Uranus and Implications for the Origin of Impacting Objects. *Icarus* 70, 517-535.
- [6] Colwell, J. E., and L. W. Esposito 1992. Origins of the Rings of Uranus and Neptune: I. Statistics of Satellite Disruptions. *J. Geophys. Res.*, 85, 10,227-10241.
- [7] Ohtsuki, K., Y. Nakagawa, and K. Nakazawa 1990. Artificial acceleration in accumulation due to coarse mass-coordinate divisions in numerical simulation. *Icarus* 83, 205-215.
- [8] Spaute, D., S. J. Weidenschilling, D. R. Davis, and F. Marzari 1991. Accretional Evolution of a Planetesimal Swarm: 1. A New Simulation. *Icarus* 92, 147-164.
- [9] Wetherill, G. W. 1990. Comparison of Analytical and Physical Modeling of Planetesimal Accumulation. *Icarus* 88, 336-354.

H64018

5161-90

LPSC XXIV

327

ABS. N 94-12176

**THE EXPERIMENTAL PRODUCTION OF MATRIX LUMPS WITHIN CHONDRULES: EVIDENCE OF POST-FORMATIONAL PROCESSES.** Harold C. CONNOLLY Jr. and Roger H. HEWINS. Dept. of Geological Science, Rutgers Univ. New Brunswick, NJ 08903.

P 2

**INTRODUCTION** The processes that acted upon chondrules after their formation are as important clues to the nature of the early solar nebula as are the exact processes that formed chondrules. Recent experiments (1,2,3,4,5,6) have studied the rim forming processes and the effects the processes have on chondrules. We present below information on how matrix inclusions (7) found within chondrules may have been formed and the potential usefulness of this information.

**BACKGROUND** It has been shown that the dominant process by which chondrule textures are produced is heterogeneous nucleation (8,9,10,11). With heterogeneous nucleation any solid, unmelted material present within a melt at the onset of crystallization will act as nucleation sites for the development of crystals. The experiments of (11) have shown that any particles introduced into a molten charge from outside of the charge will also act as nucleation sites and induce crystal development. Therefore, any relict material or introduced material in a molten chondrule will affect the type of texture produced, and clearly acts as nucleation sites. Therefore, because the "inclusions" reported by (7) had no effect on the crystallization of the chondrules that enclosed them it is unlikely that the "inclusions" were present at the onset of crystallization.

**EXPERIMENTS** Often, synthetic charges are produced that contain holes, or cavities where shrinkage during formation has permitted forming phenocrysts to grow in a pattern that uses all available melt and form a cavity (Fig. 1). Various synthetic chondrules that represent a wide range of initial formational conditions were selected based on the presence of small cavities or surface irregularities. Two techniques were used to produce matrix lumps, both utilizing Fa100 material with a grain size of 23 micrometers and less. The first technique followed the procedure of (1) and puffed dust onto charges that were placed back into the furnace. The second technique, after (1), coated charges with dust and placed them back into the furnace at 1000C for one minute.

**RESULTS AND DISCUSSION** Sections through dust filled cavities appear to show included lumps (Fig. 2) The production of these inclusions or "matrix lumps" within synthetic chondrules depends on the presence of cavities or surface irregularities on charges before a rim forming event occurs. It also depends on how a section is made through the charges. If the section is not exactly through the cavity area, then the matrix lump is never observed. The production of cavities and surface irregularities within charges is a random and infrequent event. By analogy, the production of cavities and surface irregularities within natural chondrules must have also been an infrequent, random event. It has been stated (7) that matrix lumps may have been chondrule precursors that survived the melting event. An extensive search of experimental chondrule data has failed to reveal any experiments that report the survival of precursor material similar to matrix lumps. Even the recent flash melting techniques of (12,13) have failed to produce anything similar to matrix lumps. Clearly, if any precursor material did survive the melting event, it would act as nucleation sites for phenocryst development. It should be noted that it may also be possible to produce matrix inclusions by collision with a dusty surface (4), thus simulating some type of chondrule/parent body interaction.

**CONCLUSIONS** The production and observation of matrix lumps within chondrules depend on (1) the production of cavities and surface irregularities within chondrules during formation; (2) some type of rimming event that fills the voids and coats the chondrules with dust and (3) the exact sectioning techniques that will reveal these filled cavities. From our experiments matrix inclusions appear to be either rim or normal matrix material.

**REFERENCES** (1) Connolly, H.C.Jr. and Hewins, R.H. (1990) LPSC XXII, 233-234. (2) Bunch et al (1990) Icarus (3) Connolly, H.C. Jr. and Hewins, R.H. (1992) LPSC XXIII, 239-240. (4) Connolly, H.C.Jr. and Hewins, R.H. (1992) LPSC XXIII, 241-242. (5) Connolly, H.C.Jr. and Hewins, R.H. (1992) LPSC XXIII, 243-244. (6) Podolak et al. (1992) submitted to Icarus. (7) Scott E.R.D. et al. (1984) GCA 48, 1741-1757. (8) Lofgren, G.E. and Russell, W.J. (1986) GCA 50, 1715-1726. (9) Lofgren, G.E. and Lanier, A. (1990) GCA 54, 3537-3558. (10) Radomsky, P.M. and Hewins, R.H. (1990) GCA 54, 3475-3490. (11) Connolly, H.C.Jr. and Hewins, R.H. (1990) Meteoritics 25, 354-355. (12) Hewins, R.H. (1992) Meteoritics 26. (13) Connolly H.C.Jr. et al. (1993) LPSC this volume.

**ACKNOWLEDGEMENTS** This research was supported by NASA training grant NGT-50836. Several experiments were performed at Johnson Space Center, Experimental Petrology Labs. We would like to thank Dr. Gary Lofgren and Al Lanier for the use of the equipment and for constant attention in maintaining the equipment operational.

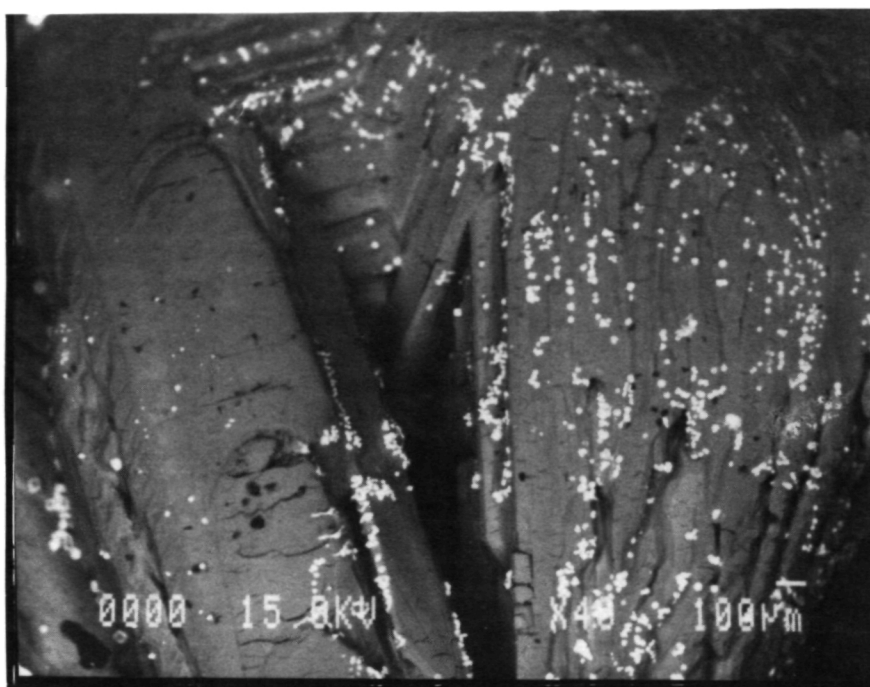
**MATRIX INCLUSION EXPERIMENTS: CONNOLLY, H.C.Jr. and HEWINS, R.H.**

Figure 1. A backscatter image of the surface of a charge. Note the cavity in the center of the charge.

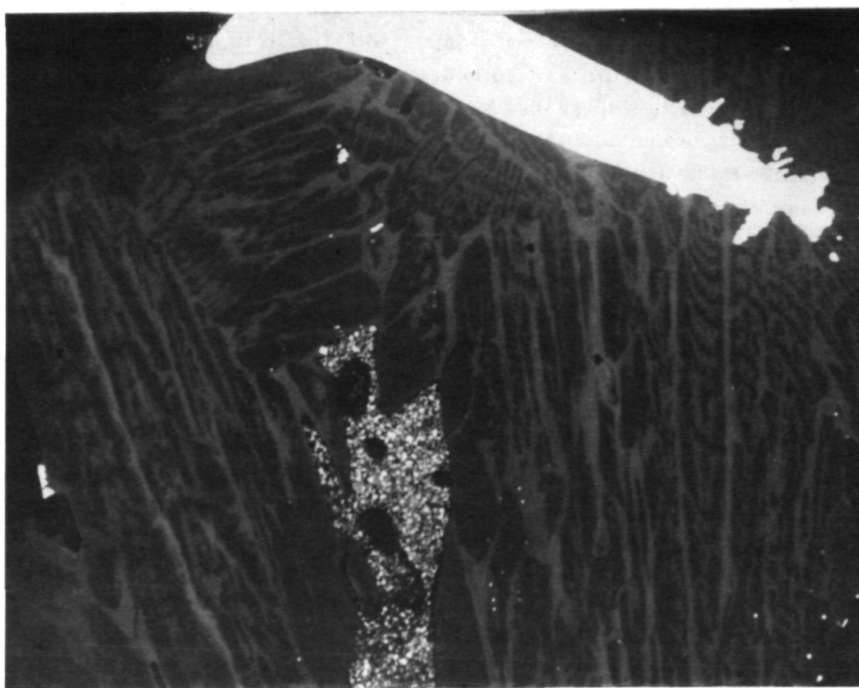


Figure 2. A backscatter image of a section from the charge in Fig.1. Note the cavity is now filled with dust. Both images were photographed at 40x.



**FLASH MELTING OF CHONDRULE PRECURSORS IN EXCESS OF 1600°C. SERIES I: TYPE II (B1) CHONDRULE COMPOSITION EXPERIMENTS.** Harold C. CONNOLLY Jr., Roger H. HEWINS<sup>2</sup> and Gary E. LOFGREN<sup>2</sup>. Dept. Geological Sciences, Rutgers University, New Brunswick, NJ 08903 and <sup>2</sup>NASA-Johnson Space Center SN-4, Houston, Texas 77058.

**INTRODUCTION** Several questions in chondrule production remain an enigma despite years of experiments. What were the melting temperatures experienced by chondrules? What were the physical characteristics of chondrule precursors? How and why did volatile elements (i.e. Na) found within chondrules survive the formation process? We present the initial results of a series of experiments designed to investigate the above questions by using flash melting to duplicate the melting stage of chondrule formation.

**EXPERIMENTAL TECHNIQUE** For these experiments a Type II (B1) chondrule analog composition with a grain size of 23-45 micrometers was prepared from mineral separates including Fa100 and San Carlos olivines. A liquidus of 1550°C was determined experimentally. Experiments were performed at JSC-Experimental Petrology labs using an Astro furnace. A standard hang wire technique (2) was used. Charges were pushed up into the hot spot when the desired temperature was reached and the furnace was then cooled. The average melting time was approximately two minutes (Fig. 1). The  $fO_2$  of the furnace was set at 1700°C for -1.5 log unit below IW using a CO/CO<sub>2</sub> gas mixture. All charges were quenched from the furnace at 1000°C with a final  $fO_2$  at quench of -2.0 log units below IW.

**RESULTS** Chondrule textures were produced from flash melting at temperatures from 1650 to 1825°C (Table 1). The total time any charge was above its liquidus (1550°C) did not exceed 3 mins. However, our experiments do not show as systematic a relationship between texture and flash conditions as was reported by (1). Early analysis of the charges indicates that at least 90 wt.% Na<sub>2</sub>O has been retained by all the charges. We also observe that approximately 75% of the phenocrysts within the microporphyritic (defined here as a texture of abundant phenocrysts approximately 50 micrometers or smaller) charges contained small relict San Carlos grains. With higher degrees of melting almost no relict grains are observed (i.e. porphyritic texture).

**DISCUSSION** Our experiments produced chondrule textures from flash melting at temperatures between 1650-1825°C, i.e. up to 300°C above the liquidus. However, our experiments failed to produce barred olivine (BO) textures (because the melting temperature was not high enough for the melting time to eliminate nuclei) or a systematic relationship similar to that of (1) between the flash melting events and the textures. The observed inconsistency of textures vs. flash conditions between our experiments and (1) may be due to either initial melting time differences; initial mass differences of charges or because we produced multiple charges in close proximity at the same time. Because BO textures may be a function of near total melting of a precursor aggregate (2,3) our experiments may indicate that flash melting conditions needed to produce near total melting were not obtained. Using the same melting times, future experiments may need to obtain temperatures in excess of 1825°C to produce BO texture.

Even though microporphyritic textures are not typical of Type II (B1) chondrules, we are able to produce them none the less. Unlike the experiments of (1), with very short heating times we cannot yet place the approximate upper transition temperature from microporphyritic to porphyritic textures. Within our microporphyritic charges we have observed a high density of relict San Carlos olivine grains. Compared to natural Type IA (A1) microporphyritic chondrules the high density of relict grains makes our charges poor analogs. Either the relict grains in our experiments are due to refractory San Carlos in a fayalite-rich melt or Type IA (A1) chondrule precursors were finer grained than our experiments. Further experiments using a Type II (B1) with only an intermediate olivine component and a Type IA (A1) chondrule analog will be needed to understand this problem better.

With the exception of the experiments of (4) the retention of sodium within experimental charges has been a serious problem with accurately producing analog chondrules within the lab. The experiments of (1) and especially the current experiments indicate that sodium may not be lost from charges providing they experience very short melting times (flash melting). If natural chondrules experienced a flash melting event the retention of sodium may be dependant on the duration or temperature of melting and not totally an exchange process with a nebular gas (4). However, textures indicative of near total melting (i.e. BO) may have needed to react with a nebular gas enriched in sodium to produce the measured sodium contents of natural BO chondrules. However, recent laser experiments (Hewins, pers. comm.) show that even with nearly total melting (equivalent to BO) very little Na is lost provided that the melting time is short.

# CHONDRULE EXPERIMENTS: CONNOLLY, H.C.Jr. et al.

## CONCLUSIONS Several important conclusions can be made from the above experiments:

1. If chondrules were formed by a flash melting mechanism, no exact temperature limit or time limit on the event can yet be precisely defined. What can be discussed is the combination of melting temperatures and melting times that chondrules experienced.
2. Type II (B1) chondrules could have experienced flash melting temperatures in excess 1825 °C and still have produced chondrule textures from relict grains or nuclei. If Type II (B1) chondrules were produced by dust encounters with totally molten chondrules (S) then the flash melting temperatures could be substantially higher than 1825 °C.
3. Type IA (A1) microporphyrritic chondrules may have been formed from precursor material finer than 23 micrometers.
4. Chondrule formation by flash melting permits the retention of such volatile elements as sodium. A nebular model where chondrules must totally equilibrate with a nebular gas enriched in sodium vapor to produce the measured sodium content of natural chondrules is not required when flash melting is the dominant chondrule-forming mechanism. Our experiments do not totally eliminate the possibility that exchange between a sodium rich gas and forming chondrules occurred. It may have been necessary for totally molten chondrule (i.e. BO) to have exchanged with a sodium-rich gas to produce the measured sodium contents. Further experiments using our Type II (B1), a modified Type II (B1) and a Type IA (A1) chondrule composition will be conducted in the future.

**REFERENCES** (1) Connolly et al. (1991) *Meteoritics* 26,328-329. (2) Lofgren, G. and Lanier, A. (1990) *GCA* 54,3537-3558. (3) Radomsky P.M. and Hewins, R.H. (1990) *GCA* 54,3475-3490. (4) Lewis, R.D. and Lofgren, G.E. (1991) *LPSC XXII*, 805-806. (5) Connolly, H.C.Jr. and Hewins, R.H. (1990) *Meteoritics* 23,354-355.

**ACKNOWLEDGEMENT** This research was supported by NASA training grant NGT-50836. Experiments were performed at JSC Experimental Petrology Labs and a generous thanks to all those who helped. A special thanks Al Lanier (Lockheed) for his constant help on these experiments.

Table 1

Charge	Flash Conditions	Texture
AST1	1665C	PO
AST2	1665C	PO
AST5	1727C	MicroPO
AST6A	1727C	PO
AST12	1747C	MicroPO
AST8A	1817C	PO/BO
AST18	1825C	PO/BO

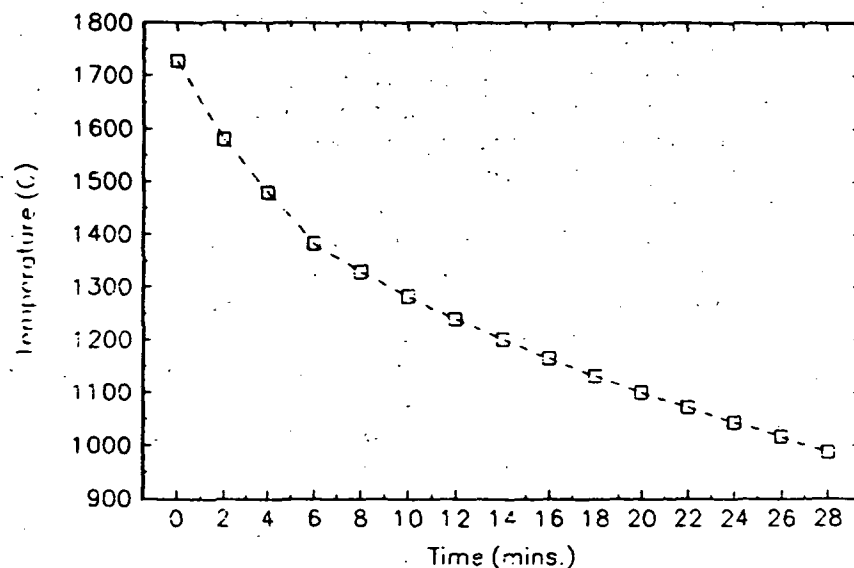


Fig. 1 A general plot of experimental flash conditions.

**MODELLING HYPERVELOCITY IMPACTS INTO ALUMINUM STRUCTURES BASED ON LDEF DATA;** C.R. Coombs, D.R. Atkinson, A.J. Watts, J.R. Wagner, M.K. Allbrooks, C.J. Hennessy, POD Associates, Inc., 2309 Renard Place, SE, Suite 201, Albuquerque, NM 87106.

## INTRODUCTION

Realizing and understanding the effects of the near-Earth space environment on a spacecraft during its mission lifetime is becoming more important with the regeneration of America's space program. Included among these potential effects are erosion and surface degradation due to atomic oxygen impingement, ultraviolet exposure embrittlement, and delamination, pitting, cratering and ring formation due to micrometeoroid and debris impacts. These effects may occur synergistically and may alter the spacecraft materials enough to modify the resultant crater, star crack and/or perforation. This study concentrates on modelling the effects of micrometeoroid and debris hypervelocity impacts into aluminum materials (6061-T6). Space debris exists in all sizes, and has the possibility of growing into a potentially catastrophic problem, particularly since self-collisions between particles can rapidly escalate the numbers of small impactors. We have examined the morphologies of the Long Duration Exposure Facility (LDEF) impact craters and the relationship between the observed impact damage on LDEF versus the existing models for both the natural (micrometeoroid) and manmade (debris) environments in order to better define these environments.

LDEF was designed as a reusable platform for launching and returning long duration (~1 year) space environment exposure experiments. LDEF was launched on April 7, 1984 from STS 41-C into a circular orbit about the Earth. The LDEF mission exposed 57 separate experiments to Earth's space environment at 12 different angles at an altitude of 450 km and an inclination of 28.4° for 53/4 years. Because the satellite was gravity-gradient stabilized, and flew its mission with one end constantly facing space and the other constantly facing Earth, the experiments were constantly oriented in known directions. To better characterize the effects of the near-Earth space environment, this study compared the results of actual impact crater measurement data and the SPace ENVironment (SPENV) program developed in-house at POD to theoretical models established by Kessler<sup>1</sup> and Cour-Palais<sup>2</sup>, and the CTH hydrodynamic computer code developed by Sandia National Labs.

## BACKGROUND

Two major components currently exist within the dynamic LEO environment; namely natural micrometeoroids from the solar system and manmade debris dating back to the onset of space exploration in 1957. While micrometeoroids arrive at the Earth from almost all directions, the debris is in both near-circular and elliptical orbits around the Earth. Although both types of particles exist all the way out to geosynchronous (GEO) orbits, the major populations of debris are within the altitude range of 350-2000 km. Micrometeoroids arrive at the Earth with differential speeds of from below 12 km/s to 72 km/s. However, when spacecraft orbital speed is included, the resulting impact speeds range from below 5 km/s to 79 km/s, yielding an overall average collisional speed of 20 km/s. The flux of particles is approximately isotropic in free space, but the effect of Earth shielding causes an asymmetry, resulting in a minimum number of impacts for Earth-facing satellite surfaces. As a result, either the RAM (velocity vector) surface or the SPACE-facing surfaces receive the highest number of impacts, depending upon altitude.

## RESULTS AND DISCUSSION

Experimental data for these analyses were collected by the authors and/or provided by several LDEF Principal Investigators, Meteoroid and Debris Special Investigation Group (M&D SIG) members, and by the Kennedy Space Center Analysis Team (KSC A-Team). These data were collected from various aluminum materials from different locations on the LDEF satellite. In addition, POD has written a PC-based computer code (SPENV) to calculate the expected number of impacts per unit area as functions of altitude, orbital inclination, time in orbit, and direction of the spacecraft surface relative to the velocity vector, for both micrometeoroids and debris. Scaling laws relate the models to the actual data (see Watts *et al.*, this volume for more information on the scaling laws). In addition, POD has performed many CTH hydrodynamic compute runs of various impact events, and has identified certain modes of response, including simple metallic cratering, perforations, and delamination effects of coatings, all of which were observed during our LDEF analyses.

Results of the damage analyses on the thermal painted LDEF aluminum panels indicated that more than 5% of surfaces examined were damaged by impact cratering and its coincident effects (i.e., spallation, delamination, and blow-off) causing damage areas to extend as far as 100 crater diameters from the central crater. Since the plates were located at different orientations, their responses to the hypervelocity impacts varied. Crater morphologies range from a series of craters, spall zones, domes, spaces, and rings to simple craters with little or no spall zone. Each of the crater morphologies is associated with varying damage areas, which appear to be related to their respective bay locations, thus exposure angle. In addition, an interesting phenomenon was noted: three "types" of ringed impact features were identified and loosely characterized as "young", "middle" or "old" as an indication of their relative sequence of formation. The "young" group is characterized by the presence of distinct crater "lips" and excavation cavity rims with distinct, visible "flaps" or folds composing the ring zone. The "middle" group appears slightly degraded, with ring edges still distinct and traces of fold-over layers still visible but less pronounced. In the "old" stage, the impact feature is noticeably eroded, with little or no foldover flaps visible and the rings appear as masses of rubble. Following discussions with Dr. Banks<sup>3</sup> we have concluded that these features are due to the interaction of atomic oxygen with the paint surfaces, with the cratering events occurring early to late (young-old) during LDEF's tenure in space.

CTH was used to simulate hypervelocity impacts into coated materials in an effort to begin to understand the formation of the "ring" and "dome" structures commonly observed on painted aluminum surfaces (Figure 1). POD has been successful in replicating "dome" structures but is not yet able to cause a "freezing" of waves to produce a permanent ring structure. The CTH runs have, however, produced transient "ring" motions which may be Rayleigh wave ripples propagating away from the impact site. One interesting note, all high speed ( $>9$  km/s) impacts modelled to date have forged the impactor into a jet structure which is expelled from the hole, leaving very little residue behind.

Results of the data and modelling comparisons and hypervelocity impact simulations show good agreement for spacecraft surfaces. It is interesting to note that hypervelocity impacts into painted aluminum surfaces are morphologically similar to those observed on some planetary surfaces. With the addition of gravity, similar modeling techniques may be used to model impacts into planetary surface materials and structures (e.g., soils, volcanic terrains, crustal materials) to evaluate their strengths and ability to withstand impacts of differing magnitudes (i.e., 4)

**REFERENCES:** (1) Kessler D.J. et al. (1987) *NASA TM-100471*. (2) Cour-Palais et al. (1969) *NASA SP-8013* (3) Bell R.L. *et al.*, (1991) Sandia Nat'l Lab. . (4) Dr. Bruce Banks, personal communication, 1991. (5) Melosh H.J. and Kipp (1989) *LPSC XX*, pp. 685-686.

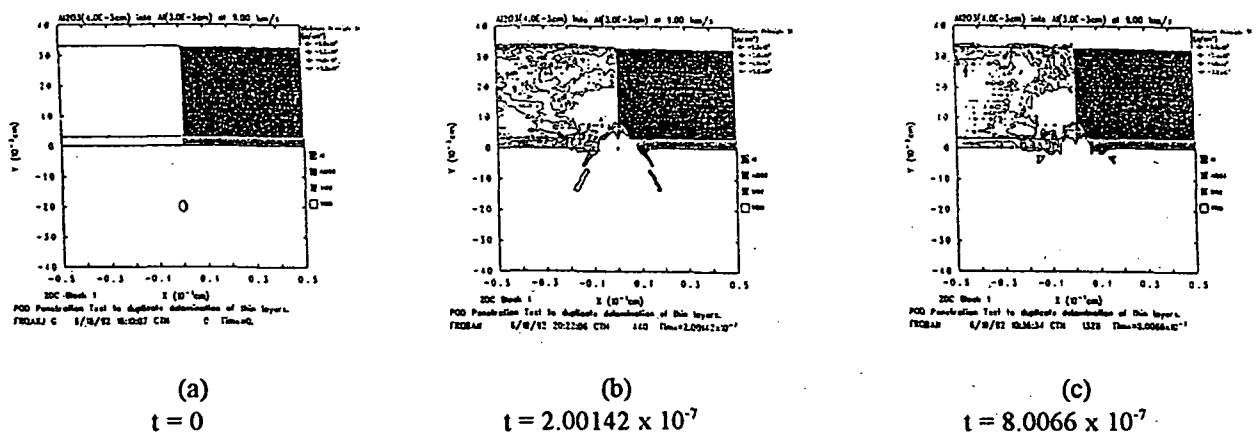


Figure 1: Example results from a CTH run where an  $\text{Al}_2\text{O}_3$  projectile impacted a 2-layer target at 9.0 km/s.

~~464024~~

464024

5164-91

LPSC XXIV

333

18

ABS ONLY

N94-12179

P 2

USING LUNAR SOUNDER IMAGERY TO DISTINGUISH SURFACE FROM SUBSURFACE REFLECTORS IN LUNAR HIGHLANDS AREAS; Bonnie L. Cooper<sup>1</sup> and James L. Carter<sup>2</sup>, (1) Lunar and Planetary Institute, 3600 Bay Area Blvd., Houston TX. (2) The University of Texas at Dallas, Programs in Geosciences, Richardson, TX.

We have developed a method using the Apollo 17 Lunar Sounder imagery data which appears capable of filtering out off-nadir surface noise from highland area profiles, so that subsurface features may now be detected in highlands areas as well as mare areas. Previously, this had been impossible because the rough topography in the highlands areas created noise in the profiles which could not be distinguished from subsurface echoes (1). The new method is an image-processing procedure involving the computerized selection of pixels which represent intermediate echo intensity values, then manually removing those pixels from the profile. Using this technique, a subsurface feature with a horizontal extent of about 150 km, at a calculated depth of approximately 3 km, has been detected beneath the crater Riccioli in the highlands near Oceanus Procellarum. This result shows that the ALSE data contain much useful information that remains to be extracted and used.

Figure 1 shows the frequency distribution curve of intensity values for the ALSE imagery over the crater Riccioli. The intensity distribution curves of other imaged areas were compared to this area. Using that comparison as a basis, a cutoff value of 176 was chosen as the intensity level above which data points would be considered as originating from the subsurface, and all pixels with intensity values below 176 (darker) would be considered as originating from either nadir or off-nadir surface reflections. The second vertical line in Figure 1 shows this cutoff value. Another dashed vertical line at intensity level 50 denotes the estimated division between nadir and off-nadir surface returns.

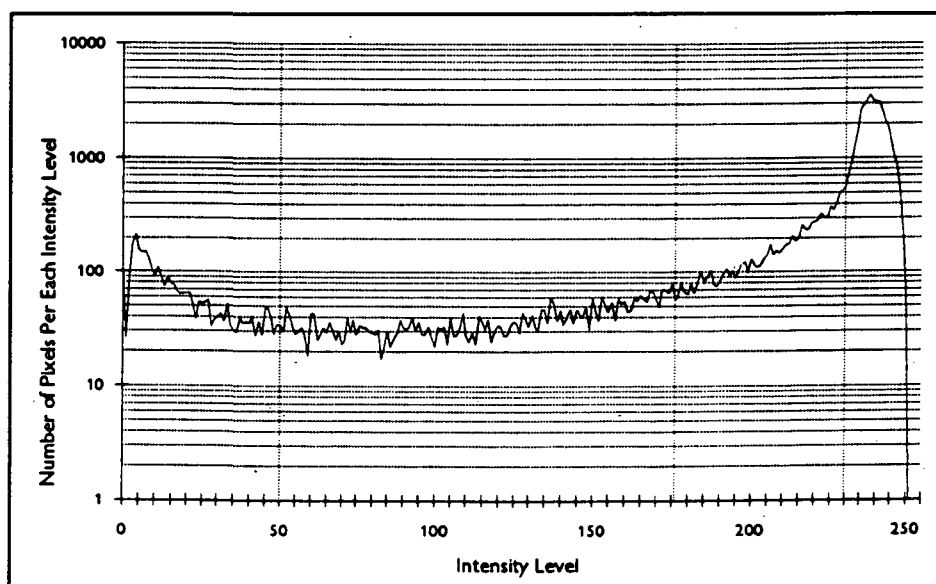


Figure 1. Frequency Distribution Curve for Pixel Intensity Values for area including Crater Riccioli and western Oceanus Procellarum.

Using this cutoff criterion, a profile was created from the original profile (Figure 2a) which contained only points that had been identified as surface returns (Figure 2b). That mask was overlaid on the original profile in a bitmap graphics program, then the off-nadir surface points were manually removed from the profile. The result is shown in Figure 2c, and the interpretation is shown in Figure 2d.

The procedure appears to be filtering out off-nadir surface returns, as evidenced by the larger number of pixels identified for removal below the highlands (83 out of 166) as compared to only 3 out of 57 pixels identified for removal from below the mare in Figure 2b. Consequently it seems probable that the horizontal reflector identified below the crater Riccioli is a subsurface feature. The relative dielectric constant in a highlands-area material of density  $2.9 \text{ g/cm}^3$  is 6.73, using the relation  $K=1.93^F$  as given by (2). The speed of electromagnetic radiation in that material would be  $c/(K^{1/2}) = 1.1556 \times 10^8 \text{ m/sec}$ . Using the value  $1.266 \times 10^{-6} \text{ sec/pixel}$ , vertical pixel resolution over highlands areas will be approximately 146 meters per pixel. This value produces calculated depths for the highlands subsurface features ranging from 2482 m to 3650 m. A loss tangent appropriate to highlands material, based on the loss tangents of the Apollo 16 samples reported by (1), was used to calculate the power ratio between the surface and subsurface returns using the formula

$$\Delta \text{dB} = 27.2 f \tan \delta,$$

as given by (3),

## SUBSURFACE REFLECTORS IN HIGHLANDS AREAS: Cooper, B.L.

where  $f = 5 \times 10^6 \text{ Hz}$ ,  $t = 6.316 \times 10^{-5} \text{ sec}$ , and  $\tan \delta = 0.0039$  (mean), to 0.0029 (median). Using this formula with both the mean and median loss tangents, power losses of 25 dB to 33.5 dB were calculated. The reflector should be within detection range if the median loss tangent of the Apollo 16 samples, 0.0029, is an appropriate estimate. The subsurface material causing the reflection at depth may be a mafic rock, because whatever is causing a subsurface reflection in the highlands would require a significant dielectric contrast from the anorthositic rock at the surface. Noritic and troctolitic layered plutons are hypothesized to have intruded the lower (4) or entire (5) crust, and detection of horizontal reflectors in the highlands subsurface would be consistent with that hypothesis.

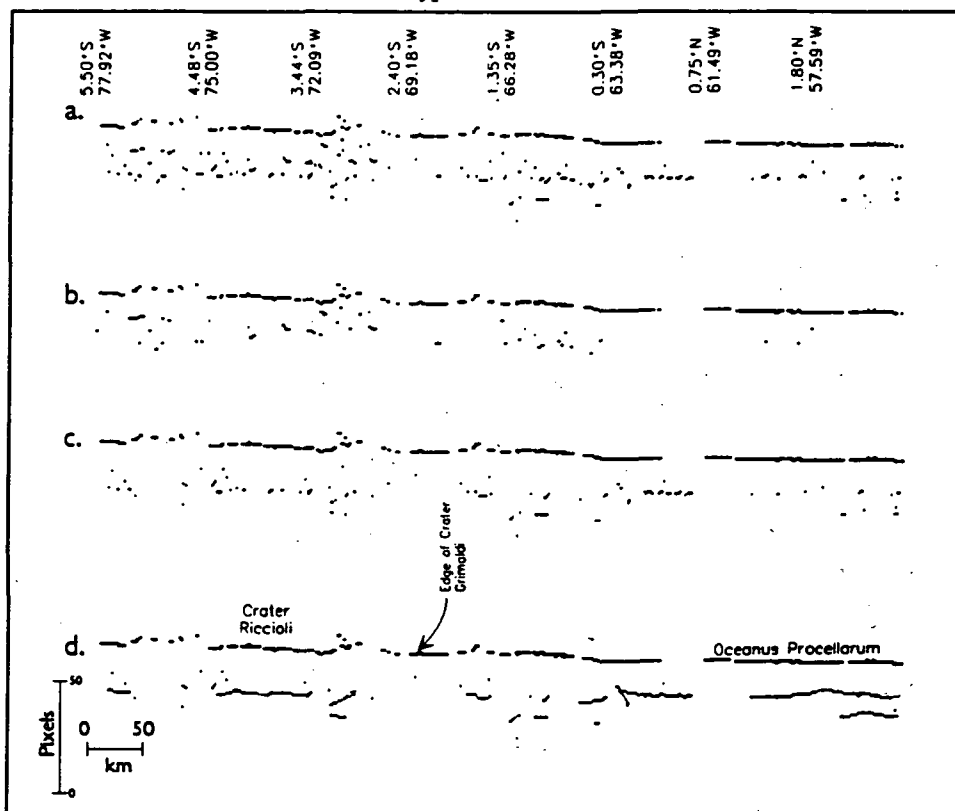


Figure 2. Procedure for removing pixels which are probably off-nadir surface returns. a) Original correlated profile of orbits 17 and 18 across western Oceanus Procellarum. b) Probable surface returns determined by masking pixels with values above 176. c) Correlated profile after removing pixels that are probable surface returns. d) Interpretation of subsurface horizons.

However, the slightly smoother surface of the crater floor may allow better radar penetration so that a feature which is continuous over a greater distance is only being imaged in that area. Alternatively, impact-triggered melting may have occurred beneath Riccioli. Impact-triggered melting seems unlikely to have produced the subsurface feature because a melt produced from anorthositic crust immediately after impact would be likely to erupt to the surface through fractures in the rock above. However, a zone of decompression below the crater may have been filled later by a mafic intrusion, when temperatures had decreased sufficiently to prevent the intrusion from remaining liquid long enough to reach the surface. Intrusives could have entered the zone during the lava filling of the Grimaldi basin, next to Riccioli.

<sup>1</sup>Peeples et al. (1978) JGR, 83, 3459.

<sup>2</sup>Olhoeft G. and Strangway D. (1975) *Earth & Planet Sci. Ltrs.*, 24, 394.

<sup>3</sup>Brown, W.E. (1972) *Lunar Geophys.*, 113.

<sup>4</sup>Warren P.H. and Wasson J.T. (1980) *Proc. Conf. Lunar Highlands Crust*, 81.

<sup>5</sup>James, O.B. (1980) *Proc. L.P.S.C. 11th*, 365.

464025

5165-91

ARBS

LPSC XXIV  
N 94-12180  
163385

335

P 2

**GEOLOGIC HISTORY OF CENTRAL CHRYSE PLANITIA AND THE VIKING 1 LANDING SITE, MARS;** *Robert A. Craddock<sup>1</sup>, L.S. Crumpler<sup>2</sup>, and Jayne C. Aubele<sup>2</sup>*; <sup>1</sup>Center for Earth and Planetary Studies, National Air and Space Museum, Smithsonian Institution, Washington, D.C. 20560; <sup>2</sup>Department of Geological Sciences, Brown University, Providence, R.I. 02912

1:500,000 scale geologic mapping was undertaken to synthesize the broad-scale geology of Chryse Planitia [1] with the local geology of the Viking 1 landing site [2]. The geology of MTM's 20047 and 25047 has been presented previously [3]. As part of the goals for the Mars Geologic Mapping program, the rational and scientific objectives for a return mission to Chryse Planitia and the Viking 1 Lander have also been presented [4]. However, in mapping central Chryse Planitia our principle objective was to determine the depositional and erosional history of the Chryse Planitia basin. These results are outlined and illustrated (Figure 1) below.

The Chryse Planitia topographic depression was formed during the Noachian (~4.2 Ga), probably as the result of a giant impact [5]. The northern rim of this basin was destroyed when Acidalia Planitia was formed, which may have also been the result of a giant impact [6]. The intersection of these two basins, or the resulting overlap in topography, produced a large trough connecting Chryse Planitia to the northern plains (topography from [7]).

Emplacement of the Ridged plains materials, unit 1 (Hr<sub>1</sub>) occurred during the early Hesperian (~3.5 Ga). These materials are seen primarily in southern Chryse Planitia and also as windows (i.e., fensters) in the central portion of the basin. Because they pre-date most of the other material in the region, their exact extent is uncertain. Morphologically they are very similar to ridged plains materials seen elsewhere on Mars. Crater size-frequency distribution curves indicate that they are also identical in age to the ridged plains materials in Lunae Planum bordering Chryse Planitia immediately to the west. They probably represent flood lavas extruded through deep-seated faults associated with the formation of the Chryse Planitia impact basin or, alternatively, they may represent fluvial sediments from early channel forming events. The sharply defined wrinkle ridges suggest that regardless of lithology, these materials have been subjected to a compressional stress regime which was stable for a long period of time (early Hesperian through at least the middle Amazonian; ~3.5-1.5 Ga).

During the late Hesperian (~2.8 Ga), Maja Valles formed. These channels cut volcanic material from Lunae Planum and carried the sediments into Chryse Planitia, debouching them into the lowest portions of the basin. Perhaps as much as 62,500 km<sup>3</sup> of volatiles were released during the formation of these channels [DeHon, personal communication, 1992], forming a standing body of water several hundred meters deep in the central portion of the basin. Formation of the circum-Chryse outflow channels to the south occurred soon after, releasing as much as 6.3 x 10<sup>6</sup> km<sup>3</sup> of water into the Chryse basin [8]. Such a large volume of water would have exceeded the volume of the basin contained within the -1 km topographic contour line and flowed northward into Acidalia Planitia.

Kasei Valles appears to have been the last outflow channel to have debouched into Chryse Planitia, forming during the late Hesperian through the early Amazonian. Sediments from the formation of these channels would have debouched into a pre-existing standing body of water emplaced by the younger circum-Chryse outflow channels. Kasei Valles sediments may have discharge across Chryse Planitia by hypopycnal flow so that suspended clays and silts were carried into Acidalia Planitia (as suggested by [9]). Because of the subdued nature of the wrinkle ridges in Ridged plains materials, unit 2 (Hr<sub>2</sub>), it is especially likely that these materials consist of fluvial deposits from the late-stage, Kasei Valles episodes of channel formation. Additional observation suggesting that these materials are fluvial in origin is the fact that they are at one of the lowest elevations on the planet (approximately -2.5 km below Mars datum; topography from [7]), have a very gradational contact with Maja and Kasei Valles channel materials, contain several partially buried craters, and are surrounded by a large outflow channel complex.

Analysis of the buried and modified craters (i.e., *eroded* craters, Figure 2) in Ridged plains materials, unit 2 yield possible information about the spatial distribution of this material. Using equations for fresh martian craters [10], the rim heights for the buried craters (2.3-11.3 km in diameter) were calculated. These values were then compared to the actual rim heights calculated through shadow measurements. By subtracting the difference between predicted and measured rim height values, we calculated that Ridged plains materials, unit 2 are ~50 m thick along the southern contact and possibly become thicker towards the basin interior. This is probably the case because the sharp bend-over in the crater production curve at 5-km-diameter (Figure 2) suggests that most craters smaller than this diameter were eradicated during the emplacement of the unit. This requires a substantially thicker deposit with a mean value of ~170 m. Throughout the Amazonian to the present, this unit has been reworked by aeolian activity.

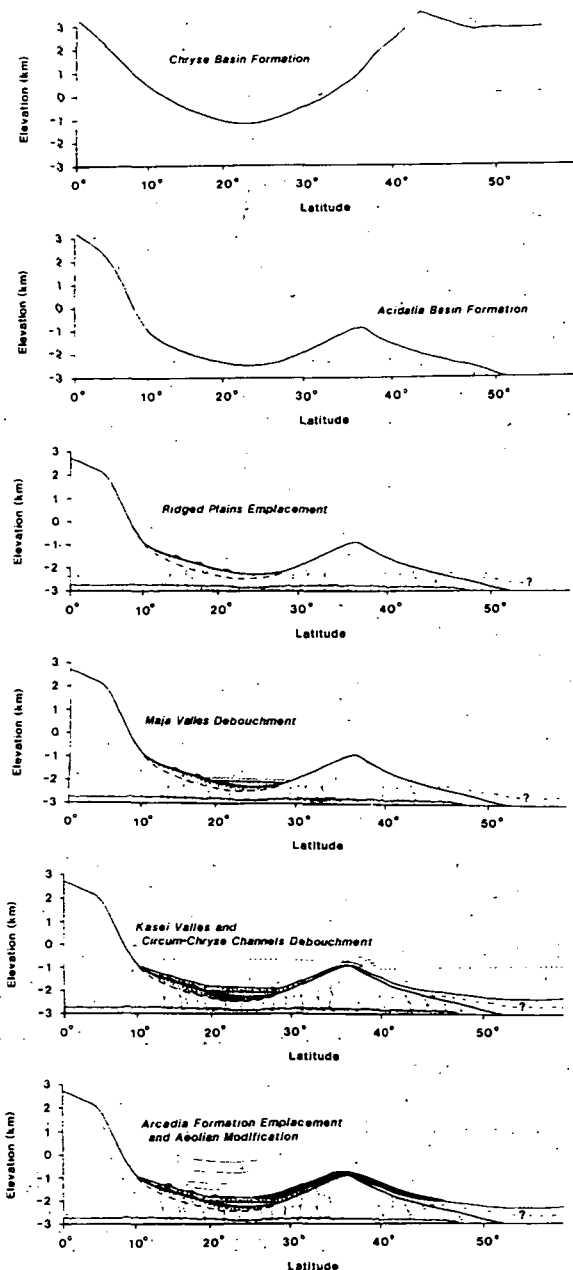


Figure 2 (right). Crater counts for Ridged plains material, unit 2 ( $H_{r2}$ ). Craters are classified as either fresh, rampart, or eroded (i.e., modified or buried). Note the bend over in the production curve at  $\sim 5$  km suggesting that  $H_{r2}$  is  $\sim 170$  m thick.

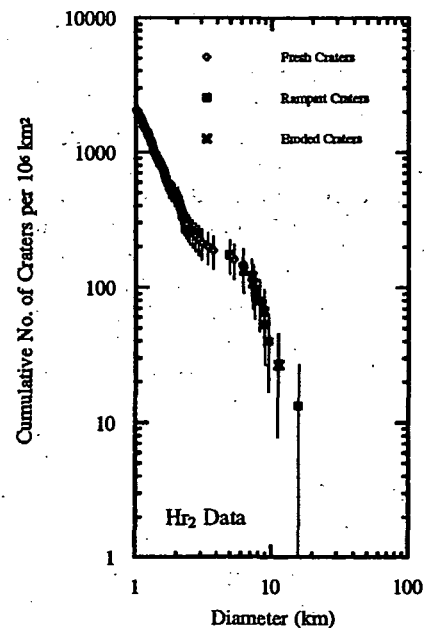


Figure 1 (left). Geologic history of Chryse Planitia. Oldest is at the top. Noachian: 1. Formation of the Chryse Planitia depression from an impact. 2. Formation of Acidalia Planitia depression from an impact and possible subsidence of Chryse Planitia. Hesperian: 3. Emplacement of Ridged plains material, unit 1 in central and southern Chryse Planitia. Deposition of these materials in Acidalia Planitia is questionable. 4. Maja Valles debouches material from Lunae Planum into Chryse Planitia, perhaps filling the the lowest portion of the basin with sediments and volatiles. 5. Kasei Valles debouches material from northern Lunae Planum into Chryse Planitia. The total volume of water discharged by the circum-Chryse outflow channel complex is approximately 6x the volume of the Chryse Planitia below -1 km in elevation. Volatiles would have overflowed into Acidalia Planitia, carrying finer-grained sediments into the northern plains. Were the boulders and rocks seen by the Viking 1 lander deposited by Kasei Valles as they emptied into a standing body of water? Amazonian: 6. Arcadia formation emplaced in northern Chryse Planitia and southern Acidalia Planitia (not seen in area investigated). If volcanic, the emplacement of these materials may have induced by further Chryse basin subsidence. Note also continued formation of wrinkle ridges, suggesting that the compressional stress regime remained since the beginning of the Hesperian. Aeolian processes continued to winnow away finer-grained materials from Chryse Planitia.

#### References:

- [1] Greeley, R. et al., *J. Geophys. Res.*, 82, 4093-4109, 1977. [2] Binder, A.B. et al., *J. Geophys. Res.*, 82, 4439-4451, 1977. [3] Craddock, R.A. et al., *Lunar Planet. Sci.*, XXIII, 257-258, 1992. [4] Craddock, R.A., *Proc. Space '92 Conf.*, 3rd, 1488-1499, 1992. [5] Schultz P.H. et al., *J. Geophys. Res.*, 87, 9803-9820, 1982. [6] Schultz, R.A. and H.V. Frey, *J. Geophys. Res.*, 95, 14,203-14,214, 1990. [7] U.S.G.S., *Misc. Invest. Ser. Map I-2030*, 1989. [8] Carr, M.H. et al., *Lunar Planet. Sci.*, XVIII, 155-156, 1987. [9] Scott D.H. et al., *Proc. Lunar Planet. Sci. Conf.*, 22, 53-52, 1992. [10] Pike, R.J. and P.A. Davis, *Lunar Planet. Sci.*, XV, 645-646, 1984.



**MACROSCOPIC ELECTRIC CHARGE SEPARATION DURING HYPERVELOCITY IMPACTS: POTENTIAL IMPLICATIONS FOR PLANETARY PALEOMAGNETISM.** D. A. Crawford and P. H. Schultz, Department of Geological Sciences, Brown University, Providence, RI 02912.

The production of transient magnetic fields by hypervelocity meteoroid impact has been proposed to possibly explain the presence of paleomagnetic fields in certain lunar samples as well as across broader areas of the lunar surface [1-6]. In an effort to understand the lunar magnetic record, continued experiments at the NASA Ames Vertical Gun Range allow characterizing magnetic fields produced by ~5 km/s impacts of 0.32-0.64 cm projectiles over a broad range of impact angles and projectile/target compositions [7-10]. From such studies, another phenomenon has emerged, macroscopic electric charge separation, that may have importance for the magnetic state of solid-body surfaces. Adushkin and Soloviev observed this phenomenon during explosive cratering experiments [11,12] but the magnetic consequences of macroscopic electric charge separation (as opposed to plasma production) during explosion and impact cratering have not, to our knowledge, been explored before now. It is straightforward to show that magnetic field production due to this process may scale as a weakly increasing function of impactor kinetic energy although more work is needed to precisely assess the scaling dependence.

The original intent of our experiments was to assess the character of purely electrostatic signals for comparison with inferred electrostatic noise signals acquired by shielded magnetic sensors buried within particulate dolomite targets (Fig. 1). The results demonstrated that electrostatic noise does affect the magnetic sensors, but only at relatively short distances (< 4 cm) from the impact point (our magnetic studies are generally performed at distances greater than ~5.5 cm [7-10]). However, to assess models for magnetic field generation during impact, measurements are needed of the magnetic field as close to the impact point as possible [9,10]; hence, work with an improved magnetic sensor design is in progress. In this paper, we focus on electric charge separation during hypervelocity impacts as a potential transient magnetic field production mechanism in its own right.

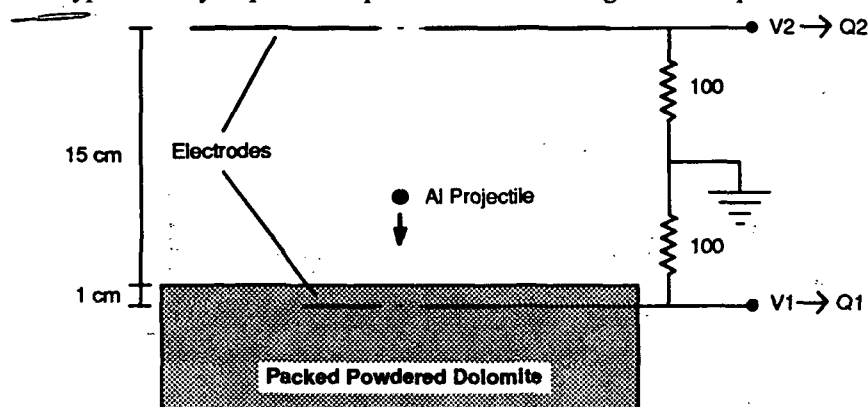


Fig. 1 Setup used for the measurement of macroscopic charge separation during the exploratory hypervelocity impact experiments reported here. Each electrode consists of an aluminum plate with a 5-cm hole to allow passage of the projectile through the upper electrode and to insure that no early-time interaction occurs between the projectile and lower electrode. Ongoing experiments with greater electrode coverage are being performed to better identify the charge distribution in space and time for various projectile and target materials.

Adushkin and Soloviev measured electric fields produced by electric charge separation during explosive cratering experiments in dry and wet soil [11,12]. They obtained an empirical relationship between electric charge ( $q$ ), explosive charge ( $W$ ) and crater diameter ( $D$ ) of the form:  $q = 2.92 \times 10^{-4} \cdot W^{0.65 \pm 0.05} = 7.2 \times 10^{-4} \cdot D^{2.0 \pm 0.1}$  (MKS) [11,12]. The latter relationship can be transformed using the scaling relations for hypervelocity impacts (5 km/s, terrestrial gravity) into dry sand [13] to obtain a relationship between electric charge and equivalent projectile kinetic energy ( $E$ ) of the form:  $q = kE^\alpha = 5.5 \times 10^{-7} \cdot E^{0.56 \pm 0.03}$  (MKS). For comparison, an  $\alpha$ -value of 0.67 implies that charge production is a contact phenomenon proportional to the projectile area whereas an  $\alpha$ -value of 1.0 implies that charge production is proportional to projectile volume (at constant impact velocity). Similar empirical relationships can be derived from charge collection data that were obtained during hypervelocity impact experiments into dolomite targets (Fig. 2). The relationship between electric charge ( $q_1$ ) collected on the lower electrode (see Fig. 1) and projectile kinetic energy ( $E$ ) fits an expression of the form:  $q_1 = 5.5 \times 10^{-12} \cdot E^{0.93 \pm 0.09}$  (MKS). A similar relationship derived from data acquired by the upper electrode is of the form:  $q_2 = 5.4 \times 10^{-9} \cdot E^{0.63 \pm 0.14}$  (MKS).

A first-order estimate of the average azimuthal magnetic field ( $B$ , in Tesla) produced by vertical transport of charge ( $q$ ) during vertically incident hypervelocity impacts can be represented by an equation of the form:

$$B(x') = 2 \times 10^{-7} \frac{q}{x' L \Delta t} = 2 \times 10^{-7} \frac{kE^\alpha}{x' L \Delta t} \quad (1)$$

where  $x'$  is dimensionless length,  $L$  is the dimensional length scale (in meters),  $\Delta t$  is the length of time (in seconds) during which charge transport occurs,  $k$  and  $\alpha$  are empirical constants (as shown earlier), and  $E$  is projectile kinetic energy (in Joules). There are two potential length scales for this problem: projectile radius ( $L = R_p$ ) or crater radius ( $L = R$ ). To simplify matters, we consider projectiles with equal velocity and density impacting a single planet; hence, the length scales can be written in terms of projectile kinetic energy [13]:  $L = R_p \propto E^{0.33}$  or  $L = R \propto E^{0.26-0.28}$ . Likewise, there are several potential time scales bracketed by two extremes: projectile penetration time ( $\Delta t \propto R_p/V_p \propto E^{0.33}$ ) and crater formation time ( $\Delta t \propto E^{0.13-0.14}$ ). Of particular interest is the case where charged impact products possess a velocity independent of the length scale ( $\Delta t \propto L$ ). In any case, the azimuthal magnetic field of this first-order model can be written in the form:

$$B(x') = \frac{k}{x'} E^{\alpha-\beta} \quad (2)$$

where the constants of proportionality have been absorbed into  $k$ ,  $\alpha = 0.53-1.02$ , the empirical exponent shown earlier and  $\beta = 0.39-0.67$ , depending on the particular combination of length and time scales. For instance, if the transient magnetic field strength experienced by target material near the crater rim is of interest, then the crater radius would be an appropriate length scale. Furthermore, if the charged impact products expand at a scale-independent rate (e.g., entrained within the expanding vapor/plasma plume), then an appropriate value for  $\beta$  would be 0.52-0.56; hence, the magnetic field experienced by target materials near the crater rim ( $x' \sim 1$ ) would scale as a weakly increasing function of impactor energy for most of the experimentally derived  $\alpha$ -values. Clearly, better estimates of  $\alpha$  and  $\beta$  are required if reasonable extrapolations of this process to larger scales are to be made. Ongoing experiments are being performed that will hopefully improve the precision of the empirically derived  $\alpha$  and  $\beta$ -values and lead to a better understanding of the process.

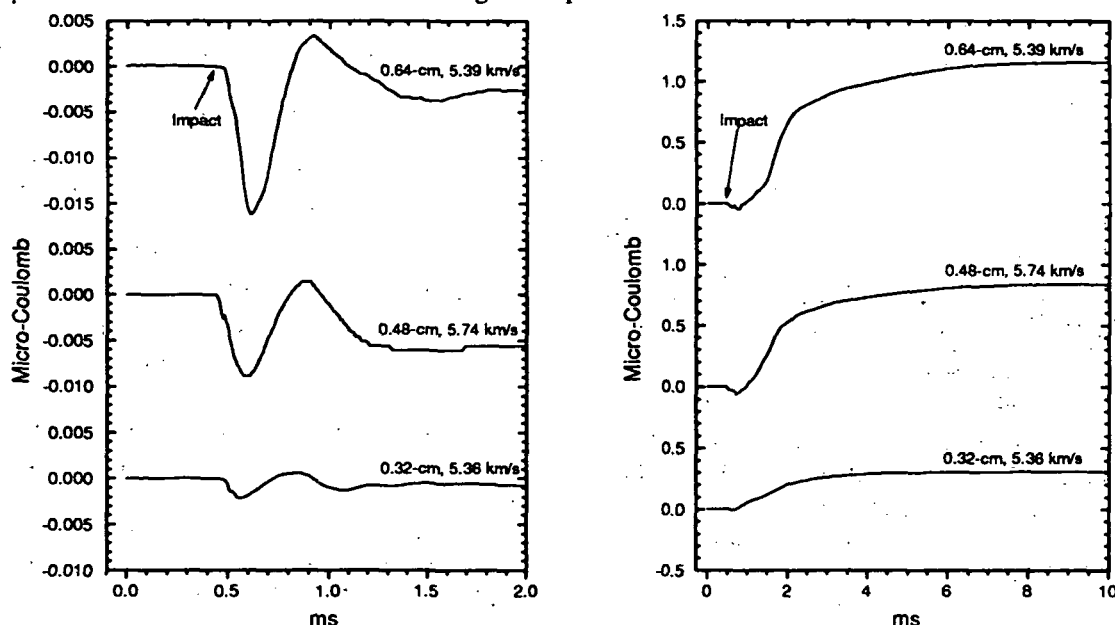


Fig. 2 Charge measured by the lower electrode (shown on left) and upper electrode (right) during three impact experiments performed with spherical aluminum projectiles (0.64, 0.48 and 0.32-cm diameter) impacting a packed powdered dolomite ( $\text{Mg}_{0.5}\text{Ca}_{0.5}\text{CO}_3$ ) target at vertical incidence. These plots were obtained by numerically integrating the charge collection currents recorded by each of the electrodes. Note the time-scale changes.

**References:** [1] Gold, T. and Soter, S., *Plan. Space Sci.* 24, 45-54 (1976) [2] Srnka, L.J., *P. Lunar Sci. Conf.* 8, 893-895 (1977). [3] Srnka, L. J. et al., *Earth Planet. Sci. Lett.* 42, 127-137, (1979). [4] Schultz, P.H. and Srnka, L.J., *Nature* 284, 22-26 (1980). [5] Hood L.L. and Vickery, A., *J. Geophys. Res.* 89, C211-C223 (1984). [6] Hood, L.L. and Huang, Z., *J. Geophys. Res.* 96, 9837-9846 (1991). [7] Crawford, D.A. and Schultz, P.H., *Nature* 336, 50-52 (1988). [8] Crawford, D.A. and Schultz, P.H., *J. Geophys. Res.* 96, 18807-18817 (1991). [9] Crawford, D.A. and Schultz, P.H., *Lunar Planet. Sci.* 23, 259-262 (1992). [10] Crawford, D.A. and Schultz, P.H., *Int. J. Impact Engng.*, (in press). [11] Adushkin, V.V. and Soloviev, S.P. *Izvestia AN SSSR, Ser. Fizika Zemli*, No. 3, 51-59 (1989, in Russian). [12] Adushkin, V.V. and Soloviev, S.P., *Lunar Planet. Sci.* 22, 3-4 (1991). [13] Schmidt, R.M. and Housen, K.R., *Int. J. Impact Engng.*, Vol. 5, 543-560 (1987).

464027

5167-90

ABS. 94

PSC XXIV 82<sup>339</sup>  
163387

## RHENIUM-OSMIUM ISOTOPE SYSTEMATICS OF GROUP IIA AND GROUP IVA IRON METEORITES.

R. A. Creaser<sup>1</sup>, D. A. Papanastassiou and G. J. Wasserburg, The Lunatic Asylum, Division of Geological and Planetary Sciences, Caltech, Pasadena, CA 91125; <sup>1</sup>Present address: Dept. of Geology, 1-26 Earth Sciences Bldg., University of Alberta, Edmonton, Alberta Canada T6G 2E3.

We are investigating the Re-Os isotope systematics of two groups of magmatic iron meteorites (IIA, IVA) in an attempt to establish precise "total rock" isochrons by the Re-Os system. The <sup>187</sup>Re-<sup>187</sup>Os isotope system is recognized as a method by which the ages of iron meteorites can be directly determined [1,2], and provide information on the timing of FeNi segregation and core formation in planetesimals. The Re-Os isotope system permits the direct absolute dating of the metal phase in iron meteorites. Indirect dating of iron meteorites has been achieved in the past through the Rb-Sr, K-Ar, and most recently, Sm-Nd for silicate inclusions, where present [cf 3-6]. Relative dating has been obtained directly by extensive studies of the short-lived system <sup>107</sup>Pd-<sup>107</sup>Ag for the metal and sulfide phases [7] and indirectly using <sup>129</sup>I-<sup>129</sup>Xe in silicate and sulfide inclusions [8].

The major experimental difficulties with Re-Os analyses derive from: a) the multiple oxidation states of Os with slow kinetics for exchange to achieve Os isotope equilibrium between sample and tracer Os; b) the volatility of OsO<sub>4</sub>; and c) the difficulty of the reliable preparation of an Os gravimetric normal for calibration of the Os tracer. Our analytical technique for addressing the first and second problems for Os now uses a sealed-tube (pyrex glass) H<sub>2</sub>SO<sub>4</sub> decomposition of the sample with attendant (closed system) Os oxidation to OsO<sub>4</sub>, using Cr<sup>VI</sup>, to equilibrate the tracer and sample Os isotopes. Osmium is then removed by solvent extraction and further purified by micro-scale anion exchange. Rhenium is separated from the aqueous phase of the solvent extraction by anion exchange. Re and Os are measured by negative thermal ion mass spectrometry [9,10]. The precision for the <sup>187</sup>Os abundance is typically 0.2-0.3%, for intense ion beams on a Faraday collector. Reproducibility for this sealed-tube technique appears good from the duplicate samples of the IVA iron meteorites currently analyzed (Table 1). Duplicate analyses of adjacent samples of Bishop Canyon have nearly identical <sup>187</sup>Os/<sup>188</sup>Os isotopic compositions and yield <sup>187</sup>Re/<sup>188</sup>Os ratios in agreement to better than ±0.2%. Duplicate samples of other meteorites that gave similar <sup>187</sup>Os/<sup>188</sup>Os isotopic compositions yield <sup>187</sup>Re/<sup>188</sup>Os ratios in agreement to ±1-3%. We had not been able to achieve routinely results with this level of reproducibility with sample decomposition methods that we have previously described, using HBr [11]. For Hill City we obtain a large discrepancy between the duplicate analyses at the 5% level, for which we have no identified cause. This shows the need for improvements in the techniques, as the matter of data reproducibility appears reasonably complex. It is clear from Table 1 that replicate analyses of Gibeon, Yanhuaitan, and Bishop Canyon show substantial variation in the concentrations of Os and Re within each meteorite. This shows that these elements are concentrated heterogeneously even in the adjacent small samples analyzed. Therefore, simple replicate analyses are not sufficient and reproducibility can be addressed only to the extent that the individual samples follow well defined Re-Os systematics. We show in Fig. 1 the data on a <sup>187</sup>Re-<sup>187</sup>Os evolution diagram. The IIA irons show a wide range in <sup>187</sup>Re/<sup>188</sup>Os and define a linear correlation. The slope of  $0.0785 \pm 0.0004$  of this IIA correlation agrees well with previous studies [12] and corresponds to an age of  $4609 \pm 29$  Ma, using the <sup>187</sup>Re decay constant of  $1.64 \times 10^{-11} \text{ a}^{-1}$  [13]. The initial <sup>187</sup>Os/<sup>188</sup>Os value of  $0.0959 \pm 0.0002$  also agrees well with previous work [2,12]. The fundamental problem of absolute tracer calibration is now being addressed.

The IVA irons analyzed for Re-Os show a very limited range of Re/Os and considerable scatter relative to the IIAs and do not define an isochron. We have shown the IVA data in Fig. 1 for comparison with the IIA data. We also show the deviations of the IVA data from the IIA correlation line in Fig. 2. To the extent that Re/Os values limit the precision, we have assigned the deviations (ζ in permil) from the correlation line to the <sup>187</sup>Re/<sup>188</sup>Os. The deviations ζ for duplicate analyses of Gibeon, Yanhuaitan and Bishop Canyon are in good agreement; the deviations for these three different IVA irons from the IIA correlation line range from ζ -0.5 to -11.2%. The data for Hill City duplicates are greatly displaced by different amounts from the IIA correlation line, as is the datum for Mart. We note that negative values of ζ correspond to points lying above the correlation line in Fig. 1. Assuming a similar initial <sup>187</sup>Os/<sup>188</sup>Os for both IIA and IVA groups, the IVA irons yield apparent Re-Os model ages up to 40 Ma older than the IIA iron meteorites. The presence of significant amounts of live <sup>107</sup>Pd and relatively uniform inferred initial <sup>107</sup>Pd/<sup>108</sup>Pd in these IVA irons at the time of segregation of the metal and sulfide phases limits the timing of their origin to approximately 10<sup>7</sup>a since nuclide production and within a few 10<sup>6</sup>a from each other [7]. If the relatively uniform initial <sup>107</sup>Pd/<sup>108</sup>Pd indicates formation within a few 10<sup>6</sup>a, then the range of 40x10<sup>6</sup>a in the Re-Os model ages of the three IVA irons analyzed that yield reproducible results is inconsistent with the Pd-Ag systematics. Therefore, there is as yet no clear correlation between Pd-Ag and Re-Os for these samples. It is known

from Pd-Ag in sulfide inclusions that the Pd-Ag system is disturbed and from petrographic studies [cf 14] that the IVA irons have been strongly metamorphosed. We will attempt to establish the extent to which the Re-Os system reflects this complex history and whether internal isochrons can be determined in favorable cases.

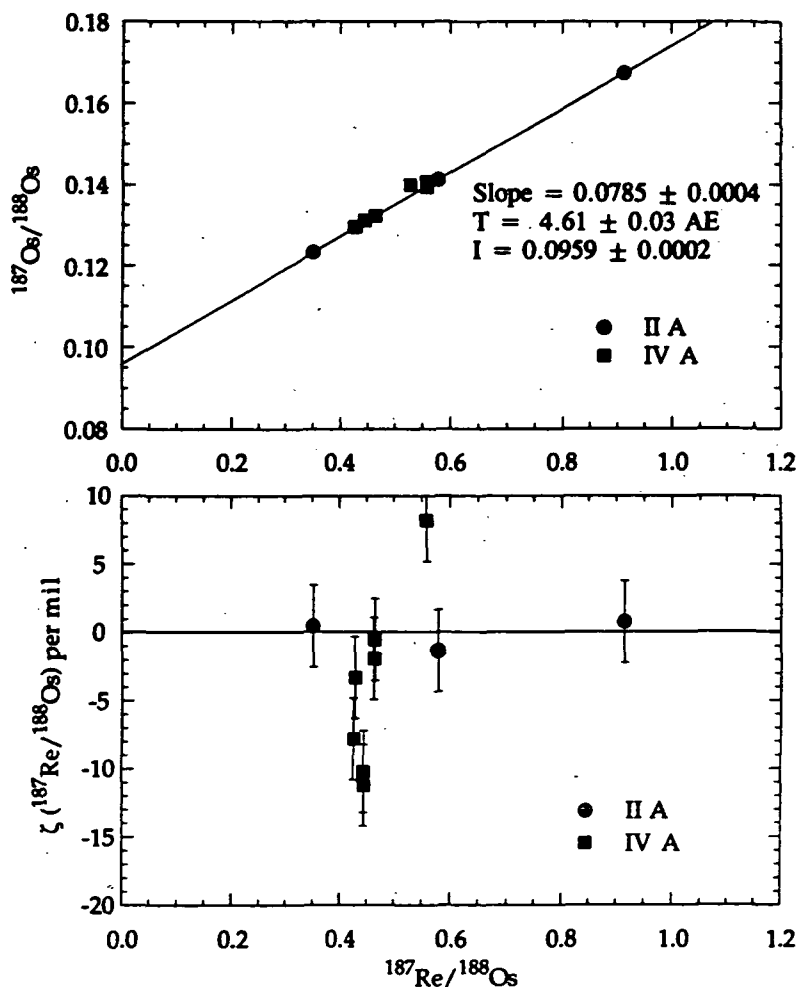
Table 1. Re-Os Analytical Results

Sample	Os (ppm)	Re (ppb)	$^{187}\text{Re}/^{188}\text{Os}$	$^{187}\text{Os}/^{188}\text{Os}$	$\epsilon(^{187}\text{Re}/^{188}\text{Os})$ (‰)
IIA Iron Meteorites					
Negrillos	67.1	4487	0.3507	0.12337	0.5
Coahuila	12.33	1478	0.5788	0.14135	-1.3
Tocopilla	1.212	228.7	0.9136	0.16751	0.8
IVA Iron Meteorites					
Gibeon	4.641	446.7	0.4641	0.13230	-0.5
Gibeon	2.775	266.4	0.4629	0.13226	-1.9
Yanhuitlan	5.417	478.2	0.4255	0.12952	-7.8
Yanhuitlan	5.002	444.6	0.4284	0.12960	-3.3
Bishop Canyon	4.432	408.3	0.4442	0.13108	-10.2
Bishop Canyon	4.591	423.1	0.4443	0.13113	-11.2
Hill City	1.023	118.2	0.5579	0.13934	8.2
Hill City	1.056	115.6	0.5287	0.13992	-57.4
Mart	0.677	78.2	0.5575	0.14073	-23.8

References: [1] Herr W. *et al.* (1961) *Z. Naturforsch.* 16a, 1053; [2] Luck J.M. & Allègre C.J. (1983) *Nature* 302, 130; [3] Burnett D.S. & Wasserburg G.J. (1967) *EPSL* 2, 137; [4] Bogard D.D. *et al.* (1968) *EPSL* 3, 179; [5] Niemeyer S. (1979) *GCA* 43, 1829; [6] Stewart B.W. *et al.* (1993) *LPSC XXIV*; [7] Chen J.H. & Wasserburg G.J. (1990) *GCA* 54, 1729; [8] Niemeyer S. (1979) *GCA* 43, 843; [9] Creaser R.A. *et al.* (1991) *GCA* 55, 397. [10] Völkening J. *et al.* (1991) *Int. J. Mass Spect. Ion Proc.* 105, 147. [11] Creaser R.A. *et al.* (1992) *LPSC XXIII*, 263; [12] Horan M.F. *et al.* (1992) *Science* 255, 1118; [13] Lindner M. *et al.* (1989) *GCA* 53, 1597. [14] Teshima J. *et al.* (1986) *GCA* 50, 2073. Contribution 5232(796). Work supported by NASA, NAG9-43.

Fig. 1.  $^{187}\text{Re}$ - $^{187}\text{Os}$  evolution diagram for IIA and IVA iron meteorites. Correlation line drawn through IIA data.

Fig. 2. Deviations  $\epsilon$ , in permil, from IIA correlation line ( $\epsilon=0$ ) in Fig. 1.



464028  
IP

5168-90

ABS ONLY

LPSC XXIV

N. 94-12183  
163 38.8  
P. 2  
341SEPARATION OF SPALLATION AND TERRESTRIAL  $^{14}\text{C}$  IN CHONDRITES

R. G. Cresswell, R. P. Beukens and J. C. Rucklidge, IsoTrace Laboratory, University of Toronto,  
60 St. George St., Toronto, Ontario, Canada. M5S 1A7

Weathering products and contamination severely hamper our ability to accurately measure the  $^{14}\text{C}$  spallation component in meteorites, but can give insights into a sample's terrestrial history. A procedure has been developed to measure the  $^{14}\text{C}$  in these components using CO and  $\text{CO}_2$  separations from temperature extractions from 200-500mg of material. The Bruderheim (L6) chondrite was chosen as a standard following the practice of previous workers [1,2], cross-checked against Peace River (L6), Abee (EH4) and Juvinas (EUC). Low temperature fractions ( $< 900^\circ\text{C}$ ) give  $^{14}\text{C}$  signatures consistent with a modern terrestrial  $^{14}\text{C}$  source; melt fractions show elevated levels attesting to a spallogenic origin. Higher yields of CO in the melt fraction are less affected by the low levels of experimental contamination than the  $\text{CO}_2$ . This fraction gave a mean  $\text{CO}:\text{CO}_2$  ratio in Bruderheim of  $81.6 \pm 7.7$ ; the ratio of the spallation component is  $79.8 \pm 8.1$ . These values suggest equilibrium release of gases on the olivine-silica-pyroxene-iron buffer. This is corroborated by approximately equal release of the two components at  $900^\circ\text{C}$ . The chondrites gave an average saturation level of  $54.3 \pm 2.9$  dpm/kg; the achondrite gave  $49.6 \pm 2.0$  dpm/kg. No clear correlation with oxygen content is apparent, though shielding effects have yet to be evaluated.

Measurement of  $^{14}\text{C}$  from separated gas species from the step-wise pyrolysis of meteorites has been undertaken to further constrain and isolate the spallation component, and assess the role of recent weathering of meteorites, with particular reference to Antarctic samples. A series of samples of Bruderheim, ranging from 306 to 486mg, were step-heated under helium in a coil furnace, then taken to melt temperatures using induction heating of the molybdenum crucible. For each temperature step chosen, the evolving gases were removed by continuously cycling the helium using a peristaltic pump, trapping the condensibles in a variable temperature trap held at  $-180^\circ\text{C}$ , and passing the non-condensibles over heated (to  $650^\circ\text{C}$ ) cupric oxide, oxidizing any Co and  $\text{CH}_4$  to  $\text{CO}_2$ , which was then trapped in two liquid nitrogen-cooled traps.  $\text{CO}_2$  was further purified by fractional distillation, diluted to give  $\approx 3\text{cc}$  and transferred to vials. Each aliquot is reduced over heated lithium to produce lithium carbide; water is added to generate acetylene, and this is dried and bled into a cracking chamber. A glow discharge is created between two aluminium pellets by means of a current controllable 60Hz, 1kV AC power supply, dissociating the gas and depositing 200-400 $\mu\text{g}$  of low density graphitic material on the surface of each pellet [3,4]. Each pellet provides a target for accelerator mass spectrometry, with  $^{14}\text{C}$  analysis carried out as described elsewhere [4]. The number of  $^{14}\text{C}$  atoms for each aliquot is determined and backgrounds are subtracted as outlined elsewhere [5].

To assess each fraction for contamination it is assumed that the recovered gas is entirely of recent origin, and the expected  $^{14}\text{C}$  content is calculated. This is subtracted from that observed to give a delta-14 value, relative to modern. Figure 1 shows the results from Bruderheim together with single runs on each of the other three falls. Almost all fractions up to  $900^\circ\text{C}$  plot within error (approximately three times the size of the symbols) of modern, indicating a terrestrial source. Above this temperature, breakdown of silicates and any indigenous graphite distorts the picture. The elevated levels from the melt fraction (here designated as  $1600^\circ\text{C}$  for Bruderheim and  $1650^\circ\text{C}$  for the other falls for clarity) are due to the spallation component, which is particularly evident in the CO fraction. Graphite in Abee and Juvinas act as natural dilutants, hence the low delta-14 for two of the other falls.

Spallation and terrestrial  $^{14}\text{C}$  in chondrites. Cresswell, R.G. et al.

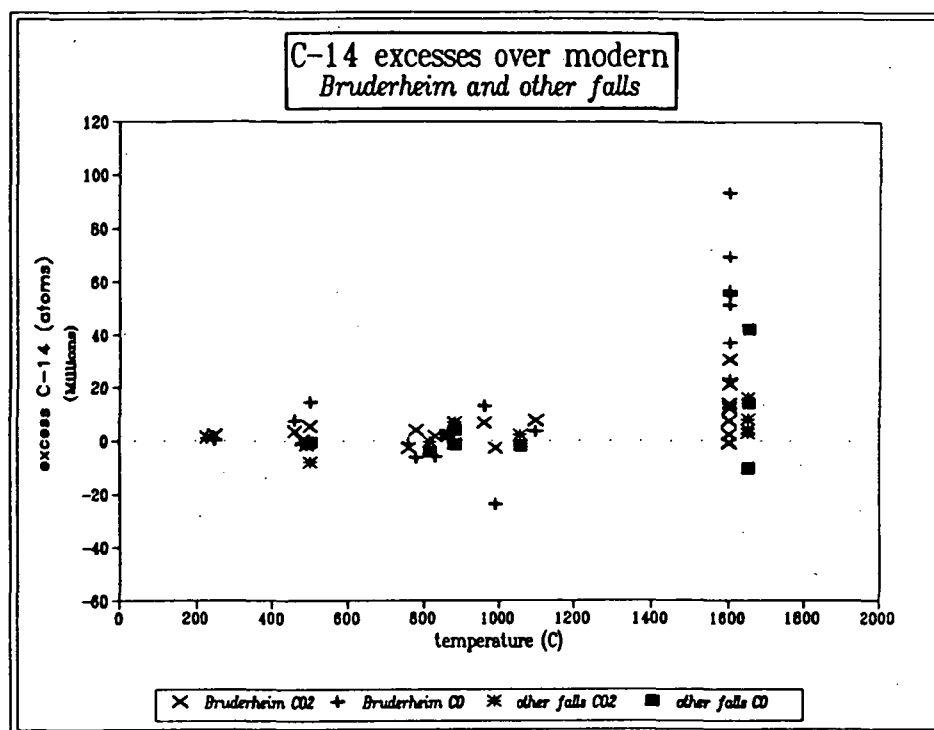


Figure 1.  $^{14}\text{C}$  excesses in Bruderheim and three other falls as a function of temperature and gas species. Zero represents a modern (terrestrial) carbon source. The excess  $^{14}\text{C}$  from spallation is clearly seen in the melt ( $1600^\circ\text{C}$ ) CO fraction.

The variable excess  $^{14}\text{C}$  in the melt is explained by incomplete diffusion for melts of less than six hours duration. Unlike the combustion method employed by Jull [2], whereby oxidation of the carbon facilitates rapid release of the spallation component, these pyrolysis extractions are controlled by diffusion, with expected diffusion rates of  $\approx 10^{-5.5}\text{cm}^2/\text{s}$  [6]. A diffusion rate of  $10^{-6}\text{cm}^2/\text{s}$  has been estimated from the results of this work on Bruderheim [7], requiring a minimum of five hour melts for complete extraction of the spallation component.

Kotra *et al.* [8] showed that finely ground carbonates decompose between  $400^\circ\text{C}$  and  $800^\circ\text{C}$  during continuous heating. Some finely crushed dolomite was tested using the same procedure adopted here for meteorites and found to completely decompose between  $550^\circ\text{C}$  and  $920^\circ\text{C}$ . This suggests an alternative to the hydrolysis method of separating weathering components used by Jull, *et al.* [9,10]. This has been used to assess the weathering component of nine Antarctic meteorites, and is reported elsewhere [5].

- REFERENCES. [1] Fireman, E. L. *et al.* (1976) *Earth Planet. Sci. Letts.*, 32, 185. [2] Jull, A. J. T. *et al.* (1989) *Geochim. Cosmochim. Acta*, 53, 2095. [3] Beukens, R. P. and Lee, H. W. (1981) in Henning, W. *et al.* (eds) *Symp. Accel. Mass Spect.* 2nd Proc. Argonne Nat. Lab., 416. [4] Beukens, R. P. *et al.* (1986) *Radiocarbon*, 28, 229. [5] Cresswell, R. G. *et al.* (in press) *Proc. NIPR Symp. Antarct. Meteorites*, 6. [7] Cresswell, R. G. (1993) PhD diss. Univ. Of Toronto. [8] Kotra, R.K., *et al.* (1982) *Icarus*, 51, 593. [9] Jull, A. J. T., *et al.* (1988) *Science*, 242, 417. [10] Jull, *et al.* (1992) *Lunar Planet. Sci.*, XXIII, 641

464029

1P

5168-91

HBS-ONLY

LPSC XXIV

343

N 94-3121 84

**NEAR-INFRARED SPECTRA OF THE MARTIAN SURFACE: READING BETWEEN THE LINES;** D. Crisp (Jet Propulsion Laboratory/Caltech, MS 169-237, 4800 Oak Grove Drive, Pasadena, CA) 91109, and J. F. Bell III (MS 245-3, NASA Ames Research Center, Moffett Field, CA 94035)

Moderate-resolution near-infrared (NIR) spectra of Mars have been widely used in studies of the Martian surface because many candidate surface materials (weathered basalts, iron minerals, carbonates, bicarbonates, sulfates, hydrates, etc.) have distinctive absorption features at these wavelengths. Recent advances in NIR detector technology and instrumentation have also encouraged studies in this spectral region. The use of moderate spectral resolution ( $200 < \lambda/\Delta\lambda < 2000$ ) has often been justified for NIR surface observations because the spectral features produced by most surface materials are relatively broad, and easily discriminated at this resolution. In spite of this, NIR spectra of Mars are usually very difficult to interpret quantitatively. One problem is that NIR surface absorption features (particularly for mineral mixtures) are often only a few percent deep, requiring observations with great signal-to-noise ratios. A more significant problem is that gases in the Martian atmosphere ( $\text{CO}_2$ ,  $\text{H}_2\text{O}$ , and  $\text{CO}$ ) contribute numerous absorption features at these wavelengths. Ground-based observers must also contend with variable absorption by several gases in the Earth's atmosphere ( $\text{H}_2\text{O}$ ,  $\text{CO}_2$ ,  $\text{O}_3$ ,  $\text{N}_2\text{O}$ ,  $\text{CH}_4$ ,  $\text{O}_2$ ). The strong  $\text{CO}_2$  bands near 1.4, 1.6, 2.0, 2.7, 4.3, and 4.8  $\mu\text{m}$  largely preclude the analysis of surface spectral features at these wavelengths. Martian atmospheric water vapor also contributes significant absorption (several percent) near 1.33, 1.88, and 2.7  $\mu\text{m}$ , but water vapor in the Earth's atmosphere poses a much larger problem to ground-based studies of these spectral regions. The third most important NIR absorber in the Martian atmosphere is  $\text{CO}$ . This gas absorbs most strongly in the relatively-transparent spectral windows near 4.6 and 2.3  $\mu\text{m}$ . It also produces 1-10% absorption in the solar spectrum at these NIR wavelengths. This solar  $\text{CO}$  absorption cannot be adequately removed by dividing the Martian spectrum by that of a star, as is commonly done to calibrate ground-based spectroscopic observations, because most stars (even "solar-analog" stars, which have similar color temperatures) do not have identical amounts of  $\text{CO}$  absorption in their spectra.

Here, we describe two effective methods for eliminating contamination of Martian surface spectra by absorption in the solar, terrestrial, and Martian atmospheres. Both methods involve the use of very-high-resolution spectra that completely resolve the narrow atmospheric absorption lines. Figure 1 shows a high-resolution ( $10^3 \text{ cm}^{-1}$ ) synthetic radiance spectrum generated with an atmospheric/surface radiative transfer model. This segment of a weak  $\text{CO}_2$  band near 2.15  $\mu\text{m}$  shares many properties with other weak  $\text{CO}_2$  and  $\text{CO}$  bands in the Martian atmosphere. For example, it consists of an array of very narrow absorption lines separated by distances that are large compared to their widths. Another important feature of these lines is that their cores are completely saturated for one-airmass optical paths. They therefore show little airmass dependence. Efforts to discriminate surface and atmospheric absorption by searching for airmass dependence therefore have little value. Figure 2 shows a synthetic spectrum of the 2.3- $\mu\text{m}$  (K-band) window that has been convolved with a triangular slit function of FWHM  $0.1 \text{ cm}^{-1}$ . At this resolution, the 2.15  $\mu\text{m}$   $\text{CO}_2$  band and 2.33- $\mu\text{m}$   $\text{CO}$  band appear to be only 10% deep, in spite of the fact that most of their lines are completely saturated. Their apparent lack of airmass dependence might therefore be a surprise to some observers. These spectra still have adequate resolution to show completely transparent regions between the strongest lines. At

much lower resolutions, these "micro-windows" are completely filled.

These examples suggest two approaches for identifying and removing atmospheric contamination from surface spectra: First, one can simply take spectra that completely resolve atmospheric absorption features. Surface features can then be reliably identified by simply "reading between the lines." Second, when this is not possible or practical (when high-resolution spectra do not provide adequate signal-to-noise or spatial resolution), one should use sophisticated atmospheric/surface radiative transfer models to assist in the analysis of the spectra.

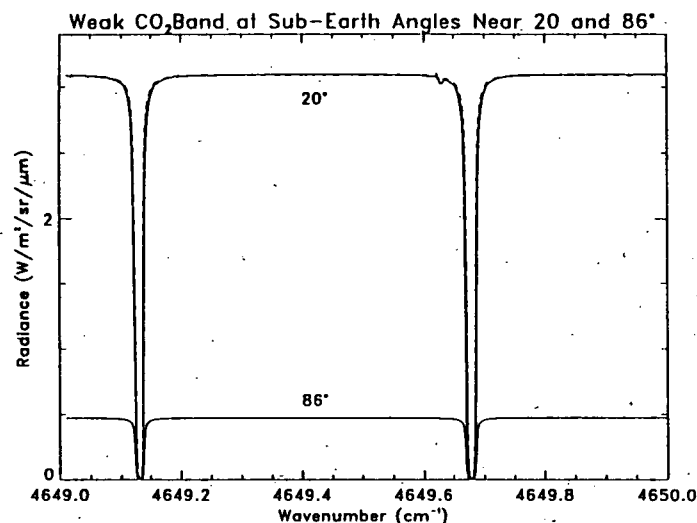


Figure 1: Synthetic radiance spectra showing two absorption lines near the center of the 2.15- $\mu\text{m}$  CO<sub>2</sub> band for emission angles (and solar zenith angles) near 20 and 86 degrees (solid lines). The 86-degree values can be scaled to the 20-degree values by simply multiplying by a constant factor that accounts for the difference in solar illumination (dashed line).

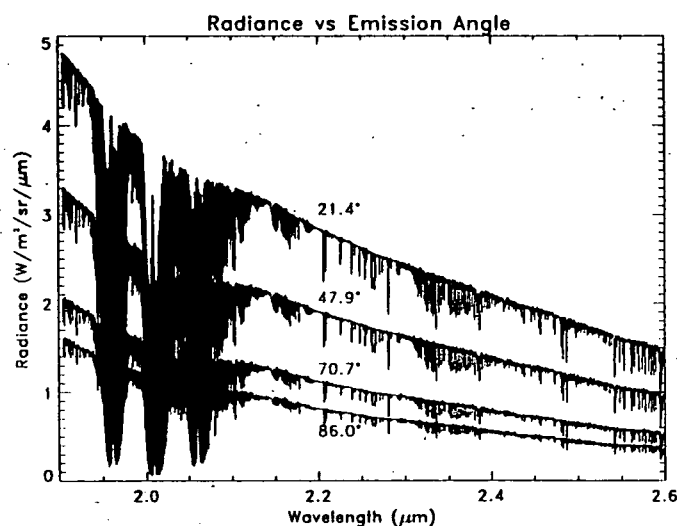


Figure 2: A synthetic spectra of the K-band (2.3- $\mu\text{m}$ ) window for emission angles near 21.4, 47.9, 70.7, and 86.0 degrees. The 2.15- $\mu\text{m}$  CO<sub>2</sub> band appears only 10% deep at this resolution. Only the strong CO<sub>2</sub> bands near 2.0 and 2.7  $\mu\text{m}$  show appreciable airmass dependence.



464030

570-91

1P

ABS. ONLY

LPSC XXIV

N94-12185 345

463370

P 2

**GEOMORPHOLOGY OF TRITON'S POLAR MATERIALS;** Steven K. Croft, Lunar & Planetary Laboratory, University of Arizona, Tucson, AZ 85721.

**Summary.** One of the Triton's most debated puzzles is the nature, distribution, and transport of its atmospheric volatiles. The full potential of constraints provided by detailed observations of the morphology and distribution of the polar deposits has not been realized. The objective of this study is characterization of the morphology, distribution, stratigraphy, and geologic setting of Triton's polar materials.

**Description of Polar Materials.** In the south polar mosaic of Triton (1), two primary types of polar materials are readily apparent: the slightly reddish south polar cap (SPC) itself and the bluish polar fringe with its north-trending rays. The bright fringe provides a continuous border to the SPC along its entire length with the exception of a small gap between 290°E and 320°E. **Fringe Materials.** The fringe is typically 100 to 200 km wide, broadening where it extends northward into the bright rays which are also 100 to 200 km wide where they seamlessly join the fringe, but typically broaden to the north. Fringe materials have the spectral characteristics of a frost (1). Fringe and ray materials range from translucent to opaque, and, except in the center of the equatorial "bar" near Yasu Sulci, show no topographic expression or visible "softening" of underlying features. The fringe overlaps the SPC along much of their common border, but a thin zone (nearly) free of bright material between the fringe and the cap edge begins near the center of the "bar" and continues eastward out of the high-resolution region. Color comparisons on the low resolution global mosaic suggest that the "detached" zone extends east to around longitude 150°E. **Geologic Subdivisions of the SPC.** These divisions represent a more detailed description of polar materials than given in the preliminary discussions (2,3). **Bright Smooth Terrain** (Bs) is a bright, flat plains unit with surface textures ranging from very smooth to slightly rough. The albedo of the surface is non-uniform, ranging from a predominate albedo estimated near  $A \approx 0.85$  to relatively diffuse bright patches with  $A \approx 0.9$ . Albedo patterns of adjacent plains are discernable within the unit, indicating that unit Bs consists of a dark "bedrock" plains surface coated with bright material translucent in most places, but becoming opaque in the high albedo spots. **Bright Rugged Terrain** (Br) consists of a maze of rugged linear ridges and troughs with a few rugged, rimmed, quasi-circular depressions. The albedos of unit Br range from  $\approx 0.85$  to  $A \approx 0.9$ , the ridges being generally darker than the troughs. The size, distribution, and texture of the ridges and depressions are similar to like features in the cantaloupe terrain, indicating that unit Br consists of cantaloupe terrain coated with a bright material. The brightest opaque material occurs in topographic lows. **Bright Featureless Terrain** (Bf), a new division, consists of very bright ( $A \approx 0.92$ ) featureless surfaces occurring in both isolated and connected patches. The bright patches are separated by a few narrow, slightly darker ( $A \approx 0.88$ ) and higher ridges into large (few hundred km) quasi-circular to linear lobate planforms. Patches of unit Bf within unit Br are small, irregular, and conform to topographic lows. The largest connected patches of unit Bf seen in high resolution images occur near 45°S, 300°E and 50°S, 350°E. Large patches of similar-appearing material are seen in the lower resolution images between about 40°S and 60°S with only isolated patches occurring to the north or south. **Maculae and Plumes** are features with albedos between 0.65 and 0.75 are seen on the SPC. Most are "wind streaks" (2,4). A second type of dark feature comprises the plumes (2,5). A third class of dark features, apparently not previously described, comprises the diffuse dark patches. These patches have very complex albedo patterns: multiple fuzzy dark centers imbedded in a thick to diffuse matrix with feathered and diffuse edges. They are probably atmospheric phenomena: 1) the edges of the diffuse dark patches strongly resemble the diffuse edges of the plumes, 2) the relative darkness of the patches increases with the obliquity of the viewing angle as do the plumes, and 3) the areal extent of the edge of a patch near the Mahilani plume changed substantially between different images. The patches are suggested to be low hazes. The patches appear to exist at latitudes between about 35°S and 70°S all around the south pole. **Bright Lineations** (a new unit) are bright linear features seen to cross the SPC in medium resolution images, including a prominent one within 10° of the south pole. The bright lineations seen at high resolution are all linear ridges, suggesting that those seen at low resolutions are also linear ridges. **Guttae and Aureoles** (the "mushrooms" of 2 & #) are dark ( $A \approx 0.7$ ) irregular spots with bright ( $A \approx 0.9$ ), annular aureoles around them (3). The guttae have not previously been considered polar materials (2,3), but are reinterpreted as such here because: 1) they occur in a well-defined latitudinal band between 5°S and 45°S, on or near the edge of the SPC, 2) aureole materials are visually indistinguishable from the opaque bright material on the SPC, and 3) they rest unconformably underlying units like other polar materials.

**Interpretation.** The materials of the SPC appear to be a layer of bright material coating a darker bedrock of plains and cantaloupe materials. The thickness of the coating is non-uniform, changing from centimeters in the translucent sections that cover most of the polar region regardless of topography to tens of meters in the opaque sections that tend to cluster in topographic lows (3). The patches of unit Bf are interpreted as somewhat thicker

## TRITON'S POLAR MATERIALS; Croft, S.K.

deposits, perhaps as much as a few hundred meters, that nearly fill valleys between the barely visible ridge crests. Their lobate and elongated planforms may result from glacier-like flow in these thicker deposits. Thus the SPC materials within the high-resolution area do not form a thick, continuous, sheet-like deposit. Medium-resolution images covering the south pole and mid-latitude areas to the west of the high-resolution area show bright lineations that are probably linear ridges right down to the pole and albedos like the translucent areas of the Br and Bs units. The bright Bf units that may be thick materials occur in only local patches. A high-resolution (but high phase angle) image, FDS 11401.38, shows another large swath of the SPC in the anti-Neptune facing hemisphere. Although the surface is partially obscured by hazes and clouds, circular features with sizes and cluster patterns like the cavi in the cantaloupe terrain can be seen as well as groupings of larger circular and elongate features with planforms and groupings like either paterae or patches of Bf material. The similarity of these features to those seen at high resolution suggest that the 1/3 of the SPC seen at high resolution is representative of the whole.

Models for seasonal transport of volatiles on Triton (e.g., 6,7) indicate that only centimeters of material can be moved in a tritonian year. Thus the thicker opaque materials must represent a permanent cap while the translucent materials apparently represent seasonal deposits. The transport models also predict significant sublimation near the current sub-solar latitude near 45°S and frost deposition in the equatorial regions and in the entire northern hemisphere. The plumes and diffuse dark patches may represent sublimated materials. The dark equatorial and northern plains raise the question: where is the freshly deposited frost? Suggestions have included dark frosts (6), deposition on N-facing slopes where it would be difficult to see in current images (8), and high internal heat flow in the north which prevents frost deposition (9). It is suggested here that frost deposition is going on, the frosts are bright, and the deposits are in plain sight: the polar fringe and the N-trending rays. These materials behave spectrally as frosts; they cover virtually the entire equatorial area and much of the northern plains. The rays darken (thin?) to the north, but then the amount being transported is very small. In addition, the light scattering properties of the rays may make them appear darker as they are seen at low phase angles near the terminator. Assuming that the fringe and rays are the sought-for frost deposits, the locations of the deposits are decidedly non-uniform. At least two possibilities exist: 1) to date, the transport models are 1-D; the frost deposition environment on Triton is 3-D: there are winds related to a Hadley cell circulation pattern (9), and presumably planetary waves propagating along the equator (suggested by the scallop pattern) that could create uneven frost distribution. Once started, a lightly frosted area would tend to be cooler than its surroundings and collect more frost. The association of the fringe with the edge of the SPC rather than some arbitrary latitude is further evidence of circulation on deposition: the fringe could be due to condensation caused by air heating and rising sharply at the cap's edge like at the edge of the martian caps (10). 2) The frost could sinter quickly, becoming transparent (11). There is some evidence that the entire zone north of the fringe and between the rays is covered with transparent frost (12). The patches of dark, i.e., transparent, frost could be caused by different ground albedos; indeed the gap in the fringe is associated with a localized patch of dark mantling. Only a few degrees difference in surface temperature is needed to cause great differences in the sintering rate (10).

The conclusion that most of the SPC materials represent a permanent cap implies that it is residual. Similarly, I propose that the guttae are residual deposits of an even more extensive cap. The morphologies of the guttae are similar to outliers of the permanent martian caps which are shaped by ablation; the sharp SPC edge, with high topography exposed is also best explained by ablation. This may be viewed as morphological evidence that Triton's atmosphere was significantly thicker earlier in its history, as has been suggested on theoretical grounds (13). As the atmosphere thinned, it "dried" relative to the volatiles in the cap, causing net ablation. The guttae may be layered: the aureole extending under the guttae; candidate materials are N<sub>2</sub> with over CH<sub>4</sub>, or CH<sub>4</sub> over CO<sub>2</sub> (14). Alternatively, the guttae may be the remnants of a less volatile material and the aureoles a later deposit; likely candidate materials are CH<sub>4</sub> guttae surrounded by N<sub>2</sub> aureoles. Is there a permanent northern cap? That it was not seen by Voyager is irrelevant: the martian permanent caps differ greatly in size. However, there has been no change in Triton's color since 1933 (15), when the sub-solar and sub-earth points were in the northern hemisphere, suggesting both a permanent northern cap and fringe. **References.** 1) McEwen, A.S. (1990) *Geophys. Res. Lett.* 17,1765. 2) Smith, B.A. et al (1989) *Science* 246,1422. 3) Croft, S.K. (1990) *LPS XXI*,248. 4) Hansen, C.J. et al (1990) *Science* 250,421. 5) Soderblom, L.A. et al (1990) *Science* 250,410. 6) Spencer, J.R. & J.M. Moore (1992) *Icarus* 99,261. 7) Hansen, C.J. & D.A. Paige (1992) *Icarus* 99,273; Stansberry, J.A. et al (1992) *Icarus* 99,242. 8) Yelle, R.V. (1992) *Science* 255,1553. 9) Brown, R.H. & R.L. Kirk (1991) *BAAS* 23,1210. 9) Ingersol, A.P. (1990) *Nature* 344,315. 10) Haberle, R.M. et al (1979) *Icarus* 39,151. 11) Eluszkiewicz, J. (1991) *J.G.R.* 96,19217. 12) Lee, P.E. et al (1992) *Icarus* 99,82. 13) Lunine, J.I. & M.C. Nolan (1992) *Icarus* 100,221. 14) Cruikshank, D. et al (1993) *Science*, submitted. 15) Buratti, B.J. et al (1993) *Icarus*, submitted.

464031

5171-90

ABS ONLY

LPSC XXIV

347

N 946-3121 8p2

**POROSITY AND THE ECOLOGY OF ICY SATELLITES;** Steven K. Croft, Lunar & Planetary Laboratory, University of Arizona, Tucson, AZ 85721.

**Summary.** The case for a significant role for porosity in the structure and evolution of icy bodies in the Solar System has been difficult to establish. Here are presented a relevant new data set and a series of structure models including a mechanical compression, not thermal creep, model for porosity that accounts satisfactorily for observed densities, moments of inertia, geologic activity and sizes of tectonic features on icy satellites.

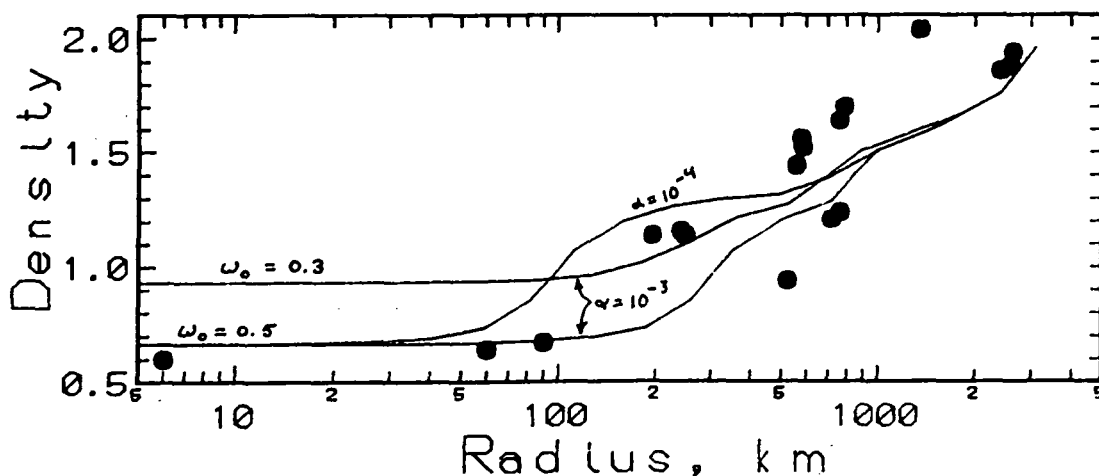
Several types of observational data sets have been used to infer significant porosity, but until recently, alternative explanations have been preferred. 1) Occurrence of cryovolcanism as a function of satellite radius: simple radiogenic heating models of icy satellites suggest minimum radii for melting and surface cryovolcanism to be 400 to 500 km, yet inferred melt deposits are seen on satellites half that size. One possible explanation is a deep, low conductivity (high porosity) regolith which lowers conductivity and raises internal temperatures (1), but other possibilities include tidal heating or crustal compositions of low conductivity (2). 2) Occurrence and magnitude of tectonic strain: tectonic structures seen on icy satellites as small as Mimas and Proteus. The structures are almost exclusively extensional, with only a few possible compressional features, and inferred global strains are on the order of 1% expansion (2,3). Expansions of this order in small bodies like Mimas and prevention of late compressional tectonics due to formation of ice II mantles in larger bodies like Rhea are attained only in structure models including low-conductivity, and thus possibly high porosity, crusts (4). 3) Inferred moments of inertia less than 0.4 in Mimas (5) and Tethys (6) can be explained by high-porosity crusts, but also by differentiation of a high density core. 4) The relatively low densities of smaller satellites like Mimas and Miranda relative to larger neighbors can be explained by deep porosity, but also by bulk compositional differences. Recent work has strengthened the case for significant porosity. Halley's nucleus was found to have a density near  $0.6 \text{ g/cm}^3$  (7), Janus and Epimetheus were proposed (and recently confirmed) to have densities near  $0.7 \text{ g/cm}^3$  (8), densities almost certainly due to high porosity. The irregular-spherical shape transition of icy satellites was quantitatively explained by low conductivity (probably high porosity) regoliths (9). A creative structure/thermal history model for Mimas (10) simultaneously accounts quantitatively for Mimas' low density and moment of inertia by invoking initial high-porosity and subsequent compaction in the deep interior by thermal creep. The main problem with this promising model is that it predicts  $\approx 7\%$  reduction in Mimas' radius, implying significant compressional failure and prevention of extensional tectonics, in contradiction to the observed extensional features and inferred 1% expansion in radius.

**Data.** Measurements were made of the widths of the largest graben-like structures on both rocky and icy bodies throughout the solar system. Based on terrestrial experience with continental rifts (grabens) and theoretical modeling, these largest grabens are assumed to represent structures cutting the entire lithosphere on each body, and thus their widths are a measure of the lithospheric thickness at the time of graben formation. Assuming further conductive heat flow through the lithosphere and radiogenic heating in the interior, the following ratio between the effective thermal conductivity,  $K_e$ , and mean thermal conductivity,  $K_o$ , derived from low porosity laboratory samples is obtained: (1)  $K_e/K_o = \rho f R L Q(t) / [3 K_o (T_i - T_s)]$ , here  $\rho$  is the lithospheric density,  $f$  is the mass fraction chondritic rock,  $R$  is the planet/satellite radius,  $L$  is the lithospheric thickness estimated from the largest grabens,  $Q(t)$  is chondritic radiogenic heating as a function of time,  $t$ ,  $T_i$  is the temperature at the bottom of the lithosphere, and  $T_s$  is the surface temperature. The resulting ratios for reasonable estimates of age and composition are near unity for planets/satellites larger than  $\approx 1000 \text{ km}$  in radius, but drop sharply and systematically by one to two orders of magnitude for bodies the size of Mimas and Miranda. This implies that effective conductivities in the lithospheres of large bodies correspond reasonably well to laboratory conductivities, while effective conductivities in the lithospheres of smaller decreases systematically with radius. Some ratios do fall off of the trend: the Moon, Io, Enceladus, and Triton. In the case of the Moon, based on other estimates, the largest grabens are probably associated with the megaregolith and not the much thicker lithosphere, the other three all have or had significant tidal heating, which in eq. 1 corresponds to abnormally small conductivity ratios.

The systematic decrease of  $K_e$  with decreasing radius eliminates mechanisms not dependent on gravity or physical size. Models that work include deep porous regoliths that decrease in thickness with increasing satellite radius. This relationship can be achieved by the thermal creep model of (10): the depth at which  $T_i$  is reached is proportional to  $1/R$ ; since  $T_i$  represents the temperature of significant creep, pore closure by creep will occur below the bottom of the lithosphere. However, any thermal creep model will produce compression in the lithosphere, not extension as observed. I propose an alternative: mechanical compression and closure of accretion-impact induced pores. Mechanical compression experiments of porous rocks and soils (11) show different behaviors depending on pore shape: 1) bubble-like pores as commonly found in terrestrial rock are difficult to close and thus do not reduce

## POROSITY ON ICY SATELLITES: Croft, S.K.

bulk moduli significantly, while 2) crack-like pores such as found in impact-generated regoliths close easily, closing linearly with increasing pressure. Complete closure is achieved at pressures near  $\alpha E$ , where  $\alpha$  is the crack aspect ratio and  $E$  is Young's modulus. This relationship suggests that as bodies accrete, pressures inside small bodies are low, impact induced cracks remain open and bulk densities remain low. Above some diameter, internal pressure become significant compared to  $\alpha E$ , crack closure becomes significant and bulk density begins to increase. Impact shaking due to continued accretion should keep stresses near lithostatic, thus in progressively larger bodies, the thickness of the porous layer should decrease roughly as  $1/R$ . The result at the end of accretion should be a suite of bodies with systematically increasing densities, progressively thinner porous layers, and progressively higher  $K_0$ 's. Experimentally,  $\alpha \approx 10^{-2}$  to  $10^{-4}$ . Thus for rocks, crack-like pores close at pressures of a few kilobars and compaction effects should become important for rocky bodies larger than about 500-600 km (i.e., only the largest asteroids). However, for ices, assuming the same physical dependence (supported by the limited data available), crack-like pores should close at pressures of a few hundred bars, pressures occurring in icy bodies with radii near 100 to 200 km. These radii fall in the middle of the observed population of icy satellites, thus the mechanical compaction model can be tested for icy bodies. The mechanical compression model was tested by constructing a series of icy satellite structure models including crack closure using parameters appropriate for ice. Both densities and effective thermal conductivities were computed for comparison. Note that these two data sets are largely independent of each other. The density results are shown in figure 1, which compares model densities as a function of radius for reasonable ice/rock fractions with observed icy satellite densities. The mechanical compression models bracket both the observed densities and the effective conductivities. Depending on the value of  $\alpha$ , pore closure effects are significant for radii between 100 and 500 km; bulk compression and phase changes in  $H_2O$  ice dominate at radii above 600 km. Some of the observed density differences are still due to composition differences, particularly between satellite systems, but it is apparent that porosity differences can also significantly affect bulk densities. Thus some density differences within a satellite system may be due to geological processes affecting porosity; e.g., melting and cryovolcanism closing pores on Dione or the giant Odysseus impact opening pores on Tethys. Possible density differences due to these processes have not yet been modeled, but they are clearly potentially significant. The mechanical compaction model predicts porosity structures at the end of accretion similar to the thermal compaction model at the end of thermal evolution. However, in the mechanical compaction model, the porosity structure is achieved before radiogenic heating becomes significant. Now as heating becomes important, any thermal compaction will be much less because it will occur at the base of the porous layer where stresses and hence strain rates are significantly lower. Thus further compaction could be negligible, and density and moment of inertia relations derived from the thermal compaction model should be preserved. The dominant effect of heating should be simple thermal expansion of the interior. The advantage of this is that now, instead of compaction and compressional tectonics, radiogenic heating should cause expansion and extensional tectonics, in agreement with the nature of tectonic features observed on the icy satellites. References. 1) Stevenson, D.J. (1982) *Nature* 298,142. 2) Croft, S.K. & L.A. Soderblom (1991) in *Uranus*, p. 561. 3) Croft, S.K. (1992) *LPS XXIII*, p. 267. 4) Croft, S.K. (1991) *RPGGP-1990*, p. 95. 5) Dermott, S.F. & P.C. Thomas (1988) *Icarus* 73,25. 6) Thomas, P.C. & S.F. Dermott (1991) *Icarus* 94,391. 7) Sagdeev, R.Z. et al. (1988) *Nature* 331,240. 8) Yoder, C.F. et al. (1989) *A.J.* 98,1875. 9) Croft, S.K. (1992) *Icarus* 99,402. 10) Eluszkiewicz, J. (1990) *Icarus* 84,215. 11) Stephens, D.R. & E.M. Lilley (1970) *PLSC 11th*, p. 2427.



464032

5172-91

ABS ONLY

LPSC XXIV

349

N 9 4-1 2187

TECTONICS ON TRITON; Steven K. Croft, Lunar & Planetary Laboratory, University of Arizona, Tucson, AZ, 85721.

**Summary.** Tectonic features on Triton have been mapped as part of a larger study of the geology of Triton. Few purely tectonic structures are found on Triton: some grabens and possibly some compressive ridges. However, most of the other structures seen (primarily cryovolcanic in origin) exhibit tectonic control. A regional tectonic network has dominant orientations of: N-S, E-W, NE-SW, and NW-SE. Most of the orientations are consistent with tidal deformations related to Triton's decreasing orbital radius. Localized quasi-concentric patterns may be due to interior processes such as mantle plumes.

**Tectonic Features.** A sketch map of tectonic features seen on the USGS 1:5 M shaded relief map of the Slidr Linea quadrangle is shown in figure 1. Of the features mapped, few are apparently unmodified tectonic structures. The most readily identifiable tectonic features are the fossae, which appear to be simple grabens. The fossae occur in two width classes: 1) narrow fossae 2-3 km wide, including Jumna Fossae, a parallel pair of valleys  $\approx 300$  km long, and Yenisey Fossa, a single valley  $\approx 800$  km long, and 2) the wide fossae  $\approx 15$  km wide, occurring in a single group, Raz Fossae, which is an en echelon pair of valleys about 350 km long. Another type of possibly unmodified tectonic features are the sinuous ridges and scarps which occur in three groups: the Awib dorsa (center near 7S, 77E), an unnamed group just southwest of Raz Fossae (3N, 14E), and another unnamed group near Bheki cavus (15N, 310E). The Raz group of ridges are 15 to 50 km long, highly sinuous in plan, axisymmetric in section with sharp to rounded crests and steeply sloping sides. Structures in the Awib Dorsa and the Bheki group are morphologically somewhat different: the structures are longer, 30 to 150 km, broadly curvilinear in plan, and their crests are more rounded. The crests of these structures are axially asymmetric, steep slopes on one side and much shallower slopes on the other, morphologically reminiscent of the lobate scarps on Mercury and might be more appropriately referred to as scarps rather than ridges. While few purely tectonic features are seen on Triton, the locations and orientations of many features exhibit strong tectonic control, including the grid-like network of the linear ridge materials, the network of rugged ridges in the cantaloupe terrain, and pit chains, notably Set Catena. These features are cryovolcanic or tectono-volcanic in origin, though interpretations differ: e.g., the linear ridges were interpreted as flooded grabens by (1) but as dike-related deformations and cracks by (2).

**The Tectonic Network.** Directional trends of these different geologic features are similar, both locally and globally. Taken together, these features define a network with four major trends: N-S, E-W, NW-SE, and NE-SW. Most individual structures follow one or another of these trends, while several of the long linear ridges switch from one trend to another: e.g., Tano Sulci (NE-SW to N-S) and Vimur Sulci (E-W to NW-SE and back). Mapping of the dense network of rugged ridges and linear ridges in the cantaloupe terrain suggest minor tectonic trends concentric and radial to two centers (one near 10°N, 310°E and the other near 15°N, 355°E in figure 1), confirming the observations of (3). While best seen in the cantaloupe terrain, the dominant tectonic trends also affect structures in the plains areas of Monad and Bubembe Regiones. The long axes of the sinuous ridges south of Raz fossae run mostly E-W. The long axis of Tuonela Planitia is N-S. Indeed, a major NW-SE "cryovolcanic" axis is defined by the locations of all four of the walled plains, most of the ring paterae, the long axes of many of the pit paterae (e.g., Kibu Patera), and the crests of the Awib Dorsa and Bheki group of scarps.

There is some localization of tectonic trends. Features trending N-S and E-W are mostly within  $\approx 20^\circ$  of the equator (Tuonela Planitia is an exception). NW-SW and NW-SE trending features tend to occur at higher latitudes. The single bright linear ridge near the south pole runs nearly parallel to a constant longitude line: 120°E over the pole to 300°E.

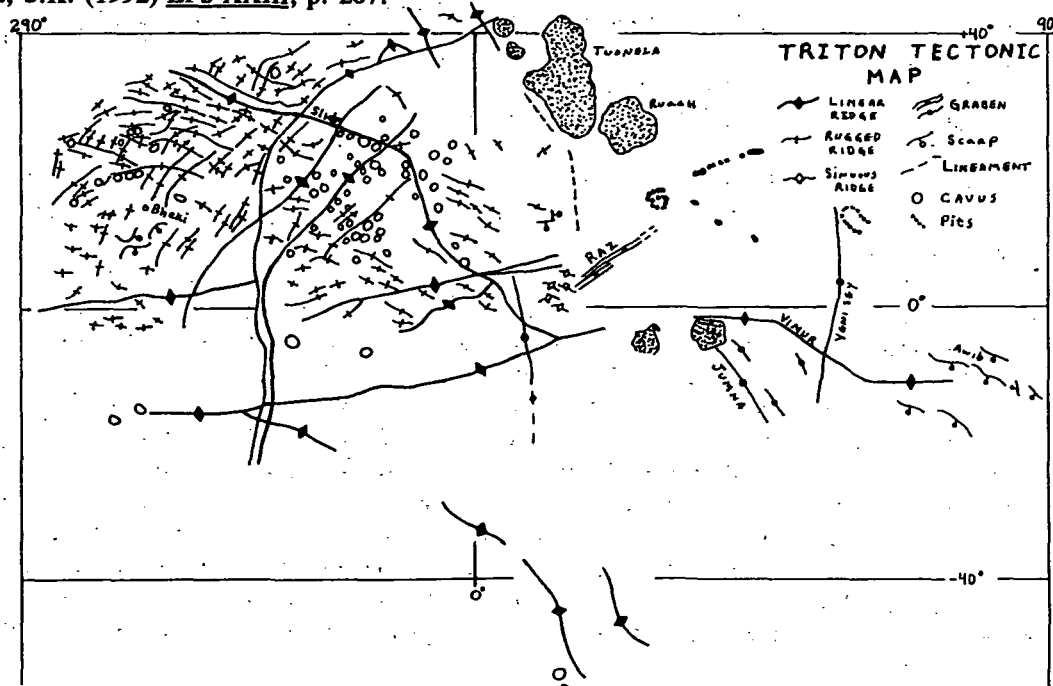
**Discussion.** Most of the observed tectonic trends are consistent with models of despinning (4) and tidal distortion (5). However, the nature of the surface failure on Triton is opposite to that usually considered, because instead of despinning and decreasing distortion due to tidal recession from a primary, Triton has undergone spin-up and increasing distortion due to its tidally-driven approach to Neptune, regardless of origin. For this case, the predicted tectonics due to increasing distortion along an axis through Neptune include N-S trending normal faults in a circular zone centered on the sub-Neptune point, NW-SE and NE-SW trending strike-slip faults over the rest of the equatorial and mid-latitude bands, and compressional faults parallel to the 0° long meridian over the poles. This predicted pattern corresponds well to most of the trends and even the extensional nature of the fossae seen on the map, noting that the map is centered on the sub-Neptune point. The somewhat broader than expected distribution in longitude of N-S trending features may be accounted for by adding a globe-girding equatorial bulge due to spin-up. However, the E-W trend and the 120° trend of the single polar ridge are unaccounted for by either model. The two concentric trends followed by the rugged ridges and linear ridges in the cantaloupe terrain are

## TRITON TECTONICS; Croft, S.K.

apparently due local stress fields or tectonic imprints due possibly to ancient large impacts or endogenic processes (3). An endogenic model is favored here, specifically mantle plumes are proposed. Radial and concentric patterns are formed by a rising, then cooling plume head. Concentrations of the possibly cryovolcanic cavi are found in the interiors of both concentric patterns and clusters of likely cryovolcanic features such as dark lobate and bulbous smooth deposits dominate the center of the eastward pattern, consistent with the location of cryovolcanic activity that would likely be associated with a plume. Additional evidence of interior activity interacting with surface tectonic patterns is provided by the "cryovolcanic" axis: virtually all of the smooth materials and paterae interpreted as cryovolcanic in origin lie along this axis. It is a global-scale feature. Although the areal density of cryovolcanic structures and the predominance of stratigraphically younger features tends to increase to the NW along the axis, stratigraphic ages along the axis do not change uniformly, suggesting a mantle "hot line" rather than a moving "hot spot". Using stratigraphy, a few events can be established about Triton's tectonic history. The formation of the tectonic grid, and presumably most of the strain and failure, occurred before the formation of the current surface formations: the piercement locations of upwelling cryovolcanics were apparently governed by weaknesses in the grid. The oldest surface is the cantaloupe terrain, which is superposed by smooth plains units. Raz Fossae lie partly under a patch of smooth high plains, while Yenisey Fossa cuts a different patch of smooth high plains and a linear ridge. This indicates that either the fossae or the patches of smooth plains were formed at different times. The smooth material in the walled plains superpose both the Jumna Fossae the smooth high plains, making them the youngest deposits on Triton. The average global extensional strain represented by the fossae is very small: only about  $10^{-4}$ , orders of magnitude smaller than the  $\approx 1\%$  strain seen on other icy satellites (6). The sinuous ridges and lobate scarps also superpose smooth materials, but no general time relation between the fossae and ridges can be established. If the ridges and scarps are compressional tectonic features, the strain represented is also small.

The stress fields directly responsible for forming the fossae, ridges, and lobate scarps are ambiguous. They may have been formed by local stress systems associated with movements of mantle material or magmas at depth: their total strains are very small, they are areally restricted in location, and their times of formation appear interleaved with cryovolcanic events. On the other hand, they formed towards the end of significant melting, and presumably heating, which, if related to capture, came after circularization of Triton's orbit. However, the orbit would continue to decay, tidally stretching the globe near the sub-Neptune point, which is where most of the fossae are found. The suggestion was made in (1) that (mis)alignments of some linear features indicate large-scale strike-slip movement to the NW of Raz fossae. However, topographic features in this area are numerous and tend to follow the NW-SE, NE-SW grid directions, so the perceived alignments may be fortuitous. There is no corroborating evidence of large horizontal movements elsewhere.

**References.** 1) Smith, B.A. et al (1989) *Science* 246,1422. 2) Croft, S.K. (1990) *LPS XXI*, p. 246. 3) Boyce J.M. & P.G. Rogers (1992) *LPS XXIII*, p. 145. 4) Melosh, H.J. (1977) *Icarus* 31,221. 5) Melosh, H.J. (1980) *Icarus* 43,334. 6) Croft, S.K. (1992) *LPS XXIII*, p. 267.



464033

5173-46

LPSC XXIV

351

AB5 ON 127 N9 4-1 2188

7-2

**POST-IMPACT ALTERATION OF THE MANSON IMPACT STRUCTURE; L.J. Crossey and P. McCarville, Department of Earth and Planetary Sciences, University of New Mexico, Albuquerque, NM 87131**

Core materials from the Manson impact site (Manson, Iowa; Fig. 1) are examined in order to evaluate post-impact alteration processes. Diagenetic interpretation of post-impact events is based on petrologic, mineralogic, and geochemical investigation of core materials; including target strata, disturbed and disrupted strata, ejecta, breccias, microbreccias, and impact melt. The diagenetic study utilizes research cores obtained by the continental scientific drilling project (CSDP) at the Manson structure, as well as core and cuttings of related materials (Alvina Luebke core, Manson 1-A, Manson 2-A, Amoco Eisheid #1 Deep Petroleum Test Well). Samples include impactites (breccias, microbreccias, and melt material), crater fill material (sedimentary clast breccias), disturbed and disrupted target rocks, and reference target material (Amoco Eisheid #1 materials). The study of multiple cores will permit development of a regional picture of post-impact thermal history. The specific objectives are: (1) provide a detailed description of authigenic and alteration mineralogy from diverse lithologies encountered in research drill cores at the Manson impact structure, and (2) identify and relate significant post-impact mineral alteration to post-impact thermal regime (extent and duration). Results will provide mineralogical and geochemical constraints on models for post-impact processes (including infilling of the crater depression; cooling and hydrothermal alteration of melt rocks; and subsequent long-term, low-temperature alteration of target rocks, breccias, and melt rocks). Preliminary petrologic and x-ray diffraction examination of fracture linings and void fillings from research core M1 indicate the presence of quartz, chlorite, mixed-layer clays, gypsum/anhydrite, calcite, and minor pyrite.

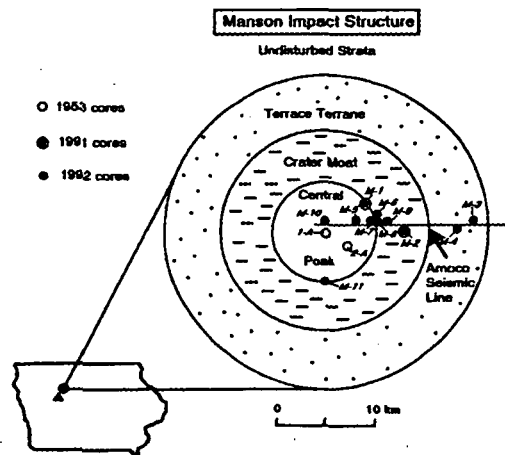


**Fig. 1: Location and schematic of Manson impact structure in NW Iowa. Triangle indicates location of Amoco Eisheid #1.**

alteration mineralogy and geochemistry will provide constraints on models for the cooling history of the impact site. Of particular focus in this study are (1) secondary minerals filling voids and fractures, (2) alteration mineral paragenesis of the reactive glasses encountered in several of the research drill cores, and (3) degree of thermal alteration of sedimentary clasts encountered in breccia units distributed across the Manson study area.

Analysis will include petrography (quantitative mineralogy and paragenetic sequence of alteration mineralogy), scanning electron microscopy (qualitative analysis of alteration phases

While much emphasis has been given to establishing mineralogical and geochemical affinities among boundary layer clay, ejecta, impactor, and target rocks, little attention has been given to post-impact processes. Re-equilibration processes occurring after the physical and thermal disruption associated with large impacts may include: infilling of the crater depression, cooling of melt rocks, development of a related hydrothermal circulation system, and mineralogical and geochemical alteration of target rocks, ejecta, and melt rocks. The availability of core material from the post-impact crater fill, breccia lens, ejecta blanket, and melt rocks provides the opportunity for detailed investigations of post-impact alteration not possible from cuttings, and less affected by surface weathering phenomena operative at currently exposed (and well-studied) crater sites. Examination of



## ALTERATION - MANSON IMPACT STRUCTURE: Crossey, L.J. and McCarville, P.

and textural interpretation), electron microprobe analysis (quantitative analysis of selected authigenic phases; including zeolites, feldspars, pyrite, chlorite, and illite), and x-ray diffraction analysis (mineralogical analysis of clay-size materials). Preliminary examination of core M1 reveals the presence of mineralized fracture surfaces and vugs. Petrographic analysis indicates the presence of abundant quartz, clay, calcite, minor pyrite, gypsum/anhydrite, and zeolites; x-ray diffraction and scanning electron microscopy indicates that the most abundant authigenic clay phases coating fractures are chlorite and an expandable mixed-layer clay (Figs. 2 and 3). A similar assemblage has been noted in fractures of the Siljan Ring, Sweden [1] and altered

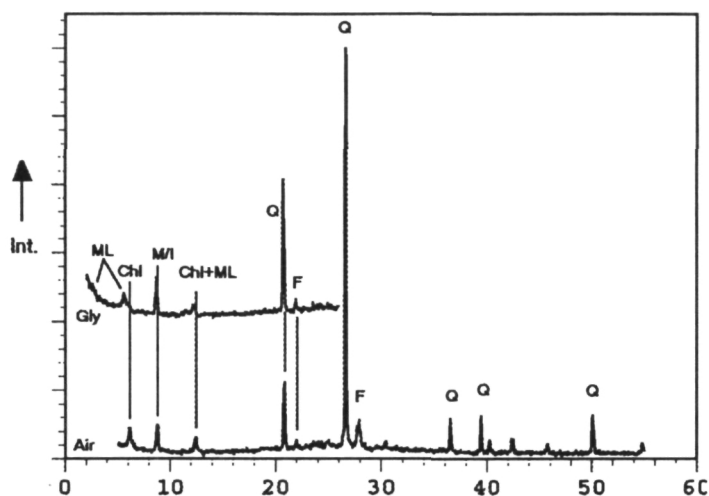


Fig. 2: X-ray diffractogram of fracture surface materials from 128m depth in the M1 core. Chl = chlorite, ML = mixed-layer clay, M/I = muscovite/illite, Q = quartz, and F = feldspar. X-axis is degrees 2-theta. Upper pattern illustrates shift of expandable mixed-layer clay upon solvation with glycol.

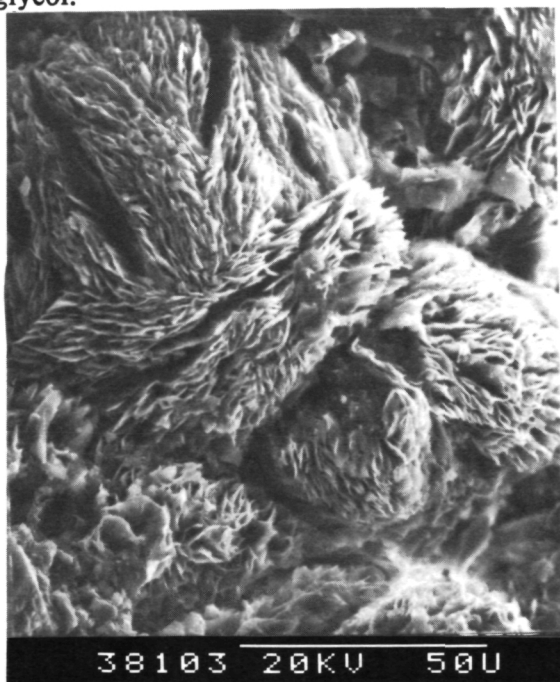


Fig. 3: Scanning electron photomicrograph of authigenic clay from 122m depth in the M1 core. Morphology and energy-dispersive X-ray analysis indicates an Mg- and Fe-rich mixed-layer clay.

materials of the Ries Crater, Germany [2], [3], and [4]. Shocked quartz, feldspar, and biotite are noted in varying degrees of abundance within breccias of the M1 core: remnant grains of recrystallized quartz typically contain a central pore. X-ray diffraction analysis of laminated, pyritic, black shales (interpreted to be displaced Proterozoic Nonesuch Shale) from the M1 core indicates that minimal, if any, graphitization has occurred.

**Acknowledgments:** This project is supported by the Department of Energy through the Office of Basic Energy Sciences. Ray Anderson and Brian Witzke of the Iowa Department of Natural Resources assisted in sampling of the cores. X-ray analysis was performed at the X-Ray Diffraction Laboratory in the

Department of Earth and Planetary Sciences at the University of New Mexico. **References:** [1] Komor, S.C., Valley, J.W., and Brown, P.E. (1988) *Geology*, 16, 711-715; [2] Newsom, H.E., Graup, G., Iseri, D.A., Geissman, J.W., and Keil, K. (1990) *GSA Spec. Pap.* 247, 195-206; [3] Allen, C.C., Gooding, J.L., and Keil, K. (1982) *JGR*, 87, 10083-10101; [4] Englehart, W.v., and Graup, G. (1984) *Geologische Rundschau*, 73, 447-481.



464035

S174-74  
ABS ONLY

LPSC XXIV

353

N94-12189

P 2

# MODEL OF OPTICAL SCATTER FROM MICROIMPACTS ON THE HUBBLE TELESCOPE, L.B. Crowell, POD Associates, 2309 Renard #201, Albuquerque, NM 87106

The investigation and modelling of optical scatter from damaged or contaminated mirrors is of interest to those who wish to estimate the working life cycle of an optical system. A space born telescope faces a threat to its survivability from naturally occurring micrometeoroids and man-made debris. High velocity, in the range of 4.0 to 14. km/s, impacts of small particles, in the range of 1 to 100 microns, will produce small craters on the impacted surface. These microcraters will typically have a size range of 3 to 300 microns for debris impacts and 6 to 600 microns for micrometeoroid impacts. If the microcraters accumulate on a telescope mirror, then there will be an increase in optical scatter and a loss of image resolution.

The micrometeoroid model of Cour-Palais [1] and the orbital debris model of Kessler [2] have been encoded in a computer program (SPENV) by the author at POD associates. The output from this program has been matched with previous calculations and compared with impact data on the LDEF satellite [3]. Subsequent work has been done to marry this computer program with an algorithm to compute optical scatter.

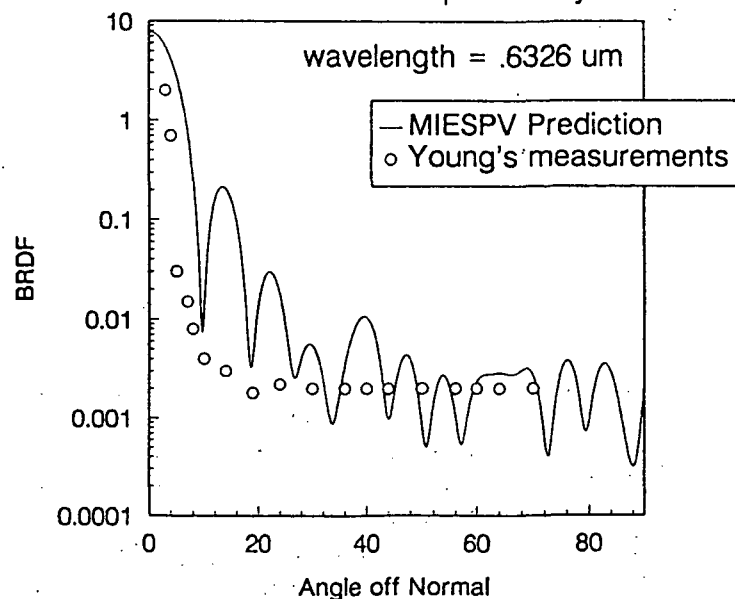
The optical scatter algorithm employs Mie theory of scatter from small particles. Mie theory [4] derives asymptotic solutions to Maxwell's equations that match the boundary conditions on spherical particles. The incident plane wave scatters off of the particle in spherical wave fronts. Consequently light is scattered in directions outside the incident light wavefront. The degree of scatter then is dependent on the size of the particles and their number.

The Mie scatter algorithm uses the assumption that craters on a reflective substrate scatter light in much the same way as particles sitting on the substrate [5], whose optical properties match the substrate. Reflection coefficients of the scattered light must further be computed to adequately model the scatter of light from these particles sitting on a substrate. The BRDF is computed for a range of viewing angles relative to the normal of the mirror surface. The first figure compares the resultant bidirectional reflection distribution function (BRDF) from this algorithm with the measured BRDF by R. P. Young [5].

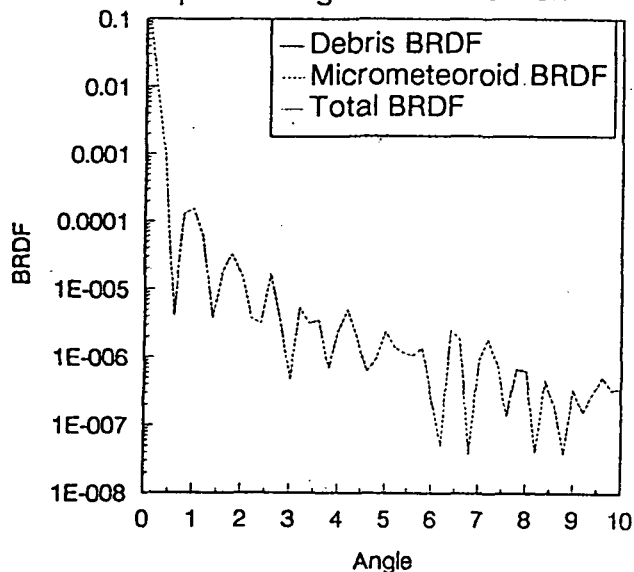
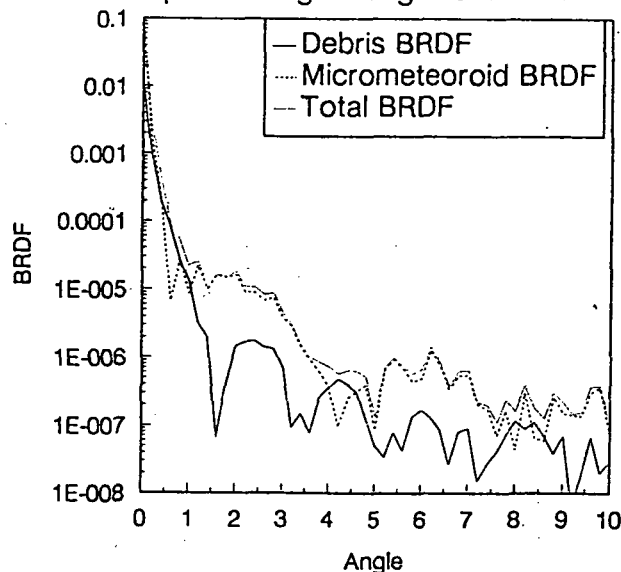
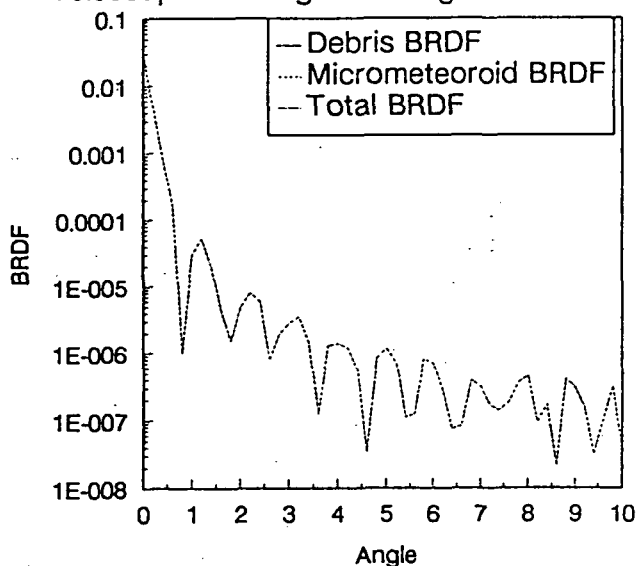
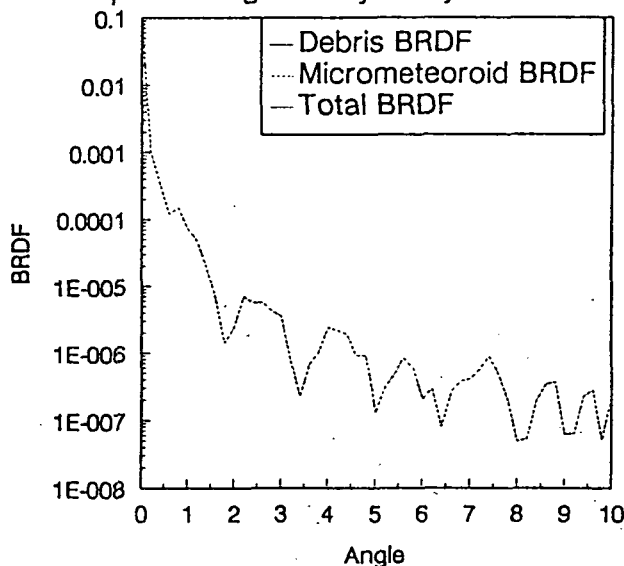
The marriage of the SPENV program with the Mie scatter program (MIESPV) was run for the Hubble telescope over the projected lifetime of the system 1990-2005. The optical wavelength used was .5 microns. The next four figures illustrate results obtained if the telescope is assumed to point in various directions, the forward direction or RAM, 45°, 90° and 180° from RAM and Space pointing, throughout the life of the system. Even though this is an artificial assumption, it bears out several lessons. Optical scatter due to debris impacts were worse when the telescope pointed within angles [20° <  $\theta$  < 60°] of RAM. Here the incident lobe in Kessler's model [2] was incident on the mirror. For larger angles away from RAM as well as angles closer to RAM the mirror was shielded from most of the debris impacts with the telescope tube. Micrometeoroid impacts were largest in the RAM direction and minimum in the rear direction. The preferable pointing direction is trailing end of the spacecraft.

This is an area that deserves further study so that optical systems may be made more survivable in the future. Future developments along these lines might include additional modelling and BRDF measurements on mirrors that have flown in space. In addition, guidelines for the design of future optical systems and the operations of existing systems may be drawn up to enhance their survivability.

BRDF for Young's Distribution of Particles on a Mirror v.s. Numerical computation by MIESPV.



## MODEL OF OPTICAL SCATTER: Crowell L. B.

BRDF vs View Angle on Mirror For Hubble  
Telescope Pointing in RAM DirectionBRDF vs View Angle on Mirror For Hubble  
Telescope Pointing 45 deg From RAMBRDF vs View Angle on Mirror For Hubble  
Telescope Pointing in Trailing DirectionBRDF vs View Angle on Mirror For Hubble  
Telescope Pointing Radially Away From Earth

- 1 B.G. Cour-Palais et. al., "Micrometeoroid Environment Model", NASA SP-9013, March 1969
- 2 D.J. Kessler, R.C. Reynolds, "Orbital Debris Model for Spacecraft Designed to Operate in Low Earth Orbit", NASA-TM-100471, Sept. 1988.
- 3 C. Coombs, A. Watts, J. Wagner, D. Atkinson, "LDEF Data: Comparison With Existing Data, NASA JSC and Lockheed ESC, July 1992.
- 4 H. V. van de Hulst, "Optical Scattering by Small Particles", Dover, New York, NY, 1981.
- 5 R. P. Young, Optical Engineering, Vol. 15, no 6, 1976.

464036

5175-91

ABS ONLY

LPSC XXIV

355

N 94-12190

163375-

**VOLCANISM IN SOUTHERN GUINEVERE PLANITIA, VENUS: REGIONAL VOLCANIC HISTORY AND MORPHOLOGY OF VOLCANIC DOMES;** *David A. Crown, Ellen R. Stofan, and Jeffrey J. Plaut, Jet Propulsion Laboratory, California Institute of Technology, 4800 Oak Grove Drive, Pasadena, CA 91109*

Guinevere Planitia is a low-lying region located between the highlands of Beta Regio and Eistla Regio. Analyses of Pioneer Venus, Goldstone, and Arecibo radar data suggested that the surface of Guinevere Planitia is dominated by volcanism, primarily in the form of bright, dark, and mottled plains units [1-4]. Also identified in this region was the Beta-Eistla Deformation Zone, composed of ovoids and discontinuous segments of lineament belts that have been embayed by the surrounding plains [4,5]. The resolution of Magellan SAR images allows detailed investigations of the volcanic deposits found in the area in order to determine the types of eruptive activity which have occurred and to constrain the regional volcanic history. Analyses of an area of southern Guinevere Planitia between 0° - 25°N and 300° - 330° indicate the presence of a wide variety of volcanic landforms, including large shield volcanoes, widespread plains, lava flow fields, and small domes, cones, and shields as well as coronae and other circular structures that have associated volcanic deposits.

#### *Volcanic Geology of Southern Guinevere Planitia*

Southern Guinevere Planitia is dominated by three broad, low-relief volcanic edifices, which have smaller volcanic constructs built upon their flanks and summit regions. The northernmost volcano (13°N, 314.5°) is ~600 x 800 km across and has a ~100 x 200 km field of low shields at its summit. It rises an average of ~600 m above its surroundings, and its flanks consist of a series of narrow, lobate flows which radiate from the summit region. To the north, a large flow field extends onto the plains and coalesces with a secondary eruptive center that is delineated by a cluster of small edifices and flows. At the summit of the westernmost volcano (9.5°N, 309°), which exhibits an average total relief of ~1.4 km relative to its surroundings, radial flows surround a small shield or cone with a large (~12 km diameter) central pit. The flanks of this edifice (~1000 km across) are composed of lobate flows which extend in all directions from the summit: to the north, flows embay a corona; to the west, a large, fan-shaped flow field, which may include some of the youngest deposits in the region, covers the adjacent plains; and to the south, flows embay a remnant of complexly-deformed terrain.

The southernmost volcano (1.5°N, 316°) has a complex summit region consisting of a shield field, a collapsed and embayed steep-sided dome, and a large, irregular dome. The southern flank is composed of narrow, lobate flows which extend for ~500 km where they overlie dark, ridged plains. This volcano exhibits an average total relief of ~2 km. A prominent rift zone extends from the summit to the north for a distance of 250 km where it terminates in a cluster of ring structures. The rift zone is embayed by summit flows. North of the rift zone, four or more corona-like structures, with diameters between ~70 and 250 km, are partially embayed by flank flows and also appear to be source regions for other flows on the plains. These features obscure the boundaries between deposits from the three major eruptive centers. Stratigraphic relationships in this area are further complicated by dark mantling deposits [6] associated with the 50 km-diameter crater at 7.3°N, 309.4°; mantling deposits overlie the lower flanks of the western volcano and remnants of complexly-deformed terrain, but superposition relationships with upper flank materials are unclear. Relative age relationships both within and between the major eruptive centers are difficult to determine due to the complex nature in which flows interfinger and overlap. Each volcano appears to have had an extensive period of eruptive activity with several major phases emplacing large flow fields and more localized activity occurring both at vents on the flanks of the volcanoes and at their summits.

A series of plains units surround the major eruptive centers in southern Guinevere Planitia. Typically, the volcanoes are superposed on the plains; however, locally plains may embay the flanks of the major volcanoes. Within the plains, bright and dark lobate flows and small domes and shields can be identified. Remnants of complexly-deformed terrain are also observed and, though not prominent, ridges and fractures are found in many areas. At 3°N, 304° a morphologically distinct network of irregular valleys appears to have formed by collapse of the surface due to the migration of subsurface fluids [7].

#### *Volcanic Domes in Southern Guinevere Planitia*

In addition to identification of three major volcanic centers, Magellan data have revealed the presence of a variety of small volcanic landforms in southern Guinevere Planitia which provide information on the styles and diversity of Venusian volcanism. Among these, steep-sided domes are of particular significance as their morphology has been used to suggest that they are silicic in composition [8-11]. The well-defined margins of most steep-sided domes also commonly provide clear cross-cutting relationships from which to assess local changes in volcanic activity.

In southern Guinevere Planitia, 23 domes have been observed, ranging in size from ~5 to 70 km across (Table 1). Domes are circular to highly irregular in plan view and may have pits and/or fractures on their upper surfaces. Dome margins are generally steep, but many domes have poorly defined edges in some areas and may have slumps or

flows extending from them. Many of the domes are flat-topped, but variations in relief on the upper surfaces of the domes are also common. Two types of pits are observed: 1) centrally located collapse pits which may have concentric fractures surrounding them, and 2) pits with prominent raised rims which are randomly located on dome surfaces and are most likely indicative of secondary eruptions and the accumulation of pyroclastic material. Domes in southern Guinevere Planitia are found at the summits and on the flanks of the major volcanic centers, in association with coronae and corona-like structures, and in clusters or groups of small edifices on volcanic plains. Degradation of the domes occurs by burial, fracturing, and collapse of the margins and/or interior [e.g., 8,11].

While the domes observed in southern Guinevere Planitia have morphologic characteristics similar to steep-sided domes as defined by [11] and they fit into the general classification of steep-sided domes, many aspects of their morphology do not directly support comparisons previously made between Venusian domes and terrestrial rhyolite and dacite domes [9,11]. Domes in Guinevere Planitia are generally comparable in radar roughness or slightly rougher than their surroundings, whereas the surfaces of silicic domes on Earth are extremely rough. Venusian domes are also directly associated with volcanic vents from which thin, lobate flows of similar morphology to terrestrial basaltic flows emanate and also occur in groups with low shields, which are presumably due to basaltic volcanism. Thin, lobate flows appear to originate from some domes, a relationship not observed at terrestrial silicic domes. Catastrophic failure of dome margins and interiors also appears to be common on Venus but is not typical on Earth. In southern Guinevere Planitia, the domes exhibit widely disparate profiles, with both steep and shallow margins and irregular summit regions, making it uncertain whether the domes are a distinct morphologic class or are part of a continuum of small volcanic edifice morphology that reflects variations in eruption conditions rather than differences in composition. Further study of small volcanic landforms will assist in documenting the evolution of volcanic centers on Venus and in determining the types of eruptive activity and resulting volcanic deposits.

Table 1. Volcanic Domes in Southern Guinevere Planitia

Latitude	Longitude	Diameter (km)	Dome Morphology	Surface Features	Volcanic Associations
0.0	302.2	15.9	irregular	summit pit	corona center
3.6N	309.3	58.1	circular	summit pit, fractures	cluster in plains
1.6N	316.1	24.3	irregular	summit pit	volcano summit
1.9N	315.9	8.1	circular		volcano summit
4.3N	315.7	23.8	irregular	pit w/ rim	volcano flank
2.5N	316.1	4.7	circular		volcano summit
2.6N	314.1	25.8	circular		volcano flank
2.7N	301.3	10.8	irregular	pit w/ rim	corona
7.4N	305.5	10.8	circular	fractures	volcano flank
10.3N	301.0	17.6	irregular	summit pit	cluster in plains
10.1N	302.1	31.0 x 71.6	irregular	fractures, pits	cluster in plains
11.0N	301.5	31.1	circular	fractures	cluster in plains
14.1N	303.0	15.9	circular		corona?
15.1N	313.8	10.8 x 17.6	irregular	pits	volcano flank
7.8N	311.0	35.8	irregular	fractures	volcano flank
11.0N	313.4	11.9	circular	pit w/ rim	group in plains
10.8N	313.4	11.9	irregular		group in plains
12.3N	316.4	15.9 x 19.9	~circular	fractures	plains
23.1N	319.4	11.9	circular	summit pit, fractures	plains
25.0N	313.8	17.9	irregular	fractures	corona margin
25.0N	314.0	15.9 x 31.8	irregular	pit w/ rim	corona margin
24.4N	314.1	19.9	irregular	summit pit, fractures	corona margin
24.7N	314.3	17.9	circular	pit w/ rim	corona margin

**References:** [1] Campbell, D.B., et al. (1989) *Science*, 246, 373-377. [2] Arvidson, R.E., et al. (1990) in *Proc. Lunar Planet. Sci. Conf.*, 20th, 557-572, LPI, Houston. [3] Senske, D.A. (1990) *Earth, Moon, and Planets*, 50/51, 305-327. [4] Senske, D.A., et al. (1991) *Earth, Moon, and Planets*, 55, 163-214. [5] Stofan, E.R., J.W. Head, and D.B. Campbell (1990) in *Lunar Planet. Sci. Conf.*, XXI, 1208-1209, LPI, Houston. [6] Campbell, D.B., et al. (1992) *J. Geophys. Res.*, 97, 16249-16278. [7] Baker, V.R., et al. (1992) *J. Geophys. Res.*, 97, 13421-13444. [8] Guest, J.E., et al. (1992) *J. Geophys. Res.*, 97, 15949-15966. [9] Head, J.W., et al. (1992) *J. Geophys. Res.*, 97, 13153-13198. [10] McKenzie, D., et al. (1992) *J. Geophys. Res.*, 97, 15967-15976. [11] Pavri, B., et al. (1992) *J. Geophys. Res.*, 97, 13445-13478.

464038

5176-90

APBS. ONLY

LPSC XXIV

357

N94-12191

# ANOMALOUS REE PATTERNS IN UNEQUILIBRATED ENSTATITE CHONDRITES: EVIDENCE AND IMPLICATIONS.

Ghislaine Crozaz and Weibiao Hsu. Dept of Earth and Planetary Sciences and McDonnell Center for the Space Sciences, Washington Univ., One Brookings Drive, St. Louis, MO 63130.

We present here a study of REE microdistributions in unequilibrated enstatite chondrites (EOCs). Although the whole rock REE contents are similar in both unequilibrated and equilibrated chondrites, the host minerals of these refractory elements are different. In the least equilibrated ordinary chondrites (UOCs), the REE reside mainly in glass whereas, in their more equilibrated counterparts, the bulk of the REE is in calcium phosphate, a metamorphic mineral that formed by oxidation of phosphorous originally contained in metal. In the smaller group of enstatite (E) chondrites, calcium phosphate is absent and the phase that contains the highest REE concentrations is a minor mineral, CaS (oldhamite) [1,2], which contains approximately 50% of the total Ca present. In E chondrites, elements typically considered to be lithophiles (such as Ca and Mn) occur in sulfides rather than silicates. This indicates formation under extremely reducing conditions, thus in a region of the solar nebula distinct from those that supplied the more abundant ordinary and carbonaceous chondrites. Previously, we observed [2] a variety of REE patterns in the oldhamite of UECs; they range from almost flat to some with pronounced positive Eu and Yb anomalies. Here, we searched for complementary REE patterns in other minerals from E chondrites and found them in the major mineral, enstatite. Whenever Eu and Yb anomalies are present in this mineral, they are always negative.

In oldhamite, most of the REE patterns belong to one of the following types. Pattern A is almost flat. Pattern B is relatively flat but with a small positive Yb anomaly; the LREE are somewhat enriched ( $\sim 60$ - $100 \times C1$ ) over the HREE ( $\sim 40$ - $70 \times C1$ ). Pattern C is characterized by both positive Eu and Yb anomalies. The Yb anomaly is more pronounced and the REE abundances are lower in C than in B. Pattern D is characterized by still larger positive Eu and Yb anomalies and much lower abundances of the remaining REE [3]. The variety of REE patterns observed in oldhamite is reminiscent, but not as extensive, of that observed in hibonite [4], a refractory mineral present in Ca-Al-rich inclusions (CAIs) of carbonaceous chondrites and which is among the first to form when a gas of solar composition condenses. In reducing environments, oldhamite may be the high temperature counterpart of refractory minerals such as hibonite (and perovskite). In oldhamite, the presence of Eu and Yb anomalies is most likely due to the relatively higher volatility of these two elements, when compared to that of the remaining REE [5]. The smaller diversity of REE patterns, when compared to that seen in hibonite, results from the more limited range of condensation temperatures of the REE in oldhamite than in hibonite [5].

The measurement of REE concentrations in other minerals of E chondrites presents more difficulties as they are typically 100 to 1,000 times lower than in oldhamite. Therefore, much larger primary ion beams are required and special attention has to be paid to the possibility of contamination by CaS. This was done by monitoring the S signal throughout the course of every single measurement. Data are most extensive for Qingzhen (EH3) but we have also obtained preliminary data for Y 691 (EH3), MAC 88136 (EL3), ALHA 77156 (EH3-4) and Indarch (EH4).

In addition to oldhamite, REE are present above the detection limits of the ion microprobe in only three minerals: in enstatite, the major constituent of E chondrites, and in niningerite and alabandite, minor minerals present respectively in EH and EL chondrites. In the last two of these minerals, the HREE are always strongly enriched over the LREE. Typically, there is an increase, by a factor of 10 of the chondrite-normalized abundance from Gd to Lu (from  $\sim 0.1$  to  $0.5 \times C1$  for Gd to  $\sim 1$  to  $5 \times C1$  for Lu), and sometimes there is also a hint of a positive Yb anomaly. Ningerite and alabandite are not major sources of REE. In enstatite, the steep pattern (with HREE enrichment) usually observed in low-Ca pyroxenes is rarely encountered; instead REE patterns tend to be mirror images of those in oldhamite, either relatively flat or with modest (and almost constant) HREE enrichments. Eu and Yb anomalies, when present, are always negative. Although not usually as depleted as Eu, Sm is often present in lower abundances than expected

## REE in E CHONDRITES: Crozaz G. and Hsu W.

by extrapolating the REE pattern from La to Nd. This may suggest that Sm, to a lesser extent than Eu and Gd, is also a relatively volatile element under reducing conditions. Examples of complementary REE patterns in oldhamite and enstatite are shown in Figs. 1 and 2.

The negative Yb anomalies present in some enstatite grains are consistent with INAA data from mineral separates of Y-691 obtained by Ebihara[6]. According to [6], an acid residue of this unequilibrated chondrite (which included the major mineral enstatite) had low REE concentrations (less than  $0.5 \times C_1$ ) and its REE pattern was characterized by a pronounced negative Yb anomaly, the remaining REE in this meteorite being located in the leachate (i.e., in oldhamite). The present study not only shows that REE patterns in oldhamite and enstatite can be complementary (e.g., positive Eu and Yb anomalies in oldhamite and negative in enstatite) but also that there is a diversity of REE patterns represented in individual grains of the same mineral. As in the case of hibonite, this reflects the variety of conditions that prevailed where these grains formed. Many of these observations have no simple explanation. In particular, the complementary REE patterns in oldhamite and enstatite cannot be the result of simple sequential condensation as one would expect the most refractory mineral (i.e., oldhamite) to be depleted (rather than enriched) in the volatile REE, Eu and Yb.

REFERENCES: [1] Larimer J. W. and Ganapathy R. (1987) EPSL **84**, 123-134. [2] Lundberg et al. (1991) LPSC XXII, 835-836. [3] Lundberg L. and Crozaz G. (1993), in preparation. [4] Ireland T. et al. (1988) GCA **52**, 2841-2854. [5] Lodders K. and Fegley B. (1992) LPSC XXIII, 797-798. [6] Ebihara M. (1988) Proc. NIPR Symp. Ant. Met. **1**, 102-112.

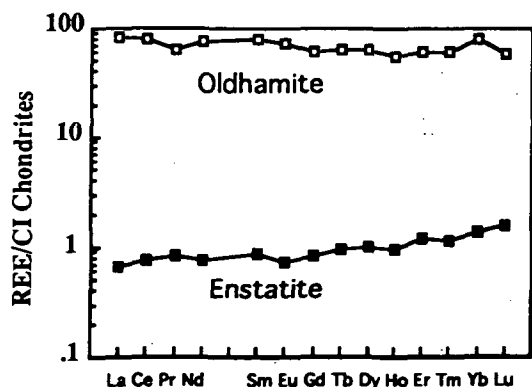


Fig. 1 CI normalized REE patterns without anomalies for oldhamite and enstatite

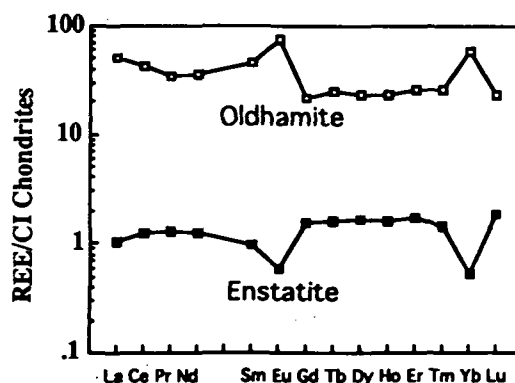


Fig. 2 Complementary CI normalized REE patterns with Eu and Yb anomalies for oldhamite and enstatite

464039

5177-91

LPSC XXIV

359

ABS ON 94-12192  
163397

# COMPARISON OF THE DISTRIBUTION OF LARGE MAGMATIC CENTERS ON EARTH, VENUS, AND MARS; L.S. CRUMPLER, Department of Geological Sciences, Brown University, Providence, RI 02912

R 2

**INTRODUCTION.** Volcanism is widely distributed over the surfaces of the major terrestrial planets Venus, Earth, and Mars. Anomalous centers of magmatic activity occur on each planet and are characterized by evidence for unusual concentrations of volcanic centers, long-lived activity, unusual rates of effusion, extreme size of volcanic complexes, compositionally unusual magmatism, and evidence for complex geological development. The purpose of this study is to compare the characteristics and distribution of these magmatic anomalies on Earth, Venus, and Mars in order to assess these characteristics as they may relate to global characteristics and evolution of the terrestrial planets.

**DISTRIBUTION OF MAJOR CENTERS.** Global maps showing the location of all major volcanic centers were prepared based on the Magellan volcanic feature catalog [1] and from existing compilations of volcanism on Earth [2] and Mars [3]. The centers and regions of volcanism included for each planet were selected because they are in each case among the largest in size, greatest in volume, or most active with respect to volcanism elsewhere (Figure 1, 2, and 3.). For Venus this consists of volcanoes exceeding 100 km in diameter [1]; for Mars, the selection is simple as this includes all known volcanic centers greater than a few kilometers in diameter; and for Earth, the residual of all active [4] volcanoes is taken for comparison after removal of the volcanic centers related to plate boundaries as discussed below.

**Venus.** Volcanism is nearly ubiquitous on Venus and ranges from small shield volcanoes near the limit of resolution [5] of Magellan data to large rises and major volcanic complexes [6]. Although widespread, the annual volume rate of volcanism is estimated [1] to be  $\sim 1 \text{ km}^3/\text{yr}$  globally, or about that of the intraplate volcanism on Earth. The global history of Venus volcanism volume-rates is currently debated, but a net decline in the magmatic budget from an initial high rate with a half-life of 2Ga is a reasonable approximation. Many of the smaller centers occur in association with the larger volcanic centers and coronae [1;7], and to first order the distribution of major centers on Venus may be taken as representative of the distribution of anomalous melting and corresponding interior anomalies. Based on the distribution of large volcanoes and coronae in the global volcanic catalog [1] the distribution of anomalous magmatism on Venus occurs in regional concentrations, groupings, and clusters. Regional (Eistla) [6] concentrations as well as hemispheric-scale (BAT) concentrations are known to occur and have been correlated to several characteristics of global tectonism [1]. The Beta-Atla-Themis concentration anomaly [1] comprises (and probably influences) a significant ( $\sim 25\%$ ) fraction of the global surface area.

Linear arrangements of the pattern of magmatic center are rare, despite the abundance of linear deformation belts, extensional fractures, and rifts, despite the correlation of volcanism with extensional fracture belts [1] at regional scales. Volcanism appears not related to plate boundary processes at any scale and must arise through other mechanisms. However, some of the largest centers of volcanism occur in association with major topographic rises and are accompanied by significant positive gravity anomalies attributable to dynamic support [8]. In this respect, the processes associated with major centers of volcanism on Venus are analogous to those frequently ascribed to mantle plumes, particularly large rises.

**Earth.** On Earth the global distribution of volcanism is widespread and occurs in both plate boundary and intraplate settings. Plate boundary volcanism arises through instabilities introduced at the divergent boundaries through crustal thinning and corresponding mantle upwelling, and at convergent boundaries through complex processes associated with the introduction of water into the deep lithosphere and upper mantle during subduction.

Intraplate or "hot spot" volcanism differs from plate boundary volcanism in several respects. The total volume rate of intraplate volcanism is exceeded by an order of magnitude by divergent and convergent plate boundary volcanism. Unlike the frequently silica-saturated, calc-alkalic, and hydrous-phase rich composition of plate boundary magmas, intraplate volcanism is typified by silica-undersaturated, alkalic, large-cation enriched melts derivable from relatively undepleted mantle. Centers of intra-plate volcanism are also known to be long-lived ( $>10^7 \text{ m.y.}$ ), relatively stable with respect to the motion of the lithosphere, and often occur in association with significant evidence for plume-like, possible deep mantle upwelling. In addition, the global distribution of intraplate volcanism is non-random, occurs in two global concentrations ("African" and "Pacific") [2] with some evidence for synchronicity of activity within global concentrations [9] and, and has been correlated with a variety of characteristics of the global patterns of mantle structure, interior convection [10], and global tectonism [11]. The African hot spot concentration encompasses an area of about 25% of the global surface and accounts for a large fraction of the known hot spots.

The pattern of distribution, relative stability, intraplate setting, and association with dynamic plumes of hot spots on Earth is comparable to many of the characteristics of volcanism on Venus. For this reason, the mapped distribution of "hot spots" on Earth (Figure 2) is considered appropriate for comparison with the distribution of volcanism on Venus.

**Mars.** The total number of volcanoes as well as the estimated global volume-rate of magma production [12] on Mars are about two orders of magnitude less than on Earth or Venus. Most of the central volcanism consists of relatively low, but physically large shield volcanoes thought to have formed through dominantly effusive processes, but with locally important components of volatile-rich magmatic activity [ref]. The rate of magmatism on Mars associated with the emplacement of major volcanic surface units has apparently decreased steadily over Martian history [12], and the same is likely of magmatism associated with the known volcanic centers. Volcanic centers occur in three settings, Tharsis, Elysium, and Hellas, and the later two are approximately antipodal to Tharsis such that there are two global occurrences (Figure 3). In either division, the global distribution is dominated by the Tharsis concentration. The origin of the Tharsis tectonism and volcanism are the subject of previous detailed studies [13]. Whatever the origin, it

## VOLCANISM ON EARTH, VENUS, AND MARS; CRUMPLER

clearly represents a major anomaly influencing the tectonic and magmatic activity in an area exceeding 25% of the global surface.

**INTERPRETATION/DISCUSSION.** Subtraction of those volcanic centers directly attributable to plate boundary processes from the mapped distribution of volcanism on Earth results in global pattern of major volcanic centers similar in several respects to the distribution of major volcanic centers on Venus and Mars. The most striking characteristic of the distribution of volcanic centers on Venus, Earth, and Mars is that it occurs in global concentrations and that each planet is characterized by a dominant globally anomalous area of unusually concentrated volcanism and/or tectonism. In addition, on both Earth and Mars there are two fundamentally antipodal concentrations.

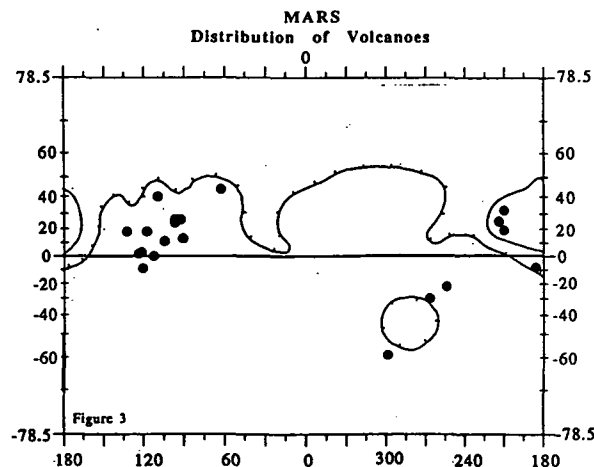
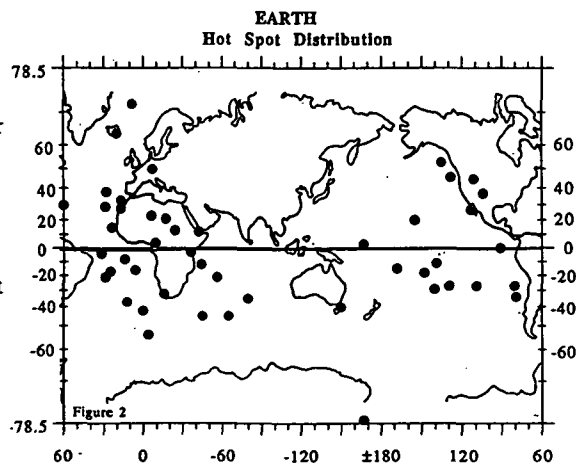
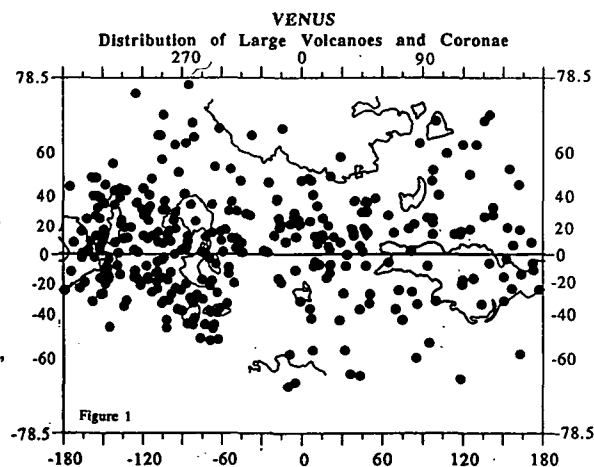
In terms of scale, association with global tectonic processes, location with respect to the inertial equator, and association with possible convective anomalies, the Beta-Atla-Themis Region of Venus, the African hot spot concentration on Earth, and the Tharsis region of Mars all share some characteristics in common. Several observations suggest that the BAT concentration on Venus and the African hot spot cluster on Earth might reflect global upwelling anomalies. Many discussions have recently centered on the possible origin of the two antipodal global hot spot concentrations on Earth [10], its relationship to global patterns of tectonism, and its possible origin through deep-seated broad-scale mantle upwelling. And many previous interpretations of Tharsis on Mars [14] have cast this topographic and volcanic anomaly on Mars as a consequence of similar deep mantle processes. The anti-correlation in arrangement of hot spot concentrations and subduction zones on Earth, and the observed anti-correlation of volcanic concentrations and crustal shortening in the lowlands of Venus may be manifestations of similar convection cycles characterized by integrated patterns of down welling and broad regions of isolated upwellings.

**REFERENCES.** [1] Head et al., 1992, JGR, 97, 13153; Crumpler et al, 1993, this volume; [2] Crough and Jurdy, 1980, EPSL, 48, 15; [3] Greeley and Spudis, 1981, Rev.Geophys.Sp. Phy, 19, 13; Hodges, 1979, NASA TMX,80339,247; [4] Simkin et al, 1981, Volc.of the World, 232pp; [5] Guest et al, 1992, JGR, 97, 15966; Aubele and Slyuta, 1990EMP, 50/51, 493; [6] Senske et al., 1992, JGR, 97, 13395; [7] Pavri et al, 1992, JGR, 97, 13445; [8] Smrekar and Phillips, 1991, EPSL, 107, 582; [9] Larson et al, 1991, Geology, 19, 547; [10] Richard et al., 1988, JGR, 93, 7690; Cazenave et al, 1989, Nature, 340, 54; Olson et al, 1990, Nature, 344, 209; [11] Vigny et al, 1991, Tectonophy, 187, 345; [12] Greeley and Schneid, 1992, Science, 254, 996; [13] Banerdt et al, 1982, JGR, 87, 9723; [14] Carr, 1981, Geol.Mars, chpt.8.

Figure 1. Distribution of large volcanoes and coronae, Venus.

Figure 2. Distribution of intraplate volcanism on Earth.

Figure 3. Distribution of major volcanoes on Mars.





464040

5128-91

ABS ONLY

LPSC XXIV

361

N 94-12193  
76 3 3 78

## THE MAGELLAN VOLCANIC AND MAGMATIC FEATURE CATALOG;

L.S. CRUMPLER, JAYNE C. AUBELE, and J.W. HEAD, Department of Geological Sciences, Brown University, Providence, RI 02912

**INTRODUCTION.** A catalog summarizing the location and characteristics of 1663 volcanic and magmatic centers identified in Magellan radar images of the surface of Venus is in final preparation to be submitted as a Geological Society of America Special Paper. The following is a brief summary preview of the contents and methods used in assembling the final data set, the organization of the catalog, and other notes of interest to potential users.

**METHODS.** The global survey data base represents a carefully compiled list of volcanic features that were identified, measured, and classified. The actual survey was refined through several preliminary iterations in order to establish the range of diversity, problems associated with identification, classification, and related problems typical of large data sets.

The characteristics used as criteria for identification, classification, and definition of volcanic features on Venus were initially determined through a detailed preliminary survey of FBIDRS. This preliminary survey was conducted when the total global orbital coverage was approximately 2/3 of the final nominal first cycle coverage. This file was then used to note the most common volcanic feature types, their range of morphological variation, their surface areal density, and their detailed characteristics. The initial FBIDR analysis established some of the criteria that identify and distinguish the different types of volcanic features. However, identification and classification of large scale volcanic features (such as corona and large volcanoes) in the FBIDRS was inconsistent; some features were detected, while others of equal scale were not identifiable. These difficulties with large scale features were alleviated in the regional perspectives of C1-MIDRS without significant reduction in the detectability and identification of the smallest volcanic features (e.g., small pits on small shields). The initial FBIDR analysis formed a reference set of criteria that enabled us to link identifications based on the appearance of volcanic features in FBIDRS with identifiable characteristics in C1-MIDRS. The final global survey was performed and compiled using a C1-MIDR data base.

Working definitions of the volcanic features, including dimensions that characterized the different sub-types (e.g., the difference between intermediate and small volcanoes) were compiled from a variety of sources, including the initial surveys of FBIDRS, the stated definitions as used in previous published treatments based on Venera 15/16 data [1], and published definitions in the 45-day report [2] and Spring '91 AGU Magellan summary abstracts [3]. Using these definitions, another trial survey of volcanic features in 35 C1-MIDR images was made and in which potential sources of inconsistency in definition, interpretations, or recognition criteria were identified.

After adjusting the identification and definition criteria to account for these potential sources of inconsistency, the complete survey of volcanic and magmatic features was carried through to completion. The actual survey was done by two people working on each image *jointly* verifying identification, classification, and numerical entries, and acting in a check-and-balance mode to verify each observation. The tandem survey was agreed upon in order to avoid "drifts" in identification and interpretation criteria that often occur in efforts of this type requiring observations over an extended period by a single individual. We believe that every effort was thus made during compilation to check and re-check the the *consistency* of identification and accuracy of locations, dimensions, and physical tabulations. As with any carefully assembled, large geophysical data set of this size and complexity, an inevitable low percentage (generally  $\leq 5\%$ ) of transcription and related "mechanical" errors occurs (see discussion of Pacific intraplate seismicity maps [in EOS, 72, page 468]) and catalog users will be requested to contact us with with these errors.

**Summary of Identification Criteria.** Altimetric considerations were not included when classifying volcanic features because (1) altimetry was not available or there were significant uncertainties in its reduction during the early part of the survey, (2) altimetric resolution is lower than the diameter of the smallest features included in the catalog and therefore would be inconsistently used as a definition, (3) even for large features there are uncertainties in overlaying altimetric and image information that would not be of concern in a comparison between features but would be of concern in an attempt to define maximum or minimum heights as part of a consistent classification scheme, and (4) as in the case of tectonic features on Venus [4], the primary morphologic characteristics by which volcanoes are identified will be preserved in the absence of significant erosion [5] even where the regional topographic characteristics are modified through later superimposed tectonism or isostatic adjustments. Therefore, all identification and classification algorithms are based solely on SAR image characteristics. On this basis, volcanic features in Magellan images may be divided into centers of volcanism or volcanic flow features such as lava channels or festoon flows. Under the centers category, they may be sub-divided into individual centers (vents) defined by extrusive flow patterns, or groups of centers (fields), or features consisting mainly of structural patterns, which may be interpreted as dominantly intrusive centers.

The presence or absence of radial flows was considered an important primary characteristic in classifying volcanic features. Radial flows indicate a vent that has been the site or source of multiple eruptions and has acted as a "center" for several extrusive events, as is generally typical of features that are identified as volcanoes elsewhere in the solar system. In addition, a radial pattern of lava flows represents geologic evidence for a topographic gradient radially from an edifice (at least at the time that the flows were emplaced). Not all magmatic centers are extrusive and other criteria generally associated with volcanism are used for their identification. Based on the initial survey and a review of the characteristics of previously identified features from Venera 15/16 and Arecibo results, we determined that the presence of either dominantly radial or dominantly concentric patterns of associated fractures, linear structures, and ridges can be used to distinguish structurally expressed volcanic and magmatic centers.

Final definitions used are summarized from preliminary reports of the global volcanic survey given in [6] and further discuss some of the criteria developed in the above sections. The classification was not modified throughout the course of the survey and every effort was made to insure that there was no "drift" in either the criteria or its usage. The corresponding

## **MAGELLAN VOLCANO CATALOG: CRUMPLER, AUBELE, and HEAD**

classification of features widely distributed over the surface has been accordingly consistent. A flow chart is included in the catalog and summarizes the steps that were developed from a compilation of the observed characteristics of volcanic centers and features on Venus and used in categorizing each of the ~1600 observed volcanic centers and features on Venus.

**Features Included in the Catalog.** The following is a list of features and common abbreviations used in the final catalog: small shield field (SF); large volcano (LV); intermediate volcano (IV); radially-pattern volcano ("anemone")(IV/RF); steep-sided dome ("pancake")(IV/SD); fluted dome ("scalloped margin dome or tick")(IV/FD); arachnoid (AR); corona (CO); nova (N); large lava flow or lava flood (LF); lava channel (LC); and festoon flow (FF). Many of these feature designations are informal as the terminology of volcanic features on Venus has evolved rapidly from that used early in the mission in order to encompass the greater diversity of volcanic morphologies seen in later mission data. The terms "radially-patterned volcano", "dark flow field", "steep-sided dome", and "scalloped margin or fluted dome" depart from the more colorful and imaginative terms used to identify these features early in the mission, but are used in the catalog to reduced ambiguity and in an effort to introduce a nomenclature that is as descriptive and non-process specific as possible. New terms and/or original terms [7] in each case are clearly identified in the catalog legend and introductory material. Gradational or transitional features, showing characteristics of more than one feature type, were assigned to the category which they most fitted and annotated by a query ("?") symbol.

**Magellan Volcanic Feature Catalog number/Formal Names of Individual Features.** Names assigned to individual features are those approved by the International Astronomical Union as of the time of this writing. In general, the only systematic attempt to assign names has been for craters and coronae. Because so few features are named as yet, we have assigned a Magellan Volcanic Feature Catalog number ("MVC#") to each feature to assist in identification, a technique used in astronomical catalogs. The MVC number is simply an abbreviated description of the latitude, longitude, and volcanic feature type for each entry; for example MVC 20/88 LV.

With the exception of two or three well-known and frequently used names such as Eve Corona and Heng-O Corona, preliminary names or suggested names which are not on the official IAU Venus nomenclature list are included parenthetically. In some cases the co-ordinates listed in the IAU list for a feature may differ from those judged from Magellan data as representing the center of a particular volcanic feature. IAU names for which no corresponding volcanic feature is identified in the survey have not been included.

**CONTENTS OF MAGELLAN VOLCANIC FEATURE CATALOG.** The final catalog lists locations to the nearest 0.5°, dimensions, brief descriptions or comments, existing names, and an "MVC (Magellan Volcanic feature Catalog) Number" consisting of the latitude, longitude, and short abbreviation for the feature type. The catalog is arranged in two listings: One list is organized by C1-MIDR starting with north latitudes and prime meridian; the second list arranges features by alphabetical ordering of feature type, starting with north latitudes and prime meridian for each type. Either of these lists enable rapid location of a feature. In addition to the tabulated listing of all volcanic and magmatic features, the final catalog includes sections on user information, definitions, initial analysis of the global distribution and size-frequency characteristics, and multiple example images of each feature type.

**REFERENCES:** [1] Barsukov et al., (1986), JGR, 91, 378; Slyuta and Kreslavsky (1990), Lunar Planet Sci 21st, 1174; Senske (1990), EMP 50/51, 3305; Pronin and Stofan (1990), Icarus, 87, 452; Aubele and Slyuta (1990) EMP 50/51, 493; Garvin and Williams (1990), GRL 17, 1381; [2] Head et al 45 day report; [3] Head? Crumpler?; [4] McKenzie et al (1992), JGR, 97, 13533; [5] Arvidson, et al (1992), JGR, 97, 13303; [6] Head et al, (1991), submitted to JGR, Magellan Issue; Crumpler et al, 1991, GSA Abstracts, 23, A400; [15] Crumpler et al, 1992, Lunar Planet Sci 23rd; [7] Head et al. (1992a), "Large volcanoes", Lunar Planet Sci 23rd; Guest et al. (1991), JGR 97; Stofan et al. (1991), JGR 96, 20933; Schubert et al. (1991), EOS 72, 175; Aubele et al. (1992), Lunar Planet Sci 23rd; Parker and Komatsu (1991), GSA Abstracts 23, A277; Pavri et al. (1992), JGR 97, E8, 13,445; Magee Roberts, et al. (1992) JGR 97, E10, 15-991.

46404/

579-91

ABS ONLY

LPSC XXIV

363

N94-12194

P. 2

# SYNTHESIS OF GLOBAL THEMATIC MAPPING, VENUS: GEOLOGIC CORRELATIONS / QUESTIONS FOR THE MAGELLAN GRAVITY MISSION;

L.S. CRUMPLER, J.C. AUBELE, AND J.W. HEAD, Department of Geological Sciences, Brown University, Providence, RI 02912

**INTRODUCTION.** An important characteristic of the Magellan mission and the resulting data [1] is that it is both global in coverage as well as extremely high in resolution. As a result, global questions may be addressed based on the constraints of extremely detailed geological evidence. An important first step in the task of interpreting the global geological record will be a synthesis of the primary geological characteristics and their relationship to significant questions [2]. The following is a brief synthesis based on a comparison of mapped distributions, initial interpretations, and some questions that these results raise.

**METHODS AND TYPES OF MAPS PREPARED.** Global maps showing the distribution of fundamental geological characteristics have been prepared of fracture belts and rifts (Figure 2); ridge belts, mountain belts, and ridged plains (Figure 3); tesserae (Figure 4); and the distribution and magnitudes of gravity anomalies (Figure 5). Global mapping of these geological features was done at a scale of 1:8 M for ~90% of surface.

Fractures are frequently resolved as graben or simple scarps, consistent with the general geological interpretation that fractures belts are the sites of crustal extension and rifting [3]. Both ridge belts and mountain belts are interpreted to be the results of focused, belt-like styles of crustal shortening. Ridged plains were identified on the basis of the presence of numerous, sub-parallel, frequently uniformly-spaced, and sinuous ridges analogous to ridges common on the lunar mare and plains surfaces of Mars ("wrinkle ridges"). Ridged-plains are common on Venus in many of the topographically low-lying and morphologically uniform plains [3] and often exhibit uniform orientations over areas hundreds to thousands of kilometers across [4]. By analogy with similar plains deformation elsewhere in the Solar System [5], mare-type ridged plains on Venus are interpreted to represent the presence of crustal shortening of a few percent. Tessera distribution is adapted from the results of Ivanov et al [6]. Tessera are the sites of generally elevated topography, often plateau-like, complex, multi-phase deformation, including evidence for both extension and compression and evidence for long-lived development [7; 8]. Tessera are the oldest local, and perhaps global, stratigraphic units. The high elevation and gravity signatures associated with extensive areas of tessera imply that they are sites of greater than nominal crustal thicknesses [9].

**REGIONAL/GEOLOGICAL DISTRIBUTIONS/CORRELATIONS.** Comparison of the different thematic maps indicates that interconnected regions of distinctive regional geological characteristics occur and correlate with patterns of both altimetry and volcanic concentration. Volcanic centers are least abundant where ridged plains are common, including Helen Planitia, Lavinia Planitia, and Aino Planitia in the southern hemisphere, and Snegurochka Planitia and Atalanta Planitia in the northern hemisphere. Most of the lowland regions are characterized by broad plains consisting of vast sheets of lava and associated sinuous channels [10; 11]. Anomalously low concentrations of volcanic centers also occur in tesserae. The large volcanic centers which do occur in this setting are frequently characterized by geological evidence for large subsurface magma reservoirs (calderas, concentric depressions, etc.).

**DISCUSSION.** There are apparent global-scale correlations between altimetric, geologic, and geophysical characteristics. Our maps agree with other recent results [9] and suggest that mass anomalies corresponding to anomalously positive geoid anomalies are correlated with concentrations of volcanic centers. This includes the major volcanic rises Atla Regio, Beta Regio, Themis Regio, and Eistla. On the other extreme, the largest negative geoid anomalies occur in areas characterized by low volcanic center concentrations, such as Lavinia Planitia and Atalanta Planitia. Although it is well-known that the geoid is strongly correlated with topography on Venus, the magnitude of the anomalies in many of these areas frequently exceeds that attributable to topography alone [12], and a significant dynamic (upwelling and downwelling) component to the geoid signal is implied under certain assumptions. Two origins for the regional compressional stresses responsible for both ridged plains and ridge belts include stresses related to (1) regional topographic slopes [4], or (2) sub-crustal mantle convergence and downwelling [13; 14; 15]. While elements of both models are likely, the absence of volcanic centers in lowlands might reflect cooler mantle, lower regional heat flow, and relative inhibition of melting in areas of mantle downwelling. Because tessera represent likely areas of greater crustal thickness, magma ascending into tessera will attain neutral buoyancy at the base of a relatively thicker crustal column and at correspondingly greater depths. Additional factors in the altimetric correlations in occurrence of volcanic centers might relate to altitude-induced differences in magma density such that neutral buoyancy of the magma may be attained at greater depths in the areas of greatest elevation [16].

**CONCLUSIONS.** Some preliminary results of the thematic geologic mapping are summarized in Table 1. Altimetrically, extensional characteristics and high concentration anomalies both appear to occur in uplands, whereas compressional deformation and low concentration anomalies occur at both the lowest and highest altitudes. Geologically, the distribution of volcanic centers is globally correlated with the areas over which the crust has been extended (fracture belts), and anti-correlated with areas characterized by compressional deformation (ridge/mountain belts and ridged plains) and greater crustal thickness (tesserae) [17]. The BAT anomaly is almost encircled by low plains characterized by compressional ridges, anomalous geoid lows, and other characteristics previously interpreted as potential indicators of mantle downwelling [15; 13; 14; 9]. This together with the abundance of extensional fracture belts and rifts in the BAT region supports the interpretation that it is a probable region of broad mantle upwelling and corresponding peripheral mantle return flow.

Tessera are not strongly correlated with these global distribution characteristics and do not appear to be correlated with areas interpreted to be present sites of mantle upwelling or downwelling. Not all tessera may identify sites of current

# THEMATIC GEOLOGIC MAPS OF VENUS; L.S. CRUMPLER AND OTHERS

formation. They could represent the end result of continuing processes of downwelling [8], in which some represent relics of thickened crust and no corresponding evidence remains in the gravity signal for mantle downwelling. Alternately, they may have all formed at a given time in a catastrophic overturn related to global lithospheric [18] or depleted mantle layer [19] instabilities, with subsequent deformation being largely related to gravitational relaxation [20]. Global high-resolution gravity data will help to resolve these issues.

**REFERENCES.** [1] Saunders et al, 1992, JGR, 97, 13067; [2] Saunders et al., 1992, EOS, 73, 178; [3] Solomon et al. 1992, JGR, 97, 13199; [4] Bilotti and Suppe, 1992, GSA Abstracts, 24, A195; [5] Watters, 1988, JGR, 93, 10236; [6] Ivanov et al., 1992, LPSC 23, 581; [7] Bindschadler and Head, 1991, JGR, 96, 5881; [8] Bindschadler et al., 1992, JGR, 97, 13495; [9] Herrick and Phillips, 1992, JGR, 97, 16017; [10] Baker et al. 1992, 97, 13421; [11] Guest et al. 1992, 97, 15949; [12] G. Bills et al., 1987, JGR, 92, 10351; [13] Bindschadler and Parmentier, 1990, JGR, 95, 21329; [14] Phillips et al. 1991, Science, 252, 651; [15] Zuber, 1990, GRL, 17, 1369; [16] Head and Wilson, 1992, JGR, 97, 3877; [17] Crumpler et al, this volume; [18] Turcotte, 1992, Int. Coll. Venus, 127; [19] Parmentier and Hess, 1992, GRL, 19, 2015; [20] Smrekar and Solomon, 1992, JGR, 97, 16121.

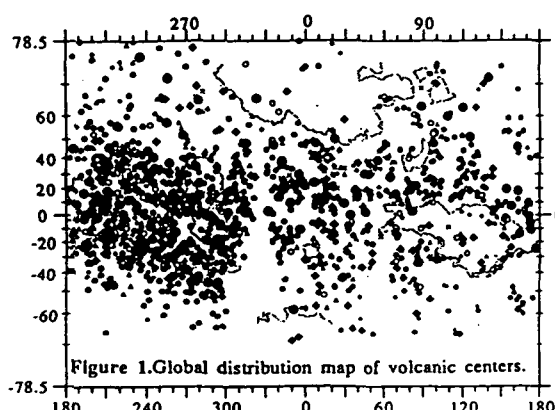


Figure 1. Global distribution map of volcanic centers.

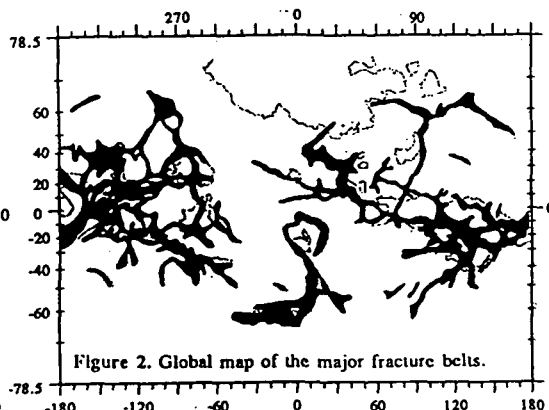


Figure 2. Global map of the major fracture belts.

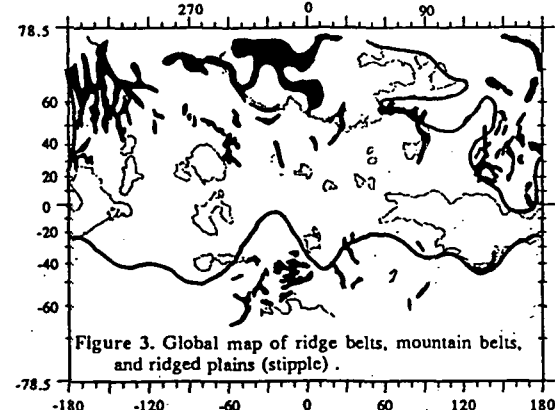


Figure 3. Global map of ridge belts, mountain belts, and ridged plains (stipple).

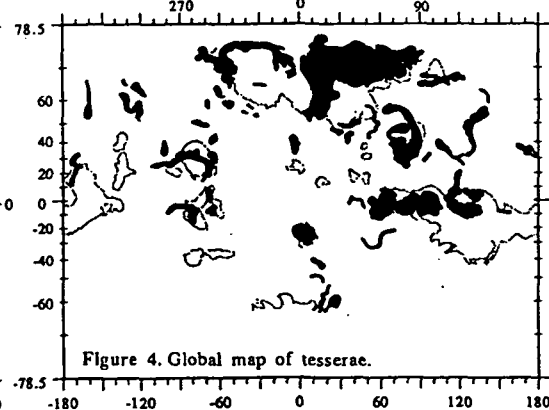


Figure 4. Global map of tesserae.

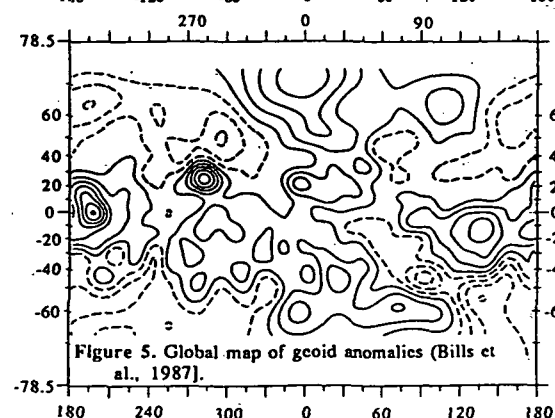


Figure 5. Global map of geoid anomalies (Bills et al., 1987).

Table 1. Summary of the global occurrence and geologic setting of volcanic and magmatic centers on Venus.

Altitude Setting	UPLANDS	LOWLANDS	HIGHLANDS
1 km			
Volcanic Centers	ABUNDANT	FEW	FEW
Geologic Characteristics	FRACTURES FAULTS TROUGH RFTS	RIDGED PLAINS RIDGE BELTS LAVA PLAINS LAVA CHANNELS/FLOODS	MOUNTAIN BELTS COMPLEX RIDGE AND TROUGH TERRAIN '(TERRA)'
Geologic Interpretation	REGIONAL EXTENSION RIFTING	REGIONAL COMPRESSION REVERSE FAULTING FOLDING	REGIONAL COMPRESSION CRUSTAL THICKENING SHALLOW EXTENSION FOLDING
Geologic Significance	MANTE UPWELLING	MANTE DOWNWELLING?	GLOBAL DOWNWELLING, REGIONAL UPWELLING

H64042

5/80-91

ABS ONLY

LPSC XXIV

365

N94-12195  
163400

p 2

# LARGE VOLCANOES ON VENUS: EXAMPLES OF GEOLOGIC AND STRUCTURAL CHARACTERISTICS FROM DIFFERENT CLASSES;

L.S. CRUMPLER, J.W. HEAD and J.C. AUBELE, Department of Geological Sciences, Brown University, Providence RI 02912.

**INTRODUCTION.** Large volcanoes (>100 km) characterized by radial lava flows and similar evidence for a topographic edifice are widely distributed over the surface of Venus and geologically diverse. Based on the global identification of more than 156 examples [1] and preliminary geologic mapping, large volcanoes range from those characterized geologically as simple lava edifices to those bearing evidence of complexly developed volcanic and structural histories. Many large volcanoes exhibit characteristics transitional to other large magmatic center types such as coronae and novae [1,2]. In this study we examine the geology and structure of several type examples of large volcanoes not addressed in previous studies which are representative of several of the morphological classes.

**MORPHOLOGIC CLASSIFICATION.** Nine fundamental types of large volcano morphology were identified previously [2] and include: (Type I) Simple large edifice characterized by a symmetric, radial distribution of flows and few prominent structural features; (Type II) Large edifice containing central or summit caldera(s); (Type III) Large edifice with one or more flanking rift zones that are arranged more or less along radial directions from the summit region (as in Hawaii). (Note that this type differs from Type VII below); (Type IV) Large edifice with elongated summit often with multiple caldera-like features (e.g., Gula Mons); (Type V) Large edifice with multiple morphologic or topographic summits (e.g., Sapas Mons); (Type VI) Large edifice surrounded by an exterior set of radial fractures, commonly pre-dating the flow units from which the edifice is constructed; (Type VII) Large volcanoes arranged astride through-going regional rift zones or fracture belts; (Type VIII) Large volcanoes in which there is a nova-like central region consisting of a high density of radial fractures radiating from the morphological or topographic summit; and (Type IX) Large volcano in which a corona-like central area comprises a large fraction of the volcano diameter, but does not obscure the radial lava flows distinguishing large volcanoes from more intrusive morphologic features such as coronae.

**PRELIMINARY GEOLOGIC MAPS OF TYPE EXAMPLES.** In the following, geologic maps prepared at a scale of 1:~4 M of Types II, VI, VII, VIII, and IX (Figures 1,2,3,4, and 5) are discussed briefly. No attempt is made to give the full details or stratigraphic history of each example because the limited space here, and only some salient characteristics are addressed. Maps of the remaining types are not presented because Type I is relatively simple and requires little explanation, and because the type examples of III (Tepev, Sif Mons), IV (Gula Mons), and V (Sapas Mons) are relatively well known from initial Magellan data analysis, and have been mapped and discussed in several previous reports [3].

**Type II (Caldera).** The apparent simplicity of the type example (MVC 19/80LV, Figure 1) of this class is deceptive, and actually represents one of the more challenging and informative volcanoes mapped. Two radial lava units pre-date an adjacent large volcano (V), and rest on pre-existing fractured plains near the juncture of two, and perhaps three fracture belts, the lower unit (S) relatively smooth, the upper unit (D), more digitate in appearance. A discontinuous annulus of radial fractures denotes the rim of a central and summit depression, the floor of which is covered by relatively smooth flows (Si) surrounding a fractured pre-existing central peak-like area (C); these flows also largely post-date the flank unit (D), the radially fractured caldera rim unit (R), and are superposed by late concentric fractures and small central pit calderas. The central region appears to represent an area structurally sagged during an intermediate stage in the development of the large volcano.

**Type VI (Radially Fractured Exterior).** Sekmet Mons (MVC 44.5/240.5LV, Figure 2) is a relatively simple example of this class, although topographically higher than many large volcanoes on Venus. It lies at the intersection of at least two sets (belts) of fractures distinctly radial to the edifice on the lower flanks. The lava patterns are asymmetric, and early and widespread digitate unit (D) flood plains to the east and pre-existing fractures. Flows and fractures are centered on a relatively small central region characterized by smaller digitate flows, and radial to a centrally concentrated field of unusual, very small (~1 km) shield volcanoes (C). Stratigraphically decreasing size of the edifice lavas and late, summit small shield fields suggest that the volume rate of volcanism at Sekmet steadily diminished with time.

**Type VII (Rift-related).** This type (MVC -12/261.5LV, Figure 3) graphically illustrates the relatively simple situation in which a fracture belt or rift has been the site of early digitate lavas (D1). Repeated eruptions of digitate flows (D2) thereafter became centralized and a large volcano developed astride the rift trend. In this example the volcano is the last event, but in several other examples of this class, continued rifting subsequent to the last eruptions have deformed and overprinted the volcano.

**Type VIII (Nova-like Interior).** The example chosen (MVC -8/243LV, Figure 4) actually has some characteristics transitional to Type IX, but dramatically illustrates the basic characteristics of Type VIII. Early ridged and fractured plains (P) and a fracture belt (F) were inundated by radially dispersed, smooth plains-forming flows (S) and later digitate flows (D). Initial mapping suggests that the radially fractured proximal interior (R) was concurrent with the regional fracture belt and was itself a source of radial flows. Within this elliptical region of radial fractures lies an annulus identifiable as a circular discontinuity in the radial pattern, interior to which radial fractures attain an even greater density comparable to the plexus of fractures identified as nova. In this example, although the central nova-like structure was one of the last events, the exact timing of the emplacement of nova-like fractures during volcano formation will require more detailed geological mapping from both the VMAP program and topical studies.

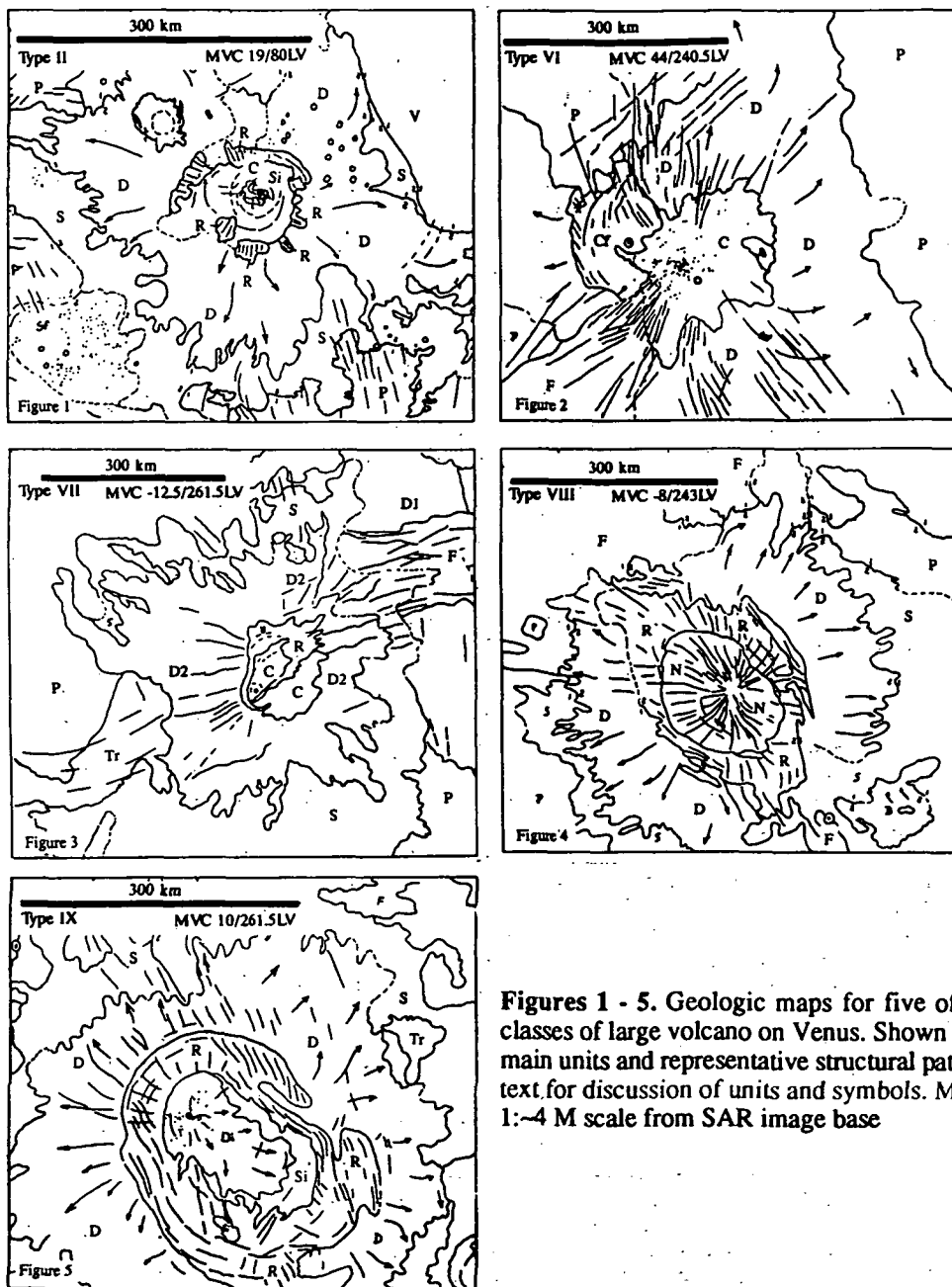
**Type IX (Corona-like Interior).** Many large magmatic centers on Venus, such as MVC 10/261.5LV (Figure 5), have the geologic characteristics of radial flow (D) emplaced on a pre-existing surface (S) and are superimposed by a concentric deformation annulus (R) meeting the criteria for coronae. The corona-like annulus frequently consists of a combination of radial and concentric fractures. A central depression with a smooth floor (Si) and central edifice consists of a

# LARGE VOLCANOES ON VENUS; CRUMPLER, HEAD, AND AUBELE

digitate, radial flow pattern. Edifice development has clearly continued subsequent to the development of corona-like characteristics.

**SUMMARY.** Geologic mapping of some examples of large volcanoes from among the nine previously identified classes, illustrates that both lava flow accumulation and structural deformation have been important in most magmatic centers. In addition, many large volcanoes are transitional to other defined types of magmatic centers such as novae and coronae. Based on this study, the stratigraphic sequence frequently follows a pattern of early, generally voluminous, lava flows to late radially patterned, digitate flows followed by some type of central structural deformation. However, in many examples the volcano developed at a site bearing pre-existing structural characteristics. A simple sequence in which large magmatic centers evolved from one feature type to another (for example, large volcano to corona, or *vice versa*) is not universal, and considerable diversity in evolution of each center is indicated.

**REFERENCES.** [1] Head et al, 1992, LPSC, 23, 513; [2] Head et al., 1992, JGR, 97, 13153; [3] Senske et al., 1992, JGR, 97, 13395; Keddle and Head, 1992, LPSC, 23, 669].



**Figures 1 - 5.** Geologic maps for five of the nine classes of large volcano on Venus. Shown are the main units and representative structural patterns. See text for discussion of units and symbols. Mapped at 1:~4 M scale from SAR image base

464046

5181-91

ABS-ONLY

LPSC XXIV

367

N 9 4 1 2 0 1 9 6

P-2

# REGIONAL MANTLE UPWELLING ON VENUS: THE BETA-ATLA-THEMIS ANOMALY AND CORRELATION WITH GLOBAL TECTONIC PATTERNS;

L.S. CRUMPLER, J.W. HEAD and JAYNE C. AUBELE, Department of Geological Sciences, Brown University, Providence, RI 02912.

**INTRODUCTION.** The morphology and global distribution of volcanic centers and their association with other geological characteristics offers significant insight into the global patterns of geology, tectonic style, thermal state, and interior dynamics of Venus. Magellan data [1] permit the detailed geological interpretation necessary to address questions about interior dynamics of Venus particularly as they reflect relatively physical, chemical, and thermal conditions of the interior. This paper focuses on the distribution of anomalous concentrations of volcanic centers on Venus and regional patterns of tectonic deformation as it may relate to the identification of global internal anomalies, including mantle dynamic, petrological, or thermal patterns.

**DISTRIBUTION OF VOLCANIC AND GEOLOGIC CHARACTERISTICS.** Initial results of the identified distribution of volcanism, geological interpretation of individual volcanic features, and some general global results of the initial survey are covered in previous discussions of the global volcanic survey [2,3]. Additional detailed discussions of coronae [4] and plains volcanism [5] are also presented elsewhere. Criteria for identification and for the classification systems of volcanic features on Venus are discussed in [6].

The largest concentration of moderate to high volcanic center areal abundance ( $>3$  to  $7$  centers/ $10^6$  km $^2$ ) occurs in the expanse of intermediate altitudes (uplands) lying between Beta, Atla, and Themis Regiones (BAT) and centered near the equator at longitude  $\sim 250^\circ$ . The BAT concentration accounts for 25% of the global surface such that together with the other smaller areas in the opposite hemisphere, the number density over  $\sim 50\%$  of the surface significantly exceeds the global mean. The areal abundance of volcanic centers in the remaining  $\sim 50\%$  of the surface area are correspondingly less ( $<3$  centers/ $10^6$  km $^2$ ) than the global mean. This distribution appears correlated with both altitude and geological setting.

**Altitude Setting of Anomalies.** The distribution of volcanic centers is non-random with respect to altitude, such that extreme high or low elevations of occurrence are infrequent (Figure 1) and most volcanic centers occur in the "uplands". BAT comprises a large fraction of the total global area of upland (0-2 km MPR) elevations.

Areas of lowest concentration include: (1) relatively contiguous lowlands oriented east-west in the mid-north or -south latitudes (Sedna, Niobe, Aino, and Helen) and north-south swaths approximately 30 degree-wide along meridians centered at the longitudes of Eastern Aphrodite ( $165^\circ$ , Atalanta, Rusalka, Helen) and Eistla Regio ( $345^\circ$ , Guinevere, Lavinia); and (2) include the main highland regions of Aphrodite Terra and Ishtar Terra, as well as minor highlands, Beta Regio, Alpha Regio, and Tellus Regio.

**Geological Setting of Anomalies.** In order to assess the regional geological environment in which concentration anomalies occur, complementary global geological thematic maps were prepared of five fundamental geological features mapped using 1:8 M Magellan mosaicked image data, including: fracture belts (Figure 2), ridge belts, mountain belts, ridged plains (Figure 3), and tesserae (Figure 4). Fracture belts locally are associated with troughs thought to result from crustal extensional, and ridge belts are frequently associated with the lowest plains areas [11] and are possibly related to focused crustal shortening [7]. Elsewhere, vast plains on Venus are characterized by sub-parallel, frequently uniformly-spaced, and sinuous ridges analogous to ridges common on the Lunar mare and plains surfaces of Mars ("wrinkle ridges") that are associated with minor regional crustal shortening are identified as ridged plains [7]. Tesserae distribution was adapted from the results of Ivanov et al. [8]. Tesserae originate through a complex history of deformation and represent anomalously thicker crust [15].

Geologically the distribution of volcanic centers is globally most strongly correlated with the areas of extension (Figure 5), and anti-correlated with areas characterized by compressional deformation and greater than nominal crustal thicknesses. The greatest concentration of fractures and rifts occurs in BAT where a complex mosaic of extensional fractures is distributed over a region centered near the equator and approximately 10,000 km in diameter. Volcanic centers are infrequent in regions characterized by mountain belts, ridge belts, and ridged plains, where compressional deformation has been common, and in tessera where the crust is thicker. The BAT anomaly is almost encircled by low plains characterized by compressional ridges, anomalous geoid lows [10], and anomalous underabundances of volcanic centers [2].

The similarity in distribution of coronae and volcanic centers is additional evidence for the presence of mantle upwelling in association with concentration anomalies. Because coronae are thought to represent local, intense mantle upwelling, possibly associated with mantle plumes [9], the similarity in distribution of coronae, extension, and other types of volcanism may reflect the characteristics of greater than nominal mantle upwelling. The close association of coronae and extension implies that areal extension is also associated with mantle upwelling phenomena.

Mass anomalies corresponding to topographic rises within concentrations of volcanic centers, such as Atla Regio, Beta Regio, Themis Regio, and Eastern Aphrodite Terra, and volcanic center, the magnitude of which frequently exceed that attributable to topography alone [10], implying a significant dynamic (upwelling and downwelling) component to the geoid signal. The largest negative geoid anomalies occur in areas characterized by low volcanic center concentrations, such as Lavinia Planitia and Atalanta Planitia. Different treatments of gravity data result in alternate geophysical interpretations, as is the case for Lakshmi Planum where both mantle upwelling and downwelling can be supported.

**INTERPRETATION.** The anomalous concentration of volcanic centers (BAT) occurs in a region with geological evidence for extension and geological characteristics of mantle upwelling phenomena. The presence of concentrations of (1) central volcanism, indicative of anomalous shallow melting and elevated regional heat flow into the shallow mantle, (2) coronae, indicative of regional, cellular mantle upwelling swarms; and (3) extensional faulting, indicative of regional crustal extension and crustal thinning support this interpretation.

# THE BETA-ATLA-THEMIS ANOMALY; CRUMPLER, HEAD, AND AUBELE

The peripheral regions, where volcanic centers are infrequent, are characterized by general evidence for compression (ridged plains, ridge belts, and mountain belts). Regions where volcanic centers are relatively few bear many geological characteristics frequently attributed to the effects of mantle downwelling [11]. The lower regional heat flow, relative exclusion of melting, and infrequent emplacement of shallow magma bodies in lowland regions as a result of large-scale mantle downwelling might contribute to a diminished probability of volcanism in these settings.

**CONCLUSIONS.** Figure 6 summarizes the observations, interpretations, and global significance of variations in volcanic center abundances. The large size of anomalous volcanic center concentrations, high number density of volcanic centers, and associated complex global fracture patterns imply the presence of a significant mantle anomaly underlying the BAT region. Evidence for upwelling are correlated with volcanism, positive gravity anomalies, coronae, and intermediate topography. Evidence for large areas of downwelling are correlated with sparse volcanism, low plains, tesserae, ridge belts, and ridged plains.

The scale of both upwellings and downwellings is several thousand kilometers and the current geological arrangement may be due to (1) fundamental patterns of deformation arising from normal cycles of fluid thermal convection in planetary interiors as described by the modeling of Schubert et al. [12]; (2) forced convection arising from cyclical lithospheric instabilities such as that proposed by Turcotte [13] or [Parmentier and Hess [14] in which anomalies like BAT might represent the residual effects of the rapid overturn of deep mantle or detachment and loss of a depleted layer; (3) an initial chemical or structural inhomogeneity in the deep interior dating from the formation of Venus or shortly thereafter; or (4) an as yet unidentified and unexamined mechanism. Whatever the mechanism, similar global-scale inhomogeneities appear to occur on the other major terrestrial planets [16].

**REFERENCES CITED.** [1] Saunders et al., 1992, JGR, 97, 13067; [2] Head et al. 1992, JGR, 97, 13153; [3] Crumpler et al. 1992, Int. Ven. Coll. 25; [4] Stofan et al., 1992, JGR, 97, 13347; [5] Guest et al. 1992, 97, 15949; [6] Crumpler et al., this volume; [7] Solomon et al. 1992, JGR, 97, 13199; [8] Ivanov et al., 1992, LPSC 23, 581; [9] Stofan et al., 1991, JGR, 96, 20933; Squyres et al., 1992, JGR, 97, 13612; [10] Bills et al., 1987, JGR, 92, 10351; [11] Zuber, 1990, GRL, 17, 1369; Phillips et al. 1991, Science, 252, 651; Squyres et al., 1992, JGR, 97, 13579; [12] Schubert et al., 1990, JGR, 95, 14105; [13] Turcotte, 1992, Int. Coll. Venus, 127; [14] Parmentier and Hess, 1992, GRL, 19, 2015; [15] Bindshadler and Head, 1991, JGR, 96, 5881; [16] Crumpler et al., 1992, this volume.

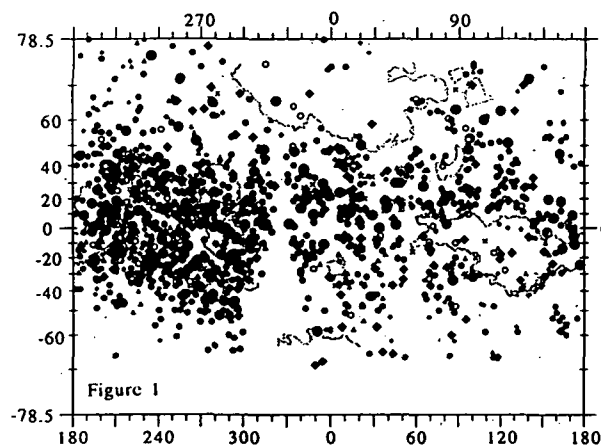


Figure 1

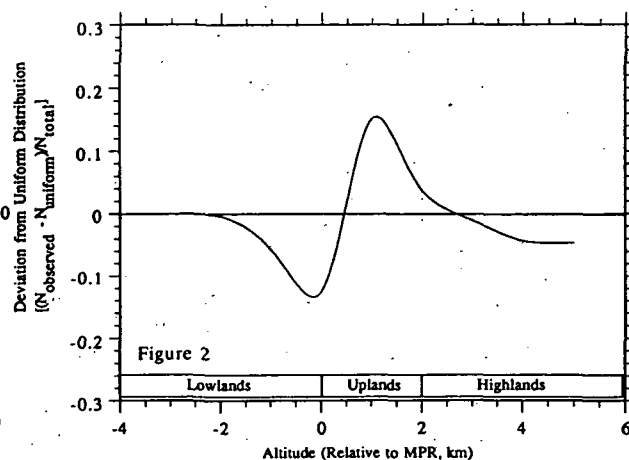


Figure 2

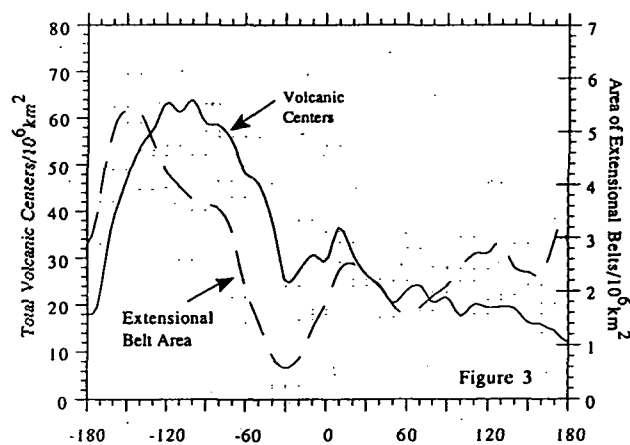


Figure 3

Figure 1. Observed global distribution of all volcanic and magmatic centers on Venus. Outlined areas indicate the major highlands.

Figure 2. Observed altimetric distribution of volcanic centers expressed as the fraction of the total that deviation from uniform case.

Figure 3. Longitudinal correlation of volcanic centers and total area of crustal extension (within  $\pm 45^\circ$  Lat).



464047

5182-46

ABS ONLY

LPSC XXIV

369

N 94-12197

**THE GRANULITE SUITE: IMPACT MELTS AND METAMORPHIC BRECCIAS OF THE EARLY LUNAR CRUST** J.A. Cushing, G.J. Taylor, M.D. Norman, and K. Keil (Planetary Geosciences, Dept. of Geology and Geophysics, SOEST, University of Hawaii, Honolulu HI 96822 U.S.A.)

The granulite suite consists of two major types of rocks. One is coarse-grained and poikilitic with many euhedral crystals of olivine and plagioclase. These characteristics indicate crystallization from a melt; the poikilitic granulites are impact melt breccias. The other group is finer-grained and granoblastic, with numerous triple junctions; the granoblastic granulites are metamorphic rocks. Compositional groups identified by Lindstrom and Lindstrom [1] contain both textural types. Two-pyroxene thermometry indicates that both groups equilibrated at 1000 to 1150 °C. Calculations suggest that the granoblastic group, which has an average grain size of about 80 μm, was annealed for  $< 6 \times 10^4$  y at 1000 °C, and for  $< 2500$  y at 1150 °C. Similar equilibration temperatures suggest that both groups were physically associated after impact events produced the poikilitic melts. Granulitic impactites hold important information about the pre-Nectarian bombardment history of the Moon, and the composition and thermal evolution of the early lunar crust.

Granulitic impactites [2] are widely considered to be an important rock type in the lunar crust, but how they formed is poorly understood. Metal compositions and elevated concentrations of meteoritic siderophile elements suggest that most lunar granulites are impact breccias. Their occurrence as clasts in ~3.9 Ga breccias, and  $^{40}\text{Ar}$ - $^{39}\text{Ar}$  ages  $\geq 4.2$  Ga for some granulites show that they represent a component of the lunar crust which formed prior to the Nectarian cataclysm. Petrographic characteristics of lunar granulites indicate at least two endmember textural variants which apparently formed in fundamentally different ways. One type has granoblastic textures consisting of equant, polygonal to rounded grains, and abundant triple junctions with small dispersions around 120° indicating a close approach to textural equilibrium. As suggested by many authors, granoblastic granulites probably formed by subsolidus annealing and recrystallization of fragmental or glassy protoliths. Examples of this type include 15418, 78155, and 79215.

The other textural type consists of poikilitic to poikiloblastic rocks with euhedral to subhedral plagioclase and olivine enclosed by interstitial pyroxene. In some cases, the texture resembles that of an orthocumulate. Examples of this type include 60035, 67955, and 77017. Rounding of grain edges is common in poikilitic granulites, but the regular crystal shapes and widely dispersed dihedral angles show they are far from textural equilibrium. The textures of poikilitic granulites are more consistent with the formation of these rocks by crystallization from a melt than by subsolidus metamorphism. A few samples have been recognized with textural characteristics transitional between those of the granoblastic and poikiloblastic endmembers (e.g., 72559, 78527) [3].

Pyroxene compositions taken from the literature and determined for this study by electron microprobe were used to calculate equilibration temperatures. The Kretz [4] Ca transfer (solvus) thermometer and the Lindsley and Anderson [5] graphical method both give similar temperatures, which range from ~1000 °C to 1150 °C (Fig. 1). There is no apparent temperature difference between granoblastic and poikilitic varieties, but there is a hint in these data that the more ferroan varieties equilibrated to lower temperatures. Additional studies are in progress to test this possibility.

Although clearly metamorphic, the granoblastic group has a matrix grain size of only about 80 μm. We can constrain the duration of metamorphism by estimating the rate of grain growth from Ostwald ripening, a process in which large grains grow at the expense of smaller ones to minimize surface free energy. If grain growth is controlled by Ostwald ripening, growth would follow a law such as the following [6]:

$$a^n = a_0^n + \frac{8\gamma v^2 \gamma_c D t}{9RT}$$

where  $a$  is the crystal size after time  $t$ ,  $a_0$  is the initial size,  $v$  is the molar volume of typical silicate crystals ( $4.2 \times 10^{-6}$  m<sup>3</sup>/mol for olivine),  $\gamma$  is the surface free energy of the crystal-crystal interface

## LUNAR GRANULITES Cushing et al.

(about  $1 \text{ J/m}^2$ ),  $c$  is the equilibrium concentration of solute (taken as the Fa content of granulite olivine,  $4 \times 10^4 \text{ mol/m}^3$ ),  $D$  is the diffusion coefficient,  $R$  is the gas constant, and  $T$  is temperature. The exponent  $n$  is 2 if the process is interface controlled and 3 if volume (diffusion) controlled. Most metamorphic systems seem to be volume controlled. The diffusion coefficient is not really known with certainty; we use that of olivine [7] because it is reasonably well determined and because its use gives self-consistent results for chondrite metamorphism [8 and our unpublished calculations]. Results are shown in Fig. 2 for an assumed initial grain size of  $10 \mu\text{m}$ . The two vertical dotted lines provide estimates for the duration of granulite metamorphism. It appears that the present grain size of granoblastic granulites ( $80 \mu\text{m}$ ) could be attained in a setting that allowed annealing at  $1000^\circ\text{C}$  to  $1150^\circ\text{C}$  for  $< 10^5 \text{ y}$ .

References: [1] Lindstrom MM and Lindstrom DJ (1986) PLPSC 16, 263 [2] Warner JL, Phinney WC, Bickel CE, and Simonds CH (1977) PLPSC 8, 2051 [3] Cushing JA, Taylor GJ, Norman MD, and Keil K. (1992) Workshop on the Geology of the Apollo 17 Landing Site, LPI Tech. Rept. 92-09, 4 [4] Kretz R (1982) GCA 46, 411 [5] Lindsley DH and Anderson DJ (1983) PLPSC 13, 887 [6] Greenwood GW (1969) Particle coarsening. In: The Mechanism of Phase Transformations in Crystalline Solids, 103-110 [7] Meisner DJ (1974) In: Geochemical Transport and Kinetics, 117-129 [8] Jones RH and Rubie CC (1991) Earth Planet. Sci. Lett. 106, 73

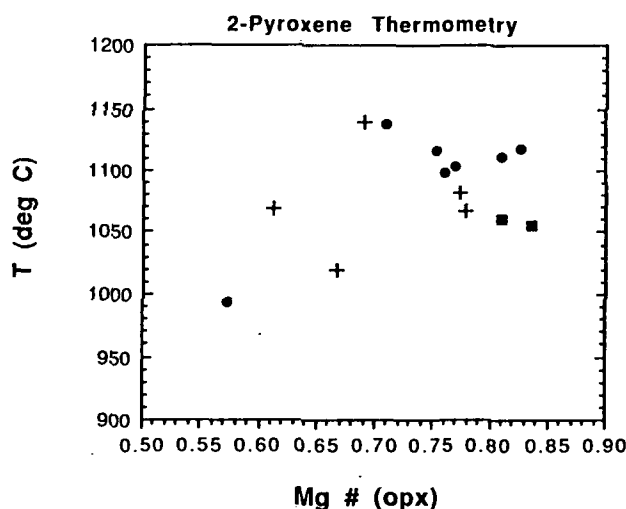


Figure 1. Pyroxene equilibration temperatures of lunar granulites plotted against the Mg/Mg+Fe of the low-Ca pyroxene. Symbols refer to textural types: granoblastic (+), poikilitic (•), and transitional (■). There is no difference in temperature between the different textural types, but the less magnesian samples may have equilibrated to lower temperatures.

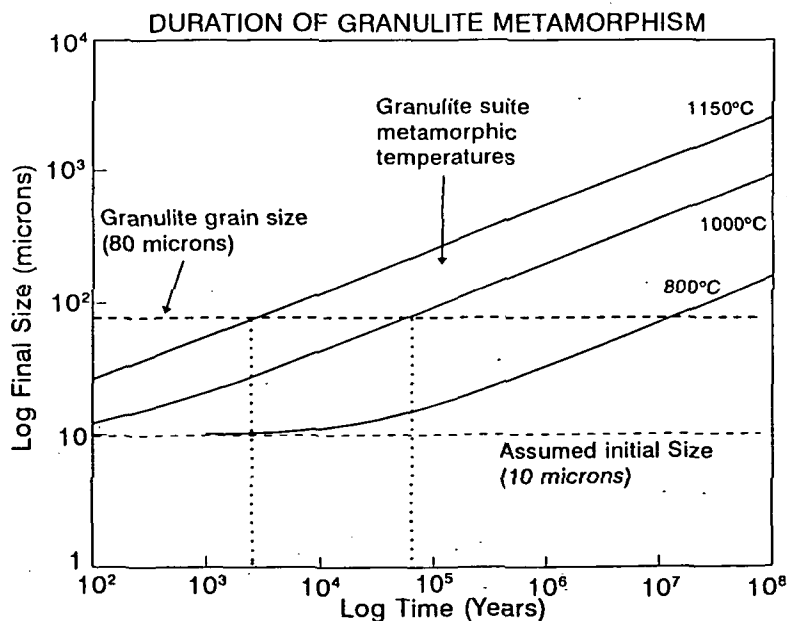


Figure 2. Thermal models for the duration of metamorphism based on the grain size and pyroxene temperatures of granoblastic granulites. Grain growth by Ostwald ripening is assumed. Metamorphic timescales of  $< 10^5$  years are indicated by these models.

LK 4064

5/83-9/

LPSC XXIV

371

AK 94-12198  
163703

P-1

**GALILEO EM-2 CONTRIBUTIONS TO THE LUNAR CONTROL NETWORK;**  
M. E. Davies and T.R. Colvin, RAND; M.J.S. Belton, N.O.A.O.; R. Greeley,  
Arizona State University; and the Galileo SSI Team.

A local control network is being developed using Galileo images that cover the region north of the Apollo area and lie between 10 and 100 degrees east longitude. This network is tied to the Apollo control network and will have a positional accuracy of approximately 500-1500 m. This region has been photographed by Earth-based telescopes and the Mariner 10 and Lunar Orbiter spacecraft, but the Galileo images are preferred for control because of their superior viewing angles, resolution, and Galileo's geometrically stable sensor.

Based on Davies et al., 1987, the positional accuracy of the near-side Apollo network is estimated to be between 50 and 300 m. The laser ranging retroreflector locations at the Apollo 11, 14, and 15 sites and the Lunikhod 2 site have been determined with an accuracy of about 10 m. (~~Williams et al., 1987~~). The locations of the ALSEP transmitters relative to the retroreflectors have also been measured (~~King et al., 1976~~). These known coordinates are used to estimate errors in the Apollo network.

The telescopic control is approximately bounded by 75 degrees north and south latitude and 75 degrees east and west longitudes. The accuracy of the telescopic network is thought to be about one to two km. Thus, the Galileo network might improve coordinates in the telescopic area as well as north and east of it.

#### References

- (1) Davies, M.E. et al., 1987, JGR 92, 14177-14184.
- (2) King, R.W. et al., 1976, JGR 81, 6251-6256.
- (3) Williams, J.G. et al., 1987, Proceedings of the International Symposium, Figure and Dynamics of the Earth, Moon, and Planets, Astronomical Institute of the Czechoslovak Academy of Sciences, 643-648.

**IRON AND NICKEL ISOTOPIC MASS FRACTIONATION IN DEEP-SEA SPHERULES;** Andrew M. Davis<sup>1</sup> and Donald E. Brownlee<sup>2</sup>; <sup>1</sup>Enrico Fermi Institute, University of Chicago, 5640 S. Ellis Ave., Chicago, IL 60637; <sup>2</sup>Department of Astronomy, University of Washington, Seattle, WA 98105.

Magnetite-wüstite spherules collected from deep-sea sediments are thought to have originally been Fe-Ni metal particles at the top of the atmosphere that were oxidized and melted during entry into the earth's atmosphere. Some likely sources for the metal particles are Fe-Ni interplanetary dust particles (IDP's) and metal or sulfide from stony IDP's that separated after melting. Davis *et al.* [1] reported that four of these spherules are enriched in the heavy isotopes of iron, with enrichments of 8–23 ‰/amu. Herzog *et al.* [2] analyzed a separate collection of spherules and found enrichments in the heavy isotopes of nickel of 10–25 ‰/amu. We have developed a technique for analysis of both iron and nickel isotopes on the same ion microprobe spot and have applied this technique to a number of deep-sea spherules in order to better understand the processes leading to isotopic mass fractionation. Eight spherules show iron and nickel isotopic mass fractionation, with iron and nickel enriched in the heavy isotopes by 10 to 19 ‰/amu and 4 to 32 ‰/amu, respectively. If the mass fractionations are due to Rayleigh fractionation during evaporation, these spherules lost 76 to 94% of their original mass.

We analyzed the four magnetite-wüstite spherules for which iron isotopic data were reported by Davis *et al.* [1] as well as four new spherules. The spherules range in diameter from 170 to 600 µm. Iron and nickel isotopic analyses were made at low mass resolution ( $M/\Delta M = 300$ ) using a modified AEI IM-20 ion microprobe. <sup>54</sup>Fe was corrected for <sup>54</sup>Cr interference by measuring <sup>52</sup>Cr and assuming that chromium is of normal isotopic composition. <sup>58</sup>Ni is interfered with by <sup>58</sup>Fe. A correction was made assuming that <sup>56</sup>Fe/<sup>54</sup>Fe and <sup>58</sup>Fe/<sup>54</sup>Fe fractionate in nature and in instrumental mass fractionation in the same way and that the fractionation factor follows an inverse square-root of mass relationship. There are a number of molecular interferences that can occur in samples high in lithophile elements: Mg<sub>2</sub> interferes with <sup>52</sup>Cr; Al<sub>2</sub> with <sup>54</sup>Cr; CaO with <sup>56</sup>Fe, <sup>58</sup>Ni and <sup>60</sup>Ni; Si<sub>2</sub> with <sup>56</sup>Fe, <sup>57</sup>Fe, <sup>58</sup>Ni and <sup>60</sup>Ni; and TiO with <sup>62</sup>Ni and <sup>64</sup>Ni. We analyzed only samples low in magnesium, aluminum, silicon, calcium and titanium. Molecular interferences were suppressed by operating under energy-filtering conditions. Energy-filtering decreases secondary ion current, but molecular ion intensities fall off more rapidly with increasing energy than do monatomic ion intensities. When the ion microprobe is tuned for maximum secondary beam intensity for Fe<sup>+</sup>, machine fractionation of iron and nickel isotopes is quite large, ~30 and ~15 ‰/amu, respectively. In addition to cutting down on molecular interferences, use of energy-filtering has the added benefit of lowering the machine fractionation for iron and nickel isotopes to ~10 and ~4 ‰/amu, respectively. The primary standards used were synthetic magnetite and NiO. Data are reported as  $\delta$  values, for example,  $\delta^{56}\text{Fe} = \{[(^{56}\text{Fe}/^{54}\text{Fe})_{\text{sample}}/(^{56}\text{Fe}/^{54}\text{Fe})_{\text{std}}] - 1\} \times 1000$ . <sup>54</sup>Fe and <sup>60</sup>Ni were used as reference isotopes. For comparison, the Cape of Good Hope iron meteorite was analyzed and found to be of near-normal iron and nickel isotopic composition. An example of the data collected is shown in Fig. 1, where  $\delta$  values are plotted vs. mass. The error bars are  $\pm 1\sigma$ , for clarity; uncertainties in  $F_{\text{Fe}}$  and  $F_{\text{Ni}}$  (see below) are  $\pm 2\sigma$ . It can be seen that isotopic compositions of iron and nickel in spherule KK191D-8 follow a mass fractionation relationship, whereas Cape of Good Hope shows no fractionation. In some samples, including both plotted in Fig. 1, there appears to be excess  $\delta^{57}\text{Fe}$ , presumably due to <sup>56</sup>FeH.

For each spherule analyzed, the average iron and nickel mass fractionation,  $F_{\text{Fe}}$  and  $F_{\text{Ni}}$ , are plotted in Fig. 2. The error bars shown are  $\pm 1\sigma$ .  $F_{\text{Fe}}$  is based on  $\delta^{56}\text{Fe}$  alone, because of hydride interferences on  $\delta^{57}\text{Fe}$ . Most  $F_{\text{Ni}}$  values are based on all five nickel isotopes, but for a few samples there is excess  $\delta^{61}\text{Ni}$ , due to <sup>60</sup>NiH. Two spherules are high in titanium (~0.5 %

# FE AND NI ISOTOPES IN COSMIC SPHERULES; Davis A. M. & Brownlee D. E.

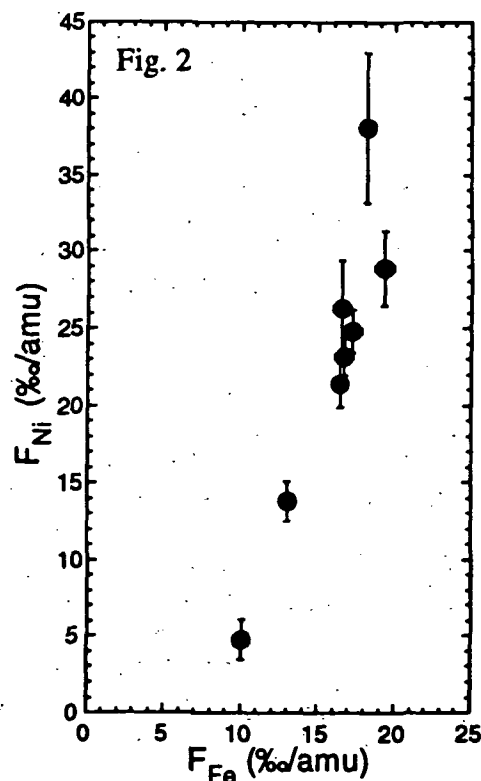
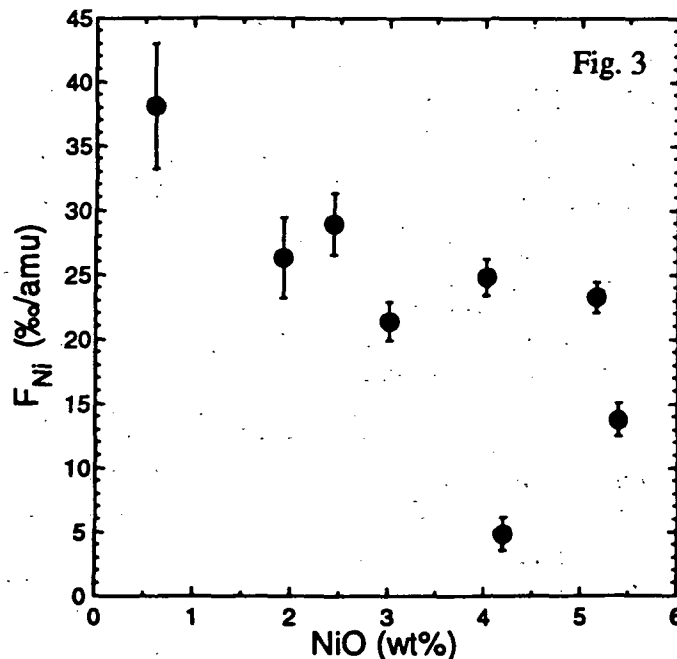
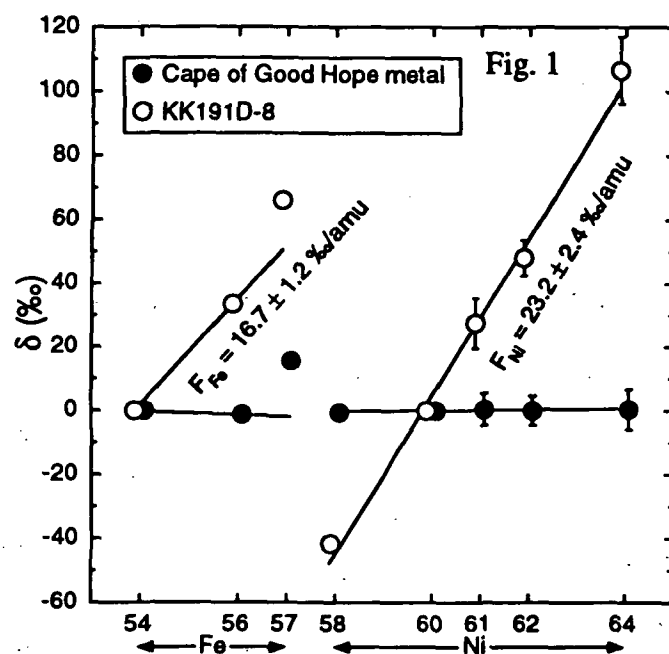
TiO<sub>2</sub>), so <sup>64</sup>Ni was not used. There is a good correlation between  $F_{Fe}$  and  $F_{Ni}$ . It appears that iron evaporates first, up to  $F_{Fe} = 8-10\text{ ‰/amu}$ , then  $F_{Ni}$  increases with increasing  $F_{Fe}$ . The maximum  $F_{Fe}$  and  $F_{Ni}$  values observed so far are 19 and 37 ‰/amu, respectively.

Davis *et al.* [1] inferred that iron evaporated as FeO from the spherules, based on the agreement between the amount of isotopic mass fractionation of iron and oxygen. We calculated the fraction of iron and nickel evaporated from each spherule, assuming Rayleigh fractionation and using FeO and NiO as the gas phase species involved in the evaporation reaction. The fraction of iron evaporated ranged from 76 to 94%, the fraction of nickel evaporated ranged from 52 to 99.2 % and ratio of original mass to present mass ranged from 4 to 18. Most of the spheres

were two to three times as large in diameter prior to evaporation. No relationship was found between present spherule diameter and  $F_{Fe}$  or  $F_{Ni}$ .

$F_{Ni}$  vs. NiO content are plotted in Fig. 3. The error bars shown are  $\pm 1\sigma$ . There is an inverse correlation between these parameters, indicating that nickel evaporates more rapidly from the spherules than does iron.

References. [1] Davis A. M. *et al.* (1991) *LPS XXII*, 281. [2] Herzog G. F. *et al.* (1992) *LPS XXIII*, 527.



**TRACE ELEMENT DISTRIBUTIONS IN PRIMITIVE ACHONDRITES;** Andrew M. Davis<sup>1</sup>, Martin Prinz<sup>2</sup> and Michael K. Weisberg<sup>2</sup>; <sup>1</sup>Enrico Fermi Institute, University of Chicago, 5640 S. Ellis Ave., Chicago, IL 60637; <sup>2</sup>Department of Mineral Sciences, American Museum of Natural History, 79th St. at Central Park West, New York, NY 10024

The primitive achondrites have approximately chondritic bulk chemical composition but achondritic textures. Clayton *et al.* [1] showed that nine of these meteorites, the acapulcoites and the lodranites, have similar oxygen isotopic compositions. The acapulcoites appear to be highly metamorphosed, but undifferentiated, meteorites of chondritic composition, whereas the lodranites appear to have lost a feldspathic partial melt. In order to learn more about metamorphic processes and partial melt removal, we have measured the trace element compositions of constituent phases of a number of primitive achondrites by ion microprobe. We have analyzed two acapulcoites, Acapulco and ALH81261 (paired with ALH77081), and three lodranites, Lodran, LEW88280 and MAC88177. In addition, we analyzed LEW88663, which has the bulk composition, mineral chemistry and oxygen isotopic composition [R. N. Clayton, pers. comm.] of L-chondrites, but is metal-free and has an achondritic texture; and Divnoe, a plagioclase-poor, olivine-rich primitive achondrite with an oxygen isotopic composition similar to that of the group IAB iron meteorites [2]. These meteorites show a variety of REE patterns in their constituent phases, and there are consistent differences between acapulcoites and lodranites that are consistent with removal of a LREE- and Eu-enriched melt that is apparently responsible for the low plagioclase content of lodranites.

Modal abundances and mineral chemistry of analyzed phases are given in Table 1. REE patterns of constituent phases are shown in Fig. 1, along with expected REE patterns for chondritic composition (uniform bulk REE enrichments of  $1.5 \times \text{CI}$  chondrites), assuming equilibrium partition coefficients. Sources of partition coefficients are as follows: olivine [3], orthopyroxene [3], clinopyroxene [4], plagioclase [5], whitlockite [6] and apatite (estimated from apatite and whitlockite REE patterns in ordinary chondrites [7]). All Eu was assumed to be present as  $\text{Eu}^{+2}$  and  $\text{Eu}^{+2}$  was assumed to have the same partition coefficient as  $\text{Sr}^{+2}$ . An equilibration temperature of  $1200^\circ\text{C}$  was assumed, based on mineral thermometry of Acapulco [8].

**Acapulcoites.** Only Acapulco shows near-equilibrium REE partitioning. The other acapulcoite, ALH81261, has REE concentrations in phosphates that are lower than expected.

**Lodranites.** The three lodranites have rather unusual REE patterns in their phosphates. LEW88280 phosphates are especially low in REE, with apatite containing lower enrichments of HREE than clinopyroxene. Phosphates in both LEW88280 and MAC88177 are enriched in HREE, unlike acapulcoite phosphates. This may have resulted from extraction of a plagioclase-rich melt from an original chondritic bulk composition, but does not explain the lack of equilibrium between phosphates and silicates. Lodran apatite has an especially unusual pattern that is suggestive of two components, a HREE-enriched one like that in the other two lodranites and a LREE-enriched one that is most enriched in Ce, Pr and Nd. Phosphates and clinopyroxene apparently did not equilibrate with one another in Lodran, as clinopyroxene has a large negative Eu anomaly and the phosphates do not show Eu anomalies.

**LEW88663.** This meteorite shows near-equilibrium REE partitioning, consistent with metamorphism of an L-chondrite. The complete absence of Fe-Ni metal implies metal loss, because L-chondrites contain 3-4 vol% metal and silicate mineral chemistry of LEW88663 indicates that the metal was not oxidized into silicates.

**Divnoe.** Only olivine and clinopyroxene could be found in our thin section of Divnoe. Clinopyroxene is lower in REE than clinopyroxene in the other primitive achondrites analyzed here. The pattern is strongly HREE-enriched, with more Lu/La fractionation than is normally seen in clinopyroxene. This might have been achieved by removal of a partial melt more enriched in LREE than in other primitive achondrites. Divnoe clinopyroxene is also unusual in that it does not have the strong negative Eu anomaly seen in clinopyroxene from other primitive achondrites. If plagioclase and phosphate extraction was responsible for the REE pattern of Divnoe clinopyroxene, one would have expected Eu to have been extracted along with the LREE, unless conditions were so oxidizing that all of the Eu was present as  $\text{Eu}^{3+}$ .

**Conclusions.** Despite the equilibrated-looking textural features of acapulcoites and lodranites, most of these meteorites do not show the equilibrium distribution of REE. Several different melt transport processes may have been involved in the formation of lodranites. Trace element data indicate that Divnoe is not related to the acapulcoites and lodranites; contrary to the relationship suggested by McCoy *et al.* [2].

References: [1] Clayton R. N. *et al.* (1992) *LPS XXIII*, 231-232. [2] McCoy T. J. *et al.* (1992) *Meteoritics*

REE IN PRIMITIVE ACHONDRITES; Davis A. M. *et al.*

27, 288. [3] Colson R. O. *et al.* (1988) *GCA* 52, 539. [4] Kuehner S. M. *et al.* (1989) *GCA* 53, 3115. [5] Phinney W. C. & Morrison D. A. (1990) *GCA* 54, 1639. [6] Neal C. R. & Taylor L. A. (1991) *GCA* 55, 2965. [7] Crozaz G. *et al.* (1989) *EPSL* 93, 157. [8] Palme H. *et al.* (1981) *GCA* 45, 727.

Table 1. Modal abundances and mineral chemistry.

Phase	Acapulco	ALH61261	Lodran	LEW88280	MAC88177	LEW88663	Divnoe
Olivine	33.9	33.4	52.6	54.1	52.5	55.1	80.3
<i>Fa</i>	11.9	10.3	12.6	12.5	12.9	24.0	26.6
Orthopyroxene	40.4	43.6	47.1	37.3	39.4	27.1	11.5
<i>Wo</i>	1.2	1.8	2.6	2.0	2.7	3.0	2.0
<i>Fs</i>	12.6	9.8	13.3	11.0	12.4	20.1	23.3
Clinopyroxene	7.4	7.2	trace	7.9	7.6	3.9	6.3
<i>Wo</i>	44	44.2	43.3	43.0	42.5	44.9	43.3
<i>Fs</i>	5	4.3	6.4	5.2	5.4	7.6	9.0
Plagioclase	15.9	14.3	—	—	0.2	12.8	—
<i>An</i>	14	14.3	—	—	—	20	—
<i>Or</i>	4	4.5	—	—	—	2	—
Chromite	0.9	1.5	0.3	0.7	0.3	1.1	1.9
Apatite	1.2	trace	trace	trace	trace	trace	—
Whitlockite	0.3	trace	trace	—	—	—	—

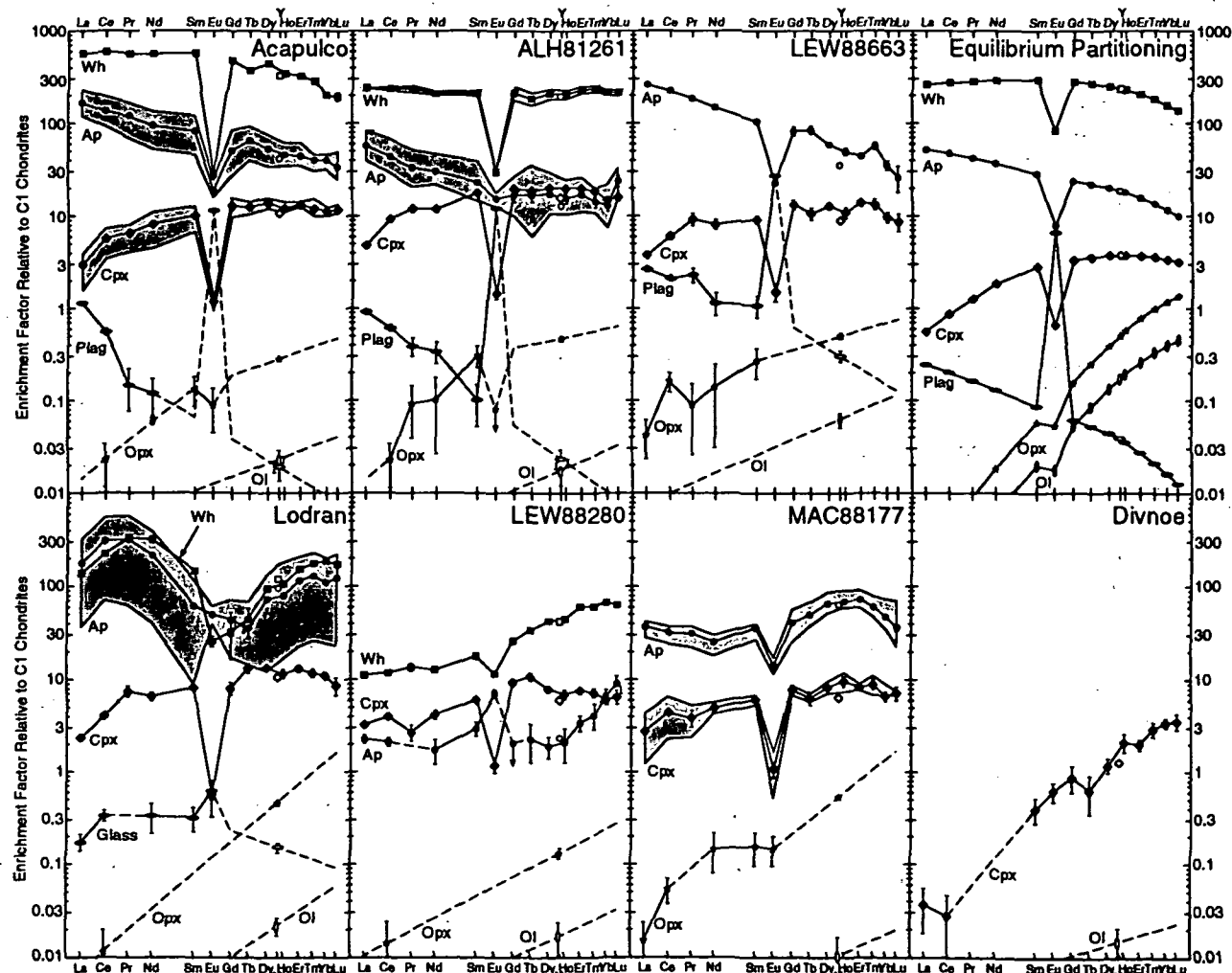


Fig. 1. REE in primitive achondrites, normalized to CI chondrites. Uncertainties are based on counting statistics and are  $\pm 1\sigma$ ; upper limits are  $<2\sigma$ .

464073

5186-90  
ABS ONLY

LPSC XXIV

377

N 94-312201

p. 2

DEVIATIONS FROM THE STRAIGHT LINE: BUMPS (AND GRINDS) IN THE COLLISIONALLY EVOLVED SIZE DISTRIBUTION OF ASTEROIDS; D.R. Davis, (PSI, Tucson AZ); P. Farinella, P. Paolicchi, and A.C. Bagatin, (Univ. of Pisa); A. Cellino and E. Zappalà (Torino Observatory)

Dohnanyi [1,2] established that the size distribution of a collisionally relaxed population is a power-law with a -3.5 slope (incremental diameter), provided that: (i) collisional parameters are independent of size and (ii) there is no lower limit on the population size for shattering impacts. In the course of studying collisional effects over a wide range of asteroid sizes (cm up to hundreds of km range), we have investigated the consequences of relaxing the second condition, while maintaining the first one.

Consider the evolution of a population using a collisional model with a constant impact strength, no gravity and no cratering effects, but with a lower bound on the population. Figure 1 shows the evolved size distribution for three different starting populations: a) power law, initial slope = -4.0; b) power law, initial slope = -3.0; c) non-power law. In all cases, the evolved population shows a wave-like structure which differs from the straight power-law distribution found for the pure Dohnanyi case, i.e., one that meets both of the above conditions. However, the evolved populations shown in Fig. 1 do have a mean slope of -3.5, but with a superimposed "wave" structure.

The "wave" structure is produced by the small-size boundary condition as follows: i) for the smallest bin, only shattering collisions within the bin remove bodies from the bin; (ii) for the second smallest bin, projectiles from the smallest bin are an additional source for removing bodies from the bin, etc. Thus there is an increasing depletion rate with increasing size up to the size body ( $D_1$ ) that can just be shattered by the smallest body in the population. Thus the population develops a steeper than -3.5 size distribution, and shows a relatively large depletion. Bodies larger than  $D_1$  are less depleted since there are fewer projectiles to shatter them due to the above depletion. Thus the population develops a shallower slope than -3.5 in this range. Repeating this pattern leads to development of the wave structure.

The wavelength of this structure depends on the impact strength of the population. As shown in Fig. 2, the wavelength varies inversely with the impact strength: the larger the strength, the shorter the wavelength.

Next we include gravity and cratering in the collisional model. Adding gravity to the model produces some changes, but the wave structure persists (Fig. 3a). Adding cratering produces a similar result, as does including both effects into the collisional model (Figs. 3b and 3c).

What are the possible implications of the result for asteroids? There is a real lower bound to the size distribution that is the result of radiation effects. For one, P-R drag produces a cutoff in the size distribution at about the cm size scale, although this is not a sharp size cutoff.

We included this effect in our simulation by removing small particles during a timestep by:

$$\Delta N/N = (1 - e^{-\Delta t/\tau})$$

where  $\Delta N/N$  is the fraction of particles of diameter  $D$  (meters) removed in time  $\Delta t$  (years);  
 $\tau = 4.5 \times 10^9 \cdot D \cdot \text{yrs.}$

Including this loss mechanism into a simplified version of our asteroid collisional evolution program gives an evolved population with a wave structure superimposed on a quasi-power law distribution (Fig. 4). Hence we might expect that the size distribution of real asteroids in the small size range may differ from that predicted based on Dohnanyi's work. Further work is in progress to better understand how real size distributions may differ from the pure power-law case.

References: [1] Dohnanyi, J.W. (1969) *JGR* 74, 2531-2554; [2] Dohnanyi, J.W. (1971) NASA SP-267, 263.



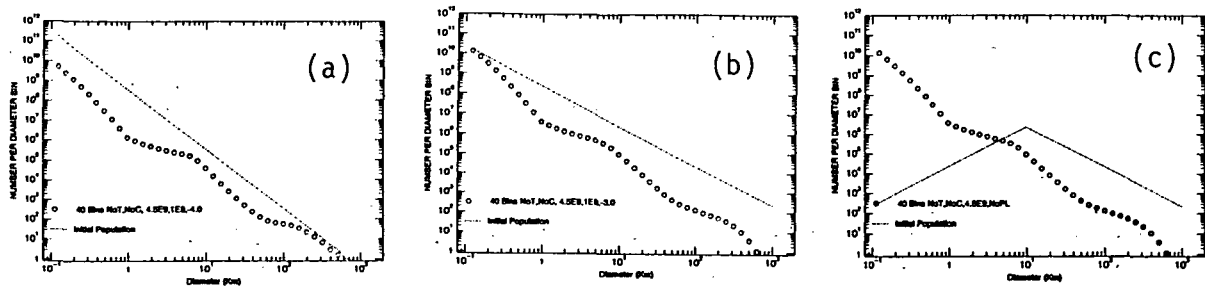
SIZE DISTRIBUTION BUMPS: Davis, D.R. *et al.*

Figure 1. Evolved size distribution for three different starting populations: (a) power-law, initial slope = -4.0; (b) power-law, initial slope = -3.0; (c) non-power-law.

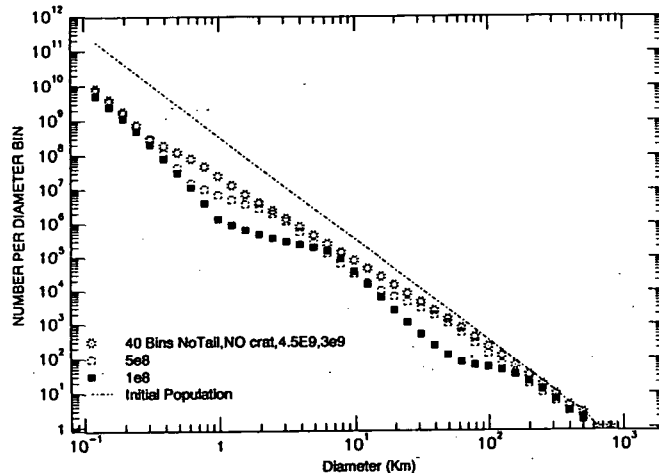


Figure 2. Effect of varying the impact strength on the structure of the first population.

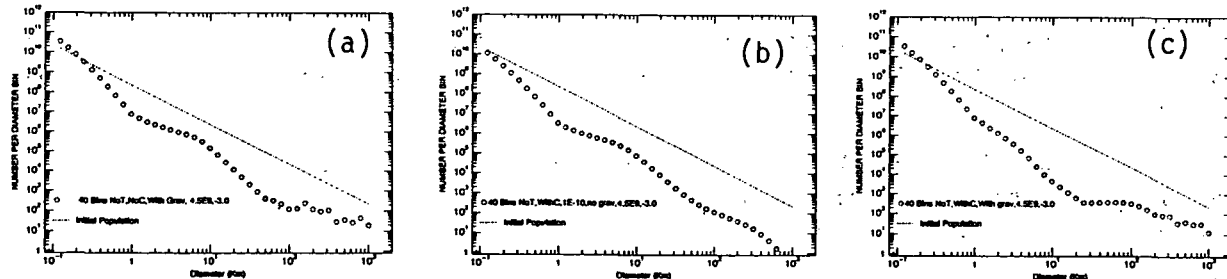


Figure 3. Evolved population using an initial power-law with a -3.0 slope. Part (a) gravity only added to the collisional outcome mode; (b) cratering only added; (c) both gravity and cratering added.

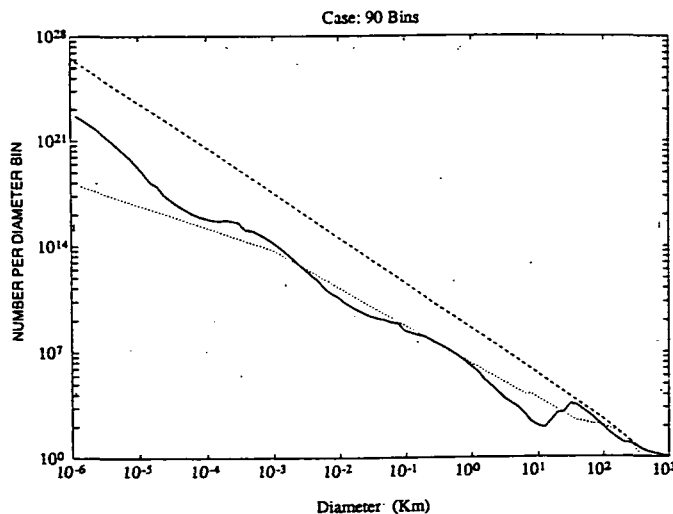


Figure 4. Evolved population from an initial power-law with a -4.0 slope, over the size range from about 1 mm to 1000 km. Cratering, gravity and P-R drag are included. The dashed and dotted curves correspond to slopes -4 (dashed), -3.5 (dotted, diameters > 1 m) and -3 (dashed, diameters < 1 m), respectively.

3187-91  
464074 ABS. ONLY  
N 94-12202

SMALL VOLCANOES IN TEMPE TERRA, MARS: THEIR DETAILED  
MORPHOMETRY AND INFERRED GEOLOGIC SIGNIFICANCE: P.A. Davis and K.L.  
Tanaka, U.S. Geological Survey, Flagstaff, AZ 86001

The Tempe Terra province contains a variety of volcanic landforms that range in size from small vents (less than 10 km in diameter) to moderately sized volcanoes (150 km in diameter) [1-6]. The volcanoes are aligned along the dominant northerly and northeasterly trends of the faults in this region, and many of the volcanoes occur on grabens [2,4,5]. Some workers have speculated on the nature of some of the volcanoes on the basis of their general morphology, shadow-measurement height, lateral dimensions, and geologic setting [1-4]. As part of a larger study, we have obtained detailed photoclinometric profiles across five of the more conspicuous small volcanoes in the Tempe Terra region (Fig. 1). From these data, we extracted for each volcano its flank width and edifice height and the width and depth of its summit crater. We statistically compared these dimensions for each volcano with a set of average dimensions for each type of terrestrial volcanic feature listed in [6]. These comparisons indicate that the morphometries of the Martian volcanoes 1, 2, and 3 most closely match Earth's cratered basaltic lava shields, and the morphometries of volcanoes 4 and 5 are similar to those of terrestrial basaltic tuff rings.

All five of the studied volcanoes are on or near grabens or fractures. All five have two morphologic characteristics in common: summit pits and a diffuse basal contact with the surrounding plains (except where the local topographic gradient causes ponding of associated lava flows). The volcanoes' summit pits differ: volcano 1 has a small circular pit, volcano 2 has an elongate pit whose trend parallels the local faults and whose length is approximately equal to the volcano's flank width, volcanoes 3 and 5 have two similar-sized circular pits aligned parallel to a local fault trend, and volcano 4 has a large rectangular pit aligned parallel to a local fault trend. The flank slopes of volcanoes 1 and 2 are about  $7.8^\circ$ ; those of volcanoes 3 and 5 are  $5.3^\circ$  and  $5.5^\circ$ , respectively; and that of volcano 4, the lowest, is  $2.6^\circ$ .

Our quantitative morphometric comparisons of the five Martian volcanoes with various types of terrestrial volcanoes [6] suggest that volcanoes 1, 2, and 3 are most similar to terrestrial cratered basaltic lava shields that have little tephra; volcano 1 is most similar to a low lava shield (e.g., Mauna Iki), whereas volcanoes 2 and 3 are most similar to Icelandic lava shields. Our comparisons further suggest that the morphometric characteristics of volcanoes 4 and 5 are similar and most closely match those of basaltic tuff rings.

On Earth, tuff rings form as a result of volcanic eruption through a zone of either ground water or ground ice [7-8]. The occurrence of tuff rings on Mars, which is indicated by the morphometries of volcanoes 4 and 5, suggests that water existed in the shallow Martian crust during the time of formation of these volcanoes.

Our quantitative analysis of volcanoes 1, 2, 3, and 5 indicates that their flank width, edifice height, and summit-crater dimensions are statistically close to those of cratered table mountains. Such an affinity has been suggested for similar small volcanic domes in the Olympus Mons region [9]. We do not, however, believe that the four Tempe Terra volcanoes are table mountains, because their profiles (Fig. 1) do not have the flat tops and steep flanks characteristic of table mountains [6]. Thus, our next analysis will be more rigorous and will include additional morphometric parameters (such as flank slope) so that we can more precisely constrain the morphometric classification.

References: [1] Hodges (1979) *NASA TM 80339*, 247; [2] Hodges (1980) *NASA TM 81776*, 181; [3] Moore and Hodges (1980) *NASA TM 82385*, 266; [4] Plescia (1981) *Icarus*, 45, 586; [5] Scott (1982) *J. Geophys. Res.*, 87, 9839; [6] Pike and Clow (1981) *U.S. Geol. Surv. Open-File Rep. 81-1038*, 40 p.; [7] Wohletz and Sheridan (1983) *Amer. Jour. Sci.*, 283, 385; [8] Lorenz (1986) *Bull. Volcanol.*, 48, 265; [9] Hodges and Moore (1979) *J. Geophys. Res.*, 84, 8061.

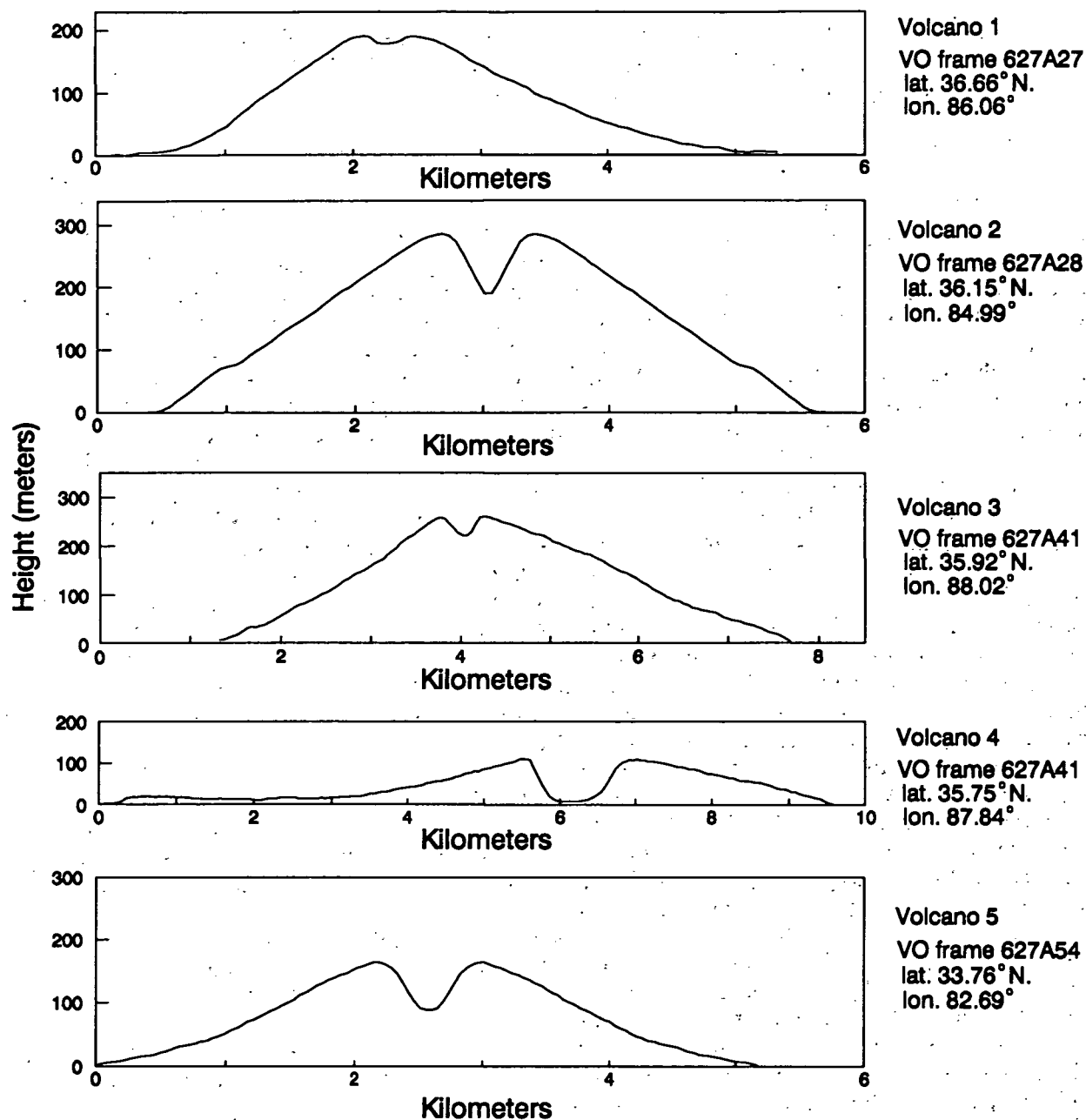


Figure 1. East-west photoclinometric profiles of five small volcanoes in Tempe Terra. Vertical exaggeration X5. Viking Orbiter (VO) frame used to derive each profile and the latitude and longitude of the summit of each volcano are listed next to the respective profile.

SHALLOW CRUSTAL DISCONTINUITIES AND GRABEN AND SCARP  
FORMATION IN THE THARSIS REGION OF MARS; P.A. Davis and K.L. Tanaka,  
U.S. Geological Survey, Flagstaff, AZ 86001 and M.P. Golombek, Jet Propulsion Laboratory,  
Pasadena, CA 91109.

We recently obtained photoclinometric profiles across all simple grabens and erosional landforms (e.g., troughs, pits, wall-valley heads, and scarps that are bounded above and below by flat surfaces) that occur within Tempe Terra. These data, together with similar data that we obtained for Syria, Sinai, and Lunae Plana [1,2] and the Alba Patera region [3], allow regional examination of shallow crustal discontinuities between latitude 30° S. and 50° N. and longitude 50° W. and 112° W. The profile for each simple graben was used with an appropriate structural model [2,4] to estimate the depth to the base of the faulted layer. The depths of erosional wall scarps may also indicate the depths of mechanical discontinuities such as a local lithologic or cryospheric boundary. Examination of these data indicates a surprisingly consistent set of shallow crustal discontinuities for the Tharsis region at depths of 0.4-0.6 km, 1.0-1.4 km, and 2 km; the maximum depth of the features in most study areas appears to be about 4 km (Fig. 1).

The concentration of values between 0.4 and 0.6 km in most scarp and some faulted-layer depth data is similar to the range in estimated thicknesses of individual exposed Noachian and Hesperian plains units [5-7] in the Tharsis region. The regional depth data also show two modes near 1 and 2 km in some study areas and a maximum depth near 4 km in most study areas (Fig. 1); the faulted-layer depths in excess of 4 km at Alba Patera occur near the summit of the caldera and could be attributed to volcanic loading. Our detailed examination of these depth data includes the following observations: (1) The mode at 1.0-1.4 km depth transcends age and geologic setting in this broad study area. (2) The 2-km mode is most obvious at Alba Patera and moderately well developed at Syria and Sinai Plana, but it is muted at Tempe Terra, which is in the same latitude range as Alba Patera but older. (3) The 2-km-depth mode is not present in all areas that have features of Amazonian age [2].

We suggest two possible explanations for our observations in the Tharsis region [see 8]:

(1) The cryosphere thickens from 1 km to 2 km toward higher latitudes, as suggested by thermal-diffusion models [9-11], but it did not fully develop to a thickness of 2 km at latitudes above 30° until Amazonian time [11]. (2) In these volcanic terrains on Mars, the 1.0- to 1.4-km depth represents a possible physical limit to non-eruptive dike ascent, which may be controlled by the depth of onset of magma vesiculation [12-13]; the 2-km depth represents the interface between the Martian megaregolith above and more solid basement below [9,14,15], which locally may reach a depth of 4 km. Dike intrusion and, in places, eruption in these volcanic terrains are supported by photogeologic observations of lava flows that originated from grabens [1,16-18]. A combination of the cryogenic and volcanic scenarios is probably most likely.

References: [1] Tanaka and Davis (1988) *J. Geophys. Res.*, 93, 14,893; [2] Davis and Golombek (1990) *J. Geophys. Res.*, 95, 14,231; [3] Davis et al. (1991) *Lunar Planet. Sci. XXII*, 285-286; [4] Golombek (1979) *J. Geophys. Res.*, 84, 4657; [5] Plescia and Saunders (1980) *Proc. 11th Lunar Planet. Sci. Conf.*, 2423; [6] De Hon (1985) *Lunar Planet. Sci. XVI*, 171; [7] Frey and Grant (1990) *J. Geophys. Res.*, 95, 14,249; [8] Tanaka et al. (1991) *J. Geophys. Res.*, 96, 15,617; [9] Fanale (1976) *Icarus*, 28, 179; [10] Rossbacher and Judson (1981) *Icarus*, 45, 39; [11] Fanale et al. (1986) *Icarus*, 67, 1; [12] Parfitt (1991) *J. Geophys. Res.*, 96, 10,101; [13] Head and Wilson (1981) *J. Geophys. Res.*, 86, 2971; [14] Woronow (1988) *LPI Tech. Rep. 88-05*, 135; [15] MacKinnon and Tanaka (1989) *J. Geophys. Res.*, 94, 17,359; [16] Moore and Hodges (1980) *NASA TM 82385*, 266; [17] Plescia (1981) *Icarus*, 45, 586; [18] Schneeberger and Pieri (1991) *J. Geophys. Res.*, 96, 1907.

## SHALLOW MARTIAN DISCONTINUITIES: Davis, P.A. et al.

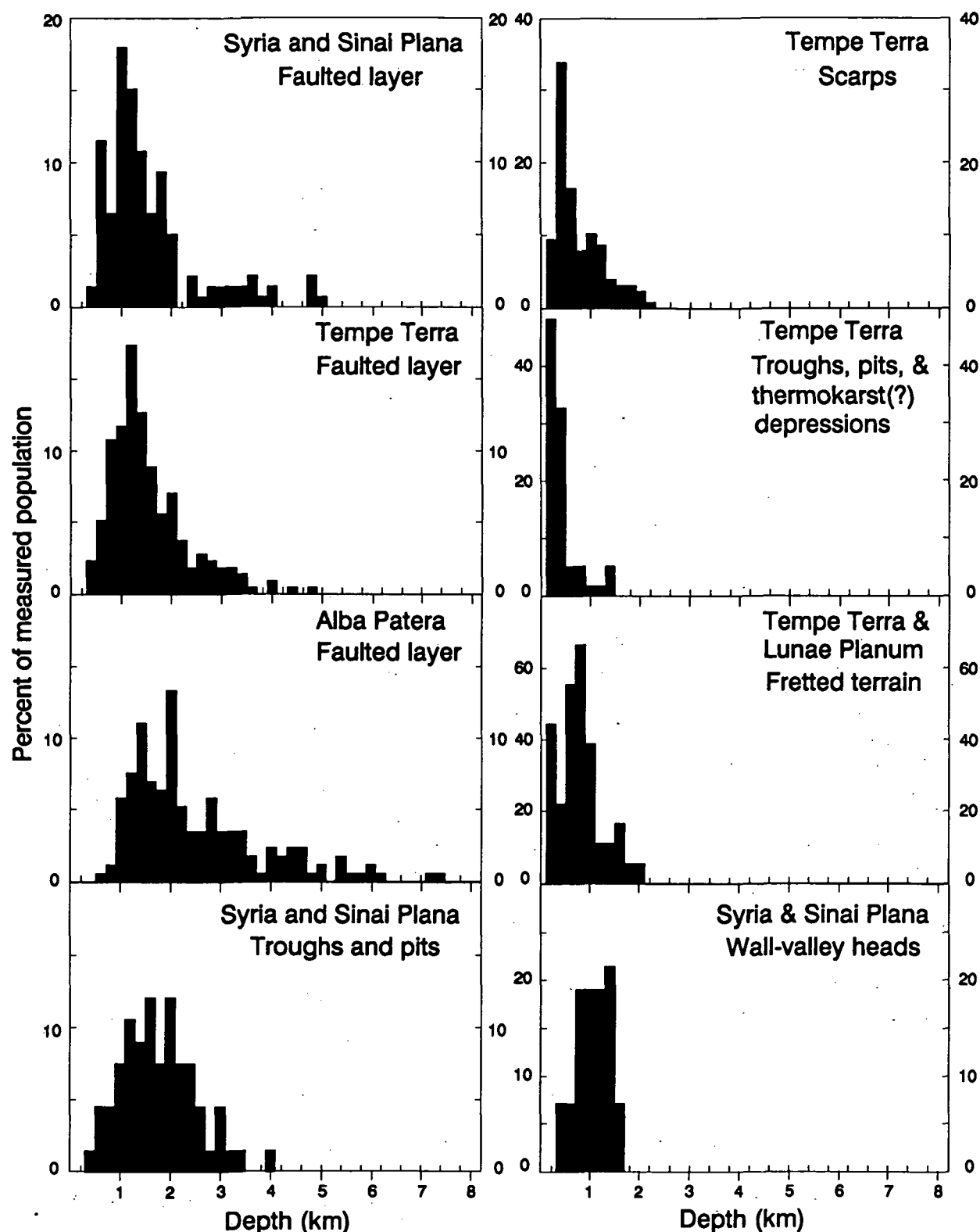


Figure 1. Calculated depths to the faulted layer and measured depths of various types of erosional scarps in several study areas in the Tharsis region of Mars.

464077

5189-91

LPSC XXIV 383

ABS. ONLY

N 9/43 462204

P-2

**CHARACTERISTICS OF ARACHNOIDS FROM MAGELLAN DATA** C.B. Dawson and  
L.S. Crumpler, Department of Geological Sciences, Brown University, Providence, RI 02912

**Introduction** Current high resolution Magellan data enables more detailed geological study of arachnoids, first identified by Barsukov et al. (1) as features characterized by a combination of radar-bright, concentric rings and radiating lineations, named "arachnoids" on the basis of their spider and web-like appearance. Identification of arachnoids in Magellan data has been based on SAR images, in keeping with the original definition. However, there is some overlap by other workers in identification of arachnoids, corona (predominantly bright rings), and novae (predominantly radiating lineations), as all of these features share some common characteristics. Features used in this survey were chosen based on their classification as arachnoids in Head et al.'s (2) catalog and on SAR characteristics matching Barsukov et al.'s original definition. 259 arachnoids have been currently identified on Venus (3), all of which were considered in this study. Fifteen arachnoids from different regions, chosen for their "type" characteristics and lack of deformation by other regional processes, were studied in depth, using SAR and altimetric data to map and profile these arachnoids in an attempt to better determine their geologic and altimetric characteristics and possible formation sequences.

**SAR Characteristics** Figure 1a shows a "type" region of arachnoids originally identified in Venera 15/16 data. Based on this study, the outer ring diameter of arachnoids ranges from 50-175km, most commonly falling between 100-125km. (Fig. 2a) Arachnoids are commonly multi-ringed structures with two to four rings, frequently occurring as arcs rather than complete rings. The radiating lineations have an average width of 1km and may extend for more than 200km, often curving to merge with lineations of regional deformation belts. (Fig. 1a,b) As most lineations are below current resolution capabilities, it is difficult to determine if the relief of these lineations is negative or positive; where visible, however, radar shadows would suggest a combination of both ridges and, more commonly, graben.

**Altimetric Characteristics** Magellan altimetry data shows that arachnoids are typically depressions (maximum 1 km deep) with a very shallow slope (Fig. 2b). The center of the bright rings does not always coincide with the center of the depression. Bright rings or arcs do not always have corresponding altimetric changes visible in profiles. The outermost ring may represent the beginning of a depression, an annulus, or may have no apparent topographic correlation at current resolution capabilities. In one example the actual depression begins 75km west of the outermost bright ring (C1MIDRP.30S207, (-25,211)), while the bright rings do not correspond to any specific feature visible in the profile. Altimetric profiles show small scarps in some of the depressions, suggesting that small-scale faulting has occurred; these scarps often correspond to bright arcs on the SAR images. A few arachnoids have profiles similar to that previously identified as typical of coroneae (4), although these arachnoids account for only a very small number of the overall arachnoid population.

**Geologic Characteristics** Arachnoids are typically found in clusters along deformation belts [(45,220), (-15,220), (45, 15)]. (Fig. 1) They are found in all latitudes, with no apparent relation between latitude and frequency. Small volcanic shields within arachnoids suggest related small-scale volcanism. Shields are typically <10km in diameter and occur both outside and, more frequently, inside the bright ring formation. Small volcanic flows are visible in some arachnoids, but appear to be related to the small shield fields. There is no apparent pattern to shield distribution within arachnoids, suggesting that they are not specifically correlated with any interior structure of the arachnoid. There is evidence of volcanism both predating and postdating subsidence: some flows show no correlation with current topography and are cut by rings and radiating lineations. In one case, the flow must have occurred before subsidence as it is unlikely that the flow would have moved upward out of the depression (FMIDRP.20S221); this would imply the occurrence of volcanic activity prior to final regional subsidence. Darkening and lack of lineations toward the center of some arachnoids suggests the occurrence of volcanism that postdates subsidence as well. Radiating lineations and bright rings seem to form concurrently, as lineations both cut and are cut by rings. Since some of the bright rings represent scarps and are thus related to

## CHARACTERISTICS OF ARACHNOIDS C.B. Dawson and L.S. Crumpler

subsidence, this would suggest that subsidence and formation of the radiating lineations occur simultaneously, with small-scale volcanism occurring throughout formation of the arachnoid.

**Interpretations/Conclusions** The high resolution Magellan data has allowed a much more detailed study of arachnoids than previous Venera data. Arachnoids show a complex history of formation of radar-bright concentric rings and radiating lineations during subsidence. The absence of arachnoids much greater than 200km in diameter or deeper than 1km suggests size restrictions in the formation of arachnoids. The shallow depression and lack of large-scale faulting seem to imply gradual rather than sudden subsidence, which may be a result of the gradual evacuation of an underlying magma chamber. The pattern of radiating lineations associated with arachnoids closely resembles that of terrestrial dike swarms. Calculations by McKenzie et al. (5) support that such lineations could be surface manifestations of Venusian dike swarms. Evacuation of the magma chamber through dikes would explain the lack of large-scale surface flows or volcanic edifices, and would be conducive to a gradual evacuation of the magma chamber.

### References

(1) V.L. Barsukov et al. (1986) *JGR*, 91, 378. (2) J.W. Head et al. (1993) in print. (3) J.W. Head et al. (1992) *JGR*, 97, 13153. (4) E. Stofan and J.W. Head (1990) *Icarus*, 83, 216. (5) D. McKenzie et al. (1992) *JGR*, 97, 15977.

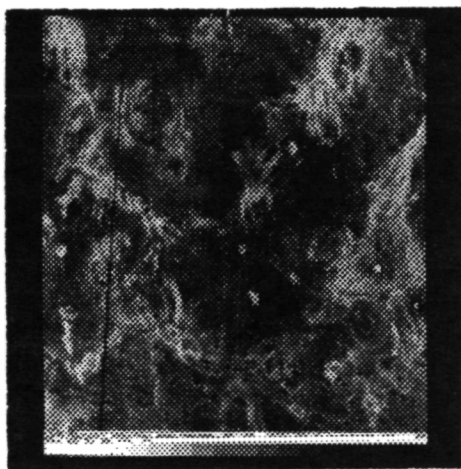


Figure 1a. Arachnoid "type" region identified by Venera 15/16. (C1MIDRP.45N011)



Figure 1b. Sketch map of radar-bright ring and lineation patterns in Fig. 1a.

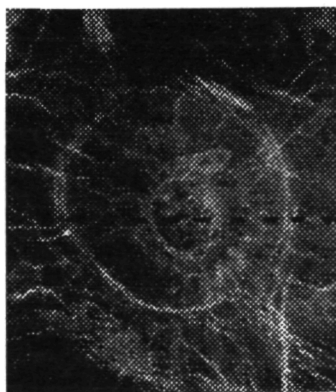


Figure 2a. Example of a "type" arachnoid, centered on (44, 14). (C1MIDRP.45N011)

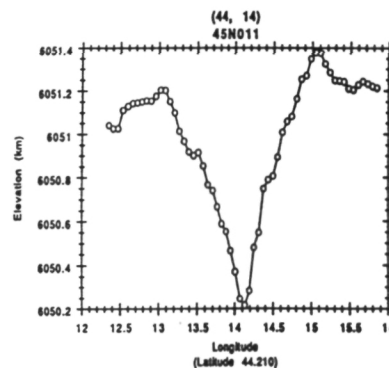


Figure 2b. Profile of arachnoid in Fig. 2a, along latitude 44.2 (shown by dotted line in Fig. 2a).

464079

5190-90  
ABS. ONLY

LPSC XXIV

385

94-12205

163410

P-2

## A METHOD TO DETERMINE ASTEROID POLES

G. De Angelis, Planetary and Space Science Division, Space Science Department, ESA/ESTEC, Keplerlaan 1, 2200 AG Noordwijk, The Netherlands.

**Introduction.** The determination of spin axis and shape is well known to be of fundamental importance for studies about the rotational and physical properties of asteroids. In particular, knowledge that the pole coordinate distribution is random or not could indicate the probable non-Maxwellian distribution of asteroid spin axes (see, e.g., [1]), while the distribution in terms of size and shape could place important constraints on the theories about the collisional history of some individual asteroids, of asteroid families, and of the asteroid population as a whole (see, e.g., [2], [3], [4], [5]). Many kinds of methods have been developed to determine pole coordinates. One is to use the epochs of maximum light in the observed photometric lightcurves and to calculate the number of synodic cycles between them. The synodic period changes with time in a way depending on the coordinates of the north pole, which so can be calculated. This method has been expressed in many ways, but the collective term "Epoch method" (E method) is used for all the pole determination methods that, like Photometric Astrometry, are based on observed epochs in the lightcurves. These methods are not based on any specified model of the asteroid, so from them you can derive no shape information. On the contrary, sidereal period and sense of rotation can be derived from these methods.

Another way to determine pole coordinates is to use the amplitudes and/or the magnitudes of the observed photometric lightcurves: if only the amplitudes are used this is an A method, if only the magnitudes this is a M method, and if you use both of them this is a AM method. The fundamental principle common to all these methods is the assertion of an amplitude-aspect angle and a magnitude-aspect angle relationship, based on some model of asteroid, usually a triaxial ellipsoidal model. With these methods the shape (model dependent) and poles can be derived, but the sidereal period and the sense of rotation cannot be found. The A, M and AM methods can be applied only to objects with very regular lightcurves. Each of these methods alone can provide only a part of the required information, and composite methods, realized by putting E, A and M techniques together, can be very useful both to give complementary information, and to give complementary constraint on pole coordinates. Many EA and EAM methods have been developed (see, e.g., [6], [7], [8]), but never these methods were really used together: every method is used separately, and not with a fit technique, but with trial poles and shape parameters as input. Only Michalowski and Velichko [9] used the E and the A information together, by linking the E and the A parts as elements of a nonlinear system of equations. In this paper a EA method is presented, from which it is possible to obtain the solution with no trial poles, but with a simultaneous least square fit on both the E and A part.

Results for rotational and shape parameters have been obtained for 18 asteroids: the value of the obtained parameters are generally in close agreement with those by other authors.

**Photometric Astrometry.** The changing relative geometry of the Sun, Earth and the asteroid (see, e.g., [6]) as they move in their orbits causes variations in the observed synodic period of rotation. The actual size and sign of these variations depend on the orientation of the spin axis and the sense of rotation, thus in principle the coordinates of the pole can be deduced by studying the changes in the synodic period.

The "Photometric Astrometry" method ([10]; [11]) was the first Epoch method to take this into proper account. A time shift of half the difference in astero-centric longitude of the Earth and the Sun is added to the number of rotational cycles. Synodic intervals between subsequent epochs are converted to sidereal periods, and the north pole giving the lowest mean deviation from the sidereal period is chosen.

The classical formula of the Photometric Astrometry ([11]; [12])

$$P_{sid} = \frac{\Delta T_c}{\Delta N \pm ((\Delta L / 360^\circ) + (\Delta S / 360^\circ) + \Delta n)} \quad (1)$$

has been used in this paper in a slightly changed version taken from Michalowski [13] and used also in Michalowski and Velichko [9]. Let "s" be a parameter denoting the sense of rotation (s=1 for prograde and s=-1 for retrograde rotation), and if we use the frame reference of the phase angle bisector (i.e., bisector of the angle between the asteroid-Sun and asteroid-Earth directions), the expression  $(\Delta L / 360^\circ + \Delta S / 360^\circ)$  can be replaced with  $(\Delta L / 360^\circ)$ , where L is the astero-centric longitude of the "sub phase angle bisector point", and so eq. (1) becomes

$$P_{sid} = \frac{\Delta T_c}{\Delta N + s ((\Delta L / 360^\circ) + \Delta n)} \quad (1a)$$

In this way, with simple calculations, it's possible to write eq. (1a) as

$$\Delta N + s ((\Delta L / 360^\circ) + \Delta n) - (\Delta T_c / P_{sid}) = 0 \quad (2)$$

If you have several lightcurves from different oppositions, you can choose pairs of them and substituting in eq. (2) the expressions for the parameters of this equation given in Michalowski [13] a set of nonlinear equations is obtained depending only on  $P_{sid}$ ,  $\lambda_p$  and  $\beta_p$ ,

$$f_l(P_{sid}, \lambda_p, \beta_p) = 0 \quad l=1, \dots, k \quad (3)$$

where "k" denotes the number of pairs of epochs. In this way the Photometric Astrometry consists in finding the solution of a set of nonlinear equations for the unknown parameters.

**Amplitude-Magnitude Method.** The fundamental principle common to all A and M methods is assertion of an amplitude-aspect or magnitude-aspect relationship, based on some model of the asteroid. Furthermore, a correction for the changing solar phase angle must be made. A triaxial ellipsoidal model is mostly used in these methods (for a wider discussion see,



## A METHOD TO DETERMINE ASTEROID POLES : G. De Angelis

e.g., Magnusson [6]).

In the present work it is used only the amplitude equation used in [6] (but the aspect angle  $\phi$  is the more usual Earth-referred aspect angle)

$$A = 1.25 \log \left[ \frac{(b/c)^2 \cos^2(\phi) + \sin^2(\phi)}{(b/c)^2 \cos^2(\phi) + (b/a)^2 \sin^2(\phi)} \right] + \beta_A \alpha \quad (4)$$

where  $A$  is the observed amplitude,  $\phi$  is the aspect angle,  $\alpha$  the phase angle,  $\beta_A$  the linear phase correction coefficient. For every lightcurve an expression is obtained

$$f_l(\lambda_p, \beta_p, b/a, b/c, \beta_A) = 0 \quad l=1, \dots, m \quad (5)$$

where  $m$  is the number of Amplitude-aspect relations.

Linking the two methods. From Photometric Astrometry it is obtained

$$f_i(P_{ast}, \lambda_p, \beta_p) = 0 \quad i=1, \dots, k \quad (3)$$

and from the amplitude-aspect relationship

$$f_l(\lambda_p, \beta_p, b/a, b/c, \beta_A) = 0 \quad l=1, \dots, m \quad (5)$$

If all these expressions are put together you obtain

$$f_i(P_{ast}, \lambda_p, \beta_p, b/a, b/c, \beta_A) = 0 \quad i=1, \dots, (k+m) \quad (6)$$

like in Michalowski and Velichko [9]. Now the parameters are obtained in a way different from that used in [9].

All these expressions (7) cannot be used all together if they are in this shape. Since the epoch and amplitude parts of the  $f_i$  are measured in different units, a procedure of standardization of the variables is needed. This is done simply by dividing each  $f_i$  by the standard deviation  $s$  of all the  $f_i$  of the same kind. This operation has to be made separately for each part (epochs and amplitudes). The new resulting variables are in the so called standard normal form

$$z_i = \frac{f_i}{s} \quad (7)$$

so they constitute a vector  $F=(z_1, \dots, z_{k+m})$  and the chosen parameters are those ones composing the vector  $X=(P_{ast}, \lambda_p, \beta_p, b/a, b/c, \beta_A)$  that minimizes the square norm of the vector  $F$

$$\|F\|^2 = \sum_{i=1}^{k+m} z_i^2 \quad (8)$$

In this way with a single simultaneous fit it is possible to obtain sidereal period, pole orientation, shape, amplitude-phase correction for an asteroid, and also the sense of rotation, making the fit first for  $s=1$  and then for  $s=-1$ , and finding for which value of  $s$  there is a solution.

**Results.** Pole and shape solutions have been obtained with this method for 18 asteroids: 9 Metis, 15 Eunomia, 16 Psyche, 22 Kalliope, 43 Ariadne, 44 Nysa, 55 Pandora, 79 Eurynome, 87 Sylvia, 130 Elektra, 201 Penelope, 511 Davida, 532 Herculina, 584 Semiramia, 624 Hektor, 694 Ekard, 951 Gaspra and 1862 Apollo. For all of them it has been possible to obtain a complete solution, and for many of them (9 Metis, 15 Eunomia, 22 Kalliope, 43 Ariadne, 87 Sylvia, 130 Elektra, 201 Penelope, 511 Davida, 532 Herculina, 624 Hektor, 951 Gaspra and 1862 Apollo) it has been even possible to remove the solution symmetry ambiguities present in asteroid pole solutions (see, e.g., [14]). For some of them (9 Metis, 43 Ariadne, 87 Sylvia, 624 Hektor, 951 Gaspra and for some aspects 532 Herculina and 1862 Apollo) this one is the first pole solution resolved from ambiguities. For sake of brevity it is not possible to describe the solutions for each individual asteroid in detail. The values of the parameters obtained for these asteroids are in close agreement with those by other authors.

**Conclusions.** The method presented in this paper allows to derive all the parameters ( $P_{ast}$ ,  $\lambda_p$ ,  $\beta_p$ ,  $a/b$ ,  $b/c$ ,  $\beta_A$  and sense of rotation) to describe the rotational and shape properties of an asteroid. All the parameters are derived by linking together the well-established techniques of Photometric Astrometry and Amplitude-Aspect relationship, and not with trial solutions, but with one only simultaneous least square fit, bypassing the problems given by each method taken alone.

The method has been applied to 18 asteroids. The values of the parameters obtained for these asteroids are in close agreement with those by other authors, some ambiguities have been resolved for the first time, and that is strongly encouraging for further applications and developments of this mathematical procedure.

**References.** [1] Harris A.W. and Burns J.A. *Icarus* 40, 115-144 (1979). [2] Tedesco E.F. and Zappalà V., *Icarus* 43, 33-50 (1980). [3] Dermott, S.F., Harris A.W. and Murray C.D., *Icarus* 57, 14-34 (1984). [4] Farinella P., Paolicchi P. and Zappalà V., *Astron. Astrophys.* 104, 159-165 (1981). [5] Lagerkvist C.-I. In *Highlights of Astronomy, Vol.6* (R.M. West, Ed.), pp.371-376. Kluwer, Boston, 1983. [6] Magnusson P., *Icarus* 68, 1-39 (1986). [7] Drummond J.D., Weidenschilling S.J., Chapman C.R. and Davis D.R., *Icarus* 76, 19-77 (1988). [8] Drummond J.D., Weidenschilling S.J., Chapman C.R. and Davis D.R., *Icarus* 89, 44-64 (1991). [9] Michalowski T. and Velichko F.P., *Acta Astron.* 40, 321-332 (1990). [10] Gehrels T., *Astron. J.* 72, 929-938 (1967). [11] Taylor R.C. In *Asteroids* (T.Gehrels, Ed.), pp.480-493. Univ. of Arizona Press, Tucson, 1979. [12] Taylor R.C. and Tedesco E.F., *Icarus* 54, 13-22 (1983). [13] Michalowski T., *Acta Astron.* 38, 455-468 (1988). [14] Zappalà V. and Knezević Z., *Icarus* 59, 436-455 (1984).

5191-20  
ABS ONLY

LPSC XXIV

387

N 94-372206

**Cathodoluminescence Properties of Components in Enstatite Chondrites.** John M. DeHart\* and Gary E. Lofgren<sup>+</sup>. \*Core Laboratories, 420 W. 1st St., Casper, WY 82601. +Mail Code SN2, Johnson Space Center, Houston, TX. 77058

**Introduction.** As a group, the enstatite chondrites are notable by the extremely low FeO content of most of their silicates. This property predisposes many of these materials to emit Cathodoluminescence (CL). Since examination of the CL properties of meteoritic components in ordinary and carbonaceous chondrites have proven to be a useful technique (1-3), we have initiated a survey of the enstatite chondrites in order to better characterize the chemical and physical properties of their luminescing phases. Because of the diversity encountered in this study, it is first necessary to describe the number and types of materials observed to emit CL in these meteorites.

**Experimental.** The meteorites listed in Table 1 were examined in this study. Two CL techniques were used. First, the initial survey work was conducted at low magnification using a Nuclide (now MAAS) Luminoscope mounted to a Wild MP binocular microscope equipped for photomicroscopy. The beam conditions used were  $14 \pm 1$  KeV and  $7 \pm 1$  milliamps, with the beam focussed to the diameter of the field of view of the microscope at 20x (approx. 1.25 cm). Photomosaics were produced for each section using Ecktar 1000 film and an exposure time of 15 to 30 seconds. Second, high magnification (400x) photos were obtained of individual components of interest by mounting a 35mm camera to the optical system of the Cameca Camebax microprobe located at the Johnson Space Center. Beam conditions used were 15 KeV and 600 nA. Ecktar 1000 film was also used, but exposure times of 6 minutes were necessary to produce a useful image.

**Observations.** The components in E chondrites that produce CL can be divided into four broad categories. These are; 1.) Clasts and aggregates, 2.) Chondrules, 3) matrix components, and 4.) refractory objects. Components in each category are discussed below. **END**

**Clasts and aggregates.** These objects have an irregular, often elongate outline, and can be divided into metal/sulfide assemblages and silicate assemblages. Most of the metal-sulfide objects are nonluminescent, but several are associated with grains of red luminescing enstatite, whitlockite that emits a bright yellow CL, or blue luminescing enstatite. Those metal/sulfide assemblages associated with blue luminescing pyroxene appear to have a range in the abundance of pyroxene, from containing a few randomly oriented "whiskers" of blue enstatite less than 3 microns in diameter to being predominately composed blue luminescing enstatite with interstitial metal and sulfide., however the second case appears limited in occurrence to EL chondrites.

The silicate clasts and aggregates can be divided into two distinct groups. First are pyroxenite clasts. These clasts are composed of; (1) blue luminescing enstatite that is sometimes associated with a red luminescing albite-normative glass, (2) microcrystalline blue luminescing enstatite (grain size <10 microns) set in a red luminescing, pyroxene-normative mesostases, or (3) a red luminescing enstatite that contain 5 to 10  $\mu$ m -sized oval regions of diopside. Second, there are clasts and aggregates of red luminescing pyroxene that often poikilolithally enclose a brighter red luminescing olivine. These assemblages are also occasionally associated with overgrowths of blue pyroxene after red pyroxene, an albite-normative glass, or a blue luminescing plagioclase-normative glass.

**Chondrules.** Although there are a few instances of similar chondrules, the CL properties of most of the chondrules in enstatite chondrites are clearly different compared to the FeO-poor type A chondrules observed in the ordinary and carbonaceous chondrites. Although occasional barred and radial chondrules were observed, porphyritic chondrules are the dominant textural type as in other chondrite groups. The following are the different types of chondrules according to their observed CL.

1. Red grains in a dull red mesostases. This is the dominant type of chondrule observed in most of the enstatite chondrites, especially the EH3 and EH4 classes. The grains are most often En98-99 enstatite occasionally enclosing Fo98-99 olivines. The mesostases has extremely high Na<sub>2</sub>O content (4 to 9 weight percent).

2. Similar to the chondrules above, but the red luminescing pyroxene encloses a blue luminescing phase, most often a nearly pure (En99.5 and greater) blue luminescing pyroxene. The different chemistry and unique physical properties of the enclosed blue pyroxene strongly suggest these are relict grains (4). A few instances of blue luminescing olivines enclosed in red luminescing pyroxene were also observed in PCA82518 (EL4).

3. Red luminescing pyroxenes enclosed by a blue luminescing, plagioclase-normative mesostasis. The composition and CL of the phases in these chondrules compare well to the type A3 chondrules in ordinary chondrites (1).

# CL of Enstatite Chondrites, DeHart, J.M. and Lofgren, G.E.

4. Blue luminescing enstatite (>En99.5) associated with a Na<sub>2</sub>O-rich dull-red luminescing mesostasis. This enstatite is clearly different than the relict pyroxene described above, and are found only in chondrites indentified as EL3s.

5. Red luminescing grains associated with a yellow luminscing mesostasis. These chondrules compare well to the type A1 and A2 chondrules observed in the ordinary chondrites.

**Matrix Components.** The interchondrule matrix in both E3 and E4 chondrites is clastic in nature and composed of smaller clasts (<50  $\mu$ m) of the types described above, smaller, isolated grains or fragments of red and blue luminescing enstatite, small regions (approx. 20  $\mu$ m in diameter) of dull-blue-luminescing SiO<sub>2</sub> and small pockets of a dull-red luminescing albite-normative glass. The proportions of each type of phase appear to vary with chemical group. Blue luminescing phases, principally enstatite, is the predominant matrix componant in the EL3 and EL4 chondrites, and is the only identifiable matrix component in LEW87223 (EL3).

**Refractory Objects.** Some components in the E3 chondrites are assemblages of refractory minerals. Although CAIs and refractory objects were previously reported as being rare in E chondrites, their unique CL made them easily identifiable in all sections of E3s, and are especially abundant in LEW87223 (EL3). Assemblages identified are;

1 Refractory chondrules with either a.) blue luminescing olivine and/or pyroxene set in a yellow-luminescing, anorthite-normative mesostases, or b.) a red luminescing spinel enclosed by laths of blue-green plagioclase set in a mesostasis of a duller blue-green luminescing, dendritic fassaite and nonluminescent glass.

2. Spherical assemblages of dendritic to subhedral blue luminescing pyroxene set in a yellow-luminescing anorthite-normative mesostasis. These objects differ from the chondrules described above by having many small dull-blue or dull-red luminescing SiO<sub>2</sub>-rich ovoid inclusions scattered in them, and is the type of object found in all E3 chondrites.

3. Concentrically layered assemblages of refractory materials (anorthite and enstatite) and/or metal. These objects are found only in LEW87223 (EL3).

**Conclusions.** The CL properties of the phases in enstatite chondrites highlight subtle, but important differences that are difficult to identify or study by other techniques, such as electron imaging or optical petrographic methods. Because most of the silicate phases emit some type of CL, examining the CL properties of these phases in enstatite chondrites can be an extremely powerful tool in deciphering their petrographic and petrologic relationships.

**REFERENCES.** (1) DeHart et. al. (1992) *GCA*, Vol. 56, pp. 3701-3807. (2) Steele, I.M. (1989) *GCA*, Vol. 53, pp. 2069-2079. (3) Keck, B. D. and Sears D.W. G. (1987) *GCA*, Vol. 51, pp. 3013-3021. (4) Logren G.E. and DeHart, J.M. (1992) *XXIII Proc. LPSC*, pp. 801-802.

Table 1  
Listing of Meteorites used in this study.

Meteorite	Chem. Class.	Weath. Class
Quinzhen	EH3	A
ALH84170	EH3*	B
LEW87223	EL3**	C
MAC88136	EL3	A
Indarch	EH4	A
ALH84206	EH4*	A/B
PCA82518	EL4**	B
ALH85159	EH4*	B/C
EET83254	EH4*	Ce
RKPA80259	EL5	B/C
ALHA81021	E6	A

\* Chemical classification tentative, and based on comparison of the CL properties to other E-chondrites of known chemical group.

\*\* Chemical classification based on same as above and the INAA results of Chin and Sears (this volume).

46087  
5192-91  
ABS ONLY  
10-9-42-12207  
2

CLASSIFICATION OF MARTIAN DELTAS; R.A. De Hon, Department of Geosciences, Northeast Louisiana University, Monroe, LA 71209.

Introduction. Water-bourne sediments in streams are deposited, upon eventual cessation of flow, either as deltas or as alluvial fans or plains. Deltas and alluvial fans share a common characteristic; both may be described as depositional plains at the mouth of a river or stream. A delta is formed where a stream or river deposits its sedimentary load into a standing body of water such as an ocean or lake. An alluvial fan is produced where a stream loses capacity by a greatly decreased gradient. A delta has subaerial and subaqueous components, but an alluvial fan is entirely subaerial. In terrestrial conditions, deltas and alluvial fans are reasonably distinct landforms. The juxtaposition of concomitant features composition and internal structure are sufficiently explicit as to avoid any confusion regarding their proper identification.

On Mars, the recognition of deltas and their distinction from alluvial fans is made difficult by low resolution imaging. Further, although it may be demonstrated that standing bodies of water existed on the surface of Mars, many on these bodies may have existed for extremely short periods of time (a few days to months ~~and~~); hence, distinctive shoreline features were not developed. Thus, in an attempt to derive a martian classification of deltas, the inclusion of wholly subaerial deposits may be unavoidable.

A simple, broad, morphologic classification of martian deltas, based primarily on planimetric shape, includes (1) digitate deltas, (2) fan-shaped deltas, and (3) re-entrant deltas. A fourth, somewhat problematical class includes featureless plains at the end of many valley systems.

Digitate deltas. Digitate deltas are characterized by parallel, longitudinal bars projecting from the valley mouth onto the basin floor. Terrestrial digitate deltas such as that of the modern Mississippi River, are composed of multiple, branching, distributary channels. Longitudinal bars of digitate levees are formed by accretion of suspended load as it spreads laterally under plane-jet flow [2]. Possible martian digitate deltas consisting of a single, leveed channel are found in Terra Sirenum [3] and Elysium Planitia [4] at breaches in basin walls. An alternate interpretation as lateral moraines is considered unlikely.

Fan-shaped deltas. As a broad classification, this includes classical deltaic forms ranging from the Gilbert-type, lacustrine delta and marine Nile delta to wave- and current-modified forms of lobate and arcuate deltas. Gilbert-type deltas are built by axial-jet flow and complete mixing very close to the mouth [5]. Martian examples include (1) a small delta on the interior wall of a crater at lat. 8.7° S long. 159.4° in Terra Sirenum and (2) a low relief, dissected fan at the mouth of Maja canyon on the western edge of Chryse Planum [6]. In the absence of reliable indicators of deposition

## MARTIAN DELTAS: De Hon R.A.

into standing water, similar deposits may be fan-deltas or alluvial fans.

Re-entrant deltas. Re-entrant or estuarine deltas, such as those of the Susquehanna and Seine Rivers, consist of fluvial sediments filling embayments in the coast line. The planimetric shape of estuarine deltas is controlled by the enclosing topography. Martian examples of re-entrant deltas include plains in re-entrants at the mouths of valleys dissecting the highland-northern plains boundary scarp.

Featureless plains. Many valleys on Mars merge with featureless plains. Some valleys are partially buried by prograding basin sediments. It is uncertain whether deposition is subaerial or subaqueous. The formation of featureless plains at the mouths of valleys, on Earth and Mars, appears to be associated with a continuous low gradient with no distinct break in slope between valley floor and depositional surface.

Discussion. The morphology of a delta is a function of the interdependence of competing environmental influences, including sediment load of the stream, tectonic stability of the coast density contrast between inflow and standing water, and currents, waves, and tides in the basin. The morphologies of martian deltas reflect conditions prevalent on the surface at the time of formation and subsequent modification. Although a range of deltaic forms is present, they are simple variants, suggesting a restricted range of environmental factors. Most martian deltas are high-constructive deltas [7] in which fluvial action dominates; most are small by terrestrial standards; and most indicate short-lived inflow into basins of standing water without significant wave or current action.

High-destructive deltas, in which current and wave energy in the basin are dominant factors [7], are not obvious on Mars. Such forms require current or wave action which is unlikely in small, short-lived catchments. Presumably, if an ocean did exist in the northern plains [8, 9], deltaic sedimentation along the highland-northern plains boundary may have been masked by later burial, by subsequent thermokarst or glacial modification, or by complete destruction by interbasinal currents.

## References:

- [1] De Hon R.A. and E.A. Pani (1992) Earth, Moon, and Planets 56, 95-122.
- [2] Morgan J.P. (1970) Journ. Geol. Edu. 18, 107-117.
- [3] De Hon R.A. (1989) 4th International Conf. on Mars, 90-91.
- [4] Mouginiis-Mark P J. (1985) Icarus 64, 265-284.
- [5] Ritter D.F. (1978) Process Geomorphology, 603 p
- [6] Rice J.W. et al. (1988) Lunar Planet. Sci. Conf. XIX, 976-977.
- [7] Scott A.J. and W.L. Fisher (1969) Delta Systems in the Exploration of Oil and Gas, Univ. of Texas, Bur. Econ. Geol., Austin, 10-39.
- [8] Parker T.J. et al. (1987) NASA Tech. Mem. 89971, 319-324.
- [9] Baker V R. et al. (1990) Lunar Planet Sci. Conf. XXI, 40-41.

464088 5193-90  
 ABS-ONLY  
 N946P2208

# Fe/Mn CONSTRAINT ON PRECURSORS of BASALTIC ACHONDRITES.

Jeremy S DELANEY; Joseph S BOESENBERG; Dept Geological Sciences, Rutgers University,  
 New Brunswick, NJ08903

Most achondritic meteorites have Fe/Mn ratios that are lower than those of carbonaceous chondrites and of course are lower than the solar system abundance ratio of these elements [1]. Models of the origin of achondritic assemblages must therefore account for these ratios. Fe/Mn ratios are suggested to be distinctive for samples from each achondrite parent body [2] and for the Earth and Moon, but the correspondence between the Fe/Mn systematics of achondrites and chondritic precursors is unclear. Most models of achondrite genesis involve magmatic differentiation of chondritic precursors. The Fe/Mn difference between achondrites and chondrites is particularly significant since Fe and Mn are geochemically similar elements with similar partitioning behavior in familiar magmatic systems and are generally coupled during crystal-liquid fractionation. In contrast, however, Mn is more volatile than Fe in a nebular setting. Variation of Fe/Mn ratios based on the relative volatility of these elements in the early nebula provides a constraint for models by which the basaltic achondrites (with Fe/Mn ratios  $\approx$  25-50) are derived from mixtures of nebular components that were enriched in volatile components such as Mn [3]. However, such volatile enriched components have not been identified in chondrites. When the abundance in achondrites of elements of similar volatility is examined, anomalies appear [4,5]. For example, Na is massively depleted in basaltic achondrites when compared to Mn. These anomalies might be explained using current models but the alternative hypothesis, that Fe/Mn ratio is controlled not by nebular volatility constraints, but by planetary differentiation should be explored.

**REDOX DRIVEN FRACTIONATION:** Source-region, crystal-liquid fractionation models for achondrites are based on indirect evidence that oxygen fugacities were close to the iron-wüstite buffer, enabling the production of both FeO-bearing silicates and limited metallic iron. At oxygen fugacities below iron-wüstite, however, conventional magmatic processes are modified by the effect of metal fractionation. If metal occurs at, or above, the solidus of an achondrite precursor system, then metal-silicate fractionation will drastically modify the oxidized Fe content of the silicate fraction and hence the Fe/Mn ratio of the silicates. Thus redox driven removal of metal will reduce the Fe/Mn ratio of a silicate assemblage. Although redox modification of Fe/Mn is recognised in ureilites [6] the application of redox exchange models to other achondrite suites has been limited. In carbonaceous chondrites typical Fe/Mn ratios are 90 to 150 similar to, or higher than, the solar system value of 97 [1]. Euclites, howardites and diogenites have Fe/Mn ratios between 30 and 45. If basaltic achondrites ultimately evolved from a precursor material with solar system average composition then Fe-Mn fractionation occurred. Partial melting experiments using a CM-chondrite composition [7] carried out at  $fO_2$  slightly below the iron-wüstite buffer, produced little difference between the precursor Fe/Mn and that of the coexisting 'achondritic' magma, presumably because relatively little iron metal was produced. If, however, melting of a carbonaceous chondrite occurred under more reducing conditions, fractionation of metallic iron could alter these results. Murchison contains 1.85%wt of elemental C [8]. Initial melting of such material may therefore be buffered by the reaction  $C + FeO = CO + Fe$ , rather than the iron-wüstite buffer, at least until the carbon is exhausted. If all the carbon present reacted to reduce FeO, about 11%wt FeO in Murchison would be reduced to Fe. This is almost half the FeO in Murchison and is equivalent to reduction of Fe/Mn from about 110 to about 55-60. Reduction of FeO to Fe by the reaction  $C + FeO = CO + Fe$  can therefore reduce the Fe/Mn of the silicate fraction dramatically. If the reaction involved the production of  $CO_2$  as well, even greater reduction of Fe and the Fe/Mn ratio would occur. Preliminary experiments on a CM analogue system [Boesenberg; in progress] indicate that melting of high Fe/Mn material under very reducing conditions produces low ratios (5-60) at all temperatures from 1180 to 1550°C.

Reduction of a CM precursor does not alter any cosmochemically significant ratios except those ratios involving Fe (and Ni). Thus Mg/Si, Ca/Al and refractory/volatile ratios remain at generally

Delaney & Boesenberg: Fe/Mn in achondrites

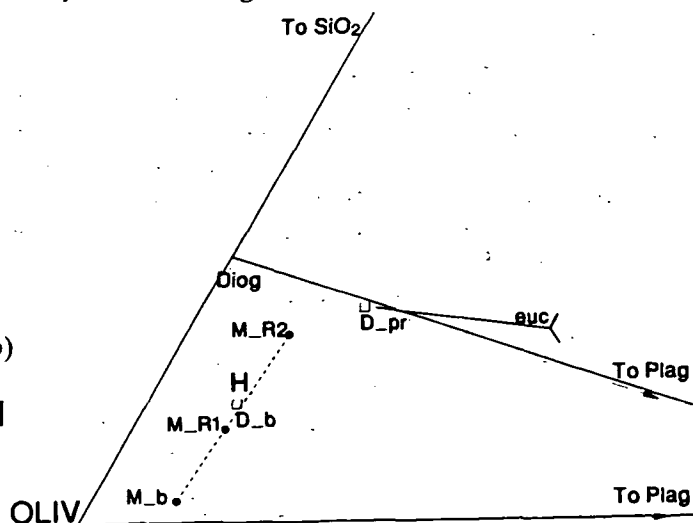
solar system values. Of course, the  $\text{Fe}/(\text{Fe} + \text{Mg})$  ratio is significantly reduced. Reduction of a CM host provides a better match for the eucrite source region than the H-chondrite model of [4]. Reduction of metal from a CM bulk composition, leaves the  $\text{Mg}/\text{Si}$  ratio unaffected although the silicate portion becomes more pyroxene normative. This is of particular importance for the basaltic achondrite suite as they are comprised of basalts approximating the peritectic point in the olivine-plagioclase- $\text{SiO}_2$  system [9] and orthopyroxenites. Olivine in basaltic achondrites is rare, either because it was seldom excavated by the impacts that sampled the basaltic achondrite parent body, or because olivine was not as abundant as would be expected for simple melting of a chondritic precursor. Reduction of metal from a CM-like precursor reduces the amount of FeO available to form olivine, increasing the normative pyroxene content of the silicates and also reduces the discrepancy between the Fe-Mn systematics of the most plausible chondritic precursors and the observed achondrites (Fig. 1). Source region compositions that are capable of yielding both diagenetic assemblages and eucritic assemblages in the abundance seen in the basaltic achondrite suite are much more tightly constrained than those capable of yielding only eucrites. Source regions that are more silica normative than C-chondrites are required. Clearly this reduction model provides a potentially powerful means to generate the required compositions. The main anomaly of this model lies in the  $\text{Fe}/(\text{Fe} + \text{Mg})$  ratio of the silicate portion ( $\approx 0.25$ ), but this might be controlled by crystal-liquid fractionation at higher oxygen fugacities

Bulk compositions estimates of the source region of basaltic achondrites are typically more  $\text{SiO}_2$  normative than bulk CM chondrites [4,5] and are also more appropriate for the production of abundant diogenites and eucrites with relatively minor intermediate compositions that are typical of howardites and polymict eucrites. Remarkably the model compositions of the EPB compositions based on trace elements are almost colinear with the reduction trend for CM chondrites when projected into the ol-plag- $\text{SiO}_2$  pseudoternary [9]. Reduction of a Murchison-like precursor, implies the presence of at least 8.5% metallic Fe in the parent body if all C were oxidized as described.

**CONCLUSIONS:** If partial melting of CM-composition material is buffered by C-CO or C- $\text{CO}_2$  reactions until the original C content of the CM material is exhausted, removal of abundant metal from the melts will reduce the  $\text{Fe}/\text{Mn}$  of the silicate fraction from the original high solar system ratio ( $\approx 100$ ) down to values that are compatible with the compositions needed in the eucrite source regions. This reduction also increases the normative  $\text{SiO}_2$  of the silicate and produces a bulk silicate composition similar to independent EPB estimates. The melt fraction may then act as the source region for eucritic/diagenetic assemblages with melt buffering probably close to the iron-wüstite buffer. Achondrite and some planetary  $\text{Fe}/\text{Mn}$  ratios, therefore, need not reflect nebular volatile/refractory fractionation, but are probably a consequence of early metal-silicate fractionation caused by oxidation of all or part of the parent body's carbon budget

REFERENCES: [1] Anders & Ebihara (1988) GCA 46; [2] Laul & Schmitt (1973) PLSC 4; [3] Ganapathy & Anders (1978) PLPSC 8th; [4] Morgan et al (1978) GCA 42; [5] Dreibus & Wänke (1980) Z. Naturforsch 35a; [6] Goodrich C (1992) Meteoritics 27; [7] Jurewicz et al, (1992) GCA in press; [8] Jarosewich (1990) Meteoritics 25 [9] Longhi & Pan (1988) PLPSC 18

FIGURE 1: Detail of Ol-plag- $\text{SiO}_2$  pseudoternary diagram [9] showing composition change of bulk CM-silicate ( $M_b$ ) after reduction by C to form CO ( $M_{R1}$ ) or  $\text{CO}_2$  ( $M_{R2}$ ). EPB estimates by [4] "H" and [5] "D\_b" and the eucrite peritectic composition are also shown.



464090

594-91  
ABS ONLY

LPSC XXIV

393

N 94612/209

# COMPOSITIONAL HETEROGENEITY WITHIN A DUMBBELL-SHAPED APOLLO 15 GREEN GLASS: EVIDENCE FOR SIMULTANEOUS ERUPTION OF DIFFERENT MAGMAS;

J. W. Delano, Department of Geological Sciences, State University of New York, Albany, NY 12222

The Apollo 15 green glasses that occur most prominently in 15425, 15426, and 15427 consist of compositionally distinct groups [1-7]. The six groups that have thus far been defined [5-7] are thought to represent different batches of magma [1,11] that were erupted as fire-fountains, probably at different times in lunar history; although isotopic analyses of representative glasses within some of these groups have not yet found any differences in age at the  $\pm 100$  Ma precision [8]. While the petrogenesis of these picritic magmas has been contentious [e.g., 1,2,4,5,6,7,9,10,11], the discovery of a compositionally heterogeneous, dumbbell-shaped green glass raises additional questions and problems about their origin.

Figure 1 shows a dumbbell-shaped Apollo 15 green glass that was handpicked from 15427,67. Its shape could be either the result of (a) spin-induced fission of a single droplet or (b) accretion of two droplets. The compositional heterogeneity observed within this sample is most readily consistent with the latter view. This sample was ground, polished, and analyzed by high-precision electron microprobe techniques involving the following conditions: 15 keV acceleration potential; 20-micron beam diameter; 50 nA specimen current; 300-second count-time per element per analysis for Fe, Al, Na, K, and S; 150-second count-time on both backgrounds for each element per analysis. At the time of writing this abstract, 280 5-element analyses of this sample have been completed in order to construct the map shown in Figure 1. For the purposes of this report, the relative proportions of Fe and Al will be discussed since these two elements show the clearest evidence for compositional heterogeneity within this volcanic glass. With the operating conditions listed previously, a typical analysis for Fe and Al yielded about 370,000 and 860,000 counts above background, respectively, resulting in a relative error for Fe and Al of  $\pm 0.04$  wt. % and  $\pm 0.01$  wt. %, respectively.

Figure 1 shows a preliminary contour map of this green glass using observed values of the  $\text{FeO}/\text{Al}_2\text{O}_3$  ratio (by weight). Since the values for this ratio varied typically between 2.50 and 2.63, only the last two digits are shown in Figure 1 (e.g., "50-54" means that the ratio varies between 2.50 and 2.54). However, Figure 1 is only an approximation to the actual heterogeneity within this glass since the A-A' traverse (Figure 2) displays a complex interfingering on the A-side of the major compositional boundary separating the "60-63" region from the "50-54" region. Mixing is also evident in the lower left portion of the glass where the compositional geometry is complex. This, and other, evidence for mixing between two melt compositions in this dumbbell-shaped glass suggests that two droplets of hot melt collided and were quenched before homogenization could occur. Based on a modified Stefan-Boltzmann equation [12], this 525x260-micron glass would have cooled from its liquidus temperature of about 1410°C [13] at a rate of at least 1000°C/second in a vacuum. At this high cooling rate, the complex interfingering of compositions within this glass may be due more to turbulent mixing caused by the collision of two melt droplets having low viscosity (about 5 poise) than to chemical diffusion. Less probable alternatives to this view might include: (a) collision between a soft melt droplet and a pre-existing glass; or (b) incorporation of a pre-existing piece of green volcanic glass into a later fire-fountaining event and its partial dissolution in the later magma.

The significance of this compositionally heterogeneous, dumbbell-shaped green glass lies principally in the surprise at its existence. The major-element compositions of all analyzed regions within this sample indicate that it belongs to Group A green glasses [1]. Steele and co-workers [5,6,7] have shown that the Group A green glasses, which were defined originally on the basis of major elements only [1,3], actually consists of two sub-groups that are distinguishable on trace-element abundances, principally Sm and other rare earth elements. The data of Steele [5] suggest that these two sub-divisions of the group A green glasses may also be resolvable using high-precision analyses for Fe and Al, as in the current investigation. Although currently speculative, the high ratios in Figure 1 may correspond to the high-Sm group A magma of Steele [5], while the low ratios in Figure 1 may correspond to the low-Sm group A magma of Steele [5]. Ion microprobe analyses would be capable of testing this hypothesis. Nonetheless, the current data seem to show that two volcanic melt droplets collided and merged during an eruption. Either this requires that (a) the magma being emitted from a single vent was compositionally varying on a time-scale of a few minutes (e.g., the ballistic flight-time of a spherule in the lunar vacuum ascending to an altitude of 5 km and falling back to the lunar surface is 2.6 minutes) or (b) two fire-fountaining events occurred simultaneously, and in close proximity, so that droplets from one eruption collided with droplets from another. In either instance, this sample raises questions about



## APOLLO 15 GREEN GLASS: Delano J. W.

the compositional uniformity of magmas during individual eruptions. This will have importance in discussions not only for lunar volcanic glasses but also for mare basalts.

REFERENCES: [1] Delano (1979) Proc. Lunar Planet. Sci. Conf. 10, p. 275-300. [2] Delano and Lindsley (1982) Lunar Planet. Sci.-XIII, p. 162-163. [3] Ryder (1986) Lunar Planet. Sci.-XVII, p. 738-739. [4] Galbreath et al. (1990) Geochim. Cosmochim. Acta, 54, p. 2565-2575. [5] Steele (1990) M.Sc. Thesis, Washington Univ., St. Louis, 201 pp. [6] Steele et al. (1990) LPI Tech. Rpt. 90-02, p. 62-63. [7] Steele et al. (1992) Geochim. Cosmochim. Acta, 56, p. 4075. [8] Spangler et al. (1984) Proc. Lunar Planet. Sci. Conf. 14, p. 487-497. [9] Grove (1981) Proc. Lunar Planet. Sci. Conf. 12, p. 935-948. [10] Hughes et al. (1988) Geochim. Cosmochim. Acta, 52, p. 2379-2391. [11] Steele et al. (1991) Lunar Planet. Sci.-XXII, p. 1317-1318. [12] Arndt et al. (1984) Proc. Lunar Planet. Sci. Conf. 15, p. 225-232. [13] Delano (1990) Proc. Lunar Planet. Sci. Conf. 20, p. 3-12.

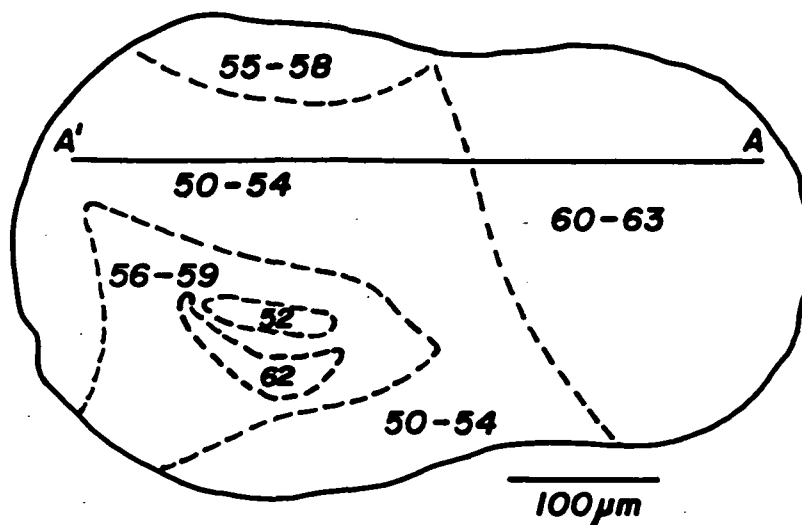


FIGURE 1

Compositional map of the Apollo 15 green glass showing values for the  $\text{FeO}/\text{Al}_2\text{O}_3$  ratio (by weight). Within this sample, the ratio typically varies between 2.50 and 2.63. The numbers shown refer to the two digits to the right of the decimal point (e.g., "50-54" means that the ratio lies between 2.50 and 2.54). The true compositional variation within this green glass is more complex than indicated by this approximation. The map is based on analyses of 280 spots on this glass by electron microprobe.

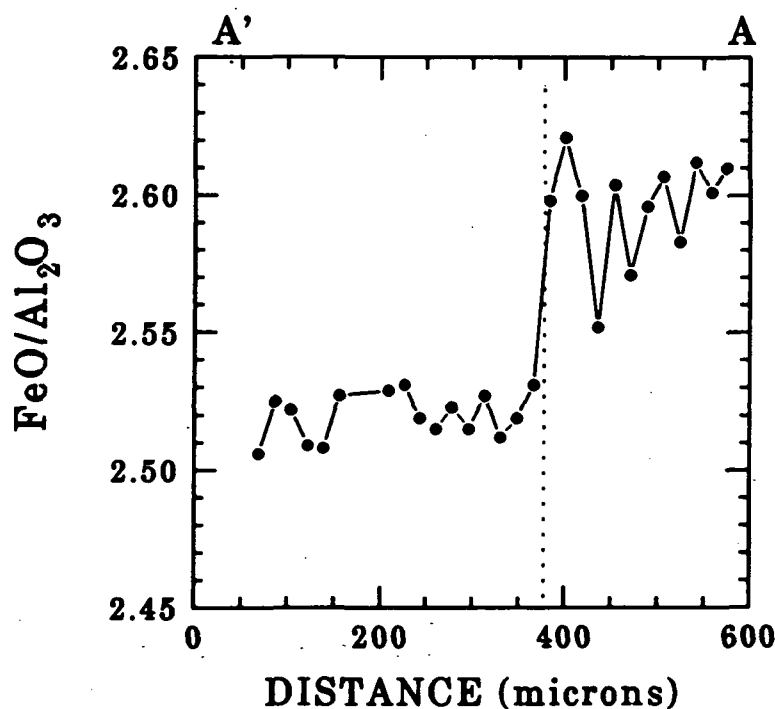


FIGURE 2

Traverse along the A-A' line (refer to Figure 1) showing the variation of the  $\text{FeO}/\text{Al}_2\text{O}_3$  ratio in this Apollo 15 green glass. Note that the boundary between the two sides of the dumbbell-shaped glass, although prominent in this traverse, is characterized by an interfingering of compositions that becomes most apparent near the boundary. The location of the boundary illustrated in Figure 1 between the "60-63" region and the "50-54" region is indicated by the vertical dotted line in Figure 2.

# OXIDATION STATE OF THE EARTH'S UPPER MANTLE DURING THE LAST 3800 MILLION YEARS: IMPLICATIONS FOR THE ORIGIN OF LIFE.

J. W. Delano, Department of Geological Sciences, State University of New York, Albany, NY 12222

*"The gossamer web of life, spun on the loom of sunlight from the breath of an infant Earth, is Nature's crowning achievement on this planet." [1]*

A popular, as well as scientifically rigorous, scenario for the origin of life on Earth involves the production of organic molecules by interaction of lightning (or other forms of energy) with a chemically reducing atmosphere in the early history of Earth [e.g., 2-7]. Experiments since the 1950's have convincingly demonstrated that the yield of organic molecules is high when the atmosphere contains molecular hydrogen, methane, ammonia, and water vapor. Additional work has also shown that such a highly reducing atmosphere might not, however, have been sufficiently long-lived in the presence of intense solar ultraviolet radiation [e.g., 8, 9] for life to have formed from it. One way of maintaining such an atmosphere would be to have a continual replenishment of the reduced gases by prolonged volcanic outgassing from a reducing Earth's interior. The length of time that this replenishment might need to continue is in part constrained by the flux of asteroids onto the Earth's surface containing sufficient energy to destroy most, if not all, life that had developed up to that point in time. If a reducing atmosphere is a key ingredient for the origin of life on Earth, the time of the last environmental sterilization due to large impacts would be an important constraint. In a deep marine setting (e.g., hydrothermal vent), the last global sterilization might have occurred at 4200-4000 Ma [14]. On the Earth's surface, the last global sterilization event might have occurred at 4000-3700 Ma [14-16]. If these are meaningful constraints, how likely is it that a reducing atmosphere could have survived on the Earth until about 3800 Ma ago? Due to the importance of replenishing this atmosphere with reducing components by volcanic outgassing from the mantle, geochemical information on the history of the mantle's oxidation state would be useful for addressing this question. Geochemical and experimental data discussed in this abstract suggest that extrusive mafic volcanics derived from the upper mantle have had oxidation states near the fayalite-magnetite-quartz buffer throughout the last 3800 Ma. At magmatic temperatures, the gases released from volcanoes having this oxidation state would have been, as they are today, composed dominantly of carbon dioxide and water vapor [e.g., 17-20], and hence would not contain the ingredients for maintaining a reducing atmosphere. Consequently, geochemical data do not favor the survival of a reducing atmosphere until about 3800 Ma. Alternative venues and pathways for the origin of life need to be investigated (e.g., hydrothermal vents along oceanic ridges) [21-25].

To constrain the oxidation state of mafic volcanics throughout the last 3800 Ma of Earth history, a new method will be relied upon that still needs additional experimental calibration. The principal concept of this approach is the following: the abundance of chromium (Cr) in a spinel-saturated, mafic magma is a strong function of oxidation state and temperature [e.g., 26, 27]. Experimental data conducted during the current investigation, as well as that from earlier workers [26, 27], has been used to define the IW (iron-wustite) and FMQ (fayalite-magnetite-quartz) buffers in Figure 1. The parameter MgO in Figure 1 is a proxy for temperature. The two groups of whole-rock data plotted in Figure 1 show the compositions of mid-ocean ridge basaltic glasses [open circles near FMQ; data from 28-34] and lunar mare volcanics (half-filled circles near IW). These data indicate, in agreement with other independent methods [e.g., 35-37], that modern terrestrial volcanics are relatively oxidizing (i.e., FMQ), whereas lunar mare volcanics are reducing (i.e., IW).

This approach can also be applied to older mafic volcanics in order to infer their *original* oxidation state, if subsequent metamorphism has not caused the whole rock to be an open system with respect to either Mg or Cr. For example, Figure 2 shows the compositions of Early Archean lavas [3000-3500 Ma; data from 38-40]. Those data suggest that these lavas had oxidation states near the FMQ buffer at the time of their eruption. This characteristic is observed in mafic volcanics throughout geologic history, including those from Isua, Greenland having an age of 3800 Ma.

In conclusion, these results suggest that the oxidation state of mafic volcanics derived from the Earth's upper mantle during the last 3800 Ma has been consistently near FMQ. If this accurately reflects the oxidation state of those portions of the mantle that contributed gaseous components to the early atmosphere, then these data indicate that a reducing atmosphere could not have been sustained by volcanic outgassing at 3800 Ma, or later. This same conclusion has been reached using other independent evidence [e.g., 41]. Although more reduced regions of the mantle may have existed [42], their contribution to the atmosphere may not have been significant

# OXIDATION STATE OF THE EARTH'S UPPER MANTLE: Delano J. W.

since no ancient volcanics from such regions have yet been identified. The impact constraints on the old side of 3800 Ma, as well as the geochemical constraints on the young side of 3800 Ma, seem to make a "traditional" view of life's origin unlikely. Alternative scenarios for the origin of life need to be investigated.

REFERENCES: [1] Cloud (1988) "Oasis in Space: Earth History from the Beginning". W. W. Norton, New York. 508pp. [2] Urey (1952) Proc. Natl. Acad. Sci. USA, 38, p.351-363. [3] Miller and Orgel (1974) "The Origins of Life on Earth". Prentice-Hall, New York. 229pp. [4] Miller and Urey (1959) Science, 130, p.245-251. [5] Miller (1953) Science, 117, p.528-529. [6] Oro et al. (1990) Ann. Rev. Earth Planet. Sci., 18, p.317-356. [7] Lasaga et al. (1971) Science, 174, p.53-55. [8] Abelson (1966) Proc. Natl. Acad. Sci. USA, 55, p.1365-1372. [9] Ferris and Nicodem (1972) Nature, 238, p.268-269. [10] Shimizu (1976) Precamb. Res., 3, p.463-470. [11] Owen et al. (1979) Nature, 277, p.640-642. [12] Kuhn and Atreya (1979) Icarus, 37, p. 207-213. [13] Kasting et al. (1983) Precamb. Res., 20, p.121-148. [14] Maher and Stevenson (1988) Nature, 331, p.612-614. [15] Oberbeck and Fogleman (1989) Origins of Life Evol. Biosphere, 19, p.549-560. [16] Oberbeck and Fogleman (1990) Origins of Life Evol. Biosphere, 20, p.181-195. [17] Gerlach (1980) J. Volcanol. Geotherm. Res., 7, p.295-317. [18] Gerlach and Graeber (1985) Nature, 313, p.273-277. [19] Greenland (1984) Geochim. Cosmochim. Acta, 48, p.193-195. [20] Muenow et al. (1980) Earth Planet. Sci. Lett., 47, p.272-278. [21] Corliss et al. (1981) Oceanologica Acta, 59. [22] Nisbet (1987) "The Young Earth. An Introduction to Archaean Geology." Allen and Unwin. 402pp. [23] Kerr (1980) Science, 210, p.42-43 for overview of subject. [24] Baross and Hoffman (1985) Origins of Life Evol. Biosphere, 15, p.327-345. [25] Shock (1990) Geochim. Cosmochim. Acta, 54, p.1185-1189. [26] Barnes (1986) Geochim. Cosmochim. Acta, 50, p.1889-1909. [27] Murck and Campbell (1986) Geochim. Cosmochim. Acta, 50, p.1871-1887. [28] Allan et al. (1989) J. Petrol., 30, p.1245-1298. [29] Bender et al. (1984) J. Petrol., 25, p.213-254. [30] Bryan et al. (1981) J. Geophys. Res., 86, p.11815-11836. [31] Clague et al. (1981) J. Geophys. Res., 86, p.9469-9482. [32] Davis and Clague (1987) J. Geophys. Res., 92, p.10467-10483. [33] Langmuir et al. (1977) Earth Planet. Sci. Lett., 36, p.133-156. [34] Perfit et al. (1983) J. Geophys. Res., 88, p.10551-10572. [35] Eggler (1983) Geophys. Res. Lett., 10, p.365-368. [36] Haggerty (1978) Geophys. Res. Lett., 5, p.443-446. [37] Christie et al. (1986) Earth Planet. Sci. Lett., 79, p.397-411. [38] Condie et al. (1977) Contrib. Min. Pet., 64, p.75-89. [39] Gill and Bridgwater (1979) J. Petrol., 20, p.695-726. [40] Nesbitt et al. (1979) Canad. Mineral., 17, p.165-186. [41] Walker "Earth History: The Several Ages of the Earth." Jones and Bartlett, Boston. 199pp. [42] Kasting et al. (1993) Science (in press).

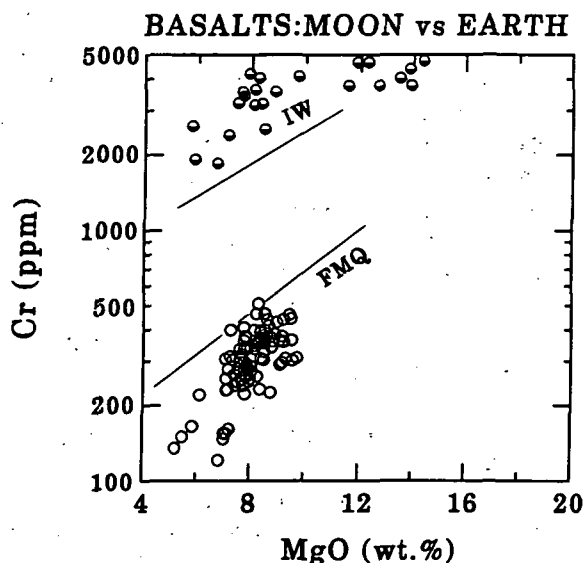


**FIGURE 1**

Compositions of terrestrial [26-34] and lunar basalts and glasses display evidence for different oxidation states.

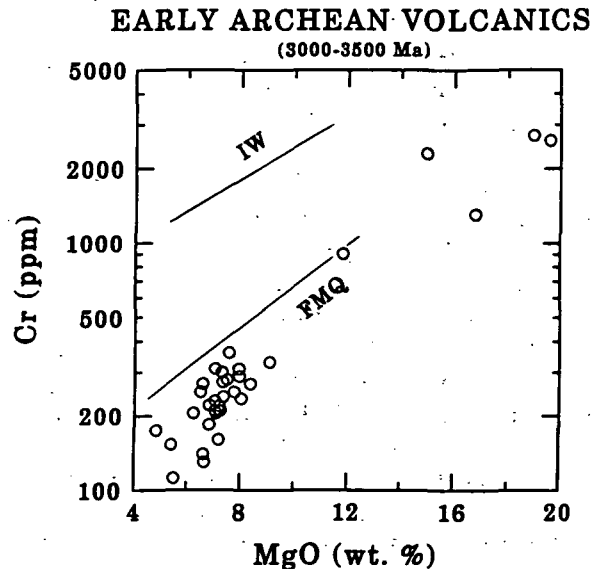


**FIGURE 2**

Mafic and ultramafic volcanics of Early Archean age [3000-3500 Ma; data from 38-40] were erupted having oxidation states near FMQ.

S996-90  
ABS ONLY

N94-12211

**SORET DIFFUSION: A POSSIBLE CAUSE OF COMPOSITIONAL HETEROGENEITY WITHIN TEKTITES;** J. W. Delano<sup>1</sup>, Y.-G. Liu<sup>2</sup>, and R. A. Schmitt<sup>3</sup>. <sup>1</sup>Department of Geological Sciences, State University of New York, Albany, NY 12222. <sup>2</sup>Depts. of Chemistry, Geosciences, and the Radiation Center, Oregon State University, Corvallis, OR 97331. <sup>3</sup>College of Oceanography, Oregon State University, Corvallis, OR 97331

Although a terrestrial origin for tektites is well-established on geochemical evidence [e.g., 1-3], the physical processes involved in tektite formation have been largely ignored by geochemists and petrologists. For example, two observations that potentially bear on the physics of their origin are the following: (a) The flange of an australite is often *more* heterogeneous than its core; and (b) microtektites are compositionally more diverse than tektites [e.g., 4,5].

The first observation contradicts the traditional view of flange formation [e.g., 6] since a second heating to super-liquidus temperatures [i.e., >1350°C; 7] during atmospheric re-entry should, by chemical diffusion and mixing, have tended to homogenize the melt as it flowed off the leading edge of the core to form the flange. Analyses of an australite flange have been performed by electron microprobe (15 keV acceleration potential; 25 nA specimen current; 40-second count-times per element, plus backgrounds collected on each analysis). The results of those analyses (Figure) emphasize the magnitude of the heterogeneity, as well as the well-defined elemental correlations that may constrain the process responsible for it. Specifically, note the inverse correlations with Si of Al, Fe, Ca, and Mg. Of special importance, note the positive correlations with Si of Na and K at SiO<sub>2</sub> < 75 wt.%, but their negative correlation with Si at SiO<sub>2</sub> > 75 wt.%. To explain these data, we offer a working hypothesis that is currently undergoing experimental investigation in collaboration with C. E. Leshner. The hypothesis is that some process operated *during* flange formation that promoted compositional heterogeneity (Figure). The process may have been Soret diffusion, which operates at super-liquidus temperatures in the presence of strong thermal gradients. Support for this hypothesis includes the remarkable resemblance of the elemental correlations (Figure) with experimental results for Soret diffusion on peraluminous compositions [8]. In addition, super-liquidus temperatures and strong thermal gradients are conditions that would have prevailed during atmospheric re-entry of australites [e.g., 9,10]. The principal question is whether sufficient time existed for Soret diffusion to occur. Although this is currently unresolved, our preliminary calculations based upon Soret coefficients [8,11] suggest that (a) temperatures in excess of 1000°C above the liquidus, (b) for times approaching ten seconds, and (c) in the presence of strong thermal gradients along the leading edge of the tektite [9,10], seem adequate. However, Soret experiments are being conducted on a natural tektite to furnish better quantitative constraints on the exact values for the Soret coefficients so that this hypothesis can be rigorously tested. If these experiments ultimately furnish additional support for Soret diffusion, the use of australite flar as flight data recorders [12] should provide information about the physics of each tektite's passage through Earth's atmosphere (e.g., temperature/time history is relevant to entry angle and velocity). In the current absence of any other competing hypothesis for these observations, the possibility of Soret diffusion warrants investigation due to the new insights that it may offer for the physics of tektite formation.

The second observation that the bulk compositions of microtektites are more diverse than the tektites within the same strewnfield is a well-known characteristic [e.g., 4,5,13,14], for which no quantitative explanation has been offered. The current investigation has involved the analysis of forty-three Australasian microtektites from the Wharton Basin (core V19-153; samples kindly supplied by B. P. Glass) by electron microprobe, as well as trace-element abundances on fifteen of these microtektites by INAA (Table). As noted by Cassidy et al. [13], individual microtektites often display large compositional heterogeneities. Our work has shown that the heterogeneities *within individual microtektites* often display the same patterns of elemental correlation previously noted for the australite flanges (Figure). This observation, in tandem with the fact that domains within australite flanges resemble bulk microtektites [14,15], seems to underscore a genetic relationship between the formation of australite flanges and microtektites. In response to those observations, we propose that microtektites are droplets of Soret melt shed from australites during their atmospheric re-entries. Owing to their low masses (Table: generally <100 micrograms), they would have settled through the atmosphere more slowly than the larger tektites, and hence been more widely distributed by upper atmospheric winds than the tektites.

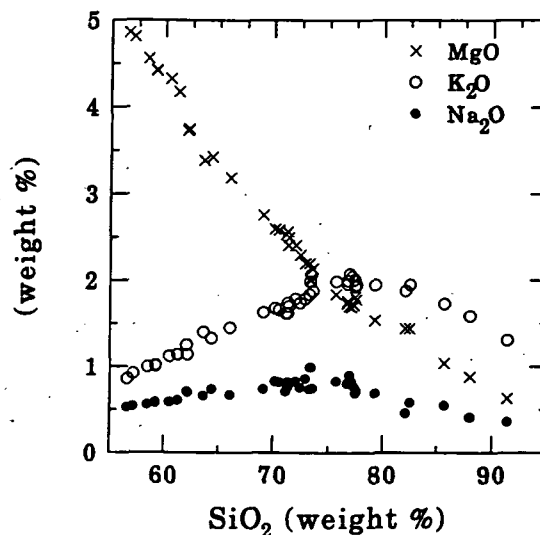
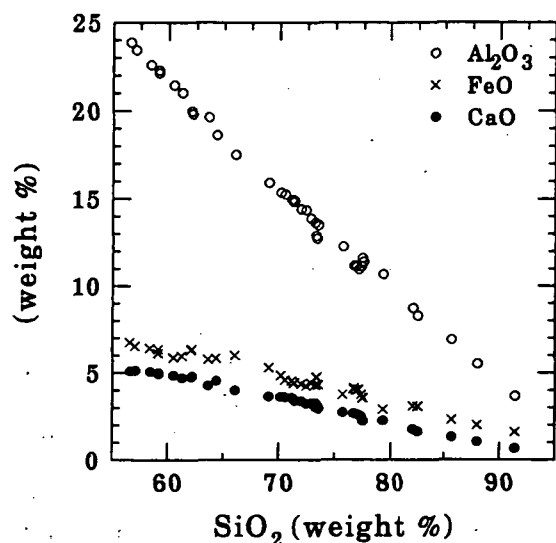
**REFERENCES:** [1] Taylor (1973) *Earth Sci. Rev.*, 9, p.101-123. [2] Koeberl (1990) *Tectonophys.*, 171, p.405-422. [3] Love and Woronow (1988) *Geochim. Cosmochim. Acta*, 52, p.2085-2090. [4] Mason (1979) *Smithson. Contrib. Earth Sci.*, 22, p.14-26. [5] O'Keefe (1969) *J. Geophys. Res.*, 74, p.6795-6804. [6] Baker (1958) *Amer. J. Sci.*, 256, p.369-383. [7] Cassidy (1964) *Geochim. Cosmochim. Acta*, 28, p.999-1008. [8] Leshner and Walker (1991) in *Advances in Physical Geochemistry*,

**SORET DIFFUSION:** Delano J. W. et al.

vol. 8, chap. 12, p.396-451. Springer-Verlag, New York. [9] Chapman (1964) *Geochim. Cosmochim. Acta*, 28, p.841-880. [10] Chapman et al. (1962) NASA TR-134, 24pp. [11] Leshner (1986) *J. Geophys. Res.*, 91, p.6123-6141. [12] Delano (1992) *Lunar Planet. Sci.-XXIII*, p. 301-302. [13] Cassidy et al. (1969) *J. Geophys. Res.*, 74, p.1008-1025. [14] Glass (1990) *Tectonophys.*, 171, p.393-404. [15] Glass (1970) *Earth Planet. Sci. Lett.*, 9, p.240-246.

**FIGURE**

Systematic compositional variations observed within an australite flange.  
Note in particular the change in behavior of Na and K at about 75 wt. % SiO<sub>2</sub>.



Sample	MT1	MT2	MT3	MT4	MT5	MT6	MT8	MT9	MT25	MT27	MT28	MT36	MT43	MT44	MT45	Uncertainty
Wt. ug	243.6	72.1	81.9	4.4	8.4	1.9	3.4	2.5	4.4	2.6	2.6	6.1	2.6	3.1	2.6	%
(wt. %)																
FEO	6.00	5.18	6.99	5.89	4.68	5.15	6.70	4.02	4.88	4.70	7.15	6.43	5.65	5.65	5.65	<3
CAO	2.1	3.3	2.8	—	—	—	—	—	—	—	—	—	—	—	—	15-20
NA <sub>2</sub> O	0.61	1.53	0.77	1.32	1.38	1.35	2.04	1.48	1.55	1.19	1.18	1.76	1.60	1.15	1.81	5-10
(ppm)																
SC	10.3	13.3	11.6	14.8	9.6	13.9	19.1	10.1	12.1	13.4	20.6	18.2	14.3	15.6	13.6	<3
CR	357	76	481	284	187	151	130	59	91	95	130	138	80	105	118	<3
CO	28.5	16.1	36.8	23.4	24.7	15.4	16.3	12.1	13.6	13.5	12.6	17.0	16.9	19.1	18.3	3-5
RB	55	99	65	110	114	111	175	136	124	133	90	158	76	119	139	10-20
SR	138	177	195	—	—	—	—	—	—	—	—	—	—	—	—	15-30
CS	2.6	4.7	2.3	4.2	6.1	6.9	10.2	6.0	8.2	7.6	6.8	9.6	9.9	8.4	7.8	10-15
BA	292	442	318	387	360	471	541	—	—	—	—	—	—	—	—	10-30
LA	30.6	42.3	33.1	36.5	30.4	41.1	56.2	38.2	41.6	43.1	58.6	53.6	50.4	42.8	46.0	3-5
CE	68.1	87.3	72.9	75.7	66.0	84.9	119.3	82.0	85.1	74.6	114.3	110.3	125.4	94.4	98.8	3-5
ND	27.0	36.2	28.7	25.1	24.8	36.0	37.4	13.6	24.9	23.8	23.5	34.8	35.3	28.2	28.8	5-15
SM	5.39	7.74	5.85	6.81	5.68	7.17	10.1	6.98	7.24	6.69	9.71	9.09	7.44	7.23	8.91	3-5
EU	1.20	1.48	1.23	1.91	1.25	1.64	2.15	1.63	1.36	1.55	1.72	1.80	1.62	2.06	2.13	5-20
TB	0.64	0.73	0.73	0.95	0.59	0.69	1.32	0.51	0.92	0.93	1.50	1.07	0.97	0.73	0.85	15-30
YB	2.54	3.47	2.75	3.03	2.57	3.19	4.58	2.88	3.17	2.76	4.09	3.98	3.28	3.39	3.66	5-10
LU	0.29	0.40	0.30	0.37	0.29	0.35	0.53	0.41	0.44	0.36	0.52	0.51	0.41	0.31	0.49	5-10
HF	6.1	5.7	6.3	5.7	5.5	5.8	6.4	7.1	6.5	4.1	5.6	5.9	4.6	4.9	7.9	5-10
TA	1.1	1.2	1.1	1.4	1.1	1.5	1.9	—	—	—	2.5	1.6	1.9	1.4	—	10-30
TH	12.8	15.4	14.1	17.4	12.7	16.9	21.8	13.7	15.5	14.7	23.8	20.8	15.9	16.9	17.2	3-5
U	0.55	0.90	—	—	1.05	—	—	—	2.32	1.82	—	—	—	—	—	20-30

ISOTOPIC AND TRACE ELEMENT CHARACTERISTICS OF AN UNUSUAL REFRACTORY INCLUSION FROM ESSEBI; E. Deloule<sup>1,2</sup>, A. K. Kennedy<sup>1,3</sup>, I. D. Hutcheon<sup>1</sup> and A. El Goresy<sup>4</sup>, <sup>1</sup>Div. Geol. Planet. Sci., Caltech; <sup>2</sup>CRPG-CNRS, Vandoeuvre, France; <sup>3</sup>Curtin Univ. of Technology, Perth, Australia; <sup>4</sup>Max Planck Institut für Kernphysik, Heidelberg, Germany. P 2

The isotopic and chemical properties of Ca-Al-rich inclusions (CAI) provide important clues to the early solar nebula environment. While the abundances of refractory major and trace elements are similar to those expected for high temperature condensates, the variety of textural, chemical and isotopic signatures indicate most CAI experienced complex, multi-stage histories involving repeated episodes of condensation, evaporation, and metamorphism. Evidence of multiple processes is especially apparent in an unusual refractory inclusion from Essebi (URIE) described by El Goresy *et al.* [1]. The melilite (mel)-rich core of URIE contains polygonal framboids of spinel (sp) and hibonite (hb) or sp and fassaite (fas) and is surrounded by a rim sequence consisting of five layers (Table 3 in [1]). In contrast to rims on Allende CAI [2], the mineralogy of the URIE rim layers becomes increasingly refractory from the core outwards, ending in a layer of spinel-Al<sub>2</sub>O<sub>3</sub> solid solution + Sc-rich fassaite. The chemical and mineralogical features of URIE are inconsistent with crystallization from a homogeneous melt and El Goresy *et al.* [1] proposed a multi-step history involving condensation of sp + hb and aggregation into framboids, capture of framboids by a refractory silicate melt droplet, condensation of rim layers and alteration of mel to calcite and feldspathoid. The PANURGE ion probe was used to investigate the isotopic and trace element characteristics of URIE to develop a more complete picture of the multiple processes leading to formation and metamorphism.

Trace elements were measured on a previously unstudied fragment (URIE-3). The mineralogy is similar to URIE-2 [1] with two important differences: (1) hb is much more abundant, occurring as aggregates of bladed crystals surrounded by feldspathoid + calcite and (2) an unidentified, hydrous silicate (phase X; approximately CaAl<sub>2</sub>SiO<sub>6</sub> · 3 H<sub>2</sub>O) occurs as a large, 60x60 μm crystal within a framboid and as small isolated crystals within melilite. The REE data from URIE (Figs. 1 and 2) display six prominent characteristics: 1) REE abundances are highly variable, even within a single phase, with CI-normalized La abundances of 35 to 100 in pv, 20 to 120 in hb, 40 to 60 in mel, 12 to 45 in fas and ~2 in phase X; 2) Mel, pv and hb exhibit flat REE patterns; 3) Fas and phase X exhibit mildly HREE-enriched patterns with CI-normalized Er/La ratios of 1.5 to 2; 4) Negative Eu anomalies are found in ~70% of the analyses and the absence of an Eu anomaly is always accompanied by lower total REE; 5) Hb is a possible host phase for Ba with abundances of up to 150 x CI; 6) REE abundances in rim phases are uniformly lower than in interior phases and no evidence for a Sc-rich, ultra-refractory component was found. The relatively flat REE patterns and similar REE abundances for co-existing phases in URIE contrast sharply with the complementary REE patterns characteristic of mel, pv and fas in Allende Type A CAI [3] and are inconsistent with equilibrium partitioning of REE during crystallization from a homogeneous melt. The REE patterns in URIE pv are similar to those of pv in Type A CAI, but abundances are ~3 to 10x lower. Overall, the distribution of REE supports the suggestion that URIE is an aggregate of condensates.

Mg and Ca isotopes were measured in URIE-3 and in URIE-2. Mel, hb, sp and phase X from the core are uniformly enriched in the heavier Mg isotopes,  $F_{Mg} = 8.2 \pm 1.5$  ‰/amu. In contrast, rim phases have isotopically lighter Mg; hb in rim layer C has  $F_{Mg} = 0.2 \pm 1.3$  ‰/amu, while spinel in layer D has  $F_{Mg} = 3.1 \pm 1.0$  ‰/amu. Excess  $^{26}Mg^*$  was detected in all mel and hb with  $^{27}Al/^{24}Mg > 10$  and data from hb, sp and mel define a linear array with slope  $^{26}Mg^*/^{27}Al = (4.7 \pm 0.4) \times 10^{-5}$  (Fig. 3). Both interior hb and rim hb lie along a single array, despite different  $F_{Mg}$ . Within the measurement precision of 5 to 8 ‰ (2σ), no Ca isotope anomalies were found in URIE mel or hb. Isotopically normal Ca in URIE fits the pattern reported by Ireland for Murchison PLAC hibonites [4]; large Ca isotope anomalies are generally absent when  $^{26}Al$  is present. Excess  $^{26}Mg^*$  is also present in phase X. In contrast to data from hb, sp and mel,  $\delta^{26}Mg$  is not correlated with the Al/Mg ratio;  $\delta^{26}Mg = 7.0 \pm 2.1$  ‰ for all.

AN UNUSUAL REFRACTORY INCLUSION FROM ESSEBI: Deloule E. *et al.*

analyses of phase X with  $^{27}\text{Al}/^{24}\text{Mg}$  ranging from 10 to 365 (Fig. 4). The D/H ratio of the water in phase X was determined with PANURGE. The instrumental mass fractionation factor was calculated from analyses of amphibole glasses and minerals (see Watson *et al.*, this volume). Three analyses gave consistent  $\delta\text{D}_{\text{SMOW}}$  of  $920 \pm 180$  ‰. This large deuterium enrichment indicates that phase X is not a terrestrial weathering product and suggests that the growth of secondary phases in URIE may have accompanied the production of hydrous matrix phases on the Essebi parent body.

The new isotope and trace element data allow us to refine the model for the formation of URIE outlined in [1]. The uniform  $F_{\text{Mg}}$  of sp and mel in the core indicates either formation of sp-framboids and the silicate precursor melt from a common reservoir enriched in the heavier Mg isotopes or an initial cooling rate of URIE sufficiently slow to allow Mg isotopic re-equilibration of initially isotopically disparate phases. Redistribution of REE did not occur due to much lower diffusion rates of REE. The differences in  $F_{\text{Mg}}$  and REE patterns between core and rim require condensation of hb and sp to form rim layers from distinct reservoirs; condensation must have occurred within  $\sim 2 \times 10^5$  y of the "solidification" of the core to preserve the  $^{26}\text{Mg}^*/^{27}\text{Al}$  correlation (Fig.3). The hydrous alteration and redistribution of Mg isotopes in phase X occurred much later, following the decay of  $^{26}\text{Al}$ . Division Contribution 5236(800). References: [1] El Goresy A., Palme H., Yabuki H., Herrwerth I. and Ramdohr P. (1984) *GCA* 48, 2283; [2] Wark D.A. and Lovering J.F. (1982) *GCA* 46, 2595; [3] Kennedy A.K., Hutcheon I.D. and Wasserburg G. J. (1991) *LPSC XXII*, 709; [4] Ireland T.R. (1990) *GCA* 54, 3219.

Fig. 1. REE abundances in URIE hb and pv. Pv#2 has a pattern identical to pv#1 but with  $\sim 3\times$  higher REE.

Fig. 2. REE abundances in URIE mel and fas.

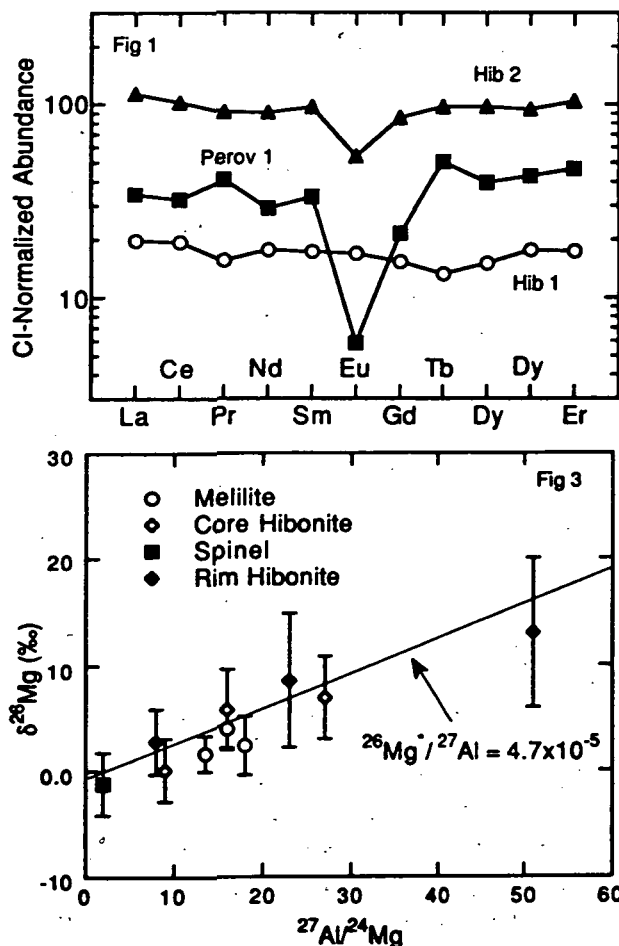


Fig. 3.  $^{26}\text{Al}$ - $^{26}\text{Mg}$  evolution diagram for URIE.

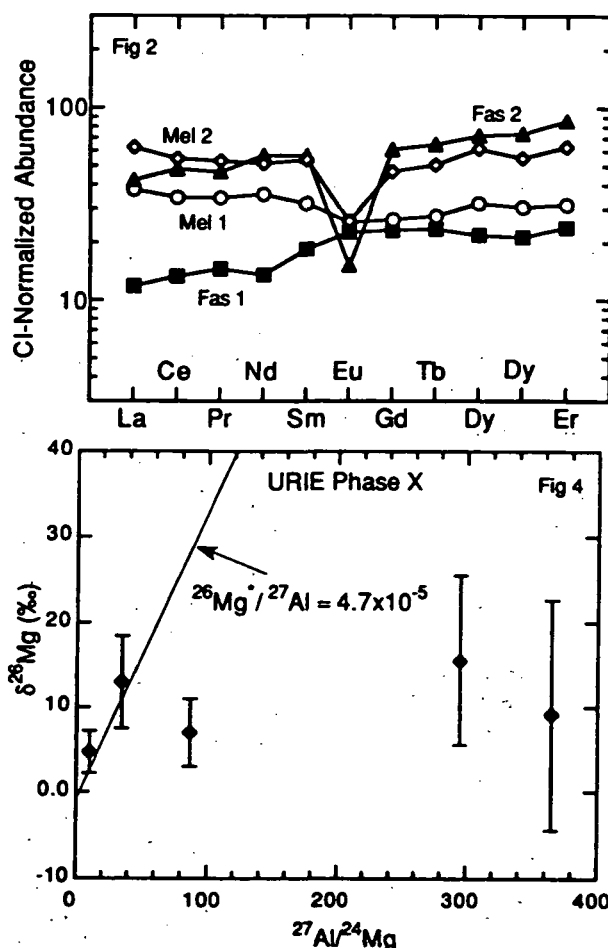


Fig. 4.  $^{26}\text{Al}$ - $^{26}\text{Mg}$  evolution diagram for URIE phase X.

N 94-12213

## Disk-Resolved Spectral Characteristics of Saturn's Medium-Sized Satellites

Tilman DENK, Ralf JAUMANN, and Gerhard NEUKUM

DLR, Institute for Planetary Exploration, Berlin-Adlershof/Oberpfaffenhofen, Germany.

Voyager-1 and -2 images of six Saturnian satellites have been investigated in the orange, green and violet spectral range (Table-1). The objective of this study is to examine and compare spectral differences of surface features in order to obtain information about compositional trends.

Although Voyager provided spectral information only at five different wavelengths, spectral differences can be identified by comparing color variations. For this purpose violet to green (VI/GR) and orange to green (OR/GR) ratios of a number of points within selected, photogeologically homogeneous regions of six satellites are calculated (Tab. 1). Each of the 50 investigated regions is characterized by its mean ratio value and standard deviation ( $\sigma$ ). Within a VI/GR and OR/GR ratio diagram all measured regions fit into a "three-component-system" defined by spectral endmembers (Fig. 1). Two of these endmembers are characterized by specific terrains on Iapetus (CM) and on Dione (GM) while the third endmember (NM) describes spectrally inactive materials. The normalized spectra of the endmembers are shown in Fig. 2, their ratios, properties, and possible compositions are given in Table 2.

With respect to the spectral differences as shown in Fig. 1 and to previous studies [1,2] the compositional trends can be interpreted as follows (the numbers in parentheses show the OR/GR and the VI/GR ratios of selected points):

- There are at least two different

	FDS (OR)	FDS (GR)	FDS (VI)	Visible surface
Mimas	34932.16	34932.20	34932.08	crater Herschel; terrain of the anti-saturn facing hemisphere
Enceladus	44000.46	44000.48	44000.44	northern saturn-facing hemisphere
Tethys	43992.24	43992.28	43992.20	trailing side
Dione	34930.11	34930.15	34930.03	trailing side (wispy streak terrain)
Rhea	34907.48	34907.52	34907.40	trailing side
Iapetus	43894.40	43894.44	43894.32	parts of Cassini Regio and Roncevaux Terra

Table 1 Utilized Voyager images

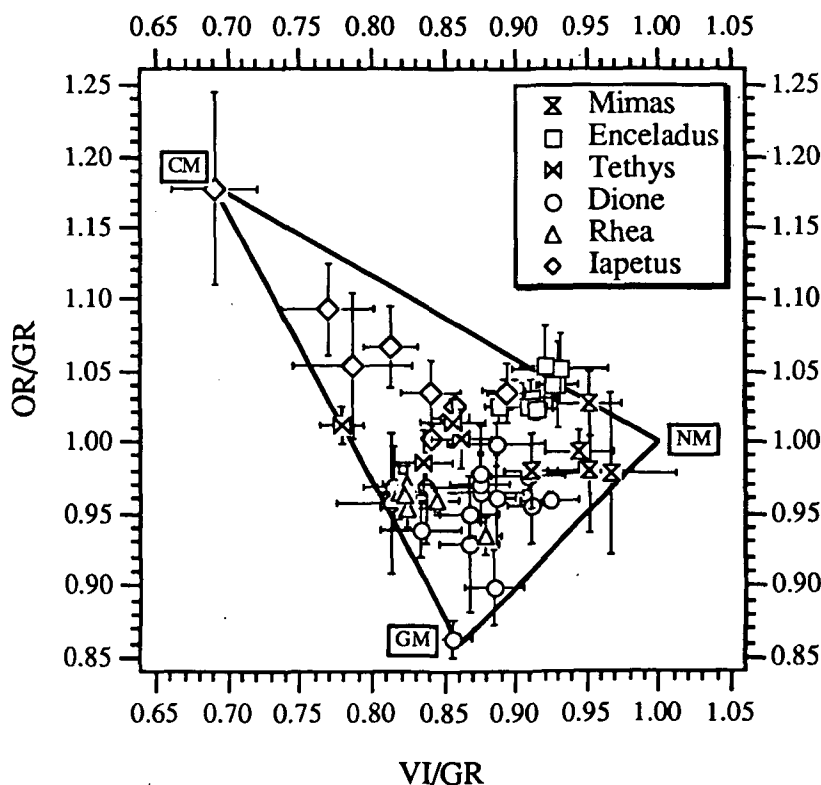


Fig. 1 Ratio diagram of the 50 examined regions



## DISK-RESOLVED SPECTRAL CHARACTERISTICS: Denk T. et al.

spectral active components on the surfaces, one with a "CM characteristic" (OR/GR > 1) and one with a "GM characteristic" (OR/GR < 1).

- All satellites except Dione and Rhea are spectrally different.
- *Mimas* has the largest NM contribution of all. Thus, it probably has the most icy surface of all six satellites.
- The surface near crater Galahad (1.026;0.953) on *Mimas* has no GM, while the area near Bors (0.979;0.911) is greener and contains more of this "mixture".
- All parts of *Enceladus* must be covered with a spectral active material, that means that there is not only ice, but also an additional material with a spectral characteristic of CM.
- The reddish feature on the trailing side of *Tethys* (1.011;0.780) contains relatively less NM. Therefore, it should have a higher silicate to ice ratio than the other regions of this satellite.
- *Dione's* "wispy streaks" contain less CM but more NM than the dark, cratered regions. They are not uniform, but differ in their spectral characteristics. A point east of crater Amata (0.863;0.857) contains most of GM on all satellites.
- Most of the wispy streak features on *Rhea* (0.96;0.83) have a similar spectral characteristic as the cratered terrain, although they are brighter.
- The region near the *Iapetus* north pole (1.034;0.894) has a similar spectral characteristic as parts of *Enceladus*.
- The Roncevaux Terra is comparable with some *Tethys* terrains (but darker).
- All parts of *Iapetus* contain CM.

In general, the results demonstrate significantly non-uniform spectral characteristics of the Saturnian icy satellites implying that the surfaces are composed of a variety of ice/mineral mixtures. A more detailed discussion is given in [3].

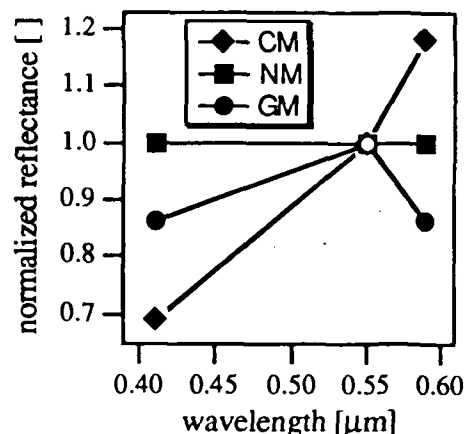


Fig. 2 Normalized spectra of the endmembers

endmembers	OR/GR	VI/GR	properties	possible compositions
CM (Cassini Regio material)	1,18	0,69	reddish	carbonaceous (organic) polymers + hydrated silicates + elemental carbon + ice [4]
NM (spectral neutral material)	1,00	1,00	no spectral activity	ice (bright component); carbon, „shadow“ (dark component)
GM (greenish material)	0,86	0,86	greenish	ice with siliceous minerals

Table 2 Characteristics of the endmembers

### References:

- [1] BURATTI, B.J.: Voyager Disk Resolved Photometry of the Saturnian Satellites. *Icarus* 59, 392-405 (1984).
- [2] BURATTI, B.J., J.A. MOSHER and T.V. JOHNSON: Albedo and Color Maps of the Saturnian Satellites. *Icarus* 87, 339-357 (1990).
- [3] DENK, T.: Untersuchung der spektralen Charakteristik von Saturnmonden. Diploma thesis, Institut für Raumfahrtssysteme, Universität Stuttgart and Institut für Planetare Erkundung of the DLR, Berlin-Adlershof/Oberpfaffenhofen, Germany, 1993 (in preparation).
- [4] BELL, J.F., D.P. CRUIKSHANK and M.J. GAFFEY: The Composition and Origin of the Iapetus Dark Material. *Icarus* 61, 192-207 (1985).

599-25  
ABS. ONLY

LPSC XXIV

403

N 94-12214

p-2

THE CORRELATION OF ALKALIS AND ALUMINUM DURING HIGH-TEMPERATURE VOLATILIZATION OF ALBITE AND NEPHELINE.

Yu.P. Dikov (1), M.V. Gerasimov (2), O.I. Yakovlev (3), F.Wlotzka (4).  
Russian Academy of Sciences: 1- Institute of Ore Deposits, Geology, Petrography, Mineralogy and Geochemistry, 2 - Space Research Institute, 3- Vernadsky Institute of Geochemistry and Analytical Chemistry, Moscow, Russia. 4- Max-Planck-Institut für Chemie, Mainz, Germany.

Our previous study of high-temperature evaporation of mafic targets has shown a systematic enrichment of newly-formed condensates in silicon and alkalis and depletion in refractory elements (Al, Ca, Ti) [1,2,3]. This effect, which is consistent with the volatility of the elements, was also tested for several experiments with acidic targets. In one case it was the impact evaporation of granite targets using a light-gas gun facility [4]. Analyses of the condensate which was collected during the impact show that it was enriched in Al and Na so that the composition of the condensate became close to nepheline. In the work of Nagahara [5,6] an incongruent evaporation of alkali feldspars under stationary conditions has been also proposed. These discoveries required a more detailed study of high-temperature evaporation of monomineralic Al-silicate targets.

In the these experiments we have used samples of oligoclase (K=0.6, Na=6.3, Al=9.0, Si=21.4, O 61.5 at.%) and of nepheline (K=2.1, Na 12.1, Al 13.5, Si 14.4, O 57.9 at.%). Vaporization of samples was performed in a hermetic cell filled with helium at normal temperature and pressure using a powerful Nd-laser focused on the sample. Laser pulses had the following parameters: luminous energy 600 J, duration  $10^{-3}$  s, density of luminosity was  $5 \times 10^6$  W/cm<sup>2</sup>, the temperature of vaporization is about 3000-4000 K [7,8]. About 4 cm from the sample a nickel foil was placed on which the condensate was collected. Films of condensate were analyzed using X-Ray Photo-Electron spectrometer ES-2401. The measurement of internal chemical composition and of the charging state of elements through the whole depth of the condensed films was made layer by layer with argon-ion-etching of 200 Å of the film per step. Results of this study are given in Table 1 and 2. The bottom layers of condensed film correspond to the front parts of the evaporated cloud or to condensation at the beginning of the evaporative process and surface layers to condensation at the end of the process.

Table 1 shows that the condensed film from the experiment with albite has three different zones: A bottom layer (13200 to 11400 Å) relatively enriched in Al and Na; an inner zone (2000 to 11400 Å) enriched in Si with slight deficit of Na and Al; and Na,Si-enriched upper layers (0 to 2000 Å). The bottom layer of the condensed film is most interesting from our point of view. This layer is noticeably enriched in volatile Na and refractory Al at the same time. In this layer the Na/Al ratio is ~1. This observation gives additional support to the idea of an incongruent mechanism of evaporation where volatilization of Na and Al occurs via a stable atomic group or cluster with Na-Al bonds. Volatilization of these clusters in the beginning the of evaporative process proves relatively high volatility of such clusters. This mechanism can act as a transportation mechanism for refractory aluminum to the vapor cloud during the evaporation process. The inner Si enriched layer of the condensed film can be considered as evaporation from a modified residual melt which was depleted in Na and Al by the above mentioned mechanism. It is important that the Na/Al ratio close to one is found also in the inner zone. The upper layer of the condensed film is considered to be formed by precipitation of atoms and radicals on

the cooled surface of the film after the end of the laser pulse [9].

Table 2 shows that the condensed film from nepheline has no distinct zonal structure. Here the ratio of (K+Na)/Al is ~1 showing that K can replace Na in the transportation mechanism for Al. It is also remarkable that for the whole thickness of the nepheline condensate and for the bottom layer of the albite condensed film we have the element ratio (Na+K):Al:Si = about 1:1:2. This proportion suggests that Si also participates in the above mentioned cluster mechanism. XPS also shows that Na and Al have bonds which are typical for silicates, there are no non-silicate bonds.

Previous results and data presented here allow us to suppose that the mechanism of volatilization of Si, Al and Na(K) during high-temperature evaporation of alkali-Al-silicates can be dominated by volatilization of Na(K)-Al-Si clusters. We have presented here only preliminary experimental results and a more sophisticated experimental and theoretical investigation of the problem is necessary. Nevertheless, this mechanism can be rather important for the formation of an early crust in the process of impact differentiation by providing a transportation mechanism for Al together with alkalis and silicon.

REFERENCES: [1] Yu.P.Dikov, M.V.Gerasimov, L.M.Mukhin, F.Wlotzka. Lunar Planet. Sci. XXI, 1990, 289. [2] Yu.P.Dikov, M.V.Gerasimov, O.I.Yakovlev. Lunar Planet. Sci. XX, 1989, 244. [3] Yu.P.Dikov, M.V.Gerasimov, L.M.Mukhin. Lunar Planet. Sci. XV, 1984, 226. [4] O.I.Yakovlev, Yu.P.Dikov, M.V.Gerasimov. Lunar and Planet.Sci. XXIII, 1992, 1557. [5] H.Nagahara. Lunar Planet. Sci. XXI, 1990, 837. [6] H.Nagahara, B.O.Mysen, N.Shimizu. Lunar Planet. Sci. XXIII, 1992, 961. [7] M.V.Gerasimov, L.M.Mukhin, Yu.P.Dikov, V.I.Rekharsky. Vestnik Acad. Nauk USSR, 1985, 9, pp.10 (in Russian). [8] M.V.Gerasimov, Yu.P.Dikov, F.Wlotzka, L.M.Mukhin. Lunar Planet. Sci. XXIII, 1992, 407. [9] M.V.Gerasimov, Yu.P.Dikov, L.M.Mukhin, V.I.Rekharsky. Lunar Planet.Sci. XIX, 1988, 383.

Table 1. Composition of zones in the condensed film from evaporation of albite (in atom %)

Zone	Depth from the surface	Elements					
		O	Si	Al	Na	K	Ca
I	0-2000 A	61.5	22.4	3.2	10.5	1.5	0.8
II	2000-10000 A	61.2	27.7	5.6	4.7	0.5	1.2
	10000-11400 A	59.4	25.4	7.3	5.8	0.9	1.2
III	11400-13200 A	58.7	17.8	11.4	9.8	0.8	1.3

Table 2. Composition of condensed film layers from evaporation of nepheline (atom%)

Depth from the surface (in A)	Elements				
	O	Si	Al	Na	K
Surface	56.0	19.6	8.7	11.3	4.3
100	59.2	16.3	9.8	11.0	3.7
200	58.8	20.3	9.4	8.0	3.5
300	57.8	20.9	10.7	7.5	3.1
500	59.6	20.0	11.4	5.9	3.1
700	58.9	19.8	11.5	6.8	3.0
900	59.1	19.8	11.3	6.8	3.1
1100	59.2	18.8	11.8	7.3	3.0
1300	57.8	19.5	11.6	7.9	3.3
1500	59.9	19.1	11.3	6.7	3.0
1700	59.8	18.6	11.7	7.0	2.9
1900	60.4	17.8	11.6	7.4	2.7
2100	59.7	19.1	11.3	7.4	2.5
2300	58.4	18.5	11.8	8.8	2.5
2500	59.7	18.0	11.3	8.7	2.3

5200-90  
 ABS ONLY

N94-3420152  
 122

A CM CHONDRITE CLUSTER AND CM STREAMS; R.T. Dodd, Department of Earth and Space Sciences, SUNY at Stony Brook, Stony Brook, NY 11794, and M.E. Lipschutz, Department of Chemistry, Purdue University, West Lafayette, IN 47907.

An elongate year-day concentration of CM falls between 1921 and 1969 (Figure 1) is inconsistent with a random flux of CM meteoroids and suggests that most or all such meteorites, and perhaps the Kaidun C-E chondrite breccia, sampled streams of meteoroids in nearly circular, Earth-like orbits.

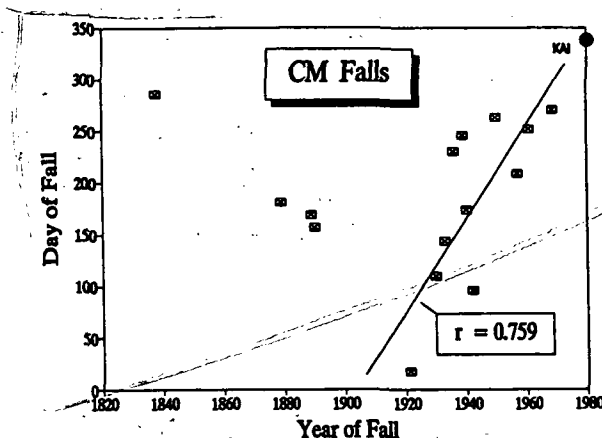


Figure 1. Year-day distribution of CM falls. The least-squares correlation line excludes Kaidun (KAI), a complex C-E chondrite breccia. Day one = 1 January.

To establish whether the post-1920 cluster might have arisen from random sampling, we determined the year-day distribution of 14 falls between 1879 and 1969 by treating each as the corner of a cell of specified dimensions (e.g. 30 years x 30 days) and determining how many falls occur in that cell. We then compared the CM cell distribution with random distributions over the same range of years. The results (Table 1) show that for 30 x 30 and 45 x 45 cells, fewer than 5% of random sets match the CM distribution with respect to maximum cell content and number of one-fall cells.

Cell		CM		Random (Frequencies)		
Years	Days	$N_{max}$	$N=1$	$(N_{max}) \geq CM$	$(N=1) \leq CM$	Both
30	30	4	9	0.04	0.25	0.024
45	45	5	6	0.04	0.16	0.012

Table 1. Frequencies of matches to CM distribution in random data sets, based on maximum cell content ( $N_{max}$ ), number of one-fall cells ( $N=1$ ), and both criteria. Based on 100 random sets for each criterion, 1000 sets for both criteria.

A product-moment least-squares calculation for the 11 post-1920 falls confirms that the CM distribution is non-random. The correlation coefficient ( $r = 0.759$ ) corresponds to a probability of only 0.007 that year and day of fall are

uncorrelated [1]. Repeating the calculation with Kaidun lowers the probability of non-correlation to 0.001.

The only plausible explanation of the distribution of post-1920 CM falls is that they sampled either one broad stream of meteoroids or two or more smaller streams. We prefer a three-stream interpretation (Figure 2), for although it is based on the post-1920 CM falls, it accommodates the earlier falls as well.

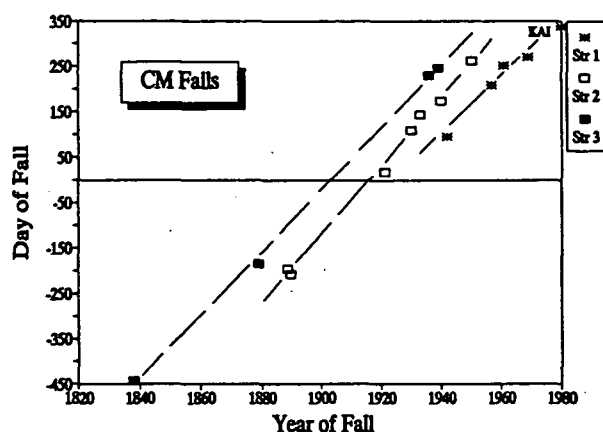


Figure 2. Three-stream interpretation of CM falls. We have subtracted 730 from the day of fall for Cold Bokkeveld (1838) and 365 from the days for other 19th Century falls.

This interpretation of the CM distribution implies that the CM streams are almost tangent to the Earth's orbit and that the points (days) of tangency advance rapidly with time. The first implication is consistent with an unusually high proportion of CM falls (8 of 14) in the Earth's forward (apical) hemisphere, which in turn suggests unusually low geocentric velocities [2]. It is also consistent with the geocentric radiant calculated for the Murchison fall ( $281-286^\circ$  -- [3]).

The second implication is more troublesome. The day range of encounter for objects in a typical asteroidal orbit can change over time because of precession, but the rate of change is modest -- at most about a week in 50 years. H and L chondrite streams [4-6] show appropriately low rates, but the CM streams in Figure 2 clearly do not. Their rapidly advancing encounter intervals strongly suggest that the CM meteoroids are in almost circular, Earth-like orbits. Although this conclusion is startling, it is consistent with orbital data for Murchison [3] and with a recent report that some small, near-Earth asteroids have such orbits [7].

- REFERENCES: (1) Rohlf, F.J. and Sokal, R.R. (1981) Statistical Tables. (2) Halliday, I. (1964) Meteoritics 2, 271. (3) Halliday, I. and McIntosh, B.A. (1990) Meteoritics 2, 339. (4) Dodd, R.T. (1992) Meteoritics 27, 214. (5) Wolf, S.F. and Lipschutz, M.E. (1992) Meteoritics 27, 308. (6) Dodd, R.T., Wolf, S.F., and Lipschutz, M.E. Science (submitted). (7) Rabinowitz, D. et al. (1992) Bulletin American Astronomical Society 24, 964.

N 94-1432416

**RELATION BETWEEN AGES AND ELEVATIONS OF MARTIAN CHANNELS;**

James M. Dohm and David H. Scott, U.S. Geological Survey, 2255 N. Gemini Dr.,  
Flagstaff, AZ 86001

**Introduction.** Mapping highland and lowland channels and reassessing their time-stratigraphic positions shows that many channels in the cratered highlands are younger than Noachian, that all channels in the lowland plains are Hesperian or younger, and that although Martian channels formed throughout the planet's history, the rate of their formation appears to have declined with time [1]. This detailed examination of the age relation between Martian terrains and the channels that transect them was made possible by the completion of the global geologic maps of Mars [2,3,4] and the availability of other geologic maps at scales of 1:5,000,000, 1:2,000,000, and 1:500,000. The present study focuses on the sources (heads) of the channels of the initial study [1,5] to see if there is a relation between channel age and elevation. CAD

**Methods used.** We have mapped and documented over 1600 highland and lowland channels and their tributaries longer than about 30 km in all of the 120 Viking 1:2,000,000-scale photomosaic quadrangles of Mars. We have excluded many small channels (mostly <30 km long) that occur around the rims and walls of impact craters, because their origins, even if fluvial, are probably more related to their respective impacts than to climate and regional processes such as endogenic heating. We assigned each channel a maximum age based on the age of the youngest material cut by the channel. (This procedure, however, provides very conservative ages, because a channel may be much younger than the rocks that it cuts.) These data were compiled on topographic maps of the western and eastern equatorial and polar regions of Mars at 1:15,000,000 scale [6] to document the elevations of the channel sources. A few sources are buried by younger materials and are only approximately located; for example, the source of Kasei Valles is covered by lava flows of the Tharsis Montes Formation [2]. Channel sources of a particular age were documented in elevation intervals of 1 km because of error margins as great as 1500 m in the contour values [6].

**Implications of the data.** A plot showing the number of channel sources vs. elevation (Fig. 1) indicates that indeed there is a relation between channel age and elevation, and, as expected, this relation generally agrees with that between terrain ages and elevation (not shown). Some of the more important observations that can be made from the plot are (1) the number of Noachian channel sources peaks between 4 and 5 km, and (2) Hesperian and Amazonian channel sources cover a relatively wide elevation range. (At the highest elevations, many of the sources of Amazonian channels occur on the flanks of volcanoes [7,8].) Some preliminary explanations for the spatial and temporal distribution of Martian channels are readily apparent. For example, our work may support the ideas that volatiles gradually migrated to lower elevations [9] and that Mars' early atmosphere was relatively thick [10] and that, with time, a gradual thinning may have resulted both in isolating the higher elevations from degradation [9] and in decreasing the rate of channel formation [1]. The lowering of channel sources with time may also have been affected by the gradual waning of geothermal heating and the decrease in the high impact flux after Noachian time.

## AGES AND ELEVATIONS, MARTIAN CHANNELS: Dohm, J.M. and Scott, D.H.

This channel study will be refined with improved topographic data provided by Mars Observer.

**References cited.** [1] Scott, D.H., Dohm, J.M., and Rice, J.W., Jr., submitted to *JGR*, 1993. [2] Scott, D.H., and Tanaka, K.L. (1986) *U.S. Geol. Surv. Misc. Inv. Series Map I-1802A*. [3] Greeley, Ronald, and Guest, J.E. (1987) *U.S. Geol. Surv. Misc. Inv. Series Map I-1802B*. [4] Tanaka, K.L., and Scott, D.H. (1987) *U.S. Geol. Surv. Misc. Inv. Series Map I-1802C*. [5] Scott, D.H., and Dohm, J.M. (1992), *Proc. Lunar and Planet. Sci. Conf.* 23, p. 1251-1252. [6] U.S. Geological Survey (1989) *U.S. Geol. Surv. Misc. Inv. Series Map I-2020*. [7] Gulick, V.C., and Baker, V.R. (1989) *Nature*, 341, 514-516. [8] Mouginis-Mark, P.J. (1990) *Icarus*, 84, 362-373. [9]. Maxwell, T.A. and Craddock, R.A. (1992) *Proc. Lunar and Planet. Sci. Conf.* 23, p. 863-864. [10] Carr, M.H. (1989) *Icarus*, 79, 311-327.

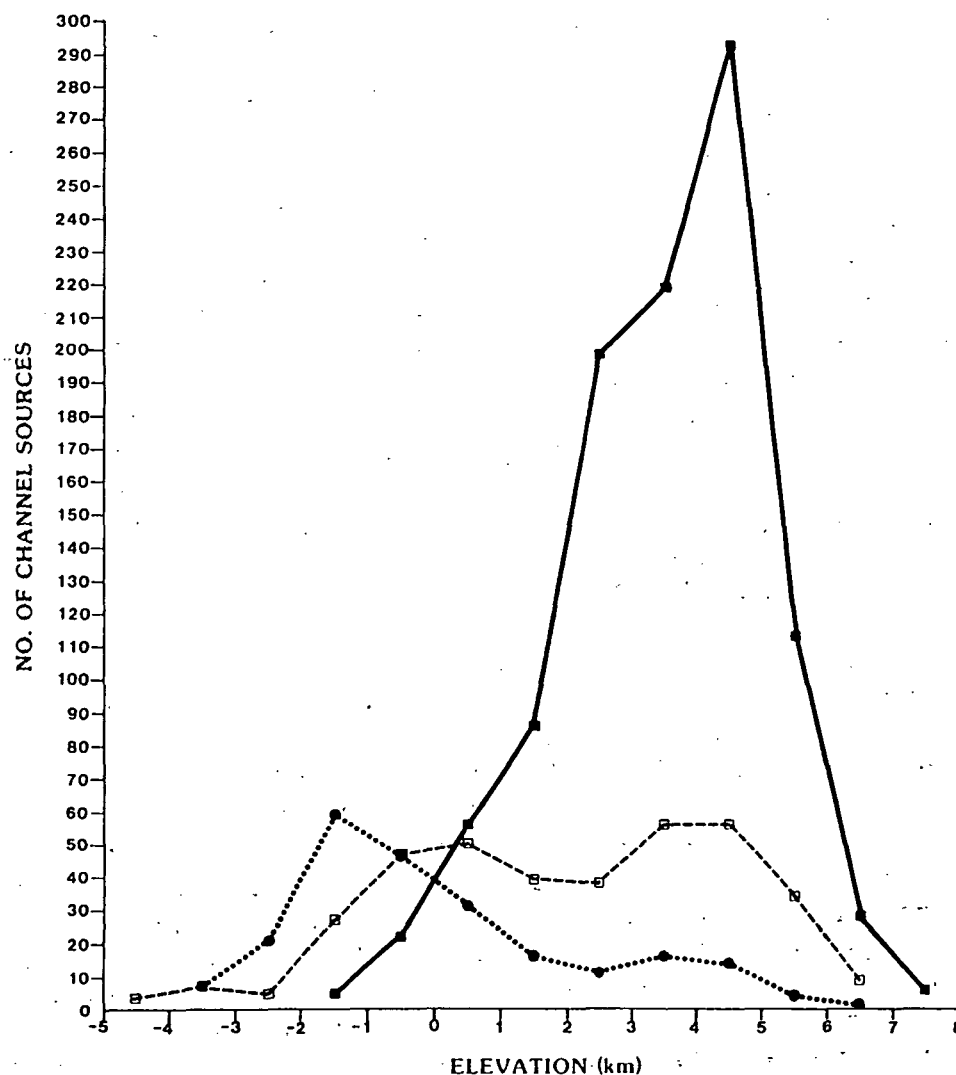


**Figure 1.** Sources of channels vs. elevation, on all Martian terrains. Solid boxes, Noachian; open boxes, Hesperian; circles, Amazonian.

N 9 46-342217  
P. 2 - -

## DOES THE THERMAL WIND EXIST NEAR THE EARTH'S CORE BOUNDARY ?

A.Z. Dolginov, *Lunar and Planetary Institute, 3600 Bay Area Blvd., Houston, TX 77058*

Temperature distribution in the Earth core determine many important processes such as convective motion, magnetic field generation, matter exchange between the core and the mantle, the thermal flux etc. This distribution depends on conditions on the core-mantle boundary and on the distribution of the thermal conductivity in the mantle. Seismic tomography shows that large horizontal temperature and compositional gradients exists at the core-mantle boundary [1, 2]. The simple assumption that these inhomogeneities are extended into the top of the core contradicts to the common opinion that the horizontal temperature gradient ( the thermal wind ), wipes them out in a short time [3]. However, this conclusion has been obtained without taking into account that the core volume is closed and the motion, if it started, can lead to a small redistribution of composition that stops this motion.

The common estimate of the thermal wind velocity at the top of the core is based on the Navier-Stokes equation. The curl of this equation admits a steady solution of the form

$$2\nabla \times \rho \Omega \times \mathbf{u} = \nabla \rho \times \mathbf{g} \quad (1)$$

where  $\Omega$  is the angular velocity,  $\mathbf{g}$  is the gravitational acceleration, and  $\rho$  is the density. One can see that the state with zero velocity,  $\mathbf{u} = 0$ , can exist only if  $\nabla \rho \parallel \mathbf{g}$  and, hence, any horizontal gradient of the density, if it exists, creates a thermal wind. However, the horizontal temperature inhomogeneities may exist if the medium is chemically inhomogeneous. In this case

$$\rho = \rho_0(1 - \beta T) \quad \nabla \rho = \nabla \rho_0 - T \nabla \rho_0 \beta - \beta \rho_0 \nabla T \quad (2)$$

where  $\beta$  is the coefficient of thermal expansion that depends on the distribution of molecular weight  $\mu$  in the medium, and  $T$  is the deviation of the temperature away from some mean core adiabat. In the absence of thermal perturbations  $\rho = \rho_0$  and  $\nabla \rho_0 \times \mathbf{g} = 0$ .  $\beta$  depends on the molecular weight,  $\mu$ , of the medium. One can see from equation (2) that in the case of nonhomogeneous  $\mu$  the horizontal temperature gradient may exist in the core near the mantle boundary. It does not create the thermal wind because the temperature gradient may be compensated by the gradient of composition. The state with  $\mathbf{u} = 0$  corresponds to the following  $\mu$  distribution

$$\nabla \mu = \left( \frac{\partial \mu}{\partial \beta} \right) \nabla \beta, \quad \frac{\nabla \beta}{\beta} = - \frac{\nabla T}{T} \quad (3)$$

This distribution seems rather special but it is naturally selected. The steady state with zero velocity is a state with the minimum production of entropy. Any other state tends to this state if possible.

Consider the time evolution of the temperature and composition in a volume where the temperature distribution on the boundary is stationary. According to equations (1) to (3) the thermal wind velocity is smaller in regions where the molecular weight distribution is closer to (3). It makes these regions more stable.

Equation of continuity in the case of incompressible fluid ( $\nabla \cdot \mathbf{u} = 0$ ) has the form

$$\frac{\partial \rho}{\partial t} + \mathbf{u} \cdot \nabla \rho = -\rho_0 T \left( \frac{\partial \beta}{\partial t} + \mathbf{u} \cdot \nabla \beta \right) - \rho_0 \beta \left( \frac{\partial T}{\partial t} + \mathbf{u} \cdot \nabla T \right) + \mathbf{u} \cdot \nabla \rho_0 = 0 \quad (4)$$

Using equation of heat propagation

$$\frac{\partial T}{\partial t} + \mathbf{u} \cdot \nabla T = \nabla (D_T \nabla T) \quad (5)$$

we can rewrite (4) in the form

$$\frac{\partial \beta}{\partial t} + \mathbf{u} \cdot \nabla \beta = - \frac{\beta}{T} \nabla (D_T \nabla T) + \frac{\mathbf{u} \cdot \nabla \rho_0}{\rho_0 T} \quad (6)$$

Terms in the right hand side of (6) are small because the characteristic scale of density is small and the diffusion is slow. We can see that evolution of composition and temperature are described by similar equations and characteristic timescale is the same.



Taking into account that terms with  $\nabla\rho_0$  are small compared to other terms in (1) and neglecting also terms of the order of  $u^2$  we obtain

$$2\rho(\Omega\nabla)\mathbf{u} = \rho_0\beta gT\left(\frac{\nabla\beta}{\beta} \times \mathbf{g} + \frac{\nabla T}{T} \times \mathbf{g}\right) \quad (7)$$

We can see that the condition (3) is sufficient to have  $\mathbf{u} = 0$ . According to (6) and (7) the state with  $\mathbf{u} = 0$  is stationary.

If there is a heterogeneous mixture of different substances ( say Fe and Si ) but not a homogeneous solution then transport by flux is essential. If the medium is mixed at the molecular scale, then only diffusion can lead to the molecular weight redistribution. However, the diffusion is too slow and is insignificant in the core. Gases in the Earth's atmosphere are mixed at the molecular scale and characteristic time of perturbations in the atmosphere is much shorter than the time necessary for the compositional redistribution.

There are direct seismic observations that apparently show the stable stratification and heterogeneous structure of the top core regions ( see Lay, Young 1990 ). The heterogeneous structure may be supported by the core - mantle exchange of the matter and extremely slow rate of mixing by the diffusion.

There is another example of stable compositional inhomogeneities in astrophysical conditions. Chemical anomalies in the form of large patches where the abundance of some elements ( including He ) may by ten or more times greater or smaller than in the surrounding medium were observed on the surface of magnetic Ap stars. Such inhomogeneities themselves are absolutely hydrodynamically unstable , but may be self-consistently stabilized by the temperature or magnetic fields.

The horizontal temperature inhomogeneities may persist at the top of the core even if there exists a slow convective motion. The viscosity of the core is less than  $10^5 \text{ cm}^2/\text{s}$  and apparently is  $\sim 10^{-3} \text{ cm}^2/\text{s}$  [5]. In this case the Reynolds number is large even for a small velocity and the motion may be turbulent at small scales. The turbulent diffusivity that also determines the thermoconductivity is of the order of  $\chi \sim u_t l_t$ , where  $u_t$  and  $l_t$  are the turbulent velocity and characteristic scale respectively. The turbulence may be driven by friction with the mantle boundary. Taking  $u_t \approx 10^{-2} \text{ cm/s}$  and  $l_t \approx 10^5 \text{ cm}$  we obtain  $\chi \approx 10^3 \text{ cm}^2/\text{s}$ .

The flux with the velocity  $u$  passes the distance  $l_T$  of the size of the typical temperature inhomogeneity on the core-mantle boundary in the time  $\tau \sim l_T/u_T$ . It is about  $3 \cdot 10^4 \text{ yr}$  if  $l_T \approx 10^8 \text{ cm}$  and  $u \approx 10^{-2} \text{ cm/s}$ . This time is enough to warm the flux throughout to a depth of about  $l \approx \sqrt{4\chi\tau} \approx 60 \text{ km}$ .

The molecular diffusivity for the liquid iron is  $\chi_m \approx 1 \text{ cm}^2/\text{s}$ . Thus only a few km can be warmed throughout by the molecular diffusion during  $3 \cdot 10^4 \text{ yr}$ .

Significant horizontal temperature inhomogeneities in regions with large electric conductivity may produce an electric current and magnetic field of much larger values than had been previously estimated in the literature.

**References :** [1] Stevenson D. J., (1987) *Geophys. J. Roy. Astr. Soc.* 88, 311 ; [2] Dziewonski A. M. , (1984) *J. Geophys. Res.* 89, 5929 ; [3] Morelly A., Dziewonski A. M. (1987) *J. Geophys. Res.* 95, 678 ; [4] Lay T., Young C. J. (1990) *Geophys. Res. Lett.* 17, 2004 ; [5] Zharkov V. N. (1983) *Interior Structure of the Earth and Planet*, Harwood Acad. Publ. Switzerland

N 94-12218  
D-2

## MAGNETIC FIELDS AND NONUNIFORM STRUCTURES OF THE MOON

A.Z. Dolginov *Lunar and Planetary Institute, 3600 Bay Area Blvd., Houston, TX 77058*

Direct magnetic measurements performed by space probes demonstrated the existence of small-scale, stationary surface magnetic fields on the Moon [1]. The magnetic field averaged over a region of  $\sim 600$  km was found to be no larger than  $\sim 10^{-5}$  G, that of the regions  $\sim 100 - 200$  km is  $\sim 10^{-5} - 10^{-4}$  G, and that of  $\sim 10 - 100$  km reaches  $\sim 10^{-3}$  G. Investigations of certain lunar rocks reveal stable residual magnetization, which could have been acquired during the crystallization of the rocks in the presence of the outer magnetic field, provided such a field existed at the initial stage of lunar evolution. Estimates show that  $4 \cdot 10^9$  yr ago the field was small, then it rose to  $\sim 1.3$  G at the beginning of  $3.9 \cdot 10^9$  yr with a subsequent exponential decrease during the period of  $3.9 \cdot 10^9$  yr to  $3.2 \cdot 10^9$  yr ago [2]. Small-scale fields have been explained by some authors as due to mechanical impacts produced by meteors. The theory of this effect is not elaborated in detail. This can in no way explain the paleomagnetic data. These data are commonly explained as a result of the dynamo action in the liquid lunar core. This action can cease for various causes, for example, when the core temperature decreases. To obtain the field  $\sim 10^{-2} - 1$  G on the surface, the field on the core boundary must be larger than  $\sim 10$  G if the core radius was less than  $\sim 400 - 500$  km. Should this field be the result of the dynamo, the convective velocity in the lunar core have to be much larger than that in the Earth's core. The motion can amplify the field only if the kinetic energy density is larger than the magnetic energy density i.e., if  $\rho u^2 > B^2/4\pi$ , where  $\rho$  is the matter density,  $u$  is the velocity of the medium, and  $B$  is the magnetic field. Hence  $u$  must be larger than  $1 - 10$  cm/s. Motions of this kind should lead to rapid smoothing of the temperature in the core, and the temperature gradient will drop below its adiabatic value. It switches off the convection. The gravitational separation of the heavy and light fractions cannot support convection of the necessary intensity in the considered case. Gravitational energy release in the process of the lunar core formation has been estimated in [3] as  $\sim 10^{15}$  erg/s. The energy needed for the large-scale magnetic field generation is no less than  $10^{17}$  erg/s if the field is about 1 G. This is a serious problem of the dynamo hypothesis. One of the alternatives is the assumption that the lunar field was induced by the Earth. This hypothesis requires the assumption that the Earth used to be much closer to the Moon ( $3 - 4$ )  $\cdot 10^9$  yr ago (at a distance  $\sim 5 - 10$  Earth radii) than today and the Earth's field was significant larger ( $\sim 10 - 50$  G). There is no evidence for these values.

A new possibility arises for the lunar field explanation if we take into account that the Moon's interior is very inhomogeneous. Large gravitational anomalies were observed by space probes. Thermal fluxes from different regions of the lunar surface differ by a factor  $\sim 1.5$  [4]. This is due to the large difference in the heat diffusivity of different rocks and gives supplementary evidence for lunar nonuniformity. There is no evidence that observed magnetic anomalies on the Moon's surface are connected with concentration of magnetized substances on or below the surface. The other possibility is the creation of a magnetic field by a current. The current needs a medium with sufficiently high conductivity. The conductivity of the Moon's surface is too small. However, it is possible that partly molten regions exists not far below the Moon's surface. Conductivity of such regions might be enough to provide a sufficiently strong current. Let us show that the observed small-scale magnetic anomalies on the Moon's surface may be explained as due to currents in such regions below the surface. The current is driven by the electric field created by chemical and temperature inhomogeneities. A similar explanation can be presented for the large-scale paleomagnetic field.

The stationary magnetic field value created by this current can be obtained from equation

$$\nabla^2 \mathbf{B} = \frac{4\pi}{c} \nabla \times \sigma [\eta \nabla T]_{\text{curl}} \quad \eta = \frac{k_B}{e} \left[ 2 + \ln \frac{2(2\pi m_e k_B T)^{3/2}}{n_e h^3} \right] \quad (1)$$

where  $[\dots]_{\text{curl}}$  denotes the vortex component. The potential component is compensated by the charge redistribution.  $\eta$  is the thermopower and  $\sigma$  is the electric conductivity. The conductivity of lunar rocks is of the nondegenerate semiconductor type. In this case  $\eta$  reaches the value  $(3 - 15) \cdot 10^{-4}$  volt/degree. Conductivity of the lunar upper mantle (up to the depth  $\sim 800 - 900$  km) is less than  $10^7 - 10^9 \text{ s}^{-1}$ , but the conductivity of the partially molten silicates which apparently are typical for the lower mantle (at least for some regions) and may exist in the upper mantle in the form of magma cavities is of the order of  $\sim 10^{12} - 10^{13} \text{ s}^{-1}$ . Conductivity of the liquid iron core, if such a core exist, reaches the value  $10^{15} \text{ s}^{-1} = 3 \cdot 10^3 \text{ ohm}^{-1} \text{ cm}^{-1}$ .

## MAGNETIC FIELD OF THE MOON

A. Z. Dolginov

[4]. The trace element doping might well change the conductivity by a large factor. This doping in most cases increases the conductivity of substances which are insulator in a pure state ( e.g. silicon ), and does not decrease substantially the conductivity of good conductors ( e.g. molten iron ). Thus the doping might work in favor of the field generation mechanism.

Consider a partially melted spherical region with the radius  $R \sim 100 \text{ km}$  at a depth of  $\sim 100 \text{ km}$  below the Moon's surface. Assume that the temperature distribution there is  $T(r, \theta) = T_a(r) + T_1(r) \cos \theta$  and  $\sigma(r, \theta, \varphi) = \sigma_a(r) + \sigma_1 \sin \theta \sin \varphi$ . The distribution of temperature has to be different from that for the conductivity ( or thermopower ) to create a current. In this case the solution of (1) is

$$(B_{tor})_\varphi \approx \frac{4\pi}{c} \sqrt{\frac{1}{3}} \frac{r}{R} \left(1 - \frac{r^3}{R^3}\right) \eta_a \sigma_a T_1 \sin \theta, \quad (B_{pol})_r \approx \frac{2\pi}{5c} \sqrt{\frac{2}{3}} \frac{r^2}{R^2} \eta_a \sigma_1 T_1 \sin \theta \cos \varphi \quad (2)$$

$(B_{pol})_\theta$  and  $(B_{pol})_\varphi$  have the form similar to  $(B_{pol})_r$ . Only the first nonvanishing terms are included in these formulae.

According to experiments [4], a melted fraction of (5 - 10) % increases the conductivity of silicates from  $\sim 10^7 \text{ s}^{-1}$  to  $\sim 10^9 \text{ s}^{-1}$ . If there are more molten substances, then  $\sigma$  may reach  $10^{10} \text{ s}^{-1}$ . Taking  $\sigma = 10^{10} \text{ s}^{-1}$ , thermopower  $\eta = 5 \cdot 10^{-6} \text{ esu}$  ( as for a semiconductor ) and temperature difference inside this region of the order of  $(2 - 5) \cdot 10^2 \text{ K}$ , and using the solution of equation (1) we obtain the field on the lunar surface above the considered region of about  $\sim 10^{-4} \text{ G}$  that is just of the order of the observed local field values.

The observed local magnetic anomalies may be either connected with regions above the existing magma cavities or with regions on the surface or below the surface that were melted in ancient times ( say by a meteorite impact ) and magnetization was fixed in substances that can be magnetized and have a magnetic memory.

Analysis of the physical characteristics of lunar rocks leads to the conclusion that at the early stage of evolution a large part of the lunar volume or even the whole Moon was in a molten state [5].

Let us assume that the Moon had a molten Fe + FeS core with a size of  $\sim 600 \text{ km}$ , temperature  $1.5 \cdot 10^3 - 2 \cdot 10^3 \text{ K}$ , temperature gradient  $\sim 100 \text{ K per } 10^3 \text{ km}$ , thermopower  $6 \cdot 10^{-8} \text{ esu}$  and conductivity about  $10^{15} \text{ s}^{-1}$ . Then, using formula (2) we obtain the surface field about of  $0.01 \text{ G}$ . If the whole Moon was melted, then the following estimates of parameters are apparently true:  $\sigma \sim 10^{13} - 10^{14} \text{ s}^{-1}$ ,  $\eta \sim 5 \cdot 10^{-6} \text{ esu}$  ( because the thermopower of molten silicates is closer to that of nondegenerate semiconductors than that of metals ), the temperature of the molten volume  $\sim 2 \cdot 10^3 \text{ K}$  and the temperature, conductivity and thermopower inhomogeneities about 10 - 20% of the average values, i.e.,  $T_i/T_a \approx 0.1 - 0.2$  etc. Using these estimates we obtain the dipole magnetic field of the ancient Moon of the order of  $0.1 - 1 \text{ G}$ . We can see that a thermoelectric current in a small lunar core is not strong enough to provide the observed paleomagnetic field value. However, this current creates a permanent existing seed field that can be amplified by the dynamo, if there are favourable conditions for the dynamo.

This paleomagnetic field is a large-scale, one but it is not a dipole field. In the formula (2) we have taken into account only the first multipole. If the distribution of inhomogeneities is strongly nonuniform the generated field may have various multipole components. It is shown by author ( see this volume ) that the field amplified by the dynamo does not forget the seed field distribution.

The paleomagnetic field may be not necessarily connected with the lunar core. It is possible that there were many large-scale local melted regions on or near the surface of the ancient Moon. Such regions may create the field as well as the Moon core and may be responsible for the lunar paleomagnetism. Using  $\sigma$ ,  $\eta$ , and  $T$  values as for partially molten silicates, and assuming the gradient of these quantities is  $\sim 10 - 20\%$  per  $10^3 \text{ km}$  the magnetic field obtained in these regions is about  $0.1 - 1 \text{ G}$ . This field may be fixed in some rocks after the crystallization process.

References : [1] Dyal P. et al (1978) Proc. Lunar Planet. Sci. Conf. 9, 231 ; [2] Cisowski S. M. et al J. Geoph. Res., 88, A 691; [3] Stevenson D. J., (1987) Rep. Progr. Phys., 46, 555; [4] Zharkov V. N., (1983), Interior Struct. of the Earth and Planet, Harwood Acad. Publ. [5] Binder A., Gungy H. (1985) Icarus 63, 421

N 94-163424  
P- 2 2 1 9**POLARITY REVERSALS AND TILT OF THE EARTH'S MAGNETIC DIPOLE**A.Z. Dolginov, *Lunar and Planetary Institute, 3600 Bay Area Blvd., Houston, TX 77058*

There is evidence that the terrestrial magnetic field is connected with the Earth's mantle: (1) There are magnetic anomalies that do not take part in the westward drift of the main field, but are fixed with respect to the mantle [1, 2], (2) The geomagnetic pole position flips in particular way by preferred meridional paths during a reversal [3], (3) Magnetic polarity reversals are correlated with the activations of geological processes [4]. These facts may be explained if we take into account that a significant horizontal temperature gradient can exist in the top levels of the liquid core because of the different thermoconductivity of the different areas of the core-mantle boundary. This temperature inhomogeneities can penetrate in the core because fluxes along the core boundary (the thermal wind) can be strongly suppressed by a small redistribution of the chemical composition in the top of the core (see Dolginov this volume). The nonparallel gradients of the temperature, density, and composition on the top of the core create a curled electric field that produces a current and a magnetic field. This seed - field can be amplified by motions in the core. The resulting field does not forget the seed - field distribution and in this way the field on the Earth surface (that can be created only in regions with high conductivity, i.e. in the core) is connected with the core-mantle boundary.

Contrary to the usual approach to the dynamo problem we will take into account that the seed field of thermoelectric origin is acting not only at some initial moment of time but permanently. *END*

The equation that governs the magnetic field amplified from the seed field by differential rotation and convection in the core has the form

$$\frac{\partial \mathbf{B}}{\partial t} - \nabla \times (\alpha \mathbf{B} + \mathbf{v} \times \mathbf{B}) - D_m \nabla^2 \mathbf{B} = Q_\varphi \quad (1)$$

where  $\alpha \mathbf{B} + \mathbf{v} \times \mathbf{B}$  is the electromotive force created by convection and differential rotation ( $\alpha \omega$  dynamo).  $Q_\varphi = -c \nabla \times [\eta \nabla T]_{\text{curl}}$ ,  $\eta$  is the termopower. If the conductivity is of the metallic type then  $\eta = \pi^2 (k_B/e) (k_B T / \zeta)$ , where  $T$  is the temperature and  $\zeta$  is the chemical potential. The trace element doping might well change the conductivity by a large factor. This doping in most cases increases the conductivity of substances which are insulator in a pure state (e.g. silicon), and does not decrease substantially the conductivity of good conductors (e.g. molten iron). Thus the doping might work in favor of the field generation mechanism. The brackets  $[\dots]_{\text{curl}}$  denote the vortex part of the expression. As an example we take the temperature distribution in the form  $T(\mathbf{r}) = T_a(r) + T_1(r) \cos \theta$ , where  $T_1 = T_1^0 \exp[-(R-r)/L]$  and  $L \ll R$ . We assume that horizontal gradients of temperature are maximum near the core-mantle boundary ( $r = R$ ). The similar expressions are taken for the thermopower and electric conductivity distributions. In this case only the  $\varphi$  component of the seed field is non zero. We use the simplest model of the  $\alpha \omega$  dynamo that allows us to show the dependence of the resulting field from the permanent existing seed field and allows us to estimate characteristic time of the field evolution. Consider the case when the velocity field is a much sharper function of space coordinates than the magnetic field and disregard the term  $(\mathbf{v} \nabla) \mathbf{B}$  as compared with  $(\mathbf{B} \nabla) \mathbf{v}$ . Estimate the term  $D_m \nabla^2 \mathbf{B}$  as  $\mathbf{B}/\tau$ , where  $\tau = L^2/D_m$  and  $L$  is the characteristic space scale of the  $\mathbf{B}$ . We will use the representation employed by many authors  $\alpha = \alpha_0(r) \cos \theta$  for  $\alpha$  effect and  $\mathbf{v} = \omega(\mathbf{r}) \times \mathbf{r}$ . In this approximation equation (1) has the following solution

$$B_\varphi = \frac{Q_\varphi \tau}{4 + \lambda^2 \tau^2} \left\{ \frac{2}{\lambda \tau} \left[ \sinh \frac{\lambda t}{2} + \frac{\lambda \tau}{2} \cosh \left( \frac{\lambda t}{2} \right) \right] \exp \left( -\frac{t}{\tau} \right) - 1 \right\} \quad (2)$$

$$\lambda^2(r, \theta) = -4 \frac{\alpha_0}{r^2} (\alpha_0 + r \frac{\partial}{\partial r} (r \omega)) \sin \theta - 4 \left( \frac{\partial \alpha_0}{\partial r} + \omega \right) \cos \theta > 0 \quad (3)$$

In the case  $\lambda = 0$  and  $t \rightarrow \infty$  we obtain from (2) the stationary solution for the seed field

$$(B_{\text{tor}})_\varphi = Q_\varphi \frac{\tau}{4} = \frac{4\pi}{c} \sqrt{\frac{1}{3}} \frac{r}{R} \left( 1 - \frac{r^3}{R^3} \right) \eta_a \sigma_a T_1^0 \sin \theta \quad (4)$$

The stationary value of the seed field created in the top of the core can be estimated from the formula (5). Taking the upper core conductivity as  $\sigma = 3 \cdot 10^{15} \text{ s}^{-1} \sim 3 \cdot 10^3 \text{ ohm}^{-1} \text{ cm}^{-1}$ ,  $\eta_a \approx 2 \cdot 10^{-5} \text{ volt/degree}$ ,  $\sigma_1$  is

about 10 - 20 % of  $\sigma_a$ , and temperature inhomogeneities  $T_1 \approx 10$  K, we obtain the seed toroidal field inside the core of the order of 0.1 - 1 G. Because the real parameters of the Earth's core are poor known larger values of  $T_m$ ,  $\sigma_m$  and  $\eta$ , and, hence, the large field estimate are possible. It is important to emphasize that the obtained seed field values are of the same order of magnitude as the magnetic anomalies observed on the Earth surface. If  $\lambda > 2$  the field increases exponentially with time. In the  $\alpha\omega$  dynamo theory the strength of the  $\omega$  and  $\alpha$  effects are measured by magnetic Reynolds numbers  $R_\omega = \omega\tau$  and  $R_\alpha = \alpha\tau/L$ . The dynamo works if  $(R_\omega R_\alpha)^{1/2} > 1$ . One can see from (3) that  $\lambda^2$  is of the order of  $4\alpha\omega/L$  and the condition  $\lambda\tau > 2$  coincides with the dynamo criteria. The field amplification stops when the nonlinear effects begin to act.

We can see from (2) that the space structure of the resulting field does not coincide with that of the seed field because of the radial and angular dependence of  $\alpha$  and  $\omega$  but the dependence on the seed field structure remains. Expressions for  $B_r$  and  $B_\theta$  can be easily obtained from (1) and (2)

$$B_r = \frac{Q_\varphi \tau^2}{4 + \lambda^2 \tau^2} \frac{\alpha_0}{r} \sin \theta \left\{ 1 - \left[ 1 + \frac{2}{\lambda \tau} \sinh \frac{\lambda t}{2} + \frac{4}{\lambda^2 \tau^2} (\cosh \frac{\lambda t}{2} - 1) \right] \exp\left(-\frac{t}{\tau}\right) \right\} \quad (5)$$

$B_r$  increases with time under the same conditions as  $B_\varphi$ . The expression of  $B_\theta$  is similar to that of  $B_r$ . Solutions of (1) with  $Q_\varphi = 0$  may be added to (2) and (5). These solutions are usually considered in the dynamo theory. We have not use these solutions assuming that the initial initial field is zero.

Some surface magnetic anomalies do not travel with the main field but remain fixed with respect to the mantle [1, 2]. It can be explained taking into account that the seed field are tight to the mantle and travel with it. The field amplified by the dynamo does not forget the seed field distribution that provides connection of some surface magnetic anomalies with the mantle.

It was demonstrated in [4] that periods of the Earth's field reversal coincide with the strong activation of geological processes. This result connects field reversals with mantle convection that exhibits itself in the surface tectonic activity. Magnetic field reversal frequency seems to correlate inversely to mantle plume activity, corresponding to convective intensity in Earth's outer core. Apparently a significant thermal flux is created in the core, as would be expected in the process of the inner core formation. The mantle acts as a thermal blanket. The hot matter is concentrated at the top of the outer core until the temperature on the mantle bottom reaches some critical value that radically changes the thermoconductivity and viscosity of the mantle lower levels and may change the mode of convection. It provide more effective heat transport and the core gets rid of the thermal excess. The change of thermoconductivity and viscosity distribution on the core-mantle boundary leads to the change of the seed field distribution, which depends on the temperature and density gradients. It may result in total magnetic field reversal.

The assumption that both the seed field distribution and convection patterns in the core are dependent on the inhomogeneous distribution of the temperature, composition and density near the mantle boundary suggests the natural explanation that the tilt of the magnetic axis reflects the deviation of this distribution from the axialsymmetric one. This statement may be generalized to the case of the giant planets. Some of them have a magnetic axis highly tilted to the axis of rotation. A magnetic field is commonly assumed to be generated in the highly conducting metallic core or in layers immediately above the core. The planet's interior above the core and possibly inside the core is in a high turbulent state. However, it does not prevent the existence of very long lived well organized structures there. Even on the surface we can observe long lived zonal flows and solitonlike spots ( for example the Jovian red spot ). The temperature and substance distributions in zonal fluxes and spots are not homogeneous. Thus we have grounds to expect that very long lived inhomogeneities exist in regions with high conductivity. These inhomogeneities may create a magnetic field as in the cases considered above. The field structure will reflect the distribution of the inhomogeneities. For example, Uranus' axis of rotation is strongly inclined to the orbital plane . It makes the tides inside Uranus, which are driven by its satellites, nonaxialsymmetric. It may lead to a slightly nonaxial symmetric distribution of temperature, composition, and velocities in the highly conducting interior of Uranus and, as a result, to the highly tilted magnetic axis.

References : [1] Bloxham J., Gibbins D., (1987) *Nature*, 325, 511 ; [2] Gibbins D., Bloxham J. (1987) *Nature*, 325, 500 ; [3] Constable C., *Nature*, 358, 230, (1992); [4] Larson R., *Geology* 19, 963 (1991)

N 9 46-142320  
P. 2

ARE COSMIC RAYS EFFECTIVE FOR IONIZATION OF THE SOLAR NEBULA? A. Z. Dolginov  
and T. F. Stepinski, Lunar and Planetary Institute, 3600 Bay Area Blvd., Houston, TX 77058

Most models of the presolar nebula predict that beyond a certain maximum radius  $R_{\max} \sim 1$  A.U. the gas temperature is too low to cause thermal ionization of any important gas constituent. In the nebular regions beyond  $R_{\max}$  significant levels of electrical conductivity require some nonthermal ionization sources. Two such sources have been identified and considered in the literature; these are cosmic rays [1] and radioactive nuclei  $^{26}\text{Al}$  and  $^{40}\text{K}$  [2]. The effectiveness of those nonthermal ionization sources is crucial for our understanding of the hydromagnetic state of the nebula. It has been shown [3] that dynamically significant nebular magnetic fields cannot arise as the result of the compression of interstellar magnetic field during the nebula collapse, but have to be contemporaneously regenerated by the dynamo mechanism. Models of nebular dynamos [3,4] showed that ionization levels due to *in situ* radioactive nuclei alone are generally too low for a nebular dynamo to operate. The ionization rate (per H atom) due to cosmic rays is given by  $\chi_{\text{cr}} = 10^{-17} \exp\{-l/l_0\}$ , where  $l \approx \rho S$  is the column density of mass traversed by cosmic rays from the nebular surface to the given point inside the nebula,  $l_0 \approx 100 \text{ g cm}^{-2}$  is a characteristic attenuation length, and  $S$  is the length of the path traveled by cosmic rays. Nebular disk surfaces are defined at  $\pm h$  from the midplane, where  $h$  is the disk half-thickness. Thus, in the parts of the nebula that are too cool for thermal ionization to occur, directly penetrating cosmic rays may provide levels of ionization that are sufficient for maintaining a nebular dynamo, provided that the surface density at those regions is not much larger than

$l_0$ .  
ADS In this paper we argue that the effectiveness of cosmic rays to ionize the bulk of the nebular gas may be further impaired by the influence of the magnetic field on the propagation of cosmic rays. When cosmic rays enter the nebular disk they ionize the gas and make the dynamo generation of magnetic fields possible. However, once magnetic fields are embedded in the nebular gas, the upcoming cosmic rays can no longer penetrate directly into the nebular disk because they start to interact with the magnetic field and lose their energy before propagating significantly toward the midplane. That, in turn, undercuts the ionization source within the bulk of the gas stopping the dynamo action. Nebular dynamo models [3,4] ignored this back reaction of magnetic fields on cosmic rays. We calculate this back reaction effect, but for the sake of mathematical simplicity we ignore the effect of magnetic field weakening due to diminishing ionization by cosmic rays.

END  
In general, cosmic rays cannot penetrate across the region pervaded by magnetic fields if the Larmor radius  $R_L = E_p/eB$  of cosmic ray particles is less than the characteristic size of the magnetic field structure. Here  $E_p$  is the energy of a particle,  $e$  is the charge of an electron, and  $B$  is the strength of magnetic field measured in Gauss. On the basis of evidence from carbonaceous chondrites [5], as well as theoretical considerations [4], we may assume that dynamo-generated magnetic fields in the solar nebula attained a magnitude of about 1 Gauss at the midplane of the region of present-day terrestrial planets. The structure of the nebular magnetic field is unknown, but it is conceivable that field lines extend beyond the surfaces of the nebular disk and form a magnetosphere. The characteristic size of such a magnetosphere is expected to be of the order of  $h$ , or about  $10^{12}$  cm for the nebular regions under consideration. Thus a magnetospheric field of only about  $10^{-5}$  Gauss is needed to prevent cosmic rays with energies up to 1 GeV from penetrating directly into the nebula. Nebular magnetospheric fields of such small magnitude are quite conceivable; however, the detailed assessment of their role in cosmic rays screening must await the development of models that can predict the actual structure of nebular magnetic fields.

Because a magnetic field *inside* a nebular disk is maintained by a turbulent dynamo process, a large-scale field,  $B$ , is inevitably accompanied by a small-scale, random component,  $b$ , that has a zero mean value but a nonvanishing  $\langle b^2 \rangle$ . In the nebular regions capable of maintaining a magnetic field, fluctuations at least as strong as the mean field occur [4] and we may assume  $\langle b^2 \rangle^{1/2} \sim B \approx 1$  Gauss. Cosmic rays that pass through the disk's magnetosphere and enter the nebular disk must now pass through the medium permeated by a magnetic field that fluctuates in space and time. For the overwhelming majority of cosmic rays (those with energies of about 1 GeV) the Larmor radius  $R_L$  is much smaller than the characteristic length of magnetic inhomogeneities  $L_0$ , and particles rotate around and travel along lines of force. In a turbulent nebula those lines are highly tangled and lose the "memory" about their previous direction after

## IONIZATION OF THE SOLAR NEBULA A. Z. Dolginov and T. F. Stepinski

distance approximately equal to the correlation length of turbulent streamline  $L_0$ . We may assume that  $L_0$  is of the order of the size of the largest turbulent eddy, which in a turbulent nebula is estimated to be of the order of  $\sqrt{\alpha}h$ , where  $\alpha$  is the dimensionless measure of the strength of turbulent viscosity.

Thus cosmic rays are scattered on magnetic inhomogeneities and their motion inside the nebula more closely resembles diffusion than direct passage. If the distribution of scatter centers (which one can visualize as "nodes" of tangled magnetic field lines) is inhomogeneous enough, the particle would follow the random walk with the mean free path,  $\Lambda$ , given by [6]

$$\Lambda = \left( \pi N_M \int_0^\pi \sigma(E_p, \theta) \theta^3 d\theta \right)^{-1} \quad (1)$$

In this expression  $N_M$  is the number of scattering centers per unit volume, which, within the order of magnitude, is equal to the number of turbulent cells per unit volume, or  $N \approx L_0^{-3}$ . The scattering cross section  $\sigma(E_p, \theta)$  is, in the first approximation, independent of energy and scattering angle  $\theta$ , and proportional to  $L_0^2$ . Using all these estimations we find that  $\Lambda \approx 10^{-2} \alpha^{1/2} h$ , or assuming  $\alpha = 0.01$ ,  $\Lambda \approx 10^9$  cm. The cosmic ray diffusion coefficient  $D_{cr} = c\Lambda$  is about  $10^{19}$  cm<sup>2</sup>/sec.

In the absence of a magnetic field, cosmic rays penetrate without any scattering into the nebula, but are unavailable for ionization after passing the vertical distance  $d_{dir} \approx l_0/\rho$ . For the nebular region under consideration  $\rho \approx 10^{-10}$  g/cm<sup>3</sup> and  $d_{dir} \approx h$ , and the bulk of the gas can be ionized by directly penetrating cosmic rays. However, cosmic rays that undergo a random walk are unavailable for ionization after traveling the path  $S = cd_{diff}^2/4D_{cr}$ , where  $d_{diff}$  is the vertical distance penetrated by cosmic rays. Comparing those penetration depths we obtain

$$\frac{d_{diff}}{d_{dir}} = \sqrt{\frac{4D_{cr}\rho}{cl_0}} \quad (2)$$

For conditions characteristic for the regions of the nebula under consideration the ratio  $d_{diff}/d_{dir}$  is about 0.1 – 0.01. Therefore, in the presence of magnetic fields, cosmic rays can, at best, penetrate only a very small fraction of nebular thickness before becoming unavailable for ionization. In the presence of a nebular magnetosphere even more effective screening is possible. This result underscores the necessity of taking into account the back reaction of a magnetic field on cosmic rays when studying the nebular dynamo. A self-consistent, nonlinear model has to be constructed, in which resistive diffusivity of nebular gas is a function of magnetic field  $B$  in the fashion described here. We expect that, if this effect is incorporated, only the surface layers of the nebula would have a degree of ionization high enough to couple a magnetic field to the gas. The dynamo can, in principle, still work, but the character of the generated magnetic field would be very different from the one we currently envision.

**References:** [1] Hayashi, C. (1981) *Prog. Theor. Phys. Suppl.*, **70**, 35; [2] Consolmagno, G.J. and Jokipii, J.R. (1978) *Moon and Planets*, **19**, 253; [3] Stepinski, T.F. (1992) *Icarus*, **97**, 130; [4] Stepinski, T.F., Reyes-Ruiz, M., and Vanhala, H.A.T. (1993) submitted to *Icarus*; [5] Brecher, A. (1972) in *Origin of the Solar System* (Reeves, H. ed.), pp. 260-272. C.N.R.S., Paris; [6] Dolginov, A.Z. and Toptygin, I.N. (1968) *Icarus*, **8**, 54.

ON THE UNIQUE STRUCTURE OF THE MAGNETIC FIELDS OF URANUS  
AND NEPTUNE ; Sh.Sh.Dolginov (IZMIRAN, 142092, Troitsk, Moscow  
Reg. Russian Federation)

N 9 4 4 B 2 2 2 1

The magnetic fields of Uranus and Neptune, that have comparable dipole, quadrupole and octupole harmonics, are unique in the present-day Solar system but they resemble the geomagnetic field at the epochs of excursions and reversals known from paleomagnetic data. R 2

The precession dynamo model -(Dolginov [1]), in which the dominant role in the generation of the planetary magnetic fields is played by external gravitational forces, allows to propose the following scenarios for the formation of the unique topology of the magnetic fields of Uranus and Neptune :

(a) Tidal flows in the "oceans" of these two planets extend down to the depths where the matter has a noticeable electric conductivity and velocity. A hydromagnetic interaction of the moving conducting fluid with the planetary magnetic field outside the generation region results in the deformation of the field and the deceleration of the motion under the action of the radial magnetic field.

(b) The deformation of the field facilitates drastic changes in cyclonic cells within the generation region causing instabilities that result in a multi-polar field structure, excursions and even inversions, (Parker [2]), (Levy [3]). Consider this problem in more detail taking the system Neptune-Triton as an example. END

The energy of zonal flows in Neptune's "ocean" is supplied by the planet's rotational energy. A tidal crest involves the whole gas-fluid structure of the planets. The velocity of the tidal flow is smaller than the tidal crest speed,  $v < v_1 = \omega R_N = 2680$  m/s and decreases with depth. (The velocity of the cloud are 600 m/s).

The volume per unit area encompassed by the tide is equal to the depth  $H$ . The Height of the tidal crest is  $h = 3mR_N^4 / 4Mr^3$  (2) where  $M$  and  $R_N$  are the mass and radius of Neptune,  $m$  and  $r$  are the mass and orbit semi-axis of Triton (Goldreich [4]). At the depth  $H$ , the tidal crest height is  $h/H$ .  $H = \omega R_N h / v$  (3)  
 $V = \Omega \sin \alpha r / z f$  (4).



The depth  $H$  at which the linear velocity in the precessing spheroid, (Stewartson and Roberts [5]) reaches  $v = -0.1$  m/s can be determined from eqs. (2) and (3) to be  $H = 3200$  km. At this depth, the conductivity can reach  $\sigma = 10^2 \text{ ohm}^{-1} \text{ m}^{-1}$ .

The depth of  $H = 3200$  km exceeds the upper boundary of the magnetically active region of Neptune (19150 km [1]) by 2400 km. The magnetic field of the planet is being deformed in this region following the magnetohydrodynamic scenario suggested for Jupiter and Saturn by Kirk and Stevenson [7]. The zonal tidal flows are braked by the radial magnetic field. This magnetic field component has a maximum near the equator where the velocity of zonal flows is less than the rotation velocities in Neptune and Uranus. The width of the region of deceleration is larger in the Neptune because the Triton orbit is inclined to the Neptune equator at a larger angle than the satellite system of Uranus.

Tidal deformations lead to differential rotation and directed mass transport, as studied in laboratory experiments (Bobryakov [6]).

Under a high electric conductivity, such motions result in the generation of toroidal fields and under moderate conductivity, the field is only deformed. The regions of the deformed field are transformed into magnetically active regions and facilitate changes in cyclonic cells and a phase of multi-polar field structure 3. The similarity of the phases and topology of the magnetic fields in the twin planets, Uranus and Neptune, is a manifestation of a property of rotating bodies which have close parameters to synchronisation under arbitrarily weak interactions (Blechman [8]).

#### REFERENCES

1. Dolginov Sh.Sh. Precession of Uranus and Neptune and their magnetic fields (this USE)
2. Parcer E.N. Astrophys.J.1969.v.158 p.815
3. Levy E.H. Astrophys.J.1972 v.175 p.573
4. Goldreich P. Icarus 1966 v.5 N4 p.375
5. Stewartson K. and Roberts P. Fluid mech.1963.v.43 N17 p.1
6. Bobryakov A.P. et al.Geotectonika 1991 N6 p.21 (in Russian)
7. Kirk R.L and Stevenson D.J. Astrophys J,1987 v.316 p.836.
8. Blechman I.I. Synchronism in nature and thechnik 1981,35Op. (in Russian).

## PRECESSION OF URANUS AND NEPTUNE AND THEIR MAGNETIC FIELD

Sh.Sh.Dolginov 142092. IZMIRAN Troitsk Moscov, Reg.RF.

N 94-12222

163427

p 2

The strength of the dipole magnetic fields of a planet,  $H_p$ , can be estimated, relatively to that of the Earth at the epoch of the observation,  $H_e$ , as follows:

$$H_p = H_e \frac{Q_E^3 \cdot R_{CP}^3 \cdot \omega_P \cdot \Omega_P \cdot \sin \alpha_P \cdot \rho_P \cdot \sigma_P}{Q_P^3 \cdot R_{CE}^3 \cdot \omega_E \cdot \Omega_E \cdot \sin \alpha_E \cdot \rho_E \cdot \sigma_E} (1); \Omega = 1.5 M G f [\cos \alpha / \omega_P r^3] (2)$$

where  $\omega$ ,  $\Omega$ ,  $\alpha$ ,  $\rho$ ,  $\sigma$ ,  $f$  are the angular velocities of rotation and precession, the angle between  $\vec{\omega}$  and  $\vec{\Omega}$  the density, electric conductivity and dynamic flattening the planets, respectively.  $M$  and  $r$  are the mass and the distance to the body causing the precession.  $Q = R_n/R_c$  with  $R_n$  the planet radius and  $R_c$  the upper boundary of the magnetically active region. For Uranus and Neptune,  $R_c$  can be determined from the spectrum of Gaussian harmonics.

$$C_n = (2n+1)^{-1/2} \left( \frac{R_n}{r} \right)^{n+2} \sum_n [g_n^m^2 + h_n^m^2]^{1/2} (3)$$

from the following condition: at  $r = R_c$ ,  $C_1 - C_2 = 0$ , where  $C_1$  and  $C_2$  are the moduli of the dipole and quadrupole harmonics, respectively [1,2]. The parameters entering eqs. (1) and (2) are given for Uranus and Neptune in Refs. [3,4-7] basing on the Voyager 2 results. The values of  $\sigma$  have been obtained from laboratory studies for the Uranus and Neptune materials [8].

Table 1, The determination of  $R_c$  for Neptune and Uranus

$C_{N1} = 12244$  nT.  $C_{N2} = 14222$  nT,  $C_{U1} = 22837$  nT.  $C_{U2} = 15967$  nT +  $\Delta$

where  $\Delta$  is the uncertainty of  $C_{U2}$  according to [1]

$r_{Nkm}$	20000	9500	19200	19150	19100	19000	18500	18000
$\Delta C_{12N}$	564	297	57	0	-15	-123	-694	-1317

Similar arguments yield  $R_c = 13800$  km for (Uranus) and  $R_c = 14700$  km for (Uranus 2)

The generation of magnetic fields in Uranus and Neptune occurs at very different depths, at very different values of  $\sigma$ . This assertion is confirmed by the estimations of the Reynolds number  $R_m$  and agrees with the difference of the contributions of the Joule heat losses into the observed heat fluxes of Uranus and Neptune (see below).

END

Tabl.2 The parameters in eq(1) Tabl.3 The parameters in eq(2)

PARAMETERS	EARTH	NEPTUNE	URANUS-1	URANUS-2	PRECESSION RATE				
$R_n$ , km	6371	24765	25600	25600	SATELLITES	MG $10^{15}$	$r$ $10^3$ km	$\alpha^\circ$	$\Omega''/\text{YEAR}$
$R_o$ , km	3480	19150	13800	14700					
$\rho$ gr $\text{cm}^{-3}$	10	1,9	3,4	3,1	TRITON	$1428,5 \pm 4,5$	354,3	20	48,39
$\alpha^\circ$	23,5	21	Tab.1	Tab.1	MIRANDA	$4,6 \pm 1,2$	129,4	4,22	3,96
$\omega/10^5 \text{ sec}^{-1}$	7,27	10,83	10,12	10,12	ARIEL	$84 \pm 12$	191,01	0,31	22,6
$\Omega''/\text{year}$	50,2	48,39	Tab.2	Tab.2	UMBRIEL	$89 \pm 13$	266,3	0,36	7,38
$\sigma \text{ cm}^{-1} \text{ s}^{-1}$	$3 \cdot 10^5$	$1,2 \cdot 10^3$	$0,67\sigma_e$	$0,67\sigma_e$	TITANIA	$232 \pm 9$	436,9	0,14	51,6
$H$ measured	30320	14240	22840	22840	OBERON	$202 \pm 7$	583,4	0,10	1,2
$H$ calculated		14240	16885	22915					
$f_e = 3,27 \cdot 10^3$ , $f_u = 1,95 \cdot 10^{-2}$ , $f_n = 1,81 \cdot 10^{-2}$									

Magnetic Reynolds  $R_m = R_c \cdot \sigma \cdot V$   $V = \Omega \sin \alpha \cdot R_c / 2f$

(a) For  $R_c = 19150$  km and  $\sigma = 1,20 \text{ cm}^{-1}$ , we have for Neptune  $R_m = 32 > R_m \text{ cri.}$ , whereas for Uranus we obtain  $R_m = (4,8-12) < R_m \text{ cri.}$  where  $R_m \text{ cri.}$  is the critical value of  $R_m$  at which the magnetic field generation is still possible (see eq.(3) and Table 2).

(b) The Joule heat losses associated with the dynamo activity are inversely proportional to the electric conductivity squared, [11]. For the strength of the Uranus field within the planet being four times the Neptune field strength, the losses in the magnetically active region of Uranus can be  $2,5 \cdot 10^3$  times smaller than in the Neptune since  $\sigma_U = 10^2 \sigma_N$  (see Table 2),

#### References.

1. Connerney I.E.P. et al. J.G.R. 1989 v.92 NA13 p.15329.
2. Connerney .E.P. et al. J.G.R. 1991 v.96 Supplement- p.19023.
3. Tyler G.L. et al. Science 1989 v.246 N4936 p.1466.
4. Anderson J.D. J. Geophys Res, 1987 v.92 NA13 p.14877.
5. Podolak M. et al. Geophys Res. Let. 1990 v.17 N10 p.173.
6. Hubbard W.B. et al. Science 1991 v.253 N5020 p.648.
7. Zharkow V.N. Astronom Vestnik. 1991 v.26 N6 p.627 (in Russian)
8. Nellis W.J. et al. Science 1988 v.240 p.779.
9. Stewartson and Roberts P.H. Fluid. Mech. 1963 v.43 N17 p.1.
10. Rearl J.C. and Conrath J, J. Geophys. Res. 1991 v.96 Supplement p.18921.
11. Rochester M.G. et al. Geophys. Roy. Astr. Soc. 1975 v.43 p.661.

## DUST IN THE MARTIAN ATMOSPHERE : POLARIMETRIC SENSING

A. Dollfus, Observatoire de Paris, 92195 Meudon, France,  
S. Ebisawa, Planetary Research Observatory, Hino-Shi, Tokyo, Japan

Telescopic optical polarimetry over planet Mars enables to detect and localize scatterers in the Martian atmosphere. Polarization discriminates between crystal clouds (phase angle dependence of polarization  $B$  in Fig. 1) and dust particles (curve  $C$ ). For dust grains, sizes can be derived. There is an increase in size from very small grains forming the permanent dust haze to sub-micrometer size grains for the local dust veils and the several micrometer size pieces found in the dust storm clouds.

Constant dust haze. The Martian gaseous atmosphere appears to be seldom completely clean of airborne dust particles. A faint almost permanent planet-wide residual pollution appears in optical polarization by a signal scattering at least  $6.0 \times 10^{-4}$  stilb.  $\text{phot}^{-1}$  at  $\lambda = 600\text{nm}$ . The spectral variation of  $\lambda^{-4}$  requires very small particles in the size range  $0.1$  to  $0.3 \mu\text{m}$  [1]. The polarimeter VPM on board the MARS-5 orbiter indicated also particles in the same size range, and an optical depth  $\tau$  no greater than  $0.1$  [2].

Dense dust clouds. Over the yellow clouds which may expand to planet-wide storms, the polarimetric measurements available ([3] to [7]) produce the curve  $C$  of Fig. 1 which was extended up to phase angle  $V = 90^\circ$  with the polarimeter VPM on board MARS-5 orbiter [8]. Theoretical and laboratory work proved this polarization behavior to be compatible with irregular absorbing grains of several micrometers in size [8] [9] [10].

Local dust veils. Beside the occurrence of these large scale dust clouds, polarimetry discloses the presence of thin and transparent dust veils. They usually remain localized and may stay for weeks. Their existence was first noted in 1977 by S. Ebisawa when conducting the Tokyo Mars Polarization Survey in Japan. In Fig. 2, the solid curve is the predicted polarization by the Martian surface when observed through a clean atmosphere. Dots are the observations pertaining to this case. The dashed line and the circles are for the case of crystal clouds. Some measurements (crosses and dotted lines) depart drastically in a-b-c, again in d-e-f, then again in g and finally in h. This polarization disturbance occurred over Tempe-Arcadia, each time this region faced the Japanese observatory. Such kind of events were also recognized during the Mars apparitions of 1982, 1986-87 and 1988-89. They were observed essentially over the Martian areas known to be the emergence sites of dense dust storms, in addition to the northern area Tempe-Arcadia. They usually occur during the season of maximum integrated daily solar insolation for the corresponding latitude [11].

All these data produce the curve of polarization  $A$  in the Fig. 1. When corrected from the polarization by the Martian surface, the relevant measurements produce the dots in Fig. 3. Mie theory computations developed at Université de Lille by J.L. Deuzé are fitting best the observed dots when assuming a refraction index  $1.56$  and values  $r_0 = 0.05$  and  $\gamma = 4.4$  in a Junge size distribution model, which corresponds to  $r_{eff} = 0.35 \mu\text{m}$ . The optical depth is rather transparent, typically  $\tau = 0.35$ .

Conclusion. From all these polarimetric results, an overview emerges about the dust particles behavior into the Martian atmosphere. There is an increase of grain size from the very small particles producing the permanent dust haze able to remain suspended in the air for long periods of time, to the sub-micrometer size grains found in the faint dust veils probably

## DUST IN THE MARTIAN ATMOSPHERE. Dollfus A. and Ebisawa S.

resupplied by lifting from the surface under wind effect, and to the large grains of the dense storms when, on the same locations as for the faint veils, conditions are such that bigger grains can be raised, producing an opaque cloud and a self-triggered thermodynamical process.

END

## References

- [1] Dollfus A. (1966), Comptes Rendus Acad. Sci. Paris 262, 519-522.
- [2] Santer R. et al (1986), Astron. Astrophys. 158, 247-258.
- [3] Lyot B. (1925), Comptes Rendus Acad. Sci. Paris (June 2), 1645-1647.
- [4] Dollfus A. (1965), Ann. Astrophys. 28, 722-747.
- [5] Dollfus A. et al. (1977), Cospar Space Research XVII, 667-671.
- [6] Dollfus A. et al. (1984a), Astron. Astrophys. 131, 123-136.
- [7] Dollfus A. et al. (1984b), Astron. Astrophys. 134, 343-353.
- [8] Dollfus A. et al. (1974), Astronomischeski Vesnik 8, n° 4, 211-220.
- [9] Morozhenko A.V. (1979), Icarus 39, 81-87.
- [10] Santer R. et al. (1986), Astron. Astrophys. 158, 247-258.
- [11] Ebisawa S. and Dollfus A. (1983), accepted in Astron. Astrophys.

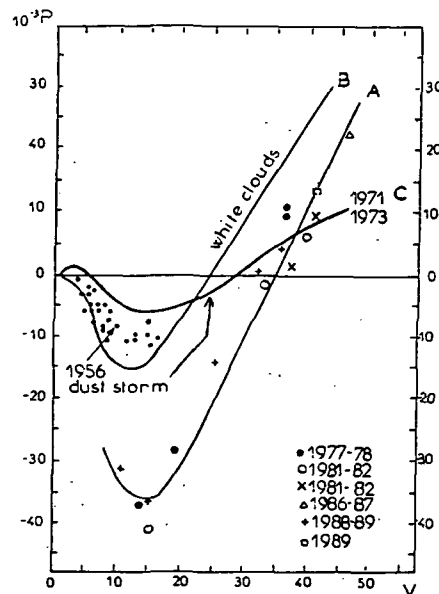


Figure 1

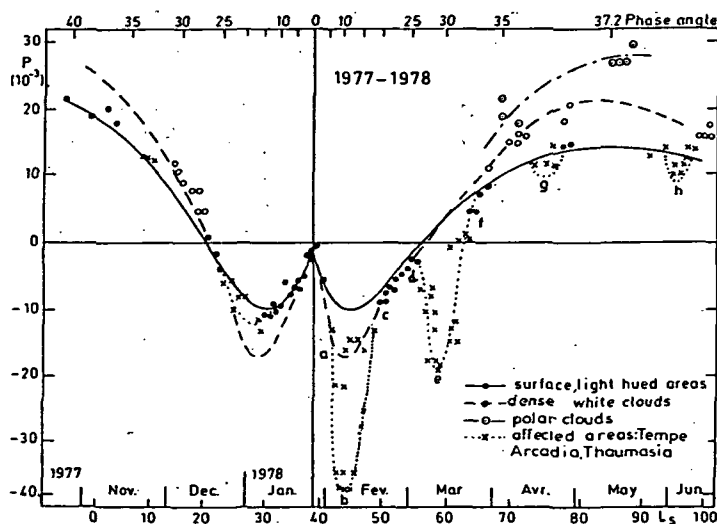


Figure 2

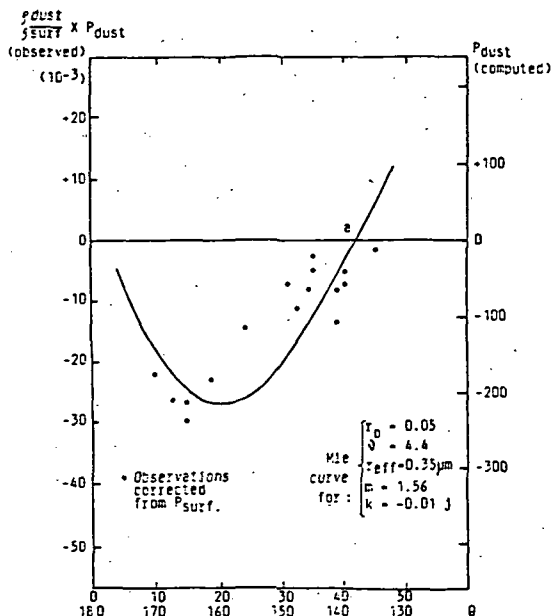


Figure 3

**DEVELOPMENT OF A MOLECULAR BEAM TECHNIQUE TO STUDY EARLY SOLAR SYSTEM SILICON REACTIONS;** *Q. W. Dong and M. H. Thiemens*, Department of Chemistry, 0356, University of California, San Diego, La Jolla, CA 92093

P. 2

ABS Silicon monoxide is one of the major gas phase silicon bearing components observed in astronomical environments.<sup>1,2,3</sup> Silicon oxide serves as the major rock forming material for terrestrial and meteoritic bodies.<sup>4</sup> It is known that several gas phase reactions produce mass independent isotopic fractionations<sup>5</sup> which possess the same  $\delta^{17}\text{O}/\delta^{18}\text{O}$  ratio observed in Allende inclusions.<sup>6</sup> The general symmetry dependence of the chemically produced mass independent isotopic fractionation process suggests that there are several plausible reactions which could occur in the early solar system which may lead to production of the observed meteoritic oxygen isotopic anomalies. An important component in exploring the role of such processes is the need to experimentally determine the isotopic fractionations for specific reactions of relevance to the early solar system. It has already been demonstrated that atomic oxygen reaction with CO,<sup>7</sup> a major nebular oxygen bearing species, produces a large (~90 ‰), mass independent isotopic fractionation. The next hurdle regarding assessing the involvement of symmetry dependent isotopic fractionation processes in the pre-solar nebular is to determine isotopic fractionation factors associated with gas phase reactions of metallic oxides. In particular, a reaction such as  $\text{O} + \text{SiO} \rightarrow \text{SiO}_2$  is a plausible nebular reaction which could produce a  $\delta^{17}\text{O}=\delta^{18}\text{O}$  fractionation based upon molecular symmetry considerations. While the isotopic fractionations during silicate evaporation and condensation have been determined,<sup>8</sup> there are no isotopic studies of controlled, gas phase nucleation processes. In order to carefully control the reaction kinetics, a molecular beam apparatus has been constructed. This system produces a supersonic, collimated beam of SiO molecules which is reacted with a second beam of oxygen atoms. An important feature of molecular beams is that they operate at sufficiently low pressures and high temperature in the jet that avalanche nucleation and clustering processes may be avoided.

The oxidation reaction of silicon monoxide (SiO) is conducted in a vacuum chamber equipped with a silicon monoxide molecular beam and a radio frequency (rf, 13.56 MHz) glow discharge flow system which produces atomic oxygen from O<sub>2</sub>. Commercial silicon monoxide powder is used as the volatile SiO precursor. The SiO beam is provided by high temperature jet expansion through a ~0.1mm aperture into a high vacuum chamber. The beam gun is designed for heats to 1900 °C and is made of an alumina tube using tungsten as the heating element. The temperature of silicon monoxide is monitored by a thermocouple inside the alumina tube and close to the nozzle exit. A second jet of oxygen atoms, produced in the rf discharge, is admixed with the SiO jet and the reaction product (SiO<sub>x</sub>) is condensed on a silver plated copper substrate. The actual temperature on the surface of substrate is not known, but may be assumed to be below room temperature for a nozzle temperature of 1700 °C. The substrate is maintained at low temperature via vacuum feedthroughs to a cryogenic reservoir. The total pressure of the reaction is about 18µm. The inert gas used for the backing pressure of the SiO molecular beam is ~6 Torr. The presumed O atom flux under the output power (40 W) of generator for an oxygen pressure 200~400 millitorr is estimated at  $10^{17}\sim 10^{18}$  (molec. cm<sup>-2</sup> s<sup>-1</sup>),<sup>9</sup> which insures an excess of oxygen atoms. The silicon monoxide vapor pressure is then the kinetic rate limiting factor for the reaction.

The SiO<sub>x</sub> condensation product has been examined by a scanning electron microscope equipped with an energy dispersive spectrometer (SEM/EDXS). The deposition rate of the vapor on the substrate is estimated at over 1000Å per minute. The semi-transparent thin film of 50µm thickness on the surface of the substrate has been examined for surface morphological characteristics and elemental analysis with X-ray spectroscopy. Using fused quartz and starting

SiO material as the references for the unknown thin film, a stoichiometry for the condensate collected on the substrate of SiO<sub>1.8</sub> is obtained. At least two reaction possibilities to account for this stoichiometry may be considered. If, during warm-up and cool down periods for the gun body, a small amount of SiO vapor may have exited the nozzle and condensed on the collection surface prior to oxygen plasma ignition, a stoichiometric number between one and two for oxygen with each silicon would be observed. Alternatively, and more likely, the reaction:



is collisionally limited, e.g., there are insufficient molecular collisions for stabilization of the vibrationally excited SiO<sub>2</sub><sup>\*</sup> species and re-dissociation occurs. Therefore, a mixture of SiO<sub>2</sub> and unreacted SiO is achieved. The collisional dependence of this process will be investigated by third body pressure and compositional variations. Based upon the present observations and analytical examinations, it is apparent that the beam system has successfully produced gas phase nucleation. The morphological characterizations are of interest for comparison with, e.g. interstellar grains recovered from meteoritic material. Ultimately, the physico-chemical characterization of the relevant parameters, such as molecular number density, composition, temperature and time (viz. kinetics) will be of importance in evaluation of interstellar grains and their histories. The molecular beam apparatus and collection features are such that studies involving other astrophysically interesting molecules, e.g. AlO, FeO<sub>x</sub> and MgO may be studied, thus providing an enhanced kinetic-mechanistic understanding of the initial nucleation processes in the pre-solar nebular. Isotopic analyses will be of even greater interest since they are of direct importance in the interpretation of meteoritic isotopic measurements.

<sup>1</sup>Langer W. D. & A.E. Glassgold (1990) Silicon chemistry in interstellar clouds. *The Astrophysical Journal*, 352, 123

<sup>2</sup>Bujarrabal V., J. Gomez-Gonzalez & P. Planesas (1989) CO and SiO thermal emission in evolved stars. *Astron. Astrophys.*, 219, 256

<sup>3</sup>Roche P.F., D.K. Aitken and C.H. Smith (1991) Silicon monoxide in Supernova 1987A. *Mon. Not. R. Astr. Soc.*, 252, 39

<sup>4</sup>Clayton R. N., R.W. Hinton and A.M. Davis (1988) Isotopic variations in the rock-forming elements in meteorites. *Phil. Trans. R. Soc. Lond.*, A325, 483

<sup>5</sup>Thiemens M. H. (1992) Mass-independent isotopic fractionations and their applications. (ed) Jack A. Kaye, *Isotope effects in gas-phase chemistry*, ACS Symposium Series No. 502

<sup>6</sup>Clayton R. N., L. Grossman and T. k. Mayeda (1973) A component of primitive nuclear composition in carbonaceous meteorites. *Science*, 182, 485

<sup>7</sup>Bhattacharya S. K. and M.H. Thiemens (1989) New evidence for symmetry dependent isotope effects: O+CO reaction. *Z. Naturforsch.*, 44a, 435

<sup>8</sup>Hashimoto A. (1989) Kinetics of evaporation of MgO, SiO<sub>2</sub>, and Mg<sub>2</sub>SiO<sub>4</sub>, and their effect on isotope mass fractionations. *Lunar Planet. Sci.* XX, 385

<sup>9</sup>Carruth, Jr., M. R., R.F. DeHaye, J.K. Norood & A.F. Whitaker (1990) Method for determination of neutral atomic oxygen flux. *Rev. Sci. Instrum.*, 61(4), 1211

5210-90  
ABS ONLY  
N 94-13225  
P-2

ON HIGH-TEMPERATURE FORMATION OF IRON-RICH OLIVINE IN THE EARLY SOLAR SYSTEM; V.A. Dorofeyeva, A.B. Makalkin, A.V. Vityazev 1—Vernadsky Institute of Geochemistry, Russian Acad.Sci., Kosygin str.19, 117334 Moscow, 2,3—Schmidt Institute of Physics of the Earth, Russian Acad.Sci., B.Gruzinskaya 10, 123810 Moscow, Russia

Kinetic restriction on formation of fayalite-rich olivine in equilibrium with the cooling solar-composition gas appears to exist at low temperature ~500 K (1). We offer a high-temperature formation mechanism (different from simple condensation) which operates at high hydrogen depletion (up to 300 times) relative to solar abundance. We show how the necessary depletion rate decreases with temperature (thermodynamical equilibrium is suggested). Consequence for planet formation is considered.

Fayalite-rich olivine is a significant component of most of chondrites, but its formation mechanism has not been well-determined yet. It was stated in many thermodynamical calculations that formation of 10-25%-fayalite-rich olivine in equilibrium with solar-composition gas is possible only at 430-530 K (at  $P = 10^{-4} - 10^{-6}$  bar) by oxidation with water vapor of iron, condensed earlier at 1250-1350 K. But at such low  $T - P$  parameters the reaction gas-solid should be kinetically inhibited (1). Palme and Fegley (1) have considered condensation mechanism of formation of iron-rich olivine at  $T > 1500$  K and  $P = 10^{-3}$  bar from the gas of solar composition, excluding water, which is added to  $10^3$  times its solar-gas abundance. Formation of fayalite occurs through the reaction:



However a physical mechanism, supplying such enrichment of gas with water vapor, has not been proposed.

Results of our simulation of recondensation in the system with chondritic bulk composition (at planetesimal intercollisions), partially presented in (2), show that in the system with high depletion of hydrogen condensation of enstatite and metallic iron occurs in the range 1500-1800 K.

In the following we consider the possibility of formation of iron-rich olivine by reaction



at  $T > 1500$  K, assuming absence of kinetic restrictions in the system gas-solid at such high temperatures. From Eq.2 one can see, that fayalite concentration in olivine ( $x$ ) strongly depends on the ratio  $[\text{H}_2\text{O}]/[\text{H}_2]$ . Approximately this dependence can be expressed using the equilibrium constant for this reaction  $K$  as

$$\log K = \log[x(1-x)](P_{\text{H}_2}/P_{\text{H}_2\text{O}})^2 \quad (3)$$

Equilibrium concentrations of fayalite in olivine as function of  $\log([\text{H}_2\text{O}]/[\text{H}_2])$ , obtained from this equation are shown in Fig. 1. It follows from the figure, that with decreasing temperature stability range for solid solution of the fixed composition moves to the lower values of the ratio  $[\text{H}_2\text{O}]/[\text{H}_2]$ . At 600-550 K iron-rich olivine becomes thermodynamically stable in the gas of solar composition (this corresponds to the intersection points for curves 1-4 with line A. Dashed line A-A' corresponds to condition when reaction  $\text{CO(g)} + \text{H}_2\text{(g)} = \text{CH}_4\text{(g)} + \text{H}_2\text{O(g)}$  at  $T < 800$  K is kinetically inhibited, and therefore the value of  $[\text{H}_2\text{O}]/[\text{H}_2]$  at lower temperatures remains constant. In this case the temperature of formation of iron-bearing olivine (solid solution) in the solid-composition gas decreases by 100 K.



HIGH-TEMPERATURE FORMATION OF IRON-RICH OLIVINE; Dorofeyeva, V.A. *et al.*

From the obtained results it follows, that formation of iron-rich olivine according to reaction 2 is possible, if condensation occurs from the gas containing all chemically active elements in solar proportion, except for hydrogen which should be 200-300 times less abundant than in the solar-composition gas. This abundance of hydrogen, though very low relative to solar composition, is too high for chondritic material, even so highly enriched in volatiles as Orgueil (3). Possible source materials and conditions which allow the appropriate value of  $[H_2O]/[H_2]$  are considered in (4).

If mechanism presented in this paper was sufficiently common in the formation region of the terrestrial planets, it could have important consequences for the composition of planetesimals and planets. Oxidation of the metallic iron at high temperatures could significantly lower formation of FeS, which would occur at  $T < 600 - 800$  K. The iron sulfide, existing in the source material, decomposes with a loss of the volatile sulfur at gas escape from the Hill sphere of colliding planetesimals. Therefore dynamically reprocessed planetesimals and planets could have significantly lower abundance of sulfur with respect to its equilibrium value for solar-composition gas. And as a consequence, higher content of FeO (relative to equilibrium calculations for the solar-composition gas) could be accreted by planets.

REFERENCES. 1. H.Palme, B.Fegley, Jr. (1990) *Earth Planet.Sci.Lett.* 101, 180-195. 2. V.A.Dorofeyeva, A.B.Makalkin, M.V.Mironenko, A.V.Vityazev (1993) This volume. 3. A.V.Vityazev, V.A.Dorofeyeva, A.B.Makalkin (1993) This volume. 4. A.B.Makalkin, V.A.Dorofeyeva, A.V.Vityazev (1993) This volume.

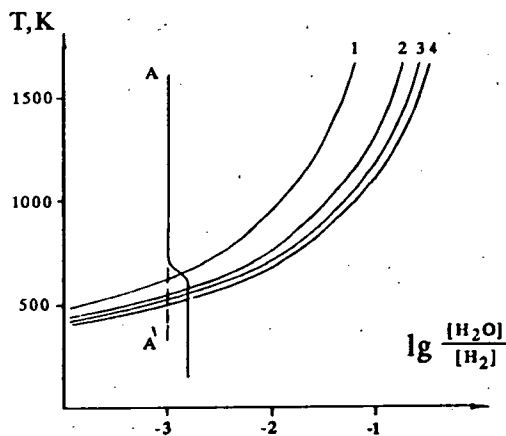


Figure 1. Fayalite content in olivine (mole %) at different temperatures as a function of mole ratio  $[H_2O]/[H_2]$ . Curve 1 corresponds to 1% fayalite content, curve 2 = 10%, curve 3 = 25% and curve 4 = 50% fayalite. Line A represents variation with temperature of  $[H_2O]/[H_2]$  ratio in the solar composition gas. Dashed line A-A' represents kinetic inhibition of the reaction  $CO + 3H_2 \rightarrow CH_4 + H_2O$ .

N94-16343/1  
12226  
p. 2

RECONDENSATION OF CHONDRITIC MATERIAL IN THE  
EARLY SOLAR SYSTEM: RESULTS OF THERMODYNAMIC SIMULATION;  
V.A.Dorofeyeva, A.B.Makalkin, M.V.Mironenko, A.V.Vityazev, 1,3-  
Vernadsky Institute of Geochemistry Russian Acad.Sci., Kosygin str.19, 117334  
Moscow, 2,4-Schmidt Institute of Physics of the Earth, Russian Acad.Sci.,  
B.Gruzinskaya 10, 123810 Moscow, Russia

~~We~~ We have performed a thermodynamic simulation of recondensation of evaporated meteoritic material. We suggested that evaporation and recondensation occurred in impact events during intercollisions of planetesimals during the early evolution of the solar system. The source materials adopted for our modeling are chondrites CI Orgueil and H5 Richardton, as the examples of the opposite extremes regarding volatile content and oxidation state (1). We calculated equilibrium mineral compositions of the closed systems of the Orgueil's and Richardton's elemental composition at the  $P - T$  conditions characteristic for the explosion cloud formed at a planetesimal collision. These  $P - T$  conditions, adopted from (1) are  $10^{-4}$  bar and 1500 and 2000 K. Results are presented in Tables 1 and 2. Before discussing the results in more details, we only mention the difference in the oxidation state of iron obtained for both source materials, with respect to the system of solar composition.

It seems interesting to compare the mineral composition obtained in our modeling (Table 1 and 2) with that reconstructed for the source material (Tables 2 and 3 in (1)). It is also of use to compare results of our calculations with those obtained from the calculations for the cooling gas of solar composition. The following conclusions can be made from the comparison.

1. Composition of refractory condensates formed from the gas of chondritic composition is similar to composition of refractories condensed from the gas of solar composition, but iron is exception. In the case of recondensation of Richardton (H5) material only 70% of iron condenses as metal. At recondensation of Orgueil (CI) metallic iron is absolutely absent, as elementary sulfur reduces  $\text{Fe}^{+3}$  to  $\text{Fe}^{+2}$  only. From this result it follows that the material of ordinary chondrites, containing significant amount of metallic iron, as well as the Earth's protomaterial, also with high abundance of iron metal, could not be obtained from the material of carbonaceous chondrites by evaporation and subsequent recondensation.

2. If hydrogen and helium are removed from the system, condensation temperatures of mineral phases become higher by 300-500 K. At evaporation and recondensation of H5 chondrite Na and K are completely condensed at 1500 K. In the case of CI chondrite at this temperature only one third of all potassium and a little more than one half of sodium are in condensed form. One can conclude, that impact reprocessing of H5 type chondritic material would accompany with much lower loss of moderately volatiles than impact reprocessing of CI type material.

3. At condensation of chondritic elemental composition formation of 10% of fayalite in olivine at  $T > 1500$  K at  $P \sim 10^{-3} - 10^{-4}$  bar appears to be possible only in the narrow range of variations of oxygen partial pressure. This result in more details is discussed in (2).

REFERENCES. 1. A.V.Vityazev, V.A.Dorofeyeva, A.B.Makalkin. (1993) This volume. 2. V.A.Dorofeyeva, A.B.Makalkin, A.V.Vityazev (1993) This volume.

Table 1  
Equilibrium Mineral Composition of the Solid Phase,  
Formed by Heating Carbonaceous Chondrite CI  
Orgueil at  $T = 1500$  K and  $2000$  K and  $P = 10^{-4}$  bar

Mineral	Chemical Formula	Abundance in Mass %	
		$T = 1500$ K	$T = 2000$ K
Spinel	$MgAl_2O_4$	---	6.4
Rankinite	$Ca_3Si_2O_7$	---	6.1
Forsterite	$Mg_2SiO_4$	11.3	32.2
Enstatite	$MgSiO_3$	44.0	55.3
Anorthite	$CaAl_2Si_2O_8$	6.9	---
Diopside	$CaMgSi_2O_6$	2.3	---
Wustite	$Fe_{0.95}O$	35.5	---

Table 2  
Equilibrium Mineral Composition of the Solid Phase,  
Formed by Heating Ordinary Chondrite H5 Richartson  
at  $T = 1500$  K and  $2000$  K and  $P = 10^{-4}$  bar

Mineral	Chemical Formula	Abundance in Mass %	
		$T = 1500$ K	$T = 2000$ K
Spinel	$MgAl_2O_4$	---	3.9
Rankinite	$Ca_3Si_2O_7$	---	2.6
Forsterite	$Mg_2SiO_4$	6.7	40.0
Enstatite	$MgSiO_3$	48.4	53.5
Anorthite	$CaAl_2Si_2O_8$	3.8	---
Diopside	$CaMgSi_2O_6$	2.9	---
Metal	Fe	22.8	---
Wustite	$Fe_{0.95}O$	11.2	---
Natur. Nepheline	$Na_{0.78}K_{0.22}AlSiO_4$	2.9	---
Nepheline	$NaAlSiO_4$	1.3	---

ANALYTIC EXPRESSION FOR EPITHERMAL NEUTRON SPECTRA AMPLITUDES AS A FUNCTION OF WATER CONTENT: Darrell Drake. Space Science and Technology Division. Los Alamos National Laboratory. Los Alamos, NM 87545.

The epithermal portion of an equilibrium neutron spectrum in a planetary body is a sensitive function of the water content of its material. The neutrons are produced at high energies but moderate by elastic and inelastic scattering until they either are captured by surrounding nuclei or escape.

The neutron equilibrium spectrum is normally divided into three energy regions which are not precisely defined in terms of energy but in terms of the type of interactions they undergo. High energy neutrons are those whose energy is large enough to scatter inelastically from surrounding nuclei. The lower boundary of this group is usually somewhere near one to two hundred keV but is dependent on the material surrounding the neutron source.

Epithermal part of the neutron spectrum begins just below the fast neutrons where the most important reaction in earthlike materials is elastic scattering. Neutron capture leading to gamma ray emission can also occur in this energy region and can contribute to observed gamma-ray spectra. The epithermal flux is reduced by these captures, especially at the lower energies where the capture cross sections are larger and more collisions are made.

The thermal neutron spectrum is complicated by both energy gaining and energy losing collisions due to thermal motion of the surrounding nuclei and by inelastic atomic reactions.

The epithermal part of the neutron spectrum is the most sensitive indicator of the presence of small amounts of hydrogen (presumably in the form of water), and fortunately it is the easiest to treat analytically. This work develops an expression that explicitly shows the dependence of the epithermal spectrum on the amount of water present in the medium and compares it to two codes that are frequently used to calculate neutron leakage spectra.

The expression for the amplitude of the epithermal spectrum [1] is given by

$$E_{pi} = Q / n \sigma \xi \quad (1)$$

where  $Q$  is the neutron source,  $n$  is the atom density,  $\sigma$  is the elastic cross section, and  $\xi$  is the logarithmic energy decrement taken as  $2/A$  for most elements and one for hydrogen. For a medium composed of several elements, the denominator of Eq. 1 can be written as

$$\sum_i n_i \sigma_i \xi_i \quad (2)$$

where  $i$  indicates the  $i$ th element of mixture. This expression can be rewritten to show the effect of a small amount of water by taking out the hydrogen component explicitly so that Eq. 1 becomes

$$E_{pi} = Q / \left( (1.33 f_{water}) + \sum_i n_i \sigma_i \xi_i \right) \quad (3)$$

where  $f_{water}$  is the weight fraction of water in the material, 1.33 is the product of the hydrogen cross section and the number of hydrogen nuclei per cubic angstrom in water of density one. The ratio of the epithermal spectrum moderated by a dry medium to the epithermal spectrum moderated by a water containing medium can be written as

$$\frac{E_{pidry}}{E_{piwet}} = 1 + \frac{1.33 f_{water}}{\sum_i n_i \sigma_i \xi_i} \quad (4)$$

This equation shows explicitly the linear dependence implied by Feldman *et al.* [2] and also shows explicitly the slope dependence as a function of the scattering cross sections of the other elements of the medium.

## ANALYTIC EPITHERMAL NEUTRON EXPRESSION: Drake, D.

Two of the codes used to compute neutron equilibrium spectra are MCNP [3], which uses Monte Carlo methods and ONEDANT [4], which uses the Boltzman transport technique. The table below presents the results of calculations of epithermal neutron amplitude for both MCNP and ONEDANT as well as the analytic expression of Eq. 4. The moderating materials were pure silicon, pure oxygen (the main components of most soils, and a proposed lunar soil. The calculations were made with no water and 0.1% water for the three materials, infinite media, and with starting neutrons of 0.2 MeV.

*EPIDRY/EPIWET*

	ONEDANT EQUATION 4		MCNP
Silicon	1.378	1.396	1.36 (high energy)
	1.17	1.20	1.18 (low energy)
Oxygen	1.0767	1.0748	1.0767
Lunar Soil	1.139	1.137	1.135

Silicon has two entries representing the high (20 keV) and low (0.5 eV) portions of the epithermal spectrum. The result for the low energy part under Eq. 4 has been corrected for neutron capture by silicon by use of an equation of Fermi [1] which accounts for the probability that a neutron is absorbed each time it collides with a silicon nucleus. The difference in the high and low energy results calculated by ONEDANT for silicon are consistent with a second part of the ONEDANT calculation shows that approximately 40% of the neutrons are captured by wet silicon and 51% are captured in the dry silicon before they reach thermal energy. The results calculated by MCNP for the lower energy epithermal neutrons agrees with those of ONEDANT and the corrected formula. Because epithermal neutrons are generally counted with cadmium covered detectors whose efficiency is proportional to the neutron velocity, most of the counted neutrons are in the energy region just above the cadmium cutoff (0.4 eV).

Oxygen has such a small capture cross section that the correction for absorption is unnecessary, and the agreement among the three calculations is excellent. Agreement among the three calculations for the lunar soil, ferroan anorthosite, is also excellent.

In summary, we have derived an expression that explicitly shows the dependence of epithermal neutron spectra on water content, compared its predictions to calculations done by a Boltzman transport code for infinite media for silicon, oxygen, and a possible lunar composition and have obtained very good agreement. *END*

References: [1] Fermi, E. (1950) *Nuclear Physics*, Univ. of Chicago Press. [2] Feldman, W. C., et al. (1991) *Geophys. Res. Lett.*, **66**, 2665. [3] Briesmeister, J., et al. Los Alamos National Laboratory report LA-9184-MS (1982).

**NOBLE GAS EVIDENCE OF AN AQUEOUS RESERVOIR NEAR THE SURFACE OF MARS MORE RECENTLY THAN 1.3 Ga;** Michael J. Drake\*, Toby Owen#, Timothy Swindle\*, and Donald Musselwhite\*. \*Lunar and Planetary Laboratory, University of Arizona, Tucson, Arizona 85721. #Institute for Astronomy, University of Hawaii at Manoa, Honolulu, Hawaii 96822. P. 2

Considerable evidence points to a Martian origin of the SNC meteorites. One of these meteorites, Nakhla, contains a leachable component which has an elevated  $^{129}\text{Xe}/^{132}\text{Xe}$  ratio relative to its  $^{84}\text{Kr}/^{132}\text{Xe}$  ratio when compared to the approximately linear array defined by Chassigny, most shergottites, and lithology C of EETA 79001. This array is thought to be a mixing line between Martian mantle and Martian atmosphere. The leachable component probably consists in part of iddingsite, an alteration product produced by interaction of olivine with aqueous fluid at temperatures lower than  $150^\circ\text{C}$ . The radiogenic Xe component may represent a distinct reservoir in the Martian crust or mantle. More plausibly, it is Martian atmosphere, fractionated by solution in liquid water and by interaction with sediment. The crystallization age of Nakhla is 1.3 Ga. Its low shock state suggests that it was ejected from near the surface of Mars. Liquid water is required for the formation of iddingsite. These observations provide further evidence for the near surface existence of aqueous fluids more recently than 1.3 Ga.

There is both direct and indirect evidence for the existence of liquid water at the surface of Mars in the distant past [1]. Evidence of stable water is seen in the existence of ancient dendritic drainage channels that mimic terrestrial desert streams and, more controversially, in the suggestion that fossil shore lines of ancient oceans are visible in Viking Orbiter imagery [2]. Evidence for metastable water exists in the form of catastrophic outflow channels. Indirect evidence for the existence of substantial bodies of liquid water 4.5 Ga ago comes from considerations of the fractionation of Xe isotopic reservoirs on Mars [3]. Of considerable interest is the possible presence of liquid water close to the Martian surface in more recent times. Its presence has been suggested on the basis of O isotopic measurements [4], vacuum pyrolysis studies [5], and mineralogical studies of alteration products [6] of SNC meteorites.

Young crystallization ages and similarities in elemental and isotopic compositions of  $\text{N}_2$ ,  $\text{CO}_2$ , and noble gases between the Martian atmosphere as measured by the Viking landers and lithology C of EETA 79001 have led to a strong consensus that SNC meteorites are samples of the Martian surface [7, 8].

Much of the elemental and isotopic structure of the noble gases may be explained as a mixture of two components [9-14]. One, perhaps mantle derived, is found in Chassigny, while the other is the Martian atmosphere-like component in EETA 79001, C. However, on a plot such as Figure 1, all nakhlites have  $^{129}\text{Xe}/^{132}\text{Xe}$  ratios that are too high to fall on the mixing line. Ott *et al.* [10] showed that the radiogenic Xe component in Nakhla itself was largely removed by leaching in 6N HCl. These authors noted that the leached component constituted 15% of the sample, and concluded that it was largely olivine. However, iddingsite is prevalent in Nakhla and, almost certainly, it was dissolved as well. Iddingsite is a weathering product of olivine consisting of smectites, hematite, ferrihydrite, Ca carbonate and Ca sulfate and its formation requires the presence of liquid water at temperatures of  $<50^\circ\text{C}$  to  $150^\circ\text{C}$  [6, 15]. Therefore, it is plausible that iddingsite is the carrier of the radiogenic Xe.

What is the source of the radiogenic Xe in Nakhla? Possibly the aqueous solution responsible for the formation of iddingsite sampled a crustal or mantle reservoir with a distinct noble gas isotopic composition. However, it is also plausible that the radiogenic component is a fractionated sample of the atmosphere, a possibility raised by Ott *et al.* [10]. Fractionation by water alone is inadequate. The Kr/Xe ratio in water is about a factor of two lower than a gas in equilibrium with it [16], while the radiogenic component of Nakhla is a factor of 5 - 8 lower in this ratio. However, terrestrial sedimentary rocks have Kr/Xe ratios lower than the atmosphere by factors of 2 - 1000 [16]. This range of sediment/atmosphere fractionation factors is consistent

# AQUEOUS RESERVOIR/MARS: Drake *et al.*

with the radiogenic Xe in Nakhla being contained in iddingsite, a sedimentary weathering product.

The conclusion that iddingsite contains the radiogenic Xe component is also consistent with the absolute abundance of  $^{132}\text{Xe}$ . Unetched Nakhla contains approximately  $6 \times 10^{-12}$  ccSTP/g, while etched Nakhla contains approximately  $3 \times 10^{-12}$  ccSTP/g. Thus, the leachate contained about  $3 \times 10^{-12}$  ccSTP/g of  $^{132}\text{Xe}$ . If iddingsite constituted, say, 1% of the leach, and all  $^{132}\text{Xe}$  was contained in it, the abundance of  $^{132}\text{Xe}$  in iddingsite would be  $3 \times 10^{-10}$  ccSTP/g. Terrestrial sedimentary rocks contain between  $6 \times 10^{-12}$  and  $5 \times 10^{-7}$  ccSTP/g [16], bracketing the iddingsite value.

Our conclusion is that Nakhla interacted with an aqueous fluid sometime after its crystallization at 1.3 Ga ago. Nakhla shows virtually no evidence of shock and, hence, must have been ejected from Mars by impact as a near surface "Grady - Kipp" fragment [17]. Thus, liquid water was present near the surface of Mars more recently than 1.3 Ga, at least in the region of origin of the nakhlites.

**References:** [1] Carr M. H. (1981) The surface of Mars. *Yale University Press*. [2] Baker V.R., Strom R.G., Gulick V.C., Kargel J.S., Komatsu G., and Kale V.S. (1991) *Nature* **352**, 589. [3] Musselwhite D.M., Drake M.J., and Swindle T.D. (1991) *Nature* **352**, 697. [4] Karlsson H.R., Clayton R.N., Gibson E.K., and Mayeda T.K. (1992) *Science* **255**, 1409. [5] Gooding J.L., Aggrey K.E., and Muenow D.W. (1990) *Meteoritics* **25**, 281. [6] Gooding J.L., Wentworth S.J., and Zolensky M.E. (1991) *Meteoritics* **26**, 135. [7] Bogard D.D. and Johnson P. (1983) *Science* **221**, 651. [8] Becker R.H. and Pepin R.O. (1984) *Earth Planet. Sci. Lett.* **69**, 225. [9] Ott U. and Begemann F. (1985) *Nature* **317**, 509. [10] Ott U., Lohr H.P., and Begemann F. (1988) *Meteoritics* **23**, 295. [11] Ott U. (1988) *Geochim. Cosmochim. Acta* **52**, 1937. [12] Swindle T.D., Caffee M.W., and Hohenberg C.M. (1986) *Geochim. Cosmochim. Acta* **50**, 1001. [13] Swindle T.D., Garrison D., Hohenberg C.M., and Olinger C.T. (1987) *Lunar Planet. Sci.* **18**, 984. [14] Swindle T.D., Nichols R., and Olinger C.T. (1989) *Lunar Planet. Sci.* **20**, 1097. [15] Treiman A.H. and Gooding J.L. (1991) *Meteoritics* **26**, 402. [16] Ozima M. and Podosek F.A. (1983) Noble Gas geochemistry. *Cambridge Univ. Press*. [17] Melosh H.J. (1989) Impact Cratering. *Oxford Univ. Press*.

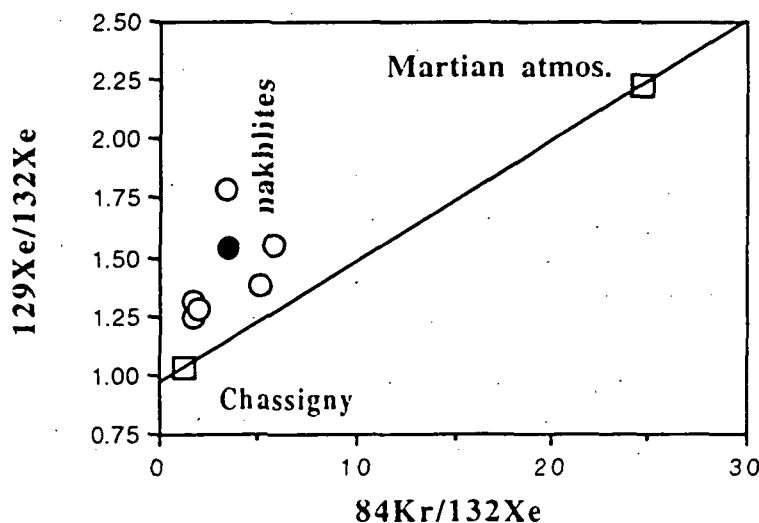


Figure 1.  $^{84}\text{Kr}/^{132}\text{Xe}$  versus  $^{129}\text{Xe}/^{132}\text{Xe}$  for some SNC meteorites. The Martian atmosphere point is lithology C of EETA 79001. Most shergottites (not shown) fall near this line, which is interpreted as a mixing line between Martian mantle (Chassigny) and Martian atmosphere. Open circles are from [9-11], filled circle is from [12-14].

N 94-163434  
122/29  
P-7

EXPLORATION PLANNING IN THE CONTEXT OF HUMAN EXPLORATION AND  
DEVELOPMENT OF THE MOON; Michael B. Duke and Donald A. Morrison, Johnson  
Space Center, Houston, TX 77058

It is widely believed that the next step beyond low Earth orbit in attaining the United States' stated goal of "Expanding human presence beyond the Earth" should be to reestablish a lunar capability, building on the Apollo program, and preparing the way for eventual human missions to Mars. The Moon offers important questions in planetary and Earth science, can provide a unique platform for making astronomical observations of high resolution and sensitivity, and can be in the development path for unlocking resources of the inner solar system to support space activities and return benefits to Earth. NASA's Office of Exploration has undertaken the planning of future lunar exploration missions, with the assistance of the Solar System Exploration Division in matters dealing with the quality of scientific data and the manner in which it will be made available to the scientific community. The initial elements of the proposed program include the Lunar Scout missions, which consist of two small identical spacecraft in polar orbit around the Moon, which can accomplish most of the objectives associated with previous proposals for Lunar Polar Orbiters (Lunar Observers). These missions would be followed by "Artemis" landers, capable of emplacing up to 200 Kg payloads anywhere on the Moon. In addition, the exploration program must incorporate data obtained from other missions, including the Galileo lunar flybys, the Clementine high orbital observations, and Japanese penetrator missions. In the past year, a rather detailed plan for a "First Lunar Outpost (FLO)" which would place 4 astronauts on the lunar surface for 45 days has been developed as a possible initial step of a renewed human exploration program. In the coming year, the FLO concept will be reviewed and evolved to become more highly integrated with planning for the initial human exploration of Mars, which could come perhaps 5 years after the reestablishment of lunar capability. Both programs could benefit from the common development of systems and subsystems, where that is sensible from a performance perspective.

The environment for obtaining approval for new space missions has changed dramatically in the past few years. Human exploration missions are particularly in question, because they tend to require new space transportation systems (eg. heavy lift launch vehicles, space habitats), greater investments in power and life support, and have significant operations costs. Like the Space Station Freedom, which is viewed as a long term operational facility, a lunar outpost could be associated with continued costs that would make it difficult for new programs to start in a period of severe budget restrictions. The "cheaper, faster, better" slogan adopted by NASA's recent management is a movement to address that concern. It is relatively clear how such direction can be implemented with robotic missions, which can be terminated when their initial objectives have been accomplished. It is less clear how to apply such an approach to human missions. The Office of Exploration's strategy is designed to develop a new exploration management culture by focusing first on robotic missions, doing them quickly, inexpensively and well, and applying the management techniques developed in the process to the human missions.

In the long run, however, it will be up to the communities involved to demonstrate that the development of a lunar program is a sound investment. The lunar and planetary science community is in the position of being able both to contribute to and benefit highly from a renewed and vigorous lunar exploration program.



N 94-16-34350

## PRIMORDIAL LIGHTNING: EVIDENCE PRESERVED IN CHONDRITES; D.

Eisenhour and P. R. Buseck, Departments of Geology and Chemistry, Arizona State University, Tempe, Arizona 85287.

**Introduction:** An increasing body of evidence suggests that transient heating events were important in forming or modifying many constituents of chondritic meteorites. For example, chondrule compositions and textures imply high cooling rates ( $\sim 5$  to  $>2000^\circ\text{C/hr}$ ) with only limited exposure to elevated temperatures ( $>1200^\circ\text{C}$ ) [1]. Similarly, experimental studies of CAIs exhibiting igneous textures suggest cooling rates from  $0.5$  to  $1000^\circ\text{C/hr}$  [2], and thermal pulses as short as milliseconds may be responsible for CAI rim formation [3]. Additionally, the spectrum of organic compounds observed in chondrites suggests that transient heating may also have played an important role in their formation. [4]. The exact nature of these transient events is less clear. A variety of mechanisms have been proposed (e.g., shock melting, drag heating, volcanism, electric discharges, and magnetic reconnection). However, a consensus is lacking as to which or what combination of these mechanisms was responsible for the range of features we observe in chondrites today. Much of the difficulty lies in the inability to identify features unique to any given process. Here we discuss electric discharges ("lightning") as a transient heat source and describe its unique signature preserved in chondrites. END

**Discussion:** Previous discussions of electric discharges have focused on those mechanisms considered most efficient: a) heating by collisions with electrons and ions within the conducting channel [5], and b) by the magnetic pinch effect, i.e., heating by channel collapse resulting from a self-induced magnetic field [6]. Unfortunately, the products produced by these mechanisms are unlikely to preserve unambiguous evidence of the unique character of their formation. Primordial lightning has, therefore, been evaluated more in terms of its physical plausibility than on its record preserved in meteorites [5,6,7].

We address the less efficient, but far more diagnostic mechanism of radiative heating produced by the electromagnetic pulse associated with an electric discharge. The property of the EM pulse that makes it unique is its frequency-dependent interaction with various types of chondritic matter. Terrestrial lightning, which produces an EM pulse that can be approximated by a blackbody radiating at  $\sim 20,000$  to  $25,000$  K, emits approximately 90% of its EM energy in the  $300$  to  $1100$  nm range [8]. For lower pressures, such as those expected in the solar nebula at  $3$  AU (although we by no means presume such a setting *a priori*), channel temperatures of  $\sim 10,000$  K may be more plausible [5]. Under these conditions, the corresponding blackbody curve would be shifted to slightly lower frequencies, and lower channel opacities would make atomic transition lines more pronounced. However, for the present argument the exact spectral distribution is not important, only that the bulk of the EM output be between  $\sim 300$  and  $1600$  nm, which is easily satisfied.

Over thicknesses of several to several tens of micrometers, most chondritic silicates absorb little energy in the visible and near infrared (typically less than 10%) [9], especially those silicates low in transition metal cations (e.g., forsterite, enstatite, gehlenite). These minerals are heated inefficiently by a passing EM pulse in this frequency range. Other minerals such as magnetite, pentlandite, troilite, and metals absorb strongly in this energy region and are, therefore, heated much more efficiently. The result is preferential melting and or evaporation based on optical properties rather than on volatility. (For a similar discussion on grain survival in a supernova environment see [10].) This preferential heating is still not helpful in itself, because little is gained by comparing the thermal history of one grain to another, both of uncertain parentage. We already know that some components of chondrites were heated and cooled more rapidly than others. However, the preferential heating effect is distinctive when opaque phases are enclosed in non-opaque silicates. The ensuing quench produces a variety of "dirty snowball" textures similar to that shown in figure 1. These "dirty snowballs" occur in a variety of chondrite components and are composed of a range of phases. In chondrules they appear as  $<1$ - to  $20$ - $\mu\text{m}$  assemblages of spherically dispersed opaque minerals such as troilite, pentlandite, taenite, and magnetite in a matrix of olivine or pyroxene. Similar features also occur in individual matrix olivines. In CAIs they are most commonly distributed within or adjacent to rims exhibiting a wide range of compositions, from pentlandite and taenite within andradite to refractory noble metals dispersed in olivine, pyroxene, melilite, and spinel hosts. The only feature these "snowballs" have in

# PRIMORDIAL LIGHTNING: *Eisenhour, D. and Buseck, P. R.*

common is that all are composed of optically opaque phases spherically distributed in optically transparent hosts.

An estimate of the magnitude of a discharge necessary to produce the observed features can be made by using terrestrial lightning as an analogue. We use as an example a dirty troilite + olivine "snowball" of radius 5  $\mu\text{m}$ , with each phase constituting one half by volume. The pre-lightning assemblage would then be an  $r \sim 4\text{-}\mu\text{m}$  sphere of troilite enclosed within olivine. If we assume an ambient temperature of 500 K, an olivine liquidus temperature of 2000 K ( $\sim\text{Fog5}$ ), mean heat capacities of 185 and 65  $\text{J mol}^{-1} \text{K}^{-1}$ , and heats of fusion of 75 and 32  $\text{kJ mol}^{-1}$  for olivine and troilite, respectively, a minimum of  $\sim 40$  ergs is required to melt the assemblage, assuming no heat is conducted to the remaining host olivine. Taking 50  $\mu\text{m}^2$  as the cross section of the initial troilite sphere gives a time integrated flux (net energy density) of 80,000  $\text{J m}^{-2}$ . Assuming olivine and troilite reflectances of 10 and 40%, respectively, and neglecting olivine absorption, raises the value to 150,000  $\text{J m}^{-2}$ .

Measurements of terrestrial lightning indicate a mean, 300 to 1100 nm, single-stroke EM density of 15,000  $\text{J m}^{-2}$  at the lightning channel surface [11]. Given the magnitude range of terrestrial lightning [8],  $\sim 1\%$  of strokes may have outputs as high as 150,000  $\text{J m}^{-2}$ . Considering that the EM energy accounts for only  $\sim 0.5\%$  of the total input energy [11], the electrical potential energy released in a single discharge is equivalent to that required to form 10,000,000 millimeter-sized chondrules. Of course no real process would form chondrules at 100% efficiency, and this says nothing about the frequency with which these discharges may have occurred. However, it is clear that discharges of this magnitude would release ample energy to form chondrules by one of the more efficient mechanisms mentioned earlier. It should be noted that the use of the terms "electric discharge" and "lightning" here are not meant to exclude the potentially similar processes associated with magnetic reconnection [12]. The important point is that an intense EM pulse of short duration is characteristic of the process.

Although evidence of lightning is preserved in chondrites, it is unlikely that this was the sole means of transient heating. While it is easily argued that chondritic material can be melted in an electric discharge, it is more difficult to account for cooling rates as low as  $\sim 5^\circ\text{C/hr}$ . A combination of processes, inclusive of lightning, seems more plausible. In fact, it may not be unreasonable to envision these processes working together. Other proposed mechanisms such as heating in turbulent shear zones [13] may, as a byproduct, provide the differential gas/grain velocities necessary to produce the charge separation required for the production of lightning. Estimates of discharge magnitude, similar to those presented here, may help to constrain such associated processes. The important point, however, is that a process analogous to lightning did play an important role in producing the features we observe in chondrites today.

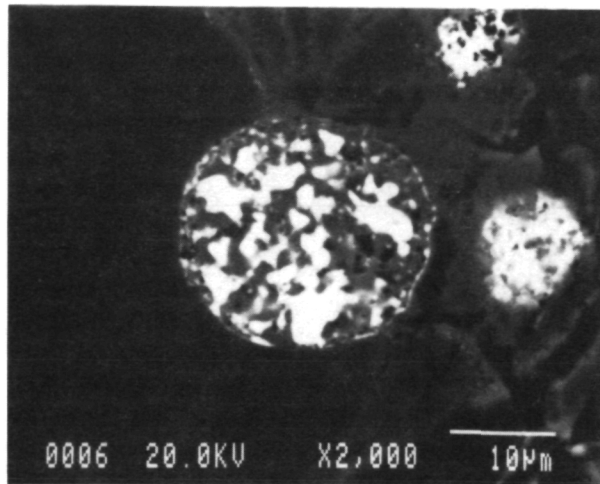


Fig. 1. "Dirty Snowball" composed of troilite and olivine (from Allende).

**References:** (1) Hewins, R. H. (1988) in *Meteorites and the Early Solar System*, U of A Press, Ch. 9.2. (2) Stolper, E. and Pague, J. M. (1986) *GCA* 50: 1785-1806. (3) Murrell, M. T. and Burnett, D. S. (1987) *GCA* 51: 985-999. (4) Miller, S. L., Urey, H. C., and Oro, J. (1976) *J. Mol. Evol.* 9: 59-72. (5) Cameron, A. G. W. (1966) *Earth Planet. Sci. Lett.* 1: 93-96. (6) Whipple, F. L. (1966) *Science* 153: 54-56. (7) Sonett, C. P. (1979) *Geophys. Res. Lett.* Vol. 6, No. 8: 677-680. (8) Uman, M. A. (1984) *Lightning*, Dover, Inc. (9) Rossman, J. R. (1988) in *Reviews in Mineralogy*, vol. 18, Ch. 7. (10) Falk, S. W. and Scalo, J. M. (1975) *Ap. J.* 202: 690-695. (11) Krider, E. P., Dawson, G. A., and Uman, M. A. (1968) *J. Geophys. Res.* 73: 3335-3339. (12) Levy, E. H. and Araki S. (1989) *Icarus* 81: 74-91. (13) Wood, J. A. (1986) *LPSC XVII*: 956-957.

5216-90  
ABS. ONLYN 9/4-12231  
P-2

**MICRO-ZONING IN MINERALS OF A LANDES SILICATE INCLUSION.** D. D. Eisenhour<sup>1</sup>), P. R. Buseck<sup>1</sup>), H. Palme<sup>2</sup>) and J. Zipfel<sup>2</sup>); <sup>1</sup>) Departments of Geology and Chemistry, Arizona State University, Tempe, Arizona 85287, USA, <sup>2</sup>) Max-Planck-Institut für Chemie, Saarstrasse 23, 6500 Mainz, Germany.

There is an increasing number of meteorites with chondritic bulk composition but completely different textures than the conventional chondrite groups. Winonaites, Acapulcoites and silicate inclusions in IAB-iron meteorites have in common coarse grain size, highly equilibrated mineralogy with frequent 120° triple junctions and they record a significantly lower degree of oxidation than ordinary chondrites. They all have equilibration temperatures, based on Ca-exchange among pyroxenes, of around 900 to 1100°C. However, on cooling disequilibrium features may develop: (a) Olivine in IAB-inclusions has lower Fa-content than equilibrium Fs-content of pyroxenes requires<sup>(1)</sup> (b) CaO-zoning in olivine was established at temperatures of around 500°C, several hundred degrees below pyroxene equilibration temperatures<sup>(2)</sup>. Obviously, olivine responded faster to changes in fO<sub>2</sub> (Fa in olivine) and temperature (Ca-zoning) than pyroxenes. Differences in diffusion coefficients can readily explain the observed trends. Here we report on much more subtle zoning features in pyroxenes. TEM-observations reveal large compositional gradients in Ca, Na, Cr, Ti and Fe within the first micrometer of cpx and opx crystals.

**Experimental:** Representative grain boundaries were identified in a Landes thin-section by SEM/EMPA, and then removed from the section and ion-thinned to electron transparency. Analyses were performed on a JEOL 2000FX TEM equipped with a Kevex thin-window, energy-dispersive x-ray spectrometer. A fixed probe diameter of 50 nm and a constant beam current were used for analyses. From time-resolved diffraction and EDS data it was determined that the resulting beam-current density caused no structural damage or volatile element loss from any of the phases analysed. Inter-element K-factors were determined by analyzing cpx, opx, and olivine grain interiors and comparing these values to WDS microprobe data acquired from the same grains prior to removal from the thin section. ZAF corrections to the data were performed using thicknesses determined by oxygen K<sub>α</sub> absorption.

**Results and discussion:** Zonation profiles in cpx and opx are shown in the Figure. Results are given as number of atoms per 4 cations. Element concentrations 2 μm from grain boundaries are typical of the concentrations for average Landes inclusions and agree with literature data. Extensive zoning begins at a distance of 0.5 to 1 μm from grain boundaries. Some "large scale zoning" of Ca in opx is common in Landes inclusions<sup>(3)</sup> and can be easily determined with the electron microprobe. According to the calibrations of<sup>(4)</sup>, Ca in opx cores records temperatures of about 980°C, while the lower Ca at opx rims reflects temperatures of about 840°C. A temperature decrease produces a CaO decrease in opx and an increase in coexisting cpx. Surprisingly, Ca decreases in both cpx and opx within the first μm of their boundaries. The decrease of Ca in cpx appears to be compensated by an increase in Na. The combination of both would, according to the formalism of<sup>(4)</sup>, result from an overall small temperature decrease. The parallel increase of Cr suggests that one Cr and one Na ion may substitute for Ca + Mg. The driving force for this replacement could be the formation of Ca-phosphate which is commonly found in these inclusions. Cpx may then act as a source for Ca.

Formation of Ca-phosphate would also provide an explanation for the FeO-zoning since it involves the oxidation of metallic P to P-oxide and a simultaneous reduction of FeO to Fe. Since diffusion in olivine is much faster than in pyroxenes, olivine crystals would be affected much more than pyroxene-crystals. According to calculations by<sup>(5)</sup>, the transition of P dissolved in NiFe to phosphate would occur in Landes silicate inclusions at temperatures below 830°C.

The zoning of Cr, Ti, (see Figure) and also Zr (not shown in the Figure) in cpx is difficult to understand. As temperature decreases both Cr and Ti will, under equilibrium conditions, begin to move from opx into cpx just as Ca would have done in the absence of phosphate formation. In addition, both Cr and Ti may be required for charge balance to compensate for the loss of Ca.

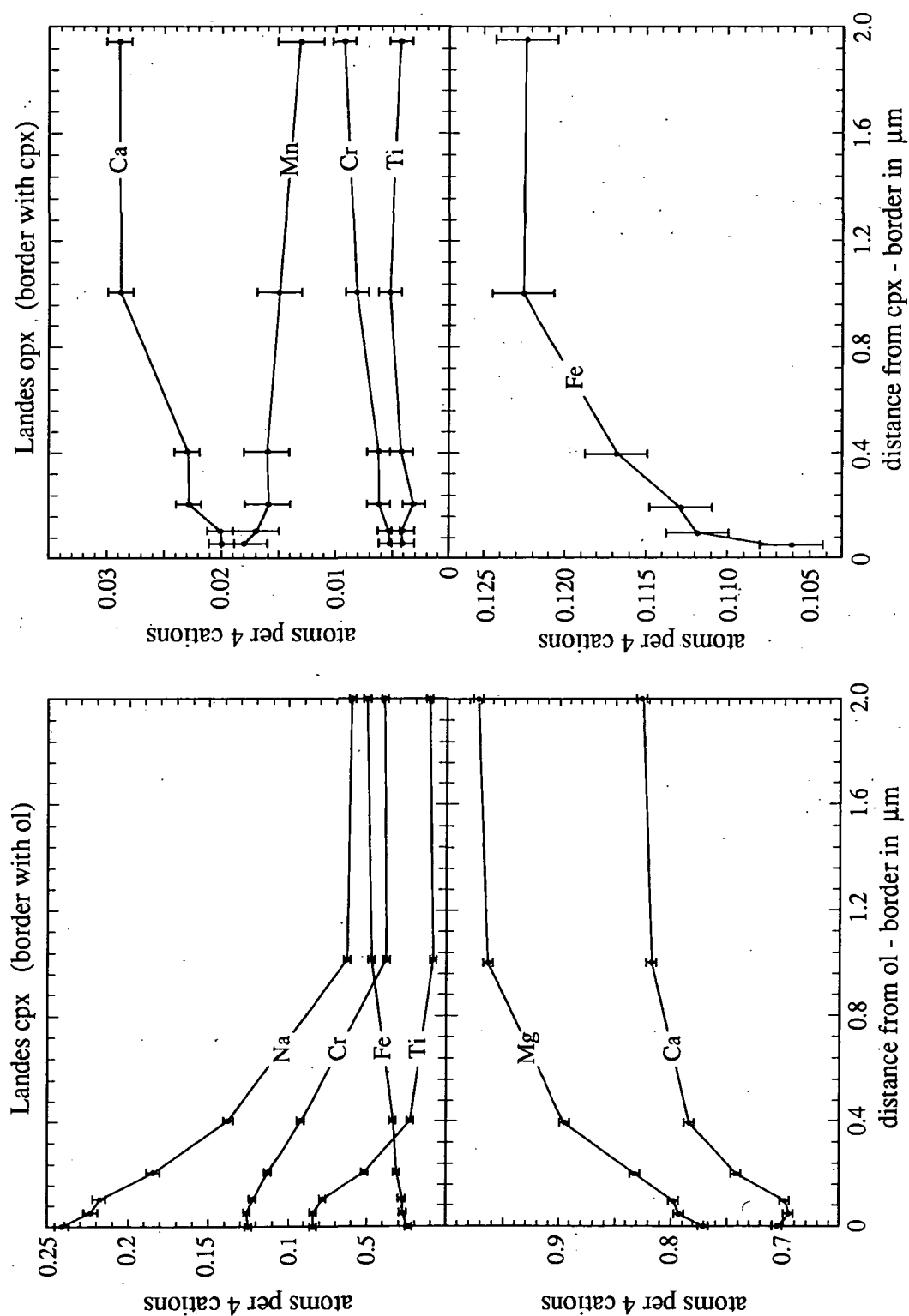
The enrichment of Na in the outer layers of cpx requires a Na source. The only reasonable source is plagioclase. A grain of Al-silicate was found associated with plagioclase, providing evidence for dissolution of plagioclase and diffusion of Na into cpx.

**In summary,** the data presented here reflect the complicated subsolidus history of a chondritic mineral assemblage that was in thermodynamic equilibrium at about 900°C and cooled slowly from this temperature whereby oxidation reactions and different closure temperatures for various minerals and elements played an important role. The oxidation of P dissolved in metal and formation of phosphate, which is thermodynamically stable at low temperatures, is suggested to be responsible for most of the observed zoning.

end

## MICRO-ZONING IN MINERALS: Eisenhour D. D. et al.

Lit.: (1) v. Seckendorff V. et al. (1992), *Meteoritics* 27, 288-289; (2) Köhler T. et al. (1991), *N. Jb. Miner. Mh.* 9, 423-431; (3) Luzius-Lange D. (1986), Ph. D. Thesis, Universität Mainz; (4) Brey G.P. and Köhler T. P. (1990), *J. Petrol.* 31, 1313-1352; (5) Olsen E. and Fuchs L.H. (1967) *Icarus* 6, 242-253.



**SOLAR WIND-INDUCED SECONDARY IONS AND THEIR RELATION TO LUNAR SURFACE COMPOSITION;** R. C. Elphic, H. O. Funsten III, Space Plasma Physics Group and Geology and Geophysics Group, Los Alamos National Laboratory, Los Alamos, NM 87545, R. L. Hervig, Center for Solid State Science, Arizona State University, Tempe, AZ 85287

Based on previous laboratory experiments simulating solar wind sputtering of lunar surface materials, it appears that solar wind ions sputter secondary ions in sufficient numbers to be measured from low-altitude lunar orbit. Solar wind protons are hundreds of times less efficient than those used in standard secondary ion mass spectrometry; nevertheless secondary ions of Na, Mg, Al, Si, K, Ca, Mn, Ti and Fe were observed sputtered from sample simulants of mare and highland soils. These secondary ion fluxes depend both on concentration in the soil and on probability of ionization; yields of easily ionized elements such as K and Na are relatively much greater than those for the more electronegative elements and compounds. The principal geochemical indicator elements Na, Mg, Al, Si, K, Ca, Ti, Mn and Fe are nevertheless detectable. However, it has not been shown that the observed secondary ions vary strictly one-to-one with their concentrations in the geochemically distinct soil simulants used here.

While we have a first order understanding of secondary ion sputtering, it is not clear that the observed ion yields can be linked with great accuracy to the simulant's composition. The simulants were analyzed by electron microprobe to establish their detailed composition. The observed secondary ion fluxes can then be compared with the microprobe results. For example  $Ti^+$  fluxes from the three simulants correspond to the true composition with accuracies of better than 10% for the high-Ti basalt, and about 20% for the low-Ti simulant. The highlands simulant produced a statistically insignificant  $Ti^+$  count rate.

Similar results were obtained for the elements Al, Fe, Ca, and K. However, the response of Mg ions did not correlate well with composition under any circumstances. Na content did not vary enough between samples to do the comparison. We suspect that cross-contamination and/or profound surface effects contributed to the lack of correlation between the microprobe results and the hydrogen sputtering results.

Here we discuss the results of further SIMS experiments using the ASU/Center for Solid State Science facility. With careful isolation and preparation of samples, we avoid the problems of the previous experiments. In particular, we will make use of ground-up sample to mimic the sputtering behavior of regolith, and will avoid charging by placing the soil on a conducting indium substrate. We report the results of a blind test of the SIMS technique using a sample of unknown composition.

end

5218-90  
ABS. ONLY

N 94-138233

**A NEW CARBON-RICH PHASE ("COPS") IN ANTARCTIC MICRO-METEORITES.** C. Engrand, M. Maurette (C.S.N.S.M., Bat. 108, 91405-Orsay, France), G. Kurat, F. Brandstätter (Naturhistorisches Museum, A-1014, Wien, Austria), M. Perreau (Laboratoire d'Etudes des Microstructures, ONERA, BP 72, 92322-Chatillon, France).

The contemporary flux of micrometeorites with sizes  $> 50 \mu\text{m}$  reaching the Earth's surface each year (about 20,000 tons/a, see [1], is much larger than the value of  $\approx 100$  tons/a, reported for conventional meteorites up to masses of  $\approx 10,000$  tons [2]. Moreover, on the average, Antarctic micrometeorites contain at least as much carbon as does Orgueil, the most C-rich meteorite [3,4]. Micrometeorites are thus responsible for most of the carbon accreted by the Earth. In this paper we report SEM observations of a new C-rich "dirty magnetite" phase observed as tiny inclusions in both melted and unmelted micrometeorites. This phase, which is enriched in C, O, P, S, Fe, frequently shows Ni contents in excess of 0.2%, strongly suggestive of an "extraterrestrial" origin. We also discovered this "COPS" phase in the fusion crust of Murchison. It appears likely that COPS is a product of meteoroid reprocessing during frictional heating in the Earth's atmosphere and/or its fast "weathering" in the upper atmosphere. Upon "catalyzed" hydrolysis this phase might have facilitated the functioning of micrometeorites as "micro-chondritic-reactors" for the synthesis of prebiotic molecules on the early Earth. — end

This COPS phase has been observed in about 1/3 of all types of chondritic micrometeorites investigated so far. This is illustrated by a selection of EDS spectra shown in Figure 1, derived from a "melted" "barred" cosmic spherule (1a), a scorian type micrometeorite (1b), a crystalline (1c) and a fine grained phyllosilicate-dominated (1d) micrometeorites. The corresponding polished sections of these grains (Fig. 2a-2d) indicate that COPS appears mostly as inclusions concentrated in isolated voids and/or cavities. The EDS spectra reported in Figure 1e illustrates our discovery of similar COPS inclusions in cavities of the fusion crust of the Murchison CM chondrite (13 inclusions with sizes  $< 10 \mu\text{m}$  observed on  $2.5 \times 10^{-3} \text{ cm}^2$ ).

COPS was never observed before in conventional meteorites and IDPs. It differs from the hydrous iron oxisulfate (tochilinite) reported from primitive meteorites [5]. It shows a clear association of phosphorus and sulfur, and also frequently contains a richer variety of minor elements, including K, Ca, Cr, Ni, Cu, Zn. These COPS inclusions are not an artefact of our polishing technique (based on an all diamond powder procedure) as they are observed either in a given object before and after polishing (see the chondritic cosmic sphere reported in Fig. 2e and 2a, respectively), or in micrometer-size crushed grains [4]. It is also unlikely that COPS be related to terrestrial weathering effective during the trapping of AMMs in Antarctica blue ice or their recovery from melted ice water [6]. Indeed they are found in the fusion crust of Murchison, a meteorite collected very soon after fall in an Australian "hot" desert. We thoroughly searched for COPS in a large number of terrestrial grains, including particles of dark rust. Only the grain reported in fig. 2f did show a COPS looking phase without Ni (see EDS spectra in Fig. 1f). We have to definitively assess whether this peculiar grain is an extraterrestrial particle.

The high concentrations of Ni generally observed in COPS inclusions are strongly suggestive of their extraterrestrial origin. However, in the Murchison meteorite, they have only been found in the meteorite fusion crust, yet. This suggests that such inclusions result from the remobilization of some progenitor extraterrestrial component during either frictional heating in the Earth's atmosphere, or a fast "weathering" in the upper layers of the atmosphere. The habit of the beautiful COPS "nugget" in a chondritic cosmic sphere (see arrows in Fig. 2e and Fig. 2a), looks very similar to that of Fe/Ni metal and/or magnetite nuggets frequently observed in similar types of spheres, and which have been attributed to the segregation of a metal bead from a melted chondritic droplet. Such similarities would rather support a frictional heating reprocessing of some unknown precursor material of COPS. But we cannot definitively rule out that most of the "dirty magnetite" COPS inclusions, as well as the ultrathin coating of magnetite observed around AMMs, might result from some poorly understood atmospheric "weathering" process [7].

Perreau et al [4] from their observation of  $\mu\text{m}$ -size crushed grains with an analytical TEM estimate that COPS represents about  $\approx 5\%$  of the total amount of C-rich material trapped in micrometeorites. This "minor" phase might be an interesting tracer of atmospheric processes, which can be hopefully monitored in the distant past looking at micrometeorites of different terrestrial ages. But COPS inclusions could have also been involved in the synthesis of prebiotic molecules on the early Earth, through a process of "catalyzed hydrolysis", effective within individual micrometeorites, which could have functioned as "micro-chondritic chemical reactors" [9].

## COPS PHASE IN ANTARCTIC MICROMETEORITES Engrand C. et al.

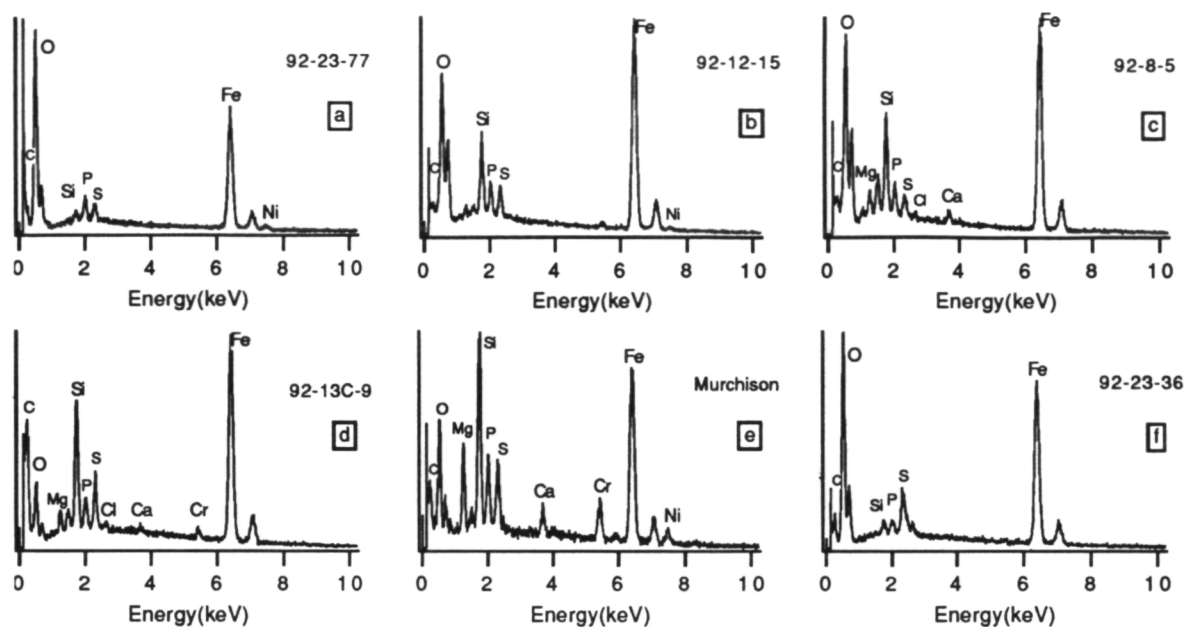


Figure 1

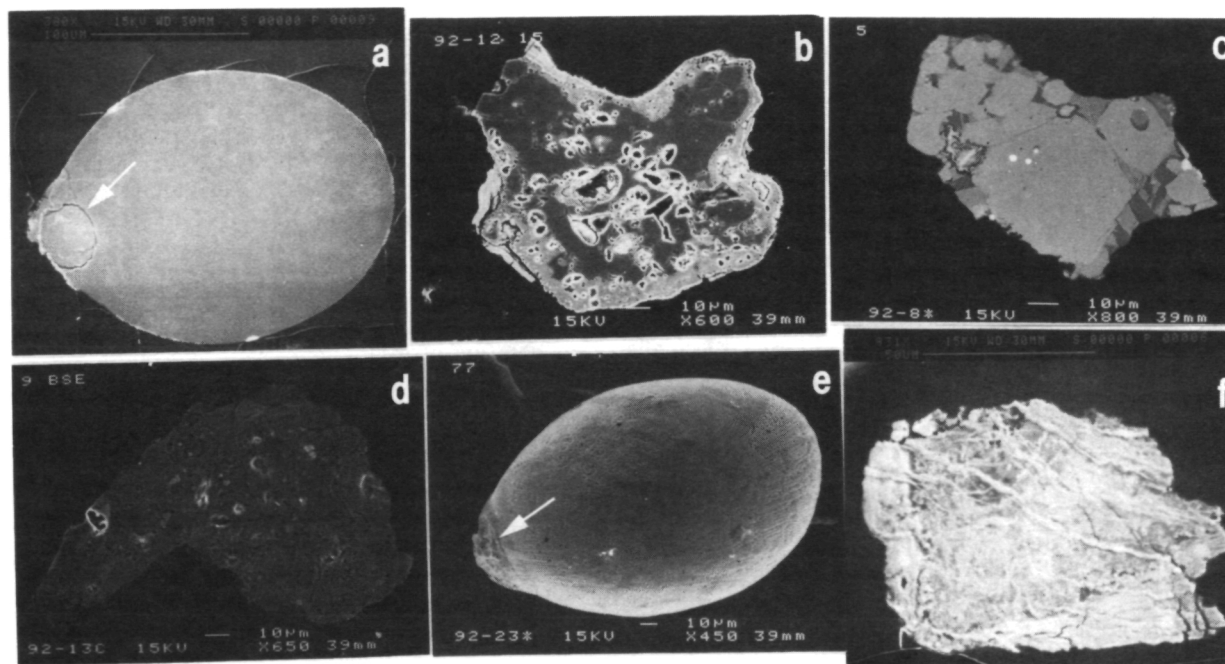


Figure 2

**REFERENCES:** [1] Maurette M., Hammer C., Pourchet M (1991), in: *From Mantle to Meteorites*, eds Gopalan K., Gaur B.L., Somayajulu J.D., MacDougall J.D., Indian Academy of Sciences, Bangalore, p.87-126; [2] Halliday I., Blackwell A.T., Griffin A.A (1989) *Meteoritics* 24, 173; [3] Perreau M., Maurette M., Kurat G., Engrand C. (1992) *Meteoritics* 27, 274; [4] Perreau et al (1993) this Abstract book; [5] Zolensky M. E. (1987), *LPSC XVIII*, 1132-1133; [6] Maurette M., Pourchet M., Perreau M. (1992), *Meteoritics* 27, 473; [7] Jessberger E.K., Bohsung J., Chavaveh S., Traxel K. (1992) *Earth Plan.Sci. Let.* 112, 1; [8] Kurat G., Koeberl C., Presper Th., Brandstätter F. and Maurette M. (1992), *Meteoritics* 27, 246; [9] Maurette M., Bonny Ph., Brack A., Jouret C., Pourchet M., Siry P. (1990) *Lecture Notes in Physics* 390, 124.



**Automatic definition of spectral units in the equatorial regions of Mars.** Stéphane Erard, Priscilla Cerroni, Angioletta Coradini. *IAS-Planetologia, viale dell'Università 11, 00185 Roma, Italy.*

**Introduction.** ISM was the first instrument that acquired spectra of small areas ( $25 \times 25 \text{ km}^2$ ) on a planetary surface. The data set consists mainly in images made up of about 3000 such pixels, each one corresponding to a near-infrared spectrum ( $0.76$  to  $3.15 \text{ }\mu\text{m}$  in 128 spectral channels) with high signal-to-noise ratio [1]. These data were used to define spectral units and to constrain the mineralogy of surface materials in the equatorial regions of the planet [2] [3]. Future spaceborne imaging spectrometers (*e. g.* OMEGA on board the Mars-94 Russian spacecraft) are expected to provide several hundred times as much data as ISM, so there's a strong need for fast and reliable processing methods. The present work is an attempt to define spectral units in the region of Syrtis Major-Isidis Planitia by means of G-mode analysis. The method allows to cluster the spectra according to their similarities; different levels of classification can be achieved by tuning a threshold of confidence [4].

**Preparation of the data set.** Since the signal doesn't only depend on the surface materials, an analysis of the whole spectra would incorporate features related to the atmosphere (mainly  $\text{CO}_2$  absorption bands) to the aerosols (overall spectral slope) and to changes in viewing geometry (spectral slope, radiance). Each pixel must thus be described by a limited number of quantities related to the surface mineralogy, *e. g.*: Reflectance corrected from photometric effects, depth, locations and surface of mineralogical bands... The variations of albedo (up to a factor of 3, see Fig. 2) are huge as compared to those of the absorption bands (in general less than 5%), so they always dominate the variance. To study more subtle features, we parametrized the spectra with 6 quantities: a) Shape of the  $0.8\text{-}1.0 \text{ }\mu\text{m}$  band, indicative of iron mineralogy (ratio of absorptions due to  $\text{Fe}^{3+}$  and  $\text{Fe}^{2+}$ , *i. e.* ferrous oxides versus mafic minerals). b) Depth of a large band centered at  $2.17 \text{ }\mu\text{m}$ , typical of Ca-rich pyroxens. c) Depth of the  $3 \text{ }\mu\text{m}$  band of hydrated minerals. d) and e) Depth of two narrow bands centered at  $2.37$  and  $2.20 \text{ }\mu\text{m}$ , related to Mg-OH and Al-OH bindings. f) Estimate of the surface contribution to the spectral slope.

**Results.** A first order analysis distinguishes between 8 main spectral types that form spatially coherent units (Fig. 1). (i) The bright regions of Isidis and Libya (class 1) cannot be separated on the basis of their spectral properties, while their morphologies are different. This was interpreted as the effect of a thin coverage by bright, hydrated dust with  $\text{Fe}^{3+}$  features [2] [3]. The craters in this regions (classe 5) have similar spectral properties due to a partial dust coverage. (ii) Conversely, the shield of Syrtis is clearly splitted in 3 main units (east, west and center, classes 4, 2 and 6). As a whole, they differ from class 1 by deep mafic features at  $1$  and  $2.17 \text{ }\mu\text{m}$ , and by a shallower hydration band at  $3 \text{ }\mu\text{m}$ . Previous interpretations of the data identified augite as a major mineral in this region [3]. (iii) Meroe Patera, which is one of the sources of the volcanic materials of Syrtis, appears as a separated unit (class 8) with stronger Ca-pyroxen absorptions and flatter spectra. Figure 2 shows the average spectra of the main five classes. One can see their differences in albedo (not included in the analysis), in spectral slope and in the shape and location of the iron band around  $1 \text{ }\mu\text{m}$ . Class 4 (east of Syrtis) has a medium reflectance, which is not normal since the albedo distribution is bimodal. This indicates that this class is not homogeneous but gathers together spectra of very different albedos on the basis of a single parameter (their unusual steep spectral slope). A deeper analysis makes appear new spectral units (Fig. 3). The eastern part of Syrtis (class 4 on Fig. 1) that was suspected to be heterogeneous, splits up in 6 sub-units on the basis of small differences in iron mineralogy. Two of this sub-units are relatively bright (classes 9 and 10), the other four are dark (classes 4, 11, 12 and 13). The bright regions remain unchanged, and do so even for high levels of analysis.



DEFINITION OF SPECTRAL UNITS ON MARS. ERARD *et al.*

**Conclusions.** The results in the Syrtis Major-Isidis Planitia area, and similar ones in the Valles Marineris region, are very close to those of the previous analysis of the same data set: The bright regions appear homogeneous, hydrated and oxidized; the dark regions exhibit deep mafic features and a shallower hydration band, with a high degree of heterogeneity. The resulting maps of the spectral types are similar to those previously obtained by other means, and are in general highly correlated to the surface morphology. Taking into account an estimate of the aerosols contribution didn't modify the limits of the spectral units. Up to 20 meaningful spectral types can be identified per observation session on the basis of 6 spectral criteria, excluding albedo. The average spectra of the classes and the numeric outputs of the analysis allow to quantify the relative importance of the spectral features and to interpret the surface materials. This qualifies the method for further analysis of ISM data and future analysis of imaging spectroscopy data, provided that the main spectral criteria (absorption features due to the surface materials) are identified prior to analysis.

Fig. 1 Low-level analysis of the Syrtis-Isidis image-cube.

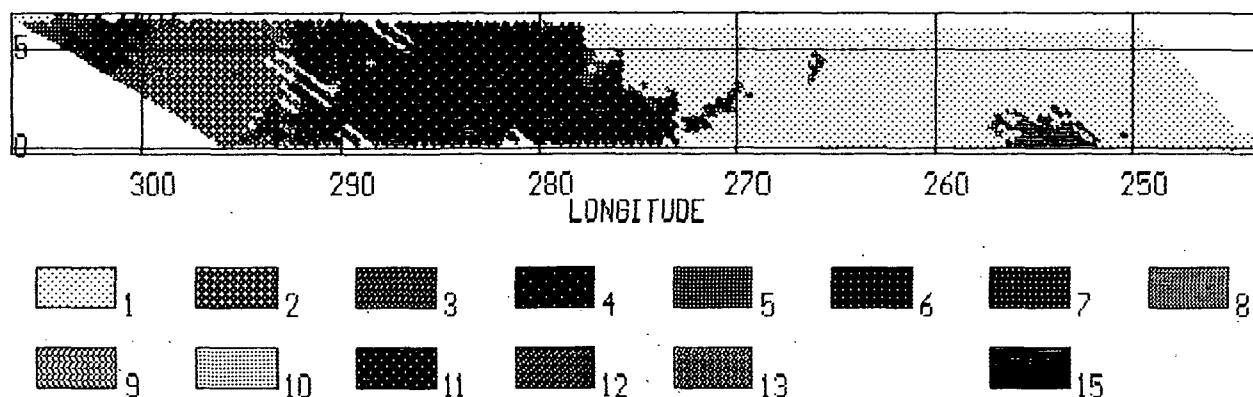


Fig. 3 High-level analysis of the same image-cube.

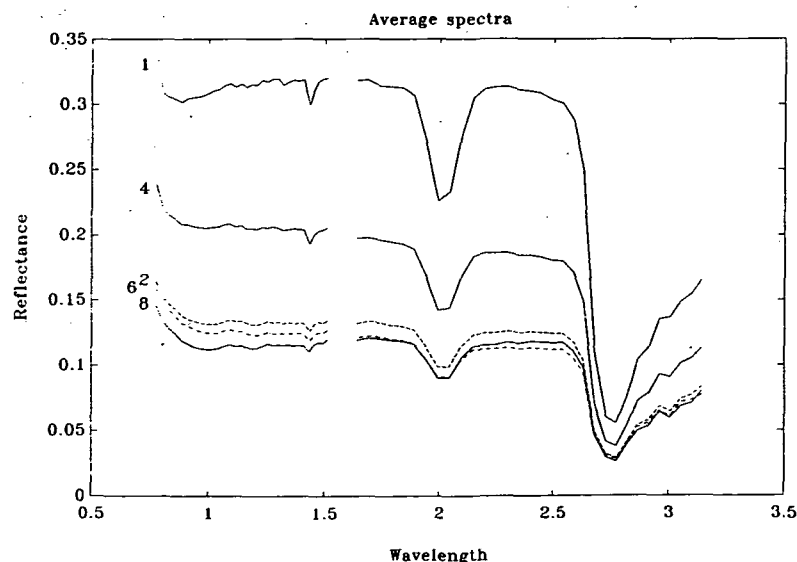
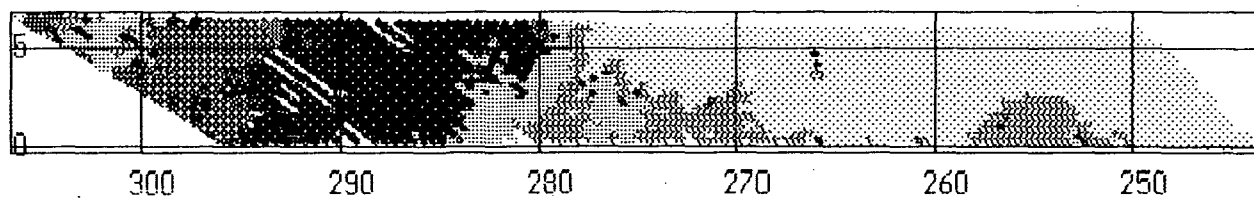


Fig. 2 Spectra of the main units in Fig. 1: 1-Isidis. 2-West Syrtis. 4-East Syrtis. 6-Syrtis center. 8-Nili Patera.

**References:** [1] Bibring *et al.*, *Proc. Lunar Planet. Sci. Conf. 20th*, 461-471, 1990. [2] Erard *et al.*, *Proc. Lunar Planet. Sci. Conf. 21st*, 437-455, 1991. [3] Mustard *et al.*, *J.G.R., MSATT issue*, 1993 in press. [4] Coradini *et al.*, *Comput. Geosci.* 3, 85-105, 1977.

N 94-12285

COMPOSITION OF THE MARTIAN AEROSOLS THROUGH NEAR-IR SPECTROSCOPY Stéphane Erard, Priscilla Cerroni, Angioletta Coradini. *IAS-Planetologia, viale dell'Università 11, 00185 Roma, Italy.* p. 2

**Introduction.** Near-infrared spectroscopy is a powerful technique to study the composition of planetary surfaces, as the main minerals exhibit absorption bands in this spectral range. It gave important informations on the mineralogy and petrology of Mars in the past twenty years [1] although in this case it is well known that a large fraction of light is scattered by the airborne particles before reaching the surface. The measured signal is thus the sum of two different contributions that should be studied separately: One from the surface and one from the aerosols that depends on their density, size distribution and composition. Data from the ISM imaging spectrometer are used here to derive the aerosols spectrum. They consist in sets of spectra (from 0.76 to 3.16  $\mu\text{m}$ ) of  $\sim 3000$  pixels  $\sim 25 \times 25 \text{ km}^2$  in size [2]. The resulting spectrum exhibits both water-ice and clay minerals features superimposed on a scattering continuum. — end

**Contributions to the measured signal.** Under low opacity and near normal viewing geometry (the conditions of ISM observations) the development of the flux reaching the detectors can be limited to the terms of single scattering. The Martian aerosols being very bright and strongly forward scattering in the near infrared, the reflectance can be further approximated as [3]:

$$r \approx r_s + \frac{\tau w_a f(\varphi)}{4\mu}$$

where  $r_s$  is the surface reflectance,  $\tau$ ,  $f(\varphi)$  and  $w_a$  are respectively the vertical opacity, phase function and single-scattering albedo of the aerosols, and  $\mu$  is the cosine of the emergence angle. This model was previously used together with the ISM data to give a large range of possible estimates of the scattered spectrum, that was then lessened by comparison with telescopic observations [4].

**Derivation of the aerosols spectrum.** A new method is applied here, exploiting the spatial overlap between two image-cubes acquired on Tharsis, East of Pavonis Mons. 600 overlapping pixels were coregistered. The pixels covering the volcano were rejected because small registration errors could result there in major differences in altitude and because peculiar wind patterns are known to exist around the volcanoes, that could perturb the aerosols opacity. We finally used 284 couples of spectra acquired under low phase angles (from  $4^\circ$  to  $11^\circ$ ). In each couple one spectrum was acquired under high emergence (from  $38^\circ$  to  $49^\circ$ ) and the other under more normal geometry (from  $27^\circ$  to  $37^\circ$ ).

According to the previous studies the aerosols contribution becomes very small at 2.5  $\mu\text{m}$ , so that normalizing the two spectra of a couple at this wavelength corrects for variations of the surface photometric function. Making the assumption that the opacity is uniform and constant, the difference between the two normalized spectra is due to the increase of the aerosols contribution with increasing emergence angle, thus an estimate of the scattered spectrum can be retrieved from each of the 284 selected pixels. The result is shown on Fig. 1 for the spectral channels outside the main atmospheric absorptions.

**Analysis.** The aerosols vertical contribution at 1  $\mu\text{m}$  is found to be  $\sim 0.04$  ( $\sim 25\%$  of the signal coming from the dark regions) which matches the estimates from Viking/IRTM under similar opacity [5]. The resulting spectrum has a strong negative slope related to Mie scattering, but isn't completely smooth. An interesting feature is the difference of reflectance between the two tracks of the instrument, which suggests that the measurements at 1.5 and 1.65  $\mu\text{m}$  are located on the wings of an absorption band. If the scattering continuum can be simulated with an exponential function,

it is then clear that absorption takes place from 1.1 to 1.7  $\mu\text{m}$ . Hence we used the nineteen channels from 0.77 to 1.09  $\mu\text{m}$  and from 1.64 to 1.85  $\mu\text{m}$  to fit an exponential continuum.

The ratio of the estimated aerosols spectrum to this continuum is showed on Fig. 2, emphasizing the absorption features due to the airborne particles. All the broad features (concerning more than two channels) are meaningful according to the statistical error (that accounts for both the instrumental noise and the spatial variability of the aerosols). Most of these features are actually very similar to those observed in water-ice spectra (*e. g.* [6]): The weak absorption from 1.09 through 1.39  $\mu\text{m}$  followed by a much stronger one up to 1.69  $\mu\text{m}$ , the strong absorption from 1.83 to 2.20  $\mu\text{m}$  and finally the drop-off below 2.20  $\mu\text{m}$ . The small inflexion from 1.74 to 1.83  $\mu\text{m}$  is also meaningful, although it doesn't appear in water-ice spectra. [6] suggested that it is indicative of very hydrated mineral, such as montmorillonite or kaolinite mixed with water. Conversely, this minerals don't exhibit all the water-ice absorption features that match the aerosols estimate, namely at 1.6 and 1.8  $\mu\text{m}$ . This would imply that two separated phases are actually responsible for the backscattered contribution, water-ice and dust composed of hydrated minerals.

To constrain more closely the latter, we made a systematical comparison of this spectrum to those of the minerals that have been proposed as major components of the Martian soils and dust, on the basis of the Viking landers analysis and spectral observations. The best fits are given by several clay minerals (montmorillonite, nontronite, saponite) and one iron oxide (gibbsite) that thus appear as the more likely components of suspended dust. No convincing similarity is found with spectra of carbonates, micas or plagioclases.

Figure 1: Aerosols contribution and modelized continuum.

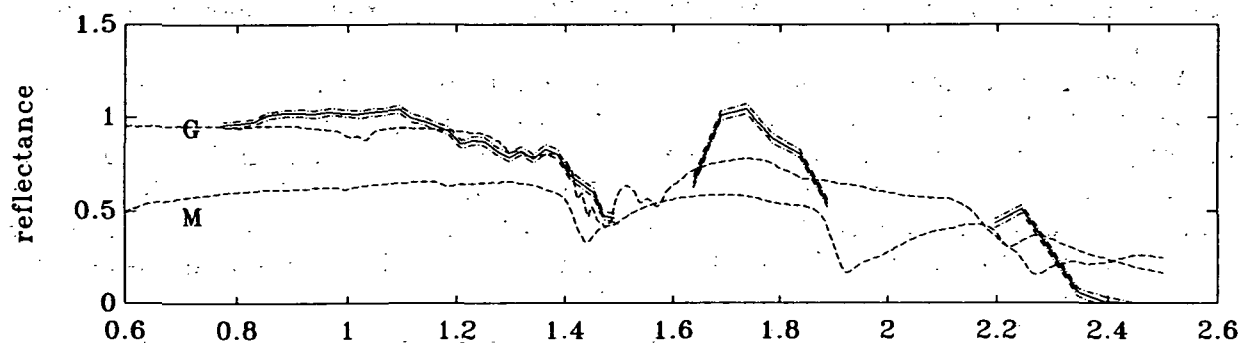
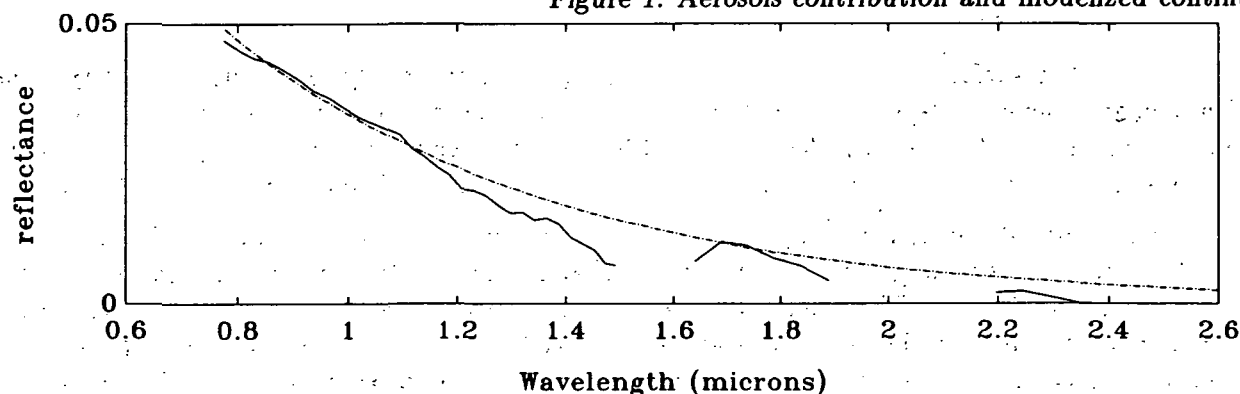


Figure 2: Aerosols to continuum ratio, gibbsite and montmorillonite spectra.

**References :** [1] Singer, *Adv. Space Res.* 5;8, 59, 1985. [2] Bibring *et al.*, *Proc. Lunar Planet. Sci. Conf. 20th*, 461, 1990. [3] Drossart *et al.*, *Annal. Geophys.* 9, 754, 1991. [4] Erard *et al.*, *Lunar Planet. Sc. XXIII*, 335, 1992. [5] Clancy and Lee, *Icarus* 93, 135, 1991. [6] Clark, *J. Geophys. Res.* 89, 6319, 1984.

5221-46  
ABS-ONLYN 94-12236  
p. 2

GIANT RADIATING DYKE SWARMS ON EARTH AND VENUS; Richard E. Ernst<sup>1</sup>, James W. Head<sup>2</sup>, Elisabeth Parfitt<sup>2</sup>, Lionel Wilson<sup>2,3</sup> and Eric Grosfils<sup>2</sup>; <sup>1</sup>Ottawa-Carleton Geoscience Centre and Dept. of Geology, University of Ottawa, Ottawa, Ontario, Canada, K1N 6N5, <sup>2</sup>Dept. of Geological Sciences, Brown University, Providence, Rhode Island, USA, 02912, <sup>3</sup>Environmental Sci. Div., Lancaster Univ., Lancaster LA1 4YQ, UK.

On Earth, giant radiating dyke swarms are usually preserved as fan-shaped fragments which have been dismembered from their original configuration by subsequent plate tectonic rifting events (1). Analysis of the largest fragments and consideration of their original configuration has led to the idea that many swarms are plume related, and that dyke swarms radiate away from plume centers (2). Magellan radar data reveal abundant intact giant radiating swarms on Venus which are similar in scale and pattern to those on Earth (3). The absence of intense weathering and plate tectonic processes on Venus accounts for the preservation of the primary radiating patterns. It is characteristic of both Earth and Venus that giant radiating dikes are emplaced laterally for distances of at least 2000 km away from plume centers (1,3). At distances beyond the influence of the plume on both Earth and Venus, the radiating dyke pattern is often swept into a linear pattern aligned with the regional stress field (2,4). There is tremendous potential synergism between the characterization and analysis of terrestrial dyke swarms (where significant erosion has revealed their structure and emplacement directions at depth) and the giant swarms of Venus (where the complete circumferential structure is preserved, and the surface fracture systems above near-surface dikes and the nature of the central source regions are revealed). In this study, we report on the characteristics of radial dyke swarms on Earth and Venus and draw some preliminary comparisons from the two perspectives.

Knowledge of terrestrial swarm distributions is still at an early stage, mainly because sufficient data exist for only a few swarms. High-precision age dating, detailed paleomagnetic study and comprehensive aeromagnetic coverage and interpretation are required in order to distinguish conclusively between swarms and to determine their full extent; this has been done for only a few swarms, mainly in the Canadian Shield. For example, the Mackenzie swarm covers an area of 2.7 million square kilometers and dramatically fans over an arc angle of about 100° from a point in northwest Canada. Thick accumulations of coeval flood basalt (Coppermine Lavas), as well as the large Muskox intrusion, occur near the focus of the swarm. Precise dating has demonstrated that the Muskox intrusion, several large sills, and the Mackenzie dyke swarm were emplaced within a period of less than 5 million years, with all the dikes being injected at  $1267 \pm 2$  Ma (5). The Coppermine lavas have not been precisely dated but are considered to also have a 1267 Ma age based on preliminary ages, similar chemistry and the fact that dyke abundance decreases upwards in the volcanic pile, implying that the dikes are feeders. The Mackenzie swarm is thought to have been initiated by a mantle plume impinging on the lithosphere (5,6); this conclusion is based on the radiating pattern, the stratigraphic evidence for uplift in the focal region preceding magma injection, and magnetic fabric evidence. Synthesis of the characteristics of this and other terrestrial swarms (2) indicates the following: **Size of Swarms:** The Mackenzie and Central Atlantic swarms extend about 2500 km away from the swarm center; based on present sampling, a more common length is typified by the Matachewan and Devonian swarms, each ~1000 km in radius from the swarm focus. **Swarm Geometry:** Some swarms have a generally subparallel to weakly fanning shape (e.g., Abitibi, British Tertiary, Gairdner, Devonian Timan swarms). Some are distinctly fanning (e.g. Mackenzie, Matachewan, Fort Frances swarms), while others are radiating (e.g. Spanish Peaks, Central Atlantic swarms). In every case, however, the swarms trend towards a coeval volcanic/plutonic center, and if they are fanning or radiating, the focal region coincides with the region of coeval activity. For the larger swarms, the focal region activity is a flood basalt related to a mantle plume event. A common characteristic is that, at some distance from the center, the swarm becomes subparallel along a trend related to a regional stress field (e.g., Mackenzie, Abitibi swarms). Another common phenomena is secondary deformation leading to a deviation from a fanning pattern (e.g., Matachewan swarm). **Flow directions:** Magnetic fabric work on Mackenzie dikes (6) has demonstrated that the magma flow in the Mackenzie swarm was vertical within about 500 km of the focus of the swarm, but horizontal from 600 km to at least 2100 km away from the focus. Since the swarm extends at least 2500 km away from the focus (7), horizontal magma flow of at least 2000 km is indicated. The vertical flow regime probably marks the outer boundary of melt generation in the mantle plume responsible for the Mackenzie igneous events (6). **Chemistry/Isotopes:** Most swarms are basaltic, ranging from quartz tholeiite to olivine tholeiites; smaller scale swarms can be more andesitic. The large swarms have trace element and Sr-Nd-Pb isotopic patterns which tie them to mantle upwellings that have been variably contaminated by lithospheric mantle or continental crust. The most reliable tool for dating the primary age has been high-precision U-Pb baddeleyite and zircon dating (e.g. 8). For swarms so far studied this way, it is clear that all parts of a dyke swarm typically tend to be intruded and crystallized within a short period of time (<5 Ma). **Intrusion and Cooling History of Individual and Adjacent Dikes:** Paleomagnetism can be utilized to detect slight differences in the timing of intrusion using secular variation, the short term wandering of the magnetic pole. In several swarms, it has been

## RADIATING DYKE SWARMS

Ernst, Richard A. et al.

demonstrated that individual dikes exhibit nearly identical directions along strike (implying that each dyke represents a single intrusion which has cooled in a short time) but that different, even adjacent dikes of the same swarm exhibit measurably different characteristic directions (on the scale of secular variation, that is, on intervals of up to thousands of years). In addition, incompatible elemental ratios are often constant along a dyke, but differ distinctly between dikes. The variation can be attributed to source inhomogeneities and bulk contamination effects. Thus, there is evidence that many dikes, even very long ones, represent distinct and rapid intrusion events, while adjacent dikes may record small amounts of evolution in the source area. Relation to Plumes: In the vast majority of the cases considered, dikes trend away from plume centers, both in the well-defined plumes associated with the breakup of Pangea and in the older Proterozoic examples. The breakup of the original configuration, however, makes study of the initial structural and stratigraphic sequence difficult on Earth.

On Venus, the discovery and analysis of central structures with distinctive radial fracture systems led to the interpretation that these features are primarily volcanic/plutonic, and that the radial fractures commonly represent the surface manifestation of dikes (3,9). A survey of Venus has been carried out to locate all radial fracture systems and to assess their association with volcanic edifices and coronae (10). They are of two broad types: 1) radiating from a point, associated with updomed topography, and displaying relatively uniform fracture lengths; 2) radiating from the outer edge of a central caldera and displaying a wider range of fracture lengths. The majority of all radial fracture systems display intensive fracturing through a full 360°. The association of many of the fractures with radial lava flows is evidence that these fractures reflect dyke emplacement; the fractures have a distribution of lengths (many short, fewer long) which is characteristic of dyke swarms, and show direct associations with calderas and lava flows consistent with a volcanic origin. In addition, the longest fractures have a radial pattern close to the center of the system but commonly bend with distance to align themselves with the regional stress field (4). For these reasons we argue that many, possibly the majority, of radial fracture systems found on Venus are the surface reflection of dyke swarms (3,9,10), those associated with positive topography primarily reflecting vertical emplacement and those radiating from calderas reflecting lateral propagation (10). On the basis of analysis of these features two preliminary evolutionary sequences are proposed (10): 1) The first sequence starts with updoming and fracturing of the surface as a mantle plume impinges on the crust; some updomes deform to form coronae and complex fracture features, while others evolve into large volcanic edifices. 2) The second sequence starts with features which have central calderas and fractures radiating from the outer edge of the caldera (reflecting lateral dyke emplacement from the central storage region). They show little or no evidence for an earlier stage of uplift. They evolve into edifices, formation of long fractures ceases, and lava flows progressively cover all but the longest fractures. In this case, a shallow storage region forms early and lateral dyke propagation from this region dominates. This pattern is likely to be related to the formation of a shallow magma reservoir and a declining rate of magma production. Early rapid melt production allows the emplacement of long dikes; as the magma production rate falls and the shallow reservoir develops dyke emplacement results in shorter dikes. One key difference seems to be that on Earth extensive flood basalt activity is associated with the early stage of development while on Venus the early stage seems to be largely intrusive. Further modelling studies are underway to develop more complete models of both evolutionary sequences.

— In summary, on both planets there is evidence for plume-related magmatic centers associated with vertical and lateral injection of magma over considerable distances (up to at least 2000 km). The abundance of very broadly radiating swarms on Venus supports the notion that the swarms on Earth were radiating over broad sectors at the time of intrusion but were dissected by later events. The Venus data show that a swarm can change from radiating (proximal) to regional (distal) subparallel orientations. An implication for Earth is that many regional linear swarms which do not have a radiating pattern may be due to fragmentation of the swarm during later plate tectonic rifting. Completion of the global classification and census of Venus features (10), comparison to the terrestrial synthesis (2), and documentation of the mode of emplacement of dikes in these environments (buffered and unbuffered conditions) (11) should lead to additional general insight into mechanisms of formation and evolution and their relation to plumes (12). *End*

**References:** 1) H. Halls and W. Fahrig (eds.) (1987) *Mafic Dyke Swarms*, *Geol. Assn. Canada SP 34*; 2) R. Ernst et al. (1993) Giant radiating dyke swarms on Earth and Venus: A synthesis and comparison; in preparation; 3) E. Parfitt and J. Head (1992) *LPSC 23*, 1029; E. Parfitt et al. (1992) *Int. Colloq. Venus*, 83; 4) E. Grosfils and J. Head (1992) *LPSC 23*, 457; (1992) *Int. Colloq. Venus*, 37; (1993) *LPSC 24*, this volume; 5) A. N. LeCheminant and L. M. Heaman (1989) *EPSL*, 96, 38; 6) R. Ernst and W. Baragar (1991) *Nature*, 356, 511; 7) W. Fahrig and D. Jones (1969) *Can. Jour. Earth Sci.*, 6, 679; 8) L. Heaman et al. (1992) *EPSL*, 109, 117; L. Heaman and J. Tarney (1989) *Nature*, 340, 705; 9) D. McKenzie et al. (1992) *JGR*, 97, 15977; 10) E. Parfitt and J. Head (1993) *LPSC 24*, this volume; 11) E. Parfitt and J. Head (1993) Lateral dyke emplacement on Earth and Venus: Implications for magma reservoir size, depth, and rates of magma replenishment, ms. in review; 12) R. Griffiths and I. Campbell (1991) *JGR*, 96, 18295.

5222-90  
ABS ONLY

N 94-12237  
LSC XXIV 449  
16341

**Re-Os DATING OF IIIAB IRON METEORITES** Tezer M. Esat and Victoria Bennett.  
Research School of Earth Sciences, The Australian National University, Canberra 2601, Australia.

Recently, Creaser et al., [1] and Völkening and Heumann, [2] have demonstrated the efficient production of large ( $\approx 10^{-11}$  A) ion beams by negative thermal ionisation mass spectrometry (NTIMS) using standard laboratory solutions of Os compounds. Horan et al., [3] have applied NTIMS to a group of 7 IIA iron meteorites and obtained a Re-Os closure age of  $4596 \pm 152$  million years. The initial  $^{187}\text{Os}/^{186}\text{Os}$  ratio was  $0.8007 \pm 0.0029$ . In addition they analysed 3 IIIA meteorite samples which indicated an age of  $4554 \pm 180$  million years and Os initial of  $0.8120 \pm 0.0075$  which does not overlap with the initial for the IIA irons. We have been independently pursuing a similar program with the direct aim of determining possible variations in the initial  $^{187}\text{Os}/^{186}\text{Os}$  ratio or Re-Os closure age of different classes of iron meteorite. We have applied NTIMS to Os extracted from the most common group of iron meteorites the IIIAB. These meteorites are believed to be of magmatic origin, formed by fractional crystallisation of molten cores of asteroidal bodies. The present results point to a significantly lower initial  $^{187}\text{Os}/^{186}\text{Os}$  ratio of  $0.7731 \pm 0.0050$  than previously determined.

Samples of iron meteorite were obtained from the ANU meteorite collection. Small (50 to 100 mg) pieces were hand sawn using clean hack-saw blades lubricated with ethanol. Samples were cut from interior portions away from ablated surfaces. Each sample was de-greased in acetone in an ultrasonic bath and rinsed with ethanol followed with high-purity water. Samples were dissolved in a mixture of HCl and ethanol, including mixed Re and Os spikes, in glass bottles at  $60^\circ\text{C}$ . Following dissolution the sample was dried and was redissolved in  $\text{H}_2\text{SO}_4$  in a sealed glass bottle at  $90^\circ\text{C}$ . An oxidant was included to ensure complete equilibration between the Os from the sample and the Os spike. This step is essential as complete sample/spike equilibration has been the single most difficult problem impeding precise Os concentration measurements. The sample in  $\text{H}_2\text{SO}_4$  solution was transferred to the distillation apparatus and gradually heated to  $120^\circ\text{C}$  using a hot air gun while small amounts of  $\text{H}_2\text{O}_2$  was added to help oxidise Os. The residue from distillation was passed through a 3 cm anion exchange column and Re eluted with  $\text{HNO}_3$ . A mixture of BaOH and KOH solutions were loaded into a V-shaped pocket in a single Pt filament followed by the addition of the sample in chloride form. All were then dried in air. We find that the presence of KOH enhances negative ion formation. Corrections for mass dependent isotope fractionation and for interference from minor oxygen isotopes were computed in a single step by first order expansion in terms of the fractionation factor. The contribution of minor tracer isotopes were handled in a similar fashion in a single step together with fractionation and  $^{17,18}\text{O}$  interferences. Statistical precision for individual runs, where  $^{192}\text{Os}$  beam intensity was larger than  $4 \times 10^{-12}$  A, is  $\pm 0.2\%$   $2\sigma$ .

The data for the 6 iron meteorites Costilla Peak, Henbury, Cape York, Duketon, Kyancutta and Carthage form a collinear array on the  $^{187}\text{Os}/^{186}\text{Os}$  vs.  $^{187}\text{Re}/^{186}\text{Os}$  diagram (Fig.1). The best linear fit to the data defines an isochron with a slope of  $0.0830 \pm 0.0012$  and an intercept of  $0.7731 \pm 0.0050$ . The slope corresponds to an age of  $4865 \pm 50$  million years. Including the uncertainties resulting from the decay constant,  $(1.639 \pm 0.050) \times 10^{-11} \text{yr}^{-1}$  ( $\pm 3\%$ ) of Lindner et al., [4] uncertainty in the Re-Os spike calibrations ( $\pm 2\%$ ) and the slope ( $\pm 1.5\%$ ) results in an age estimate of  $4865 \pm 190$  million years.

Re-Os DATING: Esat T.M. and Bennet V.C.

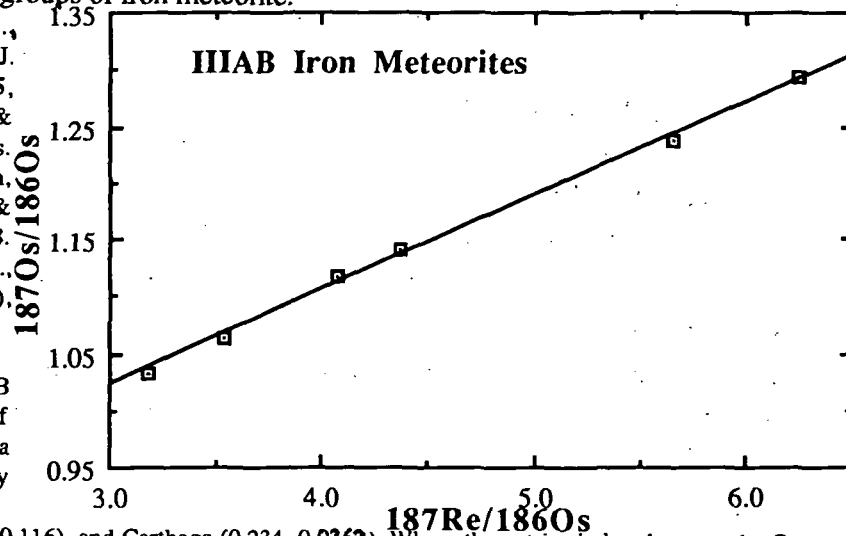
This age is incompatible with the maximum age of 4560 Ma for chondrites as the iron meteorites are expected to have evolved from chondritic precursors. It is possible that there is a larger uncertainty in the determination of the Re decay constant or that our calibration of the Re and Os spikes are in error by more than 2% (an increase of 7% in the Re/Os ratio is required to obtain an age of 4558 million years). In either of these two cases, however, the intercept corresponding to the initial  $^{187}\text{Os}/^{186}\text{Os}$  ratio should not be affected. Both us and Horan et al., [3] have analysed the IIIA iron meteorite Costilla Peak. For the Re concentration we obtain 1.420 ppm vs. 1.426 ppm; in good agreement and similarly for the  $^{187}\text{Os}/^{186}\text{Os}$  ratio of 1.0331 vs. 1.0393. For the Os concentration we have 17.98 ppm vs. 19.58 ppm indicating a difference of about 9%. This translates to a difference of about 8.5% in the Re/Os ratio. However, a decrease in our Re/Os ratios by this magnitude would lead to an even older (>5000 Ma) apparent age for the IIIAB irons.

Horan et al., [3] have determined an initial ratio of  $0.8007 \pm 0.0029$  for IIA and  $0.8120 \pm 0.0075$  for IIIA meteorites; the latter based on three analyses. As we have not as yet analysed any IIA iron meteorite samples we are unable to independently confirm any differences between IIA and IIIA initial Os ratios. Our data can only be reconciled with that of Horan et al., [3] if we assume a random error in Re/Os concentration determinations which resulted in the rotation of the isochron to produce an older age and a lower initial. This is a possibility given the difficulties of achieving complete equilibration between Os spike and sample and would require approximately a 3% increase in Re/Os ratio for the 3 high Re/Os points and a 3% decrease for the 3 low Re/Os data points to preserve the linearity of the array. In the absence of such a contrived arrangement, we are unable to offer a reasonable explanation for the differences in the initial  $^{187}\text{Os}/^{186}\text{Os}$  ratio.

If we accept the present data at face value then we can draw the following conclusions: i) The older apparent age is due to either an error in the Re decay constant or analytical problems in the calibration of our Os spike by about 7%. ii) The low initial  $^{187}\text{Os}/^{186}\text{Os}$  ratio of 0.7731 is unaffected by either of these problems. iii) The difference in the initial Os between IIA iron meteorites as determined by Horan et al., [3] and the present result for IIIAB irons may be due to the heterogeneous accretion of Os in the parent bodies of these two groups of iron meteorite.

**References:** [1] Creaser, R.A., Papanastassiou, D.A. & Wasserburg, G.J. (1991), *Geochim. Cosmochim. Acta* 55, 397. [2] Völkening J., Walczyk T. & Heumann, K.G. (1991), *Int. J. Mass. Spectrom. Ion Proc.* 105, 147. [3] Horan, M.F., Morgan, J.W., Walker, R.J. & Grossman, J.N. (1992), *Science* 255, 1118. [4] Lindner, M., Leich, D.A., Russ, G.P., Bazan, J.M., and Borg, R.J. (1989), *Geochim. Cosmochim. Acta* 53, 1597.

**Fig 1.** Re-Os evolution diagram for IIIAB iron meteorites. The 6 samples in order of increasing  $^{187}\text{Re}/^{186}\text{Os}$  ratio are: Costilla Peak (17.975, 1.420), Henbury (15.083, 1.325), Cape York (2.343, 0.237), Duketon (2.886, 0.313), Kyancutta (0.827, 0.116), and Carthage (0.234, 0.0362). Where the entries in brackets are the Os and Re concentrations in parts per million respectively. Error bars are smaller than the size of the points plotted.



# MODELLING OF DISPERSAL AND DEPOSITION OF IMPACT GLASS SPHERULES FROM THE CRETACEOUS-TERTIARY BOUNDARY DEPOSIT; J.M. Espindola (Instituto de Geofisica, UNAM, Mexico), S. Carey and H. Sigurdsson (Graduate School of Oceanography, University of Rhode Island, Narragansett, RI 02882).

The dispersal of glass spherules or tektites from a bolide impact with the Earth is modelled as ballistic trajectories in standard atmosphere. Ballistic dispersal of Cretaceous-Tertiary boundary impact glass spherules found in Haiti and Mimbral, Mexico requires a fireball radius in excess of 50 km but less than 100 km to account for the observed distribution.

Glass spherules from 1 and up to 8 mm in diameter have been found at the KT boundary at Beloc in Haiti [1], at Mimbral, Mexico [2], and at DSDP Sites 536 and 540 in the Gulf of Mexico [3], corresponding to paleodistances of 600 to 1000 km from the Chicxulub crater. In Haiti the basal and major glass-bearing unit at the KT boundary is attributed to fallout on basis of sedimentologic features [4]. When compared with theoretical and observed dispersal of volcanic ejecta, the grain size versus distance relationship of the KT boundary tektite fallout is extreme, and rules out a volcanic fallout origin. At a comparable distance from source, the KT impact glass spherules are more than an order of magnitude coarser than ejecta of the largest known volcanic events.

We model the dispersal of KT boundary impact glass spherules as ballistic ejecta from a fireball generated by the impact of a 10 km diameter bolide. Mass of ejecta in the fireball is taken as twice the bolide mass [5]. Melt droplets are accelerated by gas flow in the fireball cloud, and leave the fireball on ballistic trajectories within the atmosphere, subject to drag, depending on angle of ejection and altitude. The model for ballistic dispersal is based on equations of motion, drag and ablation for silicate spheres in standard atmosphere.

The ballistic transport range of particles is strongly dependent on decoupling radius, or the radius of the fireball when particles are no longer accelerated by the cloud and travel under their own inertia. Other factors that determine particle range are angle of ejection, particle diameter and initial velocity. Particle size is constrained by observations of the deposit [4], and initial velocity is evaluated from reasonable bolide mass and velocity [5]. Ablation is found to decrease particle radius by up to 10%. At decoupling radius <50 km the particles are severely affected by atmospheric drag and have low range. At higher decoupling radii the particle dispersal is in the range observed for KT boundary impact glass spherules (Fig. 1). Particles with high angle of ejection from the cloud and at high altitudes will travel with practically no drag and may obtain semi-orbital flight.

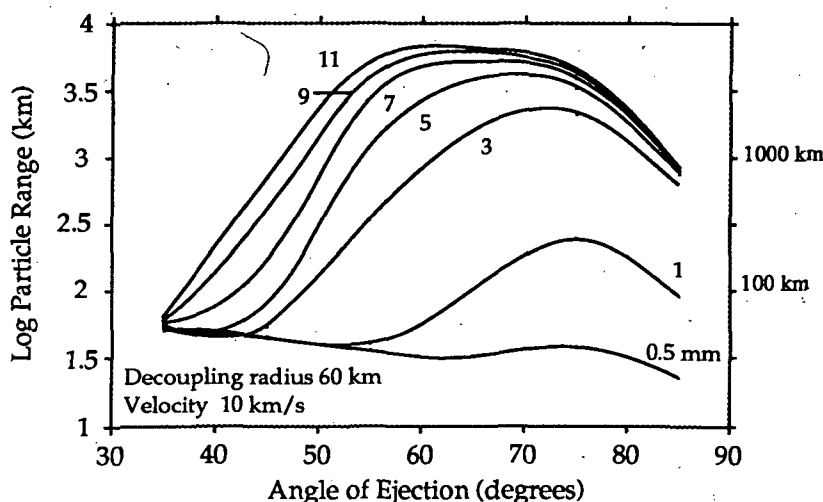


Fig. 1: Variation in the predicted transport range of particles (0.5 - 11 mm diam) as a function of ejection angle for fireball or decoupling radius of 60 km. Ballistic trajectory particle velocity at the decoupling stage is assumed 10 km/sec in all cases. This fireball radius satisfies the observed ~1000 km dispersal of glass spherules to Haiti and Mimbral, Mexico.



## MODELLING OF IMPACT EJECTA DISPERSAL: Espindola, J.M. et al.

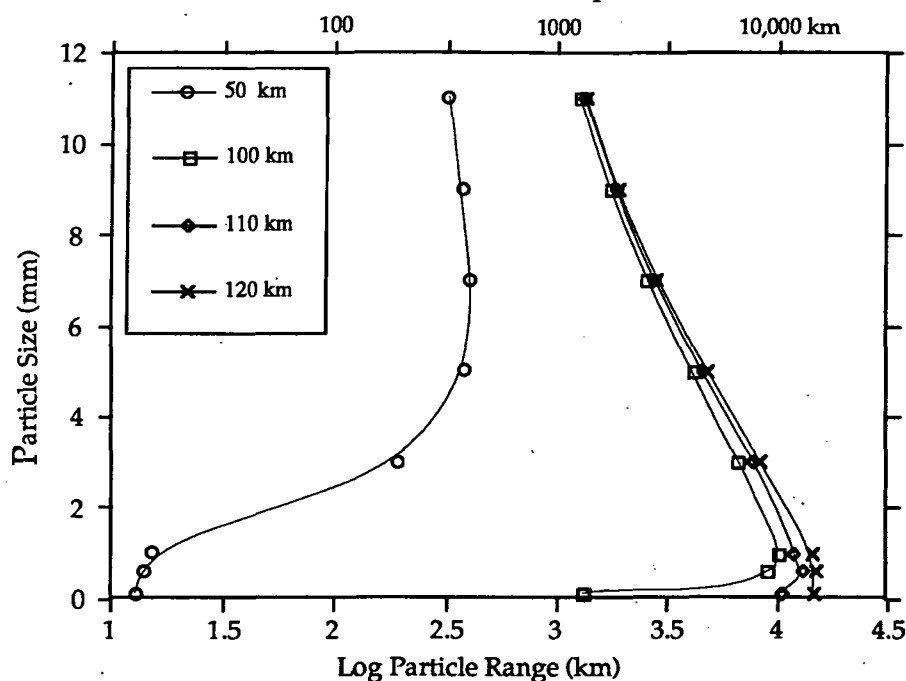


Fig. 2: Predicted maximum transport of particles from the impact of a 10 km diameter bolide at 20 km/sec. Modelling results are shown for decoupling radii of fireball of 50, 100, 110 and 120 km.

Maximum ballistic range as a function of particle size is shown in Fig.2, for decoupling radii from 50 to 120 km. The radius of 60 to 100 km required to account for the KT boundary dispersal indicates a fireball which would exceed the scale height of the Earth's atmosphere. Largest uncertainty in the ballistic model relates to the degree of melt droplet interaction with atmosphere. If atmospheric erosion is severe during impact [5], then ballistic dispersal may occur in near-vacuum conditions adjacent to the impact site. On the other hand, we model the extreme case of a standard atmosphere.

The model has also been used to estimate the thickness of the ballistic ejecta deposit, based on mass distribution in the fireball. For a 10 km diameter bolide at 20 km/sec, the axisymmetric ballistic model deposit has the same thickness/distance relation as the curve of Hildebrand and Stansberry [6] in the far-field (>1000 km), but is significantly thinner in the proximal region.

## References:

1. Sigurdsson, H., S. D'Hondt, M.A. Arthur, T.J. Bralower, J.C.Zachos, M. Fossen and J.E.T. Channell, *Nature*, 349, 482-487, 1991.
2. Smit, H., A. Montanari, N. Swinburne, W. Alvarez, A. Hildebrand, S. Margolis, P. Claeys, W. Lowrie and F. Asaro, *Geology*, 20, 99-103, 1990.
3. Alvarez et al Alvarez, L.W., W. Alvarez, F. Asaro & H.V. Michel, *Science*, 208, 1095-1108, 1980.
4. Carey et al this volume.
5. Vickery, A.M., & H.J. Melosh, 1990. In: Sharpton, V.L., and Ward, P.D., eds. Global catastrophes in Earth history. *Geol. Soc. Amer. Sp. Paper* 247, 289-300.
6. Hildebrand, A. and J. Stansberry, *Lun. Planet. Sci. Ann. Meet. Abst.*, XXIII, 537-538, 1992.

Xe-Q IN LODRANITES AND A HINT FOR Xe-L. FRO90011 ANOTHER LODRANITE?  
O. Eugster and A. Weigel, Physikalisches Institut, University of Bern, Sidlerstrasse 5, 3012 Bern, Switzerland. P. 2

→ The Lodran achondrite contains about one-quarter metallic Fe/Ni, two-thirds olivine and pyroxene, some troilite, plus minor phases [1,2]. In a previous study [3] we demonstrated that Lodran and three other lodranites - LEW88280, Yamato-791491, and MAC88177 - yield the same cosmic-ray exposure age of a few million years, suggesting that they originate from the same parent body. In the present work we show that the mineral phases of Lodran contain large concentrations of planetary-type but no solar-type trapped noble gases. Surprisingly, the highest concentrations were observed in the Fe/Ni-phase (e.g.  $1520 \times 10^{-12} \text{ cm}^3 \text{ STP/g } ^{132}\text{Xe}$ ). A large fraction of the trapped gas is released between 1200°C and 1400°C. The Xe isotopic pattern is similar to that of Xe-Q [4,5]. The 1400°C fraction of the Fe/Ni-phase shows excesses of  $^{124}\text{Xe}$ ,  $^{126}\text{Xe}$ , and  $^{128}\text{Xe}$  similar to Xe-L (pre-solar Xe enriched in the light isotopes) that has, until now, only been observed in combination with Xe-H (pre-solar Xe enriched in the heavy isotopes) [6]. — end

A 900 mg sample of Lodran was separated by handpicking into five phases - Fe/Ni, FeS, olivine, pyroxene, and  $\text{Cr}_2\text{O}_3$ . He, Ne, and Ar isotopes were measured in all phases, and Kr and Xe in a bulk sample and Fe/Ni. Bulk samples of LEW88280, Y-791491, and MAC88177 were also analyzed, the latter two only for He, Ne, and Ar. The cosmogenic, radiogenic, and fissiogenic components will be published later. Here we present the results for the trapped component. The concentrations are given in Table 1.

Although Lodran is a differentiated meteorite, its planetary-type trapped gas concentrations are high; they are in the range of those of type 3 ordinary chondrites. It is very unusual that the Fe/Ni-phase contains the highest amounts of trapped gases of all mineral phases (Table 1). The other three lodranites contain less trapped gases than Lodran. Fig. 1 demonstrates that the elemental abundance pattern is quite similar for the different mineral phases and resembles that for C3 chondrites.

The isotopic composition of trapped Ne and Ar could not be derived due to the very low concentrations. Trapped Kr shows the isotopic signature of Kr-Q [5]. Fig. 2 displays the isotopic pattern of trapped Xe in the 1200°C and 1400°C fraction of bulk Lodran and of the Fe/Ni-phase, normalized to solar wind Xe (BEOC 12001 [7]). The data points represent the measured values. As discussed below, the contributions of cosmogenic and fissogenic Xe are negligibly small. The concentrations of the target elements for cosmic-ray produced Xe in Lodran are low: 0.17 ppm Ba and 0.141 ppm La [8]. For a cosmic-ray exposure age of 3 Ma [3] we calculate a ratio  $^{126}\text{Xe}/^{128}\text{Xe}_{\text{total}}$  of less than 0.0008. The U concentration of lodranites is unknown, but it can be estimated based on a K concentration of 13 ppm [8] and a K/U concentration ratio of  $2 \times 10^4$  (ureilites). We obtain 0.65 ppb U and, for 4.55 AE,  $0.002 \times 10^{-12} \text{ cm}^3 \text{ STP } ^{136}\text{Xe}$ . However, the major progenitor of fission Xe in achondrites is  $^{244}\text{Pu}$ . Its abundance 4.55 AE ago was derived from 0.227 ppm Nd in Lodran [8] and a ratio  $^{136}\text{Xe}$  (Pu-fission)/Nd in Angra dos Reis of  $1.0 \times 10^{-12} \text{ cm}^3 \text{ STP per g and ppm Nd}$  [9] resulting in  $0.23 \times 10^{-12} \text{ cm}^3 \text{ STP/g } ^{136}\text{Xe}$  (Pu-fission). Compared with the observed concentration of trapped  $^{136}\text{Xe}$  of  $410 \times 10^{-12} \text{ cm}^3 \text{ STP/g}$  (Table 1) the fission Xe contribution is negligibly small. Radiogenic Xe from  $^{129}\text{I}$  decay might be responsible for a slight enrichment of the  $^{129}\text{Xe}$  abundance in the Xe isotope pattern in Fig. 2.

Inspection of Fig. 2 shows that bulk Lodran is depleted by about 7% in  $^{124}\text{Xe}$  and  $^{128}\text{Xe}$  relative to solar Xe. The 1200°C fraction of the Fe/Ni-phase yields a Xe isotopic pattern almost identical to that of Xe-Q [4, 5]. The 1400°C fraction of Fe/Ni contains  $370 \times 10^{-12} \text{ cm}^3 \text{ STP/g } ^{132}\text{Xe}$ . The Xe pattern can be interpreted to indicate an addition of Xe-L, with perhaps some of Xe-S [10], as  $^{126}\text{Xe}$  and  $^{132}\text{Xe}$  are enhanced. Xe-H that is highly enriched in  $^{134}\text{Xe}$  and  $^{136}\text{Xe}$  is absent in the 1400°C fraction. The Xe isotopic abundances of bulk LEW88280 are similar to those observed in bulk Lodran. We now plan to continue the Kr and Xe analyses of pyroxene, olivine, FeS, and  $\text{Cr}_2\text{O}_3$ , to search for the Xe-L carrier.

**Acknowledgements:** We thank R. Hutchison and G. Kurat for the Lodran samples and the NIPR and NASA for the antarctic meteorites. This work was supported by the Swiss National Science Foundation.

**References:** [1] Bild R.W. and Wasson J.T. (1976) *Mineralogical Magazine* 40, 721. [2] Prinz M. et al. (1978) *Lunar Planet. Sci. IX*, 919, Lun. Planet. Inst., Houston. [3] Eugster O. and Weigel A. (1992) *Meteoritics* 27, 219. [4] Lewis R.S. et al. (1975) *Science* 190, 1251. [5] Wieler R. et al. (1992) *Geochim. Cosmochim. Acta* 56, 2907. [6] Lewis R.S. and Anders E. (1981) *Astrophys. J.* 247, 1122. [7] Eberhardt P. et al. (1972) *Proc. Lunar Sci. Conf. 3rd*, 1821. [8] Fukuoka T. et al. (1978) *Lunar Planet. Sci. IX*, 356, Lun. Planet. Inst., Houston. [9] Lugmair G.W. and Marti K. (1977) *Earth Planet. Sci. Lett.* 35, 273. [10] Srinivasan B. and Anders E. (1978) *Science* 201, 51. [11] Av. of data given by Evans J.C. et al. (1982) *J. Geophys. Res.* 87, 5577 and Palme H. et al. (1981) *Geochim. Cosmochim. Acta* 45, 727.

Table 1. Trapped noble gases in lodranites

		<sup>20</sup> Ne 10 <sup>-6</sup> cm <sup>3</sup> STP/g	<sup>36</sup> Ar 10 <sup>-12</sup> cm <sup>3</sup> STP/g	<sup>84</sup> Kr 10 <sup>-12</sup> cm <sup>3</sup> STP/g	<sup>132</sup> Xe 10 <sup>-12</sup> cm <sup>3</sup> STP/g
Lodran	Fe/Ni	0.40	31.7	1700	1470
	FeS	0.62	28.9	-	-
	Bulk	0.30	21.9	1430	1330
	Cr <sub>2</sub> O <sub>3</sub>	3.6	20.7	-	-
	Px	0.24	8.2	-	-
	Ol	0.23	4.0	-	-
LEW 88280	Bulk	0.08	5.0	280	220
Y-791491	Bulk	0.03	0.45	-	-
MAC88177	Bulk	0.03	0.08	-	-
FRO90011	Bulk	0.1	1.07	-	-

Errors (2σ): 10-20%.

Table 2. He, Ne, and Ar in lodranites and FRO90011 (10<sup>-4</sup> cm<sup>3</sup> STP/g)

	<sup>3</sup> He	<sup>4</sup> He	<sup>20</sup> Ne	<sup>21</sup> Ne	<sup>22</sup> Ne	<sup>36</sup> Ar	<sup>38</sup> Ar	<sup>40</sup> Ar
Lodran	11.0	48.2	1.38	1.19	1.39	22.2	4.57	60.1
LEW88280	8.8	46.7	0.94	0.88	1.09	5.2	1.25	85.8
Y-791491	10.2	322	1.35	1.34	1.63	0.68	0.29	664
MAC88177	0.78	7.1	1.40	1.31	1.68	0.23	0.13	46
FRO90011	9.6	831	1.48	1.44	1.73	1.16	0.34	518
For comparison								
Acapulco [11]	11.6	12600	2.26	1.71	2.10	4.34	1.06	4212

Errors (2σ): 3-5%

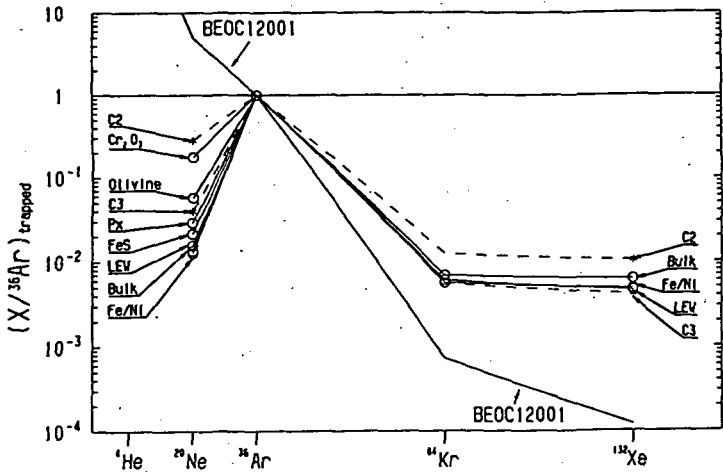


**Fig. 1** Abundance pattern of the trapped noble gases normalized to <sup>36</sup>Ar = 1 in samples from Lodran (bulk, Fe/Ni, FeS, pyroxene, olivine, and Cr<sub>2</sub>O<sub>3</sub>) and in bulk LEW88280 (LEW). C2, C3, and BEOC12001 abundances are shown for comparison.

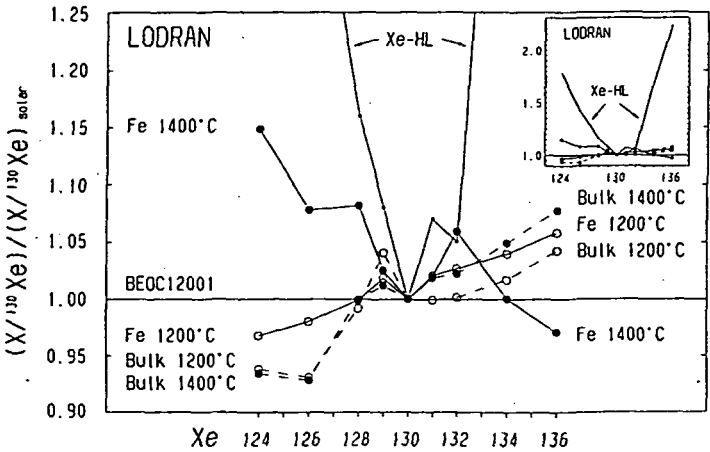


**Fig. 2** Pattern of the Xe isotope ratios in temperature fractions of a bulk sample and the Fe/Ni-phase (Fe) of Lodran normalized to solar Xe isotope ratios (BEOC12001). The pattern for Xe-HL [6] is shown for comparison. Errors (2σ): for <sup>124</sup>Xe and <sup>126</sup>Xe about 8%, for the other isotopes about 5%.

ON THE ORIGIN OF  $^4\text{He}$  AND  $^{40}\text{Ar}$  IN NATURAL GOLD; O. Eugster<sup>1</sup>, B. Hofmann<sup>2</sup>, S. Niedermann<sup>1</sup> and Ch. Thalmann<sup>1</sup>, <sup>1</sup>Physikalisches Institut, University of Bern, Sidlerstrasse 5, 3012 Bern, <sup>2</sup>Naturhistorisches Museum, Bernstrasse 15, 3005 Bern, Switzerland

→ In a first report on our investigations of noble gases in native gold we demonstrated that placer gold contains an excess of radiogenic  $^4\text{He}$  and  $^{40}\text{Ar}$  relative to the concentrations expected from in situ decay of U, Th, and K, respectively, during the geologic age of about 30 Ma of the samples [1]. We also showed that the U/Th- $^4\text{He}$  age of 36 Ma of vein-type gold from the Southern Alps agrees with its K-Ar formation age derived from associated muscovite and biotite [2]. We now studied the question of the origin of the  $^4\text{He}$  and  $^{40}\text{Ar}$  excesses of placer gold. We conclude that gold contains two components of noble gases, a low-temperature component from fluid inclusions or phases which release noble gases at  $\leq 800^\circ\text{C}$  and a high-temperature component released when gold melts ( $1064^\circ\text{C}$ ). In some samples extremely high U and K concentrations or an unreasonably high formation age would be required to explain the observed  $^4\text{He}$  abundances. Thus, trapped  $^4\text{He}$  and  $^{40}\text{Ar}$  must be present in gold. — end

A series of experiments was performed to investigate the origin of the  $^4\text{He}$  and  $^{40}\text{Ar}$  excesses. The following possible origins were considered: (a) Surficially adhering silicates on some of the gold grains. (b) Quartz inclusions inside some of the gold grains; quartz associated with gold contains high amounts of  $^{40}\text{Ar}_{\text{rad}}$  [1]. We define:  $^{40}\text{Ar}_{\text{rad}} = ^{40}\text{Ar} - 295.5 ^{36}\text{Ar}$ . (c) Zircons from the river detritus adhering on some gold grains; the high U concentration in zircons would result in high amounts of  $^4\text{He}$ . (d) Implantation of  $^4\text{He}$  into gold grains from  $\alpha$ -decay of U and Th in neighboring minerals when the gold grains were still imbedded in rock material. (e) Fluid inclusions in gold containing noble gases, and gases trapped by gold when it formed.

The following samples were analyzed: (1) Placer gold grains (88.1 mg) with abundant surface impurities (silicate inclusions). (2) Placer gold grains (65 mg) cleaned by dissolving surface silicates with HF and HCl. (3) Placer gold grains (70.4 mg) were etched with aqua regia, etching-off a surface layer of about 50  $\mu\text{m}$  thickness. (4) Placer gold (66 mg) with numerous surface silicates was completely dissolved in aqua regia, the residue (1.66 mg) was analyzed. (5) A 67 mg placer gold sample mixed with 3.3 mg zircon grains that were collected from river detritus. (6) A 66 mg placer gold sample mixed with 16.3 mg quartz that was associated with vein-type gold from the Brusson area, Southern Alps, Italy (see [1]). (7) Pure quartz as described for experiment (6). (8) and (9) Placer gold (50.0 and 50.6 mg, resp.) cleaned with HF and HCl.

Figs. 1 and 2 demonstrate the temperature release patterns of the noble gases that were obtained from the nine experiments. With respect to origins (a)-(e) we conclude: (a) Surface silicates and inclusions, if present, which are insoluble in aqua regia are poor in  $^4\text{He}$  and  $^{40}\text{Ar}_{\text{rad}}$  (experiment 4). (b) Quartz contains no  $^4\text{He}$  and shows a  $^{40}\text{Ar}_{\text{rad}}$  release pattern different from that of gold (exp. 6 and 7). (c) The release pattern of  $^4\text{He}$  from zircons differs from that of gold, in particular at  $800^\circ\text{C}$  (exp. 5). Thus,  $^4\text{He}$  originating from zircons can be excluded. Furthermore, only in this experiment we observe an excess of  $^{21}\text{Ne}$  from the reaction  $^{18}\text{O}(\alpha, n)^{21}\text{Ne}$ ; the ratio  $^{21}\text{Ne}/^4\text{He}$  is  $3 \times 10^{-8}$ . (d) The lowest concentration of  $^4\text{He}$  is obtained in experiment (6) and not in experiment (3) (etched gold); hence,  $\alpha$ -particle implantation does not explain the  $^4\text{He}$  excesses. This leaves origin (e) as the only possible source of  $^4\text{He}$  and  $^{40}\text{Ar}$  in addition to in-situ produced radiogenic noble gases.

In most experiments the release patterns of  $^4\text{He}$  and  $^{40}\text{Ar}_{\text{rad}}$  from gold show two components, a low-temperature component ( $\leq 800^\circ\text{C}$ ) and a high-temperature component (melting point of gold). Table 1 gives the noble gas concentrations for the two components. We interpret the low-temperature component to represent noble gases released from inclusions in gold that break up below  $800^\circ\text{C}$  or from radiation damaged parts of gold around these inclusions. The high-temperature component yields higher  $^4\text{He}$  but lower  $^{40}\text{Ar}_{\text{rad}}$  concentrations than the low-temperature component. It appears that the high-temperature component represents gases that were trapped by the gold when it formed (see also companion paper [3]).

**Acknowledgements:** Work supported by the Swiss National Science Foundation.

**References:** [1] Eugster O., Hofmann B., Krähenbühl U. and Neuenschwander J. (1992) *Meteoritics* 27, 219-220. [2] Diamond L.W. (1990) *Am. J. Sci.* 290, 912-958. [3] Niedermann S., Eugster O., Hofmann B., Thalmann Ch., and Reimold W.U. (1993) this issue.

Table 1. Noble gases in placer gold samples (10<sup>-8</sup> cm<sup>3</sup> STP/g Au)

Sample (Experiment #, see Figs. 1 and 2)	Low – temperature component (≤ 800°C)						High – temperature component (> 800°C)					
	<sup>4</sup> He	<sup>20</sup> Ne	<sup>36</sup> Ar	<sup>40</sup> Ar <sub>rad</sub>	$\frac{4}{40}$	$\frac{20}{36}$	<sup>4</sup> He	<sup>20</sup> Ne	<sup>36</sup> Ar	<sup>40</sup> Ar <sub>rad</sub>	$\frac{4}{40}$	$\frac{20}{36}$
Au, surf.silicates (1)	276	0.0032	0.012	2.85	97	0.27	1890	0.017	<0.05	0.33	5700	-
Au, HCl/HF cleaned (2)	87.4	0.018	0.044	5.92	15	0.41	1230	0.0060	0.0069	0.07	17600	0.87
Au, aqu.reg.etched (3)	80.1	0.0092	0.025	1.69	47	0.37	808	0.0088	0.0129	<0.1	>8000	0.68
Residue (4)	1.3	0.0032	0.0065	<0.5	>2.6	0.49	<0.2	0.0058	<0.018	<0.1	-	-
Au, HF/HCl cleaned (8)	284	0.085	0.146	8.4	34	0.58	3610	0.115	0.415	4.25	849	0.37
Au, HF/HCl cleaned (9)	219	0.090	0.229	8.0	27	0.39	1291	0.111	0.326	6.2	208	0.34

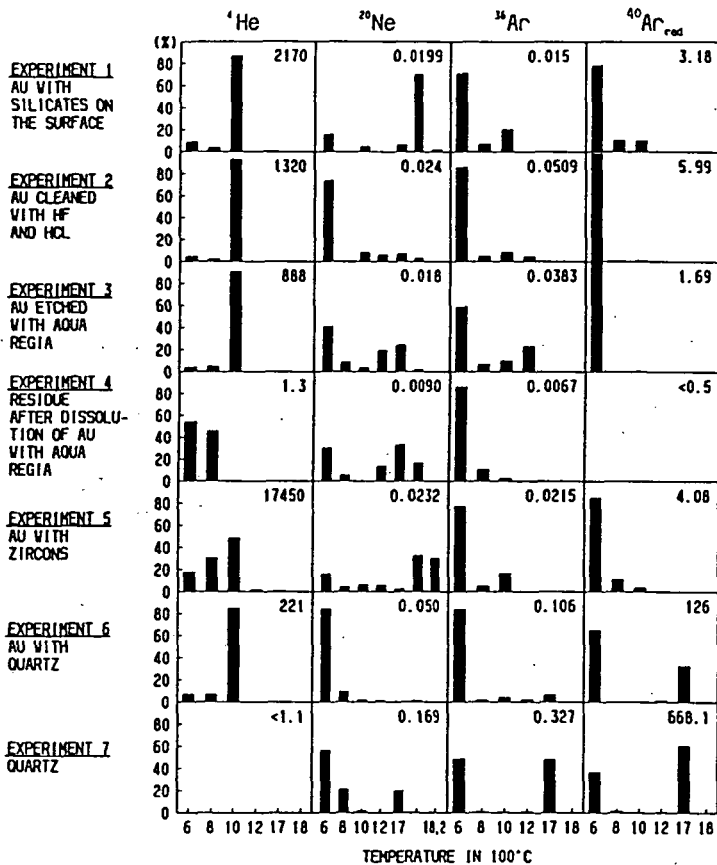


Fig. 1 Temperature release patterns of noble gases for placer gold collected from the river Grosse Fontanne in central Switzerland. Description of the experiments see text. The columns indicate the percentage of released gas. The numbers in each box give the concentrations for 100 percent in 10<sup>-8</sup> cm<sup>3</sup> STP/g Au.

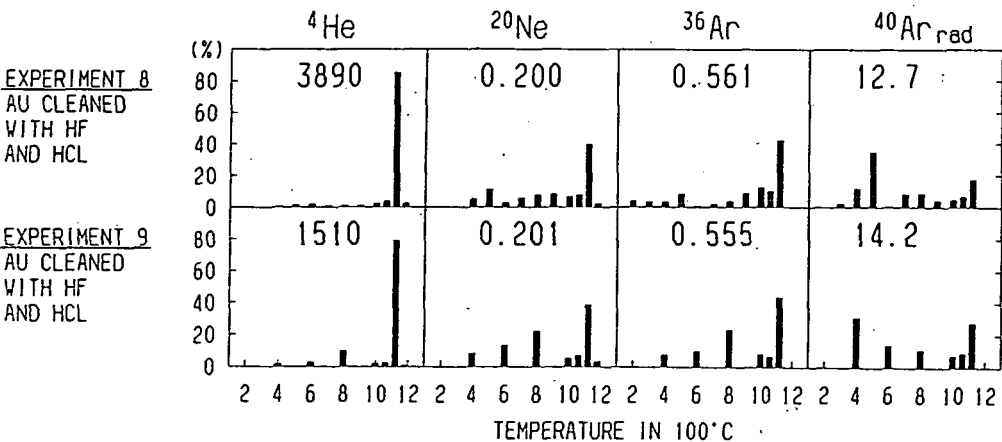


Fig. 2 Temperature release patterns of noble gases for placer gold collected from the river Kruempelgraben in central Switzerland. See also caption to Fig. 1.

5226-90  
ABS-ONLY

94-12241  
763446

p. 2

**PROJECTILE-TARGET MIXING IN MELTED EJECTA FORMED DURING A HYPERVELOCITY IMPACT CRATERING EVENT;** Noreen Joyce Evans, Thomas J. Ahrens, M. Shahinpoor and W.W. Anderson. Lindhurst Laboratory of Experimental Geophysics, Seismological Laboratory, California Institute of Technology, Pasadena, CA 91125

→ Tektites contain little to no projectile contamination (1) while, in contrast, some distal ejecta deposits can be relatively projectile-rich (eg. the Cretaceous-Tertiary (K-T) boundary clay; (2)). This compositional difference motivated an experimental study of hypervelocity target-projectile mixing processes. We hope to scale up the results from these experiments and apply them to terrestrial impact structures like the Chicxulub Crater, Yucutan, Mexico, the leading contender as the site for the impact that caused the mass extinction that marks the K-T boundary (3). Shock decomposition of the  $\approx 500\text{m}$  thickness of anhydrite, or greater thickness of limestone, in the target rocks at Chicxulub (4) may have been a critical mechanism for either global cooling via  $\text{SO}_3$ , and subsequently  $\text{H}_2\text{SO}_4$ , formation, or possibly, global warming via increased  $\text{CO}_2$  formation (4). Understanding target-projectile mixing processes during hypervelocity impact may permit more accurate estimates of the amount of potentially toxic, target-derived material reaching stratospheric heights. — end

A two-stage light gas gun was used to launch 6-7 km/s Fe alloy projectiles into Mo targets. Ejecta fragments ( $< 5\text{-}180\ \mu\text{m}$  diameter) were captured by  $0.032\ \text{g/cm}^3$  polystyrene foam (5cm thick) witness plates. After the impact, the witness plates were X-rayed and then sliced at regular longitudinal and transverse intervals to determine the depth of penetration and angular distribution of captured ejecta. Each section was dissolved in chloroform and the ejecta recovered. It was observed that a portion of the ejecta was in the form of metal spheres with distinct quench textures, indicating that melting had occurred during impact.

The spheres were analysed by electron microprobe to determine the component of target (Mo) and projectile (Fe) material in each (Figure 1). Sphere velocities were estimated by balancing the energy expended during passage through the polystyrene foam against the initial kinetic energies of the spheres. Setting these energies equal and solving for velocity yields;

$$v = \sqrt{(2AD(S_{\infty} + \rho_{\infty}E_{\text{vap}})) / m} \quad (1)$$

where A is the cross-sectional area of the hole created by the sphere penetration, D is the penetration depth,  $\rho_{\infty}$  is the foam density ( $0.319\ \text{g/cm}^3$ ) and  $E_{\text{vap}}$  is the vaporization energy of polystyrene. The force exerted by the sphere on the foam is approximated by  $S_{\infty}A$ , where  $S_{\infty}$  is the penetration strength of the foam ( $0.5\text{MPa}$ ; (5)). The mass of the sphere is given by m.

Velocity values (Figure 2) are bracketed by uncertainty in  $E_{\text{vap}}$ . If the decomposition of polystyrene produces the intermediate products acetylene and benzene, the value of  $E_{\text{vap}}$  is  $2.5 \times 10^6\ \text{J/kg}$ . However, further dissociation of the benzene monomer to acetylene brings the value of  $E_{\text{vap}}$  is closer to  $10^7\ \text{J/kg}$  (6). The limiting case for application of the above model is when the internal energy gain by the foam is less than  $E_{\text{vap}}$ . For these limiting cases, an equation for hypervelocity penetration of impact fragments into soft materials (5) was used.

Combining ejection angle, velocity and compositional data (Figures 1 and 2) reveals that high angle, high velocity ejecta contains a higher projectile component than low angle, low velocity ejecta. This supports numerical predictive calculation (7). Not predicted by calculation but observed in the present experiment is a break in the compositional trend, where from  $50\text{-}70^\circ$ , the Fe/Mo (ie. projectile/target) ratio drops dramatically (Figure 1). Although relatively fewer spheres were recovered in this section (Figure 3), the Fe/Mo ratio for this section is based on 20 analyses and is statistically significant. Although more experiments are needed to establish with confidence that this "break zone" in the sphere composition is reproducible, subsequent experiments have shown that the sphere mass distribution (Figure 3) is

reproducible.

The low angle, low velocity material generated by this experiment is not completely analogous to natural tektites for the following reasons; Firstly, the experimentally-derived material has too high a projectile component to allow a comparison with tektites which are known to contain negligible projectile contamination (2,6). Secondly, some tektites, australites for example, have travelled >5000 km from the target site and have, therefore, been ejected at relatively high angles. The high angle, high velocity material may be analogous to the projectile-rich material in ejecta deposits, such as that at the K-T boundary. If subsequent experiments support the incorporation of less than 20% target material in high angle ejecta, we may be able to more accurately model the target contribution to the stratospherically distributed dust, aerosols and gas derived from, for example, the Chicxulub target rocks.

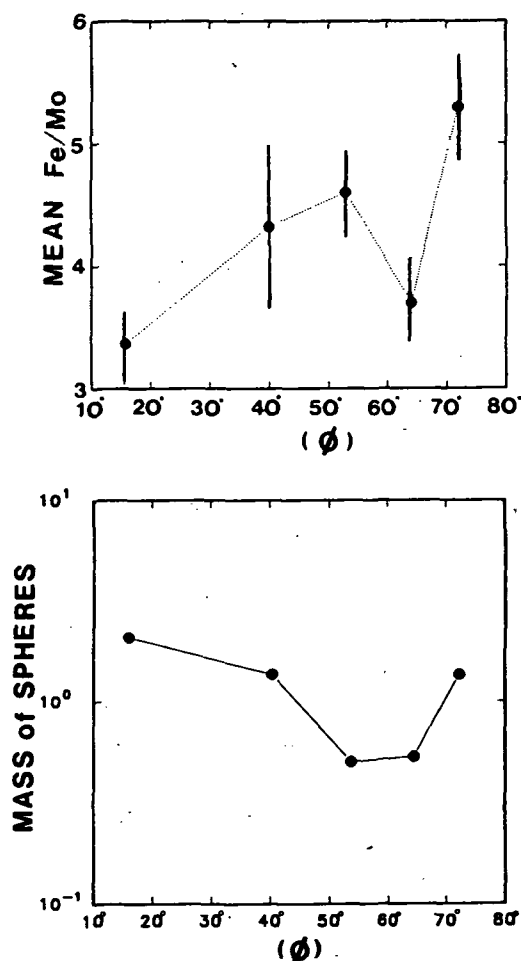


Figure 1. Mean Fe/Mo (mass ratio) versus angle of ejection ( $\phi$ , angle from target surface). A rapid increase in the Fe/Mo ratio is interrupted by a zone from 50 to 70° where the ratio drops suddenly, only to increase to the highest values at higher ejection angles.

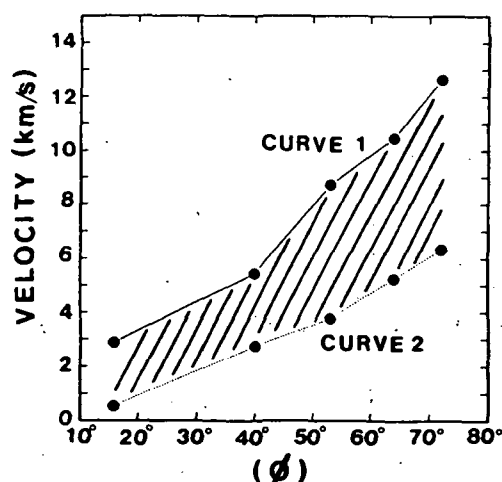


Figure 2. Mean sphere velocity (km/s) versus ejection angle ( $\phi$ ). Curve 1 and 2 correspond to  $E_{\text{vap}}$  values of  $1.0 \times 10^7$  J/kg and  $2.5 \times 10^6$  J/kg, respectively.

Figure 3. Sphere mass (normalized to the projectile mass, 0.09g) versus angle of ejection ( $\phi$ ).

- (1) Alvarez, L.W., Alvarez, W., Asaro, F. and Michel, H.V., 1980, *Science*, 208, 1095-1108. (2) Taylor, S.R., 1973, *Earth Sci. Rev.* 9, 101-123. (3) Sharpton, V.L., Dalrymple, G.B., Marin, L.E., Ryder, G., Schuraytz, B.C. and Urrutia-Fucugauchi, J., 1992, *Nature*, v. 359, p. 819-821. (4) Brett, R., 1992, *Geochim. Cosmochim. Acta*, v. 56, p. 3603-3606. (5) Shahinpoor, M., Evans, N.J. and Ahrens, T.J., Anderson, W.W., 1992, *in prep.* for Intl. J. Impact Engng. (6) Van Krevelen, D.W., 1972, *Properties of polymers; Correlations with chemical structure*. New York, Elsevier, 427 pp. (7) O'Keefe, J.D. and Ahrens, T.J., 1982, in Silver, L.T., and Schultz, P.H., eds., *Geological Implications of Impacts of Large Asteroids and Comets on the Earth*: Geological Society of America Special Paper 190, p. 103-120. (8) Blum, J.D., Papanastassiou, D.A., Koeberl, C. and Wasserberg, G.J., 1992, *Geochim. Cosmochim. Acta*, v. 56, p. 483-492.

MOSSBAUER SPECTROMETER FOR MINERALOGICAL ANALYSIS OF  
THE MARS SURFACE: MOSSBAUER SOURCE CONSIDERATIONS p 2

Evlanov E.N., Frolov V.A., Prilutskii O.F., Veselova G.V., Space Research Institute, Moscow, Russia, Rodin A.M., Moscow Physical Engineering Institute, Moscow, Russia, G. Klingelhöfer, Darmstadt Technical University, Darmstadt, Germany.

Development of space rocketry and cosmic instrument making has made it possible to create interplanetary stations to be sent to the solar system bodies. In the last decade of the century the planet Mars will be in the focus of planetary science problems. Russia, USA (the NASA) and Europe (the ESA) plan to do a new step in the study of the planetary system by spacecraft missions to Mars. One part of the programs of these missions is Martian surface measurements of iron, which is a dominant element in both the Martian soil and rocks (about 13% by weight). The chemistry of iron in space is strongly coupled to the chemistry of abundant elements (to begin with hydrogen, carbon, oxygen) and it is this coupling of chemical cycles of abundant elements that gives us the possibility of understanding some features of the chemical evolution of matter [1]. In this connection of extremely great importance for the understanding of the evolution of the solar system are the oxidation state of the iron and its mineral composition of the Mars surface. Being highly successful, the Viking landers had no instrumentation to answer these questions. Such instrumentation has to be specifically sensitive to mineralogy. For these purpose the backscattering Mössbauer spectrometer (MS-96) was proposed to be installed on a rover to be launched on board the Russian spacecraft Mars-96 mission to Mars [2]. Due to power and mass restrictions three systems of the device MS-96 (velocity transducer, detector and electronic components) have been extremely miniaturized in comparison to a standard system. In this paper we intend to place for consideration a radioactive source to find out what characteristics it should have to be suitable for purposes of the experiment. — end

Our first task was to select a matrix with which the source on the Martian surface would yield high resolution spectra with maximized signal to noise ratio. We ought to conclude that (for activity loading up to about  $2 \text{ Ci/cm}^2$ ) for assumed Martian conditions the Rh- matrix is the best matrix in any respect.

Our second task was to choose the source activity. On the one hand, an increase of the source activity allows performing the measurements in a shorter time because of the increasing count rate and the reduction of relative statistical errors. On the other hand, in order to increase the source activity without changing its dimensions it is necessary to increase the concentration of radioactive nuclei in a source matrix. As the concentration rises so the probability increases of the Mössbauer nuclei having as nearest neighbors similar atoms instead of those of the matrix element. The result is that electric field gradients are produced which cause quadrupole effects and hence line broadening. We have calculated the relative changes in a Lorentzian width  $\Gamma$ , and in a 14.4 keV Lorentzian emission line maximum  $I_{max}$  with time for a 6 microns thick Rh matrix initially containing  $1 \text{ Ci} \times \text{cm}^{-2}$  and  $5 \text{ Ci} \times \text{cm}^{-2}$ . Our calculati-



## MOSSBAUER SOURCE CONSIDERATIONS: E.N.Evlanov et.al.

ons and comparison with the first measurements with MS-96 device made by Klingelhöfer et al. [3] shows that the activity loading of  $1 \text{ Ci} \times \text{cm}^{-2}$  is the most suitable for the Mössbauer spectrometer to be sent to Mars because the use of a stronger source with the same area will diminish the resolution of the instrument. The source used for this measurements had a diameter of the active area equal to the 4 mm.

We appreciate the Obninsk Enterprise Cyclotron for the preparation of the sources for our device and the initial measurements performed with these sources.

**References:** [1] J.M.Knudsen, *Hyperfine Interactions* 47(1989) 3-31; [2] E.N.Evlanov, L.M.Mukhin, O.F.Prilutski, G.V.Smirnov, J.Juchniewicz, E.Kankeleit, G.Klingelhöfer, J.M.Knudsen, C.d'Uston, *Lunar and Planetary Science* 22(1991) 361; [3] G.Klingelhöfer, J.Foh, P.Held, H.Jäger, E.Kankeleit, R.Teucher. *Hyperfine Interactions* 71 (1992) 1449

VULCANIAN EXPLOSIVE ERUPTIONS: A MECHANISM FOR LOCALISED PYROCLAST DISPERSAL ON VENUS. S.A. Fagents and L. Wilson. Environmental Science Division, Lancaster University, Lancaster LA1 4YQ, U.K. P.2

A model of the mechanisms involved in transient (vulcanian-type) explosive eruptions has enabled us to place constraints on the velocities of blocks ejected during such events on Earth as well as on the excess pressure and concentration of gas in the vent prior to the onset of the explosion. This model, suitably modified, can predict the results of similar eruptions occurring under the differing Venusian environmental conditions. It is found that the much higher atmospheric pressure (~100 bars at the mean planetary radius) dominates the form of the resulting deposit in two main ways: (i) by inhibiting the expansion out of the vent of overpressured gas, hence reducing ejecta velocity; and (ii) by retarding the flight of ejected blocks via drag effects. Thus, it is expected that such deposits will typically extend to ~200 m on Venus as compared to several km for documented terrestrial deposits. — end

The high atmospheric pressure on Venus, especially in areas of low elevation, acts to reduce or suppress volatile exsolution from magmas erupted at the surface or intruded at shallow depths [1-3]. Steady explosive eruptions, i.e. those that involve the continuous release of gas from magma as it rises towards the surface and fragments at or below the vent to produce a steady stream of pyroclasts, may not be possible on Venus unless magma volatile contents are high relative to those commonly encountered on Earth [1]. However, when magma intrudes close to the surface but fails to erupt (most often because the rise rate is slow enough that excessive cooling intervenes), in general it becomes possible for exsolving volatiles to accumulate at the top of the magma column, initially possibly as a foam layer but later, if the foam collapses [4], as a gas pocket. Magmatic gases may be trapped efficiently beneath a rigid "lid" if magma partly invades and seals some of the near-surface fractures produced by the presence of the dike containing the magma. Alternatively, if potentially volatile compounds are present in the near-surface country rocks, these may be evaporated and trapped as high-pressure gases in any fractures not connected efficiently to the surface. It is not clear if such country rock volatiles might be present on Venus [5], but there is every reason to believe that some magmatic volatiles will commonly be released as mafic magmas approach the surface [6].

The failure of part of the lid overlying an accumulation of high-pressure gases leads to expansion of the locally released gases and acceleration of the overlying rocks. Furthermore, local decompression leads to the propagation of an expansion wave into the surroundings, and this can trigger failure of more of the lid, leading quickly to catastrophic disruption of all of the pressurised region in a vulcanian style explosion [7]. Although such activity is most commonly associated with intermediate-composition magmas on Earth, the mechanism can operate in any magma given suitable conditions controlling the approach of the melt to the surface, and may be the source of localised dark halo deposits on the Moon [8].

We have recently re-examined the details of this explosion mechanism in order to estimate the mass concentration factors and excess pressures for gases driving vulcanian explosions on Earth [9]. We computed the initial velocities and subsequent ranges in air of clasts of various sizes expelled in such explosions, using a wide range of possible initial conditions of gas pressure, gas concentration (relative to the inherent volatile content of the magma) and geometry of the exploding region. By comparing the computed ranges of clasts with the observed ranges of blocks in several eruptions for which field data are available, we have found that quite modest excess gas pressures (1 to 10 MPa, i.e., 10 to 100 bars) and gas concentrations (0.01 to 0.1 mass fraction of the explosion products, i.e. a factor of ~3 concentration over magmatic values) are needed to explain the observed dispersion of ejecta. These results differ from those of an earlier analysis [10] which overestimated the pressures and gas contents needed. This was due to the neglect, in the earlier work, of the fact that the atmosphere surrounding an explosion source must initially move outwards with about the same speed as the early explosion products, thus leading to an overestimation of the initial drag forces acting on the clasts and an underestimate of their ranges.

## VULCANIAN ERUPTIONS ON VENUS; Fagents, S.A. and Wilson, L.

A similar analysis is readily carried out for Venus with due allowance for the differing environmental conditions. Clast dispersal is computed using a model of the vertical variation of the Venus atmosphere properties. The likely ranges of gas contents in the disrupted region are estimated using calculations of gas exsolution in rising mafic magmas on Venus [6, 11]. These suggest that, since gas exsolution is likely to occur over a smaller range of vertical depths on Venus (the high surface pressure must be added to the lithostatic pressure to obtain the minimum total pressure acting on a magma at a given depth), available amounts of gas are likely to be somewhat less than on Earth. However, if the magma body degasses while remaining close to the surface for a length of time, then the ratio of the gas mass to the caprock mass may significantly exceed magmatic gas contents. Maximum gas pressures in the disrupted region are assumed to be limited (as on Earth) by the tensile or shear strengths of the overlying rocks; the high Venus surface temperature may mean that these strengths are also somewhat less than on Earth. Sizes of regions in which magmatic gas may accumulate are dictated by the typical dimensions of near-surface dikes. There are two possibilities here: if mafic dikes propagate from shallow magma reservoirs then they are likely to have similar widths to such dikes on Earth, since both the planetary gravity [12, 13] and the total range of depths at which neutral-buoyancy zone reservoirs reside [6] are similar. However, there are reasons to suspect that, in low elevation areas on Venus, shallow reservoirs will be absent and magma will rise directly from mantle partial melt zones at depths of ~10 to 20 km [6], leading to wider near-surface dikes than are common on Earth. Elasticity theory [14] suggests that the width factor will increase only as the square root of the depth factor, as a first approximation, however, implying dikes 2 to 3 times wider. On the basis of these considerations we have used gas contents in the explosion products of 0.01 to 0.1 mass fraction, excess pressures up to 100 MPa, and source region sizes up to 50 m.

The results of numerous simulated explosions with initial conditions chosen from the above ranges show that coarse clast ranges are expected to be no greater than ~350 m under the most extreme circumstances. The table below presents values of ejection velocity in m/s and range in m for blocks 2 m in diameter ejected from explosions with initial excess pressure 100 bars and gas region radii 50 m. For each of the volatile species CO<sub>2</sub> and H<sub>2</sub>O, results for two values of gas/rock mass ratio are shown. The greater molecular weight of CO<sub>2</sub> ensures that the velocities attained are lower than for H<sub>2</sub>O. Variation of the altitude of the vent location illustrates the effect of lower ambient atmospheric pressure on clast ejection velocity and travel distance: for similar initial conditions, blocks will achieve greater velocities and travel further at higher altitudes.

Altitude / (km)	CO <sub>2</sub>				H <sub>2</sub> O			
	0.05		0.10		0.05		0.10	
	vel.	range	vel.	range	vel.	range	vel.	range
0	3	49	40	140	49	153	160	200
3	15	83	52	169	64	160	112	234
10	43	181	85	266	99	285	157	341

The resolution of Magellan radar data (~100 m/pixel) may not be sufficiently high for such localised deposits to be visible, other than via their effect on sub-pixel surface roughness. It is anticipated that future work on deconvolving roughness from electrical properties of the surface may provide a tool for the detection of such deposits.

#### References.

- [1] Head, J.W. and Wilson, L. (1986). *J. geophys. Res.* **91**, 9407-9446. [2] Wood, C.A. (1979). *NASA Tech. Memo TM 80339*, 244-246. [3] Wilson, L. and Head, J.W. (1983). *Nature* **302**, 663-669. [4] Jaupart, C. and Vergnolle, S. (1989). *J. Fluid Mech.* **203**, 347-380. [5] Kargel, J.S., Komatsu, G., Baker, V.R., Lewis, J.S. and Strom, R.G. (1991). *Lunar & Planetary Science XXII*, 685-686. Lunar & Planetary Institute, Houston. [6] Head, J.W. and Wilson, L. (1992). *J. geophys. Res.* **97**, 3877-3903. [7] Wilson, L. (1980). *J. Volcanol. geotherm. Res.* **8**, 297-313. [8] Head, J.W. and Wilson, L. (1979). *Proc. lunar plan. Sci. Conf. 10th*, 2861-2897. [9] Fagents, S.A. and Wilson, L. (1992). *Geophys. J. Internat.* (in press). [10] Wilson, L. (1972). *Geophys. J. R. astr. Soc.* **30**, 381-392. [11] Garvin, J.B., Head, J.W. and Wilson, L. (1982). *Icarus* **52**, 365-372. [12] Wilson, L. and Head, J.W. (1988). *Lunar & Planetary Science XIX*, 1283-1284. Lunar & Planetary Institute, Houston. [13] Wilson, L. and Parfitt, E.A. (1989). *Lunar & Planetary Science XX*, 1213-1214. Lunar & Planetary Institute, Houston. [14] Pollard, D.D. (1987). In *Mafic Dike Swarms* (ed. H.C. Halls and W.F. Fahrig), *Geol. Assoc. Canada* **34**, 5-24.

5229-90  
ABS ONLY

N 9 4 6 1 4 2 4 4  
p. 2

**CHONDRITES, S ASTEROIDS, AND "SPACE WEATHERING": THUMPING NOISES FROM THE COFFIN?** F.P. Fanale and B.E. Clark, Planetary Geosciences, University of Hawaii at Manoa, Honolulu, HI 96822

**Introduction:** Most of the spectral characteristics of ordinary chondrites and S-asteroids in the visible and infrared can be reduced to three numerical values. These values represent the depth of the absorption band resulting from octahedrally coordinated  $\text{Fe}^{2+}$ , the reflectance at 0.56 microns and the slope of the continuum (as measured according to convention). ~~This is illustrated in Figure 1.~~ By plotting these three characteristics, it is possible to immediately compare the spectral characteristics of large numbers of ordinary chondrites and S-asteroids [1]. Commonality of spectral characteristics between these populations can thus be evaluated on the basis of overlap in position on three two-coordinate systems: albedo vs. band depth, band depth vs slope, and slope vs. albedo. In order to establish identity, members of the two populations must overlap on all three of these independent parameter spaces. In this coordinate system, spectra of 23 ordinary chondrites (representing all metamorphic grades), and 39 S-asteroids were compared [1]. It was found that there was no overlap between the two populations in terms of the slope vs. band depth parameters, nor were most chondrites identical to the S-asteroids with respect to the other criteria.

However, the controversial question remains: Where are the parent bodies of the chondrites? Perhaps an even more critical question is: Where are our samples of the S-asteroids? Considering the geography of the asteroid belt and the theory that early solar-system electromagnetic induction heating differentiated protoasteroids in the inner portion of the main belt [2,3,4], it was suggested [1] that although S-asteroids and ordinary chondrites have very similar mineralogy, the S-asteroids are mixtures of metallic nickel iron and silicates which resulted from magmatism induced by electromagnetic heating whereas chondrites were only slightly metamorphosed nebular condensates. In this scenario chondrites would have been derived from a population of bodies with thermal lag times so short that they were not subjected to melting during the phase of the electromagnetic induction heating event but only to various degrees of pervasive metamorphism. Furthermore, these objects would then have been too small to be observed and systematically included in the library of asteroidal spectra. It was also suggested in [1] that the parametric distribution of S-asteroid spectra could be reproduced by mixing various proportions of Ni-Fe meteorite and achondritic materials. This has also been demonstrated in the laboratory [5,6]. ~~end~~

In any case, it was the conclusion of [1] that ordinary chondrite meteorites possess spectral parameters which make them differ too strongly from S-type asteroids to be genetically related. It was also shown that even severe "space weathering" alteration in the form of melting, recrystallization and comminution could not change their spectral parameters enough to result in overlap with the S-type asteroids.

**New Developments:** Recently, Pieters et al. [7], have argued that maturation of long exposed surface material on the moon is not due to agglutinate formation but is instead due to another process which operates primarily on the finest grain size fraction. They suggested that this process (which we shall refer to as "process X") may also significantly affect asteroidal spectra [7]. Several physically reasonable suggestions have been proposed with respect to the identity of "process X". These include vacuum reduction of  $\text{Fe}^{2+}$  [8] and reduction of  $\text{Fe}^{2+}$  by solar wind hydrogen [9]. Because of the vast differences between lunar and asteroidal regolith meteorites, little progress can be made by simplyfying the issue to the question of whether or not "space weathering" actually occurs. Instead, three questions need to be answered: 1.) Does major alteration of spectra occur on exposed lunar material by a process other than agglutinate formation? 2.) Does the process operate on asteroids to the extent of explaining such minor spectral heterogeneities as have been attributed to Gaspra? and 3.) Does it operate on asteroids sufficiently effectively to alter the spectra of exposed ordinary chondrite material until the spectra resemble those of S-asteroids? Pieters et al. have presented a strong case that the first question will eventually be answered in the positive. In regards to the second question, the heterogeneities on Gaspra are barely demonstrable and it is unlikely that their causes will be identified. We will, however, discuss evidence relative to the third question.

**Discussion: Evidence suggesting spectral alteration of exposed asteroidal material:** To assess the relevance of "process X" to the chondrite-S-asteroid controversy we have plotted the spectral characteristics of mature and immature lunar basalts on the coordinate system referred to above [10]. On the same plots we show the positions of average S-asteroid and ordinary chondrite spectra. The spectral trends required to transform chondrite spectra into S-asteroid spectra parallel those exhibited by maturing lunar samples on all these plots. It should be borne in mind however that very diverse processes can produce similar spectral alteration. For example,

# CHONDRITES, S ASTEROIDS AND "SPACE WEATHERING": Fanale F.P. and Clark B.E.

simultaneous shallowing of absorption bands, continuum slope increase and lowering of the albedo can be accomplished by melting and recrystallization [11] or by addition of NiFe [5].

*Arguments against major alteration of asteroidal spectra by "space weathering":* 1.) The exposure age of the optical surface on the asteroids must be exceedingly short. Unlike the moon, the gravitational field of most S-asteroids is so low that almost all of the "ejecta" from impacts is, in fact, ejected from the object. In addition, any impact producing a crater >1 km on an object like Gaspra will remix many tens of meters of regolith on a global basis and much smaller impacts can cause global downslope movement [12]. Thus, unlike the case of the moon, any space weathering of the optical surface must occur on a geologically instantaneous basis in order to show up spectrally. 2.) On the asteroid 4 Vesta, the exposure of the optical surface must be much longer than on most asteroids. Yet there is no evidence of such maturation in its spectrum (see Figure 1). The possibility that the silicate mineralogy on Vesta may be somewhat different than that of chondrites is utterly irrelevant. The deep Fe<sup>2+</sup> absorption band in Vesta's reflectance spectrum testifies to the fact that there is abundant Fe<sup>2+</sup> exposed which has not been reduced significantly by either vacuum melting reduction nor by solar wind related effects. Further, the possibility of renewal of Vesta's surface by endogenic or exogenic processes such as basalt flows or the birth of "baby Vestas" is utterly irrelevant as well. In order to be relevant, such processes must have occurred on a shorter time scale than the lifetime of the optical surface of S-asteroids, which seems highly improbable.

**Conclusions:** Despite these arguments, much remains to be done before the identity or the non-identity of ordinary chondrites and S-asteroids can be established with certainty:

- 1.) First, semantic difficulties should hereafter be avoided. The question of effectiveness of space weathering must be resolved at least in terms of the three questions listed earlier. Further, it must be recognized that even if S-asteroids do not supply ordinary chondrites they still were almost certainly derived from them by various extensions of the processes which produced the various degrees of metamorphism of chondrites.
- 2.) The lifetime of the optical surface on small bodies must be modelled on a quantitative basis. While this may not be possible, at least quantitative limits could be derived theoretically.
- 3.) The precise physical cause of the spectral alteration of mature lunar soils needs to be established.
- 4.) The possibility that the lifetime of the optical surfaces on small bodies may be exceedingly short suggests that it may even be possible to duplicate the total H<sup>+</sup> dose in the laboratory. The usual heating problems associated with high beam strengths may be of little concern in this case.

**References:** [1] Fanale et al. *JGR preprint*, 1992, [2] Sonett et al. 1971, [3] Herbert and Sonett, *Icarus*, 40, 1979, [4] Bell et al. *In Asteroids II*, 1989, [5] Hiroi and Takeda, *Proc. NIPR Symp. Antarct. Meteorites*, 4, 1991, [6] Takeda et al. 1992, [7] Pieters et al. *Bull. Amer. Astron. Soc.*, 24, 1992, [8] Wells and Hapke, *Science*, 195, 1977, [9] Pillinger et al. *Proc. Lunar Sci. Conf. 5th*, 1974, [10] McKay et al. *Lunar Sourcebook*, 285-256, 1991 [11] Clark et al. *Icarus*, 97, 1992, [12] Nolan et al. *Bull. Amer. Astron. Soc.*, 24, 1992.

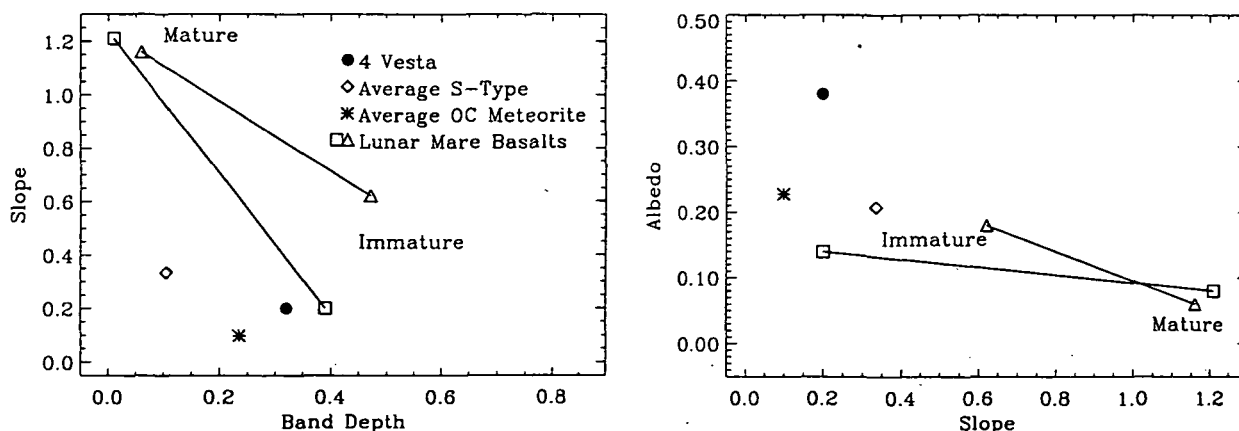


**Figure 1 A and B** These plots show the three parameters of continuum slope, reflectance at 0.56 microns (albedo) and band depth at 0.95 - 1.0 microns. The spectral trends for lunar mare basalts as they go from "immature" to "mature" are indicated. Note that the trends which would be required of OC meteorites to mature towards S-Type asteroids parallel those seen for the mare basalts. Note also that 4 Vesta appears to be spectrally immature.

A COMPARISON OF THE VISIBLE AND NEAR INFRARED REFLECTANCE OF  
HYDROVOLCANIC PALAGONITE TUFFS AND MARTIAN WEATHERED SOILS

W.H. Farrand, SAIC, 803 W. Broad St., Falls Church, VA 22031 and R.B. Singer, Planetary Image Research Laboratory, University of Arizona, Tucson, AZ 85721.

The visible and near infrared reflectance of martian weathered soils, abundant in the bright regions, have been shown to resemble certain examples of the X-ray amorphous mineraloid palagonite (e.g., [1,2]). To date, most comparisons between terrestrial palagonites and martian telescopic spectra have been done using palagonites that were formed under ambient semi-arid weathering conditions on Hawaiian volcanoes such as Mauna Kea [1,2]. Here we examine palagonites associated with the tephra deposits that make up tuff rings and tuff cones. Tuff rings and tuff cones result from hydrovolcanic activity, defined as the interaction of magmas (in this instance, of basaltic composition) with surface or near-surface water [3]. Tuff rings and tuff cones can contain variable amounts of country rock and juvenile crystals, but their primary constituent is fine grained sideromelane (basaltic glass). Sideromelane alters to palagonite. Unlike the aforementioned Hawaiian palagonites, the alteration of sideromelane to palagonite seems to occur relatively rapidly in tuff cones, on the order of days to months [3,4]. In comparing the spectra of hydrovolcanically produced palagonites with telescopic spectra of Mars, one is struck by their similarity in the VNIR and dissimilarity in the SWIR. — end

Figures 1 and 2 present overlays of several palagonite tuff sample spectra with bright region spectra. The palagonite tuff samples come from the Cerro Colorado tuff cone located in the Pinacate volcanic field of Sonora, Mexico and from the Pavant Butte tuff cone of Millard County, Utah. The Mars bright region spectrum in Figure 1 is an average of 8 spectra from Arabia collected during the 1988 opposition [5]. The spectrum in Figure 2 is an average of 3 bright region spectra (Aeolis, S. Elysium, and Amenthes) collected during the 1978 opposition [6]; the data shortwards of 0.7  $\mu\text{m}$  are an average of bright region spectra collected in 1969 [7]. All spectra are scaled to 1.0 at 0.79  $\mu\text{m}$ .

There is a very good correspondence between the position and slope of the UV/Vis  $\text{Fe}^{3+}$  absorption edge of the Cerro Colorado sample CC-2c and that of the Arabia spectrum. Differences that can be noted include the presence of a distinct 0.48  $\mu\text{m}$  band in the tuff cone spectra and its absence in the Arabia spectrum. This absorption can be ascribed to the  ${}^6\text{A}_1 \rightarrow ({}^4\text{E}, {}^4\text{A}_1)$  electronic transition of the  $\text{Fe}^{3+}$  ion [8], possibly occurring in the tuff sample due to poorly- to well-crystalline goethite and perhaps nontronite. To date, this feature has not been observed in telescopic spectra of Mars. There is also a shoulder in the tuff cone spectra centered at 0.68  $\mu\text{m}$  which can be attributed to the  ${}^6\text{A}_1 \rightarrow {}^4\text{T}_2$   $\text{Fe}^{3+}$  transition [8]. There is a weak indication of this feature in the Arabia spectrum [5] and this absorption has been noted in other telescopic spectra (e.g. [1,7,9]).

There is a disparity between Arabia (1978 and 1988) and most of the 1969-1978 bright region spectra in the 1  $\mu\text{m}$  region. The Arabia spectrum trends downward in a fashion consistent with a reflectance minimum near 0.98  $\mu\text{m}$ . This is close to the "1  $\mu\text{m}$ " band center for the PB-2b sample at 0.974  $\mu\text{m}$  [4]. In contrast, the 1978 bright region average shows a band minimum near the 0.93  $\mu\text{m}$  band center of the CC-2c sample. Farrand and Singer [4] noted that differences in the "1  $\mu\text{m}$ " band center of palagonite tuffs are related to the degree of oxidation of the constituent sideromelane. In the CC-2c sample, the sideromelane is nearly completely altered to palagonite; thus the "1  $\mu\text{m}$ " band center is more reminiscent of a ferric oxide phase such as a goethite. In the PB-2b sample, there still exist remnants of  $\text{Fe}^{2+}$  bearing sideromelane, thus its "1  $\mu\text{m}$ " band center is skewed to longer wavelengths.

What is occurring on the scale of individual pyroclasts in the palagonite tuffs might also be happening on the surface of Mars. That is to say that most bright regions observed in 1978 and before probably have a more uniform coating or soil layer of nearly completely altered palagonitic material than does Arabia. This tendency of Arabia to exhibit traits intermediate between light and dark regions was discussed by McCord et al. [6]. Those authors noted that Arabia probably has more exposed dark materials than other bright regions or perhaps a larger component of  $\text{Fe}^{2+}$  bearing grains (pyroxenes or sideromelane fragments) admixed in its soils. Recent interpretations of reflectance spectra from the Phobos ISM instrument support this evidence for compositional variety among martian weathered soils [10].

Beyond about 1.2  $\mu\text{m}$ , the resemblance between the palagonite tuff and the martian bright region spectra ends. The continua of the palagonite tuff spectra are convex in the SWIR, punctuated at 1.4 and 1.9  $\mu\text{m}$  by strong OH and  $\text{H}_2\text{O}$  absorptions and a strong fall-off in reflectance approaching the water and OH absorptions centered near 3.0  $\mu\text{m}$ . In contrast, the average bright region spectrum is relatively flat beyond 1.2  $\mu\text{m}$  with a strong

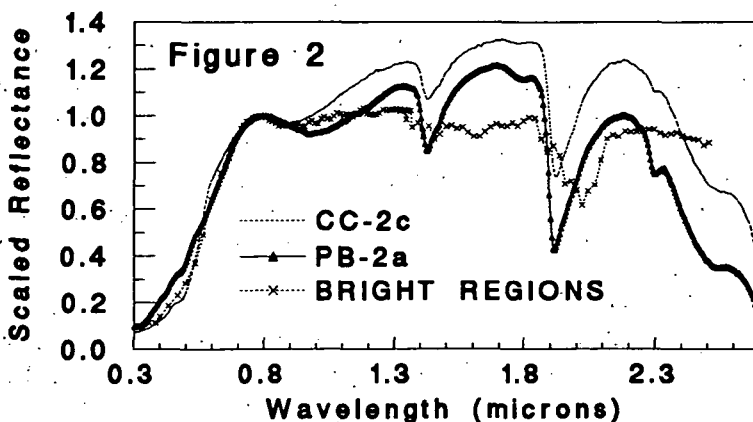
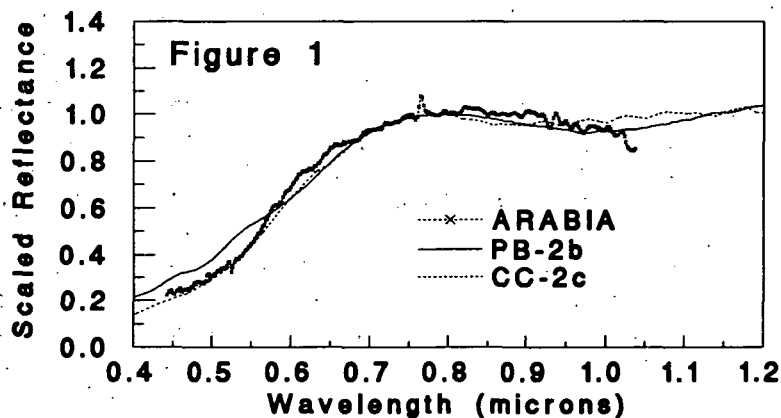
# HYDROVOLCANIC PALAGONITE TUFFS: Farrand, W.H. and Singer, R.B.

atmospheric CO<sub>2</sub> band at 2  $\mu\text{m}$ , and weaker CO<sub>2</sub> absorptions near 1.45 and 1.62  $\mu\text{m}$ . A weak but important absorption feature near 2.36  $\mu\text{m}$  was first noted in telescopic data for Mars [6, 11]. Clark et al. [12] have observed and analyzed this feature in greater detail, and conclude that it is due in part to martian atmospheric CO, but with good evidence for a surface mineral absorption as well, suggested by them to be scapolite.

The palagonite tuff spectra display a distinct absorption at 2.29  $\mu\text{m}$  which is tentatively assigned to a combination overtone of the Fe-OH bending fundamental within the smectite clay mineral nontronite. Nontronite, perhaps admixed with poorly crystalline goethite, could also be responsible for the 0.48  $\mu\text{m}$  and 0.68  $\mu\text{m}$  features in the palagonite tuff spectra. Clark et al. [13] observed a 2.29  $\mu\text{m}$  absorption in Hellespontica that was consistent with the nontronite band, but otherwise a 2.29  $\mu\text{m}$  feature with band parameters consistent with nontronite has not been seen on Mars [1, 11].

The dissimilarity of palagonite tuff and martian telescopic spectra longwards of 1.2  $\mu\text{m}$  can be attributed in large part to what is probably a greater degree of crystallinity within the terrestrial tuffs than within the martian soils. The southwestern palagonite tuffs formed in semi-arid environments but with abundant ground water and, in the case of Pavant Butte, in a standing lake. At one time conditions on Mars may have been conducive to the formation of this variety of palagonite. However, over most of its history Mars has been considerably drier. Thus, models for palagonite formation on Mars involving semi-arid ambient weathering, or other alteration involving low temperatures and minimal water, seem more appropriate for explaining the ubiquitous weathered soils.

- [1] Singer, R.B., *J. Geophys. Res.*, 87, 10,159-10,168, 1982; [2] Evans, D.L. and J.B. Adams, *Proc. Lunar Planet. Sci. Conf. 10th*, 1829-1834, 1979; [3] Wohletz, K.H. and M.F. Sheridan, *Am. J. Sci.*, 283, 385-413, 1983; [4] Farrand, W.H. and R.B. Singer, *J. Geophys. Res.*, 97, 17,393-17,408, 1992; [5] Singer, R.B. et al., *Lunar Planet. Sci. Conf. 11th*, 1154-1155, 1990; [6] McCord, T.B., et al., *J. Geophys. Res.*, 87, 3021-3032, 1982; [7] McCord et. al., *Icarus*, 31, 25-39, 1977; [8] Morris, R.V. et al., *J. Geophys. Res.*, 90, 3126-3144, 1985; [9] Bell, J.F. III, et al., *J. Geophys. Res.*, 95, 14447-14461, 1990; [10] Murchie et al, *LPI Tech. Report 92-04*, 23-25, 1992; [11] Singer et al., *Lunar Planet. Sci. Conf.*, 16th, 787-788, 1985; [12] Clark, R.N. et al., *J. Geophys. Res.*, 95, 14463-14480, 1990.



THE RATE OF CHEMICAL WEATHERING OF PYRITE ON THE SURFACE OF VENUS, B. Fegley, Jr.<sup>1,2</sup> and K. Lodders<sup>1</sup>, (1) Department of Earth & Planetary Sciences and (2) McDonnell Center for the Space Sciences, Washington University, St. Louis, MO 63130-4899 USA.

**Introduction.** This abstract reports results of an experimental study of the chemical weathering of pyrite ( $\text{FeS}_2$ ) under Venus-like conditions. This work, which extends the earlier study by Fegley and Treiman [1,2], is part of a long range research program to experimentally measure the rates of thermochemical gas-solid reactions important in the atmospheric-lithospheric sulfur cycle on Venus. The objectives of this research are (1) to measure the kinetics of thermochemical gas-solid reactions responsible for both the production (e.g., anhydrite formation [3]) and destruction (e.g., pyrrhotite oxidation [4]) of sulfur-bearing minerals on the surface of Venus and (2) to incorporate these and other constraints into holistic models of the chemical interactions between the atmosphere and surface of Venus.

**Experimental.** Experiments were done with single crystal cubes of natural pyrite (Navajun, Logroño, Spain) that were cut and polished into slices of known weight and surface area. The slices were isothermally heated at atmospheric pressure in 99.99%  $\text{CO}_2$  (Coleman Instrument Grade) at either 412° C (685 K) or 465° C (738 K) for time periods up to 10 days. These two isotherms correspond to temperatures at about 6 km and 0 km altitude, respectively, on Venus. The reaction rate was determined by measuring the weight loss of the reacted slices after removal from the furnace. The reaction products were characterized by X-ray diffraction, scanning electron microscopy, and energy dispersive spectroscopy on the SEM.

**Results.** X-ray diffraction data show the presence of unreacted pyrite and pyrrhotite in all samples. When examined in the SEM, the samples reacted at 465° C showed the growth of hexagonal platelets of an Fe sulfide phase, which is probably pyrrhotite, on the surface. These platelets became more abundant as samples were heated for longer times. The XRD peaks due to pyrrhotite also became stronger as samples were heated for longer times. Red coatings on the samples reacted at 412° C indicated the presence of hematite, and the XRD data confirmed minor amounts of hematite in these samples.

The weight loss data along the 412° C and 465° C isotherms are plotted versus time (t) in hours in Figures 1 & 2. The reaction progress is defined as  $\alpha^{1/3}$  where  $\alpha$  is the fraction of unreacted pyrite remaining in the sample. The data show a linear dependence of  $\alpha^{1/3}$  with time which indicates contracting volume kinetics [5]. The unweighted linear least squares fits to the data are:  $\alpha^{1/3} = 1.0004 - 6.352 \times 10^{-4}t$  at 412° C and  $\alpha^{1/3} = 0.997 - 1.874 \times 10^{-3}t$  at 465° C. The slope of each linear fit is the reaction rate constant for pyrite decomposition to pyrrhotite at that temperature.

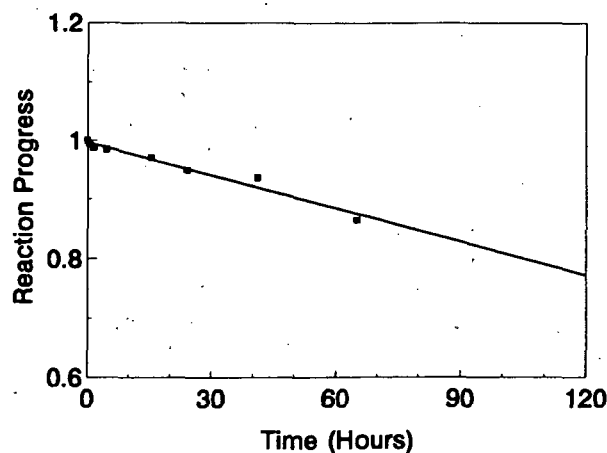
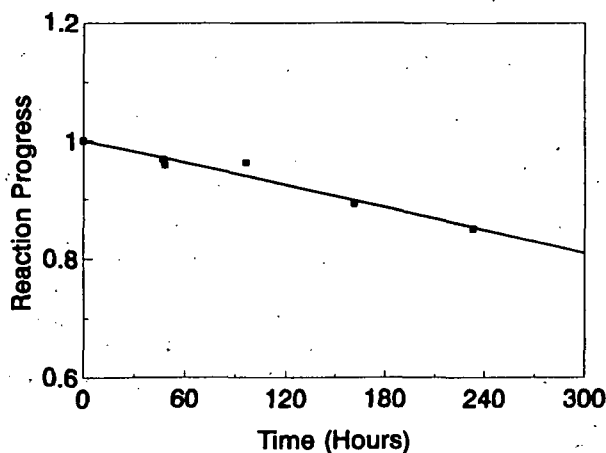


Figure 1 (left), Kinetic data at 412° C, and Figure 2 (right), kinetic data at 465° C. The reaction progress is defined by  $\alpha^{1/3}$ , where  $\alpha$  is the fraction of unreacted pyrite left in the samples.



## PYRITE CHEMICAL WEATHERING ON VENUS Fegley, B. and Lodders, K.

**Interpretation.** The weight loss data were analyzed assuming that pyrite decomposed solely to pyrrhotite. This assumption is supported by the XRD data on the reacted samples, by the phase diagram for the Fe-S system [6], and by studies of pyrite decomposition to pyrrhotite in a dynamic vacuum [7], in flowing Ar [8], and in flowing CO<sub>2</sub> [2,9,10]. Not all prior workers presented kinetic data; however, contracting volume kinetics were also found by [7]. The presence of minor hematite in the samples reacted at 412° C is unexpected because the fO<sub>2</sub> for CO<sub>2</sub> self dissociation is well within the magnetite stability field at this temperature. Minor magnetite would be expected instead if the pyrrhotite reacted with the CO<sub>2</sub> [4]. The hematite coatings are not due to reaction with air during quenching because the coatings are absent from all samples reacted at higher temperatures and because samples were not removed from the furnace atmosphere until they cooled to ≤100° C at the top of the furnace. We suggest that hematite was formed by reaction of pyrrhotite with the trace oxygen impurity in the CO<sub>2</sub>. The oxygen impurity in Coleman Instrument grade CO<sub>2</sub> is specified as ≤ 20 ppmv O<sub>2</sub>, and is plausibly high enough to make the CO<sub>2</sub> oxidizing enough for hematite to form.

**Application to Venus.** Ten years ago, pyrite was proposed as a source of reduced sulfur gases (COS, H<sub>2</sub>S, S<sub>x</sub>) at the surface of Venus [11]. Thermochemical equilibrium calculations predict that the amount of COS produced by pyrite oxidation by CO<sub>2</sub> is temperature (and hence altitude dependent) and ranges from several tens of ppmv to several ppmv in the 0-12 km altitude range [2,12]. Recent analysis of IR spectroscopic data for the 30-45 km region of the atmosphere of Venus suggests that COS abundances increase with decreasing altitude in the Venusian atmosphere [13] and supports the proposal that iron sulfides on the surface of Venus are a net source of reduced sulfur gases. The COS abundances retrieved from the spectroscopic data also agree with the predictions of [2] and [12] once an arithmetic error in the calculations of [12] for the equilibrium  $2\text{CO} + \text{S}_2 = 2\text{COS}$  was corrected.

However, neither the mechanism nor the kinetics of the weathering reaction(s) are constrained by thermochemical equilibrium calculations. Now that some observational evidence suggests a COS source on the surface of Venus, the rate of COS production is of interest. The present work, coupled with the prior studies of [1,2,4] provides information on the kinetics and mechanism of pyrite chemical weathering on the surface of Venus. The experimental results suggest that pyrite chemical weathering is a two step process with the first step involving the formation of pyrrhotite and the second step involving the oxidation of pyrrhotite to magnetite and reduced sulfur gases. The kinetic data shown in Figs. 1 & 2 show that the first step of this process is very rapid. For example, the kinetic data predict a pyrite lifetime of about 22 days at 465° C (738 K) and about 65 days at 412° C (685 K) on the surface of Venus. The second step, pyrrhotite oxidation, is not as rapid as shown by [4]. However, the fundamental result from the present work, and prior work by [1,2,4] is that sulfide chemical weathering on the surface of Venus is a relatively rapid process on a geological timescale.

**Acknowledgements.** This work was supported by a grant from the NASA Planetary Atmospheres Program (B. Fegley, P.I.). We thank D. Kremser for the X-ray diffraction data and R. Poli for polishing the samples.

**References.** [1] B. Fegley & A.H. Treiman 1990 *Bull. Amer. Astron. Soc.* 22, 1055; [2] B. Fegley & A.H. Treiman 1992 in AGU Monograph No. 66, pp. 7-71; [3] B. Fegley & R.G. Prinn 1989 *Nature* 337, 55-58; [4] A.H. Treiman & B. Fegley 1991 *Lunar Planet. Sci. XXII*, pp.1409-1410; [5] W.E. Brown et al 1980 in *Comprehensive Chemical Kinetics* vol. 22, pp. 41-113; [6] G. Kullerud & H.S. Yoder 1959 *Econ. Geol.* 54, 533-572; [7] G. Pannetier & L. Davignon 1964 *Bull. Soc. Chim. Fr.*, pp.1513-1517; [8] A.W. Coats & N.F.H. Bright 1966 *Can. J. Chem.* 44, 1191-1195; [9] G.M. Schwab & J. Philinis 1947 *J. Amer. Chem. Soc.* 69, 2588-2596; [10] F.C. Thompson & N. Tilling 1924 *J. Soc. Chem. Ind.* 43, T37-T46; [11] U. Von Zahn et al 1983 in *Venus*, pp.299-430; [12] B. Fegley et al 1992 *Proc. 22nd LPSC*, pp. 3-20; [13] J.B. Pollack et al 1992 *Bull. Amer. Astron. Soc.* 24, 996.

N 94-162242

**TERRESTRIAL CASE STUDIES OF ILMENITE EXPLORATION AND LUNAR IMPLICATIONS.** S.C. Feldman and H.A. Franklin (Bechtel Corp., San Francisco, CA 94119)

p. 2

**INTRODUCTION.** The Space Exploration Initiative (SEI) includes space resource utilization as one of the four architectures to achieve U.S. goals in space. Space resource utilization will make use of lunar resources to support long term activities on the lunar surface. Lunar ilmenite and regolith are two of the materials that can be mined and processed for lunar oxygen production. During this investigation, several sources were reviewed to assess terrestrial exploration methods used for locating ilmenite resources. These sources included published reports on terrestrial ilmenite exploration methods, analytical methods, case histories, chemical and physical properties, and associations with other minerals. Using a terrestrial analog and considering the differences between terrestrial and lunar environmental conditions, rocks, and minerals, exploration methods and analytical instruments can be recommended for a lunar orbiter and lander for assessing lunar resources.

**IMPORTANCE OF EXPLORATION IN RESOURCE PRODUCTION.** To produce a resource, such as oxygen from ilmenite, exploration is needed to gather information about the quantity and quality of the ore, the associated major, minor, and trace elements, and the depth and distribution of the deposit. These data contribute to mine planning and process plant design. Without them the life of the mine cannot be accurately predicted.

On the Earth, the initial exploration cost is extremely low compared with development and expansion costs, but provides the foundation for the operation. The same would be true for the Moon.

**TERRESTRIAL CASE HISTORIES.** Twelve terrestrial case histories were reviewed to gain insight into ilmenite exploration on the Moon. All exploration case histories follow the same pattern. They begin with a model, use remote geophysical techniques, define regional sampling sites from the model and geophysics, narrow down the area of exploration based on the preceding work, collect more samples and cores, and perform laboratory analyses of samples. An important part of this process is the collection of samples to determine the correctness of the model. Surface and core samples are collected in areas expected to contain both high and low concentration of the commodity to test the model. After samples are analyzed and the area of mineralization is defined, reserves are calculated to determine the cost/benefit ratio, the necessary capacity of the processing plant, and the life of the mine. Table 1 summarizes the exploration methods used for locating terrestrial ilmenite resources. These methods are reviewed with respect to the petrology, chemistry, and mineral associations of the terrestrial and lunar environments.

end

**ILMENITE EXPLORATION CASE STUDIES: Feldman, S.C. and Franklin, H.A.**

The number of samples collected and the size of the area of exploration in the case histories also have implications for lunar mining.

Table 1  
Exploration methods for terrestrial ilmenite resources.

Develop model
Define area of resources
Mapping
Geologic
Topographic
Geophysics
Magnetic
Seismic
Radiometric
Electrical
Gravity
Sampling
Surface samples
Cores
Laboratory analysis
Grain size analysis
Chemical analysis
Mineralogical analysis
Magnetic separation
Magnetic susceptibility
Light/heavy mineral separation
Resistivity
Induced polarization
Calculate reserves

DISCUSSION. NASA's Office of Exploration is planning two orbiting missions to the Moon. The orbiting missions are referred to as the Lunar Scout Program and will provide a basis for lunar exploration. The instruments to be flown on these missions are an X-ray fluorescence spectrometer, a gamma ray spectrometer, an imaging spectrometer, and the High Resolution Stereo Camera. The spatial resolution of chemical data gathered will be on the order of 10's of kilometers or more. Mineralogical data will have a spatial resolution of 80 to 180 m. Analytical instruments for surface missions to the Moon have been proposed for the Artemis Lunar Lander. The data needs for ilmenite exploration should to be examined together with the proposed orbiter and lander instrument requirements if ilmenite is a resource of interest for lunar oxygen production.

MORPHOTECTONICS OF VENUS; V. J. Finn and V. R. Baker, Department of Geosciences, University of Arizona, Tucson, AZ 85721; A. Z. Dolginov, Lunar and Planetary Institute, 3600 Bay Area Boulevard, Houston, TX 77058.

➤ Venus topography can be mapped morphostructurally to reveal nested hierarchical patterns of quasi-circular upland/lowland complexes. These patterns are interpreted as surficial effects of hierarchically structured, long-acting mantle convection. Beta Regio, Alpha Regio, and Artemis illustrate this process of dynamical interaction between the deforming lithosphere and the convecting mantle. — end

For the oceanic portions of Earth's surface, the kinematic theory of plate tectonics [1,2] has proven to be immensely successful [3]. Problems with its ability to explain some continental areas [4] may be resolved through the secondary theory of plume tectonics [5]. The planet Venus, with its first order geophysical similarities to Earth [6], should logically provide an objective test of the theory. Indeed, several plate-tectonic attributes were ascribed to Venus [7,8] based on inclusive pre-Magellan data. Such prediction by theoretical constructs and testing against previously unknown phenomena are considered to be philosophical essentials for proper science [9,10]. Is the theory falsified because Magellan mission data clearly indicate the inability of plate-kinematic theory to explain Venusian tectonics [11,12]? Indeed, those few local phenomena so explicable has become major foci of study [13,14]. If we accept the view that a scientific theory must not be restricted to one case (Earth) but rather should generalize to multiple cases (Earth and Venus), then a more general model than the plate-tectonic one is clearly required.

The surface of Venus is dominated by large quasi-circular topographically elevated regions separated by lowland plains, many of which also are quasi-circular in planimetric shape. These features occur at various scales and morphological types, and are given the arbitrary names coronae, arachnoids, dome-like uplands, and plateaus. They are presently explained through various processes of mantle upwelling [15,16], downwelling [17,18], or combinations of these [19].

We proposed that the various quasi-circular upland/lowland complexes of Venus comprise hierarchical patterns of morphostructures produced by endogenetic processes [20]. The quasi-circular global-hierarchical morphostructures (QGMs) include even the large Lakshmi [21] and Artemis structures [22]. Nikishin et al. [23] also proposed such a genetic association, including Lakshmi [24], but did not map the hierarchical patterns. The latter are of great importance, since they seem to reflect directly the influence of convective pattern scales arising from various levels of the mantle [25]. We believe the convective scale hierarchy to be the characteristic of long-acting mantle convection in the stratified and random inhomogeneous mantles of the terrestrial planets [25]. Venus, unlike Earth, rather faithfully records the hierarchical patterns in its topography. This may be because the lack of an asthenosphere, possibly arising from a dehydrated upper mantle [26], permits rather direct stress transfer through the Venusian lithosphere. Blocks of lithosphere are deformed into patterns that mimic the underlying patterns of mantle flux. Examples of Venusian QGMs are discussed below.

Beta Regio, previously studied for its complex history of rifting and volcanism associated with Devana Chasma [27], can be shown topographically to consist of a 3000-km megastructure divided by radial fracture zones into interior megablocks. A hierarchical pattern of daughter quasi-circular morphostructures can be discerned at successively smaller scales, as follows: 1450, 1200, 900, 500, 380, and 200 km in diameter. These extend from inside the domal megastructure to the surrounding plains. Both positive (uplifted) and negative (depressed) morphostructures occur in regular associations.

## MORPHOTECTONICS OF VENUS: Finn V.J. et al.

Alpha Regio, with its local surficial complexes of compressional ridges and lateral shear/graben structures [28], has 1450-km diameter QGM core containing hierarchically nested smaller scale QGMs of 480-500, 380 and 200 km diameters. The QGM patterns are expressed in regional topography and are independent of the local structural detail of compressional ridges.

Artemis, conventionally interpreted as an unusually large corona [29], is one of 10 very large QGMs comprising a chain that manifests itself topographically as Aphrodite Terra. Artemis itself is a 2800-km QGM. Second-order QGMs, about 1400-1500 km in diameter, fill its interior plan. Lower order QGMs in the local hierarchy have scales of 1000, 570, and 300 km. The mapped pattern [22] is analogous to laboratory simulations of mantle plume-head interactions with the lithosphere [30]. However, the global Venusian QGM pattern is much more than the mere assembly of isolated plume-head-lithosphere interactions. Various QGMs probably comprise complex stages in an evolutionary sequence.

- References. [1] Morgan, W.J. (1968) *J. Geophys. Res.*, **73**, 1959-1972. [2] McKenzie, D.P. and Parker, R.L. (1967) *Nature*, **216**, 1276-1280. [3] Allègre, C. (1988) *The Behavior of the Earth*, Harvard Univ. Press. [4] Molnar, P. (1988) *Nature*, **335**, 131-137. [5] Hill, R.I., Campbell, I.H., Davies, G.F., and Griffiths, R.W. (1992) *Science*, **256**, 186-193. [6] Kaula, W.M. (1990) *Science*, **247**, 1191-1196. [7] Head, J.W. and Crumpler, L.S. (1987) *Science*, **238**, 1380-1385. [8] Head, J.W. (1990) *Geology*, **18**, 99-102. [9] Popper, K.R. (1959) *The Logic of Scientific Discovery*, Basic Books, N.Y. [10] Popper, K.R. (1963) *Conjectures and Refutations*, Routledge and Kegan Paul, London. [11] Solomon, S.C. et al. (1991) *Science*, **252**, 297-312. [12] Solomon, S.C. et al. (1992) *J. Geophys. Res.*, **97**, 13,199-13,255. [13] McKenzie, D.P. et al. (1992) *J. Geophys. Res.*, **97**, 13,533-13,544. [14] Sandwell, D.T. and Schubert, G. (1992) *Science*, **257**, 766-770. [15] Phillips, R.J., Grimm, R.E., and Malin, M.C. (1991) *Science*, **252**, 651-658. [16] Stofan, E.R. and Saunders, R.S. (1990) *Geophys. Res. Lett.*, **17**, 1377-1380. [17] Bindschadler, D.L. and Head, J.W. (1991) *J. Geophys. Res.*, **96**, 5889-5907. [18] Kiefer, W.S. and Hager, B.S. (1991) *J. Geophys. Res.*, **96**, 20,967-20,980. [19] Bindschadler, D.L., Schubert, G. and Kaula, W.M. (1992) *J. Geophys. Res.*, **97**, 13,495-13,532. [20] Finn, V.J., Baker, V.R., and Dolginov, A.Z. (1991) *EOS*, **72**(44), 189. [21] Finn, V.J., Baker, V.R., and Komatsu, G. (1991) LPSC XXII, 377-378. [22] Finn, V.J. and Baker, V.R. (1992) LPSC XXIII, 357-358. [23] Nikishin, A.M., Pronin, A.A., and Basilevsky, A.T. (1992) in *Venus Geology, Geochemistry, and Geophysics* (eds. V.L. Barsukov et al.), Univ. Arizona Press, 31-67. [24] Pronin, A.A. (1986) *Geotectonics*, **20**, 271-281. [25] Finn, V.J., Dolginov, A.Z., and Baker, V.R. (1993) Transmantle Flux Tectonics, LPSC XXIV (this volume). [26] McGill (1979) *Geophys. Res. Lett.*, **6**, 739-741. [27] Senske, D.A., Head, J.W., Schaber, G.G., and Stofan, E.R. (1992) *J. Geophys. Res.*, **97**, 13,395-13,420. [28] Bindschadler, D.L. et al. (1992) *J. Geophys. Res.*, **97**, 13,563-15,577. [29] Stofan, E.R. et al. (1992) *J. Geophys. Res.*, **97**, 13,347-13,378. [30] Griffiths, R.W. and Campbell, I.H. (1991) *J. Geophys. Res.*, **96**, 18,295-18,310.

TRANSMANTLE FLUX TECTONICS; V. J. Finn, Department of Geosciences, University of Arizona, Tucson, AZ 85721; A. Z. Dolginov, Lunar and Planetary Institute, 3600 Bay Area Boulevard, Houston, TX 77058; V. R. Baker, Department of Geosciences and Lunar and Planetary Laboratory, University of Arizona, Tucson, AZ 85721.

Venus, Earth, and Mars have surfaces that display topographic domes and depressions with quasi-circular planimetric shapes, relief of 0 to several km, and large spatial scales ( $10^2$  to  $10^4$  km). Our morphostructural mapping reveals hierarchical arrangements of these features. They are explained by a model of long-acting mantle convection, as a particular case of convection in a stratified and random inhomogeneous medium, which develops the form of a hierarchy of different convective pattern scales, each arising from different levels in the mantle. The hypothesis of transmantle flux tectonics parsimoniously explains a diversity of seemingly unrelated terrestrial planetary phenomena, including Earth megaplumes, global resurfacing epochs on Venus, and cyclic ocean formation and global climate change for Mars.

Mars is a one-plate planet dominated by the Tharsis uplift, which is interpreted as a hot spot structure [1,2]. Earth is a multiplate planet on which the present oceanic lithospheric surfaces are well explained by the kinematic theory of plate tectonics [3,4,5]. The latter is presumably coupled to a dynamical theory of mantle convection [6,7], the details of which remain controversial [8]. A variety of second-order tectonic forms on Earth are theoretically explained by hot spots [9,10] and by mantle plumes [11,12]. The latter may be of importance in explaining various continental phenomena [13,14], many of which are anomalous with regard to the prevailing plate-tectonic paradigm [15].

Contrary to what might be predicted from its first-order geophysical similarities to Earth [16], Venus does not show plate-tectonic features, except perhaps at local scales [17,18]. Instead, the Venusian surface is dominated by quasi-circular global-hierarchical morphostructures (QGMs) at scales of  $10^2$  to  $10^4$  km [19,20]. Similar structures, though often eroded and/or deformed by lateral tectonic movements, can be recognized on Earth [21], using the morphostructural analytical procedures developed in the former USSR [22,23].

We hypothesize that all these phenomena may be parsimoniously explained by a process of transmantle flux tectonics in which long-acting mantle convection generates stresses in blocks of planetary lithosphere to produce distinctive QGM patterns. Transmantle flux tectonics differs from plume tectonics [15] in that individual plumes are not considered in isolation. Rather, a wholly interactive process is envisioned in which various spatial and temporal scales of convection operate contemporaneously and hierarchically within other scales. This process of continual change by hierarchical convective cells affects the surface at varying temporal and spatial scales, and its effects are discernable through their relic geological manifestations, the QGM patterns.

Transmantle flux tectonics derives from thermal energy released by core processes [24] and by radioactivity in the planetary mantle. The resulting convective fluxes in a stratified and randomly inhomogeneous mantle [25] will assume the form of a temporal/spatial hierarchy of convective structures in which the characteristic sizes are closely connected to the sizes of the stratification and to the correlated scales of the random inhomogeneities. Such a pattern is well exemplified by solar convection, which divides into giant cells, supergranules, mesogranules, and granules [26]. This hierarchy of surface cells corresponds to convective cells of different sizes that originate at different depths below the surface. Our preliminary calculations show that similar patterns, operating over much longer temporal scales, probably occur within terrestrial planetary mantles.

For Earth, where geophysical data provide constraints [27], it seems that temperature builds up for long periods at the core-mantle boundary (CMB) because of inner core formation.

## TRANSMANTLE FLUX TECTONICS: Finn V.J. et al.

Release of thermal energy from the CMB induces a highly energetic convective mode that alternates with a less energetic one after the core-mantle thermal gradient decreases. The process seems to be cyclic through Earth history, but characteristics of each cycle vary with the evolved state of inner core formation, compositional change in the mantle, and other factors. Temperature and chemical inhomogeneities at the CMB [28,29] may explain certain persistent magnetic anomalies that correlate to QGMs. Many more QGMs correlate to mantle inhomogeneities identified through seismic tomography [30,31].

While the above hypothesis differs in essential respects from dynamical scenarios developed to explain Earth-related plate-tectonic [27] and plume-tectonic [15] scenarios, we believe that it deserves serious consideration. It does not contradict known data; it has a theoretical basis; and it explains QGM patterns as a general phenomenon of the terrestrial planets. Moreover, it also explains some interesting quasi-cyclic phenomena, including (1) the superplume events [32] and continental flood basalt episodes [33] of Earth, (2) possible phases of global resurfacing of Venus [34] related to episodic thermal behavior of the planet [35], and (3) possible episodic, massive thermal events on Mars related to periodic outburst flooding, temporary ponding of massive water volumes, global climate change, and glaciation [36]. We hope that our preliminary hypothesis can provide a step toward the goal of identifying a unified basis for understanding these diverse phenomena.

- References. [1] Carr, M.H. (1981) *The Surface of Mars*, Yale Univ. Press, New Haven. [2] Banerdt, W.B., Golombek, M.P., and Tanaka, K.L. (1992) in *Mars* (eds. B.M. Jakosky, H. Kieffer, and C.B. Snyder), Univ. Arizona Press, 249-297. [3] Morgan, W.J. (1968) *J. Geophys. Res.*, **73**, 1959-1972. [4] McKenzie, D.P. and Parker, R.L. (1967) *Nature*, **216**, 1276-1280. [5] LaPichon, X. (1968) *J. Geophys. Res.*, **73**, 3661-3697. [6] Olson, P. (1989) in *The Encyclopedia of Solid Earth Geophysics* (ed. D.E. James), Van Nostrand Reinhold, 788-802. [7] Schubert, G. (1992) *Ann. Rev. Fluid Mech.*, **24**, 359-394. [8] Davies, G.F. and Richards, M.A. (1992) *Jour. Geology*, **100**, 151-206. [9] Wilson, J.T. (1965) *Roy. Soc. Lon. Phil. Trans.*, **258**, 145-165. [10] Richards, M.A., Duncan, R.A., and Courtillot, V.E. (1989) *Science*, **246**, 103-107. [11] Morgan, W.J. (1971) *Nature*, **230**, 42-43. [12] Loper, D.E. (1991) *Tectonophysics*, **187**, 373-384. [13] Campbell, I.H. and Hill, R.I. (1988) *Earth Planet. Sci. Lett.*, **90**, 11-25. [14] Griffiths, R.W. and Campbell, I.H. (1991) *J. Geophys. Res.*, **96**, 18,295-18,310. [15] Hill, R.I., Campbell, I.H., Davies, G.F., and Griffiths, R.W. (1992) *Science*, **256**, 186-193. [16] Kaula, W.M. (1990) *Science*, **247**, 1191-1196. [17] McKenzie, D.P. et al. (1992) *J. Geophys. Res.*, **97**, 13,533-13,544. [18] Sandwell, D.T. and Schubert, G. (1992) *Science*, **257**, 766-770. [19] Finn, V.J., Baker, V.R., and Komatsu, G. (1991) LPSC XXII, 377-378. [20] Finn, V.J. and Baker, V.R. (1992) LPSC XXIII, 357-358. [21] Baker, V.R., Finn, V.J. and Komatsu, G. (in press) *Israel Jour. Earth Sci.* [22] Volchanskaya, I.K., Kochneva, N.T., and Sapozhnikova, Y.N. (1975) *Morphostructural Analysis for Geologic and Metallogenic Research*, Nauka, Moscow. [23] Finn, V.J. (1991) LPSC XXII, 375-376. [24] Gubbins, D. (1991) *Tectonophysics*, **187**, 385-395. [25] Romanowicz, B. (1991) *Ann. Rev. Earth Planet. Sci.*, **19**, 77-99. [26] Pecker, J.C. (1991) in *Solar Interior and Atmosphere* (ed. A.N. Cox, W.C. Livingston, and M.S. Matthews) Univ. Arizona Press, 1-30. [27] Lay, T., Ahrens, T.J., Olson, P., Smyth, J. and Loper, D. (1990) *Phys. Today*, **43**(10), 44-52. [28] Young, C.J. and Lay, T. (1987) *Ann. Rev. Earth Planet. Sci.*, **15**, 25-46. [29] Jeanloz, R. (1990) *Ann. Rev. Earth Planet. Sci.*, **18**, 357-386. [30] Dziewonski, A.M. and Woodhouse, J.H. (1987) *Science*, **236**, 37-48. [31] Tanimoto, T. (1990) *Geophys. Jour. Int.*, **101**, 327-336. [32] Larson, R.L. (1991) *Geology*, **19**, 963-966. [33] Rampino, M.R. and Stothers, R.B. (1988) *Science*, **241**, 663-668. [34] Schaber, G.G. et al. (1992) *J. Geophys. Res.*, **97**, 13,257-13,301. [35] Arkani-Hamed, J., Schaber, G.G., and Strom, R.G. (in press) *J. Geophys. Res.* [36] Baker, V.R. et al. (1991) *Nature*, **352**, 589-594.

**ASSIMILATION IN LUNAR BASALTS AND VOLCANIC GLASSES:  
IMPLICATIONS FOR A HETEROGENEOUS MANTLE SOURCE REGION.**

A.B. Finnila, P.C. Hess, and M.J. Rutherford. Department of Geological Sciences, Brown University Providence, RI 02912

**Introduction:** Several scientists have called on assimilation of anorthositic crustal material or KREEP compositions to explain various lunar lithologies (1-7). In order to address the practicality of such processes, we have outlined some techniques for calculating how much assimilation is possible in magma chambers and dikes based on thermal energy balances and simple fluid mechanical constraints. In a previous effort (8) we demonstrated that dissolution of plagioclase in an iron-free basalt was too slow to contaminate magmas, and that the energy cost of melting plagioclase-rich crustal material was prohibitive both in magma chambers and in dike conduits. In the present work we have extended this analysis to include dissolution rates in an orange glass composition and to quantitatively predict the maximum contamination possible due to assimilation of both lunar crustal material and KREEP (composition shown in Table I).

**Experimental Work:** Experiments to determine diffusion coefficients and saturation chemistry of anorthite in the basalt and picrite compositions shown in Table I were run at 1 atm at temperatures of 1290, 1340, and 1390 °C for durations between 20 and 240 minutes. The iron-free basalt powder was placed in a Pt crucible with a polished, annealed An<sub>100</sub> cylinder. The orange glass composition was placed in an anorthite glass capsule, wrapped in molybdenum foil and vacuum sealed in silica glass. The mafic glass in the charges was analyzed by microprobe in transects away from the melt/anorthite interface. Diffusion coefficients for Al<sub>2</sub>O<sub>3</sub> from both melt compositions were 10<sup>-8</sup> cm<sup>2</sup>/s at 1340°C and 10<sup>-7</sup> cm<sup>2</sup>/s at 1390°C. Alumina saturation values are shown in Figure 1.

**Potential Assimilation Values:** Assimilation can occur either by partial to complete melting followed by mixing, or by dissolution. The dissolution rates of anorthite are too slow to significantly affect magma compositions in either magma chambers or dikes. Even if a magma chamber is vigorously convecting and is hot enough to avoid having chilled margins, a 10 cm nonconvecting boundary layer (9) would slow assimilation to only 0.02 cm/year at 1390°C, or a total of 2 meters of wall rock in ten thousand years. Due to the effects of chilled margins and the high melting temperature of norites and troctolites, melting of lunar crustal material by the picritic glasses is not likely (10). Using crustal temperatures between 700 - 900 °C and magma temperatures between 1300 - 1500 °C, maximum estimates are on the order of 6% contamination by the wall rock, assuming convection inside the magma chamber suppresses the formation of chilled margins (11). This would only increase the alumina content by 0.9 wt.%. If the lower crust is composed primarily of anorthosite which has a melting temperature near 1500 °C, no melting can be expected. Assimilation of KREEP is more favorable due to its low melting temperature of 1050 °C. Estimates extend up to 26% contamination of a magma chamber bounded by KREEP wall rock, but only by assuming the highest temperatures considered both for the magma and the KREEP (1500°C and 900°C respectively). Using the method of (12), the amount of crustal assimilation possible by low titanium mare basalt melts during their transit to the surface in vertical dikes is not expected to exceed 7%. The ascent mechanism for the negatively buoyant high titanium glasses reaching the surface is not understood well enough to make quantitative predictions about assimilation values.

**Discussion:** Because the volcanic lunar glasses would need 25% to 28% assimilation of noritic and troctolitic crustal compositions respectively, to explain the 5 wt.% aluminum variation in the most pristine lunar volcanic glass record, it is clear that assimilation is not responsible for the chemical variation among these glasses. When assimilation does occur, it is usually accompanied by fractional crystallization which provides the energy required by releasing latent heat of fusion. While assimilating KREEP material is energetically feasible, only the Apollo 14 high aluminum basalts and some groups from Apollo 15 and 17 of the common mare types show KREEP signatures. While isolation or actual removal of a KREEP



## ASSIMILATION: Finnila A. B. et al.

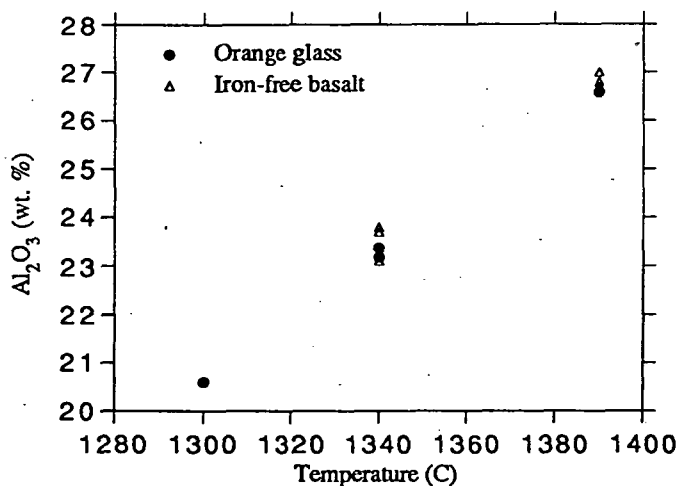
layer has been suggested to explain the selective contamination pattern (13), the thickening lunar lithosphere would prevent underplating of the crust after 3.9 b.y. Rising diapirs would tend to stall at the rheological trap at the base of the lithosphere. Even minor amounts of fractional crystallization would be apparent in the volcanic glass sample collection (14), the absence of which argues for little, if any, assimilation. Instead, as has been proposed for other reasons, most the chemical variation in the lunar basalts and volcanic glasses must be a result of distinct source regions in a heterogeneous lunar mantle.

The primary nature of these volcanic glasses has now been proposed by several lunar scientists. Hughes et al. (3) and others (15) argue for large-scale lateral and vertical heterogeneities in the lunar mantle based upon major and minor element chemistries. Hess (in this volume) argues for very deep source regions. This work shows how difficult it is to account for chemical variation using assimilative models and forces the conclusion that the lunar mantle must be extremely heterogeneous.

**Table I:**  
Experimental compositions

Oxide Wt %	KREEP	Iron-Free Basalt	Orange Glass
SiO <sub>2</sub>	55.3	44.4	38.57
TiO <sub>2</sub>	3.0	11.7	8.81
Al <sub>2</sub> O <sub>3</sub>	11.1	11.1	6.32
FeO	14.4	—	22.04
MgO	2.1	20.0	14.44
CaO	8.9	12.8	7.68
Na <sub>2</sub> O	1.1	—	0.36
K <sub>2</sub> O	2.1	—	0.09
Cr <sub>2</sub> O <sub>3</sub>	0.0	—	0.75

**Figure 1:**  
Alumina saturation  
chemistry



**References:** (1) Warren (1986) *Proc. 16th Lunar Planet. Sci. Conf., J. Geophys. Res.*, 91, D331-D343; (2) Neal, Taylor, and Lindstrom (1988) *Proc. 18th Lunar Planet. Sci.*, 139-153; (3) Hughes, Delano, and Schmitt (1990) *Proc. 20th Lunar Planet. Sci. Conf.*, 127-138; (4) Shervais, Taylor, Laul, Shih, and Nyquist (1985) *Proc. 16th Lunar Planet. Sci. Conf., J. Geophys. Res.*, 90, D3-D18; (5) Goodrich, Taylor, Keil, Kallemeyn, and Warren (1986) *Proc. 16th Lunar Planet. Sci. Conf., J. Geophys. Res.*, 91, D305-D318, 1986; (6) Dasch, Shih, Bansal, Wiesmann, and Nyquist (1987) *Geochim. Cosmochim. Acta*, 51, 3241-3254; (7) Shih, and Nyquist (1989) *Lunar Planet. Sci. XX*, 1002-1003; (8) Finnila, Hess, and Rutherford (1992) *Lunar Planet. Sci. XXIII*, 359-360; (9) Zhang et al., *Contrib. Mineral Petrol.*, 102, 492-513, 1989; (10) Marsh (1989) *Journal of Petrology*, 30, 479-530; (11) Huppert and Sparks (1988) *J. Fluid Mech.*, 188, 107-131; (12) Turcotte (1990) *Magma Transport and Storage*, ed. Ryan, 103-111; (13) Nyquist and Shih, (1992) *Geochim. Cosmochim. Acta*, 56, 2213-2234; (14) Longhi (1987) *Proc. 17th Lunar Planet. Sci. Conf.*, pp. E 349-E360; (15) Shearer, Papike, Galbreath, and Shimizu (1991) *Earth and Planet. Sci. Lett.*, 102, 134-147.

MEASURING AND DISTINGUISHING COMPOSITIONAL AND MATURITY  
PROPERTIES OF LUNAR SOILS BY REMOTE VIS-NIR SPECTROSCOPY; Erich M.  
Fischer and Carle M. Pieters; Dept. of Geol. Sci., Brown Univ., Providence, RI.

**Introduction:** Space weathering on the lunar surface affects the spectral/optical character of an exposed lunar soil in three ways: the reflectance is reduced, absorption band depths are reduced, and a red-sloped continuum is created and increased with exposure. As a result, the spectrum of a lunar soil is dependent upon both the degree of exposure at the lunar surface and the original composition. It is critical to the remote analysis of lunar soils to differentiate between the optical effects of maturity and the effects of composition. In the laboratory, it is possible to determine and consequently distinguish the degree of exposure, or soil maturity, as measured by parameters such as  $I_g/\text{FeO}$  (e.g., 1; mature defined as  $I_g/\text{FeO} \geq 60$ ), and the composition, as measured by various chemical and petrographical techniques. Lunar soils returned by the Apollo missions provide important ground truth for developing methods for remotely measuring the maturity and the concentration of Fe-bearing minerals in lunar soil. The ground truth spectral data analyzed here are from the John Adams lunar soil spectra collection. Soils collected from or near highland terrains are emphasized in the present discussion. The mineralogical makeup of mare soils results in behavior somewhat different from highland soils.

**Concentration of Fe-bearing minerals:** One method of estimating the concentration of Fe-bearing minerals in a soil (approximated by wt. % FeO) from reflectance spectra, is to measure the band depth of the one micron  $\text{Fe}^{2+}$  crystal field absorption. In the case of lunar soils, however, the one micron band is superimposed upon a distinct red-sloped continuum. Band depth is determined by measuring the depth after removing a continuum. This is normally accomplished by fitting a tangent to both shoulders of the one micron band. This method effectively normalizes the continuum created in the optical alteration process and allows the band depth of soils to be compared directly. However, as illustrated in Fig. 1, this method of estimating relative iron content is accurate only for mature lunar highland soils. Similar relations were noted by Charette et al. (2). That is, the measurement of band depth is an accurate measurement of Fe-bearing mineral concentration only for highland soils that have been exposed long enough at the lunar surface to have reached a steady state in terms of space weathering. For mature soils, the band depth is no longer changed by the optical alteration process, and is thus a function only of composition. Therefore, in order to obtain an accurate compositional measurement, it is necessary to be able to distinguish between mature and non-mature lunar soils.

**Determination of maturity:** As mentioned above, the albedo of lunar soils decreases and the red-sloped continuum increases with increasing maturity. Thus, both albedo and the slope of the straight line continuum scaled to albedo can be used to roughly distinguish between mature and non-mature highland soils. However, because the albedo of a highland soil is sensitive to the compositional properties of the soil (principally the abundance of plagioclase), the relationship between albedo and maturity is also dependent upon composition. The relationship between scaled slope and maturity is similarly offset along compositional lines.

A useful method of distinguishing between mature and non-mature highland soils incorporates a ratio between the reflectance at a wavelength outside of the one micron band and the reflectance at a point inside the band, for example  $0.76\mu\text{m}/0.99\mu\text{m}$ . The relationship between this ratio and maturity as measured by  $I_g/\text{FeO}$  is shown in Fig. 2. The  $0.76\mu\text{m}/0.99\mu\text{m}$  (or similar) ratio combines information concerning the steepness of the continuum and the depth of the one micron band. Although there is some scatter, the linear nature of the relationship in Fig. 2 for submature and immature soils ( $I_g/\text{FeO} < 60$ ) indicates that it may be possible to distinguish between different degrees of immaturity for highland soils. McEwen et al. (3) discuss the dating of Copernican craters using similar spectral properties. Thus, given the  $0.76\mu\text{m}/0.99\mu\text{m}$  (or related) ratio, in order to remotely differentiate between mature and non-mature highland soils a cutoff value can be defined below which soils can be considered mature. For the data in Fig. 2, it is estimated that soils with  $0.76\mu\text{m}/0.99\mu\text{m}$  less than approximately 0.90 can be considered mature. Although this method is not a perfectly accurate way of distinguishing between mature and non-mature highland soils, there appears to be little scatter introduced as a result of calculating the Fe-bearing concentration for soils determined to be mature using the  $0.76\mu\text{m}/0.99\mu\text{m}$  ratio rather than by determining maturity based upon  $I_g/\text{FeO}$ .

**Limited spectral data:** In the above case, the lunar sample spectra are of large enough spectral range and high enough spectral resolution for a straight line continuum to be fit tangent to both shoulders of the one micron band; thus the band depth was accurately measured. But consider the case in which the data do not include both sides of the one micron band. An example of this are the Galileo SSI data, which consist of seven channels extending from  $0.40\mu\text{m}$  to  $0.99\mu\text{m}$ . Because the true band depth cannot be measured with these type of data, several approximations for calculating the concentration of Fe-bearing minerals from this type of data have been utilized in the past. Examples of these include 1) measuring an approximate band depth after removing a straight line continuum extrapolated from the short wavelength side of the band, and 2) calculating an approximate band depth using a ratio of the reflectance on one side of the band to the reflectance near the center of the band

## COMPOSITION AND MATURITY OF LUNAR SOILS: Fischer E.M. and Pieters C.M.

(0.76 $\mu$ m/0.99 $\mu$ m in the case of the SSI data). Neither of these methods results in an accurate measurement of band depth and Fe-bearing mineral concentration among highland soils. The poor correlation between 0.76 $\mu$ m/0.99 $\mu$ m and wt.% FeO for mature highland soils is shown in Fig. 3. Indeed, it was shown in the previous section that 0.76 $\mu$ m/0.99 $\mu$ m is extremely sensitive to the slope of the alteration continuum. It is clear that data on both sides of the one micron band are required to define a slope that effectively normalizes the alteration continuum.

Although band depth of mature soils cannot be utilized in order to measure Fe-bearing mineral concentration for the SSI type of limited spectral data, reflectance can be employed as a useful substitute. Figure 4 illustrates the good correlation between the reflectance at 0.56  $\mu$ m and wt.% FeO for mature highland soils. This correlation exists because the albedo of a highland soil that has reached a steady state in terms of alteration products is controlled primarily by the amount of the two most common lunar minerals -- bright plagioclase (high Al<sub>2</sub>O<sub>3</sub>), and the more absorbing Fe-bearing mafic minerals (high FeO). Because the concentrations of plagioclase and Fe-bearing minerals are inversely correlated, the albedo of a mature highland soil provides an estimate of the amount of both the Fe-bearing mineral concentration, and the amount of plagioclase. The 0.76 $\mu$ m/0.99 $\mu$ m (or similar) ratio can be used to distinguish mature from non-mature highland soils for this limited spectral range data as well.

**Conclusion:** Comparison of lunar soil optical properties and the maturity index  $I_s/FeO$  indicates that 1) mature highland soils can be distinguished from non-mature highland soils using remote optical methods (such as 0.76 $\mu$ m/0.99 $\mu$ m), even with data of limited spectral range 2) the relative concentration of Fe-bearing minerals can be estimated remotely for mature highland soils using either the band depth or the visible albedo, and 3) the degree of immaturity of highland soils may be estimated remotely by methods such as 0.76 $\mu$ m/0.99 $\mu$ m. It is important to note, however, that although limited spectral data such as the SSI data provide extremely valuable information, the accuracy of the compositional and maturity interpretations from this type of data are limited to general properties. A larger spectral range (into the near-infrared) is necessary in order to fully analyze the lunar continuum and the character of the superimposed diagnostic absorption bands.

**Acknowledgements:** A portion of this material is based upon work supported under a National Science Foundation Graduate Fellowship (EMF). This research was also supported by NASA grant NAGW-28 (CMP).

**References:** 1) Morris R.V. (1978) *Proc. LPSC IX*, 2287; 2) Charette M.P. et al. (1976) *Proc. LSC VII*, 2579; 3) McEwen et al. (1993) These volumes.

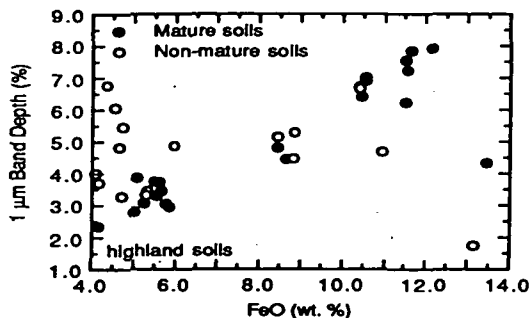


Figure 1: Iron concentration (wt.% FeO) for lunar highland soils versus band depth measured after continuum removal. Note the correlation for the mature soils (defined as soils with  $I_s/FeO \geq 60$ ; see 1).

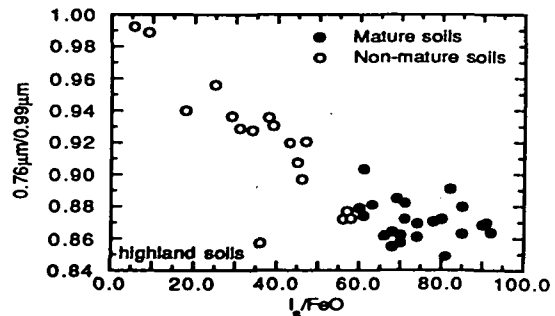


Figure 2: Maturity as measured by  $I_s/FeO$  versus 0.76 $\mu$ m/0.99 $\mu$ m for lunar highland soils. Mature soils are characterized by 0.76 $\mu$ m/0.99 $\mu$ m less than approximately 0.90. Note the linear trend for non-mature soils.

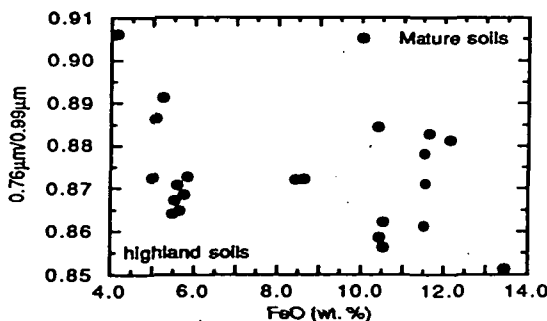


Figure 3: Iron concentration (wt.% FeO) versus 0.76 $\mu$ m/0.99 $\mu$ m for mature highland soils. Note the lack of correlation.

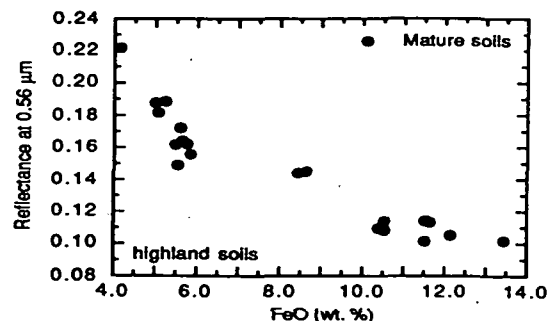


Figure 4: Iron concentration (wt.% FeO) versus reflectance at 0.56 $\mu$ m for mature highland soils.

DIAMOND THERMOLUMINESCENCE PROPERTIES OF DIFFERENT CHONDRITES  
*A.V. Fisenko, L.L. Kashkarov, L.F. Semjonova, and C.T. Pillinger*  
V.I. Vernadsky Institute of Geochemistry and Analytical Chemistry, Russian Academy of Sciences, Moscow, Russia (\*), Planetary Science Unit, Open University, Milton Keynes, U.K. (\*\*).

It has been found that TL glows of diamonds depend on a) the origin of diamonds and b) the chondrite metamorphism degree.

We have continued the investigation of thermoluminescence (TL) of diamonds [1] and here consider the results for diamonds from Murchison CM2, Krymka LL3.0, Kainsaz CO3 and Abee E4. For comparison have been analyzed also the diamonds synthesized by CVD-process (samples # 133, 159) and by detonation way from soot (DDS-B14-89). Before the TL measuring samples were annealed at  $\sim 350^{\circ}\text{C}$  during a few second and then irradiated by  $\gamma$ -rays of Cs-137 up to dose  $\sim 200$  krad. TL-measurements were performed in the air atmosphere on the standart equipment [2]. TL data for samples are shown on Figure. Here is also presented TL glow for some diamonds from [1]. The research of TL glow curves has shown following:

1) TL glow of Earth's and synthetic diamonds depend on their genesis. In equilibrated synthesis of diamonds { e.g., DN 3/2 } in TL glow curves there is only one clear high-temperature peak and in extremely unequilibrated synthesis { e.g., UDD } there is only low-temperature peak. In intermediated conditions synthesis of diamonds { film diamonds } in TL glow curves there are both high- and low-temperature peaks. The locations of peak maximum for all diamonds with the exception of DDS-B14-89 sample are observed in  $175\text{--}190^{\circ}\text{C}$  and  $290\text{--}310^{\circ}\text{C}$ . In the case of low intensity of peaks the position their maximum is displaced in more high-temperature range due to the influence of high-temperature TL glow. The correlation of TL glow peak intensities for film diamonds is not constant and probably this fact reflects the conditions of their synthesis.

TL glow curve for DDS-B14-89 also have only one peak, but with  $T(\text{max}) \sim 230^{\circ}\text{C}$ . Unfortunately the crystals structure of this sample is insufficiently studied. According to some data in this sample is perhaps lonsdaleite, but this question is being settled.

2) Presolar diamonds at least the diamonds of Efremovka and Kainsaz chondrites by TL glow are similar to UDD sample in the most degree. Therefore we suggest the presolar diamonds could be mainly formed as well as UDD in extremely unequilibrated process from carbon and/or carbonaceous compounds in gaseous phase. Perhaps this process has been proceeded in atmosphere of supernova by influence of shock waves [3].

The diamonds of Abee chondrite could be formed in the Solar system [4]. It is interesting TL glow for the Abee diamonds agrees with those for the DDS-B14-89 diamonds which contain probably lonsdaleite. The diamond crystals from Abee and DDS-B14-89 are sharply differentiated by sizes: for first the crystal sizes exceed  $0.1\text{ }\mu\text{m}$  [4], while for second they are essentially smaller ( $\sim 0.005\text{ }\mu\text{m}$ , Tatsy, pers. comm.). Nevertheless TL glows for these diamonds indicates on identical structure peculiarities of their crystals.

## DIAMOND THERMOLUMINESCENCE... Fisenko et al.

3) The intensity of TL glow for presolar diamonds in low-temperature range ( $\leq 250^{\circ}\text{C}$ ) and respectively the intensity of peak are increased relatively high - temperature TL glow for chondrites in follow sequence: Murchison, Krymka, Kainsaz, and Efremovka. The unequilibrium degree of these chondrite matters is also decreased in the same way. Perhaps the alteration of TL glow of diamonds is the result of the metamorphism process. We assume diamond crystals with most defective structure condition the persistent TL glow in large temperature intervals and that just these diamond crystals would be are lightly destroyed during metamorphism processes.

References: 1. A.V. Fisenko, L.L. Kashkarov, L.F. Semjonova, 1992, LPSC XXIII, p. 363. 2. L.L. Kashkarov et al., 1988, Meteoritika (in Russ), 47, p. 126. 3. A.V. Fisenko, A.B. Verchovsky, L.L. Semjonova, Yu. A. Shukolyukov, 1991, LPSC XXII, p. 387. 4. S.S. Russell et al., Science, 1992, v. 256, p. 206.

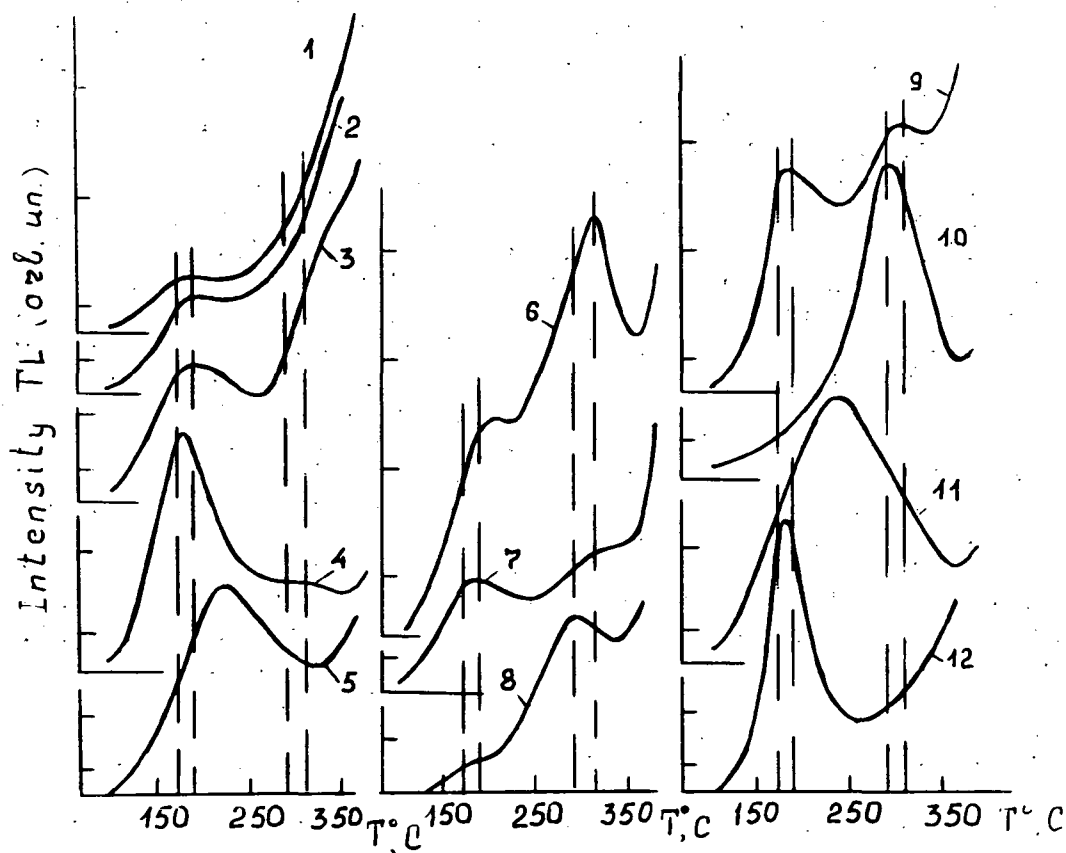


Figure. TL glow curves. 1,2,3,4, and 5 - the diamonds of Murchison, Krymka, Kainsaz, Efremovka, and Abee chondrites, respectively; 6,7,8, and 9 - the film diamonds (6,7 - sample # 133, 8 - sample # 159, 9 - sample # 21H); 10 - the diamonds (DN 3/2) from kimberlite pipe; 11 - the DDS-B14-89 diamonds; 12 - ultradis-persioned diamonds (UDD). 9,10, and 12 TL glow curves are taken from [1]. The dotted lines determine the intervals  $175-190^{\circ}\text{C}$  and  $290-310^{\circ}\text{C}$ .

THE UNUSUAL METALLIC PARTICLES IN KRYMKA LL3.0 CHONDRITE.  
A.V.Fisenko, A.Yu.Ljul, L.F.Semjonova, and K.I.Ignatenko.  
V.I.Vernadsky Institute of Geochemistry and Analytical Chemistry,  
Russian Academy of Sciences, Moscow, Russia.

It's shown the composition, structure peculiarities and possible scenario of formation of unusual metallic particles in Krymka LL3.0

In metal released from gently crushed after removal of chondrules of Krymka LL3.0 chondrite matter were detected two types unusual metallic particles. The first particles type mainly consist of coarse-grained ( $\geq 50 \mu\text{m}$ ) kamacite and fine-grained ( $\leq 10 \mu\text{m}$ ) Ni-high ( $\sim 53\text{wt.}\%$ ) taenite. These particles have well-defined zonal structure: kamacite is in central part of particles whereas taenite is in outside and the grains of taenite form the mantle around kamacite. In second particles type Fe,Ni-phase contains only fine-grained Ni-rich taenite. In both particle types there are also fine-grained phosphate, troilite and silicate. Both particle types have mostly rounded to subrounded form. For studying of detected particles some element contents in following fractions of Krymka metal were measured by INAA: a) in primordial metal with particle sizes  $\leq 75 \mu\text{m}$ ,  $140-250 \mu\text{m}$  and  $\geq 250 \mu\text{m}$ ; b) in two fractions of primordial metal  $\leq 75 \mu\text{m}$  partly etched by 1M HCl and 6M HCl; c) in the fragments of detected particles. These fragments were obtained from rounded and subrounded metallic particles ( $140-250 \mu\text{m}$ ) after treatment by 6M HCl twice. Every time from obtained mixture of particles were released particles with size  $\leq 75 \mu\text{m}$ . These particles are most probably fragments of mantle and of second type particles. The remaining particles ( $\geq 75 \mu\text{m}$ ) after etching and seiving are probably enriched by coarse-grained kamacite from zonal particles

The analysis obtained data have been shown following:

1) for the most purified from silicate the metal fractions is observed the negative linear correlation Co vs Ni (Fig.1a). The end-members of this dependence are the compositions of monomineral phases of taenite and of kamacite measured by microprobe in zonal and in second type particles. Therefore in most cases in Krymka metal  $\alpha$ - and  $\gamma$ -phases there are the equilibrated Ni-Co distribution. According to compositions of  $\alpha$ - and  $\gamma$ -phases and Fe,Ni-phase diagram this equilibration was reached at  $\sim 300^\circ\text{C}$

2) On plot Au vs Ni is observed the positive correlation (Fig.1b) but in this case the data are deviated from linear regression more than for dependence Co vs Ni.

3) On plot Ir vs Ni is absent any single correlation (Fig.1c). For metal ( $140-250 \mu\text{m}$ ) and for its fragments released after etching there is the positive correlation. But for metal  $\leq 75 \mu\text{m}$  and its fraction after etching can observed slightly negative correlation. It's to be noted on plot Au vs Ni the data for Ir-rich metal fractions are deviated from linear regression in the region of Au-low contents. Therefore, fine-grained fragments detected by us particles differ from fine-grained matrix metal at least by Ir and Au contents.

THE UNUSUAL METALLIC PARTICLES... *Fisenko A.V. et al.*

We assume the zonal particles were formed by accreted of fine-grained metal particles and Ir-rich submicron metallic grains [1] to surfaces of coarse-grained kamacite. The agglomeration of first two components only has led to formation of second type particles. Later on the short-lived heating event has led only to sintering of the agglomerates. It's to be noted the precursors of fine-grained particles were partially oxidised, perhaps during the formation of the unequilibrated chondrites matrix [2]. As a consequence Ni content in remaining part of metal is increased. Further increase of Ni content in this metal has occurred probably *in situ* during Ni diffusion between metallic particles and Ni interface diffusion at temperature right up to  $\sim 300^{\circ}\text{C}$ . All these processes have led to formation of Ni-rich mantle in zonal particles and the particles from fine-grained high-Ni taenite.

REFERENCES : 1 .E.Rambaldi, EPSL, 31, 1976, p.224. 2. H.Nagahara, GCA, 1984, v.48, p.2581.

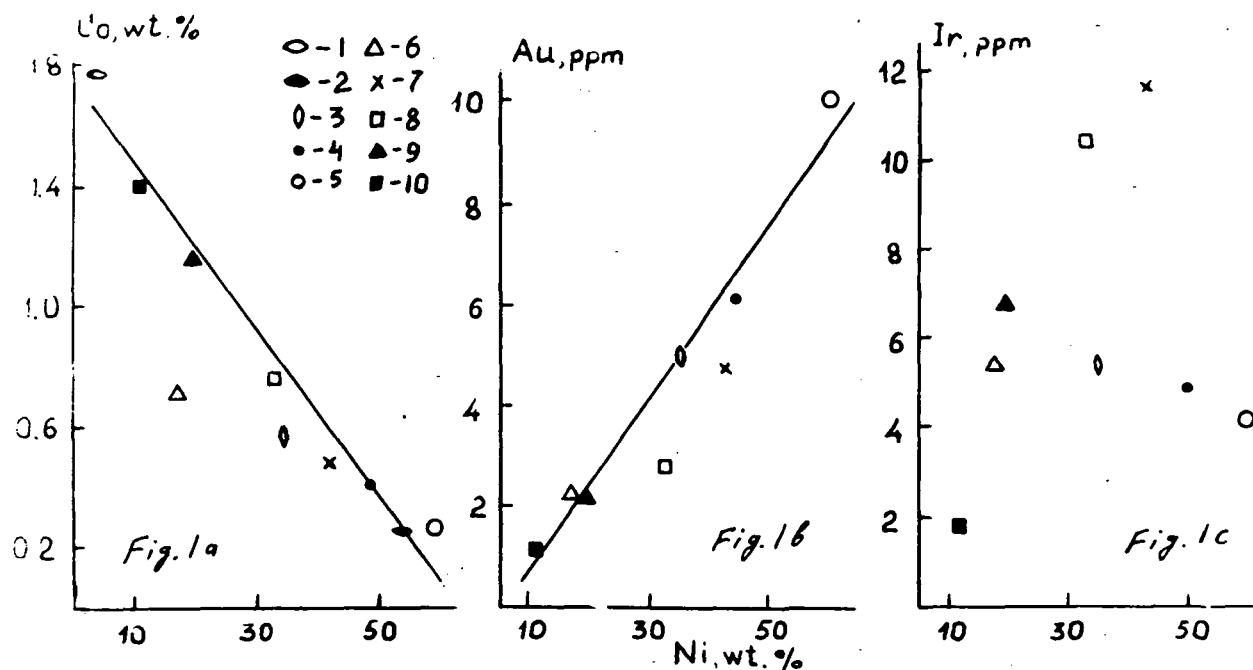


Figure. The correlation of Co, Au, Ir vs Ni in metal Krymka chondrite. 1,2 - kamacite and taenite in particles of 1 and 2 types; 3 - the primordial metal  $\leq 75 \mu\text{m}$ ; 4,5 - the primordial metal  $\leq 75 \mu\text{m}$  etched with 6M HCl and 1M HCl, respectively; 6 - rounded metal particles (140-250  $\mu\text{m}$ ); 7,8, and 9 - the fragments of rounded particles released after treatment with 6M HCl: 7,8 the fragments  $\leq 75 \mu\text{m}$  after first and second treatment, respectively; 9 - the remaining metal ( $\geq 75 \mu\text{m}$ ); 10 - the metal particles  $\geq 250 \mu\text{m}$

## ON POSSIBILITY OF DIAMOND FORMATIONS IN RADIATION PROCESS.

A.V.Fisenko, L.F.Semjonova, L.N.Bolsheva, T.V.Grachjova, A.B.Verchovsky, and Yu.A.Shukolyukov. V.I.Vernadsky Institute of Geochemistry and Analytical Chemistry, RAS, Moscow, Russia.

The possibility of diamonds formation in radiation process was checked studying of diamond contents in carburanium sample. The diamonds were not found and this result is discussed.

At present one of possible process of formation nanometer-size diamond crystals in some meteorites and Earth's diamonds (carbonado) is suggested the radiation mechanism: the formation of diamonds from carbonaceous matter in tracks of U fragment fissions and heavy fragmentation due to the action of energetic particles of cosmic rays [1,2,3]. So Bjakov et al. have carried out the calculations and shown that volume of formed diamonds in carbonaceous chondrites by radiation process correspond to discovered of diamonds volume in chondrites [1]. The discover by Ozima et al. [3] the unsupported fission Xe and Kr in carbonado supports the supposition that carbonado could be formed by radiation process [2].

The possibility of diamonds formation in radiation process can possible to check studying of diamond contents in Earth's samples enriched by uranium and carbon. For this the purpose we undertake the attempt to release the diamonds from carburanium. The contents of uranium oxide and carbon in carburanium respectively are equal to ~5 wt.% and ~65 wt.% [4] and because the carburanium is suitable the object for solution of this problem.

3.3g carburanium was used for experiment. The radiogenic age of sample is equal to  $(1.7 \pm 0.2) \cdot 10^9$  y. The quantity of diamonds which were could be formed in sample by radiation process can calculated using above mentioned parameters. The volume (V) of track high-temperature part from two fragments fission of one uranium atom we take equal to  $2 \cdot 10^{-15} \text{ cm}^3$  [1]. As note Bjakov et al. [1] in this volume P,T-conditions correspond to those at for-



ON POSSIBILITY OF DIAMOND ... *Fisenko et al.*

mation of diamonds. It was obtained the weight of diamonds in carburanium sample must to be ~150 mg. For isolation of diamonds from sample was used the stepped chemical treatment. This method is widely used for release of nanometer-sizes diamonds from chondrites and we also employ it for release diamonds from chondrites.

The carburanium sample was treated with mixture of  $\text{HNO}_3 + \text{HCl}$  at  $T \sim 20^\circ\text{C}$  and  $\sim 80^\circ\text{C}$ ; with  $\text{K}_2\text{Cr}_2\text{O}_7$  at  $T \sim 80^\circ\text{C}$ ; with  $\text{HClO}_4$  at  $\sim 140^\circ\text{C}$  and  $\sim 220^\circ\text{C}$ , and with 6N  $\text{HCl}$  at  $\sim 60^\circ\text{C}$ . The white color acid-resistant residue (~1mg) was obtained on finish dissolve stage of sample. This residue not contain of diamonds that follows from X-ray structure analysis. Thus, we have not detected the diamonds in carburanium sample whereas according to calculation this sample should contains about 150 mg of diamonds formed by radiation mechanism. Therefore used by us at calculation of diamond contents in sample the value  $V$  and supposition that the diamonds is formed in each track of fragment  $U$  fission are not real. It's probably the product  $V \cdot N$ , where  $N$  is quantity of fragments  $U$  fission forming the diamonds, must be at least 100 times less than used by us. This reference was made on the basis that we could be to release of diamonds, even if their contents in sample is about 1 mg. But in this case the calculated by Bjakov et al. [1] the quantity of diamonds formed by radiation mechanism in chondrites must also be decreased in ~ 100 times. It's led to inessential contribution of diamonds formed by radiation mechanism to total quantity of diamonds in chondrites.

Of course, it's impossible exclude that the efficiency of diamonds formation by radiation process in the carburanium can differ from those in another  $U$ -rich rocks and minerals and the more in meteorites. Because this study is would continue.

References: 1. V.M.Bjakov et al., 1990, Letters in Ap. J. (in Russ.), v.16, #11, p. 1051. 2. F.V.Kaminsky, 1987, Dokl.Akad. Nauk, USSR, v.294, p.439. 3. M.Ozima et al., 1991, Nature, v.351, p. 472. 4. M.V.Soboleva, I.A.Pudovkina, Minerals of uranium, Moscow, 1957.

5240-90  
ABS. ONLY

LPSC XXIV

485

N 9 40-142255

THE CARBON ISOTOPIC COMPOSITION OF NOVO UREI DIAMONDS. A.V.Fisenko, L.F. Semjenova, A.B. Verchovsky\*, S.S. Russell\* and C.T. Pillinger\*. Vernadsky Institute, Moscow, Russia, \*Dept. of Earth Sciences, The Open University, Milton Keynes, UK.

Herein we discuss the carbon isotopic composition of diamond grains isolated from the Novo Urei meteorite. A diamond separate was obtained from 2g of whole rock using the chemical treatments described in Fig. 1 aimed at obtaining very pure diamond. X-ray diffraction of the residue, which represented 5000 ppm of the parent mass, indicated only the presence of the desired mineral. The diamond crystals were 1 - 30  $\mu\text{m}$  in diameter, and some grains had a yellow colour. The chemical treatments were followed by a size separation to give a 1 - 10  $\mu\text{m}$  and a 5 - 30  $\mu\text{m}$  fraction, which were named DNU-1 and DNU-2 respectively.

Carbon isotope measurements were performed on a VG SIRA 24 dynamic mass spectrometer capable of measuring  $\delta^{13}\text{C}$  to  $\pm 0.05\text{‰}$  precision using a stepped combustion technique. The results from the two size separates are shown in figure 2. Both samples gave total carbon yields of  $\geq 95\%$ , demonstrating they consist of a pure carbonaceous phase. The major carbon release ( $\sim 90\%$  of the total carbon) was between 550°C to 650°C for DNU - 1 and 550 - 750°C for DNU2. The narrower combustion peak, and lower mean release temperature of DNU - 1 can be attributed to the smaller grain size in this sample, a factor known to affect combustion temperature (Wright and Pillinger 1989). The average  $\delta^{13}\text{C}$  values for carbon in the above mentioned temperature range was identical for both samples at  $-1.9 \pm 0.1\text{‰}$ . This value determines accurately an average carbon isotopic composition in Novo Urei diamonds. It differs by nearly 4‰ from the value defined by Vdovykin (1970) of  $-5.7\text{‰}$ . The difference could be ascribed to a systematic error in the isotope measurement in one of the laboratories, but a more probably explanation may be that the diamond separate used for this study is of higher purity than samples previously analysed.

The  $\delta^{13}\text{C}$  value is not constant for each temperature step of the experiment but varies by  $\sim 3\text{‰}$  over the main carbon release. This is a puzzle in view of the supposed purity of the residue. The fluctuations may be due to the fractionation of the carbon isotopes during the crystallisation of the diamond. Alternatively, the diamond may be from a mixture of isotopically distinguishable sources. Further investigations are in progress to resolve this problem.

According to the data of Grady *et al.* (1985), the average  $\delta^{13}\text{C}$  value of bulk Novo Urei is  $-2.8\text{‰}$  over the temperature range of 500 - 700°C, 0.9% lighter than the measurements made by us. The similarity in isotopic composition suggests that the diamond is genetically linked to the rest of the carbonaceous material in the meteorite, although clearly carbon measurements of samples produced at each stage of the acid dissolution will be necessary to determine whether the carbonaceous phases are isotopically distinguishable.

# THE CARBON ISOTOPIC COMPOSITION...A.V. Fisenko *et al.*

Acknowledgements - We are grateful to SERC for a research visitors grant and to Prof. Y.A. Shukolyukov for his interest and support.

## References:

1. Grady M.M., *Geochim. Cosmochim. Acta*, 1985, **49**, 903 - 915.
2. Vdovykin G.P. *Space Sciences Rev.* **10**, 483 (1970).
3. Wright I.P. and Pillinger C.T. *U.S. Geological Survey Bull.* 1890, **9** (1989).

Figure 1

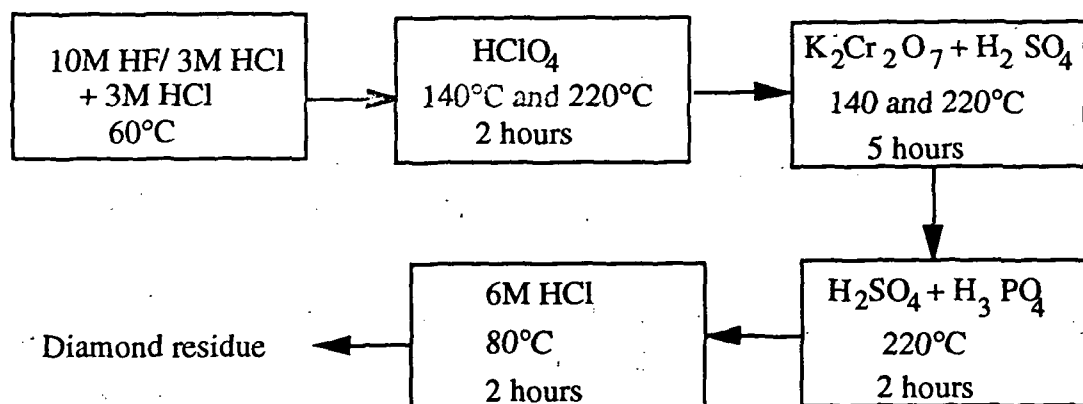
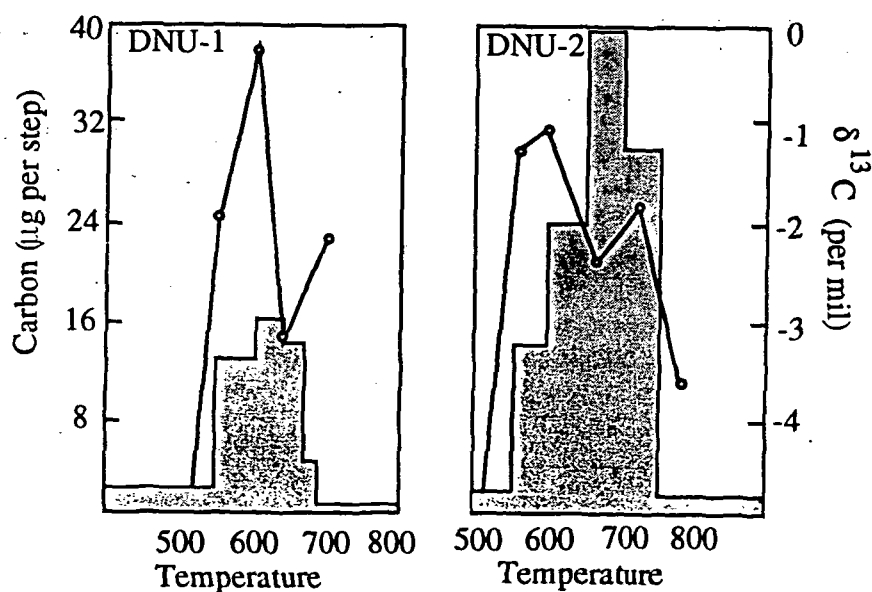


Figure 2



THE FRACTIONATION OF NOBLE GASES IN DIAMONDS OF CV3 EFREMOVKA CHONDRITE .A.V.Fisenko, A.B.Verchovsky, L.F.Semjonova, and Yu.A.Shukolyukov .V.I.Vernadsky Institute of Geochemistry and Analytical Chemistry, Russian Academy of Sciences, Moscow, Russia.

It have been shown that in diamonds of Efremovka CV3 the noble gases with normal isotopic compositions are fractionated in different degree while the correlation of isotopic anomalous components is nearly constant.

Here we consider the some data for noble gases in DE-4 sample of Efremovka chondrite. In contrast to DE-2 sample [1] the DE-4 was treated except conc.HClO<sub>4</sub>, 220°C in addition with mixture of conc. H<sub>2</sub>SO<sub>4</sub>+H<sub>3</sub>PO<sub>4</sub> (1:1), 220°C, twice. Noble gases analysis have been performed at Germany in Max Plank Institute fur Chemie. Noble gases were released by oxidation of sample at stepped heating from 420°C to 810°C and by pyrolysis at 580, 590 and 680°C.

The gases released at stepped oxidation of DE-4 sample have variable elemental composition (Fig.1) as well as for DE-2. The variation of coefficient fractionation value ( F ) at oxidation until 460°C are caused perhaps by gases diffusion at pyrolyses ( 590°C ), which has preceded of sample oxidation. At oxidation higher 460°C the quantity released gas considerable exceed those at pyrolysis. Therefore the alteration of value F at T ≥ 460°C most probably is due to that diamond grains have the gases with various elemental composition. As can be seen from Fig.1 the gases with more fractionated elemental composition are released at high temperatures, i.e. from more thermostable to oxidation the diamond grains. The value F for Ne and He is changed in less degree than for Ar. Perhaps the Ne and He origin in diamond grains is another than Xe, Kr and Ar or they are more dissolved in fine diamond grains as compared with another gases [2,3].

For reseach of possibility influence of various gases fractionation degree on scatter data on plot 86-Kr/82-Kr vs 136-Xe/130-Xe (Fig.2a) we have reduced all gas-fractions to the same value F. In calculating it has been suggested:

a) noble gases in diamonds are the mixture of solar composition gas with formed in supernova isotopic anomalous components (Xe-H + Xe-L + Kr-H) . The two-component model is the simplified variant of origin gases explanation in diamonds. It is confirmed, in particular, by linear dependence 134-Xe/130Xe vs 136-Xe/130-Xe sinse detected today the deviation of data from this dependence can be explained, for example, with few sources of Xe-H;

b) only the gas of solar composition was fractionated in different degree. This follows from insignificant variation of value ratio 86-Kr-H/136-Xe-H for all gas fractions: its mean value is equal to 0.12±0.02. As can seen from Fig.2b for corrected data there is almost linear functional dependence. Hence, the fractionation in different degree only of gases with normal isotopic composition is really the reason of data scatter on plot 2a.

FRACTIONATION OF NOBLE GASES.... *Fisenko A.V. et.al.*

On the basis of analysis of noble gases in Efremovka chondrite diamonds can be suggested:

a) the diamond grains were present or were formed in environment containing the noble gases with normal isotopic composition. Not all Xe, Kr and Ar atoms in this environment were ionized during ionization processes and because the correlation of implanted ions of these elements in diamond grains have depended on ionization gas degree. According to our data either this ionization degree was not constant or exist two groups of diamond grains. In last case these grain groups differ by fractionation degree of gas with normal isotopic composition and thermostable to oxidation [4].

b) the formed in supernova shells the nuclei of (Xe-H, Xe-L, Kr-H) were not completely neutralized until its capture with diamond grains. All these conditions could be realized at formation of diamonds in supernova atmosphere by influence of shock waves.

References: 1. A.V. Fisenko, A.B. Verchosky, L.F. Semjonova, Yu. A. Shukolyukov, 1991, LPSC, XXII, p. 387. 2. D.D. Clayton, 1989, Ap.J., v. 340, p. 613. 3. I. Matsuda, K. Fukunaga, K. Ito, 1991, G.C.A., v. 55 p. 2011. 4. A.V. Fisenko et al., 1992, Dokl. Akad. Nauk (in pres).

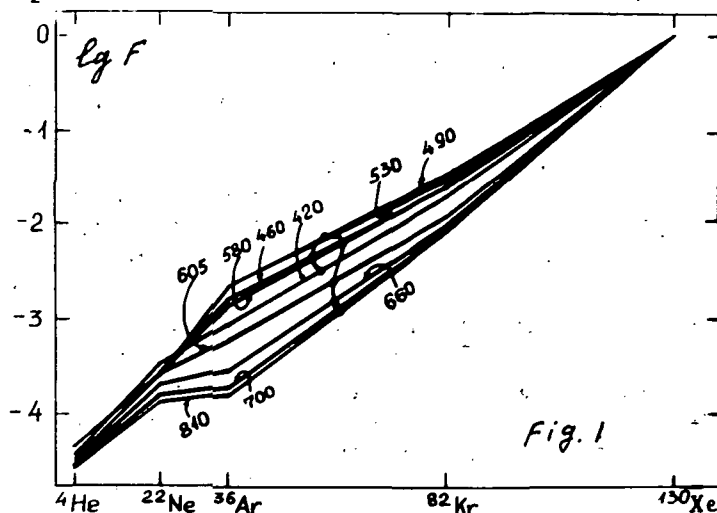
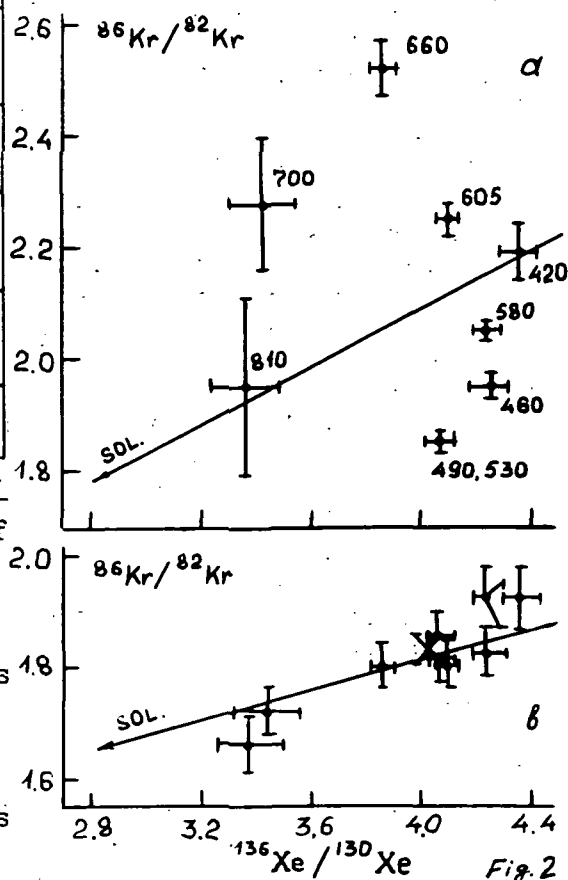


Figure captions. Fig.1. The variations of elemental composition of gases released at various oxidation temperatures of Efremovka diamonds.  $F = (A/130\text{-Xe})_{\text{samp.}} / (A/130\text{-Xe})_{\text{sol.}}$ ,  $A = 4\text{-He}, 22\text{-Ne}, 36\text{-Ar}, \text{and } 82\text{-Kr}$ . Numbers denote the combustion temperature.

Fig.2. The scatter of data on (a) is due to most probably different fractionation degree of gases with normal isotopic composition. The reducing all gas-fractions to the same fractionation coefficient  $F$  led to linear dependence  $86\text{-Kr}/82\text{-Kr}$  vs  $136\text{-Xe}/130\text{-Xe}$  (b).



N 94-13237

## CRONSTEDTITE AND IRON SULFIDE MINERALOGY OF CM-TYPE CARBONACEOUS CHONDRITES FROM CRYOGENIC MÖSSBAUER SPECTRA

Duncan S. Fisher and Roger G. Burns, Department of Earth, Atmospheric and Planetary Sciences, Massachusetts Institute of Technology, Cambridge, MA 02139. P. 2

**Overview.** Determinations of oxidation states and the crystal chemistry of iron-bearing minerals in CM meteorites by Mössbauer spectroscopy are complicated by thermally-induced electron hopping in cronstedtite and by ill-defined contributions from the hydrous iron sulphide phase believed to be tochilinite. Mössbauer spectral measurements at 30 K of several cronstedtite and tochilinite specimens have enabled modal proportions of these minerals, as well as  $\text{Fe}^{3+}/\text{Fe}^{2+}$  ratios, to be determined quantitatively for a suite of CM-type carbonaceous chondrites that included Murchison, Murray, Cold Bokkeveld, ALH 83100 and LEW 90500.

**Background.** The poorly-characterized phases (PCP) in CM carbonaceous chondrites consist of an intimate mixture of interstratified minerals comprising a hydrous iron sulfide believed to be related to tochilinite [1,2] and phyllosilicates dominated by the opaque, mixed-valence  $\text{Fe}^{2+}$ - $\text{Fe}^{3+}$  serpentine mineral cronstedtite [3,4]. Although the matrix PCP's of several CM meteorites have been studied extensively, determinations of the chemical compositions, crystal chemistry and mineral proportions continue to pose acute difficulties, despite applications of high resolution electron microbeam techniques [3-5]. In a reconnaissance Mössbauer spectral study of suites of carbonaceous chondrites [6], we demonstrated that the oxidation states and modal mineralogy of iron could be determined quantitatively in the CI, CV, CO and CK meteorite-types. However, Mössbauer spectra of CM meteorites displayed unusual temperature variations that complicated analyses of iron in these carbonaceous chondrites. To better understand the crystal chemistry of iron in CM meteorites, detailed measurements of several terrestrial cronstedtite and tochilinite specimens were made, results of which are summarized here.

**Tochilinite.** The hydrous iron sulfide phase in CM meteorites having a formula approximating  $\text{Fe}_{1.3}\text{Ni}_{0.1}\text{SO}_{1.4}$  [3-5] was identified as Fe-rich tochilinite [2]. The crystal structure of terrestrial tochilinite contains coherently stratified mackinawite ( $\text{FeS}$ ) and brucite [ $\text{Mg}(\text{OH})_2$ ] sheets [1]. The mackinawite structure contains  $\text{Fe}^{2+}$  ions tetrahedrally coordinated to sulfur in layers of edge-shared [ $\text{FeS}_4$ ] tetrahedra, while cations bound to  $\text{OH}^-$  ions occur in octahedral sites in brucite. In CM meteorites, some  $\text{Fe}^{2+}$  (+  $\text{Ni}^{2+}$ ) ions may also occur in the brucite layers of the tochilinite phase.

Mössbauer spectral measurements made on three terrestrial tochilinites at room temperature, 30 K and 4.2 K yielded a single peak, or closely-spaced doublet, located near  $0.50$ - $0.55 \text{ mm s}^{-1}$  at 30 K. The isomer shift ( $\delta \approx 0.55 \text{ mm s}^{-1}$ ) of this peak differs from that of  $\text{Fe}^{2+}$  ions in sphalerite and wurtzite ( $\delta \approx 0.65$ - $0.70 \text{ mm s}^{-1}$ ), the structures of which contain corner-shared [ $\text{ZnS}_4$ ] tetrahedra.

**Cronstedtite.** Chemical compositions of jet-black platelets of cronstedtite indicate that in this serpentine-group mineral formulated as  $[(\text{Fe}^{2+}, \text{Fe}^{3+}, \text{Mg})_3(\text{Si}, \text{Fe}^{3+})_2\text{O}_5(\text{OH})_4]$ , ferric iron is present in comparable amounts in both tetrahedral and octahedral coordinations. In octahedral sites located between layers of corner-shared  $[(\text{Si}, \text{Fe}^{3+})\text{O}_4]$  tetrahedra, each iron cation is coordinated to  $\text{OH}^-$  ions and non-bridging oxygens of the linked tetrahedra. The *cis*- $[\text{FeO}_2(\text{OH})_4]$  octahedra share edges with adjacent octahedra to form sheets parallel to the layers of corner-shared tetrahedra [7]. The close proximity of  $\text{Fe}^{2+}$  and  $\text{Fe}^{3+}$  ions in the octahedral sites causes thermally-induced electron delocalization to occur in cronstedtite so that this phyllosilicate is opaque and electrically conducting [8]. As a result, octahedral  $\text{Fe}^{2+}$  and  $\text{Fe}^{3+}$  ions cannot be distinguished in room-temperature Mössbauer spectra. When the temperature is lowered, however, electrons become localized on the  $\text{Fe}^{2+}$  ions so that ferrous and ferric cations become distinguishable in the Mössbauer spectra. At very low temperatures ( $<10 \text{ K}$ ), the onset of magnetic ordering occurs yielding very complex Mössbauer spectrum profiles. By measuring Mössbauer spectra of cronstedtites at 30 K, complications from electron delocalization and magnetic ordering are minimal so that site occupancies and relative proportions of  $\text{Fe}^{2+}$  and  $\text{Fe}^{3+}$  ions in cronstedtites and CM meteorites may be determined accurately.

## MINERALOGY OF CM-TYPE METEORITES: Fisher, D. S. and Burns, R. G.

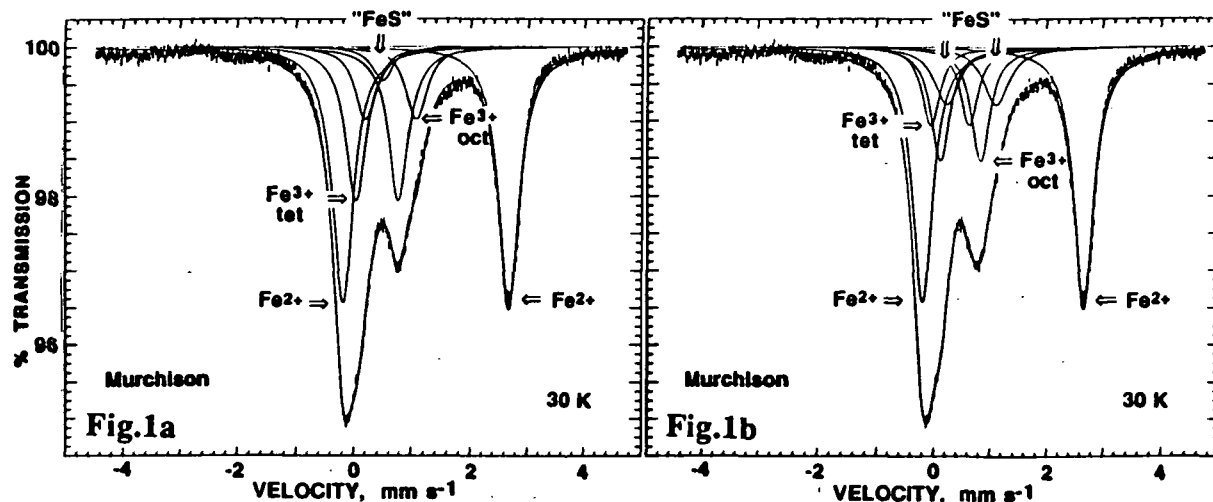
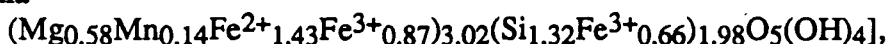


Figure 1. Mössbauer spectrum of the Murchison meteorite at 30 K. (a) 7 peak fit; (b) 8 peak fit.

Five cronstedtites assembled for this investigations included a  $\text{Mg}^{2+}$ -rich cronstedtite from Příbram, Czechoslovakia that also was used in the crystal structure determination [7]. The chemical composition determined by our microprobe and Mössbauer spectral analyses yielded the chemical formula



which closely resembles formulae of cronstedtites identified in carbonaceous chondrites [3]. Curve-fitting of the 30 K Mössbauer spectra of the cronstedtites to three doublets provided peak locations for octahedral  $\text{Fe}^{2+}$ , octahedral  $\text{Fe}^{3+}$  and tetrahedral  $\text{Fe}^{3+}$  ions. These three-doublet fits guided the curve-fitting models for resolving the Mössbauer spectra of CM-type meteorites.

**Carbonaceous Chondrites.** Specimens of ALH 83100, LEW 90500, Murchison, Murray and Cold Bokkeveld were used in the Mössbauer spectral measurements. In the course of the investigation, LEW 90500 was confirmed to be a CM-type carbonaceous chondrite. Two different curve-fitting models were used to resolve the Mössbauer spectrum profile of each meteorite. They are shown for the 30 K spectrum of Murchison in figure 1. The first approach incorporated a seven-peak fit (fig. 1a), which consisted of one  $\text{Fe}^{2+}$  doublet and two  $\text{Fe}^{3+}$  doublets (to accommodate the iron cations in cronstedtite) and a single peak at  $\approx 0.55 \text{ mm s}^{-1}$  (to represent tochilinite). However, the isomer shift ( $\delta \approx 0.45$  and  $0.65 \text{ mm s}^{-1}$ ) and quadrupole splitting ( $\Delta \approx 0.75$  and  $0.85 \text{ mm s}^{-1}$ ) parameters of the doublets assigned to ferric iron in all of the CM meteorite spectra, as well as their relative intensities, failed to match the parameters for octahedral  $\text{Fe}^{3+}$  ( $\delta \approx 0.50 \text{ mm s}^{-1}$ ;  $\Delta \approx 0.65 \text{ mm s}^{-1}$ ) and tetrahedral  $\text{Fe}^{3+}$  ( $\delta \approx 0.30 \text{ mm s}^{-1}$ ;  $\Delta \approx 0.50 \text{ mm s}^{-1}$ ) ions in the cronstedtites.

In the second approach, eight peaks were fitted to the spectra of the CM meteorites (fig. 1b). The ferric peak intensities and Mössbauer parameters for the tetrahedral  $\text{Fe}^{3+}$  ( $\delta \approx 0.30 \text{ mm s}^{-1}$ ;  $\Delta \approx 0.60 \text{ mm s}^{-1}$ ) and octahedral  $\text{Fe}^{3+}$  ( $\delta \approx 0.50 \text{ mm s}^{-1}$ ;  $\Delta \approx 0.70 \text{ mm s}^{-1}$ ) ions in the meteorites now more closely matched those for the cronstedtites. The fourth doublet attributed to iron chemically bound to sulfur yielded isomer shift parameters ( $\delta \approx 0.68 \text{ mm s}^{-1}$ ) comparable to those measured for tetrahedrally coordinated  $\text{Fe}^{2+}$  ions in iron-bearing sphalerites and wurtzites. The coordination environment of iron in the  $[\text{FeS}_4]$  tetrahedra of the "FeS" phase of CM meteorites apparently differs from that of iron in terrestrial tochilinites, perhaps reflecting different distortions of the  $[\text{FeS}_4]$  tetrahedra and next-nearest neighbor interactions with surrounding cations.

**References.** [1] N.I. Organova, V.A.Drits & A.L.Dmitrik, *Amer. Min.*, 59, 190 (1974); [2] M.E.Zolensky & I.D.R.Mackinnon, *Amer. Min.*, 71, 1201 (1986); [3] K.Tomeoka & P.R.Buseck, *Geochim. Cosmochim. Acta*, 49, 2149 (1985); [4] H.Y.McSween Jr, *Geochim. Cosmochim. Acta*, 51, 2469 (1987); [5] D.J.Barber, A. Bourdillon & L.A.Freeman, *Nature*, 305, 295 (1983); [6] D.S.Fisher & R.G.Burns, *Lunar Planet. Sci.*, XXII, 389 (1991); [7] C.A.Geiger, D.L.Henry, S.W.Bailey & J.J.Maj, *Clays Clay Min.*, 31, 97 (1983); [8] J.M.D.Coe, A.Moukarika & C.M.McDonagh, *Solid State Comm.*, 41, 797 (1982); [9] We thank M.E.Zolensky for providing the tochilinite specimens. The research is supported by NASA grants NAGW-2049 & 2220.

N 9 4 6 P 2 2 5 8

**NMR Spectroscopy of Experimentally Shocked Single Crystal Quartz: A Reexamination of the NMR Shock Barometer.** P. S. Fiske (Department of Geology, Stanford University, Stanford, CA 94305-2115, fisko@pangea.stanford.edu) A. J. Gratz and W. J. Nellis (Institute of Geophysics and Planetary Physics, Lawrence Livermore National Laboratories, L-413, Livermore, CA 94550)

Cygan and others [1,2] report a broadening of the  $^{29}\text{Si}$  NMR peak for synthetic quartz powders with increasing shock pressure which they propose as a shock wave barometer for natural systems. We expand on these results by studying single crystal quartz shocked to 12 and 33 GPa using the 6.5 m two-stage light-gas gun at Lawrence Livermore National Laboratories. Our NMR results differ substantially from those of Cygan and others and suggest that the proposed shock wave barometer may require refinement. The difference in results between this study and that of Cygan and others is most likely caused by different starting materials (single crystal vs. powder) and different shock loading histories. NMR results from single crystal studies may be more applicable to natural systems.

### Peak Position and Line Shape Studies

The spectrum for the 12 GPa sample consists of a single asymmetric peak with an intensity maximum at -107.3 ppm (relative to TMS) and a line width (FWHM=full width at half max) of 0.8 ppm. XRD shows the sample to consist solely of quartz, although its XRD peaks are broader than those for unshocked quartz. Transmission electron microscope investigations of samples shocked to similar pressures suggest that this sample contains less than 1% of an amorphous material. The shock wave barometer of Cygan and others predicts a two-fold increase in the line width at these pressures but the peak width we observe is statistically unchanged from that observed for unshocked quartz. These results suggest that any shock wave barometer using NMR peak widths may not be able to resolve differences below about 10 GPa, the region that most needs a good shock wave barometer for natural systems, because obtaining  $^{29}\text{Si}$  NMR spectra for quartz with peaks narrower than about 1 ppm is experimentally difficult.

The spectrum for the 33 GPa sample (figure 1) consists of a symmetric peak centered at -109.6 ppm (FWHM 5 ppm) and a high frequency broad peak centered at -106.1 ppm (FWHM 20 ppm). XRD peaks are about twice as broad as for the 12 GPa sample. Results from previous shock experiments suggest that this sample contains about 30% of an amorphous material [3]. In their highest pressure samples (22 GPa), Cygan and others found a single NMR peak with a four-fold increase in line width but no shift in peak position.

The shift in the narrow peak to lower frequency is consistent with a  $3^\circ$  increase in the mean Si-O-Si bond angle [4]. The broad peak is similar to those obtained for  $\text{SiO}_2$  glass quenched at high pressure (6 GPa, peak position: -108.5 ppm, FWHM: 13 ppm [5]) and  $\text{SiO}_2$  glass statically densified at room T to 18 GPa (peak position: -105.6 ppm, FWHM: 17 ppm [6]), suggesting that the amorphous material is substantially denser than 1 bar  $\text{SiO}_2$  fusion glass, with a reduction in the mean Si-O-Si bond angle of 5 to  $8^\circ$ .

### Relaxation Time Studies

Spectra were acquired using a range of delay times between excitation pulses (up to 3000 sec), and intensities were calibrated using a fully relaxed standard. Despite the use of small tip angles, the spectra with the longest delays represent only 40% of the total expected intensity due to the long relaxation time of this material.

Unlike the results of Cygan and others [7], we observe the amorphous material (found only in the 33 GPa sample) to have a longer relaxation time than the crystalline phase. This suggests that if the mechanism for relaxation is the presence of paramagnetic centers associated with structural defects [2] the amorphous material has a lower concentration of these defects than



## NMR OF SHOCKED SINGLE XTL QUARTZ: Fiske, P. S., et. al.

the crystalline material. Signal intensity measurements show that the total amount of signal obtained at each delay time is independent of shock pressure. This suggests that if paramagnetic defects are controlling relaxation in these samples, their overall concentration is not a strong function of shock pressure. However, we caution that the mechanism of relaxation in these materials is uncertain.

Finally, in order to obtain fully relaxed, quantifiable NMR spectra we are carrying out a series of experiments using single crystal amethyst. The paramagnetic Fe in amethyst has been shown to greatly reduce the relaxation time in single crystal quartz thus allowing for quicker signal acquisition and a higher ratio of signal to noise [8].

### Conclusions

The differences in these results compared to the work of Cygan and others suggest that shock experiments on compact targets produce different end products than experiments on powders, and may be more comparable to naturally shocked materials.

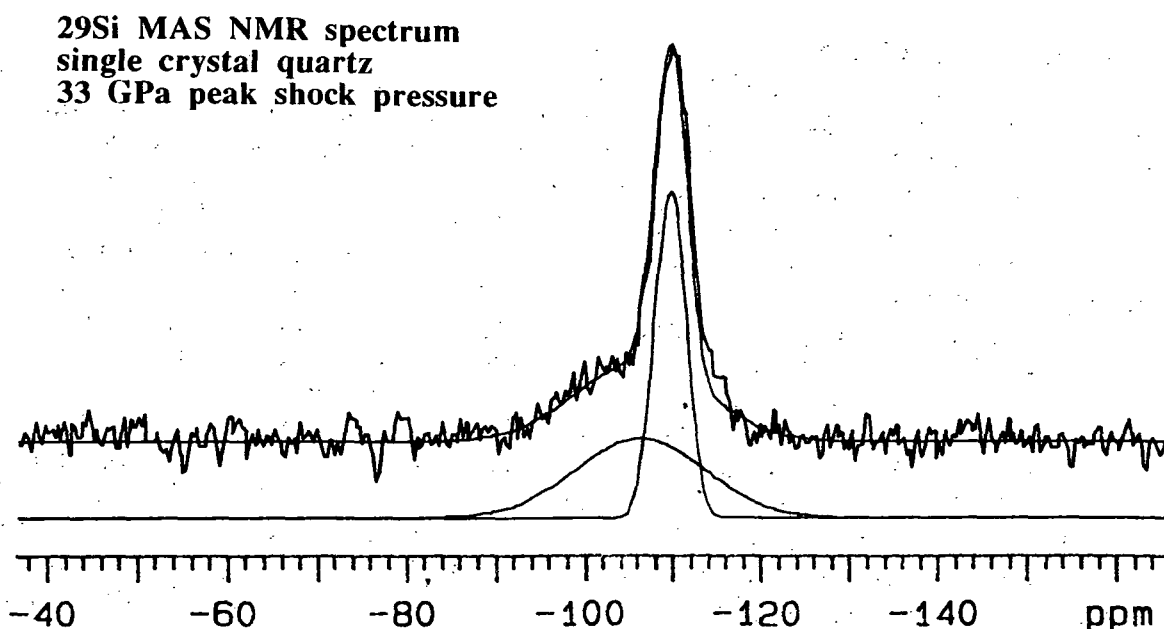


**Figure 1**

- [1] Cygan, R. T., Boslough, M. B., and Kirkpatrick, R. J. (1990) Proc. 20th Lunar Planet. Sci. Conf., 451-457.
- [2] Cygan, R. T., Boslough, M. B., and Kirkpatrick, R. J. (1992) Proc. 22nd Lunar Planet. Sci. Conf., 127-136.
- [3] Gratz, A. J., and others (1992) Phys. Chem. Min. 19, 267-288.
- [4] Oestrike, R. and others (1987) Geochim. Cosmochim. Acta 51, 2199-2209.
- [5] Xue and others (1991) Am. Min. 76, 8-26.
- [6] Stebbins, J. F. (1991) pers. comm.
- [7] Boslough, M. B., Cygan, R. T., and Assink, R. A. (1992) EOS, Trans. Amer. Geophys. Union Fall Meeting 1992, 594.
- [8] Spearing, D. R., and Stebbins, J. F. (1989) Am. Min. 74, 956-959.

**ORGANIC MATTER ON THE EARLY SURFACE OF MARS: AN ASSESSMENT  
OF THE CONTRIBUTION BY INTERPLANETARY DUST; G. J. Flynn, Dept. of  
Physics, SUNY Plattsburgh, Plattsburgh, NY 12901**

Calculations by Anders (1) and Chyba et al. (2) have recently revived interest in the suggestion that organic compounds important to the development of life were delivered to the primitive surface of the Earth by comets, asteroids or the interplanetary dust derived from these two sources. Anders (1) has shown that the major post-accretion contribution of extraterrestrial organic matter to the surface of the Earth is from interplanetary dust. Since Mars is a much more favorable site for the gentle deceleration of interplanetary dust particles (3) than is Earth, model calculations show that biologically important organic compounds are likely to have been delivered to the early surface of Mars by the interplanetary dust in an order-of-magnitude higher surface density than onto the early Earth.

Anders (1), in a detailed study of the accretion of organic-bearing extraterrestrial matter in various size ranges onto the Earth, concluded that, since organic matter cannot survive the high temperatures generated by large impacts, the major organic contribution comes from interplanetary dust particles (IDPs) small enough to survive atmospheric entry without reaching high temperatures. Mars is a much more favorable site for the deceleration of interplanetary dust than is Earth because of its lower surface gravity, giving rise to a lower average atmospheric entry velocity for IDPs, and its greater atmospheric scale height, resulting in a longer deceleration interval. In the terrestrial case, most IDPs larger than 100  $\mu\text{m}$  in diameter melt or vaporize on atmospheric entry. Flynn and McKay (3) calculate that the fraction of 100  $\mu\text{m}$  diameter IDPs surviving atmospheric entry at Earth is comparable to that for 700  $\mu\text{m}$  diameter IDPs at Mars. The survival of these larger IDPs during atmospheric entry at Mars is particularly important to the rate of delivery of organic matter to the surface of Mars because the size-frequency distribution of IDPs in space is sharply peaked (see Figure 1), with 90% of the incident mass being between  $10^{-7}$  and  $10^{-2}$  grams (4), or about 60 to 2700 microns in diameter. Thus most IDPs near the peak of the mass-frequency distribution are destroyed on Earth atmospheric entry, but a large fraction of these particles survive Mars atmospheric entry without melting.

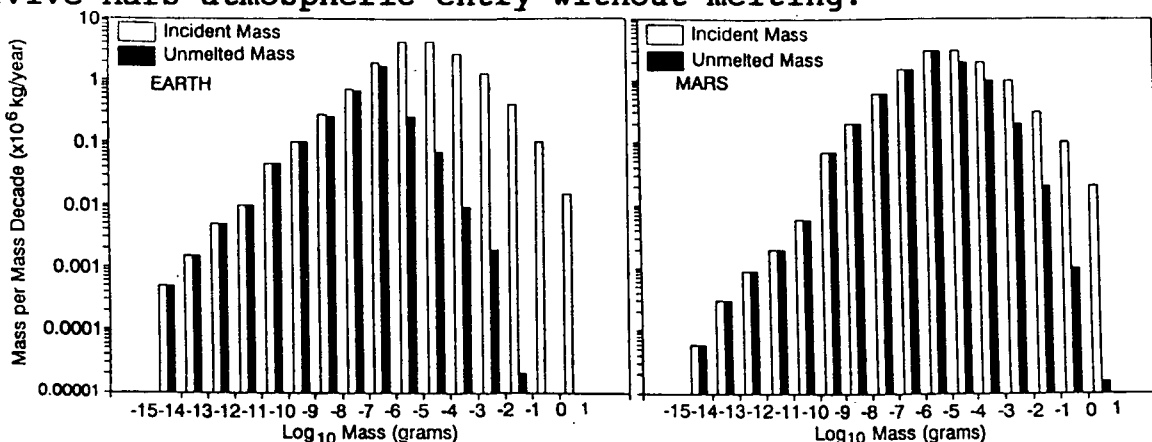


**Figure 1: The micrometeorite size frequency distribution measured at Earth (6) and calculated for Mars are shown along with the mass surviving atmospheric entry without melting. The mass of micrometeorites arriving at Earth is greater than at Mars the mass surviving atmospheric entry is greater at Mars than at Earth because Mars is more favorable for micrometeorite deceleration.**

Using the method described by Flynn and McKay (3) the size frequency distribution, and the atmospheric entry velocity distribution of IDPs at Mars have been calculated. The entry velocity distribution, coupled with the atmospheric entry heating model developed by Whipple (4) and extended by Fraundorf (5) was used to calculate the fraction of particles in each mass decade which survives atmospheric entry without melting (ie., those not heated above 1600 K). The incident mass and surviving mass in each mass decade are shown for both Earth and Mars in Figure 1. Integrating the areas under the incident and surviving mass frequency distributions gives a surviving mass of  $8.6 \times 10^6$  kg/year out of an incident mass of  $12.0 \times 10^6$  kg/year. This accretion rate for unmelted meteoritic material at Mars is almost three times the  $3.2 \times 10^6$  kg/year of meteoritic material which Anders (1) calculates to survive Earth atmospheric entry without melting, even though the incident mass at Earth is higher, approximately  $16.0 \times 10^6$  kg/year (6). Because Mars is a smaller planet than Earth, the surface density of meteoritic material which accretes onto Mars without melting is more than an order-of-magnitude higher than onto the Earth.

The average carbon content of IDPs  $\leq 20 \mu\text{m}$  in diameter collected from the Earth's stratosphere is reported to be about 10% (7, 8), with one particle having 49% carbon (7). Organic molecules, including polycyclic aromatic hydrocarbons (9), have been detected in IDPs. However, the small masses of individual IDPs ( $\sim 10^{-8}$  grams) has, thus far, precluded quantitative determination of the fraction of the carbon which is present in organic molecules. The carbon content of IDPs  $> 100 \mu\text{m}$  in diameter is not well established because most of these particles melt or vaporize on Earth atmospheric entry, but Yates et al. (10) have extracted carbon with an isotopic composition consistent with that of the macromolecular organic material in carbonaceous chondrite meteorites from melted meteoritic spherules  $> 100 \mu\text{m}$  in diameter recovered from Antarctic ices.

Repeating the entry heating calculations for IDPs not heated above 900 K, the pyrolysis temperature estimated by Anders (1) and Chyba et al. (2), indicates that approximately  $2.4 \times 10^6$  kg/year of interplanetary dust accretes onto Mars with its carbonaceous matter unaltered. Assuming, following Anders (1) the average carbon content of IDPs is 10% then the present accretion rate of unaltered (not heated above 900 K) meteoritic carbon onto the surface of Mars is about  $2.4 \times 10^5$  kg/year.

Anders (1) has suggested that the accretion of IDPs may have provided biologically important organic compounds to the primitive surface of the Earth. The more favorable conditions for low temperature accretion of interplanetary dust onto the surface of Mars provided even higher concentrations of these pre-biotic organic compounds to the early surface of Mars. This source of organic matter coupled with the possibility of more favorable climatic conditions on the early Mars (11) may have implications for the biochemical evolution of the planet.

#### REFERENCES

- 1) Anders, E. (1989) *Nature*, 342, 255-257.
- 2) Chyba, C. F. et al. (1990) *Science*, 249, 366-373.
- 3) Flynn, G. J. and McKay, D. S. (1990) *J. Geophys. Res.*, 95, B9, 14497-14509.
- 4) Whipple, F. L. (1950) *Proc. Nat. Acad. of Sci. USA*, 36, 687-695.
- 5) Fraundorf, P. (1980) *Geophys. Res. Lett.*, 10, 765-768.
- 6) Hughes, D. W. (1978) in *Cosmic Dust*, Wiley, New York, 123-185.
- 7) Blanford, G. E. et al. (1988) *Meteoritics*, 23, 113-121.
- 8) Schramm, L. S. et al. (1989) *Meteoritics*, 24, 99-112.
- 9) Allamandola, L. J. et al. (1987) *Science*, 237, 56-59.
- 10) Yates, P. D. et al. (1991) *Meteoritics*, 26, 412.
- 11) McKay, C. P. and Stoker, C. R. (1989) *Rev. Geophys.*, 27, 189-214.

**TRACE ELEMENT CONTENT OF CHONDRITIC COSMIC DUST: VOLATILE ENRICHMENTS, THERMAL ALTERATIONS, AND THE POSSIBILITY OF CONTAMINATION;** G.J. Flynn,<sup>1</sup> S.R. Sutton,<sup>2</sup> and S. Bajt,<sup>2</sup> 1) Dept. of Physics, SUNY Plattsburgh, Plattsburgh NY 12901, 2) Dept. of Geophysical Sciences, University of Chicago, Chicago IL 60637. *P, 2*

We have measured trace element abundances in 51 chondritic Interplanetary Dust Particles (IDPs) by Synchrotron X-Ray Fluorescence (SXRF). The data allow us to determine an average composition of chondritic IDPs and to examine the questions of volatile loss during the heating pulse experienced on atmospheric entry and possible element addition due to contamination during atmospheric entry, stratospheric residence and curation.

The average composition of the 51 chondritic IDPs shows a volatile enrichment for all elements with atomic numbers from Cr to Br having nebula condensation temperatures lower than 1277K (Cr) (see Figure 1). The volatiles Cu, Ga, Ge, Se, and Zn are enriched by factors of 2 to 3 over the CI meteorite abundances of these elements. Bromine is more dramatically enriched, to 30xCI. This volatile element enrichment pattern is roughly complimentary to the depletion pattern of the CM2 meteorites relative to CI, suggesting the chondritic IDPs are a new chemical type of chondritic material, more volatile rich than any known meteorite.

However, the trace element contents measured for individual IDPs may not reflect pre-atmospheric compositions because of volatile loss during atmospheric entry heating or contamination during atmospheric entry, stratospheric residence or curation. The trace element data, coupled with mineralogy, provide clues to the degree of thermal alteration and contamination.

We have shown that Zn, of all the elements measured by SXRF, is most severely depleted by heating on atmospheric entry (1). These Zn depletions correlate with the production of magnetite rims (2,3), attributed to entry heating (4), indicating that the 15 particles with low Zn ( $Zn/Fe \leq 0.2 \times CI$ ) are the most severely heated of the 51 chondritic particles studied. These low-Zn particles may also have lost other volatile elements due to heating. Removing these 15 thermally altered particles from the data set is likely to result in an average composition which more accurately reflects the pre-atmospheric composition of the IDPs. The set 36 particles lacking a Zn depletion has slightly higher abundances of the volatile elements than the set of 51 particles, but the enrichment pattern is not changed significantly (see Figure 2). The differences between the average compositions of the 15 low-Zn and the 36 normal Zn particles are more dramatic.

If the low-Zn particles are assumed to have had the same average pre-atmospheric composition as the less heated IDPs, then differences in composition between the two sets would indicate the relative volatilities of the elements in the IDPs. Comparing the two data sets, we find Zn is most extremely depleted element ( $Zn_{low-Zn}/Zn_{norm} = 0.025$ ), followed by Br ( $Br_{low-Zn}/Br_{norm} = 0.31$ ) and Ge ( $Ge_{low-Zn}/Ge_{norm} = 0.39$ ), while all other measured elements from Cr to Br agree to  $\pm 20\%$  in the low-Zn and normal-Zn averages.

We have previously identified a subset of the chondritic IDPs which shows no enrichment in volatile content above CI (5). These 9 IDPs, identified by their roughly chondritic Se and Cu contents (as described in Ref. 5), have an average composition falling between CI and CM2 meteorites for all elements from Cr to Se, but show a large Br enrichment (see "+" pattern in Figure 1). This high Br content in particles not enriched in the other volatiles suggests the mechanism for Br enrichment is different

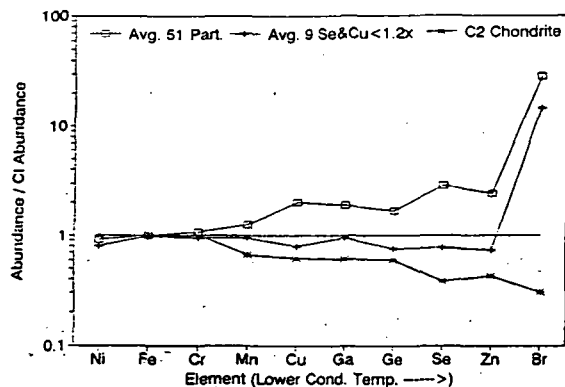


**Figure 1: Fe and CI normalized average trace element contents of 51 chondritic IDPs, 9 chondritic IDPs with Se/Fe and Cu/Fe <1.2xCI, and C2 chondrites.**

from the mechanism which resulted in the enrichment of the other volatile elements. This decoupling of the Br enrichment from the other volatile enrichments is consistent with, but does not prove, the conclusion of Rietmeijer (6) that some of the Br in the IDPs is a contaminant acquired during stratospheric residence. We note, however, that the average Br content of these 9 particles (15xCI) is only half that of the 51 particle set. If this represents the average level of Br contamination, then the chondritic IDPs would still be Br rich relative to CI.

Jessberger et al. (7) have suggested that all the volatiles above the CI level are contaminants acquired during atmospheric entry. If their hypothesis is correct, then the level of contamination they propose is 1 to 2 times CI for Cu, Zn, Ga, Ge, and Se, and a large fraction of the IDPs must receive significant contamination since 18 of the 36 chondritic IDPs not altered by entry heating have Zn contents above CI. The existence of volatile depleted particles, such as the igneous (8) and low-Zn (2) particles, indicates that contamination does not overprint the distinctive trace element abundance patterns of these unusual particles, strongly constraining the degree of contamination.

However, normal chondritic IDPs provide the best evidence against substantial trace element contamination. The measured Zn content of the 36 normal chondritic IDPs is 3.2xCI, suggesting an average contamination of 2.2xCI if the Jessberger et al. (7) hypothesis that the pre-atmospheric volatile content is CI is correct. This contamination should also affect those IDPs which were significantly heated, and thus Zn depleted, on atmospheric entry. Their proposed level of contamination is sufficient to return these Zn depleted particles to chondritic Zn abundances. Thus TEM analyses of IDPs with chondritic Zn should yield a significant number of cases exhibiting mineralogical indications (such as magnetite rims) of entry heating. No such particles have been identified among the 14 IDPs examined by SXRF and TEM in attempts to test the Zn entry heating thermometer (2,3). The good correlation between chondritic Zn content and the absence of mineralogical indicators of entry heating suggests that any Zn contamination of IDPs during atmospheric entry, stratospheric residence, or curation is substantially below the level suggested by Jessberger et al. (7) or that particles which are depleted in Zn on atmospheric entry are subsequently immune to contamination.

#### REFERENCES

- 1) Flynn G.J. and Sutton S.R. (1992) *Proc. Lun. Plan. Sci. Conf.*, V.22, 171-184.
- 2) Flynn G.J. et al. (1992) *Lunar Planet. Sci. XXXIII*, 375-376.
- 3) Klock, W. et al. (1992) *Meteoritics*, 27, 243-244.
- 4) Keller, L. P. et al. (1992) *Lunar Planet. Sci. XXXIII*, 675-676.
- 5) Flynn G. J. and Sutton S. R. (1992) *Lunar Planet. Sci. XXXIII*, 373-374.
- 6) Rietmeijer F. J. M. (1992) *Meteoritics*, 27, 280-281.
- 7) Jessberger, E. K. et al. (1992) *Earth Planet. Sci. Lett.*, 112, 91-99.
- 8) Sutton S. R. et al. (1990) *Lunar Planet. Sci. XXI*, 1225-1226.

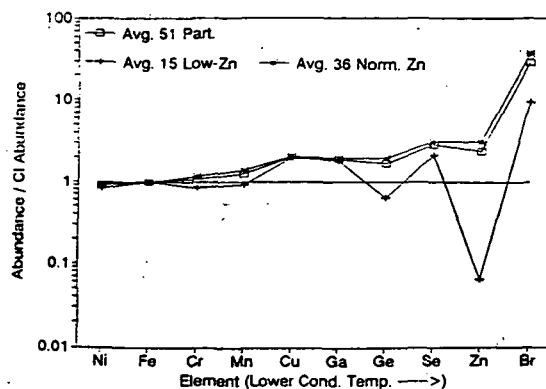


**Figure 2: Fe and CI normalized average trace element contents of 51 chondritic IDPs, 15 low-Zn chondritic IDPs, and the 36 chondritic IDPs with normal Zn.**

**DEPLETIONS OF SULFUR AND/OR ZINC IN IDPs: ARE THEY RELIABLE INDICATORS OF ATMOSPHERIC ENTRY HEATING?**; G.J. Flynn<sup>1</sup>, S.R. Sutton<sup>2</sup>, S. Bajt<sup>2</sup>, W. Klöck<sup>3</sup>, K.L. Thomas<sup>4</sup>, and L. P. Keller<sup>5</sup>, 1) Dept. of Physics, SUNY Plattsburgh, Plattsburgh NY 12901, 2) Dept. of Geophysical Sciences, The University of Chicago, Chicago IL 60637, 3) Institut für Planetologie, Westfälische Wilhelms-Universität, Münster, Germany, 4) Lockheed, 2400 NASA Rd. 1, Houston TX 77058, 5) NASA Johnson Space Center, Houston TX 77058.

The degree of heating of IDPs on Earth atmospheric entry is important in distinguishing cometary particles from main-belt asteroidal particles (1). Depletions in the volatile elements S and Zn have been proposed as chemical indicators of significant entry heating. The S and Zn contents of cosmic dust particles have been correlated with physical indicators of atmospheric entry heating, such as the production of magnetite and the loss of solar wind implanted He. The results indicate that the Zn content of IDPs is a useful indicator of entry heating, but the S content seems to be less useful.

The identification and analysis of interplanetary dust particles (IDPs) from cometary and asteroidal parent bodies is useful in defining the physical, chemical, and mineralogical properties of those parent bodies to support the design of future spacecraft to explore the comets and the asteroids. Flynn (1) has shown the peak temperature reached by an IDP on atmospheric entry is an important criterion in distinguishing main-belt asteroidal from cometary IDPs. Most cometary IDPs are heated to more extreme temperatures than main-belt asteroidal IDPs of the same size and density because of the larger relative velocities of cometary particles at Earth encounter. Mineralogical alterations, such as the production of magnetite and the alteration of olivine and hydrated silicates, the annealing of radiation damage tracks, and the loss of volatile elements all provide indications of the peak temperature reached by an individual IDP on atmospheric entry. Of these indicators, only chemical abundances allow non-destructive screening of IDPs into highly heated and not significantly heated subsets.

Fraundorf et al. (2) have demonstrated that S is lost from IDPs during laboratory pulse heating experiments, and they suggested that S depletions could serve as an indicator of substantial atmospheric entry heating. Flynn (1) suggested that Zn depletions could serve the same role, and Flynn and Sutton (3) have identified a subset of the chondritic IDPs which exhibit substantial Zn depletions. Flynn et al. (4), Thomas et al. (5), Klöck et al. (6) and Keller et al. (7) have demonstrated that Zn depletions correlate well with mineralogical evidence and He inferences of substantial atmospheric entry heating. However, since S is a major element its abundance is easier to measure than that of the trace element Zn, thus the usefulness to S content as an indicator of entry heating needs to be assessed.

Quantitative Synchrotron X-Ray Fluorescence determinations of both the S and Zn abundances on more than 30 chondritic IDPs have revealed 14 instances where the proposed S and Zn indicators differ in their heating predictions, see Table 1. One possibility is that both S and Zn contents are reliable indicators of entry heating, but one element is lost at a significantly higher temperature than the other. Although both condense at nearly the same temperature, loss temperatures depend on the specific mineralogical sites of Zn and S in IDPs (eg. pure sphalerite

## DEPLETIONS OF SULFUR AND/OR ZINC IN IDPs: G. J. Flynn et al.

Table 1: S and Zn Contents and Heating Indicators for IDPs

Particle	JSC Class.	CI Normalized S/Fe	Zn/Fe	Other Heating Observations
W7017D6	C?	0.2	0.9	
W7027E7	C?	0.2	1.7	
W7031*A5	C	1.0	0.07	low He <sup>4</sup> in related frag*
L2005C38	C	0.8	<0.02	Magnetite Rim & low He <sup>4</sup> in rel. frags*
L2005K6	C	0.3	1.8	
L2005M2	C	0.6	<0.006	
L200501	C	1.6	0.05	
L200504	C	0.8	<0.01	
L2005P2	C	0.9	<0.01	Magnetite Rim
L2005R1	C	1.4	0.3	Magnetite Rim
L2005R7	C	0.2	2.5	No Magnetite Rim
L2005U5	C?	3.2	0.02	No Magnetite Rim
L2006A18	C?	1.8	0.01	
L2006B8	C	1.3	0.1	Magnetite Rim

\* W7031\*A5 and L2005C38 are cluster particles. Nier and Schlutter (8) found low He in the related fragments W7031\*A4 and L2005C25. L2005C13 (also related to L2005C38) has a partial magnetite rim.

(ZnS) melts at 1020°C while troilite (FeS) melts at 1193°C). If the indicators monitor different temperatures, then all particles depleted in the element with the higher loss temperature would also be depleted in the one of lower temperature. This is not the case. Four IDPs (W7017D6, W7027E7, L2005K6 and L2005R7) show large S depletions but CI Zn levels, while ten (W7031\*A5, L2005C38, L2005M2, L200501, L200504, L2005P2, L2005R1, L2005U5, L2006A18, and L2006B8) show large Zn depletions but CI S levels.

Transmission Electron Microscope (TEM) observations of magnetite rims and structural alterations of olivine and hydrated silicates as well as mass spectrometric measurements of low contents of solar wind implanted He<sup>4</sup> provide independent evidence of the degree of heating experienced by IDPs. Six of the 14 particles have been examined in ultramicrotome thin section in the TEM subsequent to the SXRF chemical abundance determinations. Three particles (L2005P2, L2005R1, and L2006B8) exhibited magnetite rims, consistent with the heating inferred from the observed Zn depletions but inconsistent with the low heating inferred from their chondritic S abundances. L2005R7 showed no magnetite rim, consistent with the low heating inferred from its high Zn abundance but inconsistent with the significant heating inferred from its low S abundance. L2005U5 showed no evidence of severe heating, inconsistent with inferences from its low Zn content. The Zn in L2005U5 may be low because this particle is dominated by a 5 µm olivine. Two other particles (W7031\*A5 and L2005C38) are fragments of cluster particles. Related fragments of these particles showed low He<sup>4</sup> contents in measurements by Nier and Schlutter (8), consistent with the significant heating indicated by their low Zn contents. Another fragment related to L2005C38 showed a partial magnetite rim, also indicative of significant entry heating. In the six of the seven cases where independent evidence of heating is available that evidence is consistent with the heating inferred from the Zn/Fe indicator and inconsistent with the heating inferred from the S/Fe indicator.

In all the IDPs examined thus far except L2005U5 depletions of Zn are correlated with magnetite rims or low He<sup>4</sup> contents but S depletions correlate less well. Zn content appears to provide an efficient screen to segregate IDPs into highly heated and less heated groups, but TEM confirmation of heating remains desirable.

## REFERENCES:

- 1) Flynn, G. J. (1989) *Icarus*, 77, 287-310.
- 2) Fraundorf, P. et al. (1982) in *Comets*, U. of Arizona Press, 383-409.
- 3) Flynn G.J. & Sutton S.R. (1992) *Proc. Lun. Plan. Sci. Conf.*, V.22, 171-184.
- 4) Flynn, G. J. et al. (1992) *Lunar Planet. Sci. XXIII*, 375-376.
- 5) Thomas, K.L. et al. (1992) *Lunar Planet. Sci. XXIII*, 1427-1428.
- 6) Klock, W. et al. (1992) *Meteoritics*, 27, 243-244.
- 7) Keller L. P. et al. (1992) *Lunar Planet. Sci. XXIII*, 675-676.
- 8) Nier, A. O., and Schlutter D. J. (1992) *Meteoritics*, 27, 166-173.

NEW LOW-Ni (IGNEOUS?) PARTICLES AMONG THE C AND C? TYPES OF COSMIC DUST; G. J. Flynn,<sup>1</sup> S. R. Sutton,<sup>2</sup> S. Bajt,<sup>2</sup> and W. Klock,<sup>3</sup> 1) Dept. of Physics, SUNY Plattsburgh, Plattsburgh NY 12901, 2) Dept. of Geophysical Sciences, The University of Chicago, Chicago IL 60637, 3) Institut für Planetologie, Westfälische Wilhelms-Universität, Münster, Germany.

Low-Ni particles with major element abundances, optical properties and morphologies sufficiently similar to chondritic IDPs to receive JSC Cosmic Dust Catalog classifications of C or C?-types have been shown to have trace element contents (1, 2, 3) and mineralogies (4, 5) similar to igneous material. Examination of the JSC Catalog EDX spectra by Cooke et al. (6) has shown that 13% of the C-type and 38% of the C?-type particles are potentially low-Ni particles. We have identified two new low-Ni particles, and shown that an additional fragment from the L2002\*C cluster has an igneous composition. A newly analyzed fragment of the W7066\*A cluster has a chondritic composition. The W7066\*A cluster is important because it has yielded a fragment of igneous composition (1) and another fragment having high concentrations of He and Ne (7) suggesting an extraterrestrial origin.

Six particles with very low Ni abundances ( $\text{Ni/Fe} \leq 0.1 \times \text{CI}$ ) have previously been identified among the stratospheric dust analyzed by Synchrotron X-Ray Fluorescence (SXRF) (1, 2, 3). These particles are usually depleted relative to the CI meteorite composition in Cr, Ge, and Se, but enriched relative to CI in Rb, Sr, Cu, and Ga in a pattern similar to that seen in igneous material (1). Transmission Electron Microscope (TEM) examination of four low-Ni particles (4, 5) revealed mineralogies consistent with igneous material. Rietmeijer (5) suggested that L2002\*C is a terrestrial volcanic particle but he left open the possibility of a Martian volcanic origin.

To better constrain their source(s), we have attempted to identify and characterize additional low-Ni particles by examining particles showing no Ni peak in their JSC Catalog EDX spectra. SXRF analysis allows precise measurement of Ni at low abundances, which is important since small particles with Ni/Fe ratios near CI frequently show no Ni peak in their JSC Catalog EDX spectra. We have identified two new low-Ni particles (L2006F7 and L2006G14) and examined two new fragments (L2002\*C5 and W7066\*A6) of clusters from which other fragments (L2002\*C1 and W7066\*A4) had been identified as low-Ni (1, 2).

L2006F7, classified C-type, has a Ni/Fe ratio = 0.069. The trace element abundance pattern is unusual, having a relatively flat depletion of siderophile elements, differing from the igneous pattern in that Sr, Cu, and Ga are depleted below their chondritic abundances. This trace element pattern is similar the pattern in U2022B2 (1), a low-Ni particle dominated by a large olivine crystal (4). However, L2006F7 differs from U2022B2 in Ca content, with Ca having been detected in the JSC EDX spectrum of U2022B2 but being present at  $0.05 \times \text{CI}$  in L2006F7.

L2006G14, classified C?-type, has a Ni/Fe ratio = 0.021 and a trace element abundance pattern similar to those previously reported for igneous particles (see Figure 1). TEM examination of a small area of L2006G14 showed it to be very fine-grained like the "granular units" of primitive IDPs, but individual phases have not yet been identified.

L2002\*C5 is a second fragment of the L2002\*C cluster, related to L2002\*C1, previously examined by SXRF, which has Ni/Fe



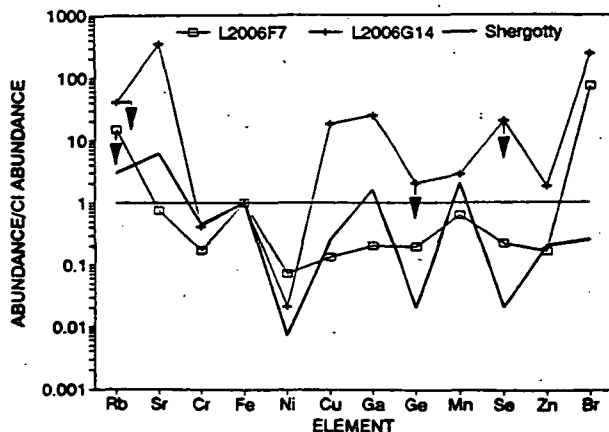


Figure 1: Trace element contents of L2006F7 and L2006G14 compared to CI and the basaltic meteorite Shergotty.

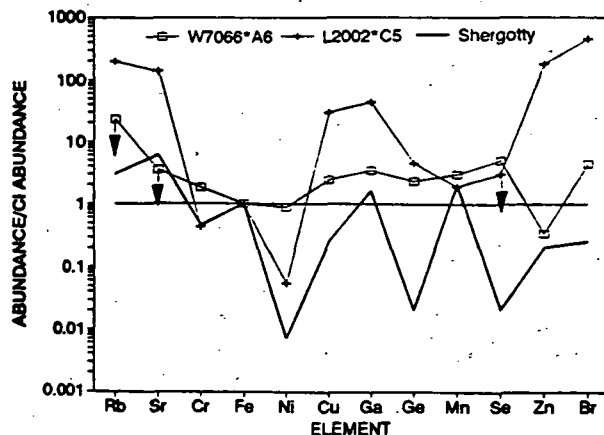


Figure 2: Trace element contents of L2002\*C5 and W7066\*A6 compared to CI and the basaltic meteorite Shergotty.

=  $0.05 \times \text{CI}$  and an igneous trace element abundance pattern (2). This cluster is not cataloged, but Hartmetz et al. (8) called L2002\*C4, another fragment of this cluster, chondritic based on major element abundances. Rietmeijer (5) has reported another fragment of this cluster, L2002\*C2, is likely to be volcanic ejecta on the basis of its layer-silicate mineralogy and major element chemistry. L2002\*C5 has a  $\text{Ni/Fe}$  ratio = 0.054, and a trace element abundance pattern (shown in Figure 2) very similar to the one previously reported for L2002\*C1, suggesting the cluster is relatively homogeneous.

W7066\*A4, a fragment of the W7066\*A cluster, was identified as a low-Ni particle with an igneous trace element pattern (1), and mineralogy consistent with an igneous origin (4). Nier and Schlutter (7) found He and Ne in concentrations comparable to those detected in extraterrestrial particles in W7066\*A5, another fragment of the cluster. This observation suggests that the W7066\*A cluster is an extraterrestrial particle of igneous composition. However, all cataloged fragments of the W7066\*A cluster except W7066\*A4 show Ni in their JSC EDX spectra. We have examined another fragment of this cluster, W7066\*A6, and found  $\text{Ni/Fe} = 0.86 \times \text{CI}$  and a trace element pattern having all detected elements except Se within a factor of 3 of their CI element/Fe ratios (see Figure 2). This pattern is consistent with other chondritic particles but quite distinct from the igneous pattern which shows both positive and negative deviations by factors of 100 or more from CI. We suspect the chondritic composition of W7066\*A6 is more representative of the W7066\*A cluster than is the igneous composition of W7066\*A4 because W7066\*A4 is the only fragment of the cluster to show a low Ni content. If so, then either the igneous material of W7066\*A4 exists as a clast within the otherwise chondritic IDP or W7066\*A4 is not related to the W7066\*A cluster. We note other evidence for contamination of the W7066\*A cluster, since W7066\*A5 consists of a chondritic fragment attached to an aluminum oxide sphere.

#### REFERENCES

- 1) Flynn G.J. and Sutton S.R. (1990) Proc. 20th Lun. Plan. Sci. Conf., 335-342.
- 2) Flynn G.J. and Sutton S.R. (1991) Proc. Lunar Planet. Sci., V. 21, 549-556.
- 3) Flynn G.J. and Sutton S.R. (1992) Proc. Lunar Planet. Sci., V. 22, 171-184.
- 4) Sutton S. R. et al. (1990) Lunar & Planet. Sci. XXI, 1225-1226.
- 5) Rietmeijer F. J. M. (1992) Proc. Lunar Planet. Sci., V. 22, 195-201.
- 6) Cooke E. et al. (1991) Lunar & Planet. Sci. XXII, 235-236.
- 7) Nier A. and Schlutter D. J. (1990) Meteoritics, 25, 263-267.
- 8) Hartmetz C. P. et al. (1991) Proc. Lunar Planet. Sci., V. 21, 557-567.

MASS AND SPATIAL DISTRIBUTION OF CARBONACEOUS COMPONENT IN COMET HALLEY; M. Fomenkova, California Space Institute, UCSD, La Jolla, CA 92093-0216 and S. Chang, NASA Ames Research Center, MS 239-4, Moffett Field, CA 94035

Cometary grains containing large amounts of carbon and/or organic matter were discovered by in situ measurements of cometary dust composition during VEGA and GIOTTO fly-by missions [1]. In accordance with the classification [2] for the data of PUMA-1 and PUMA-2 mass-spectrometers onboard the VEGA spacecraft, particles with a ratio of C to any rock-forming element (Mg, Si, Fe, Ca etc.)  $>10$ , were categorized as CHON. There are 464 such particles in PUMA-1 data and 51 in PUMA-2 data. Application of cluster analysis to these grains [3] revealed several distinct compositional classes, namely: [H,C,N,O], [H,C,N], [H,C], [H,C,O], [C,N], [C,O], [C,N,O] and [C]. Similar classes were identified among particles analyzed by PIA [4]. Also, about a third of all particles fell into groups [H] and [O] characterized by abundances of these elements beyond chemically reasonable limits.

The most numerous [H,C,N,O] particles are dominated by large grains  $>10^{-13}$ g (Table) and distributed along the whole trajectory (Figure). They display variable H:C:N:O ratios and, most probably, are multicomponent mixtures. The [H,C,N] group is dominated by medium particles  $10^{-15}$ - $10^{-13}$ g. Particles of this group are hypothesized [3] to contain nitrogen in aromatic heterocycles, or in amine, imine or nitrile substituents attached to basic hydrocarbon structures. Particles of the [H,C] group are uniformly distributed in all mass ranges and identified as mixtures of aliphatic and aromatic hydrocarbons alone or with carbon grains. The peak occurrence of [H,C,N] and [H,C] particles on the inbound leg of the VEGA-1's trajectory [about  $3 \times 10^4$  km from the nucleus] appears to be shifted further from the nucleus than that of [H,C,N,O] particles. These shifts suggest possible transformations [H,C,N,O]  $\rightarrow$  [H,C,N]  $\rightarrow$  [H,C] caused by solar flux dependent factors. Alternatively, compositional asymmetry within the coma may reflect the heterogeneity of sources on the nucleus.

Another peak in occurrence of the [H,C,N,O], [H,C,N] and [H,C] particles and a peak in occurrence of the [H,C,O] particles [uniformly represented in all mass ranges] are centered near the closest approach. Possibly these particles readily decompose by evaporation after coming out of the nucleus, thus yielding formaldehyde and CO which appear to originate from a distributed source in the coma [5].

Particles of the [C, N] and [C,O] class are more abundant among small grains  $<10^{-15}$ g while [C,N,O] particles are represented in all mass ranges. The small number of particles is insufficient for any further conclusions about mass or spatial distribution. These grains were tentatively identified as made up of polymers of cyanopolynes and multicarbon monoxides, monomeric species of which were observed in the interstellar media [6].

[C]-particles strongly prevail among small grains. This is consistent with estimates of the sizes of circumstellar and interstellar carbon particles [7]. Mass loss from carbon stars may have contributed up to 50% of all matter injected into interstellar medium, and grains of interstellar origin are believed to represent a significant part of cometary dust [8]. These particles are the most abundant at the outermost segment of the trajectory and more or less uniformly distributed otherwise. The appearance of these particles does not seem to correlate with any other classes of CHON particles and they may represent a special population of cometary grains.

The majority of CHON particles was noted [3, 9] to contain a minor mineral component, although the ratio of carbon to these elements was very high. Only 40 spectra measured by PUMA-1 are "pure" CHON [9%] (the PUMA-2 data on minor elements are not reliable [3]). Almost all pure CHON grains were encountered before the closest approach (Figure). Particles with a total lack of rock-forming elements are not randomly scattered among all classes, but rather many of them are grouped together in a few clusters within [H,C,O] and [H,C,N,O] classes, the latter being chara-

## MASS AND SPATIAL DISTRIBUTION: Fomenkova M. and Chang S.

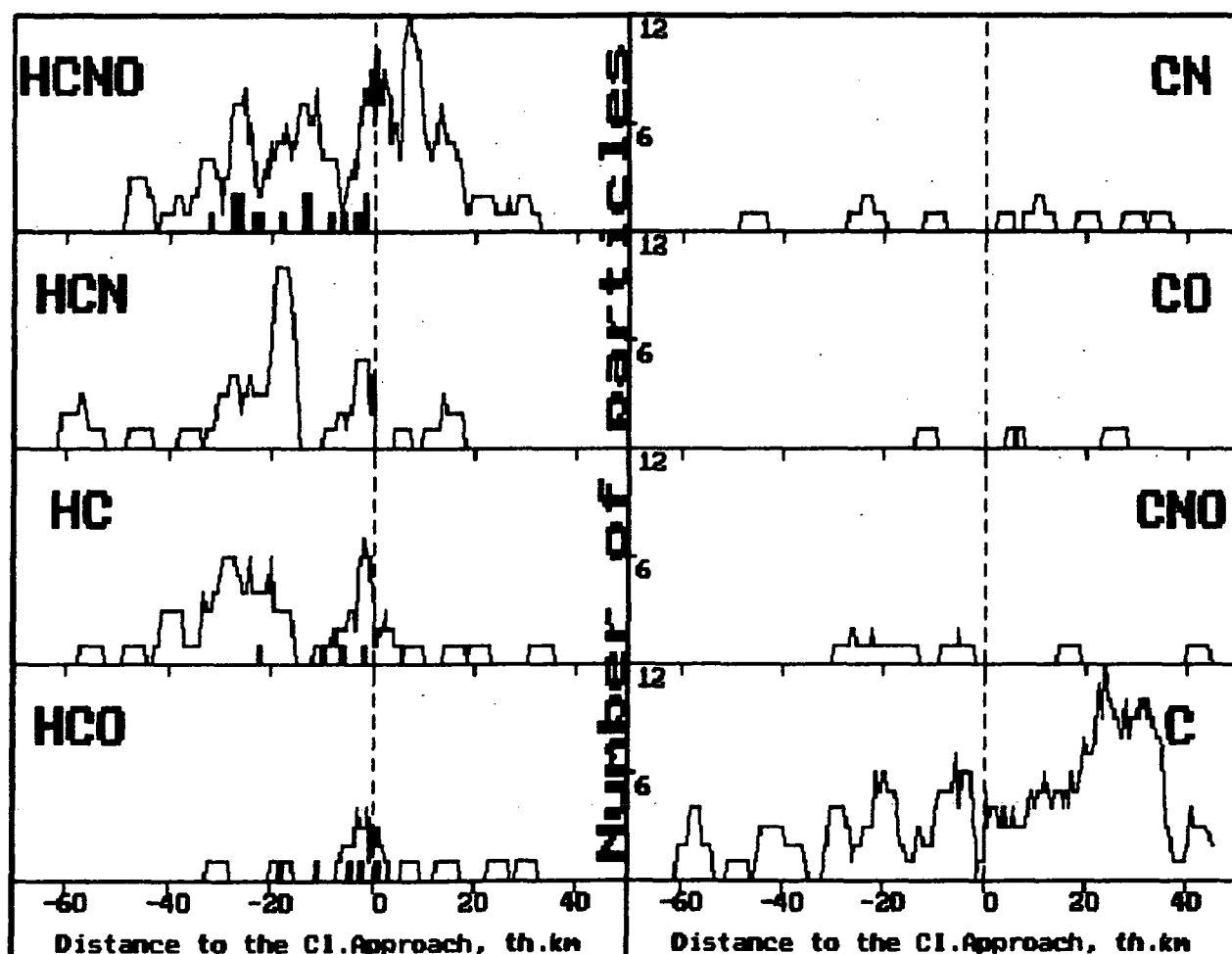
cterized by the lowest C/N ratio of about 3. In contrast, all particles of the [H,C,N], [C,N] and [C,N,O] group contain a minor mineral component and the C/N ratios vary from 8 to 50. Note that particles were combined into clusters according to the composition of their organic component while ignoring their mineral composition. Thus, the emerging correlation between composition of organic part and the lack of rock-forming elements in some groups is quite surprising.

Table. Mass distribution of different types of CHON particles. Percentages are relative to the total number of spectra in each mass range. PUMA-1 and PUMA-2 data.

mass range	H,C,N,O		H,C,N		H,C		H,C,O		C,N		C,O		C,N,O		C	
	#	%	#	%	#	%	#	%	#	%	#	%	#	%	#	%
<10 <sup>-15</sup> g	8	6	3	2	17	12	9	6	4	3	3	2	1	1	51	36
10 <sup>-15</sup> g - 10 <sup>-13</sup> g	41	19	28	13	18	8	15	7	5	2	1	<1	4	2	33	15
>10 <sup>-13</sup> g	52	33	11	7	13	8	4	2.5	1	1	-	-	3	2	16	10

REFERENCES. [1] J. Kissel et al. *Nature* 321, 280, 336 (1986); R. Sagdeev et al. *ESA SP250*, 349 (1986). [2] M. Fomenkova et al. *Science* 258, 266 (1992). [3] M. Fomenkova et al. *In press*. [4] B. Clark et al. *Astr. Astrophys.* 187, 779 (1987). [5] W. Huebner, *Science* 237, 628 (1987). [6] R. Brown et al. *ApJ* 297, 302 (1985); W. Irvine & R. Knacke, *In Origin and Evolution of Planetary Satellite Atmospheres* (1988). [7] M. Jura, *In Carbon in the Galaxy*, NASA CP3061, 39 (1987). [8] M. Greenberg and J. Hage, *Astrophys. J.* 361, 260 (1990). [9] M. Lawler & D. Brownlee *Nature* 359, 810 (1992).

Figure. The distribution of CHON particles of different types along the trajectory of the VEGA-1 spacecraft. Data were averaged by 60-seconds moving window. Vertical lines show occurrence of "pure" CHON particles. At the closest approach the distance to the nucleus was about 8900 km.



N 943162264

**PRIMITIVE SNC PARENT MAGMAS AND CRYSTALLIZATION: LOW  $P_{H_2O}$  EXPERIMENTS.** D.J. Ford and M.J. Rutherford, Department of Geological Sciences, Brown University, Providence, Rhode Island 02912.

**INTRODUCTION.** SNC meteorites are generally believed to present one of the best opportunities to study the composition and petrogenesis of Mars magmas. The crystallization ages, noble gas content, oxygen isotopic composition, and shocked minerals of the meteorites are consistent with a Martian origin [1,2]. The samples range from dunite to clinopyroxenite to microgabbro. Efforts by researchers to determine parental magmas for the more primitive SNC meteorites have been complicated by crystal accumulation and possible melt segregation and removal. This has resulted in a range of parent magma estimates [3-6], although all appear to be Fe-rich and Al-poor. One major objective of this project is to refine the Chassigny parent magma estimate [5] by forcing olivine + clinopyroxene saturation upon the proposed melt composition. EETA 79001 magma compositions are also being investigated to determine the parent magma and the origin of the coarse-grained olivine and orthopyroxene megacrysts. Low pressure experiments with small but finite  $P_{H_2O}$  are being utilized to facilitate equilibrium, and to simulate the  $H_2O$  indicated for these magmas [4,6,7].

The presence of small (0.5-1.0 wt %) amounts of  $H_2O$  in SNC magmas appears to be required by the occurrence of hydrous minerals and textures [6,7] in melts trapped by growing phenocrysts. This evidence for hydrous melts occurs in all SNC's except EETA 79001 and ALHA 77005, where the inclusion textures have been obscured by shock effects. The lack of hydrous minerals or low temperature melts in the intercumulus regions of these rocks suggests that final emplacement was sufficiently close to the surface to allow degassing as the magma equilibrated with the low P atmosphere. Any  $H_2O$  left in intercumulus phases would also tend to be lost during impact heating. Thus, although the bulk  $H_2O$  of SNC's is very low [8], we believe this is explained by the near Mars surface emplacement of SNC magmas and by shock effects. Magmatic processes involving  $H_2O$  need to be examined in order to characterize SNC magmas immediately prior to their final emplacement.

**PROCEDURE.** Two series of experiments have been performed to refine SNC parent magma estimates, obtain crystallization paths, and explore the role of  $H_2O$  in SNC petrogenesis. Series I used small fragments of EETA 79001. Series II starting materials consisted of synthetic Chassigny A\* composition [6] contained within excess Fo<sub>68</sub> olivine and 1-5% clinopyroxene (Mg# 76). Samples were placed in AgPd tubing ( $T \leq 1060^\circ C$ ) or Pt tubing pre-saturated with Fo<sub>68</sub> olivine ( $T > 1060^\circ C$ ) and run at temperatures of 950 to 1150°C in TZM or HfC pressure vessels. A small excess of  $H_2O$  and pressures of 0 to 150 bars were used to obtain melts with up to 1.5 wt % dissolved  $H_2O$ . Another set of A\* experiments was carried out under water saturated conditions at 1 kilobar. All experiments were buffered with a QFM assemblage in a separate tube.

**EXPERIMENTAL RESULTS.** Results of the series I experiments on EETA 79001 are plotted in Figure 1, a projection from olivine onto the Wo-Opx-Plag normative diagram (after [3]). Small degrees of dry melting of this rock produced a melt essentially at the previously determined four-phase reaction point. Increasing the  $P_{H_2O}$  from 0 to 10 to 100 bars yields increasingly plagioclase normative melts as predicted by [6]. These melts have low  $K_2O$  values and contain 1-3 wt %  $P_2O_5$ .

The results of the series II experiments on the A\* composition with excess Fo<sub>68</sub> and seeds of clinopyroxene are plotted in Figure 2. Experiment A-18 (dry) yields a melt essentially at the four-phase reaction point. In this experiment, calcium-rich pyroxene is present in euhedral crystals but is surrounded by a low-calcium pyroxene. The other A\* experiments illustrate how the olivine (Fo<sub>68</sub>) saturated phase boundaries move with decreasing temperature and with the addition of  $H_2O$ . Ultimately, at low T and large degrees of crystallization (A-17), the melt becomes relatively Wo and Plag depleted in contrast to crystallization at higher water pressures.

**DISCUSSION.** The experiments on EETA 79001 recreate a series of possible low pressure crystallization conditions. Comparison of the natural and experimental assemblages places limits on the crystallization history of EETA 79001. Experiments at 1080°C show the increase of

## SNC PARENT MAGMAS AND CRYSTALLIZATION: Ford D.J. and Rutherford M.J.

normative plagioclase in cotectic melts with H<sub>2</sub>O increasing from 0 to 1 wt %. Under "dry" conditions, a Mg# 46 melt coexists with two pyroxenes similar to groundmass pyroxenes in EETA 79001 [9], suggesting the final crystallization was under low pressure dry conditions. After more than 40% melting under low pressure wet conditions (1 wt% H<sub>2</sub>O), orthopyroxene is the sole EETA 79001 liquidus phase. This suggests that under no low pressure conditions could the orthopyroxene-olivine megacrysts of EETA 79001 lithology A be derived from the magma that produced EETA 79001 groundmass. The experiments also emphasize the P<sub>2</sub>O<sub>5</sub>/K<sub>2</sub>O dichotomy in EETA 79001; partial melts contain 2-3 wt% P<sub>2</sub>O<sub>5</sub> but only 0.05-0.2 wt% K<sub>2</sub>O, suggesting cumulate phosphates in the rock, and a SNC magma source with a high P/K ratio.

The experiments on the early Chassigny composition, A\*, show how H<sub>2</sub>O and temperature affect olivine (Fo<sub>68</sub>) and clinopyroxene saturated melts. As predicted by [3], clinopyroxene composition is particularly sensitive to T and X<sub>H2O</sub>. Figure 2 shows that the four-phase saturation point evolves to lower Wo with increasing crystallization at low pressure wet conditions (1 wt% H<sub>2</sub>O). Therefore it is impossible to derive the high Al<sub>2</sub>O<sub>3</sub> melts required to crystallize the kaersutites found in SNC melt inclusions except at high water contents. Given the low T (<1000°C) and high H<sub>2</sub>O required for kaersutite stability, we favor entrapment of a low (<1 wt %) H<sub>2</sub>O melt followed by buildup during cooling and crystallization.

Figure 1. Projection of EETA experiments (melt compositions) through olivine onto Wo-Opx-Plag (after [3]). Solid lines represent 1-atm dry cotectics from [3]. Dashed lines represent inferred 100 bar wet cotectics. Bulk composition of EETA from [9].

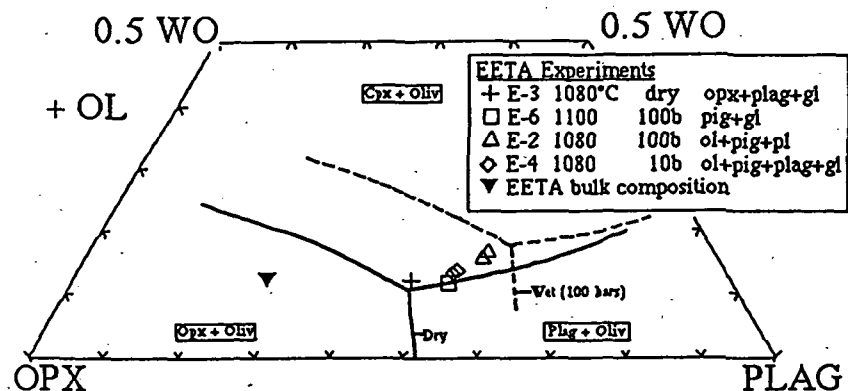
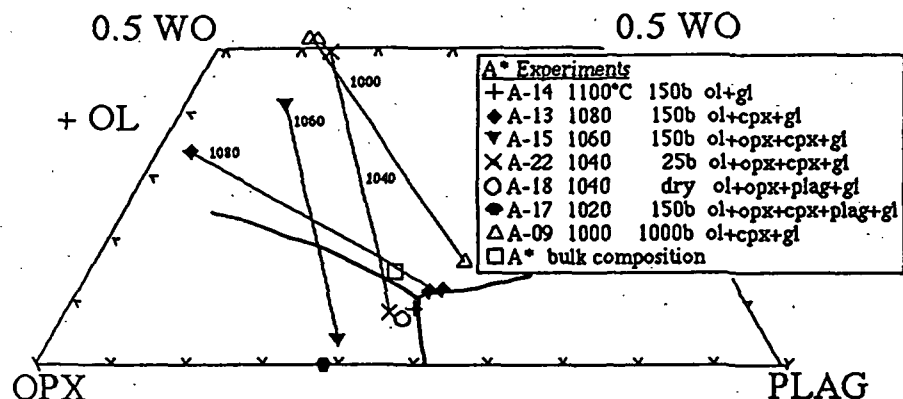


Figure 2. Projection of A\* experiments. Tie lines connect melt compositions with coexisting cpx compositions. Solid lines represent 1-atm dry cotectics from [3]. Bulk composition of A\* from [6].



- References: [1] H.Y. McSween (1985) *Rev. Geophys.*(23), pp.391-416. [2] J.H. Jones (1989) *Proc. 19th Lunar Planet. Sci. Conf.*, pp.465-474. [3] J. Longhi & V. Pan (1989) *Proc. 21st Lunar Planet. Sci. Conf.*, pp.695-709. [4] R.P. Harvey & H.Y. McSween (1992) *Earth Planet. Sci. Lett.* (111), pp. 467-482. [5] A.H. Treiman (1992) *XXIII Lunar Planet. Sci. Conf. (abstr.)*, pp.1447-1448. [6] M.C. Johnson, M.J. Rutherford & P.C. Hess (1991) *Geochim. Cosmochim. Acta* (55), pp.349-366. [7] R.J. Florin, M. Prinz, P.F. Hilava, K. Keil, C.E. Nehru and J.R. Hinthorne (1978) *Geochim. Cosmochim. Acta* (42), pp. 1213-1219. [8] M. Carr and H. Wänke (1991) *XXII Lunar Planet. Sci. Conf. (abstr.)*, pp. 181-182. [9] H.Y. McSween & E. Jarosewich (1983) *Geochim. Cosmochim. Acta* (47), pp. 1501-1513.

N 943-42262

**PHASE TRANSITIONS AND 2D SPHERICAL CONVECTION IN A LARGE ICY SATELLITE;** O.Forni <sup>1</sup>, C. Federico <sup>2</sup> and A. Coradini <sup>3</sup> <sup>1</sup>IAS - Université Paris XI, Orsay, France ; <sup>2</sup>Dipartimento di Scienze della Terra - Università degli Studi, Perugia (Italy); <sup>3</sup>IAS - Planetologia, Roma (Italy)

Three ice phase transitions, based on experimental and theoretical results<sup>1</sup>, have been incorporated into a 2D spherical convection model. These phase transitions are the exothermic Ice I-II, the endothermic Ice II-VI and the exothermic Ice VI-VIII phase transitions. The fluid is assumed isoviscous and the anelastic liquid formulation<sup>2</sup> has been used. The object is an icy satellite whose physical characteristics resemble those of Ganymede or Callisto. Structural models, similar to those of Mueller and McKinnon<sup>2</sup>, with different core sizes i.e. with different degree of differentiation have been studied. The shells i.e. the mantle of the satellite is heated both internally and from below to account for the decaying radiogenic heating and the heat flow from the solid core. The lower boundary of the mantle is rigid and isothermal, the upper boundary is isothermal. Calculations with rigid and shear stress free upper boundary are carried out in order to assess the role of the different boundary conditions. Two different Rayleigh numbers, depending on the assumed value of the viscosity, have been used in the calculations and the thermal evolution of the satellite has been studied.

The suit of calculations presented in this study demonstrates that phase transitions cannot be ignored when the thermal evolution of a large icy satellite has to be studied. The importance of the construction of realistic phase diagram for ice has been also documented. On the other hand the degree of differentiation, simulated with structures with different core's radius does not seem to drastically influence the overall behaviour of the convective activity. Within the limits of our simulations, the post-accretionnal evolution seems to be independent on the degree of primordial differentiation.

The convective style show a dramatic difference between rigid and shear stress free boundary condition. Generally it can be said that shear stress free boundary condition favours a whole mantle convection while a rigid boundary condition favours a double layered convection. In this last case the ice II-VI endothermic phase transition acts as a barrier to the convective flow. However, for both cases, the increase of the Rayleigh number enhances the layering. Above the endothermic phase transition, temperatures are high enough to produce melting only when shear stress free boundary conditions are applied and viscosity is high enough to reduce the efficiency of heat removal.

From this point of view, if the observed tectonic difference between two similar objects like Ganymede and Callisto must be explained by some degree of melting during the post-accretionnal evolution, then it must be assumed that the thermal evolution of Ganymede is controlled by a relatively large  $\Delta T$  with a relatively low Rayleigh number i.e., relatively high viscosity. This is true in our modelling as far as shear stress free boundary condition is imposed, in fact with rigid boundary condition melting never occurs. Thus, while the characteristics of Callisto can be explained by low Rayleigh number and rigid boundary, those of Ganymede require shear stress free. In the light of these results the explanation of the different tectonic activity between Ganymede and Callisto seem to reside in a more mobile lithosphere on Ganymede than on Callisto. These conclusions are also supported

PHASE TRANSITIONS AND 2D SPHERICAL CONVECTION: O. Forni et al.

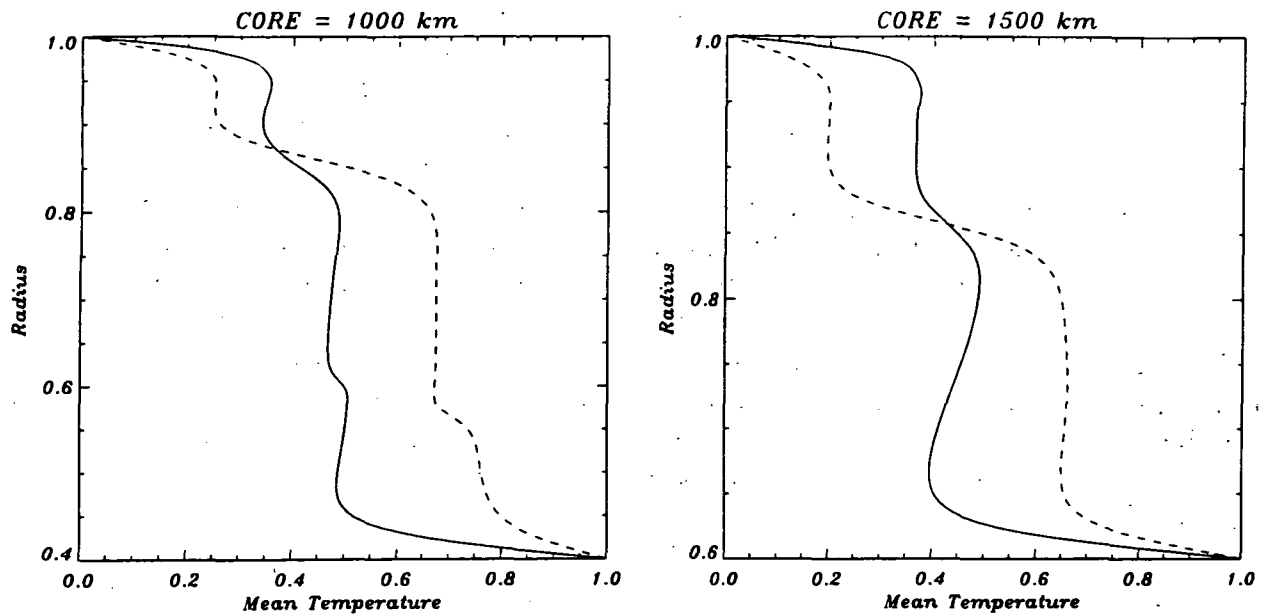


Figure 1: Mean temperature profiles for both core sizes and boundary conditions are represented. The solid lines represent the shear stress free condition and the dashed lines represent the rigid boundary condition. In the rigid case, a well developed boundary layer appears at the Ice II-VI endothermic phase transition. Mean temperatures in the upper mantle are higher for the free slip boundary condition so that melting can occur. Mean temperatures in the lower mantle are higher for the rigid case.

by the comparison between the thermal gradients we derived from our simulations and the thermal gradients obtained from the analysis of the geometry and the evolution of characteristic surficial features on Ganymede and Callisto<sup>4,5</sup>.

**References.** (1) Mishima, O. and S. Endo *J. Chem. Phys.*, **73**, 2454-2456, 1980. (2) Jarvis, G.T., and W.R. Peltier, in *Mantle convection Plate tectonics and global dynamics*, edited by W.R. Peltier, pp.479-594, Gordon and Breach Science Publishers, 1989. (3) Mueller, S., and W.B. McKinnon, *Icarus*, **76**, 437-464, 1988. (4) Allemand, P. and P.G. Thomas, *J. Geophys. Res.*, **96**, 20981-20988, 1991. (5) Passey, Q., and E.M. Shoemaker, in *Satellites of Jupiter*, D.Morrison, Ed., pp.379-454, Univ. of Arizona Press, Tucson, 1982.

## PLANETARY SCIENCE AND ASTRONOMY IN THE MIDDLE SCHOOL CLASSROOM

L. M. French, Wheelock College, 200 The Riverway, Boston, MA 02215.

Astronomy and planetary science are of great interest to most middle and secondary school students. Many who think traditional biology, chemistry, physics, or earth science courses are dry or irrelevant are fascinated by the aesthetic and philosophical appeal of astronomy, and by the adventure of exploring other worlds. This high intrinsic interest makes planetary science and astronomy ideal media for teaching basic scientific and quantitative reasoning to students who might otherwise give up on science. During the period 1989-1992 the author integrated planetary science and astronomy into a fundamental course on physical science for eighth graders.

At the Park School, an academically rigorous independent school in Brookline, MA, eighth graders study astronomy and planetary science for approximately half the school year as part of an introductory physical science course. The classroom activities in astronomy are taken from the Project STAR curriculum [1], developed at the Harvard-Smithsonian Center for Astrophysics. Planetary topics included in the Project STAR curriculum include the phases of the Moon, the Earth's seasons, gravity, and building scale models of the Solar System. The remainder of the formal curriculum can be described as "hands-on chemistry". It is based on the text *Introductory Physical Science* [2]. Fundamental characteristic properties such as density, boiling point and melting point are introduced through laboratory activities and observations. Students become familiar with laboratory techniques and important planetary materials such as methane, sulfuric acid, carbon dioxide, hydrogen, and ammonia. Near the end of the course, students study a planetary object in detail. Astronomy, chemistry, and planetary science converge with the topics of light and spectroscopy: students learn to identify ionic compounds by flame tests. They then study the atomic model and learn that the color of light emitted by an atom is characteristic of that element. Finally, they build a spectrometer, observe absorption lines in the solar spectrum, and learn how astronomers use light to study distance objects.

Twice a year, students were asked to evaluate their science classes. The questions were simple:

- 1) What topic did you enjoy most and why?
- 2) What topic did you enjoy least and why?
- 3) What should definitely be taught again next year?
- 4) What suggestions can you make to help improve this course?

The 48 students in the eighth grade class during the 1991-92 school year gave the following responses:

- 1) Overall, approximately 68% of the students preferred astronomy or planetary science topics and activities.
- 2) 85% of the girls preferred astronomy or planetary science, while approximately equal numbers of boys preferred chemistry and astronomy.
- 3) Most students preferred the mathematical approach used in the Project STAR astronomy curriculum, which was based on geometry and similar triangles. The ratio problems found in the chemistry part of the course were originally algebraic in nature, and many students had difficulties setting up the ratios initially. Once they had been introduced to similar triangles, however, several students (all girls) devised methods of solving ratio problems using similar triangles. Even the students who preferred the chemistry subject matter said that the mathematics used in astronomy was easier to comprehend.



4) All of the students (male and female) who preferred chemistry would be ranked as outstanding science students by any criterion. The group preferring astronomy and planetary science included some outstanding science students but also many who struggled more in traditional science classes.

### Sample Student Comments

#### From Girls:

- "Astronomy lets you think about where we came from and where we're going. It's cool."
- "I liked learning about photons and light and how stars shine."
- "I got ideas for new abstract artwork looking at pictures of the clouds of Jupiter for my research report."
- "Similar triangle problems helped me see how to set up ratios."
- "I preferred chemistry but doing similar triangles really helped students who had trouble. Both subjects were fun."

#### From Boys:

- "I liked both but chemistry was cooler because we got to light matches and do flame tests."
- "It was really neat to see how the different areas meet up--astronomers have to know about atoms and chemists have to know about light."
- "All the experiments with Bunsen burners should definitely be repeated. Those felt more like *real* science labs than playing with lenses did."
- "The planet project was one of the most fun research projects I've ever done. I could read scientific papers and sort of follow what they said."

### Discussion

These results suggest that astronomy and planetary science may attract and keep the interest of students more effectively than chemistry, physics, or earth science alone. Among both boys and girls there appears to be a slight tendency to see chemistry as more "real" science than either astronomy or planetary science. This may not be bad, however, as both boys and girls responded favorably to the non-traditional sciences. The results suggest that astronomy and planetary science can play valuable roles in the middle school classroom as subjects that attract diverse students and as a means for introducing basic scientific reasoning.

The survey described here was informal and obviously based upon a small number of students. One possible source of bias should be noted: the students know that their teacher was a professional planetary astronomer. Since girls are, on average, more attuned to pleasing authority figures than boys, some girls may have shaded their responses more positively (either consciously or unconsciously) toward astronomy and planetary science. A more hopeful interpretation is that perhaps having a woman astronomer for a teacher intrigued and inspired the girls. A longer term study in collaboration with the current Park School science faculty is planned.

### REFERENCES

- [1] Coyle, H. P., Gregory, B., Luzader, W. M., Sadler, P. M., and Shapiro, I. I. (1993) *Project STAR: The Universe in Your Hands*. Kendall-Hunt, Dubuque.
- [2] Haber-Schaim, U., Abegg, G. L., Dodge, J. H., Kirksey, H. G., and Walter, J. A. (1987). *Introductory Physical Science*. Prentice-Hall, Englewood Cliffs.

## DO LARGE IMPACT BASINS IN THE SOUTHERN HEMISPHERE OF MARS CONTROL THE DISTRIBUTION OF POLAR STRUCTURES AND DEPOSITS?

Herbert Frey<sup>1</sup> and Anne-Marie Reidy<sup>2</sup>, <sup>1</sup>Geodynamics Branch, Goddard Space Flight Center, Greenbelt, MD 20771, USA; <sup>2</sup>Astronomy Program, University of Maryland, College Park, MD 20742, USA.

### Introduction

Among the outstanding problems in martian geology are the cause of the off-axis and asymmetric distribution of the southern polar layered terrain and residual ice deposits and the cause of the orientation of scarps, valleys and re-entrant canyons which occur there. A perhaps related problem region is the apparently small number of large ( $D > 500$  km) impact basins seen in the relatively well-preserved cratered terrain of the south polar region. Previously only the 850 km wide South Polar Basin was easily recognized [1,2,3,4]. We have been mapping the south polar region in detail, searching for evidence of ancient, highly degraded impact basins that may have escaped earlier notice, for two reasons: (a) To determine whether the apparent absence of large impact basins is due to incomplete mapping and recognition or a fundamental characteristic of the martian crust related to the origin of the martian crustal dichotomy [5, 6], and (b) To determine whether ancient impact basins, if they exist, exert some control on the distribution of volcanic and polar deposits in the southern hemisphere and on the topography on which these deposits lie. We previously described [7] several promising candidates, including a large pre-Hellas basin in the Malea Planum region and an older but comparably sized basin overlapping South Polar [8, 9]. In this paper we concentrate on the possible influence of the candidate basins in localizing the asymmetric distribution of polar deposits and in controlling the orientation of structures found within these deposits.

### Candidate Basins in the South Polar Region

There is very good structural evidence for a multi-ring basin (Malea B) to the southwest of Malea Planum, centered at about 340°W, 75°S, near the fresh crater South. Three reasonably well-defined but incomplete rings, marked by massifs, isolated peaks and outcrops of knobby and degraded Noachian terrain bounded by scarps, have diameters 740, 950 and 1155 km. Evidence for two inner rings is weaker. Overlap of this smaller basin with South Polar Basin appears to influence the distribution of polar ice and perhaps the layered terrain deposits (see below).

South Polar Basin is the most obvious impact basin in the southern polar region, but its single recognized ring - the disjointed scarp-like Promethei Rupes - is unusual. It is impossible to fit all the segments of the exposed scarp with a single circular arc. We suggest that influence from other basins, including Malea B, South Polar B (see below), and even the distant but larger Hellas Basin, has affected the structure of the South Polar rim. As in the case of Malea B, the distribution of ridged plains, outcrops of ancient terrain, ridges, scarps, and other features suggests the *influence* of South Polar Basin greatly exceeds its variable 850-900 km diameter. We found rare individual peaks, scarps, and some ridges in spotty, sometimes concentric distribution at "diameters" of 700, 1220, 1420, 1745 and 2050 km about the center of South Polar Basin. It appears the influence of this basin extends to more than twice the diameter of the obvious ring, as does that from the much larger Hellas Basin.

Evidence exists for an overlapping basin we call South Polar B [9]. A variety of features including straightened crater rims, a subtle 45 km long scarp, a 200 km long knobby ridge, a group of massifs and mountainous peaks, a 300 km long concentric ridge, an inward-facing, 85 km long scarp 505 km from the center, and a series of short ridges, scattered knobs and small massifs all suggest a partially buried ring 1010 km wide centered at 206°W, 73°S. A possible second ring ( $D \sim 1375$  km) is suggested by a break in the rim of South Polar Basin, deflection of an 85 km NW trending ridge, a 50 km long straightened crater rim, small (10-20 km long) sinuous but concentric ridges, a small 10 km long massif, and similar features.

# IMPACT BASIN CONTROL OF POLAR DEPOSITS: Frey, H. and Reidy, A. M.

The 1000 km diameter of the most prominent (middle?) ring makes South Polar B slightly larger than South Polar, but its highly degraded state and obvious overprinting by the Promethei Rupes suggest it formed earlier.

## *Influence of Large Basins on Polar Structures and Deposits*

It appears the location and overlap of Malea B, South Polar, and South Polar B control the location of important polar terrain units. Nearly all the *Hdu* and *Hdl* units in the eastern portion of the south polar region lie within the Malea B and South Polar Basins. Likewise, the polar layered terrain (*Apl*) appears to lie mostly within South Polar and South Polar B, even though there is no obvious rim preserved on the northwestern edge of the unit. The extended distribution of *Apl* northward about 180° W longitude appears directly related to the overlap between South Polar and South Polar B.

The off-axis location of the residual ice deposits (*Api*) is more difficult to explain, being located far from the center of South Polar B and only lying within overlap of the more distant Malea B rings with South Polar. The *Api* units are located at the approximate center of a large, roughly circular region in which large craters are nearly absent. Perhaps there remains to be found a very ancient basin whose overlap with South Polar and Malea B provides the proper topographic trap not only for *Apl* units but for *Api* as well. A basin centered at 85°W, 78°S in the Cavi Agusti region would not only provide the proper overlap but also help explain the distribution of *Hdu* and *Hdl* units in the western south polar region and many of the structures found there.

Malea B, South Polar and South Polar B may influence the orientation of structures (scarps, valleys, Chasma Australe) within the layered terrains. Many of these occur along proposed rings of these basins, as arcs concentric to basin centers, or along lines radial to a basin center (sometimes where combinations of these conditions exist). Malea B appears to be particularly important in this regard. Ridges in the *Nplr* and *Hr* units of Malea Planum as well as valleys and scarps in the layered terrain *Apl* all lie on arcs concentric to the Malea B center. Chasma Australe lies within the overlap region of all three basins described, along an arc roughly concentric about the center of Malea B which may control several narrow valleys within *Api*, marks the boundary between cratered terrain and *Nplr* ridged plains that run northward from South Polar Basin rim between 280 and 290°W, and lies along several prominent ridges with Malea Planum. Several long valleys within the residual ice *Api* are oriented towards the center of either South Polar or South Polar B; shorter cross-cutting valleys in the same unit seem more aligned with the center of Malea B. Within the layered terrain away from the residual ice deposits, several long ridges at about 150°W are also radially oriented toward South Polar B. By contrast, the prominent facing scarps at 300°W, 85°S are not so obviously associated with any of these basins, and may reflect still additional influences not yet recognized.

While not explaining everything seen in the south polar region, there is intriguing but at the present time only circumstantial evidence that the three basins described above did exert substantial influence on the distribution of polar deposits (*Hdu*, *Hdl*, *Apl*, *Api*) and on the orientation of many of the structures found within these deposits. Both radial and concentric directions appear important, and in many places the combination of these from different basins may have contributed to the localization of structures.

**References:** [1] Schultz, R. A. and H. V. Frey, *J. Geophys. Res.* 95, 14,175-14,189, 1990. [2] Pike, R.J. and P.D. Spudis (1987) *Earth Moon Planets*, 39, 129-194. [3] Croft, S.K. (1981) *Proc. Lunar Planet. Sci. Conf.* 12th, 277-257. [4] Wood, C.A. and J.W. Head (1976) *Proc. Lunar Planet. Sci. Conf.* 7th, 3629-3651. [5] Frey, H. and R.A. Schultz (1990) *J. Geophys. Res.* 95, 14,203-14,213. [6] Frey, H. (1991) *LPSC XXII*, 417-418. [7] Frey, H. et al. (1991a) *LPSC XXII*, 419-420. [8] Frey, H. et al. (1991b) *LPSC XXII*, 421-422. [9] Reidy, A. M. et al., (1992) *LPSC XXIII*, 1137-1138.

**FREE-AIR AND BOUGUER GRAVITY ANOMALIES AND THE MARTIAN CRUSTAL DICHOTOMY** Herbert Frey<sup>1</sup>, Bruce G. Bills<sup>1</sup>, Walter S. Kiefer<sup>1,2</sup>, R. Steven Nerem<sup>1</sup>, James H. Roark<sup>1,3</sup> and Maria T. Zuber<sup>1,4</sup>, <sup>1</sup>Laboratory for Terrestrial Physics, Goddard Space Flight Center, Greenbelt MD 20771, 301-286-5450, <sup>2</sup>Lunar and Planetary Institute, Houston, TX 77058, <sup>3</sup>Astronomy Program, University of Maryland, College Park, MD 20742, <sup>4</sup>Dept. Earth and Planetary Sciences, Johns Hopkins University, Baltimore MD 21218.

### Introduction

This paper compares **free-air** and **Bouguer** gravity anomalies from a 50x50 field [1], derived from re-analysis of Viking Orbiter and Mariner 9 tracking data and using a 50x50 expansion of the current Mars topography [2] and the GSFC degree 50 geoid as the equipotential reference surface, with the martian crustal dichotomy. The spherical harmonic topography used in this study has zero mean elevation, and differs from the USGS maps [2] by about 2 km. In this field the dichotomy boundary in eastern Mars lies mostly at -1 to -2 km elevation.

Figure 1 shows **Bouguer gravity anomalies** on a map of Noachian, Hesperian and Amazonian age terrains, simplified from current geologic maps [3,4]. The map is centered at 300°W to show the continuity of the dichotomy boundary. Contour interval is 100 mgals. We directly compared gravity and topography along ~40 profiles oriented parallel to the dichotomy boundary topographic gradient, to determine how the geophysical character of the boundary changes along its length and what this implies for its origin and development.

### Crustal Dichotomy

Most of the heavily cratered Noachian terrain near the dichotomy boundary is characterized by 100-250 mgal *negative* Bouguer anomalies, independent of the elevation at which the cratered terrain occurs [5]. Regions as low as Tempe Terra and SE Acidalia (below -2 km) have the same negative Bouguer character as regions at +3km. Most lowlying plains units have *positive* Bouguer anomalies, ranging from 250-300 mgals in Utopia, southern Elysium, Chryse and Arcadia to 100-150 mgal at higher latitudes in northern Utopia, Acidalia and Amazonis. Where it is marked by a pronounced boundary, the crustal dichotomy is characterized mostly by a change from negative over the cratered highlands to more positive (at least in a relative sense) Bouguer anomaly over the low plains. In Xanthe Terra and further north in Tempe Terra where Noachian cratered terrain changes abruptly to younger plains, the same geophysical signature is also seen (Figure 1).

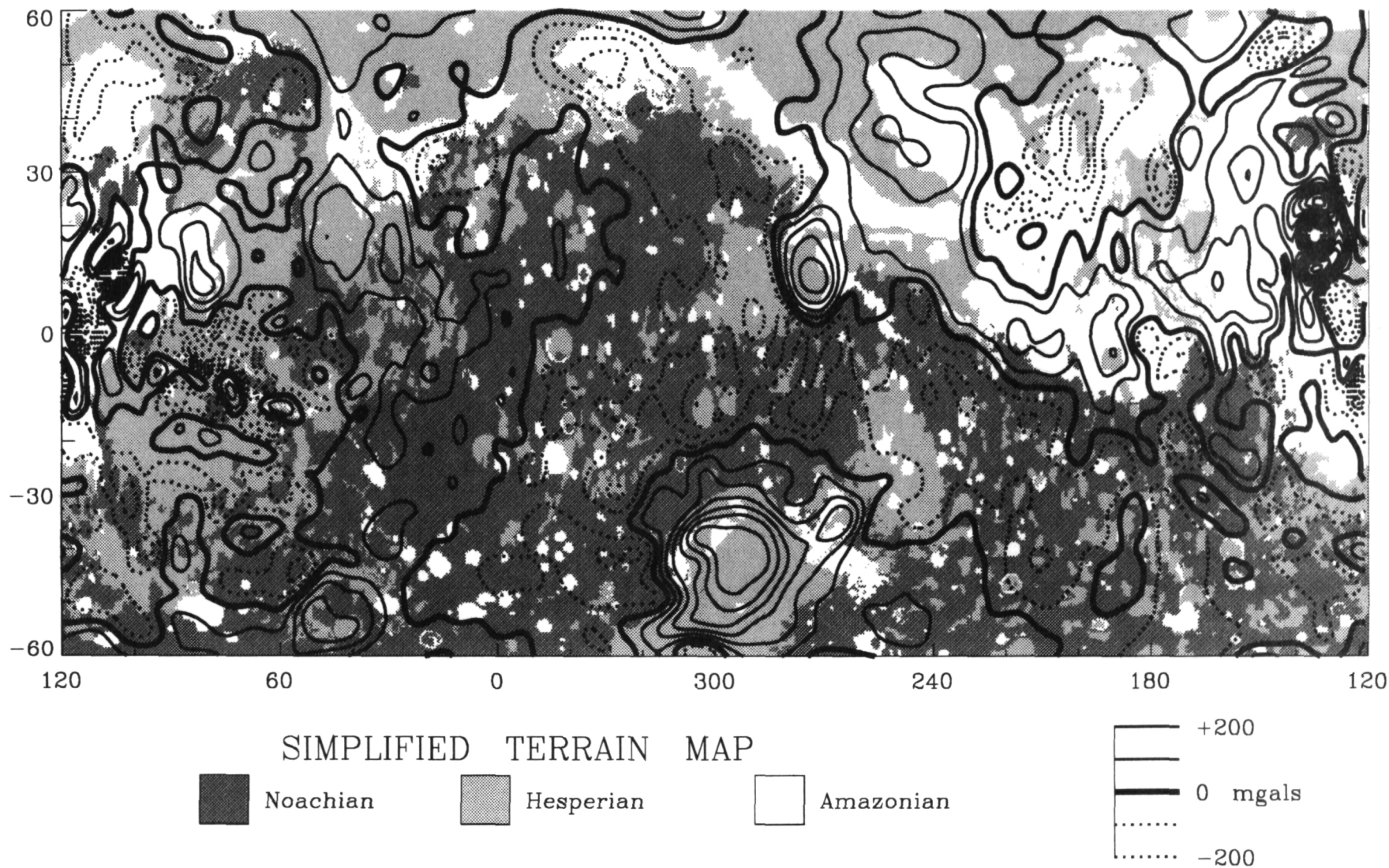
The change from negative to more positive Bouguer anomaly across the dichotomy boundary appears independent of elevation. Tempe Terra (-2 to -4 km), Xanthe Terra (+1 to -2 km), SE Acidalia (-1 to -2 km), and the rest of the boundary zone between 150 and 360°W (+1 to -1 or -2 km) all show the same pattern.

### Crustal Dichotomy Boundary

Profiles across the dichotomy boundary zone vary in a complicated way, as does the character of the boundary itself. Generally the amplitude of the **Bouguer anomaly** is intermediate over the boundary zone by comparison with the low amplitude negatives over the cratered terrain and the positives that occur over plains to the north. The amplitude swing is of order 200 to 400 mgals. East of the Isidis Basin the amplitudes associated with the generally steeper topography of the boundary are generally higher (>300 mgals). Flatter profiles characterize the region west of Isidis, where the Bouguer signature is negative even in the lowlying plains. Despite this, the 200-300 mgal change to relatively more positive from cratered terrain to lowlying plains remains. In Xanthe Terra the profiles are similar to those east of Isidis, while Tempe Terra profiles look more like those west of Isidis.

**References:** [1] Smith, D. E. et al., *LPSC XXIV*, this issue, 1993. [2] USGS *Misc. Inv. Ser.*, Map I-2030, 1:15M, 1989. [3] Scott, D. L. and K. L. Tanaka, *USGS Misc. Inv. Ser.* Map I-1082-A, 1:15, 1986. [4] Greeley, R. and J.E. Guest, *USGS Misc. Inv. Ser.* Map I-1082-B, 1:15M, 1987. [5] Frey, H. et al., *LPSC XXIV*, this issue, 1993.

FIGURE 1.  
BOUGUER GRAVITY ANOMALIES and CRUSTAL DICHOTOMY



**NEW MARS FREE-AIR AND BOUGUER GRAVITY: CORRELATION WITH TOPOGRAPHY, GEOLOGY AND LARGE IMPACT BASINS** Herbert Frey<sup>1</sup>, Bruce G. Bills<sup>1</sup>, Walter S. Kiefer<sup>1,2</sup>, R. Steven Nerem<sup>1</sup>, James H. Roark<sup>1,3</sup> and Maria T. Zuber<sup>1,4</sup>, <sup>1</sup>Laboratory for Terrestrial Physics, Goddard Space Flight Center, Greenbelt MD 20771, 301-286-5450, <sup>2</sup>Lunar and Planetary Institute, Houston, TX 77058, <sup>3</sup>Astronomy Program, University of Maryland, College Park, MD 20742, <sup>4</sup>Dept. Earth and Planetary Sciences, Johns Hopkins University, Baltimore MD 21218.

### Introduction

This paper compares free-air and Bouguer gravity anomalies from a 50x50 field (MGM-635), derived at the Goddard Space Flight Center [1], with global topography, geology and the distribution of large impact basins. The **free-air** gravity anomalies were derived from re-analysis of Viking Orbiter and Mariner 9 tracking data and have a spatial resolution of 250-300 km. **Bouguer anomalies** were calculated using a 50x50 expansion of the current Mars topography [2] and the GSFC degree 50 geoid as the equipotential reference surface. Rotational flattening was removed using a moment of inertia of 0.365 and the corrections from Table B2 of Sleep and Phillips [3]. Crustal density and mean density were assumed to be 2.9 and 3.93 gm/cm<sup>3</sup>.

The spherical harmonic topography used in this study has zero mean elevation, and differs from the USGS maps [2] by about 2 km. Comparisons with global geology use a simplified map with about 1/3 the number of units on the current maps [4,5]. For correlation with impact basins, the recent compilation by Schultz and Frey [6] was used.

### General Relations

The long wavelength **free-air anomaly** pattern [1] has a crude longitudinal dichotomy: longitudes 210 to 360°W (Elysium westward into Arabia) and 70 to 140°W (Tharsis, Alba) are dominated by positive anomalies and the remainder of Mars by negative anomalies. There is also a crude topographic relation: the highest volcanic and tectonic regions have positive and the deeper impact basins mostly negative anomalies. The relationship is imperfect, however, with strong positives in Isidis and Utopia and broad regions of highstanding ancient cratered terrain having both strong positive and moderate negative anomalies associated with them. **Bouguer anomalies** have more consistency, showing strong negative with flanking positive anomalies over major volcanoes, lower amplitude negatives over most cratered terrain, and general positives over major topographic basins. Below we examine these relations in more detail.

### Bouguer Gravity Anomalies and the Crustal Dichotomy Boundary

**Bouguer anomalies** over heavily cratered terrain are mostly *negative* (150-250 mgals) regardless of elevation [7]. That is, Tempe and portions of SE Acidalia have negative Bouguer anomalies even though they lie 2-4 km lower than most cratered terrain. Two exceptions are low elevation cratered terrain with 50-100 mgal positive anomalies east of Hellas and in Arabia. Most lowlying plains units have *positive* Bouguer anomalies, ranging from 250-300 mgals in Utopia, Chryse and Arcadia to 100-150 mgal in northern Utopia, Acidalia and Amazonis.

Profiles across the dichotomy boundary zone vary in a complicated way. Generally the amplitude of the **Bouguer anomaly** is intermediate over the boundary zone by comparison with the low amplitude negatives over the cratered terrain and the positives that occur in lowlying plains to the north. Exceptions do occur; these are discussed in a companion abstract [7].

### Bouguer Gravity Anomalies and Volcanic Constructs

All the major volcanic constructs have *negative* **Bouguer anomalies** with positive flanking anomalies. Amplitudes systematically decrease with age (not size or height) from youngest (Olympus Mons, -1000 mgal) through oldest (Elysium and Alba, -200 mgal). USGS topography and our spherical harmonic expansion both show a moat-like depression around Olympus Mons, which gives rise to a positive Bouguer flanking anomaly of +300 to +600 mgals. This is discussed in a companion paper by Zuber et al. [8]. Ascraeus Mons has a similar but lower amplitude positive flanking anomaly but this feature is missing from the older volcanoes.

## MARS GRAVITY, TOPOGRAPHY, GEOLOGY, IMPACT BASINS: Frey, H. et al.

**Bouguer Gravity Anomalies and the Valles Marineris**

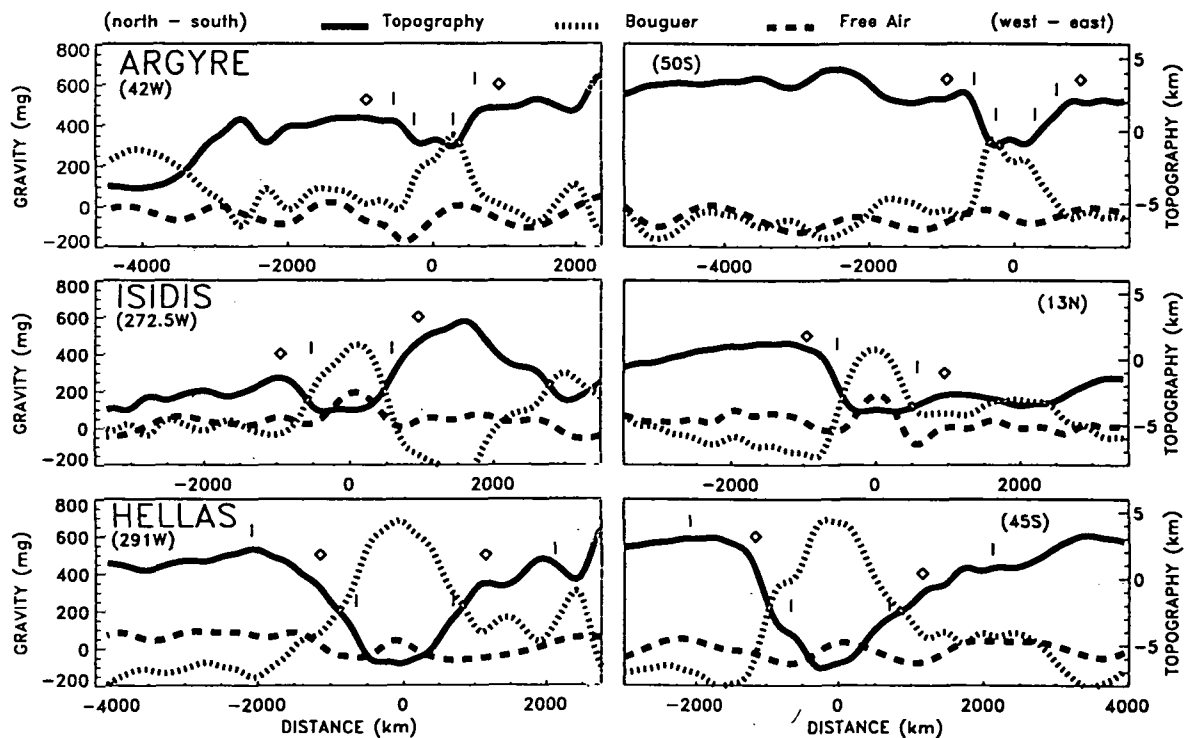
In free-air gravity, the Valles Marineris is dominated by a -250 mgal negative over the central canyons, flanked by 50-75 mgal positives over the narrower eastern and western troughs. **Bouguer anomalies** are positive for the deeper southern canyons, flanked by linear negative anomalies to the north and south. Profiles show the strong, localized positive Bouguer anomaly superimposed on a broader low; this centralized positive is most pronounced over Melas and Coprates Chasmata but also occurs over the narrow Tithonia and Ius Chasmata to the west. The shallower northern canyons (Ophir, Candor, Juventae) do not have this central positive anomaly.

**Bouguer Gravity Anomalies and Large Impact Basins**

In free-air gravity the Utopia (+200 mgals) and Isidis (+150 mgals) Basins show strong positive anomalies; weaker (< 50 mgal) positive free-air anomalies occur in Hellas, Chryse and Argyre. The **Bouguer anomalies** are different: all these basins show relatively strong positive anomalies (>250 mgals for Chryse to >650 mgals for Hellas). Smaller or less well-defined [6] basins (Ladon, Acidalia) have weaker positive (~ 150 mgal) Bouguer anomalies. For Argyre, Isidis and Hellas the positive anomaly lies within the most prominent ring (see Figure 1); the relative amplitude increases systematically from +350 to +550 mgals with basin diameter: the anomaly width at half maximum power divided by basin diameter scales linearly with the basin diameter normalized by the radius of Mars. The smaller and more poorly defined basins also show a general increase in Bouguer anomaly amplitude with increasing size.

**References:** [1] Smith, D. E. et al., *LPSC XXIV*, this issue, 1993. [2] USGS *Misc. Inv. Ser.*, Map I-2030, 1:15M, 1989. [3] Sleep, N. H. and R.J. Phillips, *J. Geophys. Res.* 90, 4469-4489, 1985. [4] Scott, D. L. and K. L. Tanaka, *USGS Misc. Inv. Ser. Map I-1082-A*, 1:15, 1986. [5] Greeley, R. and J.E. Guest, *USGS Misc. Inv. Ser. Map I-1082-B*, 1:15M, 1987. [6] Schultz, R. A. and H. V. Frey, *J. Geophys. Res.* 95, 14,175-14,189, 1990. [7] Frey, H. et al., *LPSC XXIV*, this issue, 1993. [8] Zuber, M. T. et al., *LPSC XXIV*, this issue, 1993.

**Figure 1:** N-S and W-E profiles across Argyre, Isidis and Hellas. Ring locations shown by short vertical lines; diamond shows most prominent ring. Note strong Bouguer positive anomalies.





# AUTHOR INDEX\*

OMIT  
TO  
END

A'Hearn M. F.	1261	Auchampaugh G.	49
Abakshin E. V.	53		
Adams J. B.	85, 1229	Bada J. L.	193
Adel-Hadadi M. A.	1275	Badjukov D. D.	51, 53, 699, 1051
Agerkvist D. P.	1	Bagatin A. C.	377
Agosto W. N.	3	Baguhl M.	1587
Agresti D. G.	1291	Bahar E.	73
Agrinier P.	933	Baines K. H.	253, 255, 1165
Aguirre-Puente J.	5	Bajt S.	187, 495, 497, 499, 1203, 1385, 1383
Ahrens T. J.	7, 273, 457, 1101, 1387, 1449		
Albee A. L.	1443	Baker V. R.	471, 473, 587, 723, 815
Alexander C.	1537	Baldwin S. L.	225
Alexander W. M.	915, 1403	Baloga S. M.	55
Alexandrov P. E.	1063	Balogh A.	1587
Alexeev V. A.	9, 11, 13	Bame S. J.	1587
Alexopoulos J. S.	15	Banerdt W. B.	57, 545, 931
Alibert C.	1089	Bansal B. M.	1095
Allbrooks M. K.	331	Barbera P.	287
Allen C. C.	17, 531, 963	Barkatt A.	1275
Allton C. S.	19	Barker E. S.	1043
Allton J. H.	19, 21, 963	Barlow N. G.	59, 61
Altemir D. A.	23, 25	Barnet C. D.	833
Altenberg B. H.	27	Barnouin O. S.	63
Alvarez W.	297	Barraclough B.	49
Amari S.	29	Barrett R. A.	65, 209, 1583
Anderson D. L.	31	Barsukova L. D.	1051
Anderson F. S.	563, 567	Basilevsky A. T.	67, 69, 71, 693, 1503
Anderson R.	33	Basu A.	75, 1143
Anderson R. R.	35, 87, 781, 811, 1211, 1301	Batchelder M.	1313
		Baur H.	1031, 1519
Anderson W. W.	457	Becker K. J.	255
Annexstad J. O.	37	Becker R. H.	77
Antonenko I.	623, 629	Becker T. L.	565, 623, 955
Arai T.	1393	Beckett J. R.	79
Arden J. W.	1221	Beebe R. F.	833
Ariskin A. A.	1049	Bell J. F.	197, 223, 299, 303, 515, 557, 617
Arnold J. R.	39, 193, 1085, 1195		
Artemiev V. I.	1063	Bell J. F. III	81, 83, 85, 133, 343, 617, 1229
Artemjeva N. A.	975		
Arvidson R. E.	41, 169, 585, 703, 1293	Bell M. S.	87
Ash R. D.	43	Belton M.	269, 371, 565, 569, 623, 625, 635, 1141
Asphaug E.	45, 99		
Assonov S. S.	695	Ben Othman D.	711
Atkinson D. R.	331, 1497	Benner L. A. M.	89
Attrep M. Jr.	657	Bennett M. E.	97
Aubele J. C.	47, 227, 335, 361, 363, 365, 637	Bennett M. L.	615
		Bennett V.	449

\*Page numbers refer to the first page of an abstract on which an author appears.



Benoit P. H.	91, 93, 95, 681, 1269, 1571	Brilliant D. R.	191
Benz W.	99	Brinton K. L. F.	193
Bergelson V. I.	1063	Britt D. T.	195, 197
Bernhard R. P.	65, 101, 673	Brizi E.	1001
Betterton W. J.	143, 145, 539	Brooks R. R.	593
Betts B. H.	103	Brown C. D.	199, 201
Beukens R. P.	341	Brown L. E.	307
Bibring J.-P.	915	Brown R. H.	515
Bills B. G.	105, 511, 513, 797, 1591	Browning L. B.	203
Bilotti F.	107	Brownlee D. E.	173, 205, 373, 901, 1443
Bindschadler D. L.	109, 1279	Brueneman D. J.	531
Binzel R. P.	111	Bruno B. C.	207, 283, 899
Birch P. V.	1261	Buchanan P. C.	209
Bischoff A.	113	Buck W. R.	211
Bishop J. L.	115, 117	Bullock M. A.	213, 1005
Bishop K. M.	727, 819	Bulmer M. H.	215
Black R.	781	Bunch T. E.	1259
Black S.	119, 121, 123, 125, 127	Burba G. A.	217, 221, 1077, 1079, 1081
Blaney D. L.	129, 939	Burba G. G. Jr.	219
Blanford G. E.	131, 1425	Burbine T. H.	223, 515
Blewett D. T.	133, 617, 1133	Burke K.	1283
Blum J. D.	135, 267	Burkland M. K.	225
Blumberg D.	563	Burl M. C.	227
Bobina N. N.	221, 1079, 1081	Burnett D. S.	229
Boesenberg J. S.	137, 391	Burns R. G.	115, 231, 233, 489, 1369
Bogard D. D.	139, 141, 521, 1193, 1295	Burt J. D.	235
Bohor B. F.	143, 145, 539	Burt W. W.	1019
Boles W. W.	963	Buseck P. R.	435, 437, 677
Bolsheva L. N.	483	Bussey D. B. J.	237
Borderies N.	831, 1313	Busso M.	1487
Borg J.	915	Bustin R.	239
Borisov A.	147, 667	Byrd R.	49
Borozdin V. K.	1079, 1081		
Boslough M. B.	149	Cabrol N. A.	241
Boss A. P.	151, 153, 155	Caffee M. W.	39, 1085, 1195
Bostwick J. A.	157	Calvin W. M.	83, 243
Bottke W. F. Jr.	159, 571	Cameron A. G. W.	245
Bottomley R. J.	161	Campbell B. A.	247, 249, 1577
Boundy-Sanders S. Q.	163	Campbell D. B.	1343
Bowers C.	1261	Capo R. C.	1357
Boyce J. M.	165	Carey S.	251, 451
Boyd W. T.	537	Carlson R. W.	253, 255
Boynton W. V.	167, 657	Carter J. L.	333, 963
Brackett R. A.	169	Casacchia R.	1453
Bradley J. P.	171, 173, 205	Casanova I.	257, 259
Brakenridge G. R.	175	Casier J.-G.	295
Brandstätter F.	177, 441, 1053, 1055	Cassen P.	261
Brandt D.	179, 181	Cellino A.	377
Brandvold J. B.	1497	Cerroni P.	443, 445
Brannon J. C.	1159	Chadwick D. J.	263, 265, 1241, 1397
Brearley A. J.	183, 185, 187	Chaky D. A.	515
Brekke D. W.	531	Chamberlain C. P.	135, 267
Bridges N.	189, 623	Chambers J. G.	1409

Chang S.	501	Danielson G. E.	255
Chapman C. R.	269	D'Aria D. M.	1235
Chapman M. G.	271	Dasch E. J.	683
Chen G.	273	Davies M. E.	371, 1469
Chen J. H.	275, 277	Davis A. M.	373, 375, 1131, 1479
Cheng A. F.	279	Davis D. R.	377
Chibante L. P. F.	653	Davis P. A.	379, 381
Chicarro A. F.	281	Dawidowicz G.	241
Ching D.	283	Dawson C. B.	383
Christensen P. R.	285, 287, 1175, 1505	Day T.	1429
Chyba C. F.	289	De Angelis G.	385
Cintala M. J.	291, 293, 673	DeHart J. M.	387, 893
Claeys P.	295, 297, 657	De Hon R. A.	389
Clark B. C.	299, 301, 303, 463, 909, 1207	Deines P.	1321
Clark P. E.	305	DeJong E.	569
Clarke R. S. Jr.	1131	Delaney J. S.	137, 391, 1385
Clayton D. D.	307	Delano J. W.	393, 395, 397
Clayton R. N.	685, 757, 945, 1131, 1185, 1321, 1479	Deloule E.	399
Clemett S. J.	309	Denk T.	401
Clifford S. M.	311, 313, 315, 875	Des Marais D.	845
Cloutis E. A.	317	Deutsch A.	849, 933
Cocheo P. A.	663	D'Hondt S.	251
Collins J.	851	Dickinson T. L.	893
Collins W.	1259	Dikov Yu. P.	403, 527
Collinson D. W.	319	Discovery Venera Team	1381
Colson R. O.	321, 323	Dodd R. T.	405
Colvin T. R.	371	Dohm J. M.	407, 1399
Colwell J. E.	325	Dolginov A. Z.	409, 411, 413, 415, 471, 473
Connolly H. C. Jr.	327, 329	Dolginov Sh. Sh.	417, 419
Connors C.	107	Dollfus A.	241, 421
Cook A. C.	1429	Domanik K. J.	663
Coombs C. R.	331, 617, 1497	Domergue-Schmidt N.	1195
Cooper B. L.	333	Dong Q. W.	423
Coradini A.	443, 445, 505	Dorofeyeva V. A.	425, 427, 921, 1467
Costard F.	5, 567	Douglas C.	1539, 1541
Cotugno K.	1361	Drake D.	49, 429
Craddock R. A.	335	Drake M. J.	431
Crawford D. A.	337	Drossart P.	253
Creaser R. A.	339	Dueck S.	585
Cresswell R. G.	341	Duke M. B.	433
Crisp D.	83, 129, 343	Dummel A.	1097
Croft S. K.	345, 347, 349, 1373	Durham W. B.	543
Crossey L. J.	351	Durrheim R. J.	181
Crowell L. B.	353	Ebisawa S.	421
Crown D. A.	355	Edgett K. S.	979
Crozaz G.	357, 1473	Edwards B. C.	1019
Crumpler L. S.	227, 335, 359, 361, 363, 365, 383, 637	Edwards K.	255, 805, 1207
Cushing J. A.	369	Eisenhour D.	435, 437
Cygan R. T.	149	El Eid M.	307
Dalrymple G. B.	1437	El Goresy A.	399
		Ellis S. B.	229
		Ellison M.	1231

Elmore D.	985	Fowler G. W.	1109
Elphic R. C.	439	Franchi I. A.	191, 553, 1221
Encrenaz T.	253	Franklin H. A.	27, 469
England A. W.	847	French B. M.	835
Enggrand C.	441, 1125	French L. M.	507
Epstein S.	229, 1493	Frey H.	105, 509, 511, 513, 797, 1591
Erard S.	443, 445, 1025, 1029, 1039	Fricke S. K.	861, 1317
Ernst R. E.	447	Friedman L.	41, 791
Esat T. M.	449, 1413	Frolov V. A.	459
Espindola J. M.	251, 451	Fujita T.	991
Esposito L. W.	1043	Funsten H. O. III	439
Eugster O.	453, 455, 1073	Futagami T.	1377
Evans L. G.	305		
Evans N. J.	457	Gaddis L. R.	255
Evergreen High School		Gaffey M. J.	515, 715, 787
Research Class	1231	Galileo Imaging Team	569, 623
Evlanov E. N.	459	Galileo SSI Team	371, 955, 957
		Galindo C.	1581
Fagents S. A.	461	Gallino R.	1487
Fallick A. E.	119	Ganasan J. P.	661
Fanale F. P.	255, 299, 301, 303, 463	Ganguly J.	517, 519
Farinella P.	377	Garrison D. H.	139, 141, 521, 1193, 1295
Faris J. L.	1485	Garvin J. B.	523
Farmer J. D.	845	Gaskell R. W.	611
Farrand W. H.	465	Gault D. E.	1257
Fayyad U. M.	227	Gebhard J.	1423
Fechtig H.	1587	Geissler P.	525, 569, 1029
Federico C.	505	Gektin Yu. M.	1013
Fegley B. Jr.	467	Gerasimov M. V.	403, 527
Feldman S. C.	469	Geringer M. A.	567
Feldman V.	1239	Ghail R. C.	529
Feldman W.	49	Gharakanian V.	1061
Ferrante R.	1007	Ghose S.	519
Finkel R. C.	39, 1085, 1195	Gibson E. K. Jr.	239, 757
Finn V. J.	471, 473	Gibson M. A.	531, 1411
Finnila A. B.	475	Gilmore M. S.	533
Fischer E. M.	477, 565, 623, 957, 1141, 1143	Gilmour I.	535, 679
Fisenko A. V.	479, 481, 483, 485, 487, 1011, 1461	Girard M.	253
Fisher D. S.	489	Gladstone G. R.	537
Fiske P. S.	491	Glass B. P.	145, 539
Flynn G. J.	493, 495, 497, 499	GLL Imaging Team	655
Fogel R. A.	1223, 1501	Goguen J. D.	541, 939
Foh J.	633	Gold D. P.	1303
Fomenkova M.	501	Golden D. C.	1015
Ford D. J.	503	Goldsby D. L.	543
Ford P. G.	689	Goldstein J. I.	1557
Forni O.	505	Golombek M. P.	381, 545
Forsyth D. W.	1431	Golub A. P.	975
Forsyth R.	1587	Gooding J. L.	21, 1507
Forsythe J.	255	Goodrich C. A.	547
Foster C. T. Jr.	87	Gorsline D. S.	1117
		Goswami J. N.	549
		Grachjova T. V.	483

Grady M. M.	551, 553	Haugland M.	73
Graf J.	1409	Hawke B. R.	133, 617, 629, 909, 1133, 1207, 1341
Graf Th.	555, 1163	Head J. W. III	213, 235, 361, 363, 365, 447, 533, 565, 581, 619, 621, 623, 625, 627, 629, 631, 635, 637, 691, 773, 919, 957, 1113, 1141, 1145, 1381, 1527
Graham J. A.	153	Heffernan C.	955
Granahan J. C.	255, 557	Heirath J.	1313
Grant J. A.	559, 561	Held P.	633
Gratz A. J.	491	Helfenstein P.	635
Greeley R.	371, 563, 565, 567, 623, 625, 745, 845, 957, 1111, 1141, 1521, 1545	Helgerud M. B.	637
Greenberg R.	159, 569, 571	Henderson B.	639, 911
Greenwood R. C.	573	Hennessy C. J.	331
Gregg T. K. P.	575	Herd R. A.	641
Gregoire D. C.	657	Herkenhoff K. E.	643
Grieve R. A. F.	161, 291, 1105, 1543	Herrera P.	1061
Griffin W. L.	1091	Herrick R. R.	645, 927
Grimm R. E.	199, 201, 577, 927	Hervig R. L.	163, 439
Grin E. A.	241	Herzog G. F.	647, 1547
Grinspoon D. H.	213, 579	Hess P. C.	475, 631, 649, 651, 1119
Grosfils E. B.	447, 581	Hewins R. H.	327, 329
Grossman J. N.	1477	Heymann D.	653
Grossman L.	257, 1309, 1563	Hiesinger H.	133, 617, 655
Grove T. L.	583, 1475	Hildebrand A. R.	297, 657, 1105
Grün E.	1423, 1587	Hill D. H.	167
Guest J. E.	215, 237, 843	Hingston M. P.	135
Guinness E. A.	585, 1293	Hiroi T.	659, 1395, 1465
Gulick V. C.	587	Hoffmann H.	635
Guo X.	593	Hofmann B.	455, 1073
Gurov E. P.	589, 591	Hogenboom D. L.	661
Gurova H. P.	591	Hohenberg C. M.	777
Gutierrez D. F.	593	Holloway J. R.	663
Guyot F.	933	Holmann E.	1311
Haack H.	593	Holsapple K. A.	665
Haas J. R.	595	Holzbecher J.	593
Hager B. H.	1307	Holzheid A.	667
Hall G. S.	1547	Honda M.	1085
Hall S.	1283, 1533	Hood L. L.	669
Halliday A. N.	1321, 1323, 1325, 1327	Hoppe E.	1087
Hamilton V. E.	597, 1361	Hoppin A.	1041, 1147
Hanner M. S.	1587	Horan D. M.	1469
Hansen C. J.	599	Horan M. F.	1477
Hansen G. B.	243, 601	Horanyi M.	669, 1587
Hansen V. L.	603, 775, 1135	Horn L. J.	671
Hapke B.	605, 1061	Hornemann U.	933
Hargraves R. B.	917	Hörz F.	101, 293, 673
Harlan S. S.	835	Housen K.	675
Harper C. L. Jr.	607, 709	Howell E. S.	197
Harrison S. T.	287	Howington-Kraus A.	905
Hartmann W. K.	609, 611	Hsu A.	1309, 1563
Hartung J. B.	35, 613, 811	Hsu W.	357
Harvey R. P.	615		
Hashimoto A.	1479		
Haskin L. A.	595, 729		

Hua X.	677	Juenemann D.	647, 1547
Huang H.-P.	679	Jull A. J. T.	757, 1195
Huang S.	681	Jurewicz A. J. G.	737, 739, 1491
Hudson R.	1007	Jurewicz S. R.	741, 743
Hughes S. S.	683		
Hui J.	255	Kadel S. D.	565, 623, 745
Humayun M.	685	Kalinina G. V.	759
Huss G. R.	687	Kallemeyn G. W.	747, 1555
Hutcheon I. D.	399, 687, 1103, 1493	Kamatsu G.	1231
		Kamp L. W.	253, 255
Ignatenko K. I.	481, 857	Kanamori H.	531, 1411
Ildefonse Ph.	933	Kankeleit E.	633
Iliffe J. C.	1429	Kano N.	749
Imamura M.	1085	Kargel J. S.	661, 751, 753, 755
Ingersoll A.	569	Karlsson H. R.	757
Ireland T.	1537	Kashkarov L. L.	479, 699, 701, 759, 761
Isbell N. K.	905	Kauhanen K.	763, 765, 1191
Itoi T.	1551	Kaula W. M.	767, 769, 863, 865
Ivanov A. V.	177	Keating P.	1105
Ivanov B. A.	689, 1165, 1187	Keddie S. T.	771, 773
Ivanov M.	619, 691, 693	Keep M.	775
Ivanova M. A.	695, 697	Kehm K.	777
Ivliev A. I.	699, 701	Keil K.	141, 259, 369, 777, 779, 945, 947, 1267
Izenberg N. R.	703		
Izett G. A.	705, 1171, 1275	Keiswetter D. A.	781
		Keller L. P.	173, 497, 531, 783, 785, 877, 1093, 1425
Jackson A. A.	707	Kelley M. S.	787
Jackson M. P. A.	1245	Kelly M.	119, 121, 123, 125, 127
Jacobsen S. B.	607, 709	Kelly W. D.	789
Jäger H.	633	Kempin M.	1261
Jagoutz E.	711	Kemurjian A.	791
Jakes P.	713	Kennedy A. E.	793
Jakosky B. M.	639, 911, 971, 973	Kennedy A. K.	399
Jarosewich E.	1131	Kerridge J. F.	795
Jarvis K. S.	715	Khatuncev I. V.	1225
Jaumann R.	133, 401, 617, 635, 655, 813	Kiefer W. S.	105, 511, 513, 797, 1591
Javoy M.	933	Kieffer H. H.	255
Jerde E. A.	717, 719, 1321, 1409, 1411	Kilburn C. R. J.	799, 899
Jessberger E. K.	1349	Kim J. S.	795
Johnson C. L.	721	Kim Y.	795, 801
Johnson J.	1231	Kirk R. L.	803, 805, 807
Johnson J. R.	723, 851	Kirkpatrick R. J.	149
Johnson T. V.	255, 623, 939, 957, 1141	Kissel J.	1587
Jolliff B. L.	323, 725, 727, 729	Kitamura M.	991
Jones A. C.	731	Klaasen K.	569, 623, 635, 955, 1141
Jones C. H.	27	Klein H.	845
Jones J. H.	733, 739, 741, 743, 1491	Klein J.	647, 1547
Jones K. W.	1203	Klingelhöfer G.	459, 633
Jones R. H.	185, 735	Klöck W.	497, 499, 1349
Jordan J. L.	1023	Knudsen C. W.	531, 1411
Joswiak D. J.	205, 901	Knudsen J. M.	917
		Kobayashi K.	1085
		Kochan H.	1423, 1451

Koeberl C.	135, 267, 809, 811, 1177, 1197, 1259, 1365, 1555	Lee L.	661
Koehler U.	813	Lee S.	1283
Kohl C. P.	39	Leenhouts J. M.	1315
Kohlstedt D. L.	543	Lemoine F. G.	861, 1317
Kojima H.	1553, 1555	Lenardic A.	863, 865
Kolesov G. M.	1051	Leonard G. J.	867
Kolvoord R. A.	571	Lerch F. J.	1317
Kölzer G.	1423	Le Roux F. G.	1197
Komatsu G.	525, 815	Levison H. F.	869
Konkina T. V.	1225	Levy E. H.	871
Kononkova N. N.	697, 1273	Lewis C. F.	593
Konopliv A. S.	1313	Lewis R. S.	29, 873, 1087
Korochantsev A. V.	817	Leyva I. A.	875
Korotaena N.	1239	Lindblad B.-A.	1587
Korotev R. L.	729, 819, 821	Lindsay W. L.	1099
Korotkova N. N.	761	Lindstrom D. J.	877, 1137, 1509
Korotkova Yu. Yu.	701	Lindstrom M. M.	879, 1407, 1483, 1555
Koshiishi H.	941	Linkert D.	1587
Koslov E. A.	53	Linkert G.	1587
Kousoum J.	1577	Linkin V.	791
Kremnev R.	1381	Lipschutz M. E.	405, 985, 1131, 1531
Kring D. A.	823	Liu Y.-G.	397, 881, 883, 885, 887
Król E.	825	Ljul A. Yu.	481, 857
Krot A. N.	827	Lo E.	563
Krot T. V.	1585	Lockwood J. F.	1231
Kubicki J. D.	829	Lodders K.	467
Kucinskas A. B.	831	Loeken Th.	889
Kuehn D. M.	833	Lofgren G. E.	329, 387, 793, 891, 893
Kunk M. J.	835, 1567	Long J. V. P.	573
Kuramoto K.	837	Longhi J.	895, 897
Kurat G.	177, 441, 1053, 1055, 1125, 1177	Lopes-Gautier R.	207, 255, 899
Kurosawa M.	839	Lorenz E.	1423
Kuzmin R.	567	Love S. G.	205, 901
Kyte F. T.	157	Lovell A. J.	903
LaFave N.	841	Lu J.	1269
Lampkin D. J.	1577	Lucchitta B. K.	263, 905
Lancaster M. G.	843	Lucey P. G.	133, 299, 303, 617, 907, 909, 911, 1133, 1207, 1337, 1341, 1469
Landheim R.	567, 845	Luck J. M.	711
Landry J. C.	847	Lugmair G. W.	547, 1305
Lang B.	825	Luhr J.	595
Langenhorst F.	849	Lunine J. I.	913
Lapin S. L.	1497	Maag A. J.	915
Larson S. M.	851	Maag C. R.	915, 1403
Lauer H. V. Jr.	17, 821, 1015	Macdonald R.	119, 121, 123, 125, 127
Lauer V.	1581	Madsen M. B.	917
Lavrentjeva Z. A.	857	Maechling C. R.	309
Lavrukhina A. K.	853, 855, 857, 1457	Maehr S.	1071
Layne G. D.	1289	Magee Roberts K.	627, 919, 1527
Le L.	965, 1491, 1581	Magellan Flight Team	1427
Lebofsky L. A.	197, 859	Makalkin A. B.	425, 427, 921, 1467
Lebofsky N. R.	859	Malcuit R. J.	923

Malhotra R.	925	Merényi E.	979
Malin M. C.	285, 927	Meshcherskaya V. A.	219
Manley C. R.	929	Metzger S. M.	981
Mann I.	1587	Meyer C.	983
Marbury G. S.	1275	Michaels G.	215
Marchenkov K. I.	931	Michlovich E.	985
Marín L. E.	1283, 1455	Middleton R.	647, 1547
Marti K.	555, 795, 801, 1163	Mikouchi T.	987
Martin M.	585	Miller J. S.	989
Martin R.	1261	MinMap Team	1145
Martin R. A.	1019	Mironenko M. V.	427
Martin T. Z.	243, 601	Misawa K.	991, 1437, 1555
Martinez I.	933	Misychenko N. I.	1417
Martinez R. R.	877, 1137, 1509	Mittlefehldt D. W.	739, 993, 995, 1137
Marzari F.	935	Miura Y.	997
Masarik J.	937, 985, 1195	Miyamoto M.	967, 987, 999, 1391
Masuda A.	1555	Moersch J.	569
Matson D. L.	255, 939	Molin G. M.	1001
Matsui T.	837, 1375	Montanari A.	297
Matsushima K.	941	Moore C.	1103
Matsuzaki H.	749, 943	Moore H. J.	1003
Maurasse F. J.-M. R.	1275	Moore J. M.	1005, 1247, 1249
Maurer M. J.	1311	Moore M.	1007
Maurette M.	441, 1125, 1177	Morden S. J.	319
May L.	1275	Moresi L.	1009
Mayeda T. K.	757, 945, 1131, 1185, 1321	Morfill G. E.	1587
McBride K.	75	Morgan H. F.	805, 807
McCarthy J. J.	861	Morgan J. W.	1477
McCarville P.	351	Mori H.	987
McCord T. B.	255, 625, 1145	Mori Y.	1565
McCoy T. J.	141, 259, 777, 945, 947, 1267	Morikawa N.	1047
McCulloch M. T.	1089	Moroz L. V.	1011, 1585
McDonald J. S.	537	Moroz V. I.	1013
McDonnell J. A. M.	949, 1587	Morris R. V.	17, 85, 531, 821, 1015, 1291, 1581
McEwen A. S.	565, 623, 625, 635, 951, 953, 955, 957, 1141, 1469	Morrison D. A.	433
McGee J. J.	835	Morrissey M. L.	1167
McGill G. E.	903	Morse A. D.	573, 1017
McGovern P. J.	959	Moss C. E.	49, 1019
McKay D. S.	17, 75, 531, 785, 961, 963, 1093, 1409, 1411, 1425, 1509	Mouginis-Mark P. J.	283, 1021, 1167, 1209, 1405
McKay G.	737, 965, 967, 987	Muller J.-P.	1429
McKinnon W. B.	15, 89	Murali A. V.	1023
McSween H. Y. Jr.	97, 203, 577, 615	Murchie S.	1025, 1027, 1029, 1039
Meeker G. P.	969	Murer Ch.	1031
Mehlman R.	255	Murphy D. L.	1033
Melchior R. C.	37	Murphy J. R.	1035
Melendrez D. E.	851	Murray B. C.	103
Mellon M. T.	971, 973	Murray J. B.	1429
Melosh H. J.	45, 975, 1435	Murty S. V. S.	1037
Mendell W. W.	977, 1517	Musselwhite D.	431
		Mustard J. F.	81, 629, 635, 1027, 1029, 1039, 1041, 1147, 1431, 1433

Myhill E. A.	155	Ocampo A. C.	255, 1165
Na C. Y.	1043	Oder R. R.	1409
Nagahara H.	1045	Oehler A.	1097
Nagai H.	1085	Ogawa T.	967
Nagai S.	1377	Oglesby J. P.	1099
Nagao K.	1297	Ohashi H.	1549
Nagasawa H.	1565	Okada A.	1297
Naidin D. P.	1051	O'Keefe J. D.	1101
Nakamura N.	991, 1047	Olsen E. J.	1103, 1131
Nakano G. H.	1019	Omori R.	1549
Nakashima K.	1549	Orenberg J. B.	1215
Naraeva M. K.	1013	Ortiz Aleman C.	1105
NASA Partners-in-Space Team	879	Otsuki M.	1395
Nazarov M. A.	1049, 1051, 1053, 1055, 1273	Owen T.	431
Neal C. R.	1057, 1059	Paige D. A.	599
Nellis W. J.	491	Paillat O.	1107
Nelson R. M.	1061	Palme H.	147, 177, 437, 667, 1177, 1579
Nemchinov I. V.	975, 1063, 1065, 1067, 1415, 1417	Paolicchi P.	377
Nerem R. S.	105, 511, 513, 797, 1317, 1591	Papanastassiou D. A.	277, 339, 1357, 1359
Ness R. O.	531	Papike J. J.	1109, 1285, 1287, 1289
Neukum G.	133, 269, 401, 565, 617, 623, 625, 635, 655, 745, 813, 957, 1069, 1141, 1521	Pappalardo R.	1111
Newsom H. E.	1071	Paque J. M.	969
Newton J.	1017	Parfitt E. A.	447, 1113, 1115, 1525
Nguyen T.	1291	Parker T. J.	1003, 1117
Nichols R. H. Jr.	777	Parmentier E. M.	631, 651, 1119, 1319
Niedermann S.	455, 555, 1073	Patchen A.	1409
Nier A. O.	205, 1075	Patel G. B.	1317
Nikishin A. M.	1077, 1079, 1081	Patterson W.	117
Nikolaeva O. V.	817, 1083	Pedroni A.	1121
Nishi J. M.	705	Pellas P.	1159
Nishiizumi K.	39, 1085, 1195, 1555	Peng H.	1123
Nittler L. R.	1087	Pepin R. O.	77
Nock K. T.	1381	Perelomova A. A.	1065
Nogami K.	749, 1549	Perreau M.	441, 1125
Nolan M. C.	159, 571	Perron C.	1159
Noma M.	1549	Petaev M. I.	697, 1127, 1129, 1131
Noma Y.	997	Peterson C. A.	617, 1133
Norman M. D.	369, 1089, 1091, 1413	Petrova T. L.	51
Norris J. A.	1093	Phillips J. L.	1587
Norton G.	1149	Phillips R. J.	603, 703, 1135
Nozette S.	1299, 1469	Phinney W. C.	1137
Nuth J.	1007	Piatek J. L.	515
Nyquist L. E.	683, 1095, 1295	Pierazzo E.	1139
Oberst J.	623	Pieters C. M.	115, 117, 477, 565, 623, 625, 635, 659, 957, 1011, 1041, 1141, 1143, 1145, 1147, 1379, 1431, 1433, 1469
O'Bryan M. V.	1485	Pilcher C.	623
		Pilkington M.	1105
		Pillinger C. T.	43, 191, 479, 485, 535, 551, 553, 679, 1017,



Pillinger C. T.		Roberts K. M.	843
(continued)	1221, 1461, 1539, 1541	Robertson P. B.	1543
Pimperl M. M.	1291	Robinson C. A.	1205
Pinet P. C.	1213	Robinson M. S.	301, 565, 617, 623, 955, 1207, 1209
Pinkerton H.	627, 641, 1115, 1149, 1527	Roddy D. J.	35, 1211, 1301
Plaut J. J.	355, 1003, 1151, 1237	Rode O. D.	1143
Plescica J. B.	1153, 1155, 1157	Rodin A. M.	459
Plutchak J.	623, 1141	Roest W. R.	1105
Podosek F. A.	1159	Rogers P. G.	247
Poelstra K.	1537	Romanov G. S.	1417
Pohn H. A.	1161	Rosenbaum J. G.	705
Polanskey C.	1587	Rosenblatt P.	1213
Pollack J. B.	83, 1035, 1215	Rothery D. A.	1429
Ponganis K. V.	1163	Roush T. L.	1215, 1569
Pope K. O.	1165	Rowland S.	899
Popova M. P.	1067	Rubin A. E.	827, 1217
Posado-Cano R.	5	Rubio G. S.	593
Postawko S. E.	973, 1167	Rucklidge J. C.	341
Pratt S. F.	117, 635, 1041, 1147	Rudak L. V.	1417
Premo W. R.	1169, 1171, 1173	Ruff S.	287
Presley M. A.	1175	Rulle H.	1349
Presper Th.	1125, 1177	Russell C. T.	671
Price K. H.	1179	Russell J. F.	807, 1219
Price M.	1181, 1183	Russell S.	485, 1221, 1461
Prilutskii O. F.	459	Rutherford M. J.	475, 503, 1223
Prinz M.	375, 1185, 1501, 1583	Ruzmaikina T. V.	871, 1225, 1499
Provalev A. A.	1187	Ryan C. G.	1091
		Ryan D. E.	593
Quezada-Muñeton J. M.	1283, 1455	Ryan E.	45, 1225
Quick J. E.	969	Rybakov V. A.	1063
Raitala J.	1189, 1191	Sabol D. E. Jr.	1229
Raiteri C. M.	1487	Sadeh W. Z.	1099
Rakitskaya R. B.	591	Sahuaro H.S. Astronom- ical Research Class	1231
Rao M. N.	521, 1193	Saiki K.	1393, 1395
Rasskazov S.	595	Saito J.	941
Reagan M. K.	87	Sakimoto S. E. H.	1233
Rebhan H.	635	Sakurai H.	1549
Reed K. L.	515	Salisbury J. W.	1235
Reedy R. C.	49, 521, 937, 985, 1019, 1195	Sandwell D. T.	721
Reid A. M.	209, 1419, 1421, 1533	Sappenfield P.	1403
Reidy A.-M.	509	Saunders R. S.	215, 931, 1237
Reimold W. U.	179, 181, 811, 1073, 1197, 1365, 1419, 1421	Sazonova L.	1239
Reinhardt J. W.	887	Schaber G. G.	265, 1161, 1219, 1241
Reyes-Ruiz M.	1351	Schaefer M. W.	1243
Reynolds R. L.	705	Schärer U.	933
Rice A.	229	Schenk P.	1245, 1247, 1249
Rieco S. R.	1497	Scherer P.	889
Rietmeijer F. J. M.	1199, 1201	Schloerb F. P.	903
Rivers M. L.	1203, 1383, 1385	Schlutter D. J.	205, 1075
Roark J. H.	511, 513, 797, 1591	Schmidt G.	1251
		Schmidt R. M.	1253

Schmitt R. A. 397, 881, 883, 885, 887  
 Schubert G. 109  
 Schultz L. 889  
 Schultz P. H. 63, 337, 559, 561, 1255,  
 1257, 1259, 1515  
 Schultz R. A. 1263, 1401  
 Schulz R. 1261  
 Schwehm G. 1587  
 Scott D. H. 407, 1265, 1495  
 Scott E. R. D. 593, 995, 1267  
 Sears A. S. R. 1269  
 Sears D. W. G. 91, 93, 95, 681, 1269,  
 1571  
 Sears W. D. 1271  
 See T. H. 101, 673, 995  
 Selivanov A. S. 1013  
 Semenova A. S. 1273  
 Semjonova L. F. 479, 481, 483, 485, 487,  
 1011  
 Senftle F. E. 1275  
 Senske D. A. 1237, 1277, 1279  
 Shahinpoor M. 457  
 Sharma P. 1085  
 Sharp C. M. 1281  
 Sharp L. L. 531  
 Sharpton V. L. 1283, 1339, 1455, 1533  
 Shashkina V. P. 221  
 Shearer C. K. 1109, 1285, 1287, 1289  
 Shelfer T. D. 1291  
 Shen M. H. 1291  
 Shepard M. K. 1293  
 Shih C.-Y. 1095, 1295  
 Shima M. 1297  
 Shimizu N. 1501  
 Shirey S. B. 809, 1197  
 Shoemaker E. M. 35, 1211, 1299, 1301,  
 1347, 1469  
 Short N. M. 1303  
 Shubadeeva L. P. 1067  
 Shukolyukov A. 1305  
 Shukolyukov Yu. A. 483, 487, 695, 1461  
 Shuvalov V. V. 975, 1065, 1067  
 Siddique N. 1587  
 Signer P. 1031, 1519  
 Sigurdsson H. 251, 451, 1275  
 Simon S. B. 1309, 1563  
 Simons M. 1307  
 Simpson R. A. 1311  
 Singer R. B. 465, 525, 851, 979, 989,  
 1029, 1139  
 Sjogren W. L. 1313  
 Skinner W. R. 1315  
 Skripnik A. Ya. 761  
 Smetannikov A. S. 1417

Smit J. 297  
 Smith D. E. 861, 1317  
 Smith G. 557  
 Smith J. V. 1383, 1385  
 Smith S. 293  
 Smrekar S. E. 1279, 1319  
 Smyth P. 227  
 Smythe W. D. 255, 1061  
 Snee L. W. 835  
 Snyder G. A. 719, 1321, 1323, 1325,  
 1327  
 Sobolev N. V. 1321  
 Sobolev V. N. 1321  
 Soderblom L. A. 255, 805, 953  
 Solomatov V. S. 1329  
 Solomon S. C. 959, 1307, 1331  
 Sorensen S.-A. 237  
 Sotin C. 1119  
 Southon J. 39, 1085, 1195  
 Souzis A. E. 647  
 Speidel D. H. 1333  
 Spettel B. 147, 177  
 Spilde M. N. 1109  
 Spray J. G. 1335  
 Spudis P. D. 55, 133, 617, 1133, 1337,  
 1339, 1341  
 Squyres S. W. 1469  
 Srinivasan B. 873  
 Srinivasan G. 549  
 SSI Team 1141  
 Stacy N. J. S. 1343  
 Stadum C. J. 41  
 Staubach P. 1587  
 Steele I. M. 1131, 1345, 1573  
 Steeples D. W. 781  
 Steiner M. B. 1347  
 Stephan T. 1349  
 Stepinski T. F. 415, 1351  
 Stern S. A. 869, 1043  
 Stevenson D. J. 1329, 1353, 1355  
 Stevenson T. J. 915  
 Stewart B. 1357, 1359  
 Stoewe T. L. 805  
 Stofan E. R. 355, 597, 1237, 1279,  
 1361  
 Stoker C. R. 1005  
 Stolper E. M. 79, 829, 1493  
 Stooke P. J. 1363  
 Storzer D. 1365  
 Straub D. W. 233, 1367, 1369  
 Strom R. G. 1371, 1373  
 Suarez G. 1283  
 Sueno S. 839  
 Sugita S. 1375

Sugiura N.	1377	Thouvenot E.	1213
Sullivan R.	565, 623	Titov D. V.	1013
Sunshine J. M.	565, 623, 955, 1041, 1141, 1147, 1379	Tokkonen T.	1191
Suppe J.	107, 1181, 1183	Tomeoka K.	1389
Surkov Yu. A.	1381	Tompkins S.	1431, 1433
Sutton S. R.	187, 495, 497, 499, 1203, 1383, 1385	Tonks W. B.	1435
Svedhem H.	1451	Torigoe N.	1555
Svestka J.	1587	Torigoye N.	1437
Svetsov V. V.	1067	Törmänen T.	1191, 1439
Svoboda R.	1529	Torson J.	255
Swan P. D.	309	Treiman A. H.	1441
Swindle T.	225, 431	Tribaudino M.	1001
Sylvester P. J.	1563	Trombka J. I.	305
		Trubetskaya I. A.	975
		Tsou P.	1443
		Tsukimura K.	1389
Takahashi K.	1555	Tufts B. R.	1445
Takata T.	1387	Turcotte D. L.	831, 1447
Takatori K.	1389	Tyburczy J. A.	1449
Takeda H.	967, 987, 999, 1389, 1391, 1393, 1395, 1555	Tyler G. L.	1311
Tam W.	1535		
Tanabe T.	1007	Ulamec S.	1451
Tanaka K. L.	379, 381, 867, 1397, 1399, 1401	Ulyanov A. A.	549
Tanner W. G.	915, 1403	Underwood J. R. Jr.	1453
Tatsumoto M.	1173, 1437, 1555	Urrutia-Fucugauchi J.	1283, 1455
Tatsumura M. J.	1405	Ustinova G. K.	13, 855, 1457
Taylor A.	1587	Utashima M.	941
Taylor F. W.	253		
Taylor G. J.	207, 283, 369, 617, 899, 947, 1133, 1167, 1405, 1407	Vander Auwera J.	897
		Vander Wood T. B.	173
Taylor L. A.	717, 719, 1057, 1059, 1321, 1323, 1325, 1327, 1409, 1411	Vanzani V.	935
		Veeder G. J.	939, 1459
Taylor S. R.	1413	Verchovsky A. B.	483, 485, 487, 1461
Tazzoli V.	517	Veselova G. V.	459
Tedesco E. F.	1459	Veverka J.	269, 635
Teeling M. J.	1453	Vickery A. M.	1463
Teterev A. V.	1415, 1417	Vilas F.	715, 1465, 1581
Teucher R.	633	Vistisen L.	1, 917
Thalmann Ch.	455, 1073	Vityazev A. B.	425
Therriault A. M.	1419, 1421	Vityazev A. V.	427, 921, 1467
Thiel K.	1423	Vogt S.	985
Thiemens M. H.	423	Vondrak R. R.	1033
Thomas K. L.	173, 497, 785, 1425	Vorder Bruegge R. W.	1469
Thomas P. C.	1469		
Thompson C. M.	657	Wacker J. F.	1471
Thompson T. W.	1427	Wadhwa M.	1473
Thompson W. R.	569	Wagner J. R.	331
Thorn K. S.	1203	Wagner R.	745, 1521
Thornhill G. D.	1429	Wagner T. P.	1475
Thorpe A. N.	1275	Wagstaff J.	965
		Wald A.	1235
		Walker D.	733
		Walker R. J.	1477
		Walker R. M.	309, 1087

Wang J.	1479	Xu P.	563, 1123, 1545
Wang M.-S.	1131	Xue S.	647, 1547
Wänke H.	711	Yakovlev O. I.	403, 527
Warren P. H.	1481, 1483, 1555		
Wasilewski P. J.	1485	Yamakoshi K.	749, 943, 1549
Wasserburg G. J.	275, 277, 339, 687, 793, 1107, 1281, 1357, 1359, 1487	Yamnichenko A. Yu.	591
		Yanagisawa M.	1551
Wasson J. T.	593, 1251, 1489	Yanai K.	1553, 1555
Wasylenki L. E.	1491	Yang C. W.	1557
Watson L. L.	1493	Yang H.	519
Watters T. R.	1495	Yates P. D.	1559
Watts A. J.	331, 1497	Yoder C. F.	1561
Weber E. T.	739	Yoneda S.	1563
Weidenschilling S. J.	935, 1499	York D.	161
Weigel A.	453	Yurimoto H.	839, 1565
Weisberg M. K.	375, 1185, 1501, 1583		
Weissman P. R.	255	Zappala E.	377
Weitz C. M.	69, 71, 1503	Zare R. N.	309
Wenrich M. L.	567, 1505	Zehnpfenning J.	1349
Wentworth S. J.	75, 239, 961, 1409, 1507, 1509	Zeitler P. K.	1567
		Zent A. P.	1569
Wetherill G. W.	1511, 1523	Zhang Y.	1571
Wichman R. W.	1513, 1515	Zhou L.	1251
Wieczorek M. A.	977, 1517	Zhou Y.	1573
Wieler R.	1031, 1519	Zhugin Yu. N.	53
Wiesmann H.	1095, 1295	Zimbelman J. R.	249, 637, 1209, 1495, 1575, 1577
Williams D.	623		
Williams D. A.	565, 1521	Zinner E.	29, 1087
Williams D. B.	1557	Zipfel J.	437, 1579
Williams D. R.	1523	Zolensky M. E.	65, 203, 209, 659, 679, 1465, 1581, 1583
Williams R. S. Jr.	523		
Williams S. N.	575	Zolotov M. Yu.	1585
Wills E. L.	1291	Zook H. A.	707, 1587
Wilson L.	447, 461, 621, 627, 779, 1115, 1525, 1527	Zuber M. T.	105, 511, 513, 797, 1233, 1317, 1589, 1591
Wilson T. L.	841, 1529		
Wimberly R. N.	1313		
Winters R. R.	923		
Witzke B. J.	35		
Wlotzka F.	403, 527		
Wolf S. F.	1531		
Wolfbauer M.-P.	713		
Wong A. M.	1533		
Wong P. B.	1311		
Wood C. A.	1535		
Wood C. L.	789		
Wood J. A.	1131		
Woolum D. S.	1537		
Woronow A.	1453		
Wright I. P.	553, 1539, 1541		
Wu S.	1543		
Wu S. S. C.	1209		

## SAMPLE INDEX\*

10017	719	60010	95, 821	76261	819
10022	605	60013	75, 95, 821	76281	819
10047	725	60014	75, 95, 729, 821	76321	819
10084	605, 635, 1143, 1217	60019	1143	76501	819
		60025	1169, 1173	76503	725, 727
		60035	369	76535	1091, 1169, 1173
12007	1059	60601	821	77017	369
12008	1057	61016	521, 1193	77215	1169
12011	1059	62237	1091, 1169, 1173	78155	369, 1169
12015	1057	62331	635	78221	1093
12023	795	64455	39	78235	1169, 1173, 1481
12031	1059	64801	685	78236	1169
12033	1295	67016	1089, 1091	78421	193
12038	1095	67075	1169, 1173	78527	369
12039	1095	67415	1391	79001	1509
12056	1095	67955	369	79002	1509
12057	1217	68815	39, 521, 1193	79035	795, 1519
12070	635	69941	795	79215	369
				79261	795
14078	1095	70001	95		
14163	963	70002	95		
14259	635	70003	95		
14303	1327	70004	95		
14304	1325	70005	95		
14321	719, 1295	70006	95		
		70007	95		
15386	1095	70008	95		
15388	683, 1483	70009	95		
15415	1173	70035	531		
15418	369	70135	1095		
15425	393	71055	1409		
15426	393, 1223, 1475	71501	1031, 1519		
15427	393, 1223	72415	1169, 1173		
15495	685	72417	1169		
15555	1383	72501	193, 1093		
15556	685	72559	369		
		73215	719, 1169		
24085	1143	73255	1169		
24170	1437, 1555	74001	961, 1509		
		74002	961, 1509		
60001	821	74220	649, 961, 1223, 1475, 1509		
60002	821				
60003	821	75075	1095		
60004	821	76001	819		
60005	821	76031	819		
60006	821	76131	819		
60007	821	76221	819		
60009	95, 821	76241	819		

\*Page numbers refer to the first page of an abstract in which a sample is mentioned.

# METEORITE INDEX\*

Abec	341, 479, 825, 1485	Allan Hills 84170	387
Acapulco	141, 375, 453, 801, 945, 1579	Allan Hills 84190	945
Acfer 059	1315	Allan Hills 84206	387
Acfer 111	1031, 1121	Allan Hills 85007	1085
Acfer 182	573, 1185	Allan Hills 85045	97
Acfer 277	167, 551	Allan Hills 85085	1185, 1315
Adargas	593	Allan Hills 85110	93
Adelaide	277, 573	Allan Hills 85159	387
Adhi Kot	825	Allan Hills 88013	93
Adzhi-Bogdo	113	Allan Hills 88017	93
Aioun el Atrouss	993, 1109	Allan Hills 88020	93
Allan Hills 769	1485	Allan Hills 88021	93
Allan Hills 77005	77, 139, 275, 503, 711, 1473, 1507, 1539	Allan Hills 88026	93
Allan Hills 77081	375, 945	Allan Hills 88027	93
Allan Hills 77156	357	Allan Hills 88029	93
Allan Hills 77256	993, 1109, 1289	Allan Hills 88030	93
Allan Hills 77257	547	Allan Hills 88031	93
Allan Hills 77278	1267	Allan Hills 88033	93
Allan Hills 77295	1037	Allan Hills 88035	93
Allan Hills 77307	187, 1085	Allan Hills 88039	93
Allan Hills 78084	91	Allan Hills 88042	93
Allan Hills 78134	91	Allan Hills 88047	93
Allan Hills 78230	945	Allan Hills 88049	93
Allan Hills 79035	91	Allegan	1477
Allan Hills 79039	91	Allende	137, 257, 277, 399, 435, 607, 739, 741, 749, 817, 855, 873, 969, 991, 1011, 1025, 1217, 1345, 1357, 1485, 1559, 1565, 1583
Allan Hills 80121	91	Al Rais	747, 1085
Allan Hills 80131	91	Angra dos Reis	967, 1089, 1357
Allan Hills 81002	659, 1085, 1465	Ankoher	91
Allan Hills 81005	727	Anlong	1477
Allan Hills 81021	387	Asuka 31	1555
Allan Hills 81092	91	Asuka 881757	1393, 1437, 1483, 1555
Allan Hills 81105	91	Atlanta	825
Allan Hills 81187	945, 1395	Ausson	97
Allan Hills 81251	1267	Avanhandava	1477
Allan Hills 81261	375, 945, 1579	Banten	1085
Allan Hills 81315	945	Barwell	277
Allan Hills 82100	1085	Belgica	277
Allan Hills 83100	489, 659, 1085, 1465	Belgica 7904	209, 659, 1085
Allan Hills 83101	1471	Bells	203, 659
Allan Hills 83102	1085	Bholghati	183, 209
Allan Hills 84001	993, 1109, 1289		
Allan Hills 84029	1085, 1465		
Allan Hills 84033	1085		
Allan Hills 84042	1085		
Allan Hills 84044	1085		

\*Page numbers refer to the first page of an abstract in which a meteorite is mentioned.

Bishop Canyon	339	Elephant Moraine 83243	1471
Bishunpur	827	Elephant Moraine 83252	1471
Bjurböle	97, 225, 777, 1485	Elephant Moraine 83254	387
Bondoc	519	Elephant Moraine 83271	1471
Bo Xian	93, 1267	Elephant Moraine 83274	1471
Bremervörde	1477	Elephant Moraine 83312	1471
Brenham	317	Elephant Moraine 83335	1471
Bruderheim	341	Elephant Moraine 83348	1471
		Elephant Moraine 83363	1471
Caddo	1359	Elephant Moraine 84302	945, 1395
Campbellsville	1477	Elephant Moraine 84304	1471
Canyon Diablo	749, 995, 1169, 1203, 1437, 1547	Elephant Moraine 87503	319
Cape of Good Hope	373, 647	Elephant Moraine 87513	209, 1583
Cape York	449, 593	Elephant Moraine 87521	1273, 1393, 1483
Carthage	449	Elephant Moraine 87530	1109
Central Missouri	1477	Elephant Moraine 87770	1085
Changde	1477	Elephant Moraine 90007	1085
Charlotte	647	Elephant Moraine 90020	1137
Chassigny	139, 431, 503, 711, 757, 1493	Elephant Moraine 90021	1085
Chaunskij	1131	Elephant Moraine 90043	1085
Chervony Kut	1305	Ellemeet	1109
Chupaderos	593	Erevan	1049, 1053
Claytonville	1485	Essebi	399
Clover Springs	517	Estacado	1159
Coahuila	339	Estherville	519
Cochabamba	203, 1537	Etter	1485
Cold Bokkeveld	203, 405, 489, 715, 1085, 1461, 1465, 1537	Farmington	13, 1217
Colomera	729	Fayetteville	1031
Colony	573, 1017	Fisher	97
Conquista	185	Forest City	1477
Costilla Peak	449	Forest Vale	91, 1159, 1477
		Frontier Mountain 90011	453, 801, 945, 1579
Dengli	695, 697	Frontier Mountain 90036	167, 551
Dhajala	759, 1159, 1267, 1477, 1583	Frontier Mountain 90054	167, 551
Divnoe	375, 1127, 1129	Garland	993, 1109
Duketon	449	G'Day	1583
		Gibson	141, 945
Efremovka	257, 479, 1461	Glatton	277
Elenovka	1011	Goalpara	551
Elephant Moraine 79001	77, 275, 431, 503, 553, 711, 757, 1473, 1491	Gorlovka	697
Elephant Moraine 79002	993	Grant	1477
Elephant Moraine 82608	1471	Grosnaja	549, 1085, 1177
Elephant Moraine 83204	1471	Grosvenor Mountains 85202	1085
Elephant Moraine 83206	1471	Grosvenor Mountains 85209	97
Elephant Moraine 83238	1471	Guareña	1477
Elephant Moraine 83239	1471	Guenie	695
Elephant Moraine 83241	1471		
		Hainholz	1131
		Hallingeberg	97
		Hamlet	1267
		Happy Canyon	259, 777, 1571
		Henbury	449

Hill City	339	Lewis Cliff 88055	259
Horse Creek	259	Lewis Cliff 88280	375, 453, 945, 1047
Hvittis	1501	Lewis Cliff 88516	77, 139, 275, 1473, 1507, 1539, 1541
Ibbenbüren	993, 1109, 1289	Lewis Cliff 88631	259
Ilafegh 009	259, 777	Lewis Cliff 88663	375
Imilac	317	Lewis Cliff 88763	1047
Indarch	357, 387	Lewis Cliff 90500	489, 1085, 1465
Inman	97	Lodran	375, 453, 945
Ivuna	659, 1085	Long Island	97
Jelica	1217	Lost City	739
Jhung	97	Lowicz	517
Jilin	93	Lunan	695
Jodzie	183, 209	MacAlpine Hills 87320	1085
Johnstown	319, 993, 1109	MacAlpine Hills 88100	1085
Juvinas	341, 685, 999, 1305	MacAlpine Hills 88136	357, 387, 1501
Kaba	677	MacAlpine Hills 88176	1085
Kaidun	177, 405, 761, 1217	MacAlpine Hills 88177	375, 453, 945, 1047, 1395, 1579
Kainsaz	277, 479, 759, 857, 1017	Magombedze	827
Kapoeta	183, 209, 319, 701, 1049, 1193, 1583	Manegaon	993, 1109
Karoonda	1085	Manych	1583
Kenna	547	Maralinga	783, 877, 1085
Kesen	91	Mart	339
Kiffa	91	Meteorite Hills 78008	1471
Kivesvaara	1269	Mighei	203, 277, 715, 1025, 1085, 1465, 1537
Knyahinya	95, 1195	Mihonoseki	997, 1297
Kodaikanal	729	Millbillillie	319
Kolchim	1055	Monroe	91
Kota-Kota	1501	Monument Draw	141, 945, 1579
Krähenberg	685	Moore County	999, 1357
Krymka	479, 481, 681, 827	Morito	593
Kyancutta	449	Morristown	1359
Kyushu	97	Mount Egerton	259, 1571
Lafayette	757	Mount Padbury	1357, 1359
Landes	437	Mulga (West)	1085
Leedey	277	Mundrabilla	21
Leoville	257, 685, 1485	Murchison	29, 137, 193, 203, 209, 239, 277, 301, 391, 405, 441, 479, 489, 535, 687, 715, 739, 817, 855, 873, 1085, 1087, 1089, 1125, 1269, 1309, 1449, 1537, 1563
Le Teilleul	319	Murray	203, 209, 277, 489, 659, 715, 1085, 1269, 1309, 1465, 1537
Lewis Cliff 85332	1185	Nakhla	275, 431, 553, 711, 757, 965, 1441
Lewis Cliff 85369	259	Negrillos	339
Lewis Cliff 86010	607, 967, 987		
Lewis Cliff 86024	97		
Lewis Cliff 87009	1085		
Lewis Cliff 87051	737		
Lewis Cliff 87057	1571		
Lewis Cliff 87223	387, 1501, 1571		
Lewis Cliff 87295	1583		
Lewis Cliff 88001	1085		
Lewis Cliff 88008	993		



Nejed	995	Sena	91, 1217
Ngawi	1267	Serra de Magé	999
Nilpena	183, 1221	Severnyi	1055
Nogoya	203, 715, 1085, 1537	Shalka	319, 993, 1109
Norton County	259	Shallowater	259, 777, 1571
Novo Urei	485, 547, 1221	Sharps	1477
Nuevo Mercurio	167, 749	Shaw	519, 1485
		Shergotty	139, 275, 499, 685, 711, 947, 1473, 1491
Ochansk	91	Simondium	1131
Odessa	1203	Sioux County	319
Olivenza	1485	Springwater	1573
Orgueil	239, 277, 607, 659, 685, 687, 817, 855, 1085, 1087, 1095, 1125, 1177	Stannern	1137
Ornans	187, 277, 1017, 1345	Tadjera	1025
Orvinio	823	Tambo Quemado	1103
		Tatahouine	993, 1109, 1289
Parnallee	1267	Temple	1485
Parsa	1037	Tenham	97
Pasamonte	1137	Tennasilm	93, 97
Peace River	341	Thiel Mountains 82410	993
Peckelsheim	1109	Thule	593
Pecora Escarpment 82518	387	Tieraco Creek	1477
Petersburg	319	Tlacotepec	647
Picacho	647	Tocopilla	339
Plainview	1485		
Pomozdino	1049	Vaca Muerta	1357, 1359
		Vigarano	257, 573, 659, 685, 1583
Qidong	93	Vishnupur	113
Qingzhen	357		
Queen Alexandra Range		Wabar	995
90201	197	Weekeroo Station	729
Quenggouk	185	Weston	1031
Quinzhen	387		
		Xingyang	1477
Ramsdorf	823		
Reckling Peak 80259	387	Yamato 691	357
Renazzo	659, 747, 1315	Yamato 74013	993, 1395
Revelstoke	289	Yamato 74063	945
Richmond	827	Yamato 74123	1221
Rio Cuarto	1259	Yamato 74357	945, 1047
Roda	993, 1109	Yamato 74662	1085, 1269
Rose City	823	Yamato 75032	993
Roy	1485	Yamato 75274	945, 1395
		Yamato 790981	1221
Saint Marguerite	1159	Yamato 791198	1269
Saint Mark's	1501	Yamato 791491	453, 945
Saint Severin	277, 739, 1195, 1557	Yamato 791493	945
Saratov	93	Yamato 791538	1221
Savik	593	Yamato 791717	1017
Savik	593	Yamato 793169	1393, 1437, 1483, 1555
Semarkona	681, 685, 735, 827, 1269, 1345	Yamato 793274	1393

Yamato 8002	945, 1395
Yamato 82042	177, 1053
Yamato 82162	659
Yamato 8424	1553
Yamato 86720	659, 1085
Yanhuitlan	339
Zagami	1, 139, 275, 685, 757, 947, 1473, 1491
Zaoyang	695, 1001

## KEYWORD INDEX\*

Aa	799	Apollinaris Patera	1209
Ablation	943	Apollo 11	717, 719, 1323
Acapulcoites	141, 375, 453, 945, 1579	Apollo 12	1057, 1059, 1323
Accelerator mass spectrometry (AMS)	985	Apollo 14	1475
Accretion	7, 185, 325, 1355, 1499	Apollo 15	683, 1223
Achondrites	137, 167, 317, 319, 391, 701, 737, 1047, 1109, 1357, 1473	Apollo 16	73, 821
Acoustic-gravity waves	1065	Apollo 17	333, 725, 727, 819, 977, 1223, 1323, 1509, 1517
Adsorption	1569	Apollo asteroids	197
Aerodynamics	1271, 1315	Aqueous alteration	209, 431, 715, 1005, 1269, 1389, 1465, 1507
Aerosols	445, 1013	Aquifers	311, 313, 315, 875
Age dating	67, 141, 161, 341, 449, 547, 611, 693, 745, 813, 835, 927, 957, 1073, 1089, 1567	Arachnoids	383
Age dating, uranium-lead	1169, 1171, 1173	Argon	191, 1163
Agglutinates	195, 293, 463, 795	Argon-argon age	1437
Aggregates	171, 643	Argyre Planitia	753
Alba Patera	763	Ariel	755
Albedo	537, 953, 955, 1061, 1459	Artemis	983
Albite volatilization	403	Asporina	1379
Alkali anorthosite	1325	Assimilation	717, 719
Alkali suite	1325	Asteroid belt	223
Alloy	741	Asteroid families	557, 787
Alpha Regio	619	Asteroids	45, 99, 111, 131, 205, 223, 269, 299, 301, 303, 317, 377, 385, 463, 497, 515, 557, 577, 583, 659, 715, 779, 823, 881, 1011, 1075, 1227, 1271, 1379, 1459, 1465, 1523, 1551
Alteration	203, 351, 573, 1143, 1385	C type	659
Altimetry	689, 723, 903, 1243	K type	557
Altitude dependence	773	S type	197, 299, 515, 557, 787, 1395
Aluminum-26	399, 577, 1471	Astroblemes	35, 1239
Ambrym	575	Astronomy	129, 281, 507, 841, 1033
Ames Vertical Gun Range	63, 337, 1257	Atla	769
Amino acids	193	Atla Regio	1077
Amorphous material	491	Atmosphere	7, 63, 129, 283, 343, 395, 407, 431, 579, 757, 833, 913, 1013, 1043, 1101, 1449, 1463
Amphibole	1369	breakup	1415, 1417
Analogues	85, 469, 567, 1569		
Analysis	187, 325, 589, 591		
Angrites	737, 967, 987		
Annealing	1391		
Anomalies	357, 423, 607, 749		
Anorthosites	897, 1327, 1413		
Apennine Front	683		

\*Page numbers refer to the first page of an abstract in which a term is mentioned.

Atmosphere ( <i>continued</i> )		Cartography	371, 803, 805, 807, 955
carbon dioxide	883, 887	Catastrophic flooding	1117
circulation	563	Catastrophism	631
disturbance by impact	1187	Cathodoluminescence	387, 681, 893, 1269
pressure	117	Cayley	629
Aubrite	259	CCD methods	1261
Ballistics	451, 673	Center of figure	109
Balmer	629	Central peak	15, 35, 291, 1257
Basalt	23	Central uplift	291
Basaltic magmatism	1285	Cerium anomalies	883, 887
Basaltic volcanoes	1525	Channels	5, 103, 237, 389, 407, 815, 1179
Basalts, high-titanium	717, 719, 1323, 1483	Chemical evolution	1119
low-titanium	1393	Chemical kinetics	467
Luna 24	1273	Chemical weathering	467
mare	595, 683, 1285, 1287, 1323, 1483, 1555	Chemistry	27, 101, 163, 423, 1071, 1099, 1579
very-low-titanium	1273, 1287, 1393, 1483	Chicxulub	273, 1339, 1455
Basins	201, 867, 905, 1337, 1535	Chondrite SiC grains	853
Beneficiation	1409	Chondrites	13, 277, 425, 427, 435, 463, 747, 997, 1001, 1017, 1217, 1267, 1467, 1485, 1499, 1501
Beryllium	173	C	301, 659, 1085
Beta Regio	769, 1079, 1081	C1	881
Biblis Patera	1155	C2	881
Blow-off	7	C3	969
Breccias	591, 761, 795	CH2	1309
Brightness	1033	CI	183
Brines, oxidation of iron	231	CK	783, 877
Bullialdus	1433	CM	29, 183, 203, 391, 405, 1053, 1269
Buoyancy	235, 1495	CM2	137, 209, 715, 1085, 1465
Buoyancy zones, neutral	1231	CO3	187
Calcium-aluminum-rich inclusions	79, 257, 1309	CR	747, 1185, 1315
Calibration	955	CV3	549, 677, 741, 1565
Candor Chasma	525	E	387, 825, 893, 1037, 1501, 1571
Cantaloupe terrain	1245	EH	1571
Canyons	1265	EH3	357
Capture	89, 923	EH4	357, 387
Carbon	173, 321, 551	EL3	357, 387, 1571
Carbon dioxide	1223	H	11, 91, 889, 1531, 1553
Carbon monoxide	1223	H3	1055
Carbonaceous chondrites	177, 183, 239, 399, 489, 677, 747, 817, 857, 873, 1345, 1389, 1583	L	97, 997, 1297
Carbonaceous material	43, 239, 441, 493, 785, 1053, 1125, 1221, 1425, 1539, 1541	LL	113, 1553
Carbonate sediments	883, 885, 887	LL3	681
Carburanium	483	ordinary	43, 185, 225, 299, 515, 615, 681, 735, 739, 823, 1011, 1025,
Carriers	801		

Chondrites, ordinary (continued)	1159, 1185, 1267, 1477, 1557	C1 format maps	221
origin	921	Contamination	341, 475, 1541
Chondritic breccias	1267	Contraction	545, 775
Chondritic material	1553	Convection	261, 409, 471, 473, 505, 833, 863, 865, 1009, 1135, 1319, 1329
Chondrules	153, 327, 329, 435, 669, 681, 697, 735, 759, 827, 893, 991, 1185, 1267, 1269, 1315, 1501	Convex set	1545
formation	1489	Cooling	165, 185, 1525
grain growth	1489	Cooling condition	1239
ordinary	93, 827	Cooling history	777, 1001
Chromite	827	Cooling rate	91, 97, 141, 517, 519, 731, 967, 999, 1391
Chromium	1383	Coordinate system	371
Chronology	1095, 1295, 1305, 1357, 1359	Core	147, 413, 593, 667, 743, 779, 819, 821, 837, 1071, 1353
Chronometer	225, 339, 607, 709	formation	259
Classification	47, 655, 747, 945, 1297	samples	95
Clasts	177, 183, 697	Core-mantle coupling	1561
Clays	115, 117	Corona formation	1083
Clementine mission	1337, 1469	Coronae	199, 235, 447, 529, 597, 765, 919, 1113, 1205, 1361, 1495
Climate	1167	Corvid	613
Clouds	83	Cosmic body	1063
Collapse	155, 215	Cosmic dust	205, 679
Collisions	159, 245, 269, 289, 377, 675, 1523, 1551	Cosmic rays	95, 415, 555, 1471
Colorimetry	851	Cosmic spherules	373
Comet nuclei	609	Cosmochemistry	79, 423, 685, 1007
Comet outbursts	609	Cosmogenic isotopes	9
Cometary showers	885	Cosmogenic material	139, 521, 647, 1193, 1195
Comets	131, 205, 497, 501, 609, 707, 881, 1067, 1075, 1123, 1261, 1355, 1363, 1373, 1417, 1423, 1425, 1451, 1511	Cosmogenic nuclides	39, 985, 1085
Common lunar lander	983	Cratering	63, 179, 181, 213, 269, 291, 325, 451, 457, 571, 611, 645, 657, 665, 823, 867, 1197, 1211, 1253, 1301, 1335, 1363, 1373, 1403, 1421, 1463, 1481, 1497, 1523
Compaction	347	Cratering record	1241
Compaction ages	1537	Craters	15, 61, 161, 241, 265, 269, 283, 353, 559, 589, 591, 611, 689, 703, 767, 835, 927, 957, 995, 1105, 1161, 1171, 1219, 1237, 1241, 1255, 1365, 1419, 1533, 1547, 1567
Composition	177, 287, 305, 401, 439, 469, 495, 499, 747, 819, 937, 1039, 1055, 1379	age	1365
Compression	1191, 1401		
Computer methods	227, 325, 333, 829, 1183		
Computer simulation	1391		
Concentration, trace elements	449		
Condensates	991, 1281		
Condensation	83, 245, 423, 527, 573, 677, 1093		

<i>Craters (continued)</i>		<i>Diamonds (continued)</i>	
database	1241	origin	479
floor-fractured	1513, 1515	oxidation	487
landscape	219	synthetic	479
lunar	1517	thermoluminescence of	479
modification	1513, 1515	Diapirism	1245
Venus	1513	Differentiation	113, 709, 751, 837, 947, 1095, 1329, 1435
Cretaceous-Tertiary boundary	881, 883, 885, 1051	Diffusion	225, 397, 437, 475, 517, 543, 737, 829, 967, 969, 999, 1107, 1295, 1345, 1391, 1479, 1573
Cretaceous-Tertiary event	35, 87, 143, 145, 251, 267, 273, 297, 451, 539, 811, 835, 1165, 1171, 1251, 1275, 1283, 1303, 1347, 1567	Dike swarms	447
Cronstedtite	489	Dikes	179, 447, 581, 621, 1113, 1115
Crust	455, 533, 591, 797, 837, 979, 1039, 1191, 1307	Diogenites	391, 583, 739, 1049, 1109, 1289
Crustal dichotomy	511	incompatible elements	993
Crustal spreading	631	major elements	993
Crustal structure	511	petrology	993
Cryoconite	1559	Dione Regio	771
Cryptomare	133, 617, 623, 629, 1133, 1521	Discovery	1381
Crystallization	697, 893, 1007, 1129, 1149, 1329	Disruption	99, 159, 571, 1551
Crystallization temperature	1239	Dissolution	1099
Crystals, shocked zircons	1171	Distribution	325, 943, 1181, 1439
Cumulates	649, 1109	Domes	215, 355, 929
Dark clasts	1583	Doppler methods	1313
Dating methods	341, 1073	Dorsa Argentea	753
Debris	949, 1549	Downwelling	533
Debris flow	143	Drag	1253, 1271
Deep-sea spherules	373, 901	Dunes	567
Deformation	57, 107, 603, 691, 775, 1189, 1191	Dust	175, 285, 287, 421, 501, 707, 935, 1013, 1033, 1423, 1559, 1587
Degregation, depth	649	Dust particles	1123
Deimos	861, 941	Dust storms	1035
Deltas	389	Dynamics	211, 925, 1423, 1511
Density	661, 901, 1451	Dynamism	869
Density waves	671	Early solar system	307, 855
Depleted mantle	631, 1321	Earth	569, 589, 591, 879, 1577
Depletion, elements	1177	Earth-Moon system	923
Deposition	335	Eclogites	1321
Deposits	241, 559	Education	19, 41, 59, 507, 585, 859, 879, 1167, 1405, 1407
Depth	61, 689	Effects vs. ages	13
Design	1411	Effusion rates	1525, 1577
Devonian	163	Effusive volcanism	799
Diameter	61, 689, 1335, 1419, 1421, 1459	Ejecta	143, 251, 283, 451,
Diamonds	485, 487, 1383, 1461		
formation	483		

Ejecta ( <i>continued</i> )	589, 703, 1255, 1283, 1341, 1387	Experiments ( <i>continued</i> )	891
Ejecta blanket	145, 571, 723	lunar surface	41, 279, 281, 433, 469, 941, 1469
Ejecta curtain generated winds	63	Exploration	461, 675, 1065, 1375 779
Elasticity	1009	Explosions	9, 11, 39, 139, 555, 647, 695, 889, 1085, 1193, 1471
Electron energy loss	171	Explosive volcanism	967, 987
Electron microscopy	441, 1125, 1389, 1557, 1559	Exposure ages	597, 775, 1277, 1361, 1397
Electrostatic effects	337	Exsolution	157, 1449
Element ratios	1121, 1125, 1519	Extension	1415
Elements	305	Extinctions	
Elevation	407, 903	Extraterrestrial bodies	
Elysium Mons	271		
Emissions	1587	Faulting	165, 959, 1189, 1399
Emissivity	639, 911, 1205, 1505	Faults	263, 1335
Emplacement	843	Fayalites	425
Energy	971	origin	425, 921
Energy partitioning	1387	Features	781
Energy resources	1023	Feldspathic microgabbro	683
Energy spectrum	521	Ferric minerals	1369
Enriched mantle	1321	Ferric oxides	525
Enrichment	125	Ferroan anorthosites	1089
Enstatites	777, 1501	Field studies	179, 181, 219
Environmental effects	273	Finest fraction	1143
Eolian processes	559, 567, 1255	Fire	1067
Equatorial regions	175, 581	Fissures	271
Equilibration	615, 969, 1137	Flexure	199, 721, 959
Equilibrium	429, 437	isostatic	1515
Equilibrium crystallization	1491	Flooding	1021
Equipment	633, 1299	Flow dynamics	799
Erosion	57, 237, 559, 1371	Flow fields	627, 1527
atmospheric	1463	Flow, mantle	235
crater	1517	Flows	627, 1527
Eruptions	461, 523, 961, 1021, 1153, 1375	Fluid dynamics	1375
Eskers	753	Fluids	125
Eucrites	137, 391, 583, 739, 999, 1049, 1137, 1305, 1583	Fluorides	3
	1217	Fluvial erosion	587
Euhedral metal	1445	Fluvial processes	5, 241, 389, 1429
Europa	829, 1045, 1271, 1355, 1479	Fluvial valleys	587
Evaporation	1005, 1505	Flux	101, 937
Evaporites	423, 579, 767	Flux determinations	1403
Evolution	845	Folding	1399, 1401
Exobiology	545	Formation	743
Expansion	965	Fractal methods	207
Experimental petrology	1457	Fractals	283, 763
Experimentation	147, 301, 327, 329, 713, 849, 1005, 1045, 1107, 1175, 1257, 1259, 1475	Fractional crystallization	593, 719, 897, 1057, 1491
Experiments		Fractionation	113, 121, 123, 267, 685, 713, 829, 995, 1547
		Fractionation isotope	1479
		Fractures	33

Fragmentation	293, 675, 1415, 1417, 1523, 1551	Granulitic breccias	369
Fragments	997	Graphite	29
Fremdlinge	257	Gratz number	627, 1527
Friction	1335	Gravitational waves	841
Frost	5, 83, 601, 847	Gravity	105, 211, 279, 831, 841, 931, 1009, 1157, 1253, 1279, 1307, 1319, 1427, 1447, 1533
Fullerenes	653		1283
Fusion, crust	441, 997	data	279
Fusion technology	1023	effects	279, 797, 1105, 1313, 1317
		fields	279
Galileo	253, 269, 371, 565, 569, 623, 625, 955, 957, 1207, 1459, 1521	properties	1223, 1475
Galileo Regio	1453	Green glass	887
Gamma ray methods	459, 633, 1019	Greenhouse effect	5, 311, 313, 315, 381, 973
Ganymede	1249, 1453	Ground ice	587
Gas dynamics	641	Ground water	355
Gas sputtering	1163		
Gas-rich meteorites	1031	Guinevere Planitia	617
Gaseous sulfur	1367		1139
Gases	1261	Halos	1093
Gases, fractionation	487	Hapke function	409, 939, 971
Gaspra	571	HASP	259, 1305
Geochemistry	157, 653, 655, 657, 727, 813, 1413, 1559, 1585	Heat	23
		Heat source	225, 495, 497, 577
Geodesy	371, 1069	Heat transfer	205
Geodynamics	709, 863, 865	Heating	1023
Geographic information systems	1183	Helium	867, 1179
Geographos	1469	Helium-3 inventory	1015
Geologic mapping	363, 365	Hellas	1477
Geologic traverses, lunar	891	Hematite	1309
Geology	19, 69, 71, 281, 335, 509, 511, 513, 603, 655, 973, 1229, 1453	Heterogeneity	661, 1127
		Hibonite	109, 477, 727, 1161, 1189
Geomorphology	175, 389, 555, 1021	High pressure	1319
Geophysics	181, 509, 511, 513, 781, 931, 1533	Highlands	183, 209, 583, 701, 1049, 1053, 1583
		Hot spots	623
Geothermal	971	Howardites	1133
Giordano Bruno	613		785
Glaciation	271, 753	Humboldtianum	661, 1007
Glasses	75, 171, 293, 295, 297, 393, 895, 963, 1275, 1509	Humorum Basin	151, 155, 245, 409
		Hydrated phases	3
Global compositions	1337	Hydrates	1017
Gold	455, 1073	Hydrodynamics	1389
Graben	379, 381, 545, 621, 905, 1263, 1397, 1399, 1495, 1575	Hydrofluoric acid	1215
		Hydrogen	1215
Grain size	75, 1061, 1175, 1499	Hydrothermal experiments	465
Granitic liquids	113	Hydrous carbonate	331, 457, 1403, 1497
Granulites	1391	Hydrous sulfate	
		Hydrovolcanism	
		Hypervelocity	
		Ice	175, 847, 1451



Icy bodies	401, 505, 541, 543, 661, 913, 1007, 1111, 1245, 1247, 1249, 1355, 1435	Inclusions	123, 435, 573, 877, 969, 1131, 1565
Icy satellites	755, 1445	Incompatible elements	125, 547, 733
Igneous petrology	733, 739, 1491	Incongruent evaporation	403
Igneous rock	499, 947, 1055	Infrared	129, 287, 601, 639, 909, 911, 979, 1013, 1235, 1459
Ilmenite	649	Infrared spectra	1147
Image processing	251, 333, 803, 981, 1261, 1431	Infrared spectroscopy	557
Imaging	253, 781, 851	Instruction, hands-on	507
Imaging spectrometer	625, 1145	Intact capture	915
Imbrium	623, 1481	Interdisciplinary studies	37
Impact basins	509, 513	Interferometers	1343
Impact cratering	995, 1187, 1211, 1301, 1387	Interiors	165, 359, 637
Impact craters	67, 87, 135, 149, 161, 179, 181, 219, 267, 291, 295, 351, 645, 665, 693, 781, 811, 835, 933, 1003, 1105, 1165, 1197, 1241, 1257, 1283, 1333, 1365, 1433, 1455; 1543	International cooperation	221
Impact effects	87, 351, 673, 933, 1165, 1227, 1255, 1303, 1335, 1435, 1449, 1463, 1571, 1587	Interplanetary dust	65, 101, 131, 171, 173, 205, 239, 309, 493, 495, 497, 499, 673, 935, 943, 1075, 1199, 1201, 1349, 1549
Impact experiments	51, 53	Interplanetary dust particles	205, 785, 901, 1217, 1403, 1425
Impact glasses	143, 145, 149, 995, 1093, 1259	Interstellar dust	871
Impact melting	827	Interstellar gas	871
Impact melts	51, 53, 369, 1015, 1239, 1481	Interstellar grains	29, 871, 873, 1499
Impact metamorphism	53	Io	229, 751, 939, 1249
Impact recondensation	1467	Iodine-xenon chronometry	777
Impact tektites	273	Ion imaging	1087
Impact vaporization	51	Ion implantation	1163
Impactites	351, 823, 933	Ion microprobe	399, 1285, 1289, 1473
Impactors	101, 1257	Ion probe analyses	1103
Impacts	7, 45, 99, 111, 245, 289, 331, 337, 351, 451, 583, 589, 591, 613, 665, 723, 811, 867, 975, 1051, 1063, 1065, 1067, 1105, 1227, 1251, 1253, 1365, 1417, 1421, 1497, 1511, 1549, 1551	Ion probe methods	29, 549, 573, 685, 839, 1107, 1493, 1565
Implantation	1377	Ionosphere	1063
		Iridium	729, 881, 885
		Iridium anomaly	1051
		Iron/manganese	137, 391, 1345
		Iron meteorites	339, 449, 593, 729, 779, 985, 1103, 1359, 1477, 1547
		Iron oxidation on Mars	231
		Iron recondensation	427
		Iron-60	1305
		Iron sulfides on Venus	233
		Irons	115, 647
		IIA	339
		IIIAB	449, 593
		Irradiation	463
		IRTM instrument	189, 979

ISM instrument	81, 1025, 1027, 1029	Lava flows ( <i>continued</i> )	627, 637, 731, 763,
Isochrons	121, 127, 449, 1089,		799, 815, 843, 899,
	1295		919, 929, 1233, 1265,
Isotopes	119, 121, 161, 209,		1525, 1527, 1577
	573, 687, 695, 711,	Lava pond	1525
	801, 1017, 1107,	Lavas, rheology	755
	1131, 1169, 1185,	Layers	1265
	1197, 1477, 1493,	Leaching	1177
	1539, 1541	Life	281, 395, 493
iron	373	Light element (EDX)	
nickel	373	analysis	785
ratios	1173	Light plains	565, 623
Isotopic anomalies	307, 309, 399, 687,	Lightning	435
	853, 855, 1087	Limb darkening	1139
Isotopic composition	485, 1461	Limnology	981
Isotopic fractionation	1163	Lineaments	33
Isotopic ratios	29, 43, 77, 119, 121,	Linear mixing model	1545
	123, 127, 135, 267,	Liquid	397
	449, 547, 549, 555,	Liquid immiscibility	733
	607, 685, 709, 749,	Lithology	727, 1027, 1041
	757, 795, 991, 1031,	Lithophiles	1579
	1037, 1089, 1121,	Lithosphere	721, 1135, 1213,
	1221, 1477, 1547,		1277, 1495, 1591
	1565	Venus	1515
Isotopic source	1169	Lodranites	375, 453, 945, 1579
Isotopic irradiation	1457	Long Duration Exposure	
Ivory Coast tektites	809	Facility (LDEF)	65, 101, 331, 673,
			949, 1549
Jovis Tholus	1155	LREE	547, 1537
Jupiter	1587	Lunar Scout	49, 625
Kalkkop Crater	1197	Ma'Adim Vallis	1429
Kamacite	481	Maat Mons	523
Kazakhstan	219	Magellan Imaging Gap	771
Kinetics	475, 829, 1045, 1329	Magellan mapping	221, 1077, 1079,
Kirschsteinite	987		1081
KOSI	1423	Magellan mission	15, 71, 109, 213, 215,
KREEP	897, 1327, 1413		227, 237, 247, 249,
			359, 361, 363, 365,
Laboratory studies	215, 341, 911, 1175		383, 471, 529, 637,
Lacustrine	389		689, 803, 805, 807,
Laihunite	1369		831, 843, 903, 919,
Lakes	389		1135, 1151, 1161,
Lamellae	987, 999, 1127		1183, 1205, 1237,
Landers	1293		1277, 1279, 1307,
Landing sites	567, 845		1311, 1313, 1331,
Large impact	1083		1333, 1381, 1427,
Large ring structures	217		1439, 1503
Laser impulse	1011	Magma	119, 249, 595, 1149,
Laser methods	835		1539
Laser microprobe	239	Magma flow	1115
Laser-mass spectrometry	309	Magma ocean	651, 1329, 1413
Lava	237, 595, 899, 1149	Magma processes	1169
Lava flows	55, 207, 565, 567,	Magmatic inclusions	1441

Magmatism	929, 1475	Mars ( <i>continued</i> )	
Magmatism, lunar	1173	analogues	1215
Magnesium isotopes	1479	geology	973
Magnesium suite	1327	glaciation	753
Magnetic fields	319, 411, 413, 415, 1351, 1353	gravity fields	861
Magnetic properties	319, 917, 1275	meteorites	431, 503, 757, 965, 1493
Magnetic record	1485	oxidation	231
Magnetic remanence	1347, 1485	surface	189, 971, 973, 1229
Magnetic remnants	825	weathering products	1215
Magnetics	1455	Mars '96	459, 567, 633, 791
Magnetism	337, 1533	Mars Observer	41, 1235, 1243, 1293
Magnetosphere	1063	Masaya, Nicaragua	575
Major elements	1057, 1059	Mass	671
Mangala Valles	1117	Mass extinctions	885
Manned missions	433	Mass fractionation	373
Manson impact crater	705, 811, 1157, 1211, 1301, 1303, 1347, 1567	Mass movements	55
		Materials processing	531, 1409, 1411
Mantle	147, 201, 395, 413, 473, 475, 663, 711, 797, 837, 839, 865, 1307	Mathematical methods	385
downwelling	631	Matrix	177, 187, 203, 1185
dynamics	1119	Maturity	17, 75, 195, 821
lunar	1095, 1413	Mauna Loa	523
Mapping	407, 851, 951, 953, 977, 1181	Medusae Fossae	61
Maps	335, 529	Melt	35, 147, 543, 663, 1107
Mare emplacement	621	Melt rocks	1455
Mare glasses	649	Melting	713, 1435
Mare Humorum	1133	Mesosiderites	519, 1131, 1357, 1359
Maria	393, 475, 565, 629, 655, 745	Mesostasis	1393
Mariner 7	601	Metal	147, 171, 257, 259, 741, 743, 819, 821, 1159, 1217, 1557
Mariner 9	861		1217
Mariner 10	1207	Metallic iron-nickel	97
Marquez Dome	1533	Metallography	185, 369, 437, 615, 761, 877, 1131, 1199, 1201, 1267
Mars	19, 33, 81, 83, 85, 105, 115, 117, 271, 275, 285, 311, 313, 315, 343, 443, 445, 465, 493, 509, 511, 513, 525, 553, 711, 753, 763, 797, 845, 867, 875, 917, 953, 989, 1005, 1013, 1015	Metamorphism	125, 595, 1091 985, 995
aeolian processes	563	Metasomatism	21, 79, 97, 203, 319, 327, 329, 405, 463, 517, 519, 577, 615, 647, 669, 855, 937, 997, 1137, 1407, 1457, 1461
atmosphere	421	Meteor Crater	889, 1047, 1109, 1471, 1507, 1541
dunes	563	Meteorites	1537
dust	563		499
erosion	563	Antarctic	489, 1537
evaporite/precipitate		chronology	1017
		CI	1537
		CM	111, 319, 999
		CO3	
		formation	
		HED	

Meteorites ( <i>continued</i> )		Moon	201, 255, 537, 613,
residues	1087		625, 975, 1207, 1291,
SNC	1, 77, 139, 275, 503,		1337, 1341, 1343,
	553, 711, 757, 947,		1407, 1469, 1475,
	1441, 1473, 1491,		1529, 1577
	1493, 1507, 1539,	astronomy	983
	1541	composition	49
stony iron	1395	core	651
streams	405, 1531	crater volcanic field	169
Meteoroids	93, 95, 949, 1415	crust	369, 1089, 1091
Microbreccia	695	crustal history	1337
Microcraters	1549	finis	1023
Micrometeorites	441, 493, 495, 497,	hydrogen content	49
	499, 679, 729, 1125,	light plains	813
	1177, 1199, 1201	mantle	1287
Micrometeoroids	353, 901, 1403	meteorites	1273, 1393, 1437,
Microprobe methods	1203, 1385, 1409		1483, 1555
Microstructure	1557	outpost, first	891
Microtektites	145, 163, 295, 297,	plumes	651
	397, 539, 1251	resource utilization	3, 281, 531
Middle school	507	samples	477
Midinfrared optical		soils	191, 193, 1075
properties	1215	surface	977, 1517
Mineral analysis	31	uranium/lead content	1437
Mineral compositions	427, 1091	volatiles	1023
Mineralization	525	Morphology	283, 471, 589, 815,
Mineralogy	81, 85, 177, 203, 255,		843, 1429
	323, 443, 445, 549,	Morphometry	379, 381, 523, 815
	591, 633, 725, 787,	Mössbauer	459, 633, 1291
	909, 951, 1027, 1029,	Mössbauer spectra	1, 489, 1015
	1053, 1055, 1103,	Mountains	603
	1199, 1201, 1297,	Multiring basins	15, 1339, 1341
	1393	Multispectral imaging	133, 625, 655, 745,
Minerals	17, 79, 963, 1001,		907, 951, 953, 955,
	1041, 1229, 1395		1141, 1431, 1433,
Mining	531		1469, 1521
MinMap	1145	Nakhlites	431
Minor elements	79	Navajo	19
Miranda	1111	Near-Earth asteroids	159, 951, 1469
Mission description	907, 951, 1299	Near-Infrared Mapping	
Mission planning	433, 891, 941, 1299	Spectrometer (NIMS)	255
Mission simulation	19	Nebula	1467
Mixing	123, 457, 659, 1119	lightning	1489
Modal analysis	73, 75, 909	origin	1055
Modeling	55, 57, 63, 237, 261,	processes	307
	331, 683, 959, 981,	Neodymium isotopes	1325, 1327
	1033, 1041, 1049,	Neodymium-strontium	
	1057, 1059, 1105,	isotopes	1321
	1229, 1379, 1429,	Neon	521
	1497	Nepheline volatilization	403
Models	299, 303	Neptune	417, 419
Monazite	725	Neptune-Triton system	89, 789, 913
Monte Carlo methods	213, 767, 937, 985,	Neutral buoyancy zones	773
	1195		

Neutrinos	1529	Oxide interstellar grains	1087
Neutron activation		Oxides	653, 873
analysis	657, 877, 1251	Oxygen	25, 1345
Neutron spectrometer	49	fugacity	677, 1223
Neutrons	429, 555, 1529	production	1411
Nitrates	553	Ozone	653
Nitrogen	191, 551, 599, 795, 1037, 1377	Pahoehoe	799
Nitrogen cycle	553	Pairing	139
Nitrogen isotopes	553	Pairing of lunar meteorites	1483
NMR spectroscopy	491	Palagonite	465
Noble gases	9, 453, 455, 487, 695, 1031, 1037, 1519	Paleoclimatic change	587
Nomenclature	1219	Paleomagnetism	1347
Nubium Basin	1433	Pallasites	743, 1573
Nuclear cascade	1457	Pancake domes	1233
Nucleosynthesis	749, 855, 1487	Parallax-relief	1003
Nuclide distribution	1457	Parameters	385
Nuclides	1195	Parent bodies	91, 141, 185, 787
Numerical methods	923, 935	Parent chondritic material	921
Numerical simulation	975, 1415, 1417	Parent melt	965
		Partial melting	125, 137, 739, 743, 895, 1057, 1129
Obliquity	1561	Particles	189, 1557
Occultation	671	Partition coefficients	667, 733, 793
Oligoclase	699	Partitioning	323, 741, 895, 1137
Olivine	677, 1127, 1129, 1345, 1573, 1581	Paterae	575
Olivine inclusions	857	Pathfinder mission	845
Olivine-rich asteroids	1379	Peak-ring craters	15
Opacity	261	Perryite	259
Opaque assemblage	257	Petrogenesis	503, 649, 651, 895, 897, 1047, 1059
Optical properties	17, 195, 301, 303, 435, 605, 957	Petrography	87, 1297, 1303
Orange glass	719, 1223	Petrology	329, 717, 735, 787, 1409
Orbital debris	353	Phase transitions	505, 661
Orbiters	907, 1299	Phobos	861, 941, 1025
Orbits	89, 93, 405, 707, 869, 935, 971	Phobos 2	81, 103, 1025, 1039
Organic material	1123	Phoebe Regio	1081
Organic matter	501, 817	Phosphate	725
Organic molecules	309	Photogeology	1445
Organic survivability	193	Photometry	537, 541, 635, 851, 1061, 1097, 1139
Organics	535	Physical properties	1061, 1123, 1175, 1529
Orientale Basin	745	Picritic glasses	1285, 1287
Origin	151, 153, 155, 245, 697, 741, 869, 913, 1511	Picritic material	895
of metallic particles	481	Plagioclase	783, 1581
Orthopyroxene	519, 701, 1289, 1581	Planar features	849
Osmium isotopes	809	Planet formation	1467
Outflow craters	265	Planetary evolution	1119
Outgassing	395, 609	Planetary magnetic fields	417, 419
Overturn of cumulates	651	Planetary surfaces	443, 445
Oxidation	395, 1383, 1385	Planetary systems	1511
		Planetesimals	925

Planetology core curriculum	37	Radiogenic helium	455
Planets	561	Radiogenic material	121
Plate tectonics	235	Radiometry	723
Plumes	473, 529, 769, 865, 1113, 1279	Radionuclides	135, 607, 709, 1195, 1487, 1547
Pluto	599, 869	Rare earth elements	167, 323, 357, 375, 717, 883, 887, 991, 1047, 1103, 1131, 1473, 1563
Plutonic rock	1295	partitioning	965
Polar caps	243, 601, 1247	Rare gases	77, 225, 873, 889, 1073, 1121, 1297
Polar regions	255, 345, 509	Recondensation	425, 427, 921, 1467
Polarimetry	421	Recrystallization	1137
Polarization	541, 1151	Reduction	17, 713, 1129, 1411
Polycyclic aromatic hydrocarbons	309	Reflectance	17, 635, 659, 1097
Popigai	161	Reflectance spectra	1011, 1581
Porosity	347, 641, 731	Reflectance spectroscopy	465, 989, 1015
Porphyritic material	735	Reflectivity	643, 1097
Potassium/argon	695	Refractory inclusions	387, 399, 1309, 1563
Pre-irradiation	761	Refractory material	549, 749
Preplanetary bodies	1467	Refractory trace elements	1103
Preplanetary disk	151, 153, 155	Regolith	75, 113, 195, 293, 381, 477, 541, 605, 609, 635, 795, 819, 821, 963, 977, 1011, 1519, 1553
Presolar grains	687, 1461	Relict grains	893
Pressure	27, 1253	Remote sensing	169, 227, 343, 469, 541, 605, 731, 833, 851, 907, 909, 981, 1041, 1043, 1207, 1235, 1293, 1313, 1431, 1545
Pretoria Saltpan	1365	Residence time	127
Primitive achondrites	141, 375, 945	Residue	1479
Primitive material	441, 681, 749, 1125, 1281, 1559	Resonance	925, 935
Production rate	937, 1195, 1261	Resources	23, 25, 469, 531, 941, 1409, 1411
Project STAR	507	Resurfacing	213, 645, 767, 1179, 1331
Projectile target	457	Rhenium	809
Proton microprobe	1091	Rheology	207, 543, 755, 1115, 1149
Pyrite	1367	Rhyolite	929
decomposition	467	Ridge belts	637
on Venus	233	Ridges	1439, 1589
Pyroclastics	617, 961, 1265, 1375	Rifting	1077, 1079, 1081, 1277, 1399
Pyroclasts	461	Rifts	107
Pyrometamorphism	1199, 1201	Rift zones	67
Pyroxene	989, 1129	Rima Parry	621
Pyrrhotite	467	Rims	187
Quartz	491, 849	Ring spacing	1339
Quartz monzodiorite	1325		
Radar	247, 643, 723, 1151, 1311, 1343, 1427		
methods	73, 561, 803, 805, 807, 1003, 1311		
reflectivity of Venus	233		
Radial fractures	1113		
Radiation	459, 1067, 1529		
effects	1529		
history	759		
process	483		
Radiogenic argon	455		

Rings	671, 1283	Silica aerogel	679
Ringwoodite	1127	Silica minerals	697
Robotic field geologist	983	Silicate inclusions	729
Robots	791, 841	Silicate minerals	761
Rocks	285	Silicon carbide	687
Rotation	385	Silicon, lunar	3
Roughness	1293	SIMS	1349
Rovers	791, 841, 983	Simulants	963, 1099
R-process age	277	Simulations	89, 459, 675, 1227, 1389, 1423, 1451
Samarium-neodymium age	1325, 1437	Sintering	23, 25
Samples, lunar	531, 635, 1095, 1169, 1173, 1407	Size distribution	377
terrestrial	23, 1073	Size frequency	1333
Sand	285	Slate Islands	1543
Sand dunes	1575	Smoke	1007
Sapping	587	Soil	115, 957, 963, 1027, 1029
Satellites	89, 347, 401, 939, 1111	spectra	1147
outer planets	1453	Solar abundances	277
Saturation	611	Solar-cosmic-ray neon	1193
Scaling	291, 337, 665, 673, 675	Solar cosmic rays	39
Scandium, in mare basalts	1483	Solar energetic particles	1031, 1121, 1519
Scarp	271	Solar flares	305, 1193
Scattering	73, 353, 833, 1033, 1311	Solar nebula	79, 151, 153, 155, 261, 415, 425, 427, 607, 669, 871, 921, 925, 1315, 1351, 1499
Schiller-Shickard	629	Solar protons	521
Science education	981	Solar system	1225
Sculptured Hills	1341	Solar wind	191, 1031, 1037, 1121, 1377, 1519
Sediment	295	Solubility	321, 663, 1099
Sedimentary rock	923, 1243	Soret effect	733
Sedimentation	389	Sorting	1315
Sedimentology	251, 285	Sounder instrument	333
Segregation	743, 1395	Source, ages	1173
Seismic effects	841	impact ejecta	1171
Serenitatis Basin	1341, 1481	Space	879
Shape	385	debris	915
Shergottites	77, 275, 503, 1473, 1491	grant consortium	37
Shield volcanos	47, 523	solar power	3
Shock	699, 1101	weathering	477, 515, 1143
Shock attenuation	1543	Spacecraft observations	907, 1123, 1313
Shock effects	157, 293, 491, 827, 849, 933, 1197, 1449, 1567	Space studies minor	37
Shock metamorphism	87, 149, 539, 823, 933, 1303, 1545	Spacewatch	289
Shock waves	855, 875, 1065	Spectra	243, 601, 617, 715, 847, 1133, 1235, 1465
Shock-thermal history	701	Spectral analysis	115, 117, 303, 401, 515, 565, 617, 831, 847, 979, 1133, 1229, 1379, 1505
Siberia	217	Spectral mixing	1431
Siderophile elements	481		
Siderophiles	167, 667, 713, 991, 995, 1071, 1563		

Spectral properties	299	Surface-atmosphere interactions	1035
Spectrometer	459, 1019	Synchrotron X-ray fluorescence microprobe	1203, 1383, 1385
Spectrometry	305	Taenite	481
Spectrophotometry	129, 715, 909, 1097, 1293, 1465	Tectonics	57, 107, 211, 347, 349, 381, 471, 473, 529, 545, 597, 603, 619, 645, 691, 765, 769, 927, 959, 1111, 1135, 1161, 1189, 1191, 1213, 1237, 1263, 1307, 1331, 1361, 1397, 1399, 1401, 1439
Spectroscopy	111, 133, 149, 195, 197, 255, 287, 343, 443, 445, 477, 633, 639, 659, 911, 1025, 1027, 1029, 1039, 1041, 1043, 1097, 1275, 1431, 1433, 1569	Tectonism	33, 363, 637
Spherules	143, 145, 157, 943, 1259	Tektites	135, 251, 267, 397, 539, 657, 809, 1275
cosmic	1177	Australasian meteoritic component	397, 1251
Spinel-rich inclusions	1563	Telescope methods	81, 353
Sputtering	439	Telescopic data	83
SSI instrument	1521	Temperature	27, 119, 151, 153, 261, 615, 939, 1001
Stability	653, 1367, 1369	Termoskan instrument	103
Stable isotopic composition	551	Terraces	1575
Statistical methods	1531	Terrain	73
Steep-sided domes	1233	Terrestrial age	341, 1471
Stereo	1249	Terrestrial analogues	217
Stereo imaging	1117	Terrestrial planets	359, 411, 413, 473, 579, 711, 863, 1435
Strain	775, 1331	TES instrument	979, 1505
Stratigraphy	561, 637	Tesserae	533, 581, 619, 631, 691, 693, 1181, 1189, 1381, 1439
Strength	1263, 1523	Texture	641
Stress	57, 581, 1263	Tharsis	33, 189, 263, 1153, 1397, 1399, 1575
Strontium	1159	Thaumasia	1399
Strontium isotopes	1325, 1327	Theoretical studies	27
Structure	179, 603, 775, 781, 1263, 1399, 1401, 1419, 1421, 1445, 1495	Thermal divide	897
Subduction	235, 863, 1191, 1205	Thermal effects	21, 91, 731, 1295
Subsolidus	969	Thermal emissions	103, 639, 911, 977, 1235, 1517
Subsurface	333	Thermal evolution	201
Sudbury	1339, 1481	Thermal histories	577, 1531
Sulfate devolatilization reactions	273	Thermal inertia	1575
Sulfides	1091	Thermal infrared spectra	31
Sulfur	173, 229, 751	Thermal metamorphism	783
Sulfur cycle	1043	Thermal properties	103, 169, 189, 411, 643, 1175
Sulfur dioxide	229	Thermal radiation	975
Sulfur volcanism	751		
Sun	521, 1225		
Supernova explosion	13		
Surface	129, 253, 301, 343, 559, 561, 589, 639, 703, 903, 1061, 1311, 1505		



Thermoanalytical features	825	Vega missions	69, 1381, 1503
Thermoconvection	1119	Velocity	131
Thermodynamics	21, 27, 323	Venera missions	71, 1381, 1503
Thermoluminescence	91, 93, 95, 699, 759	Vents	379
Thermoluminescence analysis	701	Venus	47, 109, 199, 253, 355, 359, 361, 363, 365, 461, 597, 619, 637, 637, 645, 691, 703, 721, 765, 771, 773, 803, 805, 807, 831, 927, 929, 931, 1083, 1101, 1135, 1151, 1213, 1219, 1237, 124
Thermometry	369	chemistry	467
Thin sectioning	173	coronae	217
Thorium-232/uranium-238 ratio	277	craters	1513
Tidal effects	789, 923	geology	221, 1077, 1079, 1081, 1231
Tidal friction	1561	impact craters	1187
Timescale	123, 127, 159, 571, 1095	landforms	1003
Tochilinite	489	lithosphere	1515
Topography	105, 109, 211, 241, 471, 581, 637, 797, 831, 903, 905, 931, 1009, 1181, 1213, 1243, 1343, 1429	magma volatile contents	1513
Toutatis	197	mineralogy	233
Trace elements	187, 657, 793, 839, 1047, 1059, 1091, 1203, 1285, 1287, 1289, 1501, 1531	volcanism	1233, 1513
Tracks	131, 759, 761	Vertical structure	833
Transfer	127	Vesta	111
Transient crater	1481	Viking missions	41, 175, 335, 861, 953
Triton	165, 345, 349, 599, 755, 1245, 1247, 1363, 1373	Viscosity	201, 211, 641, 1009, 1149, 1577
Troilite	21	Visibility	1067
Tumuli	1405	Volatiles	239, 275, 321, 345, 495, 641, 757, 779, 913, 1355, 1449, 1563
Tunguska	289	Volatilization	403, 713, 1177, 1449
Turbulence	55	Volcanic constructs	513
Ultraviolet, extreme	537	Volcanic rock	499
Ulysses	1587	Volcanics	119, 899, 961
Ulysses Patera	1155	Volcanism	47, 207, 213, 215, 247, 249, 321, 355, 359, 361, 363, 379, 393, 575, 595, 597, 619, 621, 637, 691, 745, 755, 815, 899, 905, 919, 939, 1021, 1043, 1113, 1115, 1155, 1233, 1237, 1279, 1513
Undergraduate education	37		227, 365, 379, 447, 771, 899, 959, 1153, 1231, 1591
Uplands	533, 611		
Upwelling	919		
Uranium-thorium-lead age	275, 1437		
Uranus	417, 419		
Ureilites	167, 485, 547, 551, 1221		
Ushas Mons	771		
Valles Marineris	263, 525, 905		
Valleys	5, 103, 241, 389		
Vallis	1179		
Vapor	321		
Vapor pressure	1045		
Vaporization	527, 605, 685, 961, 1045, 1093		

Volcanos ( <i>continued</i> )	
distribution	773
height	773
small	47, 1003
Volcanology	1209
Voyager missions	401, 671, 1249
Vredefort	1419, 1421
Wadsleyite	1127
Water	117, 311, 313, 315, 429, 503, 579, 663, 837, 839, 875, 1021
Water ice	973, 1271
Water trapping	527
Wavelength	1139
Weathering	11, 43, 85, 605, 1005, 1029, 1099, 1205, 1243, 1367, 1507, 1585
Whitlockite	323, 725
Wrinkle ridges	107, 335, 545
Xenoliths	839, 1053
X-ray fluorescence	1291
X-ray methods	305, 519, 987, 1203, 1383, 1385
Yakutia, Siberia	1321
Yasour	575
Yield strength	1115, 1577
Yukon	163
Zhamanshin Crater	219
Zoning	437, 517, 735, 1565